Μελέηη συποσπονικών ππoηύπυν μικποζειζμικόηηηαρ για ηην ζκιαγπάθηζη σαπακηηπιζηικών ενεπγών πηγμάηυν ηη σπήζει ηηρ μεθόδος διπλών διαθοπών και εηεποζζζσέηιζηρ ζειζμικών κσμαηομοπθών.

Kapetanidis Vasilis

NATIONAL AND KAPODISTRIAN UNIVERSITY OF ATHENS

SCHOOL OF SCIENCE
FACULTY OF GEOLOGY AND GEOENVIRONMENT
DEPARTMENT OF GEOPHYSICS AND GEOTHERMICS

Spatiotemporal patterns of microseismicity for the identification of active fault structures using seismic waveform cross-correlation and double-difference relocation.

PHD DISSERTATION

KAPETANIDIS VASILIS

VOLUME I

ATHENS

17 **MARCH 2017**

ΕΘΝΙΚΟ ΚΑΙ ΚΑΠΟΔΙΣΤΡΙΑΚΟ ΠΑΝΕΠΙΣΤΗΜΙΟ ΑΘΗΝΩΝ

ΣΧΟΛΗ ΘΕΤΙΚΩΝ ΕΠΙΣΤΗΜΩΝ
ΤΜΗΜΑ ΓΕΩΛΟΓΙΑΣ ΚΑΙ ΓΕΩΠΕΡΙΒΑΛΛΟΝΤΟΣ
ΤΟΜΕΑΣ ΓΕΩΦΥΣΙΚΗΣ - ΓΕΩΘΕΡΜΙΑΣ

Μελέτη χωροχρονικών προτύπων μικροσεισμικότητας για την σκιαγράφηση χαρακτηριστικών ενεργών ρηγμάτων τη χρήσει της μεθόδου διπλών διαφορών και ετεροσυσχέτισης σεισμικών κυματομορφών.

ΔΙΔΑΚΤΟΡΙΚΗ ΔΙΑΤΡΙΒΗ

ΚΑΠΕΤΑΝΙΔΗΣ ΒΑΣΙΛΕΙΟΣ

(Αρ. Μητρώου: 118)

ΤΟΜΟΣ Α΄

ΑΘΗΝΑ

ΜΑΡΤΙΟΣ 2017

ADVISORY COMMITTEE	P. PAPADIMITRIOU	Professor, NKUA (supervisor)
	N. VOULGARIS	Professor, NKUA
	K. MAKROPOULOS	Professor Emeritus, NKUA

EXAMINATION COMMITTEE	P. PAPADIMITRIOU	Professor, NKUA
	N. VOULGARIS	Professor, NKUA
	K. MAKROPOULOS	Professor Emeritus, NKUA
	G. TSELENTIS	Professor, NKUA
	A. KIRATZI	Professor, AUTH
	I. KASSARAS	Assistant Professor, NKUA
	G. KAVIRIS	Assistant Professor, NKUA

ΣΥΜΒΟΥΛΕΥΤΙΚΗ ΕΠΙΤΡΟΠΗ	Π. ΠΑΠΑΔΗΜΗΤΡΙΟΥ	Καθηγητής ΕΚΠΑ (Επιβλέπων)
	Ν. ΒΟΥΛΓΑΡΗΣ	Καθηγητής ΕΚΠΑ
	Κ. ΜΑΚΡΟΠΟΥΛΟΣ	Ομότιμος Καθηγητής ΕΚΠΑ

ΕΞΕΤΑΣΤΙΚΗ ΕΠΙΤΡΟΠΗ	Π. ΠΑΠΑΔΗΜΗΤΡΙΟΥ	Καθηγητής ΕΚΠΑ
	Ν. ΒΟΥΛΓΑΡΗΣ	Καθηγητής ΕΚΠΑ
	Κ. ΜΑΚΡΟΠΟΥΛΟΣ	Ομότιμος Καθηγητής ΕΚΠΑ
	Γ. ΤΣΕΛΕΝΤΗΣ	Καθηγητής ΕΚΠΑ
	Α. ΚΥΡΑΤΖΗ	Καθηγήτρια ΑΠΘ
	Ι. ΚΑΣΣΑΡΑΣ	Επίκουρος Καθηγητής ΕΚΠΑ
	Γ. ΚΑΒΥΡΗΣ	Επίκουρος Καθηγητής ΕΚΠΑ

SUBJECT AREA: Seismology

KEYWORDS: Multiplets, waveform cross-correlation, automatic picking of arrival-times, seismotectonics, Corinth Gulf

ΘΕΜΑΤΙΚΗ ΠΕΡΙΟΧΗ: Σεισμολογία

ΛΕΞΕΙΣ ΚΛΕΙΔΙΑ: Όμοιοι σεισμοί, ετεροσυσχέτιση κυματομορφών, αυτόματος προσδιορισμός χρόνων άφιξης, σεισμοτεκτονική, Κορινθιακός Κόλπος

Abstract

Earthquake sequences are often characterized by distinctive patterns, such as spatial and temporal clustering, unilateral or bilateral/radial migration and outbreaks in the seismicity rate. These may depend on the fault network geometry, the regional stress regime with localized anomalies due to stress redistribution after large events or aseismic factors such as creeping and diffusion of pressurized fluids. Earthquakes with similar focal parameters, also known as multiplets, are commonly observed during spatially clustered seismicity, producing recordings with similar waveforms. In the present dissertation, the phenomenon of waveform similarity is exploited in order to increase the spatiotemporal resolution of earthquake catalogues by increasing data quantity, through semi-automatic detection and location methods, and improving quality by performing high-resolution double-difference relocation which reduces the relative location uncertainties. The cross-correlation maximum in the time-domain is preferred as a method of measuring waveform similarity. Its characteristics are examined with respect to several parameters, such as the applied frequency filters, the window length and source duration, as well as the optimal threshold for nearest-neighbor linkage. A semi-automatic arrival-time picking method has been developed, based on the technique of the correlation detector which exploits waveform similarity on multiple stations. It is modified into a hybrid algorithm that combines the high detectability of single-station-detection and a high-sensitivity automatic picking technique based on Akaike's Information Criterion and higher order statistics. A method for the determination of seismic moment magnitude is also described, with emphasis on modifications which permit its calculation for local microearthquakes with narrow frequency content and low SNR. The developed algorithms are capable to increase the available information by more than ten times and decrease the completeness of a catalogue by up to about one order of magnitude.

Several case studies are presented, including mainshock-aftershock patterns (e.g. the 2008 Andravida, 2014 Cephalonia and 2015 Lefkada sequences), as well as earthquake swarms (e.g. 2007 Trichonis lake, 2011 Oichalia, 2013 Helike). The main study area is the western Corinth Rift, with special emphasis on earthquakes recorded by the Corinth Rift Laboratory (CRL) network during the period between 2000 and 2007. The relocated catalogues, after proper spatial clustering and division to sequential temporal periods, are explored in multiple cross-sections and spatiotemporal projections. The evolution history of multiplets and their generation rate provide implications on how seismicity spreads to new, previously unbroken fault patches, the existence of activity in regions that later produced strong clusters in the form of outbursts and the continuous recurrence of repeating earthquakes on other parts of a seismically active region. Composite focal mechanisms are constructed for spatial clusters or multiplets, where data from local networks permit their calculation, complementing the spatial analysis for the determination of the activated fault structures. Spatiotemporal migration is sought to reveal possible interaction of fluids during swarms and estimate parameters such as hydraulic diffusivity and migration velocity. The contribution of aseismic factors is also examined through ETAS modeling, which, in addition, provides information on the aftershocks productivity and decay rate.

Περίληψη

Οι σεισμικές ακολουθίες χαρακτηρίζονται συχνά από διακριτά μοτίβα, όπως χωρικές και χρονικές συστάδες, μονόπλευρη, αμφίπλευρη ή ακτινική μετανάστευση υποκέντρων και εξάρσεις στο ρυθμό σεισμικότητας. Αυτά εξαρτώνται από τη γεωμετρία του δικτύου ρηγμάτων, το καθεστώς τάσεων περιφερειακής κλίμακας με τοπικές ανωμαλίες εξαιτίας ανακατανομής τάσεων ύστερα από ισχυρά γεγονότα ή ασεισμικούς παράγοντες όπως ερπυσμό και διάχυση ρευστών υπό πίεση. Είναι σύνηθες στη χωρικά συσταδοποιημένη σεισμικότητα να εμφανίζονται σεισμοί με όμοιες εστιακές παραμέτρους (σμηνοσεισμοί, ή multiplets), οι οποίοι παράγουν όμοιες σεισμικές αναγραφές. Στην παρούσα διδακτορική διατριβή αξιοποιείται το φαινόμενο της ομοιότητας κυματομορφών με σκοπό τη βελτίωση της χωροχρονικής κατανομής των σεισμών ενός καταλόγου, τόσο σε ποσότητα δεδομένων, μέσω μεθόδων ημιαυτόματης ανίχνευσης και εντοπισμού, όσο και σε ποιότητα, εφαρμόζοντας επαναπροσδιορισμό υψηλής ευκρίνειας με τη μέθοδο των διπλών διαφορών που ελαχιστοποιεί τις αβεβαιότητες των σχετικών υποκεντρικών θέσεων. Η προτιμώμενη μέθοδος για τη μέτρηση της ομοιότητας κυματομορφών είναι το μέγιστο της συνάρτησης ετεροσυσχέτισης στο πεδίο του χρόνου. Τα χαρακτηριστικά της εξετάζονται ως προς διάφορες παραμέτρους, όπως τα συχνοτικά φίλτρα που εφαρμόζονται, το μήκος παραθύρου και η διάρκεια της σεισμικής πηγής, καθώς και τη βέλτιστη τιμή κατωφλίου για συσταδοποίηση με σύνδεση του «πλησιέστερου γείτονα». Αναπτύχθηκε μια ημιαυτόματη μέθοδος προσδιορισμού χρόνων άφιξης, βασισμένη στην τεχνική του «ανιχνευτή συσχέτισης» που αξιοποιεί την ομοιότητα κυματομορφών σε πολλαπλούς σταθμούς. Η μέθοδος αυτή έχει τροποποιηθεί σε έναν υβριδικό αλγόριθμο που συνδυάζει την αυξημένη ανιχνευσιμότητα ενός μεμονωμένου σταθμού με έναν υψηλής ευαισθησίας αυτόματο αλγόριθμο προσδιορισμού του χρόνου άφιξης σεισμικών φάσεων, ο οποίος βασίζεται στο Κριτήριο Πληροφορίας του Akaike και σε στατιστική ανώτερης τάξεως (κύρτωση και λοξότητα). Περιγράφεται, επίσης, μία μέθοδος προσδιορισμού του μεγέθους σεισμικής ροπής μέσα από φασματική ανάλυση, με έμφαση σε τροποποιήσεις που επιτρέπουν τον υπολογισμό του σε τοπικούς μικροσεισμούς με στενό συχνοτικό εύρος και χαμηλό λόγο σήματος προς θόρυβο. Οι αλγόριθμοι που αναπτύχθηκαν επιτρέπουν τον δεκαπλασιασμό της ποσότητας σεισμών ενός σεισμικού καταλόγου και τη βελτίωση της πληρότητάς του κατά περίπου μία τάξη μεγέθους.

Παρουσιάζονται διάφορες μελέτες περιπτώσεων που περιλαμβάνουν πρότυπα μετασεισμικών ακολουθιών (όπως για τους σεισμούς της Ανδραβίδας το 2008, της Κεφαλονιάς το 2014 και της Λευκάδας το 2015) καθώς και σεισμικών σμηνών (όπως στη Λίμνη Τριχωνίδα το 2007, την Οιχαλία το 2011 και την Ελίκη το 2013). Η κύρια περιοχή μελέτης είναι ο δυτικός Κορινθιακός Κόλπος, με ειδική έμφαση σε σεισμούς που καταγράφηκαν την περίοδο 2000-2007 από το τοπικό δίκτυο Corinth Rift Laboratory (CRL). Οι επαναπροσδιορισμένοι κατάλογοι, ύστερα από χωρική συσταδοποίηση και διαχωρισμό σε διαδοχικές χρονικές περιόδους, διερευνώνται μέσω πολλαπλών εγκάρσιων τομών και χωροχρονικών προβολών. Η εξέλιξη του ιστορικού των σμηνοσεισμών δίνει μία εικόνα για τον τρόπο με τον οποίο εξαπλώνεται η σεισμικότητα σε νέα τμήματα ρηγμάτων που δεν είχαν διαρρηχθεί, την προϋπάρχουσα δραστηριότητα σε περιοχές που αργότερα έδωσαν ισχυρές σεισμικές συστάδες και την επαναλαμβανόμενη σεισμικότητα σε τμήματα ρηξιγενών ζωνών. Όπου τα δεδομένα το επιτρέπουν, κατασκευάζονται σύνθετοι μηχανισμοί γένεσης για

χωρικές συστάδες ή ομάδες σμηνοσεισμών που βοηθούν συμπληρωματικά στην ερμηνεία της χωρικής ανάλυσης και τον προσδιορισμό των ενεργοποιημένων ρηξιγενών δομών. Αναζητούνται μοτίβα χωροχρονικής σεισμικής μετανάστευσης που αποκαλύπτουν την πιθανή επίδραση ρευστών κατά τη διάρκεια σεισμικών σμηνών και προσδιορίζονται παράμετροι όπως η υδραυλική διαχυτικότητα και η ταχύτητα μετανάστευσης. Τέλος, εξετάζεται η συνεισφορά ασεισμικών παραγόντων μέσα από μοντέλα ETAS (Μετασεισμική Ακολουθία Σποραδικού Τύπου) που παρέχουν, επιπροσθέτως, πληροφορία για την παραγωγικότητα μετασεισμών και τον ρυθμό απόσβεσης.

Acknowledgements

I would like to express my gratitude to the members of the advisory committee, Professors Nikolaos Voulgaris and Konstantinos Makropoulos for their important advice that helped improve the structure of my PhD thesis. I would especially like to thank the supervisor of my dissertation, Professor Panayotis Papadimitriou, for his insightful advisory and collaboration during the past ten years, which offered me the opportunity, among other things, to be involved in the installation of the "Athenet" seismological network of the University of Athens and gain significant technical experience. Special thanks are also in order for the members of the examination committee, Professors Gerasimos-Akis Tselentis and Anastasia Kiratzi, for their constructive comments and remarks, as well as Assistant Professors Ioannis Kassaras and George Kaviris, with whom I've had the opportunity to collaborate in case studies related to the subject of my thesis but also to other interesting subjects, such as regional stress distribution and shear-wave anisotropy.

This dissertation would not be complete without the contribution of the Greek institutes which participate in the implementation of the Hellenic Unified Seismological Network (HUSN). For this reason I would like to thank the personnel of the Institute of Geodynamics of the National Observatory of Athens, the Seismological Station of the Aristotle University of Thessaloniki, the Seismological Laboratory of the University of Patras and of course the personnel of the Seismological Laboratory of the University of Athens who have worked on the installation and maintenance of HUSN. I am also grateful to the French colleagues of CNRS who maintain the Corinth Rift Laboratory (CRL) network which continues to provide vital data for the important area of the western Gulf of Corinth. More importantly, I would like to thank Dr. Pascal Bernard, Dr. Anne Deschamps and Dr. Hélène Lyon-Caen for their collaboration, constructive advice and contribution to our publication for the 2013 Helike swarm.

I would also like to thank my colleagues, especially Andreas Karakonstantis who has done a great deal of work on manual analysis and construction of velocity models which are imperative for the improvement of the quality of the initial catalogue data in most of the case studies described in the present work, George Bozionelos and Alexandra Moshou, who have worked on focal mechanisms of major events using body-wave modeling during some of the sequences presented in case studies, Apostolos Agalos and Kostas Lentas, for manual analysis of the 2000-2001 CRL data and several under-graduate and post-graduate students who have helped with the routine analysis of seismicity at the Seismological Laboratory.

Double-difference relocation has been performed using the HypoDD algorithm (Waldhauser & Ellsworth, 2000; Waldhauser, 2001). Most map and cross-section figures were drawn using the Generic Mapping Tools (GMT) software of Wessel & Smith (1998). Calculations of the magnitude of completeness, G-R law and *b*-value mapping have been performed using the ZMAP software (Wiemer, 2001). ETAS and MOF models have been determined using the SaSeis2006 software (Ogata, 2006). Thank you all for freely providing your software that has been essential for the processing and presentation of earthquake data.

Last but not least, I would like to express my gratitude to my parents who have been fully supportive through all these years.

Στους γονείς μου

Table of Contents

Introduction

The present thesis deals with the detailed spatial and temporal description of microseismic patterns with emphasis on techniques and methods for the automatic processing of the large volume of waveform data which are nowadays available in Greece. Manual analysis is usually preferred over simple automatic solutions, as it ensures adequate picking quality with small arrival-time reading errors. However, it is time consuming when the amount of earthquakes is of the order of tens of thousands. It necessarily leaves out a large number of smaller events, which are not only numerous but also harder to analyse because of their low signal-to-noise ratio. This leads to a magnitude of completeness value in the final catalogue which could have been lower had smaller events been incorporated by applying an automatic algorithm. The hypocentral absolute location uncertainties can be reduced by the determination of a suitable velocity model and the application of station corrections, which reduce systematic travel-time errors that may be observed at stations in various azimuths due to lateral inhomogeneities of the medium. However, even after these improvements, the resolution of the hypocentral distribution could be limited to within scales of the order of km as a result of both the small number of events and their location uncertainties, prohibiting the discrimination of small-scale details in the activated structures.

To improve the hypocentral distribution both in terms of quantity (number of events) and quality (location uncertainties), the phenomenon of waveform similarity is taken into account. Similar waveforms are produced from the so called "repeating earthquakes", seismic events with similar source parameters (hypocenter, source size and focal mechanism). By definition, such events occur in small spatial volumes, but they are very often clustered in time as well. Waveform similarity is a feature that can be exploited in many ways. In the present study, it is mainly used for the calculation of P- and S-wave differential travel-time data which, along with the respective catalogue travel-times, can be used for the relocation of hypocenters by employing a double-difference algorithm. This effectively reduces the relative location errors, thus increasing the resolution of the hypocentral distribution which may enable the distinction of individual structures that were previously indiscernible. Waveform similarity can also be exploited for the propagation of arrival-time measurements from manually picked earthquakes to other events which have not been analysed yet.

Chapter 1 deals with waveform similarity and earthquake patterns. Methods of measurement of similarity are presented as well as clustering techniques which are required for the grouping of earthquakes into clusters of similar events called "multiplets", based on their waveform similarity. Grouping can also be performed into spatial clusters for, usually larger, groups of earthquakes in order to divide an area of study in individual volumes of clustered activity. Common earthquake patterns such as aftershock sequences and swarms are discussed, along with spatiotemporal patterns, such as earthquake migration, and their implications on the causative physical mechanism. Finally, the double-difference relocation method is briefly presented.

Chapter 2 concerns focal mechanisms, a significant requirement for a complete seismotectonic analysis. A brief introduction to stress and moment tensors is presented, along with basic properties

of the P- and S-wave radiation patterns and the polarization of particle motion. Simple focal mechanisms for individual events can be estimated by using the P-wave first motion polarities, weighted by factors that depend on discrepancies between theoretically expected and observed S-wave polarization directions and S to P amplitude ratios. Composite focal mechanisms can be determined for multiplets or spatial groups of earthquakes, providing information that is related to the local stress field and the fault planes.

Chapter 3 presents a method for the automatic determination of seismic moment magnitude by spectral fitting, aiming to enhance the quality of magnitude measurements for small earthquakes. The main difficulty with the spectral analysis of such events is that their waveforms have a low signal-to-noise ratio, especially at the lower frequencies which are essential for the determination of seismic moment.

Chapter 4 discusses different methods for automatic picking of P- and S-wave arrival-times. It begins with the simple STA/LTA signal-detection method which can also be used for preliminary arrival-time picking. Then a fully automatic, "classic" picking technique that employs Akaike's Information Criterion (AIC) is presented. This method, although sensitive down to relatively low SNR levels, is only efficient on the condition that preliminary/theoretical arrival-times have been pre-determined and associated with a certain event. The next technique is a semi-automatic picking algorithm called the "Master-Events" method. This exploits waveform similarity to propagate P- and S-wave arrival-time picks from a small set of manually picked master-events, with strong SNR, to a larger set of unresolved smaller events with low SNR. Finally, a new method called Hybrid Automatic Detection and Association of Earthquake Signals (HADAES) is presented. It is called a "hybrid" algorithm as it combines 1) single-station-detection using a modified STA/LTA method, 2) the main concept of the master-events method which is the "correlation detector" using "template waveforms" at a reference station and 3) a classic automatic picking algorithm in the form of the "AIC-picker". It also employs a method for the determination of "relative magnitude", an approximation of magnitude difference between similar earthquakes, which, when combined with master-events of known magnitude for reference, can be transformed to absolute magnitude.

A series of applications of the various methodologies discussed in the first 4 chapters are presented in Chapter 5. They concern earthquake sequences that have occurred during the last decade in Greece. It should be noted that, besides from spatial clustering, cross-correlation measurements, multiplet clustering and double-difference relocation, not every other method has been used in each of the case studies. This was mainly due to the fact that most of the presented applications had been completed and/or published before some of the methods, such as HADAES, were fully developed.

The last Chapter (6) is also an application to a case study, but is dedicated to the processing, analysis and seismotectonic interpretation of a large dataset of earthquakes that were recorded by the Corinth Rift Laboratory (CRL) local seismological network in the western Corinth Rift during 2000-2007. Several methods were employed for the analysis, including the HADAES method for the automatic picking of a large amount of events, determination of seismic moment by spectral fitting and composite focal mechanisms for different multiplets.

The detailed spatial analysis is complemented by the determination of the gross geometrical characteristics of several small activated structures, their apparent faulting types and their probable relation to mapped superficial faults. The temporal analysis includes a study of the variation of the seismicity rate per spatial cluster and its relation to significant earthquakes in each sequence. The energy release rate is investigated either in terms of cumulative magnitude or based on the earthquake productivity, by applying ETAS modeling or the modified Omori's Formula. Multiplet productivity and temporal evolution, related to spreading of ruptures to new areas or repeated slip at the same areas, respectively, are also examined in case studies. The findings are discussed in the context of the regional stress and tectonic regime, with emphasis on possible local perturbations of the stress-field and the activation of smaller structures which have become delineated as a result of high-resolution relocation.

Abbreviations

AIC : Akaike's Information Criterion
AoI : Area of Interest
AR system: Aki-Richards coordinate system
DC (SC) model: Double-Couple (or Single-Couple) model
DS : Day-Specific (multiplet)
CF : Characteristic Function
CLID : CLuster IDentification number
C(L)TF(Z) : Cephalonia(-Lefkada) Transform Fault (Zone)
CLVD : Compensated Linear Vector Dipole
CRLnet : Corinth Rift Laboratory network
EMR : Entire Magnitude Range (method)
ETAS : Epidemic Type Aftershock Sequence
FFT : Fast Fourier Transform
FM : Focal Mechanism
FMD : Frequency-Magnitude Distribution
FMP : First Motion Polarities
FPS : Fault Plane Solution
G-R : Gutenberg-Richter
HADAES : Hybrid Automatic Detection and Association of Earthquake Signals
HUSN : Hellenic Unified Seismological Network
LSQR : Least-Squares QR decomposition (or conjugate gradients method)
ME(m) : Master-Events (method)
MID : Multiplet IDentification number
M_{int}/M_{ext} : Internal/External master-events
MLE : Maximum Likelihood Estimation
MOF : Modified Omori's Formula
MT : Moment Tensor
RE : Reference Event
RMS : Root Mean Square
RPP : Residual Point Process
R_{st} : Reference Station
SaM : "Slaves as Masters" (procedure)
SE : Slave-Event
SNR : Signal-to-Noise Ratio
SoI : Stations of Interest
SPR : S/P amplitude Ratio
SRF : Site Response Function
SSD : Single-Station Detection
STA/LTA: Short-Term Average / Long-Term Average
STF : Source Time Function
SVD : Singular Value Decomposition
SWP : S-Wave Polarization
XC_{max} : (global) Cross-Correlation maximum

Chapter 1

Waveform similarity and earthquake patterns

1.1 Waveform similarity

Earthquakes are generally defined as the mechanical vibrations of the Earth (Aki & Richards, 2002) and seismology as the scientific discipline that primarily studies their source of origin, their physical mechanisms and the propagation and characteristics of their elastic waves. Tectonic earthquakes are generated by the sudden slip on active faults. This can occur either due to the accumulated stress surpassing the material strength or to the decrease of the coefficient of friction caused by increased pore-pressure pushing the fault walls apart and enabling slip. Other types of seismic events or tremors can be caused by various phenomena which produce abrupt crustal displacements, such as volcanic eruptions (e.g. Hotovec *et al.*, 2013), nuclear detonations (e.g. Zhang *et al.*, 2014), meteoroid blasts (e.g. Antolik *et al.*, 2014), landslides (e.g. Bozzano *et al.*, 2011), ice-quakes at glaciers (e.g. Carmichael *et al.*, 2013) etc.

The released energy is radiated outwards from the source in the form of elastic waves which propagate through the Earth's interior before eventually reaching the surface where they are recorded by seismological instruments. The resulting waveform is briefly described by Eq. 1.1 (Lay & Wallace, 1995):

$$\mathrm{u}_n(\vec{\mathrm{x}},\mathrm{t}) = s(t) * i(t) * g(\vec{x},t) = s(t) * i(t) * \sum_{j=1}^{5}\left(m_j \cdot G_{jn}(\vec{\mathrm{x}},t)\right) \tag{1.1}$$

where u_n is the time-series of the n^{th} component (vertical, radial or tangential) of ground displacement at position $\boldsymbol{x}$, the symbol * represents the mathematical operation of convolution, $s(t)$ is the source time function (STF), $i(t)$ is the instrument recording function or instrument response, $g(\mathrm{t})$ is the propagation function, where the coefficients m_j refer to the moment tensor elements which represent the radiation pattern of the corresponding wave-type and G_jn are the respective Green's functions for the moment tensor's element j and displacement's component n at position $\mathbf{x}$ and time t.

For a certain position at the surface, any earthquakes which may have similar terms $\boldsymbol{x}$, $s(t)$, $i(t)$ and $g(\boldsymbol{x},t)$ should produce similar displacement time-series, $\boldsymbol{u}(\boldsymbol{x},t)$. That is to say, two earthquakes recorded at a certain station, preferably with the same instrumentation during both events (thus the term $i(t)$ is the same and can be eliminated), originating from approximately the same hypocenter (thus $\boldsymbol{x}$ and $G_{in}(\boldsymbol{x})$ are similar), with comparable focal mechanism (similar terms m_i) and, preferably,

comparable magnitude, to exclude dissimilarities in the term $s(t)$, are expected to produce similar waveform recordings.

Reversing the argument, earthquakes with similar waveform recordings at a certain station are also expected to have similar source parameters (mainly hypocenter and focal mechanism). This implies that the medium's properties also remain relatively unchanged, so that the ray-paths and waveform spike-trains (G_{in}) are comparable. Such events are called similar or repeating earthquakes, doublets (for a pair) or multiplets / earthquake families for groups of more than 2 events (Geller & Mueller 1980; Poupinet *et al.*, 1984). Such events are of particular interest in studies of hypocentral relocation (Hauksson & Shearer 2005; Bohnhoff *et al.*, 2006; Waldhauser & Schaff 2008; Statz-Boyer *et al.*, 2009), propagation velocity variations (Poupinet *et al.*, 1984; Nishimura *et al.*, 2000; Pandolfi *et al.*, 2006; Cociani *et al.*, 2010), empirical Green's functions (Ichinose *et al.*, 1997) and others.

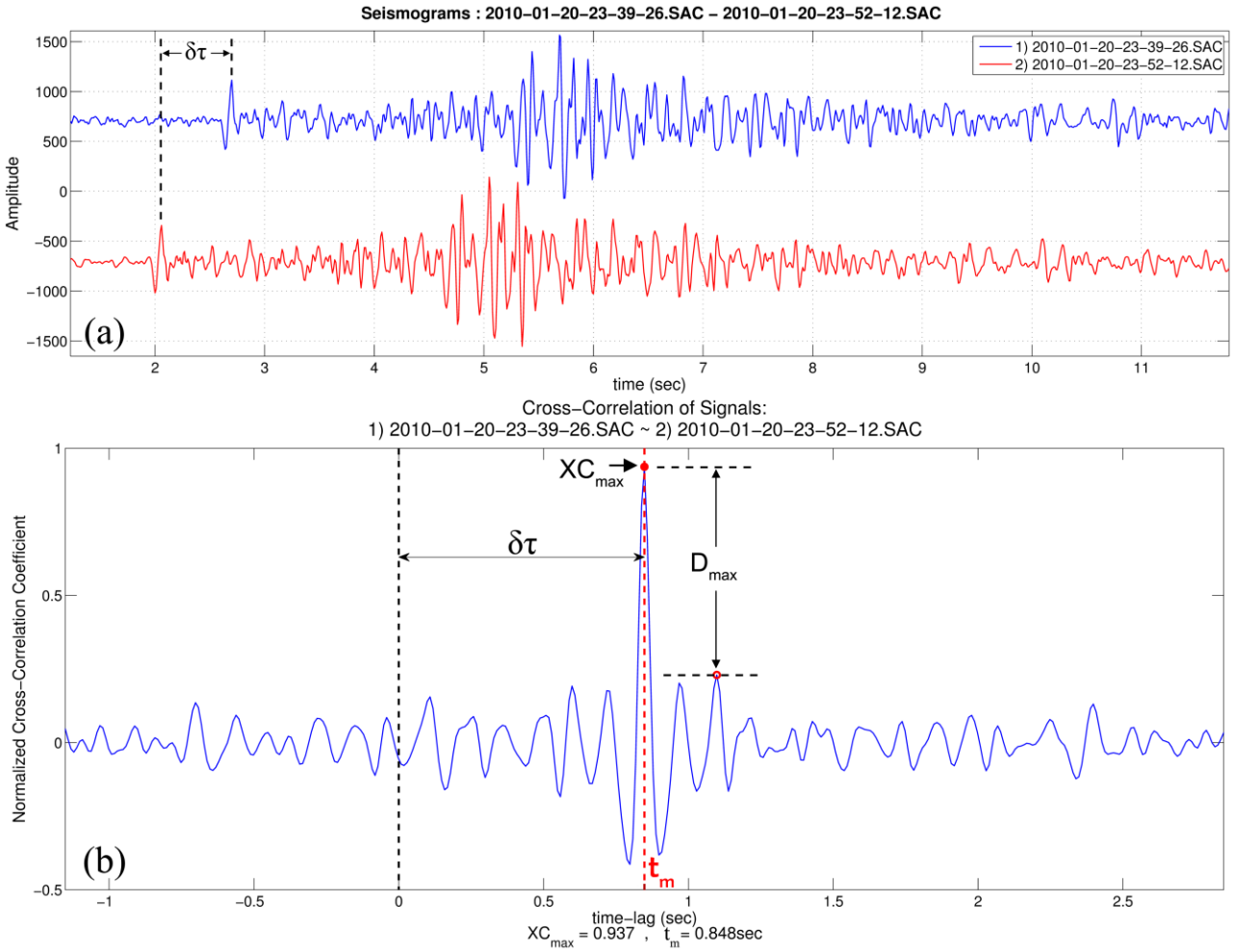

Figure 1.1: (a) two similar waveforms recorded at the vertical component of station KALE during the 2010 Efpalio swarm (Section 5.2), band-pass filtered at 2 – 23 Hz, normalized and shifted by a small time-lag, $\delta\tau$, with respect to the temporal alignment where their similar shapes fit best. (b) Cross-correlation (Eq. 1.2) between the time-series of panel (a), where XC_{max} is the global maximum at time-lag $t_m \equiv \delta\tau$ and D_{max} is the difference between the global and the major secondary maximum.

1.1.1 Measures of similarity

There are several ways to quantify the similarity between a pair of waveforms $x(t)$, $y(t)$. The most frequently used method is through the normalized cross-correlation function in the time-domain (Fig. 1.1), $XC(d)$:

$$XC(d) = \frac{\frac{1}{N}\sum_{n=0}^{N-1}\left(x(n)-\bar{x}\right)\cdot\left(y(n+d)-\bar{y}\right)}{\frac{1}{N}\sqrt{\sum_{n=0}^{N-1}\left(x(n)-\bar{x}\right)^2}\cdot\sqrt{\sum_{n=0}^{N-1}\left(y(n)-\bar{y}\right)^2}} \quad , \quad XC(t_m) = \max(XC) = XC_{\max} \tag{1.2}$$

where N is the number of samples of the longer time-series (the shorter one is padded with trailing zero samples to reach N) and d is the time-lag measured in samples, with $1 - N \le d \le N - 1$. The global maximum $XC_{max} = XC(t_m)$ is considered as a measure of the similarity between the two waveforms. The corresponding time-lag, t_m, represents the required shift (in samples or equivalent time units, depending on the context) that must be applied to the one time-series in order to align with the other so that their matching shapes (peaks and troughs) overlap. If the two time-series are sufficiently similar and the waveforms are cropped at the window of best-alignment, the correlation coefficient between their corresponding amplitudes should have a high value, near unity. For $x \equiv y$, Eq. 1.2 becomes the auto-correlation function.

The denominator of Eq. 1.2 is a normalization factor that makes $XC(d)$ independent of the absolute amplitudes of waveforms. However, $XC(d)$ is biased by a factor that depends on the absolute time-lags compared to the window length; its values are bounded by an envelope that causes them to reduce linearly with increasing time-lag (Kapetanidis, 2007). To acquire the unbiased, normalized cross-correlation value, Eq. 1.2 must be corrected by a factor, C_e:

$$C_e(d) = 1 - \frac{|d|}{N} \tag{1.3}$$

Before applying the cross-correlation function, a band-pass filter is required in most cases, mainly for the removal of long-period trends and DC offset/bias which can greatly affect the results of the cross-correlation, but also for the reduction of high frequency noise that may be present. For local microearthquakes, the frequency band between about 2.5 and 23 Hz is usually adequate in most cases. More details on the selection of filters are described in Section 1.2.2.

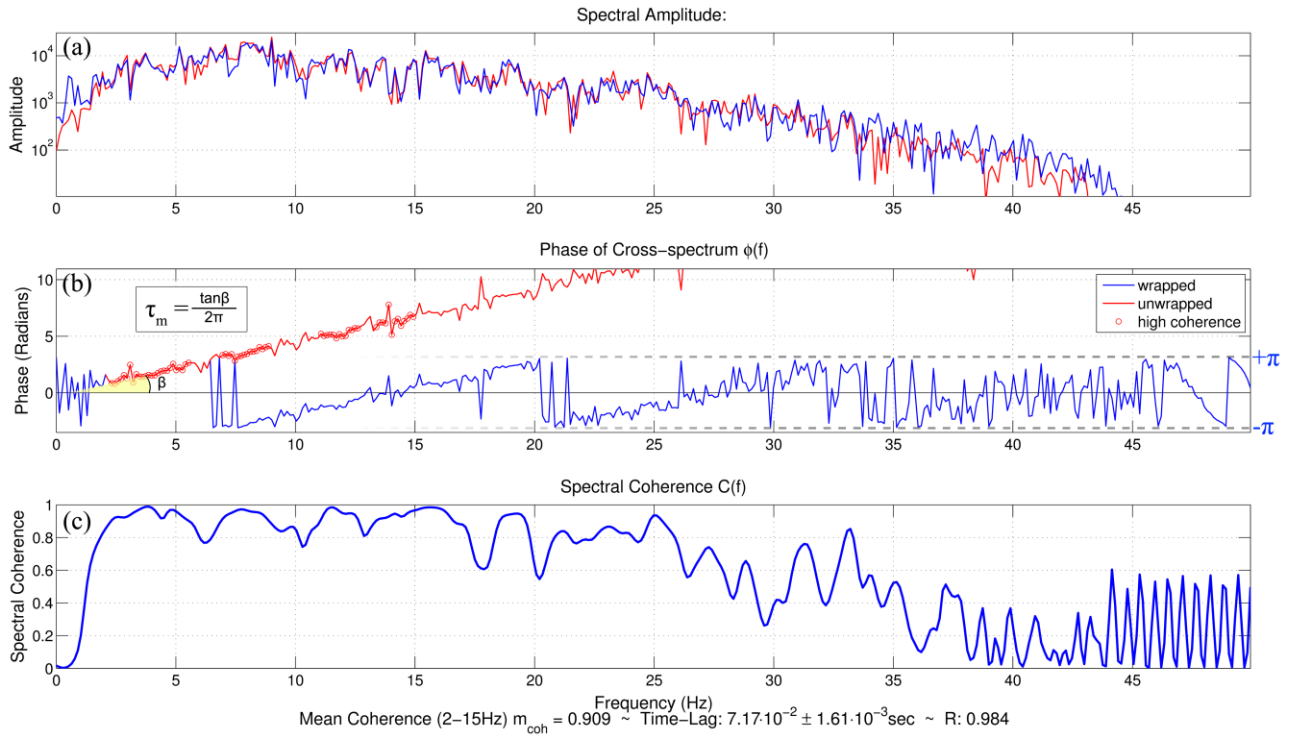

Figure 1.2: (a) Spectral amplitudes of the two similar waveforms of Fig. 1.1a, (b) wrapped between [-π, +π] (blue) and unwrapped (red) phase of the cross-spectrum (Eq. 1.5) for waveforms of Fig. 1.1a, shifted by a small time-lag, τ_m. The time-lag, τ_m, can be retrieved by the angle between the frequency axis and the linear part of the unwrapped cross-spectral phase, by applying linear regression using the encircled points that correspond to high coherence between 2 and 15 Hz. (c) Spectral coherence (Eq. 1.4) of the two similar waveforms.

An alternative measure of similarity, in the frequency-domain, is the spectral coherence (Poupinet *et al.*, 1984):

$$C_i(f) = \frac{S_i^2(f)}{A_{xi}(f)A_{yi}(f)} \tag{1.4}$$

where A_{xi}, A_{yi} the smoothed spectra of $x(t)$ and $y(t)$, respectively. The index i represents the temporal shift between the two time-series (their relative alignment) and $S_i(f)$ is the cross-spectrum function (Fig. 1.2a):

$$S_i(f) = A_{yi}^*(f) \cdot A_{xi}(f) \tag{1.5}$$

where $A_y^*(f)$ are the conjugate values of the complex coefficients of the Fast Fourier Transform (FFT) of $y(t)$. The cross-spectrum is typically the FFT of the cross-correlation function. The spectral coherence (Fig. 1.2c; Fig. 1.3) measures similarity between the shapes of the spectra of the two time-series around different frequencies. It is the equivalent of the cross-correlation in the frequency domain and has been preferred by several authors (Poupinet *et al.*, 1984; Got *et al.*, 1994; Kilb & Rubin, 2002) or used as an additional weight (Schaff *et al.*, 2004). In the case of local microearthquakes, the mean spectral coherence, m_{coh}, between 2 and 15Hz could be used as a

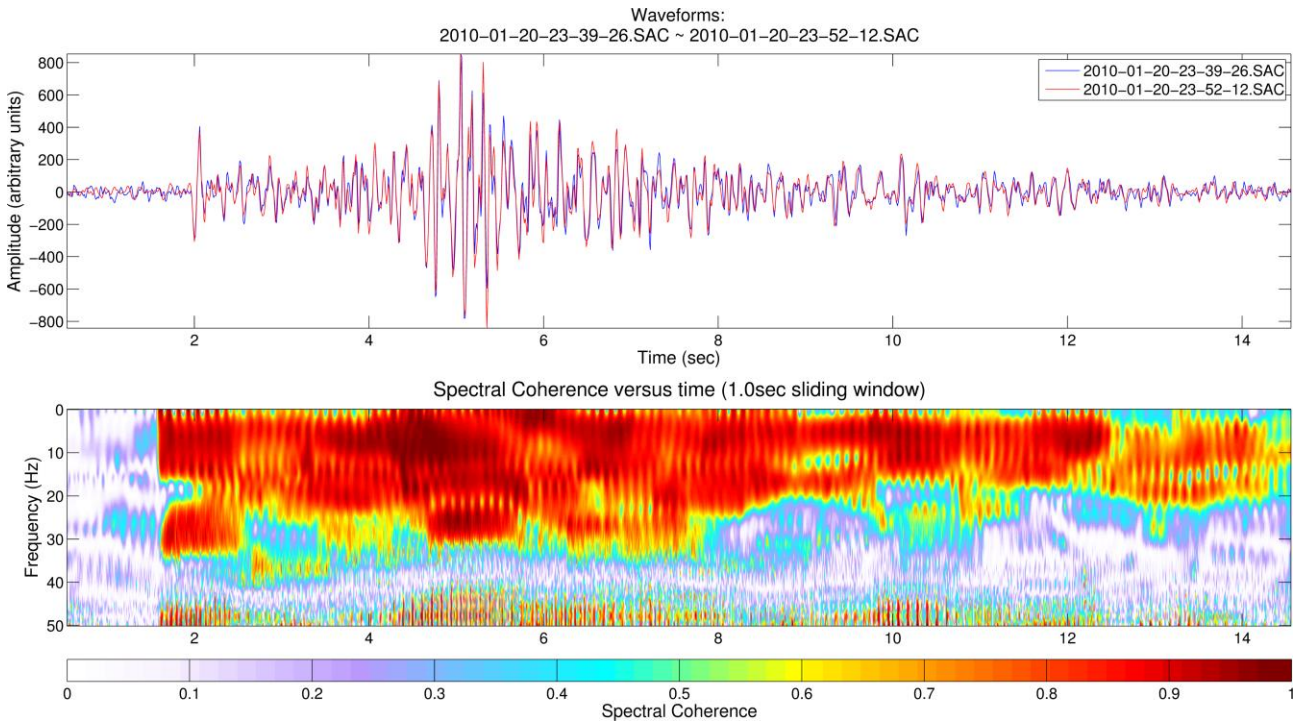

Figure 1.3: (top) the waveforms of Fig. 1.1a shifted to their best-fit temporal alignment. (bottom) spectral coherence on a 1 sec - long sliding window with 1-sample step, windowed using a 25% cosine taper (Tukey) windowing function. It only resembles a simple spectrogram due to the high degree of similarity along the whole length of the waveforms and the fact that they are temporally aligned to match (zero time-lag).

measure of similarity between pairs of waveforms. This spectral region avoids long period as well as high frequency noise, while it contains most of the energy content that is generated by a local event.

In the case of auto-correlation, the phase of the cross-spectrum is, by definition, zero for all frequencies. This is due to the auto-correlation being an even function; hence the coefficients of its FFT are real. A similar observation can be made between the waveforms of two highly similar earthquakes: when aligned at t_m, the cross-correlation function $XC(d)$ will be nearly symmetrical with respect to d=0 and the cross-spectral phase will be roughly zero in the band of highly coherent frequencies (Kapetanidis, 2007). If, however, the two similar waveforms are not aligned, the cross-spectral phase will deviate from zero proportionally the increasing frequency (Fig. 1.2b). The equivalent value of the time-lag, τ_m, in the spectral domain, which can be used as an offset for the best temporal fit of two similar waveforms, can be estimated by the slope angle, β (Fig. 1.2b), of the cross-spectral phase (Poupinet *et al.*, 1984):

$$\tau_m = \frac{\tan\beta}{2\pi} \tag{1.6}$$

While the t_m given by the cross-correlation function (Eq. 1.2) has a precision limited by the sampling interval $\delta\tau=1/F_s$, where F_s is the sampling frequency of the waveform recording, the time-lag τ_m via Eq. 1.6 could provide a result of greater precision, as the angle values are continuous rather than discrete. Even if the original time-series have already been shifted by t_m (Eq. 1.2), the

cross-spectral phase angle could be $\beta \approx 0$ with $|\tan\beta/2\pi| = |\tau_m| < |\delta\tau|$. However, in practice, measuring τ_m could present difficulties, as the linear segment of the cross-spectral phase could include outliers, where the corresponding coherence is low, or be wrapped around $\pm\pi$ if the time-lag is relatively large. In any case, the phase has to be unwrapped before any calculations of its slope take place, and the unwrapping procedure is not always successful, especially when the coherence is poor. The limited range for which cross-spectral methods can provide valid τ_m measurements has been examined by Schaff *et al.* (2004), who concluded that for the waveform recordings of earthquakes at local distances it is not recommended when the time-lag is larger than 8 samples, or 80 ms for 100sps sampling rate, thus they recommend the cross-correlation function for large time-lags as it is more robust.

A suggested practice for the safer use of the cross-spectral phase is:

1. Shift the original time-series by t_m (Eq. 1.2).
2. Calculate cross-spectrum and spectral coherence on the shifted time-series.
3. Measure the remaining time-lag, τ_m by the angle of the cross-spectral phase (total time-lag: $t_m+\tau_m$).

Step #2 prevents wrapping around $\pm\pi$, so that no unwrapping techniques (which can often be problematic) need to be applied. For step #3, the angle is only measured using samples of the cross-spectral phase in frequencies where the coherence is sufficiently high (Got *et al.*, 1994), in order to avoid outliers. The measurement of the slope, $\tan\beta$, and its standard error can be derived by least-squares linear regression, weighted by the corresponding spectral coherence values (Poupinet *et al.*, 1984; Got *et al.*, 1994).

Alternatively, to avoid unnecessary FFT and other time-consuming calculations in the frequency domain, the precision of t_m (Eq. 1.2) can be improved by resampling the cross-correlation curve around its global maximum at a higher sampling frequency, such as $10 \cdot F_s$. This can be done e.g. by fitting a 2nd degree polynomial (Deichmann & Garcia-Fernandez, 1992; Schaff *et al.*, 2004) or using non-linear spline interpolation, either on $XC(d)$ or on the waveforms themselves (Hauksson & Shearer, 2005; Lin *et al.*, 2007; Kapetanidis *et al.*, 2010). The latter method is mostly adopted in the present work, as it has been widely tested in various applications of hypocentral relocation with satisfactory results. The mean spectral coherence, m_{coh}, can provide additional weighting information (Kapetanidis & Papadimitriou, 2011; Section 4.3). However, it is not practical or robust enough to be a primary similarity measure, as, besides the problems with the calculation of the time-lag from the cross-spectral phase, m_{coh} saturates faster than the corresponding XC_{max}, as similarity decreases (Kapetanidis, 2007; Kapetanidis *et al.*, 2010).

Various other measures of similarity are also used in the literature. Some of the more interesting ones take into account the partial similarity between segments of waveforms or work at both time and frequency or time-scale domains. In the Syntactic PAttern Recognition Scheme (SPARS) algorithm (Zhizhin *et al.*, 2006; Pacchiani, 2006) the waveforms pass through wavelet decomposition and are represented in the form of discrete scalograms. Their dissimilarity is then measured by their (syntactic) Levenshtein distance (Levenshtein, 1966), which takes into account local delays in phase-arrivals (the most outstanding being the difference between S-P arrival-time

differences, $T_{S\text{-}P}$), differences in frequency content and energy envelopes. The Fingerprint And Similarity Thresholding (FAST) algorithm (Yoon *et al.*, 2015) analyzes signals by extracting key discriminative features from their spectrograms and scalograms, compressing and storing them in a database in the form of binary "fingerprints" which are then used for fast nearest-neighbor search using hashing techniques. Some other similarity measurement or similarity-based classification techniques, which have been used by some authors, include (but are not limited to): chirplet atomic decomposition (Bardainne *et al.*, 2006), cumulative shape dissimilarity (Benvegna *et al.*, 2011) and phase cross-correlation / instantaneous phase coherence (Schimmel, 1999; Schimmel *et al.*, 2011).

When dealing with absolute times, the difference between the times of the first sample of each time-series, $t_x(1)$-$t_y(1)$, has to be taken into account. This is crucial because it allows for a calculation of the time-lag of XC_{max} for a custom initial temporal alignment. More specifically, the two time-series could be shifted so that the manually (or automatically) picked arrival-time of their P- or S-waves, coincide. The alignment is done by subtracting the corresponding absolute time of the pick, e.g. t_{px} and t_{py}, from the time values of the windowed waveforms x and y, respectively, so that for $t_x'=t_x-t_{px}$ the relative time $t_x'=0$ corresponds to the respective P- or S-wave arrival-time, t_{px}. To acquire the real time-lag with respect to t_{px} and t_{py}, a correction by the offset $t_{off}=t_y'(1)-t_x'(1)$ is required. Then, if these waveforms are similar, the time-lag t_m, corrected by adding t_{off}, provides a measure of the difference that arises between the corresponding arrival-time picks, which have been used for the temporal alignment, when the similar waveforms are shifted in time to fit together. Naturally, if the waveforms are cropped to an equal number of samples before t_{px} and t_{py}, then $t_{off}=0$ and the t_m value can be used directly as a differential measurement. For a set of highly similar earthquakes, these time-lags can provide a rough estimate of the arrival-time reading errors (Seggern, 2009). Together with differential travel-times derived from catalogue data, they can be used for the double-difference relative relocation of earthquake hypocenters (see Section 1.4).

1.1.2 Degrees of similarity

Geller & Mueller (1980) in their study of similar earthquakes concluded that for a pair of earthquake waveforms to be similar, their hypocentral separation distance cannot be greater than 1/4 of the dominant wavelength, λ_d, based on the idea that they should be within a common first Fresnel zone. In their example, the examined $M\approx2.7$ earthquakes had a dominant frequency f_d = 5Hz, which, taking into account V_S = 3.5 km/s at the source, results in λ_d = 0.7km and $\lambda_d/4 \approx$ 175m, suggesting a maximum separation distance of about 200-400m. Baisch *et al.* (2008), on the other hand, have shown that the $\lambda_d/4$ criterion is not as restrictive as Geller & Mueller (1980) suggested, but various degrees of similarity can be observed at larger distances. They used high-frequency synthetic examples to demonstrate how waveform similarity can be affected by small differences in the major factors of Eq. 1.1, namely hypocentral separation distance and source-receiver geometry relative to the radiation pattern, but, also, to technical parameters such as the correlation window length, L_{XC}, and the frequency band (filtering). The $\lambda_d/4$ criterion holds for high frequency signals and for very high degrees of similarity ($XC_{max} \geq 0.95$). However, it can also hold for separation distances larger than $\lambda_d/4$, if the signal is low-pass filtered so that the bandwidth is limited to low frequencies, reducing waveform complexity and increasing XC_{max}. The cross-correlation maximum decreases at

a lower rate with respect to the separation distance for low-frequency signals than for those which include higher frequencies. On the other hand, sources separated by less than $\lambda_d/4$ can exhibit lower XC_{max}, if L_{XC} (the length in samples of the time-series x and y being cross-correlated) increases. Decreasing the window length makes more likely for some arbitrary wave trains to match, resulting in larger XC_{max} values. Baisch *et al.* (2008) suggest an $L_{XC}=2.8\cdot(t_s-t_p)$, with the first 20% of the window containing noise before the P-waves and the rest including the whole P-wave train, an adequate length of S-waves and some of their coda. Baisch *et al.* (2008) also examine the XC_{max} dependence on source-receiver geometry and find that, even for events with a separation distance nearly $\sim\lambda_d$, the XC_{max} can become abnormally high when the stations are near the nodal planes or the stress axes, where S- and P-waves, respectively, exhibit high amplitudes.

An example for the relation between XC_{max} and inter-event separation distance is presented in Fig. 1.4 for a spatial group that occurred in the western Corinth Rift (Chapter 6; Section 6.3.5). The highest XC_{max} values are found, as expected, at very short distances, while the highest observed XC_{max} tends to decrease with increasing source spatial offset. Han *et al.* (2014) examined the XC_{max} dependence on source separation distance using synthetic waveforms. They found that the hypothesis of Menke (1999) that XC_{max} declines exponentially with increasing inter-event distance is only valid as a first approximation. Interestingly, if the two foci are offset only horizontally, in a direction that is perpendicular to the source-station direction, then, provided that the spatial offset of the sources is much smaller than their (roughly common) distance from the station, the XC_{max} can hardly detect any difference at all (it doesn't decrease with increasing tangential source distance). On the other hand, a vertical offset has a stronger effect on XC_{max} than a radial horizontal offset (Han *et al.*, 2014).

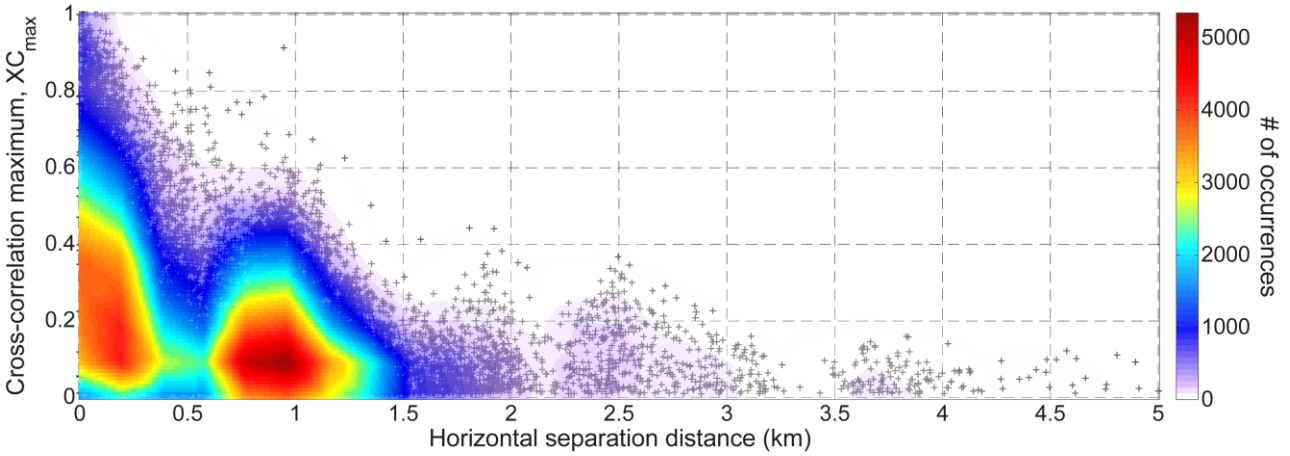

Figure 1.4: Variation of XC_{max} (station DIMT, vertical, filtered between 2 and 20 Hz) with respect to the horizontal source separation distance for relocated seismicity from the spatial group #4 of 2004 in the western Corinth rift (Chapter 6). The colour-scale applies to the very dense areas of the plot while in low density areas the respective values are plotted with crosses.

1.1.2 Degrees of similarity

Deichmann & Garcia Fernandez (1992) examined two microearthquake sequences that occurred in 1987, at the Jura Mountains, northern Switzerland. They observed events with identical S-P travel-times ($T_{S\text{-}P}$) that had significant differences in their S/P amplitude ratio, including even P-wave first motion polarity reversals and attributed these variations to small perturbations in the focal mechanisms. However, the main faulting type remained strike-slip with a stable P-axis and the subtle differences were attributed to different orientation of the slip vectors but on the same fault plane. While this effect could also be caused by tangential separation, which in general does not affect $T_{S\text{-}P}$, it is possible for events within a relatively tight spatial cluster to have a high degree of variance in their radiation pattern. Schaff (2010) notes that a couple of "semi-similar" events with even a 60° difference in their rake could exhibit a high degree of correlation in e.g. 2 of their 3 components. In such cases it may even be appropriate to also examine the cross-correlation for strong negative global minima, as in rare cases there can be events with reversed polarities in all their components (e.g. Ma & Xu, 2013). It is, however, also possible that such reversals are due to an instrumental malfunction, in which case the issue must be investigated and corrected. P-wave first motion reversals between events within a multiplet can be expected if the station is close to a nodal plane so that small perturbations in the focal mechanism can place the station's trace in the opposite quadrant of the radiation pattern. However, larger deviations may be observed if the degree of similarity is relatively low.

Concerning the fault plane solutions of repeating earthquakes, it is usually expected that most events within a narrow seismogenic volume have little variation in their focal mechanisms, indicating that the rupture occurs on the same fault surface and with a similarly oriented slip vector (rake). It is possible, though, that several faults are cross-cutting each other or branching to comprise a fault network. Antithetic faults are a common case where a regional stress regime can produce slip on either fault. Furthermore, it may be ambiguous to distinguish whether an event has occurred on the synthetic or antithetic fault, if the nodal planes of its focal mechanism are compatible with both fault planes. However, if there are, under certain conditions, strong localized stress concentrations, it is possible that slip occurs on other types of discontinuities, e.g. old, "inactive" structures, or on expected faults but at a different rake angle.

In some rare cases, even pairs of events may exist whose waveforms are highly anti-correlated (very strong negative minimum in the cross-correlation function) for all components. Ma & Xu (2013) observed such occurrences for 5 "negative doublets" in the aftershock sequence of the 2008 Wenchuan earthquake in China, but were unable to conclude whether this was a result of opposite fault plane solutions, as they used a single station. White *et al.* (2011) observed coexistence of opposite focal mechanisms at a common focal region, flipping between normal and reverse, in seismic events that occurred due to melt injection within propagating dykes in the ductile mid-crust of the Kverkfjöll volcanic system, Iceland. Although the authors have not calculated cross-correlation values to demonstrate the reversal, they present a series of waveforms for two events with all stations having opposite polarities, which otherwise appear to be visually identical. They proposed several possible mechanisms to explain the flipping fault plane solutions, including parallel fractures ahead of the dyke tip that slip in opposite directions due to the dyke's propagation, or the involvement of a solidified but fractured basalt plug inside the dike whose parts may slide in

alteration, producing opposite slips relative to the respective dyke wall, depending on the plug segment that breaks and gets pushed by the intruding melt.

The dependence of waveform similarity on magnitude difference can be demonstrated in terms of a variable STF, as the relative amplitude differences alone do not affect the *XC* function. It is theoretically expected that the relation of seismic moment, M_o, to source duration, τ, is $M_o \propto \tau^3$ (Kanamori & Anderson, 1975; Harrington & Brodsky, 2009). The relation between seismic moment and moment magnitude (Kanamori, 1977), M_w, is:

$$M_w = \frac{2}{3}\left(\log_{10}\frac{M_o}{N \cdot m} - 9.1\right) \tag{1.7}$$

So the relative magnitude, or magnitude difference, is roughly given by:

$$M_{diff} \approx \frac{2}{3} \cdot 3\log_{10}\tau_r \tag{1.8}$$

where τ_r is the ratio between the source durations of two events with similar source parameters.

A simple synthetic test was performed to investigate this relation using the following steps:

1) A random spike train was created, with variable amplitudes of random polarity, to simulate a Green's function.
2) A reference waveform was generated by convoluting a windowing function (e.g. a Gaussian) with the spike train to simulate the source duration.
3) Step (2) was repeated using windowing functions of gradually increasing length (duration) to generate a waveform similar to that of (2) but with larger magnitude.
4) The waveforms of step (3) were cross-correlated with the reference waveform of step (2) and the XC_{max} value was registered.

The results are displayed in Fig. 1.5 with respect to the source duration ratio, τ_r, and magnitude difference, M_{diff} (Eq. 1.8), using various windowing functions (Gaussian, Triangular, Tukey and Rectangular) and two wavelets (Morlet, Mexican Hat) for comparison. At τ_r=1, the two waveforms are equal (auto-correlation). As the source duration increases, the pulses which comprise the waveform that corresponds to the larger relative magnitude become wider. As a result, the two time-series become gradually more dissimilar and XC_{max} drops.

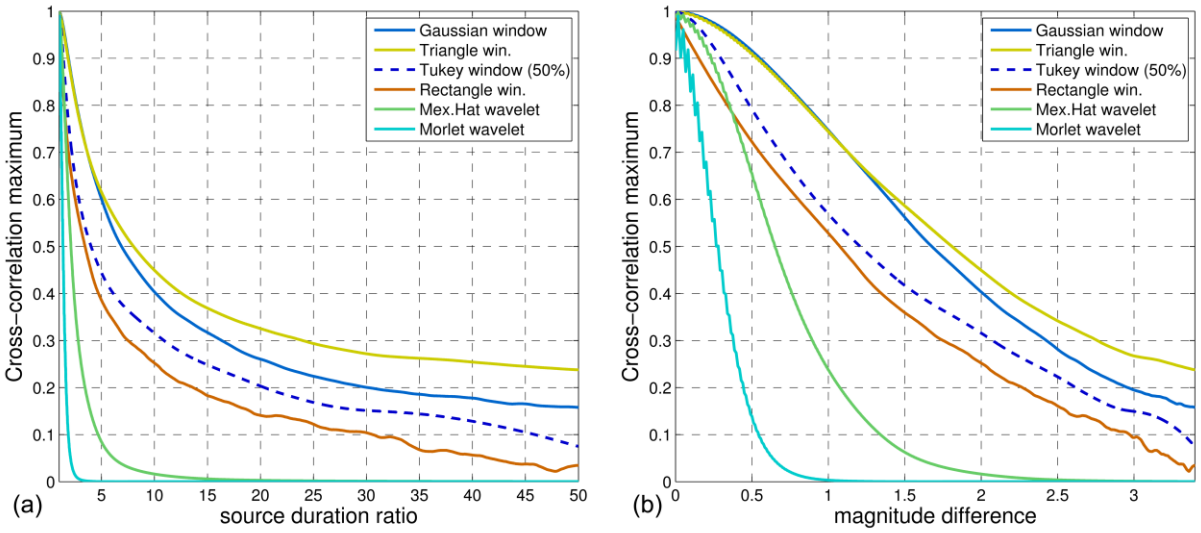

Figure 1.5: Synthetic test for the influence of source duration on the correlation coefficient (see main text for details) using various "source shapes" with respect to (a) the source duration ratio, (b) relative magnitude difference.

Although the test is certainly oversimplified, it provides a sense on how waveform similarity is likely affected by the difference in magnitudes. With all other parameters being equal, differences of ±0.5 in magnitude may cause a drop in XC_{max} in the range 10-30%, depending on the windowing function. The Gaussian window is smoother, thus the effect of increase in its length is weaker. It is also more stable in terms of t_m derived by cross-correlation. However, with many of the other windowing functions the cross-correlation quickly becomes unstable, resulting in erroneous t_m. For this reason, the plots of Fig. 1.5 have been drawn after forcing a temporal shift by the expected t_m value due to the expected offset produced by the convolution, which is half the source duration difference, and the linear correlation coefficient is calculated instead. This produces the same result as the XC_{max} for the unbiased (corrected by the factor of Eq. 1.3) normalized XC. The triangular windowing function gives similar results to the Gaussian (albeit a bit more unstable), for M_{diff} up to 1.1, with a 30% drop in XC_{max}. From that point on, the triangular source has higher correlation values than the others. The rectangular window, being the least smooth/stable, provides generally lower correlation coefficients. The plot of the 50% Tukey window, which starts and ends smoothly with a cosine taper but is flat in its middle segment, ranges between the rectangular and Gaussian plots. The wavelet functions, on the other hand, which have a shape that also includes negative values, have correlation coefficients that drop much faster. Using a Morlet wavelet as a "source" shape, the correlation drops by 30% at M_{diff}=0.18, while with the smoother Mexican Hat wavelet it drops by 30% at M_{diff}=0.45.

These relations are not considerably affected if the number of spikes is modified or the data length is increased. They do not depend much on the reference source duration (for τ_r=1) either, provided the waveform window is large enough. At M_{diff}>3 the correlation becomes lower than 0.3 for all source functions, suggesting very little correlation between earthquakes when their magnitude difference is so great. However, this doesn't mean that such correlations are impossible to detect, as

demonstrated by Schaff & Waldhauser (2010), who measured XC_{max}=0.26 between two similar events with a magnitude difference of ~3.3, where the smaller one could be used as an empirical Green's function to retrieve the relative STF (Ichinose *et al.*, 1997). Concerning the frequency filters, events with significant differences in their source duration, despite their similarity in the other source parameters, may have higher XC_{max} values when filtered at lower frequencies, e.g. 2-4 Hz, rather than higher frequencies, e.g. 16-32 Hz, with 8 Hz considered as a threshold above which the source may have a significantly negative impact on XC_{max} (Nakahara, 2004).

An example with real data is presented in Fig. 1A.1, with the magnitude determined using the method described in Chapter 3. The result is compared to the theoretical curve derived from sources of triangular shape as in Fig. 1.5. The expected curve, which is also the one with the shallowest slope, envelopes the portion of the density map with 10 or more occurrences, but there are in fact several dispersed measurements which fall outside this region. This shows that the tolerance of XC_{max} to source size difference can be even higher than expected in some cases. There are, of course, differences in the overall distribution of XC_{max} versus ΔM_w from station to station which may depend on other factors that negatively affect the XC_{max}. The image in Fig. 1A.1 is not representative but highlights the existence of signals with adequate waveform similarity despite the significant difference in the magnitude of their respective events.

An important observation derived by Fig. 1.5 is that events of comparable magnitude are more likely to have similar waveforms. The expected number of earthquakes in a given seismically active region may increase tenfold with a drop of magnitude by 1.0, according to the Gutenberg-Richter (G-R) law for the frequency-magnitude distribution (Gutenberg & Richter, 1954) for a *b*-value near unity, which is the global estimate. This makes it more probable for smaller earthquakes to be similar, especially if they are spatio-temporally clustered. It also implies that a reference station must be in a relatively small epicentral distance from the seismogenic zone in order to record the smaller, more likely to be similar, events with adequate SNR. The other significant result is that similarity can drop drastically when M_{diff} is large, even though the point sources may coincide (they are separated by less than $\lambda_d/4$).

1.2 Clustering methods

When analyzing multiplets and spatio-temporal earthquake patterns, one of the most important procedures is the linkage and hierarchical clustering of earthquake events into groups. The sense of clustering is that objects (signals or events) within a group have certain features more similar to each other than between objects that belong to different groups. In this section a brief introduction into the basics of clustering techniques will be presented, focused on those which are of interest in applications concerning earthquake events.

The classification in multiplets can be helpful for several reasons, such as:

- Segmentation of the dataset to reduce processing time during further analyses, for example:
  - Cross-correlation measurements for double-difference relocation (Section 1.4).
  - Correlation detector procedures for arrival-time (re-)picking (Chapter 4).

- Examination of the temporal evolution of multiplet activity, their generation rate and life-span.
- Examination of their spatial distribution (applications in Chapters 5 and 6).
- Determination of composite focal mechanisms (Chapter 2).

Generally, in clustering methods the property of interest could either be the similarity between waveforms of earthquake signals (multiplets) or the proximity of earthquake hypocenters (spatial clustering) or their origin times (temporal clustering). Either way, a measure of proximity or dissimilarity has to be defined before the linkage between objects is calculated. In the case of hypocentral locations, the inter-event separation distance, between pairs of hypocenters, for a 3D, or epicenters, for a 2D distribution, respectively, is an appropriate measure of dissimilarity with Euclidean metric. Likewise, inter-event times (origin time differences) can be used for temporal clustering. In multiplets, however, the correlation coefficient, XC_{max}, is a measure of similarity rather than dissimilarity. In this case, the dissimilarity can be simply given by $1\text{-}XC_{max}$, a simple form of "correlation distance".

The most common hierarchical linkage methods are agglomerative, that is they begin with a total of n objects, each one in a single one of the n individual 1-event "groups", and are gradually merged into larger clusters according to criteria based on a relation between the inter-object/subcluster distance or dissimilarity. The basic input for the linkage procedure is the matrix that contains the inter-event distances or waveform dissimilarities ($1\text{-}XC_{max}$).

1.2.1 Linkage algorithms

The simplest and most intuitive clustering method is the "single" or "nearest neighbor" linkage. The first link is created between the closest objects, which also comprise their own single-object cluster. The procedure ensues by linking clusters whose distance is the smallest, where distance between two clusters is defined as the minimum distance between one of the former group's objects and an object of the latter. At each step of the linkage, the referring minimum distance or "fusion level", which typically increases (except for rare cases in certain linkage algorithms) as the subclusters are merged into larger groups, also indicates the current threshold value. This sort of linkage is commonly used to define multiplets according to a minimum similarity threshold, C_{th}, above which two events, A and B, are considered as similar or "direct / close-relatives", or $XC(A,B) \geq C_{th}$. According to the nearest-neighbor linkage, a third event, C, is also considered similar to A and B (belongs to the same multiplet) as long as e.g. $XC(A,C) \geq C_{th}$, even if $XC(B,C) < C_{th}$, in which case B and C are "indirect / distant-relatives", linked together through event A (Kapetanidis *et al.*, 2010; Kapetanidis & Papadimitriou, 2011). The downside of single linkage is that it may create a so called "chaining effect", linking two distinctly irrelevant groups through a "narrow neck" of intermediates or "bridge" objects (Hartigan, 1975). This can be counteracted by visual inspection of the spatial distribution of the resulting (large) multiplets or their internal consistency/structure (individual correlation matrices) which may reveal that a single, large multiplet would be better broken in two or three smaller ones. It is also suggested that similarity is met in more than one station before

creating a link. However, this could considerably reduce the number of events contained in multiplets.

On the opposite side of the linkage techniques, the "complete" or "furthest neighbor" method also makes links between clusters having the smallest distance, but defines as the distance between two clusters the maximum separation/dissimilarity between two of their objects. If furthest-neighbor linkage is applied to a waveform dissimilarity matrix, according to a certain threshold, the property of the created multiplets is that all events within a multiplet have $XC_{max} \geq C_{th}$ between them (they are all direct relatives). This usually results in a large number of small multiplets, but with strong internal consistency.

Both single and complete linkage methods do not take the internal structure of the clusters into account; they do not consider the overall effect of agglomeration within the resulting merged cluster. The "centroid linkage" algorithm, on the other hand, considers the distance, $d_c(a,b) = d(\bar{a},\bar{b})$ between the centroids of clusters *a* and *b* to be merged, either using the raw data (with $\bar{a}$ and $\bar{b}$ being the mean values of the corresponding observations) or requiring a matrix with Euclidean distances. This means that it takes into account the internal structure, as the fusion between two sub-clusters modifies the centroid of the resulting clusters, thus its distance from the centroids of the others. The linkage algorithm of Ward (1963) creates a link (merges two clusters *a* and *b*) when the within-cluster sum of squares between the objects and the resulting cluster's centroid is minimized, compared to all other combinations of cluster fusions. The objective function to be optimized in Ward's linkage, $d_w(a, b)$, also called the "error sum of squares", is defined by Eq. 1.9:

$$d_w(a,b) = \frac{n_a n_b}{(n_a + n_b)} d_c^2(a,b) \tag{1.9}$$

where d_c is the centroid distance, as defined earlier for the centroid linkage method, n_a and n_b the size (number of objects) of subclusters *a* and *b*, respectively. Ward's linkage requires a matrix of Euclidean distances, hence it is not proper for waveform dissimilarity matrices which have a different metric. It is, however, computationally efficient, as well as a recommended option for the distinction of spatial clusters in several studies (Pirli *et al.*, 2010; Kassaras *et al.*, 2014a, 2014b; Lasocki, 2014; Zamani & Hashemi, 2004; Kapetanidis *et al.*, 2015).

1.2.2 Stopping rules / thresholds

It is meaningful to specify a certain quantity of spatial clusters to define at which point the agglomerative linkage is to be stopped. The preferred number of groups can either be considered visually, by observing the spatial distribution for evidently distinct groups that should be distinguished, or aided by a procedure such as "Mojena's stopping rule" (Mojena, 1977). This method examines the change in the fusion level against the number of clusters that are formed. If a_0, a_1, …, a_{n-1} are the fusion levels corresponding to *n*, *n*-1, …, 1 clusters, where *n* is the total number of objects, then $g = n - j$ is the optimal number of clusters, such that as the agglomerative procedure reaches up to stage *j* the following relation is true:

$$a_{n-g+1} \equiv a_{j+1} > \bar{a} + cs_a \tag{1.10}$$

where $\bar{a}$ is the mean fusion level, s_a the corresponding unbiased standard deviation, $j \in [0, n\text{-}2]$ and c is a critical value, usually in the range of 2.75 to 3.50 (Mojena, 1977) or ~1.25 (Milligan & Cooper, 1985). This can also be decided graphically, by plotting against the number of clusters either the raw or the standardized fusion level (Martinez *et al.*, 2010):

$$\frac{a_{j+1} - \bar{a}}{s_a} \tag{1.11}$$

which should have a pattern similar to a "scree plot" in applications using principal component analysis (Cattell, 1966), with a characteristic "elbow" at the optimal number of clusters, just below the critical value c if the raw levels are used. Alternatively, instead of $\bar{a}$ and s_a measured over all fusion levels, the corresponding values in Eq. 1.11 can be calculated over the first j levels (Martinez *et al.*, 2010), in what could be called "modified Mojena's stopping rule". The number of clusters can be decided graphically at one of the distinct elbows that could arise, or chosen automatically by finding the global minimum of the plot's differential, as it happens that the optimal number usually

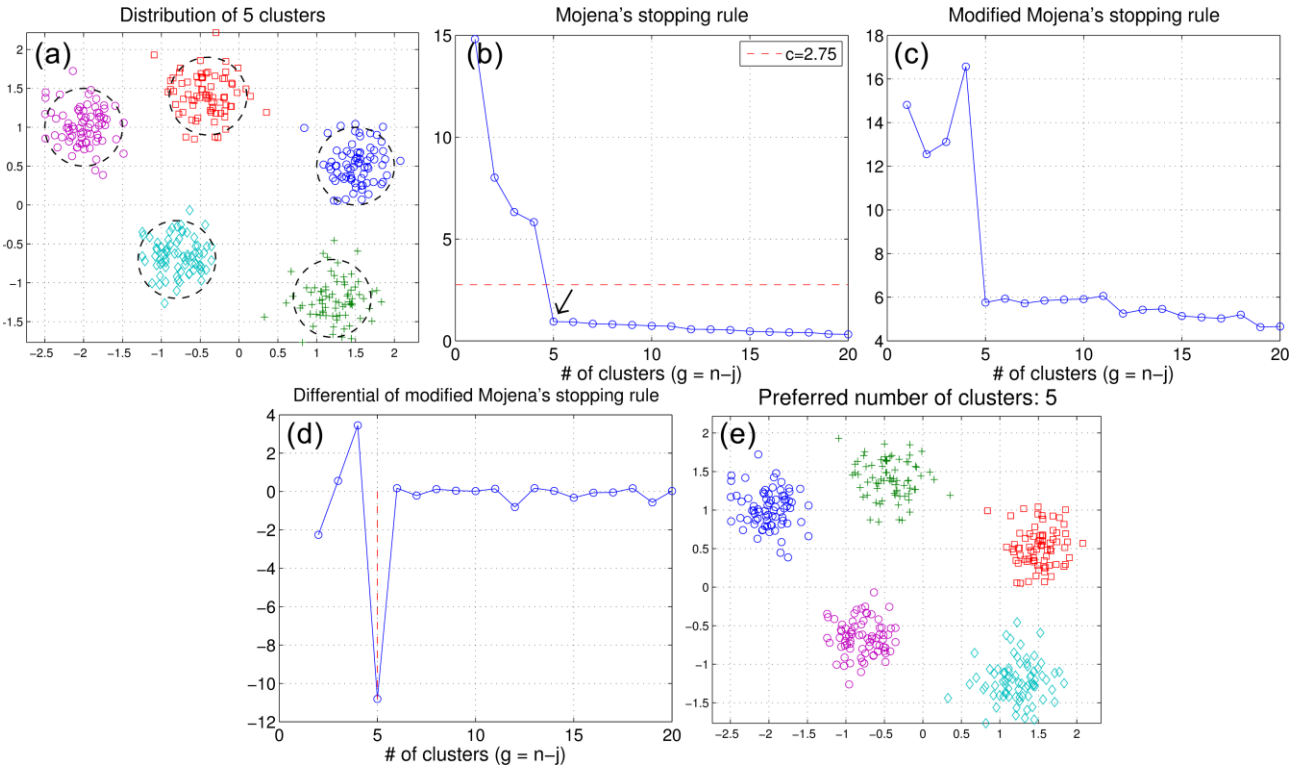

Figure 1.6: Synthetic test for the distinction of 5 non-overlapping spatial clusters using Ward's linkage (a) initial distribution and true grouping, (b) Mojena's stopping rule (Mojena, 1977), with the vertical axis corresponding to the raw fusion level where the arrow points at the "elbow" below the critical value c=2.75, indicating the preferred number of clusters, (c) modified Mojena's stopping rule (Martinez *et al.*, 2010), with the vertical axis corresponding to the standardized fusion level, (d) differential of (c) with its global minimum suggesting the preferred number of clusters and (e) the 5 reconstructed clusters with different colours/symbols indicating different clusters in random order, thus different than those of (a).

coincides with the largest step-down of the modified plot. The "scree plot" shows how much "improvement" is achieved by stopping the agglomerative clustering procedure at an earlier stage, thus breaking the distribution to a larger number of clusters. The abrupt flattening at the "elbow" shows that further division into smaller clusters is meaningless / artificial, or rather it indicates that the resolution of data does not permit the distinction of more details.

A synthetic example is presented in Fig. 1.6a, where five 2D clusters are plotted, generated by Gaussian distributions. Fig. 1.6b is an application of Eq. 1.10 on the raw fusion level and Fig. 1.6c the result of Eq. 1.11, after applying Ward's linkage and performing the calculation of the standardized fusion levels. The horizontal axis represents the number of clusters [1, 2, …, n], or equivalently [n-1, n-2, …, 0], if it represented the number of partitions, j. In this case, the five clusters are completely non-overlapping, so the algorithm can easily find the correct number either by the level where j+1 (or, equivalently, g-1, reading the plot from right to left) crosses the critical level c=2.75 (Fig. 1.6b), or by the minimum of the differential plot (Fig. 1.6d). The reconstruction is presented in Fig. 1.6e.

If, however, the distributed points of the five clusters are overlapping (Fig. 1.7a) then the elbow of the "scree plot" may not be located below the c=2.75 level, but higher. This means that it is unsafe to presume a fixed critical value. However, the differential of the modified plot (Fig. 1.7d) is still

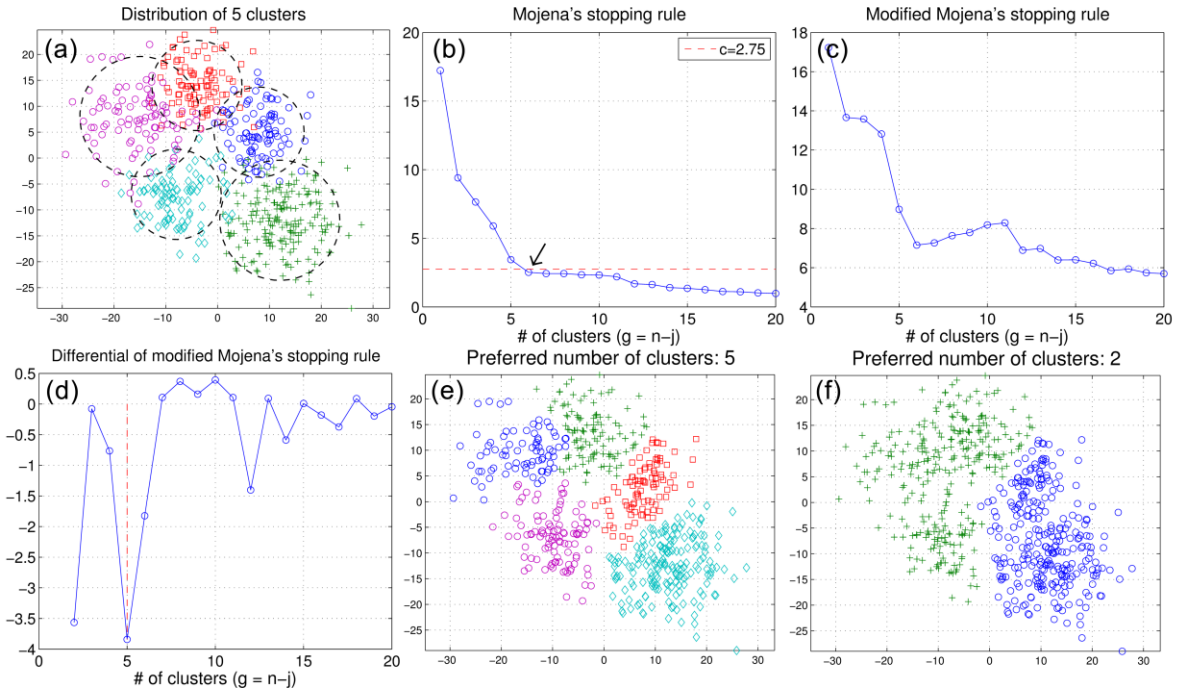

Figure 1.7: Synthetic test for the distinction of 5 partially overlapping spatial clusters using Ward's linkage (a) initial distribution and true grouping, (b) Mojena's stopping rule (Mojena, 1977) where the arrow points at the the first point below the critical value c=2.75, erroneously suggesting 6 clusters, (c) modified Mojena's stopping rule (Martinez *et al.*, 2010) indicating at least three possible elbows at 2, 6 and 12 clusters, (d) differential of (c) with its global minimum suggesting 5 clusters, (e) the 5 reconstructed clusters and (f) an alternative reconstruction using 2 clusters as indicated by the largest secondary minimum of (d).

able to detect the optimal number of clusters by the plot's minimum, without having to assume a critical level. Naturally, the reconstruction cannot be without errors at the intersecting regions (Fig. 1.7e). This problem in unavoidable when there is strong overlapping and may also lead to a false number of clusters, larger or smaller than its true value, as in Fig. 1A.2 of the Appendix, where the relatively sparser points in an overlapping region were distinguished as a separate cluster. The secondary minima of Fig. 1.7d could also indicate alternative groupings, corresponding to local "elbows" of Fig. 1.7c, for example the minimum at g=2 could sometimes be even stronger than the one at g=5, in which case the alternative reconstructions (Fig. 1.7f) must be evaluated by the analyst, depending on the grouping that is deemed more realistic for a particular case.

The above method can also be applied to a temporal distribution, e.g. origin times of earthquakes, to decide how to best separate the period of study into sub-periods that may include episodes of temporally (and, quite possibly, also spatially) clustered seismicity. However, as in the case of Fig. 1A.2, the resulting temporal segments may be such that they include intervals of sparse seismicity between sub-periods of significant seismic outbursts. A large list of various other stopping rules is presented and evaluated by Milligan & Cooper (1985).

Concerning cross-correlation values, the clustering (grouping into multiplets) has to be chosen based on different principles than those of the spatial or temporal distributions which have Euclidean distance matrices. Instead of selecting a (relatively small) preferred number of clusters, an optimal threshold value must be determined and let the cluster number be acquired from that choice. There are several different methods in the literature for the selection of a threshold or even completely different set of criteria to decide whether a subset of earthquakes actually belongs to a multiplet. Schaff *et al.* (2004) consider as a condition for two events be included in the same group that $XC_{max} + m_{coh} > 1.70$, with the mean spectral coherence, m_{coh}, being calculated in the band between 2.5 and 12 Hz. Han *et al.* (2014) require that $XC_{max}>0.8$ in at least 3 stations for a pair of events to belong to the same multiplet. Schaff & Waldhauser (2005) make a selection of events below a maximum inter-event separation distance of 5km, to avoid unnecessary processing time, and set C_{th}=0.7 for the cross-correlation of P-wave trains. They also point out that lower thresholds, such as C_{th}=0.6 or even below, may also be meaningful when the reason for the reduced XC_{max} is not the signal but the superimposed environmental noise (low SNR), which may depend on the distance from the station or the low magnitude of the events. Very low threshold, C_{th}=0.4, has been used by Okubo & Wolfe (2008) but under the condition that the separation distance is lower than 0.5 km. For correlation detector procedures, such as those presented in Sections 4.3 and 4.4, the threshold for valid similar waveforms can drop down to extremely low values, as demonstrated by Schaff & Waldhauser (2010), who measured XC_{max}=0.26 averaged simultaneously over 3 components (thus ensuring validity) between an M=2.5 and an M=5.8 event. It is important to note that such low thresholds can be valid (not triggering false positives) when the window is sufficiently large (tens to hundreds of seconds) and/or multiple channels/stations are used (Harris & Dodge, 2011).

Using a separation distance limit is a strong criterion that can be used when the hypocentral locations are previously known with adequately low uncertainties, which must be accounted for. This, however, is not possible when the signals are derived from (yet) unknown sources, or the locations are calculated by automatic procedures which may be prone to serious errors. In the latter,

some events which in reality are similar could be separated by a disproportionally large distance due to significant location errors in one or both events, so a distance limit would lead to a "miss" (false rejection). This indicates that before any such criterion is applied, automatic locations must be revised. A similar technique to reduce unnecessary processing time is to divide the data in spatial groups before applying the cross-correlation procedure. This also permits the selection of a different reference station for each cluster. However, spatial clustering also requires sufficiently small location errors, otherwise the distribution may be too "cloudy" and the sub-clusters indistinguishable or overlapping. This method is presented in several applications (Chapter 5) while the improvement of automatic locations is a major issue in Chapter 6 for the seismicity of western Corinth Rift during the period 2000-2007.

Green & Neuberg (2006) justify the selection of a correlation threshold by plotting the histogram of all correlation coefficient values between a 30-min waveform and a wavelet that is known to appear in the data. The plot has the form of a Gaussian curve that encompasses the "noisy" part of the histogram at the low positive and the negative correlation values which breaks at about 0.5, from which point on it appears constant, indicating a different distribution between highly correlated events. They choose the threshold at C_{th}=0.7, well outside the right "edge" of the Gaussian curve, which represents the correlation between random noise and the seismic wavelet. Petersen (2007) and Thelen *et al.* (2011) also use the same rule to justify their selection of threshold. Likewise, Cannata *et al.* (2013) apply a fixed threshold at C_{th}=0.8 to reliably isolate doublets which are sufficiently similar and their inter-event hypocentral distance, D, is also very small, as observed by

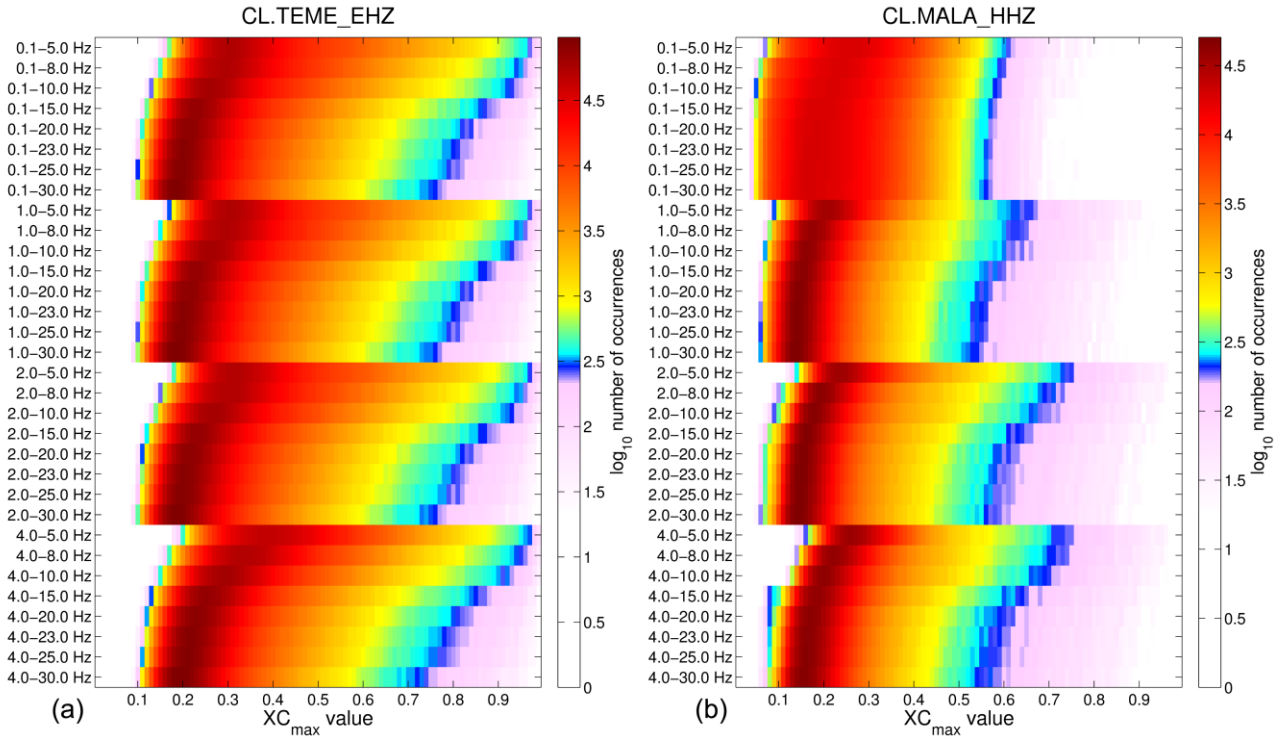

Figure 1.8: Histograms of XC_{max} values per event-pair for different band-pass filters (vertical axis) with data from the 2013 earthquake swarm in Helike (Section 5A.4) at stations TEME (short-period), within the epicentral area, and MALA (broad-band), at an average distance of 26 km from the swarm.

diagrams of XC_{max} against D. They also perform clustering separately on different stations creating station-specific families, then merge families that have been formed using data from different stations if at least one pair of events between the two families has $XC_{max}>C_{th}$.

An example of such histograms is presented in Fig. 1.8 for two stations at different epicentral distances with data from the 2013 earthquake swarm in Helike (Section 5A.4) and for a wide range of band-pass filters. The distribution generally resembles a skewed Gaussian, with a steep slope at low correlation values, while being much smoother towards high XC_{max} (positive skewness). Petersen (2007) denotes a breaking in the Gaussian at mid-high XC_{max} and even a secondary Gaussian and high XC_{max} values, representing the distribution of correlated event-pairs. Cannata *et al.* (2013) note a similar, but less distinct breaking. However, in general, the Gaussian curve may degrade too smoothly, without any apparent sign of being mixed with a different distribution at higher correlation values. It is interesting to note that the histograms are strongly dependent on the selection of the frequency band, being wider towards higher XC_{max} values when the band is narrow, especially when limited at the lower frequencies, its noisy dominant part reaching lower XC_{max} values when higher frequencies are included and being generally narrower and more restricted to low correlation values when the station is further away from the epicenters.

A new method for the selection of the optimal correlation threshold for a given correlation matrix is suggested in the present study. Nearest-neighbor clustering is performed and the various clustering configurations for a wide range of correlation values are depicted in the form of cluster size (number of events contained) against threshold value (Fig. 1.9, top). The total number of clustered events (those contained in doublets or larger multiplets, but excluding orphans). As the threshold is lowered, at some point a very large cluster is formed (main branch) which gradually integrates the smaller ones, until all events are incorporated in this one group. Naturally, the agglomerative clustering must be stopped before this occurs, as further fusion would be mostly attributed to chaining effects due to the applied nearest neighbor's linkage. It is suggested that the optimal threshold value $C_{opt.th}$ is the one which maximizes the difference between the size of the largest cluster, C_{max}, and the sum of clustered events, Σ_C. It is at this point that the main branch starts augmenting out of control, as seen in Fig. 1.9 (bottom), where the plot of the size of the largest cluster resembles a "scree plot", with the "elbow" right at the point where the abovementioned condition is true. At about the same point, the total number of formed clusters (with size $\geq 2 = C_{min}$ for doublets) begins to decrease. However, this only defines a low boundary for the threshold below which the (larger) formed groups will surely contain more than one real multiplet. It must be noted that this method does not work for farthest neighbor (complete) linkage, as the behavior of the largest cluster with respect to the sum of clustered events is very different.

In intense seismic sequences and for reference stations at local epicentral distances, $C_{opt.th}$ can be reasonably high if most of the recorded events have strongly correlated waveforms. However, if the correlated events are sparse (which can also be due to low SNR, if the station is relatively far),

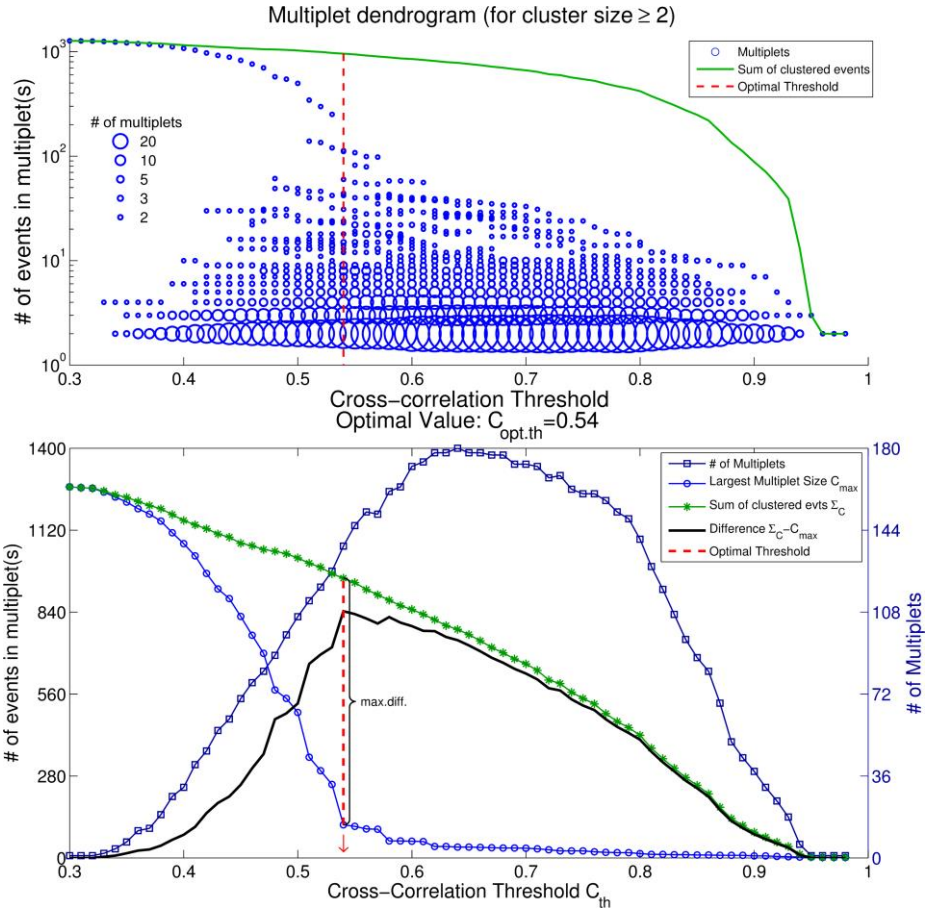

Figure 1.9: Multiplet configurations formed by cross-correlation of waveform recordings of the vertical component of station KALE for the seismicity of the 2010 Efpalio swarm (Kapetanidis & Papadimitriou, 2011), filtered between 2 and 23 Hz. (Top) Multiplet-tree diagram and selection of the optimal threshold, $C_{opt.th}$ = 0.54. Circles represent the size (number of events, logarithmic vertical axis) of multiplets formed at different correlation thresholds with their radius being proportional to the number of multiplets of the same size. The green envelope curve shows the sum of clustered events. The main branch (top-left circles) starts to develop for threshold values below the optimal. (Bottom) plots of various clustering parameters such as the number of multiplets (right vertical axis), the size of the largest multiplet (left vertical axis), the sum of clustered events, the difference between the sum of clustered events and the size of the largest multiplet and the optimal threshold, $C_{opt.th}$. This does not coincide with the threshold that creates the maximum number of clusters (solid line, left axis), here at C_{th} = 0.64. (modified after Kapetanidis & Papadimitriou, 2011)

$C_{opt.th}$ may be very low. In such cases, it is advised to use a higher threshold value to avoid the formation of inconsistent groups, or recalculate the dendrogram of Fig. 1.9 with a slightly higher C_{min} value (instead of the default C_{min}=2, for doublets), excluding the smaller clusters. Alternatively, a different band-pass filter can be used to acquire a higher threshold value. Some tests for the values of $C_{opt.th}$ with respect to the corresponding frequency band are presented in Fig. 1.10, using data from the spatial Group #4 of the 2004 seismicity in the western Corinth Rift (Section 6.3.5). It is an intense swarm that occurred within the gulf, ~6-7 km offshore Aigion, with a large number of correlated events. One of the closest stations, primarily suggested as a reference station, is DIMT (or DIM) of the Corinth Rift Laboratory network, at about 7.5 km from the

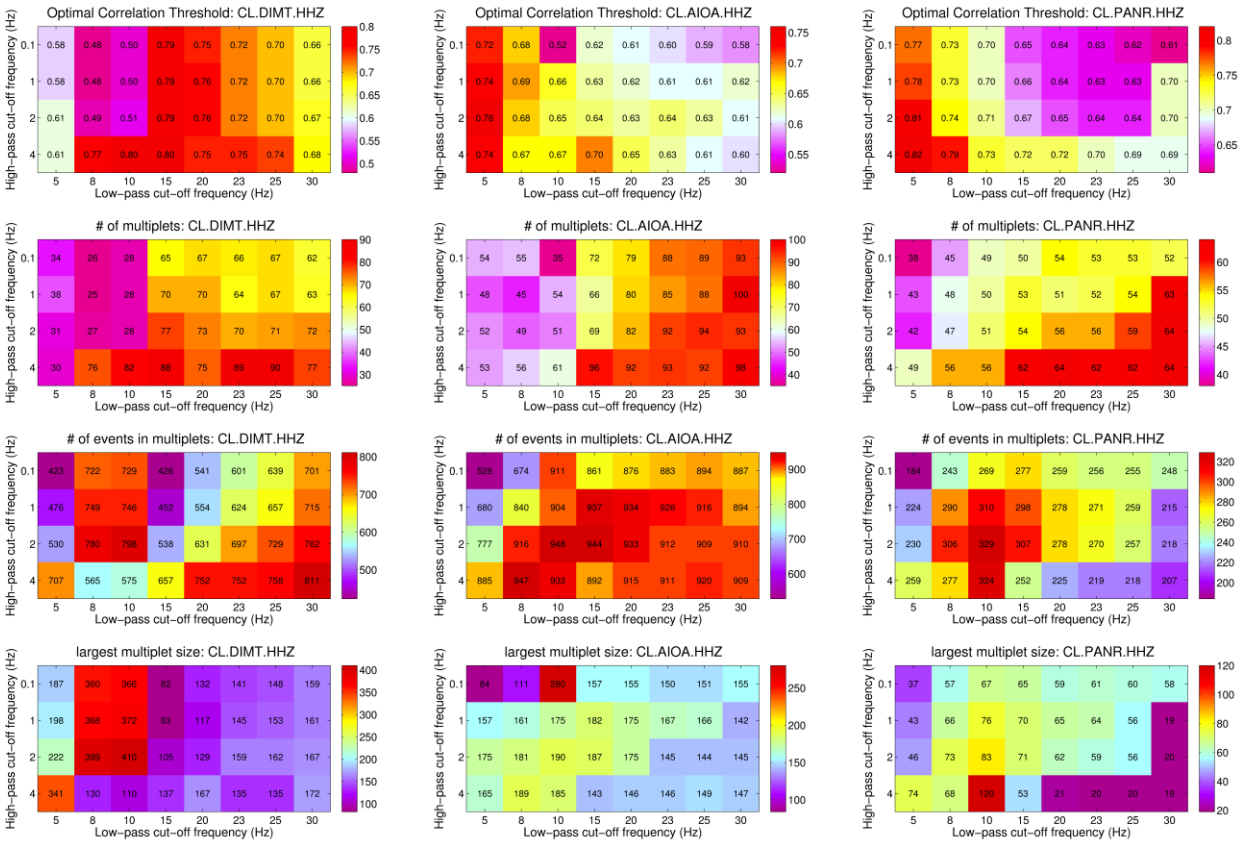

Figure 1.10: Correlation thresholds (top) and other values for multiplets formed using different band-pass filters for events of the seismicity of the western Corinth rift in 2004, Group #4 (Section 6.3.5) using data from the vertical component of stations DIMT, AIOA and PANR, at average epicentral distances 7.5, 13 and 17km, respectively, with C_{min}=2. The high-pass and low-pass cutoff frequencies are represented by the vertical and horizontal axes, respectively. Thresholds are defined at the value which maximizes the difference between the size of the largest multiplet (panels in the last row) and the sum of clustered events (panels in the second row from the bottom).

centroid of the group. With C_{min}=2, the highest thresholds are acquired when the cutoff frequency of the low-pass filter (f_{LP}) is about 15-20 Hz, independently of the corresponding high-pass cut-off frequency (f_{HP}), as the station's sensor is a short-period instrument and its waveforms have minimal long-period noise. The high-pass filter starts affecting the threshold when f_{HP} becomes high enough (f_{HP}=4 Hz) to start altering the lower frequency content of the earthquake signals themselves. The threshold values range between ~0.5 and ~0.8, depending on the band-pass filter. By examining the multiplet dendrogram itself (Fig. 1.11), it appears that there are significant differences in the branching between the 2-10 Hz and the 2-23 Hz bands. In the first one, $C_{opt.th}$ is very low (0.51) and there are very few multiplets with size > C_{min} and smaller than the largest cluster at lower thresholds (they fuse with the largest one almost immediately).

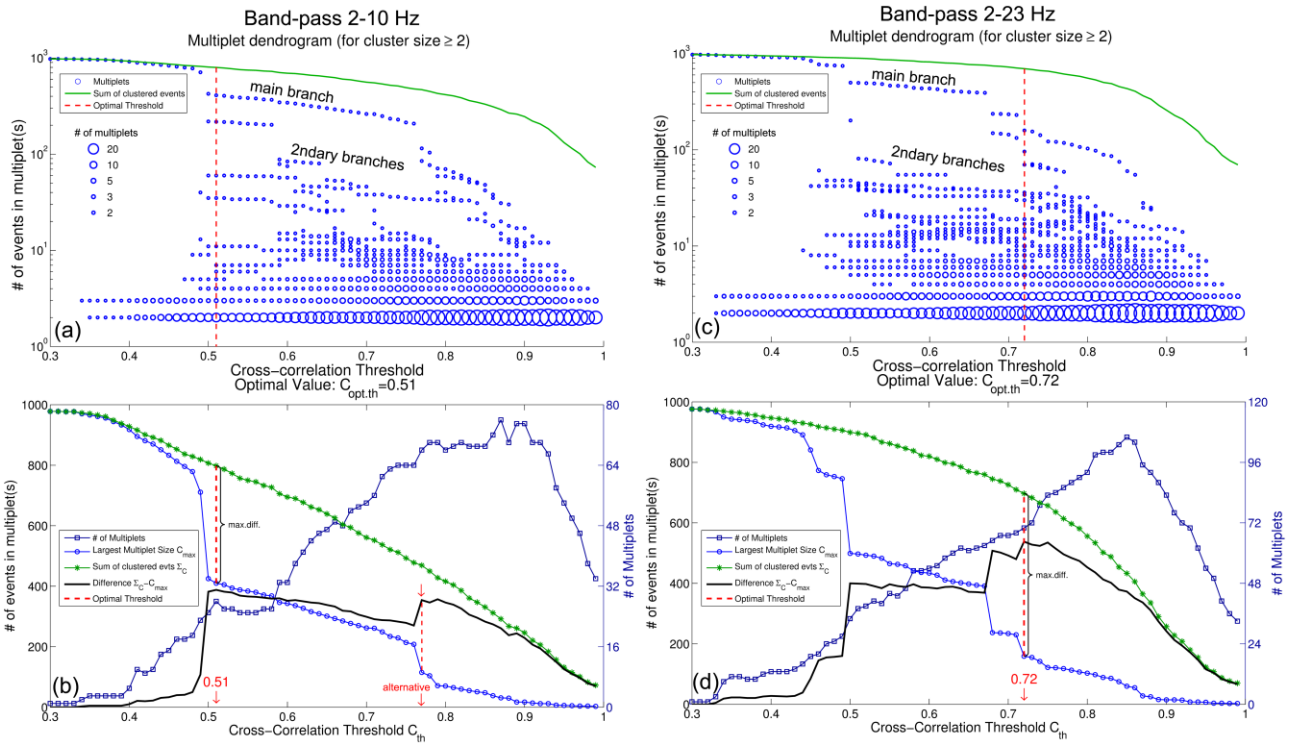

Figure 1.11: Multiplets formed for the seismicity of 2004, Group #4 in the western Corinth rift (Section 6.3.5), station DIMT, vertical component, using different band-pass filters (a,b) at 2 – 10 Hz and (c, d) at 2 – 23 Hz. (a, c) multiplet dendrograms, same as the top panel of Fig. 1.9, (b, d) plots of various clustering parameters, same as the bottom panel of Fig. 1.9.

On the other hand, in the band 2-23 Hz, $C_{opt.th}$=0.72 and the multiplet dendrogram shows that quite a few large multiplets can be formed for lower thresholds between 0.5 and 0.7, before they all fuse with the largest one. This is a result of the simplification of waveforms that occurs when the higher frequencies of the signals, thus, their complexity, are reduced. An alternative, and better choice, of threshold for the 2-10 Hz band would be C_{th}=0.77, as what could be called "the main branch" emerges at C_{th}=0.76, with many of the largest multiplets being fused. In this case, increasing C_{min} could possibly alter the $C_{opt.th}$ choice, however this is not the case for this particular example, as $C_{opt.th}$ drops to 0.5 for C_{min}>6. If a low frequency band is required and the dendrogram behaves in such a way, it is suggested that $C_{opt.th}$ is used as a minimum C_{th} value, but a better choice would be a higher threshold that should be set manually at the point where the largest cluster size is reduced abruptly due to its division into many smaller multiplets. Increasing the frequency band at 2-23 Hz increases complexity and the smaller multiplets are fused more gradually into the main branch. In such circumstances, the $C_{opt.th}$ criterion can indeed select an optimal threshold value high enough to ensure adequate waveform similarity. In general, it is safer to set an absolute lower threshold at e.g. $C_{th.min}$=0.6 to override values of $C_{opt.th}$<$C_{th.min}$ and avoid thresholds which could create highly inconsistent clusters, but this depends on the type and quality of data, the application's requirements and the SNR conditions at the reference station. As mentioned above, another reason for the reduction of XC_{max} when higher frequencies are retained may be attributed to differences in the source time function (Nakahara, 2004), which means that the events/multiplets which are fused into larger groups at lower frequencies could also have larger magnitude differences.

Another example presenting the dependence of C_{th} and other clustering values on the frequency band is presented in the Appendix (Fig. 1A.3) for the seismic swarm of 2013 in Helike (Section 5A.4; Kapetanidis *et al.*, 2015), including two stations with broad-band instruments. For the closer stations, TEME and LAKA, the various values are, in general, comparable, despite the different distances and sensors. In both cases the thresholds increase with decreasing low-pass filter cut-off frequency. The major difference is that in LAKA station, due to the broad-band sensor and the larger epicentral distance (smaller SNR), at the lowest high-pass filter cut-off frequency (0.1Hz) the threshold drops significantly, as the smaller events are super-imposed on the long-period background noise. A high-pass filter with a reasonably high f_{HP} is required (at 1 Hz or 2 Hz) to remove this trend before the signals are cross-correlated. At the more distant station MALA, the results are very different. Despite the lower $C_{opt.th}$ values, the number of multiplets as well as the total number of events within them is significantly lower. The only common characteristic is that, being equipped with a broad-band sensor, at f_{HP} = 0.1Hz the behavior is similar to that of LAKA, while in TEME there is not much difference with either 0.1 Hz or 1 Hz.

For the case of microearthquakes recorded by stations in local distances, Kapetanidis & Papadimitriou (2011) have performed extensive tests with correlation detectors in a wide range of frequency bands (Section 4.3.2). The tests have shown that a frequency range between 2.5 Hz and 23 Hz is usually adequate for a default filter. The 2.5 Hz corner frequency of the high-pass manages to remove the long-period trend, which can be significant in broad-band stations, while the low-pass filter at 23 Hz preserves enough signal complexity in the waveforms to enhance the distinction between neighboring multiplets. Similar frequency bands, permitting frequencies higher than 10 Hz, have also been used for cross-correlation by other authors in the literature (Scarfì *et al.*, 2003; Carmona *et al.*, 2009; Häge & Joswig, 2009; Chun *et al.*, 2010; Yukutake *et al.*, 2010). It is important that the filter is focused in the frequency range where the signals are coherent (Kita *et al.*, 2010), include their dominant frequency (Massin *et al.*, 2013) and also aim to improve or retain adequate signal-to-noise ratio (Hemmann *et al.*, 2003; Massa, 2010). A wider frequency range is also useful to prevent cycle-skipping (Akuhara & Mochizuki, 2014). However, frequencies below 10 Hz have been preferred in other studies (Shearer, 1998; Massa, 2010; Myhill *et al.*, 2011; Massin *et al.*, 2013; Pirli *et al.*, 2013; Vavryčuk *et al.*, 2013), which may depend on factors such as the type of earthquakes (e.g. volcano-tectonic), the longer epicentral distances or, simply, the requirement for less waveform complexity to achieve higher correlation coefficients.

An example of similar waveforms from the 2013 Helike swarm (Kapetanidis *et al.*, 2015; Section 5A.4) recorded at the vertical component of station LAKA, situated at an epicentral distance of ~10 km, is presented in Fig. 1.12. While, in this case, the lowest XC_{max} value is 0.795 (the bottom waveform compared against the top one), there can be many events in the same multiplet with their waveforms having an XC_{max} value well below the C_{th}, when compared against the top waveform of Fig. 1.12 due to the nearest neighbor linkage. The same events are presented in Fig. 1.13 from recordings of station TEME, situated within the epicentral region, but in the same order and using the same filter (2.5 Hz - 23 Hz) as in Fig. 1.12. It is worth noting that, in this case, the degree of similarity between individual waveforms and the top one is significantly different than in Fig. 1.12.

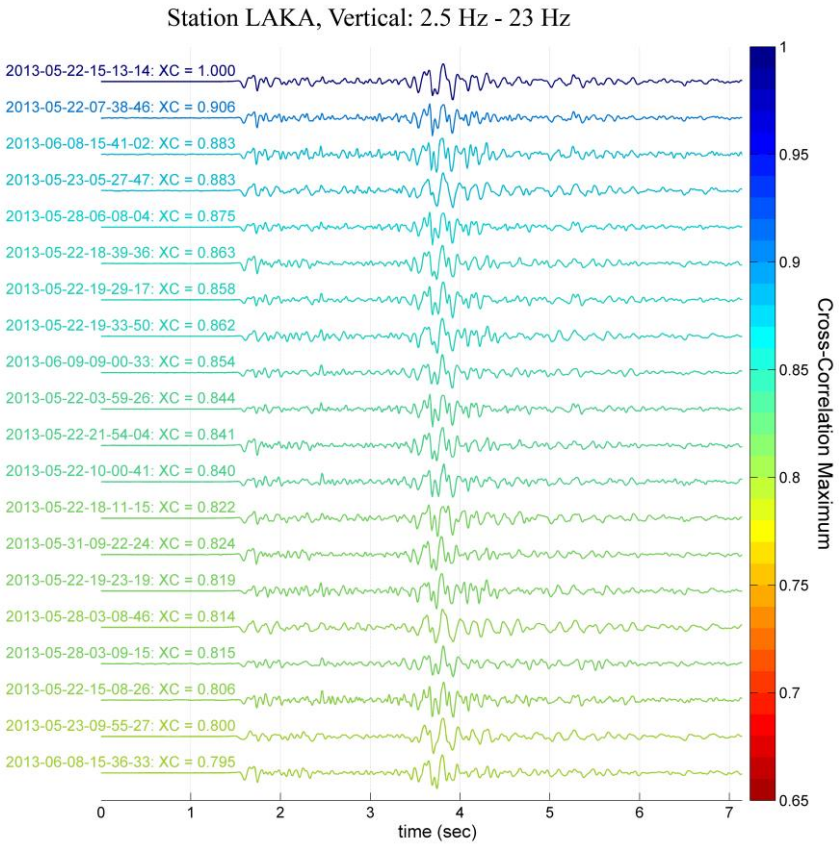

Figure 1.12: Waveform recordings from a multiplet during the 2013 Helike swarm (Section 5A.4; Kapetanidis *et al.*, 2015) on the vertical component of station LAKA, filtered between 2.5 and 23 Hz. The waveforms are sorted by order of their similarity to the first one at the top. Colours refer to the $XC_{\max}$ value for the cross-correlation of each waveform with the one at the top of the stack (indicated as *XC*).

Although the station is very close to the epicenters, thus the signal-to-noise ratio is expected to be larger than in LAKA, many XC_{max} values are below 0.7. There are, also, significant variations in the relative amplitudes of the S-waves, which in some cases are largely responsible for the reduction of XC_{max}. The low correlation values are not due to noise, but can be mainly attributed to changes in the radiation pattern caused by variations of either the focal mechanisms (or the relative position of the station on the stereo-net) or in the hypocentral locations, especially the focal depth. The former is more significant for stations such as TEME, within the epicentral region and most likely near the P-axis, than for stations at longer distances. The latter may introduce extra phases in the wave-train due to reflections/refractions on small-scale discontinuities in the crustal structure. This situation is partially improved, similarity-wise, when a stronger filter is applied between 2.5 Hz and 10 Hz, removing the higher frequencies in the 10 Hz - 23 Hz band (Fig. 1.13_B). While the radiation pattern effects still remain (polarities and S/P amplitude ratios) and the time-lags, t_m, are unchanged, the waveform complexity is reduced, leading to larger XC_{max} values. This increases the tolerance and enables more events to be grouped in the same multiplet, which may be necessary when similar events are scarce. However, the wider 2.5 Hz - 23 Hz band is useful when the enhancement of dissimilarities between neighboring multiplets is required. This allows for the distinction of several sub-clusters within the swarm, which would have been merged if a narrower band was used.

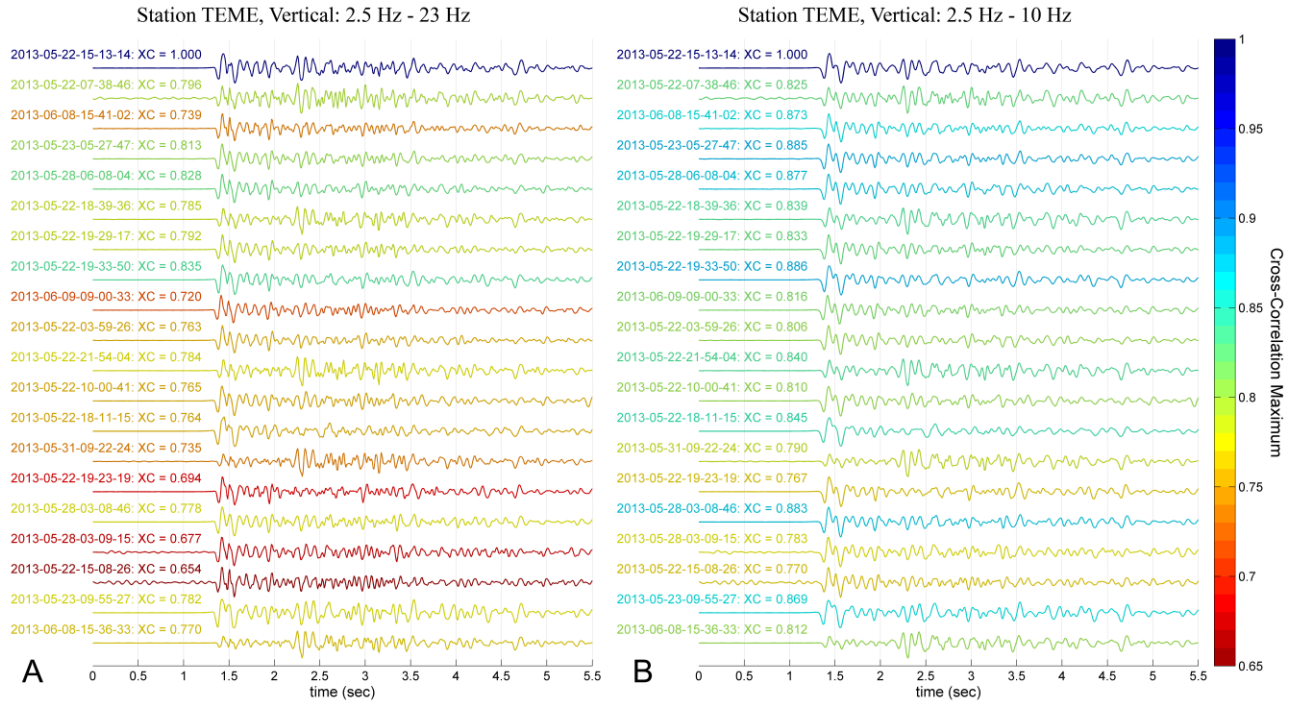

Figure 1.13: Waveform recordings for the same events as in Fig. 1.12, but recorded in station TEME, A) filtered between 2.5 and 23 Hz, B) filtered between 2.5 and 10 Hz. The waveforms are sorted by the same order as in Fig. 1.12, regardless of their similarity to the first one at the top. Colours refer to the XC_{max} value for the cross-correlation of each waveform with the one at the top of the stack (indicated as XC).

The optimal correlation threshold, $C_{opt.th}$, typically drops with increasing L_{XC} (total number of samples of the time-series being compared), as presented in Fig. 1.14. The XC_{max} values tend to be, on average, larger for smaller sample lengths, but the statistical significance of the correlation becomes lower, increasing the risk for two irrelevant signals to be registered, by accident, as being highly correlated. Thus, it is safer to use the largest windows permissible, despite the lower threshold. As window length increases, the respective multiplet dendrogram (see Appendix, Fig. 1A.4) appears to shift towards lower thresholds. At the same time, the stronger multiplets (at high thresholds) tend to "unwrap"; they require a lower threshold before they fuse into larger ones. As a result, the multiplet dendrogram becomes more "detailed". The optimal threshold simply follows the "elbow" of the largest multiplet's size that shifts towards lower values. The total number of multiplets may remain constant, due to the reduction of $C_{opt.th}$, except for low window lengths (and still high $C_{opt.th}$), where the behavior of the clustering values can be drastically different. At average window lengths (S-waves included) and unless $C_{opt.th}$ changes abruptly (selects a different "elbow"), the size of the largest multiplet remains almost the same as $C_{opt.th}$ slowly decreases. At some point, increasing the window length does not provide more information but rather fills the time-series with uncorrelated noise. This can cause $C_{opt.th}$ to halt at a constant value or decline very slowly, while the number of multiplets begins to increase but C_{max} and Σ_C typically decrease. Apparently, this may begin to occur at different window lengths when different band-pass filters are used (Fig. 1.14). The reduction of $C_{opt.th}$ with increasing L_{XC} is a generally observed feature; however the behavior of the other values may vary, depending on the data.

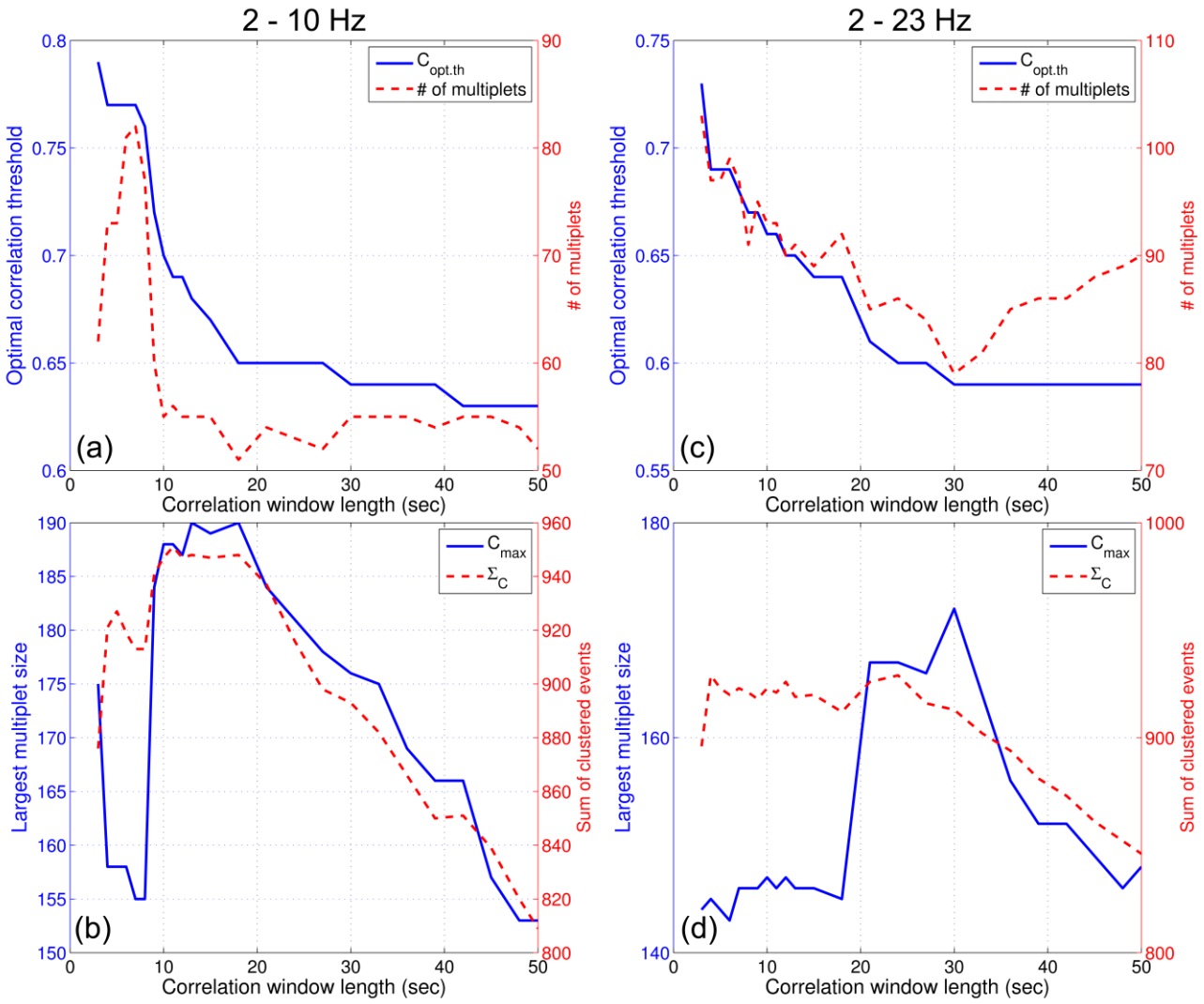

Figure 1.14: Correlation thresholds and other values for multiplets formed using different correlation window lengths (L_{XC}) for events of the seismicity of the western Corinth rift in 2004, Group #4 (Section 6.3.5) using data from the vertical component of station AIOA at average epicentral distance 13km, (a, b) using a 2 – 10 Hz band-pass filter, (c, d) using a 2 – 23 Hz band-pass filter. The optimal correlation threshold, $C_{opt.th}$ is selected as the value that maximizes the difference between the size of the largest multiplet, C_{max}, and the sum of clustered events, Σ_C.

1.2.3 Internal structure of multiplets

An insight into the changes in the internal structure of the formed multiplets with varying correlation threshold can be explored by plotting the average XC_{max} value of all combinations of pairs within formed multiplets, excluding pairs that belong to different multiplets. This is presented in Fig. 1.15 in an example with 3 different L_{XC} values, but in the form of average dissimilarity (1 – $\overline{XC_{max}}$) to better resemble a "scree plot", as in Fig. 1.6b for spatial clustering with Ward's linkage. While the general pattern is similar for all 3 curves, the preferred "elbow" points corresponding to $C_{opt.th}$ are different for each L_{XC} value. As in the case of spatial clustering, "elbow" points at higher

thresholds / lower average dissimilarity can be reckoned as possible alternative choices that may provide interesting cluster configurations. The average dissimilarity is higher than 1-C_{th} due to the nearest neighbor linkage, which permits pairs of events within the same multiplet to have $XC_{max}<C_{th}$. At lower thresholds, the formed clusters, especially the larger ones, can become highly inconsistent, which is why $(1 - \overline{XC_{max}})$ may become high. On the contrary, had "farthest neighbor" linkage been applied, the dissimilarity would always be smaller than 1-C_{th}, as event-pairs within a multiplet would have, strictly, $XC_{max}\geq C_{th}$.

Large groups may require re-evaluation and their internal structure be re-examined for possible bridging effects which may indicate that they should be further divided into smaller multiplets. To reduce this problem, a combined cross-correlation matrix can be constructed, taking into account multiple components or reference stations that may give a different "perspective" to the degree of waveform/source parameters similarity for a given pair of events. A suggested combination (Kapetanidis *et al.*, 2010) is the RMS value of the individual XC_{max} values derived for each pair of events, e.g. for three correlation matrices that correspond to the three components of a single station:

$$XC_{max} = \frac{1}{\sqrt{3}}\sqrt{XC^2_{max,Z} + XC^2_{max,N-S} + XC^2_{max,E-W}} \tag{1.12}$$

Taking into account multiple components ensures that some special cases of event-pairs that could be erroneously considered as similar are excluded. For example, two events at different azimuths but the same epicentral distance and depth could possibly produce similar waveforms at the vertical component, on the condition that the velocity structure is such that the ray-paths and travel-times for both events are roughly similar and the position of the station relative to the respective radiation patterns is such that the moment tensor coefficients are also similar. An even more restrictive option is to average the cross-correlation function across all components simultaneously, eventually creating a "stacked" correlation-function (Schaff, 2008; Schaff & Waldhauser, 2010). This method takes advantage of constructive/destructive interference to reduce the noisy part and enhance the correlated signal. Multi-channel correlation detector schemes are also applicable in seismic arrays where they are able to reduce the detection threshold by up to 1.3 orders of magnitude compared to more classical methods such as STA/LTA (Gibbons & Ringdal, 2006; Junek *et al.*, 2014). Using more than one reference stations in the combined cross-correlation matrix may also enable the inclusion of multiplets from parts of a certain sequence that may be too distant for a single station to record with adequate SNR, or even fill data gaps (e.g. Section 5.4).

1.3 Earthquake patterns

The rather flexible term "earthquake patterns" applies to significant characteristics of the observed seismicity and its statistics which tend to attract the scientific attention, as they can provide insights to the underlying physical processes (Wyss *et al.*, 1999). Patterns can be anomalies from otherwise stable values, e.g. seismicity rate anomalies, such as seismic quiescence (Enescu & Ito, 2001), spatio-temporally clustered seismicity disturbing an otherwise stationary background or a temporal change in the *b*-value of the G-R law, are among the patterns with an additional potential as a

premonitory phenomenon. They can also be characteristics of seismicity that tend to recur in a certain motif, such as the temporal decay of aftershocks, following a major earthquake (Omori, 1894). Quasi-periodic or otherwise repeating phenomena are also regarded as patterns, e.g. recurrence intervals for earthquakes (Waldhauser *et al.*, 2004; Shelly, 2010). Multiplets themselves are patterns, as their equivalent term "repeating earthquakes" indicates. This section examines the relation between multiplets and spatio-temporal patterns of seismicity, as well as magnitude-time earthquake patterns and their causative physical mechanisms.

Earthquakes with similar source parameters indicate stress release and repeated slip on the same patch of a fault surface. This can happen due to inhomogeneities in the material's strength and respective irregularities in the stress-field at barriers or asperities (Geller & Mueller, 1980). With increasing data coverage from various seismogenic zones, it soon became apparent that repeating earthquakes are a commonly occurring phenomenon, especially related to spatio-temporally clustered seismicity.

Various models have been proposed in the literature to explain the phenomenon of repeating earthquakes depending on the conditions. Aki (1984) suggested that there are two types of repeating earthquakes, those whose amplitudes are similar ("asperity" type) and those whose amplitudes may differ by more than one order of magnitude ("barrier" type). Interestingly, the latter refer to events with a similar high frequency content and corner frequencies which only differ in their spectral amplitude level, thus no source-duration difference that would affect the waveforms' shape and cause $XC_{\max}$ to drop as in Fig. 1.5.

The *b*-values are considered to be inversely proportional to the regional stress, which is why they are typically used as a stress-meter (Schorlemmer *et al.*, 2005). Low *b* is related to high regional shear stress (Wyss, 1973), while, on the contrary, high *b*-values are usually associated with seismicity that causes small stress drops. Creeping or highly fractured sections of faults usually exhibit very high *b*-values while locked sections are characterized by much lower ones (Schorlemmer *et al.*, 2005). For a certain region, precursory foreshock sequences are usually characterized by lower *b*-values, while the respective aftershock sequences have relatively higher *b*-values (Suyehiro *et al.*, 1964). Spatial mapping of *b*-values can reveal regions with anomalously low *b*-values, indicating asperities where strong earthquakes are likely to occur (Wiemer & Wyss, 1997). Such anomalies can be detected even after the occurrence of a mainshock, within the aftershock zone, marking possibly unbroken, locked regions (Bayrak *et al.*, 2013). Concerning earthquake swarms, unusually high *b*-values, reaching up to 2.5, have often been observed in their frequency-magnitude distribution in volcanic areas (Smith *et al.*, 2004; Legrand *et al.*, 2011), while in other regions they may be either slightly above or below unity (Jenatton *et al.*, 2007; Ibs-von Seht *et al.*, 2008; Pacchiani & Lyon-Caen, 2010; Telesca, 2010; Kapetanidis *et al.*, 2015).

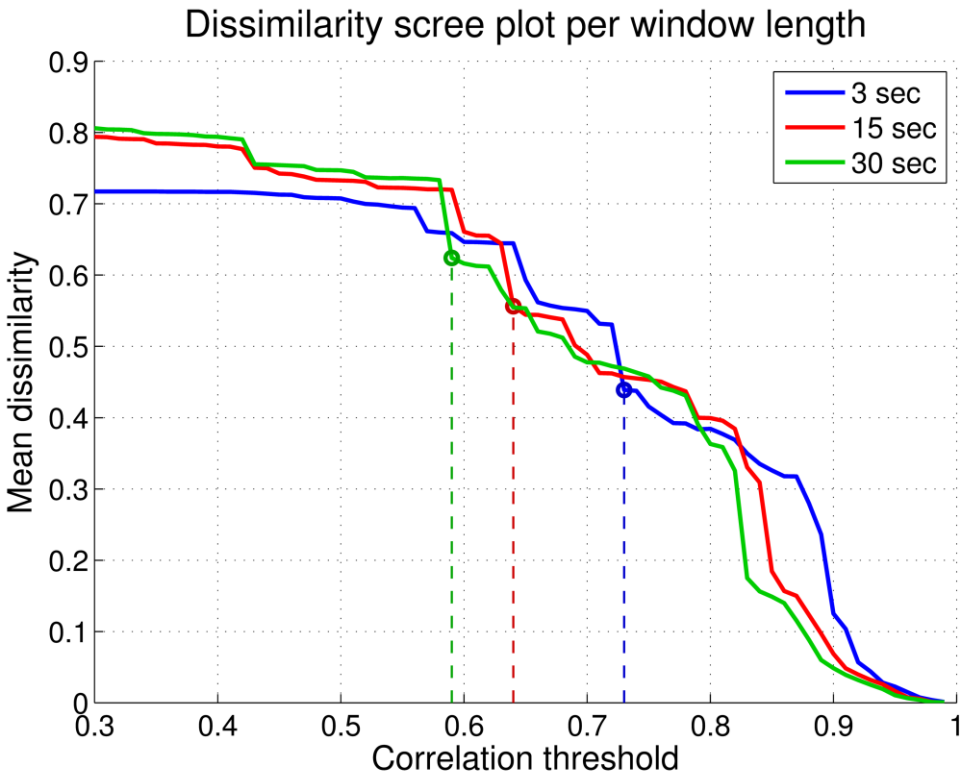

Figure 1.15: Mean dissimilarity level ($1 - \overline{XC_{max}}$) between all combinations of pairs of events that belong to the same multiplet for cross-correlations performed at 3 different window lengths (see legend) for events of the seismicity of the western Corinth rift in 2004, Group #4 (Section 6.3.5) using data from the vertical component of station AIOA. Encircled values marked with vertical dashed lines represent the corresponding optimal thresholds, $C_{\text{opt.th}}$.

1.3.1 The mainshock-aftershock sequence

The most common and significant earthquake pattern is the (foreshock-) mainshock-aftershock sequence. A major event, called mainshock, causes slip to an extensive area of a fault's surface and rearranges the stress-field. A sequence of aftershocks may begin to occur immediately after the mainshock, at a rate that typically follows an inverse power law decay, according to the Omori-Utsu or modified Omori's formula (Utsu, 1961):

$$n(t) = \frac{K}{(c+t)^p} \tag{1.13}$$

where $n(t)$ is the frequency of aftershocks per unit time interval at time t, and K, c, p are constants, with K depending on the lower magnitude boundary (typically the magnitude of completeness, M_c, of the G-R law for the aftershock distribution), c of the order of 0.01 to 1 or more days is a temporal shift representing "days after the mainshock" from which point on the law applies, with c=0 corresponding to a straight line in the log-log domain while c>0 adds a delay, and p, usually in the range 0.9-1.5 (Utsu *et al.*, 1995), controls the rate of change, with p=1 in the original formula of Omori (1894). However, the re-distribution of stress after the mainshock cannot explain on its own the delayed occurrence of aftershocks with a decaying rate, as these stress changes are nearly

instantaneous. Schaff *et al.* (1998) studied the seismicity in the aftershock zone of the 1989 Loma Prieta M7.1 earthquake and observed that, in a time-span of several years, repeating events within individual multiplets have recurrence times that follow Omori's law and proposed a model with stress-loading driven by creep at a rate that decays exponentially. Repeating aftershocks occur at fault patches that remain unbroken by the major event following a stick-slip mechanism.

Even without a mainshock, an aseismically creeping fault surface could include asperities where stress concentrates and accumulates until the threshold of material strength is reached and an asperity either breaks all at once or gradually at a large number of smaller slip events, with similar source parameters, controlled by the rate of creep (Beeler *et al.*, 2001). Seno (2003) considered a fractal asperity model where asperities are circular and each contains even smaller circular asperities and so on, embedded in a region called "barrier" that can be "invaded" by elevated pore-pressure. Rupture of an asperity within an invaded barrier can potentially cause breakage of neighboring asperities, due to low friction, leading to the slip of a larger area and producing a larger earthquake.

1.3.2 Earthquake swarms

Earthquake swarms are another significant type of seismic pattern, very commonly associated with the occurrence of repeating earthquakes. Swarms are bursts of increased seismic activity which, unlike the mainshock-aftershock sequences, lack a distinct, strong, initiating event that would also explain the spatial extent of the activated zone (Mogi, 1963; Zobin & Ivanova, 1994). Instead, they may contain several major events of comparable magnitude. The strongest one often occurs in the middle or towards the end, rather than the beginning of the sequence (Ferrucci & Patanè, 1993; Vidale & Shearer, 2006; Lohman & McGuire, 2007; Legrand *et al.*, 2011), however this is not always the case (Benetatos *et al.*, 2004; Lyon-Caen *et al.*, 2004). Swarms are mostly observed in volcanic settings (Hill, 1977; Bianco *et al.*, 2004; Smith *et al.*, 2004; Massin *et al.*, 2013; Sigmundsson *et al.*, 2014) but they have also been known to occur in non-volcanic regions (Jenatton *et al.*, 2007; Lohman & McGuire, 2007; Ibs-von Seht *et al.*, 2008; Roland & McGuire, 2009; Pacchiani & Lyon-Caen, 2010; Telesca, 2010). Mogi (1963) has suggested that swarms may occur in highly fractured zones or otherwise heterogeneous media. These conditions, combined with a gradual accumulation of regional stress, enable the local concentration of high stress in a multitude of cracks or small faults. In case this volume is seismically activated, the lack of a distinct major active fault limits the maximum magnitude potential, as well as the spatial extent of a generated swarm. Such conditions can be present in volcanic environments (Hill, 1977) or at the intersection of buried tectonic features (Bisrat *et al.*, 2012). Static stress changes caused by a swarm itself can play an important role in its evolution, especially in cases where the observed activity leaps abruptly to different focal areas (Aoyama *et al.*, 2002).

Swarms can also be caused by a source of highly localized stress. This mechanism usually implicates pressurized fluids, either of magmatic nature (Hill, 1977; Ferrucci & Patanè 1993; Sigmundsson *et al.*, 2014), hydrothermal activity (Bianco *et al.*, 2004; Massin *et al.*, 2013), meteoric origin (Kraft *et al.*, 2006; Jenatton *et al.*, 2007; Leclère *et al.*, 2012; Kassaras *et al.*, 2014b) or mantelic CO_2 degassing (Fischer *et al.*, 2014), which alter the stress-field and trigger seismicity

(Roland & McGuire 2009; Smith *et al.*, 2004; Hainzl & Ogata, 2005). A very characteristic pattern related to fluid-driven swarms is the migration of seismicity. Fluids are diffused at high pressure through the micro-crack network, increasing pore-fluid pressure while reducing the effective normal stress on pre-existing fractures, causing seismicity to expand radially away from the initial source of injection (Shapiro *et al.*, 1997; Fournier, 1999; Hainzl *et al.*, 2012), usually at low rates of 10-100 m/day (Pacchiani & Lyon-Caen, 2010; Kassaras *et al.*, 2014b). This phenomenon has been well documented in cases of seismicity induced by hydraulic fracturing (Fehler *et al.*, 1998; Parotidis *et al.*, 2005; Albaric *et al.*, 2014). The fluid-driven mechanism of swarms and the possible presence of asperities provide favorable conditions for the generation of repeating earthquakes (Hemmann *et al.*, 2003; Bourouis & Bernard, 2007; Bisrat *et al.*, 2012; Massin *et al.*, 2013).

1.3.3 Hydraulic diffusion

Shapiro *et al.* (1997) proposed a model for the spatio-temporal migration of induced seismicity by the injection of highly pressurized fluids at the KTB hydraulic-fracturing experiment, to estimate the average local permeability of the crust. The mechanism behind pressurized-fluid-induced seismicity is suggested to be the relaxation of the pore-pressure in fractured, saturated rocks. When the rocks are near a critical state of failure equilibrium, small perturbations in the pore-pressure can cause enough change in the effective normal stress to trigger earthquakes (Shapiro *et al.*, 2003). The model is based on the diffusion equation for the distribution of pore-pressure, p:

$$\frac{\partial p}{\partial t} = D \cdot \nabla^2 p \tag{1.14}$$

where D is the hydraulic diffusivity, which is related to the permeability, k:

$$D = Nk/\eta \tag{1.15}$$

where N is the poro-elastic modulus and η is the pore-fluid dynamic viscosity. Shapiro *et al.* (1997) note that k (and, consequently, the parameter D) can be highly variable even at neighboring regions due to the strong influence of cracks and other heterogeneities of the pore-space. In general, D in the crust is expected to vary between 0.01 and 10 m^2/s (Scholz, 2002). They observed that the spatio-temporal distribution gradually expands to regions further away from the source of injection. While the seismicity is mostly intense in the vicinity of the source, earthquakes begin to appear at increasingly larger distances, though at lower rates due to pore-pressure relaxation.

The expanding radius, $r(t)$, also called the "triggering front", as it bounds the seismically activated region around the injection source (Fig. 1.16), follows the relation of Eq. 1.16 (Shapiro *et al.*, 1997):

$$r(t)_{t>t_o} = \sqrt{4\pi D(t - t_o)} \tag{1.16}$$

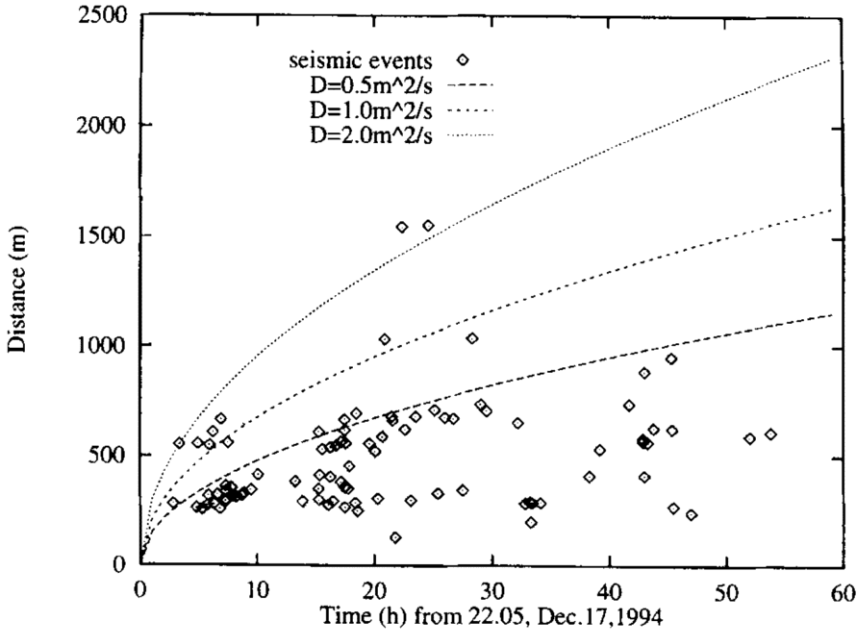

Figure 1.16: Distances of the induced microseismic events at the KTB site from the center of the injection source with respect to their occurrence times relative to the beginning of the injection. The parabolic curves are derived from Eq. 1.16. (Figure after Shapiro *et al.*, 1997)

where t is the time since the beginning of the injection at t_o. Eq. 1.16 requires the location of the injection source and the starting time, t_o, which can be known or better constrained in hydraulic-fracturing experiments. However, in non-controlled environments, the position, geometry of the source and t_o are generally unknown and have to be determined by the spatio-temporal evolution of seismicity. Eq. 1.16 also ignores the direction of migration and sometimes earthquakes may occur further/earlier than the $r(t)$ envelope for a given D value. If such events are indeed induced by pressurized fluids, this may indicate the presence of another triggering front, corresponding to higher hydraulic diffusivity, towards a different fracture zone with increased permeability, which is why it is reasonable to draw multiple parabolic envelopes for a limited set of D values. Earthquake migration during swarms usually occurs along narrow structures, either unilaterally (e.g. Section 5A.2; Kassaras *et al.*, 2014b) or bilaterally (e.g. Section 5.4 and Chapter 6), most likely asymmetrically with respect to its starting point. In such cases, a spatio-temporal projection along the most prominent direction of migration, instead of radial expansion, may provide more specific information.

The simple hydraulic diffusion model has been applied in several studies where migration of seismicity has been observed in combination with the occurrence of repeating earthquakes. Pacchiani & Lyon-Caen (2010) examined the migration pattern of the 2001 Agios Ioannis swarm in western Corinth, Greece (group #5 of 2001 in Chapter 6), and suggested a set of D values in the range of 0.08-0.20 m^2/s using the same source location but different injection starting times. Godano *et al.* (2013) measured D between 0.75 and 1.00m^2/s and a migration rate of ~100m/day for the 2010 swarm near Sampeyre, Italy. Multiple sequences, attributed to fluid-triggering, were also detected in the aftershocks of the 2008 Wenchuan earthquake in China, with a range of relatively

high hydraulic diffusivities between 1.8 and 4.2 m^2/s, including back-fronts (Liu *et al.*, 2014). It must be noted in that in many cases, the triggering front envelope may be unable to enclose the full extension of the seismically activated region at the beginning of a swarm. This may indicate either the coexistence of a different mechanism responsible for kick-starting the sequence, such as static stress changes caused by a relatively strong event, a complex fluid injection source geometry instead of a simple point source or some sort of anisotropy in the microfracture network of the medium which could be described by different hydraulic diffusivity values at different directions, including a very high one that could explain the extended range of activity at the first outburst.

The model of Eq. 1.16 applies in a homogeneous, isotropic, poro-elastic, saturated medium. An alternative for seismic migration triggered by pressurized fluids is the model of hydrofracture growth (HG), proposed by Fischer *et al.* (2009) and Dahm *et al.* (2010). It can explain the asymmetric bidirectional or unilateral spatio-temporal migration patterns of seismicity, induced by hydraulic-stimulation experiments, with a distinctive back-front marking a deficit of seismicity left behind by the propagating seismically active patch. Instead of a simple parabolic envelope, as the one derived by Eq. 1.16, the HG model divides the process in 2 to 4 stages (Fig. 1.17). The first is the injection phase, characterized by bilateral expansion of the stress-gradient-driven triggering front, while the fracture's walls also expand in a transverse direction. Depending on the net pressure gradient, g, the fracturing can be symmetric (g=0) or asymmetric ($g\neq0$), with the sign of g defining the more "preferred" direction of growth. A non-zero g depends on the various terms which comprise the net pressure gradient, such as the gravity effect within the injection fluid, a non-zero pore-pressure gradient or non-zero tectonic stress gradient (Dahm *et al.*, 2010). For g=0, the migration velocity is $v_o \propto a(t)^{-1/3}$ with $a \propto t^{3/4}$ being the distance of the triggering front from the injection source, or remain constant during the first phase at the direction in which the growth is faster, in case of asymmetric fracturing. The normalized net pressure gradient γ can be estimated by comparing the relative lengths, $a_s(t)$ and $a_l(t)$ of the short and long wings of the expansion during the bidirectional phase 1, respectively (Fischer *et al.*, 2009; Dahm *et al.*, 2010):

$$\gamma = \frac{g}{p_o^{net}} \approx \pi \left(\frac{a_l(t) - a_s(t)}{a_l(t)^2 + a_s(t)^2} \right) \tag{1.17}$$

where p_o^{net} is the net pressure at the injection point. The net gradient g can be considered to remain constant throughout the whole process (Dahm *et al.*, 2010). The other phases are all post-injection. Phase 2 (fracture self-expansion under constant volume) is still exhibiting a bilaterally growing front for a short time. The fracture walls collapse while the crack tips expand due to viscous fluid flow until the ambient net pressure within the fracture is reduced below a critical value, according to the Griffith criterion (Griffith, 1921). In the third phase, which only occurs under the condition that $g\neq0$, the fracture keeps growing unidirectionally towards the longer wing until the stress intensity factor at the expanding crack tip drops below the critical value. During phase 3, starting at the middle of the fracture where its maximal opening is expected to be at the beginning of this phase, a back-front develops behind the seismically activated patch below which the density of earthquakes drops to a minimum, once phase 3 begins (Fig. 1.17).

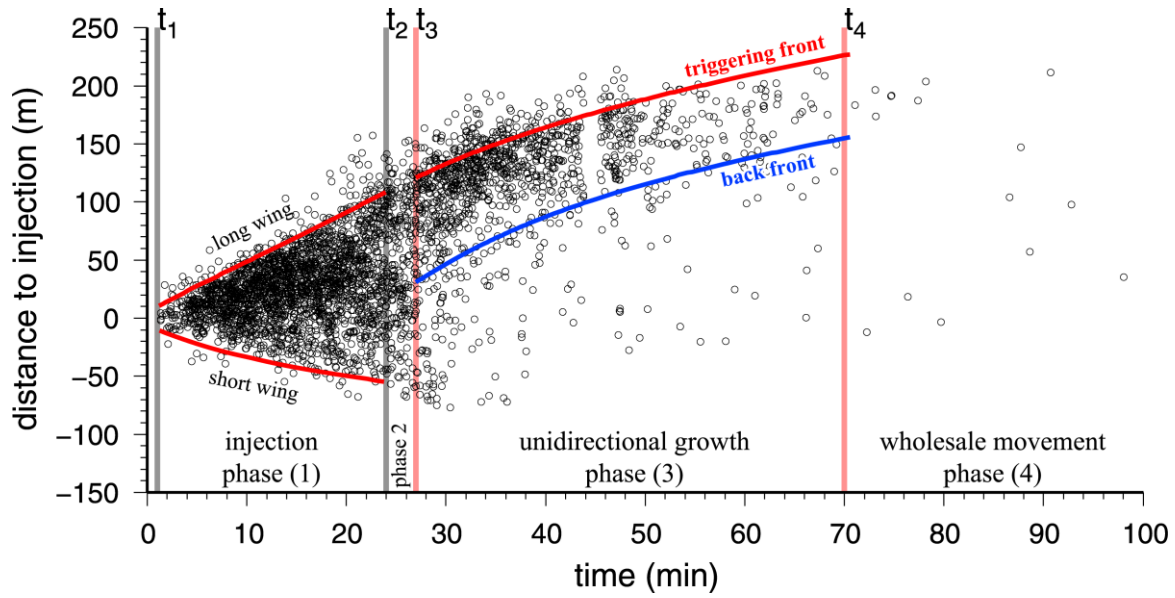

Figure 1.17: Application of the HG model on data from a hydraulic-fracture stimulation experiment in the Sawyer Canyon Sands gas field in Texas, 2005 (Dahm *et al.*, 2010), with t1, t2, t3 and t4 marking the initiation times of phases 1, 2, 3 and 4, respectively. (Figure modified after Dahm *et al.*, 2010)

The back-front pattern has been observed in several experiments of hydraulic fracturing and although it could, in some cases, follow the triggering front at the same rate (as in Fig. 1.17), that is not always the case, as it may be described by a curve that corresponds to a different D value (e.g. Parotidis *et al.*, 2004; Shapiro & Dinske, 2009). A fourth phase may sometimes be observed, if enough fluid has been injected, so that the fracture reaches an overcritical length and "wholesale movement" occurs towards the direction indicated by the net pressure gradient (Dahm *et al.*, 2010). The HG model has also been applied to the naturally occurring swarm of 2008 in Vogtland/NW Bohemia (Hainzl *et al.*, 2012). An earthquake migration pattern was observed, which appeared, on first approximation, to fit well with the simple diffusion model. However the migration was asymmetric, with D=0.3m^2/s in the up-dip and D=0.1m^2/s in the down-dip direction. The down-dip propagation stopped much earlier (9 days) than the up-dip one, which proceeded for about 30 days. The swarm lasted for about 4 weeks, but the overall seismic moment release was thrice the 2000 swarm in the same region, which lasted for ~10 weeks (Hainzl & Fischer, 2002; Hainzl *et al.*, 2012).

The hydraulic diffusion / growth models could also apply to larger scale migration patterns, such as the one observed during the deflation of Krafla volcano, NE Iceland, in 1978 (Einarsson & Brandsdóttir, 1979). In that case, the observed seismic activity began migrating, horizontally outwards from the caldera rim, due to lateral magma injection along a dyke, at a propagation velocity of ~1.6 km/h and ended up ~30 km away after ~24 hours at a rate of ~0.1 km/h in the form of a seismically active patch, followed by a back-front at about the same rate. A similar pattern of ~20 km total length and much smaller migration rates (~80m/day or ~3.3 m/h) is described in Section 5A.2, for the region of Messinia, Greece, attributed to high-pressure crustal fluids of meteoric origin (Kassaras *et al.*, 2014b). High migration rates (~1 km/h) have been usually

associated with swarms caused either by dyke propagation (Sigmundsson *et al.*, 2014) or driven by aseismic creep (Lohman & McGuire, 2007).

In the recent years, a well-known case of induced / man-made seismicity has been the seismic swarm that occurred between 4 and 12 March 2014 in Poland Township, Ohio, which has been attributed to hydraulic fracturing (or fracking) activity (Skoumal *et al.*, 2015). This included an M≈3 event that was even felt in a nearby town, a significantly large magnitude for the records of fracking experiments, with the largest being an M3.8 that occurred in 2011 in Horn River Basin, Canada (Davies *et al.*, 2013). It was noted that, during the sequence, the seismicity migrated by about 600m along a straight line, causing strike-slip faulting. The hypocenters were located at a distance of ~850m, mostly vertically, below the source of fluids injection that was performed on horizontal drilling well paths. The induced seismicity ceased a couple of days after the drilling operations in a nearby well were shut down. The measured *b*-value of the G-R law was found b=0.89, consistent with expected values for seismicity in pre-existing faults, triggered by pore-pressure changes due to fluids diffusion or even after the fluid pumping has stopped. On the contrary, $b\approx2$ is expected (Davies *et al.*, 2013) for seismic activity directly related to microfractures produced during fracking, usually with $M_w<1$.

1.3.4 The Epidemic Type Aftershock Sequence

A generalization of the modified Omori-Utsu law is formulated in the Epidemic Type Aftershock Sequence (ETAS) model (Ogata, 1988), which uses the assumption that every earthquake, either small or large, generates its own aftershock sub-sequence. It is a stochastic, magnitude-dependent point-process that is described by the following equation for the aftershock rate, $\lambda(t)$:

$$\lambda(t) = \mu + \sum_{\{i:S<t_i<t\}} K \frac{e^{\alpha(M_i - M_z)}}{(t - t_i + c)^p} \tag{1.18}$$

where α describes the ability of each earthquake to generate its own sub-sequence, μ is a constant in time (Poisson stationary process) that represents a background rate, usually considered to be close to zero, t_i and M_i are the origin time and magnitude of the i^{th} event after the starting time S, M_z is the magnitude threshold of the catalogue (smallest event), preferrably set to $M_z \equiv M_c$, the magnitude of completeness, and K, c and p are constants of equivalent physical meaning as those used in the modified Omori's formula (Eq. 1.13). The constant a has been found to range between 0.35 and 0.85 in swarms or between 1.2 and 3.1 in other types of seismic activity in Japan (Ogata, 1992). The parameters of the ETAS model μ, K, c, α and p characterize a certain seismogenic region during the particular time interval on which it is applied and they can be determined from the catalogue data by means of Maximum Likelihood Estimation (Ogata, 1983). Once the parameters are calculated, the integral of $\lambda(t)$ in Eq. 1.18, which only takes into account the magnitudes and origin times of the various events in the sequence, should give similar results to the time-series of the cumulative number of events (with $M \geq M_z$) in the real catalogue, if the model is consistent with the data.

The residuals, $\mu_r(t)$, between the modeled (temporal integral of Eq. 1.18) and the real cumulative number of events can provide insights into possible anomalies which could imply that the observed seismicity during a certain period is presenting quiescence when the real rate is lower than the modeled one (Ogata, 1989), or is driven by external causes, when the real rate deviates to higher values than the expected theoretical ones (Llenos *et al.*, 2009). Hainzl & Ogata (2005) calculated the parameters of the ETAS model on a sliding window of ~10 days for the earthquake swarm of 2000 in Vogtland/NW Bohemia. They found a correlation in the variation of parameter $\mu \equiv \lambda_o$ (in their paper) with periods of spatio-temporal migration, indicating pore-pressure diffusion. They suggested that $\mu(t)$, if considered as a time-dependent variable that introduces non-stationarity to the ETAS model, corresponds to the externally imposed "stressing rate" or "forcing rate" (seismicity not triggered by internal stress changes) that was attributed to the influence of high-pressure fluids. Other types of external causes which can trigger swarms include slow slip events, which may be detected by GPS (Wolfe *et al.*, 2007; Llenos *et al.*, 2009) or aseismic creep. It should be noted that while external forcing may initiate a swarm, the events of the swarm itself can generate, subsequently, their own aftershocks by stress-transfer. Thus, the ETAS model can be a helpful tool for the interpretation of seismic swarms and other intense sequences which are closely related to the generation of multiplets.

The comparison between the ETAS model and the catalogue can be viewed either in ordinary time units or in a "transformed time" domain. The transformed time is equivalent to the cumulative number of events as predicted by the theoretical rate of the model, thus "unwrapping" the temporally clustered seismicity. If the model describes the data sufficiently, the resulting time-series, called Residual Point Process (RPP), should represent a stationary Poisson process of constant intensity. Any deviations could indicate either inhomogeneity in the data or a behavior in the data that differs from what would otherwise be expected if all seismicity could be explained by (internal) stress-triggering, according to the selected parameters of the stationary ETAS model. The goodness-of-fit between different model configurations and data can be measured by comparing their Akaike's Information Criterion (*AIC*) values, derived by the formula (Ogata, 1988):

$$AIC = 2\cdot(-LL)+2\cdot q \qquad (1.19)$$

where $-LL$ is the negative log-likelihood (objective function being minimized during the estimation of parameters) and q is the number of variables being searched, usually q=5 for ETAS (unless some parameters are fixed) and q=4 for the Omori-Utsu model, as the variable α is fixed to zero in the latter.

A modification of ETAS is the Restricted ETAS or RETAS model (Gospodinov & Rotondi, 2006), which considers that only earthquakes above a certain threshold $M_{th} \geq M_z$ are capable of generating their own subsequences. In this frame, $M_{th} \equiv M_z$ is equivalent to the ETAS model (all events generate subsequences) while $M_{th} \equiv M_{max}$ is the Omori-Utsu law (only the largest event generates the whole sequence). Other modifications also include the spatial element of seismicity, in the sense that each earthquake can trigger localized sub-sequences within its vicinity (Ogata, 2004).

1.3.5 Spatial and temporal characteristics of multiplets

The relation between the spatio-temporal distribution and repeating earthquakes is usually very close. By definition, events within a multiplet are expected to be very localized (spatially clustered). The matrices of Fig. 1.18 have been drawn to represent multiplet similarity (XC_{max} values) in their upper triangular part and 3D inter-event distances in their lower one. In order to use a common colour-scale, the negative logarithm of distances was taken into account, to represent "proximity" instead of distance, and its values were normalized in the range [0, 1], with 1 corresponding to identical hypocenters (zero distance) and 1 to the maximum separation distance in the data. Rows and columns of events with mean XC_{max} (against all others) smaller than 0.22 were removed from the matrix to reduce the number of events and increase the size of cell (pixel) corresponding to each

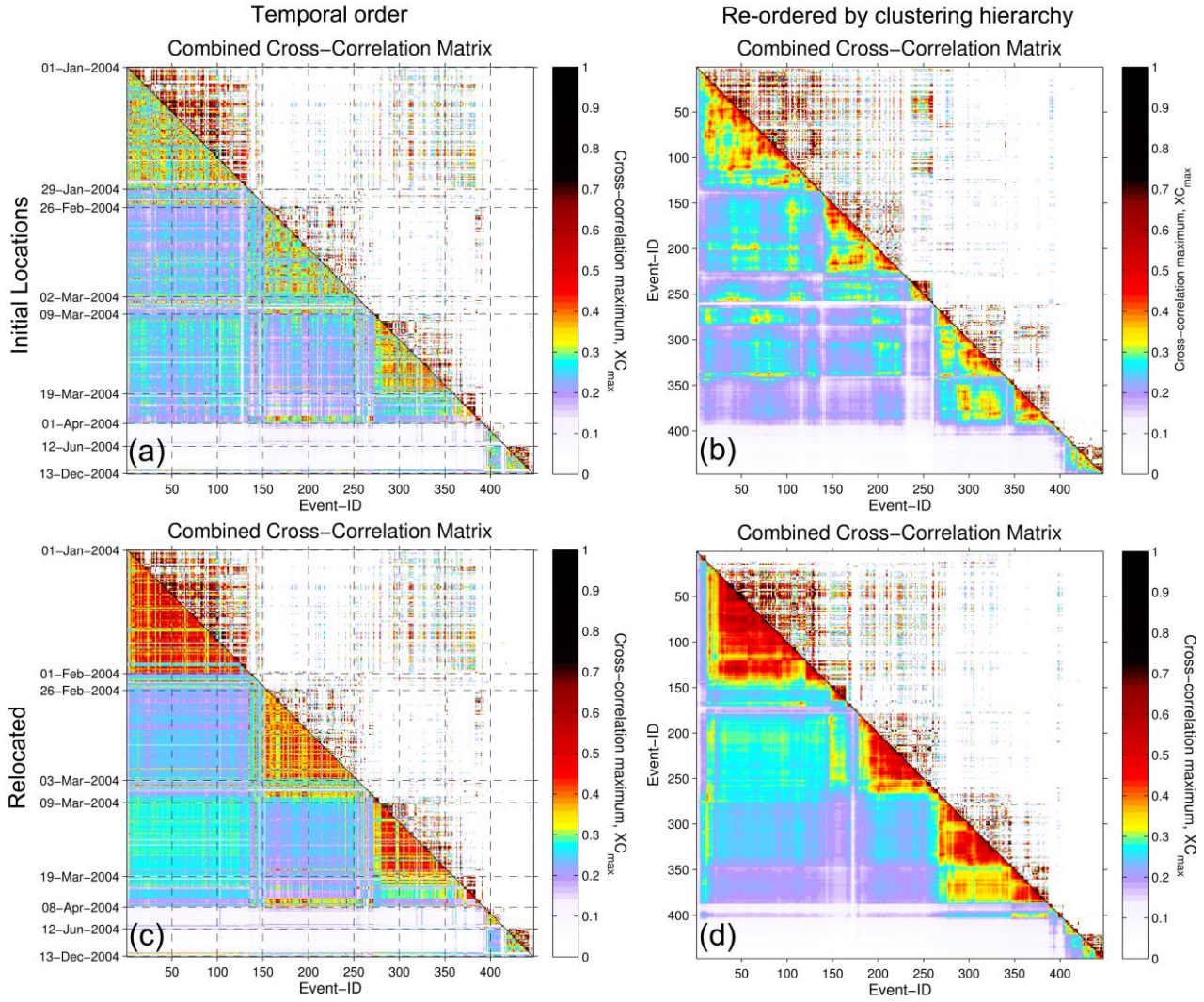

Figure 1.18: Matrices demonstrating the relation between waveform similarity (station DIMT, vertical, filtered between 2 and 20 Hz) and separation distances for selected seismicity from the spatial group #4 of 2004 in the western Corinth rift (Chapter 6). The upper triangular part of each matrix corresponds to the XC_{max} values (colour-scale) while the lower triangular part corresponds to normalized source proximity (see text for details). (a, b) initial locations, (c, d) relocated hypocenters, (a, c) event indices sorted by temporal order of their origin time, (b, d) event indices re-ordered according to the optimal leaf ordering for the hierarchical tree determined by the application of Ward's linkage on the 3D source separation distances.

event-pair for better clarity. In Fig. 1.18a the event indices are ordered by increasing origin time, while in Fig. 1.18b the matrix has been re-ordered according to the hierarchical configuration derived by Ward's linkage on the 3D spatial distribution (distances in the lower half of the matrix). In the latter, the clusters are more distinguishable in squares around the diagonal, as the temporal component has been removed. Fig. 1.18a also exhibits similar patterns due to the simultaneous temporal clustering. However, they are more likely to be interrupted by uncorrelated events, while in some cases an old multiplet may reactivate, in which case highly correlated rectangles may appear in off-diagonal regions, temporally separated from the rest of their multiplet which is found in squares around the diagonal at the same rows and columns. The same general remarks apply for Fig. 1.18c,d, where the relocated seismicity has been used for the calculation of separation distances. Even in the temporal sequence (Fig. 1.18c), the lower half-squares of spatially clustered events have become more dense and less noisy than in Fig. 1.18a, as the uncertainties were reduced and correlated events were concentrated closer to their cluster's centroid. In Fig. 1.18d the whole hierarchical linkage has been restructured producing different, typically better resolved cluster configurations. New multiplets may be generated during the time-span of a seismic dataset. They can be temporally clustered near the time of their first occurrence, spread-out throughout a sequence, recurring in bursts or simply ceasing to exist. A multiplet timeline, or history, as in Fig. 1.19 is a typical representation of how earthquake families generate, as seismicity migrates to new areas while some disappear as conditions change. In this example, almost all multiplets that were generated before the eruption of October 2007 at Bezymianny Volcano, Russia (Thelen *et al.*,

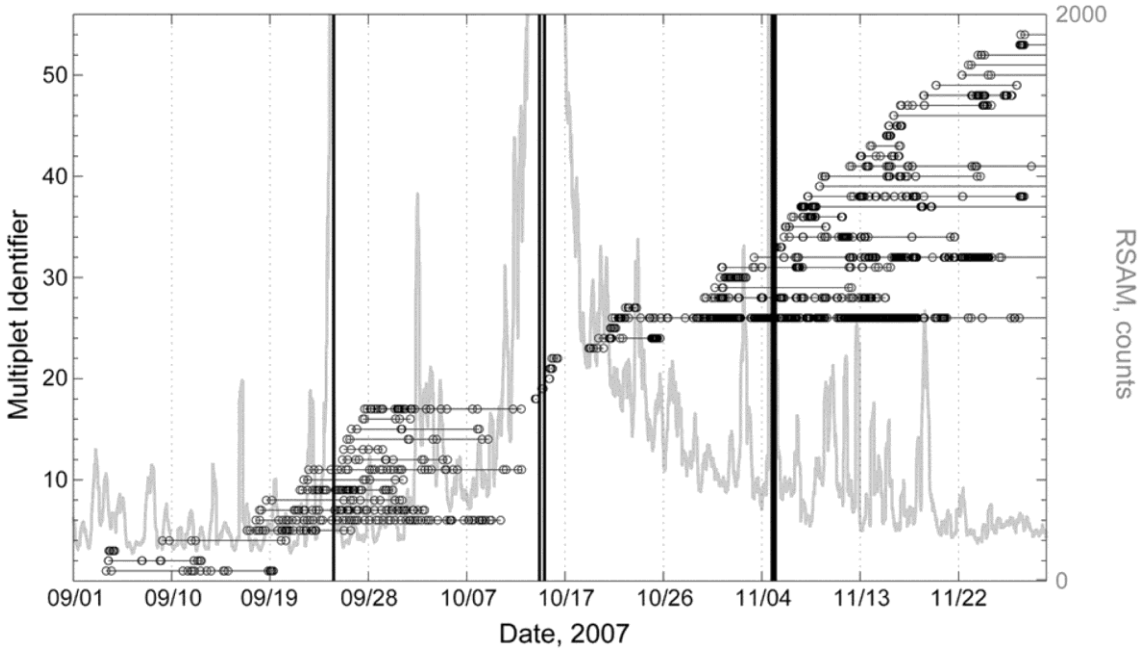

Figure 1.19: Multiplet timeline (or history) for the seismicity observed at Bezymianny Volcano, Russia, between 1 September and 1 December, 2007 (Thelen *et al.*, 2010). Each horizontal row corresponds to a multiplet, with at least 5 events, whose identifier increases with increasing generation time of the first event in each one. Circles represent earthquakes with a line connecting events that belong to the same multiplet. The gray line is the rectified seismic amplitude on a station (BELO) near the top of the volcano, while the vertical black lines mark volcanic events. (Figure after Thelen *et al.*, 2010)

2010), vanished as the conditions changed drastically after this event. In aftershock sequences, where a large region is activated in a very short time, the multiplets generation may present a very large burst in the beginning of the sequence while very few may be generated later during the relaxation stage, unless a strong secondary sub-sequence activates a previously unbroken region.

In swarms, on the other hand, new families may be generated in small bursts or gradually, as the seismicity migrates to different areas while older multiplets may diminish due to changing pore-pressure or other conditions. For example, in case of asymmetric crack propagation in the HG model, multiplets located at the short wing are expected to cease to exist after the beginning of phase 3 (Fig. 1.17). In general, there is no time-related criterion in the definition of earthquake families. Earthquakes with similar waveforms have been found to recur even after several years (Petersen, 2007; Cannata *et al.*, 2013) and, sometimes, even in quasi-periodic seismic cycles (Nadeau *et al.*, 1995; Waldhauser *et al.*, 2004). Given that the fault network and stress-field need to remain consistent in order to produce earthquakes with similar source parameters, the only other limitation is that the medium's properties have not changed utterly in a way that would significantly alter the ray-paths and their travel-times. Small variations in the propagation velocities of the order of 0.01% have been found and measured in several studies (Poupinet *et al.*, 1984; Cociani *et al.*, 2010). However, their effect on the waveform is mainly on a slight gradual stretching of the wave-coda, with unimportant effects to the overall XC_{max}.

1.4 Relocation of hypocenters

The improvements of operational seismological networks in density and azimuthal coverage around seismogenic zones have greatly enhanced the resolution and detection threshold of microseismicity in the last decades. As a result, the observed spatial seismicity patterns went from global to local scale, from the relatively simple plate boundaries to the complexity of local fault zones. Still, however, for a given seismological network geometry, traditional single-event location methods can go as far as the uncertainties of the velocity model and arrival-time reading errors permit. A velocity model in its simplest form is a set of homogeneous horizontal layers with a constant V_p/V_s ratio. Inhomogeneities in the real structure can cause systematic biases at certain directions, which in turn increase the uncertainty along the direction of the respective ray-paths, causing a spatial cluster to diffuse and deform.

The input data for a single-event location algorithm includes the stations positions, the velocity model and the P- and S-wave arrival-times. When a solution for the hypocenter and origin time is obtained, the forward modeling provides the "calculated travel-times", or T_{cal}, of P- and S-waves to the stations, while the differences between the observed arrival-times and the calculated origin time are the "observed travel-times", or T_{obs}. The differences (T_{obs}-T_{cal}) between observed and calculated travel-times are residuals that account for uncertainties mostly due to lateral variations in the velocity structure that are not included in the model. Douglas (1967) suggested that an extra term is added to the equation of the required adjustments to the approximate hypocenter and origin time, to account for "station corrections". For a group of events located in the same region, their ray-paths "sample" roughly the same velocity structure before arriving to the stations. In that case, their average P- or S-wave travel-time residual for each station is an estimate for the respective station

correction. When these corrections are applied to the P- or S-wave arrival-times (Douglas, 1967) and the location procedure is re-run, the hypocentral solutions will be corrected by the average travel-time residuals and the location uncertainties will be reduced. This is the basic idea behind the method of Joint Epicenter Determination or JED (Douglas, 1967), or, later, Joint Hypocenter Determination or JHD (Dewie, 1971) as well as of joint inversions for hypocentral location, origin time, station and velocity model corrections (Kissling *et al.*, 1994) by minimizing the mean travel-time residuals. The JED/JHD method has been used in many studies in the past (e.g. Dewey, 1972; Herrmann, 1981; Pujol, 1995), including the region of Greece (Makropoulos & Burton, 1981).

More recently, an improved relocation algorithm was developed on the concept of minimization of the double-differences, dr_k^{ij} (Eq. 1.20) between observed and calculated travel-times for event-pairs (*i*, *j*) to station, *k* (Waldhauser & Ellsworth, 2000):

$$dr_k^{ij} = \left(t_k^i - t_k^j\right)^{obs} - \left(t_k^i - t_k^j\right)^{cal} \tag{1.20}$$

where t_k^i refers to the travel-time of a P- or S-wave from the source of event *i* to a station *k*. The algorithm works on the requirement that the source separation distance for an event-pair is much smaller than their (roughly common) hypocentral distance from a station, so that their ray-paths are approximately the same (sampling the same velocity structure). On that condition, any differences between their travel-times can be attributed to their spatial offset, projected along the ray-path. By minimizing Eq. 1.20, the errors due to the unmodeled velocity structure are reduced and relative relocation is achieved after several iterations. Besides the small separation distance, events are linked to pairs and considered as neighbors when they have at least a minimum number of common observations (P- or S-wave arrivals at common stations), while strong links are usually considered as those with at least 8 arrival-time observations, as this is equal to the degrees of freedom in the system of double-difference equations which aim to resolve hypocenter (3 spatial coordinates) and origin time for every pair of events. In the same sense, for better stability, it is also recommended that cross-correlation measurements are used only for pairs of events with a minimum number of valid P- & S-wave correlations. Additional restrictions on the minimum $XC_{\max}$ and t_m values may also apply to ensure robustness (Hauksson & Shearer, 2005; Fang *et al.*, 2015; Mesimeri *et al.*, 2016).

The time-lags, t_m, of Eq. 1.2 (after resampling) can provide direct differential travel-time measurements which can account for arrival-time reading errors, thus reducing the inconsistencies between highly correlated events that belong to the same multiplet. The initial alignment, for example, of the P-waves of two similar events to their observed arrival-times (P-wave picks) is equivalent to an alignment on their respective observed travel-times ± the true travel-time difference between the two events + the arrival-time reading error, as the differences in their origin times are eliminated. Then, if the time-lag, t_m, of $XC_{\max}$ is measured, this corresponds to a difference in the pick placement between the two events relative to the similar part of their P-waveforms, or, equally, to the difference between their arrival-time reading errors. In older approaches of relative relocation, these differences were used to relocate the events of a multiplet with respect to a "master-event" or "reference-event", whose arrival-times and absolute location should be determined with the least uncertainties, so that the picking errors in the other events of the

cluster would be fully accountable for the resulting t_m measurements (Frémont & Malone, 1987). The HypoDD double-difference algorithm, on the other hand, does not require the selection of a master-event, but rather performs relocation with respect to the cluster's centroid that is re-determined on each iteration. It also incorporates catalogue data (travel-time differences derived from the initial solutions and ordinary phase picks) in order to provide links between uncorrelated events (Fig. 1.20), thus increasing the amount of events that can be relocated and correcting the relative locations between sub-clusters of repeating earthquakes. The catalogue travel-time differences themselves provide corrections for the unmodeled velocity structure, in a similar sense to the JHD method, so that the HypoDD method does not require station or velocity model corrections.

A typical relocation example and comparison between JHD and HypoDD is presented in Fig. 1.21 (Waldhauser, 2001). The double-difference relocation using both catalogue and cross-correlation data is clearly resolving with greater detail the activated structures, which appear diffused in the left panel despite being already improved by the application of JHD. The incorporation of cross-correlation measurements with increased precision (by resampling the XC function or measuring the angle of the cross-spectral phase) can potentially reduce the relative location uncertainties within multiplets to a few meters or tens of meters (Waldhauser & Ellsworth, 2000). HypoDD has been used extensively during the past decade for the high-resolution relocation of hypocenters in

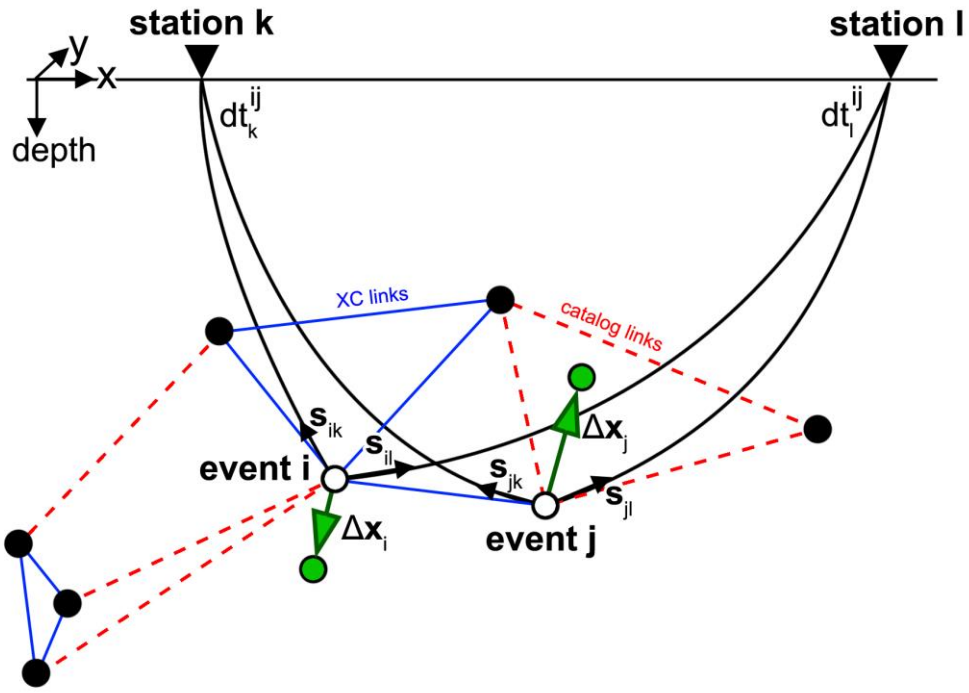

Figure 1.20: Sketch depicting the ray-paths $\mathbf{s}_{ik}$, $\mathbf{s}_{il}$ and $\mathbf{s}_{jk}$, $\mathbf{s}_{jl}$ for an event-pair (i, j) (white circles, trial locations) to stations k and l with travel-times differences dt_k^{ij} and dt_l^{ij}, respectively, as well as the two types of links (blue: cross-correlation links, red: catalogue links) between these events and their neighbors (black circles, trial locations) used in the double-difference algorithm HypoDD and the resulting relocated hypocenters (green) with the respective relocation vectors $\Delta\mathbf{x}_i$ and $\Delta\mathbf{x}_j$. (Figure modified after Waldhauser & Ellsworth, 2000).

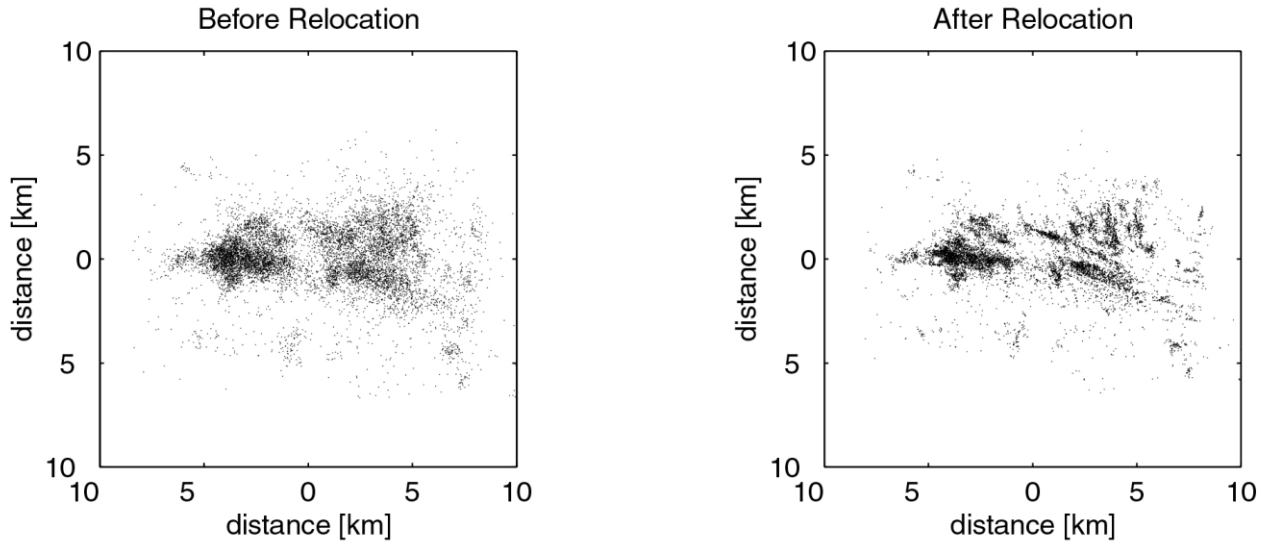

Figure 1.21: Epicenters of about 10,000 events from the 1997 seismic crisis in the Long Valley caldera, (left) resolved using the JHD method and (right) relocated using the double-difference HypoDD algorithm. (Figure after Waldhauser, 2001)

earthquake sequences worldwide (e.g. Hauksson & Shearer, 2005; Waldhauser & Schaff, 2008; Bisrat *et al.*, 2012; Cannata *et al.*, 2013; Fang *et al.*, 2015; Kapetanidis *et al.*, 2015).

The HypoDD algorithm provides two ways to run the inversion, either using Singular Value Decomposition (SVD) or a conjugate gradients scheme (LSQR). While the former is capable to determine realistic errors, it cannot be used for large systems due to memory/processing requirements. On the other hand, LSQR is very efficient for large systems, however its error estimates are likely undertermined (Waldhauser & Ellsworth, 2000; Waldhauser, 2001). To assess reliable errors, the authors suggest to either run SVD on small, representative samples of events, or, alternatively, apply statistical resampling methods to examine the robustness of the procedure to several factors. Error assessment is important to evaluate the results of HypoDD. For example, if the major semi-axes of the 95% confidence interval error ellipse have a significant length and are aligned to a direction similar to the orientation of the events in a cluster this is a clue that the delineation of the cluster is probably the result of bias and not a true hypocentral alignment. A jack-knife technique can be used to investigate the influence of individual stations to the relocation procedure. This works by removing travel-time data from one station at a time and repeating the relocation procedure using, otherwise, the same parameters and starting model (trial hypocenters). A similar test can be performed to examine the robustness of the relocation procedure against the starting model. This can be done by applying random permutations to the trial hypocenter of each event in all 3 dimensions and re-running the relocation procedure for a large number of times. The influence of each event to the relocation of the others can also be estimated by a similar jackknife method, removing one-event-at-a-time and repeating the double-difference iterative procedure. Each of the above tests provides a distribution of errors for each event from which conclusions can be drawn on the order of the uncertainties as well as possible biases. It is also important that, before relocation is applied, the initial solutions of absolute solutions have been properly constrained. This

requires that a valid velocity model is used, it could in fact negatively affect not only the absolute locations (horizontal or vertical shift, spreading, concentrations or thinning of the distribution around the model's discontinuities etc.) but also the results of the relocation (Michelini & Lomax, 2004). It is, thus, suggested as the first step before any sort of spatio-temporal analysis takes place in a dataset, that a local velocity model is either adopted or calculated for a particular region before the estimation of initial solutions.

Chapter 2

Focal mechanisms and particle motions

Introduction

Earthquakes originate from sudden slips on fault surfaces or other disturbances such as volcanic eruptions, nuclear or other explosions, cavern collapses, meteor impacts etc. which release or introduce energy in the form of elastic waves that propagate in the Earth's interior. One of the primary objectives in seismology is the understanding of the physical mechanism which generated a particular earthquake. Rarely, it is possible to measure the characteristics of a fault that ruptured directly from field observations. However, this is only possible for very large, shallow earthquakes, as the focus can be tens or hundreds of km below the surface and the rupture area and slip very small. However, information concerning the physical mechanism that caused an earthquake is transferred from the source to the surface in the form of seismic waveforms. The interpretation of the pattern of radiated energy can lead to the determination of the focal mechanism.

This chapter begins with a brief introduction into the theory of stress and moment tensors, leading to the radiation patterns and polarization of particle motion. Information on these properties is then exploited for the development of methodologies which can be useful to constrain composite focal mechanisms of clustered events, which, in combination with geometrical properties of the spatiotemporal distribution of a seismic cluster, can enable the determination of the nodal plane that corresponds to the rupture plane. Particle motion is also exploited in an application of polarization measurements to verify a probable vertical polarity reversal of surface stations due to technical issues (Section 2.5) and to obtain information on the unknown horizontal orientation of borehole sensors (Section 2.6).

2.1 Stress tensors

When the accumulated elastic strain on a rock, caused by imposed stress-load, surpasses its breaking strength, the rock ruptures and slip occurs, releasing stress and relaxing the strain. This usually takes place on a pre-existing fault surface, as it constitutes a discontinuity in the material; a weak area where the probability of rupture is higher. The dislocation on a, typically, planar fault can be either tensile (crack propagation Mode I), if the crack walls open/diverge as the crack propagates, or shear, if the displacements occur on the crack plane, parallel (Mode II) or transverse (Mode III) to the direction of crack propagation (Scholz, 2002).

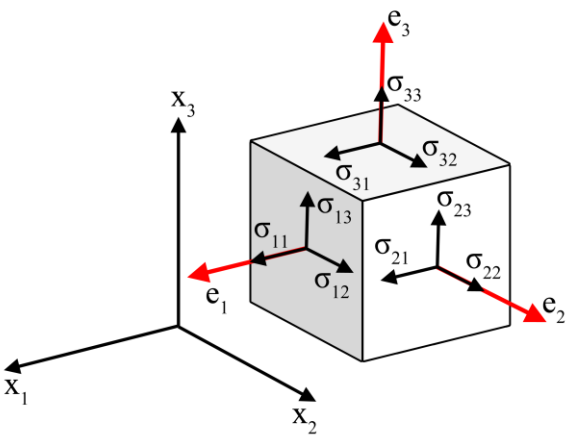

Figure 2.1: Components of stress applied on the faces of an infinitesimal cube inside a material. Vector triplets also apply at the opposite faces in the reverse directions.

In a general case, the applied stress on the surfaces of an infinitesimal cube inside a material (Fig. 2.1) can be described by a stress tensor, $\boldsymbol{\sigma}_{ij}$:

$$\sigma_{ij} = \begin{bmatrix} \sigma_{11} & \sigma_{12} & \sigma_{13} \\ \sigma_{21} & \sigma_{22} & \sigma_{23} \\ \sigma_{31} & \sigma_{32} & \sigma_{33} \end{bmatrix} \tag{2.1}$$

The stresses are applied as coupled forces at opposite sides of the cube and towards opposite directions, cancelling one another to preserve equilibrium, but producing strain. The elements of the diagonal correspond to vectors which are normal to the surface of the cube that is indicated by the first index, *i*, and responsible for strain that changes the cube's volume. The other, non-diagonal, stress elements refer to vectors which are coplanar to the applied surface and can cause shape-changing shear strain to the cube. In the literature, the latter are sometimes represented by τ_{ij} ($i \neq j$), τo distinguish between normal stress and shear stress. For equilibrium, in order to conserve the angular momentum, the stress tensor must be symmetric ($\boldsymbol{\sigma}_{ij}=\boldsymbol{\sigma}_{ji}$) to prevent rotation. This means that in the general case only 6 out of the 9 elements are required to describe the stress tensor.

The elements of the stress tensor depend on the coordinate system that is chosen; the orientation of the cube with respect to the stress field. The stress tensor is a diagonalizable matrix, which means it can be rotated to a specific coordinate system where its non-diagonal elements (shear stresses) become zero. In that system, the only stresses acting on the cube are oriented in directions indicated by the cube's normal vectors, called principal stress axes. The procedure for diagonalization of the stress tensor is called eigen-decomposition or principal component analysis:

$$\begin{vmatrix} \sigma_{11}-\lambda & \sigma_{12} & \sigma_{13} \\ \sigma_{21} & \sigma_{22}-\lambda & \sigma_{23} \\ \sigma_{31} & \sigma_{32} & \sigma_{33}-\lambda \end{vmatrix} = 0 \Rightarrow \lambda^3 - tr(\sigma_{ij})\lambda^2 + \text{minor}(\sigma_{ij})\lambda - \det(\sigma_{ij}) = \\ = \lambda^3 - I_1\lambda^2 + I_2\lambda - I_3 = 0 \tag{2.2}$$

The last part of Eq. 2.2 is the "characteristic polynomial" of the tensor, where $\text{tr}(\boldsymbol{\sigma}_{ij})=I_1$ is the trace of the original tensor matrix, $\text{minor}(\boldsymbol{\sigma}_{ij})=\sigma_{11}\sigma_{22}+\sigma_{22}\sigma_{33}+\sigma_{11}\sigma_{33}-(\sigma_{21}^2+\sigma_{32}^2+\sigma_{31}^2)=I_2$ is the "sum of the minors" and $\det(\boldsymbol{\sigma}_{ij})=I_3$ its determinant (Lay & Wallace, 1995). The roots of the characteristic polynomial are real numbers, due to the symmetry of the stress tensor, and are called eigenvalues. The coefficients of I_1, I_2, I_3 and the three roots λ_κ (or $\sigma_1 \geq \sigma_2 \geq \sigma_3$) of Eq. 2.2 are called invariants of the tensor, meaning they are independent of the coordinate system. The diagonalized stress tensor, $\boldsymbol{\sigma}_{ij}^*$, is written as:

$$\sigma_{ij}^* = \begin{bmatrix} \sigma_1 & 0 & 0 \\ 0 & \sigma_2 & 0 \\ 0 & 0 & \sigma_3 \end{bmatrix} \Rightarrow \begin{cases} I_1 = \sigma_1 + \sigma_2 + \sigma_3 \\ I_2 = -\left[\sigma_1\sigma_2 + \sigma_2\sigma_3 + \sigma_3\sigma_1\right] \\ I_3 = \sigma_1\sigma_2\sigma_3 \end{cases} \tag{2.3}$$

The new coordinate system is defined by the eigenvectors $\boldsymbol{\upsilon}_\kappa$, one corresponding to each of the eigenvalues, λ_κ. The eigenvectors are determined, with substitution of the respective eigenvalue, from the solution of the system:

$$\begin{bmatrix} \sigma_{11}-\lambda_\kappa & \sigma_{12} & \sigma_{13} \\ \sigma_{21} & \sigma_{22}-\lambda_\kappa & \sigma_{23} \\ \sigma_{31} & \sigma_{32} & \sigma_{33}-\lambda_\kappa \end{bmatrix} \begin{bmatrix} \kappa_1 \\ \kappa_2 \\ \kappa_3 \end{bmatrix} = 0 \tag{2.4}$$

Where $\boldsymbol{\upsilon}_\kappa=[\kappa_1,\kappa_2,\kappa_3]^T$ represents an eigenvector corresponding to the eigenvalue λ_κ. If the three individual eigenvectors are symbolized as $\boldsymbol{\upsilon}_x=[x_1,x_2,x_3]^T$, $\boldsymbol{\upsilon}_y=[y_1,y_2,y_3]^T$ and $\boldsymbol{\upsilon}_z=[z_1,z_2,z_3]^T$ and the eigenvalues λ_x, λ_y, λ_z, then the principal component analysis results in the following:

$$\sigma_{ij} \cdot \vec{\upsilon}_\kappa = \lambda_\kappa \vec{\upsilon}_\kappa \tag{2.5}$$

$$\sigma_{ij} = V\Lambda V^{-1} \quad \text{, where} \quad \Lambda = \begin{bmatrix} \lambda_x & 0 & 0 \\ 0 & \lambda_y & 0 \\ 0 & 0 & \lambda_z \end{bmatrix} = \sigma_{ij}^* \quad \text{and} \quad V = \begin{bmatrix} x_1 & y_1 & z_1 \\ x_2 & y_2 & z_2 \\ x_3 & y_3 & z_3 \end{bmatrix} \tag{2.6}$$

The first equation (Eq. 2.5) represents the projection of the tensor in the direction of the eigenvector $\boldsymbol{\upsilon}_\kappa$. It also reflects the basic characteristic of the eigenvectors: applying a tensor $\boldsymbol{\sigma}_{ij}$ on the eigenvector does not change its direction, but only its scale (by λ_κ). In other words, in this coordinate system the tensor can cause volume changes but not shape changes (zero shear strain). Eq. 2.6 is the compact form of the principal component analysis or eigenvalue decomposition. The 3 eigenvalues are equal to the elements of the diagonal of $\boldsymbol{\sigma}_{ij}^*$ (Eq. 2.3), that is $\lambda_x=\sigma_1$, $\lambda_y=\sigma_2$ and $\lambda_z=\sigma_3$. The eigenvectors $\boldsymbol{\upsilon}_\kappa$ are usually normalized to unit length and are orthogonal to one another, due to the symmetry of the tensor and the eigenvalues being real, while λ_κ is their respective scale.

Typically, both eigenvectors and eigenvalues are sorted by order of decreasing eigenvalue $\lambda_x \geq \lambda_y \geq \lambda_z$ (or $\sigma_1 \geq \sigma_2 \geq \sigma_3$). However, for geological applications where the stresses are all negative (compressive) they are usually sorted by order of decreasing absolute values $|\sigma_1| \geq |\sigma_2| \geq |\sigma_3|$ (Stein & Wysession, 2003). Eq. 2.6 can also be written as: $\boldsymbol{\sigma}_{ij}\mathbf{V} = \mathbf{V}\boldsymbol{\Lambda}$, meaning that $\mathbf{V}$, whose columns are the eigenvectors $\boldsymbol{\upsilon}_{\kappa,}$ can be used as a transformation matrix to rotate the tensor into the new coordinate system in which the shear tensions vanish.

The σ_1, σ_2, σ_3 are the principal stresses, while the corresponding normalized eigenvectors define the principal axes of stress. The elements σ_{11}, σ_{22}, σ_{33} of the diagonal in Eq. 2.3 are also called principal stresses; they are normal to the surface of the cube that corresponds to the first index, *i*, and responsible for strain that changes the cube's volume. Their invariant sum $I_1 = \sigma_{11} + \sigma_{22} + \sigma_{33} = \sigma_1 + \sigma_2 + \sigma_3 = \sigma_m$, is called mean stress and the $\sigma_m \cdot \mathbf{I}$ matrix defines the isotropic component, $\boldsymbol{\sigma}_{iso}$, of the stress tensor. What remains, $\boldsymbol{\sigma}_{dev} = \boldsymbol{\sigma}_{ij} - \sigma_m \cdot \mathbf{I}$, is called the deviatoric stress component.

$$\sigma_{ij} = \sigma_{iso} + \sigma_{dev} = \begin{bmatrix} \sigma_m & 0 & 0 \\ 0 & \sigma_m & 0 \\ 0 & 0 & \sigma_m \end{bmatrix}_{iso} + \begin{bmatrix} \sigma_{11} - \sigma_m & \sigma_{12} & \sigma_{13} \\ \sigma_{21} & \sigma_{22} - \sigma_m & \sigma_{23} \\ \sigma_{31} & \sigma_{32} & \sigma_{33} - \sigma_m \end{bmatrix}_{dev} \tag{2.7}$$

with $\boldsymbol{\sigma}_{ij} = \boldsymbol{\sigma}_{ji}$. If, in addition, the isotropic component is zero (no volume change), then $\sigma_m = \sigma_{11} + \sigma_{22} + \sigma_{33} = 0$, or $\sigma_{33} = -(\sigma_{11} + \sigma_{22})$, which leaves 5 independent elements remaining.

Given a specific stress field that is applied on a brittle material (e.g. rock) which is likely to break, one would intuitively expect shear rupture to occur on a surface on which the shear stresses maximize, rather than vanish as in the principal stress axes system. In a 2D stress tensor example, with only two principal stresses σ_1, σ_3 (index "3" is used for compatibility with minimum principal stress in the 3D case) and corresponding axes $\mathbf{S}_1$, $\mathbf{S}_3$, if a hypothetical plane's normal, $\mathbf{n}$, forms an angle θ^* with respect to the $\mathbf{S}_1$ principal stress axis, then the diagonalized stress tensor must be transformed by multiplying with a rotation matrix to apply to the hypothetical surface. In that case, the shear stress, τ, in the rotated system becomes (Stein & Wysession, 2003):

$$\tau = (\sigma_3 - \sigma_1)\sin\theta^* \cos\theta^* = \frac{(\sigma_3 - \sigma_1)}{2}\sin 2\theta^* \tag{2.8}$$

Then the magnitude of shear stress, $|\tau|$, maximizes where $\sin 2\theta^* = \pm 1$, that is at $\theta^* = 45°$ or $\theta^* = 135°$. This result is important as it shows that the shear stress maximizes on planes which bisect the right angle formed between the maximum stress axis, $\mathbf{S}_1$ and the minimum stress axis, $\mathbf{S}_3$ and there are two such planes.

However, a more realistic approach is given by the Coulomb-Mohr failure criterion (Eq. 2.9), which is a simple expression of the relation between the material's strength and the applied normal, σ_n, and shear stresses, τ, required for failure:

$$\tau = \tau_o + \mu \cdot \sigma_n \tag{2.9}$$

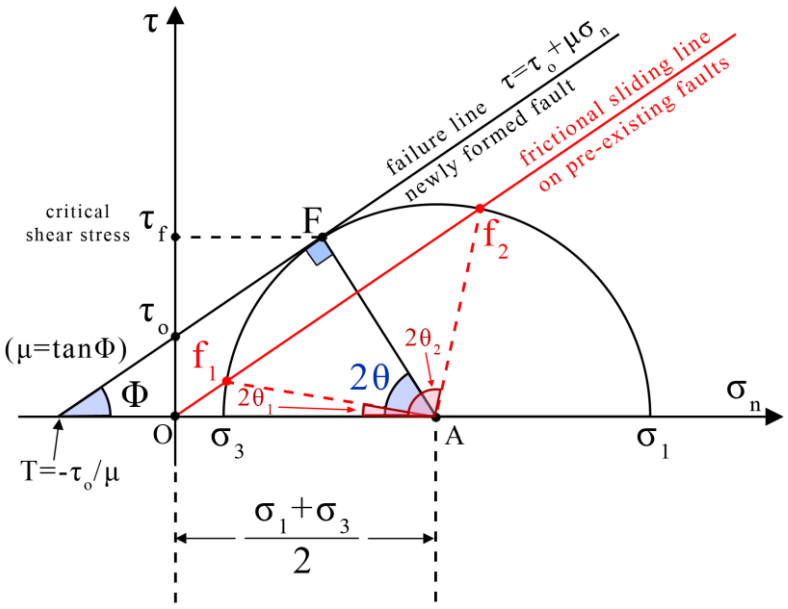

Figure 2.2: Mohr's circle for the definition of frictional slide on pre-existing faults (red line) or failure angles on newly formed faults (black line parallel to the red one), where Φ is the angle of internal friction, θ is the angle between the σ_1 axis and the failure plane (see Fig. 2.3), σ_n is the applied normal stress, τ is the applied shear stress, τ_o the cohesive strength and T the tensile stress of the material. The circle's radius is AF=$(\sigma_1-\sigma_3)/2$, that is also the value of maximum shear stress for θ=45° (if Φ=0). Note: in the literature, the angle 2θ is alternatively measured counter-clockwise from σ_n+ instead, corresponding to the angle θ between the normal to the failure plane and the σ_1 axis. (Figure based on Scholz, 2002)

where τ_o is the cohesive strength of the rock, or simply cohesion, μ = tanΦ is the coefficient of internal friction of the material and σ_n in this formula is considered positive for compression (Scholz, 2002). The parameter Φ is called angle of internal friction or effective stress friction angle and can be graphically represented in a Mohr's circle diagram (Fig. 2.2), which depicts the state of stress in a material depending on the orientation of an assumed plane, as the angle between the failure line and the axis of σ_n. In Fig. 2.2, depending on the applied stress and the strength/internal friction of the rock, if the failure line is tangential to the circle at point F, then θ represents the angle between the rupture plane and the principal axis of maximum normal stress, σ_1. From the geometry of Fig. 2.2, the general case is:

$$\theta = 45° - \Phi/2 \qquad (2.10)$$

In the special instance where μ = tanΦ = 0 $\Rightarrow$ Φ = 0 the failure line is parallel to the σ_n-axis while still crossing the τ-axis at τ_o. In that case, if it is tangential to the circle at a point F, then θ = 45°, the same result derived for the plane of maximum shear stress (θ^* in Eq. 2.8 for maximum τ) which is given by the radius of the circle $(\sigma_1-\sigma_3)/2$.

For pre-existing faults, the τ_o value is omitted from the Coulomb-Mohr criterion and the intersections, f_1, f_2, of the sliding line with the circle of Fig. 2.2 mark the corresponding $2\theta_1$ and $2\theta_2$ angles (measured counter-clockwise, same as with 2θ) where a pre-existing fault is likely to slide,

given the stress tensor and internal friction coefficient. Fig. 2.2 shows only a semicircle, but the criterion also applies to the other half, which means that the failure planes are found at $\pm\theta$ (Fig. 2.3) and the respective sliding planes at $\pm\theta_1$ and $\pm\theta_2$ angles. If pore-pressure, p_w, is also considered, the σ_n in Eq. 2.9 can be replaced by $(\sigma_n - p_w)$, with $p_w = \rho_w g y$, where ρ_w is the density of water, g the acceleration of gravity and y the depth. This effectively shifts Mohr's circle to the left, enabling frictional slip to occur at plane orientations defined by its intersection points with the failure line at lower stress states than without p_w.

A typical value for the internal friction coefficient in rocks, as measured in laboratory experiments, is $\mu \approx 0.85$ or $\Phi \approx 50°$, which, however, would require much higher stress-drops than those observed during earthquakes that is mainly attributed to the high pore-pressure of water on faults (Turcotte & Schubert, 2002). According to other estimates, the value of μ for solid rocks varies between 0.47 and 0.70, with $\mu = 0.6$ ($\Phi \approx 30°$) often being used for general calculations (Haakon, 2010). According to Eq. 2.10, this means that $\theta \cong 30°$, meaning that the maximum principal stress axis (compression) must be more parallel than perpendicular to the failure plane. Intuitively, this implies that normal faulting is more likely to occur at a steeper dip (~60°) while thrust faulting at lower dip angles (~30°), since σ_1 is sub-vertical or sub-horizontal on each case respectively. A more generalized view is presented in Fig. 2.3, derived by Anderson's theory of faulting; assuming that dip-slip faulting at pre-existing zones of weakness is expected to occur on failure planes which are at an

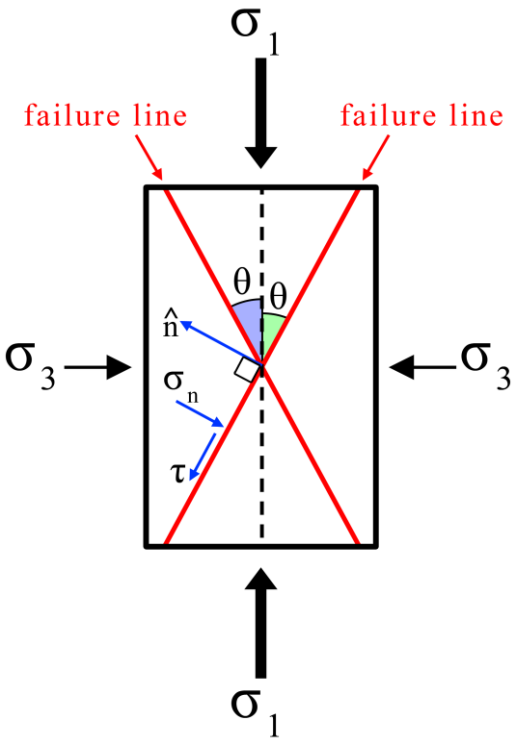

Figure 2.3: Relation between the maximum (σ_1) and minimum (σ_3) principal stress axes and failure lines (angle θ, same as in Fig. 2.2, between σ_1 and the failure plane). The normal (σ_n) and shear stress (τ) directions are also indicated for one of the failure lines. (Figure based on Scholz, 2002)

angle that requires minimal tectonic stress (Turcotte & Schubert, 2002). On this condition, dip, δ, and deviatoric stress, $\Delta\sigma_{xx}$, are given, with respect to μ=tanΦ, by:

$$\Delta\sigma_{xx} = (\sigma_{xx} - \rho g y) = \frac{\pm 2\mu(\rho g y - p_w)}{\sqrt{(1+\mu^2)} \mp \mu}$$
$$\tan 2\delta = \pm \frac{1}{\mu} \qquad (2.11)$$

where σ_{xx} is the horizontal stress at the dip direction, ρgy is the term for lithostatic pressure (equal to the vertical stress), ρ is the density of the rock ($\rho \approx 2700 kg/m^3$), with $\sigma_1 \equiv \rho gy$ considered for normal faults ($\Delta\sigma_{xx}<0$) and $\sigma_1 \equiv \sigma_{xx}$ for thrust faults ($\Delta\sigma_{xx}>0$). Fig. 2.4a shows that for μ=0 the failure planes are expected to have a δ=45° dip, but as the coefficient of internal friction increases, normal faulting occurs at steeper dip-angles while the opposite is true for thrust faulting, the former reaching δ=60° and the latter δ=30° for $\mu \approx 0.6$ at a depth of y=5km. On the other hand, the deviatoric stress, $\Delta\sigma_{xx}$, takes much larger absolute values for thrust faulting than normal faulting as μ increases (Fig. 2.4b). Typical dips of 60° for normal faults are considered in some applications of Chapters 5 and 6. The general deductions for the properties of the stress tensor, including the directions of the principal stress axes with respect to the planes of maximum shear stress, bear similarities with the respective properties of the moment tensor that is described in the following Section.

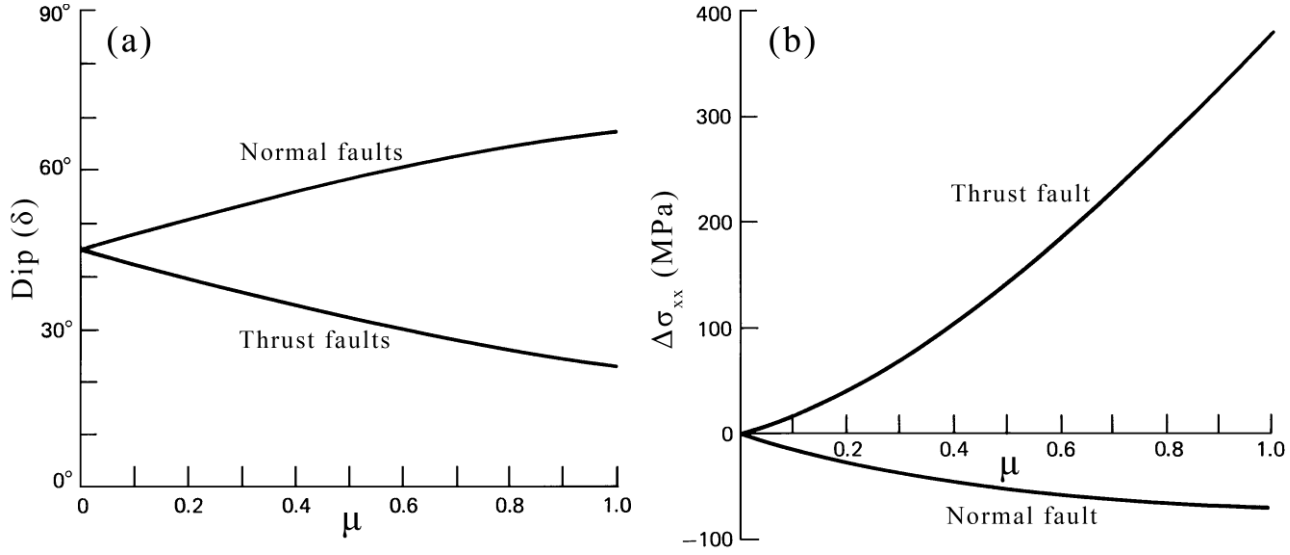

Figure 2.4: a) Relation between the expected fault dip angle, δ, for a given coefficient of internal friction, μ, for normal and thrust faults (Eq. 2.11), b) dependence of the deviatoric stress, $\Delta\sigma_{xx}$, on μ, considering $p_w=\rho_w gy$, ρ=2700kg/m^3, ρ_w=1000kg/m^3, g=10m/s^2 and y=5km in Eq. 2.11. (Figures modified after Turcotte & Schubert, 2002).

2.2 Moment tensors

During tectonic rupture, the walls of the fault are displaced in opposite directions the one relative to the other. The two blocks begin at rest, are accelerated as slip/displacement takes place and finally they stop because of energy loss due to friction or of a sudden blockage of the rupture. At first approximation, it can be considered that the seismic body waves are being radiated from a point source at the earthquake's hypocenter, disregarding the finite extent of the ruptured surface. The dynamics of the displacement are estimated by models of equivalent forces acting at the point source or, rather, at a small distance, *d*, from the source and can be either collinear (tensile/explosive or implosive) or parallel (shear).

In the point source dislocation model, the acting forces during shear rupture can be considered as a single couple (SC) of vectors applied at equal distance, *d*, from the fault plane and pointing to opposite directions. This is one of the two models which had been proposed in the past, the other being the double-couple (DC) model, where a second pair of forces is applied in opposite directions at a small distance from an auxiliary plane that is perpendicular to the fault plane and also passes through the point source. Until more observational data became available, it was debated as to which model better represented a shear rupture, with the simpler SC model being originally

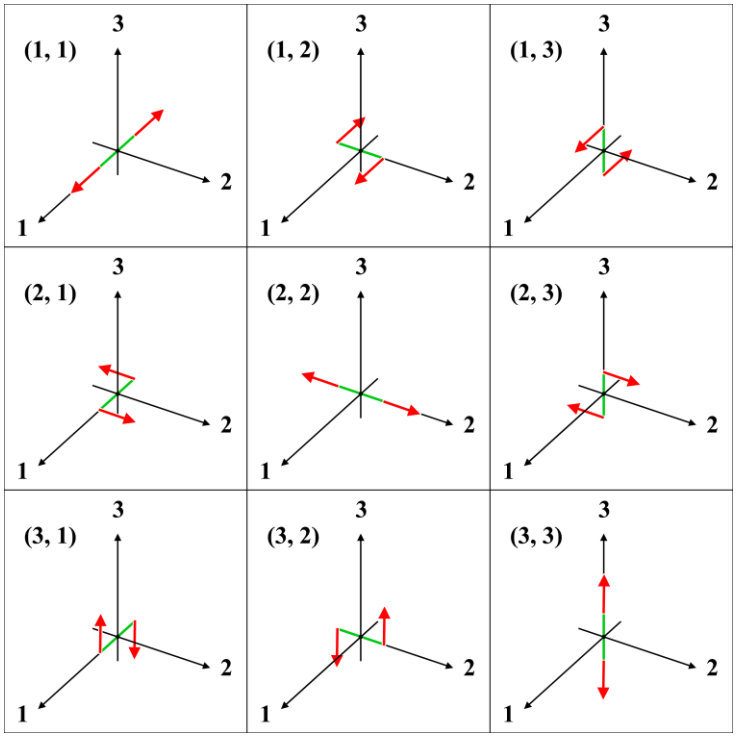

Figure 2.5: The 6 elements M_{ij} of the general 3x3 moment tensor, with coupled forces oriented along the direction indicated by the first index, *i*. Green bars indicate the 2·*d* distance between the points of application for each single couple of forces along the direction indicated by the second index (*j*). All elements have zero net-force. The elements on the diagonal ($i \equiv j$) also have zero net-moment, while the non-diagonal ones ($i \neq j$) require the presence of a second, opposing couple (*j*, *i*), in order to have zero net-moment (no rotation), thus defining a double-couple.

suggested, intuitively, as more realistic. However, near-field and polarity data later confirmed the theoretical predictions of the radiation pattern that is created by a DC system of equivalent forces (Aki & Richards, 2002). The main reason for the initial suggestion of the DC model was that the net-torque of the SC model is non-zero, which would lead to rotation. The DC model overcomes this issue by canceling changes in the angular momentum in a similar way to the stress tensor of Eq. 2.1.

As with the case of the stress tensor, the equivalent forces can be represented in terms of a moment tensor, **M**, with its elements m_{ij} implying the various products $f_{ij} \cdot d$ of the force-couples, f_{ij}, acting at a small distance, d, from a plane, whose normal vector $\mathbf{n}_i$ corresponds to the first index, i, passing through the point source (Fig. 2.5):

$$M = \begin{bmatrix} m_{11} & m_{12} & m_{13} \\ m_{21} & m_{22} & m_{23} \\ m_{31} & m_{32} & m_{33} \end{bmatrix} = \begin{bmatrix} m_{xx} & m_{xy} & m_{xz} \\ m_{yx} & m_{yy} & m_{yz} \\ m_{zx} & m_{zy} & m_{zz} \end{bmatrix} \tag{2.12}$$

The force-couples which exert each of the moments in the diagonal of the tensor, m_{11}, m_{22}, m_{33} (m_{ii}) are collinear (vector dipoles), aligned in a direction indicated by the unitary normal vector $\hat{\mathbf{n}}_i$, while the two forces corresponding to the shear elements, m_{ij} ($i \neq j$), are coplanar and aligned in the direction indicated by i, but are offset, separated by an "arm" in the direction of $\hat{\mathbf{n}}_j$. Similarly to the stress tensor, the moment tensor is symmetric ($m_{ij} = m_{ji}$), having 6 independent elements. The tensor can be uniquely decomposed in an isotropic, $\mathbf{M}_{iso}$, and a deviatoric component, $\mathbf{M}_{dev}$:

$$M = M_{iso} + M_{dev} = tr(M)/3 \begin{bmatrix} 1 & 0 & 0 \\ 0 & 1 & 0 \\ 0 & 0 & 1 \end{bmatrix} + \begin{bmatrix} m_{11} - tr(M)/3 & m_{12} & m_{13} \\ m_{12} & m_{22} - tr(M)/3 & m_{23} \\ m_{13} & m_{23} & m_{33} - tr(M)/3 \end{bmatrix} \tag{2.13}$$

where $tr(\mathbf{M})$ is the trace of the moment tensor. If the isotropic component (representing volume change) is zero, then the tensor is purely deviatoric. A zero trace also reduces the number of independent elements to 5, with $m_{33}=-(m_{11}+m_{22})$.

$$M_{dev} = \begin{bmatrix} m_{11} & m_{12} & m_{13} \\ m_{12} & m_{22} & m_{23} \\ m_{13} & m_{23} & -(m_{11} + m_{22}) \end{bmatrix} \tag{2.14}$$

In the special case where the unitary vector $\hat{\mathbf{n}}_1$ is normal to the fault plane and the slip is in the direction of the unitary vector $\hat{\mathbf{n}}_2$, a SC model would only require one couple of forces that would be represented by the element m_{21} while all others would be zero, including $m_{12}=0$. However, in the corresponding DC model the moment tensor would be symmetric, with a non-zero element $m_{12} = m_{21}$. The tensor would have the following form:

$$M = \begin{bmatrix} 0 & m_{12} & 0 \\ m_{12} & 0 & 0 \\ 0 & 0 & 0 \end{bmatrix} \xrightarrow{\text{diagonalization}} M' = \begin{bmatrix} M_o & 0 & 0 \\ 0 & 0 & 0 \\ 0 & 0 & -M_o \end{bmatrix} \tag{2.15}$$

where M_o represents the scalar seismic moment, an important quantity that is used to measure the size of an earthquake and define its seismic moment magnitude, M_w (Chapter 3).

In the general case, the coordinate system used for moment tensors is the typical (x, y, z) Cartesian system defined by Aki & Richards (2002), where the unit vector $\hat{\mathbf{x}}$ is directed towards the North, $\hat{\mathbf{y}}$ points to the East and $\hat{\mathbf{z}}$ vertically downwards. A DC focal mechanism can be represented by three parameters corresponding to one of the two nodal planes: strike ($\varphi_f \in [0°, 360°]$), sometimes symbolized simply as "φ", dip ($\delta \in [0°, 90°]$), and rake or slip direction ($\lambda \in [-180°, 180°]$). Strike and dip are characteristics of the particular nodal plane itself while the rake provides information on the slip direction and the orientation of the other nodal plane. If the selected nodal plane is the fault plane, the rake is defined as the angle between the fault's strike and the slip vector (or its projection on the fault plane), which shows the direction of motion of the hanging wall relative to the footwall (Lay & Wallace, 1995). Other characteristics of the fault geometry are presented in Fig. 2.6. With $\hat{\mathbf{n}}$ being the unit normal vector to the fault plane and $\hat{\mathbf{d}}$ the unit slip vector (coplanar to the fault plane for a pure DC mechanism), the moment tensor's elements can be written as a function of $\hat{\mathbf{n}}$, $\hat{\mathbf{d}}$ and M_o:

$$m_{ij} = M_o \cdot (n_i d_j + n_j d_i) \tag{2.16}$$

where n_i and d_i are the components of $\hat{\mathbf{n}}$ and $\hat{\mathbf{d}}$ in the direction indicated by the index, i. The relation

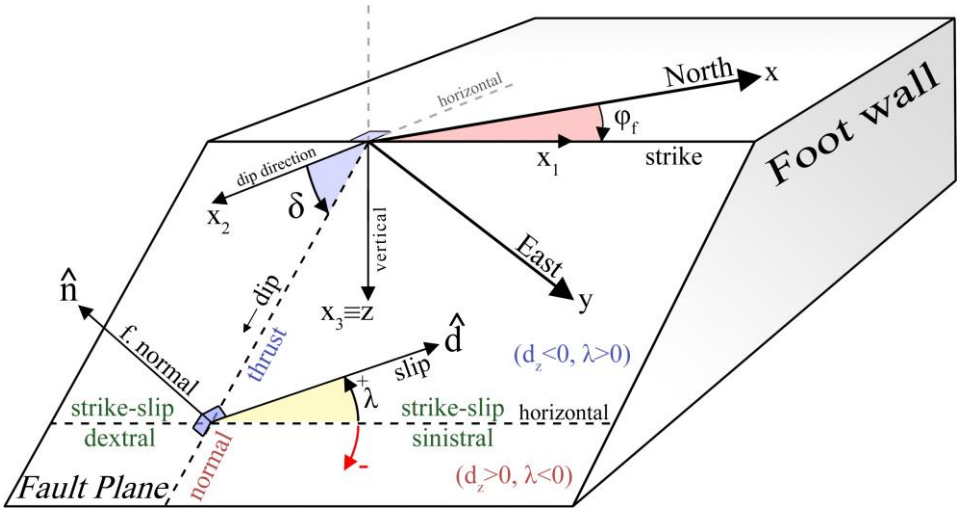

Figure 2.6: Fault geometry and associated vectors. Two types of coordinate systems are displayed, one ($\mathbf{x}_1$, $\mathbf{x}_2$, $\mathbf{x}_3$) aligned to the fault's strike ($\mathbf{x}_1$)and dip direction ($\mathbf{x}_2$) and Aki & Richards (2002) geographical coordinate system ($\mathbf{x}$, $\mathbf{y}$, $\mathbf{z} \equiv \mathbf{x}_3$), with positive orientations: $\mathbf{x}\rightarrow$North, $\mathbf{y}\rightarrow$East and $\mathbf{z}\rightarrow$downwards. The fault's normal unit vector, $\mathbf{n}$, and the slip unit vector, $\mathbf{d}$ are also displayed. (Figure based on Stein & Wysession, 2003, but using a different coordinate system)

between n_i and d_i in Eq. 2.16 shows that the two unit vectors, $\hat{\mathbf{n}}$ and $\hat{\mathbf{d}}$, are interchangeable (Stein & Wysession, 2003): the same moment tensor / radiation pattern would apply for a fault plane with a unit normal vector in the direction of $\hat{\mathbf{d}}$, which in this case corresponds to the auxiliary nodal plane, and a unit slip vector in the direction of $\hat{\mathbf{n}}$. This ambiguity between the fault plane and the auxiliary plane is one of the major characteristics of the DC model. It also means that a second set of strike, dip and rake parameters (φ', δ', λ'), corresponding to the auxiliary nodal plane, can define the focal mechanism.

In a geographic Cartesian coordinate system, where the axis $\hat{\mathbf{x}}$ is directed northwards, $\hat{\mathbf{y}}$ eastwards and $\hat{\mathbf{z}}$ downwards (as in Aki & Richards standard coordinate system), the $\hat{\mathbf{n}}$ and $\hat{\mathbf{d}}$ unit vectors (Fig. 2.6) can be defined in the following forms (Gasperini & Vannucci, 2003):

$$\hat{n} = \begin{pmatrix} -\sin\delta\sin\phi_f \\ \sin\delta\cos\phi_f \\ -\cos\delta \end{pmatrix} \tag{2.17}$$

$$\hat{d} = \begin{pmatrix} \cos\lambda\cos\phi_f + \cos\delta\sin\lambda\sin\phi_f \\ \cos\lambda\sin\phi_f - \cos\delta\sin\lambda\cos\phi_f \\ -\sin\delta\sin\lambda \end{pmatrix} \tag{2.18}$$

while the corresponding unit vectors for the auxiliary plane are $\hat{\mathbf{n}}' = \hat{\mathbf{d}}$ and $\hat{\mathbf{d}}' = \hat{\mathbf{n}}$.

The moment tensor can be diagonalized similarly to the stress tensor (Eqs 2.2, 2.3). Principal component analysis can provide the eigenvectors and eigenvalues of the rotated moment tensor:

$$M = \begin{bmatrix} m_{xx} & m_{xy} & m_{xz} \\ m_{yx} & m_{yy} & m_{yz} \\ m_{zx} & m_{zy} & m_{zz} \end{bmatrix} = V\Lambda V^{-1} = \begin{bmatrix} t_x & b_x & p_x \\ t_y & b_y & p_y \\ t_z & b_z & p_z \end{bmatrix} \cdot \begin{bmatrix} \lambda_1 & 0 & 0 \\ 0 & \lambda_2 & 0 \\ 0 & 0 & \lambda_3 \end{bmatrix} \cdot \begin{bmatrix} t_x & b_x & p_x \\ t_y & b_y & p_y \\ t_z & b_z & p_z \end{bmatrix}^{-1} \tag{2.19}$$

Or, in terms of the example in Eq. 2.15:

$$M = \begin{bmatrix} t_x & b_x & p_x \\ t_y & b_y & p_y \\ t_z & b_z & p_z \end{bmatrix} \cdot \begin{bmatrix} M_o & 0 & 0 \\ 0 & 0 & 0 \\ 0 & 0 & -M_o \end{bmatrix} \cdot \begin{bmatrix} t_x & b_x & p_x \\ t_y & b_y & p_y \\ t_z & b_z & p_z \end{bmatrix}^{-1} \tag{2.20}$$

The elements of the diagonal $\lambda_1 = M_o$, $\lambda_2 = 0$ and $\lambda_3 = -M_o$ are the eigenvalues of the moment tensor. From this form, M_o can be determined as:

$$M_o = \frac{1}{2}\left(|\lambda_1| + |\lambda_3|\right) \tag{2.21}$$

where $|\lambda_1|$ and $|\lambda_3|$ are the two eigenvalues with the larger absolute values. This definition can also cover moment tensors which are not pure DC, where $|\lambda_1| \neq |\lambda_3|$. As in the case of the stress tensor, **V** is the matrix of orthonormal eigenvectors, sorted by order of descending eigenvalue. In a pure DC moment tensor, the eigenvector corresponding to the positive eigenvalue (minimum compressional deformation) is the "tension axis", **T**, the one with the zero eigenvalue is the intermediate stress or null axis, **B**, and the last one, corresponding to negative eigenvalue (maximum compressional deformation), is the "pressure axis", **P** (Lay & Wallace, 1995). In the general case of a symmetric but non-DC moment tensor, $\mathrm{tr}(\mathbf{M}) \cong 0$ if there is an isotropic component and/or $\lambda_2 \cong 0$, but rather a different combination of eigenvalues results in $\mathrm{tr}(\mathbf{M}_{\mathrm{dev}})=0$ in the deviatoric component. In the special case of $\theta=45°$ in Eq. 2.10, the axes **P**, **B**, and **T** coincide with the principal stress axes corresponding to σ_1, σ_2 and σ_3. However, this is only true by random chance, not only because most earthquakes occur on pre-existing faults but also due to the fact that the crust can be very fragmented, crossed by many discontinuities which could rupture under the right stress and pore-pressure conditions. The orientations of the principal stress axes and their relative (but not absolute) magnitude can be estimated statistically by inversion procedures (Gephart & Forsyth, 1984; Michael, 1984) which utilize regional fault and slip data to calculate a probability density distribution of **P**, **B**, **T** and determine the reduced deviatoric stress tensor (Xu, 2004).

In the DC model, if the axes **P**, **T** are known, the orientation of **B** can be deduced from orthogonality ($\mathbf{B} = \pm\mathbf{P}\times\mathbf{T}$). More importantly, knowing the coordinates of **P** and **T** (the DC moment tensor), one can obtain φ_f, δ and λ from the geometry of Fig. 2.6. Axes such as **P** and **T** can be represented by either their Cartesian coordinates, as in the eigenvector matrix, **V** (Eq. 2.19), or by their trend, $\alpha \in [0, 360°]$ (clockwise angle between the direction of the North and their projection on the horizontal plane) and plunge, $\gamma \in [0, 90°]$ (inclination between the vector and the horizontal plane). The trend is undefined for $\gamma=90°$ while it can take two values, α and $\alpha+180°$ for $\gamma=0$. These parameters can be derived from the Cartesian coordinates of **P**, **B** and **T** in the AR system (Gasperini & Vannucci, 2003):

$$\begin{aligned} \gamma_P &= \arcsin(p_z), \quad \alpha_P = \arctan\left(\frac{p_y}{p_x}\right) \\ \gamma_T &= \arcsin(t_z), \quad \alpha_T = \arctan\left(\frac{t_y}{t_x}\right) \\ \gamma_B &= \arcsin(b_z), \quad \alpha_B = \arctan\left(\frac{b_y}{b_x}\right) \end{aligned} \tag{2.22}$$

In case $\gamma < 0$ (which happens when the z component of **P**, **B** or **T** are negative) γ is reversed and 180° are added to α (which can be wrapped if it exceeds 360°). In that case, the vector itself could be reversed so that its components correspond to the reversal of its plunge and trend. The following equations can be used for the reverse relation:

$$\begin{array}{lll} p_x = \cos\gamma_P \cos\alpha_P & t_x = \cos\gamma_T \cos\alpha_T & b_x = \cos\gamma_B \cos\alpha_B \\ p_y = \cos\gamma_P \sin\alpha_P & t_y = \cos\gamma_T \sin\alpha_T & b_y = \cos\gamma_B \sin\alpha_B \\ p_z = \sin\gamma_P & t_z = \sin\gamma_T & b_z = \sin\gamma_B \end{array} \tag{2.23}$$

The coordinates of $\hat{\mathbf{n}}$ and $\hat{\mathbf{d}}$ can be calculated from **P** and **T** with the relations (Gasperini & Vannucci, 2003)[1]:

$$n_i = \frac{-(t_i + p_i)}{\sqrt{2}}, \qquad d_i = \frac{-(t_i - p_i)}{\sqrt{2}} \tag{2.24}$$

and the fault parameters φ_f, δ and λ can be calculated from $\hat{\mathbf{n}}$ and $\hat{\mathbf{d}}$ as follows:

$$\left.\begin{array}{c} \delta = \arccos(-n_z) \\ \phi_f = \arctan\left(\dfrac{-n_x}{n_y}\right) \\ \lambda = \arctan\left(\dfrac{-d_z/\sin\delta}{d_x\cos\phi_f + d_y\sin\phi_f}\right) \end{array}\right\} n_z \neq -1, \quad or \quad \left.\begin{array}{c} \delta = 0 \\ \phi_f = 0 \\ \lambda = \arctan\left(\dfrac{-d_y}{d_x}\right) \end{array}\right\} n_z = -1 \tag{2.25}$$

The above formulae[2] take for granted that $n_z \leq 0$, which is true for the fault plane since, by definition, its normal vector points upwards (at an angle) while the vertical axis' positive orientation is downwards. However, d_z can take positive values when $\lambda<0$ (Fig. 2.6), or $t_z<p_z$ (both always positive, pointing downwards) or $\gamma_T<\gamma_P$. Swapping places for n_i and d_i, one can calculate the corresponding φ', δ' and λ' parameters for the auxiliary nodal plane. However, care should be taken so that $n_z' \leq 0$, otherwise the signs in all components of $\hat{\mathbf{n}}'$ and $\hat{\mathbf{d}}'$ must be reversed (Gasperini & Vannucci, 2003). For the fault plane, by definition, it's always $n_z \leq 0$ as long as t_z, $p_z \geq 0$, otherwise the corresponding vectors with negative vertical component (**P** and/or **T**, if required) must be reversed.

The DC moment tensors represent certain faulting types. This is usually defined by the [φ, δ, λ] parameters of the nodal planes but they can also be defined in terms of the **P**, **B**, **T** axes plunge angles (Table 2.1). There is a region of **P** and **T** plunges in which focal mechanisms are not classified in a typical faulting type, but rather as "odd" or "unknown". This is the case of either sub-horizontal faults with horizontal slip or sub-vertical faults with dip-slip (both γ_P and $\gamma_T \approx 45°$ or all three axes with $25° < \gamma < 45°$). Such cases are generally rare and may characterize very low-angle normal faults or thrusts where the principal stress field is tilted out of horizontal and vertical planes (Zoback, 1992).

[1] In the formula for d_i in Eq. 2.24 a -1 factor has been added, as the corresponding functions for the derivation of d_i from φ_f, δ, λ in the appendix of Gasperini & Vannucci (2003) actually result in opposite values and λ could not be derived correctly.

[2] An alternative formula for λ is: $\lambda = -\arccos(d_x \cdot \cos\varphi_f + d_y \cdot \sin\varphi_f)$, however this also requires a reversal of the sign of λ in case $d_z<0$.

Table 2.1: Stress regime characterization based on the plunge, γ_i, of **P**, **B** and **T** axes (on the basis of them being an approximation of the principal stress axes $\mathbf{S}_1$, $\mathbf{S}_2$ and $\mathbf{S}_3$), where NF, SS and TF refer to normal, strike-slip and thrust faulting, while NF and TF to oblique normal and thrust faulting, respectively. The trend of the maximum horizontal stress axis, $\mathbf{S}_{Hmax}$, is also indicated (after Zoback, 1992). The last two lines ("Odd" faulting type) have been added for completeness.

P ($\boldsymbol{\sigma_1}$)	**B** ($\boldsymbol{\sigma_2}$)	**T** ($\boldsymbol{\sigma_3}$)	Regime or faulting type	$S_{\mathbf{Hmax}}$ trend
$\boldsymbol{\gamma_P \geq 52°}$		$\gamma_T \leq 35°$	NF	α_B
$\boldsymbol{40° \leq \gamma_P < 52°}$		$\gamma_T \leq 20°$	NS	$\alpha_T + 90°$
$\boldsymbol{\gamma_P < 40°}$	$\gamma_B \geq 45°$	$\gamma_T \leq 20°$	SS	$\alpha_T + 90°$
$\boldsymbol{\gamma_P \leq 20°}$	$\gamma_B \geq 45°$	$\gamma_T < 40°$	SS	α_P
$\boldsymbol{\gamma_P \leq 20°}$		$40° \leq \gamma_T < 52°$	TS	α_P
$\boldsymbol{\gamma_P \leq 35°}$		$\gamma_T \geq 52°$	TF	α_P
$\boldsymbol{40 \leq \gamma_P \leq 50°}$	$\gamma_B \approx 0°$	$40 \leq \gamma_T \leq 50°$	"Odd"	-
$\boldsymbol{25 \leq \gamma_P \leq 45°}$	$25 \leq \gamma_B \leq 45°$	$25 \leq \gamma_T \leq 45°$	"Odd"	-

The DC moment tensor's elements in the AR coordinate system can be calculated directly from φ_f, δ and λ or, equivalently, from φ', δ' and λ' (Aki & Richards, 2002):

$$
\begin{aligned}
m_{xx} &= -M_o\left(\sin\delta\cos\lambda\sin 2\phi_f + \sin 2\delta\sin\lambda\sin^2\phi_f\right)\\
m_{yy} &= M_o\left(\sin\delta\cos\lambda\sin 2\phi_f - \sin 2\delta\sin\lambda\cos^2\phi_f\right)\\
m_{zz} &= M_o\left(\sin 2\delta\sin\lambda\right) = -\left(m_{11}+m_{22}\right)\\
m_{xy} &= M_o\left(\sin\delta\cos\lambda\cos 2\phi_f + \frac{1}{2}\sin 2\delta\sin\lambda\sin 2\phi_f\right) = m_{yx}\\
m_{xz} &= -M_o\left(\cos\delta\cos\lambda\cos\phi_f + \cos 2\delta\sin\lambda\sin\phi_f\right) = m_{zx}\\
m_{yz} &= -M_o\left(\cos\delta\cos\lambda\sin\phi_f - \cos 2\delta\sin\lambda\cos\phi_f\right) = m_{zy}
\end{aligned}
\tag{2.26}
$$

While the decomposition of a moment tensor to an isotropic, $\mathbf{M}_{iso}$, and deviatoric component, $\mathbf{M}_{dev}$, is unique, if $\mathbf{M}_{dev}$ does not have one eigenvalue equal to zero (pure DC), it can be further analysed in a few different ways (Jost & Herrmann, 1989). A common decomposition is to a DC component, $\mathbf{M}_{DC}$, and another called Compensated Linear Vector Dipole, or CLVD. The diagonalized form of CLVD is:

$$
M_{CLVD} = \begin{bmatrix} -\lambda & 0 & 0 \\ 0 & \lambda/2 & 0 \\ 0 & 0 & \lambda/2 \end{bmatrix}
\tag{2.27}
$$

which represents three dipoles, with one of them being -2 times the magnitude of the others (Stein & Wysession, 2003). These may occur naturally in volcanic areas, caused by the inflation of magma which can generate tensile opening of cracks, or during fissure eruptions or slip on ring-fault structures, where CLVDs with a sub-vertical tensional (T) axis may be observed (e.g. Kanamori *et al.*, 1993; Shuler *et al.*, 2013) or by a deflation that can cause subsidence, as with the observed CLVD mechanisms with a vertical compressional (P) axis during the collapse of the Bárðarbunga

caldera in Iceland (Riel *et al.*, 2015). In such cases, volume change can be expressed by an isotropic component and the deviatoric part by one or more CLVDs, which represent crack opening or closing without causing volume change. Another type of decomposition for $\mathbf{M}_{dev}$ with eigenvalues $[\lambda_1, \lambda_2, \lambda_3]$ where $|\lambda_1| \geq |\lambda_2| \geq |\lambda_3|$ is to a major and a minor DC with eigenvalues $[\lambda_1, -\lambda_1, 0]$ and $[0, -\lambda_3, \lambda_3]$, respectively (Kanamori & Given, 1981). It is useful in studies of moment tensor inversion to characterize the quality of the inversion by the percentage of DC or CLVD, usually attributing the non-DC component to noise or misfits, unless a physical mechanism could explain a real CLVD (e.g. in an active volcanic region or under the influence of pressurized fluids). The procedures of decomposition and calculation of DC percentages are described in detail by Jost & Herrmann (1989).

2.3 Radiation Pattern and polarization of particle motion

Seismic waves of tectonic earthquakes are generated when sudden slip occurs on a fault, which at first approximation can be considered as a plane surface. Both longitudinal and shear body waves radiate outwards from the earthquake's focus through the Earth's layers where they undergo through refractions, reflections, scattering, dispersion and other transformations until they finally reach a seismological station. The full waveform recording may be complex; however, the properties of the source can still be recovered from the particle motion of the wave onsets.

Intuitively, even considering the SC model, the coseismic deformation that occurs during slip on each fault wall is expected to produce pressure waves which are compressive towards the direction of the corresponding wall's displacement and dilatational to the other direction. The opposite would happen on the other half, eventually dividing the space in four quadrants of alternating P-wave first motion polarities. The typical representation of a DC focal mechanism is the stereonet, an equal area lower-hemisphere projection of the two nodal planes with four quadrants, colour coded alternately for compressional (darker colour) and dilatational (white) P-wave first motion polarities. In this projection, the σ_1 axis ($\mathbf{S}_1$) is expected to be within the same quadrant as **P** and the σ_3 axis ($\mathbf{S}_3$) within the quadrant of **T**. However, the traces of **P** and **T** are always situated at exactly 45° from the nodal planes.

Some examples of stereonet depictions, nodal planes and the respective **P**, **B** and **T** axes parameters are presented in Table 2.2. The first four represent pure strike-slip solutions, with **P**, **T** horizontal ($\gamma_P=\gamma_T=0$) and **B** vertical ($\gamma_B=90°$). Solutions 5-8 are pure (dip-slip) normal ($\gamma_B=\gamma_T=0$, $\gamma_P=90°$, $\lambda=-90°$) while 9-12 are pure reverse ($\gamma_P=\gamma_T=0$, $\gamma_T=90°$, $\lambda=+90°$). Focal mechanisms 9-19 are oblique-reverse (13-16) or oblique-normal (17-20), mainly characterized by $\gamma_B>0$, while solutions 21-25 are of the "Odd" type (Table 2.1), with $\gamma_P=\gamma_T=45$ and $\gamma_B=0$, representing vertical slip on a vertical plane (solution #1, $\delta_1=90°$) or horizontal slip on a horizontal plane (solution #2, $\delta_2=0°$).

P-wave seismic rays radiate outwards from the source and some of them eventually reach seismological stations. Unless reflected or transformed, they retain their initial polarization and polarity, compressive or dilatational towards their direction of propagation. The vertical first motion polarity is indicative of whether the ray originated from a quadrant of compressional (upward; Fig. 2.7a) or dilatational (downward; Fig. 2.7b) first motion. The trace of a P-wave seismic ray

corresponding to a station is represented on the stereonet by the station's azimuth, φ_s, with respect to the epicenter and the take-off angle (i_h), measured from nadir up to the initial ray's direction at the source. For local stations the seismic rays can be up-going ($i_h > 90°$), in which case the tangential to the ray at the focus must be extrapolated to the lower hemisphere of the focal sphere, while its trace on the stereonet will be positioned at the conjugate take-off angle $i_h' = 180° - i_h$ and at an azimuth $\varphi_s + 180°$, which is a valid approximation for the back-azimuth of the station, φ_s' (azimuth of the epicenter relative to the station), but only at small epicentral distances due to the Earth's sphericity. With enough measurements from azimuthally distributed stations, one can constrain the focal mechanism for a certain event by determining an appropriate pair of orthogonal nodal planes which divide the sphere in four quadrants of alternating first motion polarities.

Calculations on the elastodynamics of the far-field displacement generated by a point double-couple source lead to the radiation pattern for the P-waves, R_P (Aki & Richards, 2002):

Table 2.2: Nodal plane and **P**, **B**, **T** axes information for 25 examples of focal mechanisms, with φ, δ and λ corresponding to strike, dip and rake of the respective nodal plane (1 or 2), while α_i and γ_i being the trend and plunge of the **P**, **B** or **T** axes (index *i*). All values are in degrees. (Also see Table 2.3).

	φ_1	δ_1	λ_1	φ_2	δ_2	λ_2	α_P	γ_P	α_B	γ_B	α_T	γ_T
1	0	90	0	90	90	-180	315	0	90	90	225	0
2	45	90	0	135	90	-180	0	0	135	90	270	0
3	90	90	0	0	90	180	45	0	180	90	315	0
4	135	90	0	225	90	-180	90	0	225	90	0	0
5	0	45	-90	180	45	-90	0	90	180	0	270	0
6	45	45	-90	225	45	-90	0	90	225	0	315	0
7	90	45	-90	270	45	-90	0	90	270	0	0	0
8	135	45	-90	315	45	-90	0	90	135	0	225	0
9	0	45	90	180	45	90	270	0	180	0	0	90
10	45	45	90	225	45	90	315	0	225	0	0	90
11	90	45	90	270	45	90	180	0	90	0	0	90
12	135	45	90	315	45	90	225	0	135	0	0	90
13	0	60	45	243	52	141	120	5	27	38	216	52
14	90	60	45	333	52	141	210	5	117	38	306	52
15	180	60	45	63	52	141	300	5	207	38	36	52
16	270	60	45	153	52	141	30	5	297	38	126	52
17	0	60	-45	117	52	-141	324	52	153	38	60	5
18	90	60	-45	207	52	-141	54	52	243	38	150	5
19	180	60	-45	297	52	-141	144	52	333	38	240	5
20	270	60	-45	27	52	-141	234	52	63	38	330	5
21	0	90	90	0	0	-90	90	45	0	0	270	45
22	45	90	90	0	0	-135	135	45	45	0	315	45
23	90	90	90	0	0	180	180	45	90	0	0	45
24	135	90	90	0	0	135	225	45	135	0	45	45
25	180	90	90	0	0	90	270	45	180	0	90	45

$$R_P = \cos\lambda \sin\delta \sin^2 i_h \sin 2\phi - \cos\lambda \cos\delta \sin 2i_h \cos\phi + \sin\lambda \sin 2\delta \left(\cos^2 i_h - \sin^2 i_h \sin^2 \phi\right) + \sin\lambda \cos 2\delta \sin 2i_h \sin\phi \quad (2.28)$$

where [3] $\varphi \equiv \varphi_s - \varphi_f$. The pattern is characterized by four lobes, coupled as dipoles in the direction of **T** and **P** axes, with positive and negative values, respectively, at 45° from the nodal planes. Eq. 2.28 can be used for the calculation of the theoretical polarity of the P-wave (sign of R_P: positive for compression, negative for dilatation) for a given focal mechanism (φ_f, δ, λ), hypocenter and station (φ_s, i_h), which can then be compared to the observed polarity to confirm a match or discrepancy.

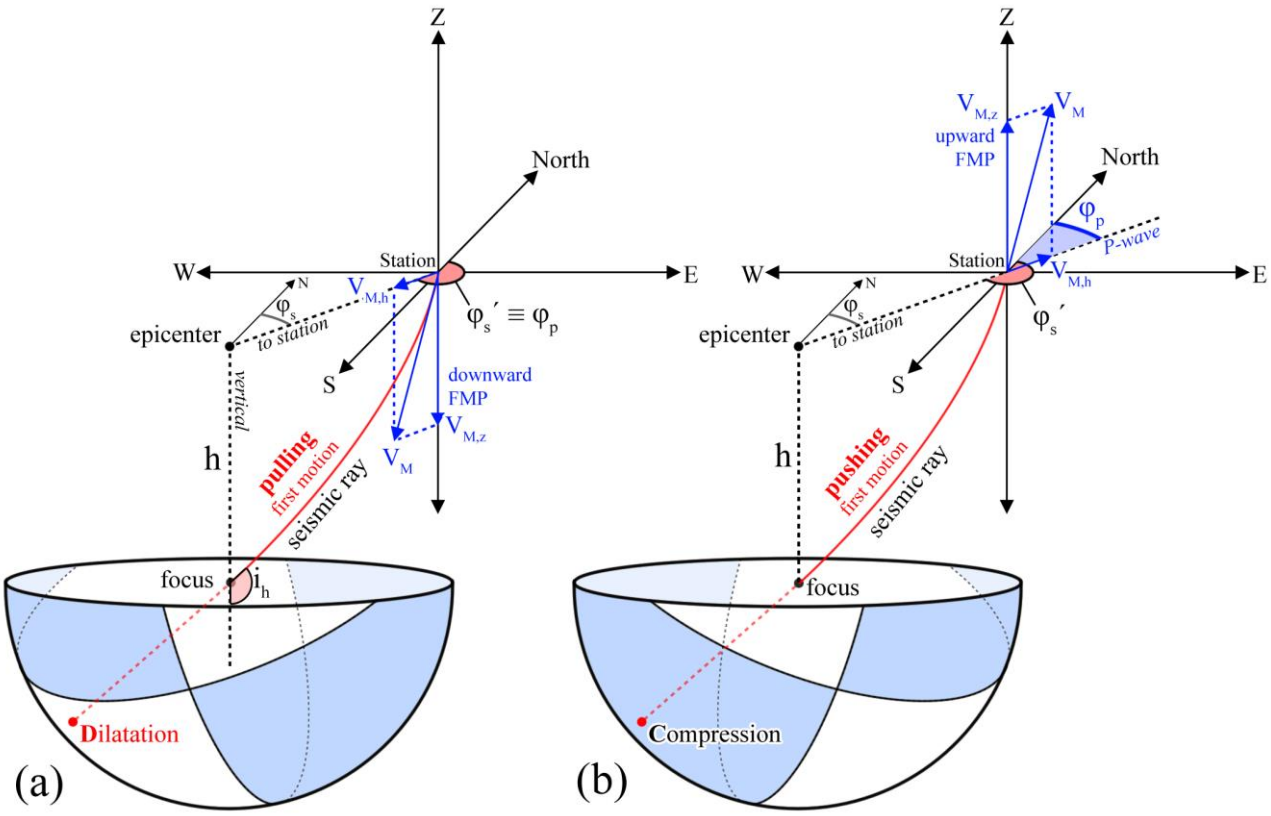

Figure 2.7: P-wave first motion for an upwards directed seismic ray radiating from a) a dilatational quadrant of the focal sphere, b) a compressional quadrant of the focal sphere. $\mathbf{V}_M$ is the vector of P-wave first motion, $\mathbf{V}_{M,h}$ its horizontal component (corresponding to the polarization direction, pol. dir.) and $\mathbf{V}_{M,z}$ its vertical component, φ_s is the azimuth of the station relative to the epicenter while $\varphi_s'=180-\varphi_s$ is the back-azimuth, φ_p is the horizontal polarization of the P-wave, i_h the take-off angle and h denotes the focal depth. The hemispheres represent a typical example of focal mechanism that is usually represented as a lower-hemisphere projection.

[3] Note: The notation of the argument $(\varphi_s-\varphi_f) \equiv \varphi$ is different in Aki & Richards (2002), where φ is used for the source-receiver azimuth (or simply station's azimuth) and φ_s for the fault's strike, thus it is expressed as $(\varphi-\varphi_s)$ and produces the correct values and polarities. The same remark goes for Eqs 2.29 and 2.30.

The absolute values of P-waves maximize in the vicinity of the **T** and **P** axes. Near the nodal planes and the null axis: $R_P \rightarrow 0$, which makes the characterization of the P-wave onset uncertain.

The first pulse of the P-waves tends to be linearly polarized, with the particle motion being collinear to the seismic ray. The P-wave radiation pattern (Fig. 2.8) indicates that the polarization direction is radial at the focus while the horizontal polarization, φ_p, at the station is in the direction indicated by the station's azimuth with respect to the epicenter. When the trace of the seismic ray that corresponds to a seismological station is in a compressive quadrant of the focal sphere, the P-wave first motion is similar to what would be caused by the shockwave of an explosion, had it occurred at the focus (Fig. 2.7b). In that case, the first motion would be directed outwards, away from the epicenter, and the vertical first motion would be upwards (compressive). The opposite is true for dilatational quadrants; the first motion would be that of an implosion, pulling towards the epicenter (Fig. 2.7a). In both cases, the direction corresponds to the azimuth of the epicenter with respect to the station or the opposite. This in fact can be used as a first approximation to the problem of epicentral location, especially when the waveform data is limited to only a few stations (e.g. Kaviris, 2003). Simply measuring the vertical polarity of the P-wave first motion at several stations, preferably distributed at various azimuths and angles of emergence, can provide useful data for the determination of an event's focal mechanism.

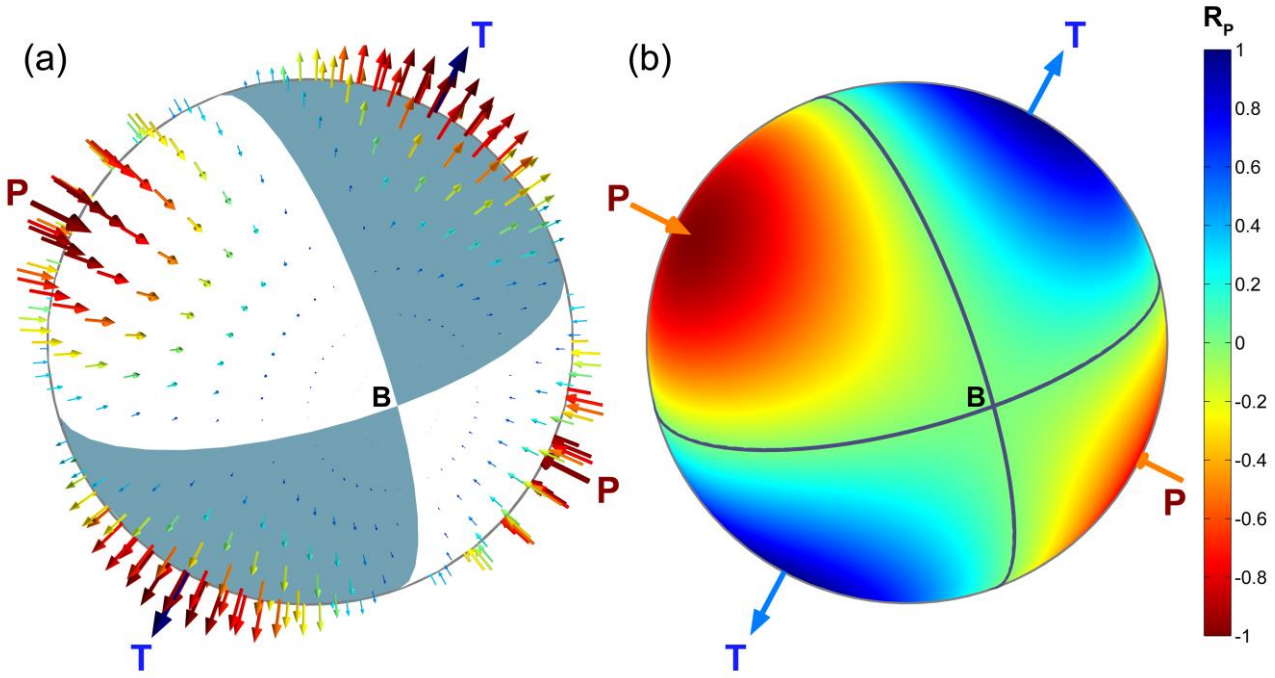

Figure 2.8: 3D representation of the P-wave radiation pattern in a double-couple focal mechanism. a) Direction and amplitude of the P-wave first motion, b) distribution of the (signed) R_P values, indicating polarity and amplitude of the P-wave first motion. **P** and **T** vectors correspond to the P- and T-axes while **B** marks the trace of the null-axis on the focal sphere.

The shear body-waves oscillate on a plane that is perpendicular to the seismic ray (Fig. 2.9). They are typically decomposed in two distinct types, SH and SV. The former is the purely horizontal component of the S-wave oscillation that is in a direction perpendicular to the horizontal projection of the seismic ray. SV, is perpendicular to both P and SH; it has both a vertical, SV_z, and a horizontal component, SV_h, with the latter being collinear with the horizontal projection of the seismic ray, pointing away from the epicenter while the ray is down-going and towards the epicenter otherwise. Aki & Richards (2002) defined a coordinate system that is oriented according to P, SV and SH, with unit vectors $\hat{\mathbf{l}}$ (along ray), $\hat{\mathbf{p}}$ (transverse, on vertical plane) and $\hat{\boldsymbol{\varphi}}$ (transverse, horizontal), with their positive axes being: $\hat{\mathbf{l}}$ towards the ray's direction, $\hat{\mathbf{p}}$ oriented so that its vertical component is directed upwards and $\hat{\boldsymbol{\varphi}} = \hat{\mathbf{l}} \times \hat{\mathbf{p}}$ (Fig. 2.9). The equations of the far-field radiation pattern of SH and SV for a point double-couple source are the following (Aki & Richards, 2002):

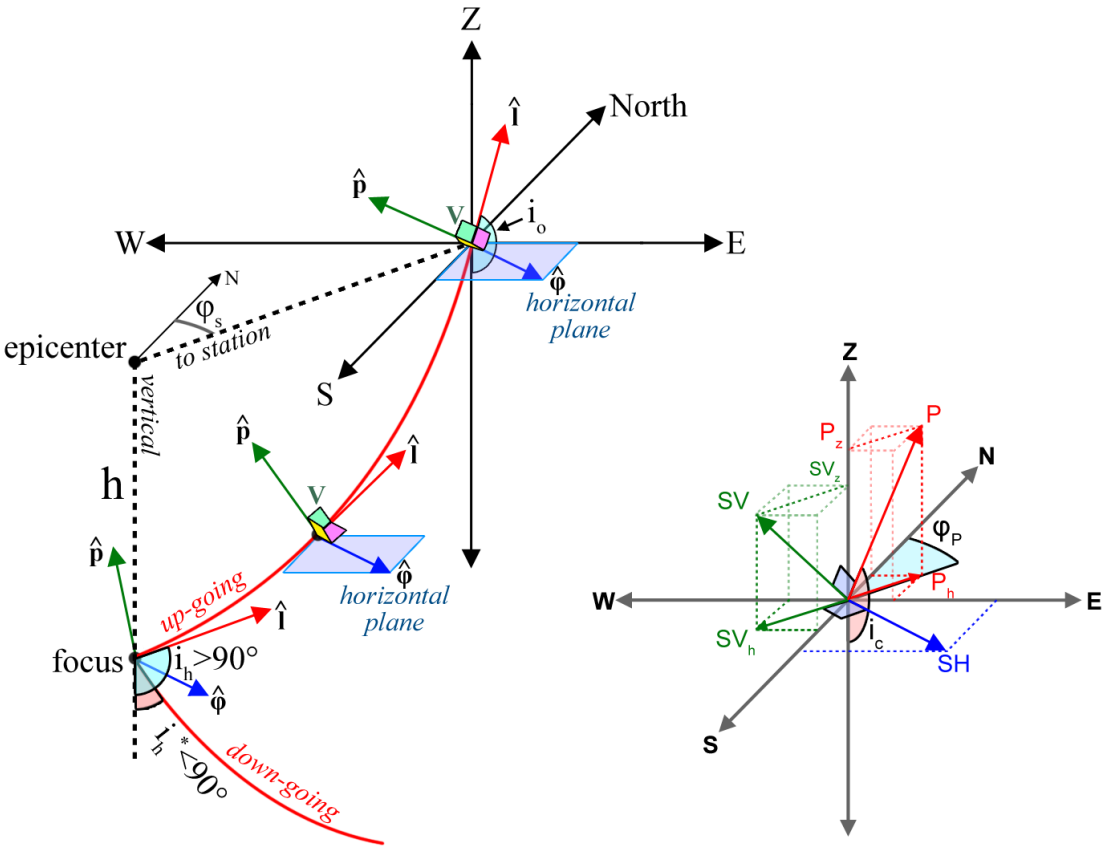

Figure 2.9: Rotation of the relative coordinate system for the polarization of P, SH and SV waves, defined, respectively, by the unit vectors $\hat{\mathbf{l}}$ (tangential to the ray-path, oriented towards the propagation direction), $\hat{\mathbf{p}}$ (transverse to the propagation direction, on a vertical plane "**V**" defined by $\hat{\mathbf{p}}$ and $\hat{\mathbf{l}}$) and $\hat{\boldsymbol{\varphi}}$ (transverse, horizontal), normal to the **V** plane. The S-waves oscillate at the plane defined by $\hat{\mathbf{p}}$ and $\hat{\boldsymbol{\varphi}}$. The vectors $\hat{\mathbf{l}}$ and $\hat{\mathbf{p}}$ rotate around $\hat{\boldsymbol{\varphi}}$ as the waves propagate while $\hat{\boldsymbol{\varphi}}$ is only translated. Vector $\hat{\mathbf{l}}$ begins at an i_h take-off angle and ends up at an i_o angle of incidence at the surface, φ_s is the azimuth of the station relative to the epicenter and h denotes the focal depth. At the lower-right diagram, SV_z and P_z are the vertical components of **SV** and **P**, respectively, while $\mathbf{SV_h}$ and $\mathbf{P_h}$ are the corresponding horizontal ones. **SH** does not have a vertical component, $\mathbf{SV_h} \perp \mathbf{SH}$, $\mathbf{SH} \perp \mathbf{P_h}$, $\mathbf{SV} \perp \mathbf{SH} \perp \mathbf{P}$ and $\mathbf{SV} \perp \mathbf{P}$, while $\mathbf{SV_h}$ is collinear to $\mathbf{P_h}$, but in opposite direction due to $P_z > 0$.

$$R_{SV} = \sin\lambda\cos 2\delta\cos 2i_h\sin\phi - \cos\lambda\cos\delta\cos 2i_h\cos\phi$$
$$+\frac{1}{2}\cos\lambda\sin\delta\sin 2i_h\sin 2\phi - \frac{1}{2}\sin\lambda\sin 2\delta\sin 2i_h\left(1+\sin^2\phi\right) \quad (2.29)$$

and

$$R_{SH} = \cos\lambda\cos\delta\cos i_h\sin\phi + \cos\lambda\sin\delta\sin i_h\cos 2\phi$$
$$+\sin\lambda\cos 2\delta\cos i_h\cos\phi - \frac{1}{2}\sin\lambda\sin 2\delta\sin i_h\sin 2\phi \quad (2.30)$$

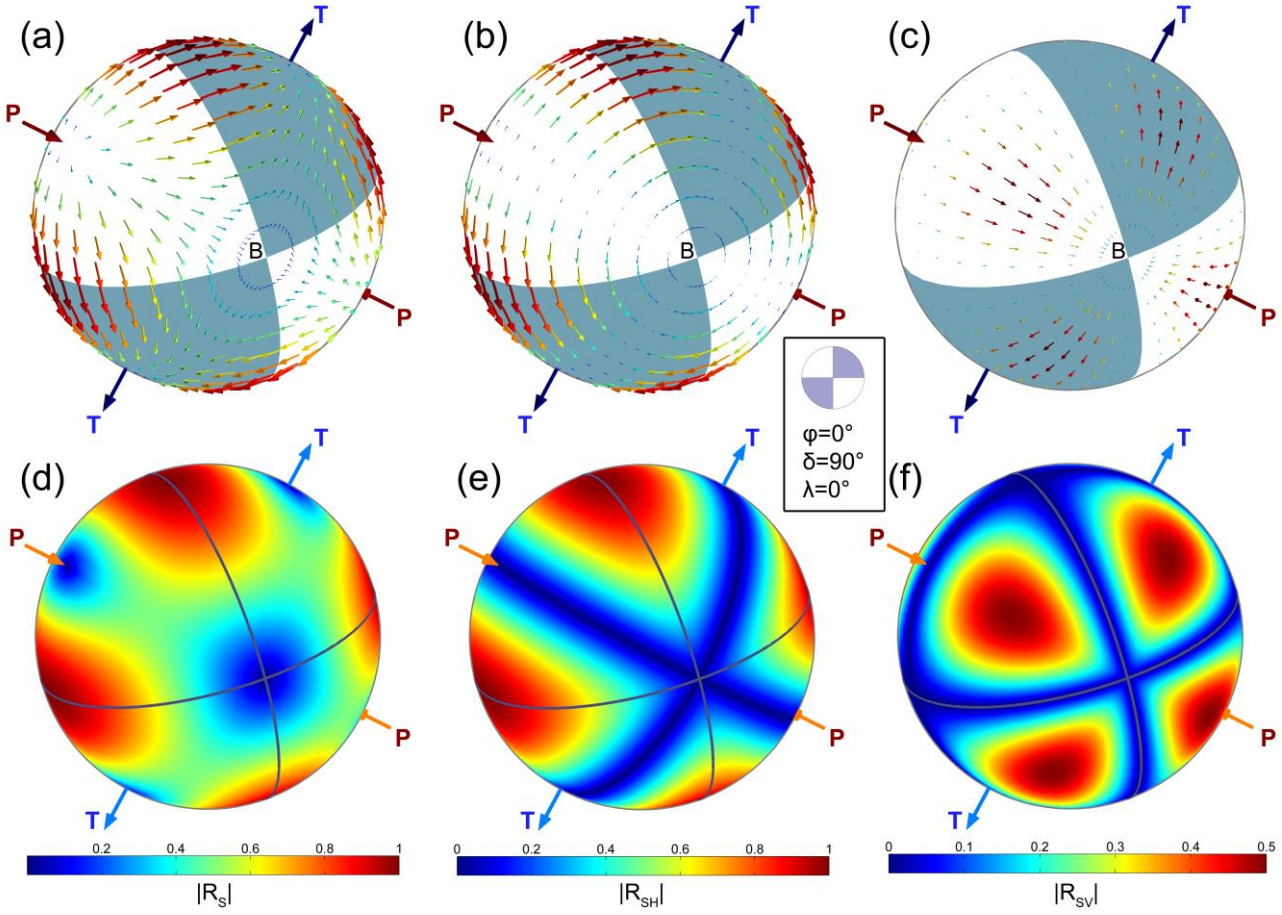

Figure 2.10: 3D representation of the S-wave radiation pattern for a pure strike-slip, double-couple focal mechanism. a-c) Direction and amplitude of the a) S, b) SH and c) SV first motion vectors, d-f) distribution of the $|R_S|$, $|R_{SH}|$ and $|R_{SV}|$ amplitude values of the respective wave-types. **P** and **T** vectors correspond to the P- and T-axes while B marks the trace of the null axis on the focal sphere. In this example, the focal mechanism is pure strike-slip (despite its appearance as an oblique-normal mechanism in this rotated 3D view), meaning that the direction of the vertical coincides with the null axis while the **P**- and **T**-axes are, in fact, horizontal. This affects both SH and SV patterns, both directions (b, c) and amplitudes (e, f) but does not change the overall S-wave pattern (a, d). For comparison, the SH and SV patterns of pure-normal (δ=45°, λ=-90°) and oblique focal mechanisms see Figs 2A.1-2A.3. Note that the maximum $|R_{SV}|$ values in this extreme case (**B**≡Vertical) reach only up to 0.5.

where $\varphi = \varphi_s - \varphi_f$. The radiation pattern for the total amplitude of the S-waves is simply:

$$R_S = \sqrt{R_{SH}{}^2 + R_{SV}{}^2} \tag{2.31}$$

The polarization direction and the respective amplitudes of the S-waves are presented in Fig. 2.10. The S-waves are stronger near the nodal planes and away from the **P**, **B**, **T** axes. Their first motion tends to be directed towards the **T**-axis, away from the **P**-axis and perpendicular to the nodal planes, directed towards the quadrant of compressional P-wave first motions (where the trace of the **T**-axis is found). In the vicinity of the null axis (**B**), the (weak) S-waves are diverting, "avoiding" the axis, while the "flow" of the vectors is directed from the dilatational (**P**) to the compressional quadrant (**T**). The vectors of S, SH and SV are always tangential to the focal sphere. The SH waves as seen from the lower hemisphere Schmidt projection, are tangential to concentric circles around the vertical axis passing through the focus, which in the example of Fig. 2.10 coincides with the **B**-axis. The SV waves, on the other hand, appear to be directed radially with respect to the center of the

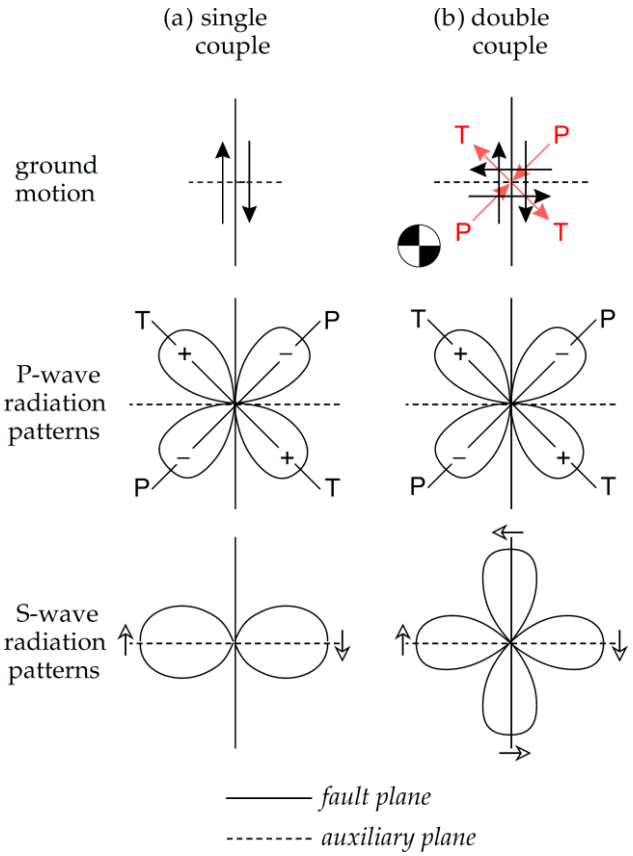

Figure 2.11: Similarities and difference between a) single-couple and b) double-couple of forces model, along with its typical focal sphere representation, in the ground motion (top), in the P-wave (middle) and S-wave (bottom) radiation patterns. (Figure modified after Lowrie, 2007).

stereonet, which represents the vertical axis passing through the focus. In a 3D focal sphere, SV and SH are tangential, with the former directed along longitudinal lines joining at the vertical and the latter along parallel circles perpendicular to the vertical axis, rather than depending on the orientation of the nodal planes. This means that while the pattern of P and the resultant S vectors on the focal sphere can be understood purely relative to the nodal planes and the compressive/dilatational quadrants, the pattern of SH and SV strongly depends on the orientation of the vertical axis relative to the nodal planes, affecting both the direction/orientation and the amplitudes of the vectors.

Interestingly, while the P-wave radiation pattern is similar in both SC and DC models, the S-wave radiation pattern is different, as the R_S value is high near both nodal planes in the DC model but is only strong near the fault plane for the SC model (Fig. 2.11). In the latter, the fault plane would be unambiguously defined by simply observing the S-wave radiation pattern. In reality, however, the S-waves follow the pattern predicted by the DC model, hence the ambiguity between fault and auxiliary planes. A special attribute of SH is that their polarity remains unaffected by reflections on horizontal surfaces, while the polarity of SV is reversed. The SV polarization axis, $\hat{\mathbf{p}}$ also rotates together with the respective P polarization axis, $\hat{\mathbf{I}}$, as the direction of the seismic ray changes (Fig. 2.9) during the propagation of waves in a vertical velocity gradient or through horizontal layers of different velocities.

Simple raytracing tests on a typical local velocity model for the western Corinth Rift (Rigo *et al.*, 1996) can provide a sense of the required axial rotation for different focal depths and up-going rays (s). Fig. 2.12a shows the dependence of the rotation angle on the epicentral distance of a hypothetical station. The first layer is up to 4 km, so at the focal depth of 3 km the rays propagate in a homogeneous medium without crossing another layer, hence no correction is required ($i_h = i_o$, where i_o is the angle of incidence at the surface). At 5 km and below an almost linear dependence of correction angle on epicentral distance can be observed, up to a certain point where "linearity" appears to break and less extra correction is required. In general this happens at nearly horizontal take-off angles ($i_h \cong 90°$), however it is questionable whether the 1D model can be trusted in these extreme cases, as the first discontinuity, even with small velocity contrasts, tends to bend the ray significantly, while the next layers do not affect the ray's direction as much. For a focal depth of 5 km the direct S-wave ray reaches stations up to ~35 km before its take-off angle becomes ~90° but its "safe" limit is up to an epicentral distance of ~12 km. The h = 5 km line has an approximate rotation change rate of 1.5° per 1 km of epicentral distance which decreases rapidly after ~12 km. For larger focal depths, the rotation change rate is slower but does not decrease systematically with increasing focal depth, e.g. it goes down to 0.54°/km at h = 30 km but rises to 0.68°/km at h = 40km and then drops to 0.52°/km at h = 50 km. However, the decrease of rate is much smoother at larger focal depths (Fig. 2.12a).

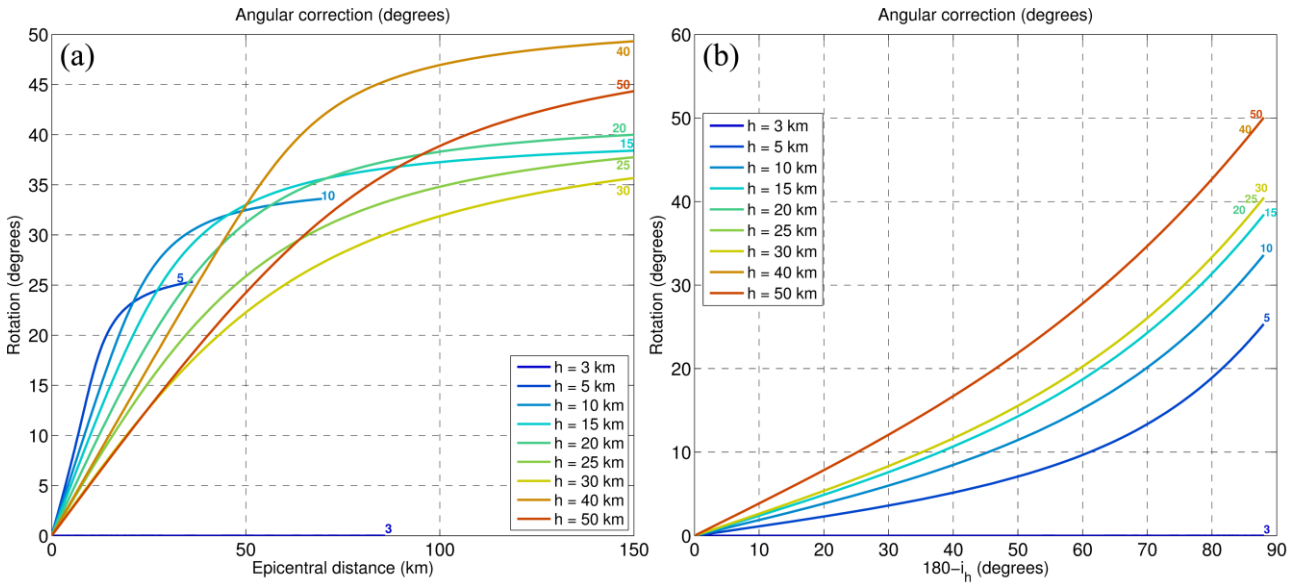

Figure 2.12: Examples of rotation between take-off angle ($91° \leq i_h \leq 180°$; up-going rays only) and angle of incidence, i_o, a) with respect to the epicentral distance and b) with respect to the take-off angle, i_h (expressed as 180-i_h), at various focal depths, h (different colours and numerical labels on each curve), for the 1D velocity model of Rigo *et al.* (1996). Focal depth h=3 km corresponds to a single layer (homogeneous velocity; zero rotation).

The dependence of angular correction from i_h (or rather 180°-i_h which is the take-off angle as measured from zenith) is more uniform (Fig. 2.12b). The curve is parameterized not by the various focal depths but by the starting layer where the hypocenter is located. Even at different depths, if the starting layer is the same the curves are identical (e.g. h = 20-30km and h = 40-50km). This is expected by the ray theory (Aki & Richards, 2002) which defines a value called "ray parameter", or horizontal slowness, $p=(\sin i)/\alpha$, where α is the propagation velocity and i the angle between the ray's direction and axis $\hat{\mathbf{z}}$. The ray parameter is constant at every point of a certain seismic ray, so $(\sin i_1)/V_1 = (\sin i_2)/V_2$, hence:

$$i_o = \arcsin[V_{top}\cdot(\sin i_h)/V_{start}] \qquad (2.32)$$

where V_{start} the velocity at the source and V_{top} the velocity of the top layer. This is the quickest way to calculate i_o without the need for raytracing. This is useful for studies of anisotropic shear-wave splitting where rays within the "shear-wave window" of i_o<45° are selected, while the selection may depend on the take-off angle, i_h, rather than a real measurement of i_o. This is required to avoid interactions with the free surface that could cause distortions in the polarization of the S-waves, mainly due to S-to-P conversions (Booth & Crampin, 1985). In Fig. 2.12, for h=3km the medium between the focus and the surface is homogeneous, hence $i_o \equiv 180°-i_h$. At larger depths i_o<180°-i_h, with $i_o \cong 45°$ for $45° < 180°-i_h <$ about 75°, depending on the focal depth / starting layer (larger tolerance at deeper layers). The rotation rate relative to the conjugate take-off angle is generally larger the deeper the starting layer.

In an isotropic medium, one can measure the horizontal polarization of the S-waves and use this information to constrain a focal mechanism solution. However, the existence of micro-cracks with a

particular orientation can define a direction of oscillation through which S-waves travel faster than on its perpendicular one. In such anisotropic media, the shear waves are split in two distinct components, a fast one, for which particle motion is polarized in a perpendicular direction with respect to the crack plane, and a slow component which arrives with a time-lag. In such cases, the polarization direction of the fast S-waves and the time-lag must be measured and the slow component shifted backwards by the corresponding time-lag. Then the S-waves can be further analysed into SH and SV and the horizontal polarization that corresponds to the initial polarization at the source measured. This, combined with amplitude ratios between SH, SV and P can be used to constrain the focal mechanism when P-wave polarities are not enough or azimuthally well distributed on the focal sphere.

The horizontal polarization direction of the S-waves can be estimated by appropriate filtering of the waveforms to remove possible anisotropic effects (low-pass at ~4 Hz), selecting a window containing the first S-wave pulse and determining its polarization. The latter can be performed in two ways, depending on whether it is the direction or the orientation that is going to be measured. For small data samples where the measurements can be performed manually, the orientation can be determined by the direction of particle motion where the vector's modulus maximizes. This can then be compared to the corresponding orientation of the horizontal projection of the S-wave polarization for a given focal mechanism solution and the necessary correction for the rotation of the $\hat{\mathbf{p}}$ axis (Figs 2.9, 2.12; Eq. 2.32). In large datasets, however, it may be necessary to implement an automatic procedure for the determination of the S-wave polarization direction (SWP). For a given S-wave arrival-time (manual or theoretical/approximate) a small window is selected such that it contains a certain number of zero-crossings at the horizontal components. This ensures that the S-wave's first pulse is contained in the window. Then the covariance matrix of the two vectors (amplitude samples from the two horizontal components) is calculated and the eigenvector corresponding to the largest eigenvalue of the covariance matrix should indicate the S-wave polarization direction. To ensure a more stable solution, sample-pairs with reversed signs are also included in the data vectors, creating a symmetric distribution, since the direction, and not the orientation, is sought and to avoid miscalculations.

To measure the amplitude of SV and SH it is important that the coordinate system is rotated to a more appropriate one, namely the one described by the $\hat{\mathbf{l}}$, $\hat{\mathbf{p}}$ and $\hat{\boldsymbol{\varphi}}$ unit vectors (oriented for P, SV and SH waves, respectively). Two parameters are required, the station's back-azimuth, φ_s', and the angle of incidence, i_o, relative to the vertical (with i_o=0 for rays which meet the surface at a right angle). The former can be derived by the location of the epicenter and the station, although it can also be measured directly from the horizontal polarization of the P-wave (Fig. 2.7). The latter can be either estimated theoretically from the ray parameter, provided the hypocentral depth, take-off angle and propagation velocities at the focus and the surface are known (Eq. 2.32), or, more appropriately, directly from the 3D polarization direction of the P-waves which can be done e.g. by the covariance matrix of the particle motion for a small window containing the first P-wave pulse (Montalbetti & Kanasewich, 1970; Amoroso *et al.*, 2012). The transformation of the coordinates can be performed by applying an appropriate rotation matrix (Plesinger *et al.*, 1986):

$$\begin{bmatrix} L^T \\ Q^T \\ T^T \end{bmatrix} = \begin{bmatrix} \cos i_o & -\sin i_o \sin \phi_s' & -\sin i_o \cos \phi_s' \\ \sin i_o & \cos i_o \sin \phi_s' & \cos i_o \cos \phi_s' \\ 0 & -\cos \phi_s' & \sin \phi_s' \end{bmatrix} \cdot \begin{bmatrix} Z^T \\ E^T \\ N^T \end{bmatrix} \tag{2.33}$$

where **Z**, **E**, **N** the data vectors of the vertical, East-West and North-South components and **L**, **Q**, **T** the transformed data vectors in the directions of the $\hat{\mathbf{l}}$, $\hat{\mathbf{p}}$ and $\hat{\boldsymbol{\varphi}}$ unit vectors. After the transformation, the P, SV and SH amplitudes can be measured on their corresponding axes either manually or automatically by selecting an appropriate window, as in the case of the S-wave polarization direction. The (unsigned) amplitude ratios SV/P, SH/P, SV/SH and S/P can then be compared to their theoretical values (Eqs 2.28-2.31). Their values may span in a large range of orders of magnitude, which is why the differences between the logarithms of the observed – theoretical values are used instead. Even if more sophisticated methods are used for the estimation of the theoretical values, e.g. through synthetic waveforms (e.g. Godano *et al.*, 2014), systematic residuals are expected to be observed due to differences between the P- and S-wave attenuation as well as site effects. Although S/P ratios account for differences in event magnitude and geometrical spreading, scattering in their values can still be significant (Hardebeck & Shearer, 2003), limiting the ability of the S/P ratios to improve the solutions. The measurements on each station should be corrected and the procedure repeated for more stable results. It should be noted that S/P ratio data alone cannot adequately constrain a reliable focal mechanism, as the solutions with the best misfit reduction may not satisfy the P-wave first motion polarity data at the same time (Hardebeck & Shearer, 2003).

2.4 Composite focal mechanisms

Kikuchi & Kanamori (1991) have suggested that any seismic point source (DC or non-DC) can be expressed as the linear combination of certain elementary moment tensors. They propose 6 elementary moment tensors as basis tensors which they use for body-wave inversion:

$$M_1 = \begin{bmatrix} 0 & 1 & 0 \\ 1 & 0 & 0 \\ 0 & 0 & 0 \end{bmatrix} \quad M_2 = \begin{bmatrix} 1 & 0 & 0 \\ 0 & -1 & 0 \\ 0 & 0 & 0 \end{bmatrix} \quad M_3 = \begin{bmatrix} 0 & 0 & 0 \\ 0 & 0 & 1 \\ 0 & 1 & 0 \end{bmatrix}$$

$$M_4 = \begin{bmatrix} 0 & 0 & 1 \\ 0 & 0 & 0 \\ 1 & 0 & 0 \end{bmatrix} \quad M_5 = \begin{bmatrix} -1 & 0 & 0 \\ 0 & 0 & 0 \\ 0 & 0 & 1 \end{bmatrix} \quad M_6 = \begin{bmatrix} 1 & 0 & 0 \\ 0 & 1 & 0 \\ 0 & 0 & 1 \end{bmatrix} \tag{2.34}$$

The solution for a general moment tensor is formulated as a summation of these elementary tensors with different individual weights. Multiplets by definition ought to have similar source parameters,

including their focal mechanism. Based on this assumption, several techniques can be developed to acquire a composite focal mechanism for a group of similar events (e.g. Shearer *et al.*, 2003; Godano *et al.*, 2014; Papadimitriou *et al.*, 2015; Kassaras *et al.*, 2014a), or even a dense spatial cluster, which can be acceptable under certain conditions (e.g. Kapetanidis *et al.*, 2015). Some methods for the determination of composite or average moment tensor solutions are described in the following sub-sections.

2.4.1 Average FM for a single event

A local seismological network can usually provide enough first motion polarities with adequate azimuthal coverage to constrain the focal mechanisms of local events up to a certain degree. After placing the polarities on a stereonet, the nodal planes can either be drawn manually, which is time-consuming and does not account for uncertainties, or automatically. In this section, an automatic procedure is described for the rapid estimation of focal mechanisms using all types of available data, including first motion polarities or FMP, S-wave polarization directions, or SWP, and SV/P, SH/P, SV/SH and S/P amplitude ratios, collectively abbreviated as SPR, for individual events.

Initially, a grid-search is performed for varying values of $\varphi \in [0, 180°]$, $\delta \in [0, 90°]$ and $\lambda \in [-180°, 180°]$, by a small step which can be set to 1°-2°, where φ refers to the strike of one of the two nodal planes. The search range for strike does not have to surpass 180°, as the second nodal plane will be necessarily in that range. The step value has to be small enough so that a plane can be defined even in case of polarities which are very close to and on opposite sides that plane, constraining its (φ, δ) bounds. With take-off angles, i_h, and station azimuth, φ_s, being known for all FMP, the sign of R_P (Eq. 2.28) indicates the theoretical (expected) FMP for a particular (φ, δ, λ) solution at each station. The term "individual solutions", in the simplest case, refers to solutions (φ_i, δ_i, λ_i) which satisfy all FMP data. The errors in i_h and φ_s values strongly depend on the uncertainties of the hypocentral location and on the used velocity model, which defines the way the seismic ray-path bends as the ray travels from the focus to the station. For local events / station geometry, it is generally more preferable that $i_h > 90°$, which means that the rays should be up-going. If discrepancies are observed at stations with $i_h \approx 90°$ or $i_h < 90°$ the data may have to be reconsidered. Sometimes it is necessary to allow for a limited tolerance to the FMP. Misread polarities, uncertainties in the hypocentral location and the degree of bending of the seismic rays (i_h) may cause certain measurements to be incoherent with a focal mechanism solution. Uncertain measurements (emergent or noisy FMP) can be given a lower weight and a threshold be set, which may also depend on the total number of measurements, to allow individual solutions which do not satisfy all FMP but are incompatible with e.g. 1 certain or 2 uncertain FMP. Alternatively, in case no individual solutions satisfy 100% of FMP, the percentage can be lowered down to a threshold where a minimum number of valid individual solutions become available, but only when a large number of data is available, as with composite solutions for multiplets (Section 2.4.3).

Let $\mathbf{M}_i$ be the normalized moment tensor (divided by its largest singular value) of an individual solution (φ_i, δ_i, λ_i). The average moment tensor, $\mathbf{M}_c$, can be given by Eq. 2.35:

$$M_c = \frac{\sum_1^N w_i \cdot M_i}{\left|\sum_1^N w_i \cdot M_i\right|} \tag{2.35}$$

where N is the total number of individual solutions, w_i a weight that corresponds to each solution while the denominator symbolizes the largest singular value of the numerator and is simply used for the normalization of $\mathbf{M}_c$. In the simplest case, $w_i=1$ for $i=1\ldots N$. Equal weighting results in an average focal mechanism whose nodal planes pass "through the middle" of the distributed individual nodal planes while the mean solution's **P**, **B**, **T** axes traces are also at the centroid of the distribution of the corresponding axes in the individual solutions. When the latter are more or less similar, this sort of mean solution is adequate. It should be noted that, although the trace of $\mathbf{M_c}$ is zero, this summation almost always results in a moment tensor that is not a pure double-couple (non-zero determinant).

Even in a network such as CRL at the western Corinth Rift, the station geometry may cause uncertainties due to the azimuthal gaps east and west for epicenters inside the gulf, as the stations are located in opposite sides of the gulf. Besides these gaps in azimuthal coverage there may also be a lack of stations in "middle" distances, despite the availability of several stations within the epicentral region or far from the epicenters, at the opposite coast (Kapetanidis *et al.*, 2015). In such cases it may be difficult to constrain the strike and dip of the nodal planes with FMP alone. For this reason, instead of simply considering the average solution of FMs which are in agreement with the FMP, variable weights on each individual solution can be calculated by taking SWP and SPR misfits into account at selected stations during the averaging procedure for each event.

A combined weight can be constructed by incorporating all types of data using the generalized formula:

$$W_i = C^{\left(C_o \cdot \frac{FMP_i}{\sum FMP} + C_1 \left(\frac{90 - \bar{\Delta}_{SWPi}}{90} \right)^{P_1} + C_2 \left(\frac{1}{\bar{\Delta}_{SPRi}} \right)^{P_2} \right)^{P_3}} \tag{2.36}$$

where the index i refers to an individual fault plane solution which is in agreement with the $\frac{FMP_i}{\sum FMP}$ percentage of FMP, $\bar{\Delta}_{SWPi} \in [0, 90°]$ is the average of the minimum angular differences between the measured and calculated directions of S-wave polarization, Δ_{SWP}, in all selected stations, $\bar{\Delta}_{SPRi} > 0$ is the absolute difference between the logarithms of observed and calculated SPR, Δ_{SPR}, averaged in all selected stations, $C>1$ and C_o, C_1, C_2, P_1, P_2, P_3 are positive constants which can be calibrated to control the effect of Δ_{SWP} and Δ_{SPR} to the averaging of individual solutions.

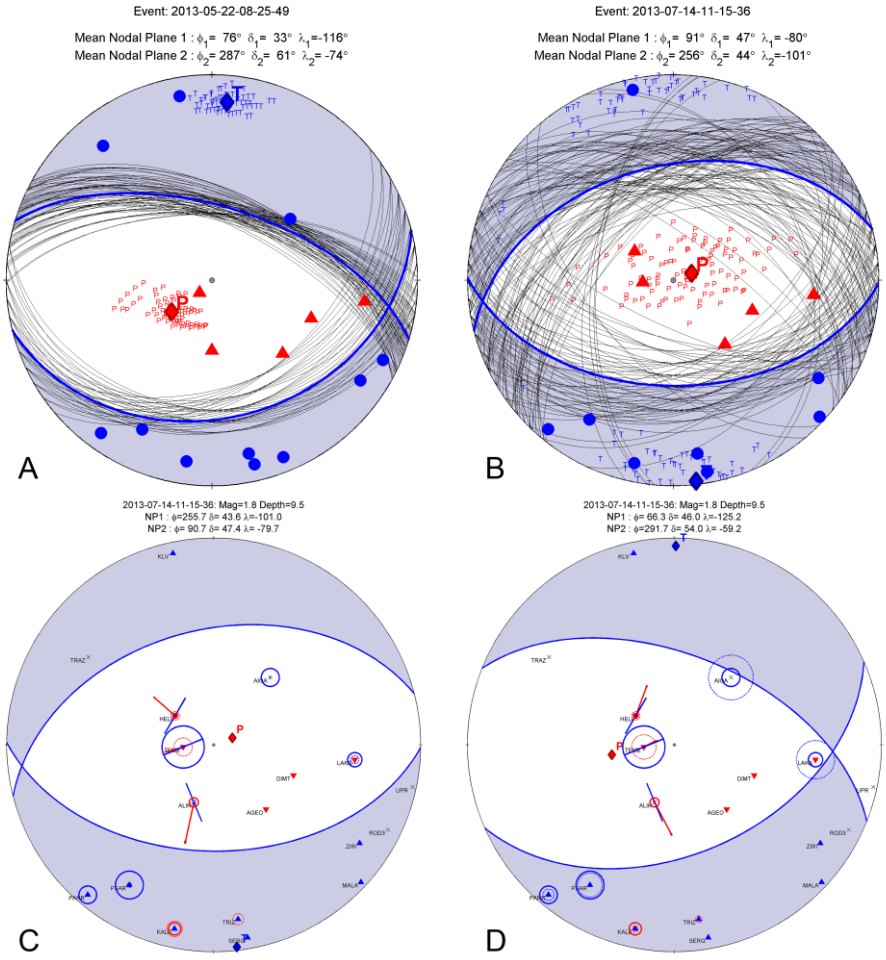

Figure 2.13: A) a well-constrained focal mechanism calculated by averaging individual solutions derived from a grid search using only FMP, B) a poorly constrained solution with FMP alone, C) indication of SWP (straight lines on stations) and SPR (circles centered on stations) for the average solution of panel (B), where the blue and red straight lines correspond to observed and theoretical SWP directions, respectively, while solid and dashed circles represent the observed and theoretical SPR, respectively. The radius of each circle is proportional to the absolute value of the logarithm of the corresponding SPR, while blue and red indicate positive and negative logarithms, respectively, and D) modified average solution, weighted by SWP and SPR differences. (Figure after Kapetanidis *et al.*, 2015)

An example is presented in Fig. 2.13 from the application of Section 5A.4 (Kapetanidis *et al.*, 2015). A 5°-step grid search for strike (ϕ), dip (δ) and rake (λ) was performed to identify ~910 individual fault plane solutions which satisfy the observed FMP. The average solution (ϕ= 256°, δ= 44°, λ = -101°) is calculated by summing the individual normalized moment tensors. In this case, the mean values of SWP and SPR are 40° and 0.45, respectively (Fig. 2.13C). The quality of an average solution derived by the grid-search on FMP is defined by the number of valid individual solutions, which in this case is very large, permitting a wide range of strike and dip values for both nodal planes, thus the quality is relatively poor. By taking into account the proposed weighting scheme of Eq. 2.36, in this case with a simple parameterization C=10, C_o=C_1=C_2=P_1=P_2=P_3=1, the normalized moment tensor of each individual solution is multiplied by the corresponding weight, W_i, before the summation. This results in a different average solution (ϕ= 292°, δ= 54°, λ = -59°),

which is also in agreement with the FMP but is biased towards reducing the mean Δ_{SWP} and Δ_{SPR} differences to 7° and 0.41, respectively (Fig. 2.13D). This is particularly useful when the focal mechanisms cannot be constrained adequately by FMP alone.

2.4.1.1 Angular differences as an uncertainty estimate

The uncertainty of the average moment tensor can be measured in terms of the RMS angular difference, $\delta\theta_{\mathrm{RMS}}$. The angular difference, $\delta\theta$, between $\mathbf{M}_c$ and an individual solution $\mathbf{M}_i$ is defined as the minimum angle of rotation, also known as "Kagan angle" (Kagan, 1991; Tape & Tape, 2012), that must be applied relative to a special axis so that $\mathbf{M}_i$ becomes equal to $\mathbf{M}_c$. In order for the angular difference to be calculated, the following procedure is employed. The optimal 3D rotation matrix, **R**, is calculated using a method called "Kabsch algorithm", which provides the transformation that minimizes the RMS deviation between two sets of vectors in their exact order (Kabsch, 1978).

The **P**, **B**, **T** eigenvectors of $\mathbf{M}_c$ and $\mathbf{M}_i$ are calculated and inserted in two matrices, $\mathbf{V}_c$, $\mathbf{V}_i$, along with their reverse **-P**, **-B** and **-T**, with each vector being multiplied by m_p, m_b, m_t, for $\mathbf{V}_c$ and m'_p, m'_b, m'_t, for $\mathbf{V}_i$, respectively, which can take values +1 or -1 (the use of these multipliers will be explained later). The rotation of the one focal mechanism to match the other should be treated as the rotation of a sphere, centered at (0, 0, 0), defined by the traces of ±**P**, ±**B** and ±**T** on its surface.

The mean value of each coordinate is subtracted from the respective elements, to account for translation, and the cross-covariance matrix of the resulting matrices is calculated:

$$
\begin{aligned}
C &= x\,\mathrm{cov}([V_c \quad -V_c],[V_i \quad -V_i]) = [V_c \quad -V_c]^T \cdot [V_i \quad -V_i] \\
&= \begin{bmatrix} m_p p_x - \bar{x} & m_b b_x - \bar{x} & m_t t_x - \bar{x} & -m_p p_x - \bar{x} & -m_b b_x - \bar{x} & -m_t t_x - \bar{x} \\ m_p p_y - \bar{y} & m_b b_y - \bar{y} & m_t t_y - \bar{y} & -m_p p_y - \bar{y} & -m_b b_y - \bar{y} & -m_t t_y - \bar{y} \\ m_p p_z - \bar{z} & m_b b_z - \bar{z} & m_t t_z - \bar{z} & -m_p p_z - \bar{z} & -m_b b_z - \bar{z} & -m_t t_z - \bar{z} \end{bmatrix}^T \cdot \\
&\cdot \begin{bmatrix} m'_p\, p'_x - \bar{x}' & m'_b\, b'_x - \bar{x}' & m'_t\, t'_x - \bar{x}' & -m'_p\, p'_x - \bar{x}' & -m'_b\, b'_x - \bar{x}' & -m'_t\, t'_x - \bar{x}' \\ m'_p\, p'_y - \bar{y}' & m'_b\, b'_y - \bar{y}' & m'_t\, t'_y - \bar{y}' & -m'_p\, p'_y - \bar{y}' & -m'_b\, b'_y - \bar{y}' & -m'_t\, t'_y - \bar{y}' \\ m'_p\, p'_z - \bar{z}' & m'_b\, b'_z - \bar{z}' & m'_t\, t'_z - \bar{z}' & -m'_p\, p'_z - \bar{z}' & -m'_b\, b'_z - \bar{z}' & -m'_t\, t'_z - \bar{z}' \end{bmatrix}
\end{aligned}
\tag{2.37}
$$

where $\bar{x} = \bar{y} = \bar{z} = \bar{x}' = \bar{y}' = \bar{z}' = 0$ the mean values of x, y and z, or the coordinates of the centroid of each system of 6 vectors, that is (0, 0, 0) by definition since both $\mathbf{V}_c$ and $-\mathbf{V}_c$ vectors have been included in each matrix. At this point, let the multipliers be $m_p = m_b = m_t = m'_p = m'_b = m'_t = +1$ for simplicity.

Singular Value Decomposition (SVD) is performed to calculate the unitary matrices of singular values, **U** and **V**, such that their dot product with the resulting diagonal matrix, **S** is:

$$C = U \cdot S \cdot V^T \tag{2.38}$$

The optimal rotation matrix, **R**, is:

$$R = V\begin{bmatrix}1 & 0 & 0\\ 0 & 1 & 0\\ 0 & 0 & d\end{bmatrix}U^T = \begin{bmatrix}R_{xx} & R_{xy} & R_{xz}\\ R_{yx} & R_{yy} & R_{yz}\\ R_{zx} & R_{zy} & R_{zz}\end{bmatrix} \tag{2.39}$$

where d is the sign (+1 or -1) of the determinant of $\mathbf{V}\cdot\mathbf{U}^T$, which corrects for reflection in case $d<0$ to ensure a right-handed system (Kabsch, 1978). Then the rotation matrix, **R**, can be converted to an axis/angle representation by a procedure known in the literature as the inverse of Rodrigues' rotation formula (e.g. Shuster, 1993) or log map from rotation group SO(3) to so(3). This is based on Euler's rotation theorem which states that any rotation of an object about a fixed point in the 3D space can be represented by a single rotation around an axis that runs through that point. This means that a single Euler axis (a unitary rotation vector) multiplied (as its magnitude) by an angle, $\delta\theta'$, which is the angular difference, can represent a transformation that is equivalent to the application of the 3D rotation matrix. The angle $\delta\theta'$ is generally given by:

$$\delta\theta' = \arctan\left(\frac{\sqrt{\left(R_{zy}-R_{yz}\right)^2+\left(R_{xz}-R_{zx}\right)^2+\left(R_{yx}-R_{xy}\right)^2}}{R_{xx}+R_{yy}+R_{zz}-1}\right) \tag{2.40}$$

or

$$\delta\theta' = \arccos\left(\frac{R_{xx}+R_{yy}+R_{zz}-1}{2}\right) \quad , \quad \delta\theta' \in (-\pi,\pi)$$

The transformation is such that the rotated $\mathbf{P}_r$, $\mathbf{B}_r$, $\mathbf{T}_r$ vectors (and their reverse) have the same orientation as the **P**, **B**, **T** and **-P**, **-B**, **-T** of the first matrix:

$$R\cdot\begin{bmatrix}V_c & -V_c\end{bmatrix} = \begin{bmatrix}V_i & -V_i\end{bmatrix} \tag{2.41}$$

This means that a rotated $\mathbf{P}_r$ will match the target **P** and not **-P**, which would also be an acceptable solution and could even yield a smaller rotation angle. In order to acquire the minimum angular difference, the procedure must be repeated for *all* combinations of the six vectors **P**, **B**, **T, -P, -B, -T** (first focal mechanism) and the other six **P′**, **B′**, **T′, -P′, -B′, -T′** (second focal mechanism) in reverse directions, by altering the values of the m_t, m_b, m_p and m'_t, m'_b, m'_t multipliers (+1 or -1) in Eq. 2.37, and selecting the angular difference with the minimum value, $\delta\theta$.

The symmetric Table 2.3 presents a comparison between the 25 types of focal mechanisms presented in Table 2.2, in terms of their minimum angular difference. These examples practically correspond to 6 types of faulting, rotated by 90° or 45° with respect to the vertical, which changes the strike of both planes by the same angle. This is reflected in the $\delta\theta$ of successive mechanisms of the same type, being $\delta\theta<90°$ for simple cases. As for larger rotations the same mechanism can be acquired by a rotation with $\delta\theta<90°$ in the opposite direction. A pure normal FM such as #5 can be converted to a pure strike-slip such as #2 with a simple rotation by $\delta\theta=90°$ around the **T**-axis.

However, the difference between #6 and #1 is larger, as two such rotations would be required, one by 90° around the **T**-axis, that would result in FM #3, then another by 90° along the (rotated) **B**-axis. Instead, the optimal rotation is such that can be performed around a single axis which does not coincide with any of the typical ones and the required minimum angle is $\delta\theta$=120°. This is also the maximum limit for $\delta\theta$, as all sorts of combinations tend to result in $\delta\theta \leq 120°$. That occurs due to the reverse axial matches, e.g. between **P** and **–P,** being acceptable, although $\delta\theta$ could theoretically reach up to 180°, above which value a similar result would be feasible with a rotation towards the opposite direction (or around a reversed rotation axis). The required rotation between a pure normal FM such as #5 and a pure reverse such as #9 is $\delta\theta$=90°, around the **B**-axis, while for the odd #21 or #25 it is half that, $\delta\theta$=45°.

Table 2.3: Minimum angular differences, $\delta\theta$, for the 25 types of focal mechanisms of Table 2.2.

		1	2	3	4	5	6	7	8	9	10	11	12	13
1		-	45.0	90.0	45.0	98.4	120.0	98.4	90.0	98.4	90.0	98.4	120.0	53.6
2		45.0	-	45.0	90.0	90.0	98.4	120.0	98.4	120.0	98.4	90.0	98.4	76.3
3		90.0	45.0	-	45.0	98.4	90.0	98.4	120.0	98.4	120.0	98.4	90.0	91.0
4		45.0	90.0	45.0	-	120.0	98.4	90.0	98.4	90.0	98.4	120.0	98.4	60.8
5		98.4	90.0	98.4	120.0	-	45.0	90.0	45.0	90.0	98.4	120.0	98.4	85.7
6		120.0	98.4	90.0	98.4	45.0	-	45.0	90.0	98.4	90.0	98.4	120.0	96.7
7		98.4	120.0	98.4	90.0	90.0	45.0	-	45.0	120.0	98.4	90.0	98.4	96.5
8		90.0	98.4	120.0	98.4	45.0	90.0	45.0	-	98.4	120.0	98.4	90.0	91.7
9		98.4	120.0	98.4	90.0	90.0	98.4	120.0	98.4	-	45.0	90.0	45.0	47.3
10		90.0	98.4	120.0	98.4	98.4	90.0	98.4	120.0	45.0	-	45.0	90.0	41.4
11		98.4	90.0	98.4	120.0	120.0	98.4	90.0	98.4	90.0	45.0	-	45.0	71.3
12		120.0	98.4	90.0	98.4	98.4	120.0	98.4	90.0	45.0	90.0	45.0	-	81.6
13		53.6	76.3	91.0	60.8	85.7	96.7	96.5	91.7	47.3	41.4	71.3	81.6	-
14		91.0	60.8	53.6	76.3	96.5	91.7	85.7	96.7	71.3	81.6	47.3	41.4	90.0
15		53.6	76.3	91.0	60.8	85.7	96.7	96.5	91.7	47.3	41.4	71.3	81.6	76.3
16		91.0	60.8	53.6	76.3	96.5	91.7	85.7	96.7	71.3	81.6	47.3	41.4	90.0
17		53.6	60.8	91.0	76.3	47.3	81.6	71.3	41.4	85.7	91.7	96.5	96.7	90.0
18		91.0	76.3	53.6	60.8	71.3	41.4	47.3	81.6	96.5	96.7	85.7	91.7	104.5
19		53.6	60.8	91.0	76.3	47.3	81.6	71.3	41.4	85.7	91.7	96.5	96.7	60.0
20		91.0	76.3	53.6	60.8	71.3	41.4	47.3	81.6	96.5	96.7	85.7	91.7	82.8
21		90.0	98.4	90.0	98.4	45.0	62.8	98.4	62.8	45.0	62.8	98.4	62.8	53.6
22		98.4	90.0	98.4	90.0	62.8	45.0	62.8	98.4	62.8	45.0	62.8	98.4	60.8
23		90.0	98.4	90.0	98.4	98.4	62.8	45.0	62.8	98.4	62.8	45.0	62.8	91.0
24		98.4	90.0	98.4	90.0	62.8	98.4	62.8	45.0	62.8	98.4	62.8	45.0	104.5
25		90.0	98.4	90.0	98.4	45.0	62.8	98.4	62.8	45.0	62.8	98.4	62.8	73.7

Table 2.3: (continued).

		14	15	16	17	18	19	20	21	22	23	24	25
1		91.0	53.6	91.0	53.6	91.0	53.6	91.0	90.0	98.4	90.0	98.4	90.0
2		60.8	76.3	60.8	60.8	76.3	60.8	76.3	98.4	90.0	98.4	90.0	98.4
3		53.6	91.0	53.6	91.0	53.6	91.0	53.6	90.0	98.4	90.0	98.4	90.0
4		76.3	60.8	76.3	76.3	60.8	76.3	60.8	98.4	90.0	98.4	90.0	98.4
5		96.5	85.7	96.5	47.3	71.3	47.3	71.3	45.0	62.8	98.4	62.8	45.0
6		91.7	96.7	91.7	81.6	41.4	81.6	41.4	62.8	45.0	62.8	98.4	62.8
7		85.7	96.5	85.7	71.3	47.3	71.3	47.3	98.4	62.8	45.0	62.8	98.4
8		96.7	91.7	96.7	41.4	81.6	41.4	81.6	62.8	98.4	62.8	45.0	62.8
9		71.3	47.3	71.3	85.7	96.5	85.7	96.5	45.0	62.8	98.4	62.8	45.0
10		81.6	41.4	81.6	91.7	96.7	91.7	96.7	62.8	45.0	62.8	98.4	62.8
11		47.3	71.3	47.3	96.5	85.7	96.5	85.7	98.4	62.8	45.0	62.8	98.4
12		41.4	81.6	41.4	96.7	91.7	96.7	91.7	62.8	98.4	62.8	45.0	62.8
13		90.0	76.3	90.0	90.0	104.5	60.0	82.8	53.6	60.8	91.0	104.5	73.7
14		-	90.0	76.3	82.8	90.0	104.5	60.0	73.7	76.3	53.6	60.8	91.0
15		90.0	-	90.0	60.0	82.8	90.0	104.5	73.7	60.0	73.7	76.3	53.6
16		76.3	90.0	-	104.5	60.0	82.8	90.0	91.0	104.5	73.7	60.0	73.7
17		82.8	60.0	104.5	-	90.0	76.3	90.0	73.7	104.5	91.0	60.8	53.7
18		90.0	82.8	60.0	90.0	-	90.0	76.3	73.7	60.0	73.7	104.5	91.0
19		104.5	90.0	82.8	76.3	90.0	-	90.0	53.7	76.3	73.7	60.0	73.7
20		60.0	104.5	90.0	90.0	76.3	90.0	-	91.0	60.8	53.7	76.3	73.7
21		73.7	73.7	91.0	73.7	73.7	53.7	91.0	-	45.0	90.0	98.4	90.0
22		76.3	60.0	104.5	104.5	60.0	76.3	60.8	45.0	-	45.0	90.0	98.4
23		53.6	73.7	73.7	91.0	73.7	73.7	53.7	90.0	45.0	-	45.0	90.0
24		60.8	76.3	60.0	60.8	104.5	60.0	76.3	98.4	90.0	45.0	-	45.0
25		91.0	53.6	73.7	53.7	91.0	73.7	73.7	90.0	98.4	90.0	45.0	-

Given that, the RMS angular difference, $\delta\theta_{\mathrm{RMS}}$ for a set of individual tensors $\mathbf{M}_{\mathrm{i}}$ with minimum angular difference $\delta\theta_{\mathrm{i}}$ relative to the average $\mathbf{M}_{\mathrm{c}}$ is simply:

$$\delta\theta_{RMS} = \sqrt{\frac{\sum_{N} \delta\theta_i^{\,2}}{N}} \tag{2.42}$$

The RMS angular difference between individual solutions and the composite can give an estimate on how well the average solution fits (Hardebeck & Shearer, 2002). Usually, an RMS difference of up to ~25° indicates a good fit. However, if there are strong differences between individual solutions, proper weighting may help to avoid badly constrained ones influencing the average. It is important to note that Eq. 2.35 does not necessarily yield a purely DC focal mechanism. Besides $\delta\theta_{\mathrm{RMS}}$, the DC (as opposed to CLVD) percentage (Jost & Herrmann, 1989) could also be used as a

measure of the quality of the composite focal mechanism, as well constrained composites ($\delta\theta_{RMS}$ < 25°) are expected to have a relatively high percentage of DC.

2.4.2 Composite FM for a multiplet using well constrained sub-events

Under certain circumstances, a multiplet may contain a subset of events with adequately constrained focal mechanisms using the procedures described in the previous section. In that case, a composite solution can be derived by averaging the individual moment tensors using appropriate weighting. The term "individual solution" here refers to the single solution for each individual event within the multiplet.

Magnitude weighting, using the equivalent seismic moment as weight, may strongly bias the mean solution towards the one of the major event in the subset. A better choice is the number of available FMP, with uncertain measurements counting for half the weight of the certain ones. Additionally, the RMS angular difference of each individual mechanism can also be employed, lowering the weight of the more uncertain sub-solutions. This creates a balance between poorly constrained events with few FMP and well constrained events with less FMP. An alternative weighting scheme to that of Eq. 2.36 could have the following form:

$$W_i = C^{\,f(M_w)\frac{FMP_i}{\left(\sum FMP\right)^{C_p}}\left(1+C_1\left(\frac{90-\bar{\Delta}_{SWPi}}{90}\right)^{P_1}+C_2\left(\frac{\Delta SPR_{\min}}{\bar{\Delta}_{SPRi}}\right)^{P_2}\right)^{P_3}} \tag{2.43}$$

Where $f(M_w)$ can either be a constant (e.g. unity) or a function of the magnitude, M_w, and C_p could typically take the value C_p=1, in which case the denominator is a normalization constant for the FMP, or C_p=0, if the raw number of satisfied FMP in an individual event's solution must be used as a weight instead (e.g. if SPR or SWP data are unavailable or their quality is inadequate, where also C_1=C_2=0). C_2 can be used as an upper limit to the SPR weight (typically ~3) in combination with a lower allowed limit, $\Delta SPR_{\min}$ (typically ~0.15), for the mean absolute difference between the log-values of the theoretical and observed SPR, $\bar{\Delta}SPR_i$.

Using FMP and RMS angular difference weighting biases the average towards the ones with the more data available and, also, the better constrained ones. This technique has been applied to acquire composite solutions for multiplets in the Trichonis lake 2007 swarm (Section 5A.1; Kassaras *et al.* 2014a) and for average focal mechanisms of spatial clusters during the Helike 2013 swarm (Section 5A.4; Kapetanidis *et al.*, 2015) and within the caldera of Santorini during the 2011-2012 seismic crisis (Section 5A.3; Papadimitriou *et al.*, 2015).

2.4.3 Composite FM for a multiplet using weakly constrained sub-events

There are cases where it may be difficult to acquire focal mechanism solutions for individual events, due to small magnitude or poor network coverage. However, the estimation of a composite

focal mechanism could still be achievable by taking into account all available data that can be collected from the sub-events which comprise the multiplet. This includes FMP, SWP and SPR.

The composite can be calculated using a similar method as described in Section 2.4.1 for the determination of a solution for an individual event, as the whole multiplet is treated as such. In this section, the term "individual solution" is used in the same sense as in Section 2.4.1 to describe a focal mechanism which could potentially apply for the multiplet. There is, however, an important difference. Using all the available measurements may not help to better constrain a solution, but, on the contrary, make it impossible for a solution to exist that satisfies all data. Even if the hypocenters are well located/relocated and the FMP measured without errors, small deviations in the real focal mechanisms of the sub-events may cause scatter in distribution of FMP such that no solution may be found that satisfies all FMP. In practice, when dealing with very small events or there is a shortage of good quality data, the analyst may decide to "guess" a large number of uncertain FMP, part of which may be of erroneous polarity.

To overcome this problem, the grid-search does not examine simply whether all FMP are satisfied or not, but, instead, the percentage of satisfied FMP is calculated. Then a percentage threshold is set, such that a minimum number of individual solutions satisfy this percentage of polarities. The rest of the procedure is similar to that of Section 2.4.1. In fact, the percentage threshold technique can also apply to the determination of focal mechanisms for individual events to reject a certain (small) number of polarities when no individual solutions (zero, rather than a minimum number) that satisfy all FMP can be derived. This method has been applied for the estimation of composite focal mechanisms of multiplets that were distinguished in the western Corinth Rift during 2000-2007, using data from the CRL network (Chapter 6).

When multiplets have been identified, a composite or reference focal mechanism can be assigned to each one on the assumption that events with adequately similar waveforms ought to have a similar focal mechanism. In cases where the geometry of a multiplet is defined with sufficiently small uncertainties, one can assume that the hypocenters are distributed on a 2d plane which should identical to the fault plane. Hence, the nodal plane of the focal mechanism with the least angular difference from this best-fit plane can be reckoned as the fault plane. However, even relocated hypocentral distributions of a multiplet could be having uncertainties too large for a best-fit plane to be defined with sufficient certainty. Their distribution could be linear, defining only a single axis that could belong to an infinite number of planes, or a small ellipsoid cloud which may not be sufficiently flat to allow for the definition of a plane.

The geometry of larger hypocentral distributions (with respect to their location uncertainties), when relocated, can usually provide more safe conclusions concerning the (main) fault plane. However, this does not exclude the possibility of multiplets that could belong to smaller antithetic faults, with the main best-fit plane of the larger seismicity cloud corresponding to the auxiliary plane of their faulting mechanism. The large distribution can be divided in sub-groups either spatially (clusters identified using Ward's linkage, Section 1.2.1) or (spatio-) temporally, by identifying distinct phases of activity in a sequence that may exhibit different geometrical characteristics, e.g. due to the activation of a neighboring fault.

2.5 Application: Confirmation of instrument's vertical polarity

The properties of the P-waves' linear polarization can be further exploited to recover information about possible polarity reversals due to technical issues with a station's instrumentation. In this section, in particular, the vertical polarity of several surface (non-borehole) stations of the CRL network will be examined.

During the application described in Chapter 6, a large number of P-wave first motion polarities were measured for the purpose of focal mechanism determination. However, it is important that these polarities correspond to the real direction of the P-wave onset. For this reason a sample of ~50 events selected throughout the period of study (2000-2007) were examined in a set of stations. The events have been relocated, so the earthquake epicenters are known with relatively small uncertainties. To determine whether the polarity of the vertical component of the instrument is correct or reversed, the P-wave's horizontal first motion should either point towards the epicenter, if the FMP is dilatational, or away from the epicenter, if the FMP is compressional. If the opposite is true, then either the polarity of the instrument's vertical component is reversed, or the polarity of both horizontal components is reversed, or the instrument's polarities are correct but it has been horizontally disoriented by 180°.

The measurements were performed manually, by picking the starting and ending time of the first pulse of the P-wave (half-period). It is important that the selected samples have:

- clear P-wave onsets
- unambiguous vertical polarity
- clear P-wave pulse in the horizontal components in the selected interval
- no long-period trend or offset in the amplitudes

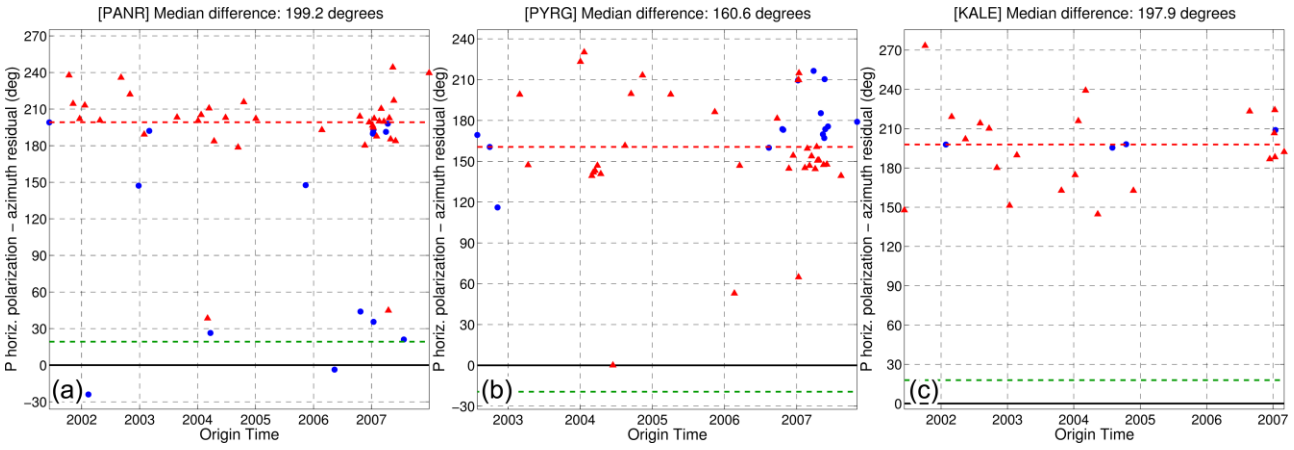

Figure 2.14: Validation of polarity reversal on the vertical component of surface stations a) PANR, b) PYRG and c) KALE, using the CRL 2000-2007 dataset (Chapter 6). Compressive and dilatational first motion polarities are denoted by blue circles and red triangles, respectively.

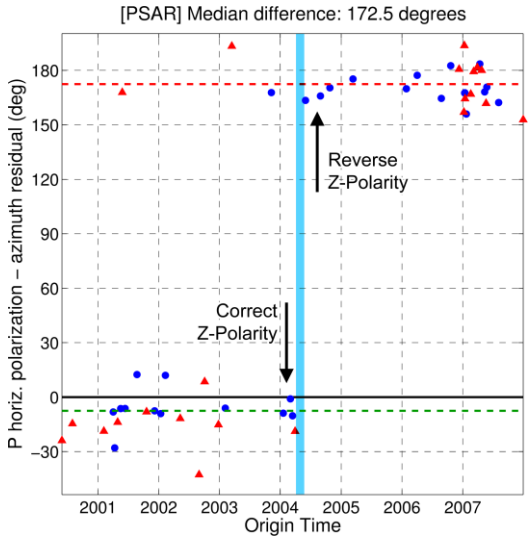

Figure 2.15: Validation of a flip in the polarity of the vertical component of the surface station PSAR between April and May 2004 (later confirmed to have occurred between 16 and 17 April), using the CRL 2000-2007 dataset (Chapter 6). Compressive and dilatational first motion polarities are denoted by blue circles and red triangles, respectively.

To ensure the last requirement, the waves go through a weak high-pass filter and it is visually confirmed that the pulses begin and end near a zero-crossing. The 3D vector of the particle motion is constructed for the selected interval and the polarization direction is measured where its modulus maximizes. The direction of the vector's projection to the horizontal plane is compared against the azimuth of the epicenter relative to the station. The sign of the Z component defines whether the first motion is dilatational or compressional. In the latter case, the measured horizontal direction of P-wave polarization must be rotated by 180° to match the epicenter's azimuth[4]. The residual between epicenter's azimuth and polarization direction should be, on average, close to 0°. A residual of ~180° indicates reversal of the polarity of the vertical component.

Reversal of the vertical component's polarity was confirmed in 4 stations of the CRL network, namely KALE (previously KAL), PYRG, PANR (Fig. 2.14). In station PSAR, however, which was also known to have a vertical polarity reversal, a discrepancy was discovered in the data, as some of the event waveforms appeared to have been preprocessed up to some point to correct for the polarity reversal. Measurements throughout the period 2000-2007 pinpointed reversal of vertical polarity somewhere between April and May 2004 (Fig. 2.15). Guided by this observation, a comparison between event waveforms and unprocessed continuous data confirmed that the event waveforms in station PSAR had been corrected up to 16 April 2004 while data after that date required polarity reversal. It should be noted that, since all the measurements presented are manual and only for strong P-wave onsets on the vertical component, outliers are usually due to miscalculation of the horizontal P-polarity that may occur if e.g. the horizontal pulse is not strong enough or there is a small phase difference that could cause a difference of ~180°.

[4] In local distances the azimuth of the station relative to the epicenter is approximately the same as the azimuth of the epicenter relative to the station +180° (or back-azimuth). However, for large distances this can differ significantly due to the Earth's sphericity.

2.6 Application: Estimation of horizontal orientation in borehole sensors

The same technique that was applied in the previous section for the validation of an instrument's vertical component polarity can be used to determine the horizontal orientation of sensors buried inside boreholes. This is true for several stations of the CRL network. Orientation corrections are particularly important for measurements of shear wave anisotropy direction or S-wave polarization to constrain focal mechanisms. It is, of course, prerequisite that the polarity of the vertical component is correct or that it is already known it is reversed, in which case it must be treated accordingly.

Table 2.4: Instrument orientation measurements for local stations in the western Corinth Rift.

Station	Depth (m)	Data-set	Median φ_r	Mean φ_r	st. dev. φ_r
AIOA	130	CRL 2000-2007	154	155	13
TEME	71	CRL 2000-2007	356	358	11
ALIK	70	CRL 2000-2007	322	320	11
AIOA	130	Helike 2013	167	167	6
TEME	71	Helike 2013	33	38	17
LAKA	0	Helike 2013	11	10	6
MALA	193	Helike 2013	291	292	9
HELI	0	Helike 2013	293	291	17
AIOA	130	Nafpaktos 2014	153	151	7
MALA	193	Nafpaktos 2014	289	289	11

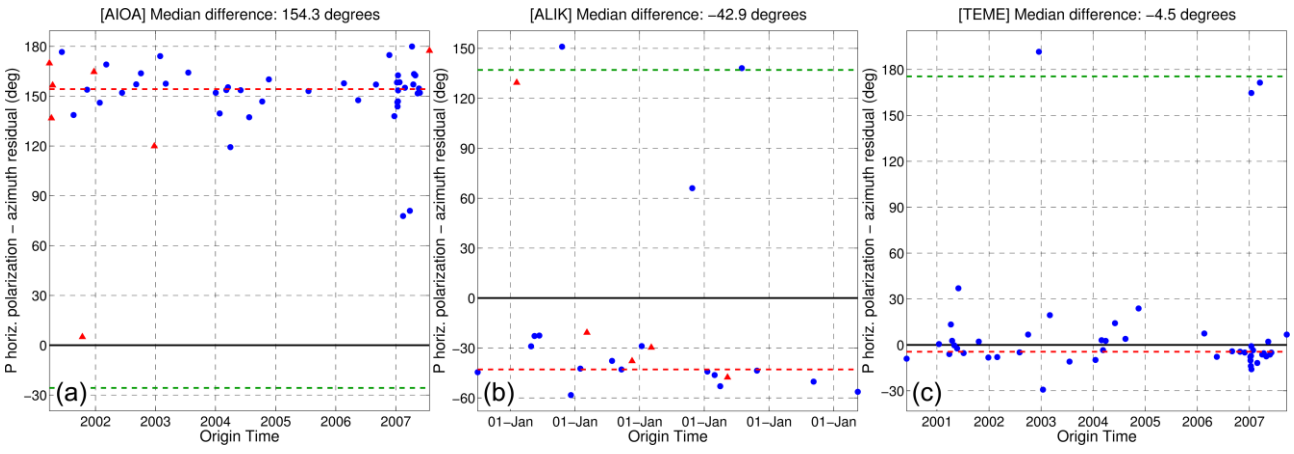

Figure 2.16: Orientation tests for borehole seismometers with correct vertical polarity, using the CRL 2000-2007 dataset (Chapter 6). Compressive and dilatational first motion polarities are denoted by blue circles and red triangles, respectively.

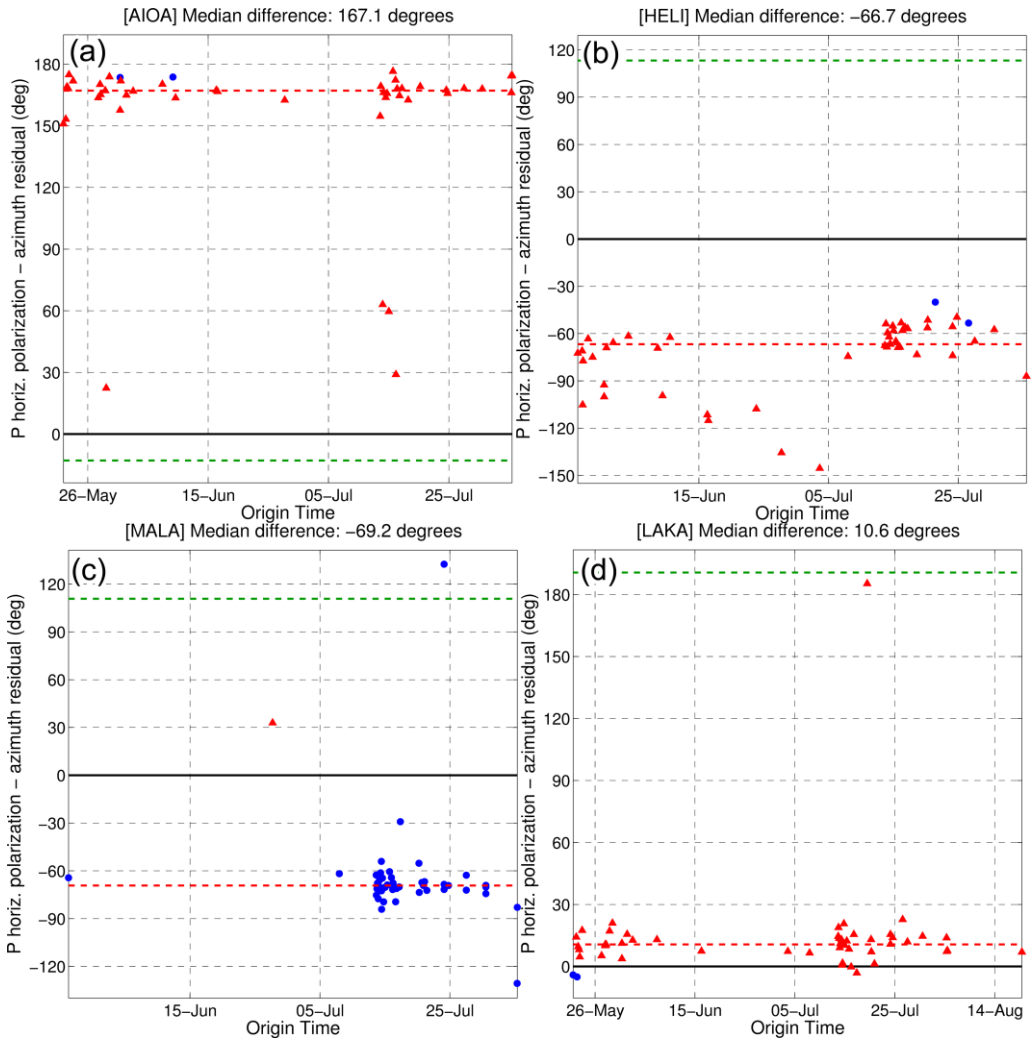

Figure 2.17: Orientation tests for seismometers with correct vertical polarity, using the 2013 Helike dataset (Section 5A.4). Compressive and dilatational first motion polarities are denoted by blue circles and red triangles, respectively.

As in Section 2.5, the interval containing the first P-wave pulse is picked and both vertical polarity and horizontal direction are measured where the particle motion vector's modulus maximizes. However, in this case, the residual between the epicenter's azimuth relative to the station and the P-wave's first motion direction should always be, on average, near 0° or 360°, if the sensor is properly oriented. Any significant deviation from 0° indicates disorientation of the horizontal components. This is the typical case of sensors inside boreholes, as they rotate during deployment and their final orientation is random.

Results of the orientation measurements for stations of the local network in the western Corinth Rift are presented in Table 2.4. In order to transform the randomly oriented horizontal components, $\mathbf{N}^*$, $\mathbf{E}^*$ to the correct N-S, E-W orientation (data vectors **N**, **E**), the following rotation matrix must be applied:

$$\begin{bmatrix} N^T \\ E^T \end{bmatrix} = \begin{bmatrix} \cos(-\phi_r) & \sin(-\phi_r) \\ -\sin(-\phi_r) & \cos(-\phi_r) \end{bmatrix} \cdot \begin{bmatrix} N^{*T} \\ E^{*T} \end{bmatrix} \tag{2.44}$$

where φ_r is the measured rotation of the sensor, hence $-\varphi_r$ the required correction. The median and other values in Table 2.4 have been measured using circular statistics (Berens, 2009) to avoid wrapping at the margins of the [0, 2π] range. Mean and standard deviation values have been measured on selected subsets after removing outliers.

Station AIOA was found with a residual that is relatively close to 180°, as measured with 3 different datasets (Figs 2.16-2.18). This is consistent with measurements of the fast shear-wave polarization directions on this station (during analysis in the framework of the study of Kaviris *et al.*, 2016) which were made before the φ_r correction was determined, but resulted in a relatively similar mean anisotropy direction compared to other local stations in the area. This hinted that the real orientation of the AIOA station was probably near zero or 180°. The orientation of station TEME was found close to 0° during the period 2000-2007. However, later measurements on TEME during the seismic crisis of 2013 in Helike resulted in a residual of ~38°, indicating that the latter is probably due to TEME being within the epicentral area of the 2013 Helike swarm, thus small differences in azimuths or polarization of the particle motion could cause large biases in the measured angle of direction. The same problem probably affected measurements in the temporary station HELI, which was found at ~293° and a relatively large standard deviation (same as TEME). Despite the reason for the systematic deviation between observed and theoretical directions, these corrections should be taken into account to reduce biases in the S-wave polarization directions which are used as additional weights for the determination of composite focal mechanisms (e.g. Section 5A.4). The borehole station MALA, which is installed on the northern shore of the rift,

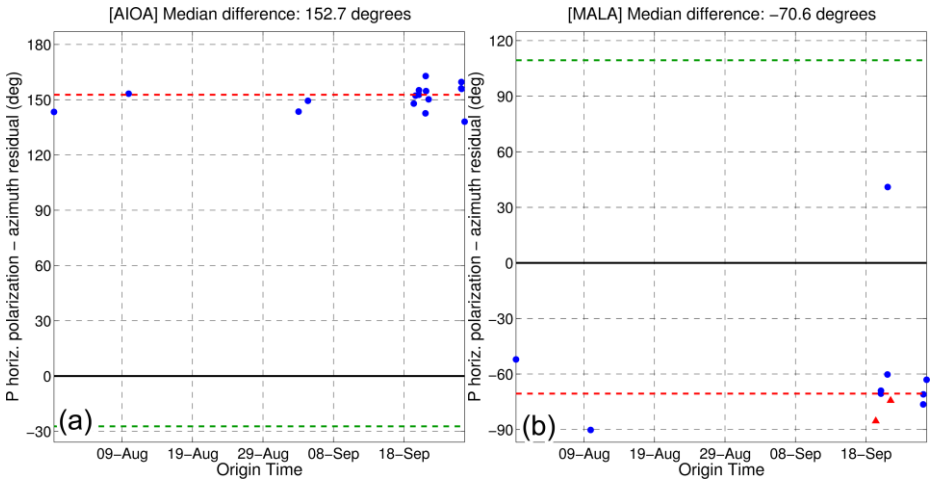

Figure 2.18: Orientation tests for borehole seismometers with correct vertical polarity, using the 2014 Nafpaktos-Psathopyrgos swarm dataset (Section 5.4). Compressive and dilatational first motion polarities are denoted by blue circles and red triangles, respectively.

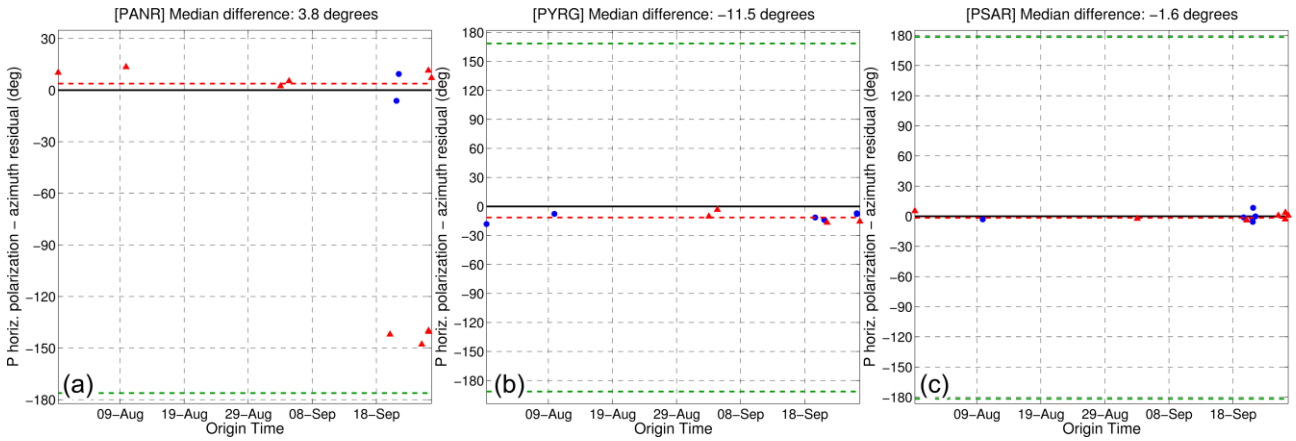

Figure 2.19: Validation of vertical polarity after the applied reversal on the vertical component of surface stations a) PANR, b) PYRG and c) PSAR, using the 2014 Nafpaktos-Psathopyrgos swarm dataset (Section 5.4). Compressive and dilatational first motion polarities are denoted by blue circles and red triangles, respectively.

below Mornos delta, was found to have a $\varphi_r \approx 290 \pm 10°$, with very consistent results in two different datasets. The correct horizontal orientation was also validated for the surface stations PANR, PYRG and PSAR (Fig. 2.19), during the 2014 Nafpaktos-Psathopyrgos swarm (Section 5.4) after their vertical waveforms were reversed. Orientation corrections for the borehole stations AGEO, DIMT and KOUL could not be measured, as at least one of their horizontal components was damaged.

It is noteworthy that there is another technique for estimating the orientation of borehole sensors which takes advantage of waveform cross-correlation. In case another, properly oriented sensor is also employed at the surface near the borehole, even when a small earthquake occurs at local distance both instruments should record a similar waveform. This is the reverse of what happens when two similar events occur and their waveforms are recorded to the same station and is due to the principle of reciprocity (Spudich & Bostwick, 1987). Had both sensors been properly oriented, the cross-correlation of a seismic waveform between their corresponding components should have a high maximum value. However, due to the random orientation of the borehole sensor, its horizontal components have to be rotated (Eq. 2.44) in order for a high cross-correlation value to be measured. Cross-correlations are performed for $\varphi_r \in (0, 360)$ and the φ_{max} which corresponds to the maximum XC_{max} value should correspond to the rotation of the borehole sensor. The same technique can, in principle, be applied using a properly oriented sensor at a neighboring station as long as the earthquake event is at an epicentral distance much larger than the distance between the two stations.

Chapter 3

Spectral analysis of seismic sources

Introduction

One of the most important seismic source parameters is the magnitude, which quantifies the size of an earthquake. The magnitude of an earthquake event was originally defined by Richter (1935) as the logarithm of the maximum trace amplitude, A (in μm), with which the standard short-period torsion seismometer would register that shock at an epicentral distance Δ = 100 km. The local magnitude, M_L, for epicentral distances Δ < 600 km, is based on measurements of peak displacement, A, on the horizontal component recordings, with M_L = 0 corresponding to A = 1μm at Δ = 100 km. While it is based on a straightforward measurement on the waveform recordings, this poses limitations as it only utilizes a small portion of the available information and is also prone to saturation for events of large magnitudes (e.g. Kanamori, 1977). A different approach on the magnitude is based on the determination of the scalar seismic moment, M_o, from field observations, as defined by the following relation (Aki, 1966):

$$M_o = \mu \cdot \bar{u} \cdot S \tag{3.1}$$

where μ is the shear modulus (or rigidity, or second Lamé parameter) at the focus, which is the ratio of shear stress to shear strain and is used as a measure of the material's resistivity to shear, the product $S=L \cdot w$ (m^2) represents the surface area for a rectangular rupture plane with length L and width w and $\bar{u}$ (m) is the average dislocation on the ruptured surface. The shear modulus can be calculated from $\mu=\beta^2\rho$, where β is the shear velocity and ρ the density of the material at the source, with typical values $\mu \cong 32$ GPa (or $\sim 3.2 \cdot 10^{11}$ dyne·cm^{-2}) in the crust and ~75 GPa in the mantle. The moment magnitude, M_w, can be derived from M_o with the following formulae (Hanks & Kanamori, 1979):

$$M_w = \frac{2}{3}\left(\log_{10}\frac{M_o}{N \cdot m} - 9.1\right) = \frac{2}{3}\left(\log_{10}\frac{M_o}{dyne \cdot cm} - 16.1\right) \tag{3.2}$$

In this chapter, the theoretical aspects of the seismic displacement spectrum are briefly presented. The primary aim is the development of an automatic procedure for the determination of M_o, mainly for relatively small earthquakes, along with other parameters such as the corner frequency, f_c and the attenuation factor, κ.

3.1 The displacement spectrum

When the ground motion is measured at a seismic station by an instrument, such as a seismometer or an accelerometer, it goes through a series of unit conversions and response convolutions; a procedure which can be reversed through deconvolution to reconstruct the real ground motion (Appendix 3A). The displacement can be calculated by integrating the velocity time-series, either in the time-domain, using a numerical method for integration, or by performing a Fast Fourier Transform (FFT) and dividing the spectrum by $i \cdot 2\pi f$ in the frequency domain. The latter is recommended as a faster solution if further analysis needs to be performed on the displacement spectrum.

A simple form of the expected theoretical shape of the displacement spectrum can be derived by assuming that the following conditions are true:

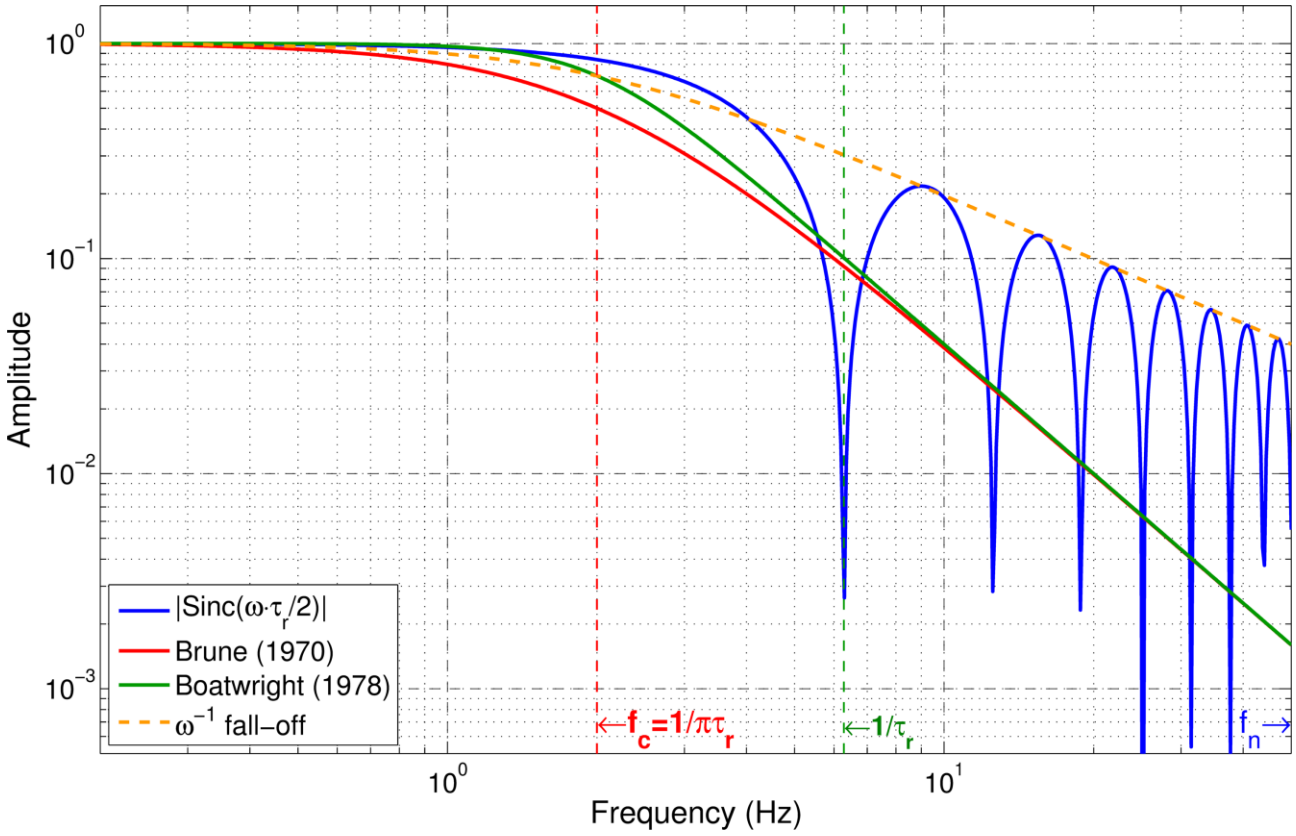

Figure 3.1: Diagrams of the Sinc function (blue), Brune (1970) model (red: n=1, γ=2 in Eq. 3.8)) and Boatwright (1978) model (green: n=2, γ=2), with κ=0, for a boxcar STF with τ_r=(1/2π)sec≈0.16sec (f_c=2Hz), where f_n=50Hz marks the Nyquist frequency for a sampling rate of F_s=100sps. Note that the Sinc function decays as ~ω^{-1} instead of ~ω^{-2} (γ=2) for the Brune and Boatwright models. An additional orange dashed line (n=2, γ=1, κ=0) follows the decay of the Sinc function for the high frequency part of the Sinc curve. The $1/\tau_r$ frequency marks the first zero-crossing of Sinc.

- The far-field seismic waves are treated as if generated by a double-couple point source.
- The seismic source time function (STF) can be approximated by a boxcar or trapezoid function.
- The ruptured surface for small earthquakes ($M_w < 5$) can be approximated by a circular fault (Brune, 1970; Madariaga, 1976) where the rupture begins at its center and propagates radially outwards.
- Unilateral ruptures can be approximated by the ribbon-like Haskell fault model (Haskell, 1964), which can also replicate directivity effects.

A boxcar STF, $B(t; \tau_r)$ corresponds to a ramp displacement history, where the rise time, τ_r, of the ramp is the duration of the boxcar function. For a ruptured fault with finite dimensions, as in the Haskell fault model, the STF can be represented by a trapezoid function, that is the convolution of two boxcars of unitary area (Lay & Wallace, 1995):

$$u(t) = M_o\left(B(t;\tau_r) * B(t;\tau_c)\right) \tag{3.3}$$

one with a duration corresponding to the displacement history of a single particle (rise time, τ_r) and the other to the effects of the fault's finiteness, represented by the rupture time, $\tau_c = x/\upsilon_r > \tau_r$, where x is the fault's characteristic dimension (length for a rectangular or radius for a circular fault model) and υ_r the rupture velocity, normally in the range $0.6\beta<\upsilon_r<0.9\beta$ for subsonic ruptures (Madariaga, 1976), typically 0.8β (Lay & Wallace, 1995).

The Fourier transform $u(\omega)$ of a boxcar with duration τ_r is the absolute value of the un-normalized cardinal sine, or "Sinc" function, $SINC(x) = \frac{\sin(x)}{x}$, with corner, or cut-off angular frequency $\omega_c = 2\pi f_c = 2/\tau_r$ (Fig. 3.1):

$$u(\omega) = M_o\left|\frac{\sin(\omega\tau_r/2)}{\omega\tau_r/2}\right| = M_o \cdot \left|SINC(\omega\tau_r/2)\right|, \tag{3.4}$$

In the more convoluted case of the trapezoid STF (Eq. 3.3), the corresponding Fourier transform is the product of the moduli of two Sinc functions with corner angular frequencies $\omega_1 = 2/\tau_c$ and $\omega_2 = 2/\tau_r$ (Fig. 3.2):

$$u(\omega) = M_o \cdot \left|SINC(\omega\tau_r/2)\right|\left|SINC(\omega\tau_c/2)\right| \approx \begin{cases} M_o & , \quad \omega < \dfrac{2}{\tau_c} \\ \dfrac{M_o}{\omega\tau_c/2} & , \quad \dfrac{2}{\tau_c} < \omega < \dfrac{2}{\tau_r} \\ \dfrac{M_o}{\omega^2(\tau_r\tau_c/4)} & , \quad \omega > \dfrac{2}{\tau_r} \end{cases} \tag{3.5}$$

The right-hand side of Eq. 3.5 represents a simplification for the trends of the spectrum at various frequency bands (Lay & Wallace, 1995), which at the lower angular frequencies ($\omega<\omega_1$) can be approximated by a plateau of constant amplitude, M_o, while the respective amplitude at the higher

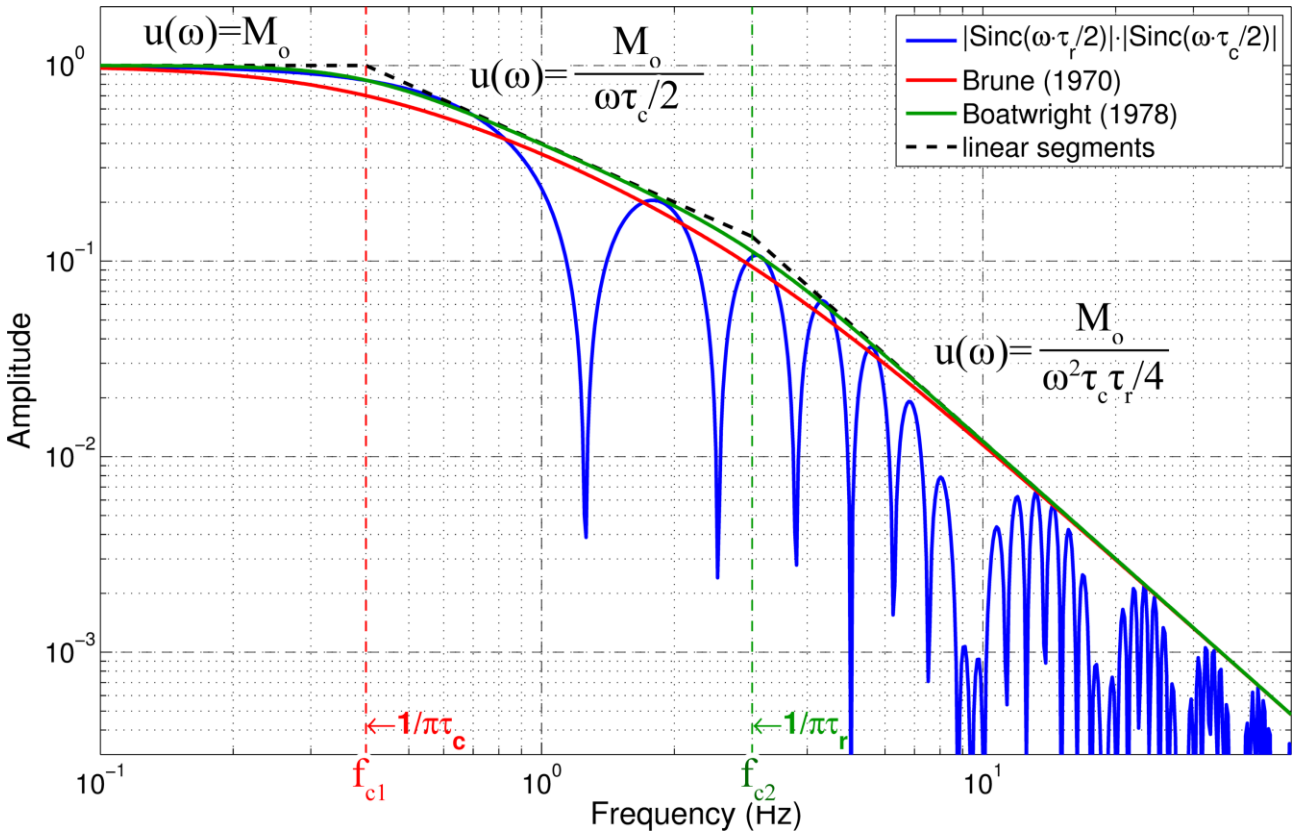

Figure 3.2: Diagrams of the product of two Sinc functions (blue) (Eq. 3.5) with corner frequencies $f_{c1}=2\pi\omega_1=1/\pi\tau_c=0.4$Hz (red dashed vertical) and $f_{c2}=2\pi\omega_2=1/\pi\tau_r=3$Hz (green dashed vertical) and their respective approximations with a Brune-type model (red: n=1, γ=2), Boatwright model (green: n=2, γ=2), with κ=0, $\gamma_1=\gamma_2=\gamma$, Ψ_o=1 (Eq. 3.7) and the linear segments (in log-log scale) of Eq. 3.5 (black dashed lines).

angular frequencies ($\omega>\omega_2$) decays in proportion to ω^{-2}. The high-frequency decay is the theoretically expected result of destructive interference between high-frequency waves in the far-field for periods smaller than the source duration. The simple boxcar spectrum, on the other hand (Eq. 3.4), falls-off in proportion to ω^{-1}, with a single cut-off angular frequency at $\omega_c=2/\tau_r$, or simple corner frequency (Hz) $f_c=1/\pi\tau_r$ (Fig. 3.1), same as the Haskell model for angular frequencies between ω_1 and ω_2. The spectral fall-off when examined in a log-log scale becomes simply linear, with ω^{-1} and ω^{-2} representing different values of its trend's slope.

An alternative approximation to the body-wave displacement spectra, $\Psi(\omega)$, has been formulated along with the respective fault model of Brune (1970):

$$\Psi(\omega)=\frac{\Psi_o}{1+\left(\frac{\omega}{\omega_c}\right)^2} \tag{3.6}$$

where Ψ_o the plateau of the displacement spectrum at the lower frequencies. The source model of Brune (1970) supposes a ramp displacement history, causing stress drop $\Delta\sigma$ in time τ_r. The STF in the Brune model can also be approximated by a boxcar, although the dynamic stress drop, which propagates at shear-wave velocity, β, precedes the rupture, which usually propagates with a velocity of the order of 80% of β at the source. The model of Eq. 3.6 falls off as ω^{-2}, with a single cut-off angular frequency at $\omega_c=2/\tau_r$. Boatwright (1978) proposed a generalization of the source spectrum formula which is more flexible for the description of different source models:

$$\Psi(\omega)=\frac{\Psi_o}{\left(1+\left(\frac{\omega}{\omega_c}\right)^{n\gamma}\right)^{1/n}} \Leftrightarrow \Psi(\omega)=\frac{\Psi_o}{\left(1+\left(\frac{\omega}{\omega_1}\right)^{n\gamma_1}\right)^{1/2n}\left(1+\left(\frac{\omega}{\omega_2}\right)^{n\gamma_2}\right)^{1/2n}} \tag{3.7}$$

where the parameter γ describes the high-frequency fall-off rate, with $\gamma=2$ for an ω^{-2} model, while n takes the value $n=2$ in the Boatwright model, which is its main difference from the Brune model that is represented with $n=1$. The second form of Eq. 3.7 can be used to incorporate two corner angular frequencies, ω_1 and $\omega_2>\omega_1$, as in the Haskell model with $\gamma_1=\gamma_2=2$ (Eq. 3.5), with fall-off in the generalized case $\sim\omega^{-\gamma}$, where $\gamma=\gamma_1/2$ for ω between ω_1 and ω_2 and $\gamma=(\gamma_1+\gamma_2)/2$ for $\omega>\omega_2$ (Boatwright, 1978). It should be noted that, in practice, the two corner frequencies are usually indistinguishable and a single frequency related to the apparent source duration is sought instead.

In addition to the source, path effects also modify the spectral shape of an earthquake record. Higher frequency waves tend to be more susceptible to attenuation because of energy loss due to a certain degree of anelasticity of the medium and energy redistribution caused by scattering effects, which become significant for wavelengths smaller than the heterogeneities. The attenuation is expressed as an extra factor in Eq. 3.7 which accounts for the degree of exponential decay (Fig. 3.3):

$$\Psi(\omega)=\Psi_o\frac{\exp\left(-\omega\kappa/2\right)}{\left(1+\left(\frac{\omega}{\omega_c}\right)^{n\gamma}\right)^{1/n}} \tag{3.8}$$

where $\kappa=\frac{T}{Q}$, sometimes symbolized with T^* or t^*, is the spectral decay parameter, mainly incorporating site-effects but also the attenuation along the seismic ray-path (Anderson & Hough, 1984), with T being the travel-time of the respective wave-type and $Q>>1$ the "quality factor", a dimensionless, path-dependent quantity that is inversely proportional to the fractional loss of energy per cycle of oscillation due to anelastic/intrinsic attenuation in the medium (Lay & Wallace, 1995). Values of Q for shear-waves usually range from hundreds to over 1000 (e.g. Abercrombie, 1995), which usually makes κ of the order of a few to tens of milliseconds (e.g. Ichinose *et al.*, 1997). It is noteworthy that for $\kappa=0$ and $n=2$, Eq. 3.8 becomes similar to the frequency response of a γ-order low-pass Butterworth filter:

$$\left|H(\omega)\right| = G_o \frac{1}{\sqrt{1+\left(\frac{\omega}{\omega_c}\right)^{2\gamma}}} \tag{3.9}$$

where ω is the angular frequency, γ is the filter order and the ω_c is the high cut-off angular frequency which corresponds to a reduction of amplitude by ~3dB (the amplitude has dropped to ~70.7% of its initial value), independently of the filter order. This can actually be seen in the example of Fig. 3.1, where the curves of the Boatwright and the ω^{-1} model, both with κ=0 and n=2 but different γ, intersect at f_c=2Hz, at a value of normalized amplitude ~$7\cdot10^{-1}$. Another characteristic is that the ω^{-1} curve (or the 1st order Butterworth filter) drops to 10^{-1} when it reaches $10\cdot f_c$=20Hz while at the same frequency the respective Boatwright model ω^{-2} curve (2nd order Butterworth filter) has dropped to 10^{-2}, same as for the Brune ω^{-2} model. The spectral fall-off, γ, generally ranges from 1.5 to 3, but is usually considered fixed at γ=2 during inversions, mainly to reduce the number of unknowns (e.g. Ichinose *et al.*, 1997).

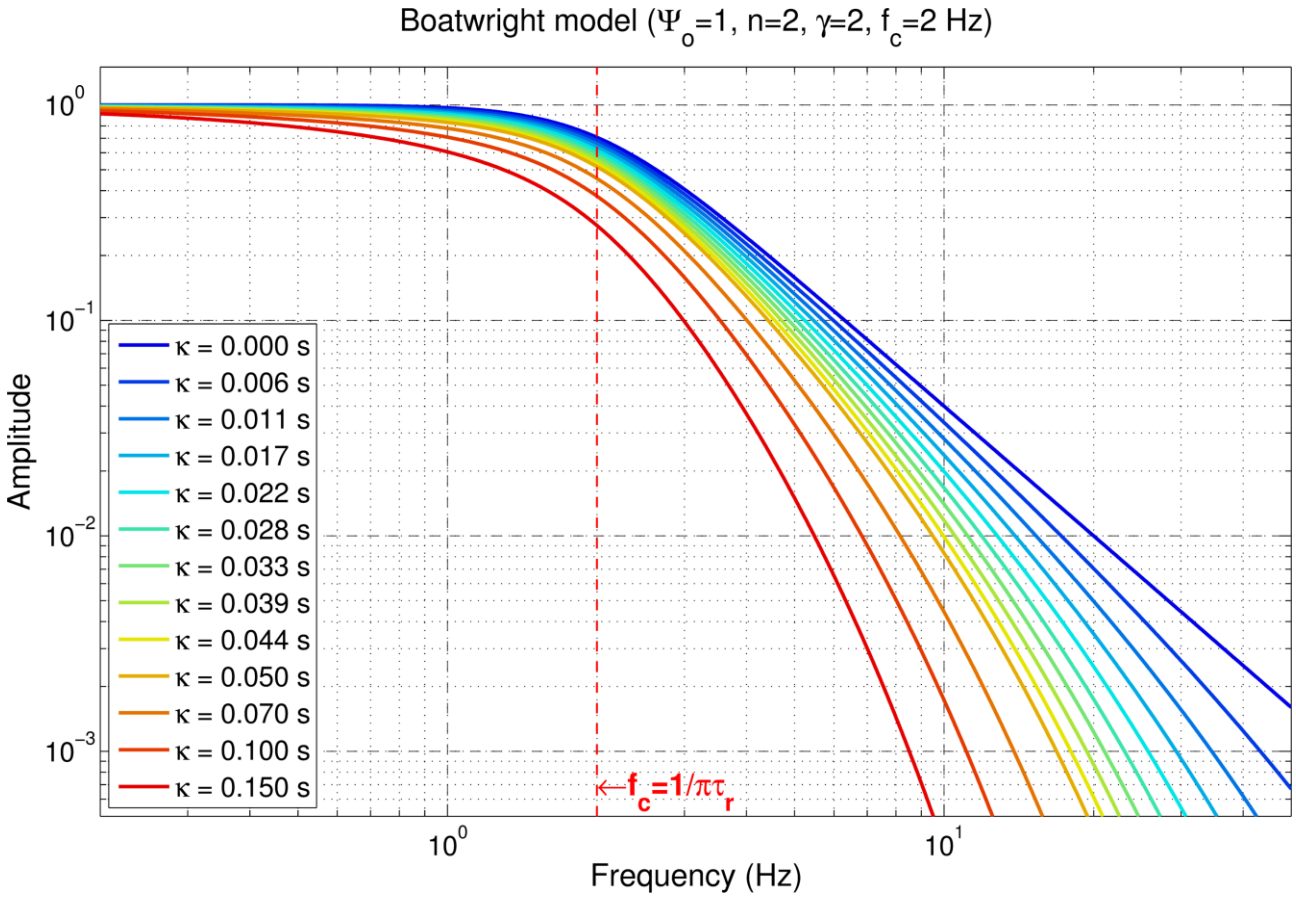

Figure 3.3: Diagrams of a Boatwright model with f_c=2Hz for various values of the spectral decay parameter, κ.

The plateau of the source displacement amplitude spectrum, Ψ_o can be converted to seismic moment, M_o, using the following equation (Boatwright, 1978; Bowers & Hudson, 1999):

$$M_o = \frac{4\pi\rho^{1/2}(\vec{x})\rho^{1/2}(\vec{\xi})\beta^{1/2}(\vec{x})\beta^{5/2}(\vec{\xi})R\left(\vec{x},\vec{\xi}\right)}{F_S(\theta,\varphi)R_S S_S}\Psi_o \approx$$
$$\approx \frac{4\pi\rho\beta^3}{F_{RMS}R_S}\frac{R}{S_S}\Psi_o = C\frac{R}{S_s}\Psi_o \quad (3.10)$$

where **x** and **ξ** represent the location of the station and the hypocenter, respectively, β is the shear-wave velocity, ρ is the material's density, β is the shear-wave velocity, R is the hypocentral distance to account for geometrical spreading, $F_S(\theta,\varphi)$ is the S-wave radiation pattern, R_S=2 is the free surface correction and S_s is the station-dependent site-effect correction. The second form of the equation is an approximation used to simplify the calculations, where $\rho\approx$2700kg/m^3 and β at the source is only taken into account. F_{RMS} is the RMS average of the radiation pattern measured over the whole focal sphere, with approximate values 0.52 for the P-waves and 0.63 for the S-waves (Aki & Richards, 2002; Boore & Boatwright, 1984), which is valid when several measurements of M_o are taken at various azimuths and a mean value is determined. The parameters which are independent of the station are merged into the constant C, leaving hypocentral distance, R, and site amplification/de-amplification factor S_S. The same relation can be used to convert the displacement spectrum $\Psi(\omega)$ into seismic moment units, $M(\omega)=C\cdot R\cdot\Psi(\omega)/S_s$, and the M_o can be determined through an inversion procedure from the spectral plateau at the lower frequencies.

3.2 Automatic determination of seismic moment

3.2.1 Preparation of signal and noise spectra

In several applications of the present study (Chapters 5-6) magnitude information is not available from pre-existing catalogues and has to be determined for each individual earthquake. An automatic algorithm has been developed for the calculation of moment magnitude, based on the abovementioned features of the displacement spectrum of the recorded seismograms. Similar procedures have been described in the literature (Kapetanidis, 2007; Edwards *et al.*, 2010; Matrullo *et al.*, 2013; Kapetanidis *et al.*, 2015; Godano *et al.*, 2015). The required data include: a catalogue of events, P- and S-wave arrival-times (T_P and T_S, respectively, replaced by their theoretical values where picks are not available), seismic waveforms, a comprehensive history of stations' instrument responses and information on the "State of Health" (SOH) of the 3 components of each station. A step-by-step description of the procedure is presented below.

An adequately large window length is selected that includes the full waveform signal and the noise before the arrival of the P-waves. The waveform is de-trended for DC offset and linear trends. Optionally, a high-pass filter with cut-off frequency at ~0.1 Hz can be applied for the removal of potentially unwanted low frequency noise, however, in the present study it is not used, leaving the low frequency spectrum unaltered. An unfiltered copy of the full waveform should also be available to re-evaluate the spectra of major events, where a high-pass filter may cause underestimation of the

spectral plateau, M_o. The seismic waveform, $S(t)$, is cropped to include the S-wave train and part of the P-wave coda (Fig. 3.4). A typical window length is [T_S - 0.5s , T_S + 20s]. A noise window, $N(t)$, is also selected, e.g. [T_P – 15s , T_P – 5s]. If a T_P measurement is not available it can be estimated by T_S-TT_{SP}, where TT_{SP}=T_S-T_P=TT_S-TT_P, with TT_P and TT_S being the P- and S-wave travel-times and TT_P≈TT_S·V_S/V_P, where V_P/V_S the P- to S-wave propagation velocity ratio, thus TT_{SP}=TT_S(1-V_S/V_P). Special care should be taken so that the signal window does not include waves of another, possibly stronger event that may arrive at the station before the T_S+20s end point (e.g. Fig. 3B.2a). This could severely influence the overall amplitude and spectral shape and likely result to a largely overestimated magnitude. To avoid this, the mean absolute amplitude of the first ¾ of the signal window is compared to the respective last ¼. Naturally, it is expected that the first segment, which contains the S-wave, should have larger mean absolute amplitudes than the ending part, where only some remaining coda or background noise should be contained. Otherwise, it could mean the arrival of an incoming, possibly stronger event which should be removed. In that case, the signal is shortened by ¼ and the procedure repeated up to another two times for the remaining window, unless the condition is satisfied. Both signal and noise windows should be de-trended, by removal of their mean value and any remaining linear trend. A multitaper with 5 3π-prolate tapers can be used to acquire a smoothed out spectra, low spectral leakage and variance (e.g. Edwards, 2008, 2010). Alternatively, a faster method is to simply apply a 20% cosine taper and then the spectra of both signal and noise can be further smoothened by calculating their 5-point average (e.g. Godano *et al.*, 2015). This reduces the variance and the outliers, which has been observed to result in more stable fit with wider bands of adequate SNR, better correlation coefficients and clearer trends in both original and corrected spectra as well as smoother weight functions which are discussed below.

A Signal-to-Noise Ratio (SNR) value is calculated by dividing the respective RMS amplitude values:

$$SNR = \frac{S_{RMS}}{N_{RMS}} = \sqrt{\frac{N_n \sum_{Ns} A_{s,i}^{\,2}}{N_s \sum_{Nn} A_{n,j}^{\,2}}} \tag{3.11}$$

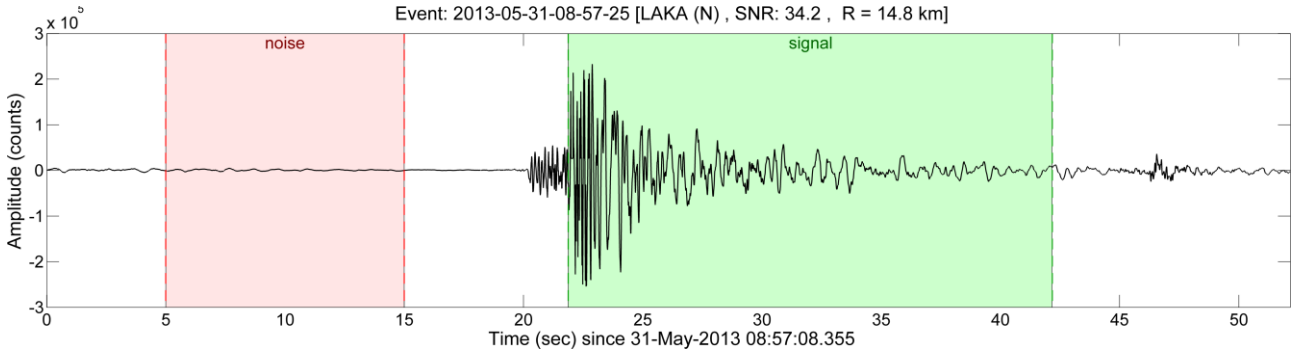

Figure 3.4: Example of S-wave signal (green) and noise (red) window selection for the calculation of the respective spectra. The SNR is ~34.

where S_{RMS} and N_{RMS}, the RMS values of signal and noise windows, respectively, $A_{s,i}$ and $A_{n,j}$ are the corresponding amplitudes of the i^{th} and j^{th} sample and N_s and N_n the total number of samples of the signal and noise windows. Signals with $SNR < 2$ are rejected, on the assumption that there should be at least one station/component with adequate $SNR>2$ for each event. This is particularly useful for small events, as the SNR can be very low in far stations, resulting in a miscalculation of the seismic moment. In such cases, the magnitude has to be determined by a small set of the closer stations with sufficiently high SNR. Both waveforms, $S(t)$ and $N(t)$, are converted to the frequency domain, by applying FFT, and resampled, if needed, so that both amplitude spectra refer to the same frequency values. To remove bias caused by the different window lengths between signal and noise windows, the latter spectrum must be normalized by N_s/N_n (Edwards *et al.*, 2010). The frequency-dependent $SNR(f)$ is calculated by dividing the signal amplitude, $S(f)$, with the noise amplitude, $N(f)$, at the corresponding common frequencies. Low values of $SNR(f)$ can be nullified, while the rest are normalized by $\max(SNR(f))$, so that the $SNR(f)$ ranges from 0 to 1 and can be later modified to a normalized spectral weight function, $w(f)$.

The instrument's response must be de-convoluted and the signal be converted from "counts" to velocity units. Specifics on the calculation of the instrument response spectra are described in Appendix 3A. The deconvolution can be performed directly in the frequency domain by dividing the signal spectrum with the respective sensor's transfer function. In terms of log-amplitude, this corresponds to a subtraction of the instrument's response from the displacement spectrum. The result of the deconvolution is presented in Fig. 3B.1.

The next step concerns the integration of the deconvolved signal to acquire the displacement spectrum. This can be performed directly in the frequency domain by dividing the velocity spectrum once by $i \cdot 2\pi f$ (or twice, in case of an acceleration spectrum), where i is the imaginary unit. The visual result on the amplitudes resembles a sort of clockwise rotation of the spectrum: in the low frequencies it is raised and becomes more "flat" (parallel to the frequency axis) while for higher frequencies it is now steeper (Fig. 3B.1). At this point, any remaining noise, especially in low SNR waveforms, will result in a slope, with amplitudes gradually increasing towards lower frequencies. Lastly, the displacement spectrum can be converted to seismic moment units by application of Eq. 3.10.

3.2.2 Inversion for the determination of spectral fit parameters

The seismic moment, M_o, along with the other parameters (f_c, n, γ and κ) of the theoretical source spectrum function (Eq. 3.8) can be calculated from the seismic moment spectrum by means of weighted non-linear least squares. Ichinose *et al.* (1997) note that there is a trade-off between γ and κ which makes the simultaneous inversion for f_c, γ and κ unstable. Boatwright (1978) ran several inversions with different fixed κ values and γ either allowed as a free parameter or fixed e.g. at $\gamma=3$ in cases of unstable solutions that resulted in $\gamma>>3$. There is also a trade-off between f_c and κ which causes an apparent scaling breakdown in earthquakes of small magnitude, limiting the ability for the proper determination of source dimensions (e.g. Anderson, 1986). Therefore, either γ or κ, or both

could be set to a constant value, at least for preliminary calculations. Alternatively, they should range within restricted bounds to ensure a stable inversion.

The M_o parameter is, in general, more stable, with its main issues being 1) the noise at the lower frequencies for events of small magnitude (low SNR), which can potentially cause overestimation of M_o, and 2) limited number of samples at the band of the spectral plateau, especially for larger events for which the f_c is also lower and may possibly cause underestimation of M_o. Ideally, the visually distinguishable plateau of the moment spectrum corresponds to the seismic moment value, M_o, which is all that is required for the calculation of M_w. However, the automatic determination of the plateau is not always self-evident, especially for low-magnitude events / low-SNR signals, where low frequency noise can significantly mask and distort the plateau towards higher values, leading to overestimation of M_o. On the other hand, an overestimated f_c, a lack of enough low frequency samples (small window length / sample size) or not strong enough weights on the plateau, might drag M_o to lower values. The latter mostly affects the larger events, as the length of the signal window, T_{win}, limits the lower resolvable frequency of FFT to $f_{low}=1/T_{win}$. Apparently, $f_c>>f_{low}$ to allow for an adequate number of low frequency samples.

To determine M_o, the function of Eq. 3.8 is used in a non-linear least-squares inversion, weighted by $w(f)$ that depends on $SNR(f)$. The first pass of the algorithm is preliminary, with the site amplification factor, S_S, set to unity for all stations and components. Several measures can be taken to mitigate the problem of noise at the lower frequencies, especially for events of low magnitude. The first, as already mentioned, is an initial selection of suitable waveforms with SNR>2 in the time-domain, mainly to avoid stations which are too far and have low SNR. The second is the use of a normalized, frequency-dependent weight function, $w(f)$. The base for $w(f)$ is the previously determined $SNR(f)$ (Fig. 3.5; blue line) which is usually lower in the low frequencies and high in the middle and higher ones. It can take very low values in the long periods when the magnitude/SNR is small, thus reducing the gravity of samples on the ascending ramp of noise which may mask the plateau at the lower frequencies, while its amplitude is comparable (even smaller at some frequencies) to that of the noise spectrum. The SNR at low frequencies is expected to be high enough for strong events, resulting in relatively large $SNR(f)$ weighting values which enable the correct determination of the plateau. However, because of the nature of the FFT, the frequency sampling is done at equidistant frequencies on a linear scale, whereas the usual presentation of seismic moment spectra, with the main "linear" features highlighted in Fig. 3.2, is in log-log scale. This practically means that the data used for the inversion will contain a lot more samples for $f>f_c$ than for $f<f_c$ where the primary target, the M_o plateau, is to be found. This can lead to a bias, as the decaying part of the spectrum adds up more weight, potentially underestimating the plateau. The solution is to resample both $S(f)$ and SNR(f) to frequencies which are equidistant in the log scale (Ide *et al.* 2003; Kapetanidis, 2007) before the inversion, thus increasing the chance for a valid calculation of M_o. This enhances the part of the spectrum which is generally of greater importance and removes unnecessary details from the very high frequencies. The same procedure can be exploited to decrease the number of spectral samples down to a specified amount (e.g. 128 samples), which may reduce the processing time of the inversion. Alternatively, an additional $1/f$ weight (Fig. 3.5; dashed red line) can be incorporated in the $w(f)$ function to balance the sampling bias (Edwards *et al.*, 2010).

In the present work, two different spectral weighting schemes are used, depending on the average *SNR*(*f*), or rather the average $\log_{10}(SNR(f))$ which yields more conservative SNR values. The weighting function, *w*(*f*) begins as $\log_{10}(SNR(f))$, normalized and bound so that it stretches between 0.3 and 1.0. If the average $\log_{10}(SNR(f))$ surpasses a high threshold, e.g. $\log_{10}(50)$, which is usually the case for relatively strong earthquakes, it is more important that the lower frequency content is taken into account. In that case, the *w*(*f*) is multiplied by a factor that begins at 1.0 at low frequencies and gradually drops to 0.2 at the higher frequencies (Fig. 3.5; solid red line). Then *w*(*f*) is again stretched to fit a range between 0.3 and 1.0 (Fig. 3.5; black line). Finally, at frequencies where the original $\log_{10}(SNR(f))<0.01$ (SNR very close to unity) the respective weights are nullified, as the noise level is comparable to the signal level. Optionally, a mid-level threshold can also be set, e.g. for $\log_{10}(SNR(f))<0.3$ (or $SNR(f)<2$) to forcibly reduce weights for frequencies where SNR is less than double the noise level. All the weighting functions are presented in Fig. 3.5, where "(norm) *SNR*(*f*)" and "(mod) *SNR*(*f*)" refer to *w*(*f*) for average $\log_{10}(SNR(f))<\log_{10}(50)$ and $>\log_{10}(50)$, respectively (also see an example for average $\log_{10}(SNR(f))<\log_{10}(50)$ in Fig. 3B.2c). Lastly, a correction for systematic residuals per frequency between the model and the data can be applied on a second pass of the procedure, described in more detail below as the Site Response Function (SRF).

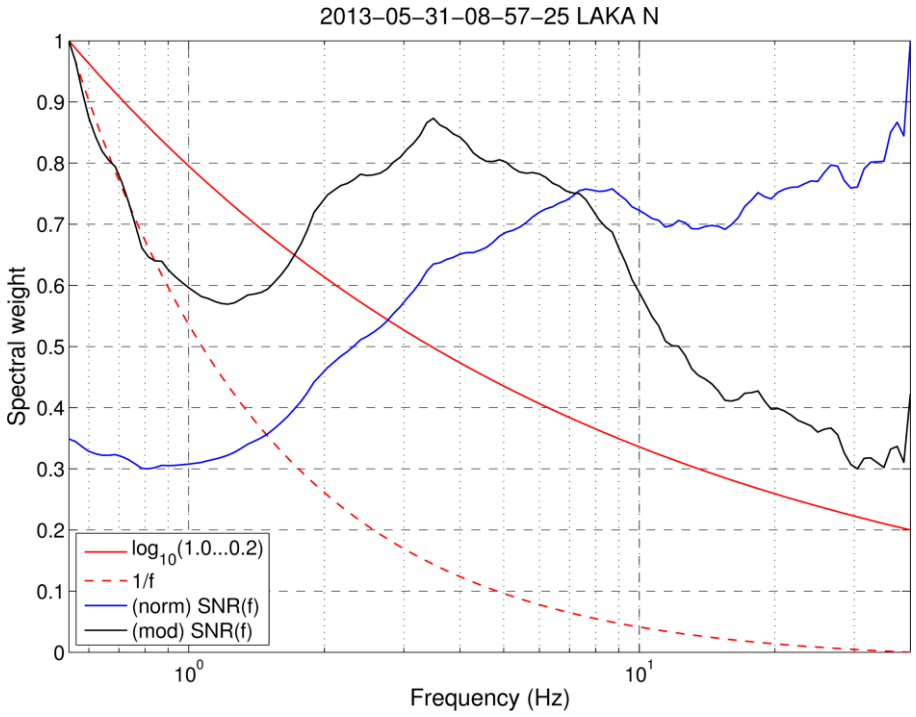

Figure 3.5: Different types of spectral weighting functions, *w*(*f*) for the waveform presented Fig. 3.4. The 1/*f* weight is proposed by Edwards et al. (2010) to account for the fewer FFT samples in the lower frequencies, "(norm) *SNR*(*f*)" is derived from the signal-to-noise spectral ratio, normalized and stretched between 0.3 and 1.0 while "(mod) *SNR*(*f*)", which is the preferred weighting function, has been multiplied with the "$\log_{10}(1.0…0.2)$" curve and re-normalized between 0.3 and 1.0.

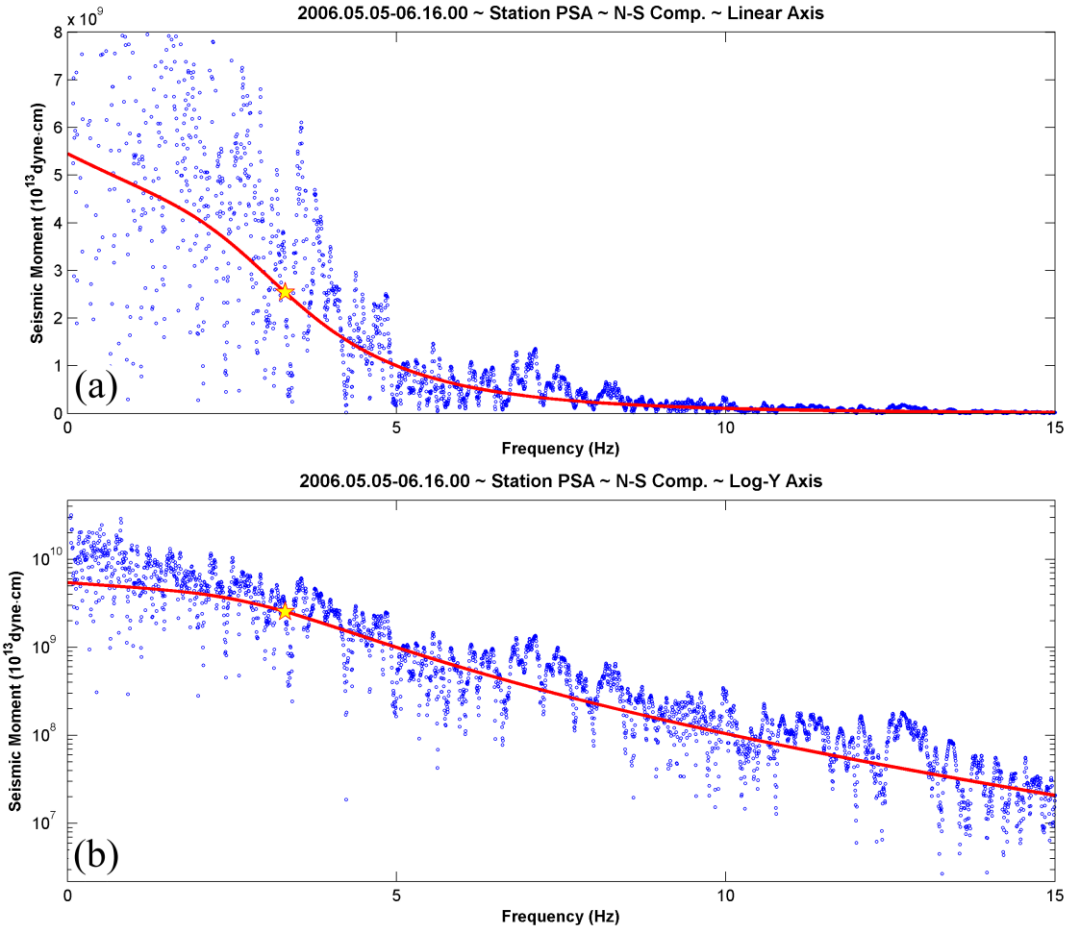

Figure 3.6: Example of a seismic spectrum a) in linear and b) in log-scale for the vertical axis of the seismic moment. Blue dots are the data points of the FFT, the red bold line is the model of Eq. 3.8 for (a) and Eq. 3.12 for (b), the star marks the f_c. (Figure after Kapetanidis, 2007)

The inversion procedure can be further aided by converting the $M(f)$ amplitudes, based on Eqs 3.8 and 3.10, to log scale (Fig. 3.6; Kapetanidis, 2007):

$$\log_{10} M(f) = \log_{10} M_o - \pi f \kappa \log_{10} e - \frac{1}{n} \log_{10} \left[1 + \left(\frac{f}{f_c} \right)^m \right] \tag{3.12}$$

This step is crucial, as the inversion using the formula of Eq. 3.8 directly can be very unstable. Eq. 3.12 smoothens the diagram on the Y-axis while the resampling of frequencies at equidistant values in the log scale aided by the $1/f$ type additional weighting is equivalent to the smoothening of the diagram and the spectral function in the X-axis. Examples of the spectral fit method are presented in Section 3.3.

Chances are that there may be significant bias between the mean M_o calculated on average, as determined by measurements in all the stations of the network for a certain event and the one derived by a certain station/component. For example, there may be a station or component which provides systematically larger M_o values relative to the mean. This systematic difference must be

removed as a correction to the M_o measurements per station/component, being an equivalent to the S_S factor of Eq. 3.10. On the second-pass of the procedure, following the previously mentioned modifications to the spectrum, the SRF is "subtracted" from $M(f)$ by division (subtraction in the log-scale). As the SRF may have different frequencies than the signal's FFT, a resampling is usually required, with the respective values determined either by linear interpolation or nearest neighbor extrapolation. This aims to correct certain frequency bands which may systematically deviate from the fit. These biases, along with the systematic M_o offset, may be due to topographic effects, badly calibrated or damaged instruments or even possible errors in the sensitivity/gain constants. In addition, the residuals, $M_R(f)$, between model and data, as calculated from the preliminary pass of the inversion procedure, are used for the estimation of the frequency-dependent Site Response Function (SRF) or "site amplification factor" for each station and component. The SRF is mainly attributed to resonant frequencies caused by near-surface fractured and weathered layers (Edwards, 2008). For long time-spans (e.g. Chapter 6), such that the instrumentation on several stations may have changed, both the average M_o residual and SRF must be calculated for each of the periods that a station has been working with a certain seismometer/digitizer configuration.

3.3 Examples of the spectral fitting method/ distribution comparisons

In order to examine the behavior of fitting Eq. 3.12 to the displacement/moment spectra, a set of different models have been considered (Table 3.1). Models #3 and #4 are the typical Brune (1970) and Boatwright (1978) models, including a variable κ parameter for attenuation. The respective #1 and #2 models are simpler in the sense that κ is forced to zero. Models #5-7 also allow γ to vary, with #7 also having n as a free variable. Naturally, M_o is always a variable, as the primary target of the spectral fit, as is f_c, which is expected to have some sort of dependence on M_o.

Table 3.1: Test models for spectral fitting.

#	n	γ	κ	model
1	1	2	0	Simple "Brune"
2	2	2	0	Simple "Boatwright"
3	1	2	(var)	Brune (1970)
4	2	2	(var)	Boatwright (1978)
5	2	(var)	0	Test #5 (γ)
6	2	(var)	(var)	Test #6 (γ, κ)
7	(var)	(var)	(var)	Test #7 (n, γ, κ)

To enable a stable inversion, the values of M_o, f_c, n, γ, κ are allowed to vary within a restricted range (Table 3.2). The range for M_o (in N·m) is equivalent to M_w between ~0.0 and 7.3, with the initial value (13) corresponding to $M_w \approx 2.6$. The corner frequency, besides the restrictions of Table 3.2, is always bound by the Nyquist frequency and the window length of the signal. Parameter γ, which represents the high frequency fall-off rate, is usually taken as $\gamma \equiv 2$ (ω^{-2}), but, if allowed to vary it should not surpass 3 and cannot be lower than 1.5 to prevent the source from radiating infinite energy (Ichinose *et al.*, 1997). The spectral roll-off, κ, is usually of the order of tens of ms. The 0.2s

value is an upper extreme that is only allowed to aid the fit in order to detect a valid M_o, which is the first priority. Lastly, the effect of n, which only varies in model #7, is the sharpness of the spectral corner at f_c, with n=1 (Brune) being smooth, n=2 (Boatwright) sharper and n=3 an even sharper corner, while n is also allowed to take non-integer values, rendering model #7 the most flexible one. The data points used for the inversion are derived from resampling at the log-scale between the frequencies 0.5 and 40Hz, with the Nyquist being at 50Hz for a typical 100sps sampling rate. The tests examined in this section have been run using the dataset of the 2013 Helike swarm (Chapter 5; Section 5A.4).

Table 3.2: Fit parameters min/max range and starting values (when variable).

	Min	Max	Start
log(M_o/Nm)	9	20	13
f_c (Hz)	0.2	30	5
n	1.0	3.0	2.0
γ	1.5	3.0	2.0
***κ* (s)**	0.0	0.2	0.0

Two examples of signal and noise spectra are presented in Fig. 3.7. Both have been converted to seismic moment units (N·m). The first event is a relatively strong one (M_w=3.7), with high SNR values in all frequencies. The lower SNR values are found at the lower frequencies (Fig. 3.5; blue line). On the other hand, the overall SNR is lower in the second example (Fig. 3.7b) for a smaller event (M_w=1.2), where for some frequencies the signal amplitude is even smaller than that of the

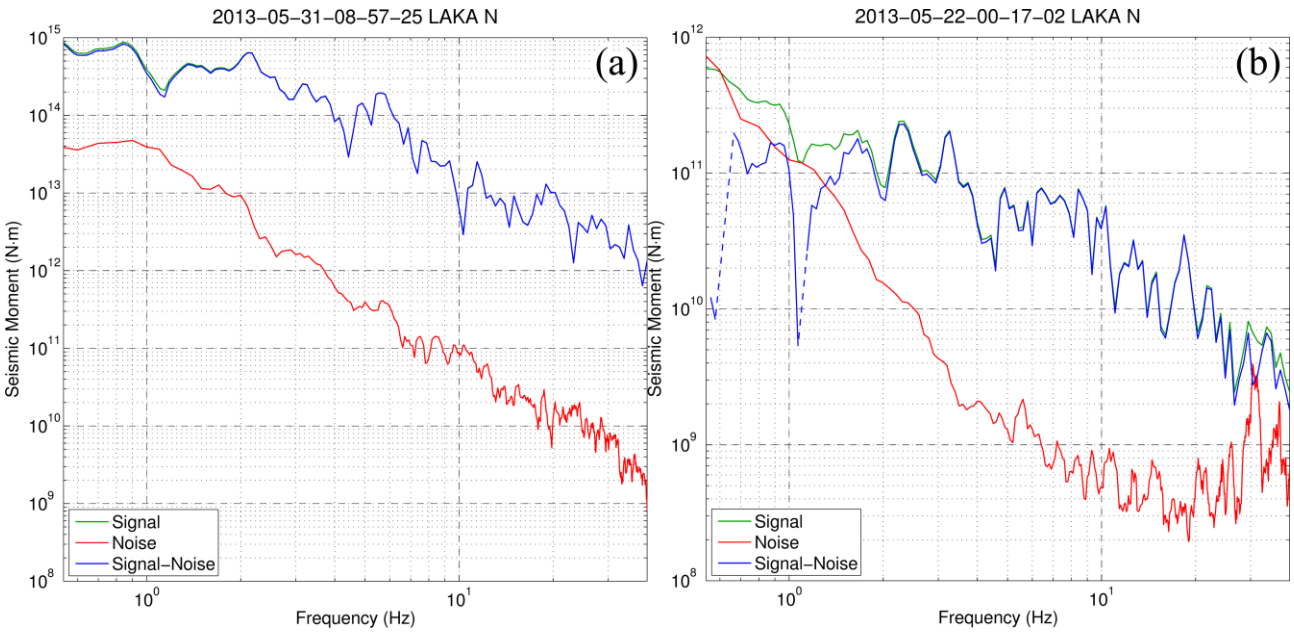

Figure 3.7: Signal (green) and noise (red) converted to seismic moment units along with the corrected "Signal minus Noise" curve (blue) for a) an M_w=3.7 event, b) for an M_w=1.2 event. Dashed segments in the blue line of panel (b) join parts of the spectrum interrupted by data points with $SNR(f)$<1.

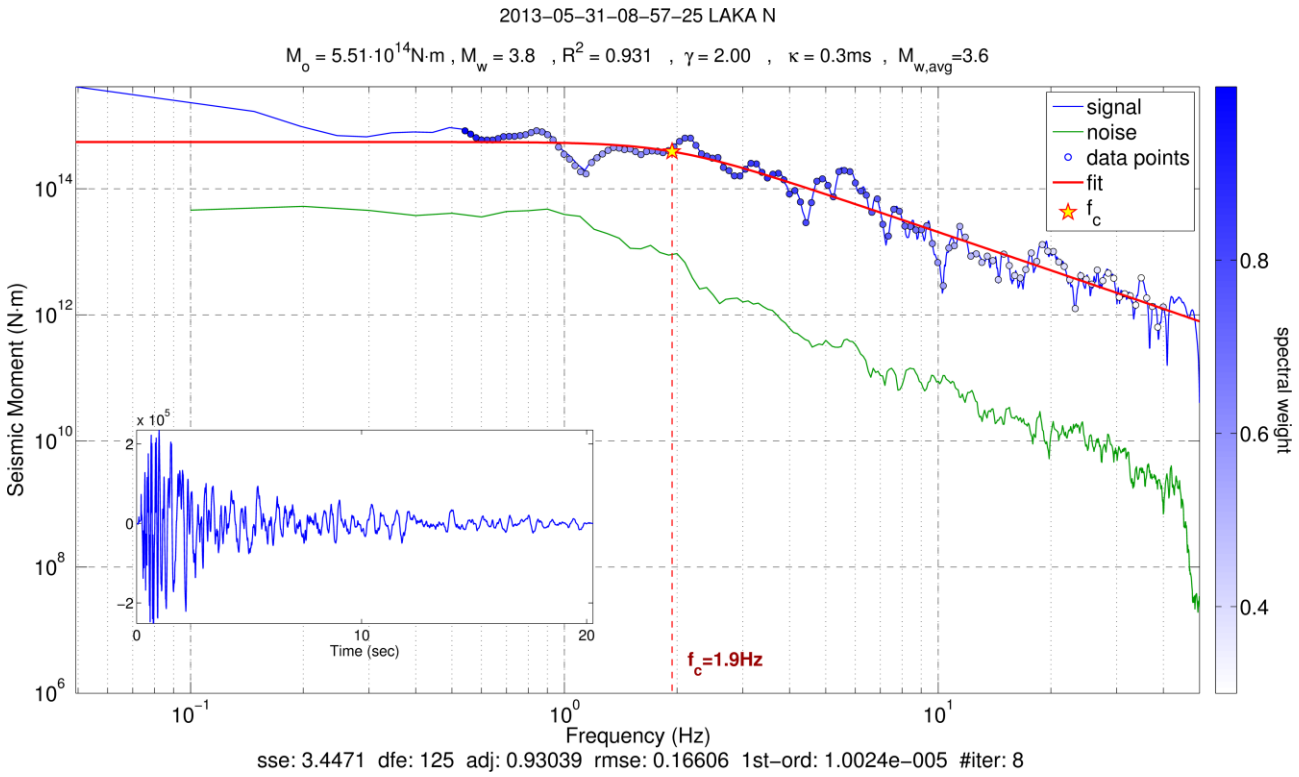

Figure 3.8: Example of seismic moment spectral fit (red bold line) using the model of Boatwright (1978). The blue curve is the full uncorrected signal while the circles are the selected points of the resampled and noise-corrected spectrum, with colour corresponding to the respective weight, $w(f)$. Star denotes the value of the theoretical spectrum at the corner frequency, f_c.

noise spectrum. At these values, the log($SNR(f)$) becomes negative and those samples are removed from the inversion. One of the modifications which are devised in order to reduce the chances of misfit to overestimated M_o is the (linear) subtraction of the noise from the respective signal amplitude values. This has negligible effect in large earthquakes, with high SNR (Fig. 3.7a; blue line) but it does affect the spectrum of smaller earthquakes, at frequencies with low SNR(f) (Fig. 3.7b; blue line). This is a countermeasure to reduce the effect of the noise ramp at the lower frequencies and also decrease the respective weights, $w(f)$, which are determined after the subtraction of noise.

The fit for the first event is displayed in (Fig. 3.8), using model #4. The smoothed signal and noise spectra are displayed with continuous, thin lines. The specific data points that were used for the inversion are shown with circles. These have been derived after resampling the spectra at equidistant frequencies in the log-scale, to a maximum of 128 points. The shades correspond to the final spectral weight function, $w(f)$ (Fig. 3.5; black line), which incorporates both $SNR(f)$ and the $1/f$ modification. As a result, the frequencies above 10Hz have significantly less weight than the ranges 0.5-0.8Hz and 2-10Hz. Also, many of the "details" of the spectrum at the higher frequencies, which have already been reduced due to smoothing, are ignored by the resampled data points. The theoretical spectrum curve (bold red line) is such that it passes through the data points in a least-squares sense at the log-scale, due to the modified formula of Eq. 3.12. This is different than the depiction of the theoretical spectra in Figs 3.1 (dashed orange line) and 3.2, which resemble

envelopes passing through the local maxima of the Sinc spectra. This may cause a systematic bias, leading to slightly underestimated M_o. Note that no SRF correction has been applied in this test. In the second example (Fig. 3.9), there is a different distribution of weights, as the low frequency data points are in fact below the noise level after the subtraction of noise from the signal spectrum. This effectively nullifies their weight, hence the white colour of the respective data points.

The M_o for an event is measured in all available stations and components, provided the SNR criteria are satisfied. Each fit provides a multivariate correlation coefficient, R^2, which can be used as the quality of the fit. The corresponding M_w can be derived by Eq. 3.2 using a weighted mean for $\log_{10}(M_o)$, after removal of bad fits (e.g. R^2<0.5) and the trimming of the extremes (one or two highest and lowest values) provided that enough measurements remain for a valid mean $\overline{M_w}$ calculation, weighted by R^2.

The residuals $M_R(f)=M_{obs}(f)- M_{calc}(f)$ of each fit are saved for the determination of the Site Response Function (SRF), along with the respective differences between the individual M_w calculated from each station/component's spectra and the weighted average $\overline{M_w}$ of the corresponding event. When the whole dataset has been processed, the $M_R(f)$ as well as the average difference between individual M_w and $\overline{M_w}$ are taken into account for the calculation of a systematic offset and the relative spectral variations (SRF) on each station/component per instrumental period (in case the instrumentation has changed during the recording of waveform data). Examples of SRF are

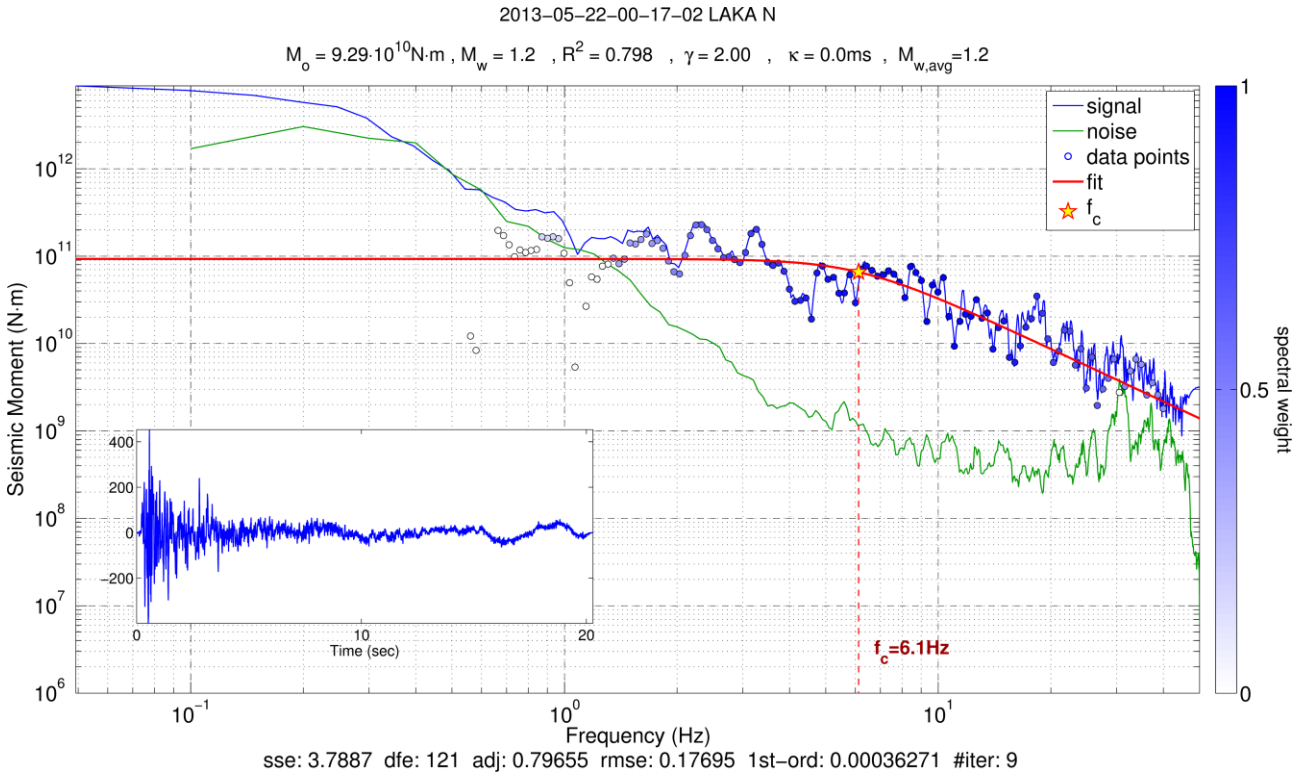

Figure 3.9: Same as Fig. 3.8 but for a smaller event with M_w=1.2 without SRF correction. Note the overlap between signal and noise at the lower frequencies and the respective decrease of spectral weight.

presented in Fig. 3.10 for different stations. LAKA and KLV are broad-band stations at average epicentral distances of ~10km and ~20km, respectively. The general impression of the SRF is that of a relatively smooth distribution around 0 (which represents unity, as the SRF are calculated on a log scale) at frequencies between ~2 and ~30Hz, slightly negative on the first part (up to ~8) and positive on the second half of this band while the residuals have a tendency towards positive values below 2Hz and especially below 0.5Hz. However, the latter is only estimated as an average, with large dispersion. On the contrary, the short-period station TEME (Fig. 3.10b), located within the epicentral area of the 2013 Helike swarm, exhibits stronger resonant frequencies and larger negative and positive offsets above ~2Hz. Also, the low frequency noise ramp is sharper and very intensely defined, with low dispersion. The latter, when the SRF is removed from the signal spectrum, has an effect similar to that of a high-pass filter, removing the trend and bringing the spectral shape closer to the theoretical one with the low frequency plateau. In Fig. 3.10, panels a-c have been rendered

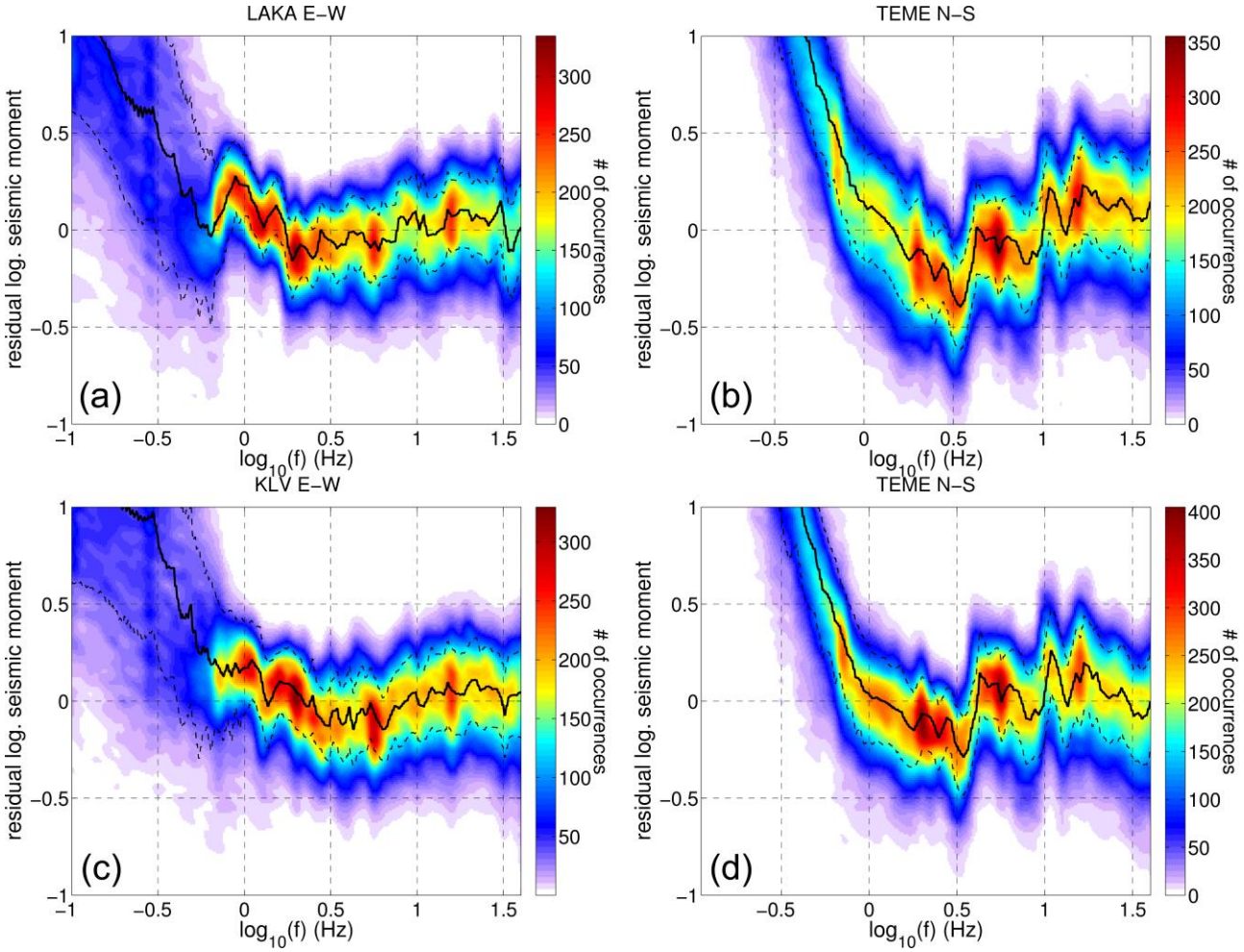

Figure 3.10: Site Response Function (SRF), or systematic spectral residuals between model and observed signal spectra for events of the 2013 Helike swarm dataset (Section 5A.4), using model #4 (Boatwright, 1978) a) for the broadband station LAKA, at average epicentral distance $\Delta \approx 10$km, b) for the short-period station TEME, located within the aftershock zone, c) for station KLV, at $\Delta \approx 20$km and d) same as (b) but using model #7.

by accumulation of spectral residuals between the observed spectra and the least squares fit of model #4. Fig. 3.10d is the same as Fig. 3.10b but using the more flexible model #7, which also happens to have, most of the time, the highest correlation coefficient compared to the other models. In this case, the shape of the SRF is similar, as far as the resonant frequencies are concerned, but the offsets are smaller, that is the residuals are closer to zero for frequencies above ~2Hz than those of model #4. Other than that, the low-frequency ramp is still strong, especially below 1Hz.

After the determination of SRF, the data are reprocessed and the SRF is removed from the signal's spectrum. This can cause changes that may affect the weighting function, $w(f)$, especially for events with low $SNR(f)$ in important frequency bands. The ($\overline{M_w}$-M_w) offset correction can be applied after the determination of the new fit. This should reduce the variance between individual measurements and the weighted mean in a relative sense, so that each station/component provides a result that is closer to the one determined by the network as an average. Together, the SRF and ($\overline{M_w}$-M_w) can be considered as the S_S factor of Eq. 3.10, but they also account for other sorts of unforeseen systematic errors, e.g. due to problematic components or incorrect instrument responses or sensitivities. An example of the difference between spectra before and after the application of the SRF on a small event can be seen in Fig. 3B.3.

Fig. 3.11a shows a test using all 7 models of Table 3.1, with parameters allowed to vary within the bounds defined in Table 3.2 on the same spectrum as in Fig. 3.8, but after the application of SRF correction. It appears that all models correctly determine the M_o and, more importantly, the M_w with differences of the order of ±0.1. Furthermore, the f_c, which is the second more important parameter of the fit, is relatively well constrained in all models, or at least its mean value, within a range of about ±0.4Hz. A similar result is derived for other, smaller events in Fig. 3.11b and Fig. 3B.4. However, this is not always the case, as the example of Fig. 3B.5 shows, where much different f_c values are determined for each model. In all these examples, the more flexible model #7, which also allows n to vary, is the best preferred one in terms of R^2. The difference in its spectral shape for n=3 is more clearly demonstrated in Fig. 3B.5b, where its f_c is also the best visual match for the corner of the spectrum. However, in Fig. 3B.5a, the f_c has taken its maximum allowed value of 30Hz, while e.g. models #4 and #6 suggest a value closer to the visually distinguished spectral corner around 11-12Hz.

In reality, in both cases these values are likely underdetermined for an earthquake with M_w≈1.2. Godano *et al.* (2015) specifically studied the problem of the determination of f_c for multiplets by calculating the spectral ratio of repeating earthquakes, thus removing all common factors such as site effects, path attenuation and radiation pattern, leaving out only the size of the source, primarily dependent on the f_c of each earthquake, and the amplitude ratio, which is suggestive of the difference in magnitudes between a couple of repeating earthquakes (also see Section 4.4.4 for a method of relative magnitude determination). They then perform an inversion to determine the two f_c parameters using a Bayesian approach. Estimating f_c without removing the effect of attenuation could be problematic due to a trade-off between κ and f_c. For example, Anderson (1986) noted a tendency for underestimation of the f_c by a factor of 2 for κ=0.01s and M_w≤2.5 while a value of κ=0.10s could cause the same degree of underestimation for even larger magnitudes, M_w≤4.0. Godano *et al.* (2015) remark another sort of saturation in its values for small magnitudes due to limitations set by the sampling rate itself: at 125sps rate / Nyquist frequency at f_n=62.5Hz, the f_c will

always be underdetermined for earthquakes with $M_o \leq 2 \cdot 10^{11}$N·m, or $M_w \leq 1.5$, resulting in overestimation of rupture length and underestimation of the stress drop. In many theoretical models, the stress drop, $\Delta\sigma$, is assumed to be roughly independent of the magnitude of an earthquake due to the slip being proportional to the fault length (Stein & Wysession, 2003). This is in fact a scaling law which implies that fault rupture is a self-similar process, a result of the same physical mechanism acting at all scales. For example, in the circular fault model (Brune, 1970; Madariaga,

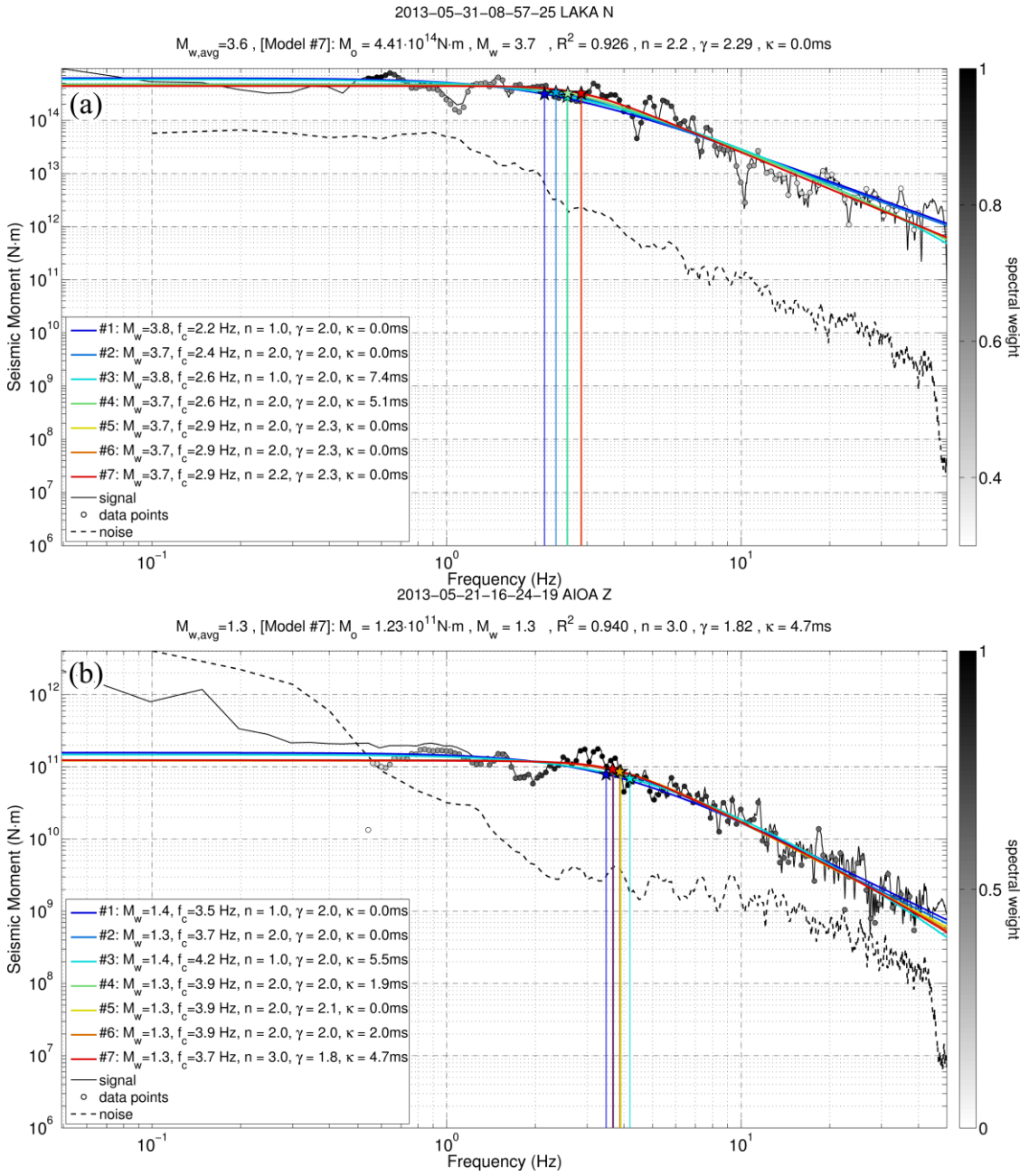

Figure 3.11: Spectral fit of multiple models (Table 3.1) on a) an M_w=3.7 event recorded at the broadband station LAKA, b) an M_w=1.3 event recorded at the short-period station AIOA. Both signal spectra have been corrected by SRF. The fit parameters are displayed in the legend. The parameters of the model with the largest correlation coefficient, R^2 are shown on top.

1976), which is usually considered for small earthquakes where the source's dimensions are very limited, the relation between M_o and the rupture radius, r, is:

$$\Delta\sigma = \frac{7M_o}{16r^3} \tag{3.13}$$

where $\Delta\sigma$ is typically in the range of 0.1 to 100 MPa (or 1-1000 bar). Since $r \approx \upsilon_r \cdot \tau_r \approx 0.8\beta/(\pi f_c)$, it follows that $M_o \sim f_c^{-3}$. However, deviations from self-similarity may result in $M_o \sim f_c^{-(3+\varepsilon)}$, where $\varepsilon \leq 1$ a scaling parameter (Kanamori & Rivera, 2004). This effectively produces larger $\Delta\sigma$ for events of larger magnitude than for the smaller ones when $\varepsilon > 0$. In any case, Eq. 3.13 provides a valid range for the expected distribution of M_o and f_c, depending on the assumed values for $\Delta\sigma$. Fig. 3.12 shows an example of M_o relative to the f_c parameter, as determined by the non-linear inversion using model #3 (Brune, 1970), calculated using waveforms of station TEME for the 2013 Helike swarm dataset. While f_c apparently decreases with increasing $M_o \sim f_c^{-(3+\varepsilon)}$, where $\varepsilon = 0.36$, however, the distribution is only partially surpassing the $\Delta\sigma = 0.01$MPa level. This indicates either a very low stress drop, which is considered unlikely, or a systematic underestimation of the f_c by about half an order of magnitude, as, indicatively, events with $M_w < 2$ (or $M_o < 1.26 \cdot 10^{12}$N·m) are expected to have f_c of the order of tens of Hz (e.g. Abercrombie, 1995; Godano *et al.*, 2015), rather than $f_c < 10$Hz. The distribution of $M_o(f_c)$ deviates even more in some of the models. This suggests that while the inversion procedure described in Section 3.2.2 is capable of measuring M_o and M_w even for events with low SNR, the other parameters remain elusive. Spectral ratio methods using repeating earthquakes (e.g. Godano *et al.*, 2015), with the waveform of one event acting as an empirical Green's function for the other, or even simply nearby events (e.g. Ide *et al.*, 2003), given that the inversion works on the general trend of the spectral ratio, are probably the only stable way for the determination of realistic f_c values for small events.

On the other hand, the $\log_{10}(M_o)$ measurement appears to be more stable. However, under certain conditions M_o could be overestimated due to noise at the lower frequencies. The spectral weighting function, $w(f)$, strongly counteracts this problem on the fit. Still, some spurious M_o measurements may be found, especially before the SRF correction (e.g. Fig. 3B.6a). To further improve the stability of M_o, independently of the choice of model, an average M_o value can be estimated in a frequency range where the spectral plateau is more likely to be found. In this study, the 0.1-5.0 Hz band was selected for the determination of $M_{w,avg}$, a weighted average moment magnitude derived using the $w(f)$ weights for the respective data points. Including higher frequencies could reduce the $M_{w,avg}$ while lower frequencies could raise its value. With the corresponding $M_{o,avg}$ as a middle point, the range of M_o could be restricted within a limited zone around this value, e.g. $M_{w,avg} \pm 0.5$. In most cases, this limit is not required, as the resulting M_o from the inversion could be identical whether M_o was allowed to vary in the range of Table 3.2 or restricted around $M_{w,avg}$. However, in certain cases such as for small events with low SNR, recorded at short-period instruments, this restriction actually helps constrain M_o to lower values, so that it is not affected by the noise ramp at low frequencies (Fig. 3B.6). This can happen if for some reason the $w(f)$ is strong due to high

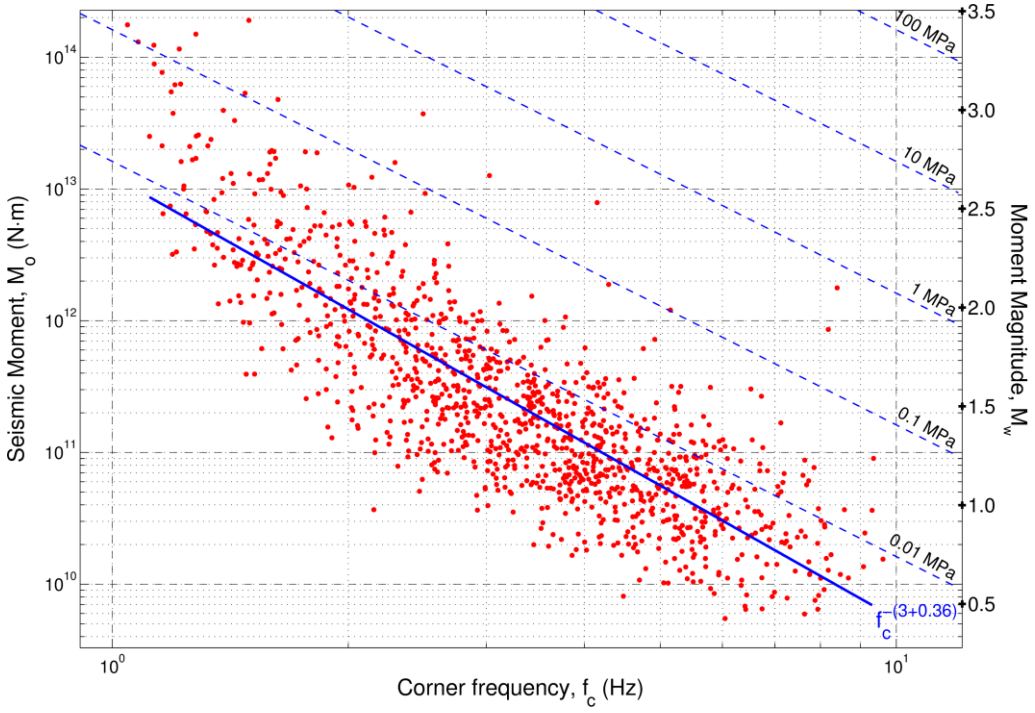

Figure 3.12: Relation between M_o and f_c for measurements of the 2013 Helike swarm on station TEME, using model #3 (Brune, 1970). A series of f^3 lines for typical values of constant stress drop, $\Delta\sigma$, are also displayed for reference.

SNR(*f*) at low frequencies, despite these values not representing actual signal amplitude. Optionally, this problem could be overcome by the application of a high-pass filter prior to the fit (e.g. Kapetanidis *et al.*, 2015), but this action could also alter the real plateau of larger earthquakes.

The relation between $M_{w,avg}$, as derived from the weighted average in the 0.1-5.0Hz band and $M_{w,fit}$ of the inversion for a single station/component (TEME, E-W) is presented in Fig. 3.13. Its characteristic is that $M_{w,fit}$ generally takes higher values than $M_{w,avg}$, with the exception of very low magnitudes. The "capped" solutions can be clearly seen in Fig. 3.13c. Both signal amplitude and *w*(*f*) are altered after the SRF correction, which also makes the $M_{w,avg}$±0.5 less significant (Figs 3.13b and 3.13d). In that case, the bias is almost constantly positive for $M_{w,fit}$ with respect to $M_{w,avg}$, while the capped measurements do not experience any more clipping at the $M_{w,avg}$+0.5 limit, at least at this station/component and, more importantly, with this specific model. The same example with model #7 has a much stronger dispersion which is reduced by stull remains after the SRF correction and the solutions are still capped at the $M_{w,avg}$+0.5 level. Even so, interestingly, the results at the higher magnitudes ($M_{w,avg}$≥3.0) are very similar in both cases after the SRF correction even with model #7. The differences are also, in general, less significant in broad-band stations, where clipping could rarely occur. However the pattern differences between the SRF-corrected capped and uncapped versions is similar to the short-period ones. A similar method is proposed by Godano *et al.* (2015) who measure $M_{w,avg}$ in the band 1-5Hz when the respective mean *SNR*(*f*) is >2, otherwise they use a wider frequency range 1-10Hz to avoid spurious M_o values. Fig. 3B.7 shows a comparison between the average (trimmed, weighted mean) M_w determined for all stations with the respective $M_{w,fit}$ from the spectral fit of a station/component (AIOA, N-S). Apparently, the capped

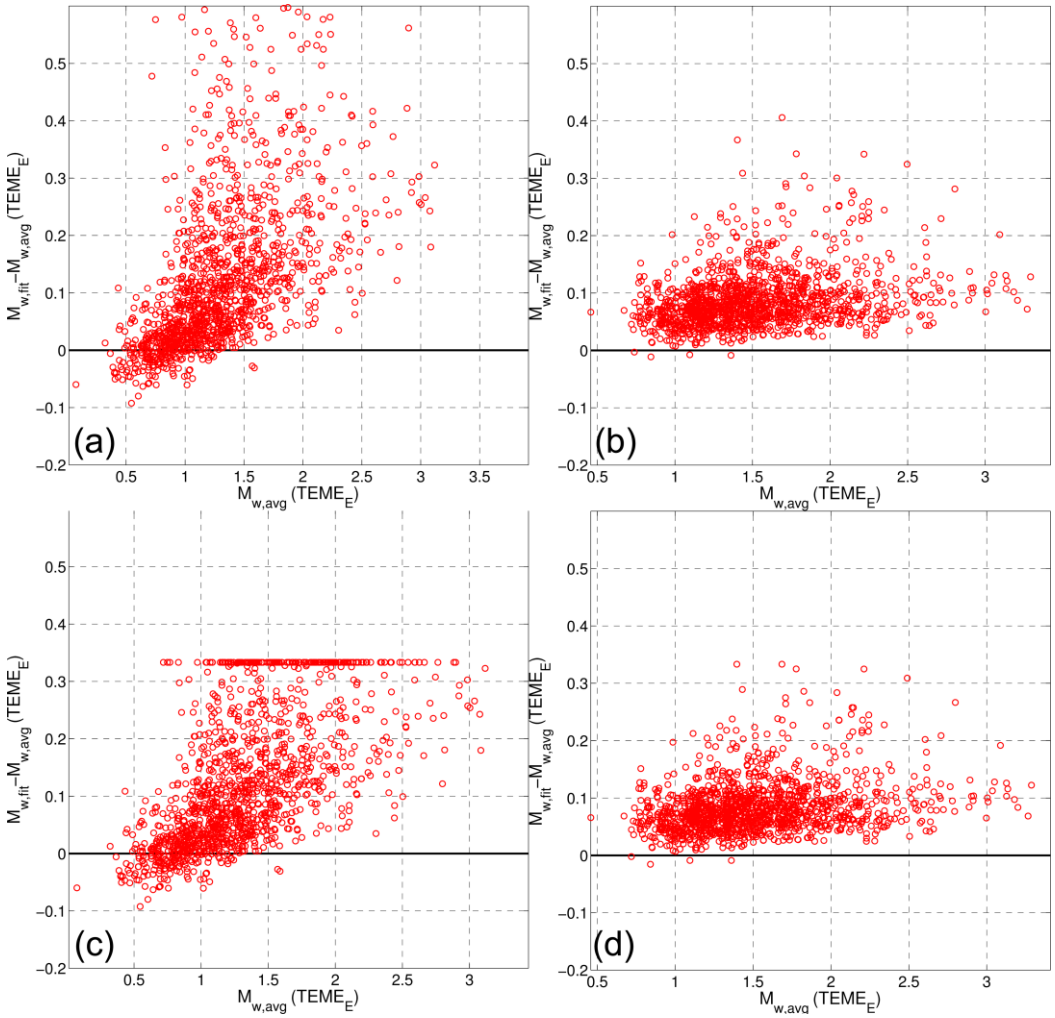

Figure 3.13: Differences between M_w derived by spectral fit and the respective average $M_{w,avg}$, in the band 0.1-5.0Hz, on the E-W component of station TEME for the dataset of the 2013 Helike swarm using model #4, a-b) with M_o free to vary according to Table 3.2, c-d) with M_o restricted within $M_{w,avg}$±0.5, before (a,c) and after the correction for the average M_w offset and the SRF (b,d).

M_o fits (lower panels) provide generally smaller mean difference from the final M_w solutions derived from all stations than the uncapped M_o fits (upper panels) and smaller dispersion, while the same is true for the SRF corrected versions (right panels) with respect to the uncorrected ones (left panels). These differences can be smaller in some stations, especially in broad-band stations where $M_{w,avg}$±0.5 capping does not play such a major role.

Fig. 3.14 shows a comparison of the trimmed weighted mean M_w as determined for all stations under different set of rules with respect to M_o-capping and SRF correction. This shows that, on average, without SRF correction the difference between capped and uncapped versions are negligible (Fig. 3.14a). The same is true for the M_o-capped version with or without SRF correction (Fig. 3.14d), with only a small deviation at the lower magnitudes where the SRF-corrected version tends to result in relatively larger magnitudes (by ~0.1). This is slightly counter-intuitive, as the SRF-correction would be expected to result in even lower magnitudes by lowering the noise level at low frequencies. However, as can be seen in the SRF plots (Fig. 3.10), besides the very low

frequencies where the corrected amplitudes are indeed reduced, there is a middle band where the residual is a bit negative, hence the signal should be amplified. This corresponds to a band where the *SNR*(*f*) is usually significant, which also further raises the respective weights, causing an overall increase in the resulting M_o value (e.g. Fig. 3B.3). On the other hand, the SRF correction has great impact on the uncapped-M_o version (Fig. 3.14c), with an offset of about +0.3 with respect to the non-corrected (for SRF and mean M_w residual) magnitudes while the residual's shape otherwise roughly resembles Fig. 3.14d. This offset by 0.3 is better presented in Fig. 3.14b for the difference between M_o-capped and uncapped versions of Mw with SRF-corrected spectra. As far as the various

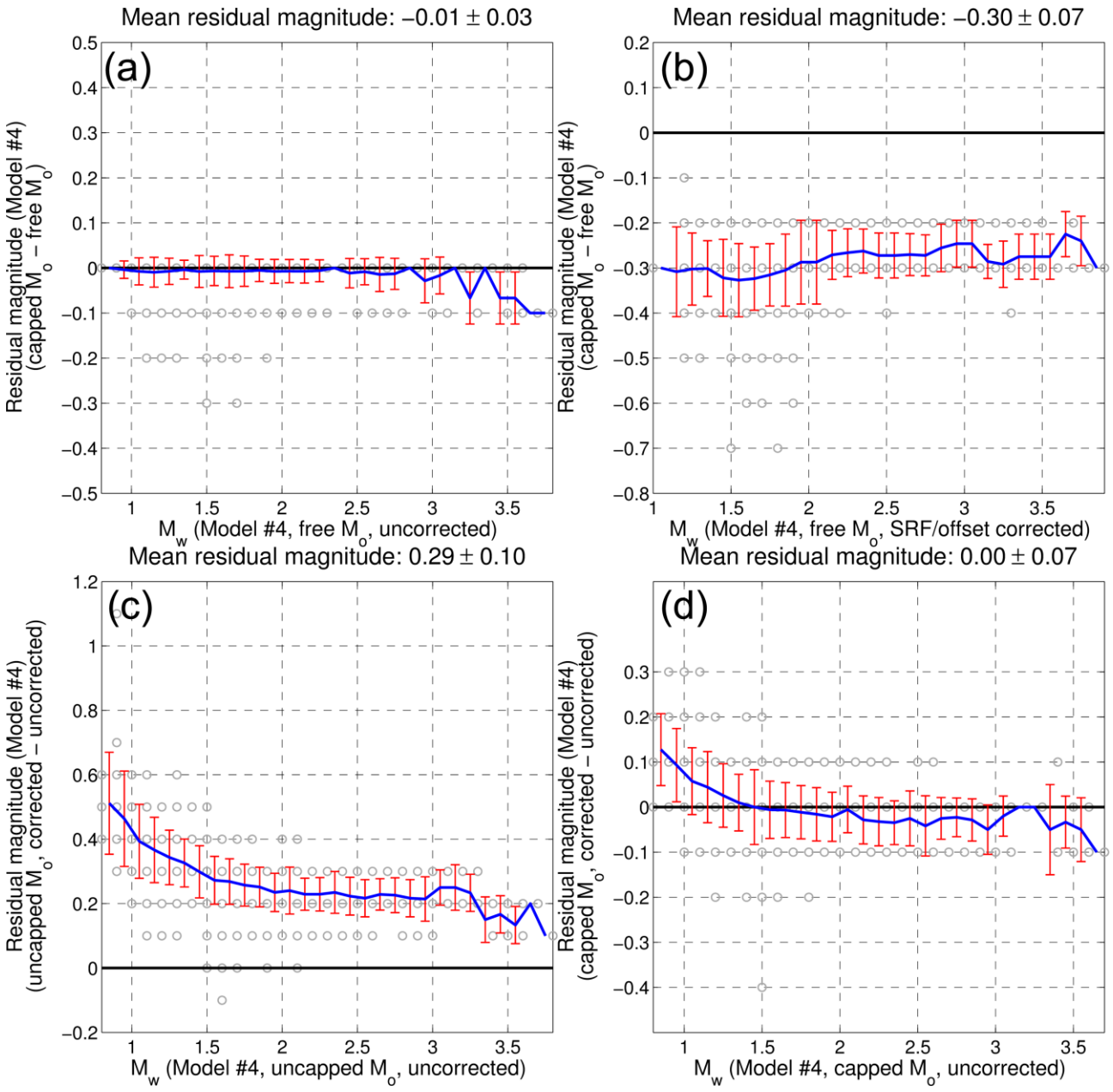

Figure 3.14: Differences between the trimmed, weighted means M_w derived using model #4 for the dataset of the 2013 Helike swarm, a) between capped M_o (restricted within $M_{w,avg}$±0.5) and uncapped M_o (ranging according to Table 3.2) without offset/SRF correction, b) same as (a) but after offset/SRF corrections, c) between corrected and uncorrected (SRF) M_w for uncapped M_o and d) same as (c) but for capped M_o.

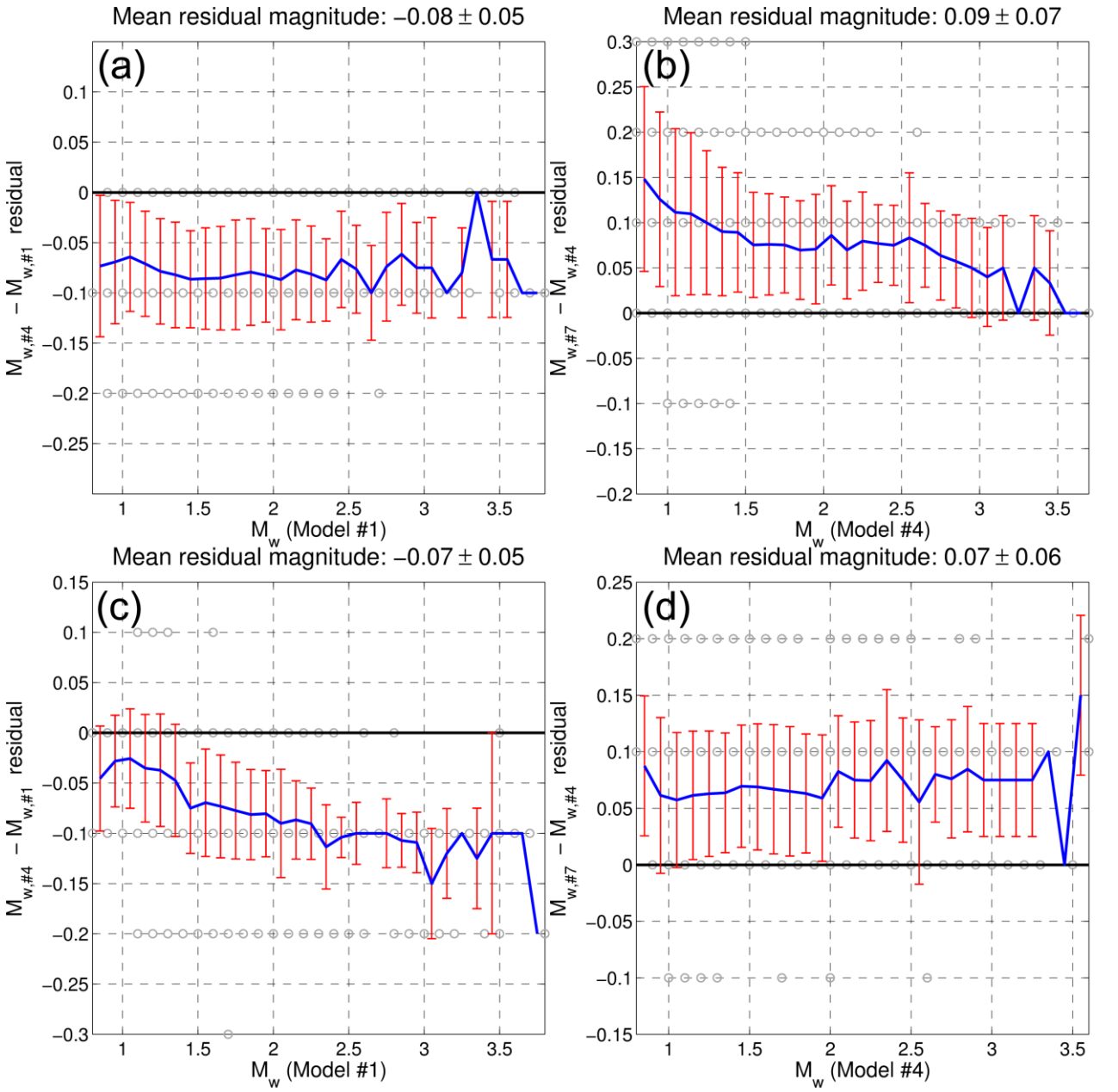

Figure 3.15: Differences between the trimmed, weighted means M_w for the dataset of the 2013 Helike swarm between a,c) models #1 and #4, b,d) models #4 and #7 for a-b) uncorrected spectra and c-d) spectra corrected for offset and SRF. In all cases M_o was allowed to vary within the $M_{w,avg}$±0.5 bounds.

models of Table 3.1 are concerned, with respect to the resulting final M_w (trimmed weighted mean from all available stations/components), Fig. 3.15 shows a comparison between #1 and #4 as well as #4 and #7 before and after the SRF correction. The differences are very small; they do not surpass 0.1. This result is independent of M_o-capping, despite the large deviation of M_o values for small events in some short-period stations or even more flexible models such as #7 if M_o is allowed to vary freely. The SRF correction manages to reduce this sort of dispersion while the average M_w offset correction reduces the variation of M_w between different stations/components. In the applications of Chapters 5 and 6, where M_w calculations by spectral fit were required, the M_o-capped version of Model #4, in combination with the SRF and average offset corrections, was

preferred and used by default, as it provided less spurious measurements and M_o values closer to those indicated by $M_{w,avg}$.

Lastly, the results of the method described in this study is compared with the similar technique that was applied in the study of Kapetanidis *et al.* (2015), using the algorithm of Matrullo *et al.* (2013), which utilizes the Brune (1970) source model (#3). The main differences is that in the latter a smaller signal window is used (5 sec), the signals are band-pass filtered between 0.5-50Hz (for broad-band sensors) or 1-50Hz (for short-period sensors) and the inversion takes place in the band 0.5-40Hz. *SNR*(*f*) is taken into account as a weighting function but without the 1/*f* correction, while a combination of the available components provides an extra spectral amplitude for fitting. The comparison between the two methods provides significantly similar results, with differences of the order of 0.05 to 0.1, depending on the model (Fig. 3.15a-c). On the other hand, a comparison between the results of either methods for M_w and the respective local magnitude, $M_{L,NOA}$ for the 2013 Helike swarm dataset, acquired from the GI-NOA public database, presents a significant bias (Fig. 3.15d) of a linear form with respect to the magnitude between 1.0 and 3.5 (also Fig. 3B.9, red line):

$$M_w=0.83\cdot M_L+0.60 \quad (3.14)$$

Or a quadratic polynomial form (Fig. 3B.9, blue line), also taking into account lower M_L values ($M_L<1$):

$$M_w=0.05\cdot M_L^2+0.56\cdot M_L+0.89 \quad (3.15)$$

which is very similar to a relevant relation of Grünthal *et al.* (2009) for earthquakes of Central Europe. Apparently, the M_w measurements from the inversion of the spectra are larger than the M_L values, with the offset being small at the larger magnitudes but increasing linearly up to ~0.5 for the smaller magnitudes. A similar observation was made by Matrullo *et al.* (2013) for earthquakes in the wider region of the western Corinth Rift, with a scaling relation of the form:

$$M_w=0.40\cdot M_L+1.03 \quad (3.16)$$

Edwards *et al.* (2010) also noted this type of deviation between seismic moment and local magnitude and derived a polynomial relation between them. It could be supposed that this difference is due to the M_L depending on simple peak-to-peak amplitude measurements in the time-domain which could possibly be contaminated by low frequency noise after integration, especially at the lower magnitudes. However, there are inherent reasons which implicate a degree of non-self-similarity of the seismic sources or the complex interaction between the Wood-Anderson filter, f_c and f_{max} (a cut-off high frequency in the acceleration spectra) with the deviation from 1:1 scaling between M_w and M_L that should be described by a polynomial relation (Edwards *et al.* 2010 and references therein). The calculation of M_w by spectral analysis is considered a more reliable method for the measurement of magnitude, as it uses a large number of samples, does not involve a Wood-Anderson filter and takes into account the noise spectrum and the respective *SNR*(*f*). Problems mostly caused by the noise level at low frequencies and low SNR can be surpassed using the methodology described in the present section.

Chapter 4

Automatic event detection and location methods

Introduction

The increasing amount of waveform data from seismological stations that is available in the recent years has made imperative the development of algorithms and methodologies to handle the utilizable information. Real-time earthquake monitoring systems such as Earthworm or SeisComP3 (Olivieri & Clinton, 2012) provide rapid estimations of the basic seismic source parameters for a large number of events, while Virtual Seismologist (Cua & Heaton, 2007) and other Early Warning Systems (Horiuchi *et al.*, 2009; Satriano *et al.*, 2011; Given *et al.*, 2014) are mainly targeted on the major earthquakes which can cause damage and fatalities, especially when their epicenter is close to densely populated areas. Manual analysis of earthquake signals is time consuming, but can provide high-quality results for a representative sample of events in a sequence. Automatic algorithms can reduce the amount of required manual work that has to be done in order to acquire a draft catalogue from real-time or archived raw waveform data.

Given the known coordinates of the seismological stations and the frequency response of their equipment, the waveforms are scanned for anomalies, which may indicate the arrival of a seismic wave, in their amplitude, spectral content or other parameters that are expressed in the form of Characteristic Functions (CF), and attempt to pick the onset time. Automatic picking algorithms include the classic Allen-picker (Allen, 1982), the CF of Baer & Kradolfer (1987), the "Short-Term Average / Long-Term Average" (STA/LTA) CF (Earle & Shearer, 1994), algorithms for stationarity analysis using Auto-Regressive (AR) modeling (Leonard & Kennett, 1999; Sleeman & Eck, 1999; Nakamula *et al.*, 2007) or the Akaike Information Criterion (AIC) on the raw waveform (Akazawa, 2004; Wang *et al.*, 2006; Turino *et al.*, 2010) or over other CF (Zhang *et al.*, 2003; Küperkoch *et al.*, 2010), high-order statistics such as skewness and kurtosis (Saragiotis *et al.*, 2002; Küperkoch *et al.*, 2010; Baillard *et al.*, 2014; Langet *et al.*, 2014), time-frequency analysis (Tselentis *et al.*, 2012) and parameters concerning the polarization of particle motion, such as directivity, planarity or rectilinearity, which can also be used to identify the type of the detected seismic phase (Sleeman & van Eck, 1999; Fedorenko *et al.*, 2008; Diehl *et al.*, 2009; Baillard *et al.*, 2014; Kurzon *et al.*, 2014). Other algorithms employ neural networks (Dai & MacBeth, 1995; Zhao & Takano, 1999; Gentili & Michelini, 2006), wavelet analysis (Sleeman & van Eck, 1999; Zhang *et al.*, 2003; Hafez *et al.*, 2010; Bogiatzis & Ishii, 2015), a manifold-based approach (Taylor *et al.*, 2011) or even fractal dimensions (Boschetti *et al.*, 1996) to automatically pick seismic wave arrivals.

The registered "triggers", which is a better term until they have been confirmed as arrival-times of seismic waves, are cross-checked between the stations of the network according to criteria which

may involve information of the medium's velocity structure from pre-calculated travel-time tables on a grid that contains the stations and the possible locations at various depths where hypocenters are expected to be located. If a sufficient number of picks are consistent with the respective travel-times, then a new event is declared and these arrivals are associated with (or "bound" to) it. The trigger-times are also checked for proximity to the expected (or theoretical, or calculated) arrival-times of an existing event's origin to which they can be associated, if they match, and the event's origin is updated/relocated. Examples of such algorithms are the "binder_ew" of Earthworm (Dietz, 2002; Friberg *et al.*, 2010) or the Global ASSociator (GLASS) which is an integral part of the Hydra system (Buland *et al.*, 2009). These procedures require a sufficient number of arrivals and relatively small travel-time residuals for an event to be located and for arrival-times to be associated with an origin. This in turn means that the picking algorithm must be able to identify the seismic wave arrivals successfully, which is usually a matter of strong Signal-to-Noise Ratio (SNR). While picking algorithms could, in principle, be able to pick a seismic wave arrival-time even under low SNR conditions, when an arrival is expected to be found within a limited window, in practice these expected arrival-times are unknown until at least a draft hypocentral location and origin time of an earthquake has already been determined. The sensitivity of such algorithms can be fine-tuned, e.g. to allow for low SNR or higher frequency arrivals to be picked. However, this will increase the amount of triggers that may be detected, which may or may not correspond to seismic wave arrivals, increasing the amount of false positives.

On the other hand, during intense seismic sequences, a station that is close to or within the epicentral area may record thousands of earthquakes in a single day, including a large number of low-magnitude events that will have very low SNR in further stations, which may render it undetectable or unresolvable. Even with sufficient SNR, waveforms of sequential earthquakes may superpose with one another, making even manual picking difficult without proper guides for the theoretical arrival-times of the seismic phases of each event. Also, the sheer number of generated events in aftershock sequences or swarms can be such that it poses practical problems in their fully manual analysis.

The completeness of a catalogue is usually quantified by the range between the magnitude of the strongest event and the magnitude of completeness, M_c: the low-magnitude margin for which the Gutenberg-Richter power law of the frequency-magnitude distribution holds true. For example, an $M_c = 5.6$ is quite acceptable for global seismicity in the more recent years (after 1964) or $6.2 \leq M_c \leq 7.5$ for the early instrumental era, with the largest earthquakes reaching over 9 magnitude units (Di Giacomo *et al.*, 2015), while for regional seismicity, e.g. in Greece, where the major earthquakes are usually $6.0 \leq M_w \leq 7.0$ and very rarely $M_w > 7.0$ (Makropoulos *et al.* 2012), a completeness of $2.0 \leq M_c \leq 2.5$ is deemed to be an important achievement (D'Alessandro *et al.*, 2011). On the other hand, in mining induced microseismicity, with major events of M≈3.0, the acceptable M_c can be of the order of $M_c = 0.0$ or even negative (e.g. Bischoff *et al.*, 2010) and, at the lowest extreme, acoustic emissions / picoseismicity, e.g. induced by mining activity or generated by dike propagation, in the range $-5.0 \leq M_w \leq -1.0$ (Kwiatek *et al.*, 2010; Plenkers *et al.*, 2011). The reduction of M_c for a particular region or seismic sequence, which can be accomplished after increasing detectability and resolvability by installing extra stations (e.g. a temporary network) or using techniques which can utilize additional information that is already available, typically leads to

a denser temporal distribution. This can also lead to denser spatial distribution when coupled with the reduction in relative location errors, which can be achieved by performing relocation, using, for example, the double-difference method (Waldhauser, 2001). The increased resolution can allow for a more detailed description of the spatiotemporal evolution of a sequence and detailed mapping of the activated structures. Reducing the M_c of a catalogue for a certain region and period requires an increase in the detectability of resolvable events. This may refer either to low-magnitude local (microseismic) events or to generally low-SNR signals at long epicentral distances.

The "Single-Station Detection" (SSD) is a method in which a single reference station can be used to detect and classify or locate a large number of earthquakes and other types of signals. (Ruud & Husebye, 1992; Agius & Galea, 2011). The simplest way to detect signals is an STA/LTA method or any of its varieties (Blandford, 1982; Sabbione & Velis, 2013; Havskov & Alguacil, 2014), but many of the other above-mentioned automatic picking methods can also be utilized for this purpose. An alternative for seismic signal detection is based on a technique called "correlation detector" (Schaff & Waldhauser, 2005) which can identify events with similar waveforms (thus, comparable seismic parameters, as described in Chapter 1) based on a "template" or "master" waveform. In the "correlation detector" technique, a sliding window that contains a strong signal (e.g. a P- or S-wave) of a known event is used as a template in search for a sufficiently similar part in a continuous waveform record on the same station and component. For each position of the sliding window the linear correlation coefficient between template and target waveform is calculated and the detections are made based on a threshold value, e.g. 0.80, that signifies high similarity between template and target. This method and other cross-correlation techniques can also be applied to re-pick arrival-times on a series of events (Rowe *et al.*, 2002; Eagar *et al.*, 2006; Okubo & Wolfe, 2008) or even pick new arrival-times on unresolved events (Kapetanidis & Papadimitriou, 2011) based on the picks made on the templates. Apart from SSD, seismic arrays can also detect and locate a great number of earthquakes in a wide range of epicentral distances, mainly depending on the aperture of the array, from local/regional to teleseismic distances (Gibbons & Ringdal, 2006; Wang *et al.*, 2006; Pirli *et al.*, 2007). Correlation detectors in a framework with seismic array data can significantly increase the detectability of signals with very low SNR, managing to lower the magnitude of completeness, M_c, by up to ~1.3 magnitude units compared to conventional signal detection methods (Gibbons & Ringdal, 2006; Junek *et al.*, 2014).

In this Chapter, two classic algorithms of automatic signal detection (STA/LTA) and phase-picking (AIC) are presented, along with two alternative methods of semi-automatic picking (MEm) and association of meta-data (HADAES) based on waveform similarity, specifically developed in the framework of the present study. These methods aim to enrich a seismological catalogue with additional data of strongly correlated microearthquakes, increasing the sample size in sparse datasets and, consequently, the resolution of the spatiotemporal distribution.

4.1 Signal Detection: The STA/LTA method

The simple STA/LTA algorithm is based on the detection of anomalies in the SNR. It measures the "background noise" level in a long window and the "signal" level in a sufficiently short window so that it is sensitive enough to incoming pulses of arriving seismic waves. It works on the time-series of a characteristic function that represents the current "energy level". A seismic waveform has to be properly filtered, so that long period trends are removed as well as any existing high frequency noise before the STA/LTA procedure takes place. Data gaps must also be smoothed-out (e.g. Appendix 4A), otherwise they may cause abrupt spikes which could generate false positives.

The complex "analytic signal" function (Fig. 4.1), $S(t)$, is defined by the formulae of Eqs 4.1 and 4.2 (Kanasewich, 1981):

$$S(t) = f(t) + i \cdot f_H(t) = E(t) \cdot e^{i \cdot \Phi(t)} \tag{4.1}$$

$$E^p(t) = \sqrt{f^2(t) + f_H^2(t)}^p \tag{4.2}$$

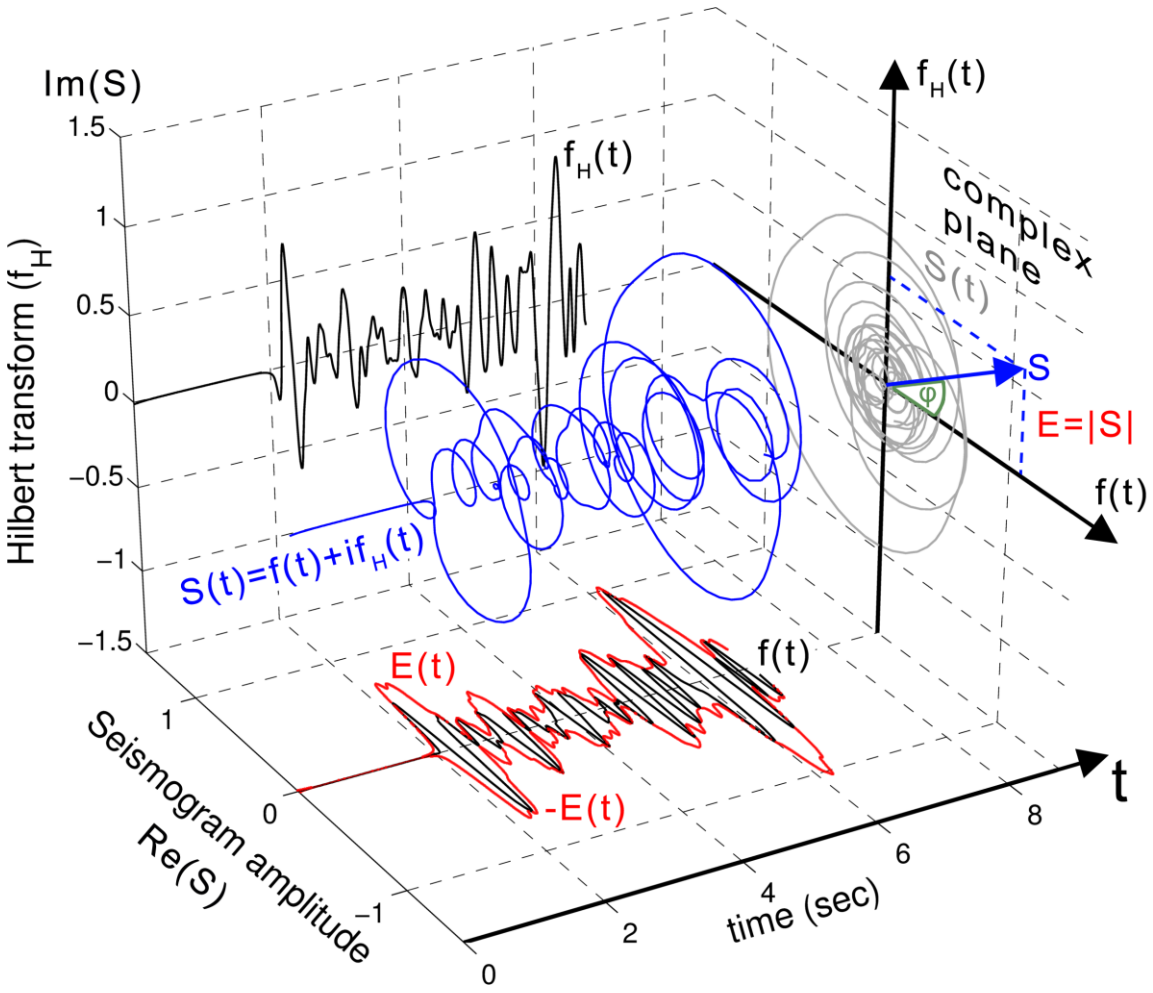

Figure 4.1: 3D representation of the complex Analytic Signal, $S(t)$, the Hilbert transform, $f_H(t)$, the envelope, $E(t)$, and the instantaneous phase, $\varphi(t)$, of a real (normalized) seismogram, $f(t)$ (see Eq. 4.1 and 4.2).

where $f(t)$ is the filtered seismogram and $f_H(t)$ the discrete-time analytic Hilbert transform of $f(t)$ (a quadrature function, having a phase-difference of $\pi/2$ with the original waveform). The amplitude, $E(t)$ (Eq. 4.2), in the exponential form of $S(t)$, at the right-hand of Eq. 4.1, is the envelope of the seismogram (shown with red line in the $f(t)$ projection at the bottom plane of Fig. 4.1), which provides an estimate of the energy level and can be used as a characteristic function (Earle & Shearer, 1994). The angle $\Phi(t)$ is called "instantaneous phase" and its usefulness will be presented in Section 4.4.5. The contrast between low and high energy levels can be amplified, if necessary, by raising $E(t)$ to a positive power $p>1$.

The STA/LTA window lengths (with typical values ~0.5 and ~10 sec, respectively, for applications concerning local micro-earthquakes) may be adjusted according to the mean epicentral distance from the reference station. The STA window is preferably attached without overlap to the end of the LTA window (Fig. 4.2), to increase sensitivity of detection for wave onsets. In simple STA/LTA procedures, two ratio (R) thresholds are usually defined, one for the initiation of a trigger (e.g. R_1=3), marking the signal onset at an approximate arrival-time t_1, and another to mark the end of the signal (e.g. R_2=1.75<R_1). However, during intense sequences this can lead to an overwhelming number of triggers, which makes necessary the selection of valid triggers according to some strict criteria.

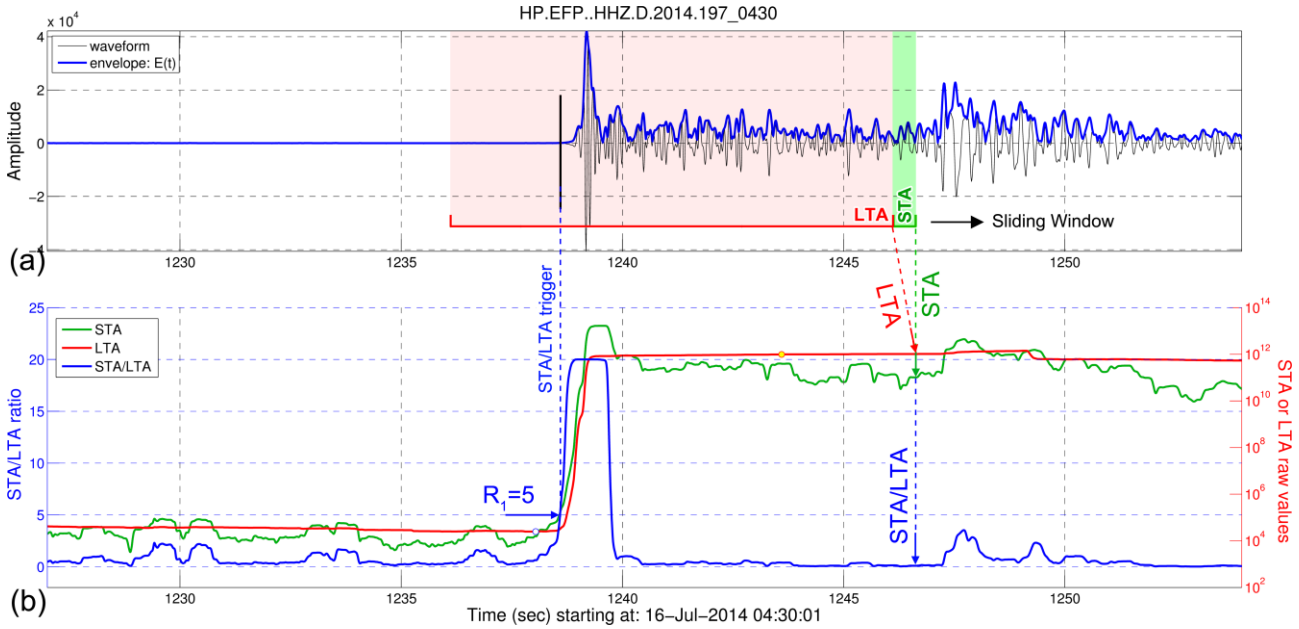

Figure 4.2: The *STA*/*LTA* signal detection method. a) The configuration of STA (green, 0.5 sec length) and LTA (red, 10 sec length) windows, sliding along the time-axis of a seismic waveform. b) the *STA* (green), *LTA* (red) and *STA*/*LTA* (blue: left vertical axis) values, measured on the E^3(t) envelope with p=3 (Eq. 4.2). The *STA* and *LTA* values are depicted on the right vertical axis (log scale). The time to which each measurement is attributed corresponds to the last sample (the "rightmost") of the STA-window. The blue vertical marker in panel (a) corresponds to the time that the *STA*/*LTA* ratio surpasses the on-trigger threshold, R_1≡5.

In applications such as the HADAES method (Section 4.4), the following modification of the STA/LTA procedure is used for the detection of signals, which is demonstrated in the example of Fig. 4.3. Note that the referred values were used for the application of Section 5.4 (Appendix 5B) and therefore are only typical. Different parameterization might be better suited for other applications. The 24-hour waveform is divided in 30-min buffers which are band-pass filtered between 2 and 15 Hz. There is a partial overlap between buffers to allow for the LTA window to obtain average background level at the beginning. The envelope of the filtered waveform, $E(t)$, is calculated using Eq. 4.2 and then raised to the 3rd power (p=3) to increase the contrast between low and high amplitude values. The background noise level is determined as the standard deviation of the filtered waveform in consecutive 1-minute windows and the smallest individual value, σ, is considered, likely corresponding to a segment without any seismic signals or other high amplitude/variance disturbances. The "on-trigger" threshold is defined at R_1=5, a value that seems high but refers to the *STA*/*LTA* ratio on the characteristic function that is raised to the 3rd power rather than a simple SNR level. Since R tends to exhibit strong but short-lived spikes, $R_2 \equiv R_1$=5 is considered, and a trigger-time, T_{trig}, is defined at the first sample that surpasses R_1. A 2σ noise threshold is applied for each wave-buffer and the triggers corresponding to signals with maximum absolute amplitude below that level are rejected, unless their maximum R has surpassed an even higher threshold, R_3=10. Several other parameters are determined for each trigger, such as the

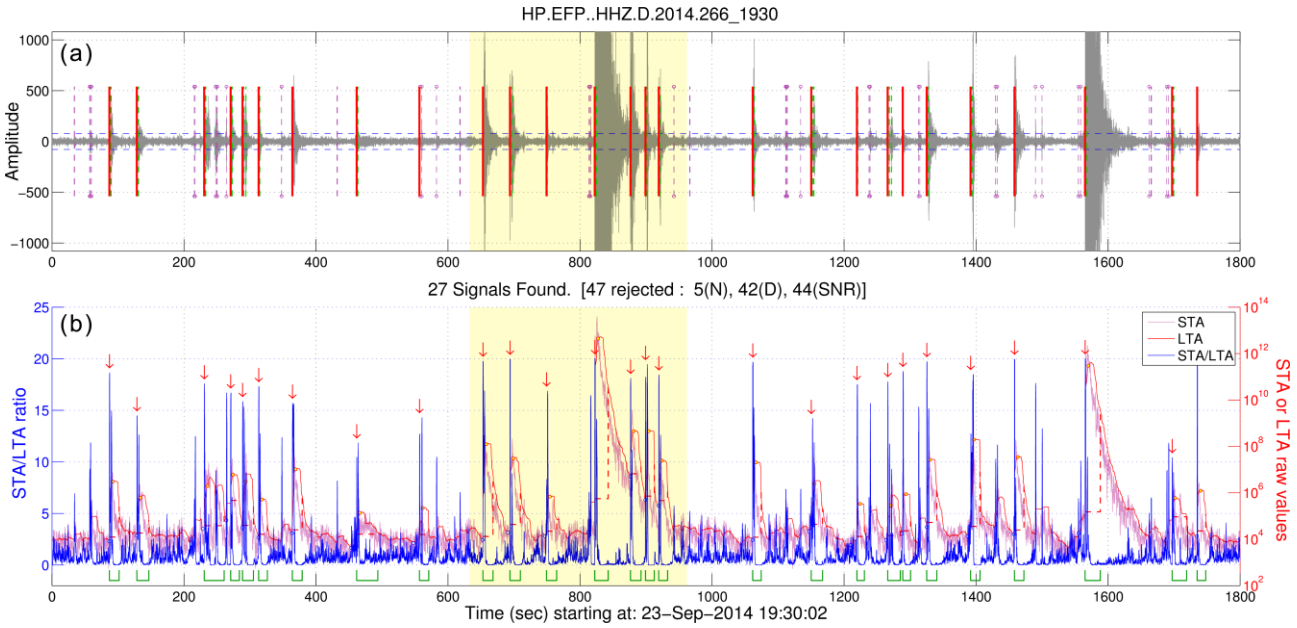

Figure 4.3: Example of event detection using the *STA*/*LTA* method. a) 30-min filtered waveform (grey) of the vertical recording of station EFP during 23 September 2014 (starting at 19:30 UTC). Markers show valid triggers (solid red), rejected triggers due to low amplitudes, the noise level (dashed purple: labeled "N") or with low LTA_{max}/LTA_{min} ratio, despite $R \geq 10$ (dashed purple with circles: labeled "SNR") and double triggers (dashed green: labeled "D"). b) The $R \equiv STA/LTA$ ratio (blue: left vertical axis, linear scale) along with the raw *STA* (light purple) and raw *LTA* values (red: right vertical axis, log scale) and typical signal durations (green brackets at the bottom). Red down-pointing arrows mark the valid triggers. The highlighted yellow area is presented in more detail in Fig. 4.4. *STA* and *LTA* values have been calculated on windows of 0.5 sec and 10 sec, respectively, on the characteristic function $E^3(t)$ (Eq. 4.2).

maximum value of R during the spike, the minimum (LTA_{min}) and maximum (LTA_{max}) values of LTA, 30 sec before and 5 sec after T_{trig}, respectively, are registered, along with their corresponding times. Another SNR threshold is considered, rejecting triggers with $\log_{10}(LTA_{max}/LTA_{min})<1.5$. This is usually a case when an event is superimposed on the coda of a strong one. This filter ensures a minimum strength of the smaller event with respect to the minimum value of the LTA shortly before the second trigger. Additional criteria can then be applied to detect possible double-triggers (e.g. P- and S-waves of the same event, or closely occurring "double" events, possibly with partially superimposing waveforms), by accepting only the trigger corresponding to the largest absolute amplitude in the characteristic function, when other triggers are found in a ±10sec window (Fig. 4.4). The remaining triggers are considered as "valid". A pulse duration is defined as the time between the trigger and the time when the $\log_{10}$(LTA) drops from its maximum value to its 80%, down to a minimum allowed duration of 5sec. The duration is also cropped before the onset of an incoming valid trigger. The final set of STA/LTA triggers can, optionally, be passed through a fast, single-component "AIC-picker" procedure (Section 4.2) which can adjust the trigger-time closer to the actual wave onset.

Besides from simple event detection, the STA/LTA method can also be used as an arrival-time picker. For clear onsets (with a high enough SNR) it can successfully pick a P-wave arrival, within a certain margin of error mainly dependent on the STA window length. However, it can also be used to detect the arrival of an S-wave. The main issue is that, especially at local epicentral distances, the S-wave is superimposed on the P-wave coda. The background level is already increased due to the P-wave-train which may have entered the LTA window, lowering the

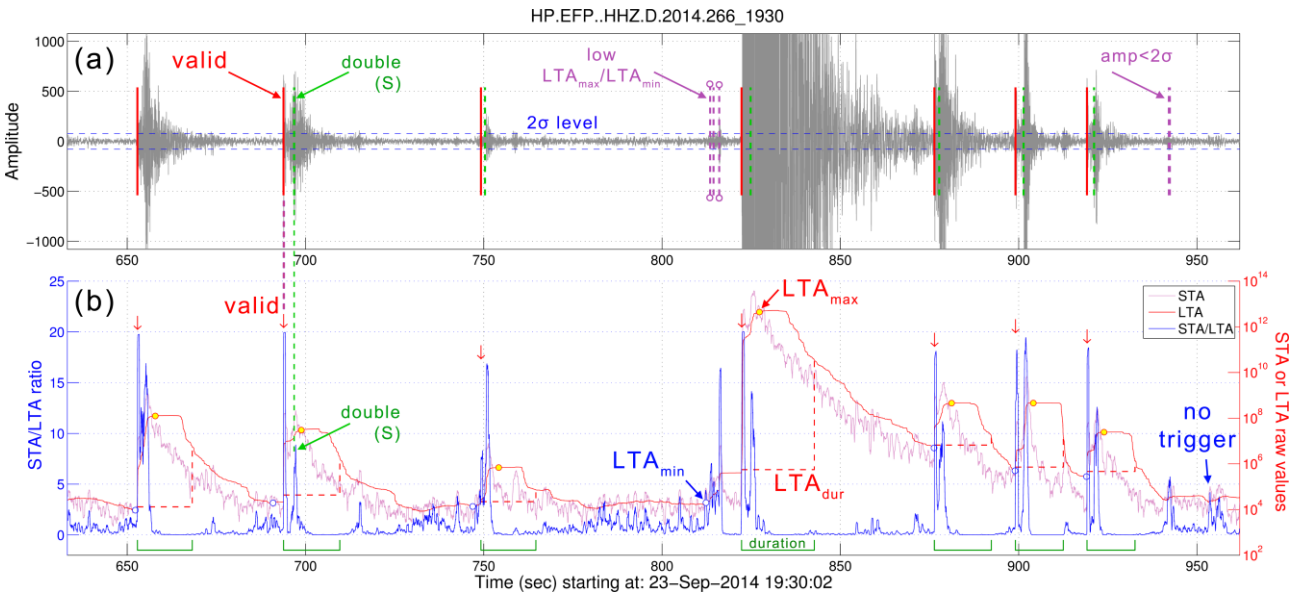

Figure 4.4: Zoom in highlighted area of the diagrams in Fig. 4.3.The double triggers are sometimes related to the arrival of S-waves. In panel (b), blue circles mark the LTA_{min} values during a short timespan before the LTA_{max} points (red circles). Dashed right angles on the LTA diagram start at the trigger point (where $STA/LTA \geq R_1 \equiv 5$) and up to where $\log_{10}(LTA)$ drops by 20% from its log10(LTA_{max}) value, unless, under certain conditions, the pulse duration is shortened (due to incoming valid triggers) or set to a minimum allowed value (see text for details).

STA/LTA ratio value. If however the STA/LTA is applied on a reversed time-axis, or, likewise, its sliding window runs backwards in time, with the STA window attached before the beginning of the LTA window, it can detect an abrupt decrease of the ratio (below unity or towards negative log values) when the STA window begins to include the, lower energy, P-wave-train right before the S-wave onset (e.g. Akazawa, 2004). However, there are more precise methods to successfully pick a wave onset, even with a relatively low SNR. Such a technique is explained in detail in the next section.

4.2 Automatic Picking: The AIC picker

The STA/LTA procedure is useful for signal detection, but its accuracy on the picking of seismic wave arrivals is mainly limited by the uncertainty introduced by the STA window length. The latter has to be wide enough to ensure stable measurements, especially if a rough CF such as the envelope of Eq. 4.2 is used, but the wider the window the less sensitive it is to small anomalies and the longer it takes for the STA/LTA ratio to overcome the triggering threshold, R_1. Other techniques have to be applied in order to increase the picking accuracy and reduce errors in the automatic location of hypocenters.

A widely used algorithm for automatic picking of arrival-times of seismic phases is the one based on the Auto-Regressive (AR) model (Sleeman & van Eck, 1999; Wang *et al.*, 2006; Nakamula *et al.*, 2007). The technique assumes that the two segments of a waveform record, one before and one after the arrival-time of a seismic phase, are locally stationary and can be described by two AR models with different coefficients. The Akaike Information Criterion (AIC) can be used for the identification of the optimal point which divides the two different AR processes and likely corresponds to the arrival-time of the seismic phase. An efficient formula for the direct calculation of the AIC function (Eq. 4.3) has been proposed by Maeda (1985), which bypasses the necessity for the estimation of AR order and coefficients:

$$AIC(k) = k \cdot \log\{\mathrm{var}(x[1,k])\} + (N-k-1)\log\{\mathrm{var}(x[k+1,N])\} \qquad (4.3)$$

where x represents the amplitude values of a (filtered) waveform segment with N samples, containing the onset of a seismic phase, with part of its wave-train, including noise before the arrival, and $k \in (1, N)$. The global minimum of AIC at $k = k_{\min}$ corresponds to the point that best divides the two AR models and potentially coincides with the arrival-time of the seismic phase. Waveform pre-processing for the enhancement of the onset before the application of the AIC-picker may include other modifications such as differentiation (Lomax *et al.*, 2012) or raising the amplitudes to the third power (Akazawa, 2004), which can be efficient for a more accurate detection of P-wave arrivals. Various filters can also be applied to account for different conditions of background noise, including coda-waves of previous arrivals, which may have contaminated the onset that needs to be detected. It is important that the filtered waveforms are properly normalized before the application of the AIC function, as its absolute values are derived by measurements of

variance, which is dependent on the absolute amplitudes of the time-series. Alternatively, the AIC values may require proper modification to account for differences in window lengths. An algorithm that takes advantage of multiple *AIC* measurements to estimate picking errors and reject picking on noise is described below.

The AIC function is more computationally intensive than the respective STA/LTA when applied to a simple window. This renders it too slow for use as a signal detector. It has to be applied

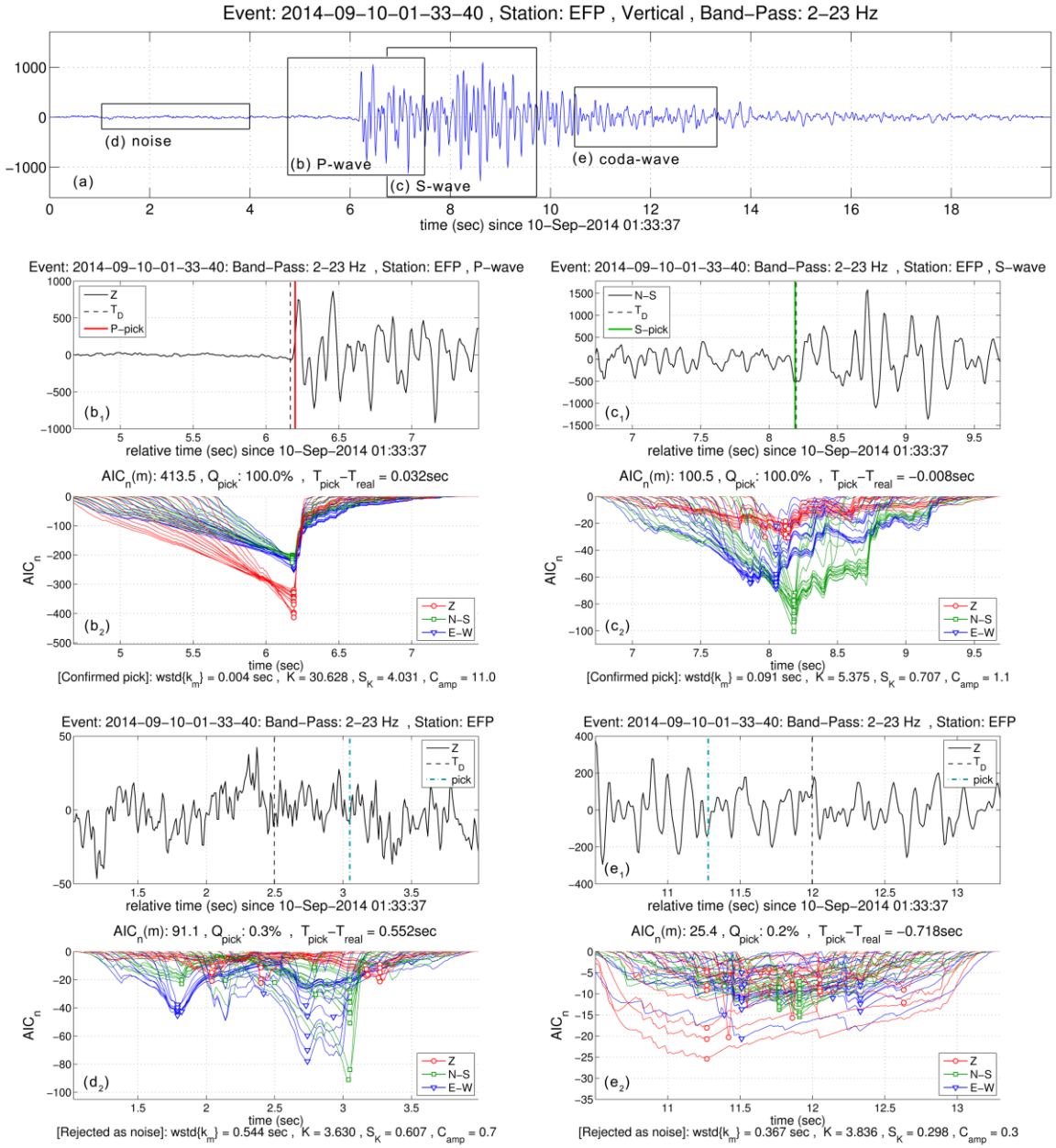

Figure 4.5: The AIC-picker. (a) vertical recording of a local earthquake recorded in station EFP. Rectangles marked b, c, d, and e refer to the targeted W_{max} windows (with a length of 3 sec) presented in the following panels, namely auto-pick on (b) a P-wave, (c) an S-wave (N-S component), (d) background noise and (e) S-wave coda. The upper sub-panels (b_1, c_1, d_1 and e_1) show a close-up of the W_{max} window with the manual and the automatic pick, while the lower sub-panels (b_2, c_2, d_2 and e_2) present the individual AIC_n curves, their global minima and the results of the preferred solutions.

selectively, on windows which are expected to contain a wave onset, such as a P- or S-wave. In the HADAES algorithm (Section 4.4), which employs the AIC-picker at its final stage, such preliminary estimates of P- or S-wave arrivals are called "dummy" arrival-times, T_D. The $AIC(k_{min})$ values are measured in windows of various sample lengths, N_i, containing the dummy arrival-time, T_D, by default at the center of the window. The length N_{max} of the largest window, W_{max}, is defined as the maximum tolerance allowed for the difference between the real onset and T_D and cannot be larger than the estimated difference between S- and P-wave arrival-times (or travel-times), T_{S-P}, or there will be risk of detecting the arrival of the wrong wave-type. In that case the windows' bounds have to be altered; otherwise the larger ones could contain both P and S onsets. The procedure is repeated in all the available components of a station and the maximum of each curve is subtracted, resulting in a set of *AIC* plots with negative-only values and, usually, a clear global minimum at the onset (Fig. 4.5).

A strong contrast between the two different AR models produces minima which become larger with increasing window length. Dividing by window length acts as a normalization of this effect. The original *AIC* curves are modified by subtraction of their maximum values, so that all their values become negative, divided by the total length of each window (in sec) and multiplied by a 15% cosine taper to remove edge artefacts. For events in local epicentral distances, the P-waves are usually more pronounced on the vertical rather than the horizontal components, while the opposite is true for the S-waves. For this reason, another modification is the amplification of *AIC* curves which correspond to the vertical component by 10% and reduction of the horizontal ones by the same amount in case the pick is intended for a P-wave onset, to reduce the chance of detection of the opposite wave-type. The reverse procedure is applied for the S-waves. The processed *AIC* curves according to the above-mentioned modifications are hereafter symbolized as AIC_n. The most negative of the minima usually corresponds to the window of maximum length, especially when the real onset is close to the center of the segments. The general idea is that the AIC_n curves of windows which contain a wave onset tend to have coherent and distinct global minima (Figs 4.5b and 4.5c), with small dispersion of k_{min} for the various lengths, N, while those records containing only noise (Fig. 4.5d) or coda-waves (Fig. 4.5e) tend to produce random minima of comparable magnitude.

This last step of classical auto-picking could, in principle, be replaced by the ME method described in Section 4.3 (Kapetanidis & Papadimitriou, 2011). However, this requires sufficient waveform similarities in all stations of interest, which may not always be the case, especially because of SNR limitations. The ME method, however, could be used in addition to the AIC-picker and provide extra data for a better evaluation of the quality of the picks.

There are 3 main tasks that the targeted automatic picker is intended to accomplish:

- pick the arrival-time of a seismic phase onset with adequate accuracy under various SNR conditions
- provide information on the uncertainty to assess the quality of a pick
- reject picks on windows containing only noise or coda-waves

As in all picking algorithms, the primary goal is to provide a large set of picked arrival-times, T_{pick}, with minimal deviation, $|dt|=|T_{pick}-T_{real}|$, from the real onset, T_{real}, and small uncertainty (high pick-

quality, Q_{pick}). To determine a method that yields adequate results, a large number of tests on synthetic examples have been performed with the following parameters:

- Variation in SNR
- Variation in filters
- Variation in initial offset of dummy arrival-time, T_D, from the real wave onset arrival, T_{real}
- Noise rejection tests

The above were tested using various combinations of the AIC-picker with additional parameters such as kurtosis, skewness and amplitude ratio (after/before T_{pick}). The measurements include the difference between real arrival-time and automatic pick time, $|T_{pick}\text{-}T_{real}|$, quality of pick (uncertainty) Q_{pick}, and whether the measurement fulfils several criteria, otherwise the pick must be rejected. This may happen on a window of noise or very low SNR, even if the pick time is, by chance, acceptable. It is done to reduce the number of false positives (erroneous picks) with the risk, however, of increasing false negatives (missed picks).

4.2.1 Pick onset

At first approximation, T_{pick} is defined as the k_{min} corresponding to the most negative minimum of $AIC_n(m)$. However, there may be k_{min} values which would provide a smaller $|T_{pick}\text{-}T_{real}|$ deviation. In case $|T_D\text{-}T_{real}|$ is relatively small (real onset near the center of the windows) this could happen when the minima point to slightly different times on each component. If $AIC_n(k_1)$ and $AIC_n(k_2)$ represent global minima at two different components and $AIC_n(k_1) < AIC_n(k_2)$ or $AIC_n(k_1) \cong AIC_n(k_2)$ (the two minima have comparable values, according to a predefined percentage of tolerance) but k_2 is closer to the median of the set of k_{min} than k_1, then k_2 is preferred over k_1.

Another case is when $|T_D\text{-}T_{real}|$ is relatively large (the onset is near the edge of the W_{max} window of maximum length, N_{max}). While the minima of the AIC_n curves in the largest windows may indeed correspond to pick times near T_{real}, their (negative) amplitude may not be strong enough to allow them to be selected as the preferred solution. In such cases, also, there may not be enough measurements (from windows of different lengths) which include the onset. Taking these observations into account, some extra parameters must be considered.

Kurtosis and skewness are higher-order statistical functions which can be used to describe the shape of a distribution of values. Kurtosis, K, is defined as a normalized form of the fourth central moment, m_4, and quantifies the heaviness of the tails of the distribution (Eq. 4.4):

$$K = \frac{\mu_4}{{\mu_2}^2} = \frac{\mu_4}{\sigma^4} = \frac{\frac{1}{n}\sum_{i=1}^{n}\left(x_i - \bar{x}\right)^4}{\left[\frac{1}{n}\sum_{i=1}^{n}\left(x_i - \bar{x}\right)^2\right]^2} = \gamma_2 + 3 \tag{4.4}$$

where μ_2, μ_4 the second (variance) and fourth central moments, respectively, σ the standard deviation and $\gamma_2 = K - 3$ the excess kurtosis. In a Gaussian distribution, typical for random noise, the value of kurtosis is $K = 3$ (or $\gamma_2=0$). If K is measured on a sliding window along a filtered seismic record, the introduction of a strong seismic wave onset at the edge of the window, otherwise filled with noise, perturbs the distribution, causing the K parameter to increase abruptly to values which may exceed 10 (Baillard *et al.*, 2014). If exactly one half of the window contains noise while the rest a P-wave-train, K may be higher but comparable to 3. The same is true for windows containing only a P- or S-wave and their corresponding coda. This means that in order for kurtosis to be useful for the enhancement of a pick quality, the window must be set to contain only a small part of the incoming wave onset while the rest should be filled with the noise that precedes the wave. The time of the last sample of the sliding window where K maximizes can also be helpful for selecting $AIC_n(m)$ measurements in cases of large $|T_D\text{-}T_{real}|$ offsets. Skewness, S_k, on the other hand, is defined as a normalized form of the third central moment, μ_3, and quantifies the lop-sidedness or asymmetry of a distribution (Eq. 4.5):

$$S_K = \frac{\mu_3}{\mu_2^{3/2}} = \frac{\frac{1}{n}\sum_{i=1}^{n}\left(x_i - \bar{x}\right)^3}{\left[\frac{1}{n}\sum_{i=1}^{n}\left(x_i - \bar{x}\right)^2\right]^{3/2}} \tag{4.5}$$

It can take either positive or negative values and is equal to zero for symmetrical distributions. Sliding windows of skewness on filtered seismic records deviate momentarily to absolute values above unity when a strong wave onset enters the window and drops soon after the first pulse. The behaviour of kurtosis and skewness in seismic records has been previously exploited for the implementation of automatic phase pickers (Saragiotis *et al.*, 2002; Baillard *et al.*, 2014). In the present work, both γ_2 (excess kurtosis) and $|S_K|$ are calculated in sliding windows along the seismic records and the maximum $|S_K|$ and γ_2 (of all components) is registered for each position. Windows with $|S_K|<1$ and $\gamma_2<1$ are nullified and the product $K_S=|S_K|\cdot\gamma_2$ is calculated for the rest. The K_S curve is considered as a characteristic function and minima of AIC_n with k_{min} close to the maximum of K_S (within ± 0.1 sec) are examined as alternative T_{pick} values.

4.2.2 Pick Quality

The standard deviation (*std*) of the k_m (time values, k_{min}, corresponding to the minima of the individual $AIC_n(m)$ measurements for each of the trial window-lengths and available components, represented by the symbol m) provides a first approximation of the uncertainty of a pick. In case of noise or coda-waves the minima are generally scattered (Fig. 4.5d and 4.5e), while for distinguishable body-wave onsets the individual k_m tend to be aligned at the arrival-time (Fig. 4.5b), which may be slightly different between different components but consistent for different window lengths that contain the onset in the same component (Fig. 4.5c). The $std\{k_m\}$, however, is significantly biased when the T_D is not adequately close to the real onset. This causes random

minima to be found in the small trial windows while only the few largest ones may provide consistent minima near the real arrival-time. Thus, setting a maximum threshold for the $std\{k_m\}$ will likely cause many picks to be missed, although the global minima may actually point to the correct arrival-time (false negatives).

It was found that for N_{max} = 3 sec (T_D ± 1.5 sec) a threshold of ~0.75 sec for $std\{k_m\}$ was adequate to reject most false positives, which was typically defined in our tests as $|dt|$ > 0.1 sec. However, this also caused a large number of false negatives when the initial offset was $|T_D\text{-}T_{real}|$ > 0.4 sec. To avoid this problem, another characteristic of the AIC_n curves was exploited. In case of windows containing noise, the k_m are randomly distributed (bound by the limits of their corresponding trial window), however, the $AIC_n(m)$ (where the index *n* symbolizes the processed *AIC* curves according to the above-mentioned modifications) also have comparable values, while their absolute values can become significantly high if there is a strong contrast (e.g. impulsive phase onset), especially in the larger trial windows. To account for this characteristic, a weighted standard deviation scheme was applied with the following formulae:

$$
\begin{aligned}
wgt(m) &= \frac{AIC_n(m)}{\min\{AIC_n\}} \\
wmean\{k_m\} &= \frac{1}{\sum_m wgt(m)} \sum_m wgt(m) \cdot k_m \\
wstd\{k_m\} &= \sqrt{\frac{1}{\sum_m wgt(m)} \sum_m wgt(m) \cdot \left(k_m - wmean\{k_m\}\right)^2}
\end{aligned}
\tag{4.6}
$$

where $wgt(m)$ is the weight of each $AIC_n(m)$ (and k_m) measurement, $\min\{AIC_n\}$ is the global minimum of all $AIC_n(m)$, $wmean\{k_m\}$ is the weighted mean and $wstd\{k_m\}$ the corresponding weighted standard deviation of all k_m measurements. The $wstd\{k_m\}$ has usually smaller values than the classic $std\{k_m\}$. This happens because small-window measurements have low $AIC_n(m)$ and $wgt(m)$, so the uncertainty is mostly attributed to the dispersion of the k_m values that correspond to larger windows. This significantly reduces the bias in cases of relatively large $|T_D\text{-}T_{real}|$ offsets and allows for the much lower uncertainty threshold $\sigma_{th} \cong 0.38$ sec for N_{max}= 3 sec (roughly one eighth the length W_{max}, but this relation doesn't hold for larger N_{max} values).

The following relation is used for the calculation of the quality of the pick, Q_{pick}:

$$
\begin{aligned}
Q_{pick} &= \left(C_{AIC} \cdot C_{std} \cdot C_{amp}\right) + C_{kurt} + C_{skew} \\
C_{AIC} &= \frac{\left|\min\{AIC_n\}\right|}{R_{min}} \quad , \quad C_{std} = \frac{\sigma_{th} - wstd(k_m)}{\sigma_{th}}
\end{aligned}
\tag{4.7}
$$

where R_{min} is a calibration parameter which depends on the order of magnitude of the AIC_n values (typically set to R_{min} = 75), $C_{amp}=A_{aft}/A_{bef}$ is a signal-to-noise amplification factor that is measured as the ratio of the area A_{aft} covered by the waveform after T_{pick} divided by the area A_{bef} before T_{pick} in the largest window, with both A_{aft} and A_{bef} normalized by their corresponding lengths, while C_{kurt} and C_{skew} are values depended on the excess kurtosis ($\gamma_2 = K - 3$) and absolute skewness measured

in windows containing all samples before T_{pick} but only a few samples after T_{pick} (typically 15 samples ≡ 0.15 sec for a sampling rate of F_s=100sps). The C_{amp} multiplier is limited to a maximum value of 3 to prevent extreme behaviour. The C_{AIC} factor is depended on the absolute values of AIC_n. In order for these to be independent of the absolute amplitudes of the filtered seismogram, the time-series of each component is divided by the mean of absolute amplitudes of the largest window (which acts as a normalization factor) and then multiplied by 100 before the calculation of $AIC(k)$ to produce results which are compatible with the abovementioned R_{min} parameter. The C_{std} factor is forced to zero if C_{std}<0. The C_{amp} scheme in sliding windows of the form $C_{amp}(k)$, with k being a mid-window sample, similar to Eq. 4.3 for $AIC(k)$, has also been attempted as a modifier of the AIC_n curves, but it turned out that, even if its contribution is set to a maximum of 5%, it randomly amplifies several local minima causing unwanted increase in $wstd(k_m)$, although it sometimes improves the detection of S-waves in largely offset windows. The $wstd\{k_m\}$ may also become relatively large if the longest windows contain two wave onsets at both ends (e.g. both P and S waves). To avoid these extreme cases a maximum threshold is set and when $wstd\{k_m\} > \sigma_{max}$ the quality is forced to $Q_{pick} = 0$, where σ_{max} = 0.75 sec, a typical value tested for a 3 sec W_{max} window. The Q_{pick} values are forcibly bound within [0, 1] in case they exceed these limits. C_{kurt} and C_{skew} are allowed to have non-zero values only if the first term of Q_{pick} is lower than 0.5, in which case they are set to increase quality by up to 0.4 and 0.1, respectively, according to the following formulas:

$$C_{kurt} = \begin{cases} 0 & , \quad \gamma_2 < 3 \\ 0.4 \cdot (\gamma_2 - 3)/17 & , \quad 3 \le \gamma_2 \le 20 \\ 0.4 & , \quad \gamma_2 > 20 \end{cases}$$
$$C_{skew} = \begin{cases} 0 & , \quad |S_K| < 1 \\ 0.1 \cdot (|S_K| - 1)/3 & , \quad 1 \le |S_K| \le 4 \\ 0.1 & , \quad |S_K| > 4 \end{cases} \tag{4.8}$$

The C_{kurt} and C_{skew} terms help improve the quality of a pick when the $|T_D$-$T_{real}|$ offset is relatively large. Besides cases when Q_{pick}<Q_{min} (with Q_{min} typically set to 0.17) or $wstd\{k_m\} > \sigma_{max}$, other noise rejection criteria include cases where $AIC_n(m)$<R_{th}, with R_{th} typically set to 30, for AIC curves multiplied by 100 as already mentioned.

4.2.3 Spectral filter tests

The results of AIC_n, kurtosis and skewness functions are strongly dependent on the choice of the filter that is applied on the waveforms. As in the case of cross-correlation, it is important that any long period trend is removed with an appropriate high-pass filter. The target P- or S-wave onset may then be further enhanced by a low-pass filter. For P-waves, especially, differentiation of the waveform can bring out the onset for better accuracy on the determination of its arrival-time, something particularly useful in early warning systems (Lomax *et al.*, 2012). A series of tests have been performed with both synthetic pulses and real seismograms to establish a default set of filters which produce the best results in terms of small $|T_{pick}$-$T_{real}|$ deviation and high Q_{pick}.

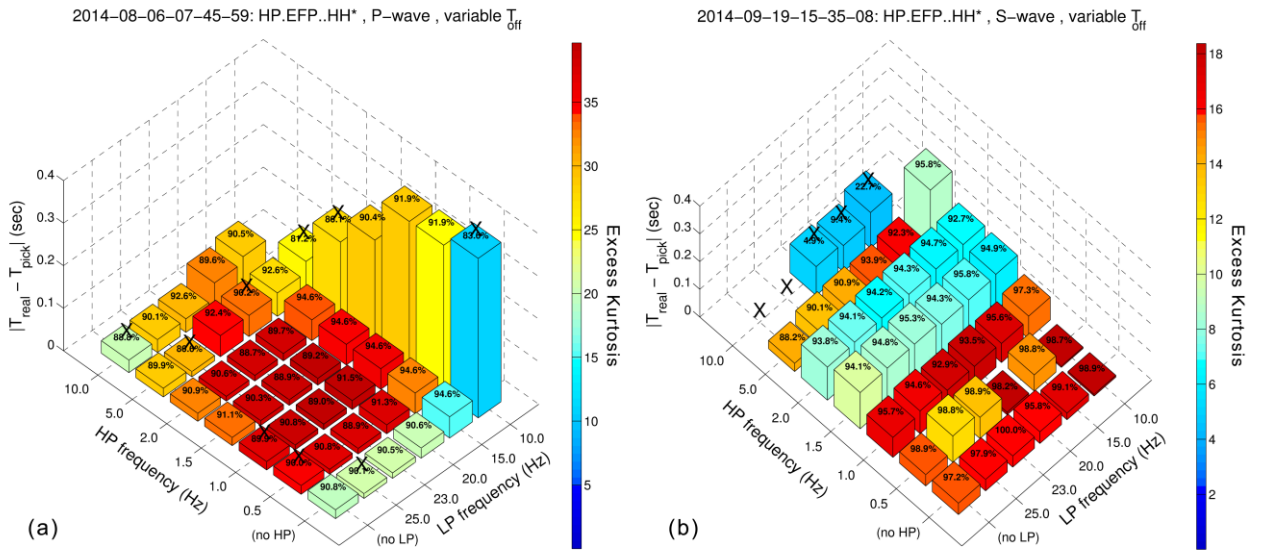

Figure 4.6: AIC-picker frequency filter tests with W_{max} length of 3 sec (a) for P-waves, (b) for S-waves. HP and LP refer to High-Pass and Low-Pass corner frequencies of the applied Butterworth filter. The bars' height corresponds to the mean of absolute deviation values, $|dt|$, calculated over a range of starting offsets $|T_{off}| \leq 1.1$ sec for the example of P-waves and $|T_{off}| \leq 0.6$ sec for the example of S-waves. Colours correspond to mean excess kurtosis values. Percentages on top of bars represent mean quality, Q_{pick}. Heights, colours and percentages are calculated over non-rejected results only. Bars with "X" on top correspond to rejection of over ~5 per cent of the results.

A total of 41 filter combinations were tested for a selected set of P- and S-waves with a varying range of initial offsets, $T_{off} = T_D - T_{real}$, to check for stability (Fig. 4.6). The algorithm works adequately with most filters when the initial offset $T_{off} = 0$ and the signal is strong enough. However, by increasing $|T_{off}|$ the deviation dt becomes larger, especially when certain frequency ranges are used, and the quality is lowered. A similar effect is observed when Gaussian noise is added to the waveforms or recordings with lower SNR are used (events of smaller magnitude or larger hypocentral distance). Fig. 4.6a shows an example with the P-wave of an $M = 0.8$ event recorded at station EFP at epicentral distance ~10 km. The presented results are mean values of $|dt|=|T_{real}-T_{pick}|$, quality Q_{pick} and excess kurtosis, γ_2, calculated over valid (non-rejected) automatic picks, with trial T_{off} varying between -1.1 and 1.1 sec, and $N_{max} = 3$ sec. Each bar corresponds to a combination of high-pass (HP) and low-pass (LP) Butterworth filters. In this example, it is apparent that the filter combinations in the middle of the grid provide the best solutions with respect to the smaller mean $|dt|$. It should be noted that $T_{S\text{-}P} \cong 1.5$ sec, which means that the S-wave onset is barely at the right edge of W_{max} when the offset is zero and is fully contained in W_{max} when $T_{off} = 1.1$ sec. This promptly affects the results, especially in the lower frequencies, which is why the deviation is larger when the low-pass corner frequency is $f_{LP} = 10$Hz, also causing rejections by more than 5% of the measurements in some combinations (bars marked with "X" on top). In terms of $wstd\{k_m\}$, the values are generally low, except for $f_{LP} = 10$Hz. High kurtosis values are observed in the middle of the grid, as these frequency bands better enhance the P-wave onset against the background noise and the incoming S-wave.

Fig. 4.6b is a similar example for the S-wave of an M_w=4.1 shallow event recorded at the same station at about the same epicentral distance. Smaller T_{off} range was used, as the preceding P-waves can strongly influence the results (see more about this issue in the offset tests section below). This test indicates that the best solutions are mainly achieved with HP filters at 0.5 or 1.0 Hz and LP filter at 10 Hz, while a significant percentage of rejections (over 20%) is observed at f_{HP}=10Hz. Deviations of the order of 0.1 sec with f_{HP}=1.5Hz or f_{HP}=2.0Hz can be due to the existence of alternate solutions for S-wave arrival, one on each of the horizontal components, with the one preferred over the other depending on small variations in the shape of the AIC_n curves.

These tests are not always conclusive, as there are several factors which affect the results, such as the level of noise or the frequency content of a particular wave (e.g. depending on the magnitude and hypocentral distance of an event). Parameters such as the length of the W_{max} window, and the criteria of pick preference, quality and rejection also play a major role in the final outcome. For this reason, no single filter is optimal for all cases, but rather a number of predefined filters must be tried out when the algorithm is applied on a dataset of events and a best solution has to be selected according to the quality or other criteria. For P-waves, frequency bands such as 1-20 Hz, 1.5-15 Hz and 2-23 Hz seem to provide adequate results for local micro-earthquakes, while for the S-waves the bands 0.5-10Hz, 1.5-10Hz and 2-15Hz can also manage most events in local distances. Smaller W_{max} window lengths (e.g. N_{max} = 2.5 sec instead of 3 sec) are also applied in cases of small T_{S-P} intervals.

4.2.4 Noise tests

It is important that the algorithm can distinguish P- and S-wave onsets under conditions of low SNR, but also manage to reject picks when the uncertainty becomes too large or the window contains only noise. For this purpose, the algorithm was tested by applying the default set of filters that were determined in the previous section while gradually superimposing Gaussian noise on the waveforms to artificially reduce the SNR. In this test, the signal level was measured as the weighted mean of the absolute amplitudes of the filtered waveform inside W_{max}. This is divided by the noise level value, which is measured in a window the Gaussian noise before it is superimposed on the signal. However, to avoid a division by zero, the noise level is represented by SNR^{-1}, with zero corresponding to "no extra noise" added to the signal.

Fig. 4.7 shows a typical example of the behaviour of Q_{pick}, $wstd\{k_m\}$, $AIC_n(m)$ and dt as the signal quality is reduced. A total of 10 measurements were repeated for each level of random additive noise in order to calculate the errors, which are mostly important for dt. The Q_{pick} is gradually reduced as the noise becomes stronger, which increases $wstd\{k_m\}$ due to the dispersion of the AIC_n minima, especially in the smaller windows. As the noise level increases, the contrast between the wave onset and the background noise becomes more obscure, lowering $AIC_n(m)$. Finally, for SNR^{-1} > 0.85 (or SNR < 1.17), the quality becomes too low and algorithm is unable to determine a pick with adequate certainty. The $|dt|$ values start to deviate from zero with significant errors, as the pick becomes completely random. An interesting observation is that for $SNR^{-1} \cong 0$, there is a deviation of

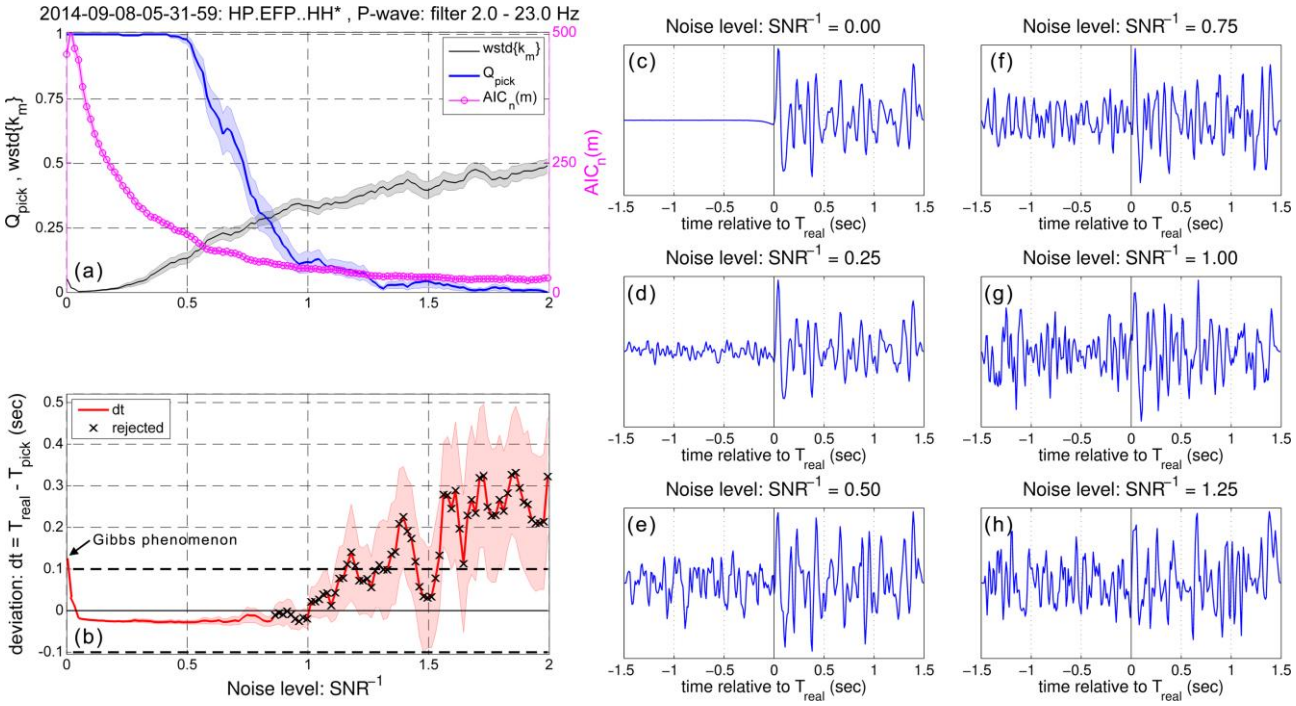

Figure 4.7: P-wave picker noise test. (a) pick quality, Q_{pick} (thick blue line, left axis), weighted standard deviation of the AIC_n minima, $wstd\{k_m\}$(black line, left axis, measured in sec) and modified AIC value at the preferred minimum, $AIC_n(m)$ (purple circles, right-hand axis), (b) deviation between T_{pick} and T_{real} with respect to the starting offset, T_{off} and (c-h) waveform segment in W_{max} window, centered at T_{real}, for increasing noise level (SNR^{-1}).

~0.13sec, with $T_{pick} < T_{real}$, a small increase in $wstd\{k_m\}$ and a slight drop of $AIC_n(m)$. This is because of the ringing effect due to acausal filtering, also known as the Gibbs phenomenon, which creates a long-period, low-amplitude pulse of opposite polarization before the impulsive P-wave onset, which, although negligible visually, affects the results of the algorithm. By increasing the noise level before the strong P-wave onset, the SNR of this artefact is reduced and the algorithm manages to pick the arrival-time with better accuracy. Although this deviation is not often an issue for signals of lower SNR but with a clear onset, it can be reduced in high SNR P-waves by applying a stronger high-pass filter (e.g. with cut-off frequency at 10Hz), optionally combined with differentiation of the waveform to further enhance the higher frequencies.

4.2.5 Offset tests

The algorithm was tested in a wide range of initial $T_{off} = T_D - T_{real}$ offsets to simulate uncertainties in the estimation of the theoretical arrival-times, T_D, which are used to guide the auto-picking procedure. The problems which may occur are 1) a P-wave onset being at the right edge of the window, the rest being noise, 2) a P- or S-wave onset at the left edge of the window, the rest being the coda wave, 3) both P- and S-waves included in the same window. The test also examines the behaviour of Q_{pick} as the offset increases. The length of W_{max} has to be a compromise that allows a suitable range in T_{off} (uncertainty of T_D) for a successful pick (larger windows increase the chances

that the targeted onset will be inside W_{max}) while it avoids having both P- and S-waves included in the same window. This means that the minimum N_{max} value can be adjusted according to the expected $T_{S\text{-}P}$ (or epicentral distance of a station) and the maximum length according to the average error in T_D. In this application a N_{max} = 3 sec was considered for most stations, and the center of the window for S-wave was altered when $T_{S\text{-}P}$ was smaller than 2 sec to allow for a safety space between the end of the window and the P-wave onset. The T_{off} is zero when the arrival-time of the onset, T_{real}, is exactly in the middle of the 3 sec window (W_{max}). Negative T_{off} means that the window is centered to an earlier time than T_{real}, the reverse is true for $T_{off} > 0$.

Fig. 4.8 shows the typical behaviour of the AIC-picker with varying T_{off} when targeted at a P-wave onset in a waveform filtered between 2 and 23 Hz. For this particular recording, the $T_{S\text{-}P}$ = 2 sec allows for a 0.5 sec safety window when N_{max} = 3 sec. The deviation $dt = T_{real} - T_{pick}$ is minimal in the range -1.1 sec ≤ T_{off} ≤ 1.3 sec, which permits an uncertainty in T_D of the order of ± 1 sec. The parameter $AIC_n(m)$ represents the preferred minimum of the AIC_n curves which corresponds to the automatic T_{pick}. It is typically in the order of hundreds when a clear onset is detected (Fig. 4.8a, right axis). The contrast is stronger in the range -0.8 sec ≤ T_{off} ≤ -0.4 sec, when the W_{max} window is mostly filled with low-amplitude noise while it also contains the strong P-wave onset in the last 1/3 of W_{max}. However, at T_{off} < -0.8 sec, the $AIC_n(m)$ starts to drop and is reduced to a minimum value at T_{off} < - 1.25 sec. The weighted standard deviation, $wstd\{k_m\}$, is at its lowest in the range 0 ≤ T_{off} ≤

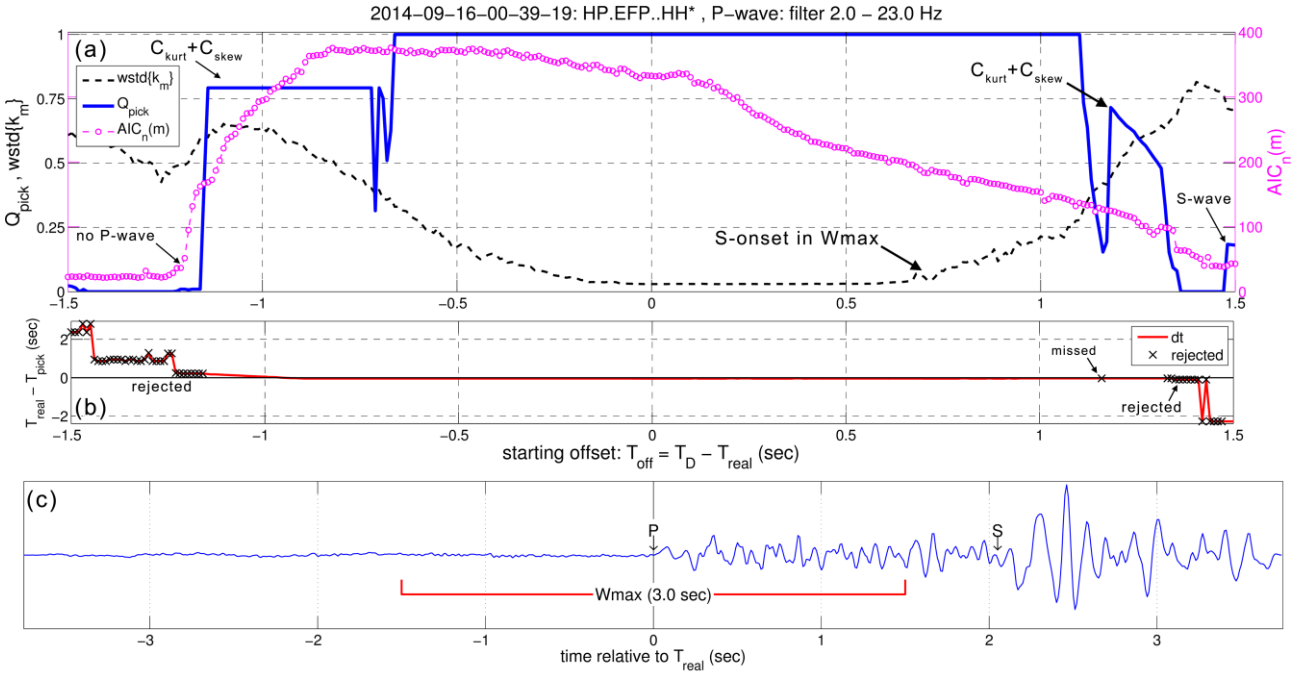

Figure 4.8: P-wave picker offset test. (a) pick quality, Q_{pick} (thick blue line, left axis), weighted standard deviation of the AIC_n minima, $wstd\{k_m\}$(dashed black line, left axis, measured in sec) and modified AIC value at the preferred minimum, $AIC_n(m)$ (purple circles and dashed line, right-hand axis), (b) deviation between T_{pick} and T_{real} with respect to the starting offset, T_{off} and (c) the positioning of the W_{max} window on the waveform record for T_{off} = 0. The manually picked arrival-times of P- (T_{real}) and S-waves are marked for reference. The waveform displayed in panel (c) is the horizontal component, in order for the S-waves to be more distinguishable, filtered between 2 and 23 Hz (the same that was used for the picker).

0.5 sec, when the W_{max} contains mostly the P-wave onset and its coda. This happens because the minima of the AIC_n curves are less dispersed. The $wstd\{k_m\}$ becomes larger than 0.5 sec at T_{off} < -0.9 sec, when the P-wave onset is at the right edge of W_{max} and, further on, the window contains only noise. On the right side, it starts to increase at T_{off} > 0.5 sec, when the S-wave enters W_{max} (Fig. 4.8c), and it briefly exceeds σ_{max} = 0.75 sec for $T_{off} \cong$ 1.4 sec. The quality, Q_{pick}, is maximum in the range -0.6 sec ≤ T_{off} ≤ 1.1 sec, largely attributed to the first term of Eq. 4.7. At $T_{off} \cong$ -0.65 sec the quality drops abruptly, but as Q_{pick} approaches the value 0.5, the C_{kurt} and C_{skew} terms kick in, with the maximum of the product $K_S=|S_K|\cdot\gamma_2$ strongly affecting the preference of possibly secondary AIC_n minima for T_{pick}. For as long as $dt \cong 0$, the C_{amp} factor (not presented in Fig. 4.8) remains constant at about C_{amp} = 9 (if left unbound), as T_{pick} does not change much. C_{amp} drops to near unity at both ends of the T_{off} range.

In the case of S-waves, the behaviour of the AIC-picker is similar but a bit more complex (Fig. 4.9). A better frequency range for this type of wave is between 1.0 and 10 Hz. The quality Q_{pick} maximizes to unity in the range -0.6 sec ≤ T_{off} ≤ 0.15 sec. The deviation, dt, remains within acceptable limits for -1.0 sec ≤ T_{off} ≤ 1.0 sec, with Q_{pick} > 0.25 for the most part. While $|dt|$ is near zero in the range 0.8 sec ≤ $|T_{off}|$ ≤ 1.1 sec, the quality is very low and the noise rejection criteria dictate that the pick is not reliable in most cases. For $T_{off} \cong$ -1.0 sec, the $wstd\{k_m\}$ > 0.75 sec and

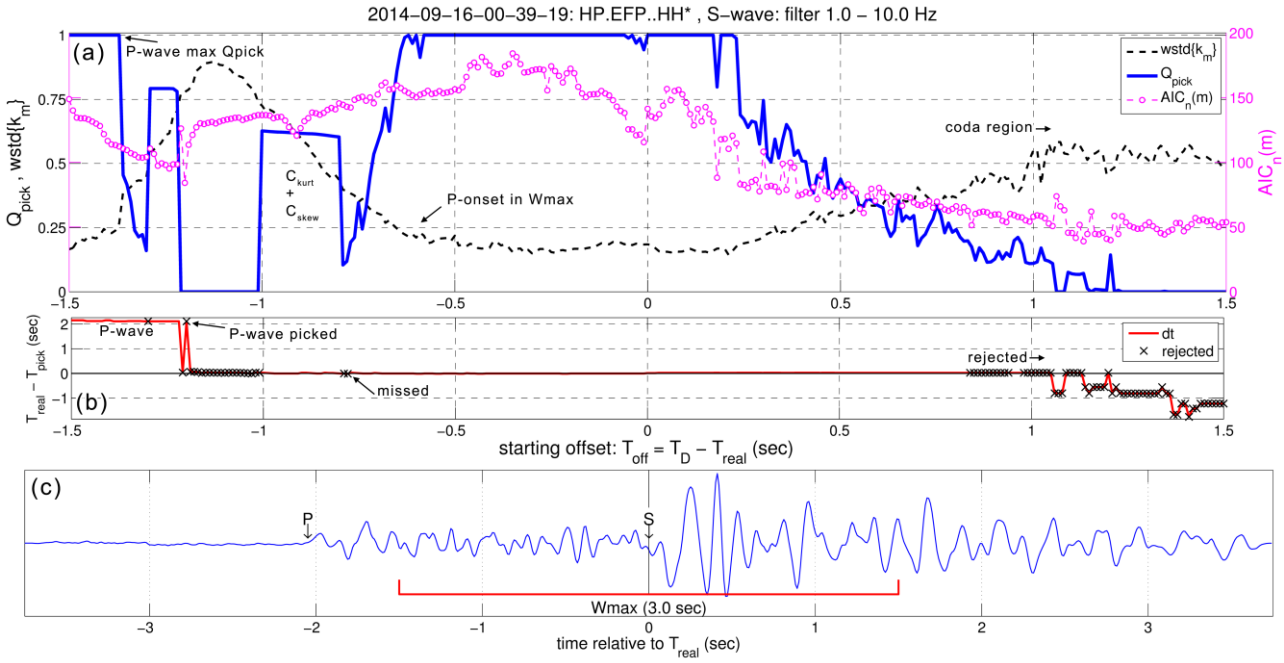

Figure 4.9: S-wave picker offset test. (a) pick quality, Q_{pick} (thick blue line, left axis), weighted standard deviation of the AIC_n minima, $wstd\{k_m\}$(dashed black line, left axis, measured in sec) and modified AIC value at the preferred minimum, $AIC_n(m)$ (purple circles and dashed line, right-hand axis), (b) deviation between T_{pick} and T_{real} with respect to the starting offset, T_{off} and (c) the positioning of the W_{max} window on the waveform record for T_{off} = 0. The manually picked arrival-times of P- and S-waves (T_{real}) are marked for reference. The waveform displayed in panel (c) is a horizontal component, in order for the S-waves to be more distinguishable, filtered between 1 and 10 Hz (the same that was used for the picker).

Q_{pick} = 0, as both the P- and S-wave onsets are clearly contained in the W_{max}. The P-wave starts to affect $wstd\{k_m\}$ at about T_{off} = -0.5 sec, but the algorithm still prefers the S-wave pick, at least in this particular frequency range. The deviation culminates and stabilizes at $dt \cong 2.0$ sec for $T_{off} < -1.2$ sec, as the picker now works on the P-wave instead of the S-wave. This means that when the algorithm runs on an operational level, it is important that extra conditions are considered to avoid this problem, such as limiting the bounds of W_{max} to not include the T_D of the P-wave or its T_{pick}, in case the P-wave was picked before the S-wave. In the case of S-waves, the C_{amp} factor has generally low values, slightly above unity, depending on the amplitude difference between the S-waves and the coda of the P-waves, in the region where T_{pick} is placed correctly at the onset. C_{amp} drops to lower values for $T_{off} > 1.2$ sec. However, when the P-wave enters the left side of the W_{max} window ($T_{off} < -0.9$ sec), C_{amp} increases abruptly to the value of ~5. It is not the same value that was observed throughout the valid T_{off} range for the P-waves, but this is only due to the different filter.

This last test for the S-waves was repeated with a variation of parameters. Filtering in higher frequencies (e.g. 2 - 23 Hz) further limits the valid T_{off} range ($|T_{off}| < 0.6$ sec), with rejection occurring earlier on both sides and the P-wave strongly affecting the picker at $T_{off} < -0.9$ sec. It also introduces secondary minima of AIC_n to be preferred, with a small difference (~0.1 sec) in their k_{min} time and amplitude, due to the early arrival of the S-wave being clearer in one of the horizontal components. Small variations in the calculations cause the algorithm to prefer one solution over the other, depending on the placement of W_{max}. Concerning the length of W_{max}, a 2 sec window slightly reduces the range of max quality and also limits the valid T_{off} region to about -0.8 sec $\leq T_{off} \leq 0.75$ sec, beyond which the $|dt|$ deviates abruptly and the pick is rejected as the quality drops. The "kurtosis criterion" region at $T_{off} \cong -0.8$ sec is also more limited (halved). A longer W_{max} window (4 sec), on the other hand, allows a greater range of T_{off} on the right side, with the S-wave being detectable even if most of the window contains its coda, as the "kurtosis criterion" provides valid solutions for T_{off} up to 1.5 sec. It is, however, prone to lower values of quality and rejection on the left side starting at T_{off} = -0.65 sec.

4.3 Semi-automatic picking: The Master-Events method (MEm)

Seismic events during intense sequences are often clustered both in space and time. Consequently, a large number of them could meet the conditions of similar focal parameters and therefore produce similar waveforms, as described in Chapter 1. Routine analysis (manual picking of arrival-times and locating of recent significant events performed by an analyst on a daily basis) in local/regional seismological networks usually dismisses a great number of events of smaller magnitudes, as the manual picking of phase-arrivals for low-energy events with a low SNR can be difficult and unreliable. Also, the seismic activity is often very intense in the time-period shortly after the occurrence of a main event. As a result, the waveforms of successive aftershocks may overlap, in which case one or both events may be ignored from routine analysis because it becomes difficult to distinguish the phase arrivals, even though the SNR may be high.

A Master-Events methodology (MEm) based on the cross-correlation of events with similar waveforms, which can be used as an alternative, semi-automatic picking algorithm (Kapetanidis &

Papadimitriou, 2011), is briefly presented in the present section. The idea is based on the fact that a reference station located close to the epicentral area can record and detect a large part of an aftershock or seismic swarm sequence, while stations in farther distances can record only the stronger events. Classic auto-picking algorithms work by detecting phase-arrivals on several stations and associating them to an event afterwards. However, the phase arrivals of events with small magnitude may be neglected when the SNR is not high enough. In the proposed methodology the events are detected *a priori* using the waveform recordings of a single reference station and the arrival-times are identified afterwards using a correlation detector technique. This has the advantage of using the whole P or S wave-train to make a statistical match between the master and slave waveforms instead of searching for the onset of an arrival which may not be easily distinguishable from the background noise.

In order to analyze an entire aftershock sequence, the detected events' waveforms are cross-correlated and organized in multiplets. A minimal number of events with larger magnitudes from each cluster are selected as "master-events" (ME). The arrival-times of their P- and S-waves are manually picked and their waveforms are used to automatically pick the corresponding arrival-times of smaller but similar "slave-events" (SE). The large number of additional aftershocks which can be located using this method may provide a higher level of detail in the spatiotemporal distribution of the rupture process. This method has been applied to the case study of Section 5.2, a significant sequence that followed two moderate earthquakes (M_w=5.1) near the city of Efpalio, western Corinth Rift, on 18 and 22 January 2010 (Kapetanidis & Papadimitriou, 2011).

Prior to the application of the MEm during an intense earthquake sequence, a reference station, whose recordings are representative of the whole sequence, must be selected. Its choice depends on the density and geometry of the seismological network around the aftershock area. It has to be close to the epicentral area to record events with small magnitudes, clearly distinguished from the background seismic noise, but also far enough for very small events to be dismissed because of their low SNR, so that most signals detected at the reference station can also be clearly detected in other stations at farther epicentral distances. It is necessary for an event to have strong signal in at least 3 stations in order for its P- or S-wave arrival-times to be picked and a solution of its location and origin time be calculated. The data quality on the available stations has to be checked to ensure that all components are operating properly. Damaged or noisy components have to be ruled out, otherwise they may cause problems. Custom frequency filters may be required in some cases to ensure better SNR and correlation coefficients (see Section 4.3.2). This information is stored in a matrix called "station-rules".

Signals recorded at the reference station can be detected using the STA/LTA algorithm of Section 4.1. The MEm requires starting times called $P_{markers}$, or approximate P-wave arrival-times, and ending times, or $D_{markers}$, which can be approximated by the time the STA/LTA ratio drops below the lower threshold value, R_2. Day-specific (DS) cross-correlation matrices are constructed with XC_{max} values measured over all combinations of signal pairs at the reference station, after proper filtering. The optimal threshold for the classification into multiplets with the nearest neighbor linkage is selected using the method described in Section 1.2.2. Partial matrices are then created for each multiplet and their events are cross-correlated with the respective ME signals in search for a direct match. A single ME can be used to locate all SE in a partial matrix, as all events within a

matrix are similar through intermediates. The events directly matching a ME are called "primary slaves", while the rest are "secondary" or "higher order slaves". Events which do not belong to a partial matrix are called "orphans", however they may still match one or more ME. The procedure described in Section 4.3.1 is first applied to the primary SE, supplying them with arrival-times and allowing them to be located. The primary SE can then be used as ME themselves, propagating the picks from the original ME to the higher order SLE within their multiplet.

4.3.1 The correlation detector

The picking algorithm runs for each ME with direct similarity to a primary slave, for each station with available manual arrival-time picks and healthy components (according to the "station-rules" matrix) on both master- and slave-event. A sliding window technique known as the "correlation detector" has been adopted here as the fitting process (Schaff & Waldhauser, 2005). The detector-window (master-waveform) slides over the target waveform data (slave-waveform) and delivers unbiased correlation measurements, C_i. This is slightly different from the cross-correlation function of Eq. 1.2, in which case, due to the difference in window lengths, the shorter master-waveform would have to be zero-padded to reach the same number of N samples as the longer slave-waveform and the XC function would deliver biased measurements due to the time-lag depended envelope, as explained in Section 1.1.1 (Eq. 1.3).

The maximum correlation-coefficient found at the best-fit window is symbolized by C_m. Fig. 4.10 shows an example of the detection of a P-wave on the slave waveform (top), using a template

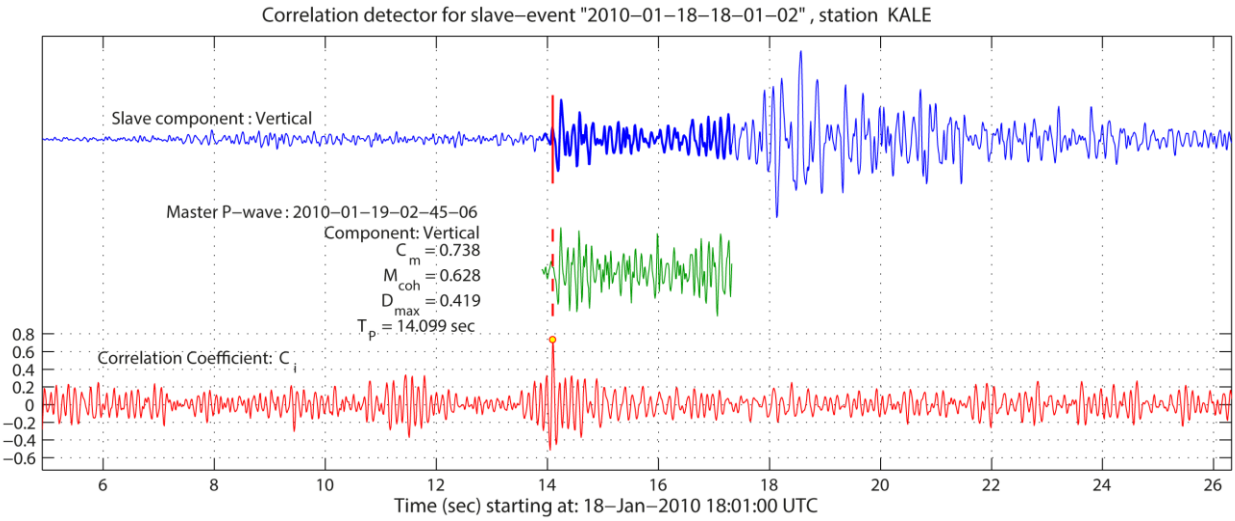

Figure 4.10: The correlation detector for a P-wave (middle waveform) slides along the slave (top waveform) and the correlation-coefficient, C_i, values are being calculated at each sample (bottom diagram). The correlation-coefficient maximizes for $t=T_P$ which corresponds to the arrival-time of the P-wave at both master and slave waveforms. C_m is the correlation coefficient at the time-lag of best-fit, M_{coh} the respective mean spectral coherence in the band 2-15Hz and D_{max} is the difference between the global and the highest secondary local maximum of the cross-correlation function. Figure after Kapetanidis & Papadimitriou (2011).

waveform as a detector (middle). The bottom diagram in Fig. 4.10 represents the calculated correlation coefficients with a maximum value C_m at the best-fit window. The D_{max} value is the difference between global and the highest secondary local maximum of the cross-correlation function of the master waveform and the best matching window of the SE, as in Fig. 1.1b of Chapter 1. The mean spectral coherence, M_{coh}, between 2Hz and 15Hz (e.g. Fig. 1.2c) is also taken into account at the best-fit window.

Suppose a certain master-event, *M*, recorded at a station *K* and the discrete time-series $M(t)$ of its P-wave on the vertical component. The manually picked P-wave arrival-time for this event on this station is at $t=t_P$, with $t=0$ at the first sample of the series. The corresponding waveform of a slave-event $S(t)$ is divided into a family of time-series called $S_i(t)$, where the index *i* refers to a certain window with equal length *N* to that of the $M(t)$ series, which starts at the beginning of $S(t)$ and shifts by one sample as the index *i* increases. In each $S_i(t)$, the relative time is $t=0$ at the first sample of the window.

The correlation-coefficient C_i is calculated between $M(t)$ and $S_i(t)$ for every window *i*:

$$C_i = \frac{\frac{1}{N}\sum_{j=1}^{N}\left(M(t_j)-\overline{M}\right)\cdot\left(S_i(t_j)-\overline{S_i}\right)}{\frac{1}{N}\sqrt{\sum_{j=1}^{N}\left(M(t_j)-\overline{M}\right)^2}\cdot\sqrt{\sum_{j=1}^{N}\left(S_i(t_j)-\overline{S_i}\right)^2}}, \tag{4.9}$$

$$\overline{M} = \frac{1}{N}\sum_{j=1}^{N} M(t_j), \tag{4.10}$$

$$\overline{S_i} = \frac{1}{N}\sum_{j=1}^{N} S_i(t_j). \tag{4.11}$$

If at some point $C_i > C_{H,th}$, where $C_{H,th}$ is a high-threshold value, the process continues for a certain number of supplementary steps (equivalent to e.g. 1-2 seconds) and then the maximum $C_{i=m}$ value and its respective index $i=m$ are registered in a matrix. In that case $S_{i=m}(t)$ and $M(t)$ should be highly similar. Suggested value for $C_{H,th}$ is 0.7, but this can be fine-tuned by trial and error and even be station- or wave-type-dependent. Then, the absolute time of the sample at $S_{i=m}(t=t_P)$ should correspond to the automatically picked arrival-time of the P-wave of the slave-event on station *K*. If, on the other hand, there is no $C_i > C_{H,th}$, the procedure stops after a specified maximum number of steps after P_d is reached (typically equivalent to about 20sec) and the maximum value, C_m, is saved.

Using multiple master-events (Fig. 4.11) presents advantages, as it is probable that there will be some P- or S-wave arrival-time picks available at a certain station for only one of those master-events. The same principle applies to the use of multiple components in order to acquire up to three P or S arrival-time picks from each station per master-event. Each measurement obtained for a pair of master/slave events on a certain station and component is called "observation". Multiple observations increase the probability to obtain a correct final pick when all measurements are post-processed according to their corresponding weights.

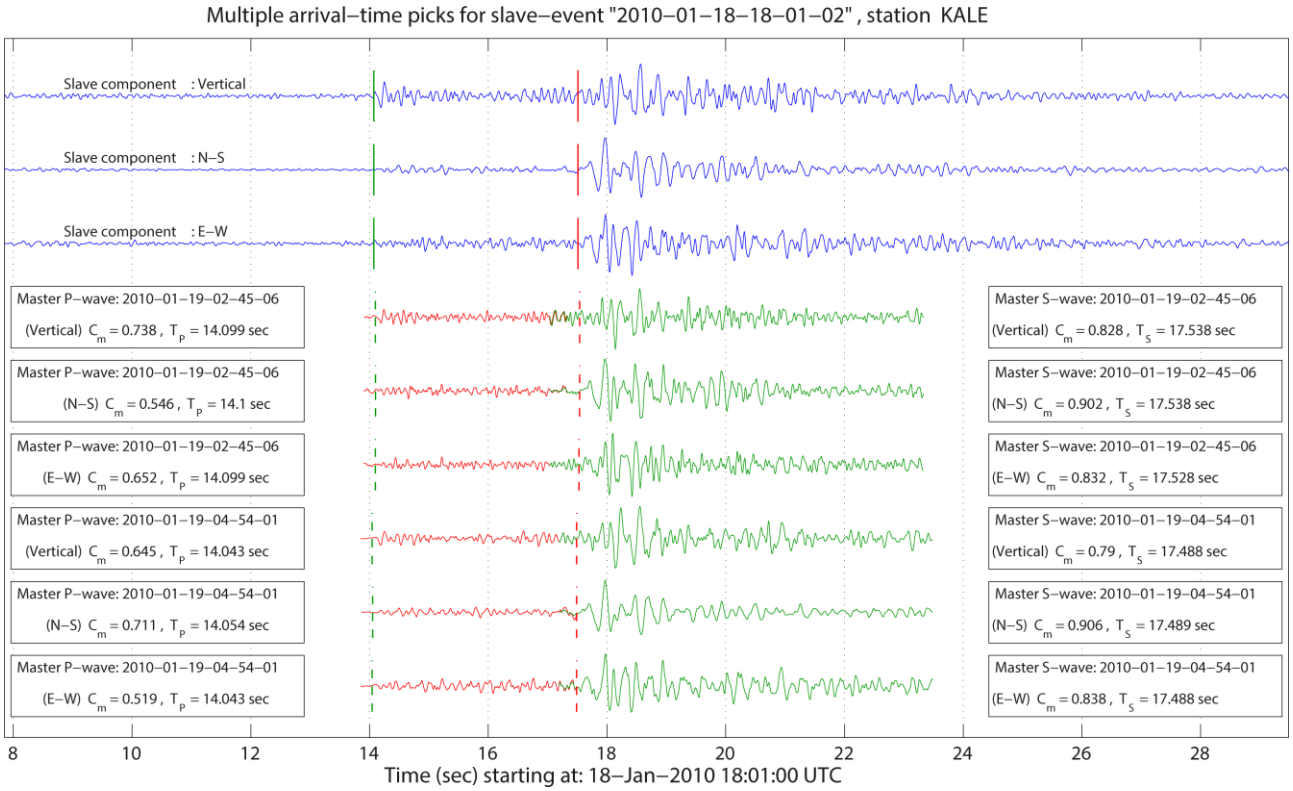

Figure 4.11: Multiple master P- and S-waves on multiple components, being fit to the corresponding slave waveforms (first three on top). Although the maximum correlation coefficients, C_m, vary from as low as 0.519 to a high value of 0.906, the derived arrival-time picks are consistent. Figure after Kapetanidis & Papadimitriou (2011).

The ME methodology is more efficient with the S-waves because of their higher energy content and SNR. During the application of the correlation detector, in some cases the P-wave arrival-times, T_P, were being detected after the S-wave arrival-time, T_S, because of the low SNR of the P-waves and to some degree of statistical similarity between the master P-wave and the coda of the slave's S-wave. To ensure that the condition $T_P<T_S$ is met, the algorithm works with the S-waves first (when there is a manual pick available for the master-event) to attempt an automatic pick at T_S, then it picks the P-wave arrival-time and examines if $T_P<T_S$ is true, otherwise it searches for other local correlation-coefficient maxima above the required threshold before the time T_S. In order to avoid such issues of "false negatives", a combined observation weight, taking into account all available measurements (C_m, M_{coh}, D_{max}) as well as the type of wave (P or S), is determined in a post-processing stage that follows the picking procedure (Kapetanidis & Papadimitriou, 2011). This characterizes the quality of the fit which is important for the estimation of the final arrival-time pick and its uncertainty level.

4.3.2 Frequency filter tests

While a global frequency filter is easier to implement into the MEm, it is usually better to use custom filters per station/component, mainly depending on their instrument type and average expected epicentral distance but also on the wave-type (P or S). Fig. 4.12 shows the C_m values calculated using band-pass filters with a wide range of combinations between low and high cut-off frequencies for P- or S-waves at different stations and components. It is evident that the vertical component (Fig. 4.12a) gives higher C_m values for a wider region of cut-off frequencies than the horizontal ones (Figs 4.12b and 4.12c) for this master/slave pair and station. The S-waves produce, in general, higher C_m values than the respective P-waves, which is expected because of their higher energy content and, consequently, higher SNR. It may also be observed that in most cases there is a low C_m value region for high-pass cut-off frequencies below ~1.5Hz. This is due to the presence of long-period noise in broad-band seismometers with high amplitudes relative to those of the signals of local micro-earthquakes which greatly affect the cross-correlation procedure in the time domain.

The plots shown in Figs 4.13c,f are different because of the "short-period" seismometer used on station PYR of the CRL network, in which case the long-period noise is filtered-out by the hardware and high-pass filters make little difference. In most cases the highest C_m values are calculated for narrow frequency bands, e.g. cut-off frequencies of the low-pass filter close to 10Hz and cut-off frequency at 2.5Hz or higher for the high-pass filter (Figs 4.12d-f and 4.13a,d-e). In some cases such as those in Fig. 4.12b,c the highest C_m values are calculated for a band between

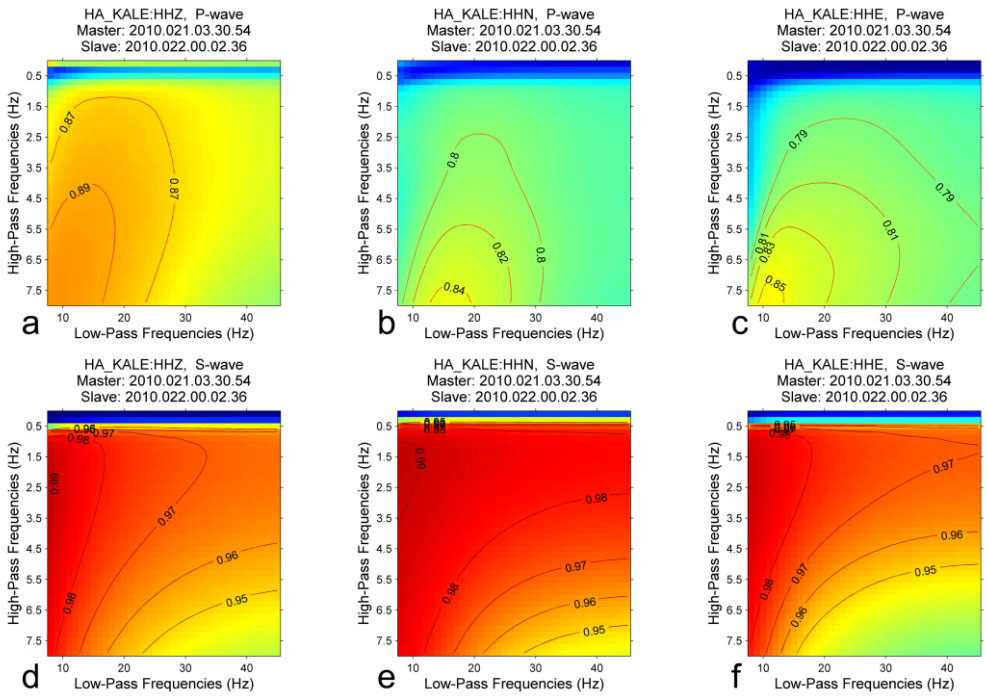

Figure 4.12: Testing of the picking algorithm for different frequency bands. Colours and contours represent C_m values. The horizontal axis indicates the high cut-off frequency of the low-pass Butterworth filter while the vertical one represents the low cut-off frequency of the high-pass filter that was used for each measurement. Panels (a-f) show the range of C_m values for a master/slave pair on the three components of the reference station KALE while picking the P-waves (a-c) or the S-waves (d-f) respectively.

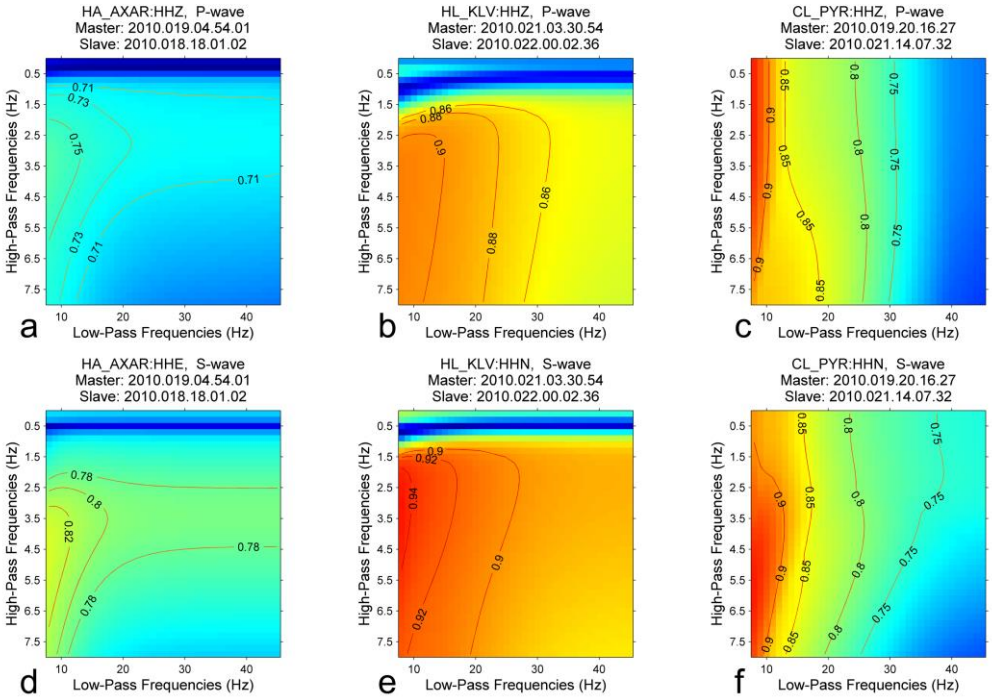

Figure 4.13: Same as Fig. 4.12 but for three different master/slave pairs. Panels (a-c) show the C_m values for P-waves on different master/slave pairs of other stations, while panels (d-f) show the corresponding C_m values for S-waves. Figure after Kapetanidis & Papadimitriou (2011).

8Hz and 13Hz. This happens because the waveforms become less complicated and easier to match when there is less frequency content, but it is not suggested to use very narrow bands as in that case the algorithm will become more prone to false positives (identifying random noise as signal because of waveform simplicity).

Waveform complexity also helps distinguish signals with different characteristics in their higher frequencies, although they may resemble more in the lower ones. These plots in combination with spectrograms of coherence (e.g. Fig. 1.3 in Chapter 1) can be used as a guide for the selection of a default filter. For waveforms with strong similarity the frequency range usually influences only the C_m value without affecting the time-lag, but in cases of signals with moderate to low similarity and significant noise level the selection of the frequency range may also affect the time-lag, so its careful selection plays an important role to the whole procedure. Further tests were performed by varying the high and low cut-off frequencies and calculating the RMS values and location errors of the hypocentral solutions of the slave-events as well as observing their spatial clustering visually. For the application of the MEm in case study of Section 5.2, the waveforms were band-pass filtered between 2.5Hz and 23Hz with additional filters depending on the information stored in the "station-rules" matrix to account for station-dependent signal and noise characteristics. This default filter is wide enough to preserve waveform complexity while eliminating long-period and high-frequency noise.

4.3.3 Sensitivity tests

In order to examine the strength of the correlation detector against low SNR a synthetic test has been conducted. Gaussian noise was being added to a filtered slave waveform, whose S-wave part is shown at the top of the matrix that is presented on the left side of Figs 4.14 and 4.15. The SNR was measured using the uncontaminated signal of the S-wave part relative to the (contaminated) noise background for an equal number of samples before the arrival of the P-wave (not shown in these figures). Each of the rows in the matrices of Figs 4.14 and 4.15 represent a slave-waveform with increasing amounts of high-frequency (Fig. 4.14) or low-frequency (Fig. 4.15) Gaussian noise being added. The values at the left side of the vertical axis show the SNR for selected waveforms which are plotted on the right side of the figures. The top waveform at the right side is the master which is used as the correlation detector and is not being contaminated by noise. The picking algorithm is run in each case and the resulting C_m values for the selected examples are shown at the right side of each waveform, along with a label that indicates a successful pick or a failure to pick the arrival-time correctly.

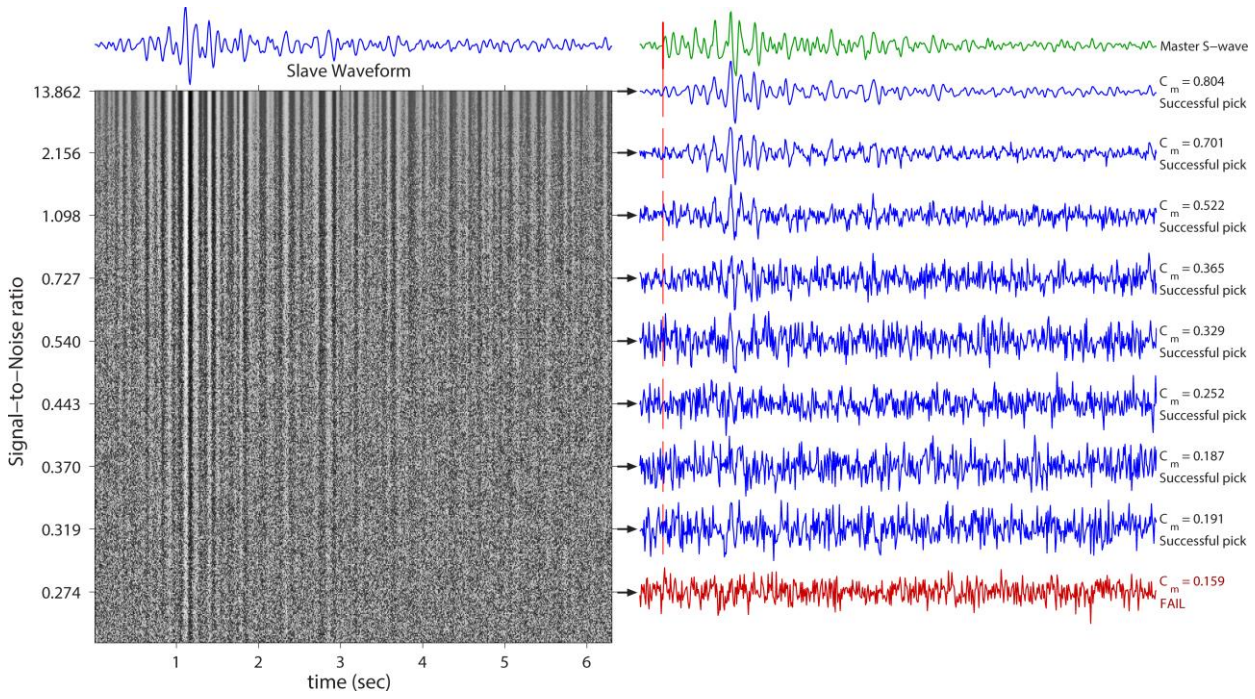

Figure 4.14: Testing of the picking algorithm on the S-waves of a master/slave pair with the addition of different levels of high-frequency Gaussian noise. The uncontaminated slave-waveform is shown on top of the matrix presented on the left part of the panel. The matrix shows the waveform amplitudes (white for positive, black for negative values, gray is zero) of the slave waveform as it becomes increasingly contaminated by Gaussian noise. Horizontal axis represents time while the vertical one denotes the signal-to-noise ratio of selected examples whose waveforms are plotted on the right. At the right side of each waveform the resulting C_m value is presented along with an indication of success or failure of the picking algorithm with respect to the correct pick time (with sample precision). Figure after Kapetanidis & Papadimitriou (2011).

The total results of this test are presented in Fig. 4.16 where it is shown that the C_m, M_{coh} and D_{max} values decrease fast as the SNR is lowered (note that the horizontal SNR axis is logarithmic). It is noteworthy that the correlation detector is still able to pick the arrival-time correctly for SNR values down to about 0.250, which can be considered as the margin of "excess noise" for the purpose of the ME methodology. However, as the C_m, M_{coh} and D_{max} values can become very low for high levels of noise the combined observation weight of such picks will force the algorithm to reject the measurement, leading to a "miss". Failure to pick the correct arrival-time such as the bottom waveform of Fig. 4.14 is due to small D_{max} value (below 0.1) which means that the global maximum of the cross-correlation function is comparable to the secondary maximum. In other words: either of these maxima could point to the correct pick, but the algorithm is unable to distinguish the right one. Some other interesting characteristics of the behavior of the parameters plotted in Figs 4.16a,b are the low effect of noise on their uncontaminated values for SNR up to ~3 while they decrease more rapidly down to about 0.250. The C_m and M_{coh} values appear to intersect at $SNR \cong 1$. It is interesting to note that in the case of contamination with low-frequency (smoothed) Gaussian noise (Figs 4.15 and 4.16b), the M_{coh} values are not affected as much as with the high-frequency one (Figs 4.14 and 4.16a). That is because the M_{coh} is calculated between 2Hz and 15Hz while the noise used in this test mainly affects lower frequencies. The D_{max} has a similar behavior as C_m, which is expected due to their dependence, maintaining values between 0.150 and 0.250 smaller than C_m.

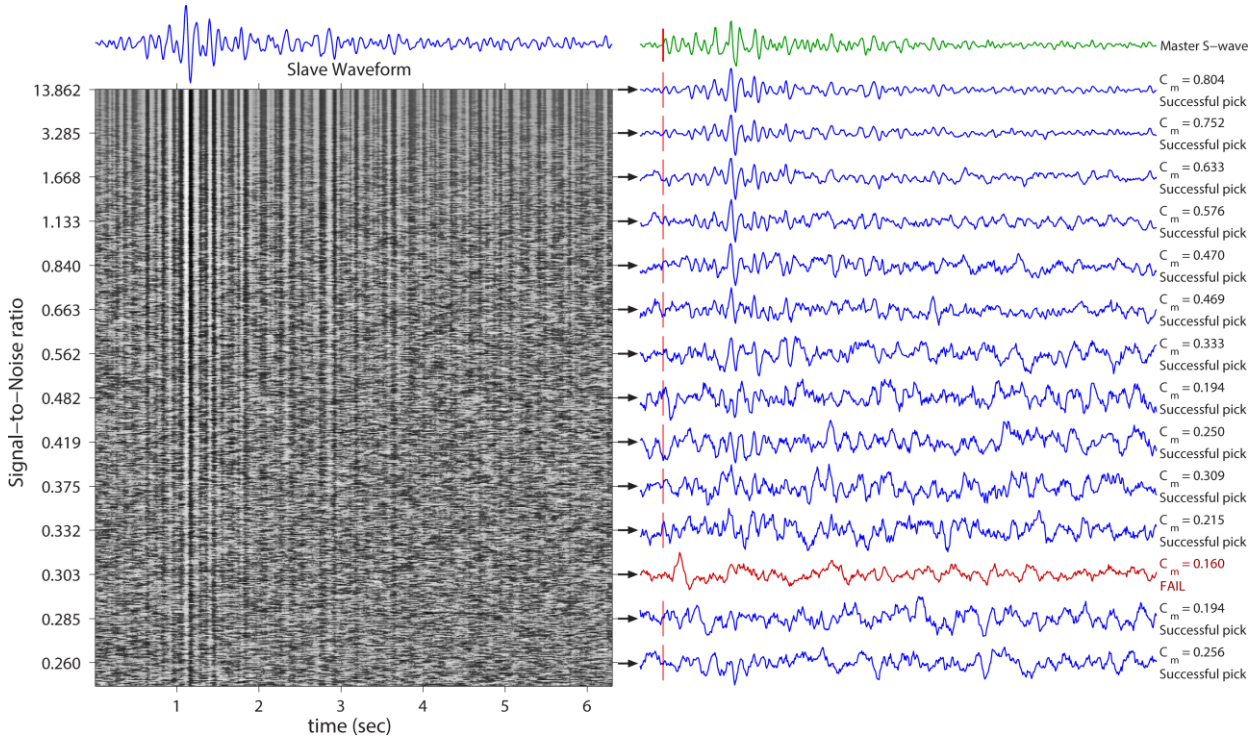

Figure 4.15: Same as Fig. 4.14, but using low-frequency (smoothed) rather than high-frequency Gaussian noise. Figure after Kapetanidis & Papadimitriou (2011).

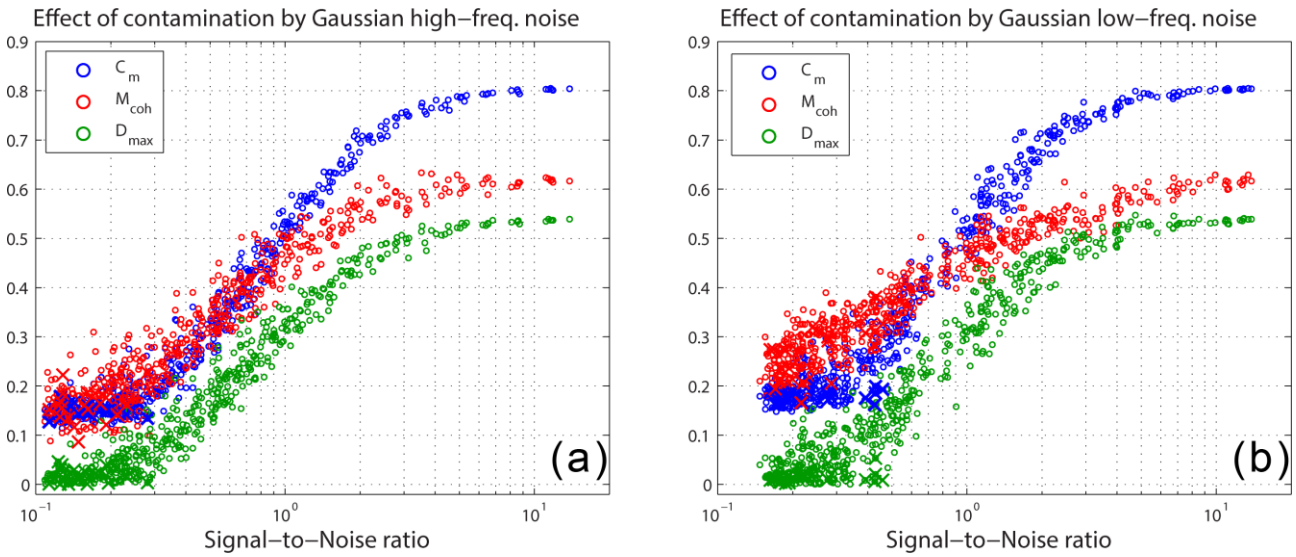

Figure 4.16: Values of C_m, M_{coh} and D_{max} for the tests with addition of (A) high-frequency and (B) low-frequency (smoothed) Gaussian noise shown in Figs 4.14 and 4.15 respectively. Horizontal axis indicates the signal-to-noise ratio. Cases for which the picking algorithm failed to identify the S-wave are indicated with "X" symbol (for low signal-to-noise ratio). Figure after Kapetanidis & Papadimitriou (2011).

4.3.4 Internal consistency of picks within a multiplet

Internal consistency between automatic picks of slave-events can decrease in cases of successful picks using different or multiple master-events, as there can be small variations between observations due to the scatter in the manual phase picks of master-events with respect to the similar part of their waveforms. This is presented in Fig. 4.17 where the waveforms from a sample of 14 slave-events are cross-correlated against each other and a set of master-events, all taken from the same multiplet. Fig. 4.17a shows the S-wave windows recorded at the E-W component of station KALE, as they were more pronounced on that horizontal direction. The temporal alignment of all the waveforms was performed by cross-correlating each of them with the master-event waveform #15 (drawn with thicker line than the rest) and subtracting the time-lag that corresponds to the cross-correlation maximum. This calculation was done with sampling interval accuracy (0.01 sec for station KALE).

The manual pick of the selected master-event (#15), shown with a short vertical thick line at the beginning of the waveform, was then imposed on the slave-events, as shown with the dashed vertical line extending above the manual pick of the #15 waveform. Below the selected master-event (#15) there are the waveforms of a few more master-events (#16 up to #20). Fig. 4.17b shows the cross-correlation matrix between all combinations of the waveforms of Fig. 4.17a, while the anti-symmetric matrix 14c represents the respective time-lags, t_m, of the XC_{max} in each case. The time-lags have been calculated with sub-sample accuracy of 1ms by fitting a parabola around the global maximum of the cross-correlation function with increased sampling rate as proposed by other authors (Deichmann & Garcia-Fernandez, 1992; Schaff *et al.*, 2004). They also include the difference of the arrival-time picks between pairs of waveforms using the time-scale shown in Fig. 4.17a.

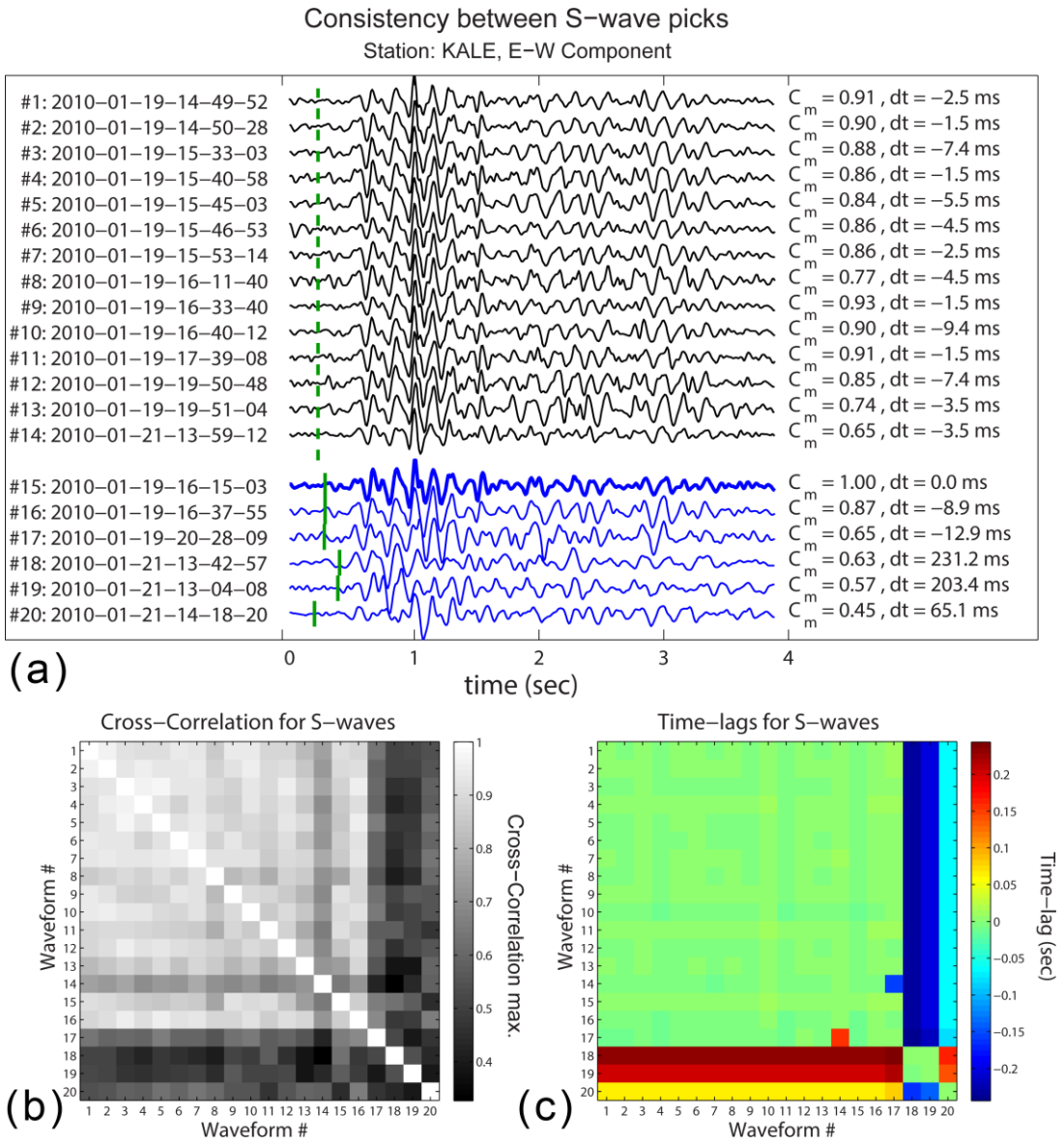

Figure 4.17: Consistency between S-wave picks. a) 14 waveforms (#1-14) belonging to slave-events and 6 more (#15-20) belonging to master-events of the same multiplet, temporally aligned by cross-correlation with #15. Relative arrival-time picks are marked with thick vertical lines at the beginning of each waveform. The dashed vertical line extending from master-event #15 to the above slave-event waveforms #1-14 is the automatic pick imposed using the ME methodology. The C_m value on the right of each waveform is the maximum correlation coefficient and *dt* is the corresponding time-lag including the relative arrival-time difference. Time-stamps on the left of each waveform are rough estimates of the P-wave arrival-time on station KALE, b) The cross-correlation matrix for waveforms shown in panel (A), c) The time-lag matrix showing the values of time-lag of the cross-correlation maximum for the corresponding elements of the matrix in panel (b), taking into account the relative arrival-time differences from panel (a). Figure after Kapetanidis & Papadimitriou (2011).

It is noteworthy that although the slave waveforms are not equally similar with one another, as seen by the variations in the top-left 14x14 square in Fig. 4.17b, their internal consistency is very high, as presented in the corresponding 14x14 square of Fig. 4.17c, where all the absolute time-lag values are below 0.01sec. The values of $XC_{\max}$ for the selected master-event waveform #15 against the rest

is shown as "C_m" at the right side of the waveforms in Fig. 4.17a, along with the respective time-lags, *dt*, which include the relative arrival-time differences. Negative time-lags correspond to earlier relative arrival-times with respect to the one of the master-event waveform #15, while positive time-lags represent later relative arrival-times. Essentially, the C_m and *dt* values shown in Fig. 4.17a are taken from the row #15 of the matrices in the corresponding panels b and c respectively. The waveforms of event #16 are very similar to those of the selected master-event #15 and the relative arrival-times are also very close (*dt*=-22.8ms). As a result, the picks that would be imposed on the slave-events if #16 was used would also be very close to those derived by using #15.

The other master-event waveforms appear to have more significant differences. The values in the cross-correlation matrices are smaller (darker colours for rows or columns #17-20 in Fig. 4.17b), but also, because of the scatter of their manually picked arrival-times, there is a systematic difference in relative arrival-times between these master-events and the slave-events, which is shown with horizontal and vertical stripes of increased absolute time-lag values in Fig. 4.17c. This suggests that, although automatically picked arrival-times for slave-events may have very strong internal consistency with small differences being revealed using cross-correlation with sub-sample precision, manually picked arrival-times are expected to have much larger differences of the order of 10ms or 100ms. These differences are also highly dependent on the epicentral distance of the station, as in far stations the manual picking error may easily reach the order of seconds due to the arrivals of head-waves or converted phases, as well as the generally longer wavelengths and likely filtering artifacts.

4.4 Hybrid Automatic Detection and Association of Earthquake Signals (HADAES)

The Master-Events methodology (Section 4.3) involves a semi-automatic algorithm that can provide arrival-time picks for large numbers of small events. It takes advantage of both the accuracy of manual arrival-time picks on master-events and the statistical similarity of the aftershocks waveforms in order to automatically duplicate the manual picks the slave-events. Ideally, the accuracy of the arrival-time picks on the slave-events is equal to that of the manually picked arrival-times of the master-events, but in practice it also depends on the filters used before the correlation of waveforms, as well as the ability of the algorithm itself to distinguish signal from noise and reject erroneous observations. The main disadvantage is that it can only be used for events with very similar waveforms in all the stations which are included in the procedure. On the other hand, a fully automatic picking algorithm can only work for events with sufficient SNR in at least a minimum of 4 stations, as long as the picks can be associated with a common origin. The AIC-picker presented in Section 4.2, despite its ability to detect wave onsets with low SNR, requires proper guidance for the expected arrival-time, which means that the approximate origin should be somehow defined prior to the actual picking.

In this section, a modification and generalization of the main idea behind the MEm described in Section 4.3 is developed and presented, in a way that can be applicable to a larger amount of detected signals. This is done by requiring similarity only at the reference station(s), to which the

ME method is applied, exploiting the full advantages of SSD, while the respective P- and S-wave arrival-times in a set of Stations of Interest (SoI) are estimated by travel-times which are transferred as meta-data from the master-events to the associated slave-events (SE), or target-events. At the same time, hypocentral information is passed to the SE as a first approximation, while a relative magnitude is also determined by comparing the amplitudes between the ME (with known magnitude) and SE, supposing a common hypocentral distance and focal mechanism. The approximate origin and travel-times for the SE provide a rough estimate for P and S arrival-times at the SoI. Targeted automatic picking can then be applied in a window around these approximate arrival-times. The modification of the Auto-Regressive Akaike's Information Criterion (AR-AIC) presented in Section 4.2 is proposed for the automatic picking of P- and S-wave onsets, as it incorporates information on skewness, kurtosis and SNR to aid the onset detection and provide additional weights.

The algorithm developed and presented in this Section is aptly named "Hybrid Automatic Detection and Association of Earthquake Signals" (HADAES), as it combines: a) SSD (Section 4.1) and meta-data from other-stations, b) a correlation detector (Section 4.3.1) and a more conventional automatic picking technique (Section 4.2) and c) relative magnitudes for the slave events, calibrated by the local magnitudes of the master-events (Section 4.4.4). The main issues with the implementation and application of this method is the sheer amount of information and generated data, which require a great deal of organization and optimization to make their processing feasible without demanding large memory and long processing time. When the reference station is sufficiently close to the epicentral region, the magnitude of completeness of the detected events can easily drop below zero, while the number of resolvable earthquakes can increase by more than 10 times compared to the used ME. For the distribution of the processing into smaller subsets, the event-detection and correlation detector procedures are performed on a daily basis within day-specific (DS) multiplets. Each multiplet is characterized by a reference waveform that is defined by a weighted stack of the individual events that it contains. DS multiplets that have been formed on subsets of different days are later grouped into larger families either by their relation to common ME or by similarity in their reference waveforms.

An overview of the basic procedures is presented in Fig. 4.18. The workflow begins at the database of the available 24-hour waveform data. The upper half of Fig. 4.18 concerns a portion of significant events which should be manually analysed. A subset of events, which comprise the master-events, is selected inside the defined Area of Interest (AoI). Travel-time (TT) information on a set of Stations of Interest (SoI) is used as metadata that is transferred later to the slave-events during the event association. The top part of Fig. 4.18 concerns the selection of "External Master-Events" (M_{ext}) for the whole timespan; a list of ME which are global (they span along the whole period of study), as opposed to internal master-events (M_{int}) which are all ME that have occurred during a certain day in the Day-Specific (DS) procedures of the lower half of Fig. 4.18. For the latter, the 24-hour waveform data at the reference station are scanned for signals through an STA/LTA procedure and a DS cross-correlation matrix is constructed from which DS multiplets are obtained through nearest-neighbor linkage. The next procedures are day-specific, but also "multiplet-specific", executed individually for each multiplet created from the DS cross-correlation

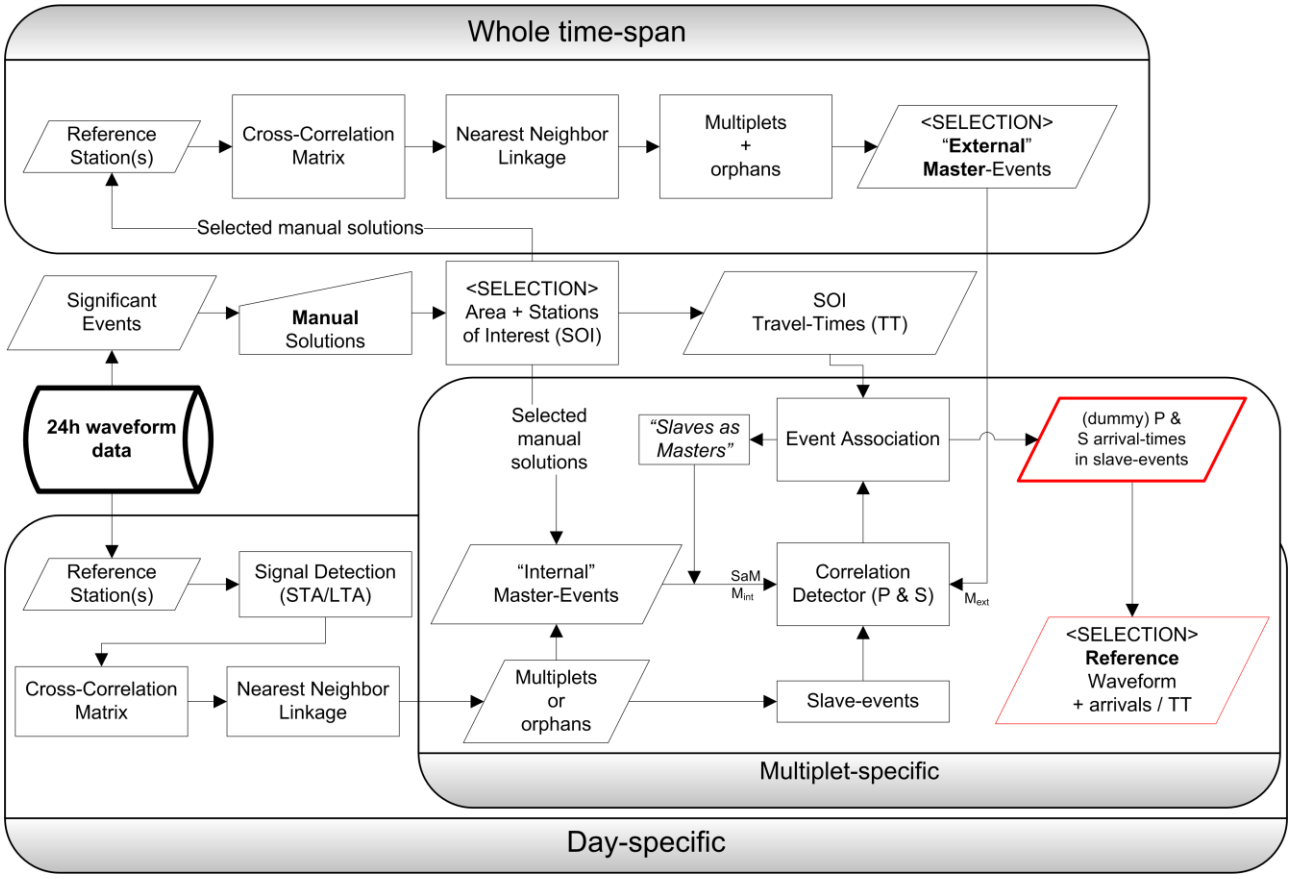

Figure 4.18: Flow-chart of the primary day-specific procedures: from a database of continuous 24-hour waveform recordings and manual solutions of the more significant events to the association of (dummy) arrival-times in slave-events correlated with at least one master-event (more details in the text).

matrix. Those signals which correspond to M_{int} are assigned their respective meta-data which have been defined through manual analysis (arrival-times at the reference station and other SoI, TT, hypocenter, origin time and magnitude). The rest of signals are treated as "slave-events" (SE). Internal masters (M_{int}) along with all external masters (M_{ext}) are used as templates for the correlation detector procedure, which propagates the P and S-wave arrival-time picks to the primary slaves. Meta-data are also passed to the SE, such as approximate hypocenter and origin time, approximate travel-times to SoI, all based on relative times with respect to the picks defined by the correlation detector, as well as relative magnitude (Event Association). Equipped with this information, the associated SE can then be used as an ME (Slaves-as-Masters, or SaM) to propagate picks and meta-data to higher order SE. Event association creates a set of "dummy" catalogue data for each multiplet which can be represented by a "Reference waveform" with its own meta-data information, that can be either an event with the highest SNR, or the one with the most direct relatives within its multiplet or a stacked waveform with averaged travel-times and approximate meta-data. These reference waveforms are later used to link a DS multiplet with a larger family of multiplets that may be defined during different days (cross-day procedures) of the study period (Section 4.4.5). More details on the various procedures are described in the following sub-sections.

4.4.1 Preparation – signal detection – multiplet classification

The preparatory stage of the HADAES method involves the selection of an Area of Interest (AoI), reference station (R_{st}) and other Stations of Interest (SoI). Signal detection is performed on the R_{st}, using the method described in Section 4.1. Only the vertical component of an R_{st} is used in all procedures from signal detection to event association, while the horizontal components are only used for the automatic picking and for the final cross-correlation stage for relocation with HypoDD (Waldhauser, 2001). The recordings are processed in 30-minute-long buffers with a small overlap. The waveform segments are band-pass filtered to remove long period and high-frequency noise. Care must be taken to smooth-out any possible data-gaps and spikes which would seriously affect both the signal detection and cross-correlation procedures (Appendix 4A).

The detected signals are initially unclassified. It is unknown whether they are earthquakes or noise which could have been generated by local human activity or other environmental factors. Even if they are earthquake signals, it is uncertain whether they are related to the defined Area of Interest or they have originated elsewhere. In the HADAES methodological approach, all procedures described in the current section are performed on a day-specific (DS) basis, to ration the amount of data that has to be loaded in memory and reduce processing time. A day-specific, symmetrical cross-correlation matrix, $\boldsymbol{XC_m}$, is constructed by applying Eq. 1.2 for all combinations of the detected signals. Afterwards, a nearest neighbor linkage is performed on the matrix data and multiplets are formed by selecting an appropriate correlation threshold (Section 1.2.2).

During intense earthquake sequences, a significant percentage of the detected signals will tend to be grouped in multiplets due to repeated stress release at the same asperity, or stress concentration, at the same patch of a fault plane (Geller & Mueller, 1980; Poupinet *et al.*, 1984; Bourouis & Bernard, 2007). However, most multiplets are of small size (e.g. with less than 5 events each). Some signals will not be included in any of the DS earthquake families, thus they can be called "orphans". This, however, does not rule out their possible similarity with events that have occurred on different days. Indeed, repeating earthquakes may persist for days and even recur after several months or even years (Petersen, 2007; Cannata *et al.*, 2013).

4.4.2 Master-Events

The notion of using manually located events with strong signals in a reference station (R_{st}) to detect smaller events with similar waveforms has been adopted in previous studies for semi-automatic picking (Kapetanidis & Papadimitriou, 2011), to detect earthquake families (Hotovec *et al.*, 2013; Junek *et al.*, 2014) and to correct automatically or manually detected phase-arrivals (Rowe *et al.*, 2002; Eagar *et al.*, 2006; Okubo & Wolfe, 2008). The master-events (ME) are typically manually located, significant events with well-recorded waveforms in one or more reference stations, coupled with meta-data of P- and S-wave travel-times in a set of Stations of Interest (SoI), within or surrounding the Area of Interest (AoI), as well as seismic source parameters such as origin time, hypocenter and magnitude. The goal is to find matching ME for each of the detected multiplets and associate their meta-data, after appropriate modifications, to slave-events (SE) with previously unknown information. This provides a set of arrival-times acquired from the direct cross-correlation

of the master to the slave waveforms, in the same sense as in Kapetanidis & Papadimitriou (2011), but will also make available approximate arrival-times to the other SoI. The estimates can be used for a guided auto-picking procedure such as the one presented in Section 4.2. It is recommended that the selected set of manually analysed events be relocated prior to the application of the HADAES method, as their hypocentral locations are used for the determination of "dummy" hypocenters for the associated slave-events in the draft catalogue.

In the generalized methodology presented in this section, the multiplets are primarily formed on a DS basis. This means that, on a first level, for a certain period which could span for several days, the total number of ME required to cover even the bigger multiplets could be exceedingly large. The ME which are found to belong to multiplets that have been formed on the same day are called "Internal" Master-Events, or M_{int}. A possible solution to overcome the aforementioned issue would be to cross-correlate all events within each DS multiplet without a M_{int} to all ME which have occurred on different days and attempt to find a match. Although in principle this is possible, in practice it would be computationally heavy when the database of manually located events in the AoI is large. To optimize this procedure, a cross-correlation matrix is constructed for the wave recordings of the manually located events in the R_{st} for the whole period of study (upper part of Fig. 4.18) and, by applying nearest neighbor linkage and selecting the optimal threshold (Section 1.2.2), multiplets are formed for the manual events. Afterwards, a "reference event" is selected for each of these master-multiplets, as explained in more detail in Section 4.4.5. It is important that these events have a high chance of being directly similar to other events in the same multiplet (and, likely, to an even larger number of SE), thus a criterion for their selection is that they have the largest number of direct relatives (above threshold) or the highest mean cross-correlation value in the matrix (Petersen, 2007). Orphan ME are not discarded, as they may still be similar to several of the smaller events which have been detected. The selected subset of manually analysed and located events forms a database of "External" Master-Events, or M_{ext}.

Links between M_{ext} and DS multiplets without a M_{int} are formed by constructing an asymmetrical cross-correlation matrix, with rows representing the events of the multiplet and columns corresponding to all M_{ext} candidates. A M_{ext} is defined for the multiplet if an element in the matrix is found with its XC_{max} above a minimal threshold value. A higher threshold is sought (e.g. the optimal for the multiplets of a specific day) if many M_{ext} are found, so as to keep only the more similar ones, while a lowest threshold value, e.g. C_{th}=0.5, is applied as a last resort.

4.4.3 Direct event-association

Once the master-events have been defined for a multiplet, either M_{int} or M_{ext}, the critical part of the ME method follows. The procedures described in this section are applied on a per-multiplet basis. For each ME, the P- or S-waveform windows must be cropped, tapered with a Tukey window and saved in the memory. P-waves are cut 1 sec before and 5 sec after their arrival-time at the R_{st}, unless the S-wave arrives earlier, in which case the right end of the window is cut 0.1 sec before the S-wave arrival. During the formation of multiplets, the portion of the DS cross-correlation matrix, $\boldsymbol{XC_m}$, that refers to the signals grouped in a single multiplet can be put together in a partial cross-correlation matrix, $\boldsymbol{C_p}$. The trigger-times, which, in case of an earthquake event, roughly correspond

to P-wave arrival-times, are compared to the manually picked P-wave arrival-times of M_{int} events of the same day. If matching arrivals are found, the corresponding M_{int} are defined for a multiplet. The other events in the multiplet are then called "Slave-Events", or SE.

Given that there is at least one M_{int}, the similarity between M_{int} and SE is already known from $\boldsymbol{C_p}$. By definition, there has to be at least one SE with cross-correlation value $XC_{max} > C_{th}$ with each M_{int} (direct relatives). The picking technique described in Section 4.3.1 is applied in the following stage. The correlation detector "carries" with it the information of the manually picked, relative arrival-time of the P- or S-wave on the master-waveform. When the C_i exceeds a threshold and maximizes at a value C_m, the pick is transferred from the ME to the SE and imposed as an arrival-time, T_P or T_S, of the corresponding wave-type, P or S, respectively, on the SE. The T_S is defined first and in case of a strong correlation (above a threshold) the T_S sets a limit for the search region of the P-wave correlation detector in order to prevent an invalid situation where $T_P > T_S$.

In the HADAES method, a third correlation detector is performed between ME and SE, this time using a strict window on the P- and S-waves of the ME instead of its broader version which had been used in the C_p. Its purpose is to approximate both P- and S-wave arrival-times, T_P^* and T_S^*, at the SE, on the hypothesis that the S-P arrival-time difference, $T_{S\text{-}P}$, is the same in both ME and SE. This is true when the two hypocenters are very close, but there is a tolerance in its variation which does not severely affect the overall XC_{max}. While the shorter P- and S-wave correlation detector windows can account for the different $T_{S\text{-}P}$, they are prone to erroneous fits in different wave-types, wave-coda or may even, sometimes, correlate with noise, because of their smaller sample size. The short-window picks, T_P and T_S, are compared to the full-waveform picks, T_P^* and T_S^*, and are allowed to differ up to some threshold value, e.g. ±1 sec, while the condition $C_m > 0.5$ is also checked, otherwise the corresponding short-window picks are rejected. If both partial P and S fits are discarded and no other candidate ME are available for a particular SE, the S-wave arrival, T_S^*, according to the full-waveform fit, is imposed on the SE instead. The S-wave is preferred as it usually dominates the cross-correlation in a full-waveform fit, because of its usually larger amplitudes and longer coda than the corresponding P-waves which may not fit well, depending on the $T_{S\text{-}P}$ difference between ME-SE. This extra correlation also yields another C_m value, which is compared against a fixed low-threshold, e.g. 0.5, and ME-SE matches of low correlation are rejected. This can happen, for example, when the broader version of the ME actually contains overlapping signals from 2 earthquakes, while the shorter version doesn't and the C_p value was referring to a similarity of the SE with the other signal. At this point, relative magnitudes can be calculated for the SE using the method described in Section 4.4.4.

The M_{int} cannot be used to directly associate arrival-times in all the SE of a multiplet, as nearest neighbor linkage enables events with indirect similarity (via intermediates) to be grouped in the same cluster. Thus, the SE which were directly matched to the M_{int} have to be used as master-events against their own direct relatives, a procedure briefly called "Slaves as Masters", or SaM. There is a risk of error propagation and accumulation in SaM of higher order (Kapetanidis & Papadimitriou 2011), however, the application only in the R_{st} combined with strict windowing in P- and S-waves, rejection of problematic correlations and comparison with arrival-times of the full-waveform match ensures an adequate quality of the fits, even at the cost of a few SE. The ME constructed by the

SaM procedure also contain relative magnitude information (Section 4.4.4), which can be used as M_L in Eq. 4.12 to provide relative magnitudes for SE of higher order.

Orphans are treated as a special group. An asymmetrical cross-correlation matrix is constructed between them and constrained windows of P- and S-waves for M_{int} and M_{ext}. They are examined against a threshold which can be lower than the optimal C_{th} (but down to a minimum of 0.5) to provide a better chance of a fit. It is worth noting that some of the manually located events, especially those of larger magnitude, may be included as a signal in the list of orphans.

Each of the P- and S-wave arrival-time picks acquired by the ME procedure are then translated to meta-data. Approximate origin times, OT^*, can be estimated by subtracting the corresponding P- or S-wave travel-times of the ME at the R_{st}, while arrival-times of the waves to the other SoI are obtained by adding their corresponding travel-times of the ME to the OT^*. In case there are multiple measurements, a weighted mean value is considered, using the correlation maxima (C_m) as weights. The mean correlation coefficient derived by the P- or S-wave fits is registered as a quality, Q_s, of the corresponding "dummy" solution. While the automatic picks in the R_{st} were obtained according to a simplified version of the ME method (Section 4.3), the arrival-times estimated for the other SoI are only "dummy" arrivals and require corrections which are made at a later stage with the application of the targeted automatic picking algorithm of Section 4.2.

Differences in the S-P arrival-times between a SE and its respective ME indicate an offset in the SE hypocenter relative to the ME either due to different epicentral distance from the R_{st} or different focal depth. The offset can be estimated by assuming a constant P-wave propagation velocity, V_p, at the roughly common source and a constant V_p/V_s ratio which enables the calculation of an "effective" (radial) inter-event distance D_d between ME and SE hypocenters, ignoring the "tangential" component with respect to the R_{st}. If the D_d is purely due to a difference in focal depths, the corresponding travel-time differences for the other stations can be estimated geometrically, given the known ME and SoI coordinates. The travel-times in stations which are closer to the epicenter will be more affected by a change in focal depth than the distant ones, but, in this approximation, the changes in all stations are going to have a common sign. However, differences in horizontal location are harder to account for, as there may be an unknown tangential component in the offset, with respect to the R_{st}, and the sign of the offset will depend on the azimuth of each SoI. It is, of course, difficult to automatically decide whether the offset is vertical or horizontal with information from a single station (R_{st}), so to simplify the problem, a vertical offset is considered and travel-time differences in other SoI are adjusted according to their hypocentral distance ratio against the one of the R_{st}. In any case, the differences are not expected to be too large, otherwise they would also greatly affect the cross-correlation maximum (Han *et al.*, 2014), and will most likely be significant only for the closer SoI with small S-P differences.

4.4.4 Relative magnitude

The best fit of either P-, S-wave or full ME waveform to the matching window of the SE waveform has already provided two useful parameters, the XC_{max}, which is used as weight or measure of quality of the fit, and the arrival-time of the P- or S-wave on the SE. But there is still another

important piece of information which can be obtained from the correlation of the two waveforms. The linear correlation coefficient, C_c, is measured on the scatterplot of amplitudes between the two time-series which correspond to samples of the same relative time, with respect to the first sample of the windows. A high value $C_c = C_m$ at the best-fit window translates to a strong linear relation between the amplitude values of the two time-series, which is how the correlation detector works. Given that the two events belong to a multiplet, thus their hypocenter and focal mechanisms are similar, the slope, B_m, given by the linear regression in this best-fit window can provide information about the difference in magnitude between the ME and the SE, something that is not reflected in the C_c which is indifferent of the absolute amplitudes. The local magnitude, M_L, for the ME is known from routine analysis, therefore one can calculate a relative magnitude difference, D_M, from the slope, B_m, and acquire a first approximation for the unknown magnitude, M_{SE}, of the SE using Eq. 4.12 (Yang *et al.*, 2009):

$$M_{SE} = M_L + D_M = M_L + \log_{10}(B_m) \tag{4.12}$$

with the slope or scaling factor, B_m, calculated from the scatterplot of the SE amplitudes (vertical axis) against the ME amplitudes (horizontal), thus $0<B_m<1$ when $M_L>M_{SE}$, which is likely the case, but can also be $B_m>1$ if the ME is of smaller magnitude than the SE. A weighted mean, using the correlation values as weights, is calculated when multiple B_m measurements are available for a single SE. As an alternative method, the value of B_m can be acquired by calculating the covariance matrix of the two time-series, applying singular value decomposition (SVD) and measuring the direction of the eigenvector that corresponds to the major eigenvalue. A robust application of SVD for the joint determination of relative magnitudes in families of highly similar multiplets in California is described by Rubinstein & Ellsworth (2010). It should be noted that the 2.5 Hz high-pass cut-off frequency, f_{HP}, that is applied before the cross-correlation procedures to filter out long period noise is well below the corner frequency, f_c, for events of small magnitude such as those targeted by the HADAES method, a required condition for the successful SVD relative moment calculations by Rubinstein & Ellsworth (2010). It could, however, cause reduction to the amplitudes of some of the larger master-events, which may, in effect, cause over-estimation of the relative magnitude values on their SE. For events with larger magnitudes, the f_{HP} can be lowered to include the f_c for use with relative magnitudes, but this is also acceptable when the SNR is high enough for the signal to be significantly stronger than any background long-period noise or trends. In any case, the results can be cross-checked with an independent procedure for the direct calculation of moment magnitude (e.g. Edwards *et al.*, 2010; Matrullo *et al.*, 2013).

An example of the procedure for the calculation of relative magnitude is presented in Fig. 4.19 for a pair of manually located (master) events. The two full-waveforms, with both P and S-waves, in Fig. 4.19a are aligned at the best-fit window, where the $C_c=C_m$ is maximized ($C_m = 0.72$). The amplitude values of the sample-pairs corresponding to the same relative time are used as coordinates of the points in the scatterplot of Fig. 4.19b. The relatively high C_m value indicates the amplitudes of the two waveforms are characterized by a significant positive correlation. However, the difference

between the known local magnitudes of the two events is $D_M = M_2 - M_1 = 2.3 - 1.2 = 1.1$. This translates to a tenfold difference between the amplitudes, which is already evident from the scale of the *x*- (~10^4) and *y*-axes (~10^5) in Fig. 4.19b. The exact relation can be measured by the slope, B_m, of the scatterplot. This measurement has been attempted in 6 ways. The dashed straight line in Fig. 4.19b has been determined by the least-squares linear regression method (LSQR), taking into account all data points, resulting in an underdetermined $D_M = \log B_m = 0.96$. A different way to measure this relation is via the direction of the major eigenvector of the covariance matrix, estimated by SVD. This is visualized by the dashed ellipsoid that corresponds to the 80% confidence interval region. Note that the ellipse is distorted due to the large difference in the scale of the axes and the direction of its major semi-axis is slightly different from what appears visually. This direction corresponds to an overestimated magnitude difference $D_M = 1.25$. Both results by the LSQR and SVD methods are affected by a large number of low-amplitude samples for which the correlation is not necessarily as high as for the higher amplitude samples, contributing to noise

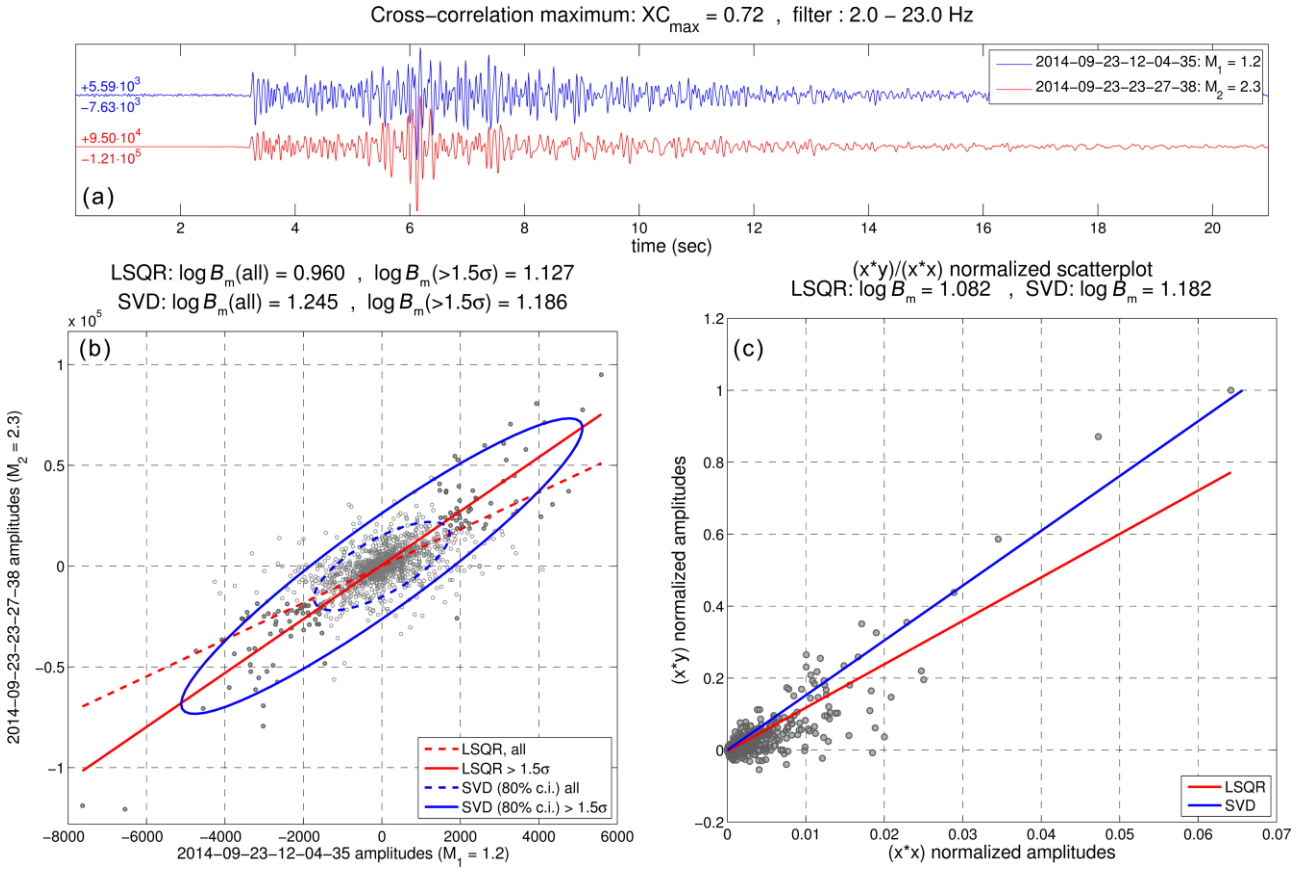

Figure 4.19: (a) A pair of normalized, similar waveforms with manually calculated local magnitudes M_1=1.2 and M_2=2.3, respectively. Numbers at the left size denote the maximum (top, positive) and minimum (bottom, negative) amplitude values of each waveform. (b) Scatterplot of amplitudes of the bottom waveform of panel (a) against those of the top one for the calculation of relative magnitude difference, $\log_{10} b$, where b is the slope, calculated in 4 ways. Dashed lines correspond to the least squares linear regression and the 80 per cent confidence interval ellipse (small one) for all the samples of the scatterplot while solid line and ellipse are for a selected set of measurements with amplitude above 1.5σ of the distribution. (c) Same as (b) but for normalized (x·x) and (x·y) values (see text for details).

that affects the measurements. To prevent this, a set of samples with amplitudes above a threshold of the order defined by the standard deviation is selected (solid circles in Fig. 4.19b). The solid straight line and ellipse correspond to the LSQR and SVD measurements for the selected samples with amplitudes >1.5σ. Interestingly, the magnitude differences are perturbed closer to the correct D_M = 1.1. An alternative approach is suggested by Gibbons & Ringdal (2006) and Slinkard *et al.* (2014) who make a first estimation of the slope from the distribution of $x(t)*y(t)$ against $x(t)*x(t)$ (hereafter mentioned as *xy*/*xx* data), with $x(t)$ and $y(t)$ representing the amplitudes of the first and

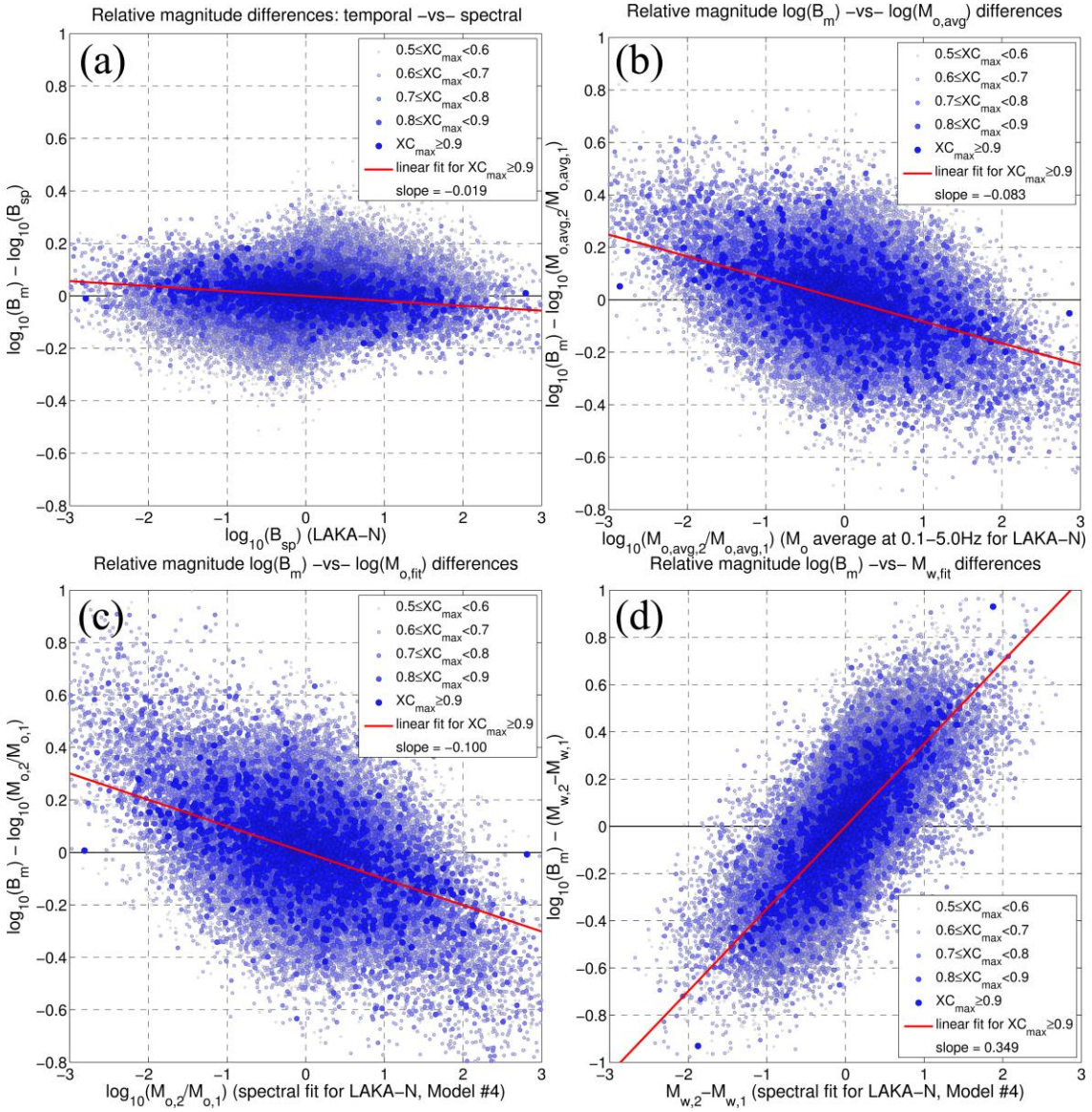

Figure 4.20: Relations between the relative magnitude difference, log(B_m) determined from xy/xx by SVD, and its spectral counterparts for repeating earthquakes of the 2013 Helike swarm dataset (Section 5A.4) measured at the N-S component of station LAKA: a) log(B_m) with respect to log(B_{sp}), calculated from the ratio of the average spectral amplitude between 1 and 8 Hz (simple FFT), c) log(B_m) relative to log($M_{o,2}/M_{o,1}$) of the averaged moment spectra, corrected for SRF, between 0.1 and 5 Hz, d) log(B_m) with respect to log($M_{o,2}/M_{o,1}$) from spectral fit using Model #4 (Section 3.3) and d) log(B_m) with respect to ΔM_w for spectral fit data as in panel (c).

second waveform, respectively. This is visualized in Fig. 4.19c, with the values being normalized by the maximum of $|x(t)*y(t)|$ and $|x(t)*x(t)|$. For the direction of the major eigenvector via the SVD method, the symmetrical data points with respect to the point (0, 0) are also used in the calculation. With this alternative technique, the LSQR method gives the closest result (1.08) to the expected D_M = 1.1, while the slope determined by the SVD method is similar to the one for $y(t)$ against $x(t)$ for amplitudes > 1.5σ. This indicates that the recommended method is LSQR in a scatterplot of *xy*/*xx* data, which can easily be applied in shorter time-series too. However, a wider sample of measurements with more event-pairs is required to investigate possible biases and deviations of relative magnitudes from manually determined ones. This is examined in the case study of Section 5.4 (Appendix 5B).

The relative magnitude can also be measured in the frequency domain, in the form of spectral ratio between two repeating earthquakes. As described in Chapter 3, the displacement spectrum is expected to exhibit a pattern of constant amplitude at the lower frequencies and the scalar seismic moment can be determined from the level of that plateau. A spectral ratio between two repeating earthquakes should remove all effects of instrument response, integration ($1/i2\pi f$ factor) as well as radiation pattern and attenuation effects, which are expected to be similar, since both events originate from the same focal area. On the other hand, the level of the spectral ratio at the frequencies of the displacement's plateau should be the equivalent to the B_m value as determined by LSQR or SVD in the time domain. Instead of calculating the spectral ratio for each event-pair, a faster method is to measure the average value of the velocity spectrum in the same way as the average M_o for $M_{w,avg}$ in Chapter 3, then calculate the ratio between the two average values, B_{sp}, which can be used as an estimate for B_m in the frequency domain. Indeed, Fig. 4.20a shows a comparison between B_m and B_{sp}, whose difference is very small even when the two events are separated by many orders of magnitude, although these two values have been determined in a different way. Note how the dispersion increases at smaller XC_{max} values. Similar results but with larger deviation (Fig. 4.20b) are derived if B_m is compared to the M_o as measured from the weighted average of the SRF-corrected spectral amplitudes in the range 0.1-5.0Hz, the equivalent of $M_{w,avg}$ (Chapter 3). This is somehow expected, as $M_{w,avg}$ is determined as an average in a modified spectrum, having passed through deconvolution of instrument response, integration, SRF correction and using a set of spectral weights that mainly depend on the $SNR(f)$. Also, $M_{w,avg}$ as well as the spectral fits are measured in the S-wave spectrum, whereas B_m in this example is determined using the full signal (P- and S-wave) on a single horizontal component. The difference becomes more significant when B_m is compared to $M_{o,fit}$ (Fig. 4.20c), derived from the fitting procedure, e.g. using Model #4 (Section 3.3). The difference is even larger in measurements taken from a short-period station (e.g. TEME), similarly to the differences between $M_{o,fit}$ and the equivalent M_o of $M_{w,avg}$, with M_w from the fitting procedure generally having slightly larger values than $M_{w,avg}$. With all other parameters of Eq. 3.10 being the same for both event pairs, thus being cancelled when the ratio is taken into account, the hypocentral distance factor, R does not significantly affect the scaling relation between B_m and M_o, as it only increases the variance rather than the scaling itself, due to the introduction of location uncertainties. The most significant discrepancy is found between the difference in M_L, as expressed by $\log(B_m)$, and the respective difference in M_w, as the latter is:

$$\Delta M_w = \frac{2}{3}\left(\log_{10} M_{o,1} - 9.1\right) - \frac{2}{3}\left(\log_{10} M_{o,2} - 9.1\right) = \frac{2}{3}\log_{10}\frac{M_{o,1}}{M_{o,2}} \quad (4.13)$$

while the various formulae for M_L or M_S (e.g. Kiratzi & Papazachos, 1984) include log$A$ (where A the maximum displacement) multiplied by unity and a function of distance that is cancelled due to subtraction, in case of repeating earthquakes. This means that there is a 2/3 scaling expected between ΔM_w and $\Delta M_L = \log_{10}(B_m)$, which is reflected in Fig. 4.20d. Ideally, if it was $\log_{10}(B_m)=\log_{10}(M_{o,2}/M_{o,1})$, the slope in Fig. 4.20c would be zero. Even so, the "double difference" $\log_{10}(B_m)-\Delta M_w$ would be 1-2/3=0.333 due to Eq. 4.13, which is close to 0.349 in Fig. 4.20d.

4.4.5 Indirect associations (cross-day procedures)

While the DS approach can yield a large number of associated SE, especially on the first days of an earthquake crisis, many events which practically belong to multiplets that were generated on previous days may remain unassociated due to the lack of a M_{int} or M_{ext} with direct similarity to one of their SE. As with similar methodologies in the literature (Rowe *et al.*, 2004; Thelen *et al.*, 2010; Rodgers *et al.*, 2013), the HADAES method includes cross-day / family links between multiplets, which enables the use of M_{int} from clusters of different days (not included in the M_{ext} subset) or even associated SE of previous days which can be used as ME.

For each multiplet, the event with the largest peak-to-peak amplitude in its waveform is initially considered as a "primary" Reference Event (RE). In associated multiplets, an extra criterion is used in case there is no solution (meta-data) linked to the event of largest amplitude or its Q_s value (mean correlation; Section 4.4.3) is below a threshold. In that case the SE with an available solution, Q_s value above threshold and the largest amplitude is considered as a RE. Alternatively, if a M_{int} is available in a multiplet it can directly be considered as a RE, as long as it does not belong to the M_{ext} subset, which would render it redundant. Orphans are treated as RE of their own.

Stacking techniques have been used in many relevant studies (Rowe *et al.*, 2004; Okubo & Wolfe, 2008; Thelen *et al.*, 2010; Cannata *et al.*, 2013; Rodgers *et al.*, 2013) for the construction of reference waveforms (or master-events, or templates). Stacking can be particularly useful in cases of event-detection with seismic arrays (Schimmel & Paulssen, 1997; Gibbons & Ringdal, 2006). While this is efficient when the degree of similarity between waveforms is high (e.g. XC_{max}>0.9), working with relatively low correlation thresholds (~0.5) and nearest neighbor linkage can introduce pairs of events with low similarity even within the same multiplet. The observed effect of partial similarity in P- and S-waves but different $T_{S\text{-}P}$ is also a problem to full-waveform stacking, which can result in a linearly (same weights in all samples for all events) stacked waveform of lower SNR than the one selected with the abovementioned criteria in each multiplet. Other problems may occur when a window actually contains the superposition of waves from two or more earthquake events, with (at least) one of them being similar to those of a corresponding multiplet. As a result, a stacked reference waveform may actually be less effective in being similar even to other waveforms within the same multiplet than a single waveform may be.

However, there are ways to gain the positive benefits of stacking while reducing these side effects. Schimmel & Paulssen (1997) have demonstrated a technique called "Phase-Weighted Stack" (PWS) which performs non-linear stacking, $g(t)$, using different weights, $w_{pws}(t)$, for each sample (corresponding to time t) according to their combined instantaneous phases ($\Phi(t)$ in Eq. 4.1), using the formulae of Eq. 4.14 and 4.15:

$$w_{pws}(t) = \left| \frac{1}{N} \sum_{k=1}^{N} \exp\left[i \cdot \Phi_k(t) \right] \right|^{\nu} \tag{4.14}$$

$$g_N(t) = \frac{1}{N} \sum_{j=1}^{N} f_j(t) w_{pws}(t) \tag{4.15}$$

Where $g_N(t)$ refers to a stack of N waveforms, aligned so to maximize their cross-correlation, alternatively denoted as $g_{ij}(t)$ when referring to a single pair of waveforms (N=2) with indices i and j, $f_j(t)$ the seismogram of the j-th event and ν is a control variable, where $\nu = 0$ for linear stacking while $\nu \geq 1$ can be used for PWS. The weights in Eq. 4.14 tend to decrease the effect of stacking for samples whose instantaneous phases are summed up destructively, while samples with coherent phases survive the filter (Schimmel & Paulssen, 1997). The weight function, $g_N(t)$, must be smoothed to reduce rapid alterations between high and low values.

The above method is efficient when the waveforms used for stacking are highly similar with the exception of random noise contamination. However, $T_{S\text{-}P}$ differences and other sorts of dissimilarities within partially or indirectly similar waveforms would decrease the weights even in parts which should contain the signal. In order to minimize this problem, a modified approach has been adopted in the framework of the HADAES method. The primary RE, selected using criteria that have already been mentioned, is considered as a starting waveform. A series of cross-correlations between this event and others within the same multiplet are performed for the calculation of time-lags between intermediates that form pairs of successive direct relatives, so that all waveforms can be aligned to their best-fit offsets in pairs. Stacking, $K_{ij}(t)$, is performed between the primary RE, $f_{i=1}(t)$, and its (first) immediate relative, $f_j(t)$ using the Eq. 4.16:

$$K_{ij}(t) = \begin{cases} \dfrac{f_i(t) + 0.5 \cdot f_j(t) \cdot XC_{1j} \cdot g_{1j}(t)}{1 + 0.5 \cdot XC_{1j} \cdot \bar{g}_{1j}} & , \quad XC_{1j} < 0.6 \\ \dfrac{\left(f_i(t) + f_j(t) \cdot XC_{1j} \right) \cdot g_{1j}(t)}{1 + XC_{1j}} & , \quad XC_{1j} \geq 0.6 \end{cases} \tag{4.16}$$

where XC_{1j} is the cross-correlation maximum (XC_{max}) between $f_{i=1}(t)$ (always with the primary RE or i=1) and $f_j(t)$, and $\bar{g}_{1j}$ the mean for the phase-stack function, $g_{1j}(t)$, over all time values. Then the stacking proceeds by replacing $f_i(t)$ with the previously calculated $K_{ij}(t)$ and $f_j(t)$ with an immediate relative of the previous $f_j(t)$. Cases of indirect relatives with XC_{1j}<0.3 are completely excluded from the stack. This procedure ensures that in case of relatively low XC_{max} the primary RE or previous

$K_{ij}(t)$ is only slightly affected by the summation with a potentially dissimilar indirect relative. However, in cases of adequately similar relatives ($XC_{1j} > 0.6$), the second formula is essentially the summation proposed by Schimmel & Paulssen (1997) for a pair of waveforms, but with the waveform j that is being added at each step being weighted according to its correlation with the primary RE and the normalization factor adjusted accordingly.

The resulting final stacked waveform, $K_f(t)$, should still have a high XC_{max} value compared to the primary RE, while its XC_{max} with many of the other events within the same multiplet should be comparable or even higher than their respective correlation with the primary RE. It's also important that immediate relatives of the primary RE keep having relatively high correlation with $K_f(t)$, although it may be reduced. The purpose of stacking, besides noise reduction and signal amplification, is that the $K_f(t)$, or "Reference Waveform" (RW), should have a higher chance of being similar with events which have originated on other days and therefore are not included in the DS multiplet. In the following, the term RE will be used to signify either a "primary", unchanged, reference event or a stacked reference waveform. It is, of course, required that meta-data are associated with a RW in the same way they did in the primary RE with the necessary adjustments. Stacked RW will obviously have arbitrary absolute times. However it is important that average travel-times are taken into account for the meta-data, which when subtracted from the respective associated arrival-times of a SE can provide an approximate origin time.

The RE of all multiplets defined for a certain day are cross-correlated to the RE of the previous days and external links are registered for pairs with $XC_{max} > 0.5$. In case of long periods of study, the correlations can be performed in a limited amount of previous days, but a chain of intermediates can still allow links to go further back in time. These links can be used for both connecting sub-multiplets into larger ones and to enable previously unassociated multiplets or orphans to be picked

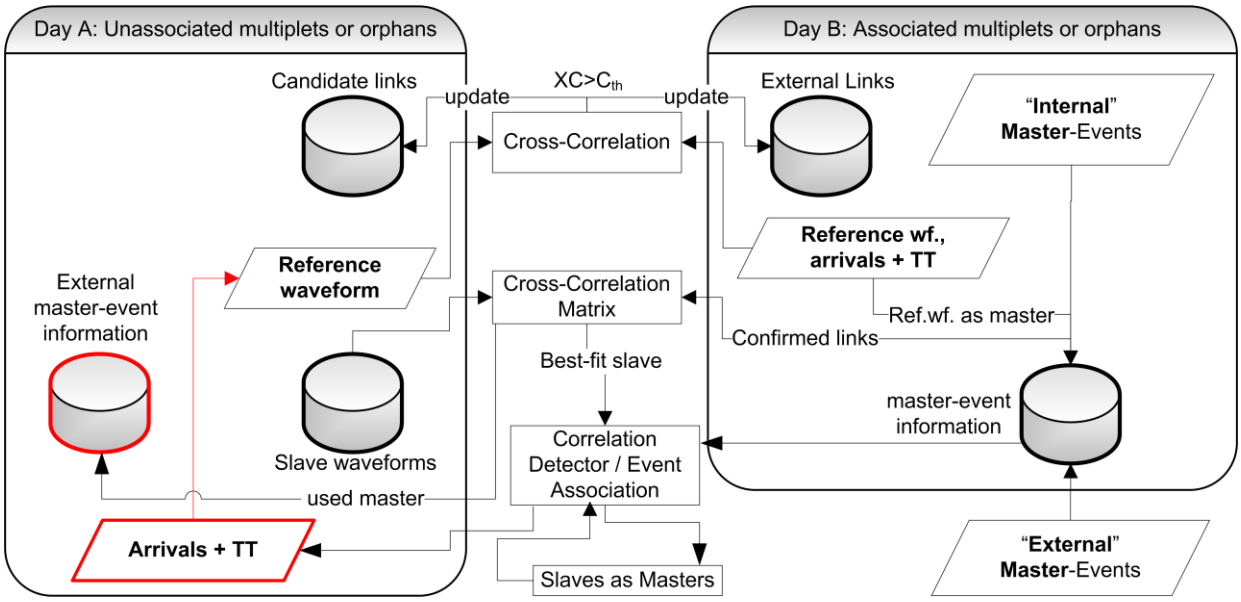

Figure 4.21: Flow-chart of the cross-day procedures: creating links between correlated day-specific multiplets of different days and using master-event information of associated multiplets from one day (B) to make event-associations in multiplets of another day (A).

and acquire preliminary solutions. The RE can act in the same way as M_{ext}, providing extra chances for association of origin, arrival and travel-times with SE that do not have M_{int} or an adequate correlation with M_{ext}.

A simplified flow-chart of the cross-day correlation procedures is presented in Fig. 4.21. In this diagram, the left panel "Day A" represents a multiplet that could not be directly associated with a M_{int} or M_{ext} with the procedures of Section 4.4.3. It may still have a chance to be associated using information from:

- Internal masters of a different day (Day B; right panel in Fig. 4.21)
- Internal master of a third day (e.g. Day C), which was used to indirectly associate a multiplet of Day B
- Reference Event/Waveform from an associated multiplet of Day B

Information on the primary master-event(s) that was used to associate a certain SE is registered to allow the algorithm to look for correlations with manual events before trying out RE with information defined by the SaM procedure, thus reducing error propagation. Events of unassociated multiplets of the day that is currently processed (Day A) are correlated to the RE of previous days and their similarity is registered. In case a strong correlation with one of the external multiplets (of a previous day) is found, the algorithm checks for possible correlations of the current day's SE with the original ME used for the external multiplet, if available. The best suited waveforms on both current and external multiplets are used in the master-event procedure to make the first associations, followed by SaM to make associations to the rest of the SE in the multiplet.

The aforementioned procedure is followed by a "second pass", after all days of the study period have been processed once. This time, the registered external links in unassociated multiplets are checked against possibly associated clusters of other days. This "second pass" can actually be performed multiple times, as more multiplets may be associated every time it is repeated. The various connections between multiplets of different days can create super-clusters. This provides information on the requirement of extra ME which may have to be manually analysed to associate large groups that remain without solutions, on the condition that they have occurred within the AoI.

4.4.6 Relocation

The main output of the HADAES method is a preliminary catalogue of dummy origin times, hypocenters and relative magnitudes as well as a phase-file with P- and S-wave arrival-times, determined by the AIC-picker. Conventionally, a single-event location algorithm, such as HYPOINVERSE (Klein, 2002) is employed to resolve absolute hypocentral locations. However, the detected events by the HADAES method can be too small for an adequate number of picks to be available, while there can also be some uncertainties in the picking of the wave onsets due to low SNR. As a result, the hypocentral distribution can become very noisy. The draft catalogue, on the other hand, while it provides a sense of location and temporal evolution, it is only based on the (relocated) master-events locations.

To improve the spatial distribution but also take advantage of the preliminary draft catalogue locations, a family-specific relocation procedure can be performed, using travel-times determined by the results of the single-event location algorithm but restricting the new locations to a narrow volume near the draft catalogue locations. This is described in more detail in the Appendix 5B for the application of Section 5.4.

4.5 Discussion

The problem of automatic event-detection and estimation of seismic source parameters, such as hypocentral coordinates, origin time and magnitude, is critical for the study of microseismicity in regions of continuous background activity or during sequences such as aftershocks or earthquake swarms. The ME-method (Section 4.3) attempts to increase the number of resolvable events by detecting earthquake families and propagating picks through all the available stations by exploiting waveform similarity. It requires sufficient similarity in all available stations but can even manage picks despite the very low SNR of the SE signals. HADAES (Section 4.4) expands MEm for use with larger datasets of continuous waveform recordings, without the requirement of strong similarity in all stations of interest, complemented by a classic automatic picking approach (Section 4.2) and upgraded with the calculation of relative magnitude in a procedure that provides a complete automatic catalogue. The HADAES method takes advantage of the high detectability by focusing on a single station close to the epicentral area and the availability of travel-times to a group of SoI, location and magnitude data acquired by routine analysis of the stronger events of a sequence. These are joined together by exploiting the property of waveform similarity.

There are several differences between HADAES and MEm. The former applies a correlation detector (Schaff & Waldhauser, 2005) only for the reference station and uses a more conventional auto-picking algorithm for the other SoI. The latter has the advantage that it applies to waveforms which are not necessarily similar to the same degree as in the reference station, in contrast with the ME method of Section 4.3. However, it also means that it requires sufficient SNR for a successful pick, while the correlation detector is capable to detect the P- or S-wave statistically, even if the target waveform is overwhelmed by noise (Kapetanidis & Papadimitriou, 2011) or buried in the coda of a previous, stronger event (Schaff & Waldhauser, 2010). It is more memory efficient, as it works on day-specific multiplets which are later merged into larger families, rather than creating a global cross-correlation matrix. It takes advantage of the relocated master-events to provide preliminary locations for the slave events, allowing for a reduction in the minimum scale for which the fractal power-law of the spatial distribution holds true (see Section 5.4.1). It compares the amplitudes between master- and slave-events to estimate relative magnitudes, expand the range of the Gutenberg-Richter law to a lower magnitude of completeness and even possibly recover a small portion of events with magnitudes larger than the original M_c which might have been missed from the routine analysis.

The downsides of the HADAES method are similar to those previously reported by Kapetanidis & Papadimitriou (2011). It can only be applied to families of repeating earthquakes, which means that if there are no master-events with sufficient similarity to the waveforms of a certain multiplet at the reference station, then it will not be resolved. There is also the problem of waveform overlapping

which is often observed in bursts of earthquakes during intense sequences and can cause confusion to either the correlation detector or the AIC-picker, leading to false travel-time and seismic source parameters associations. In addition, the HADAES method uses automatic signal detection by employing an STA/LTA procedure. Pseudo-signals generated by environmental / anthropogenic noise which may be falsely detected not only increase the workload but can also be rather problematic, as there is always a small chance for part of a seismic waveform being similar to that of artificial noise or the window of a low-amplitude signal containing noise of comparable strength. This can lead to an avalanche of erroneously reported events in the catalogue or even whole families of "repeating" (sufficiently similar) artificial signals. However, most of these occurrences are filtered out either during the AIC-picker procedure, which will probably fail to detect any arrivals at the other SoI, leading to an inability for preliminary location and, on a second level, even if the AIC-picker detects by chance some accidental "phase" arrivals, these fake "events" will most likely be ruled out during the relocation procedure. In any case, the final catalogue requires a manual check for left-overs of artificial noises being reported as earthquake events, with extra care taken in the few SE with relatively large magnitudes. The rather significant problem of environmental / anthropogenic noise can be avoided by proper selection of a reference station whose recordings are not riddled with such signals or by applying appropriate filters or thresholds to the detected signals (e.g. Ketner & Power, 2013) in order to reject them altogether before the algorithm proceeds to the rest of the procedures. More sophisticated methods for signal classification include the implementation of artificial neural networks for the recognition and distinction of earthquake signals from environmental noise (Wang & Teng, 1995; Peng *et al.*, 2014).

The use of a correlation detector for event-detection is an option that can potentially result in a larger number of usable signals, but there is always the possibility that certain families with a significant number of events do not have a suitable master-event to permit association with arrival-times and seismic source meta-data. Schaff & Waldhauser (2010) have observed that a correlation detector managed to detect about 85% of the events that were also detected by a conventional STA/LTA detector, called "pIDC". However, the correlation detector identified an additional 70% of events that were missed by the "pIDC". Using an STA/LTA algorithm for signal detection, instead, ensures that no earthquake families are omitted (unless, of course, all their events are too small to be detected by this method) and that the signals have sufficient SNR. Master-events can be manually added for such families on a second stage to allow for their solution, provided these families are inside the Area of Interest, otherwise they can be discarded altogether. Depending on the purpose of a research, a correlation detector may also be employed to study the history of specific families in more detail. The SaM procedure in the HADAES method permits associations of events with less similar waveforms which could have been rejected by a master-event used as correlation detector for the signal detection procedure. The disadvantage is that a correlation detector has a higher chance to detect signals of very low amplitude which might have been missed by an STA/LTA algorithm. A combination of STA/LTA, correlation detector and clustering in earthquake families has also been implemented in frameworks for array data (Harris & Dodge, 2011; Junek *et al.*, 2014). Gibbons & Ringdal (2006) remark that a simple correlation detector manages to detect events which are 0.7 magnitude units lower than STA/LTA, while a multi-channel correlation detector using a full array can additionally improve the detectability by 0.4

orders of magnitude lower than the single-channel correlation detector. Similarly, Junek *et al.* (2014) report a reduction of M_c by 1.3 magnitude units relative to the regional NORSAR analyst-reviewed catalogue of Storfjorden, Norway, using a framework that combines STA/LTA with correlation detectors in array data. In the application of the HADAES method (Section 5.4 and Appendix 5B), however, very low-amplitude signals, undetectable by the STA/LTA procedure or rejected by the selection criteria, would be practically unusable for proper individual location, as the SNR would be even lower in epicentral distances further than the reference station and P- or S-wave onsets would likely be indiscernible in such stations. In addition, the *b*-value was slightly increased in the final catalogue, similarly to the observations of Yang *et al.* (2009) who determined relative magnitudes in a seismic sequence at Mount Carmel, Illinois.

The significant advantages of the HADAES method can be mainly observed in the spatiotemporal distribution which is largely enriched (Section 5.4). The fractal dimensions remain unaffected while the scaling range of the power-law is expanded. This can be very useful for studies of dynamics in the evolution of a sequence, as it provides more samples to allow for increased resolution and statistical importance. The phenomenon of spatiotemporally clustered repeating earthquakes which occur in bursts of numerous events is particularly observed in volcanic regions (e.g. Rowe *et al.*, 2004; Papadimitriou *et al.*, 2015), where the influence of pressurized fluids is significant. This is impressively demonstrated during the explosive activity of the Redoubt volcano, Alaska, in 2009, where seismic bursts were observed that intensified and degenerated into harmonic volcanic tremor with its fundamental frequency gliding up from 1 to 30 Hz shortly before several eruptions (Hotovec *et al.*, 2013; Ketner & Power, 2013). However, repeating earthquakes are also observed in swarms that occur in tectonic settings, usually with the contribution of fluids (Lindenfeld *et al.*, 2012; Kassaras *et al.*, 2014a, 2014b; Kapetanidis *et al.*, 2015) or during aftershock sequences, when stick-slip repeatedly occurs on asperities surrounded by creep after the redistribution of stress caused by the mainshock (Schaff *et al.*, 1998).

4.5.1 Single-Station Detection

The scheme of Single-Station Detection has been previously applied successfully by Ketner & Power (2013) for the classification of seismic events, based on waveform similarity. The authors grouped the detected signals into families and measured several metrics, such as inter-event time, event rate, peak frequency, peak-to-peak / RMS amplitude etc. to investigate the seismic behaviour of Redoubt volcano. They discovered several swarms which were initiated in the beginning of 2009 and that seven explosions were preceded by bursts of repeating earthquakes which belonged to one or more event families. An STA/LTA technique was used for the primary event-detection, while a correlation detector method was also employed to detect events of very low amplitude. Compared to the over 125,000 SSD events, only 2% had been manually detected and located in an Analyst-Reviewed Catalogue (ARC) of events provided for the local sub-network. The authors took advantage of events of the ARC which belonged to several key-multiplets to specify the approximate location of the corresponding earthquake families while they also applied a cross-correlation technique to automatically re-pick events in certain swarms.

The analysis of earthquake families for SSD events, even without an available estimate of hypocentral location or magnitude, can provide useful information, as demonstrated by Rodgers *et al.* (2013) for the detection of possible precursory behaviour before the eruptions of Telica volcano, Nicaragua, in 1999. The authors applied a procedure quite similar to HADAES, cross-correlating the detected signals of a single station to produce day-specific (DS) correlation matrices and creating DS multiplets, stacking waveforms to produce a reference waveform (RW) per multiplet and cross-correlating RWs between multiplets of different days to merge them into broader earthquake families. They then classified each family according to the spectral characteristics of their reference waveforms in low-frequency (LF, < 5 Hz), high-frequency (HF, > 5 Hz) or mixed-frequency (MF) events and studied their temporal evolution. Their analysis revealed decrease of LF followed by increase of HF events prior to the onset of eruptive activity in May 1999 as well as a complex pattern in the rates of both HF and LF events prior to a series of eruptive episodes that occurred in the following months (Rodgers *et al.*, 2013). They also demonstrated an increase in the generation of a multitude of earthquake families (22) prior to the explosions of October 1999 which switched them off while other families were generated later. The "destruction" of previously active multiplets after volcanic events has also been observed by Thelen *et al.* (2010) at Bezymianny volcano, Russia, with eruptive episodes creating new families of repeating earthquakes, as the volume of magma or gas migrates and perturbs the distribution of stress.

The HADAES method creates a cross-correlation matrix for signals detected in a single day and attempts to classify events in groups of multiplets according to an adaptable threshold, which is practical when continuous waveforms have been already archived into 24-hour records. It then links DS multiplets into larger families by measuring the similarity of their corresponding RW. A similar scheme with DS multiplets, waveform stacking and creation of broader earthquake families has also been applied by Petersen (2007) for the seismic activity in Shishaldin volcano, Alaska. A different approach on the problem of large datasets and memory efficiency has been followed by Ketner & Power (2013), who performed cross-correlations on subsets of 2000 consecutive events with an overlap of 1000 events between sequential subsets, to allow for arrays of family member references to be passed from subset to subset. The generation of earthquake families can be broadened by processing multiple days altogether, instead of single days. This is feasible when the daily number of detected signals is small enough and can enable the creation of larger multiplets without the need to search for external links in a second stage of the procedure. This can be done by joining individual, externally linked, multiplets into larger ones, re-calculating a cross-correlation matrix for the missing pairs (between different days), thus creating a new clustering hierarchy within the merged multiplet and re-defining the master events which can be used.

4.5.2 Relative magnitudes

The property of waveform similarity between master- and slave-events is also exploited in HADAES for the calculation of relative magnitude. Two different methods, LSQR and SVD, were tested on the direct scatterplot of amplitudes but also on the *xy*/*xx* data (see Appendix 5B). Gibbons & Ringdal (2006), who introduce the *xy*/*xx* scheme, estimate the scaling factor, *a* (which is represented by B_m), as the ratio between the dot products *xy* and *xx*, where *x* is the data vector

containing the multi-station/multi-channel template signals and *y* are the corresponding waveforms of what is termed as "slave-event", at the time-lag of maximum cross-correlation with the templates (master-event waveforms). The authors determine weights which minimize the residuals of Eq. 4.17:

$$y = a \cdot x + \varepsilon \quad , \text{ or } \quad , \quad a = (x^{T} \cdot W \cdot x)^{-1} \cdot x^{T} \cdot W \cdot y \tag{4.17}$$

using an iterative procedure, where W is a $N \times N$ matrix of weights (N is the total number of samples in x or y, which are $N \times 1$ vectors) and ε represents noise which cannot be interpreted by $a \cdot x$. In the application of the HADAES method (Appendix 5B), multiple individual relative magnitude measurements are made for each slave-event using the LSQR method on the *xy*/*xx* data in both P- and S-wave parts of the master and slave waveforms and a mean value is estimated after removal of possible outliers, with a residual larger than 1σ from the median. Statistically, the unweighted *xy*/*xx* ratio of dot products (with W of Eq. 4.17 being an identity matrix), which is used as the initial value $a^{(0)} \equiv B_{\mathrm{m}}$ by Gibbons & Ringdal (2006) before the calculation of weights, is practically indistinguishable, in all aspects, from the results of the LSQR method as presented in Appendix 5B (Fig. 5A.3a). The minute differences between the two are due to the LSQR including a non-zero ε (Eq. 4.17) while the *xy*/*xx* ratio of dot products does not account for this. Of course, the iterative method of Gibbons & Ringdal (2006) could potentially decrease the variance of the results, however it also involves all components and master-events into the data vector, which is a different approach to the problem than the one followed in HADAES method. The iterative algorithm of Gibbons & Ringdal (2006) was tested on the data presented in Fig. 5A.3a for the same single-component waveforms and one master/"slave" pair at a time. The resulting slope of M_{rel} against M_{l} was found to be exactly the same as the simple LSQR (Fig. 5A.3a) but the correlation coefficient was lower ($R^2 = 0.587$) and the standard deviation slightly increased (~0.39 instead of ~0.36). The same inequalities are true if a different frequency range (e.g. 2 - 10 Hz) and higher correlation threshold (e.g. 0.7) are selected. The iterative procedure is also more time-consuming in terms of processing, as it loops until the solution for B_{m} converges to a specified precision or reaches a predefined maximum number of iterations (Gibbons & Ringdal, 2006), which is another reason why it wasn't adopted in HADAES.

It is noteworthy that the aforementioned standard deviation values are very similar to the ones determined by Schaff & Richards (2011, 2014), who estimated $\sigma \cong 0.35$ magnitude units for catalogue relative magnitudes using the method of Gibbons & Ringdal (2006), indicating the large inaccuracies in the determination of catalogue magnitudes. These imprecisions are inevitably propagated as systematic errors from the master- to the slave-events, which is why an evaluation with direct magnitude measurement, e.g. using the methods described in Chapter 3, can be helpful to detect large deviations. Rubinstein & Ellsworth (2010) have also exploited waveform similarity for the joint calculation of relative magnitudes in families of highly similar ($XC_{\max} \geq 0.85$) repeating earthquakes using SVD. They point out that after applying strict criteria for waveform similarity, SNR and filtering such that the frequency content is below the corner frequency of the examined events, the first output-basis vector (corresponding to the largest eigenvalue) can account for over 80% of the amplitude of the original seismograms while the other output-basis vectors are mostly attributed to noise or misalignment of the seismograms. Their results indicate that the uncertainty of

measurements of relative moment within groups of repeating earthquakes using the SVD method can be less than 10%, compared to an average of 75% in the catalogue moments. They also note the importance of control over potential changes in the instruments of the stations during the study period. If the seismometer, and thus its response, remains unchanged, the cross-correlation function is not affected by changes in the gain of the digitizer, in the degree that the waveform's shape is not altered. However, the calculation of relative magnitude requires that the gains are corrected before amplitude measurements take place. In HADAES, the selection criteria are intentionally left more flexible and tolerant, as the method primarily aims to increase the number of detected and resolved events. Of course, on a post-processing stage, each family, having a much more manageable number of events, can be analysed with stricter criteria to determine more accurate relative magnitudes. The additional events which were resolved using the HADAES method in the application of Section 5.4 have resulted in a reduction of the magnitude of completeness by ~0.9 units, which is comparable to the findings of Rubinstein & Ellsworth (2010) who report one magnitude unit reduction in the detection threshold using correlation detectors in large scale applications.

4.5.3 Automatic phase-pickers

The proposed AIC-picker of Section 4.2 is employed in the HADAES method for the automatic correction of the approximate P- and S-wave arrival-times, which are estimated by the association of the master-events' travel-times to the slave-events. The algorithm has been tested and fine-tuned for the requirements of the application in Section 5.4; however it has not been compared against other conventional algorithms, as the HADAES method is mostly focused on the procedures concerning the classification of multiplets into families and the association of approximate travel-times and source parameters to the slave-events. Turino *et al.* (2010) have tested the efficiency of an automatic picker based on the Akaike Information Criterion (AIC) against the classic STA/LTA approach of Allen (1978, 1982), hereafter called Allen-picker. While the Allen-picker is amply efficient for picking P-wave onsets, with results comparable to the AIC-picker, it is problematic when applied on S-waves (using the horizontal components), in which case the AIC algorithm is superior (Turino *et al.* 2010). In HADAES, the STA/LTA characteristic function (Eq. 4.2) of Earle & Shearer (1994) is only used for the purpose of signal detection. While the STA/LTA trigger times can also be considered as approximate arrival-times, sometimes the P-wave is not strong enough for the STA/LTA value to overcome the triggering threshold and it is the (stronger) S-wave which is really detected. When the correlation detector is applied and the waveform of a master-event matches the one of the analysed slave signal, it is expected to distinguish between the P- and the S-wave and provide a corrected estimate for their arrival-times (Kapetanidis & Papadimitriou, 2011). In this study, the AIC-picker combines measurements of amplitude ratio, as well as kurtosis and skewness to provide additional weight (Eq. 4.7 and 4.8) or alternate pick times when the target onset is near the edges of the W_{max} window (Figs 4.8 and 4.9). In the literature, high-order statistics have also been used exclusively for the picking procedure, either in their original form (Saragiotis *et al.* 2002), or modified to exploit a range of window lengths and frequency bands (Baillard *et al.* 2014). Küperkoch *et al.* (2010) apply AIC on the characteristic functions (CF) of skewness or kurtosis in place of the waveform's variance which is used in Eq. 4.3. They also use the SNR of the

CF and its slope immediately after the determined onset to calculate the quality of a pick. In HADAES, the pick quality is mainly dependent on the variance of the time values corresponding to the minima of the AIC function as calculated at a set of different window lengths.

4.5.4 Conclusions

Several algorithms, including single-station signal detection, multiplet classification, correlation detector and relative magnitudes have been combined in the HADAES method that was developed in the framework of the present study. HADAES can manage a large dataset of earthquakes detected in one or more reference stations by taking advantage of the high detectability of SSD, a database of correlation detectors and a simple automatic phase-picker. It can provide a preliminary catalogue by associating approximate seismic source parameters, including relative magnitude, as determined by a small set of manually analysed events, to the automatically detected and processed slave events. The final catalogue results from a combination of a conventional, but targeted, auto-picking algorithm and relocation relative to the known master-events. As in all automatic algorithms, the HADAES method has some weaknesses. It is only applicable to multiplets which can be primarily associated with master-events. The SaM technique and cross-day correlations of reference waveforms are prone to error propagation due to chaining effects which may affect the approximate arrival-times, but could also link groups of noise signals which partially match a low-amplitude slave. The latter issue can be mitigated by a proper selection of noise-free reference stations, pre-filtering of detected signals or manually discarding such false events from the final catalogue.

The HADAES method can also be applied partially, omitting several steps or ignoring some restrictions. In Section 5.2, HADAES was used to pick higher order slave-events using all the manually analysed ME and "primary slaves" of the first pass of the MEm as M_{ext}, instead of selecting a single ME for each multiplet, as the application was restricted to a short period of ~9 days. In the application of Chapter 6, HADAES was used to improve automatic locations available for a dataset of earthquakes in the western Corinth Rift. The AIC-picker was employed to verify/correct the automatic picks. Unresolvable or events with large errors were re-processed with the HADAES method. A set of manually located events were used as ME to estimate arrival-times on these slave-events and the AIC-picker was used again for onset detection. This was performed using several different reference stations and the best results were selected and visually evaluated. The events in that dataset were pre-selected, so no signal detection on 24h waveforms was performed. However, the STA/LTA method was used for some still unresolvable events to better estimate the point of the cropped waveform at which the signal emerged and to be given another chance for arrival-time estimation and picking.

The HADAES method can multiply the amount of catalogue data by more than ten times, reduce the completeness magnitude and increase spatiotemporal density and clustering accordingly, providing a more complete image of the occurred seismicity. The resulting increase in the sheer amount of data can improve the resolution in studies concerning the spatiotemporal evolution, fractal dimensions and the dynamics of a seismic sequence.

Chapter 5

Case studies of earthquake patterns in Greece

Introduction

The methodologies presented in the first 4 chapters of the present study have been applied to several case studies of earthquake sequences in various regions of Greece. Several have been published in scientific journals (Appendix 5A) while preliminary results from others have been presented in international scientific congresses. The typical method for multiplets classification can be summarized in the following steps:

- (Optional) Separation of the initial catalogue to spatial groups using Ward's linkage method (Section 1.2). This can be helpful for the rest of the procedures by reducing the number of events (per group), thus reducing the number of unknowns for the double-difference inversion but also decreasing the size of the cross-correlation matrix (number of combinations of event-pairs for cross-correlation). The rest of steps can then be applied per spatial group.
- (Optional) Determination of a group-specific, custom velocity model.
- (Optional) Calculation of mean P- and S-wave travel-time residuals and application of station-corrections. This can improve initial locations by removing the average errors caused by lateral inhomogeneities to either V_p or V_s velocities (hence introducing a V_p/V_s ratio that also varies per station).
- Selection of one or more reference stations: These have to be sufficiently close to the epicenters under study so that the signal to noise ratio is high enough. They should also have an adequate number of P- and S-wave arrival and signal duration observations which are used to properly crop the waveform time-series before cross-correlation is applied in order not to contain noise before the P-wave or after the S-wave coda.
- Full signal cross-correlation: The signals must be band-pass filtered to remove long-period noise (mainly for broad-band instruments) and high-frequency noise. For local micro-earthquakes, the frequency band 2-23 Hz is usually appropriate (see Section 1.2.2). The similarity between signals is measured by the maximum, XC_{max}, of the cross-correlation function (Eq. 1.2). The results are registered in a cross-correlation matrix. Measurements are repeated using other components or a different reference station. The matrices determined for different stations or components are then averaged by their RMS value, constructing a combined cross-correlation (or "similarity") matrix.
- Multiplet classification: Nearest neighbor linkage is performed on the combined similarity matrix. The optimal threshold is determined as the value that maximizes the difference

between the size (=number of events within) of the largest multiplet and the total number of clustered events (Section 1.2.2), usually with a lower bound e.g. C_{th}=0.60 to ensure a minimum degree of direct similarity.

- Cross-correlation measurements for P- and S-waves between events that belong to the same multiplet. The individual P- or S-waves are first aligned on their (manually or automatically) observed arrival times and the time-lag, t_m, of XC_{max} is also registered as a measurement of the difference between the two picks, with reference to the similar part of their waveforms (mostly attributed to arrival-time reading errors). At this stage, the XC_{max} and t_m for both P- and S-waves are determined for all stations, not only for the reference ones. The vertical component is preferred for the cross-correlation of P-waves while the S-waves measurements are averaged over the two horizontal components (if both are operational).

In this chapter, a selection of case studies is presented, mostly focused on the relocation of hypocenters, multiplet classification and spatiotemporal analysis, complemented by seismotectonic interpretation.

5.1 The 2008 Andravida aftershock sequence

On 8 June 2008, a major M_w=6.4 earthquake struck the region of NW Peloponnese, western Greece. The epicenter is located at ~23km ENE of the city of Andravida (Fig. 5.1), hence the name used in this section for reference to this sequence. In the literature it is more widely referred to as the 2008 Movri earthquake, after the name of the mountain in the epicentral area, or the 2008 Achaia-Ilia earthquake, after the name for the wider region. By mid-2008, the Hellenic Unified Seismological Network (HUSN) had just been fully integrated, with permanent seismological stations deployed throughout Greece and transmitting their digital recordings in real-time. When the 2008 Andravida earthquake occurred, the Seismological Laboratory of the University of Athens was operating two stations (LAKA and KALE), while the station TRIZ of the Corinth Rift Laboratory network was also operational in real-time, in the broader vicinity of the epicentral region, 50-70 km NE of the mainshock's epicenter. Waveform data from more than 20 stations of HUSN, in epicentral distances up to 150 km, as well as from the central station TR0 of the Tripoli Seismic Array (Pirli *et al.*, 2004) were used for manual *P*- and *S*-wave arrival-time picking. Preliminary results for this earthquake sequence have been announced by Papadimitriou *et al.* (2008, 2010a). In the present section a re-evaluation of the spatiotemporal distribution for a longer catalogue of this sequence is examined and compared to results from other studies.

5.1.1 Preliminary location

Initial locations were obtained using a 1D layered velocity model that was determined for the eastern Corinth Gulf area (Kaviris, 2003). In order to obtain better hypocenter locations, a velocity model for the broader epicentral area was calculated, based on the minimization of RMS errors and location uncertainties (Table 5.1; Papadimitriou *et al.*, 2008). Initial solutions were determined using the Hypo71 software (Lee & Lahr, 1972).

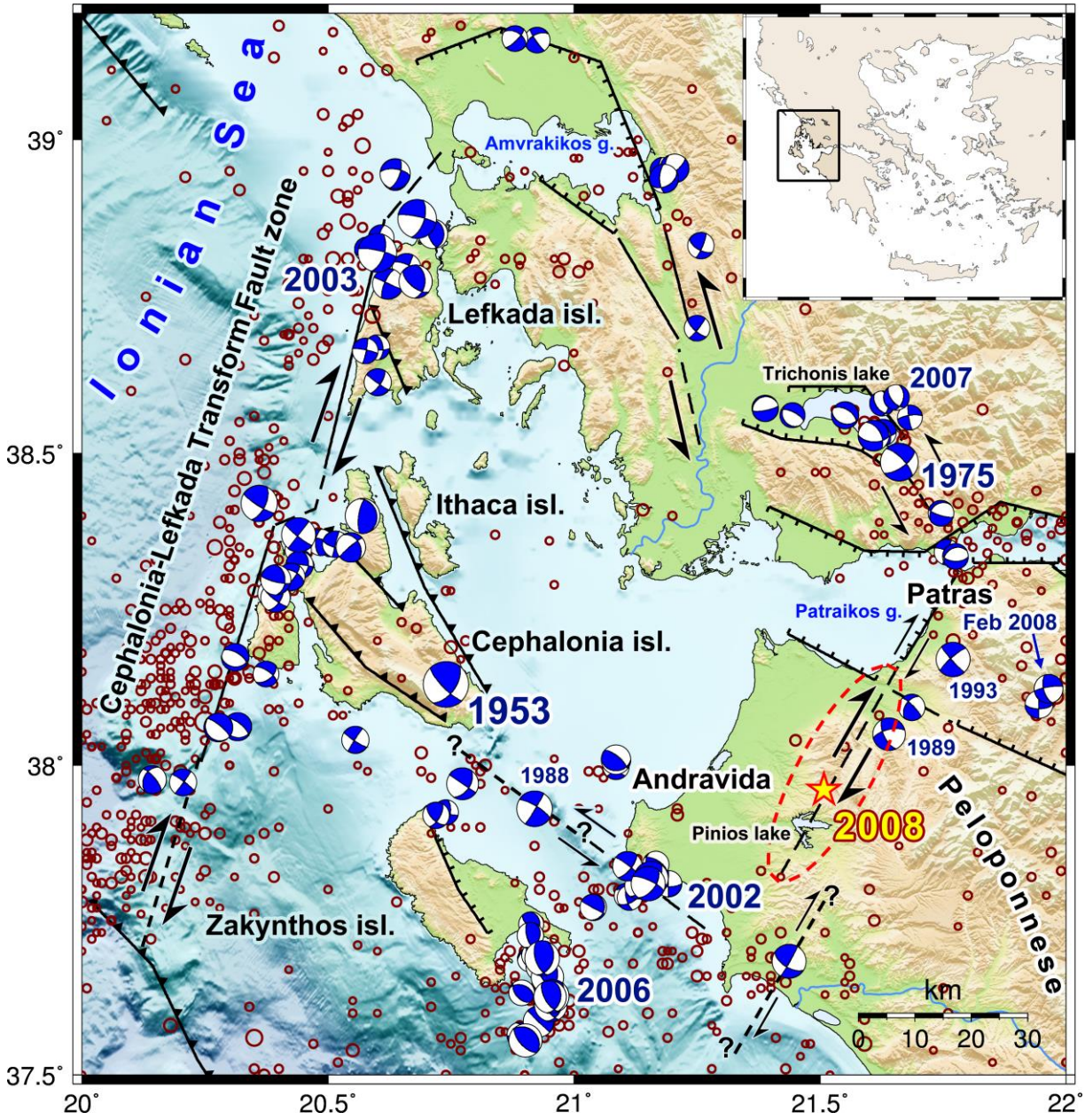

Figure 5.1: Seismotectonic map of the region of mid-western Greece, including the seismicity of 1970-2008 (Makropoulos *et al.*, 2012) with $M_w \geq 4.0$, prior to the 8 June 2008 Andravida earthquake, marked with a red-yellow star and a dashed ellipse surrounding its aftershocks zone. Focal mechanisms are a selected subset for $M_w \geq 4.0$ from the compiled catalogue of Kassaras *et al.* (2016) (see references therein). Gross fault lines for major tectonic features are based on Underhill (1989), King *et al.* (1993), Armijo *et al.* (1996) and Flotté *et al.* (2005).

During the first month after the occurrence of the mainshock, about 1250 events were manually analyzed and located in the aftershock zone and its vicinity. The study period was extended up to the end of 2010, with a total of over 2700 events in broader area and magnitudes mainly varying between 2.0 and 3.5. Most of the major aftershocks occurred within the first 5 days at distances no longer than 15 km NW of the mainshock's epicenter. The gross characteristics of the aftershocks spatial distribution can be observed in Figs 5.2a and 5.3a. The activated zone spans ~45km along a

SSW-NNE direction (N30°E). The mainshock is near the middle of the epicentral area, while the aftershocks zone is thinner in its mid-SSW part (~5km) and gets wider towards NNE (~10km). The focal depths generally vary between 12 and 27 km.

Table 5.1: Minimum 1D velocity model used for the 2008 Andravida aftershock sequence.

	Papadimitriou *et al.*, 2008	
V_p/V_s ratio	1.79	
Layer	**P-wave Velocity** (km/s)	**Ceiling Depth** (km)
1	4.9	0.0
2	5.5	3.5
3	6.2	8.0
4	6.4	16.0
5	7.1	34.0
6	7.9	48.0
7	8.4	83.0

5.1.2 Multiplet classification and relocation

The locations of the aftershocks, shown in Figs 5.2a and 5.3a, present relatively large dispersion. This is mostly due to the fact that the sequence was only recorded by regional stations of HUSN, without an additional local network that could better constrain the solutions and especially their focal depths. However, the relative location uncertainties can be reduced by applying a relocation procedure which can also contribute to the discrimination of spatial clusters. Although repeating earthquakes are more often observed during swarms, usually with the contribution of pressurized fluids (e.g. Hemmann *et al.*, 2003; Bisrat *et al.*, 2012 etc.), aftershock sequences worldwide have also been found to contain a significant number of correlated events, due to repeated slip on small, unbroken asperities that may be triggered by time-dependent mechanisms including creeping or pore fluid diffusion (e.g. Schaff *et al.*, 1998; Beeler *et al.*, 2001; Seno, 2003 etc.).

The mean P- and S-wave travel-time residuals were determined for stations in epicentral distances up to 150km and station corrections were applied to reduce biases in the absolute locations, mainly caused by unmodeled lateral inhomogeneities of the velocity structure. This was done after dividing the spatial distribution along the aftershock zone into clusters using Ward's linkage and Mojena's criterion (Section 1.2.2). The corrections were calculated and applied on each cluster separately to account for rays travelling through different paths in the crust which could exhibit different travel-time residuals, especially in stations which are in epicentral distances comparable to the dimensions of the aftershock zone.

A typical multiplet classification and relocation procedure, as already described in the introduction of Chapter 5, was applied for the 2008 Andravida aftershock sequence. To estimate the similarity between all combinations of aftershocks pairs, the waveform recordings of all three components of

the RLS station, located at ~10 km NNW of the mainshock epicenter, were employed. Data were cropped in windows containing both *P*- and *S*-waves and were band-pass filtered between 2 and 15 Hz prior to the calculation of XC_{max}, in order to eliminate linear trends, long-period and high-frequency noise. For each station/component, the XC_{max} values were registered into separate cross-correlation matrices. The data were combined into a single matrix that contains the XC_{max} values of the corresponding elements between all partial matrices. The events were then grouped in clusters, according to the degree of their waveform similarity using the nearest-neighbor linkage. 168 multiplets were formed with an optimal threshold value $C_{opt.th}$=0.65, containing 1004 events. Most

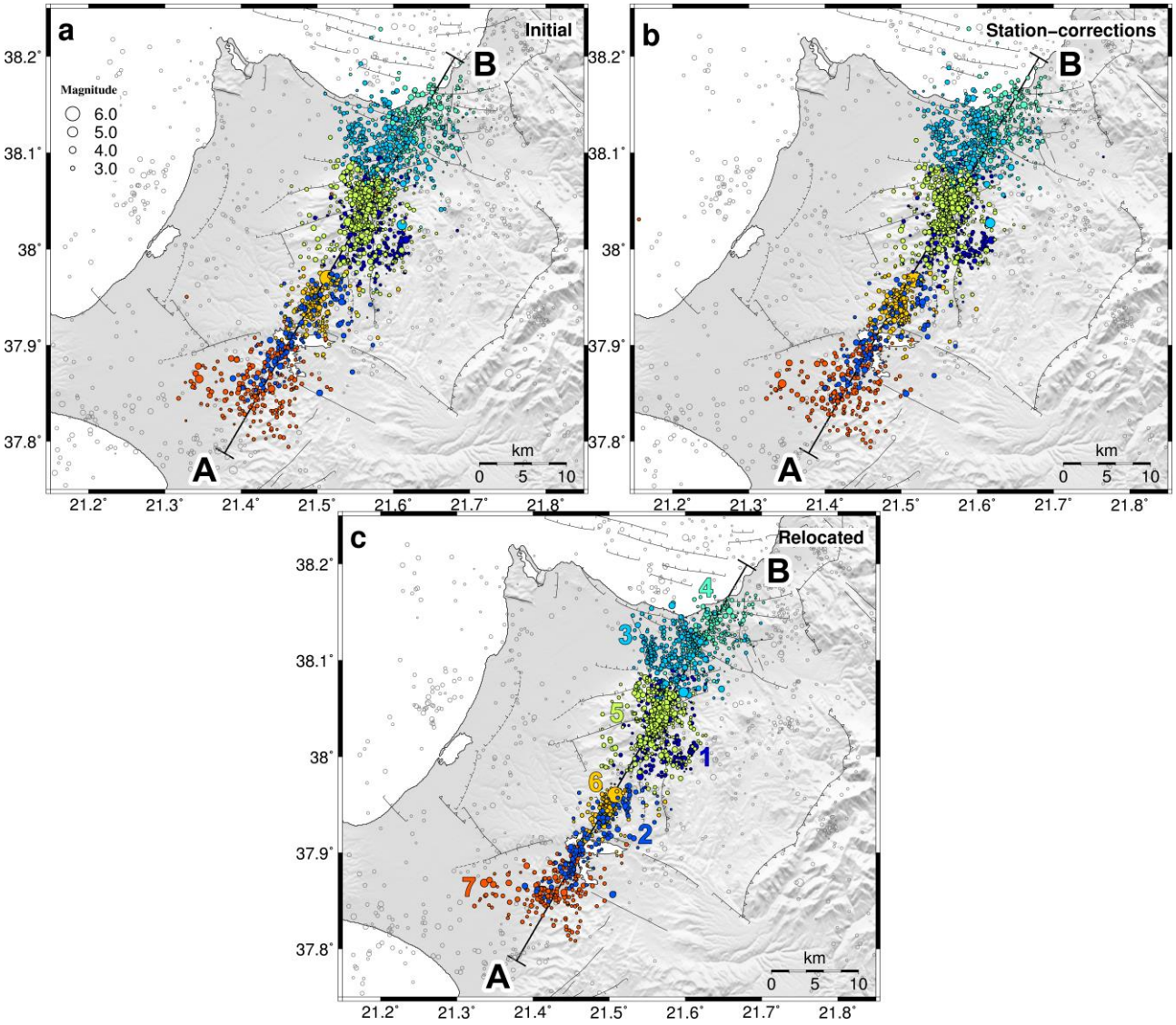

Figure 5.2: Maps of the 2008 Andravida aftershocks for a) initial, b) corrected by the average P- and S-wave travel-time residuals and c) relocated using the double-difference method. Colours represent the 7 spatial clusters (see numbers in panel c). The A-B profile line, drawn in a N30°E direction, is used for the cross-sections of Fig. 5.3 as well as the spatiotemporal projection of Fig. 5.8. Mapped superficial fault lines are after Koukouvelas *et al.* (2009) and Parcharidis *et al.* (2009).

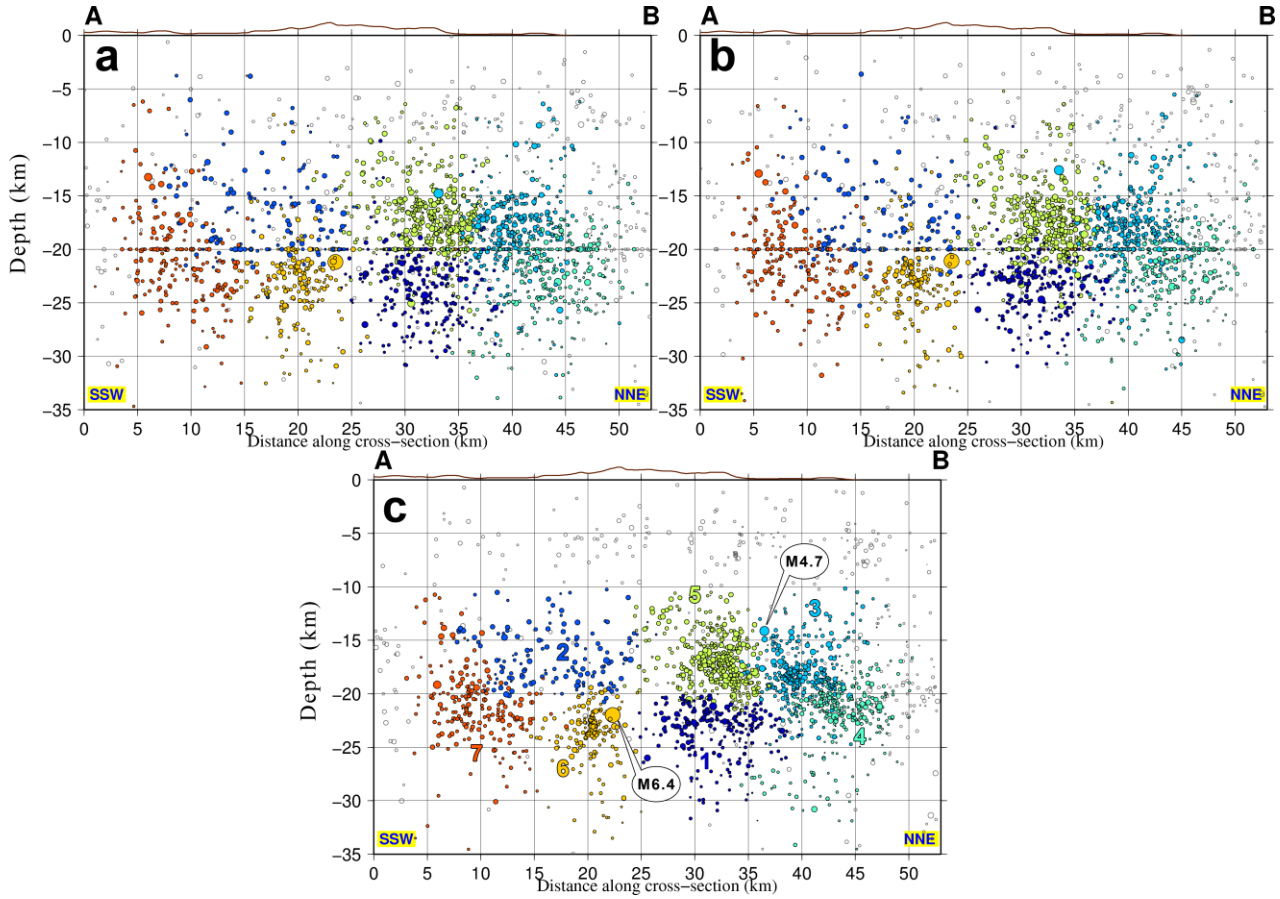

Figure 5.3: Cross sections of the 2008 Andravida aftershocks along the A-B profile-line of Fig. 5.2 in a N30°E direction for a) initial, b) corrected by the average P- and S-wave travel-time residuals and c) relocated using the double-difference method. Colours represent the 7 spatial clusters (see numbers in panel c).

of these are doublets or triplets, 26 of them are composed of 5 or more events and only 16 of them contain at least 10 events each.

The double-difference algorithm HypoDD (Waldhauser & Ellsworth, 2000) was used to relocate the aftershock sequence, using both catalogue and cross-correlation differential travel-time data up to 31 December 2008 and catalogue data (only) for the period 2009-2010. The relocation procedure is divided in two stages. At the first one, the inversion is mostly focused on the catalogue data, while a lower but non-zero *a priori* weight is applied to the cross-correlation data. In this way, the strongly correlated events remain bound to each other, while all the events linked by catalogue data are roughly relocated. In the second part, a higher *a priori* weight is given to the cross-correlation data, so that the events that belong to multiplets are being relocated relative to their cluster's centroid. A re-weighting process is also applied during the last stage, gradually breaking links between weakly correlated events, resulting to an even more local relocation. The relocation procedure was executed for different subsets of data either restricted in a narrow selection at the aftershock zone or the containing the seismicity in whole broad region around it. The results were then merged while the original locations were conserved for events which could not be relocated, to provide a more complete final catalogue. The relocation technique achieves a better concentration of events without

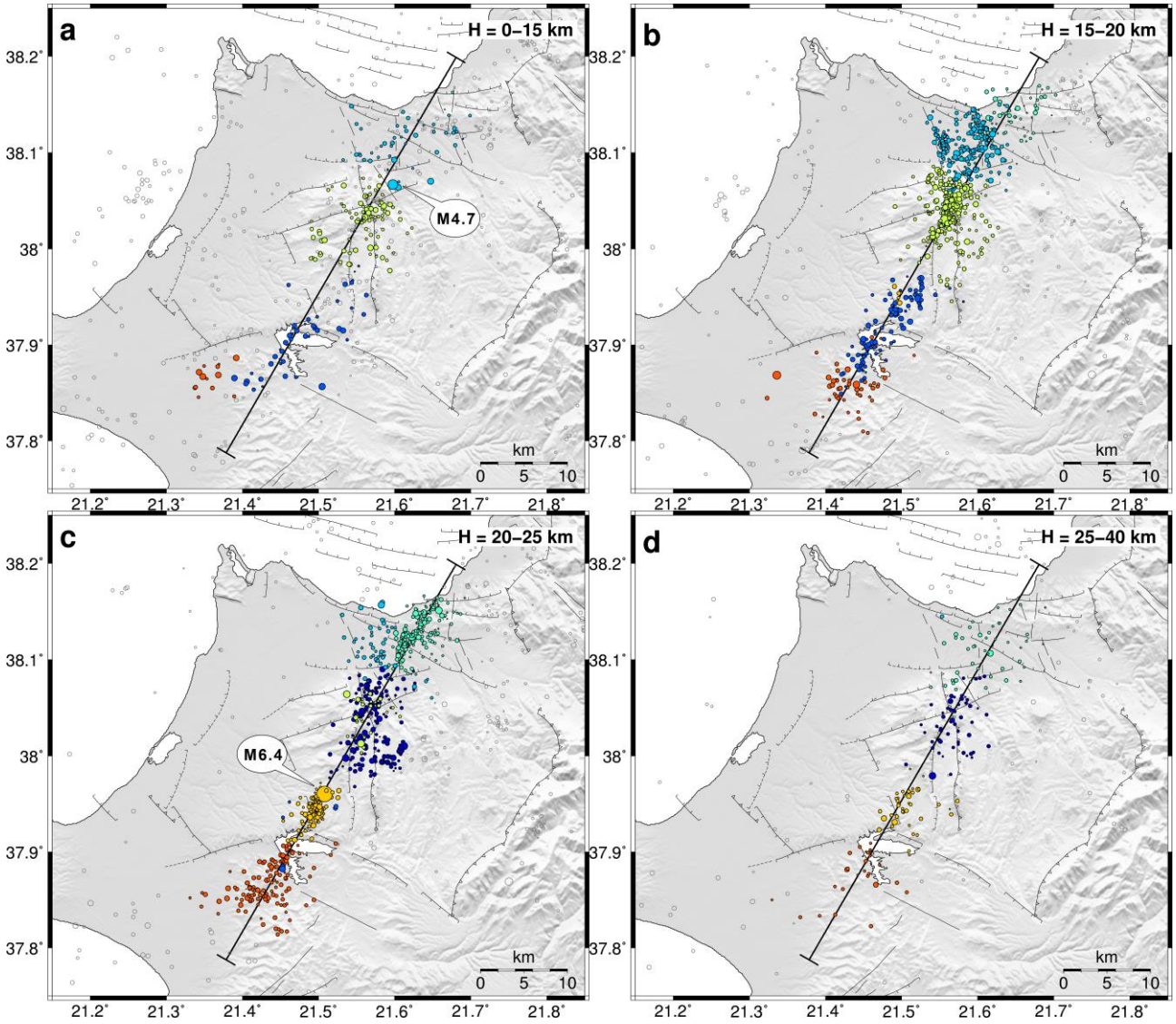

Figure 5.4: Maps of the relocated epicenters of the 2008 Andravida aftershock sequence for slices of different focal depth (H) ranges: a) 0-15km, b) 15-20km, c) 20-25km and d) 25-40km. Colours represent the 7 spatial clusters.

significant shift of each cluster's centroid (less than 1km), enhancing some details of the spatial distribution, such as several minor branches, mostly in the middle and in the north.

5.1.3 Spatio-temporal description/ multiplet analysis

The inter-event focal distance matrix was calculated using the relocated hypocenters and then Ward's linkage was applied to create a hierarchical classification, excluding epicenters outside the aftershock zone as well as very shallow (H<10km) or deep (H>40km) events. A threshold value was selected as indicated by Mojena's plot, so that a certain number of clusters (7) are formed to distinguish all the parts of the spatial distribution which present some particular interest. The

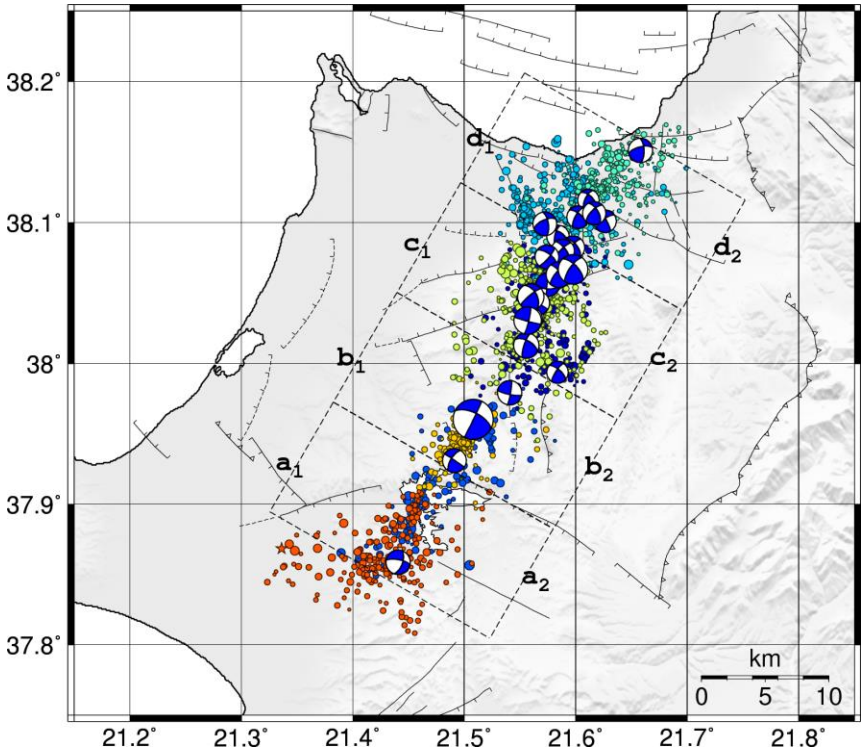

Figure 5.5: Map of the relocated epicenters of the 2008 Andravida aftershock sequence along with the focal mechanisms of the largest events (Papadimitriou *et al.*, 2008).

comparison between initial locations, corrected by travel-time residuals and relocated ones is presented in Figs 5.2 and 5.3.

The spatial distribution of the aftershock sequence covers an area of approximately 45 km length and a variable width between 5 and 10 km, with its major axis oriented in a NNE-SSW direction. Limited activity is observed near the hypocenter of the mainshock, with the exception of the tight Cluster #6, while the major part of the aftershocks is situated north of it (clusters #1 and #3-5), including most of the major ones with $M_w \geq 4.0$. To the south, significant but less intense activity is present, while at least two more clusters can be identified, one mostly north (#2) and another south of the artificial Pinios lake (#7). The depth distribution is also improved but only to a limited degree due to the lack of data from local seismological stations. It is, however, evident that the depths of the aftershocks tend to be better constrained and more concentrated at the northern segment while, in the south, clusters #2 and #7 are more vertically dispersed.

To better understand the geometry of the spatial distribution, horizontal slices for different focal depth (H) ranges are presented in Fig. 5.4. The expected characteristic is a linear feature along the direction of the main rupture at about N30°E. This can be seen more clearly in the deeper slice (20 km < H < 25 km) which also contains the mainshock's hypocenter and its respective Cluster #6 (Fig. 5.3c). A branch offset to the ENE of the mainshock can also be observed in the same slice (Cluster #1) as well as seismicity aligned along the N30°E line at the northernmost part (Cluster #4). The latter part also presents branching towards NW (Cluster #3) at the shallower slice (Fig. 5.4b; 15 km < H < 20 km).

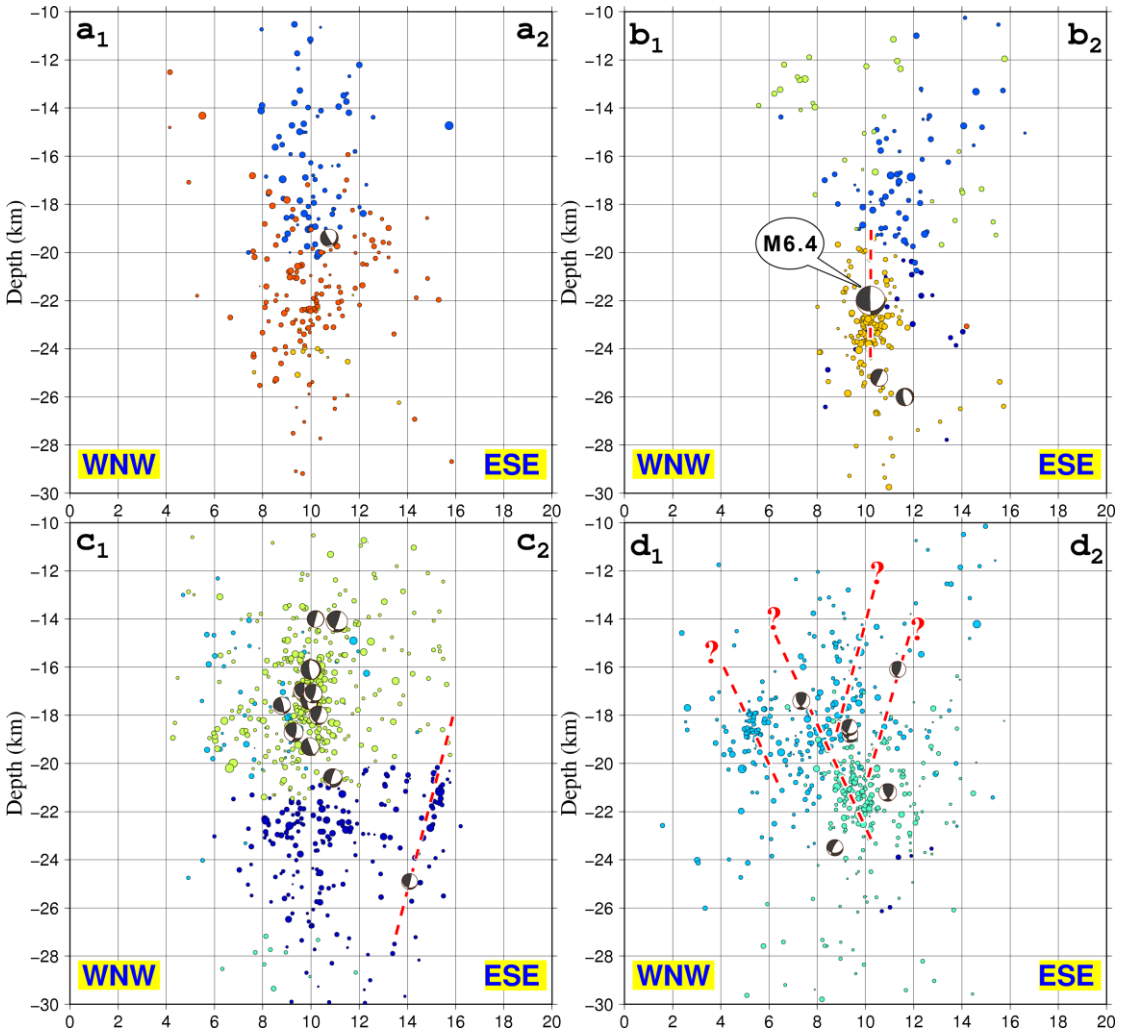

Figure 5.6: Transverse cross-sections in a N120°E direction across the relocated distribution of the 2008 Andravida aftershocks. Beach-balls represent the far-hemisphere projection of the respective focal mechanisms for the largest events of the sequence (Papadimitriou *et al.*, 2008).

Another perspective can be seen in a series of vertical slices, transverse to the main axis of the spatial distribution, in combination with the resolved focal mechanisms for the largest events of the aftershock sequence (Figs 5.5 and 5.6), derived by regional body-wave modeling at the Seismological Laboratory of the University of Athens (Papadimitriou *et al.*, 2008, 2010a). The fault plane solutions indicate almost pure strike-slip faulting near the mainshock, with an increasing degree of reverse component towards the north. In Fig. 5.6, the southernmost vertical slice a_1-a_2 shows a significant dispersion in the vertical axis that reflects the larger uncertainties at this part of the study region due to the unavailability of data from local seismological stations which would better constrain the focal depths. In b_1-b_2, the mainshock can be observed along with its very tight (2 km wide, horizontally) respective Cluster #6 at depths of 22-24 km. Interestingly, the hypocenters are less dispersed at these depths than in the shallower ones. The cross-section is nearly perpendicular to both the spatial distribution and the fault plane as indicated by the focal mechanism. The geometry becomes more complicated in the next cross-section, c_1-c_2, which also

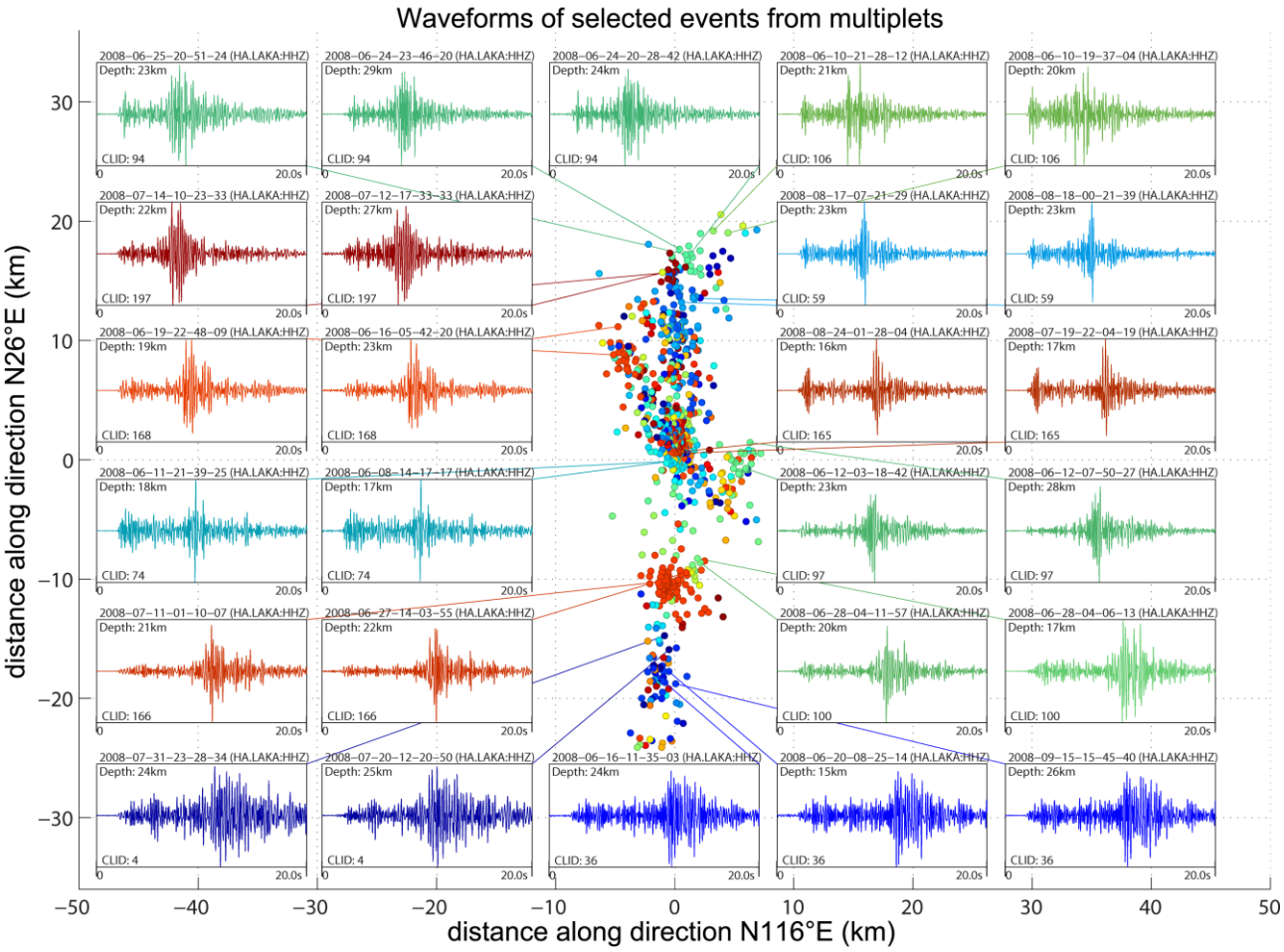

Figure 5.7: Epicenters of the largest multiplets during the 2008 Andravida aftershock sequence from a preliminary relocation, rotated by 26° counter-clockwise (Papadimitriou *et al.*, 2008). Waveforms represent the vertical component of station LAKA. CLID numbers refer to temporary multiplet IDs (see references in the text).

contains most of the major aftershocks. The latter mostly belong to Cluster #5, while a deeper one that belongs to Cluster #1 appears to be consistent with a linear feature that is offset from the main body of the sequence and could be related to the short branch to the east (Fig. 5.6c). In the northernmost cross-section, d_1-d_2, the tight deeper Cluster #4 defines activity on the main rupture plane, while the distribution is more dispersed at shallower depths, with some smaller offset clusters likely related to secondary structures near the tip of the major fault (Fig. 5.6b).

The multiplet analysis plays an important role in the relocation procedure, as correlated events are strongly bound together and their clusters tend to become denser. However, aftershocks with strong waveform similarity are relatively scarce in this sequence, given the detection capabilities of the regional network in this area (M_c=3.0). Although about 1000 events recorded in 2008 (~55%) were grouped in multiplets, only about half of them belong to large ones (more than 10 events). Fig. 5.7 presents the epicenters of events that belong to multiplets with the different colours corresponding to different Multiplet-ID (reported as CLID). The epicenters have been rotated by 26° counter-clockwise so that the vertical axis matches the approximate mean direction of the northern segment.

Waveforms of the vertical component of LAKA station are also presented for selected events from certain multiplets. The waveforms have been band-pass filtered between 3 Hz and 15 Hz and cropped between 2 seconds before the *P*-wave arrival-time and 18 seconds afterwards. Dissimilarities in waveforms are mainly attributed to differences in hypocentral location, focal mechanism and source duration (see Section 1.1.2).

Large groups of similar events are found in patches, the more populated one being a multiplet composed of over 100 events at the northern tip of the southern segment (Cluster #6), near the mainshock. Surprisingly, the dense spatial cluster located NE of the main event (Cluster #5) includes only two major multiplets with over 30 events each (shown in Fig. 5.7 with CLIDs 165 and 74 respectively) and two lesser ones with about 10 events. The waveform similarity among the rest of the events is less than required to form large multiplets, although they are all concentrated in a relatively small space. This could indicate increased complexity in the fault structure of that region, with the possibility of a flower-like structure that is also indicated by the spatial distribution itself. The northern segment is also characterized by two minor branches with significant multiplets, such as #97 (Cluster #1) and #168 in Fig. 5.7 (Cluster #3). The northern tip of the sequence includes another large multiplet (#59) with over 30 events and two smaller ones (#197 and #94) with about 15 events each, in the spatial Cluster #4. The southern segment is more simple and linear, mainly composed of the large multiplet #166 (Cluster #6) and a lesser one (#36) at the SW, under the artificial lake of Pinios (Cluster #2).

It is worth noting that it is usually the small events of a sequence that tend to have more similarities with each other and form multiplets. However, there are 22 events with $M \geq 3.5$ that belong to multiplets composed of 10 or more events. Some examples include an M_w=4.2 aftershock that occurred in 12 June 2008, 03:15 is part of the multiplet #97 and the M_w=4.2 event of 13 July 2008, 16:25 is included in multiplet #181 (situated at the northern part of the sequence). The M_w=4.6 event that occurred on 5 July 2008 belongs to the multiplet #165 owing to its strong similarity (mean XC_{max}=0.795) with the event of 10 June 2008, 20:45 with M=3.7. The latter is similar to 5 events, including the one that occurred on 5 July, but is also strongly correlated to two smaller ones: the 10 June 2008, 06:45 (M=2.4) and 18 December 2008, 10:53 (M=2.7). This chain of similar events continues to expand, because of the "nearest-neighbor" linkage used to create the similarity-based hierarchical classification, to all 38 aftershocks of multiplet #165. An important aftershock (M_w=3.9) is the 24 June 2008, 18:14 one that occurred at the northern extreme of the sequence, at the area covered by multiplet #94 to which it belongs. An apparent "bending" of the distribution towards a more E-W direction can be observed in that region, as also suggested by the more oblique-reverse fault plane solution of an M_w=3.9 event that occurred on 24 June 2008 (Fig. 5.5) which implies a dextral-slip fault striking ~N254°E, quite rotated relative to the N33°E (or N213°E, since the fault plane is sub-vertical) strike of the mainshock.

The temporal evolution of multiplets is presented in Fig. 5C.4, restricted in the first 30 days of the aftershock sequence. The activity in most of the larger multiplets was initiated within the first 4 days after the mainshock. In fact, most of the events that belong to different multiplets were generated at that time, indicating a very fast expansion of activity in most of the aftershock zone and little spread to new, unbroken areas afterwards. Some minor outbreaks can be related to strong

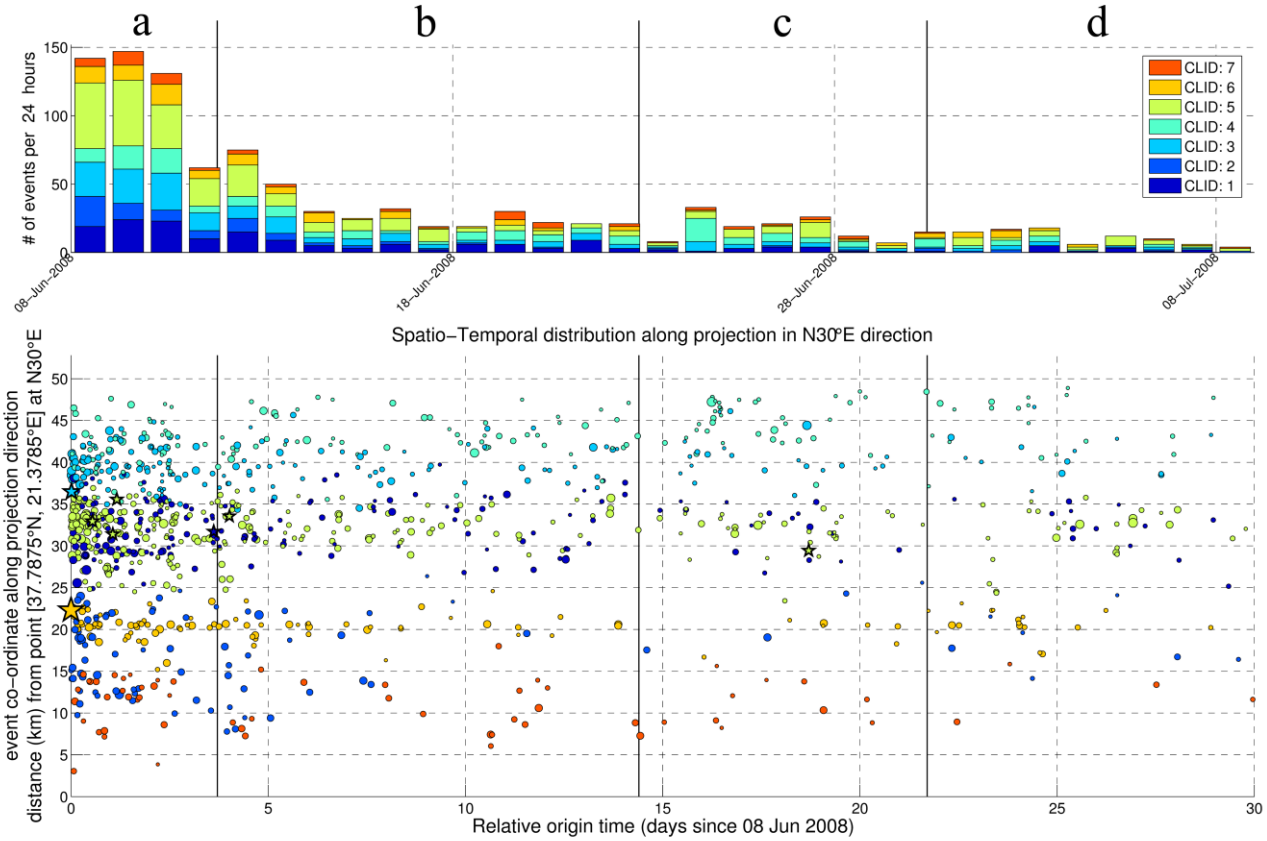

Figure 5.8: (top) Histogram of the daily occurrence of earthquakes during the first 30 days of the 2008 Andravida aftershock sequence, (bottom) spatiotemporal projection of the aftershocks' epicenters along a N30°E direction. Colours represent the 7 spatial clusters (CLID). Stars mark events with $M_w \geq 4.0$.

events, indicated by vertical gray lines in Fig. 5C.4, but in general no significant secondary subsequence can be observed that would cause a spike in the histogram. Similar observations can be made in the spatio-temporal projection of Fig. 5.8 along the major axis of the epicentral distribution, N30°E. The aftershocks cover the whole length of the aftershock zone almost immediately after the mainshock (zooming into the time-scale does not make a difference that would indicate spreading of seismicity outwards from the mainshock). The activity decays very smoothly, as evident from the histogram. Different parts of the rupture zone are characterized by different density of hypocenters and seismicity rates (Fig. 5.8). However, they all decay in the same manner.

Some of the more noteworthy, but still small, sub-sequences during the extended period of study (up to December 2010) were observed on: (a) 12 June 2008, when a small branch was activated by an M_w=4.2 aftershock SE of the northern segment, (b) on 24-25 June 2008 at the northernmost part of the sequence which appears to follow a different direction than the rest of the segment, bent slightly more towards WSW-ENE which also matches the strike of one of the nodal planes of the 24 June 2008 significant aftershock (M_w=3.9), (c) on 5-6 July 2008 at the southern part of the northern segment following the major aftershock of 5 July 2008 (M_w=4.6), (d) almost 18 months later, during November-December 2009, the southernmost part of the southern segment was reactivated with an M_w=3.9 event on 26 November 2009, followed by an M_w=3.8 aftershock under the artificial Pinios

lake on 21 February 2010, which triggered a short sequence, and (e) the last spatio-temporal cluster that occurred during July 2010 was observed south of Pinios lake, at depths of about 20-22 km, possibly affected by an M_w=4.3 event that occurred further SW (outside the study area) on 29 May 2010.

5.1.4 ETAS modeling

From the point of view of its spatio-temporal evolution, the 2008 Andravida earthquake appears to have generated a very typical and smooth aftershock sequence. Perhaps its only peculiarity seems to be the one concerning the largest aftershock, which occurred ~18 min after the mainshock and had a magnitude of M_w=4.7, quite lower than the expected M_w≈5.2 for an M_w=6.4 mainshock, according to Båth's law (Båth, 1965). However, if the Gutenberg-Richter law for the frequency-magnitude distribution is taken into account, along with the modified Båth's law suggested by Shcherbakov & Turcotte (2004), the expected magnitude of the largest aftershock, m^*, becomes m^*≈4.57 (with a=7.52 and b=1.64) for the first 30 days or m^*≈4.71 (with a=7.31 and b=1.55) for the seismicity up to December 2010, determined by least squares regression for magnitudes between 3.0 and 4.2. During the first month, the catalogue appears to be complete down to M_c=3.0 with a large b-value of about 1.50, as estimated by the maximum likelihood method. The relatively low detectability restricts the magnitude range over which the Gutenberg-Richter power-law is applicable. As is typical with aftershock sequences, the magnitude of completeness is high at the beginning, following the mainshock, reaching about M_c=3.0, then gradually drops near 2.7±0.2.

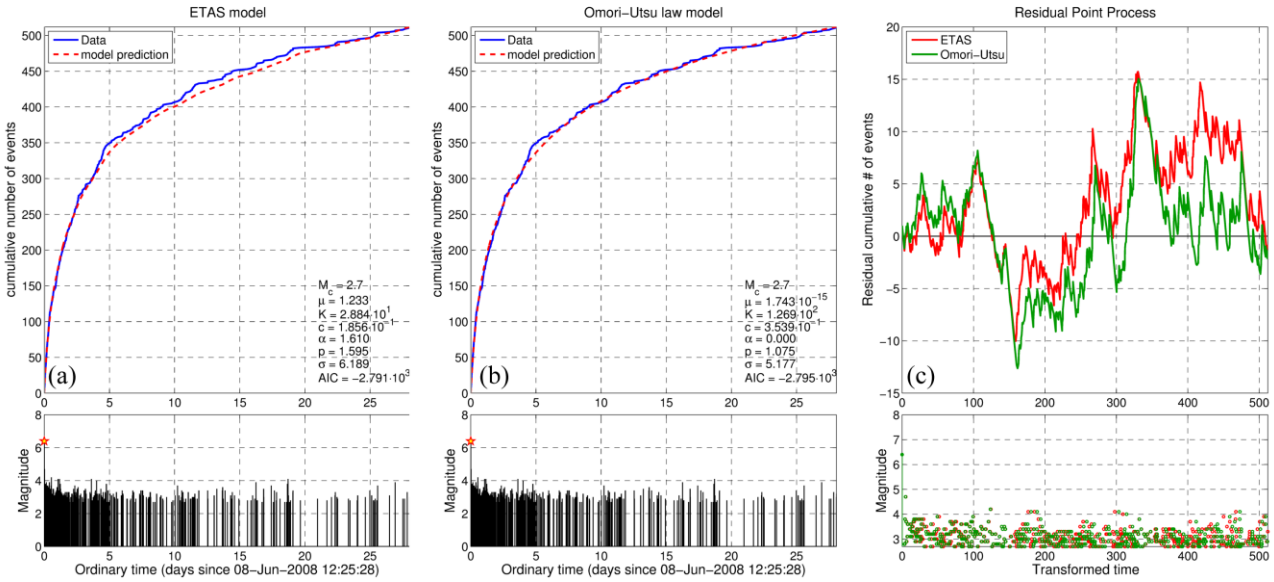

Figure 5.9: a) ETAS model and b) Omori-Utsu model for the first 30 days of the 2008 Andravida aftershock sequence, with M_c=2.7 and M_{ref}=M_{main}=6.4, c) comparison of the residuals between real and modeled cumulative number of events for the two models in transformed time.

An ETAS model was determined using the SASeis2006 software (Ogata, 2006) for a subset of 513 events with $M \geq 2.7$ during the first 30 days of the aftershock sequence (Fig. 5.9). The results are compared against the respective Omori-Utsu model (Modified Omori's Formula, or MOF), with all parameters determined by maximum likelihood estimation. Due to the lack of significant secondary sub-sequences, the MOF model seems to be a better choice than the ETAS model, as the respective *AIC* value for the latter is higher (less negative) than the former. The standard deviation σ is also slightly larger for the ETAS model, due to an offset in the calculated cumulative number of events that is observed after the 4th day which persists until the end. The MOF model has a practically zero background rate, μ, in contrast to the ETAS model. Fixing $\mu=0$ for MOF does not affect the calculation of the other parameters at all. The *p*-value as determined for the MOF model is $p=1.08$ and could reach up to $p \approx 1.15$ for different choices of M_c or a larger time interval (e.g. until the end of 2008). For the ETAS model, on the other hand, it is quite high, $p \approx 1.60$ with an equally large *a*-value, $a=1.6$, consistent with what is expected for ETAS when applied to aftershock sequences (e.g. Ogata, 1992). For $M_c=3.0$, which is more appropriate for this dataset, although it reduces the events to 300, $p=1.083$ for the MOF model but the μ value is about 100 times larger and the fit is not as good, while ETAS still has a worse fit and its *AIC* is higher than the respective MOF model. All this suggests that the whole aftershock sequence can be described adequately by stress transfer due to the mainshock, which did not leave any significant unbroken asperities in the margins or inside pockets within the ruptured surface that would break and generate secondary subsequences.

5.1.5 Discussion - Conclusions

The year 2008 had been one of the most intense in terms of seismic activity in the region of Greece, as a series of mainshocks with $M_w>6.0$ struck various parts along the broader Hellenic arc (Papadimitriou *et al.*, 2008, 2010a; Papadopoulos *et al.*, 2009). In 6 January 2008, an $M_w=6.3$ event of intermediate depth ($H=84$km) occurred below Leonidion, east Peloponnese (Zahradnik *et al.*, 2008). About a month later, in 14 February 10:09 UTC, an $M_w=6.6$ thrust earthquake struck ~40 km offshore S of the city of Methoni, SW Peloponnese, followed by an $M_w=6.1$ aftershock two hours later and yet another $M_w=6.0$ strike-slip event two days later (Roumelioti *et al.*, 2009). The $M_w=6.4$ Andravida event, studied in this section, occurred on 8 June while an $M_w=6.3$ earthquake struck Rhodes island, at the SE end of the Hellenic Arc, on 15 July 2008. In fact, year 2008 has been the year with the most events with $M_w>6.0$ since 1970 (Fig. 5.10). It is comparable only to 1981, which was marked by three significant earthquakes in the eastern Corinth Rift (King *et al.*, 1985) that caused damage and casualties in many cities including Athens, an $M_w=6.9$ mainshock between Skyros and Lesvos islands and an $M_w=6.3$ aftershock, and 1983, with two earthquakes SW of Cephalonia and another in the North Aegean trough, at the extension of the North Anatolian fault.

The 2008 Andravida earthquake was considered unexpected in terms of the causative fault and its potential. It's reportedly been the largest earthquake that has occurred in NW Peloponnese for 300 years (Papadopoulos *et al.*, 2010). It is located in a transition zone between the active subduction at the Hellenic Arc, with a compressive stress in a SW-NE direction and rifting in the Gulf of Corinth with extensional stress in a N-S direction. Until its occurrence, there had been few seismological data which indicated that strike-slip faulting occurs in the broader area, with ambiguity concerning

the strike of the respective faults and, consequently, whether the horizontal slip is dextral or sinistral. An example for this ambiguity is the 2002 Vartholomio earthquake, with a focal mechanism similar to the one of the 2008 Andravida earthquake but with some authors supporting a dextral, SW-NE striking fault (Serpetsidaki *et al.*, 2010) while others suggesting the conjugate nodal plane which defines NW-SE sinistral strike-slip faulting (Roumelioti *et al.*, 2004). In support for the latter model (e.g. Ganas *et al.*, 2009), a NW-SE striking, sinistral-slip structure could include an event that occurred in 1988 in its NW extension towards Cephalonia, also consistent with the NW-SE plane of the 1953 earthquake, if an oblique-reverse fault plane solution is considered (Fig. 5.1; source: ETHZ) instead of a pure reverse one (e.g. Stiros *et al.*, 1994). The first scenario, however, is more consistent with the faulting type imposed by the propagation of the dextral Northern Anatolian fault through the Aegean and supposedly through continental Greece and likely towards the Hellenic Arc (Serpetsidaki *et al.*, 2014).

The 2008 Andravida mainshock and its aftershock sequence provided evidence for the existence of a SW-NE trending, sub-vertical, dextral strike-slip fault in the SW continuation of the NW-dipping Rion-Patras fault zone (RPFZ; Flotté *et al.*, 2005), which is oblique-normal with a dextral component. It was unexpected, as there is no mapped superficial fault to correspond (Koukouvelas *et al.*, 2009), but rather some minor normal faults in random directions and a series of east-dipping thrusts whose traces are all oblique to the causative fault of the Andravida earthquake. No indications for such a major structure are evidenced from the hydrographic network either, as no offset in the streams can be observed (Stiros *et al.*, 2013). The fault is sub-parallel to and of the same slip direction with the major Cephalonia-Lefkada Transform Fault Zone (CTFZ). At a regional scale, the CTFZ, the subduction zone west of Zakynthos island, the Andravida fault and RPFZ, the NNW-SSE sinistral-slip faults in Aitoloakarnania and the pull-apart basins of Trichonis lake and Amvrakikos gulf, apparently demarcate the boundaries of a tectonic block with very sparse seismicity in its interior.

The lack of direct macroseismic manifestations of the coseismic slip on the main rupture, despite the significant magnitude of the mainshock, indicates that its causative fault is a buried strike-slip structure with various observed ground openings, mostly oblique to the direction of the main fault, e.g. near Nisi (Fig. 5.11), being attributed to the development of a positive flower structure (Koukouvelas *et al.*, 2009), while an impressive distortion of railway lines in Kato Achaya was explained as deformation caused by the passing SH-waves rather than due to the static displacement field at the surface (Parcharidis *et al.*, 2009; Papadopoulos *et al.*, 2010). This is consistent with the relatively large depth of its hypocenter, at ~22km. The aftershocks are mostly distributed between ~12 and ~27 km. Shallower events (H<10km) are generally considered as either mis-located, "attracted" by the velocity model's shallow discontinuities or well-located but unrelated to the aftershock sequence and rather belonging to more superficial structures.

Such smaller faults were outlined by Serpetsidaki *et al.* (2014), where the vertical distribution presents a gap at ~15km that is speculated to be caused by a layer of evaporites, decoupling the deeper from the shallower activity. In the present study the same pattern appears to occur at ~10km. This upper limit of seismicity is an approximation for the burial depth of the fault. Feng *et al.* (2010), on the other hand, who consider a fault length of ~25km, argue that a burial depth of ~10km

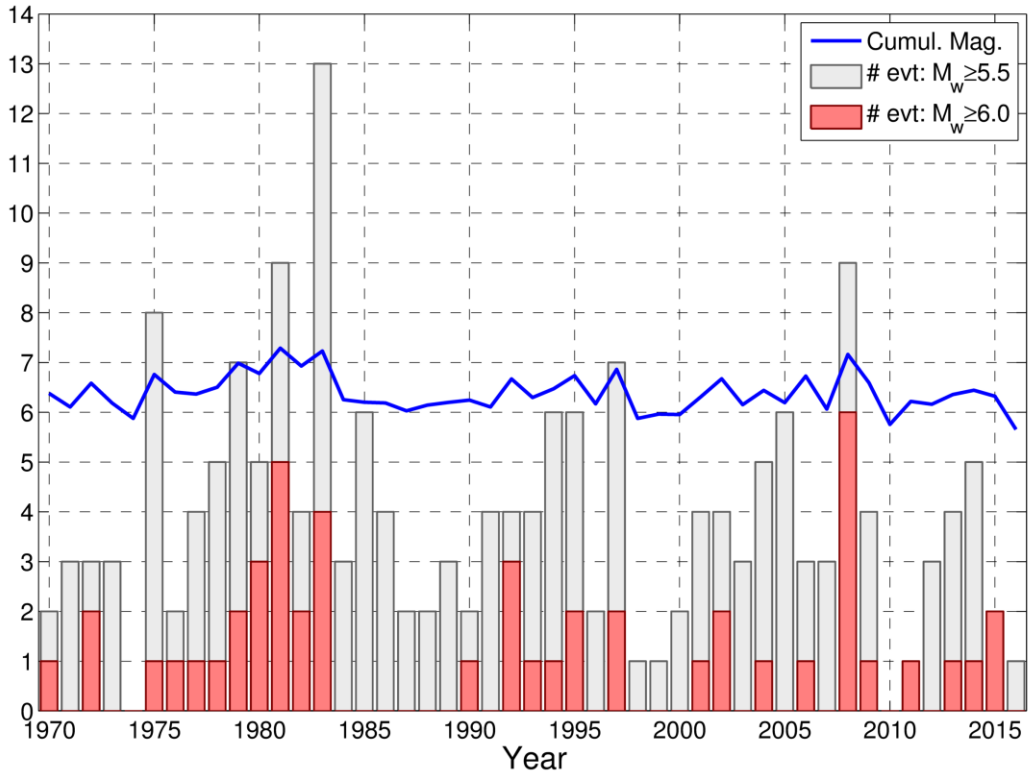

Figure 5.10: Yearly number of significant earthquakes (M_w≥5.5 or M_w≥6.0) and cumulative magnitude (summation for events with M_w≥5.0) since 1970 and up to June 2016.

would affect the length/width aspect ratio and prefer a value of 5km. They calculated that, in such a case, the expected horizontal surface deformation at a distance of 3 to 13 km from the fault should be larger than 20mm. However, measurements at the closest permanent continuous GPS station, located at Riolos (RLS) was 7.3±0.3mm (Ganas *et al.*, 2009). Feng *et al.* (2010) suggested that decoupling occurs between the subsurface deformation and the surface due to the existence of a ~3km thick flysch layer, evidenced from seismic and borehole measurements (Kamberis *et al.*, 2005). Either way, whether because of a mid-crust salt layer or a shallower flysch layer, there appears to be a separation of the activated structures and static deformation between the main fault and the surface.

Papadimitriou *et al.* (2010a) determined a slip model that is compatible with a rupture length of 25 km (Fig. 5C.6a), while the parts of the fault plane where major slip has occurred coincide with areas of sparse aftershock activity, mainly above Cluster #6 (in the area covered by the much sparser Cluster #2), north of #6 in the gap between Clusters #6 and #1, as well as above the major Cluster #5. This is a similar result as the one of Gallovic *et al.* (2009) who found maximum slip at the respective spatial gap and a more or less comparable rupture length, containing 3 sub-event sources. The dense Clusters #5 and #6, in the margins of the area of maximum slip, were triggered by highly localized stress load due to the redistribution of stress associated with the mainshock. Other authors (e.g. Papadopoulos *et al.*, 2010; Serpetsidaki *et al.*, 2014) have derived smaller fault lengths with a

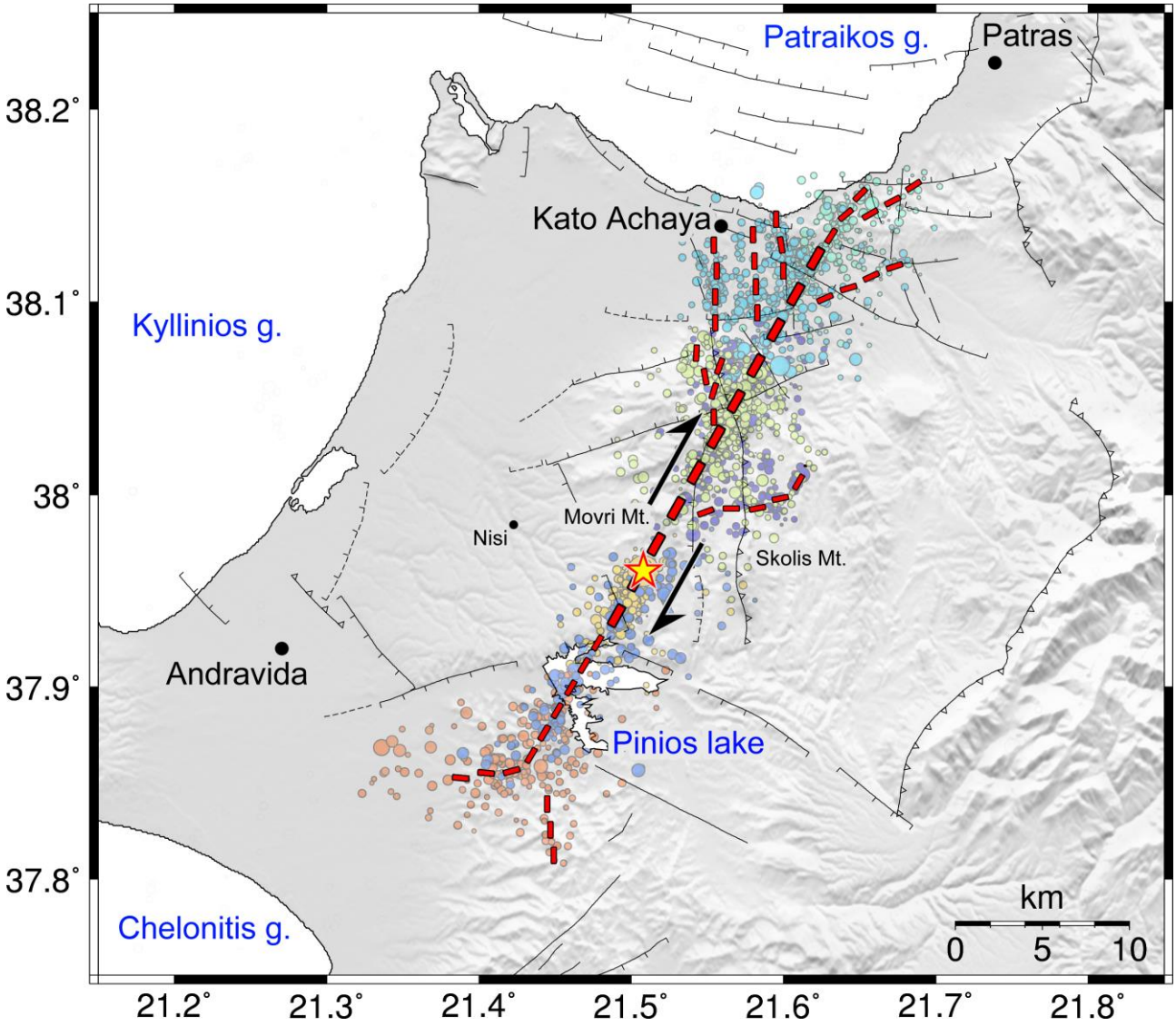

Figure 5.11: Sketch of simplified interpretation of the inferred activated structures at depth. The 25 km long, bold dashed red line corresponds to the main rupture while smaller red dashed lines are supposed secondary neighboring structures activated due to stress transfer by the mainshock (red-yellow star) and the largest aftershocks. Kato Achaya is the village which suffered the most severe macroseismic effects with a maximum intensity of VIII (Papadopoulos *et al.*, 2010). NNW-SSE to WNW-ESE directed surface breaks were also reported in the vicinity of Nisi (Koukouvelas *et al.*, 2009).

larger average slip. It's been reported that the 2008 Andravida earthquake was characterized by a relatively high stress drop, $\Delta\sigma$ = 13 bars, attributed to the increased rigidity and long recurrence time (~300 years) (Papadopoulos *et al.*, 2010). Feng *et al.* (2010) measured an even higher value of $\Delta\sigma$=5MPa (or 50 bars) and explained it as a result of large coseismic slip or fast rupture velocity, due to the rupture of an immature structure containing little fault gouge that could favor after-slip. This is consistent with the observation that the aftershock sequence was very smooth, without any significant secondary outbreaks, containing very few events with $M_w \geq 4.0$, while the determined *b*-value of the Gutenberg-Richter law was very high, indicating seismicity due to creep rather than the breaking of large asperities (Papadopoulos *et al.*, 2010).

The dimensions of the rupture area derived from the slip model of Papadimitriou *et al.* (2010a) are also compatible with the theoretically expected ones. According to the empirical relations of Wells & Coppersmith (1994), the subsurface length, *L* (km), of a strike-slip rupture is:

$$L = 10^{\frac{M_w - a}{b}} \xrightarrow{(strike-slip, length)} L = 10^{\frac{M_w - 4.33}{1.49}} \quad (5.1)$$

where *a*, *b* constants which depend on the faulting type and fault dimension. For the widely accepted M_w=6.4, the subsurface length and width (derived using *a*=3.80 and *b*=2.59 in Eq. 5.1) for a strike-slip rupture are 24.5 km and 10 km, respectively. However, the length of the activated area is much larger, reaching up to ~43 km (Fig. 5.11), that would correspond to a moment magnitude of about 6.7 to 6.8. The resulting Coulomb stress transfer using the respective slip model (Fig. 5C.6b) can explain the triggering of activity at the northern and southern edges of the sequence as well as the NW-directed branches of Cluster #3, which were not yet resolved in the preliminary results of Papadimitriou *et al.* (2010a). Other Coulomb stress transfer models have suggested that the positive lobe includes the area below the city of Patras (Ganas *et al.*, 2009) and Psathopyrgos fault and could possibly have promoted the occurrence of the two earthquakes near Efpalio in 2010 (Segou *et al.*, 2014; Section 5.2).

An important observation is that, although the mainshock's focal mechanism indicates an almost vertical fault striking at N33°, the aftershocks appear to be roughly distributed along two different linear segments, with the mainshock's epicenter lying in between. More specifically, at the southern segment (Clusters #2, 6 and 7), the orientation of the aftershocks spatial distribution is around N36°, while at the northern one (Clusters #1, 3, 4 and 5) it changes to about N27°, with a few branches deviating from the roughly linear distribution. This difference has also been observed, even more pronounced, in other studies (e.g. Feng *et al.*, 2010), which could be partially due to differences in the used velocity models causing biases, mainly at the less constrained southern segment. However, taking into account only the deeper slice at *H*=20 to 25 km (Fig. 5.4c) it appears that the N30°E profile line fits well to most clusters with the exception of the various branches. This shows that the activated fault is well defined at depth, while at shallower depths seismicity probably deviates to secondary, smaller faults, especially at the northern segment which is also much wider.

The slip model of Papadimitriou *et al.* (2010a) also provides evidence for the directivity of the rupture towards NE, similar to Gallovic *et al.* (2009). This was hinted by the early findings of the spatiotemporal distribution. Although it was evident that the whole area was immediately affected, as aftershocks filled both segments in less than a day, during the first hours following the mainshock most of the seismicity was located at the northern segment, with fewer events at the southern one. Both segments show activity during the whole study period, however, the ratio of the number of located earthquakes occurring at the southern segment divided by the corresponding number at the northern one remains around 38%, with the exception of the time-period between November 2009 and December 2010 during which the southern segment's activity was increased. Overall, ~1290 events were recorded at the northern segment while only ~550 were located at the southern one (42.6% ratio). Fig. 5.11 shows the approximate length that was ruptured with bold red

dashed lines and some inferred secondary structures branching out from the main fault (thin red dashed lines).

Serpetsidaki *et al.* (2014), who installed a temporary local network covering the northern segment of the 2008 Andravida aftershock sequence to better constrain the hypocenters, performed a relocation procedure and determined several clusters at depth. Their largest (most populated) one roughly coincides with the respective Cluster #5 of the present study, although spread to also include some activity of Clusters #6 and #2. They concluded that the main rupture occurred within this cluster, that would be like shifting the bold dashed line of Fig. 5.11 by about 7km SW, bringing the mainshock's epicenter closer to the middle of the sub-vertical plane, thus reducing the effect of the rupture's directivity. They also located the seismicity of the northern edge much offset to the west, with no evidence of NW-directed branches (e.g. Cluster #3) and very few events at the southern end of the activated zone (e.g. Cluster #7). Despite these differences, they too suggest that the mid-southern part of the activated zone, related to their large cluster, is simpler and more compatible with the faulting type of the mainshock while the northern part presents differences both in terms of location (offset from the main rupture plane) and faulting type, as they calculated many normal mechanisms in the mid-northern part and several reverse ones at the very offset NE edge. While in the present study there is no evidence for activated normal events, an oblique-reverse solution has been determined at the northern part, with the dextral-slip plane being slightly rotated clockwise (Fig. 5.5), matching a NE-trending branch (Fig. 5.11).

Concluding, the 2008 Andravida earthquake filled an important gap in the recorded seismicity of Greece and, like other significant earthquakes, it was a reminder that unknown, blind faults, with little to no background activity can break unexpectedly and surprisingly and likely re-adjust the map of seismic hazard. It also potentially fills a missing piece in the image of an extension of the North Anatolian fault through continental Greece, below the RPFZ and towards the subduction zone. On the other hand, its rupture directivity towards the North, the likely NNE propagation of the fault's tip and the redistribution of stress which increased the load below Patraikos gulf (Fig. 5C.6b) could possibly be a concern for the major city of Patras, thus the seismicity of the region should be carefully monitored.

5.2 The 2010 Efpalio sequence

The western Corinth Rift, one of the most seismically active regions in Europe, has been continuously monitored by the Corinth Rift Laboratory (CRL) local seismological network for more than a decade (Lyon-Caen *et al.*, 2004; Bernard *et al.*, 2006). Since 2007, the integration of the Hellenic Unified Seismological Network (HUSN) has also been providing complementary regional data, covering areas which were at the limits or barely outside the CRL network. Such is the region of Efpalio, at the north-western edge of the rift, N of the major E-W trending, north-dipping Psathopyrgos normal fault. One of the most important recent sequences started on 18 January 2010

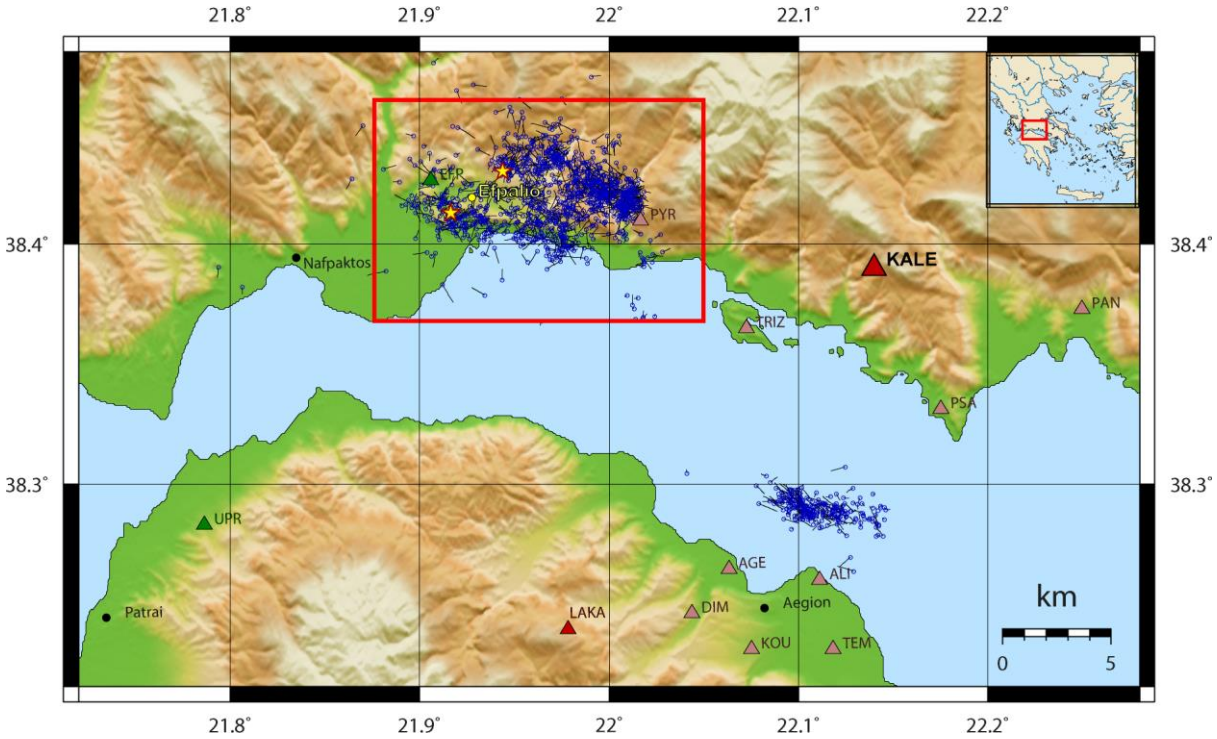

Figure 5.12: Seismicity of 18-26 January 2010 in the western Corinth Rift derived by the Master-Events method (a more detailed view is presented in Fig. 5.13) as well as the local seismological stations, including the reference station KALE. The 2010 Efpalio swarm is marked with a red rectangle. The two M_w=5.1 events are marked with stars. Figure after Kapetanidis & Papadimitriou (2011).

at 15:56:08 UTC, when an earthquake of magnitude M_w=5.1 occurred close to the city of Efpalio (Fig. 5.12). Four days later, on 22 January 2010 at 00:46:55 UTC, another moderate event of magnitude M_w=5.1 occurred, about 3km NE of the previous one. Intense aftershock activity followed both major shocks, with the epicenters covering a region about 12km long (WNW-ESE) and 6km across. In this specific area no such activity had been observed during the past few decades. It is also the strongest event to date (2016) in the western Corinth Rift since the 1995 M_s=6.2 Aigion earthquake, with the second largest being the M_w=5.0 event of 7/11/2014, offshore Aigion (see Appendix 6A).

A preliminary analysis of the seismicity during the 2010 Efpalio sequence was undertaken as an application of the Master-Events method (Sections 4.3 and 5.3.1) by Kapetanidis & Papadimitriou (2011). In this section a more complete seismotectonic and spatiotemporal analysis is conducted and described, with additional small events being added to the catalogue using the HADAES method (Section 5.2.2).

5.2.1 Application of the Master-Events method

Several stations have been installed and are operating in the broader region around the aftershocks. The station KALE of the Seismological Laboratory of the University of Athens, is located about 15km E of the aftershock area and was selected as the reference station for the application of the

Master-Events (ME) method (MEm, for short). This station is neither too close nor too far from the epicentral zone, and its data quality has been adequate during the study period between 18 and 26 January 2010. Manual event-detection was performed by visual inspection of the 24-hour continuous recordings at the reference station, to ensure that all cropped windows include a single signal, wherever it is possible, and that all signals are valid earthquakes and not local noise. Inevitably, in some cases of successive events, the signals had already begun to overlap when arriving at station KALE. For experimental purposes such events were not discarded in order to test the fitting procedure for any possible weaknesses related to this issue. In total, 9174 signals were detected at station KALE for the period between 18 and 26 January 2010, starting right after the first major event.

Day-specific cross-correlation matrices were constructed, followed by the clustering procedure and calculation of the optimal threshold $C_{opt.th}$. Over 6000 of events were found to belong to multiplets, representing the 67.4% of the detected signals. The highest values of optimal threshold $C_{opt.th}$ were found for 19 January (one day after the first major event) and 22 (the day of occurrence of the second major event) which also yielded the largest numbers of repeating earthquakes and clusters. Cluster-specific matrices were then created using the bridging technique (Cattaneo *et al.*, 1999) between individual clusters derived from different day-specific cross-correlation matrices. After the removal of clusters with less than 4 events, the remaining 219 contained a total of 4583 events.

Routine analysis at the Seismological Laboratory of the University of Athens provided arrival-time, origin-time and location data for the stronger events of the sequence. This information was used for the calculation of mean P-wave travel-times, TT_P, for all stations. Approximate mean S-wave travel-times, TT_S, were also calculated by multiplying TT_P with the mean V_p/V_s ratio. In the original application of the method (Kapetanidis *et al.*, 2011), the velocity model of Papadimitriou *et al.* (2010b) was used, with V_p/V_s=1.79. The $P_{markers}$ (approximate P-wave arrival) and TT_P (P-wave travel-time) of the reference station were used for the calculation of approximate origin times, OT_P, for each of the multiplet-events that belong to the cluster-specific matrices.

The $P_{markers}$ for a total of 388 multiplet-events were matched to the arrival-times of P-waves of manually located events (already available from routine analysis) at the reference station, KALE. These were selected as master-events, mainly distributed in the major multiplets. No extra master-events were considered for this application, other than these 388, but, in practice, there should be at least one master-event per cluster in order to produce complete results. In that case the master-event should be the strongest event of each multiplet in order to have a higher signal-to-noise ratio. Such criteria are also considered in the HADAES method for the selection of internal (day-specific) master-events. Additional P- and S-wave arrival-times were manually picked for the master-events, especially at the closer stations as well as local stations whose data were not available during the routine analysis. This concludes the preparatory stage of catalogue data.

Extensive filter tests were performed to determine the frequency bandwidths which maximize the correlation coefficient maxima of the correlation detectors, C_m (Kapetanidis & Papadimitriou, 2011). Further tests were conducted by varying the high and low cut-off frequencies and calculating the RMS values and location errors of the hypocentral solutions of the slave-events as

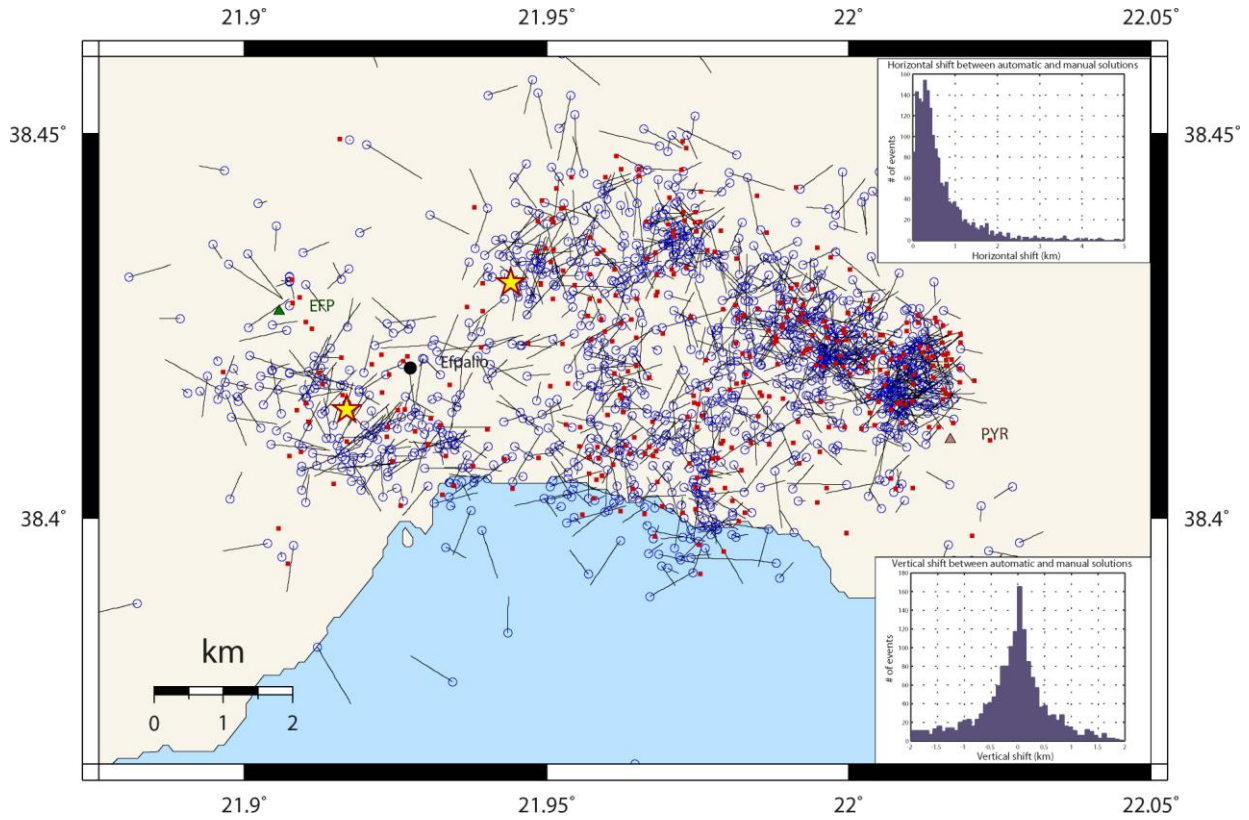

Figure 5.13: Zoom in the area of the Efpalio 2010 aftershock sequence, denoted by a rectangle Fig. 5.12. Solid squares are the master-events used to pick the arrival-times of the slave-events. The upper-right histogram shows the distribution of the horizontal shifts while the lower-right histogram shows the distribution of the vertical shifts between automatic and manual locations. Stars denote the epicenters of the two major shocks. Figure after Kapetanidis & Papadimitriou (2011).

well as visually observing their spatial clustering. For the case studied in this application, the waveforms were band-pass filtered between 2.5Hz and 23Hz with additional filters depending on the per-station stored information, to account for station-dependent signal and noise characteristics. This default filter is wide enough to preserve waveform complexity while eliminating long-period and high-frequency noise.

For the master-events, the P-wave windows were cut between 0.2sec before and 4sec after their arrival-time, unless the S-wave arrives earlier, in which case the window stops before its onset to avoid any influence of the S-wave to the correlation. There is no need for a longer offset before the P-wave onset, as the arrival-time has been manually picked with sufficient precision. The S-wave window starts 0.3sec before and stops 6sec after the S-wave arrival-time, without any concern for the P-wave coda because of its lower energy content in comparison to the S-waves. The length of the P-wave window has to be small enough to exclude noise before the arrival as well as the onset of S-waves. Even in cases where the manual arrival-time picking error is more than 0.2sec, the arrival pulse takes up only a few samples at the beginning of the correlation detector window. The coda wave is also important for the correlation as it occupies more samples. However, when the

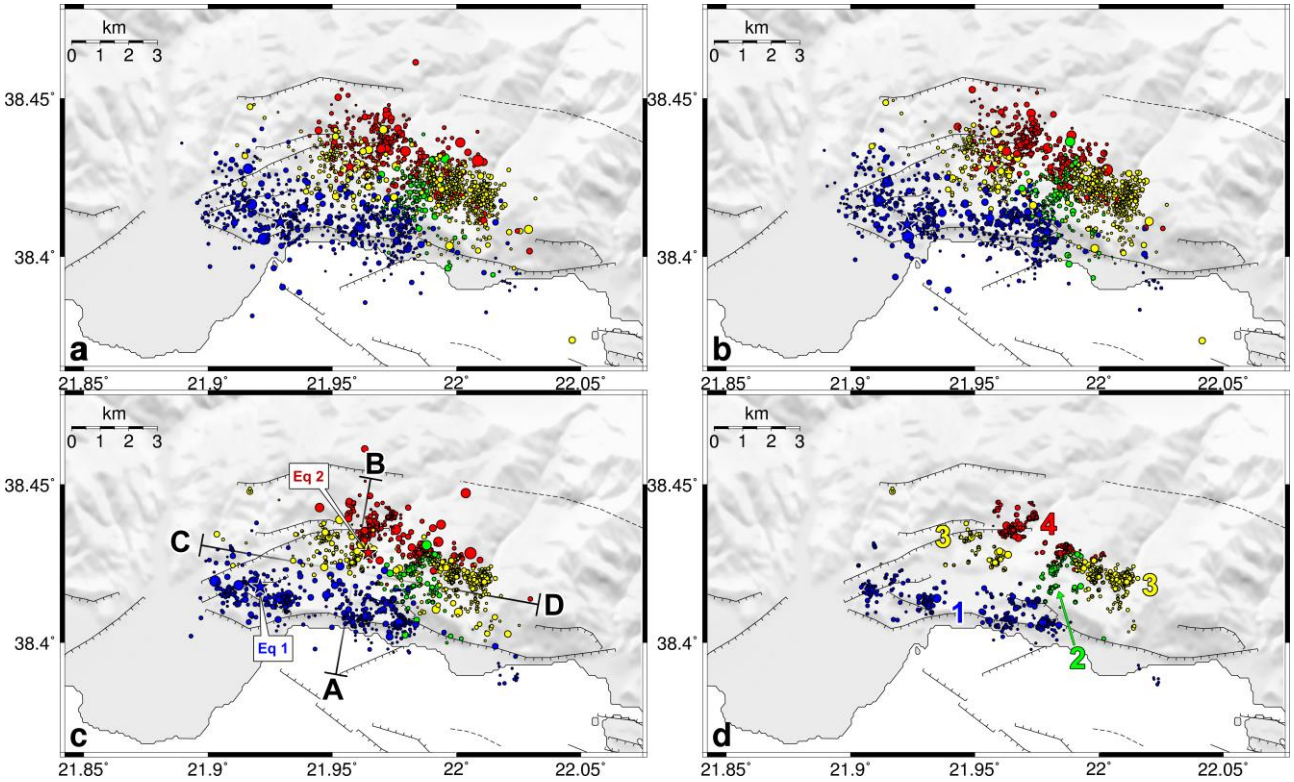

Figure 5.14: Seismicity of 18-26 January 2010 in Efpalio, including events from routine analysis and manually revised primary slaves derived from the MEm (subset A), a) initial locations, b) corrected by station travel-time residuals, c) relocated by HypoDD, d) relocated, but retaining only cross-correlation links in the last set of iterations (subset CC). The relocated epicenters of the two major M_w=5.1 events and profile lines A-B and C-D are marked in panel (c). Spatial cluster numbers are marked in panel (d). Fault lines are compiled after Doutsos & Poulimenos (1992), Flotté *et al.* (2005), Bell *et al.* (2009), Valkaniotis (2009) and Beckers *et al.* (2015).

arrival onset is impulsive, it may indeed play a major role in the level of the correlation coefficient. Experiments with different window lengths for cross-correlations in the literature (Schaff *et al.* 2004; also Figs 1.14 and 1.15) have shown that the correlation coefficient tends to decrease with increasing window length, although the fitting efficiency tends to improve in longer windows (more reliable fits despite their lower weight) as they have a better chance of capturing coherent energy, especially when the signal-to-noise ratio is low. In any case, the window length for a P-wave correlation detector cannot exceed the S-P arrival-time difference; otherwise it will include the S-wave onset, which must be avoided. The slave-event waveforms were cropped between 30sec before the approximate P-wave arrival, P_d, and 90sec afterwards, in order to include the whole signal.

The picking algorithm, which is the main part of the ME methodology, measures the correlation-coefficient maximum value, C_m, and its corresponding time-lag at the best-fit window between a master- and a slave-waveform window of equal length. For the same window, the mean coherence

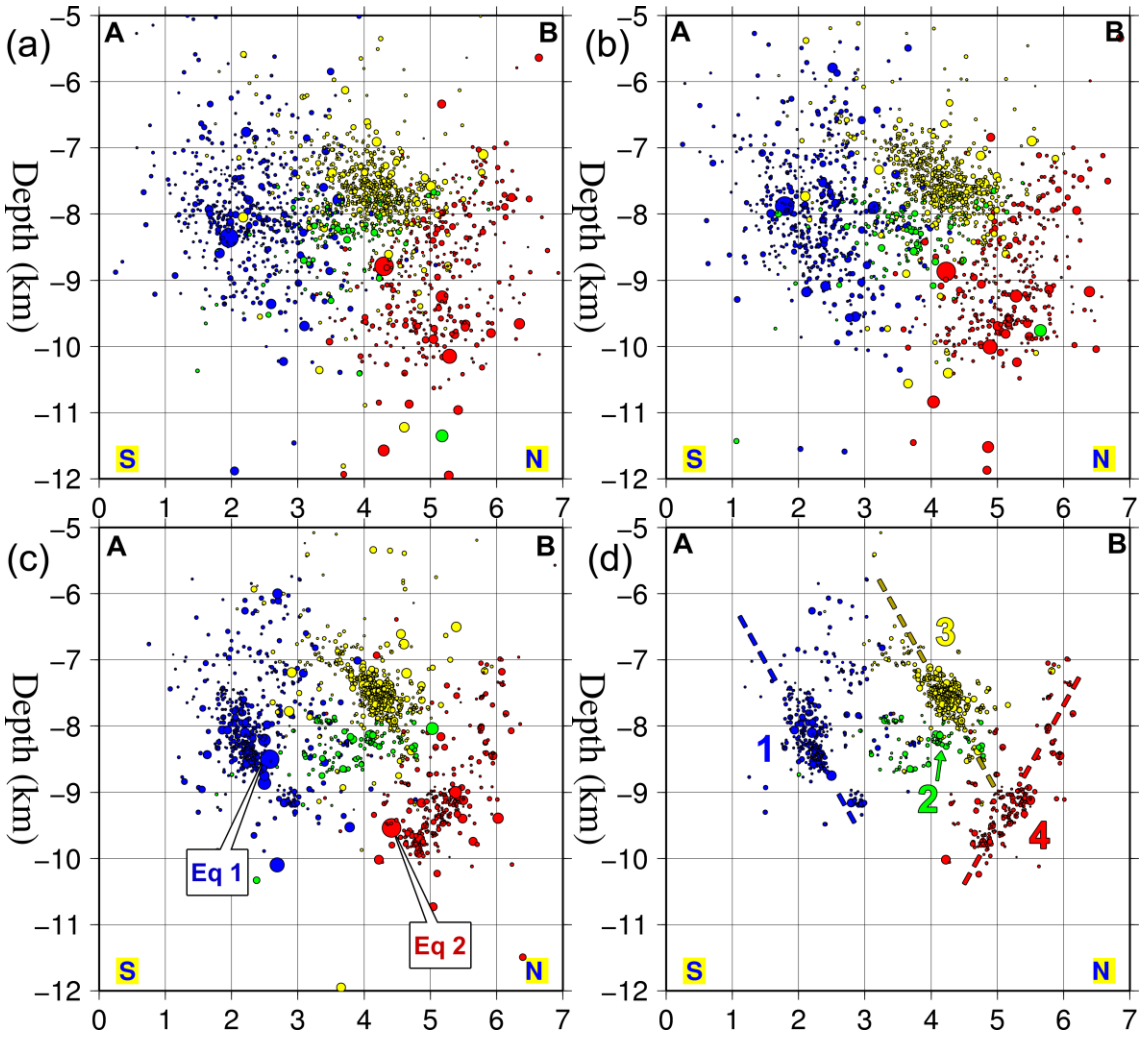

Figure 5.15: Same as Fig. 5.14 but in the N10°E oriented A-B cross-section view, a) initial locations, b) corrected by station travel-time residuals, c) relocated by HypoDD, d) relocated, but retaining only cross-correlation links in the last set of iterations (subset CC). Proposed structure geometry is indicated by dashed lines in panel (d).

between 2Hz and 15Hz, M_{coh}, and the difference between the global and the highest secondary maximum of the cross-correlation function, D_{max}, are also measured, as described in Section 4.3. Their distribution characteristics were studied by Kapetanidis & Papadimitriou (2011). The maximum values of the C_m/M_{coh} ratio and C_m/D_{max} ratio distributions were used as multipliers for the M_{coh} and D_{max} values, for observations of P- and S-waves separately, which, in addition to the C_m, can provide a combined observation weight, C_w, that takes into account all three parameters. The weighting scheme can be improved with trial and error experiments on the pre-calculated measurements in an attempt to minimize the resulting location errors and improve the visual image of the epicenters' spatial clustering. The procedure was finalized by producing a single arrival-time pick, taking into account all the available fits between master- and slave-waveforms.

A total of 1945 slave-events had their arrival-times picked automatically using the ME methodology. This is only a part of the potential number of events which can be picked, as they are the ones which are directly similar to the 388 master-events ($XC_{max}>C_{opt.th}$ in the cluster-specific

matrices). In order to evaluate the quality of the automatic results, the arrival-times of the slave events were manually revised for corrections or rejections (false positives) of automatic picks as well as for the addition of extra arrival-times that were missed. The comparison between automatic and manually corrected slave-events locations is presented in Fig. 5.13, where the line attached to each open circle (slave-event location after manual evaluation) shows the horizontal shift between the automatic and manual location. The epicenters of these slaves cover the entire aftershock region both horizontally and vertically and are generally located close to their respective master-events (red squares). The histogram in the top-right corner of Fig. 5.13 presents the distribution of the horizontal shifts, while the bottom-right one shows the distribution of the (signed) vertical shifts. The majority of shifts both horizontally and vertically are smaller than 1km. The mean horizontal (*ERH*) and vertical (*ERZ*) errors for the automatic locations are *ERH*=0.61km and *ERZ*=0.71km, while for the manual locations they are *ERH*=0.39km and *ERZ*=0.44km.

The addition of the slave events to the catalogue improved the spatial distribution of the aftershock activity which has started to delineate the activated areas. About 4 to 5 spatial clusters can be distinguished, with the most intense being the eastern one. The distribution of aftershocks is characterized by activity on faults ruptured by the two main shocks as well as in neighboring areas. In addition to the aftershock sequence at Efpalio, a swarm occurred N of the city of Aigion (shown in Fig. 5.12). During the preparatory stage of the procedure, all detected master-events were used irrespectively of their epicentral location. As a result, arrival-times of slave-events similar to those master-events were also automatically picked. Keeping master-events of other clustered sequences that have occurred in the broader region is also helpful for the HADAES method, as the association of these signals can eliminate the possibility of erroneous classification to clusters of the sequence under study due to chaining effects.

5.2.2 Application of the HADAES method

In order to complete the analysis of the cross-correlation matrices, the master/slave relations of higher degrees must be processed. Kapetanidis & Papadimitriou (2011) used the primary slave-events (SE) from the first pass of the ME procedure as master-events for the second pass to compare the uncertainties associated with these solutions when fully automatic primary SE and manually evaluated SE were used, respectively. In this section, a partial application of the HADAES method was used to automatically determine solutions for the rest of the detected signals of the earthquake sequence between 18 and 26 January 2010 in Efpalio.

In addition to the 388 ME and 1945 primary SE derived from the ME method, the rest of the manually determined routine solutions (a total of ~600) were also included in a single, large database of external master-events (M_{ext}), instead of selecting a single master-event from each multiplet. This is a deviation from the typical procedure of the HADAES method as described in Section 4.4, but it creates more opportunities for secondary slaves to be directly matched with one or more of the master-events and acquire approximate arrival-times and other meta-data. These events were first passed through the AIC picker to determine possibly missed arrival-time picks at the stations of interest and obtain additional, valid P- and S-wave travel-times. A preliminary

relocation was also performed on these external master-events to be used as temporary (dummy) hypocenters for the respective slave-events associated with them via the HADAES method.

About 3800 additional slave-events were initially associated with master-events, including 470 that belonged to the cluster offshore Aigion. The AIC picker provided automatic estimates for P- and S-wave arrival-times to all the stations of interest. From the preliminary solutions, a subset of ~2150 was selected in the narrower area of interest including only events of the 2010 Efpalio sequence and only the more constrained ones in terms of location and RMS errors. The subset was further filtered by removing possible duplicates and events that were isolated during a preliminary relocation procedure. The final selection for the catalogue in the narrow study region includes: 581 manually picked events from routine analysis, 1220 manually revised primary slave-events (ME method) and 1846 automatically picked secondary slave-events (HADAES method), a total of ~3650 events, a catalogue about 6.2 times larger than the initial one.

5.2.3 Location, multiplet classification, relocation and clustering

Having determined the final working dataset, initial solutions were obtained using HYPOINVERSE (Klein, 2002), employing the velocity model of Rigo *et al.* (1996) for the W. Corinth rift, with V_p/V_s=1.80, for compliance with other studies in the region (Fig. 5.14a). To reduce, on a first level, systematic errors due to (mostly lateral) discrepancies between the 1D velocity model and the real structure, mean P- and S-wave travel-time residuals were calculated for the stations of interest. These residuals were subtracted from the travel-times to account for station corrections. This, naturally, reduced the resulting RMS but, also, the location errors, while it led to an obvious improvement in the spatial distribution (Figs 5.14b and 5.15b), in both epicenters and focal depths. This can be visually evaluated as a stronger concentration of events in spatial clusters, with a respective reduction of the diffused seismicity between them and likely a reduction of biases/artifacts at depth, e.g. concentration of hypocenters near a discontinuity of the velocity model. Seismic moment magnitudes were determined using the methodology described in Chapter 3.

Using KALE as a reference station, cross-correlation matrices were constructed from the filtered (2-15Hz) full signal waveforms of each of the 3 components and averaged (RMS value) into a single combined matrix. Due to the mixed nature of the catalogue that contains both automatically and manually revised arrival-times, two sets of data were considered: one with only manually picked events (routine solutions and primary slaves from the MEm), briefly referred to as “subset A”, and another that also includes the secondary slaves (HADAES), hereon mentioned as “subset B”. The first can be used for the study of the spatial and spatiotemporal properties while the latter can be used to analyze the properties of the magnitude distribution and also some temporal aspects with a larger sample. Nearest-neighbor linkage was applied and the optimal threshold was determined at C_{th}=0.70 for both subsets A and B, according to the method proposed in Section 1.2.2. More specifically, for subset A, a total of 1500 events (~83.3% of the catalogue) were distributed in 151 multiplets, with 24 of them containing at least 10 events. For the events within each multiplet, cross-correlations were performed separately for P- and S-wave windows, registering XC_{max} and the respective time-lags as differential travel-time measurements.

Relocation was performed using the double-difference algorithm HypoDD (Waldhauser, 2001) at several steps, employing the conjugate gradients inversion method (LSQR). Subset A was initially considered, as it is a catalogue of better quality with manually revised picks. HypoDD was parameterized in two main types of iterations, the first with minimal a priori weight to cross-correlation data and maximum to the catalogue data while opposite rules were applied to the latter set. Another HypoDD procedure was run by completely removing catalogue data links during the last phase, thus removing events that were not strongly correlated to others and letting the rest form tight multiplet clusters, comprising "Subset CC". Common events were replaced from subset A with those from subset CC. The subset B was also treated in a similar way, substituting common events from the relocated subset A. Lastly, the compiled catalogue was checked for missing significant events which might have been isolated either at the beginning or during the relocation procedure. Such missing events were relocated using a selection of good quality neighboring smaller events and the SVD iterative procedure. The final relocated catalogues, after the removal of small magnitude outliers, contain 1775 events for subset A (98.6% relocated) and 3224 events for subset B (88.4% relocated).

5.2.4 Spatio-temporal analysis

A hierarchical clustering configuration was constructed for the relocated subset A using Ward's linkage (Ward, 1963) on the inter-event 3D distances matrix. The modified Mojena's plot (Section 1.2.2), suggests several different numbers of clusters at major and minor "elbows" of the respective fusion level diagram. By observing the 3D spatial geometry of hypocenters, several patches of clustered activity could be distinguished. However, their association into broader groups was also apparent. To reduce the complexity of the sequence, 4 spatial groups were considered (Figs 5.14 and 5.15), which, however, could not result directly by choosing 4 as the number of clusters to be formed from the Ward's linkage clustering hierarchy. The distribution was separated to a larger number of clusters which could then be sorted and merged into the 4 larger groups. Figs 5.14 and 5.15 were redrawn using the group separation that was determined after relocation. For subset B, a similar procedure was followed, creating groups roughly matching those derived for subset A and then keeping only unique events from B while retaining the original grouping for common events with A. This is only presented for comparison in Fig. 5C.7, as subset B does not provide any more details to the description of the spatial distribution but rather adds noise due to the data being only automatically determined.

At first glance, the epicenters appear to be distributed in two blocks, oriented at ~N100°E, with a length of ~7.5km, width ~2km and with the northern block being offset by ~3km towards ESE. Given the location of the two major M_w=5.1 earthquakes, at the western side of each block, a simple interpretation could be that the first earthquake triggered seismicity in the southern block and the second in the northern one. However, the distribution of hypocenters is more complex, as presented more clearly in the relocated subset CC (Fig. 5.15d). While the southern, N-dipping group (#1), at depths of ~7.5-9.2km, can indeed be associated with the first major event (hereon referred to as EQ1), the northern group is more complicated and can be divided to a shallow (~7-8km), north-dipping cluster (#3), a zone of small multiplets around ~7.8-8.8km (#2) and a deeper, probably

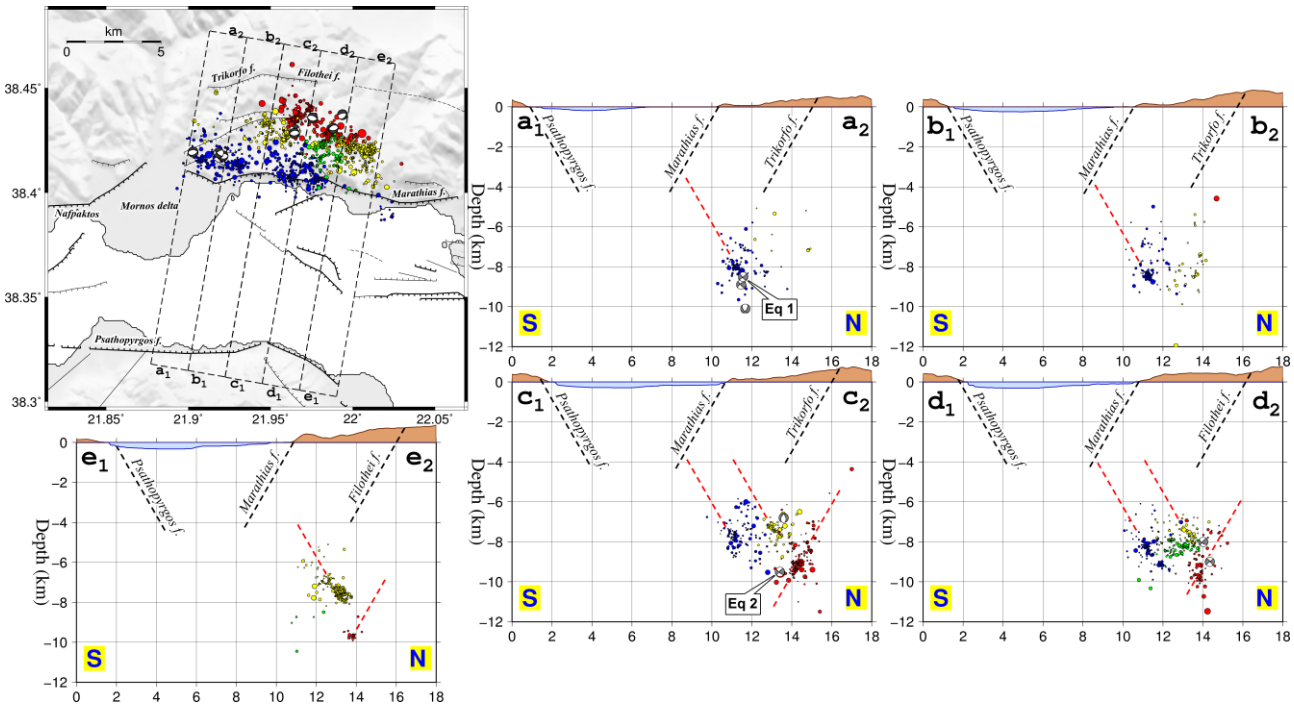

Figure 5.16: Map of the relocated epicenters from subset A of the 2010 earthquake sequence in Efpalio and the corresponding cross-sections in a N10°E direction along the profile lines a_1-a_2 to e_1-e_2. The far-hemisphere projections of the focal mechanisms for major events are also presented. Black dashed lines correspond to the extensions of mapped fault on the surface at a typical 60° dip. Red dashed lines are inferred/hypothetical faults determined from the geometry of the resolved clusters, also drawn at 60° dip. Colours correspond to the 4 spatial clusters (same as Fig. 5.14). Focal mechanisms are from the catalogues of NKUA and GEIN-NOA, placed at their respective relocated positions.

south-dipping cluster (#4) at depths of 9-10km. The second major earthquake (EQ2) is likely associated with cluster #4. However, the temporal characteristics of the sequence would have to be taken into consideration for safer conclusions to be made. Some diffuse activity between clusters #1 and #3 (Fig. 5.15c) could not be easily separated from these groups by means of Ward's linkage, but they may be considered of a similar sense as Cluster #2, which is probably activity on a relay zone between the structures corresponding to Clusters #1 and #3.

A more detailed view on the smaller clusters which comprise the broader groups and their relation to mapped fault in the area of the western Corinth Rift is presented in Fig. 5.16. Focal mechanisms for some of the larger events of the sequence are also presented (sources: Seismological Laboratory – NKUA; GI-NOA). The fault plane solutions for the major earthquakes are following the typical pattern observed throughout the rift (see Chapter 6), indicating E-W trending, dip-slip normal faulting, ambiguous as to whether the fault planes are north- or south-dipping ones. All main groups appear to be broken to a western and an eastern patch of activity, separated by a gap of low seismicity. However, both patches are compatible with the same structure geometry as the one presented in the wide cross-section of Fig. 5.15d. The sub-surface rupture length for an M_w=5.1 earthquake with normal faulting is estimated, according to the marginally applicable (due to low magnitude) empirical relation of Wells & Coppersmith (1994), as L≈3km (with a=4.34 and b=1.54 in Eq. 5.1). This is roughly the length of the western patch of activity in Groups #1 and #4. The

former can be subdivided in two even smaller eastern and western sub-clusters, with EQ1 located in between, at a depth of 8.5km, with the sub-clusters likely delineating the edges of the main rupture, where the redistribution of stress from the mainshock likely caused localized high stress conditions, inducing clustered seismicity. This is not very clear for EQ2, at a focal depth of 9.5km, whose hypocenter during relocation was persistently offset, horizontally, from the rest of Group #4, while at some experimental parameterizations of the procedure it was relocated at more shallow depths, near the bottom of Group #3. The northwards dip of Groups #1 and #3 is indicated in the cross-sections of Fig. 5.16. The south dip of Group #4 is mostly supported in section c_1-c_2, while in d and e its distribution is sub-vertical and spherical, respectively, tending to slightly larger focal depths towards the east. The most complex thin section is d_1-d_2, where activity in Group #2 is also observed near the depth of 8km. This coincides with the eastern end of the southern group, increasing the probability that Group #2 is diffuse seismicity in a relay/damage zone between two sub-parallel structures, while Group #3 extends further east with a very intense cluster in e_1-e_2.

The temporal aspect of the 2010 Efpalio sequence is presented in Fig. 5.17. The catalogue was separated in 8 periods, using Ward's linkage and Mojena's plot on the matrix of inter-event times and interfering only in the fourth period, manually dividing it to d and e, before and after EQ2. Maps for the 8 periods are presented in the Appendix (Fig. 5C.8). Apparently, the major event of 18 January (15:56) triggered seismicity in all structures at once, but mostly the southern Group #1. Activity in the deeper Group #4 was delayed until a few hours after the main event and was mostly expressed in two temporally clustered bursts during periods a and c. With the occurrence of EQ2, Group #4 was strongly activated near the major event's hypocenter but also more easterly, while some minor reactivation occurred in Group #1, including a few moderate events. By the end of period f, only Group #3 remained strongly active, persisting through periods g and h. As with the case of the 2008 Andravida earthquake, very limited migration patterns can be observed, with the seismicity quickly spreading through most of the study area. Some hints of migration are seen in period a, Group #1, with activity expanding outwards from the M_w=5.1 event, mostly eastwards, but only within a 1km radius, later persisting at the edges of the main rupture. Group #4 presents clustered activity in a certain narrow zone through periods a and c (near the Y=6km mark), but expands by ~3km eastwards and ~1km westwards after EQ2. The more pronounced migration patterns can be seen in Group #3. Although it starts with some moderate events in period a along the whole length of its structure, some minor westwards migration can be observed in its western patch (clusters through periods b to d), with almost no activity during period e (EQ2). The eastern patch also presents some signs of weak eastwards migration. The strongest pattern is observed during periods f to h, with its activity reaching the Y=10km mark, towards ESE, while backwards migration (towards WNW) is also observed by the end of period g and the beginning of period h.

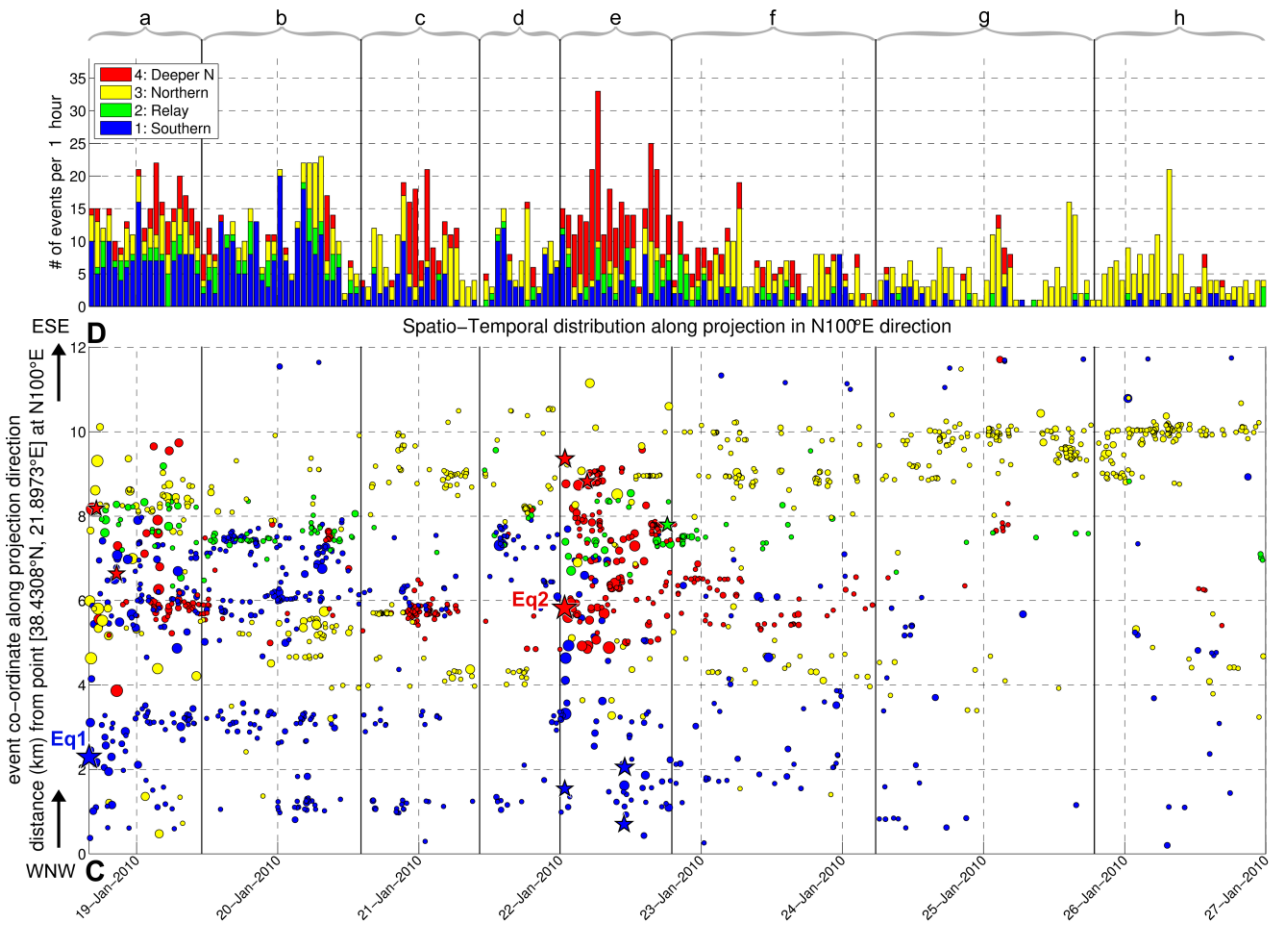

Figure 5.17: (top) Stacked histogram of hourly number of earthquakes per spatial cluster, presented by different colours, during the 18-26 January 2010 earthquake sequence in Efpalio, from the relocated catalogue of subset A, (bottom) spatio-temporal projection along the 12km-long, C-D profile line (Fig. 5.14) at a N100°E direction. Stars represent earthquakes with $M_w \geq 4.0$. The two major M_w=5.1 events are labeled as Eq1 (18 January) and Eq2 (22 January) respectively. Vertical thick lines divide the 8 successive temporal periods (see also Fig. 5C.8).

In terms of the cumulative number of events (Fig. 5.18), Group #1 appears to be the more populated one during the sequence, with Group #3 surpassing it only during the last day of the study period. However, if the other Groups (#2-4) are considered as a northern "super-group", their combined cumulative number follows Group #1 very closely and surpasses it after the occurrence of EQ2, while Group #1 gradually diminishes. The short bursts of Group #4 before EQ2 are also easily visible as steep steps. EQ2 mostly affects the cumulative number of Group #4, which also contains includes many major events, but its rate declines rapidly after 23 January. Group #2 is the smallest

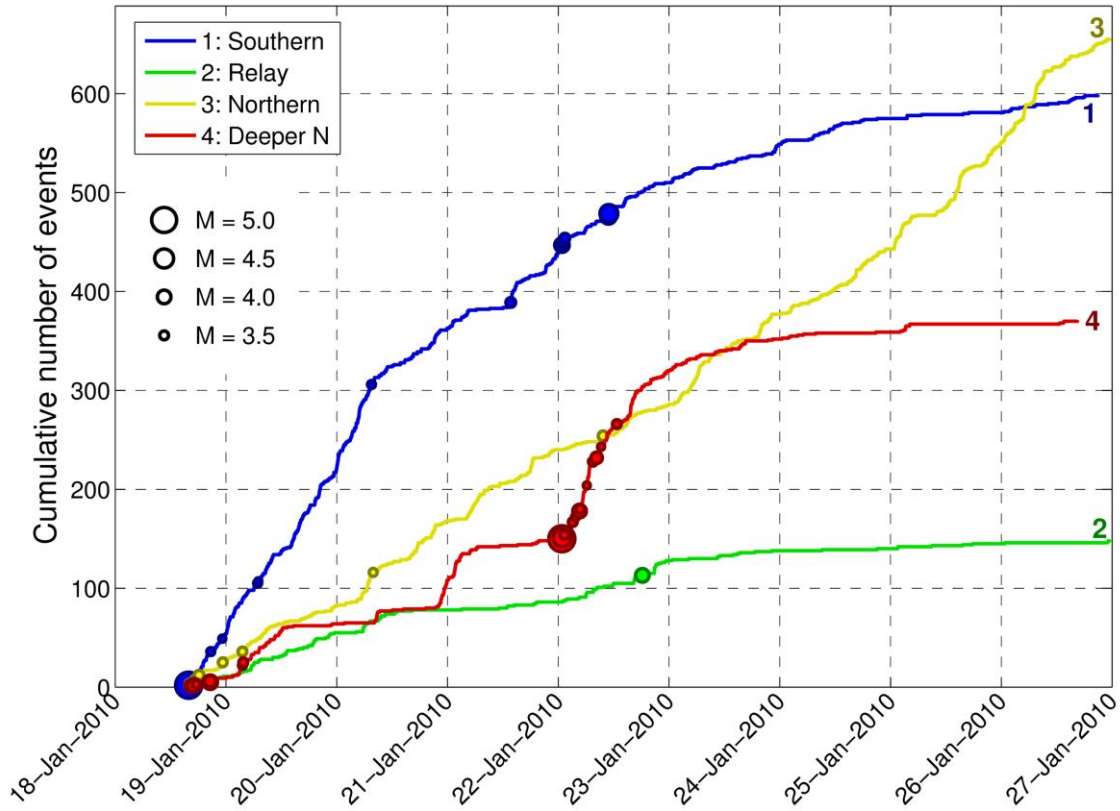

Figure 5.18: Cumulative number of events per spatial cluster, during the 18-26 January 2010 earthquake sequence in Efpalio, from subset A. Circles depict the stronger events of the sequence.

one, with a low rate of ~25 events/day and is not affected by EQ2. Interestingly, Group #3, representing the northern north-dipping cluster, has a nearly constant seismicity rate of ~70 events/day in subset A, which is lower than the starting rate of Group #1, during the first two days (~175 events/day), but surpasses it by the end of 26 January, partly due to the sudden increase of spatiotemporally clustered activity at its easternmost end.

A last insight into the spatiotemporal distribution can be given by the evolution of multiplets (Fig. 5.19). This shows high new-multiplet generation rate following major events, which is interpreted as expansion of seismicity into yet unbroken structures or patches of previously activated ones. The two largest multiplets are formed right after EQ1, a commonly observed pattern following strong events which produce aftershock sequences. Surprisingly, EQ2 did not generate any significant new multiplets, but rather several small ones. While it reactivated the largest multiplet of Group #4, which was generated a few hours after EQ1 and, also, the very first and largest multiplet that belongs to Group #1. Reactivations are less common for the smaller, short-lived multiplets, with few exceptions. In general, as observed from the histogram at the top of Fig. 5.19, "blue" multiplets mostly occupy the first 1/3 of the sequence, "yellow-orange" ones the middle 1/3 and red ones the last 1/3. One of the largest multiplets was generated on 24 January at the eastern end of Group #3 and is responsible for the last 1/3 of the histogram being red, with very weak activity in the earlier generated multiplets. An interesting observation is the low multiplet generation rate in the first half

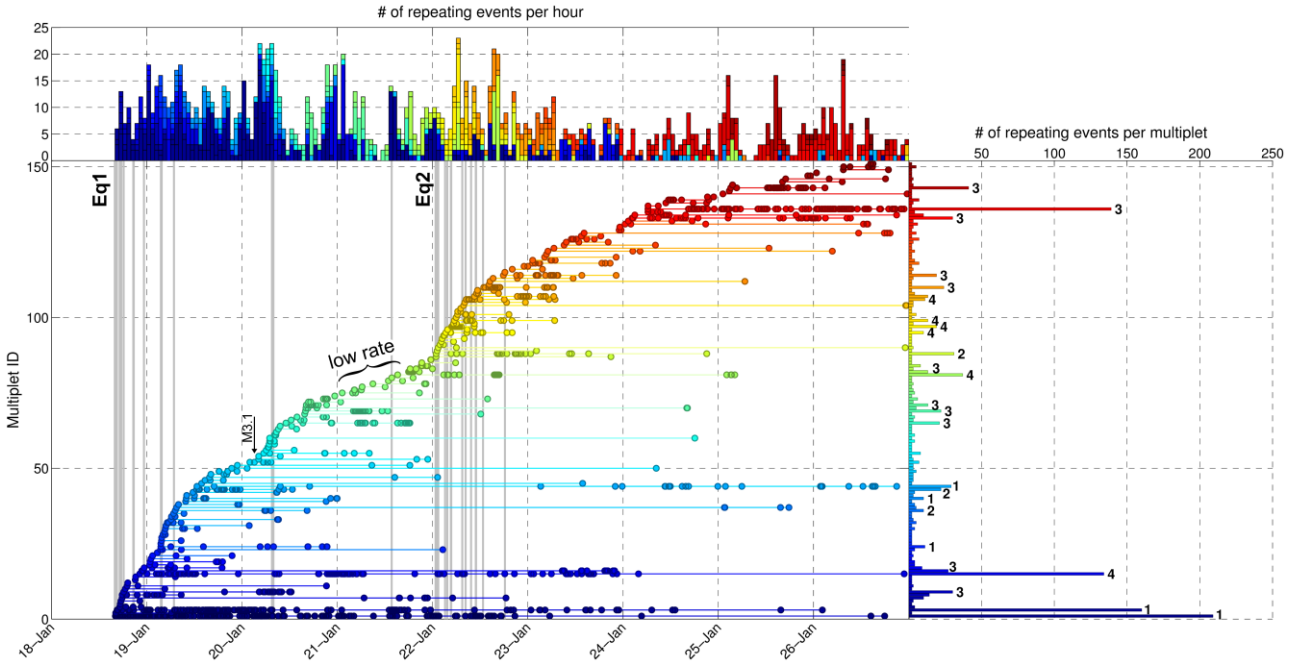

Figure 5.19: (bottom-left) Multiplet evolution history during the 18-26 January 2010 earthquake sequence in Efpalio, from subset A. Each row represents a single multiplet, with IDs sorted in increasing order according to the origin time of the first event in each multiplet. Circles represent repeating earthquakes. Vertical gray lines correspond to the origin times of major events ($M_w \geq 3.4$). The two major M_w=5.1 events are marked with Eq1 (18 January) and Eq2 (22 January), (top) histogram of the hourly number of repeating earthquakes, with colours corresponding to multiplet ID, (right) total number of repeating earthquakes per multiplet. Numerical labels next to certain large multiplets (size≥10) correspond to the spatial cluster to which they belong.

of 21 January. Very small multiplets were only generated during this period, which could be considered as a sort of short-term "quiescence". This was followed by a small increase in the multiplet generation rate during the second half of the same day, right before the occurrence of EQ2.

5.2.5 Properties of the magnitude distribution – ETAS modeling

The application of the Master-Events and HADAES methods have managed to resolve many small earthquakes, increasing the catalogue by ~6 times. This has an impact to the magnitude of completeness, M_c, as indicated by Fig. 5.20 which presents the Frequency-Magnitude distribution (FMD), with the M_c determined using the maximum curvature method (Wiemer & Wyss, 2000) and the *b*-value of the Gutenberg-Richter law estimated by Maximum Likelihood using the ZMAP software (Wiemer, 2001). The catalogue of routine solutions has an $M_c \approx 2.2$ and an inadequate

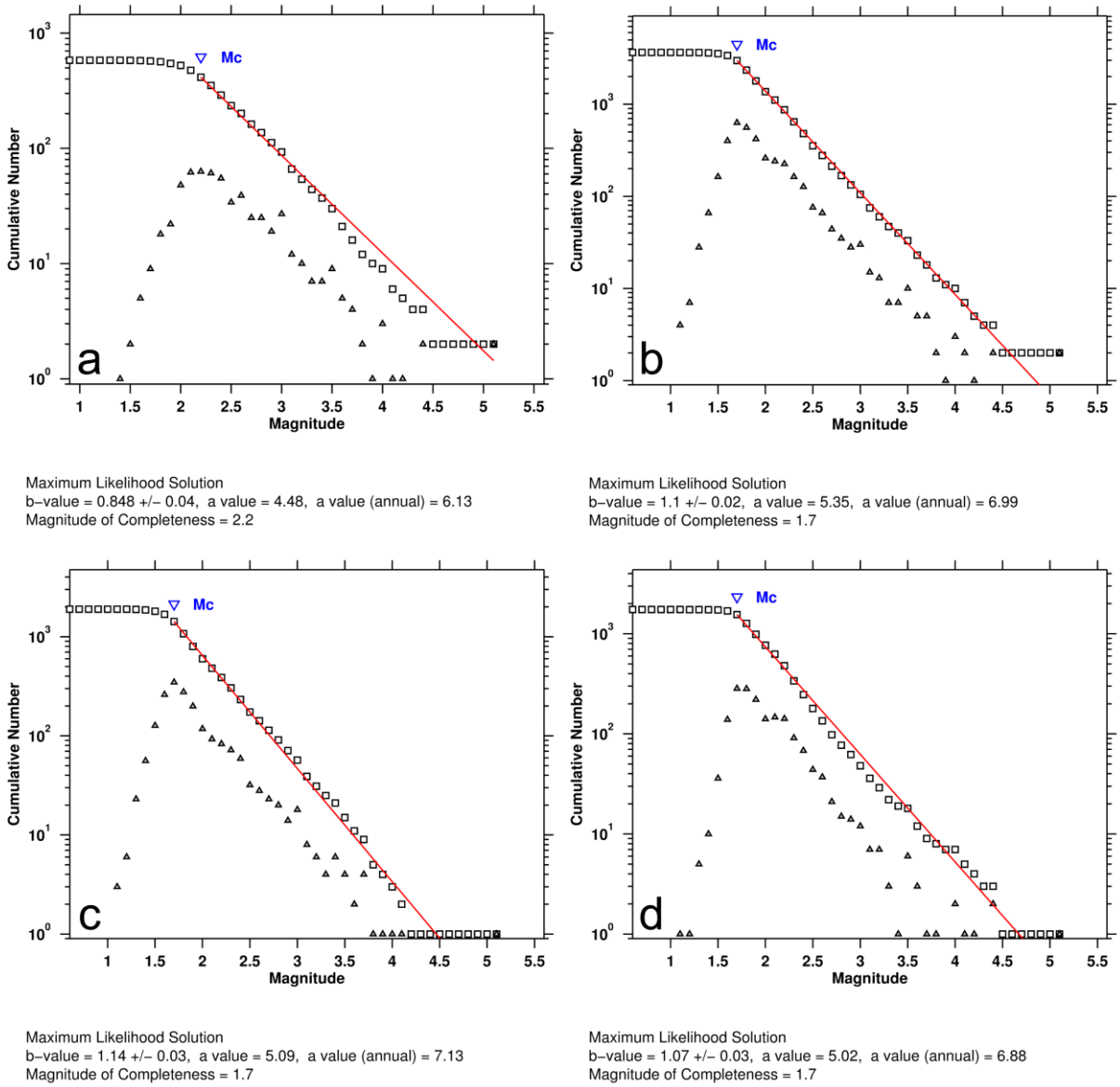

Figure 5.20: Diagrams of the frequency magnitude distribution for the seismicity of 18-26 January 2010 in Efpalio, a) using events from routine analysis only (M_c=2.2, b=0.85±0.03, or, alternatively, by least squares fit for $2.6 \leq m \leq 4.2$: b=1.02±0.02), b) with additional primary (MEm) and secondary slaves (HADAES), or subset B (M_c=1.7, b=1.10±0.02), c) same as (b) but for the first period, before the second M_w=5.1 event (M_c=1.7, b=1.14±0.03), d) for the period following the second M_w=5.1 event (M_c=1.7, b=1.07±0.03). Squares represent the cumulative number of events with magnitude≥m (x-axis) while triangles are the (non-cumulative) number of events with magnitude m.

linear fit on the FMD (Fig. 5.20a). The b-value is estimated at 0.85 in Fig. 5.20a, while a least squares fit restricted to the narrow linear part results in b=1.02, much closer to the typical b≈1. Taking the full catalogue into account (subset B), the M_c drops to 1.7, indicating a significant increase in detectability which is responsible for the sixfold growth of the catalogue (Fig. 5.20b). The linear part of the FMD is also better defined. Indeed, in the initial dataset the FMD actually

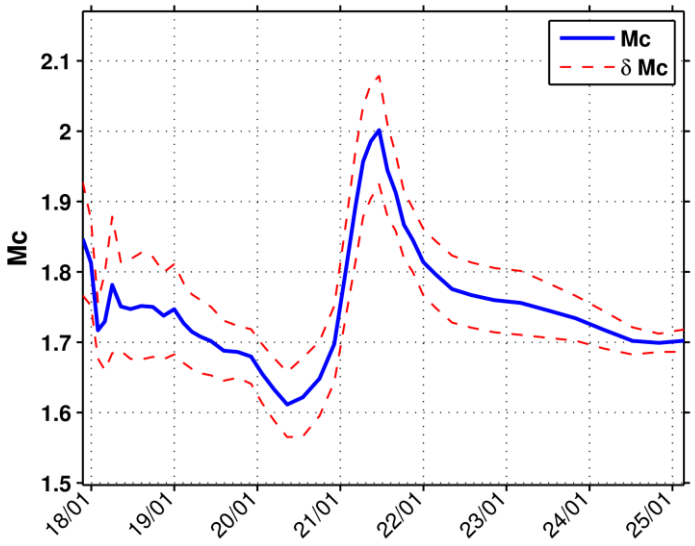

Figure 5.21: Temporal evolution of the magnitude of completeness, M_c, determined using the maximum curvature method in sliding windows of N=300 events, for the seismicity of 18-26 January 2010 in Efpalio, subset B.

begins to deviate from linearity at about M_c=2.4, with the maximum curvature method slightly underestimating it, so the actual (or, rather, maximum) drop in M_c is by about 0.7.

The M_c=1.7 for subset B persists in both parts of the sequence, before and after EQ2 (Figs. 5.20c,d). A more detailed view, however, shows that, in fact, M_c varies in time (Fig. 5.21). As commonly observed after strong earthquakes that trigger aftershock sequences, M_c is high right after the mainshock and is later reduced to a lower value. This is due to the masking of smaller events by the high aftershock activity that follows the major earthquake, leading to strong overlapping between the intensely generated small events and, very often, their superposition on the waveforms of the more energetic stronger events. This effect can even cause some major aftershocks to be undetectable/unresolved during routine/preliminary analysis. The diagram of Fig. 5.21 is actually slightly deceptive, as the abrupt increase of M_c in the middle appears to occur during 21 January when, in fact, it occurs right after EQ2, on 22 January, but it is caused by the sliding window including events from both 21 January (which has little activity) and events from the aftershocks of EQ2. The M_c reaches a maximum of M_c=2.0, which should be considered as a threshold value to ensure homogeneity of detectability during the whole sequence.

The spatial mapping of the *b*-value of the G-R law reveals some interesting characteristics (Fig. 5.22). During the first phase (periods a-d, before EQ2), the *b*-value is ~1.1 in most of the study area except for a region around the site of EQ2, where *b*-values are lower, at about 0.9. This could indicate the existence of an unbroken asperity in the vicinity of the second earthquake's hypocenter, before its occurrence. This changed in the second part (periods e-h, after EQ2), with $b\approx1.1$ in the vicinity of its hypocenter, indicating a release of accumulated stress, and much higher *b*-values ($\geq$1.3) at the eastern and western edge of the northern group. Interestingly, this part of activity at the eastern end corresponds to the intense spatiotemporal cluster of Group #3 that took place during

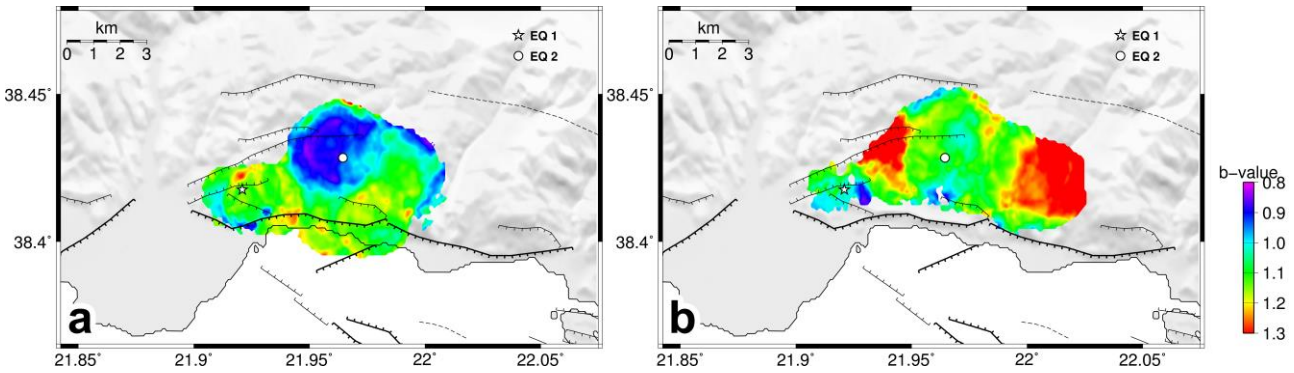

Figure 5.22: Spatial mapping of the b-value for the full catalogue (subset B) of the 18-26 January 2010 earthquake sequence in Efpalio, a) for the period before the second M_w=5.1 event, b) for the period after the second M_w=5.1 event. The *b*-values were calculated in selected hypocenters inside cylindrical vertical columns with a constant radius of 1.5km. The relocated epicenters of the first and the second major M_w=5.1 earthquakes are depicted by a star and a circle, respectively.

periods g-h, with hints of seismic migration, suggestive for the propagation of pressurized fluids and likely low stress-drop conditions or creeping in that part of the activated structure, indicated by the high *b*-values.

The full catalogue (subset B) was subjected to ETAS and Omori-Utsu (Modified Omori's formula, or MOF) modeling, to determine the nature of the sequence, mainly in terms of aftershock productivity. The high M_c=2.0 threshold value was considered to ensure homogeneity during the whole period of study. Fig. 5.23a shows the ETAS model for both parts of the sequence (before and after EQ2), with its parameters determined by MLE. Visually, the fit is very adequate for the first part (before EQ2), but it deviates afterwards, with the real cumulative events being more than the modeled ones for the seismicity after EQ2, an offset mainly attributed to the first hours after EQ2. The aftershock productivity, a=0.961<1 is low enough to indicate that this could be marginally considered as a swarm sequence, with a high *p*-value p=2.251. Typically, earthquake swarms are those sequences without a distinctive mainshock, but rather several major events of comparable magnitude, usually occurring after the swarm has been initiated. In the case of the 2010 Efpalio earthquakes, one could suppose that it is a typical aftershock sequence; that is until EQ2 occurred. The second major event is of comparable magnitude to the first M_w=5.1 event of 18 January. On the other hand, the shape of the "cumulative number of events" curve of Fig. 5.23 shows that EQ2 is not just a secondary aftershock of EQ1. It is a pattern more consistent with the superposition of two individual aftershock sequences.

In that sense, the two major M_w=5.1 events could be treated as mainshocks producing their own aftershock sequences. The ETAS and MOF models for the first part (periods a-d) are presented in Fig. 5.24. The *AIC* value for the ETAS model is smaller (more negative) than the respective value for the MOF model. The standard deviation, σ, is also smaller for the ETAS model. This indicates that, although the MOF model follows closely the main trend of decaying seismicity rate, the ETAS model is still best suited. The MOF model misses at least two outbursts (positive residual) and a deficit towards the end. The ETAS model follows these anomalies more closely. The remaining

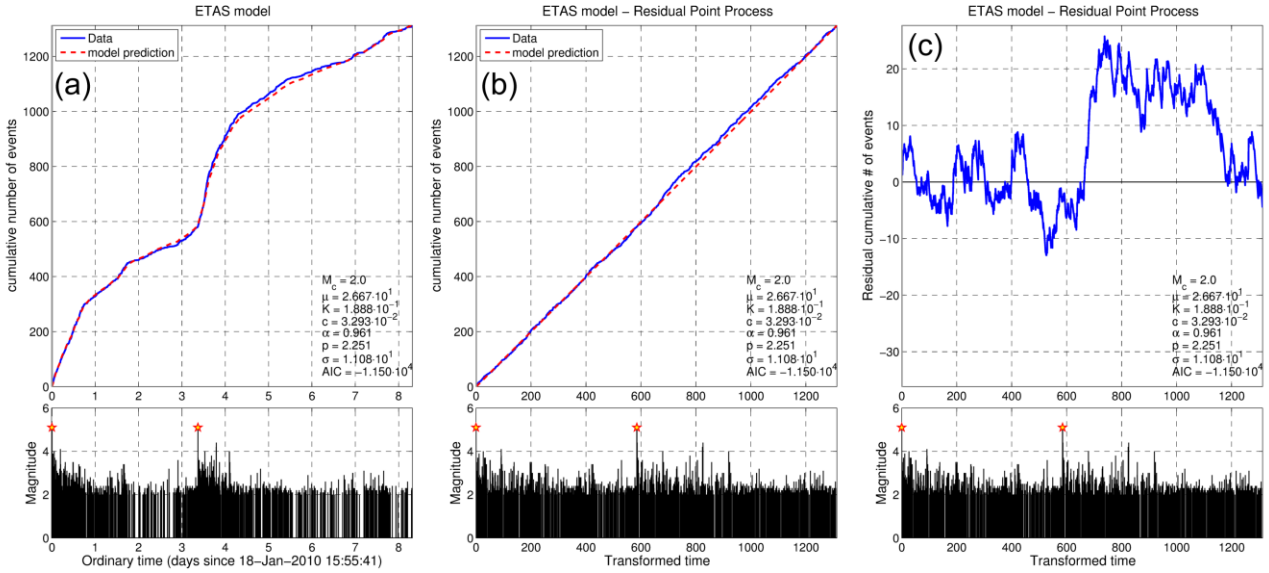

Figure 5.23: ETAS model for the seismicity of 18-26 January 2010 in Efpalio, subset B, using a threshold value at $M_{th} \equiv M_c = 2.0$ and $M_r \equiv M_{main} = 5.1$, a) data and model curves in ordinary time, b) in transformed time, c) residual between data and model in transformed time. The two $M_w = 5.1$ events are marked with a star in the histograms (lower panels).

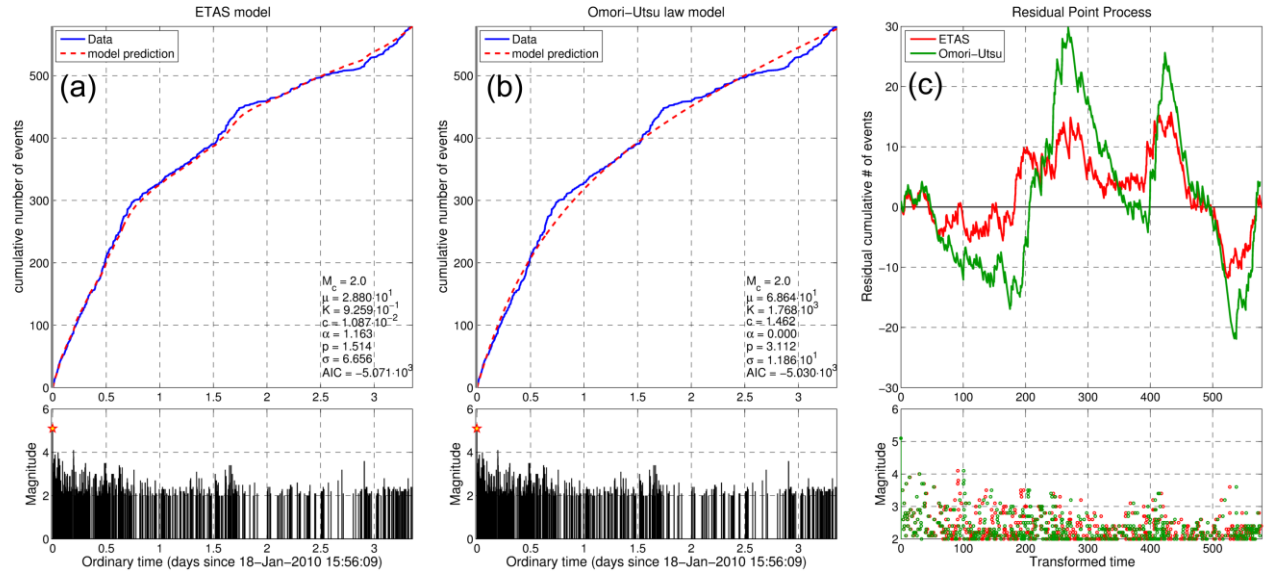

Figure 5.24: ETAS and Omori-Utsu models for the seismicity following the 1st major $M_w = 5.1$ event (18 January 2010, 15:56:09) of the 2010 sequence in Efpalio, subset B, using a threshold value at $M_{th} \equiv M_c = 2.0$ and $M_r \equiv M_{main} = 5.1$, a) data and ETAS model curves in ordinary time, b) data and MOF model in ordinary time, c) residuals between data and models in transformed time.

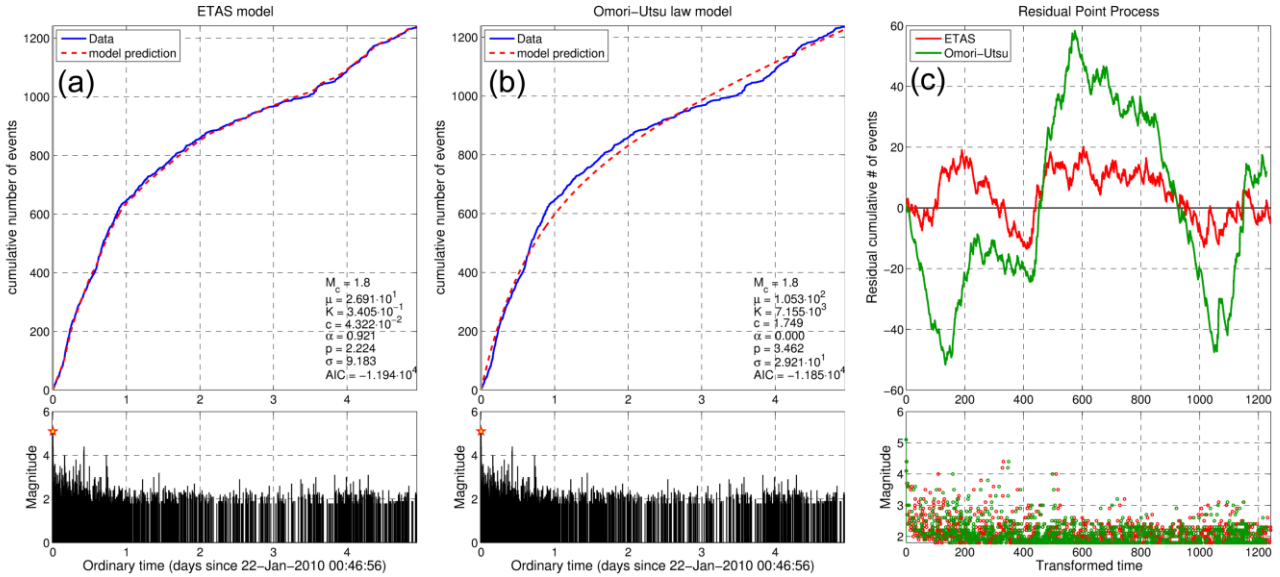

Figure 5.25: ETAS and Omori-Utsu models for the seismicity following the 2nd major M_w=5.1 event (22 January 2010, 00:46:56) of the 2010 sequence in Efpalio, using a threshold value at M_{th}=1.8 and $M_r \equiv M_{main}$=5.1, a) data and ETAS model curves in ordinary time, b) data and MOF model in ordinary time, c) residuals between data and models in transformed time. Data selected from subset B.

positive residuals could indicate an aseismic component to the triggering of those outbursts, causing non-stationarity to the parameters of the model. The observed deficit of seismicity towards the end (period d) coincides with the observed reduction in the generation rate of large multiplets (Fig. 5.24) shortly before the occurrence of EQ2. The *p*-value for the ETAS model is smaller than in the case of the whole sequence while the *a*-value is a bit higher but remains small, relative to what is usually observed for aftershock sequences in the literature (e.g. Ogata, 1992; also Section 5.1 for the 2008 Andravida sequence). On the other hand, the *p*-value for the MOF model is very high (>3). The modeling for the second part, following EQ2, is presented in Fig. 5.25. In this case, a lower threshold was selected (M_{th}=1.8), as it provided a better visual fit (smaller σ) for the ETAS model, which is preferred over the respective MOF model due to the lower *AIC* value. The *a*- and *p*-values are closer to those derived for the whole sequence (Fig. 5.23) while *p* is very large (*p*>3) for the MOF model. The μ-value, or background rate, for all 3 ETAS models are about 26-28 events/day. The abovementioned observations combined with the complex geometry of the spatial distribution lead to the conclusion that the 2010 Efpalio sequence can be characterized as a hybrid between two typical aftershock sequences and a low degree of swarm-likeness (mainly because of the low *a*-value), or rather a typical case of Epidemic Type Aftershock Sequence (ETAS), as a whole, with two major events and some non-stationarity in its parameters, likely due to a certain degree of aseismic triggering in parts of the sequence.

5.2.6 Discussion - Conclusions

The two M_w=5.1 earthquakes that occurred in 2010 near Efpalio, western Corinth, only 4 days apart, triggered scientific interest to investigate the geometry of the activated structures and the relation between the two major events. The routine locations of the stronger events revealed a complex spatial distribution of hypocenters which was attributed to the complexity of an existing network of active faults. Initially, despite the intense aftershock sequence, only a few hundreds of events were manually analyzed. In order to study this earthquake series in detail, a larger sample of events had to be resolved. For this reason, the methodology of Master-Events, as described in Section 4.3 and Kapetanidis & Papadimitriou (2011), which was already under development during that period, was applied to the first 8 days of the aforementioned sequence, between 18 and 26 January 2010. This resulted in over 1200 additional events being resolved and located as primary slaves, with direct similarity to a subset of the routinely analysed master-events. In the present work, an alternative method called HADAES (Section 4.4) was also employed to locate over 1800 extra slave-events of second or higher degrees in the narrow area of study (subset B), left out by the first pass of the MEm. As a result, the amount of data in final catalogue was increased by over 6 times.

The high-resolution relocation procedure that was applied to a set of 1800 manually revised events (subset A) revealed at least 3 structures which were activated during the 2010 Efpalio sequence. The focal mechanisms for the main events show E-W normal faulting with ambiguity as to whether the dip is towards the north or the south. The combined information of focal mechanisms, the geometry of the relocated clusters and the spatiotemporal characteristics of seismicity (such as coseismic triggering) enable the determination of the fault planes. According to the above, the first (Group #1) is a north-dipping structure, associated with EQ1. Another north-dipping structure was identified (Group #3) which does not appear to be directly related to the rupture plane of either major earthquake but was activated a while after EQ1. A deeper, south-dipping structure (Group #3) appears to be associated with EQ2, due to its hypocentral proximity and its strong coseismic activation. The latter consists of clusters which appear to be located at the down-dip extension of the north-dipping plane of Group #3. However, EQ2 did not trigger seismicity at the shallower Group #3.

Several other studies have been conducted for the interpretation of the 2010 Efpalio earthquake sequence. Sokos *et al.* (2012) determined the fault planes for the two major events, using the method of Zahradnik *et al.* (2008). They suggested that EQ1 has occurred on a south-dipping fault plane with almost no on-fault aftershocks, while EQ2, on the other hand, occurred on a north-dipping plane. These results are completely opposite to those derived from the present study, mainly due to the different method used for fault plane determination. The hypocentral distribution is also shallower, while the centroid positions are at 4.5 and 6.0km for EQ1 and EQ2, respectively, allowing for the association of EQ1 with the south-dipping Filothei fault. Sokos *et al.* (2012) used an additional 6 temporary local stations and preferred a different, gradient velocity model (Latorre *et al.*, 2004) with V_p/V_s=1.78. A test with the P-wave velocity model of Rigo *et al.* (1996) but V_p/V_s=1.78, using the data of the present study, resulted in a spatial distribution comparable to the one presented in Figs 5.14 and 5.15, with minor differences in absolute locations of the order of 100-200m which do not affect the general observations and conclusions. This makes the association

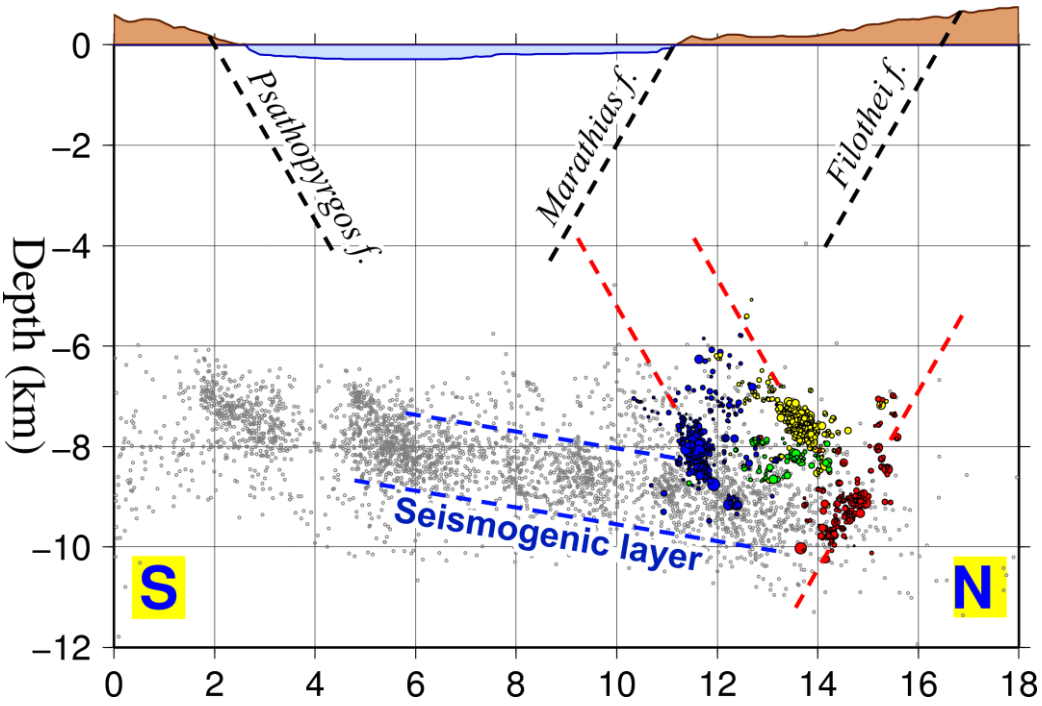

Figure 5.26: Cross-section in a N10°E direction for subset CC of the 2010 earthquake sequence in Efpalio, overlaid on the relocated seismicity of years 2000-2005 in the western Corinth Rift (Chapter 6), with emphasis on the weak seismogenic layer (blue dashed lines), dipping at 9-10° towards the north. Mapped faults (black) and inferred activated structures (red) are represented by dashed lines, typically dipping at 60°.

of the south-dipping Group #4 with Filothei fault unlikely, as it would require a vertical shift of the hypocenters by ~3km. If the causative fault had indeed a superficial expression, it would outcrop about 5-6km north of Filothei fault. The same test conducted using the model of Latorre *et al.* (2004) actually resulted in comparable RMS but higher location errors while it negatively affected the vertical distribution, concentrating most hypocenters strictly between 6 and 8 km and creating an artificial gap below. These irregularities are, in general, signs of biases to the locations caused by the velocity model which cannot always be smoothed out by a relocation procedure.

Ganas *et al.* (2013) used data from the regional HUSN only and yet another velocity model. Based on the geometrical characteristics of the relocated spatial distribution, they suggest that EQ1 occurred on a north-dipping fault, associated with the shallow-dipping seismogenic layer that is known to be present in the western Corinth Rift at depths of ~8-10km (e.g. Rigo *et al.*, 1996; Lambotte *et al.*, 2014; also presented in detail in Chapter 6) while their results are inconclusive as far as EQ2 is concerned, where an almost vertical distribution was observed. The spatial relation between the 2010 Efpalio sequence and the background seismicity on the seismogenic layer of the western Corinth Rift is presented in Fig. 5.26. Years 2006-2007 have been left out of the background seismicity presented in Fig. 5.26, because of an intense cluster that occurred during that period (Section 6.6.3) and would be projected near the horizontal mark of (10±1) km. As described in more detail in Chapter 6, clustered seismicity in the rift usually occurs on steep dipping faults near the weak layer, which, however, is also characterized by diffuse deformation due to the brittle-ductile transition near its bottom and background seismicity on small, randomly oriented surfaces.

Group #1 of the 2010 Efpalio sequence is partly embedded in the seismogenic layer, but its shallower part clearly defines a, likely blind, north-dipping structure. It should be noted that in Fig. 5.26 the seismicity to the left of the 8km horizontal mark concerns activity that occurs in the middle of the western Corinth Rift (roughly between Trizonia island and Aigion) while in the area between Psathopyrgos and Efpalio seismicity in the weak layer is mostly present to the right of the 8km mark. Group #3 is clearly above the weak layer while Group #4 appears to be completely embedded within.

GPS data from a local station at Efpalion (EYPA) reveal permanent static vertical displacement of 3.6 cm downwards (Ganas *et al.*, 2013), intuitively consistent with the area being part of the subsiding hanging wall of the main north-dipping structure that hosted the M_w=5.1 earthquake of 18 January, but also within the hanging wall of the 22 January event's south-dipping fault plane. However, Ganas *et al.* (2013) found that the GPS data are inconclusive about the geometry of the EQ1 and EQ2 causative faults, as the possible fault plane combinations produce comparable residuals from the observed values at station EYPA, verified by forward modelling on the coseismic surface deformation. An alternative scenario that EQ1 and EQ2 have both occurred on north-dipping faults is supported by Karakostas *et al.* (2012), who relocated a total of 724 events in the period between 18 January and 9 March 2010.

Interestingly, the seismic activity in the vicinity of the 2010 Efpalio sequence was spread towards the west during the next few days (27 January – 1 February), with the epicentres located within Mornos delta, while later, during May, another outbreak of clustered activity occurred near Nafpaktos. In both cases, the largest events did not exceed M_w=4.0, with only few events of magnitude between 3.5 and 3.9, north of Nafpaktos on 13-15 May 2010 (Sokos *et al.*, 2012). Ganas *et al.* (2013) suggest that the cluster in Mornos delta occurred on a north-dipping structure, at depths between 10 and 15km, certainly a bit deeper relative to the seismicity of Group #4. Karakostas *et al.* (2012) also derived a similar conclusion but at different focal depths (8-12km), roughly similar to those for the rest of the Efpalio sequence. They also measured a likely change in the direction of the local extensional stress from ~SSW-NNE at the eastern end to SSE-NNW at the western end of the activated zone.

It is noteworthy that in the present study a total of 1800 events (or over 3600 events, in Subset B) were resolved during the short time-window of ~8 days, whereas routine analysis in NOA (Ganas *et al.*, 2013) located roughly the same number of events (1892) during 5 months in a broader study area. This is, of course, due to the lowering of M_c / detectability threshold which was achieved by detecting earthquake families and exploiting waveform similarity to transfer arrival-time picks and meta-data. The latter, combined with manual revision and relocation, has enabled a significant increase in the resolution of the spatial geometry, allowing for detailed observations to be made concerning the structures which interacted during the 2010 Efpalio sequence.

5.3 The 2014 Cephalonia aftershock sequence

The island of Cephalonia is situated in the Ionian Sea, western Greece, in a region dominated by the dextral Cephalonia-Lefkada Transform Fault Zone (CLTFZ), connecting the north-western end of the Hellenic Arc, which begins roughly at the latitude of Zakynthos Island, with the Apulian Thrust in the north, near the latitude of Corfu Island (Fig. 5.27). In terms of seismic hazard, it is classified to the highest zone of the Greek seismic code (EAK2003) and is known to have hosted several catastrophic historic earthquakes. Thirty years after the 1983 M_s=7.0 major earthquake, an M_w=6.1 mainshock occurred on 26 January 2014, with its epicenter ~2 km NE of the city of Lixouri (Papadimitriou *et al.*, 2014; Papadopoulos *et al.*, 2014; Valkaniotis *et al.*, 2014; Karakostas *et al.*,

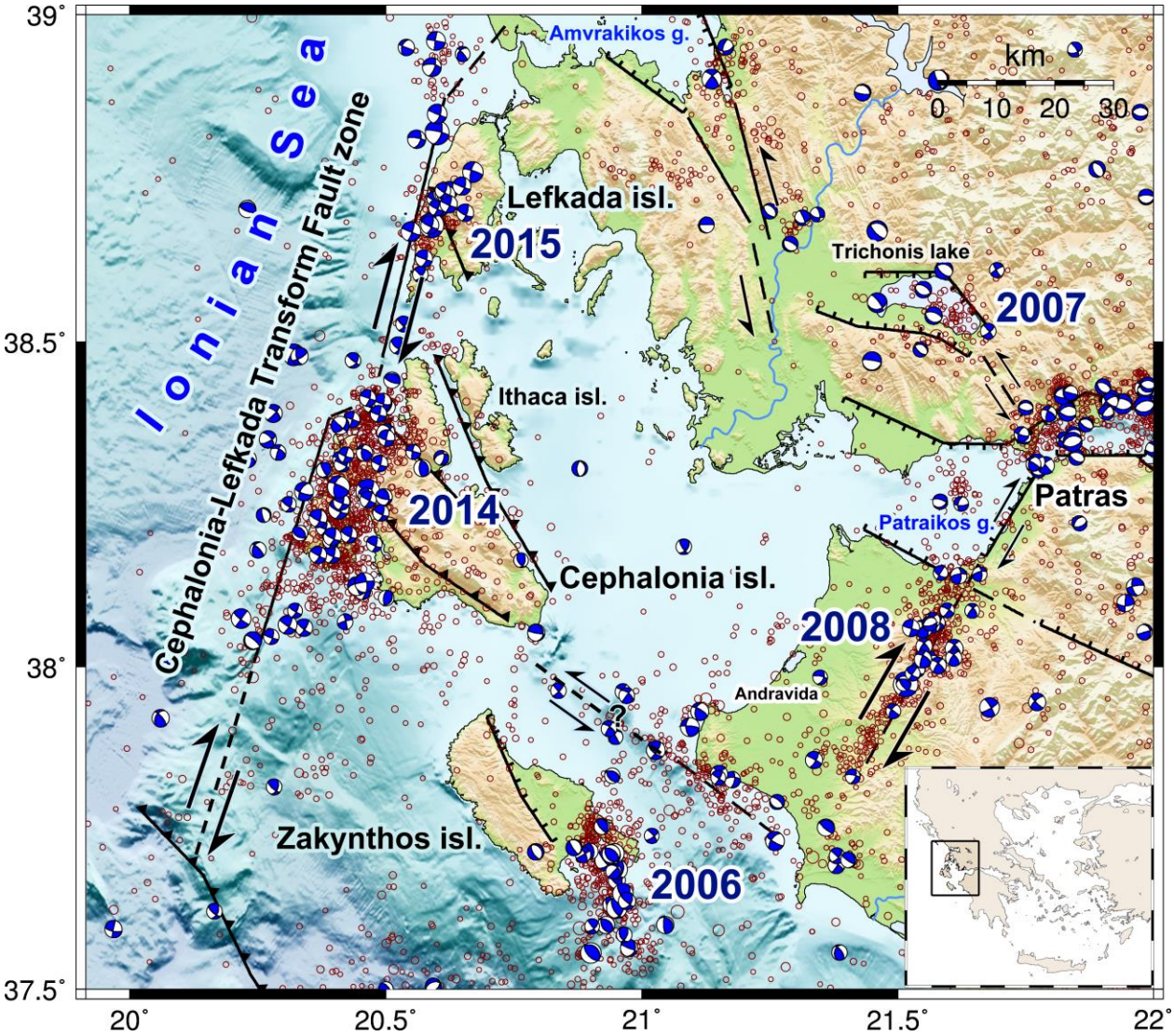

Figure 5.27: Seismotectonic map of the region of mid-western Greece, including selected seismicity with $M \geq 3.0$ from the catalogue (1996-2006) of Karakonstantis & Papadimitriou (2010) and from the routine analysis at the NKUA seismological laboratory. Focal mechanisms of are from the catalogue of NKUA, derived from regional body-wave modeling. Gross fault lines for major tectonic features are based on Underhill (1989), Armijo *et al.* (1996), King *et al.* (1993) and Flotté *et al.* (2005).

2015; Karastathis *et al.*, 2015). About one week later, on 3 February 2014, another significant earthquake of magnitude M_w=5.9 occurred at the NW part of the Paliki peninsula. The intense aftershock sequence was recorded by the Hellenic Unified Seismological Network (HUSN) and provided data of adequate quality, suitable for a detailed seismotectonic analysis which could enable the identification of the tectonic features that were activated. In this section, the aftershock sequence, that was manually analysed by the Seismological Laboratory of the University of Athens, is processed through typical cross-correlation and relocation procedures to provide high-resolution hypocentral locations for a detailed spatio-temporal analysis. Preliminary results of this analysis were presented by Papadimitriou *et al.* (2014).

5.3.1 Relocation - Clustering

Initial locations for over 7600 events in the period between 26 January and 31 December 2014 were determined using a minimum 1D velocity model that was estimated by average RMS and location uncertainties minimization for a selected subset of aftershocks (Table 5.2; Papadimitriou *et al.*, 2014). The location uncertainties and the hypocentral dispersion which resulted by the use of the local velocity model can be further decreased by applying a relocation procedure using the algorithm HypoDD (Walhauser and Ellsworth, 2000). It is necessary to divide the data in regions, because of the large number of events as well as the extend of the epicentral area. Ward's linkage (Ward, 1963) was applied to the inter-event hypocentral distances matrix, separating the sequence in 6 spatial groups (Fig. 5.28A), with all of the following procedures being repeated for each group. Similar workflow has been adopted previously for the relocation of the seismicity in the Santorini Volcanic Complex (Section 5A.3; Papadimitriou *et al.*, 2015).

Table 5.2: Custom P-wave 1D velocity model for the region of Cephalonia, with V_p/V_s = 1.80. (Papadimitriou *et al.*, 2014)

Layer	V_p (km/sec)	**Ceiling Depth** (km)
1	5.0	0
2	5.9	4
3	6.2	7
4	6.5	16
5	6.7	24
6	7.4	35

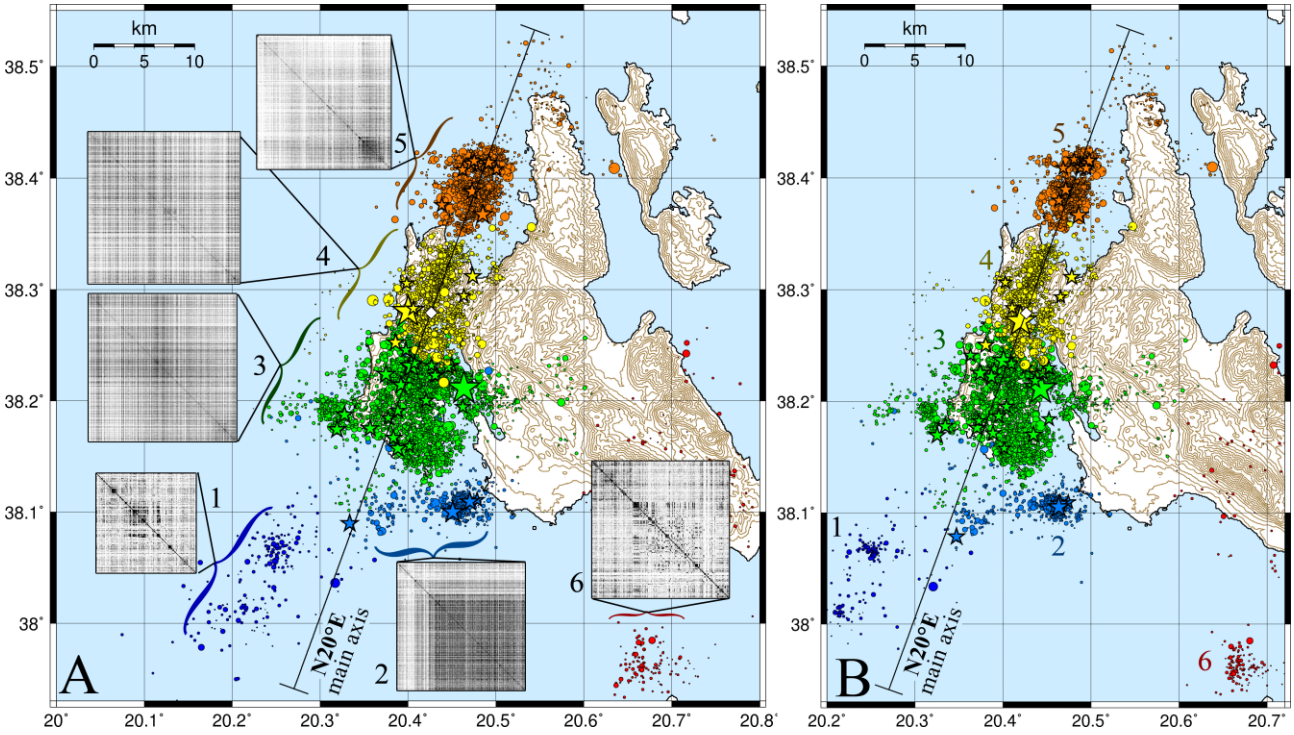

Figure 5.28: Epicenters of the 2014 earthquake sequence in Cephalonia A) before and B) after relocation with the double-difference algorithm HypoDD. Squares in panel (A) represent the cross-correlation matrices (with black referring to strong correlation) for each of the 6 spatial groups indicated by numbers and different colours of epicenters. The group-specific cross-correlation matrices are also depicted in panel (A). Major earthquakes with magnitude $M \geq 4.0$ are represented by stars. The profile line drawn at N20°E is used for the cross-sections of Figs. 5.29 and 5.30 and is referred in the text as the "main axis" of the aftershock sequence.

A cross-correlation matrix was constructed using waveform recordings from the local station VLS, situated in a minimal distance of ~17 km from the middle of the aftershock sequence and up to ~31 km from its northern tip in the Myrtos Gulf. Full signals were considered (both P, S-waves and coda), filtered between 2 Hz και 15 Hz. Individual matrices were constructed for each of the 3 components and their RMS values were then used for a combined matrix. The individual matrices for each spatial group are depicted in square panels within Fig. 5.28A, with rows and columns representing events sorted according to their origin time and dark cells corresponding to strongly correlated pairs of events. The matrices of Groups 3 and 4, which cover the Paliki peninsula, appear visually homogeneous, with alternating bright and dark lines and without large dark square areas around the diagonal, which would indicate strong, spatiotemporal clustering of repeating earthquakes, relatively uninterrupted by uncorrelated events. These groups include the majority of aftershocks directly related to the rupture zone, and the homogeneity of the matrices is consistent with the observation that the whole volume occupied by these groups was activated almost immediately after the occurrence of the major event of 26 January 2014. This is in contrast with Groups 2 and 5, corresponding to a dense spatiotemporal cluster S of Cephalonia and to the seismicity in the gulf of Myrtos. The first is dominated by high cross-correlation values while the latter shows evidence of strong spatiotemporal clustering towards the end of the study period (dark square region in the lower-right corner of the matrix). Small sets of correlated events are evident in

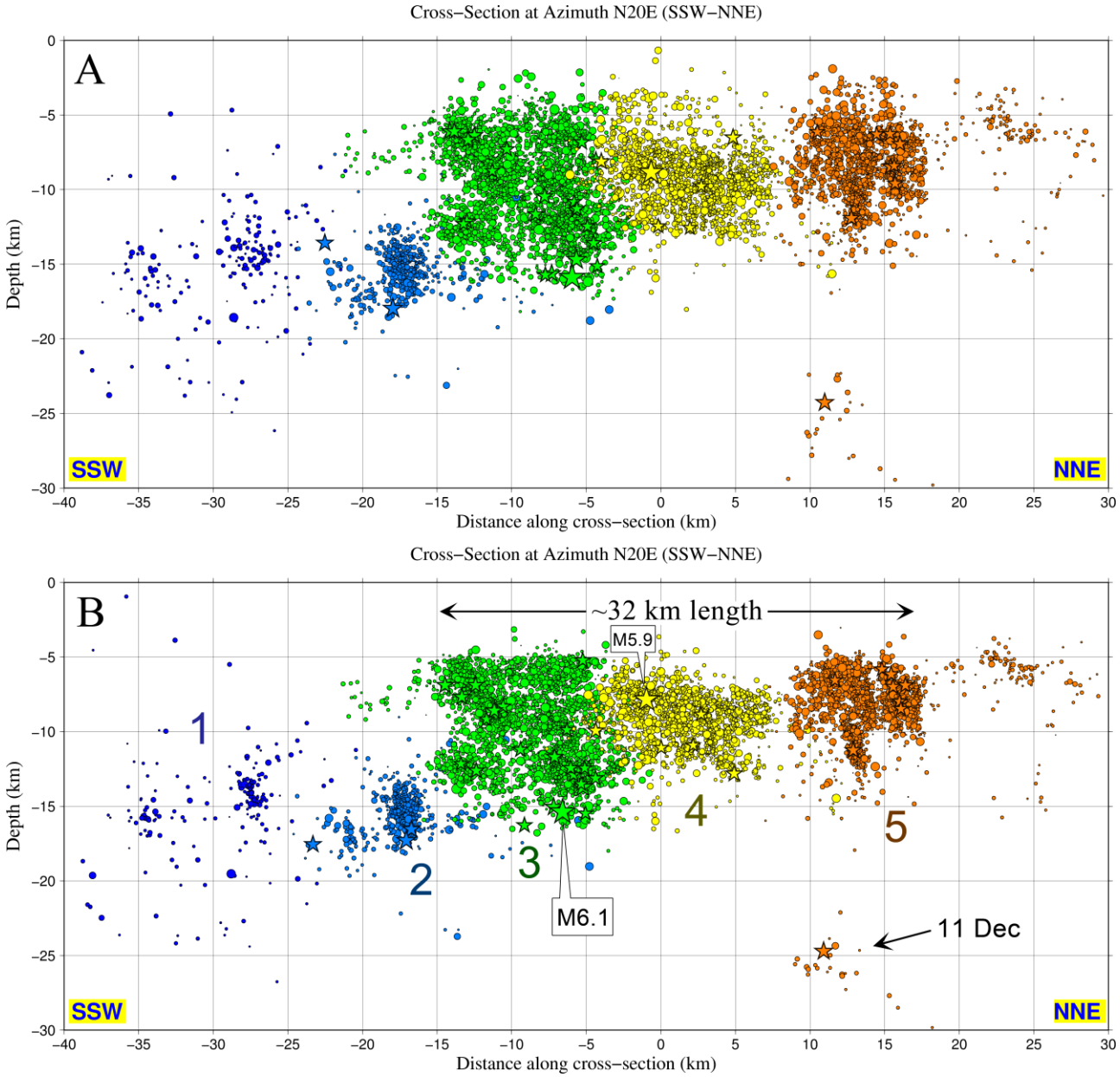

Figure 5.29: Cross-sections of the 2014 earthquake sequence in Cephalonia, drawn in N20°E direction (see profile line in Fig. 5.28) using solutions A) before and B) after the relocation procedure with HypoDD. The width of the cross-sections is ± 10 km. Numbers and colours are used to indicate the 6 spatial groups. Major earthquakes with magnitude $M_w \geq 4.0$ are represented by stars.

the matrices of the less populated Groups 1 and 6, corresponding to off-shore activity in the CLTFZ, SW of Cephalonia, and between Cephalonia and Zakynthos islands, respectively.

Nearest-neighbor linkage was applied on each matrix for the determination of clustering hierarchy of repeating earthquakes and multiplets were formed after selecting the optimal correlation threshold, $C_{opt.th}$. About 50% of events in the catalogue were found to belong in multiplets of size equal or larger than 2. More details are presented in Table 5.3. The P- and S-waves were then cross-correlated separately in each station for all pairs of events with a similarity level above the threshold value and initial alignment on their observed arrival-times. The value of the cross-correlation

maximum and its corresponding time-lag were registered as additional input data for the relocation procedure that follows. For the larger Groups 3 and 4 the travel-times obtained from catalogue consist the main input data, as the multiplets tend to be numerous but sparse, while most include small numbers of events. The vast majority of events (~99%) were successfully relocated with HypoDD (Walhauser and Ellsworth,

Table 5.3: Results of the cross-correlation and relocation procedures per spatial group.

Group	Region	# events	C_{th}	% multiplets	# reloc.	% reloc.
1	CTF (SSW)	223	0.38	66%	211	95%
2	S.Cluster	629	0.76	54%	629	100%
3	mid-S (1st EQ)	3092	0.67	40%	3059	99%
4	mid-N (2nd EQ)	1793	0.66	44%	1775	99%
5	Myrtos g.	1812	0.46	64%	1776	98%
6	SE (off-shore)	230	0.42	72%	223	97%
Total	-	**7779**	-	**49%**	**7673**	**99%**

2000), mostly using the weighted least squares method, with the exception of some small sub-clusters for which the SVD technique was feasible. The results of the double-difference relocation are presented in Fig. 5.28B and Table 5.3. The significant decrease in dispersion is especially evident in the off-shore clusters, while the width of the spatial extend in the rest of the seismicity is also reduced. Both major events have been relocated closer to the main N20°E axis of the aftershock sequence. More details on its spatial characteristics are presented in the following section.

5.3.2 Spatio-temporal and multiplet analysis

The detailed spatio-temporal description of the 2014 aftershock activity in Cephalonia requires further analysis in spatial and temporal windows to simplify and understand its characteristics. On a large scale, the relocated aftershock sequence is roughly oriented NNE-SSW (~N20°E), covering an area ~32 km long, ~5 km wide on its northern part and ~15km wide on its southern part, with its epicenters occupying most of the Paliki Peninsula, as well as a large portion of the Argostoli and Myrtos gulfs. In the cross-section of Fig. 5.29 a difference in focal depth ranges can be observed between the northern and southern halves of the sequence, with the former, more linear part (Groups 4 and 5) being constrained at depth between 5 and 12 km while the latter, more diffuse part (Group 3), extending down to ~17 km. The mainshock of 26 January, 13:55 UTC (M_w=6.1) is located at a focal depth of ~16 km, in the mid-southern part of the sequence, with its epicenter shifted by ~5 km eastwards with respect to the main N20°E axis of the distribution (Fig. 5.28). The second major event (M_w=5.9), which occurred on 3 February 2014, 03:08 UTC, is located in the middle, more linear segment of the sequence, at a focal depth of ~8 km.

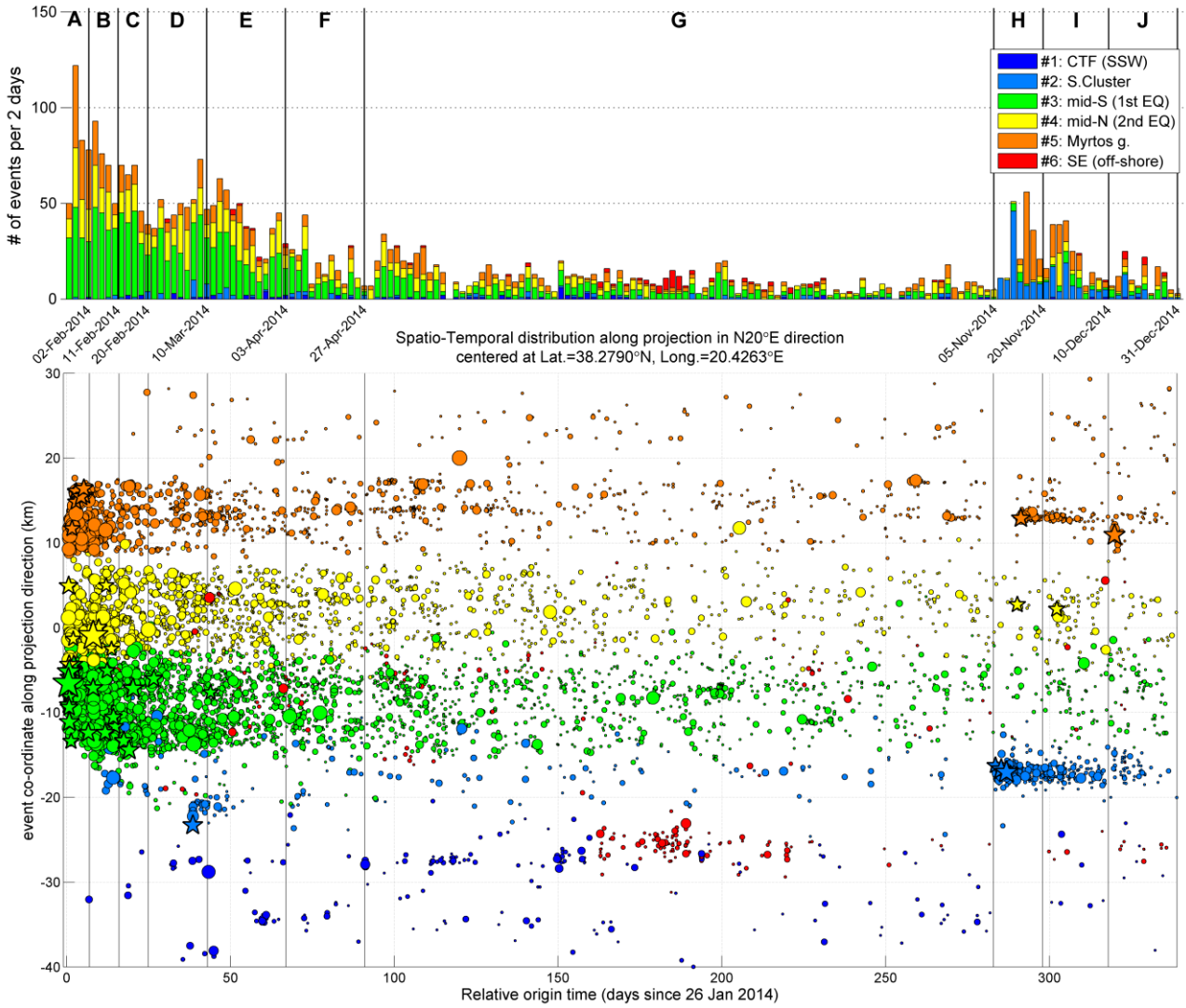

Figure 5.30: (Top) Histogram of number of earthquakes per 2 days for the 2014 aftershock sequence in Cephalonia, divided in 10 periods: A) 26 January - 1 February, B) 2 -10 February, C) 11 - 19 February, D) 20 February - 9 March, E) 10 March - 2 April, F) 3 - 26 April, G) 27 April - 4 November, H) 5 - 19 November, I) 20 November - 9 December and J) 10 - 31 December, 2014. (Bottom) spatio-temporal projection of relocated epicenters on the main N20°E axis with respect to the relative origin time (measured in days since 26 January 2014). Colours in both panels are used to indicate the 6 spatial groups. Major earthquakes with magnitude $M_w \geq 4.0$ are represented by stars.

The temporal evolution of the aftershock sequence was relatively smooth, without any major sub-sequences, but degraded at a slow rate, as is evident in the histogram of Fig. 5.30 (top panel). During the first hours after the mainshock, the activity was mainly concentrated in Group 3, but it spread throughout Groups 4 and 5 soon afterwards. Macroscopically, it is evident in the spatio-temporal projection of Fig. 5.30 (lower panel) that the larger earthquakes with $M_w \geq 4.0$, depicted as stars, mostly occurred during the first 2 months of activity, roughly in periods A-D. A gradual reduction of seismicity can be observed in periods E-G, with the exception of the activation of Group 6, SE Cephalonia (offshore) in the middle of period G. The last two months of 2014 were characterized by the activation of a strong cluster S of Cephalonia (Group 2) and re-activation of

seismicity in Myrtos Gulf (Group 5), along with two $M_w \geq 4.0$ events in Group 4 (mid-northern part of Paliki peninsula). No evidence of significant seismicity migration can be observed from the spatio-temporal diagram.

A special selection of the relocated spatial distribution (containing only activity along the main N20°E axis) has been further divided in 11 sub-clusters (Fig. 5.31) using the same clustering technique as in the previous section (Ward's linkage), enabling its study at a smaller scale in the maps and cross-sections of Fig. 5.32. This mainly separates Group 3 in four sub-clusters (c, d, e and f) and group 4 in two sub-clusters (g and h) while the main portion of Group 5 (sub-cluster "j") is separated from a small subset that is located at a much larger depth of ~25km (sub-cluster "i") and the sparse sub-cluster "k" that is located and the NE tip of Cephalonia island. Sub-clusters "a" and "b" are roughly corresponding to spatial Groups 1 and 2, respectively, while Group 6 is not discussed any further.

During period A (26 January - 1 February 2014), the seismic activity reached the northernmost part of the sequence in Myrtos Gulf. A linear segment is indicated by an arrow in the map of Fig. 5.32A

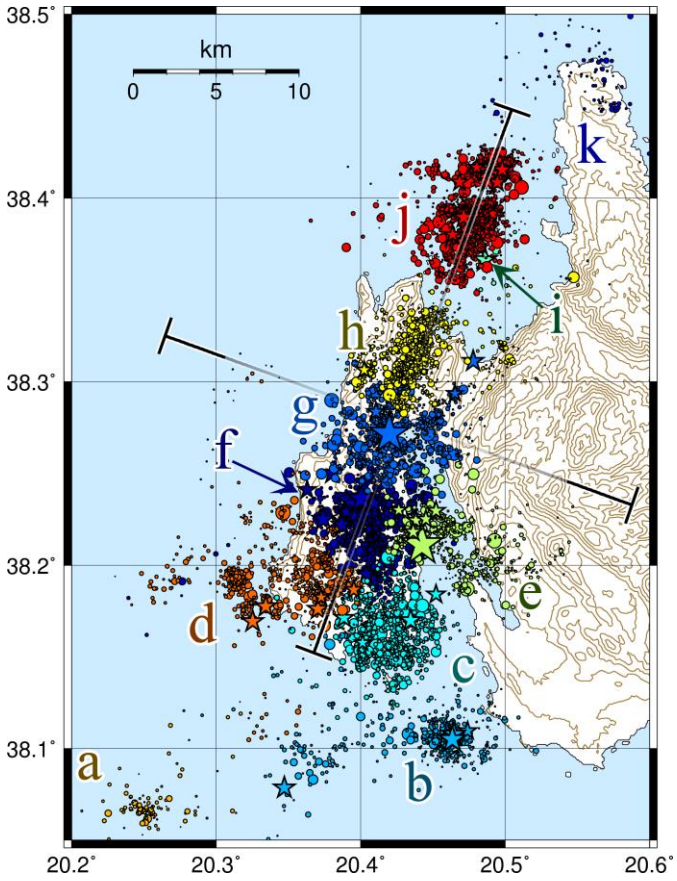

Figure 5.31: Relocated epicenters of the 2014 aftershock sequence in Cephalonia, further divided in 11 spatial sub-clusters. Profile lines drawn in N20°E and N110°E directions are used for the parallel and perpendicular cross-sections in Fig. 5.32. Major earthquakes with magnitude $M_w \geq 4.0$ are represented by stars.

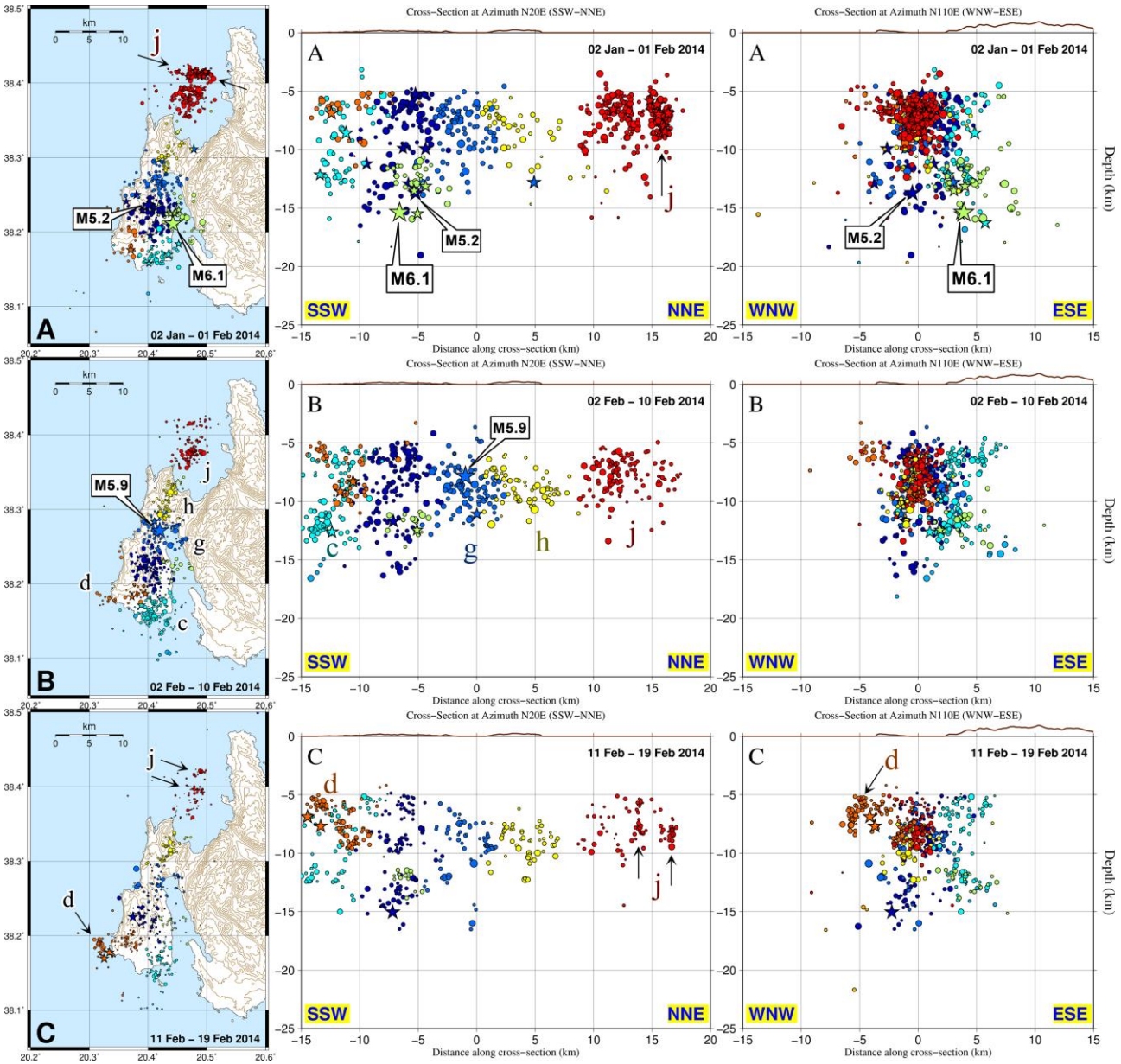

Figure 5.32: Map (left), parallel (middle, N20°E) and perpendicular (right, N110°E) cross-sections of the relocated 2014 aftershock sequence in Cephalonia for the 10 sequential temporal periods, indicated by capital letters. Colours and small letters indicate the 11 sub-clusters shown in Fig. 5.31. Major earthquakes with magnitude $M_w \geq 4.0$ are represented by stars.

for sub-cluster "j", while its distribution at depth suggests activity on a sub-vertical WNW-ESE oriented plane at depths between 5 and 9 km, separated by a small gap from the rest of the seismicity in the same sub-cluster. The hypocentral locations of the mainshock (M_w=6.1) of 26 January and the large aftershock (M_w=5.2), which occurred ~5 hours later the same day, are also indicated in the same figure and belong to sub-clusters "e" and "f", respectively. The main rupture is considered along a SSW-NNE oriented plane. However, it appears that activity is occurring mostly SSW (sub-cluster "c") and WNW of the mainshock's epicenter, where the large aftershock also occurred. Despite the lack of seismicity NNE of the mainshock, the tip of the suggested main

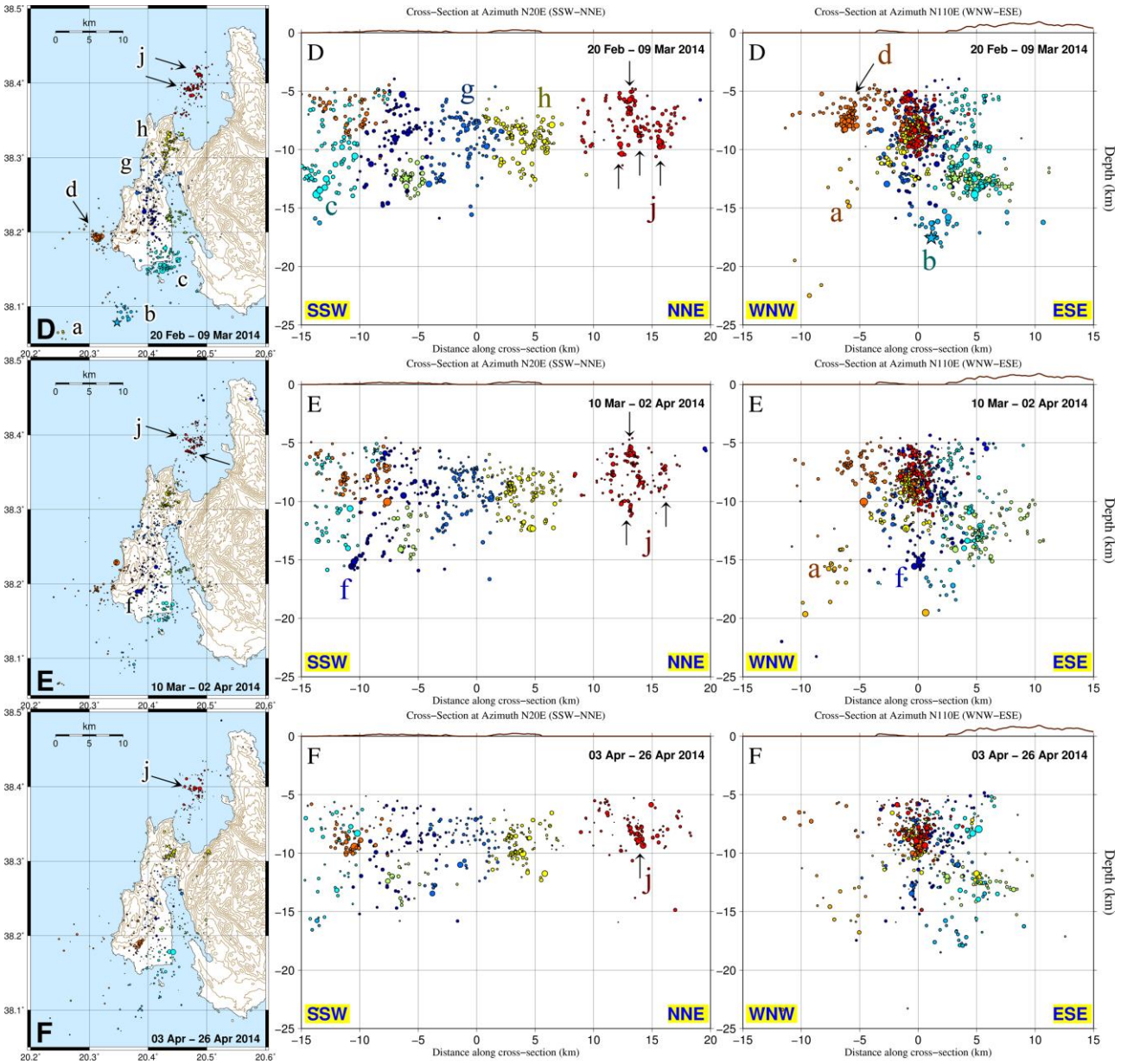

Figure 5.32: (continued)

rupture is marked by a $M_w \geq 4.0$ event grouped in sub-cluster "g", with its epicenter close to the junction between Paliki peninsula and the rest of Cephalonia Island.

The second period (Fig. 5.32B) roughly begins with the occurrence of the second major event (M_w=5.9) of 3 February 2014, the seismic activity was concentrated mostly on a SSW-NNE oriented linear segment including the large aftershock and sub-clusters "g" and "h". Although this region was already active during period A, its activity has slightly expanded towards NNE. It also appears limited in a narrower depth range between ~7 and ~12 km, getting even narrower at its NNE end where it is concentrated between 8 and 10 km. At the south of Paliki peninsula the

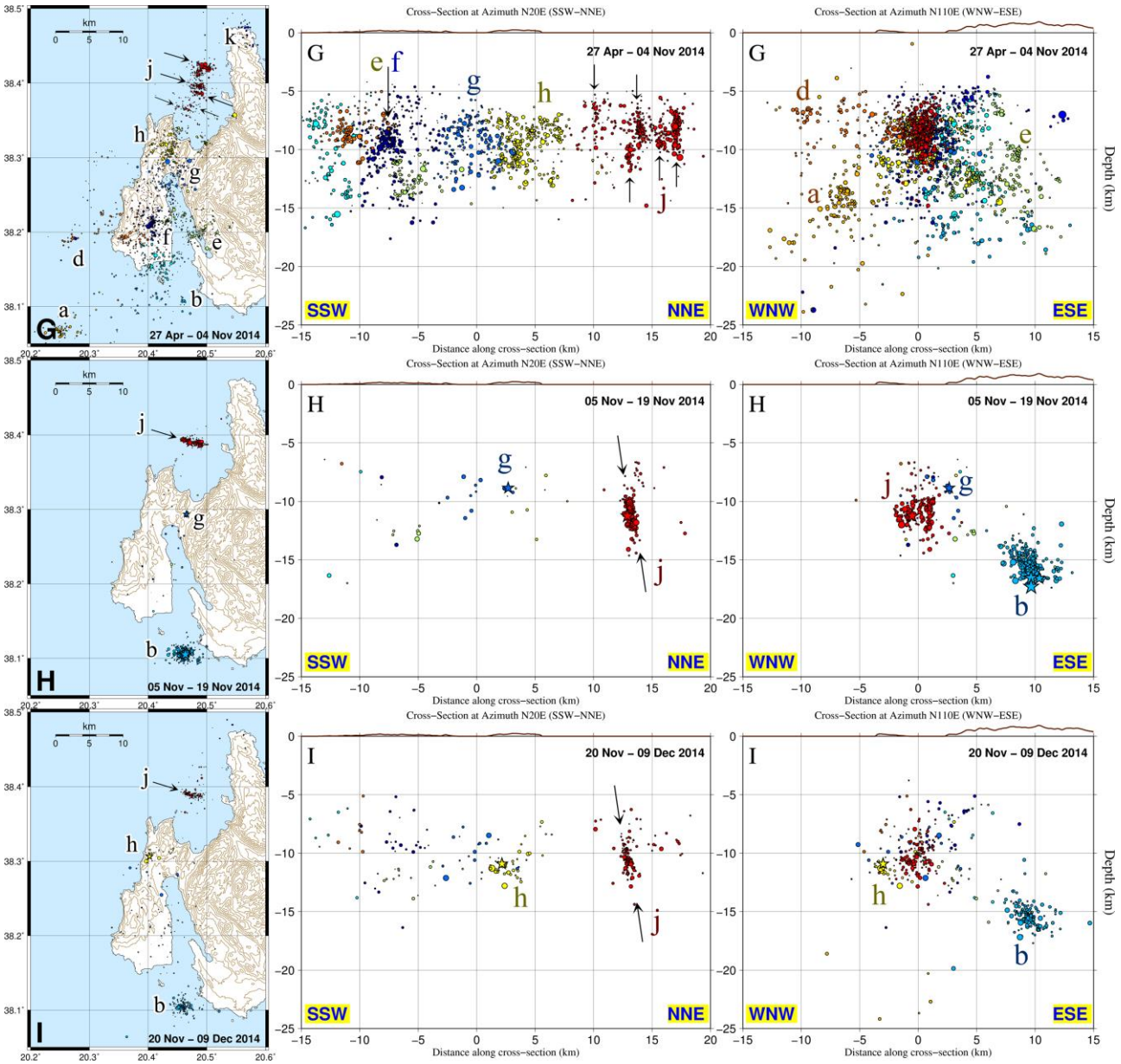

Figure 5.32: (continued)

activity is also slightly expanded to the south (sub-cluster "c") mostly at a depth of ~12 km and to the west (sub-cluster "d") at depths shallower than 10 km.

During the third period (Fig. 5.32C) the seismicity in the main body of the aftershock sequence persists, but is characterized by gradual degradation, while the branch of sub-cluster "d" is expanded westwards at shallower depths. There is also some evidence of a second linear structure in sub-cluster "j", ~2 km south of the previously activated surface in period A. All regions remain active in the following periods (D-F) with further expansions in sub-clusters "c" and "d" and the activation of a small sub-cluster (b) ~10 km to the south, offshore Cephalonia Island. Gradual

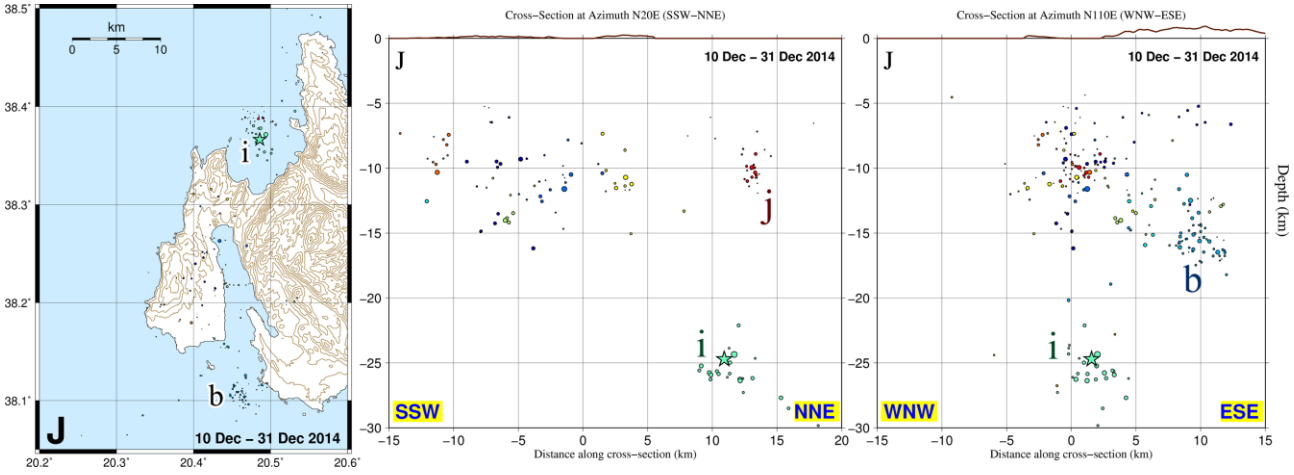

Figure 5.32: (continued)

degradation and slight outwards expansion of seismicity is observed throughout the longer period G (Fig. 5.32G), during which sub-clusters "a" and "k" were activated, SW offshore, at the CLTFZ and at the northernmost part of Cephalonia Island, respectively. The slow degradation and expansion is indicative of a relaxation process while numerous parallel individual segments can be distinguished within sub-cluster "j".

The last periods (H-J) are characterized by the activation of the strongly clustered Group 2 (sub-cluster "b"), in focal depths between 15 and 17 km, offshore south of Cephalonia Island. This activity began with an M_w=4.2 event on 5 November which was followed by an M_w=4.8 event two days later and culminated with an M_w=5.0 event in 8 November at the same area. On 12 November, an M_w=4.0 event occurred at the junction between Paliki peninsula and the main island (sub-cluster "g") which was followed by an M_w=4.3 event inside Myrtos gulf (sub-cluster "j") during the same day. The latter follows the same pattern of activity in a sub-vertical WNW-ESE plane. Activity in Groups 2 and 5 was gradually reduced towards the end of 2014. During the last period (Fig. 5.32J), an M_w=4.8 event occurred on 11 December at a depth of ~25km beneath Myrtos Gulf, activating the small sub-cluster "i".

The evolution history of multiplets per spatial group is presented in Fig. 5.33. It is evident that the occurrence of the mainshock triggered the emergence of large multiplets such as those marked with "2", belonging to Group 3) in the right panel of Fig. 5.33, while the one marked with "3" belongs to Group 5 with the seismicity inside Myrtos Gulf. Multiplet labeled with "4", belonging to Group 4 of activity in the mid-northern Paliki peninsula, was first generated with a small number of events before the occurrence of the major earthquake of 3 February, but it became more active soon afterwards. Other multiplets belonging to the major groups 3 and 4 were generally smaller, with the exception of the one labeled "6" in Fig. 5.33, which was generated in the beginning of March (period D), when an increase in new multiplets is observed within a few days. A peak in multiplet activity was observed towards the end of Period D and during the beginning of period E, with Group 3 (mid-southern Paliki) being the most intense ones. This activity is almost exclusively attributed to the two large multiplets labeled with "2". The multiplet marked "7" concerns the

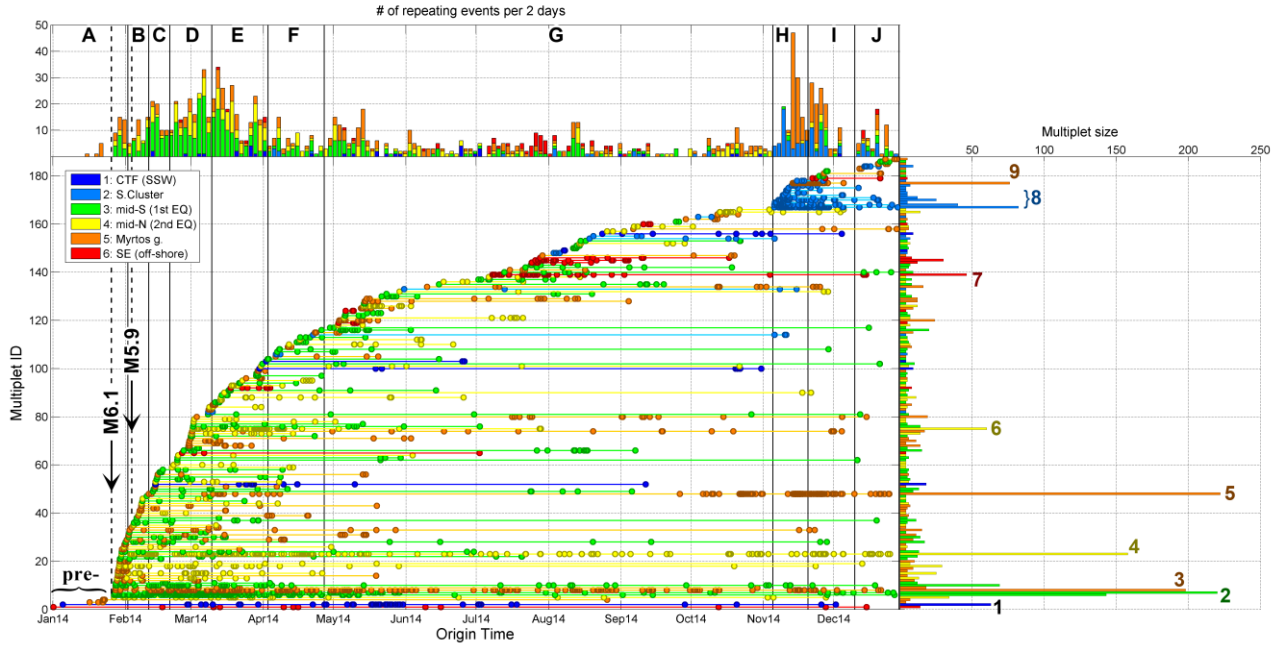

Figure 5.33: (Bottom-left) Multiplet history dendrogram for the 2014 aftershock sequence in Cephalonia. The vertical axis shows the Multiplet ID, sorted by increasing origin time (horizontal axis) of the first event, that is considered as the generation time of the corresponding multiplet. The circles drawn in the same line represent events belonging to the same multiplet. (Right) Multiplet size, indicating the number of events contained in each multiplet (for numerical labels refer to the text). (Top) histogram of the total number of repeating events occurring per 2 days. Colours in all panels indicate the 6 spatial groups.

activity in Group 6, offshore between Cephalonia and Zakynthos islands, in the middle of period G. The largest multiplet is labeled "5" and belongs to Group 5 (Myrtos Gulf). This was first activated at the beginning of period C with a few events in the following periods. It then vanished until the end of period G when it was reactivated. In period H the multiplets labeled "8" were triggered by the occurrence of the major events in sub-cluster "b", at the south of Cephalonia Island, followed by the re-activation of seismicity in Myrtos gulf with multiplet "9", concurrently with more events in the pre-existing multiplet "5". It is also interesting that during January, before the mainshock, a few small multiplets could be detected among the background seismicity, including some which belong to Group 1, SW offshore Cephalonia island on the CLTFZ (multiplet labeled "1") which kept generating events during the aftershock sequence. However, it should be noted that, given the relatively low correlation thresholds, C_{th}, in most groups (Table 5.3), and the simple linkage method that has been applied for the formation of multiplets, the large ones may in fact be a group of individual real multiplets in a relatively broader area than expected for strictly defined multiplets. During the relocation procedure these do not collapse to a single source but rather concentrate to their respective individual centroids, together with their more (relatively) similar events. This is rather true for the two large multiplets of Group 3, labeled "2" in Fig. 5.33, which were formed soon after the mainshock occurred. Large multiplets in this sequence were formed in regions most densely occupied by hypocenters, in almost all the defined sub-clusters.

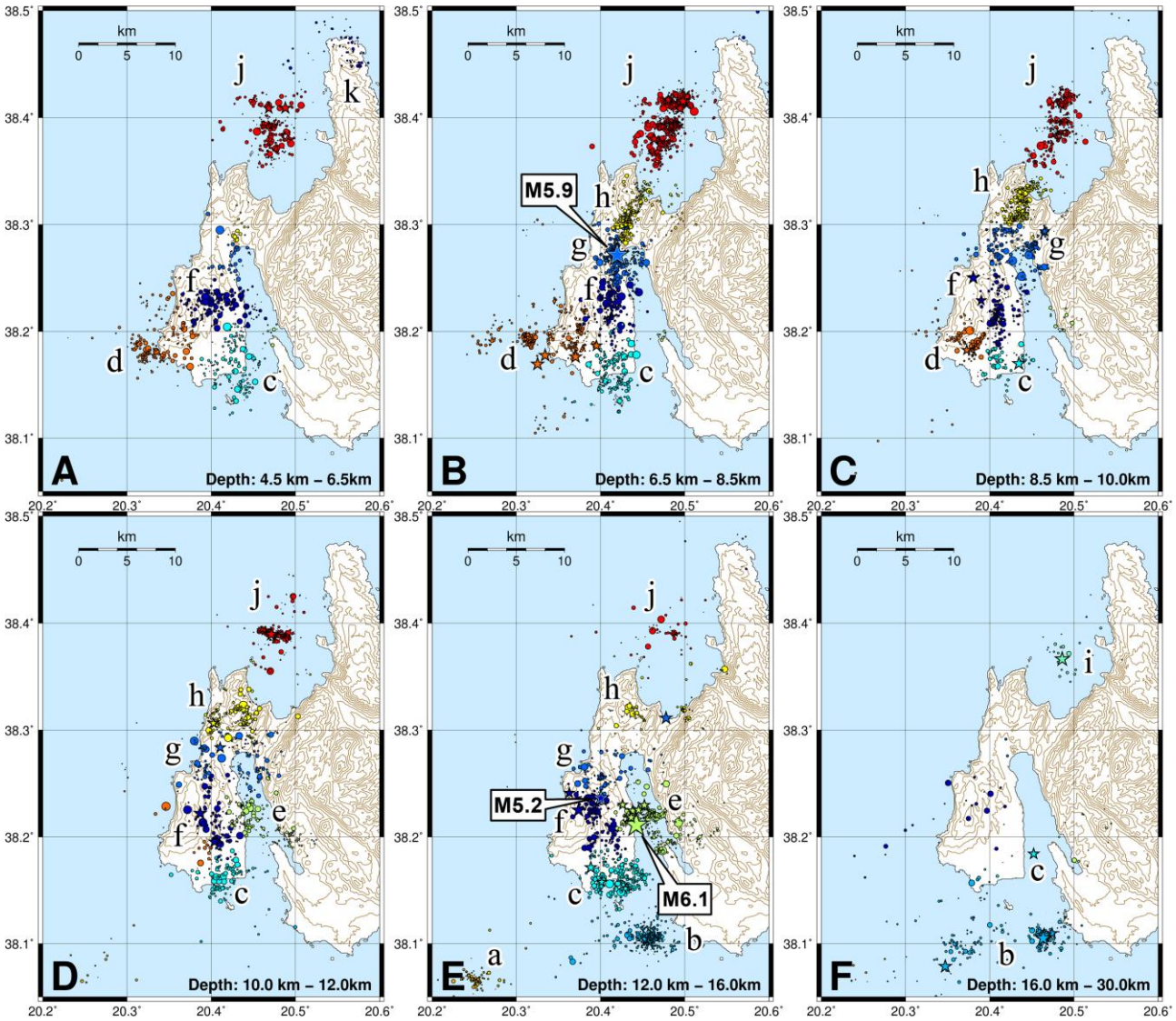

Figure 5.34: Maps of the relocated epicenters of the 2014 aftershock sequence in Cephalonia for selected subsets of different depth ranges: A) 4.5 - 6.5 km, B) 6.5 - 8.5 km, C) 8.5 - 10.0 km, D) 10.0 - 12.0 km, E) 12.0 - 16.0 km, F) 16.0 - 30.0 km. Colours and small letters indicate the 11 sub-clusters shown in Fig. 5.31. Major earthquakes with magnitude $M_w \geq 4.0$ are represented by stars.

Some interesting details can be discriminated by observing the seismicity in narrow bands of different focal depths (Fig. 5.34). The shallower events (at focal depths H<6.5 km) mostly occupy regions in the mid-southern part of Paliki peninsula and Myrtos Gulf (Groups 3 and 5, respectively). Some E-W delineations are roughly evident in the northernmost part of sub-cluster "j" while the rest, including the shallow activity of sub-cluster "k" in the northernmost part of the island, are too diffuse to allow for any safe conclusions. The next depth slice (Fig. 5.34B) has a major feature of two roughly linear segments with the epicenter of the major event of 3 February in the middle, sub-cluster "h" to its north, oriented almost SW-NE, and sub-clusters "g" and "f" to its south, oriented roughly N-S. Several small spatial clusters can be observed in the southern part of Paliki as well as in Myrtos Gulf. In the band of 8.5 km ≤ H ≤ 10.0 km (Fig. 5.34C) some small linear segments can be observed in sub-clusters "c", "d" and "f". The SW-NE oriented cluster "h" persists while a

branch of sub-cluster “g” is spread NE of the major event of 3 February, in the junction between Paliki peninsula and the rest of Cephalonia Island. This activity, although it does not clearly form a linear segment, can be linked, with hindsight, to sub-cluster “e” deeper and further south, near the region where the hypocenter of the mainshock of 26 January is located (Fig. 5.34E). At depths 10 km $\leq H \leq$ 12 km (Fig. 5.34D) the most remarkable feature is the WNW-ESE oriented linear segment of sub-cluster “j”, belonging exclusively to the activity of this spatial group in November, while the next depth slice (Fig. 5.34E) contains most of sub-cluster “b” that was activated during the same month. This slice also includes the mainshock and largest aftershock of 26 January 2014 in sub-clusters “e” and “f”, respectively. It is noteworthy that these clusters are aligned along a WNW-ESE orientation, which corresponds to the auxiliary plane of the mainshocks focal mechanism, but there is also significant seismicity in sub-cluster “c” which lies SSW. In the same depth range sub-cluster “a”, located at the CLTFZ, can also be observed. The deepest slice (Fig. 5.34F) reaches the depth of 30 km and contains the deepest part of sub-cluster “b”, but also the activity at depth of ~25 km beneath Myrtos Gulf (sub-cluster “i”).

The main characteristics of the spatial distribution are summarized in the sketch of Fig. 5.35. More specifically, two main faults are suggested (solid bold lines); by taking into account both the results of the spatiotemporal analysis, the focal mechanisms of the major events and deformation patterns, which suggest dextral slip along SSW-NNE oriented sub-vertical faults. The ~15 km long rupture caused by the mainshock of 26 January lies at depths between 10 km and 15 km, along the line between sub-clusters “e” and “f”, reaches the junction between Paliki peninsula and the rest of Cephalonia island in the north (sub-cluster “g_2” in Fig. 5.35) and the diffuse activity of sub-cluster “c” in the south of Paliki. This is the most probable scenario is mostly forced by the focal mechanism and deformation data rather than the spatial distribution itself, as the hypocenter of the mainshock tends to be offset by several km away eastwards of the main N20°E axis and quite a few of the major events happen to be situated on the auxiliary plane of its focal mechanism, which would suggest a WNW-ESE plane which is not supported by other observational data. However, the rupture plane for the second major event of 3 February is straightforward, as evidenced by the very linear, ~10 km long, SSW-NNE oriented segment marked by “g_1” and “h” in Fig. 5.35, at the depths of 6 - 12 km. The rupture is likely ended at the spatial gap between sub-cluster “h” and the activity in Myrtos Gulf (sub-cluster “j”). The latter is characterized by smaller spatial (and some also temporal) sub-vertical clusters which seem to be parallel, oriented WNW-ESE, separated by small gaps. Since the focal mechanisms of their major events are similar to the rest of the distribution it is suggested that they are in fact sinistral strike-slip faults. It is also observed that they become wider the further away they are from the shore of Paliki. This is consistent with a flower-structure of antithetic small faults created between two larger strike-slip faults (e.g. those related to the major ruptures of the 2014 sequence and the large CLTFZ to the west of the island), likely connected to the opening of Myrtos Gulf. The description of the activity in the southern part of Paliki peninsula

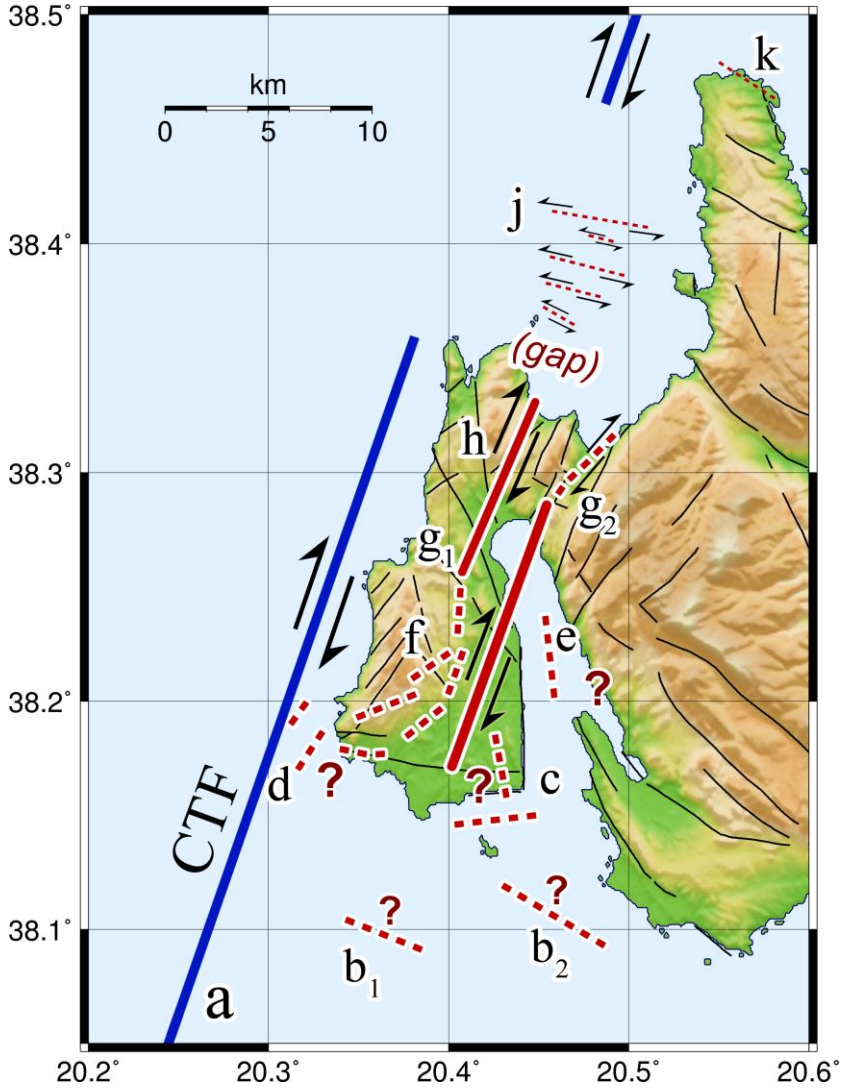

Figure 5.35: Simplified sketch for the main faults (solid red lines) and sub-faults (dashed lines) which were activated during the 2014 earthquake sequence in Cephalonia. Small letters indicate the 11 sub-clusters. Mapped neotectonic fault lines are after Sakkas & Lagios (2015).

is more uncertain. Dashed lines close to the labels “c”, “d”, “e” and “f” in Fig. 5.35 are drawn in places where small linear segments were observed after careful examination of thin, overlapping depth slices as well as small spatiotemporal clusters. The suggested slip directions are according to the orientation of the lines with respect to the dominant focal mechanism solution. It is noteworthy, that many lines can be related to neo-tectonic faults which have been mapped on the surface of the island. This is also true for the very shallow sub-cluster “k” on the northern tip of Cephalonia, which may be sparse but contains a multiplet that is roughly aligned in a NW-SE direction, parallel to the superficial fault traces to its south. Lines “b_1” and “b_2” are mostly hypothetical, as there is no clear delineation in sub-cluster “b”, which occurred at larger depths than the rest of the sequence (~13 - 19 km).

5.3.3 Magnitude distribution - ETAS modeling

As typical during aftershock sequences, the magnitude of completeness, M_c, varies significantly with time. Fig. 5.36 shows the M_c values, calculated by the maximum curvature method (Wiemer & Wyss, 2000) in sliding windows of 300 events, starting as high as ~3.0 at the beginning, right after the mainshock, and gradually decreasing down to ~1.7±0.2. In fact, the M_c is still not at its lowest point after the second major event of 3 February. This suggests that if the whole sequence is to be studied in terms of its magnitude distribution, a higher threshold would have to be chosen to ensure homogeneity.

A significant effect of this issue is that when the cumulative number of events curve is viewed without a threshold, the largest aftershock of 3 February appears to not affect the sequence at all (Fig. 5.37, blue line). The curve is very smooth and this major earthquake behaves as just another aftershock. However, if a threshold as high as M_{th}=2.8 is selected, it immediately becomes apparent that the major earthquake of 3 February produces a secondary aftershock sequence. Taking this into account, these two parts of the sequence, before and after the second major event, should be studied separately.

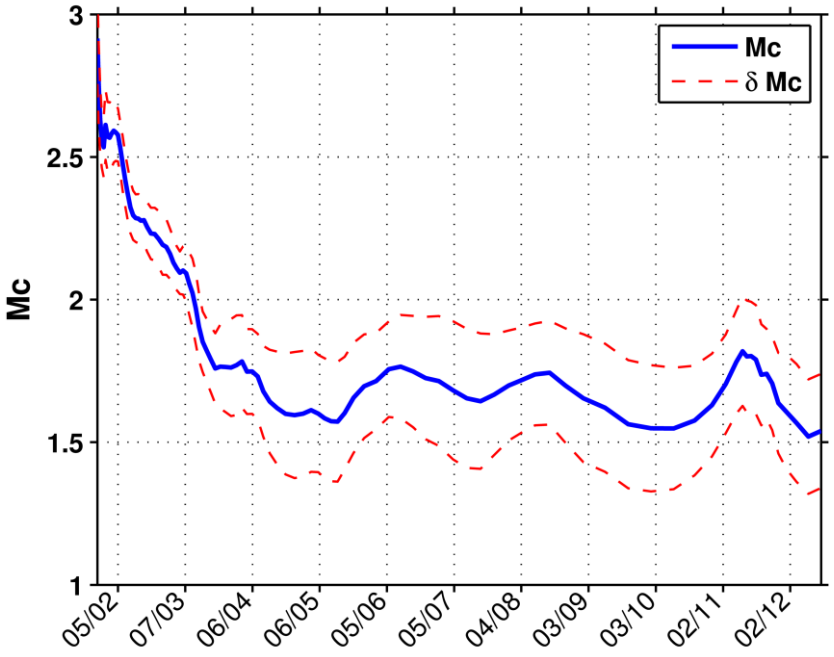

Figure 5.36: Temporal variation of the completeness magnitude, M_c, for the 2014 Cephalonia aftershock sequence, calculated using the maximum curvature method at sliding windows of 300 events.

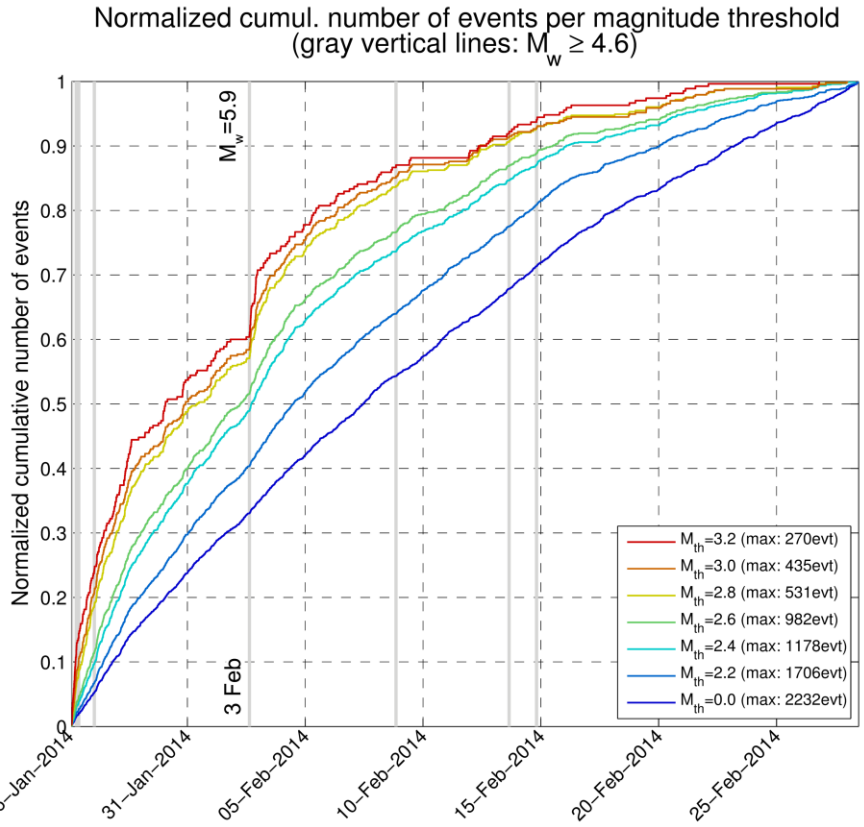

Figure 5.37: Cumulative number of events for different magnitude thresholds, M_{th}, normalized by their respective total number of events, for the first 34 days of the 2014 Cephalonia aftershock sequence. Gray vertical lines mark the origin times of the largest events (M_w≥4.6).

Interestingly, the frequency-magnitude distribution of the first part exhibits a relatively low *b*-value for an aftershock sequence, *b*=0.87±0.04. Moreover, considering the modified Båth's law (Shcherbakov & Turcotte, 2004), the magnitude of the largest aftershock is expected to be around 5.8 (Fig. 5.38a), rather than the average 6.1-1.2=4.9, estimated by the original Båth's law (Båth, 1965). The M_w=5.8 value is very close to the observed M_w=5.9 for the earthquake of 3 February. The calculated M_c for the second part (Fig. 5.38b) is already lower than the first one and the *b*-value is higher after the second largest event. In fact, the *b*-value soon stabilizes to a range near unity with some variation and a few "bursts" of slightly higher values during the rest of the sequence.

The evolution of the cumulative number of events could be modeled by either the simple Modified Omori's Formula (MOF), which depends only on the elapsed time since the mainshock, or the more complex ETAS model, which uses the assumption that every aftershock produces a secondary sequence depending on its magnitude. The two models for the first part of the 2014 Cephalonia aftershock sequence are presented in Fig. 5.39. It is immediately apparent that this part of the time-series can be described by a simple decay rule, with minor deviations. In this case, the MOF model is preferred over ETAS, mainly due to its lower *AIC* value, while, in addition, it also has a slightly lower standard deviation, σ. The decay rate for the MOF model is relatively low (p<1), indicating that the decline of the aftershocks rate is slow. The *a*-value for the ETAS model, which is also

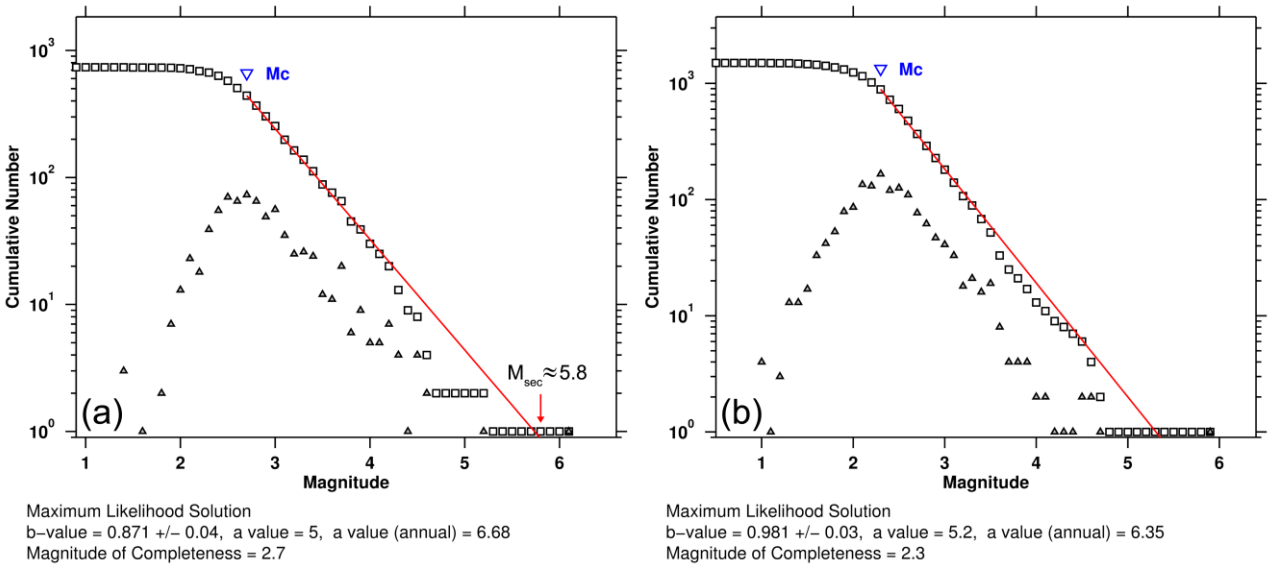

Figure 5.38: Frequency-magnitude distribution for the 2014 Cephalonia aftershock sequence, a) first part (26 January – 2 February), where M_{sec}≈5.8 is the predicted magnitude of the largest aftershock according to the modified Båth's law (Shcherbakov & Turcotte, 2004), b) second part (3 – 28 February).

adequate, even though not preferred, is very high (a≈5.8) even for a mainshock-aftershock sequence. In both models, the residuals are well distributed, alternating between positive and negative values (Fig. 5.39b).

The separate modeling for the part of the sequence following the major M_w=5.9 earthquake of 3 February is presented in Fig. 5.40. In this case, a lower magnitude threshold was selected (M_{th}=2.6), still valid within the acceptable range for M_c, as it provided a better fit. Again, the MOF model is marginally better than the respective ETAS model, with lower *AIC*, although it has a higher σ. The latter is due to ETAS being better at following seismicity rate variations between days ~3-9, during which the MOF model has a significant negative residual. The *p*-value is slightly increased for both models while the *a*-value of the ETAS model is lower. The ETAS model deviates after day ~9 (12 February), when there is an increase in the seismicity rate that cannot be explained by the current ETAS model. This coincides with the occurrence of a major M_w>4.0 event in Group #3 on that day and the spreading of activity in the offshore branch of sub-cluster d, which is a small sign of migration (Fig. 5.32C). Another positive residual is observed after day ~34 (4 March; not included in the window of Fig. 5.40) that is likely related to the spreading of activity in the relatively deep (H>15km) sub-cluster b of the southern Group #2 during period D (Fig. 5.32D). These deviations do not necessarily imply the influence of an aseismic factor to the triggering of these small clusters (although it cannot be ruled out), but possibly an incompatibility of the current ETAS parameters. It should be noted that despite using a relatively high threshold value, in both Figs 5.39b and 5.40b there appears to be a deficit in the smaller magnitudes at the very beginning, indicating a still slightly higher M_c value during the period that these events occurred.

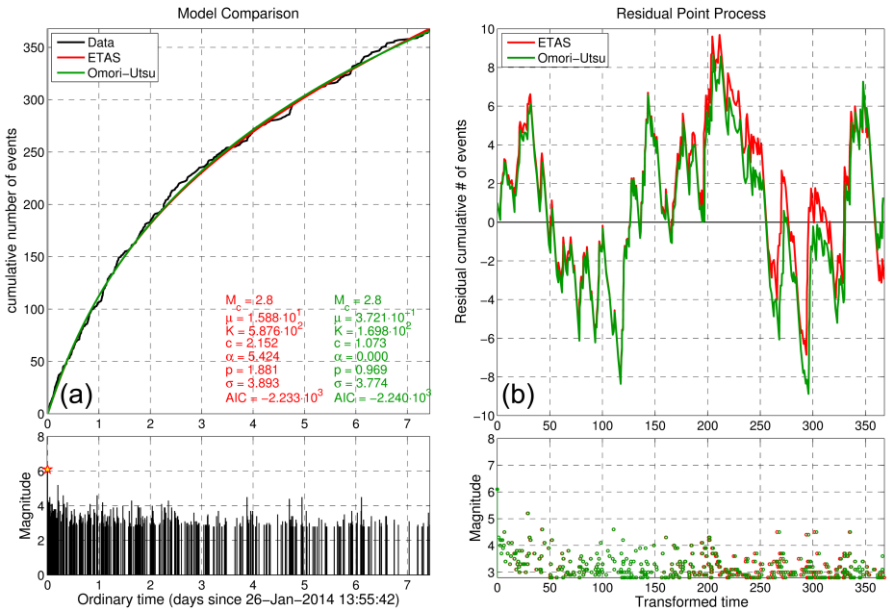

Figure 5.39: ETAS and MOF models for the first part of the 2014 Cephalonia aftershock sequence, up to the occurrence of the second major event (26 January – 3 February, T_{end}=7.5 days), using a threshold $M_{th}\equiv M_c$=2.8 and $M_r\equiv M_{main}$=6.1, a) data and ETAS model curves in ordinary time, b) residuals between data and model in transformed time.

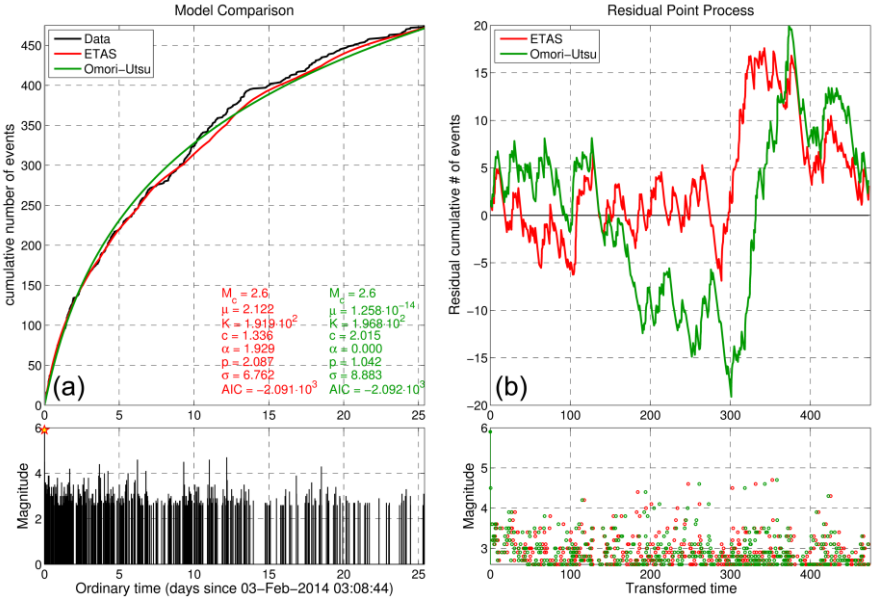

Figure 5.40: ETAS and MOF models for the second part of the 2014 Cephalonia aftershock sequence, for T_{end}=26 days after the occurrence of the second major event (3 February – 1 March), using a threshold M_{th}=2.6 and $M_r=M_{sec}$=5.9, a) data and ETAS model curves in ordinary time, b) residuals between data and model in transformed time.

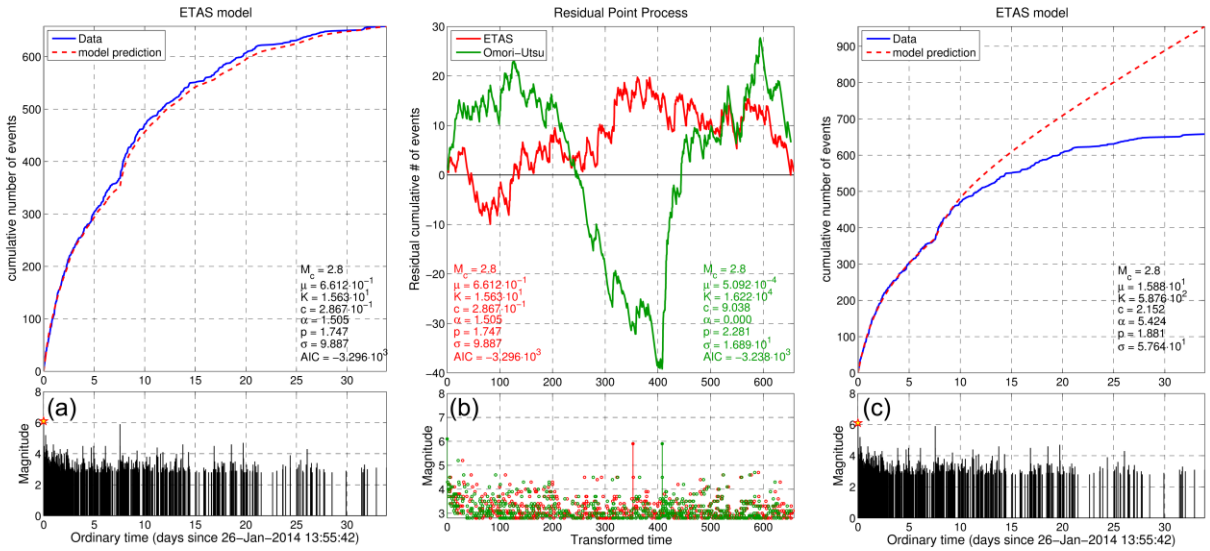

Figure 5.41: Models for the first T_{end}=34 days of the 2014 Cephalonia aftershock sequence (limited before a significant secondary outbreak on around 6 March), using a threshold $M_{th} \equiv M_c$=2.8 and $M_r = M_{main}$=6.1, a) data and ETAS model curves in ordinary time, b) residuals between data and model in transformed time, including the respective MOF model (green), c) forward ETAS modeling using parameters determined by MLE for the first part of the sequence (Fig. 5.39).

If a larger portion of the seismicity is taken as a whole, it cannot longer be treated as a simple aftershock sequence. Fig. 5.41 shows that the second major earthquake causes a secondary aftershock sequence that alters the shape of the "cumulative number of events" curve in a way that cannot be modeled by the simple MOF (Fig. 5.41b). In this case, the ETAS model is clearly preferred over the MOF model, with both *AIC* and σ being lower than the respective MOF values. The *a*-value is still high enough to be consistent with mainshock-aftershock patterns observed elsewhere (e.g. Ogata, 1992). However, there is a deviation from the model which begins 1 day after the mainshock and becomes more significant 5-6 days later (~1 February), that is before the second large earthquake occurred. If forward modelling is performed using the parameters of the ETAS model that was derived from the first part of the sequence (Fig. 5.41c), the fit is exceptional up to day ~9 (4 February). In this case, the deviation is not up to a constant value but becomes increasingly high, with the data being gradually further from the values predicted by the model. This is also suggestive that the whole sequence cannot be adequately described by a single model, as there is an apparent change that occurs shortly after the second major earthquake, likely due to an increase of the decay rate.

5.3.4 Discussion - Conclusions

The 2014 aftershock sequence in Cephalonia provided a rich dataset of over 7000 events, which were located with sufficiently small location uncertainties, despite the azimuthal gap due to the lack of seismic stations west of the epicenters. The southern and northern parts of the spatial distribution could be considered as two distinct groups, the first related to the mainshock of 26 January and the latter to the largest aftershock of 3 February 2014. The epicenters of the northern one are more linearly distributed along a SSW-NNE direction and limited to shallower depths, while the southern one has about twice the horizontal (~18 km) and vertical width (~10 km). The southern group is also characterized by a larger number of distinct activated volumes, indicating increased complexity.

Focal mechanisms for small events could not be calculated properly by first motion polarities because of the unavailability of a dense local network. However, the large number of major events allowed for the determination of several focal mechanisms by regional modeling, using stations of HUSN, and teleseismic waveform modeling, using IRIS DMC stations (Papadimitriou *et al.*, 2014). These all indicate dextral strike-slip faulting in a SSW-NNE direction, with the fault plane dipping steeply SE, similar to the dominant tectonic regime as defined by the Cephalonia Transform Fault in the west (Figs 5B.18 and 5B.19). However, because of the existence of distinct spatial clusters, mostly at the southern part, which are offset from the main axis of the aftershock distribution, related to the main causative fault, and taking into account the mapped neo-tectonic faults (Fig. 5.35), certain clustered events may be characterized by faulting consistent with the second nodal plane of the focal mechanisms. Concerning the events located in the Myrtos Gulf, the fault plane is possibly the one that strikes WNW-ESE. The increased complexity of the spatial distribution in the southern part, compared to the northern, is revealed in the cross-sections of Fig. 5C.19. In particular, distinct branches begin to appear at the cross-section e_1-e_2, whereas the main earthquake of 26 January and the largest aftershock that occurred ~5 hours later (M_w=5.2) are located at g_1-g_2, along with the majority of the strong aftershocks of the sequence. The spatial distribution becomes more linear to the north, starting from the cross-section h_1-h_2 (including the second main event of February 3rd).

Estimations from the determined seismic moment of the two major events indicate rupture lengths of 15 km and 10 km for the earthquake of 26 January and 3 February 2014, respectively (Papadimitriou *et al.*, 2014). Combined with the observed spatial distribution, this suggests that each earthquake is associated with a different fault or fault segments of different dimensions, approximately parallel to each other and to the major Cephalonia-Lefkada Transform Fault Zone. Since there were no surface ruptures of the order of 15 cm - 25 cm in a length of several kilometers in Paliki, it is proposed that the activated faults are those presented in Fig. 5.35. It is reasonable to assume this fault segmentation or the existence of a significant asperity in the northern part was fortunate, as it did not permit the main rupture to break both southern and northern parts in a dynamic cascade. Such a scenario would have resulted in an even stronger mainshock (e.g. $M_w \approx 6.6$ for subsurface length L≈36km, according to the empirical relations of Wells & Coppersmith, 1994) that would certainly cause extensive damage and fatalities on the island.

The seismicity detected both offshore, SSE of Cephalonia, and within the Myrtos Gulf, does not seem to be directly associated with the main rupture but rather corresponds to activation of secondary neighboring small structures due to stress-transfer mainly caused by the two major earthquakes. It is worth noting that between the spatial group #5 (Myrtos Gulf) and the northern end of the main epicentral region, an area with very few located events is identified. This area could be the transition between different tectonic structures, likely the formation of a negative flower structure or a zone of extensional step-overs within Myrtos gulf, formed between the Cephalonia and Lefkada segments of the Cephalonia-Lefkada Transform Fault Zone (CLTFZ) such as the one proposed by Karakostas *et al.* (2015). Activity in the very same structure was also triggered after the M_w=6.4 earthquake that struck Lefkada island on 17 November 2015 (Section 5.5).

It should be noted that the seismic sequence was characterized by a long duration, while the temporal reduction of the number of aftershocks was very slow. Especially during the first weeks of the sequence, the frequency of aftershocks was very high, nearly one per minute, implying that a significant number of events could not been analyzed, as can be clearly observed from the high completeness magnitude at the beginning, which dropped gradually (Fig. 5.36). The slow decay was confirmed by the relatively low *p*-value (smaller than unity) of the Omori-Utsu law, especially at the first part of the sequence between the two major earthquakes, which however became more rapid during the second part.

The seismicity can be explained by simple stress-transfer mainly due to the two major events, with negligible aseismic forces, as its temporal evolution can be better predicted by two separate MOF models rather than a single or two individual ETAS models. Gospodinov *et al.* (2015) calculated day-specific MOF and (Restricted-) ETAS models for the 2014 Cephalonia aftershock sequence and measured even lower *p*-values during the first days (down to 0.514). They estimated which type of model best fits each part of the sequence and related it to the type of clustering, e.g. relating the MOF model to clustering in the vicinity of the mainshock and RETAS to more random clustering (more sub-clusters). They also detected a significant negative residual before the second large earthquake, but do not consider it as a sign of quiescence. In the present study, the simple application of MOF and ETAS models on the first part of the sequence did not indicate any such deficit of observed seismicity near the end of period (Fig. 5.39).

5.4 The 2014 Nafpaktos-Psathopyrgos swarm

The western Corinth Rift has been the primary study area of the present work, with Chapter 6 being dedicated to it, not only because of the interesting spatiotemporal patterns that its seismicity exhibits, but also owed to the availability of data from the local stations of the Corinth Rift Laboratory network (CRLN; e.g. Lyon-Caen *et al.*, 2004; Bernard *et al.*, 2004), reinforced by stations of the Hellenic Unified Seismological Network (HUSN). As such, methodologies aiming to increase the detectability of microseismicity, as those described in Chapter 4 as well as in the case study of Section 5.3, can be tested during seismic crises of particular interest.

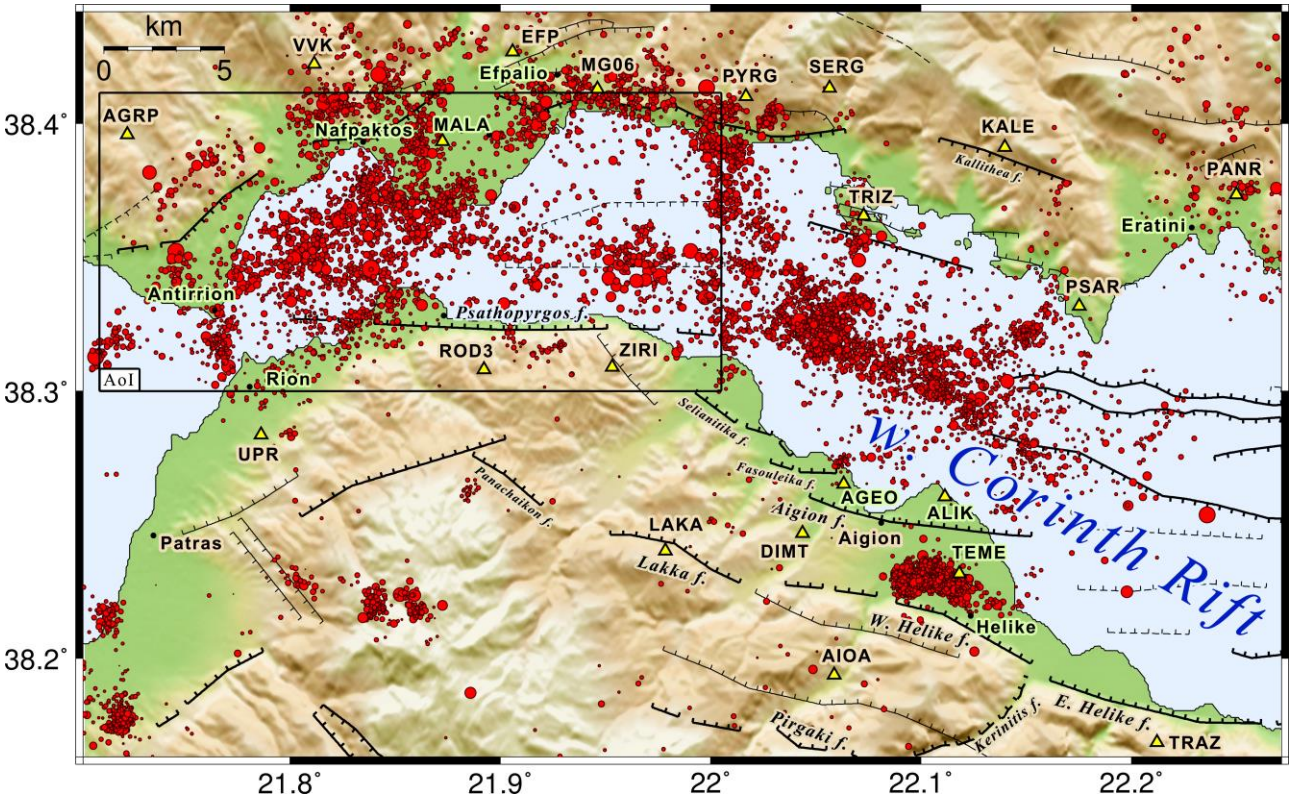

Figure 5.42: Relocated epicenters of seismicity in the western Corinth Rift during the period between September 2011 and October 2014. The rectangle marked "AoI" is the Area of Interest defined for this study (see Fig. 5.43). Thick/thin serrated lines represent major/minor normal faults while dashed lines correspond to inferred/uncertain faults. Fault lines are based on Doutsos & Poulimenos (1992), Armijo *et al.* (1996), Flotté *et al.* (2005), Bell *et al.* (2009), Valkaniotis (2009) and Pacchiani & Lyon-Caen (2010).

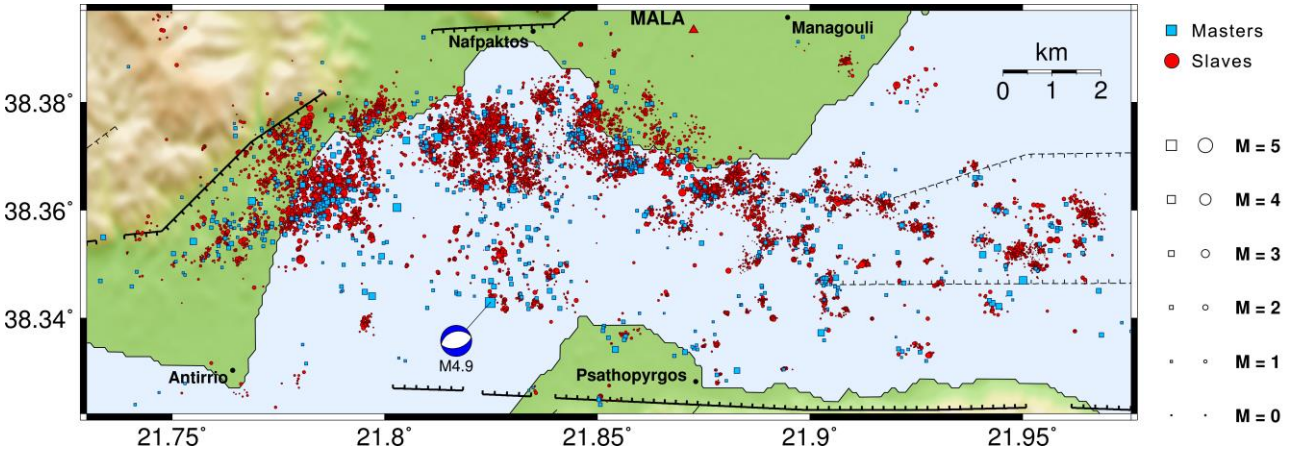

Figure 5.43: Relocated epicenters of master-events (squares) and slave-events (circles). The focal mechanism of the M_w=4.9 event of 21 September 2014 is also presented (φ = 254°, δ = 39°, λ = -91°).

An intense earthquake swarm took place between 15 July and 31 October 2014 at the offshore region between Nafpaktos and Psathopyrgos, near the western end of the Corinth Rift in Central Greece (Fig. 5.42, rectangle). The swarm covered a relatively large epicentral area, 20 km long in an approximate E-W direction and about 3 - 5 km wide. The HADAES methodological approach (Section 4.4) has been applied to this earthquake sequence and the detailed results are presented in this section. The technical aspect of this particular HADAES application is described in detail in the Appendix 5B.

5.4.1 Overview of the results

The map of the final catalogue is presented in Fig. 5.43, with both master- (squares) and slave-events (circles). The densest clusters are located at the western part of the distribution, while a large number of smaller clusters comprise the eastern part. The full catalogue was divided in 3 spatial groups (Fig. 5.44), using Ward's linkage (Ward, 1963) on the matrix of 3D inter-event distances. The distribution at depth is presented in the two series of roughly transverse cross-sections, Fig. 5.45 for the profile-boxes (a-i) of Fig. 5.44, and Fig. 5.47 for the respective boxes (j-r) of Fig. 5.46.

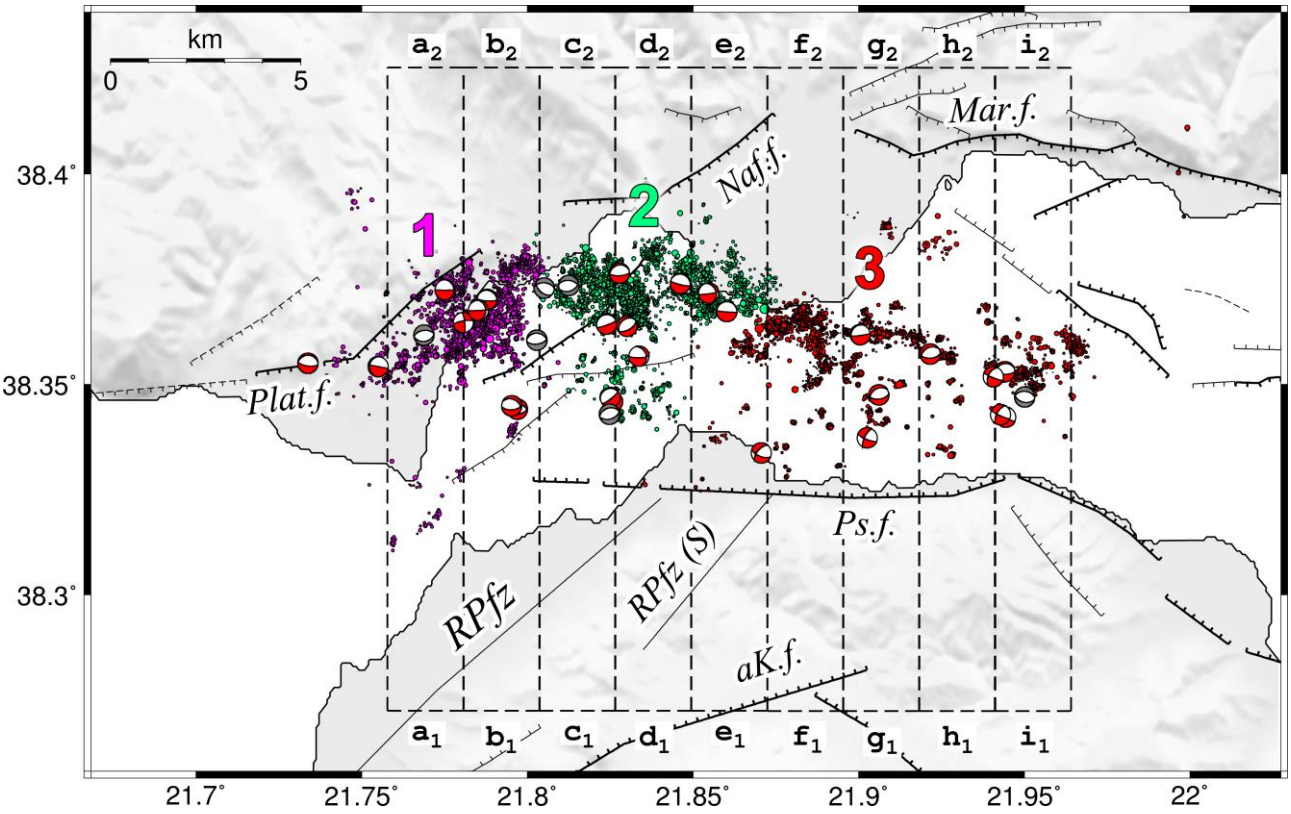

Figure 5.44: Seismotectonic map of relocated slaves. Focal mechanisms of the largest events are derived either by moment tensor inversion (grey; source: NKUA, NOA) and first motion polarities (red; this study). The successive, parallel boxes, oriented in a S-N direction correspond to the cross-sections (a-i) of Fig. 5.45. The colours of the epicenters represent the 3 spatial clusters. (Plat.f.: Platanitis fault, Naf.f.: Nafpaktos f., Mar.f.: Marathias f., RPfz: Rion-Patras fault zone, aK.f.: Ano Kastritsi f., Ps.f.: Psathopyrgos fault).

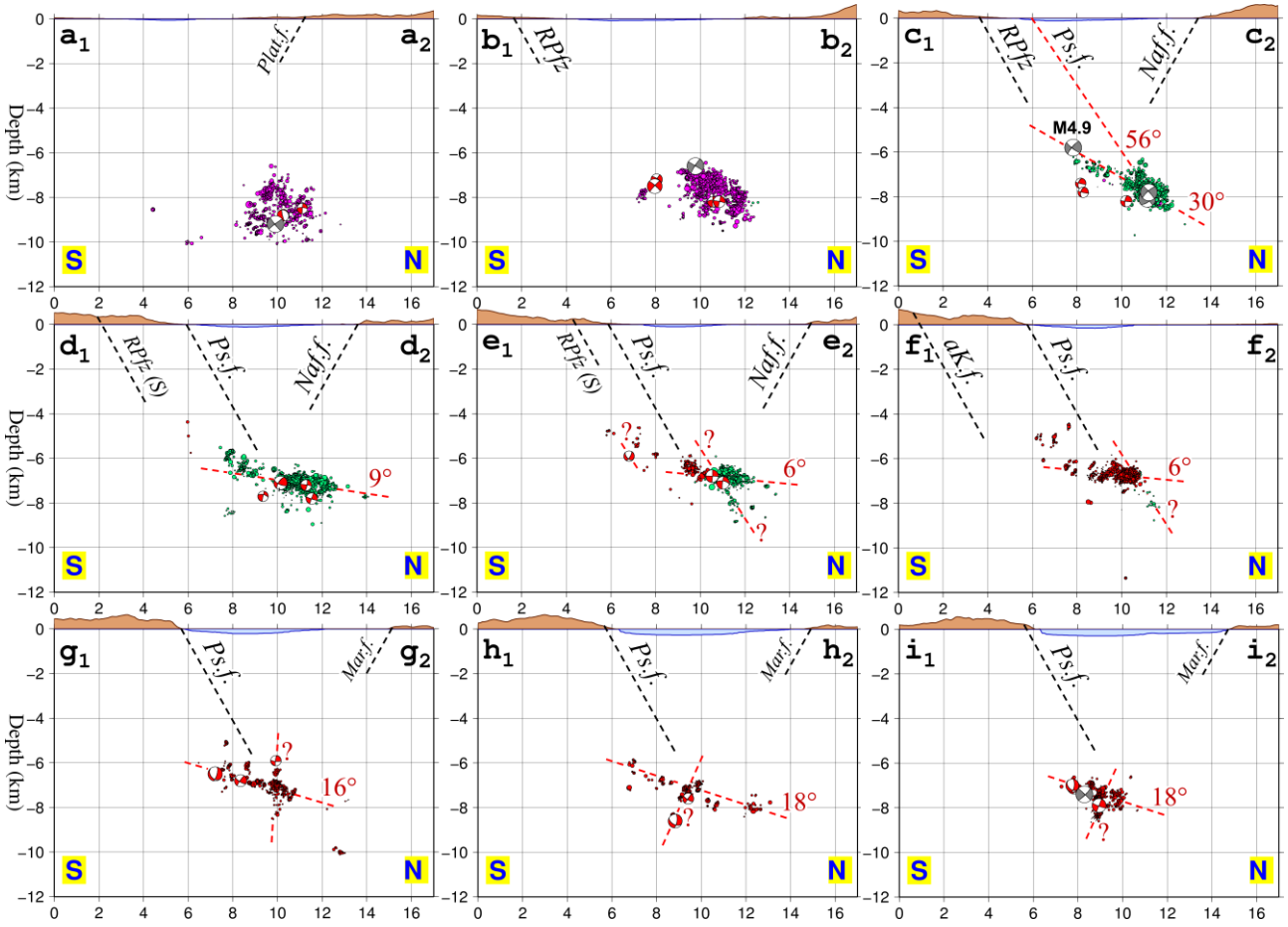

Figure 5.45: Cross-sections (a-i) drawn in S-N direction with width ± 1km, corresponding to the profile boxes of Fig. 5.44. Black dashed lines are used for reference to the known, mapped faults, drawn at a typical dip of 60°. Red dashed lines are inferred structures identified from the relocated seismicity and focal mechanisms along with their apparent dip in degrees.

The hypocenters are mainly distributed on a north-dipping surface, with groups #2 and #3 apparently belonging to about the same plane while the western Group #1 is slightly rotated, dipping ~NNW. The plane of Group #3 is also tilted, deepening towards the west. The focal depths range mainly between 6 and 8 km for Group #3, consistent with previous observations in the western Corinth Rift (Rigo *et al.* 1996; Lambotte *et al.* 2014), while groups #1 and #2 seems to reach down to 9 km, with the southern portion of Group #2 being more dispersed and shallow.

From west to east in Fig. 5.45, Group #1, appears thick due to the cross-sections a_1-a_2 and b_1-b_2 not being perpendicular. In c_1-c_2, seismicity of Group #2 is distributed in a plane, dipping ~30°N. At this point, the extension of this inferred structure towards the surface does not correspond to any mapped fault. However, the down-dip extension of Psathopyrgos fault at 60° roughly matches the hypocenter and focal mechanism of one of the major events of the sequence. In d_1-d_2, the low-angle weak layer, known to exist in the western Corinth Rift (Chapter 6), begins to appear at a ~9°N dip, consistent with some focal mechanisms derived by FMP. This pattern persists in cross-sections e-f

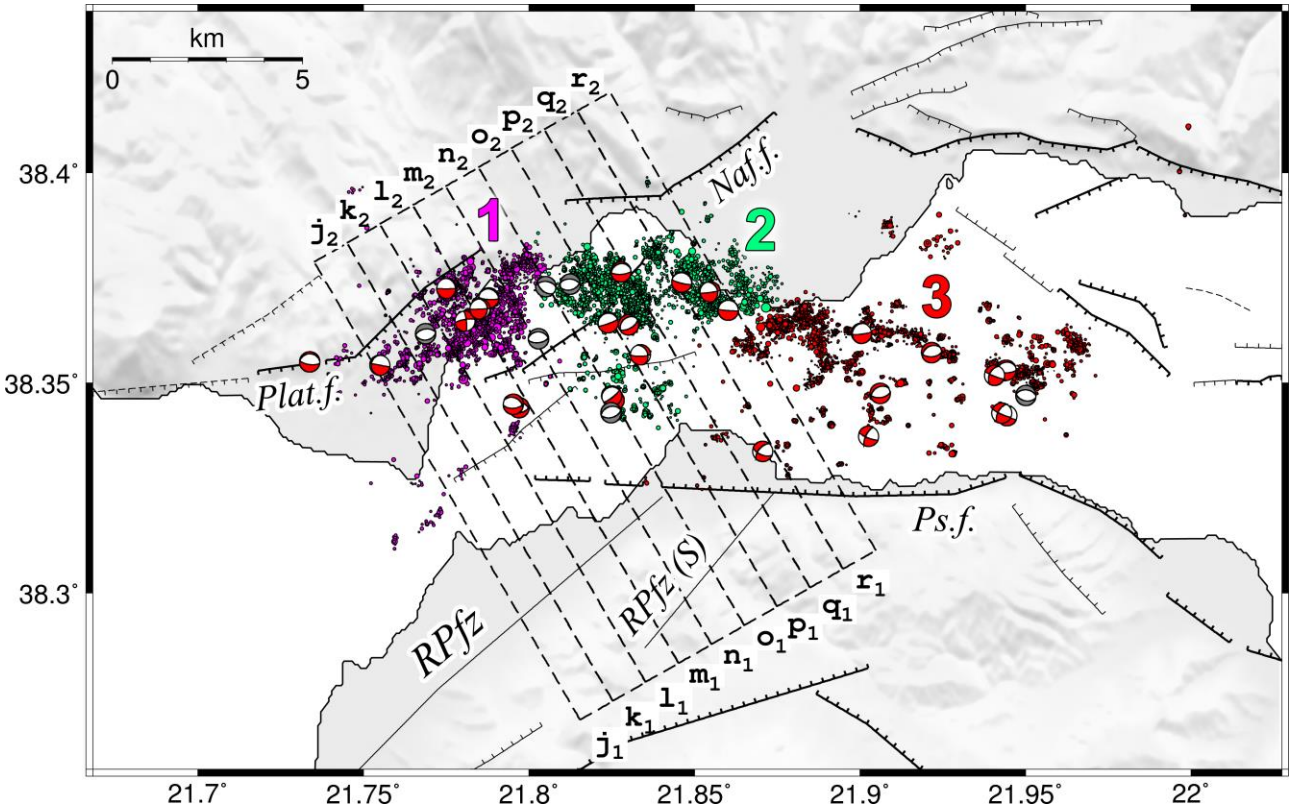

Figure 5.46: Same as Fig. 5.44, but for the set of profile lines j-r, oriented in a SSE-NNW direction, for the cross-sections of Fig. 5.47.

at a slightly lower angle, with a hint for seismicity below the weak layer roughly corresponding to Psathopyrgos fault, while some oblique focal mechanisms further south might be related to the right-lateral Rion-Patras fault zone. In cross-sections g-i there are indications for some small antithetic, steep south-dipping structures cross-cutting the weak layer, which seems to be dipping at 16-18°N. The other set of thin SSE-NNE cross-sections (j-r) of Fig. 5.47 are almost perpendicular to the Rion-Patras fault zone (RPfz), which is a right-lateral, oblique-normal NNW-dipping structure. Group #3 is presenting a diffuse distribution, due to the tilt. In m_1-m_2 there are indications for a low-angle (15°) NNW-dipping feature at ~7km depth and a slightly deeper and steeper one further NNW. The latter is clearer in n_1-n_2, dipping at 50°NNW, with its up-dip extension matching RPfz. The sub-parallel structure "RPfz (S)" could also match the SSE part of the hypocentral distribution at o_1-o_2. The apparent dip of the activated structure in cross-sections o-p is at 25°. The low-angle weak layer of the rift appears at cross-sections q-r, the eastern half of Group #2.

Concerning the frequency-magnitude distribution, the Gutenberg-Richter law diagrams for the catalogues of master-events and the full catalogue are presented in Fig. 5.48a. The *b*-value is similar in both datasets, 0.89 and 0.97, respectively, with the former being lower probably because of a portion of missing weak events even above the estimated magnitude of completeness (Yang *et al.* 2009). However, following the HADAES method, the catalogue is now more complete, with the magnitude of completeness, M_c, dropping from 1.4, for the master-events in the initial catalogue, to

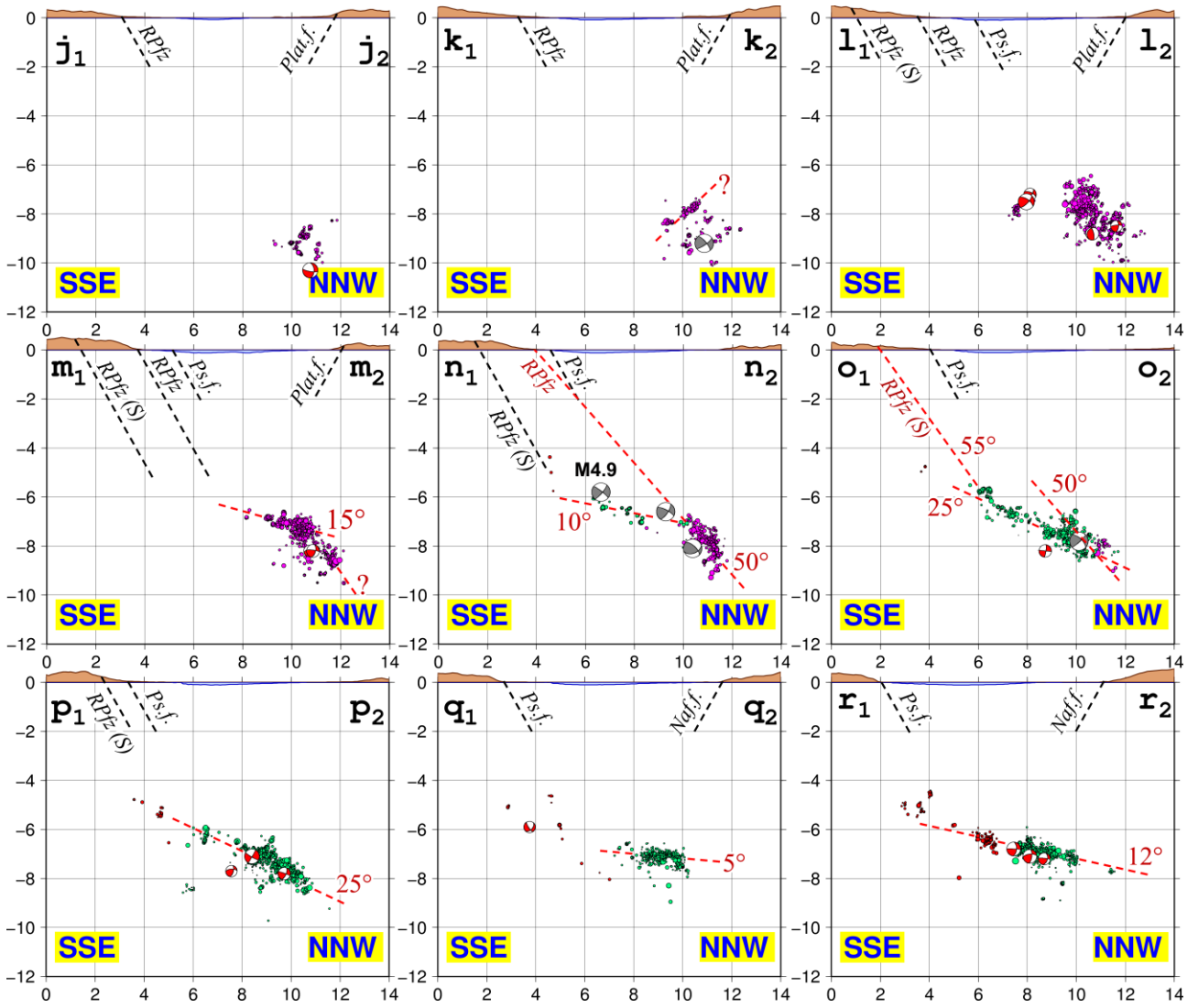

Figure 5.47: Cross-sections (j-r) drawn in N330°E direction with width ± 0.5km, corresponding to the profile boxes of Fig. 5.46. Black dashed lines are used for reference to the known, mapped faults, drawn at a typical dip of 60°. Red dashed lines are inferred structures identified from the relocated seismicity and focal mechanisms along with their apparent dip in degrees.

a minimum of 0.5 in the final results, although it can be disputed that this is a bit underestimated. The *b*-value has also been calculated for each spatial group separately (Table 5.4) and, surprisingly, is very close to 0.97 in all of them.

Interestingly, a similar improvement is observed in the fractal geometry of the spatial distribution. Fig. 5.48b presents the correlation integral, $C(r)$, as defined by Grassberger & Procaccia (1983):

$$C(r) = \frac{2}{N(N-1)} \sum_{i,j=1}^{N} H\left[r - \left|\vec{x}_i - \vec{x}_j\right|\right] \quad , \quad i \neq j \tag{5.2}$$

Table 5.4: Numbers of events per spatial group, master- and slave-events along with calculated b-values of the Gutenberg-Richter law and correlation dimension, D_2, of spatial (2D) and temporal (1D) distributions. The additional master-events used at the secondary reference station, AGRP, are also included in the corresponding numbers.

Description	Group	Events	Masters	Slaves	*b*	$D_{2,\text{spatial}}$	$D_{2,\text{temporal}}$
western	1	3119	270	2849	0.98 ± 0.02	1.52 ± 0.03	0.91 ± 0.03
central	2	4725	311	4414	0.95 ± 0.02	1.59 ± 0.02	0.87 ± 0.02
eastern	3	4250	242	4008	0.96 ± 0.02	1.38 ± 0.03	0.89 ± 0.02
masters	-	823	823	-	0.89 ± 0.02	1.52 ± 0.03	0.88 ± 0.01
all	-	12094	823	11271	0.97 ± 0.01	1.50 ± 0.03	0.93 ± 0.02

where N is the total number of events in a dataset, corresponds to the inter-event distance between the pair of events i and j, r is the scaling parameter and $H(x)$ is the Heaviside function:

$$H(x)=\begin{cases}0 & ,x<0\\ 1 & ,x>0\end{cases} \tag{5.3}$$

For distributions which are characterized by fractal geometry, hence self-similarity or, rather, scale invariance in a statistical sense, the following relation is true:

$$\log_{10}\big(C(r)\big)=D_2\cdot\log_{10}(r) \tag{5.4}$$

where D_2 is the correlation dimension. The exponential law is valid for a range of scales $r\in[r_{\min}, r_{\max}]$. The plots in Fig. 5.48b are without the normalization factor $\frac{2}{N(N-1)}$, in order for the diagram corresponding to the full catalogue to be more separated from the other two, for better visualization and to reflect the difference in the number of events between the two catalogues. The shape of the plots in Fig. 5.48b does not change if the normalized correlation integrals are used instead, however they are vertically offset and become overlapping, which makes it harder to distinguish differences. The correlation dimension, D_2, is calculated from the slope of the linear part of the log-log graph of the correlation integral $C(r)$ with respect to the scaling parameter, r. In Fig. 5.48b, the initially located master-events (squares) have a D_2 value of 1.87, which is very close to the embedding dimension 2. This implies for a spatial distribution that is almost homogeneously distributed on a 2D surface. The maximum scale, $r_{\max}$ is about 3.6 km and the exponential law remains true down to the smallest scale. The correlation integral of the relocated master-events (circles) has a lower slope which corresponds to $D_2 = 1.52$. This signifies that the relative relocation has caused hypocenters of groups of strongly correlated earthquakes to become more clustered in space, with the scaling law, however, breaking at $r_{\min} \approx 38$ m. The fractal power-law is very similar to the one of the relocated master-events, with a slightly lower dimension $D_2 = 1.50$. However, the increase in the density of clustered micro-earthquakes which have been resolved, has caused the

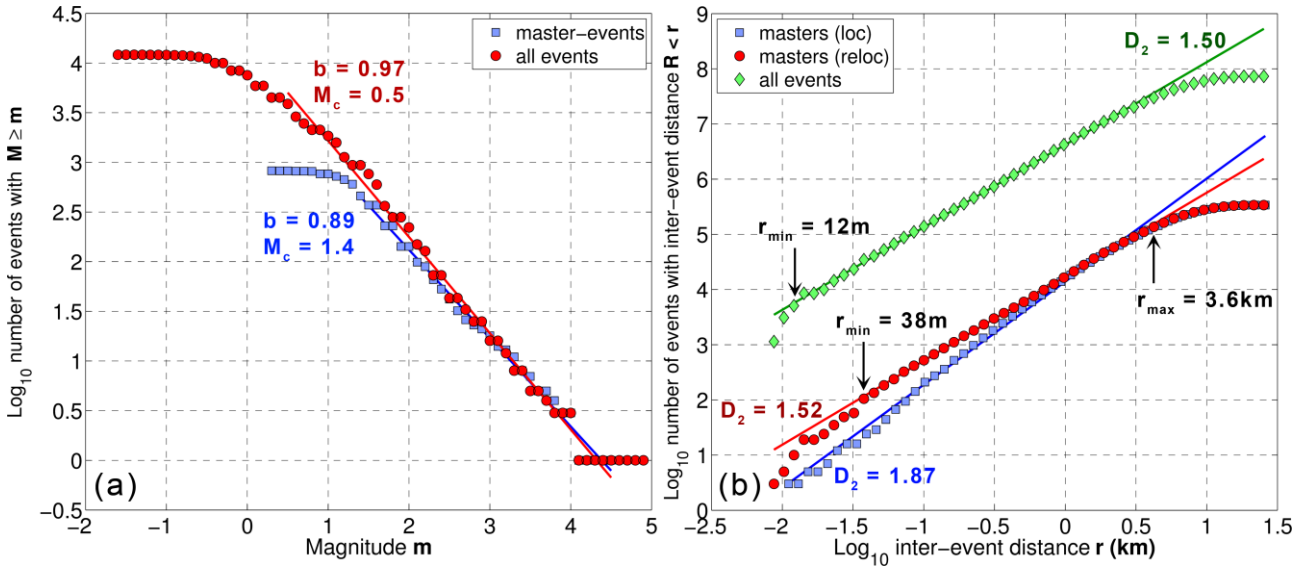

Figure 5.48: (a) Gutenberg-Richter law for the master-events (squares) and the full catalogue containing both master- and slave-events (circles) along with the best-fit line on the linear segment of their distribution and with emphasis on the decrease of the magnitude of completeness, M_c, in the full catalogue dataset, (b) correlation integral (without normalization) calculated for the epicenters (2D inter-event distances) of the initially located master-events (squares), their relocated epicenters (circles) and the full catalogue of relocated master- and slave-events (diamonds) with emphasis on the decrease of the lower scale, r_{min}, for which the fractal law remains true in the full catalogue dataset. D_2 values denote the fractal correlation dimensions.

scaling law to be true at even lower distances, down to r_{min} = 12 m. The D_2 values have also been calculated for each spatial group separately (Table 5.4). The western Group #1 has similar fractal characteristics to those which describe the whole distribution, with D_2 = 1.52, the central group #2 is slightly closer to being homogeneously distributed on a 2D surface while the scaling law for the eastern Group #3, with D_2 = 1.38, is between the 2D Cantor dust set (capacity dimension D_0 = log(4)/log(3) ≅ 1.26) and the box fractal (D_0 = log(5)/log(3) ≅ 1.46), reflecting the stronger nucleation in separated sub-clusters which is also visually confirmed (e.g. Fig. 5.44). Similar conclusions, concerning the range of scales for which the fractal law holds true, are drawn for a 3D embedding dimension (hypocentral inter-event distances).

The temporal aspect of the catalogue is also largely enriched, with the resolved slave-events being over 13 times more numerous than the master-events, surpassing the gross estimates of Kapetanidis & Papadimitriou (2011). Fig. 5.49a shows a histogram of the daily occurrence of events, with the bars corresponding to slave events being stacked over the master events. At this scale, the master-events are mostly visible during the outburst of 21 September 2014, following the major M_w = 4.9 and a couple of M = 4.0 events. The same can be observed in the log diagram of cumulative number of events (Fig. 5.49b), where the number of master-events appears to be negligible. On the other hand, the contribution of slave-events to the cumulative magnitude (Fig. 5.49c) is important only for short periods before major events which are already included in the ME catalogue. The M_w = 4.9

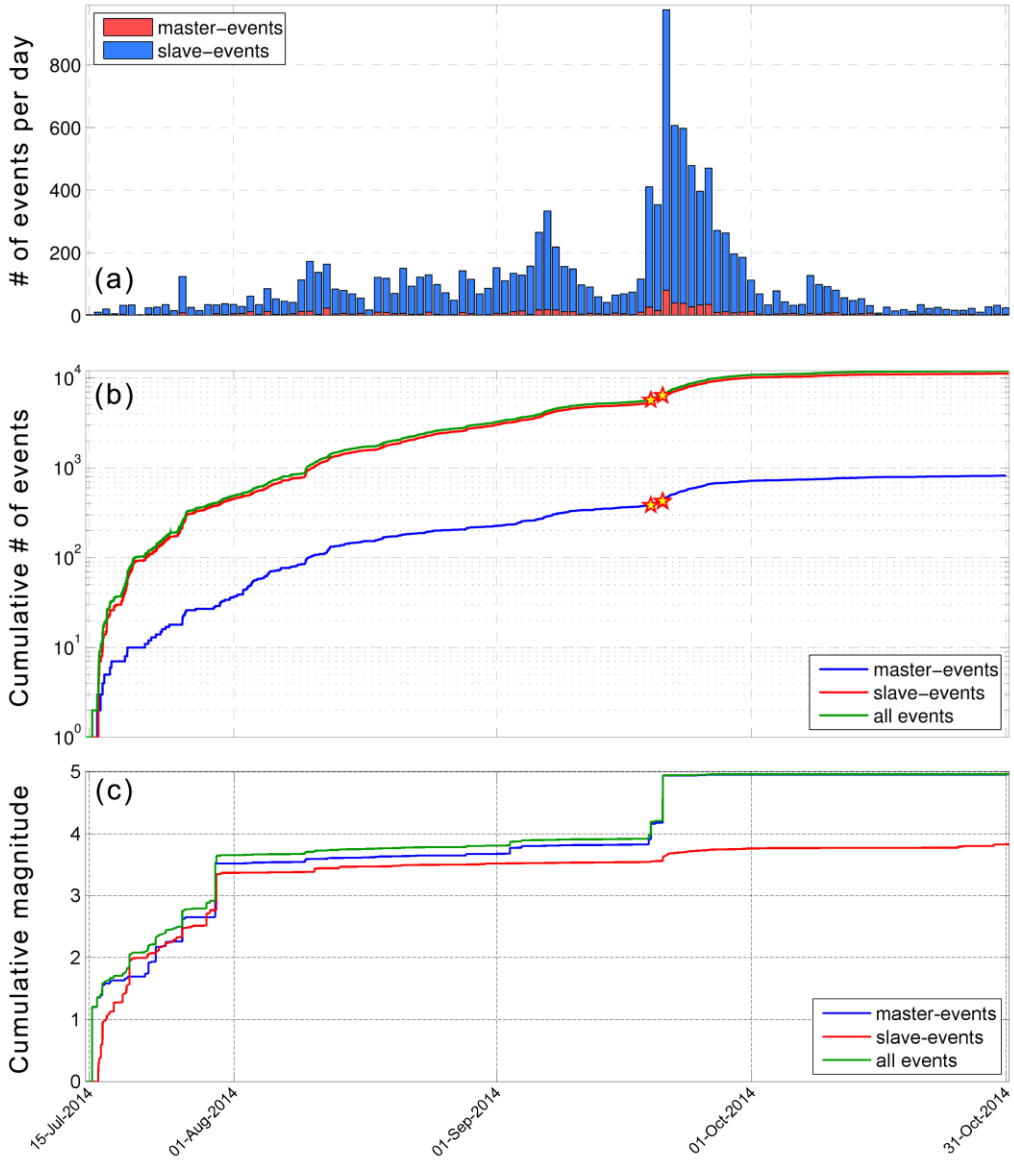

Figure 5.49: (a) Stacked histogram of number of master and slave events per day, (b) cumulative number of events with stars marking earthquakes with $M \geq 4.0$, (c) cumulative magnitude.

event of 21 September 2014 overwhelms the plot, with the cumulative magnitude of the total catalogue being practically equal to the magnitude of this major event. The cumulative magnitude of the slave-events is around $M = 3.9$, mostly attributed to a few events with $2.8 \leq M \leq 3.3$ that were missing from the routine locations.

5.4.2 Spatio-temporal analysis

The spatiotemporal evolution of the 2014 swarm in W. Corinth is presented in the sequential maps of Fig. 5.50. The swarm began offshore Nafpaktos in late July 2014 and the activity started spreading bilaterally in a WNW-ESE direction. This pattern persisted gradually up to mid-

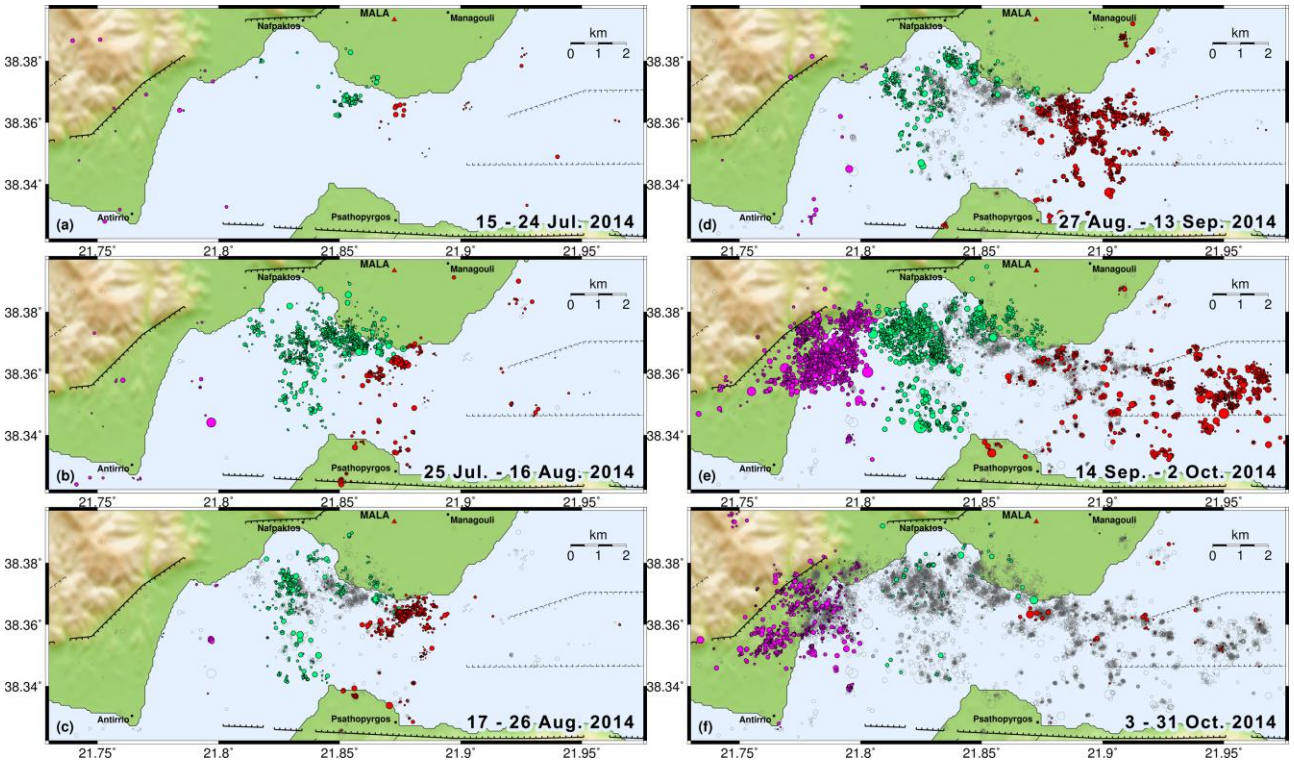

Figure 5.50: Maps of spatiotemporal distribution for the periods a-f. Colours represent the 3 spatial groups. Hollow circles represent epicenters of previous periods for spatial reference.

September 2014, when two major events with $M_w \geq 4.0$ struck at the western part on 21 September 2014. This activated Group #1 but it also triggered seismicity towards the east. The bilateral migration of seismicity is presented in the spatiotemporal diagram of Fig. 5.51. The strongest events in the central Group #2 occurred concurrently with the activation of the western group on 21 September 2014. The easternmost part of Group #3 was activated a short while afterwards, but microseismicity in that region was also detected by the automatic procedure before its final outburst. Another interesting characteristic is the spatial gap between groups #2 and #3 during periods c, d and half of period e.

The initial radial expansion of seismicity during periods a and b is compatible with the propagation of a triggering front of pressurized fluids, $r(t)$, according to the model of Shapiro *et al.* (1997) (Section 1.3.3). A parabolic envelope corresponding to $D = 0.15$ m^2/s can be fitted to the denser part of the spatiotemporal distribution, closer to the starting injection point, or $D = 0.4$ m^2/s for a broader envelope which is compatible with the first ~50 days of activity, up to the middle of period d, when the expansion of group #3 towards the east is accelerated shortly after an $M_w = 3.4$ event on 3 September 2014. Migration rates begin at 100 m/day, increase to 200 m/day in periods d and e for Group #3 while the corresponding rate for Group #2 slows down to 30-50 m/day. The occurrence of the $M_w = 4.9$ event on 21 September triggered a new episode of rapid migration, radiating outwards from the epicenter of an $M_w = 4.0$ event that followed on the same day, near the edges between Groups #1 and #2. This was preceded, two days earlier by increased clustered activity in the same

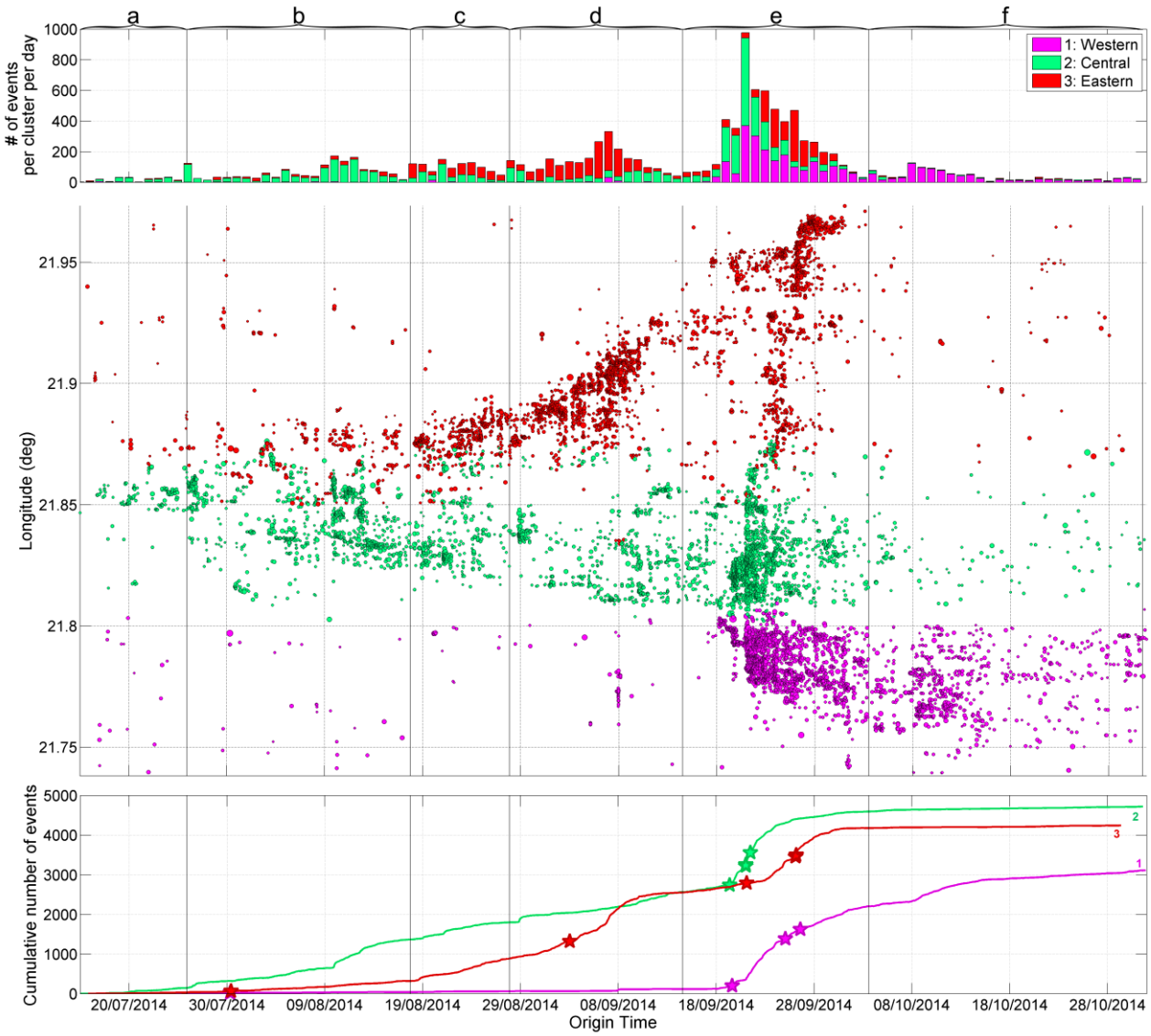

Figure 5.51: (top) stacked histograms of daily occurrence of events per spatial cluster, (middle) spatiotemporal diagram of latitude with respect to origin time and (bottom) cumulative number of events per spatial cluster with stars depicting events with magnitude $M \geq 3.2$. Colours represent the 3 spatial clusters and thick vertical lines separate the 6 temporal periods a-f, as labeled at the top.

region, following two events with magnitudes M_w = 3.5 and M_w = 4.0 on 19 September 2014. The seismic front expanded with a rate of ~1.2 km/day, but in the form of bursts after the occurrence of major events, while the initial migration of seismicity during the first periods was more gradual. The last activity at the easternmost part of Group #3 was triggered by a series of events with $M_w \geq$ 3.3 on 26 September 2014. In the final period, f, the seismicity was mainly focused at the westernmost part of Group #1. It is noteworthy that a small cluster of events with deeper foci ($H \cong$ 16 km) and epicenters at the south-western part of the area of study occurred between 7 and 8 September 2014, a few days before the major outbreak of 19-23 September 2014.

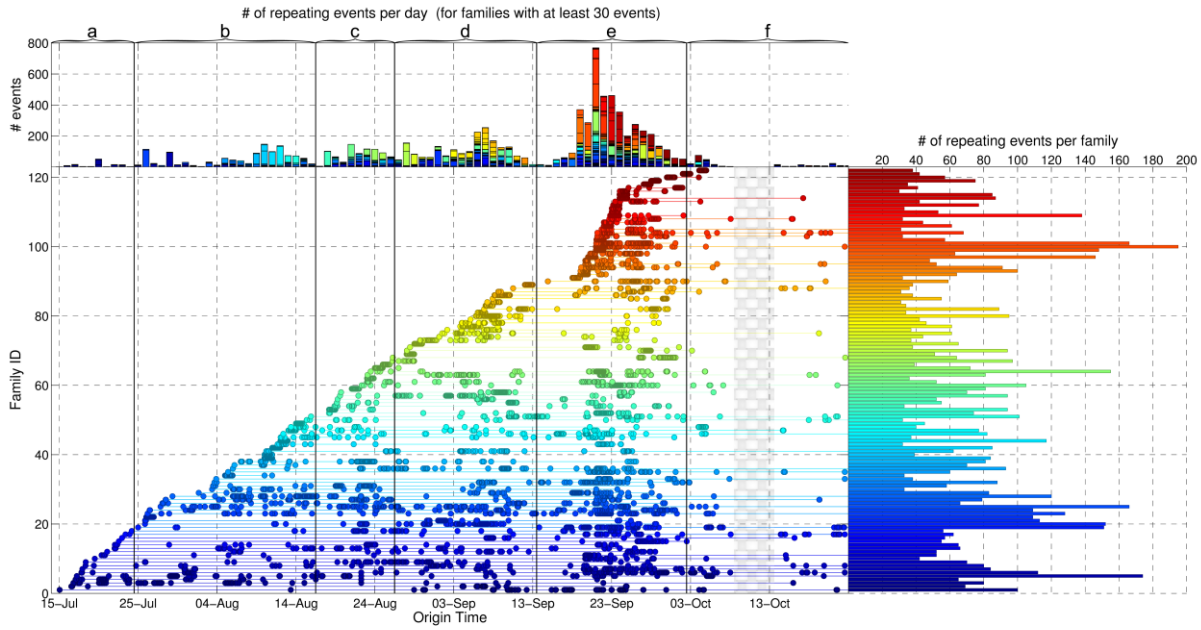

Figure 5.52: Family history dendrogram of the seismic swarm for families with at least 30 events formed with the reference station EFP. (Main panel) The circles represent repeating earthquakes linked by horizontal lines to indicate that they belong to the same family. The vertical axis shows the Family ID, sorted by the origin time of the first event of each family. Families with lower ID were initiated earlier than others with higher ID. The horizontal axis represents origin time. (Right panel) family size, indicating the number of events contained in each family. The vertical axis is shared with the history dendrogram. (Top panel) histogram of the total number of repeating events occurring per day. The horizontal axis is shared with the family history dendrogram. Letters on top denote the 6 consecutive periods a-f, divided by vertical black lines. The checkerboard pattern in October marks a data gap in the reference station.

The generation and temporal history of earthquake families is presented in Fig. 5.52. The bilateral migration of seismicity during periods a-d (Fig. 5.51) is also reflected at an almost constant generation rate of 2 large families (with over 30 events) per day, as the seismicity spreads into new territories. A significant decrease of this rate is observed between 10 and 17 September 2014, followed by the generation of new multiplets on 18 September, when the first signs of activity in the western Group #1 appear, culminating on 21 September. It is noteworthy that the large outburst of activity in Group #1 is complemented by re-activation of older families, with some exceptions in those with IDs 63 - 84, which were generated in period d (mostly belonging to the middle Group #3), and those with IDs around 40 (mostly in Group #2), generated in the second half of period b. Some of the families with IDs 63 - 84 were re-activated a bit later, after 23 September, which is also evident from the re-appearance of events of Group #3 in the spatiotemporal diagram at the easternmost portion between 25 and 30 September, when the generation rate drops to a very low rate at about ~0.7 new families per day. Note that the family dendrogram of Fig. 5.52 represents only the major families generated by the analysis of waveforms in the reference station EFP. The checkerboard pattern in the main panel between 8 and 14 October marks a data gap that has been filled with additional analysis on the continuous records of station AGRP for the final catalogue and the spatiotemporal distribution of Fig. 5.51, where it coincides with a small increase in the activity of the western group #1. Smaller multiplets/doublets present roughly similar characteristics, an

almost constant generation rate up to 21 September, followed by a sudden, but short-lived increase, with a few extra outbursts on 4, 13 and 15 September which were not observed in the larger families.

5.4.3 ETAS modeling

The 2014 Nafpaktos-Psathopyrgos sequence bears the typical characteristics of an earthquake swarm, such as the non-existence of a single major event at the beginning, large dimensions compared to the cumulative seismic moment and very distinct spatiotemporal migration patterns. The latter is usually linked to aseismic factors such as the diffusion of pressurized fluids or creeping. ETAS modeling was attempted to examine whether or not the sequence can be explained as a stationary residual point process. Fig. 5.53 shows the best fit ETAS model for the whole sequence. The magnitude threshold M_{th}=0.8 was selected after several tests in the acceptable M_c range and different T_o and T_{end} values to achieve an adequate fit. There are significant deviations from the model, especially in the second part of the sequence, following the major M_w=4.9 event of 21 September 2014. The *a*-value (~1.22) is relatively large for a swarm and within the lower bounds defined by Ogata (1992) for other types of sequences. The T_o=14d was selected so that the range for the determination of parameters by MLE begins right before a couple of major (M_w>3.0) events that occurred on 30 July 2014. These did not produce any notable burst of seismicity rate, hence the negative residuals, which become even lower after day 30 (~14 August) and increase near zero after 6 September 2014. The data began surpassing the values predicted by the model after the M_w=4.1 event of 19 September and even more so after the major M_w=4.9 earthquake of 21 September. The latter did not cause a single-step deviation but rather a gradual one over a period of ~4 days. A step-down occurred on 26 September, following an M_w>3.0 event that did not produce any significant sub-sequence, then began to decrease during October 2014.

Change-point analysis showed that the minimum combined AIC value is obtained if the sequence is split at ~65 days, shortly before the M_w=4.1 event of 19 September. Fig. 5.54 shows the ETAS model for the first part, using the same threshold M_{th}=0.8. The model has a good fit with the data but the a-value is very large (3.27) and the *p*-value is very low (0.48). There are no signs of decay in the seismicity rate, but rather a pattern of constant to increasing seismicity rate.

The ETAS model estimated for the second part (Fig. 5.55) is still not fitting properly, with significant and persistently positive residual. This shape does not change much if higher thresholds are selected. The *a*-value is lower than the one of the first part but still high for a swarm-type sequence, while the *p*-value is higher (1.23) but within a normal range, which is expected because of the decay observed in the cumulative number of events curve. It is also noteworthy that the μ-value for both models of the whole sequence and the first part is relatively high (4-6 events/day), while for the second part it is practically zero.

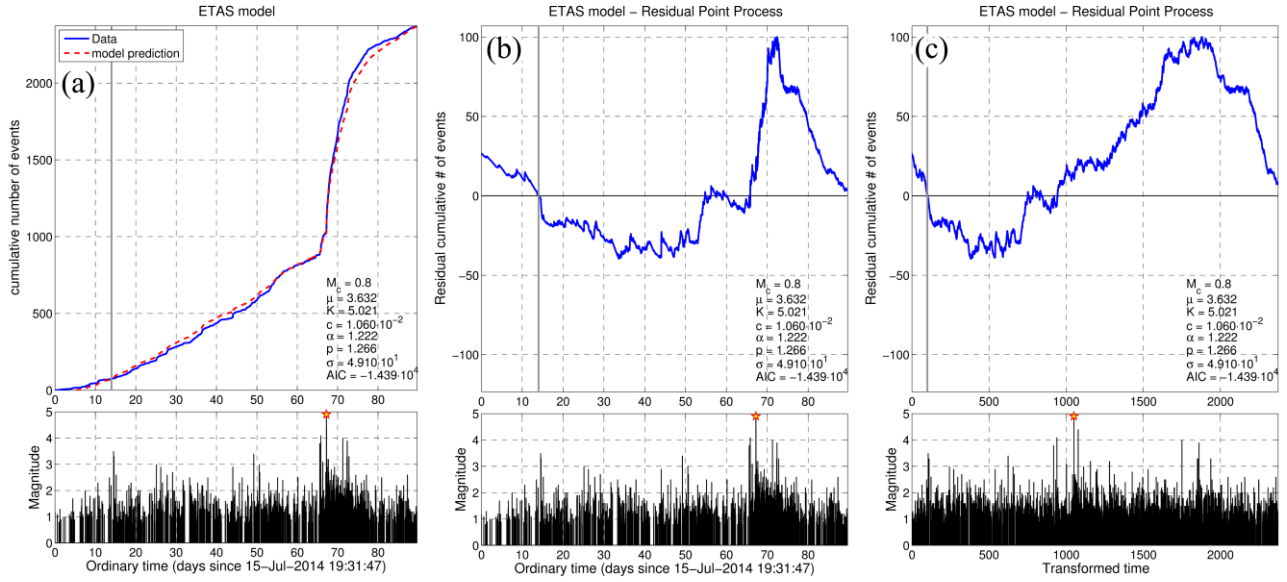

Figure 5.53: ETAS model for the 2014 Nafpaktos-Psathopyrgos swarm (15 July– 13 October), using a threshold M_{th}=0.8 and M_r=4.9 (major event of 21 September 2014, depicted by a star), with the model parameters estimated by MLE ignoring the first T_o=14 days, a) data and ETAS model curves in ordinary time, b) residuals between data and model in ordinary time, c) residuals between data and model in transformed time.

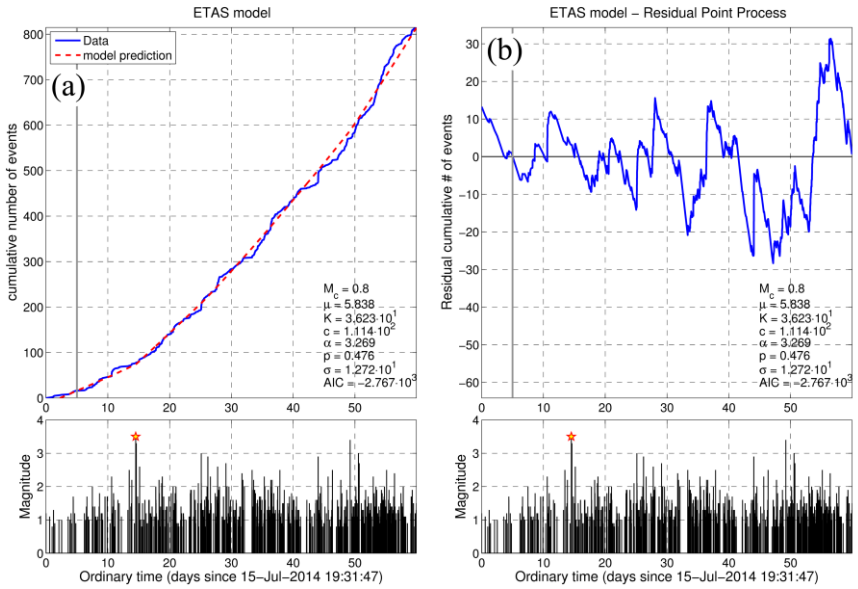

Figure 5.54: ETAS model for the first part of the 2014 Nafpaktos-Psathopyrgos swarm (15 July– 13 September), using a threshold M_{th}=0.8 and M_r=3.5, with the model parameters estimated by MLE ignoring the first T_o=5 days, a) data and ETAS model curves in ordinary time, b) residuals between data and model in ordinary time.

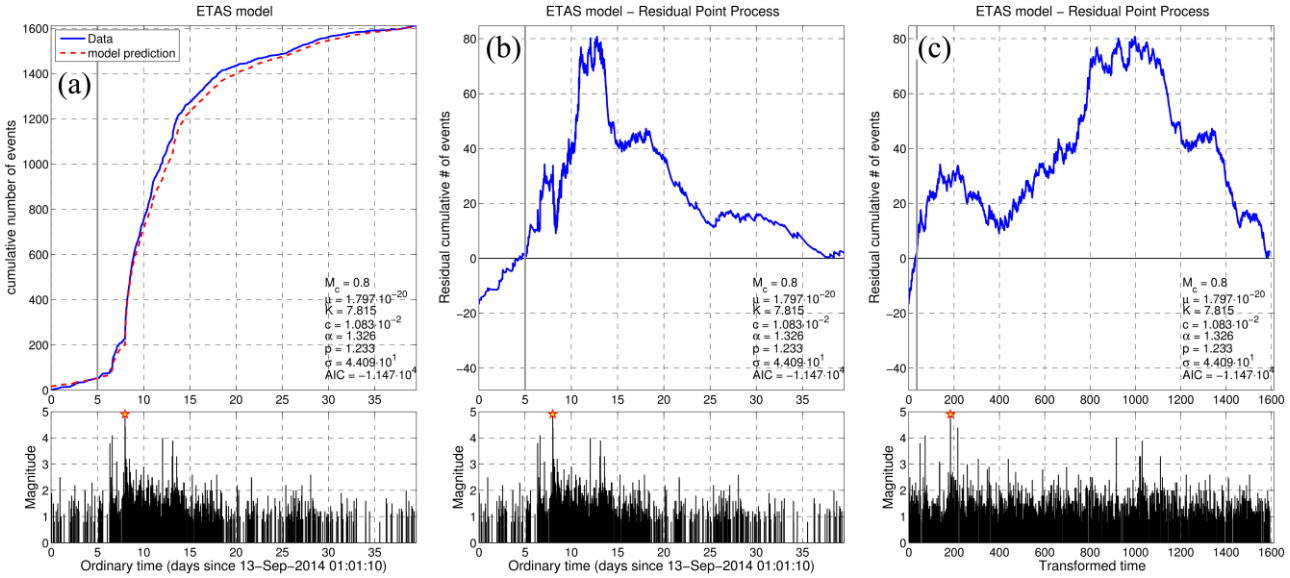

Figure 5.55: ETAS model for the second part of the 2014 Nafpaktos-Psathopyrgos swarm (13 September – 23 October), using a threshold M_{th}=0.8 and M_r=4.9, with the model parameters estimated by MLE ignoring the first T_o=5 days, a) data and ETAS model curves in ordinary time, b) residuals between data and model in ordinary time, c) residuals between data and model in transformed time.

The inability for a proper fit indicates non-stationarity in the parameters of the ETAS model, which is expected because of the observed migration patterns. However, in contrast to other cases (e.g. Sections 5.4 and 5.6) where fluids had significant influence on the migration but not into triggering subsequences themselves, as the latter were controlled by stress-transfer caused by previous earthquakes, in the 2014 Nafpaktos-Psathopyrgos swarm they appear to have a more important role. The degree of non-stationarity can be approximated by calculating ETAS model parameters for sliding windows over the sequence, with the time-dependent μ-value reflecting a "forcing rate" (e.g. Hainzl & Ogata, 2005). Fig. 5.56 shows the temporal variation of μ for consecutive windows of 5 days. Several bursts of increased μ-value can be observed, with the strongest on 19-24 August and 23-28 September, 2014. These are roughly consistent with periods during which strong migration patterns were observed. Measurements of low μ-value such as on 3-13 September and 28 September – 13 October could possibly be related to periods of "random" seismicity or, rather, controlled by seismic stress-transfer. However, during the former (second half of period d), significant spatiotemporal migration takes places towards the east (Group #3). This could indicate a similar condition as in the 2nd and 3rd phases of the hydrofracture model (Section 1.3.3; Fig. 1.17), during which there is no active fluids injection but there is still strong (likely unilateral) migration due to stress imbalance around the volume that has been infiltrated by pressurized fluids. It should be noted that the models are relatively stationary during 3-13 September, with low *a*-values, indicative of swarm-type behavior, and *p*-values that remain at a normal / slightly elevated range (1.0-1.5) until the end of September. This suggests that this part of the sequence is mostly controlled by

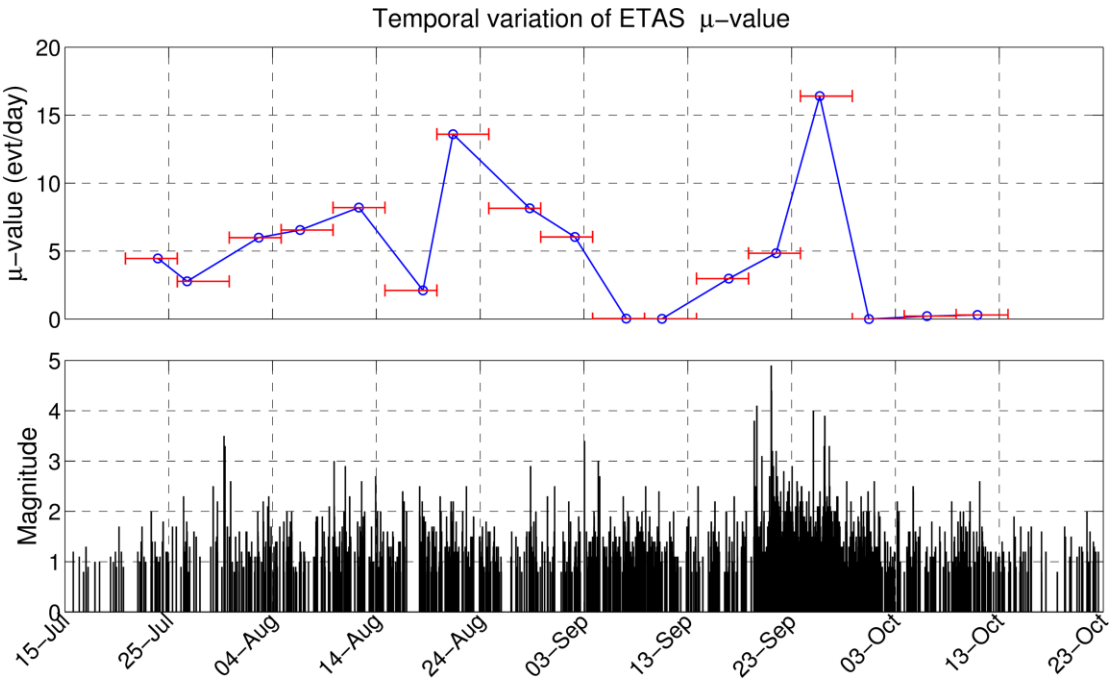

Figure 5.56: (Top) Temporal variation of the μ-value of the ETAS model determined by MLE over successive windows of 5 days, with ranges depicted by red horizontal bars and circles representing median origin time of the events, (bottom) time-series of earthquake magnitudes.

earthquake-induced stress-transfer, with fluids diffusion playing a secondary role, while the expansion is almost linear, at the almost constant and relatively high migration rate of ~250m/day towards the east, instead of parabolic, as expected for the triggering front of Eq. 1.16 (Shapiro *et al.*, 1997).

5.4.4 Discussion - Conclusions

The seismic swarm of 2014 in the western Corinth Rift provided an opportunity for the development and application of the HADAES method (Section 4.4), an algorithm that exploits single-station detection and waveform similarity to increase the number of available data tenfold. During the study period between 15 July and 31 October 2014, about 830 events were available by routine analysis in the offshore region between Nafpaktos and Psathopyrgos. The expansion of the database with the HADAES method to about 12000 events mainly enriched the spatiotemporal distribution with clusters of many tens to hundreds of earthquakes where only a few were previously detected and located. It also revealed the existence of several "precursory" clusters in areas which were strongly activated later in the sequence. The spatiotemporal distribution is described by complex migration patterns radiating outwards, bilaterally, or back-propagating at several phases of the swarm, at relatively large migration rates for the standards of the western Corinth Rift (e.g. Section 5A.4, Chapter 6), but also elsewhere in Greece (e.g. Section 5A.2).

Examination of the spatial distribution using thin vertical cross-sections showed that the mid-eastern part of the seismicity is related to the weak, north-dipping seismogenic layer known to exist

beneath the western Corinth Rift (Chapter 6). Some sub-clusters could be related to the down-dip extension of Psathopyrgos fault. The western part of the swarm was mainly triggered during the second phase, following an M_w=4.9 event on 21 September 2014. While its association with known structures is not very clear, its eastern part is compatible with the RPfz, dipping at ~55° NNW. The resolved focal mechanisms are mainly normal but also include some right-lateral strike-slip ones that could be related to the RPfz or other related sub-parallel buried structures. Low-angle focal mechanisms which are consistent with the geometry of the weak layer were also determined. As is further discussed in Chapter 6, very low-angle focal mechanisms are rarely observed under the western Corinth Rift. That is because such events are generally not expected to occur without the aid of bursts of fluids or due to the deformation process itself, as the maximum principal stress component is sub-vertical, which increases friction on sub-horizontal fault planes, requiring high pore-pressures to initiate slip (Bourouis & Cornet, 2009).

Despite the large number of very small earthquakes, which could be expected to raise the slope of the G-R diagram, *b*-values slightly lower than unity were found for the sequence (Table 5.4). At smaller samples, when examined throughout time and space, even lower values could be determined. Low *b*-values usually indicate increased stress in an area. However, the intense presence of fluids or aseismic creep, evidenced by the strong migration patterns and non-stationarity of the μ-value of the ETAS model, may imply that this is not the case of a locked structure. The latter was also suggested by Bernard *et al.* (2004), who measured a strain transient that was attributed to a silent earthquake of equivalent magnitude M_w=5.4, originating from about the same area. Moreover, ETAS modeling showed that the 2014 Nafpaktos-Psathopyrgos swarm can be described in two phases, the first exhibiting constant or increasing seismicity rate, with very high *a*-value and very low *p*-value, and the latter closer to a mainshock-aftershock decay pattern, but with significant positive residuals. These can be explained by non-stationarity that indicates influence of aseismic factors to the triggering of earthquakes, although some periods of strong migration can still be explained by earthquake-induced stress-transfer with little contribution by fluids.

The 2014 Nafpaktos-Psathopyrgos swarm bears some similarities to the 2013 Helike swarm that occurred in the broader region of study (Section 5A.4; Kapetanidis *et al.* 2015). That sequence started with a series of earthquakes which included several bursts, some of which containing events with magnitudes $3.4 \leq M_w \leq 3.7$, with 3.7 being the maximum magnitude observed. Its spatiotemporal distribution was also characterized by a roughly bilateral migration during its first phase of activity, between 21 May and mid-July 2013, in an approximate E-W direction with D = 0.4 m^2/s and a slow one-sided eastwards migration at 30-40 m/day at its later part. A second phase was initiated on 12 July 2013 with intense activity at the western portion of the swarm, including three M_w = 3.6 events and a rapid seismic moment release, in contrast to the more gradual release in bursts during the first phase. While the magnitudes and time/space/energy scales involved in the 2013 swarm in Helike are smaller than those in the 2014 swarm in the western Corinth rift, there is some resemblance between the second phase of the first and period e of the latter. This is due to the denser spatial distribution and larger energy release in a short time that is observed in both. Also, the gradual migration of the seismicity front in both cases during the first phase, which is probably linked to triggering by pressurized fluids, is another general characteristic that is shared between the two of them. This can lead to a similar explanation on the triggering of the “second phase” (period

e) for the 2014 swarm, as the redistribution of stress caused by the migrating fluids and possibly other aseismic mechanisms such as creeping, could have induced the M_w = 4.9 event of 21 September which lead to the major outbreak of the 2014 swarm.

5.5 The 2015 Lefkada aftershock sequence

Lefkada Island is located at the northern part of the Cephalonia-Lefkada Transform Fault Zone (CLTFZ), the major dextral strike-slip tectonic feature of the Ionian Sea (Fig. 5.57). As with Cephalonia, seismicity in the vicinity of Lefkada Island during the last decades has been mainly concentrated offshore, with the exception of a sequence that took place in November-December 1994 (Makropoulos *et al.*, 1996). The strongest earthquakes have been known to occur in the NW side of the island, as was the case with the major M_w=6.3 event of 14 August 2003 (Benetatos *et al.*, 2005; Zahradnik *et al.*, 2005; Papadimitriou *et al.*, 2006). A strong M_w=6.4 earthquake occurred on 17 November 2015 in Lefkada Island, with its epicenter located near the mid-southern part of the west coast. In this section the spatiotemporal and seismotectonic characteristics of its aftershock sequence are analysed in detail. Preliminary results were announced by Papadimitriou *et al.* (2016a) and reported to EMSC (Papadimitriou et al., 2016b).

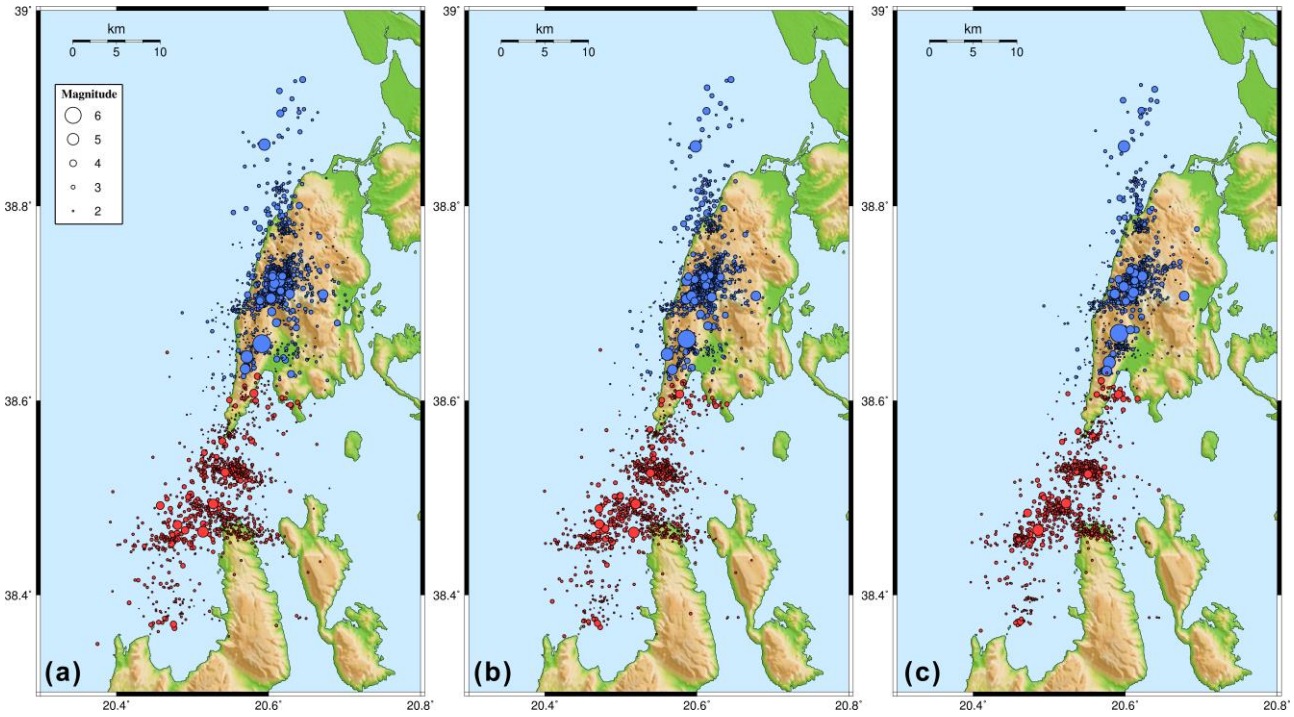

Figure 5.57: Epicenters of the aftershock sequence in Lefkada island between 17 November and 3 December, 2015. a) Initial locations with the custom velocity model of Papadimitriou *et al.* (2016a), b) after application of station-corrections, c) relocated epicenters using HypoDD. Colours represent the two main spatial groups (blue: North, red: South) for which the station corrections and relocation procedures were applied separately.

5.5.1 Relocation - Clustering

Over 1100 events of the 2015 Lefkada aftershock sequence in the period between 17 November and 3 December 2015 have been manually analysed by the Seismological Laboratory of the University of Athens. In addition, the HADAES method (Section 4.4) was partially applied to enrich the catalogue with a large number of highly correlated, smaller events, mainly in the vicinity of the mainshock, resulting in a total of over 2700 events. Moment magnitudes for the additional events were calculated using the spectral fitting method described in Chapter 3. A subset of the best located events were used for the determination of a local 1D velocity model for the broader area of Lefkada by minimizing the average travel-time residuals and location uncertainties (Table 5.5; Papadimitriou *et al.*, 2016a).

Table 5.5: Custom P-wave 1D velocity model for the 2015 Lefkada aftershock sequence, with V_p/V_s=1.81 (Papadimitriou et al., 2016a).

Layer	V_P (km/s)	**Ceil. Depth** (km)
1	4.9	0.0
2	5.2	4.0
3	5.9	7.0
4	6.2	11.5
5	6.4	13.0
6	6.5	16.0
7	7.3	39.0

Using the determined local velocity model, the location uncertainties were reduced and sparse events were concentrated closer to regions of clustered activity without significantly affecting the absolute locations of the spatial clusters centroids. The relative hypocentral dispersion, however, may be further reduced to enable the distinction of several sub-clusters which comprise the aftershock sequence. Ward's linkage was applied on the inter-event distance matrix to create a clustering hierarchy based on Euclidean distances. The spatial distribution was divided in two groups by selecting an appropriate threshold. The northern group contains about 52% more events than the southern one. From this point on, each group was further processed individually. For each station, the mean P- or S-wave travel-time residuals were calculated and station corrections were applied. As a result, both mean RMS errors, location uncertainties (Table 5.6) and hypocentral dispersion (Fig. 5.58b) were reduced, as events which belong to certain sub-clusters became better concentrated.

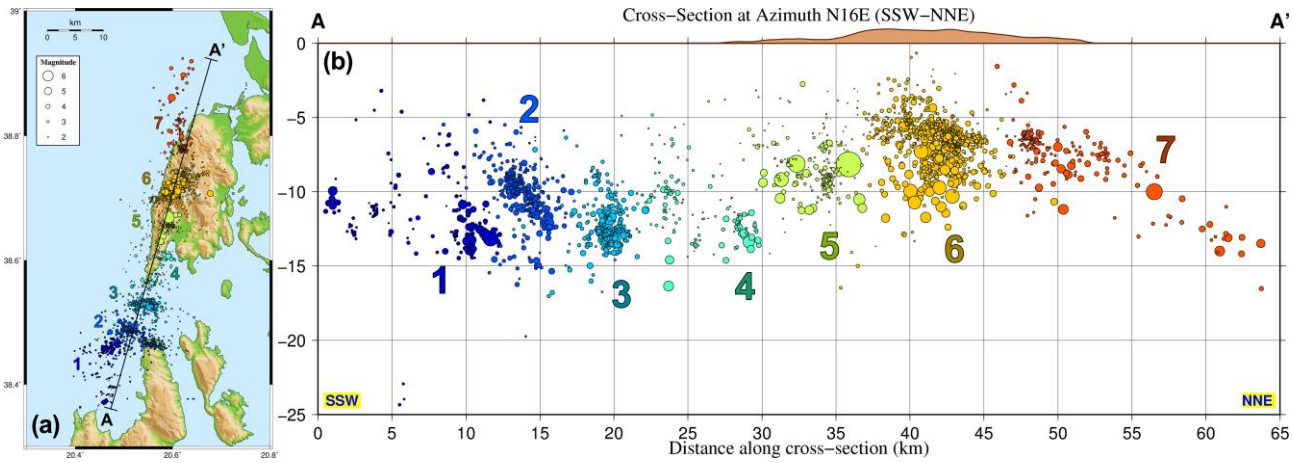

Figure 5.58: (a) Map of relocated epicenters divided in 7 spatial clusters, (b) vertical cross-section in a N16°E direction along the line A-A' presented in panel (a). Colours and numbers represent the 7 spatial clusters while the hypocenter size is proportional to the magnitude of the corresponding event.

Table 5.6: Error statistics of the two major spatial groups before and after the application of station corrections using the velocity model that was derived in the present study.

Group	**Northern**		**Southern**	
	initial	after stat. corr.	initial	after stat. corr.
Mean RMS (s)	0.12	0.10	0.14	0.10
Mean ERH (km)	0.74	0.68	1.16	1.04
Mean ERZ (km)	1.16	1.04	1.48	1.27
Median Depth (km)	6.33	6.48	11.66	11.42

The relocation algorithm, HypoDD (Waldhauser & Ellsworth, 2000), was employed to reduce the relative location errors. The cross-correlation measurements were performed on the filtered (2 - 23 Hz) full-signal (P & S) waveforms of station EVGI, which is situated on Lefkada island, about 8 km SE of the epicenter of the mainshock and up to 30 km of both SSW and NNE edges of the aftershocks distribution. The matrices which were derived of the 3 components were averaged by the respective RMS values for each event-pair. A clustering hierarchy was created by applying nearest-neighbor linkage on the combined cross-correlation matrices and the optimal threshold that was found to be the same, C_{th}=0.57, for both groups, leading 68% and 63% of events to be contained in multiplets with size≥2 for the northern and southern group, respectively. For each multiplet, all combinations of pairs of P- or S-wave segments were then cross-correlated in all stations where manual arrival-time picks were available to acquire differential travel-time measurements, with the corresponding XC_{max} used as observation weight.

Table 5.7: Information on the multiplets and number of relocated events for each of the two major spatial groups.

Group	# evt	C_{th}	# multiplets	# evt in multiplets	# relocated evt
North	1662	0.57	155	1124	1642
South	1089	0.57	125	689	1052

Iterative relocation was performed using the HypoDD algorithm for each group. A weighted least squares inversion was used for the full set of data with a distance and residual reweighting scheme to maintain links within correlated spatial clusters and achieve stable results. Travel-times and locations acquired from the solutions that were derived after the application of station corrections were used as data and initial conditions in HypoDD. On a second stage, selected smaller groups containing large events were relocated separately using a Singular Value Decomposition method. About 98% of events from the initial catalogue were successfully relocated (Table 5.7). The final results are displayed in Fig. 5.57c. The mainshock and largest aftershock of 17 November 2015 are well aligned in a SSW-NNE direction. Several linear structures can be distinguished, many of which offshore, south of Lefkada island, trending roughly E-W. The aftershock distribution appears mostly aligned in a N16°E direction with several branches oriented ~N32°E, including the northernmost and southernmost tips.

5.5.2 Spatio-temporal / Multiplet analysis

The spatial clustering method that was used to separate the seismicity in two major groups can also be applied to further divide the sequence in smaller sub-clusters. This can be useful for a detailed spatio-temporal description. After re-calculating the inter-event 3D distance matrix from the relocated catalogue the distribution was separated into 7 spatial clusters, numbered (1-7) with increasing mean latitude order (Fig. 5.58, Table 5.8). The cross-section drawn at N16°E, roughly parallel to the CLTFZ, indicates that the total length of the activated area is approximately 60 km. The focal depths are distributed between 5 and 15 km, with the clusters in the northern group (5 - 7) being generally shallower than those of the southern group (1 - 4). The mainshock, as well as the strongest aftershock (M_w=5.0) of 17 November are contained in cluster #5, the one with the lowest percentage of events with $M \geq 2.0$ (30%). This is due to the many small events that were introduced to the catalogue by the HADAES method for the area near the mainshock, which mostly revealed a small cluster of weak events between the mainshock and the largest aftershock at ~9 km depth. The epicenter of the major events of this cluster are mainly aligned SSW-NNE, with the smaller sub-cluster being apparently oriented E-W. By far the largest cluster is #6, which contains nearly 1200 events, or 44% of the catalogue. Detailed observation in thin horizontal slices (Fig. 5.59) shows that its shallower parts (4-6 km) are divided in two branches, one SSW-NNE, similar to cluster #5, and another trending WSW towards the western coast and extending a bit deeper (8-9 km) ENE. The described hypocentral distribution is probably related to fault network complexity, which has possibly acted as a barrier, prohibiting the main rupture to extend further north. It also contains most of the major aftershocks (13 events with $M_w \geq 3.9$) which are, on average, located at slightly

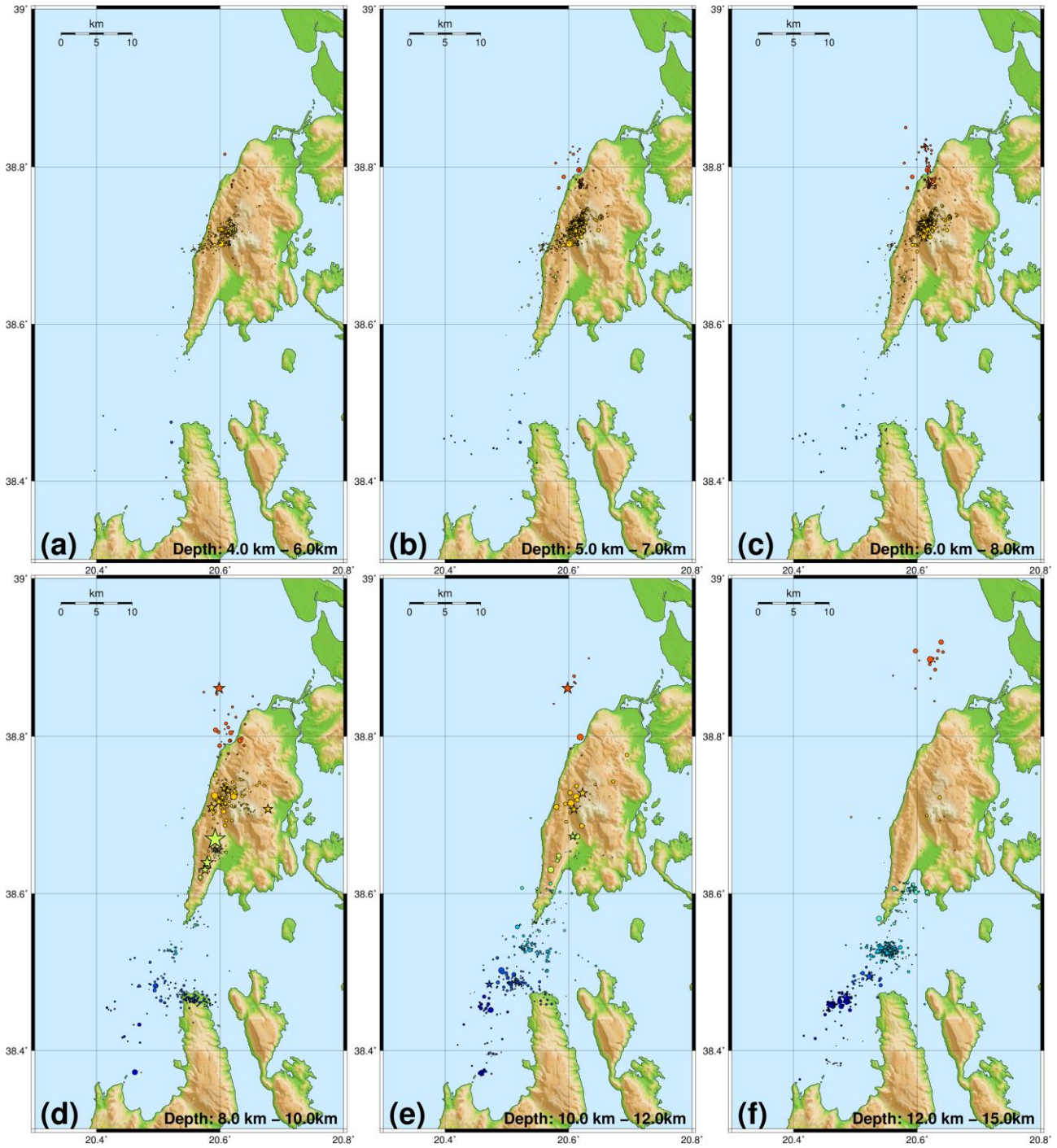

Figure 5.59: Maps of consecutive, thin horizontal slices at various depth ranges. Colours represent the 7 spatial clusters.

larger focal depths (~9.3km) than the smaller ones (~6.6 km). Further north, cluster #7 extends ~17 km and deepens from ~6 km onshore (excluding a few sparsely located shallower events) down to ~15 km and includes the second largest aftershock (M_w=5.0) which occurred on 18 November 2015, 12:15 UTC. The cluster could be further divided in 2 sub-clusters, the one for the shallower,

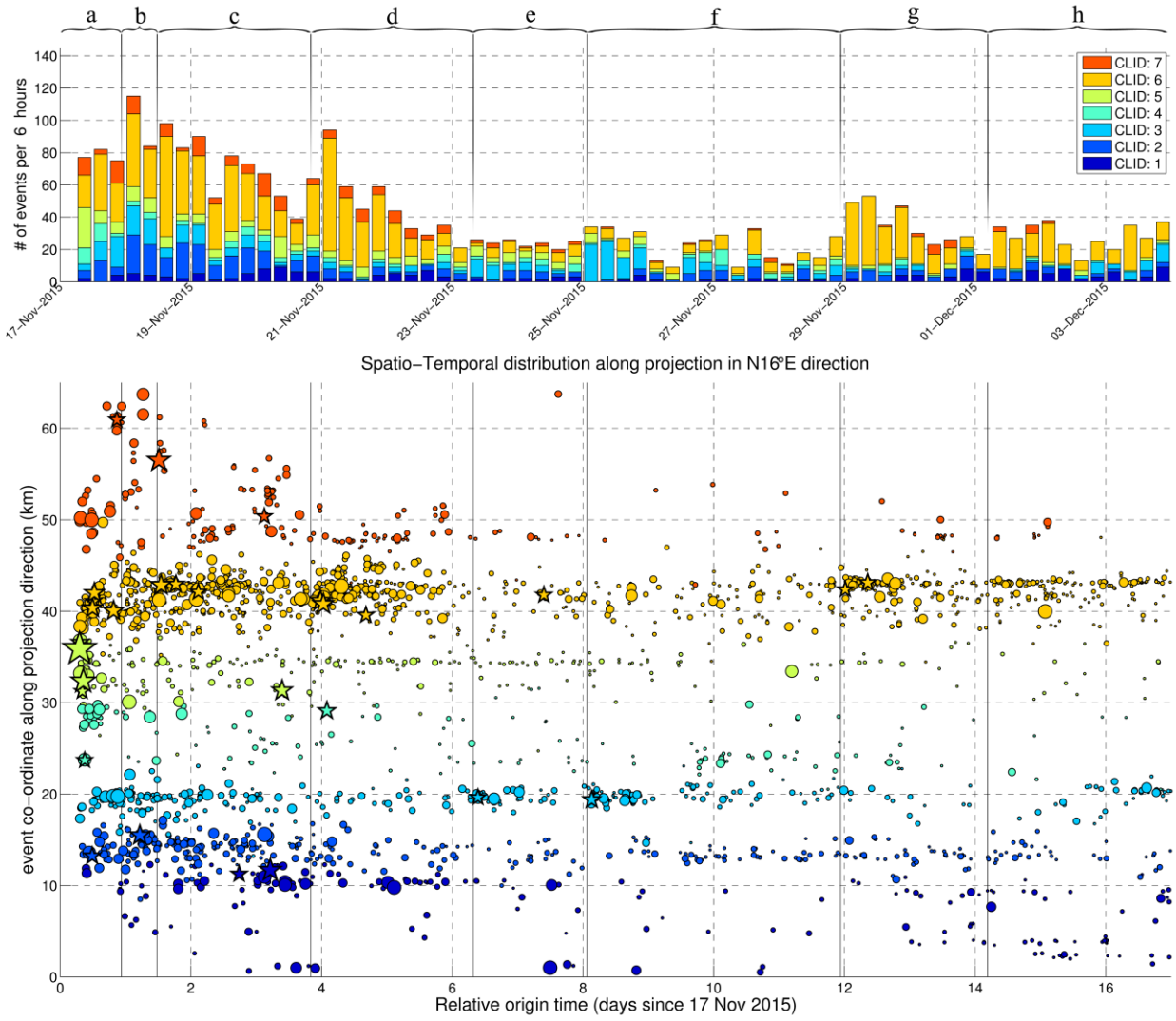

Figure 5.60: (Top) Histogram of earthquake occurrence per calendar day. (lower panel) Spatiotemporal projection of the aftershock sequence. The vertical axis represents the position along the N16°E trending A-A' line of Fig. 5.58, horizontal axis marks the origin time. Stars mark major events ($M_w \geq 4.0$). Colours represent the 7 spatial clusters.

roughly onshore events, trending S-N and the other, offshore further north, containing fewer events and apparently trending SW-NE.

At the southern group, the northern tip of cluster #4 is ~4-5 km south of the mainshock and the cluster extends another 7.5 km SSW while its median focal depth (11.6 km) is larger than the one for cluster #5 (8.8 km, Table 5.8). It probably belongs to the same fault plane as the one of the main rupture and defines its deeper seismogenic part. It contains several smaller sub-clusters, likely related small asperities which generate multiplets. Clusters #2 and #3 are less dispersed than cluster #4 and their distribution is roughly oriented E-W. Cluster #2, in particular, contains 2 large sub-clusters at 8 – 13 km depth and a smaller sub-cluster at 15 km depth. The southernmost cluster #1 is a bit offset from the cross-section line A-A´ (Fig. 5.58a). Its main body is located at 7-9 km depth and it also includes several sub-clusters dispersed further south, related to small multiplets. The

seismic activity in the area covered by the southernmost clusters is likely triggered by positive Coulomb stress transfer caused by the mainshock. It is worth noting that the same was observed during the 2003 Lefkada aftershock sequence (Papadimitriou *et al.*, 2006). At the very southern edge of the study area, a group of 3 deeper events at ~23-24 km, with epicenters between Ithaki and Cephalonia islands, are also included in cluster #1.

The Lefkada 2015 aftershock sequence is typical in terms of its spatio-temporal characteristics. The catalogue was divided in 8 periods, each including small secondary outbursts (Figs 5.60, 5.61 and 5B.20), to enable the understanding of the evolution of the seismic activity. Aftershocks were generated at both northern and southern edges of the zone within minutes to hours following the mainshock, as evident from both the map of the first period (Fig. 5.61a) and the spatiotemporal projection (Fig. 5.60), while the largest one (M_w=5.0) occurred in less than 2 hours after the main

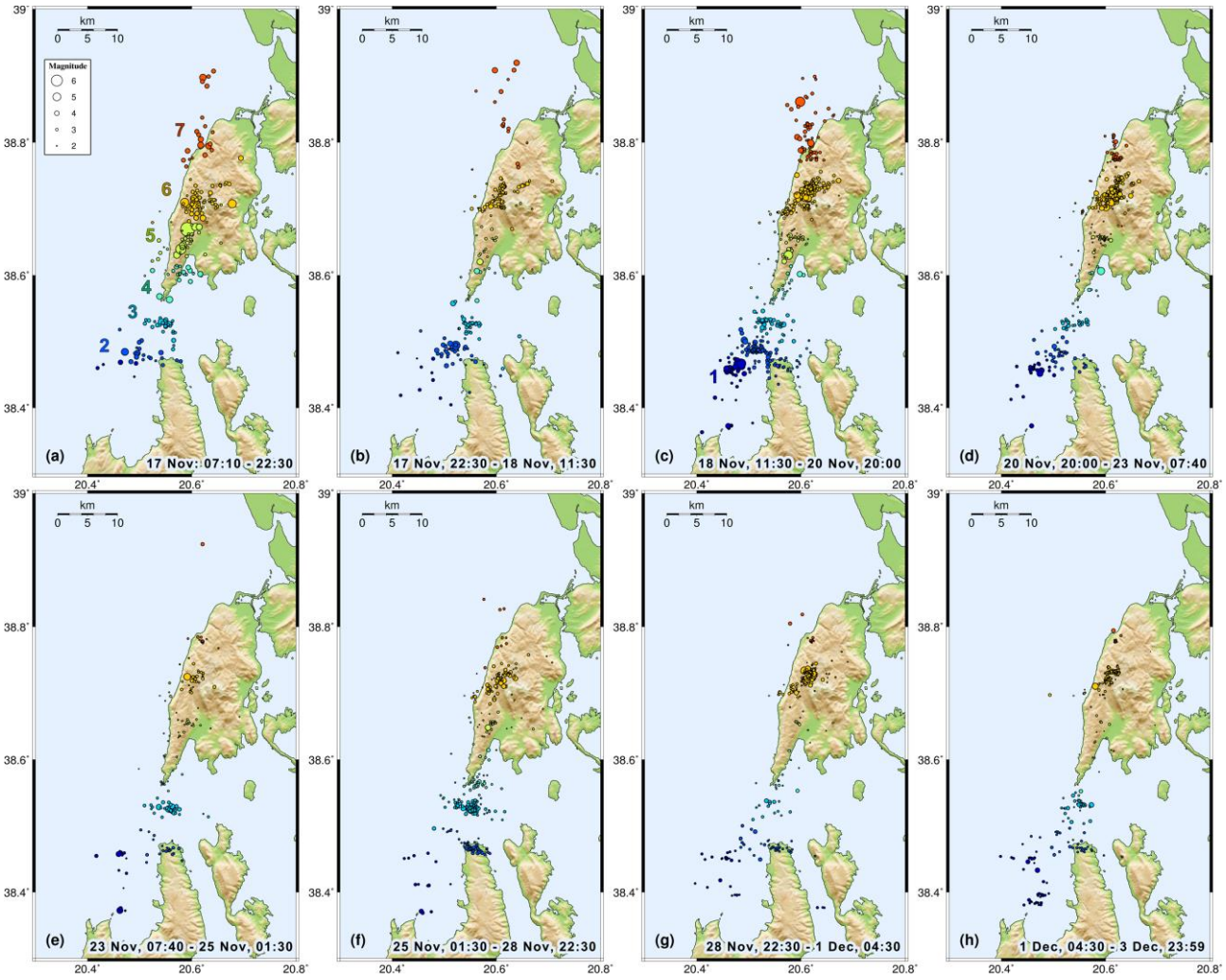

Figure 5.61: Maps of temporal evolution of the aftershock activity divided in 8 periods: a) 17 Nov: 07:10-22:30, b) 17 Nov, 22:30 - 18 Nov, 11:30, c) 18 Nov, 11:30 – 20 Nov, 20:00, d) 20 Nov, 20:00 – 23 Nov, 07:40, e) 23 Nov, 07:40 – 25 Nov, 01:30, f) 25 Nov, 01:30 – 28 Nov, 22:30, g) 28 Nov, 22:30 – 1 Dec, 04:30 and h) 1 Dec, 04:30 – 3 Dec, 23:59. Colours represent the 7 spatial groups.

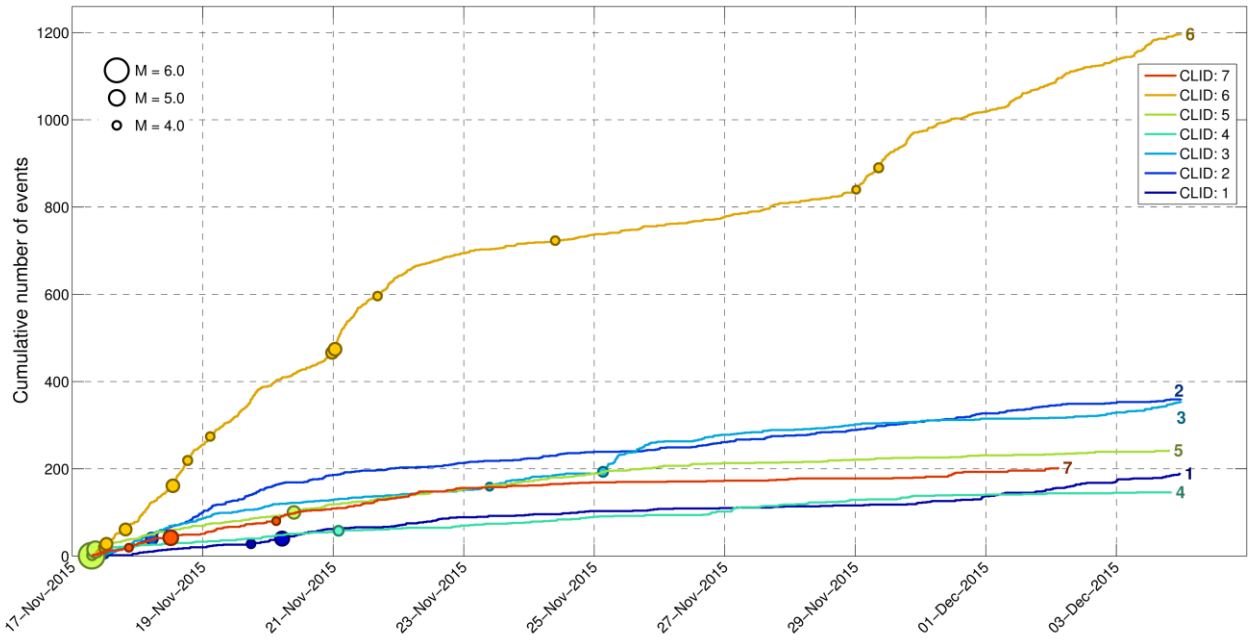

Figure 5.62: Cumulative number of events for each of the 7 spatial groups. Circles denote major events ($M_w \geq 4.0$)

event, in the same cluster (#5; 2nd largest star in Fig. 5.60). Some secondary/minor sub-sequences are related to strong events ($M_w \geq 4.0$), indicated by stars in Fig. 5.60 at the beginnings of some periods and associated with increase of the respective bar height in the histogram. The activity is mostly persistent in the clusters labeled (CLID) #6, #3 and #2 (Fig. 5.58), near the edges of the inferred ruptured surface. The most notable secondary outbreaks occurred on 21 November (CLID #6), 25 November (#3) and 29 November (#6), causing increase in the seismic rate of the respective cluster (Fig. 5.62). Weak activity in cluster #5 is mostly generated by a multiplet of small events located between the two major events of 17 November 2015. By the end of December 2015, the activity in most of the spatial groups had diminished (Fig. 5.61h), with the exception of cluster #6, and the sequence was typically over, as confirmed by routine observations of the seismicity rate during the following months.

The history of multiplet evolution for the northern and southern groups is presented in Fig. 5.63. New multiplet generation is abrupt in the beginning, as is typical for aftershock sequences, especially in the northern part that contains the large Group #6. While this first outburst produced several large multiplets it was a second wave that produced the largest one (MID:52 in Fig. 5.63a) on 18 November, at the beginning of period c. A third wave, on 21 November mainly reactivated MIDs 52 and 77 of the northern group. It also caused spreading to new areas (new multiplets) but only of very small size. The large significant outburst that occurred on 29 November mainly affected MID 52. In the southern group, on the other hand, the largest multiplet (MID: 23) was generated on the first day, ~14 hours after the mainshock, during a secondary outburst of period b,

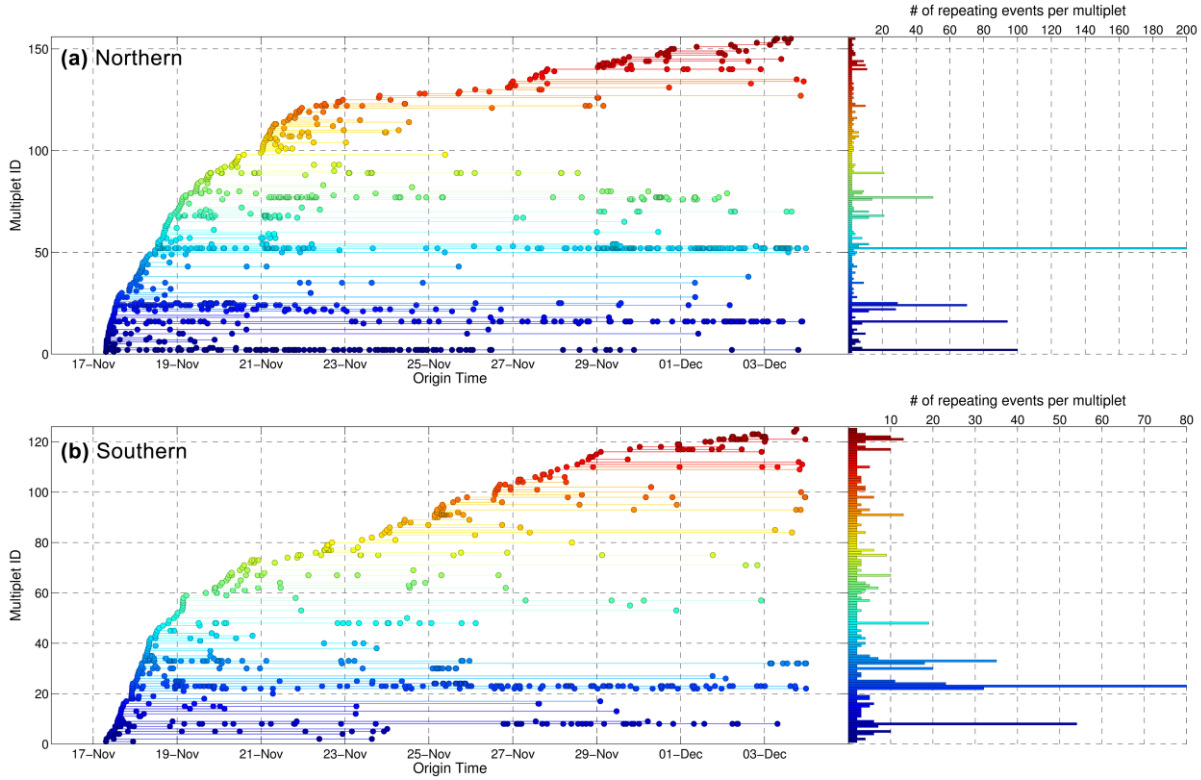

Figure 5.63: (Left) Multiplet evolution history during the 2015 Lefkada aftershock sequence a) for the northern group (including sub-groups 5-7) and b) for the southern group (including sub-groups 1-4). Each row represents a single multiplet, with IDs sorted in increasing order according to the origin time of the first event in each multiplet. Circles represent repeating earthquakes. (Right) total number of repeating earthquakes per multiplet.

Table 5.8: Error statistics and other information on the 7 spatial clusters.

CLID	1	2	3	4	5	6	7	total
Mean RMS (s)	0.11	0.10	0.09	0.10	0.09	0.10	0.10	0.10
Mean ERH (km)	0.91	1.07	1.03	1.13	0.95	0.57	0.91	0.81
Mean ERZ (km)	1.15	1.00	1.00	1.42	1.35	0.89	1.30	1.04
Median Depth (km)	12.1	9.9	12.6	11.6	8.8	6.5	7.2	8.08
Mean latitude	38.43	38.48	38.53	38.58	38.65	38.72	38.80	-
Max. mag.	4.8	4.5	4.2	4.2	6.4	4.6	4.9	6.4
# evt	190	360	354	147	243	1197	203	2694
% of total evt	7.1%	13.4%	13.1%	5.5%	9.0%	44.4%	7.5%	-
# evt with M ≥ 3.9	2	2	2	2	5	13	3	29
# evt with M ≥ 2	120	226	240	61	73	643	131	1494
% evt with M ≥ 2	63%	63%	68%	41%	30%	54%	65%	55.5%

and persisted throughout the sequence. The burst of 21 November, however, hardly affected the southern group at all. Also, several of the relatively large multiplets perished before 24-27 November or were mostly active for only a few hours.

5.5.3 Composite focal mechanisms (Group #6)

The large spatial Group #6 contains a significant number of small multiplets concentrated at different parts of its volume. This part of the aftershock zone is likely related to the end of the main rupture and the damage zone surrounding the main fault. The large number of multiplets is indicative of increased complexity. For this reason, it is of particular interest to investigate the possibility of existence of secondary faults in a small-scale fault network. Most events contained in multiplets usually have smaller magnitude, which makes it difficult or impossible to determine their focal mechanism with the method of waveform inversion. The availability of data from local stations of HUSN on Lefkada Island, complemented by some stations on Cephalonia Island, permits the estimation of focal mechanism using the technique of first-motion polarities (FMP). To obtain a focal mechanism solution for an individual event, a grid search was performed to determine whether the resulting quadrants of compressive and extensional radiation correspond to the observed first-motion polarities. However, the local stations are very few, unevenly distributed and they do not always provide reliable FMP data, e.g. when the event is too small or the station is near one of the nodal planes. A small degree of tolerance was also used to avoid erroneous observations due to uncertain polarity measurements. To constrain the solutions, the S-wave polarization direction and S- to P-wave amplitude ratio were also measured and used as weights according a

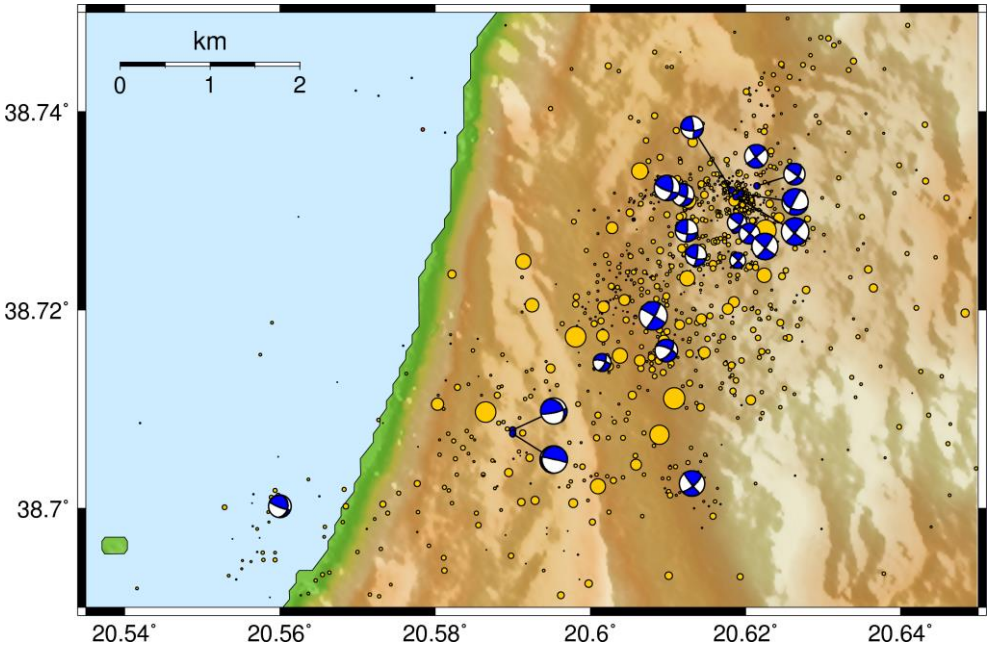

Figure 5.64: Zoom on Group #6 with composite focal mechanisms for 20 selected multiplets.

combined weight function (e.g. Section 2.4.3), also including the percentage of first-motion polarities which lie in the correct quadrants. A composite focal mechanism was calculated for each multiplet by summing the moment tensors of its events. The RMS angular difference between the composite solution and the individual focal mechanisms was used as an error estimate. A mean solution is accepted when it has a relatively small RMS error or it represents most of events after visual inspection. In the latter case, the RMS can be improved by removing some badly constrained solutions from the multiplet.

The results of the composite focal mechanism solutions are presented in Fig. 5.64, with their location corresponding to the mean coordinates of each multiplet. The focal mechanisms are mostly strike-slip, compatible with the solutions that were determined for the larger events by waveform modeling; with a few representing oblique slip. However, some more significant differences are observed towards the "western branch" of Cluster #6, where sub-vertical/sub-horizontal nodal planes solutions are observed in 3 well-constrained (RMS < 25°) composite focal mechanisms. These suggest either a sub-horizontal fault with footwall sliding towards the north or a sub-vertical, E-W trending fault with the southern wall subsiding. Another, minor observation, is that several multiplets in the middle of Cluster #6 appear to be aligned so that the WNW-ESE to NW-SE trending, sub-vertical plane could be seen as patches of a common fault surface that is transverse to that of the main rupture, suggesting the possible existence of antithetic structures with sinistral slip under the common shear-stress regime.

5.5.4 Magnitude distribution – ETAS modeling

The frequency-magnitude distribution for the 2015 Lefkada aftershock sequence is complete down to M_c=2.2. The temporal distribution of M_c has little variation, starting at 2.2 and dropping to 2.0 halfway through the period of study. The *b*-value is found to be near unity (1.01±0.03), with insignificant temporal variation but with lower values around the region of the mainshock and higher values in the vicinity of Group #6 and the southern, offshore groups.

ETAS modeling was applied to examine whether the sequence can be described as a simple mainshock-aftershock pattern following the Modified Omori's Formula (MOF) or it is more complex and consists of a superposition of multiple subsequences. Fig. 5.65 shows the ETAS and MOF models. Both are relatively well fitted on the data. However, both *AIC* and σ values are lower for the ETAS model, which renders it preferred over the MOF model. The *a*-value (1.202) is within the lower margin for non-swarm types of sequences while the p-value is relatively high for both models, indicating fast decay of the aftershock series. Small, positive deviation of the data is observed between 18 and 24 November for the ETAS model, being even more pronounced in the residuals of the MOF model between 20 and 24 November. During that time (roughly period d), a secondary subsequence occurred that mainly affected the large Group #6. The smaller subsequence of period g did not cause significant positive residuals.

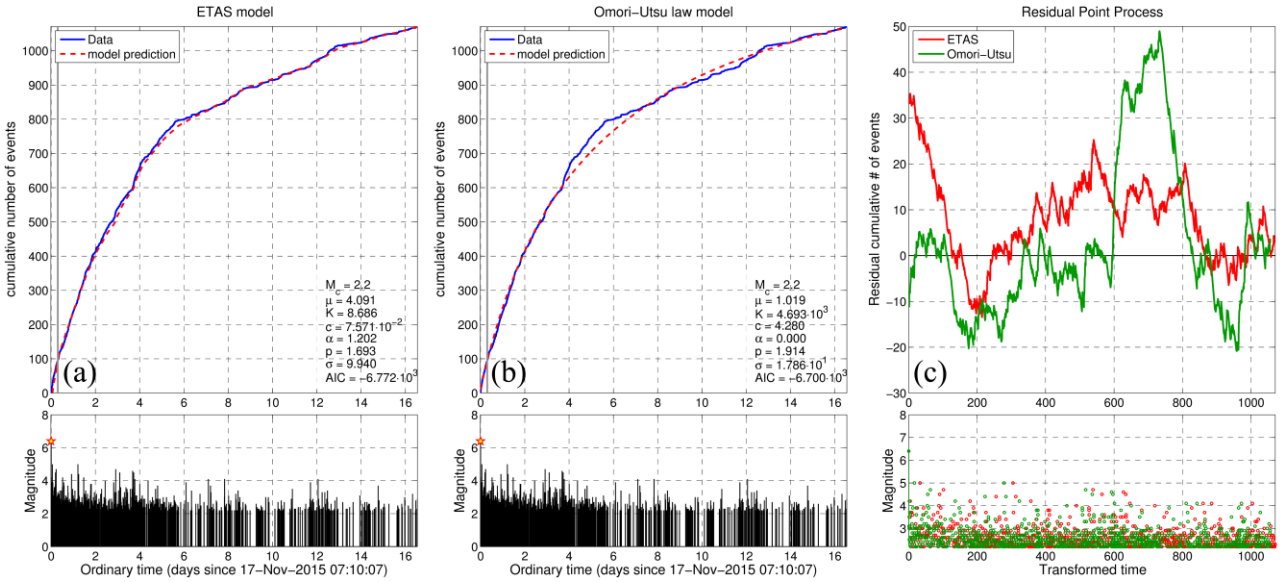

Figure 5.65: ETAS and Omori-Utsu models for the 2015 Lefkada aftershock sequence (17 November – 3 December, 2015), using a threshold value at $M_{th} \equiv M_c = 2.2$ and $M_t \equiv M_{main} = 6.4$, with the model parameters estimated by MLE ignoring the first $T_o = 0.3$ days (grey line). a) data and ETAS model curves in ordinary time, b) data and MOF model in ordinary time, c) residuals between data and models in transformed time.

5.5.5 Discussion – Conclusions

The 2015 aftershock sequence in Lefkada mainly struck the mid-southern part of the island. The epicentral distribution extends to a length of ~60 km, much larger than the expected sub-surface rupture length $L \approx 25$km from the empirical relations of Wells & Coppersmith (1994) for strike-slip faulting with $M_w = 6.4$. This implies that the mainshock ruptured nearly half of the activated area, while the rest of seismicity is a direct result of stress redistribution. The area defined by the spatial groups #5 and possibly #4 is considered to be the main rupture area, likely a barrier that left few unbroken asperities where the seismic clusters are observed. Only few aftershocks were located in the vicinity of the mainshock's epicenter, including a low energy cluster in group #5 that was only resolved due to the application of the HADAES method that was employed to detect smaller events, particularly in that area. On the contrary, the most intense activity was observed in a cluster N of the mainshock, at the central part of the island. This is approximately the same area where a significant sequence occurred in 1994 (Makropoulos *et al.*, 1996), when an $M_w = 5.1$ occurred on 29 November 1994, followed by an $M_w = 4.8$ aftershock on 1 December 1994. Intense activity in the same area was again triggered during the 2003 aftershock sequence of an $M_w = 6.3$ earthquake that occurred in the northern half of the island (Papadimitriou *et al.*, 2006; Karakostas & Papadimitriou, 2010). The temporal evolution of the aftershock sequence is generally smooth, with 2 - 3 detectable smaller sub-sequences following major events. No significant migration patterns were observed, as almost the full extent of the aftershock zone was activated within the first 24 hours after the mainshock.

Seismic activity is numerous, less populated clusters, also occurred to the south, close to the NNW part of Cephalonia Island, mostly not directly related to the main rupture these clusters are not located along the CLTFZ but are shifted to the east. They are also stretched in a roughly WNW-

ESE direction, separated by gaps between them, possibly indicating parallel small left-lateral structures, transverse to the main CLTFZ. It is noteworthy that activity this area was also triggered by Coulomb stress transfer after the M_w=6.3 earthquake of 2003 in Lefkada island (Papadimitriou *et al.*, 2006), but also during the 2014 Cephalonia aftershock sequence (Section 5.3).

The geometry of the activated structures leads to an interpretation of the tectonics in the broader area presented in Fig. 5.66. This is similar to the suggestion of Karakostas *et al.* (2015) for the northern part of the Cephalonia sequence, but with the transverse structures extended further to the north towards Lefkada Island. The up-dip extension of the causative fault, given the determined

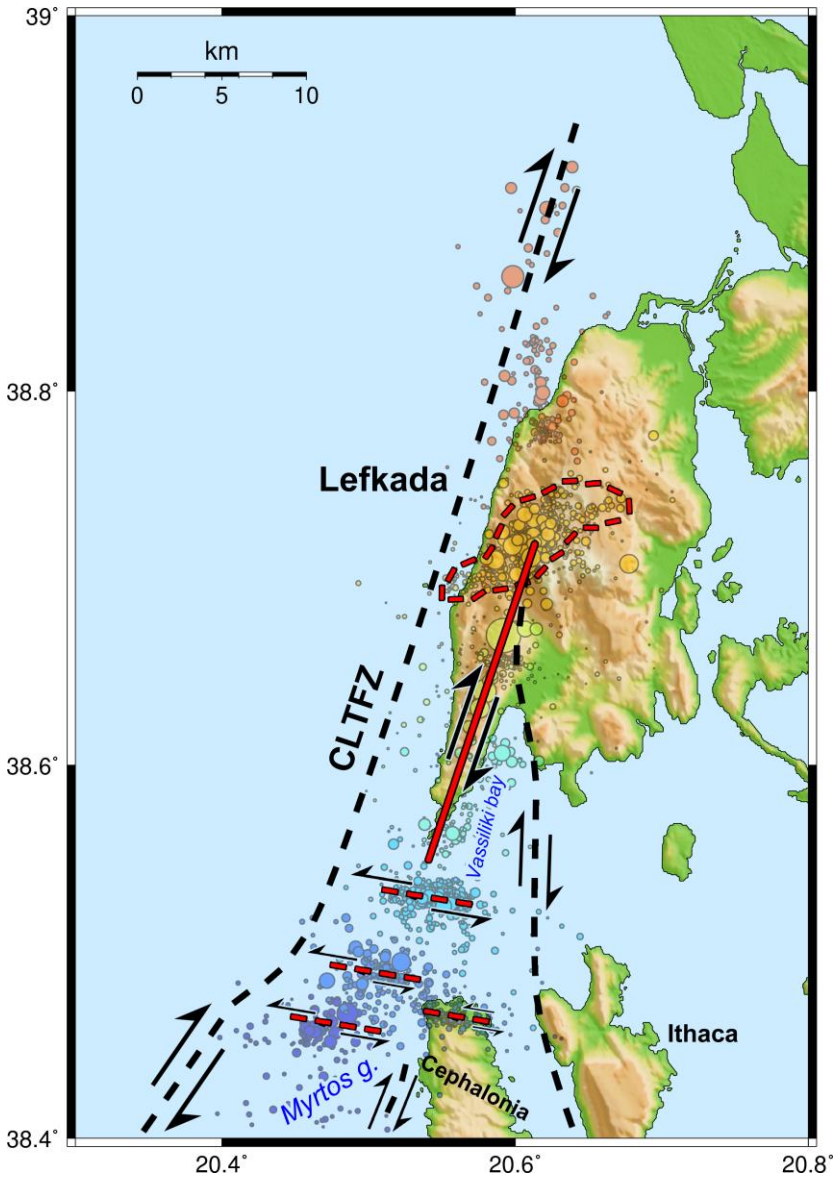

Figure 5.66: Simplified sketch for the main rupture of the 2015 Lefkada earthquake at the mainshock's depth (20km-long solid red line) inferred transverse structures (dashed red lines) and traces of known superficial structures in the area (black dashed lines). Group #6 is encircled in by red dashed lines to highlight its geometry.

focal mechanism of the 2015 mainshock, meets the surface at about 1km offshore west of Lefkada. This could be related to the northern part of the CLTFZ, which is, however, is shifted by a few km to the west at the latitude of Cephalonia Island. The transverse E-W trending, sinistral-slip structures would be a result of a negative flower structure that could also be responsible for the observed topography at the northern part of Cephalonia (Myrtos gulf), and also, possibly, the geomorphology of the southern part of Lefkada Island (Vassiliki bay). These small structures are likely less capable to sustain high stresses, as suggested by the relatively higher *b*-values observed in that area, which could render them sensitive to triggering by stress transfer due to large mainshocks in their vicinity.

The role of the large cluster in the middle of Lefkada (Group #6) is less clear, as composite focal mechanisms for several multiplets revealed insignificant deviations from the expected regional stress field, with little evidence for possibly transverse structures. However, the latter might be supported by the overall geometry of the cluster (surrounded by a red dashed closed shape in Fig. 5.66) and by the fact that it apparently divides two segments of the CLTFZ in Lefkada that were activated separately (2003 and 2015) rather than both at once, which could produce a much larger earthquake (e.g. $M_w \approx 6.8$-6.9 for a rupture length $L \approx 50$km). Karakostas & Papadimitriou (2010) determined a similar direction for the 2003 "central-eastern" cluster, characterized by right-lateral strike-slip, and suggested that it was kinematically related to the main fault. The likely existence of an offset between the northern and souther segments would suggest some sort of relay zone in the volume of Group #6 that would also mark the northern edge of the 2015 rupture and the southern one of 2003. The mainshock greatly increases the local stresses at the edges of the main rupture's surface which can explain the triggering of clustered activity in between the two offset segments.

Chapter 6

Seismicity of 2000-2007 in the western Corinth Rift

6.1 Introduction

The Gulf of Corinth is an E-W trending rifting zone, one of the most seismically active regions in Europe and the fastest-spreading intracontinental rift on Earth (Jolivet *et al.*, 2010). It is characterized by a nearly orthogonal extension of 10±4 mm/yr in a N19°E direction at its eastern end to 14±2 mm/year at N9°E at its western end (Briole *et al.*, 2000), reaching a maximum of 16 mm/year near Aigion (Avallone *et al.*, 2004). It is mostly considered as an asymmetric half-graben with the major structures being those bounding it from the south, with uplifted footwalls, while only minor antithetic faults are observed in the north, experiencing long-term subsidence (Armijo *et al.*, 1996). On the other hand, observations on the offshore faults (Moretti *et al.* 2003; Beckers *et al.*, 2015) suggest that the rift is less asymmetric than previously thought and support a model of more homogeneous spreading at the lower crust with a significant portion of the deformation being accommodated on the south-dipping faults. The faults are *en echelon*, right-stepping from W to E, with the major fault segments in the south having lengths between 15 and 25 km, striking ~N90-105°E on average, with a ~50° northwards dip near the surface (Armijo *et al.*, 1996). The formation of the rift began in the Quaternary, as evident from the faults cutting through sediments of Miocene and Plio-Pleistocene age, while its opening is oblique, almost orthogonal, to the fabric and topography of the Hellenic belt (Armijo *et al.*, 1996). During the last 1.5-1.8 Myr the deformation has been migrating gradually towards the north, leaving the older faults in the south inactive or with slow slip rate, while the extension rate has been increasing (Sorel, 2000; Ford *et al.*, 2013).

Several strong earthquakes have been recorded in this region during both historical and instrumental eras (Makropoulos & Burton, 1981; Ambraseys & Jackson, 1990; Papazachos & Papazachou, 2003; Makropoulos *et al.*, 2012; Stucchi *et al.*, 2013), including tsunamogenic ones, such as the 373 BCE earthquake that destroyed the city of Helike and the 23 August 1817 earthquake that caused severe damages and fatalities in Aigion at the shallower southern coast (Kortekaas *et al.*, 2011). In the more recent years, the most significant events in the Gulf of Corinth have been the three earthquakes of 24-25 February and 4 March 1981. They ruptured in sequence the Corinth, Perahora and Kaparelli faults in the east, with M_s magnitudes 6.7, 6.4 and 6.2, the first two occurring 1 day apart (Jackson *et al.* 1982; King *et al.*, 1985; Armijo *et al.*, 1996) and the M_s=6.2 event of 15 June 1995 which struck the city of Aigion in the west (Tselentis *et al.*, 1996; Bernard *et al.*, 1997). The latter, along with the M_w=5.8 Galaxidi earthquake of 18 November 1992 (Hatzfeld *et al.*, 1996) activated shallow north-dipping (30-35°) offshore faults, differing significantly from the 45° to 50° dipping planes of the three earthquakes of 1981, at the eastern end of the rift (Bernard *et al.*, 2006).

During the last 400 kyr, the focus of extension has been migrating gradually from the center towards the western side of the gulf (Bell *et al.*, 2011), with the currently maximum extension rate being measured near Aigion. The western Corinth Rift is of particular interest as it is currently generating thousands of microearthquakes every year. Some first details on its microseismic activity were highlighted by a seismological experiment in July-August 1991 with the installation of a temporary network of 51 stations covering an area of 40x40 km² around Psathopyrgos-Aigion (Rigo *et al.*, 1996; Hatzfeld *et al.*, 2000). The events of 1992 and 1995 attracted more scientific attention

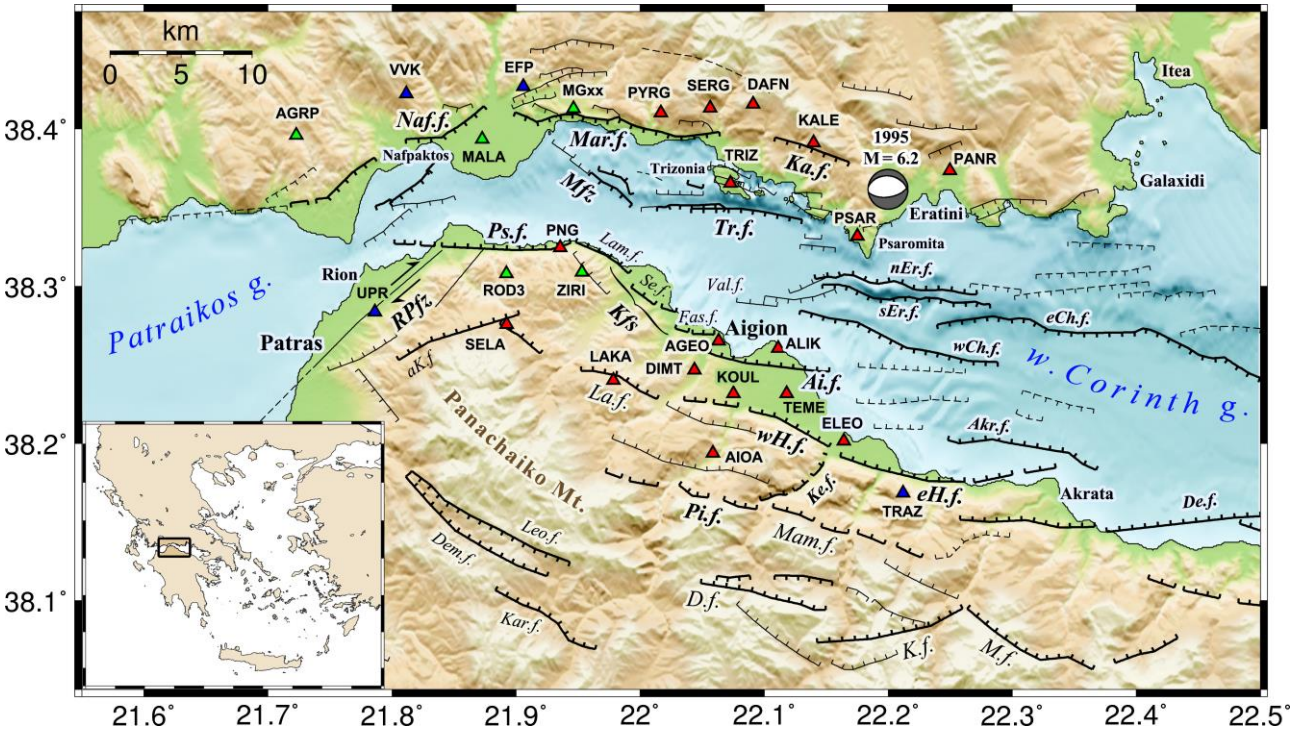

Figure 6.1: The western Corinth Rift covered by the Corinth Rift Laboratory (CRL) seismological network (red triangles: period 2000-2007, green triangles: additional stations in later periods) and HUSN stations (blue triangles). Stations which are also parts of HUSN include LAKA, KALE (University of Athens) and SERG (Charles University of Prague in collaboration with the University of Patras). MGxx represents an array of 8 stations at Managouli. The focal mechanism of the M_S=6.2 earthquake of 1995 is presented at its epicenter. Fault name abbreviations:, Dem.f.: Demesticha fault, Leo.f.: Leontio f., Kar.f.: Karousi f., D.f.: Doumena f., K.f.: Kerpini f., M.f.: Marmati f., Pi.f.: Pirgaki f., Mam.f.: Mamousia f., De.f., Derveni f., Akr.f.: Akrata f., eH.f.: east Helike f., Ke.f.: Kerinitis f., wH.f.: west Helike f., La.f.: Lakka f., aK.f.: Ano Kastritsi f., Ai.f.: Aigion f., Kfs: Kamarai fault system (Fas. f.: Fassouleika f., Se.f.: Selianitika f., Lam.f.: Lambiri f.), Ps.f.: Psathopyrgos f., RPfz: Rion-Patras fault zone, Naf.f.: Nafpaktos f., Mfz: Managouli f.z., Mar.f.: Marathias f., Tr.f.: Trizonia f., Ka.f.: Kallithea f., nEr.f.: north Eratini f., sEr.f.: south Eratini f., wCh.f.: west channel f., eCh.f.: east channel f. Fault lines are a composition of major (bold), and minor (thin) or inferred (dashed) faults after Doutsos & Poulimenos (1992), Armijo et al. (1996), Stefatos et al. (2002), Flotté et al. (2005), Bell et al. (2009), Valkaniotis (2009), Pacchiani & Lyon-Caen (2010) and Beckers et al. (2015). Digital elevation model from NASA SRTM (http://srtm.csi.cgiar.org/) and bathymetry from EMODnet (http://portal.emodnet-hydrography.eu/).

which later leaded to the development of the multidisciplinary Corinth Rift Laboratory (CRL) project (Moretti *et al.*, 2003; Avallone *et al.*, 2004; Lyon-Caen *et al.*, 2004; Bernard *et al.*, 2004, 2006).

Focused studies in the Corinth Rift have produced detailed maps revealing the most prominent local tectonic features and estimating their past activity through geomorphology and paleoseismology (Pantosti *et al.*, 2004; Koukouvelas *et al.*, 2001). High resolution bathymetry and multichannel seismic tomography has also revealed details on the geometry and kinematics of major and minor offshore structures (Brooks & Ferentinos, 1984; Stefatos *et al.*, 2002; Sakellariou *et al.*, 2003; Bell *et al.*, 2009; Beckers *et al.*, 2015). A map with the major and minor faults in the region of the western Corinth Rift is presented in Fig. 6.1, along with the local seismological stations which have been installed in the area since 2000. Information on the major faults' strike, dip and faulting type are available in Table 6.1. At the surface, their dips mainly range between 40° and 70°. Shallower dip angles ~30° are probably not newly formed, but rather constitute pre-existing weak zones which were originally dipping at ~45° and have been tilted by ~15° on a horizontal axis because of an increase in the extension rate (Hatzfeld *et al.*, 2000). Such discontinuities could also be cross-cut by younger faults, with the older structures providing weak surfaces that could, under certain conditions, slip at their current low angle. Similarly, there is evidence for slip on structures which are oblique to the rift, e.g. thrust formations along the Hellenic belt, now acting with oblique-normal slip under the current stress regime, or relay zones between the *en echelon* faults, during aftershock sequences (Rigo *et al.*, 1996) or swarms (Lyon-Caen *et al.*, 2004; Kapetanidis *et al.*, 2015). Several low-angle, north-dipping, normal focal mechanisms have been determined for events located at depths between 9.5 and 10 km, mainly in the northern part of the western Corinth Rift (Rigo *et al.* 1996; Rietbrock *et al.*, 1996). There is seismological (Hatzfeld *et al.*, 1996; Rigo *et al.*, 1996; Bernard *et al.*, 1997; Lambotte *et al.*, 2014) and geophysical evidence (Le Meur *et al.*, 1997; Pham *et al.*, 2000; Gautier *et al.*, 2006) that the younger active faults, bordering the southern shore, are rooting at a depth of 6 - 8 km beneath the gulf, in a zone which generates continuous background microseismic activity while producing the observed deformation (Bernard *et al.*, 2006). However, it is debated whether this zone is simply the result of random diffuse deformation caused by the brittle-ductile transition (Hatzfeld *et al.*, 2000), or it comprises a detachment zone (Rigo *et al.*, 1996) or it is a weak seismogenic layer which has not yet degenerated into a single low-angle fault while an immature north-dipping detachment has been growing in the north (Lambotte *et al.*, 2014).

In the present study, a large dataset of waveform recordings from the seismicity of the western Corinth Rift during 2000-2007 is analysed. The general workflow that was followed for the data processing is briefly described in the following steps:

- Creation of a proper data structure
- Examination of the data quality and stations' State of Health (SoH)
- Manual or automatic picking of P- and S-wave arrival-times
- Gross division to spatial groups per year.
- Calculation and application of station corrections per spatial group.
- Determination of multiplets.

- Double-difference relocation.
- Calculation of seismic moment magnitude.
- Determination of first-motion polarities.
- Determination of corrections to the polarity of vertical components.
- Determination of corrections to the orientation of the horizontal components (borehole stations).
- Automatic estimation of composite focal mechanisms per multiplet.
- Automatic estimation of single focal mechanisms for the largest events.

The initial purpose is the creation of a catalogue of relocated hypocenters and a database of composite or simple focal mechanisms for events that cover all activated parts of the study area. The examination of their spatial distribution will enable a detailed seismotectonic analysis that

Table 6.1: Brief fault geometry information. Dip refers to measured fault dip angle at the surface. NF stands for normal and NS for oblique-normal faulting (dextral or sinistral).

Full name	Abbrev.	Strike	Dip (deg)	Faulting	Reference(s)
Aigion	Ai.f.	289	60 NNE	NF	[3,8]
Akrata	Akr.f.	280	60 N	NF	[1]
Doumena	D.f.	281	75 NNE	NF	[3]
East Helike	eH.f.	278	50-75 NNE	NF	[3]
Fasouleika	Fas.f.	285	70 NNE	NF	[3]
Kallithea	Ka.f.	109	SSW	NF	
Kerinitis (near Pi.f.)	Ke.f.	242	70 NW	NS (dex.)	[3]
Kerinitis (foc.mec.)	>>	220	40 NW	NS (dex.)	[6]
Lakka	La.f.	277-305	65-70 NNE	NF	[3]
Lambiri	Lam.f.	300	NE	NF	
Mamousia	Mam.f.	283	70 NNE	NF	[3]
Managouli f.z.	Mfz	126/306	64-72 SW/?NE	NS (sin.)	[2]
Marathias	Mar.f.	98	55 S	NF	[5]
North Eratini	nEr.f.	277	60 N or 39-52 N	NF	[1,2]
Pirgaki	Pi.f.	280	50-70 NNE	NF	[3]
Psathopyrgos	Ps.f.	270	50 N	NF	[7]
Rion-Patras f.z.	RPFZ	220-228	NW	NS (dex.)	[2]
Selianitika	Se.f.	300	70 NE	NF	[3]
South Eratini	sEr.f.	97	50-60 S or 55-74 S	NF	[1,2]
Trizonia	Tr.f.	96	64-72 S	NF	[2]
Valimitika	Val.f.	290	N	NF	[4]
West Channel	wCh.f.	106	45-60 S	NF	[1]
West Helike	wH.f.	285	50 NNE	NF	[3]

References: [1] Bell *et al.* (2008), [2] Beckers *et al.* (2005), [3] Ghisetti & Vezzani (2005), [4] Stefatos *et al.* (2002), [5] Gallousi & Koukouvelas (2007), [6] Zahradnik *et al.* (2004), [7] Bell *et al.* (2009), [8] Cornet *et al.* (2004).

could reveal possible relations of the seismically activated structures at depth with known tectonic features at the surface or uncover the existence of blind active faults or other minor local features. It can also provide information on places where the stress-field might exhibit local perturbations that could induce activity on minor structures, especially in areas which are likely more fragmented. Spatio-temporal analysis can bring out clustering or migration patterns which can give insights on the dynamics of the deformation process and the possible role of fluids. Spatial mapping of the *b*-value of the frequency-magnitude distribution can reveal areas which are probably more fragmented or likely to creep as well as the location of possible asperities. Finally, the modeling of the magnitude-dependent seismicity rates can indicate whether the observed seismicity can be described as a residual point process, controlled by stress transfer, or there is a significant degree of non-stationary external forcing which modifies the earthquake productivity.

6.2 Data availability / preparation

The available data from the Corinth Rift Laboratory network begin around 16-20 May 2000 with 4 stations (ALIK, KOUL, PSAR and TEME). During the following months, data from more stations gradually became available, reaching a total of 12 stations by the beginning of 2001. At the southern part of the western Corinth Rift many stations are installed in boreholes, which helps to reduce the noise, as the upper ground layer consists mostly of soft soils. However, this renders the orientation of the horizontal components unknown. The waveforms were already archived in a structure of SAC files per detected event. Available data also include files with P- and S-wave arrival times per detected event, including a few manual, but mostly automatic ones for the years 2002-2007. However, the latter have to be strongly re-evaluated.

Waveform data were re-structured to a typical directory structure that has also been formulated for event files from HUSN in the Seismological Laboratory of the University of Athens (yyyy/mm/dd/yyyy-mm-dd-HH-MM-SS). Events are labeled after an "event-code", roughly related to the origin time, which is used for the filenames of phase/catalogue files per-event and to link them with the corresponding waveform data. The original 3-letter CRL-net station codes were also renamed to match their current officially registered 4-letter codes. The sampling frequency, F_s, in all data is normally at F_s = 125 sps. However, several changes to the F_s have been occasionally observed. This is problematic for procedures such as cross-correlation, which require a common sampling rate between the compared time-series. For this reason, any waveforms with different F_s were resampled to 125 sps (except for SERG, whose typical F_s is 100 sps) by cubic interpolation.

The 3 components of each station were visually examined in several sub-periods to obtain information on their state-of-health. This is very important, as any automatic picking or cross-correlation algorithm must be informed on whether a component is working properly or must be ignored to avoid miscalculations. Some components of borehole stations were flagged as damaged for most part of the period of study. Another problem which was observed is the issue of periodic spikes which affected some stations during some periods. A special filter (Appendix A.6 in Kapetanidis, 2007) must be applied in these cases to enable more valid cross-correlation measurements and auto-picking attempts. The results of the stations' state-of-health examination are

presented in Fig. 6B.1 (Appendix 6B). Some marked as "noisy" could be contemporary (low SNR for a certain event), so only persistently noisy components are flagged as "damaged".

The location algorithm Hypo-Inverse was employed for the calculation of the hypocentral coordinates, origin time and travel-times. The mean arrival-time reading error, which affects location error estimates, was set to 0.2 sec, to account for possibly large errors in some automatic picks. Trial depth was set to 8 km. The 1D velocity model of Rigo *et al.* (1996) was used for compliance with other studies in this area. Distance weighting was configured to start dropping from 13 to ~40 km (3·13km) with a cosine taper, unless the second closer station is located at an epicentral distance D_2>13 km, in which case the weight begins reducing from D_2 and up to $3 \cdot D_2$.

6.2.1 Arrival-time data

A quick look to the initial data reveals that there are large location uncertainties in years 2002-2007, as the arrival-times were derived from a simple automatic picking algorithm. By observing the waveform data it also appears that a significant portion of detected signals belong to events at regional distances, which however have been mis-located inside the western Corinth Rift. Because of the large number of events (~60000 during this 7 and a half year period), an automatic processing approach was devised to reduce the portion of events that would require manual analysis. The procedures involved take advantage of methodologies which were described in previous chapters, such as spatial group clustering, the HADAES method and the AIC picker.

For easier management, the dataset was divided by year. Several attempts to obtain automatic solutions were made, taking advantage of the already available information.

1. For years 2002-2007, taking into account the initial preliminary automatic solutions, the theoretical arrival-times of P- and S-waves in all available stations were used to guide a simple AIC-picker procedure. This helped to confirm, reject, improve or add extra arrival-times to the dataset.
2. A set of best resolved events, regarding their RMS errors and location uncertainties, were selected as master-events for the application of the HADAES method. This excludes the event-detection part of HADAES, as a relevant procedure has already been run for the creation of the dataset.
3. The HADAES method was repeated using several reference stations at both southern and northern parts of the western Corinth Rift. As multiple automatic solutions became available for the same events, the best results were selected by preferring those with the smaller location uncertainties.
4. The AIC-picker procedure was re-run several times, iteratively, to re-pick the arrival-times guided by their updated theoretical values.
5. All resolved events' waveforms were visually inspected to ensure that the P- and S-wave arrival-times at the three closest stations were picked with enough accuracy and minimal travel-time residual to ensure a valid location. Problematically picked events were flagged for manual re-picking. Cases of events with mis-picked waveforms included:

   a. Very noisy signals.
   b. Double or multiple events with partially or completely super-imposed waveforms.
   c. Mis-picked P- or S-waves. This is the case when the calculated arrival-time of an S-wave is too close to the P-wave onset. The AIC-picker may accidentally pick the P-wave and mark it as the arrival-time of the S-wave while the algorithm searches for a P-wave arrival within the preceding noise.
   d. Events at regional distances which have been detected and erroneously located within the area of study. Such events can be completely removed from the dataset.
6. A simple STA/LTA procedure was also run for the remaining unresolved events to determine candidate P-arrival times. Reverse STA/LTA was used for approximate S-arrival times. Then the AIC picker was applied to determine valid picks and their respective weights.
7. A manageable number of events for manual re-picking were randomly selected from regions where the automatic solutions reveal the existence of clustered activity but no manually picked events were previously available.
8. All manually picked events can be used as master-events in a last attempt to pick and locate the remaining unresolved data. The HADAES method can be configured to use all individual master-events instead of selecting one master-event from each of the determined multiplets. This increases the processing time but also the chance of a successful match.
9. Step #4 was repeated for the remaining automatically resolved events.
10. The final catalogue was cross-checked with public databases, including the National Observatory of Athens, EMSC and the catalogue of Makropoulos *et al.* (2012), to ensure that events of relatively larger magnitude within the area of study have been successfully picked and located.

6.3 Spatial clustering, Multiplet classification and Relocation

The 30x30 km^2 area covered by the CRL network in the western Corinth Rift includes several sub-regions of strongly clustered microseismic activity. To improve the hypocentral locations, the spatial distribution has to be divided in groups that should be processed separately. For the seismicity of each year, the inter-event hypocentral distance was calculated for all pairs of events, thus constructing a Euclidean distance matrix. Ward's linkage was applied to create a clustering hierarchy and the "scree plot" (Section 1.2.2) was considered to decide the number of spatial clusters that is most appropriate. The following procedures were then followed for each of the resulting clusters.

The P- and S-wave travel-time residuals at each station were calculated and their median value was reckoned as a station-correction. These values are subtracted by 80% directly from the respective P- and S-wave arrival-times, under the condition that an event has at least 7 such measurements. This step produces corrected travel-times but it also slightly affects the origin time. The hypocentral locations and travel-times derived from this procedure are later taken into account as initial locations and catalogue data during the double-difference relocation that follows. However, the initial arrival-times are strictly used for all cross-correlation measurements. An approximate origin

time correction can be considered in the final catalogue, depending on the bias caused by the modified arrival-times at the available phases of each event.

Further on, a reference station is selected for each group. The criteria include:

- Proximity to the epicentral area.
- Availability of picked arrival-times.
- State of Health (SoH).

While the proximity is a very important factor for the selection of a reference station, in case multiple stations have a comparable average epicentral distance the one with the largest total number of picks is preferred, provided its SoH is also acceptable.

A combined cross-correlation matrix is created at the reference station using all available components. Nearest neighbor linkage is applied and a threshold, C_{th}, is selected according to the value that maximizes the difference between the size of the largest multiplet and the sum of clustered events (Section 1.2.2), with a minimum allowed value of 0.6 to ensure an adequate degree of similarity. Cross-correlation measurements are then taken for all P- and S-waves at all stations and operable components according to their SoH information. XC_{max} and t_{max} values are registered in the dt.cc file for HypoDD, while travel-time and hypocentral information from the dataset corrected for systematic residuals is written to an input file for the ph2dt program.

The double-difference relocation procedure is performed for each spatial group separately by calibrating the configuration individually, depending on the geometry of the corresponding spatial distribution. That is:

- the total epicentral area covered,
- whether a group consists of one or more large-scale clusters,
- whether it contains several small-scale multiplets,
- the dimensions of the multiplets compared to the general distance between their centroids,
- the total number of events in the group.

The preferred configuration is usually a compromise between maintaining most of the events of the initial catalogue down to the last iteration and achieving a stable relative relocation with minimal origin shift of the centroids. In sparse groups which, however, contain a large number of small clusters, or otherwise groups which could be further divided in a small number of larger sub-clusters, the build-in clustering algorithm of HypoDD was also taken into account to break weak links between sub-clusters and improve the inversion. The same was also performed in groups with a large number of events in order to reveal details within the initial seismic cloud. However, this also greatly reduces the percentage of relocated events, as many become isolated due to their small number of available observations. The results of the 4 basic steps (preliminary/initial, re-picked, application of station corrections and relocation) for the seismicity of each year are presented collectively in figures and tables at the Appendix 6B (Figs. 6B.3-10, Tables 6B.1-8). The enumeration of spatial groups in Sections 6.3.1 to 6.3.8 is mainly temporary, with their scope limited to their own sub-section. “Global” spatial groups as defined in Section 6.3.9, covering the whole 2000-2007 seismicity, will be used as reference in the rest of the Chapter.

6.3.1 Seismicity of 2000 (23 May – …)

The available data begin on 16 May 2000, starting with station ALIK, soon joined by stations KOUL, PSAR, TEME, AIOA and TRIZ. However, reliable solutions are typically available after 23 May 2000. The seismicity was initially split in a total of 8 spatial groups. However, because of large errors it was not possible to achieve reliable relocation in 2 of the groups, so they were omitted from the rest of the procedures and are not described henceforward. The relocated epicenters for the 6 remaining groups are presented in Fig. 6.2. PSAR and KOUL were selected as reference stations to cover the seismicity at the northern and southern shoulder of the rift, respectively (Table 6.2). Details on the calculation of seismic magnitudes which are mentioned henceforth are described in Section 6.4.

The seismicity in 2000 is mainly characterized by two clusters, within the same spatial group (#1), east of Trizonia island. They were likely triggered by an M_L=4.6 event that occurred on 27 April 2000 in about the same region. However, their temporal distribution shows that they occurred on two discrete intervals, the southern one between 19 and 21 June, including an M_w=3.1 event on 20 June, while the northern one between 29 June and 2 July 2000, with the largest event on 30 June (M_w=3.6). The strongest event occurred on 22 August 2000, with M_w=3.7, near Sergoula. Another, smaller cluster (Group #5) is located west of Trizonia. A notable small cluster appeared within Patraikos gulf (Group #2) and another near Sela. The rest is mostly sparse seismicity, including the region around Eratini (Group #6), which is of particular interest, as it overlaps with part of the aftershock sequence of the major M_s=6.2 earthquake of 1995 (Fig. 6.1) and also marks some of the deeper activity of the rift, with depths at about 10-11 km.

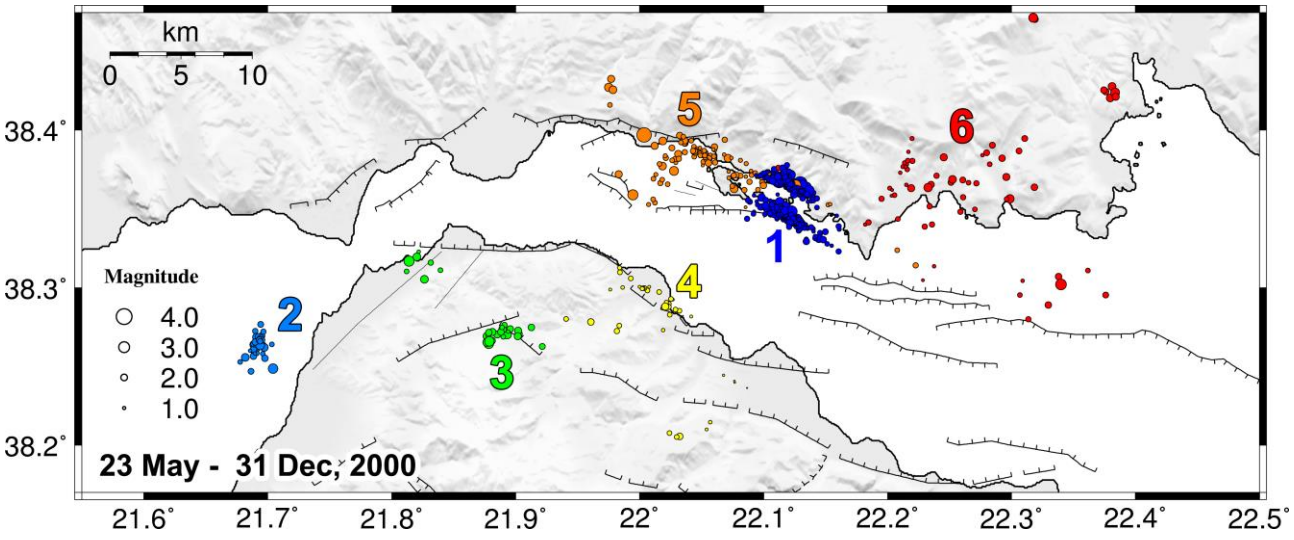

Figure 6.2: Relocated epicenters in the western Corinth Rift for year 2000. Colours and numbers correspond to the 6 spatial groups (Tables 6.2 and 6B.1) on which station corrections, multiplet classification and relocation were separately performed.

An example of similar waveforms from selected multiplets of Groups #1 (southern and northern clusters) and #2 are presented in Fig. 6B.2. For Group #2, despite being completely outside of the network, it was possible to perform relocation and reduce the relative location uncertainties due to the fact that it occurred as a spatiotemporal cluster with enough waveform similarity for cross-correlation data to constrain the relative locations, up to some degree.

Table 6.2: Information on multiplet classification per spatial group for the seismicity of year 2000 in the western Corinth Rift.

Group	Ref. Station	Comp.	avg. Dist. (km)	# evt	# phases	C_{th}	# mult.	# evt in mult.	largest mult.	# reloc
1	PSAR	ENZ	5.9	797	786	0.60	42	639	266	415
2	KOUL	EN	33.9	48	41	0.60	3	30	19	36
3	KOUL	EN	19.9	63	59	0.75	4	18	7	30
4	KOUL	EN	7.6	72	68	0.80	10	33	8	43
5	PSAR	ENZ	13.8	428	416	0.60	57	231	30	112
6	PSAR	ENZ	10.2	120	120	0.60	16	50	7	67

6.3.2 Seismicity of 2001

In 2001, waveform data were available from about 12 stations of CRLnet, increasing detectability and resolvability. A more typical distribution of the background activity inside the western Corinth gulf can be observed, with sparse seismicity, which however contains several small multiplets, offshore between Aigion and Trizonia (Fig. 6.3). The most significant sequence in 2001 was a seismic swarm (Group #5), in the vicinity of Ayios Ioannis station, AIOA (or AIO) that began around 25 March 2001 and its most intense part lasted for ~85-100 days. The swarm, briefly termed as the "2001 AIO swarm", is examined in more detailed in Section 6.6.1. Some small clusters were also located far outside of the network, SW of the swarm. Sparse seismicity is also observed near Sergoula (SERG station) and inland towards Pyrgos (PYRG station). The largest earthquake (M_w=4.1) occurred on 8 April 2001, 06:12 within the swarm of Ayios Ioannis, which also included a couple of M_w≈3.8-3.9 on 31 May and 1 June. Another M_w=3.8 event occurred in Group #3, west of Nafpaktos, on 24 December 2001.

It should be noted that the location errors of earthquakes in the out-of-network region of Group #3 are significant (Table 6.3). Unless an important spatiotemporal cluster occurs (e.g. Group #2 of 2000, in Patraikos gulf), the relocation procedure can only work using catalogue data, with limited efficiency. The largest uncertainties, as expected, are found in the focal depths, which are mostly fixed at 10 km to enable more stable solutions for the epicenters.

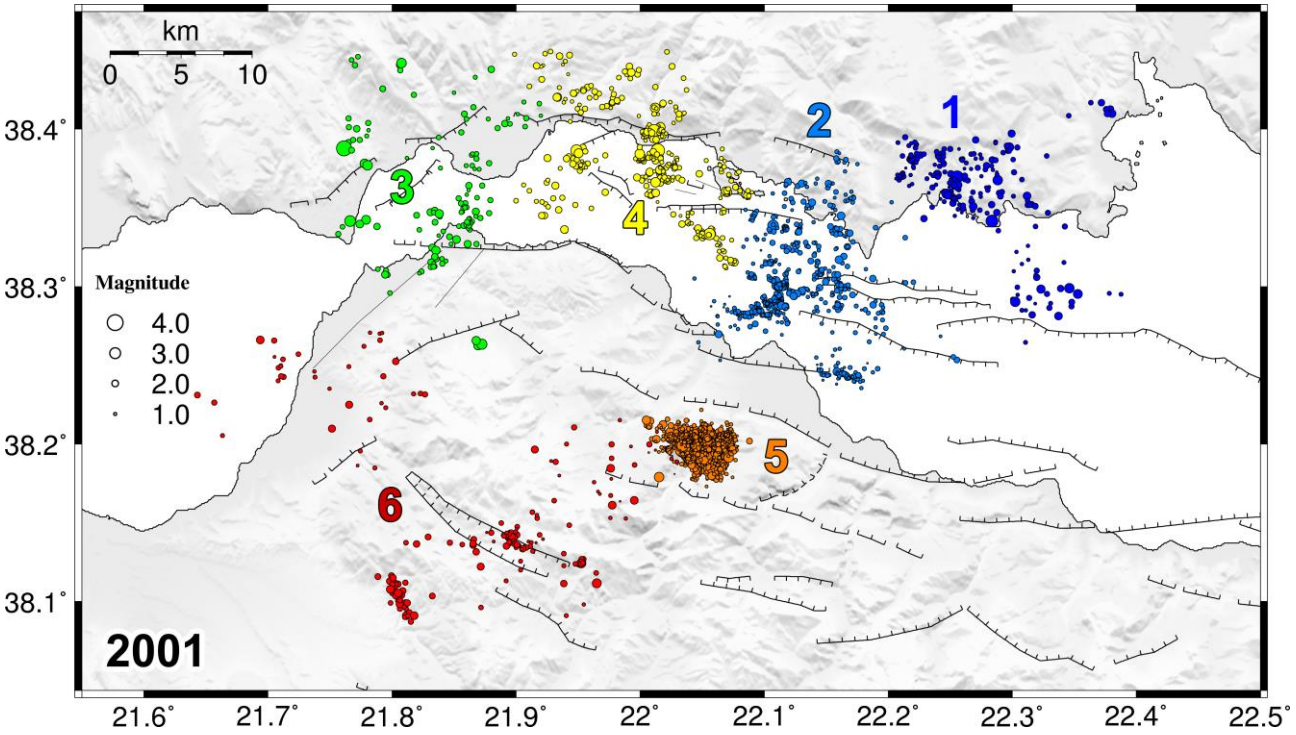

Figure 6.3: Same as Fig. 6.2, but for the seismicity of year 2001. Details on the 6 spatial groups are presented in Tables 6.3 and 6B.2.

Table 6.3: Information on multiplet classification per spatial group for the seismicity of year 2001 in the western Corinth Rift.

Group	Ref. Station	Comp.	avg. Dist. (km)	# evt	# phases	C_{th}	# mult.	# evt in mult.	largest mult.	# reloc
1	PSAR	ENZ	9.6	240	238	0.66	27	128	20	233
2	PSAR	ENZ	6.5	977	937	0.64	115	677	61	706
3	TRIZ	ENZ	21.0	303	276	0.60	32	120	24	131
4	TRIZ	ENZ	7.6	743	646	0.62	76	495	42	380
5	DIMT	EZ	5.5	2751	2612	0.88	179	1845	217	2257
6	DIMT	EZ	20.3	219	201	0.60	18	150	49	187

6.3.3 Seismicity of 2002

In 2002, the activity is spread all around the study area in several small clusters, including some remaining seismicity in the area of the Ayios Ioannis swarm (Group #5) on 9-10 February and a few short outbreaks within the gulf. The largest events occurred on 27 January 2002 (M_w=3.7) and on 7 July 2002 (M_w=3.6) at Group #6 and #1, respectively, while another M_w=3.7 on 21 February followed by an M_w=3.6 three days later, occurred in Group #4. However, these were not directly related to a significant subsequent increase of activity. On the other hand, the most intense outburst was detected in the timespan of 10 to 16 January, with a spatiotemporal cluster near Psathopyrgos (Group #4) continuing from some similar activity in late 2001, and mid-gulf, between Aigion and Psaromita (PSAR station) in the period 4 – 12 September, 2002. Another activity of

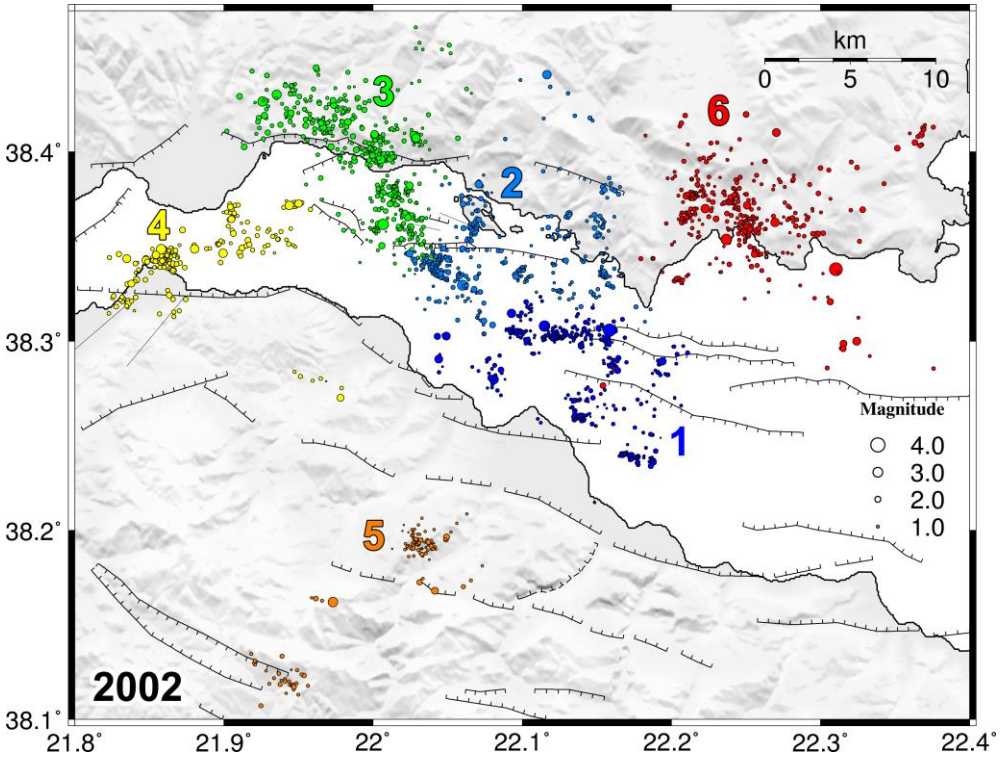

Figure 6.4: Same as Fig. 6.2, but for the seismicity of year 2002. Details on the 6 spatial groups are presented in Tables 6.4 and 6B.3.

Table 6.4: Information on multiplet classification per spatial group for the seismicity of year 2002 in the western Corinth Rift.

Group	Ref. Station	Comp.	avg. Dist. (km)	# evt	# phases	C_{th}	# mult.	# evt in mult.	largest mult.	# reloc
1	PSAR	ENZ	6.8	480	464	0.64	56	364	62	446
2	PSAR	ENZ	8.5	503	489	0.67	76	345	36	485
3	TRIZ	ENZ	8.0	498	454	0.61	67	343	22	476
4	DIMT	EZ	18.7	416	400	0.60	39	339	105	193
5	KOUL	E	9.1	141	141	0.66	12	110	28	121
6	PSAR	ENZ	7.9	397	387	0.66	40	267	47	389

particular interest began in 20 November in Group #4 and lasted until the end of 2002, including an M_w=3.5 event on 3 December 2002. The latter was related to a transient strain anomaly observed at the station of Trizonia Island about 15 km NW (Bernard *et al.*, 2004).

6.3.4 Seismicity of 2003

In year 2003 the most important pattern was a sequence of clusters in a 20-25 km, NW-SE extent, mid-gulf (Groups #5, #4 and #8). It was initiated on 6 January with some diffuse events in Group #8, followed by clustered activity on 12 – 18 and 27 – 30 January in the same region, while sparse seismicity was observed in Group #5. Activity in Group #5, at the NW end, intensified with a couple of spatiotemporal clusters on 2-7 February and 3-6 March, 2003. While the spatial extend of Group #5 seems larger, Group #8 actually contains more events, albeit concentrated in 2 dense, distinct clusters and a couple smaller ones. The strongest events were an M_w=4.2 that occurred on 18 November near Efpalio (Group #2) and an M_w=3.8 on 31 October (Group #6). Sparse seismicity persisted in the vicinity of Eratini (Group #9), offshore Sergoula (Group #1) and towards Efpalio (Group #2), while a small cluster (Group #7) was observed in the region of the 2001 AIO swarm, between 24 and 27 January, 2003.

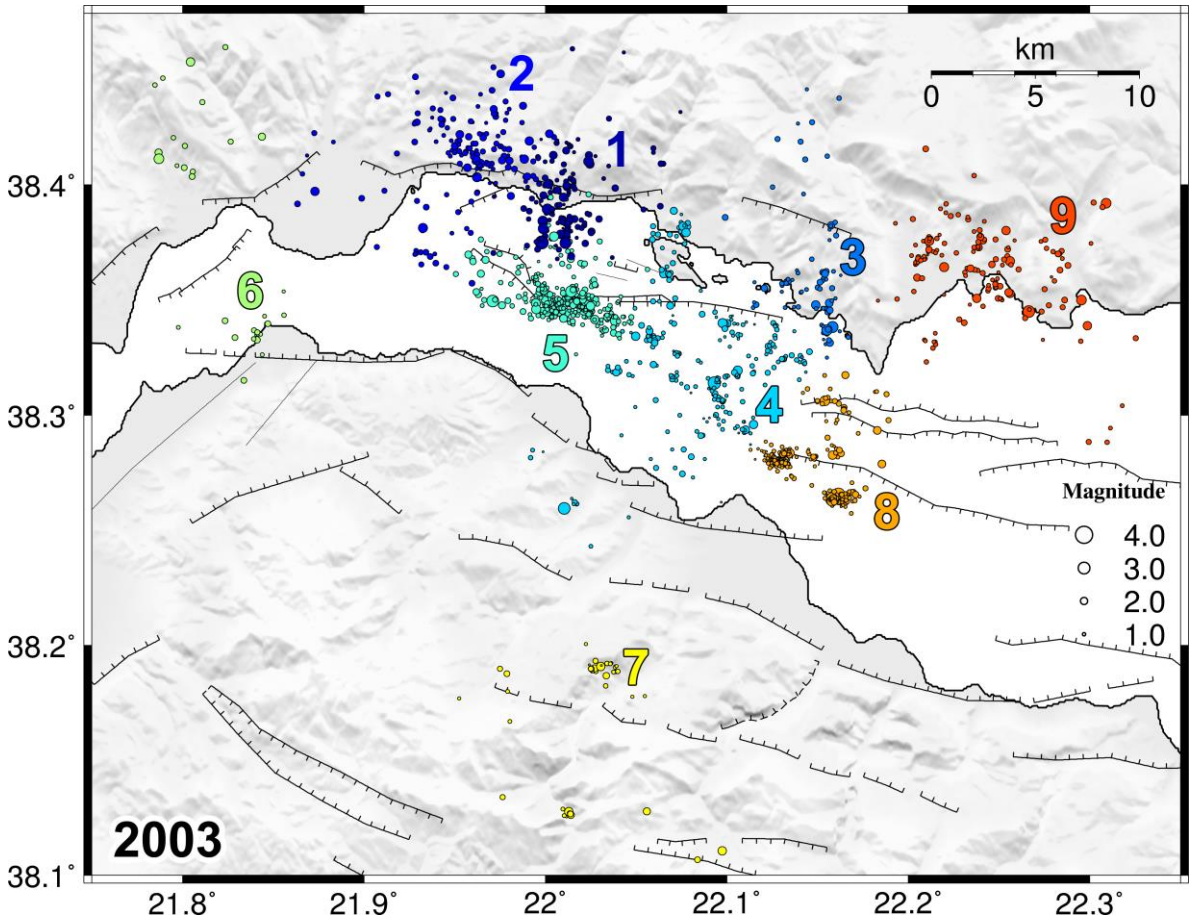

Figure 6.5: Same as Fig. 6.2, but for the seismicity of year 2003. Details on the 9 spatial groups are presented in Tables 6.5 and 6B.4.

Table 6.5: Information on multiplet classification per spatial group for the seismicity of year 2003 in the western Corinth Rift.

Group	Ref. Station	Comp.	avg. Dist. (km)	# evt	# phases	C_{th}	# mult.	# evt in mult.	largest mult.	# reloc
1	TRIZ	ENZ	6.4	151	120	0.69	18	87	13	142
2	TRIZ	ENZ	11.8	161	133	0.71	21	78	16	152
3	PSAR	ENZ	4.4	90	85	0.60	12	58	16	86
4	ALIK	EN	7.9	264	258	0.69	35	184	37	262
5	AGEO	EZ	10.6	380	337	0.60	35	218	30	374
6	AGEO	EZ	23.9	38	29	0.60	4	16	10	31
7	AIOA	ENZ	4.9	49	49	0.60	7	37	10	43
8	ALIK	EN	4.4	491	486	0.64	27	442	167	402
9	PSAR	ENZ	7.4	157	153	0.64	21	96	16	153

6.3.5 Seismicity of 2004

In 2004, a significant pattern of spatiotemporal clusters occurred within the gulf. Combined with the 2003 activity, it will be analysed in more detail in Section 6.6.2 as a swarm sequence. It is mainly divided in Groups #4 and #5, with the largest events being two $M_w \approx 3.5$ on 2 and 6 March, respectively. Other relatively major events include another $M_w=3.4$ on 3 March, west of Sergoula (Group #2), an $M_w=3.5$ event on 24 May in the Eratini region (Group #6) and an $M_w=3.8$ event in the Rio straits (Group #3). An $M_w=3.3$ event on 16 September is related to spatiotemporally clustered activity in Group #8, south of the 2001 AIO swarm region, at the relatively large mean focal depth of ~10 km. The activity in Group #8 occurred in two outbursts on 14 August and between 10 and 17 September, 2004. Group #7 in Patraikos gulf also exhibited clustered activity in the period 14 – 18 October, 2004.

Table 6.6: Information on multiplet classification per spatial group for the seismicity of year 2004 in the western Corinth Rift.

Group	Ref. Station	Comp.	avg. Dist. (km)	# evt	# phases	C_{th}	# mult.	# evt in mult.	largest mult.	# reloc
1	TRIZ	ENZ	12.3	203	169	0.73	22	103	21	194
2	TRIZ	ENZ	5.3	410	359	0.79	50	274	31	401
3	TRIZ	ENZ	14.6	123	112	0.75	16	77	9	109
4	DIMT	EZ	7.6	1040	977	0.73	80	749	135	993
5	PSAR	ENZ	5.7	915	868	0.65	92	738	93	870
6	PANR	ENZ	3.3	239	223	0.71	22	140	47	237
7	AIOA	ENZ	30.3	119	117	0.73	13	96	25	102
8	TEME	E	10.0	388	388	0.76	42	303	107	221

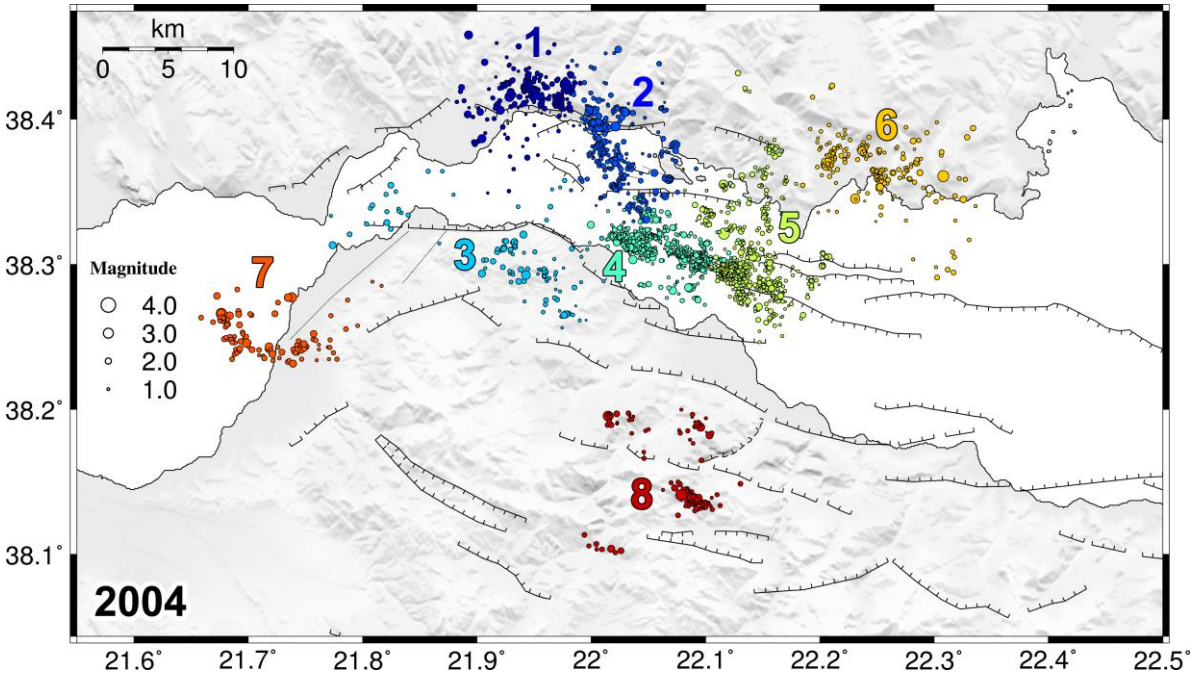

Figure 6.6: Same as Fig. 6.2, but for the seismicity of year 2004. Details on the 8 spatial groups are presented in Tables 6.6 and 6B.5.

6.3.6 Seismicity of 2005

A significant drop in the detected seismic activity was observed in year 2005. The available data show a sparse distribution of very small multiplets throughout the region. The most significant events occurred near Psathopyrgos (Group #9). However the largest was an M_w=4.0 event that occurred offshore Selianitika (Group #2) on 12 November.

Table 6.7: Information on multiplet classification per spatial group for the seismicity of year 2005 in the western Corinth Rift.

Group	Ref. Station	Comp.	avg. Dist. (km)	# evt	# phases	C_{th}	# mult.	# evt in mult.	largest mult.	# reloc
1	AGEO	EZ	7.6	78	76	0.60	10	49	18	78
2	AGEO	EZ	7.3	91	88	0.61	8	39	14	88
3	AGEO	EZ	14.6	78	72	0.61	7	38	20	77
4	AGEO	EZ	17.8	84	79	0.60	14	49	12	73
5	AGEO	EZ	15.5	10	10	0.79	2	7	4	9
6	AGEO	EZ	4.3	61	61	0.60	6	31	13	60
7	PSAR	ENZ	5.2	164	164	0.60	27	103	12	64
8	PSAR	ENZ	7.0	77	75	0.60	12	35	6	72
9	DIMT	EZ	18.1	80	79	0.86	13	44	5	69
10	PSAR	ENZ	8.1	77	77	0.64	10	44	11	75

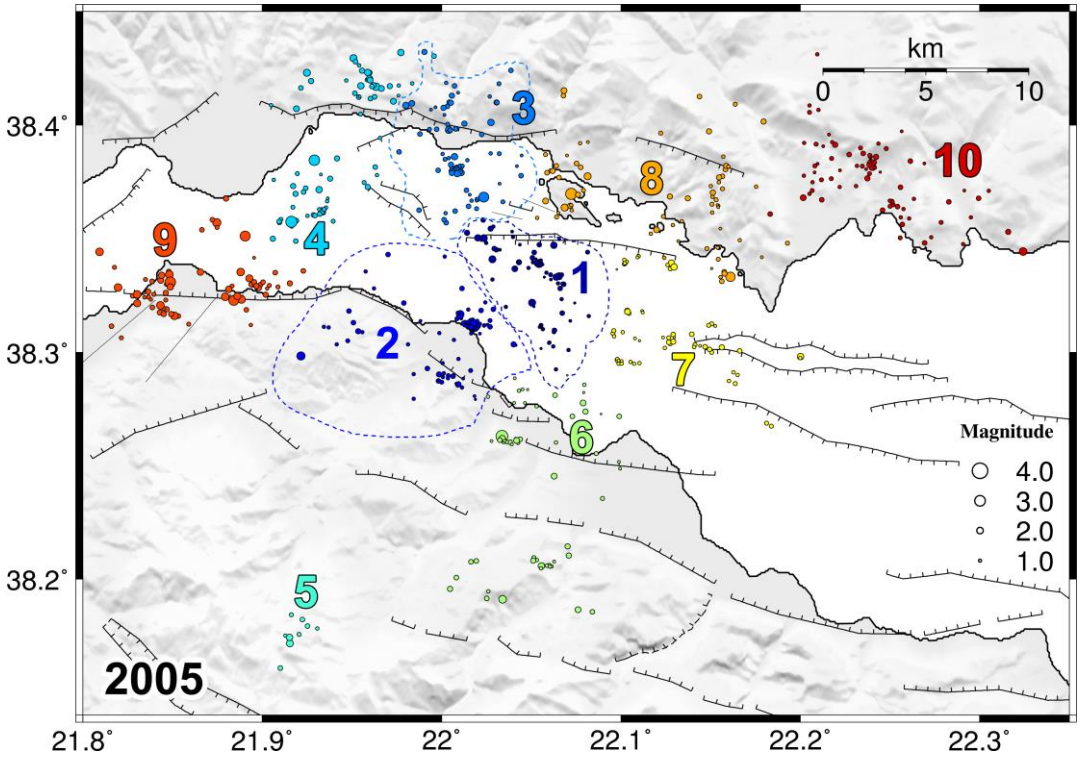

Figure 6.7: Same as Fig. 6.2, but for the seismicity of year 2005. Details on the 10 spatial groups are presented in Tables 6.7 and 6B.6.

6.3.7 Seismicity of 2006

Year 2006 was characterized by a significant cluster mid-gulf (group #7) in the period 19 February – 20 March, initiated by an M_w=3.0 event on 19 February, including an M_w=3.2 event on 20 February. Also, an intense sequence (Group #6) began on 19 October with an M_w=3.2 event, followed by an M_w=3.6 event on 21 October, and persisted through 2007 in approximately the same area. The 2006-2007 sequence will be discussed in more detail in Section 6.6.3.

Table 6.8: Information on multiplet classification per spatial group for the seismicity of year 2006 in the western Corinth Rift.

Group	Ref. Station	Comp.	avg. Dist. (km)	# evt	# phases	C_{th}	# mult.	# evt in mult.	largest mult.	# reloc
1	DIMT	EZ	4.1	81	78	0.60	14	56	19	78
2	TRIZ	ENZ	5.8	1679	1505	0.60	77	827	239	717
3	PSAR	ENZ	4.9	325	324	0.75	37	209	39	280
4	PSAR	ENZ	3.7	280	280	0.76	43	184	35	237
5	AIOA	ENZ	6.7	53	53	0.60	7	27	6	26
6	TRIZ	ENZ	8.5	1330	1289	0.87	122	552	50	1216
7	TRIZ	ENZ	4.2	1113	1044	0.61	57	827	304	1011
8	PSAR	ENZ	7.8	186	186	0.64	27	154	38	136

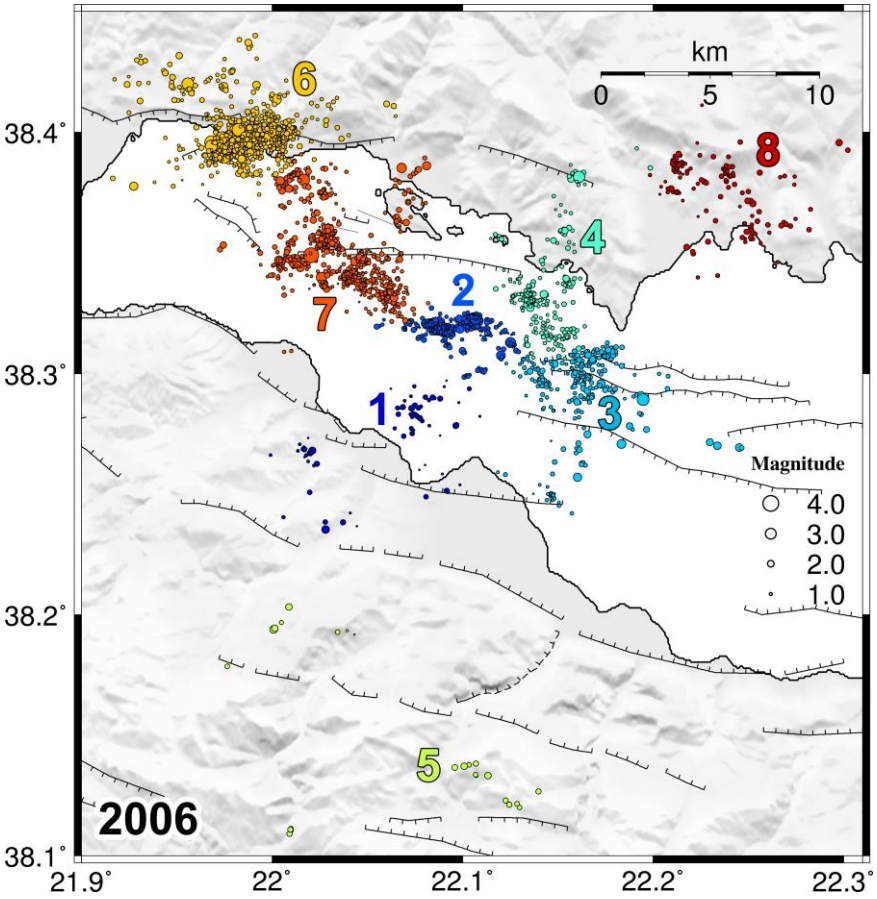

Figure 6.8: Same as Fig. 6.2, but for the seismicity of year 2006. Details on the 8 spatial groups are presented in Tables 6.8 and 6B.7.

6.3.8 Seismicity of 2007

Year 2007 began with a very intense spatiotemporal cluster on 7 January, including an M_w=3.6 event in Group #6 (near Sergoula), lasting for ~9 days, with simultaneous activation of two distinct clusters in Group #2, mid-gulf. The largest event (M_w=3.8) occurred on 19 March in Group #6. Group #4, in between, was mostly active between 15 April and 3 May, 2007, following an M_w=3.2 on 15 April and an M_w=3.6 on the following day. Two spatial clusters were detected in Patraikos gulf (Group #7). The one near the coast occurred on 18-25 February while the other was temporally spread in small bursts following a series of events with $M_w \geq 3.0$ between 14 April and 2 November, 2007. The earthquake swarm at Trichonis lake (Section 5A.1) occurred at about the same time (April 2007), roughly 30 km N of Patraikos gulf. It is noteworthy that an event of intermediate depth ($H \approx 60$km) occurred on 15 December, with M_w=3.8 and its epicenter north of Psaromita, while a quadruplet of intermediate depth events ($H \approx 48$km) was also detected mid-gulf, offshore Psaromita, occurring between February and October. Another intermediate depth event ($H \approx 70$km) was located beneath Patraikos gulf, on 25 May, 2007.

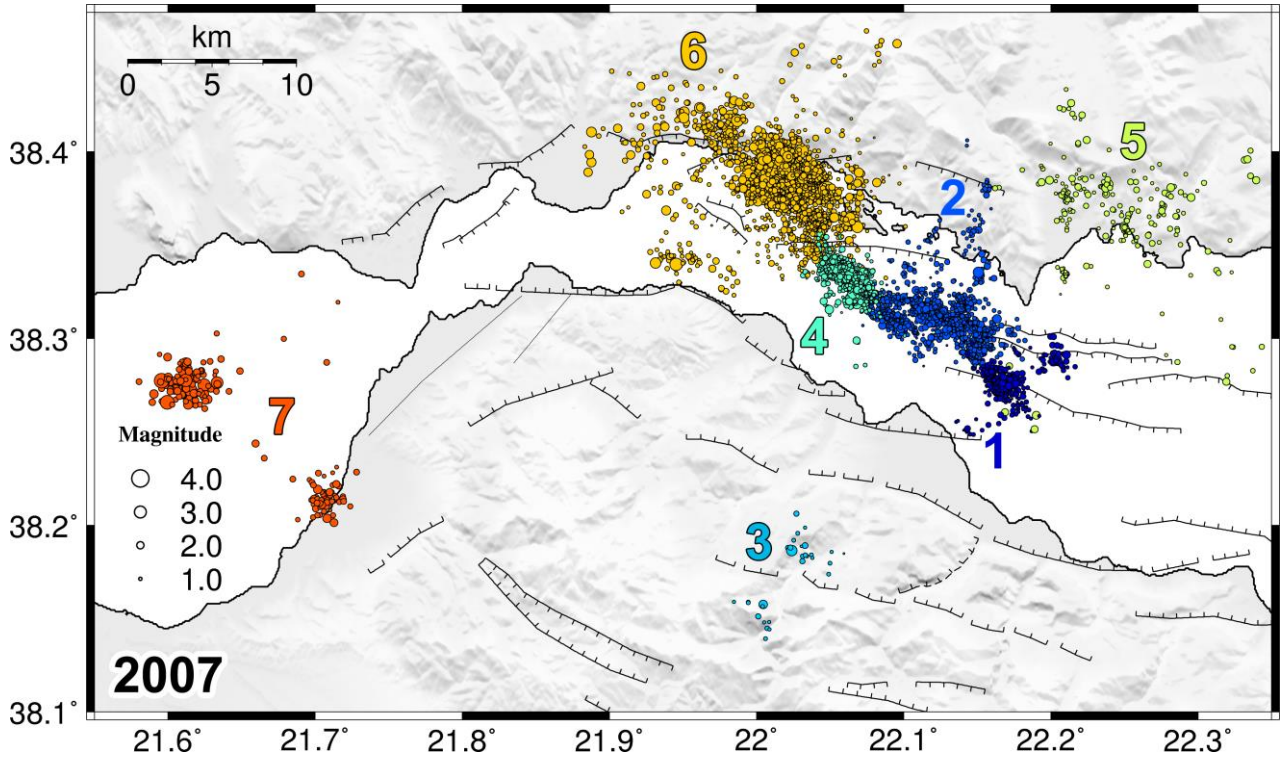

Figure 6.9: Same as Fig. 6.2, but for the seismicity of year 2007. Details on the 7 spatial groups are presented in Tables 6.9 and 6B.8.

Table 6.9: Information on multiplet classification per spatial group for the seismicity of year 2007 in the western Corinth Rift.

Group	Ref. Station	Comp.	avg. Dist. (km)	# evt	# phases	C_{th}	# mult.	# evt in mult.	largest mult.	# reloc
1	PSAR	ENZ	6.4	525	470	0.69	55	366	89	445
2	PSAR	ENZ	5.6	1678	1261	0.67	146	1014	139	1406
3	KOUL	E	8.2	67	64	0.60	6	38	11	32
4	DIMT	EZ	9.5	1712	1660	0.72	137	1104	94	1551
5	PANR	ENZ	4.2	278	272	0.66	27	218	54	256
6	TRIZ	ENZ	5.1	4809	3960	0.83	350	2183	216	4534
7	AIOA	ENZ	36.8	314	308	0.86	32	229	21	216

6.3.9 Overview

The final relocated catalogue is composed of the individual results from the spatial groups of each year. During the relocation procedure, several events were discarded due to large errors or few/weak links with their neighboring ones which did not allow for them to be properly relocated. To ensure that major events are not excluded from the final catalogue, the initial locations were added for missing events with $M_w \geq 3.5$.

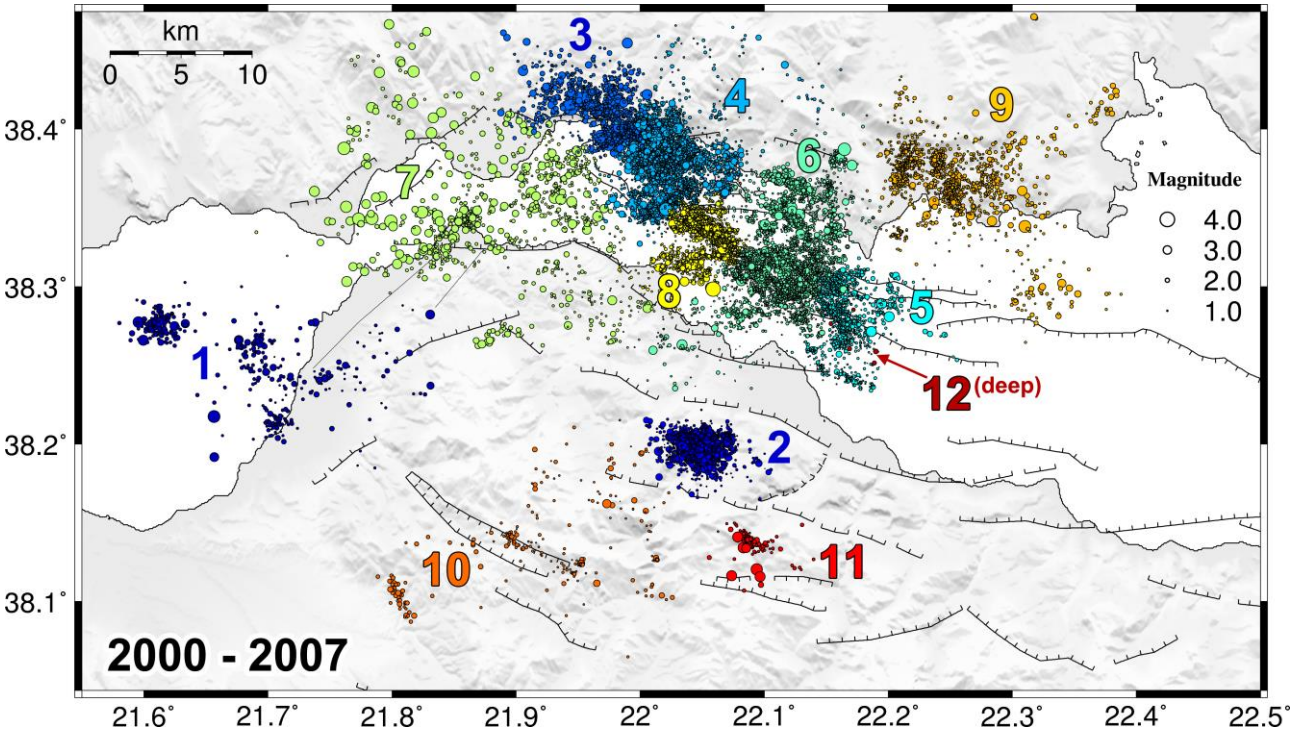

Figure 6.10: Relocated epicenters in the western Corinth Rift for the whole period of study (2000-2007). Colours and numbers correspond to 12 spatial groups determined by Ward's hierarchical clustering on the inter-event 3D distances. Group #12 is comprised of 4 events at a hypocentral depth of ~48 km and another at ~70km, separated from the rest of the seismicity.

To enable the distinction of different regions of seismic activity in the spatiotemporal and seismotectonic analysis that follows, the spatial distribution was divided into 12 groups, determined using Ward's linkage (Fig. 6.10). In summary, the groups are: 1) Patraikos gulf, 2) Ayios Ioannis 2001 swarm region, briefly called "AIO group", 3) a cluster mainly N of Marathias fault scarp, 4) south of Marathias fault, east of Group #3, 5) easternmost mid-gulf activity, 6) mid-gulf, W-NNW of Group #5, including clusters E of Trizonia island, 7) mostly sparse seismicity near Nafpaktos and Psathopyrgos-Rion, with relatively large errors, 8) mid-gulf, NE of the Kamarai fault system, 9) seismicity near Eratini, below PANR station, partially overlapping with aftershock zone of the 1995 M_s=6.2 earthquake, briefly called "Eratini group", 10) sparse clusters SW of the AIO group, 11) a cluster SSE of the AIO group and 12) a group containing 5 events at intermediate depth that occurred in 2007, four at ~48 km below Group #5 and one at ~70km below Group #1.

The focal depths generally vary between 5 and 12 km. Within the gulf, the shallower seismicity is observed N-NE of Helike and SSW of Psaromita (Fig. 6.11a). At larger depths, a low-angle seismically active layer is observed, covering the whole area of the gulf (Fig. 6.11c) which deepens towards the north, mainly NW (Fig. 6.11e-f). Group #9 is mainly concentrated deeper (8.5 – 12 km) while Group #2, in the south, is confined between 5.5 and 9 km. Interestingly, despite the bathymetry becoming deeper towards the east, the seismicity generally deepens towards WNW along the axis of the gulf. Areas with dense spatial clusters are highlighted in Fig. 6B.11. The more

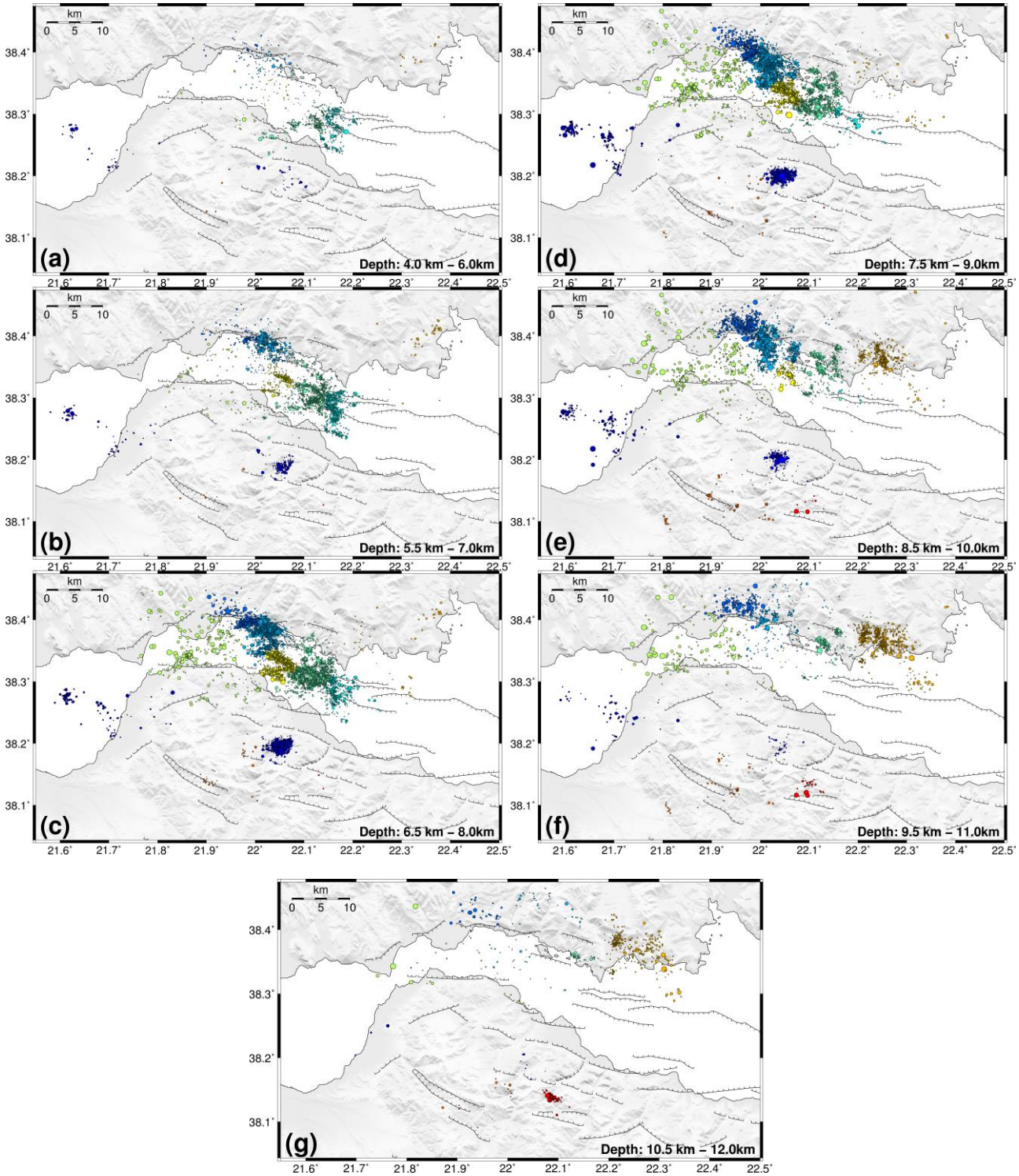

Figure 6.11: Epicenters of relocated seismicity in the western Corinth Rift for years 2000-2007 at various, partially overlapping, depth slices: a) 4-6 km, b) 5.5 – 7.0 km, c) 6.5 – 8.0 km, d) 7.5 – 9.0 km, e) 8.5 – 10.0 km, f) 9.5 – 11.0 km and g) 10.5 – 12 km.

active regions include mid-gulf between Trizonia island and Aigion (northern part of Group #8), NW and W of Trizonia island and south of Marathias fault (Groups #3 and #4). More widespread activity is observed at the eastern part, including several small clusters NE and E of Trizonia island (Group #6). Activity in Group #9, although sparse throughout the years, apparently occurs in 3 or 4 spatially limited patches.

6.4 Moment Magnitude

The methodology described in Chapter 3 was used for the estimation of seismic moment magnitude. For this purpose, a database of instrument responses was prepared, containing information about the history of changes in either the seismometer or digitizer. Corrections for systematic errors (residuals in the frequency domain and offset from the median preliminary M_w solutions) were calculated separately for the periods during which a station was operating using the same instrumentation. A list with the largest events ($M_w \geq 3.5$) in the period 2000-2007 are presented in Table 6.10. These events were cross-checked with public databases to ensure that no significant earthquakes were missing and no events of the catalogue had erroneously overestimated magnitudes. Some differences are expected due to different magnitude types (e.g. M_L) or methods of seismic moment calculation.

The Gutenberg-Richter (G-R) frequency-magnitude distribution (FMD) diagrams for the whole catalogue and for various subsets are presented in Fig. 6.12. The magnitude of completeness, M_c, was determined using the EMR method (Woessner & Wiemer, 2005) and the *b*-value with Maximum Likelihood Estimation (MLE), as implemented in the ZMAP software (Wiemer, 2001). Other, less computationally intensive methods for M_c, such as "maximum curvature" (MAXC), also yielded similar results when applied on large samples and are generally preferred for the estimation of the temporal or spatial distribution of M_c. On average, M_c=1.2 for the whole dataset. However, not all regions have the same network coverage and detectability, while strong spatial clusters should be considered as separate subsets with their own M_c and *b*-value. Fig. 6.12c shows the respective FMD plot for the 2001 swarm in Ayios Ioannis and Fig. 6.12b the corresponding diagram for the mid-gulf activity (Groups #3, #4, #5, #6 and #8). While the 2001 AIO swarm is at the southern edge of the network, marginally outside, its M_c is also 1.2. A different result (M_c=1.5) is obtained for the FMD plot of Group #9, near Eratini, with the MAXC method yielding an equally acceptable M_c=1.3. Although it is also marginally outside of the network its seismicity is very different, generally sparse with a few spatial clusters and low seismicity rate. Its high *b*-value (1.37±0.06) suggests a low-stress region, likely creeping, without significant asperities. The *b*-value in the rest of the catalogue is around 1.1-1.2, which is normal for a region with continuous background activity and a multitude of swarms and other spatiotemporal clusters.

The M_c was also examined through time (Fig. 6.13, using the EMR method). Its high value (up to ~1.5) at the beginning of the catalogue is suggestive of the lower network coverage during 2000. It then varies around 1.3±0.1, reaching its lowest values in 2004 during a swarm with many small events, and, also near the beginning of 2006. It spikes for a short time by the end of 2006, at the beginning of the intense sequence described in Section 6.6.3, apparently due to masking of the smaller events by larger ones. It should be noted that for the smaller sample lengths used for the

calculation of M_c against time, the MAXC method tends to underestimate the respective results obtained by the EMR method (Fig. 6.13) by about 0.05-0.10 or even higher in some cases. The more significant differences are observed in the early period, before the 2001 AIO swarm, with EMR yielding M_c=1.8±0.1 compared to M_c≈1.5 calculated by MAXC. The *b*-value for the seismicity within the gulf varies in time between 1.1 and 1.3, reaching lower values before the swarm of 2004 and before the 2006-2007 sequence, at which point it becomes unstable, varying between 1.2 and 1.6 (Fig. 6.14). The method used for the determination of M_c does not cause much

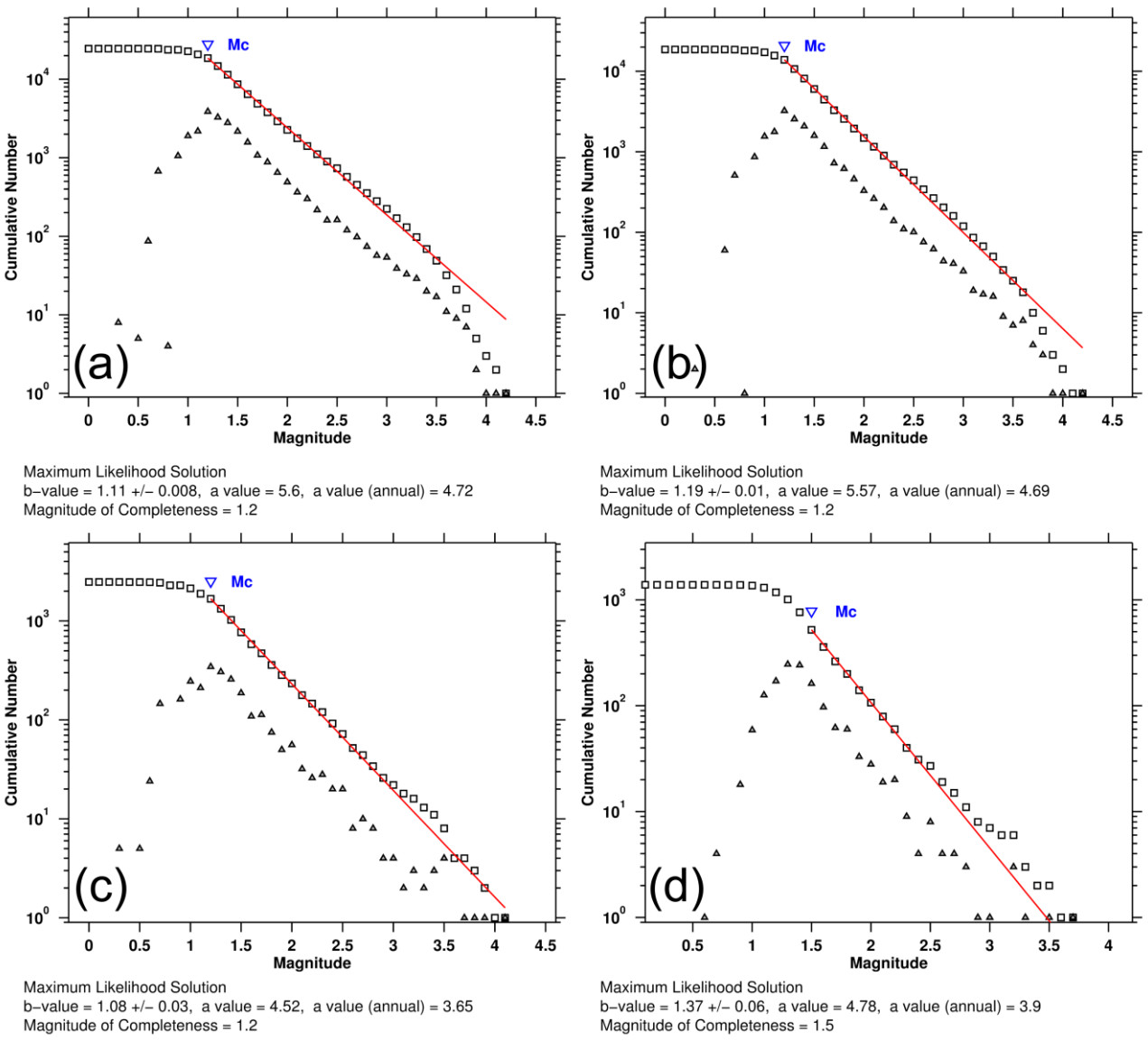

Figure 6.12: Gutenberg-Richter diagram for the frequency-magnitude distribution of earthquakes during years 2000-2007 in the western Corinth Rift a) for complete catalogue, b) only for events located within the gulf (groups #3, #4, #5, #6 and #8), c) for the 2001 Ayios Ioannis swarm (group #2) and d) for group #9 (Eratini). The M_c has been determined using the EMR method (Woessner & Wiemer, 2005) and the b-value using MLE, as implemented in the Zmap software (Wiemer, 2001).

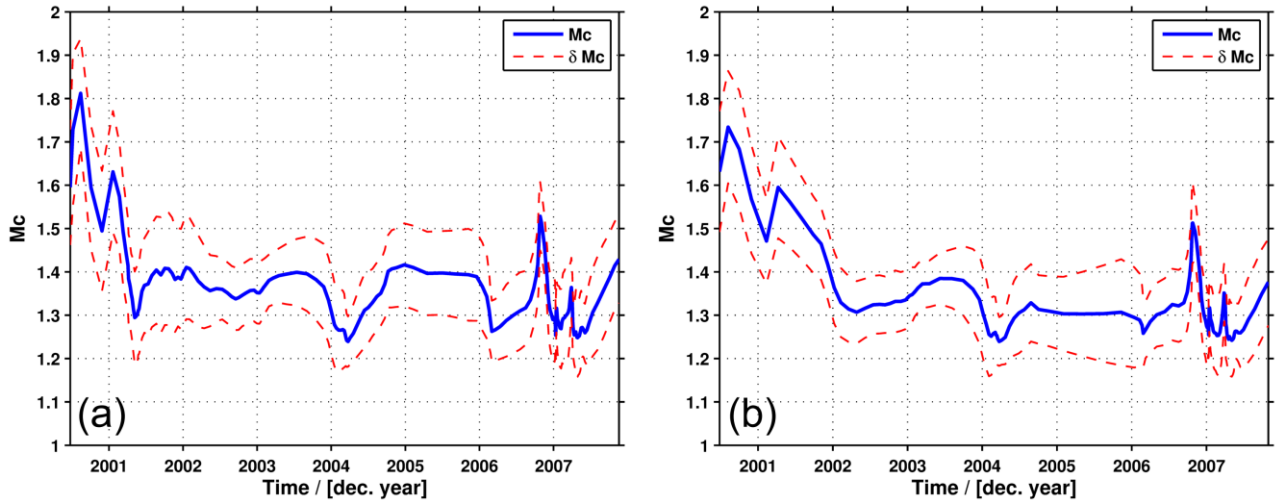

Figure 6.13: Temporal variation of the completeness magnitude, M_c for the seismicity of years 2000-2007 a) from the complete catalogue, b) only for events located within the gulf (groups #3, #4, #5, #6 and #8). The M_c values have been determined using the EMR method (Woessner & Wiemer, 2005), in sliding windows of 500 samples with the uncertainties computed using 200 bootstrap samples.

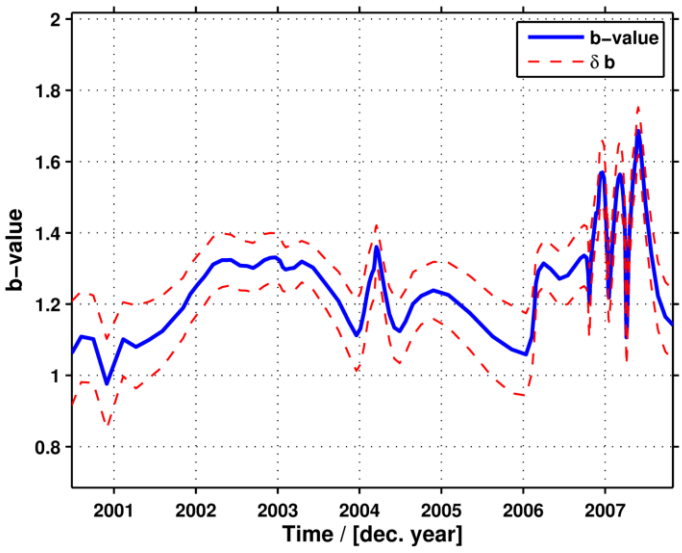

Figure 6.14: Temporal variation of the b-values of the G-R law for events located within the western Gulf of Corinth (groups #3, #4, #5, #6 and #8) in the period 2000-2007 in sliding windows of 500 samples. The M_c values have been determined using the EMR method (Woessner & Wiemer, 2005).

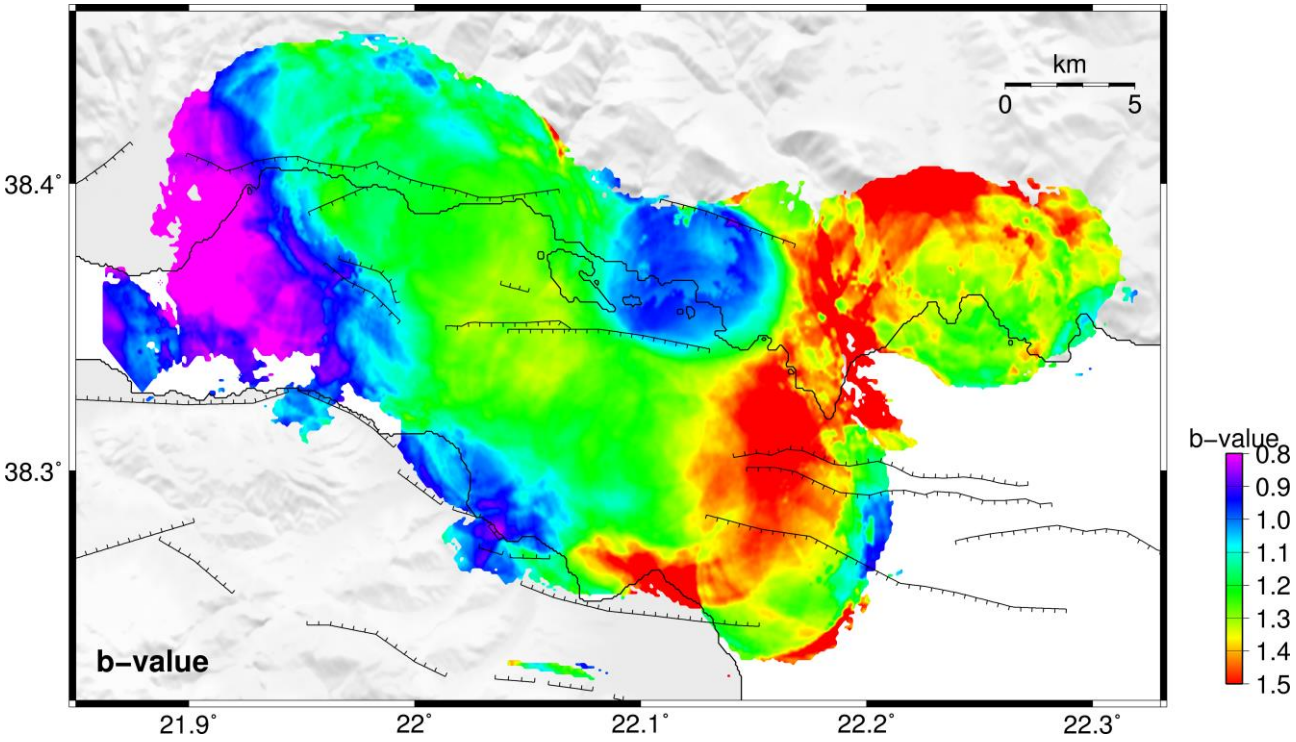

Figure 6.15: Spatial distribution of the *b*-value in the western Corinth Rift for the seismicity of 2000-2007. The values were calculated on a grid with ~0.1km spacing in volumes defined by vertical cylinders with a constant radius of 3km. The M_c values were calculated using the maximum curvature method.

difference to the resulting *b*-values, with the exception of the early period 2000-2001 for which MAXC yields smaller *b*-values, dropping from ~1.1 to ~0.9.

The spatial distribution of *b*-values for the seismicity of 2000-2007 in the western Corinth Rift is presented in Fig. 6.15. The values have been calculated with a grid spacing of 0.001 degrees (roughly 0.11 km) and a constant search radius of ~3 km. The goodness of fit is adequate (≥85%) throughout most of the region, with few exceptions e.g. at the northernmost part of Group #9 and near the trace of Aigion fault.

To summarize the most important characteristics:

- Along the main NW-SE direction of the gulf, from the region N of Marathias fault down to W of the offshore west Channel (wCh.f.) and Eratini faults (nEr.f. and sEr.f.), the *b*-value is ~1.2.
- At the west part of the abovementioned faults and towards NNE, the *b*-value is very high, nearly ~1.5.
- The region of Group #9 (Eratini) has *b*-values above 1.2.
- The *b*-value appears lower (~0.95) east of Trizonia Island, mainly attributed to the clusters that occurred in 2000 (Group #1 in 2000).
- Low *b*-values (~0.9) are observed near Selianitika (Se.f.) and Fasouleika faults (Fas.f.).
- Very low *b*-values (≤0.8) are observed N of Psathopyrgos fault (Ps.f.).

High *b*-values may mark either highly fragmented volumes or regions where creeping is likely to occur, as with the SSW-NNE area presented with red in Fig. 6.15, while low *b*-values could indicate regions where the faults are more or less locked or asperities are likely to exist. The seismicity in

those regions mainly consists of relatively larger events and fewer small ones than expected for a "normal" *b*-value around unity.

Table 6.10: List of major events ($M_w \geq 3.5$) in the western Corinth Rift during 2000-2007. Events with $M_w \geq 3.9$ are marked with bold.

Origin Time	Latitude	Longitude	Depth (km)	M_w	φ (°)	δ (°)	λ (°)	Group
19/06/2000 15:02	38.3500	22.1216	9.8	3.7	118.0	48.6	-59.4	6
19/06/2000 16:16	38.3455	22.1281	9.0	3.7	251.8	55.0	-138.0	6
30/06/2000 20:00	38.3660	22.1297	10.3	3.6	150.6	43.8	-58.1	6
22/08/2000 08:55	38.3969	22.0035	10.0	3.7	296.8	42.6	-74.5	4
09/02/2001 20:38	38.3001	22.1198	7.5	3.7	255.4	45.4	-120.2	6
29/03/2001 00:25	38.2023	22.0431	8.0	3.5	217.5	34.9	-136.9	2
08/04/2001 06:12	**38.1994**	**22.0449**	**8.0**	**4.1**	**228.8**	**30.1**	**-117.3**	**2**
08/04/2001 06:36	38.1934	22.0444	8.2	3.5	255.6	8.5	-69.6	2
13/04/2001 01:06	38.1873	22.0486	7.1	3.5	295.8	37.1	-64.6	2
28/04/2001 11:57	38.2040	22.0369	8.7	3.7	217.0	38.7	-141.3	2
21/05/2001 09:58	**38.3620**	**22.0092**	**8.8**	**3.9**	**144.8**	**52.1**	**-48.2**	**4**
26/05/2001 09:03	38.2046	22.0522	8.3	3.5	198.2	35.1	-155.0	2
31/05/2001 09:42	**38.2022**	**22.0709**	**7.5**	**3.9**	**222.4**	**48.5**	**-141.5**	**2**
01/06/2001 03:21	38.1965	22.0342	8.9	3.8	80.1	57.3	-33.1	2
10/06/2001 14:51	38.3863	22.0143	9.6	3.5	137.7	61.7	-27.3	4
24/12/2001 20:55	38.3878	21.7613	9.8	3.8				7
27/01/2002 08:44	38.3381	22.3103	10.8	3.7	289.0	25.6	-71.1	9
21/02/2002 09:15	38.3974	21.8317	9.4	3.5				7
21/02/2002 18:20	38.3429	21.7729	10.7	3.7				7
24/02/2002 00:31	38.3507	21.7630	8.5	3.6	50.0	27.0	7.0	7
07/07/2002 05:30	38.3059	22.1585	8.0	3.6	320.0	39.0	-12.8	5
03/12/2002 23:04	38.3502	21.9148	8.0	3.5				7
14/12/2002 11:50	38.3563	21.9309	8.0	3.5				7
05/02/2003 00:13	38.3526	21.9946	8.4	3.5	139.9	22.1	-58.1	4
28/08/2003 12:01	38.4027	21.9844	8.0	3.5				3
31/10/2003 02:33	38.3414	21.7992	9.8	3.8	277.5	74.3	-2.1	7
18/11/2003 18:32	**38.4137**	**21.9438**	**8.0**	**4.2**	**114.4**	**37.6**	**-42.4**	**3**
06/03/2004 04:34	38.2947	22.1216	7.9	3.5				6
28/04/2004 07:26	38.3433	21.7837	10.1	3.8	101.3	51.3	-30.4	7
24/05/2004 00:03	38.3689	22.2065	10.2	3.5				9
14/08/2004 22:08	38.1342	22.0832	11.7	3.5	328.9	31.1	-56.1	11
12/09/2004 09:16	38.1203	22.0940	10.5	3.6	264.1	25.4	-148.4	11
05/10/2005 10:20	38.3472	21.8241	8.0	3.7				7
12/11/2005 21:52	**38.2984**	**22.0589**	**8.3**	**4.0**	**10.0**	**22.0**	**32.0**	**8**
20/11/2005 17:56	38.4365	21.8174	10.8	3.6	272.7	45.4	-30.4	7
15/12/2005 19:17	38.3624	22.0247	8.1	3.6	248.8	29.8	-153.0	4
21/10/2006 07:42	38.3900	21.9746	8.0	3.6	228.7	43.3	-153.9	3

Table 6.10: (continued)

Origin Time	Latitude	Longitude	Depth (km)	M_w	φ (°)	δ (°)	λ (°)	Group
28/10/2006 16:02	38.3956	21.9683	8.5	3.6	260.2	47.7	-145.1	3
24/11/2006 02:58	38.3173	22.0938	7.3	3.5	252.0	38.7	-141.3	6
24/11/2006 09:03	38.3491	22.0206	8.7	3.8	261.9	41.5	-135.1	4
07/01/2007 14:47	38.3818	22.0220	8.2	3.6	82.3	44.2	-46.9	4
10/01/2007 14:15	38.3852	22.0305	7.5	3.5	325.7	33.8	-74.3	4
19/03/2007 20:53	38.3796	22.0476	7.0	3.8	225.3	28.8	-104.0	4
25/03/2007 08:01	38.3967	22.0108	6.7	3.5	233.7	42.7	-168.1	4
07/04/2007 11:10	38.4024	22.0008	9.3	3.6	289.6	18.2	-80.8	4
16/04/2007 21:42	38.3244	22.0670	8.7	3.6	97.8	42.3	-81.3	8
09/05/2007 01:46	38.2176	21.6564	8.8	3.7	174.6	6.0	136.6	1
20/06/2007 22:08	38.2775	21.5955	8.6	3.5	79.2	37.0	-50.1	1
15/12/2007 14:41	38.3872	22.1646	53.8	3.8				6

Spatial mapping of *b*-values in two successive periods, 2000-2005 and 2006-2007 (Figs 6B31-32) shows that high *b*-values are observed during both periods along the eastern end of the seismically activated area, while for Group #9 they are generally high during the second period. Low *b*-values north of Ps.f. are mostly resolvable during the first period, with a hint also observable during the second period but not covering the whole area due to lack of seismicity. Interestingly, relatively low *b*-values are also observed in the region between the Managouli fault zone and Marathias fault in the first period while in the second one, which includes highly clustered and intense seismicity

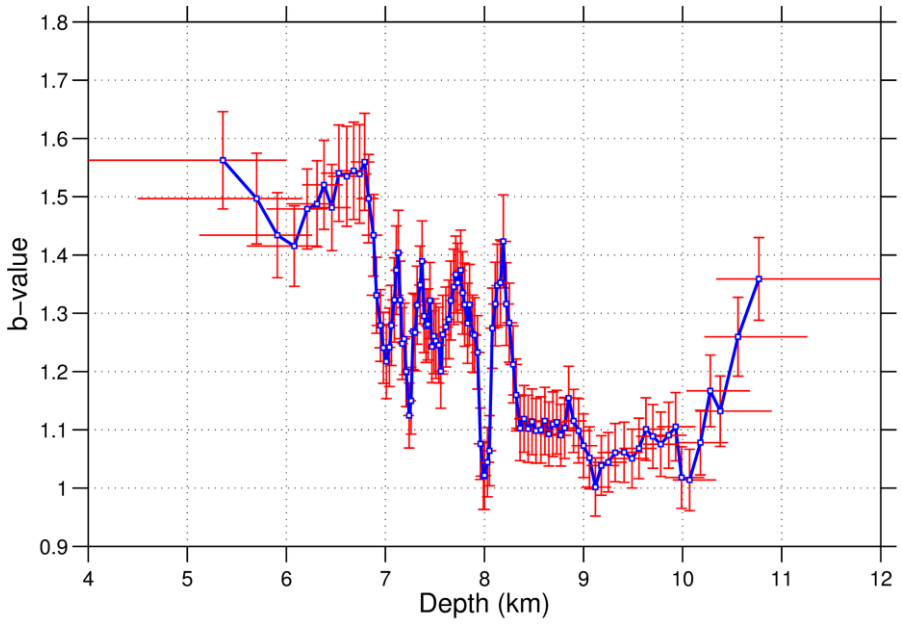

Figure 6.16: Distribution of b-value with respect to depth for the seismicity of the western Corinth Rift (2000-2007), including Group #9, in overlapping windows of N=400 samples with a fixed M_c=1.4.

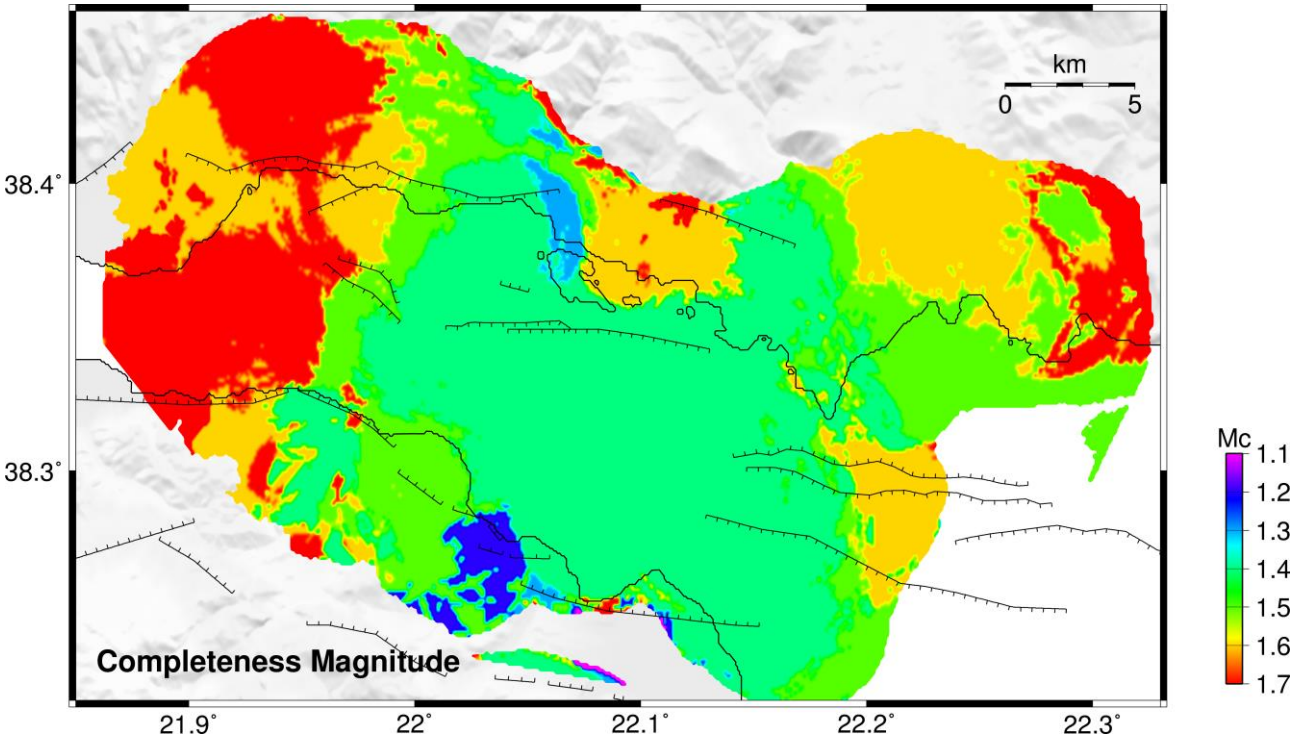

Figure 6.17: Spatial distribution of the completeness magnitude, M_c, in the western Corinth Rift for the seismicity of 2000-2007. The values were calculated on a grid with ~0.1km spacing in volumes defined by vertical cylinders of constant radius 3km. The M_c values were calculated using the maximum curvature method.

during the 2006-2007 crisis, the *b*-values are high. That could possibly indicate the rupture of a small asperity. In the mid-gulf region, the *b*-values are normal to high, with an exception west of the major offshore faults wCh.f. and sEr.f. and near Se.f. and Fa.f., mostly in the first period. The *b*-value also appears to drop with increasing focal depth (Fig. 6.16). It can be roughly divided in 4 ranges, the shallower focal depths (H<7km) with $b\approx1.5$, then dropping to 1.3±0.1 for 8km≤H≤7km, further deep between 8 and 10 km it is reduced to about 1.1±0.1 and then increases up to 1.3-1.4 for the events between 10 and 12 km.

The spatial distribution of M_c, derived using the MAXC method, is presented in Fig. 6.17. It appears to be homogeneously distributed offshore, in the middle of the region at ~1.4, lower (~1.2) near Se.f. and Fa.f. and much higher ($M_c\geq1.7$) N of Ps.f. (Group #7) and at Group #9 ($M_c\geq1.6$). It should be noted that, in areas with fewer samples, the MAXC underestimates M_c values relative to the respective M_c derived by the EMR method. However, the *b*-values and goodness-of-fit is not significantly different with either method.

6.5 Focal mechanisms and local stress-field

The tectonic regime in the western Corinth Rift is characterized by regional extension in an approximately N10°E direction (Briole *et al.*, 2000; Lyon-Caen *et al.*, 2004). E-W trending normal faulting is dominant, with several major normal fault scarps mapped at both shoulders of the rift as

well as inside the gulf (Fig. 6.1). However, the identification of multiplets that leads to spatial clustering by relative hypocentral relocation can potentially provide details on the small-scale fault network or local stress variability.

By definition, similar earthquakes are expected to share similar focal mechanisms. However, multiplets usually contain events of small magnitude, which makes the determination of fault plane solutions by waveform inversion difficult or practically impossible, as the SNR is very small at the low frequencies and there are inherent limitations for the construction of Green's functions, as the response in higher frequencies / smaller wavelengths is affected by smaller structural details of the medium which are hard to model properly. For this reason, the First Motion Polarities (FMP) technique was employed for the determination of focal mechanisms.

While the availability of the local seismological network enables the application of the FMP technique, as the seismic rays usually have an angle of emergence > 90° (directed upwards), the gulf itself creates a significant physical azimuthal gap. This means that it is usually difficult to constrain the Fault Plane Solution (FPS) of a single event with FMP alone. The FPS is even more uncertain when the number of available FMP is small. A lack of FMP can be due to either low SNR or to the ambiguity of the first motion itself, which may be the case when a station is situated close to one of the nodal planes.

To mitigate the above issues, composite solutions are considered, taking into account the FMP observed in all, or a subset of events of a multiplet. In addition, S-wave polarization directions and S to P amplitude ratios are also incorporated to provide weights, biasing the solutions towards reducing the difference between theoretical and observed directions or ratios.

Multiplets with ≥ 5 events were selected from each spatial group. For those with more than 20 events, the largest ones (higher magnitude/amplitudes) were selected. The FMP were measured for ~5300 events in multiplets, tagging uncertain polarities to be used with caution (reduced weight). The polarities were reversed for stations PSAR, PYRG, KALE and PANR to correct for vertical component reversal according to the observations made in Section 2.5.

A grid search, with a step of 2°, was applied to determine the FPS which satisfies the FMP. The unified FMP data from the events belonging to a multiplet may contain measurements of both positive and negative polarities to the same station. This could indicate that the station is possibly nodal, but there is also a chance that a few of these measurements are actually erroneous, or, in some cases, that some of the selected events in the multiplet are less similar than others (due to chaining effects). This is especially the case for uncertain measurements of emergent, noisy or otherwise ambiguous polarities which are given a lower weight, e.g. 0.5 or 0.3, instead of 1.0 for the certain measurements. For each FPS in the grid search, a percentage of polarities may correspond to the correct quadrant of the focal sphere. A score value was set for the ratio of the sum of weights of the validated polarities to the sum of weights of all the measurements. When the grid search is completed, the algorithm begins by looking for FPS with a 100% score. If a minimum number (typically 10-30) of such solutions is not available, the percentage threshold is lowered e.g. by 1% until at least 10-30 FPS are found with a score greater or equal to the threshold. The latter threshold

value may be regarded as a measure of error, as it shows how many measurements had to be discarded in order for the algorithm to find an adequate number of individual FPS.

The individual FPS may or may not be coherent, in the sense that the nodal planes are sufficiently constrained or not. In case they are, the mean solution (measured as described in Section 2.4.3) will have a small RMS angular difference, $\delta\theta_{RMS}$. However, a high $\delta\theta_{RMS}$ value (e.g. $\delta\theta_{RMS}$>30°) can lead to an average MT solution that is more random than representative of the composite focal mechanism. To reduce this randomness, additional measurements of S-wave polarization (SWP) directions and S to P amplitude ratios (SPR) are also incorporated. These values, along with the percentage of satisfied FMP for each individual solution, are taken into account in the determination of a combined weight (Eq. 2.43) for each individual moment tensor during the calculation of the average solution, following the procedures described in Section 2.4.3. This also affects the mean focal mechanisms of groups with a relatively small $\delta\theta_{RMS}$, however, in those cases, the solutions are bound to a limited range, thus it does not lead to radically different FPS than the simple average with uniform weights.

In some cases where the averaged solutions were questionable, with large $\delta\theta_{RMS}$, the procedure was re-run with the restricted to individual FPS that corresponded to normal, oblique-normal and "odd" (subvertical or subhorizontal slip) faulting, according to Zoback's (1992) criteria (Table 2.1), excluding reverse and strike-slip solutions which are less likely to be observed in the area of study. In addition to the 284 composite mechanisms that were calculated for multiplets, another 116 large events were considered for the estimation of individual focal mechanisms, as their SNR is sufficient in most stations to allow for the measurement of enough FPS to constrain a solution with small $\delta\theta_{RMS}$, aided by SWP and SPR, using the procedures of Chapter 2.

The full results of FPS are presented in the map of Fig. 6.18 and in exploded view in the Appendix (Figs. 6B.12-13), including composite solutions (small focal spheres) and single solutions for major events (large focal spheres). The hypocenters of composite FM are determined by the mean hypocentral coordinates of the selected events in the multiplet, weighted by the number of FMP observations. The composite focal mechanisms were associated with a spatial group according to the proximity of their averaged hypocenter to the centroid of the respective cluster. Most solutions are located, expectedly, within the gulf, in the AIO and Eratini groups and a few in Group #7 (Psathopyrgos) and in sparse clusters at the south. Although most solutions have a strong normal component, a significant number seems to represent oblique-normal slip. Also, while some the solutions are more or less uniform in certain regions, in others there appears to be a higher degree of variation, suggesting increased complexity of the faulting network or localized stress perturbations in a relatively small volume.

A series of thin, parallel cross-sections were performed in a N10°E direction, as presented in Fig. 6.19, across the western Corinth Rift (Fig. 6.18). Major fault traces are also depicted with a typical 60° dip for reference, unless stated otherwise. An attempt is made to match known mapped faults to specific earthquake clusters at depth, by combining their approximate geometry and the resolved focal mechanisms.

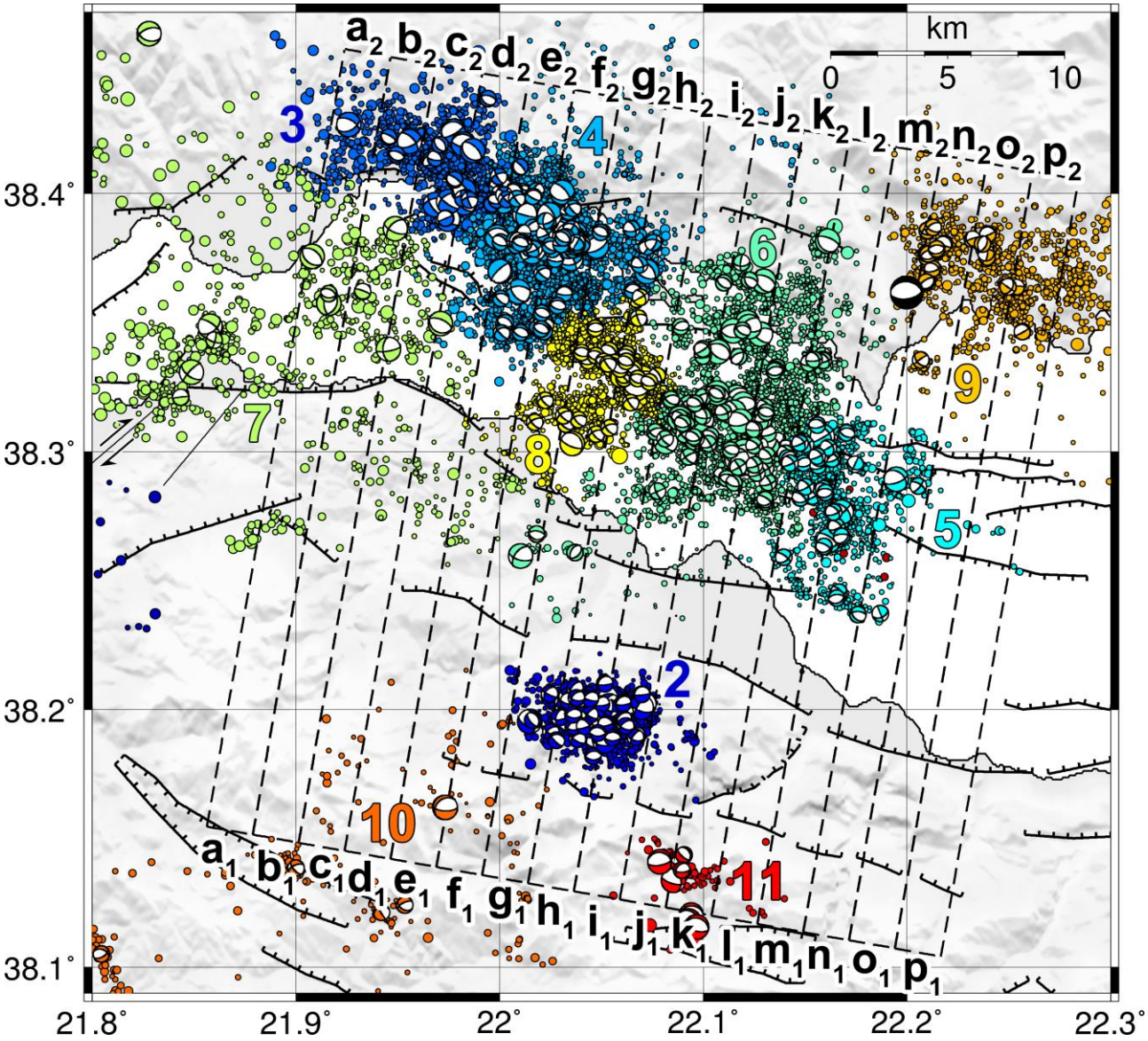

Figure 6.18: Map of resolved composite focal mechanisms for multiplets (small beachballs) and single focal mechanisms (larger beachballs) for major events ($M_w \geq 3.0$) in the western Corinth Rift for the period 2000-2007. Numbers and colours correspond to the same spatial groups as in Fig. 6.10. Dashed rectangles represent the bounds of cross-sections a_1-a_2,…,p_1-p_2 of Fig. 6.19. The focal mechanism with black compressive quadrants near group #9 is the M_s=6.2 mainshock of 1995.

Starting from the westernmost section a_1-a_2, some seismicity of Group #7 at a depth of $H \approx 8$km can possibly be related to the Psathopyrgos fault. However, these hypocenters are essentially outside of the network and their depths cannot be adequately constrained. To the north, activity in Group #3 is likely associated with a N-NW dipping fault plane. No cross-sections were performed west of a_1-a_2, as the solutions are getting sparser with the exception of a small spatial cluster near Psathopyrgos fault scarp. This activity could be related to the right-lateral oblique-normal Rion-Patras Fault Zone, as indicated by a couple of resolved major events focal mechanisms. Further east, Group #3 begins to concentrate at depths mainly between 8 and 10 km, delineating a north-dipping structure which,

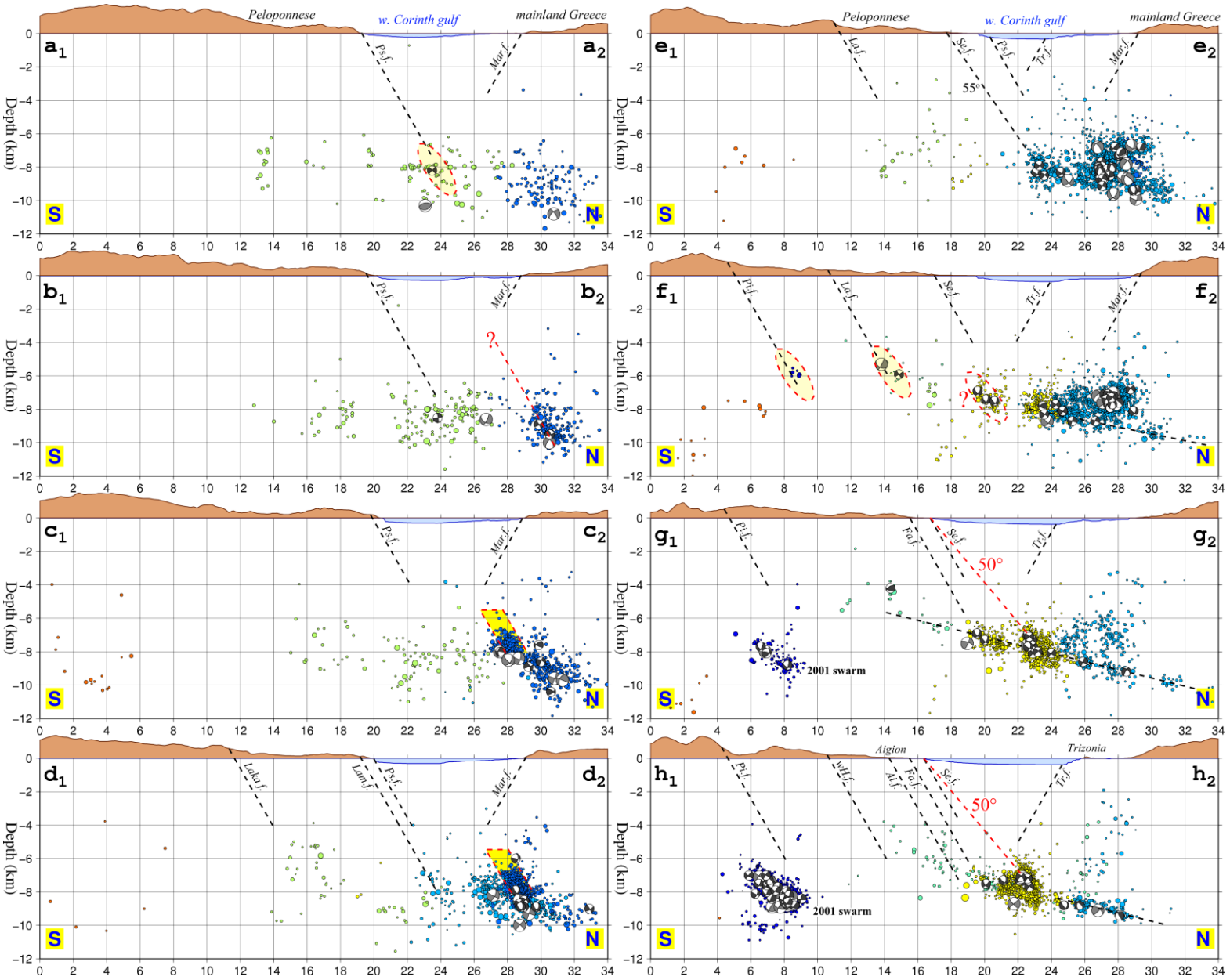
Peloponnese
w. Corinth gulf
mainland Greece
a1
a2
b1
b2
c1
c2
d1
d2
e1
e2
f1
f2
g1
g2
h1
h2
Psf.
Marf.
Lakf.
Lamf.
Laf.
Sef.
Trf.
Pif.
Faf.
wHf.
Aif.
55°
50°
?
2001 swarm
Aigion
Trizonia
S
N
Depth (km)

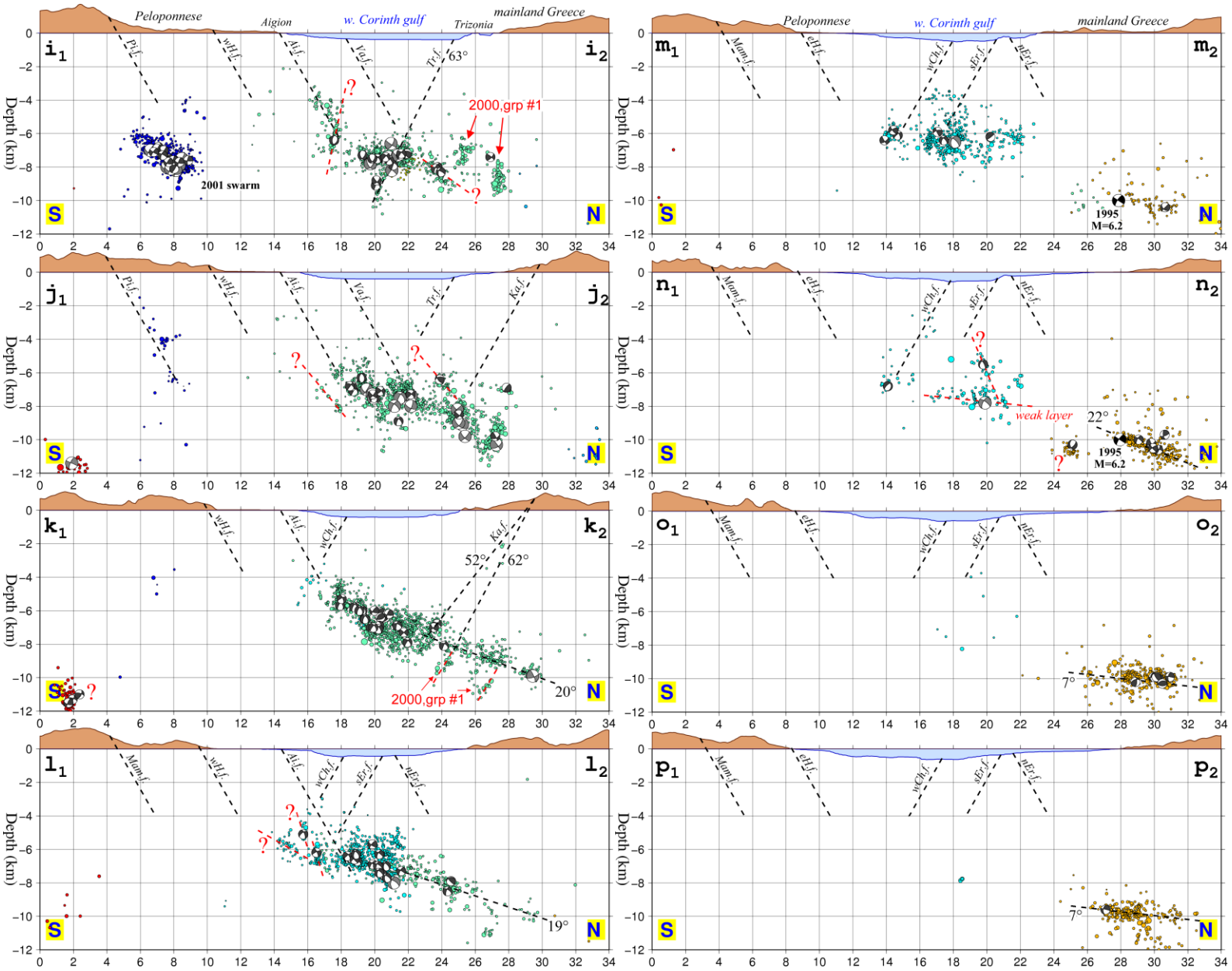
Peloponnese
Aigion
w. Corinth gulf
Trizonia
mainland Greece
i1
i2
Pi.f.
wH.f.
Ai.f.
Va.f.
Tr.f.
63°
2000,grp #1
2001 swarm
S
N
Depth (km)
m1
m2
Mam.f.
eH.f.
wCh.f.
sEr.f.
nEr.f.
1995
M=6.2
j1
j2
Ka.f.
n1
n2
weak layer
22°
k1
k2
52°
62°
20°
o1
o2
7°
l1
l2
19°
p1
p2

Figure 6.19 (previous pages)**:** Thin (±1km), non-overlapping, parallel cross-sections in a N10°E direction across the western Corinth rift (Fig. 6.18). The beachballs correspond to the projection of the respective focal mechanisms (small = composite solutions, large = single events). Black dashed lines mark the extension of known faults at depth with a typical dip angle of 60°, unless stated otherwise. Red dashed lines mark the extension of possible blind faults or the seismogenic layer. The horizontal/vertical length proportions are 1:1 so that true angles can be directly observed while topography and bathymetry are also plotted without exaggeration.

however, cannot be directly associated with a mapped offshore fault, as indicated by the red dashed extension of the respective nodal plane at ~60°, derived by composite focal mechanisms. In c_1-c_2 another dense cluster is observed in Group #3 further south, at shallower depths (6.5 – 8 km), with a likely lower dip. It should be noted that the N10°E is not always perpendicular to the nodal planes of the focal mechanisms, indicating either a fault plane that is not crossed at a right angle or oblique slip on a fault that is perpendicular to the respective cross-section, or both. Section d_1-d_2 introduces Group #4, dipping at a low angle. The cluster of Group #3 appears shifted towards the north but at the same depths as in c_1-c_2 (yellow rectangle with red, dashed edge in c_1-c_2 and d_1-d_2), likely indicating a SW-NE striking fault plane. This could correspond to a series of oblique-normal composite focal mechanisms, suggesting a NNW dipping fault plane with dextral component, roughly at the extension of the RPFZ towards NE. The alternative for these oblique-normal events would be a series of sub-vertical SE-NW faults in parallel, across a WSW-ENE direction, but is considered unlikely.

In e_1-e_2 the distribution below Marathias fault becomes increasingly complex, possibly a result of the interaction between multiple structures at different orientations within a small volume at depths of 6-8 km. Below that, a low-angle seismically active zone begins to form, spreading at shallower depths towards the south. However, very few low-angle normal faulting mechanisms can be observed, as most appear to dip at angles of 30-60°. The southernmost part could possibly be related to Selianitika fault (extended at 55° dip). The cross-section is not perpendicular and it passes near the end of Se.f. An alternative could be Lambiri fault, whose fault scarp, however, is slightly offset to the north. The general description of the mid-northern part remains similar in f_1-f_2, with a small cluster in Group #8 including focal mechanisms that indicate oblique normal faulting. Some small clusters further south coincide with the extensions of Lakka and Pirgaki faults at 60°, the former also supported by a composite focal mechanism. In section g_1-g_2, mid-gulf, at the northern part of Group #8 a probably north-dipping cluster is observed, but its extension at ~45°, as inferred from the focal mechanisms, meets Fasouleika fault at the surface. However if a steeper dip is used, judging from the geometry of its spatial distribution, it does not correspond to any of the known structures, implying for a small, blind fault at depth. The southern part of Group #8, continued from f_1-f_2, is still ambiguous in terms of fault plane. Measurements on its geometry suggest a 30° dip towards the north but one of the nodal planes dips NW rather than N. On the other hand, the strike of the SSW-dipping nodal plane better suits the direction of the main axis of the cluster's horizontal distribution. The case that these multiplets belong to small, south-dipping antithetic structures could be supported by the geometry of small subclusters, roughly visible in f_1-f_2.

The seismicity of Group #4 in the north becomes sparse, with its floor, however, following the ~13° low-angle seismic layer. Group #2 (Ayios Ioannis swarm region) begins to appear at the south. The cluster seems to be north-dipping, however the majority of focal mechanisms show that there is a significant degree of obliqueness. The swarm will be discussed in more detail in Section 6.6.1.

In cross-section h_1-h_2 there are no significant differences from g_1-g_2. The southern part of Group #8 as well as the shallower seismicity of Group #4 vanish and there are still indications of activity at the northern part of the low-angle seismic layer. The latter changes in sections i_1-i_2 and j_1-j_2, where the northern clusters correspond to two seemingly high-angle south-dipping clusters that occurred in 2000 (spatial Group #1 of 2000) east of Trizonia island. It should be noted that their hypocenters become gradually deeper towards ESE, however this seems to contradict with the resulting composite focal mechanisms. The geometry of the northern cluster indicates dip towards S while the southern one dips towards ESE. However, both have a very high rectilinearity value (>0.9), so their dip and dip-direction cannot be reliable. The orientation of their elongated horizontal distribution is compatible with the main axis of the rift and these clusters likely belong to south-dipping structures reaching a bit below the weak seismogenic layer. The extension of Kallithea fault (Ka.f.), dipping at 60-62°, meets the southern cluster at about 8 km in j_1-j_2 and the northern part of the weak layer at a dip of 52° in k_1-k_2, presenting two alternative scenarios.

Mid-gulf, in i_1-i_2 a group of single normal focal mechanisms is observed at the extension of Trizonia fault (Tr.f.), following a 63° dip dashed line. According to Beckers *et al.* (2015) the Trizonia fault dips at 64-72°, thus, allowing for a small reduction due to the cross-section's direction not being exactly rectangular to the fault's trace, this is a plausible case. A small cluster is also located mid-gulf at larger depth than the mostly active seismogenic layer, between 8 and 10 km, still in the same direction as the extension of Tr.f. Interestingly, a shallower cluster is observed further south, offshore, apparently meeting Aigion fault (Ai.f.) at ~4-7 km. However, a well-constrained composite mechanism suggests almost pure strike-slip faulting (Fig. 6B.21), likely a rare exception which, however, retains the direction of the extensional axis. In this section, the offshore, north-dipping Valimitika fault (Va.f.) (Stefatos *et al.*, 2002) appears ~4km N of the Ai. f. Its dip is not known, although it's supposedly more shallow-dipping than Ai.f. (Ghisetti & Vezzani, 2005; displayed as an unnamed offshore fault in Fig. 4 therein). At 60° dip, its extension passes through a cluster at ~24km horizontal distance, but then it would have to cross Trizonia fault.

In j_1-j_2 the activity at the horizontal range 17 – 20 km could probably associated with the Ai.f., although several different types of focal mechanisms are observed which are not compatible with this fault plane. Sparse, shallow seismicity in Group #2, but unrelated to the 2001 AIO swarm, as these events occurred in 2004 (Fig. 6.6), is located at the extension of Pirgaki fault, although it could possibly be equally compatible with Kerinitis fault as its horizontal distance from both scarps at the surface is comparable.

Cross-section k_1-k_2 is characterized by many oblique events mid-gulf, near the root of Ai.f., including an apparently south-dipping cluster at 4-6 km, beneath the trace of the west Channel fault, likely a small structure that was activated in late 2003. The more oblique mechanisms, including some almost pure strike-slip, are concentrated in this small-zone. The low-angle (≤20°) north-dipping seismic layer is mostly active mid-gulf, and extends to the north with some small clusters.

The deepest events of the two clusters of 2000, Group #1, seem to "breach" below the seismic layer, reaching down to 10-11 km. A single focal mechanism characterized by E-W normal faulting is located at a cluster near the Kallithea fault's scarp at a depth of ~10 km. However its nodal planes are not compatible with the low-angle layer, possibly suggesting a small antithetic fault.

In l_1-l_2 the activity of the deep seismic layer withdraws to the mid-southern gulf region which still exhibits mostly oblique normal faulting. A small, shallower cluster is observed at the extension of the south-dipping west Channel fault (wCh.f.), which, however, intersects with the Ai.f. at about 3.5 km, if they both have a 60° dip angle. Activity beneath wCh.f. persists through cross-section m_1-m_2 while mid-gulf seismicity becomes sparser at its edges, being limited to its central part. Apparently, the pure normal faulting observed in the middle of the gulf (Group #8) becomes gradually more oblique towards the eastern end, where the offshore seismicity stops almost abruptly.

In the north, Group #9 begins to appear at a depth of ~10km, in a focal region near the hypocenter of the 1995 M_s=6.2 Aigion earthquake (Tselentis *et al.*, 1996; Bernard *et al.*, 1997; Bernard *et al.*, 2006). While several types of composite focal mechanisms are resolved in that group, its spatial distribution suggests a low-angle layer, dipping at 20° at its western side to 10° at its eastern side. Most composite mechanisms of Group #9 are for multiplets aligned almost SSW-NNE along n_1-n_2 and indicating normal faulting. A few multiplets also indicate very low-angle faulting (focal mechanisms of "Odd" / "Undefined" faulting type, with B-axis plunge ~0° and P- and T-axes plunge ~45°), compatible with the direction of slip on the inferred detachment zone that has been suggested to exist in that region in several studies (Rigo *et al.*, 1996; Bernard *et al.*, 2006; Lambotte *et al.*, 2014). Such mechanisms are also observed towards the NW end of the seismicity in Groups #3 and #7 and a few in the 2001 AIO swarm (Group #2), including many with strongly oblique normal faulting.

The stress field, as indicated by relatively stable T-axis direction (Fig. 6.20), roughly associated with the σ_3 minimum principal stress axis (see Section 2.2), is extensional in a dominant SSW-NNE direction. It is slightly different for the 2001 AIO swarm (Group #2) and the Eratini Group (#9) (SSE-NNW), with in the latter varying mostly around S-N in its western half and being SSE-NNW in its eastern half. Near Marathias fault (Groups #3 and #4), despite the variance due to some oblique-normal events, the dominant direction remains SSW-NNE. In the middle of the gulf (northern part of Group #8), where pure normal faulting is indicated by the composite focal mechanisms, the lowest variance in the T-axis is observed. The B-axis, on the other hand, is expected to be roughly parallel to the strike of the causative faults, when the degree of obliqueness is small. It follows an approximate WNW-ESE direction in the mid-NW part of the rift and becomes more E-W in the mid-eastern part (Fig. 6B.14). The P-axis is almost vertical in events with

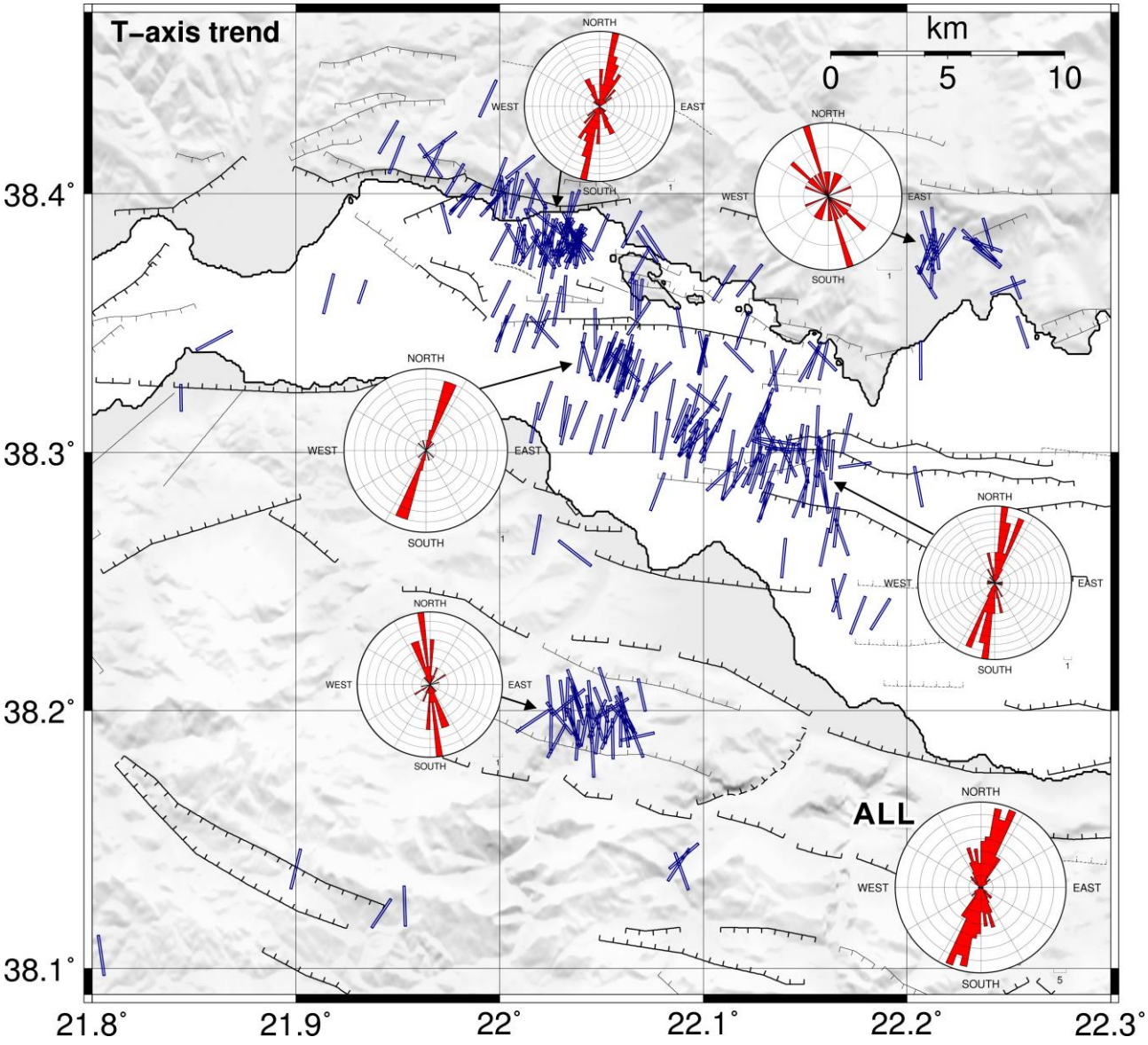

Figure 6.20: Directions of the composite focal mechanisms' T-axes for multiplets in the western Corinth Rift in 2000-2007. Line length is proportional to $\cos T_{pl}$, where T_{pl} is the T-axis plunge angle. Rose plots show the distribution of T-axis directions for various regions (pointed by arrows) and for all resolved composite solutions (lower-right)

pure normal faulting, however its horizontal component becomes more significant when oblique slip is involved or the nodal planes become subhorizontal/subvertical. Fig. 6B.15 shows the P- and T-axes for multiplets with an oblique component, as estimated by the plunge of the B-axis, being 90° for pure strike-slip and 0° for pure normal/thrust or otherwise dip-slip. Besides the complex part underneath Marathias fault, in the rest of the gulf the obliqueness of slip tends to increase S and SE of Group #8, mostly near the western end of the West Channel and Eratini faults, possibly indicating increased small-scale fault complexity and/or perturbations in the local stress field, likely associated with relay zones between the overlapping faults' segments or near their extremities.

6.6 Spatio-temporal analysis

The reduced uncertainties achieved by the double-difference relocation enable a detailed description of the seismicity patterns that have occurred in the western Corinth Rift. These potentially include spatiotemporal clusters, swarms, seismicity migrations and mainshock-aftershock sequences. Having determined the moment magnitudes and composite focal mechanisms, an overview of the seismicity throughout the period of study, 2000-2007, can be examined.

Initially, after visual examination of the number of events per day, the catalogue was divided in two periods: 2000-2004 and 2005-2007, to halve the number of events per part. Then, Ward's linkage was attempted on the inter-event origin time differences, as a measure of "temporal distance", and

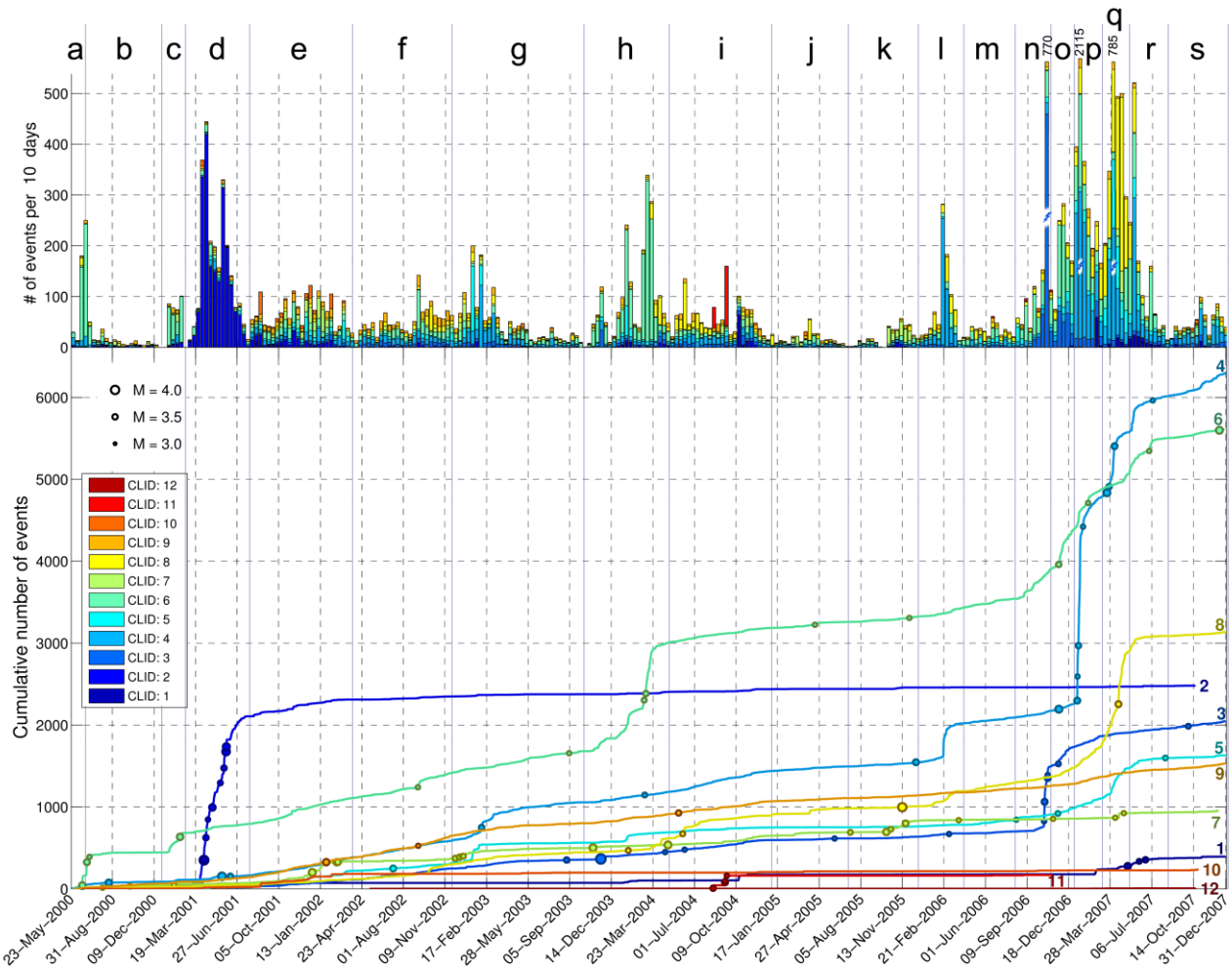

Figure 6.21: (Top) Stacked histogram of number of events per 10 days for the seismicity of the western Corinth Rift during 2000-2007, with colours corresponding to the 12 spatial groups of Fig. 6.10. Small-case letters on top represent the 19 temporal periods to which the catalogue has been divided (See Fig. 6B.34 in the Appendix). Some bars in 2006-2007 have been shortened, with the number on top corresponding to the total height of the respective bar. (Bottom) Cumulative number of events per spatial group drawn on the same time-scale as the top panel. Circles represent major events ($M_w \geq 3.0$).

examining the respective "scree plot" per part. The minimum of the "differential Mojena's method" plots was found at 7 and 10 periods for parts #1 and #2, respectively. Most intervals tend to include major temporal (and spatial) clusters. However, manual division is still required in some cases for the proper separation of significant clusters. Ultimately, a division in 19 sub-periods was considered (Fig. 6.21).

The western Corinth Rift is characterized by complex seismicity patterns, including regions of with an almost constant background rate, others where migration patterns are frequently observed, many spatiotemporal clusters, swarms and, less often, typical mainshock-aftershock sequences. As evident from the histogram and cumulative number of events per spatial group (Fig. 6.21), during 2000-2007 the major outbreaks include the 2001 AIO swarm (period d), the 2003-2004 mid-gulf sequence (period h) and the 2006-2007 sequence near Marathias fault (periods n-r). In the latter, Group #4 became dominant in terms of the total number of events, especially during period p, or more specifically between 7 and 16 January 2007, when over 2000 events occurred within 10 days. Group #2 (AIO) has a comparable number of events but they are more widespread in a time-frame of ~120-140 days. Many of the more significant seismicity outbreaks are triggered by or contain several (relatively) major events ($3.0 \leq M_w \leq 4.2$), either in the same spatial group or in a neighboring one. Group #6, the second largest, was mostly active during the 2003-2004 sequence (period h). Group #9 (Eratini) is the larger group without any significant outbreaks. On the contrary, it has an average rate of 17 events/month (evt/mon), in the full catalogue, or ~15 evt/mon above the group's M_c=1.2 threshold. Mid-gulf, Group #6 also presents a nearly constant rate of 34 evt/mon (25 evt/mon for $M \geq M_c$=1.2) between periods d and g, or 17 evt/mon (13 evt/mon for $M \geq M_c$=1.2) during periods i-m. Group #4, near Marathias fault, follows Group #9 closely up to period f with 22 evt/mon, then after a small burst in period g it proceeds with 20 evt/mon up to period k (or 21 and 17 evt/mon, respectively, for $M \geq M_c$=1.2). The other mid-gulf group, #8, has a rate of 7-12 evt/mon, excluding some occasional bursts, and an average of 21 evt/mon up to period n (11 evt/mon for $M \geq M_c$=1.3). Then a smooth increase is observed during the 2006-2007 sequence, along with the other mid-gulf Groups #5 and #6, reaching a maximum of activity in period q, before it drops to a low rate in periods r-s.

6.6.1 The 2001 swarm near Ayios Ioannis

Increased activity in a region ~6km SSW of Aigion, near station AIOA (Ayios Ioannis), began in late January 2001 with a few events concentrated in a radius of ~0.5 km. An M_w=3.5 event on 29 March 2001 triggered abrupt increase in the seismicity rate, initiating a swarm with several events of $M_w \geq 3.0$, including an M_w=4.1 on 8 April 2001, the largest event of the sequence. The 2001 AIO swarm defines most of Group #2. In this section, however, the study period will be limited between 17 January and 22 July 2001. The spatial distribution was further divided into 6 subclusters (Fig. 6.22) using Ward's linkage and consulting Mojena's plot. The major M_w=4.1 event occurred in Group #5, which is also the more populated one (Fig. 6.23). From the histogram and the diagram of cumulative number of events it is apparent that while all sub-groups are involved during the evolution of the swarm, there are several small outbursts and differentiations. For example, the sub-

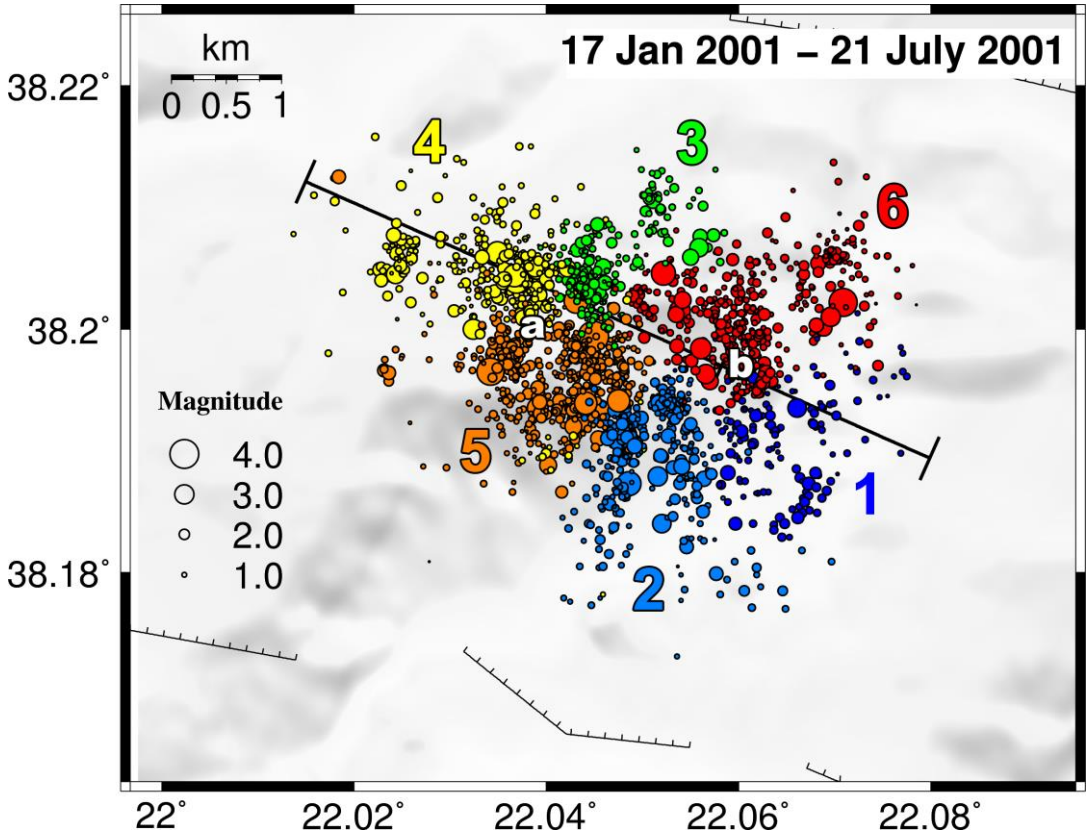

Figure 6.22: Epicenters of relocated seismicity of the 2001 Ayios Ioannis swarm. The line drawn at N114°E is used for the spatio-temporal projection of Fig. 6.25. Colours and numbers represent 6 spatial clusters determined using Ward's linkage to better distinguish the various part of the swarm. Letters "a" and "b" mark the approximate location of the hypothetical injection source centers used in Figs 6.26 and 6.27, respectively.

group #5, is mostly active between 28 March and 18 April 2001, while the second larger sub-group, #6 (NE part of the swarm), is more active in a later period, with outbreaks on 1 and 26 May 2001. Activity in sub-group #1, at the eastern end of the swarm, is delayed until about 9 May – 2 June 2001.

A cross-correlation procedure for the 2001 AIO swarm was re-run using the working components of station DIMT, at an epicentral distance of ~5.5km N of the swarm, filtered between 2 and 15 Hz. Clustering into multiplets was performed with nearest neighbor's linkage at the optimal threshold of C_{th}=0.93. The multiplet history diagram of Fig. 6.24 shows that the first multiplets, including the largest one in sub-group #5, were initiated before the occurrence of the first major event (M_w=3.5) on 29 March 2001. In fact, at least two outbursts related to the generation of new multiplets occurred before the M_w=4.1 event on 8 April 2001. The latter triggered the initiation of several new multiplets, which, however, belonged to sub-group #4, in the NW side of the swarm. This sudden increase of activity in sub-group #4 is also evident from the diagram of the cumulative number of events (Fig. 6.23). It is also apparent that several major events are related to the initiation of new multiplets (spreading of activity to new, unbroken areas), or re-activation of previously generated

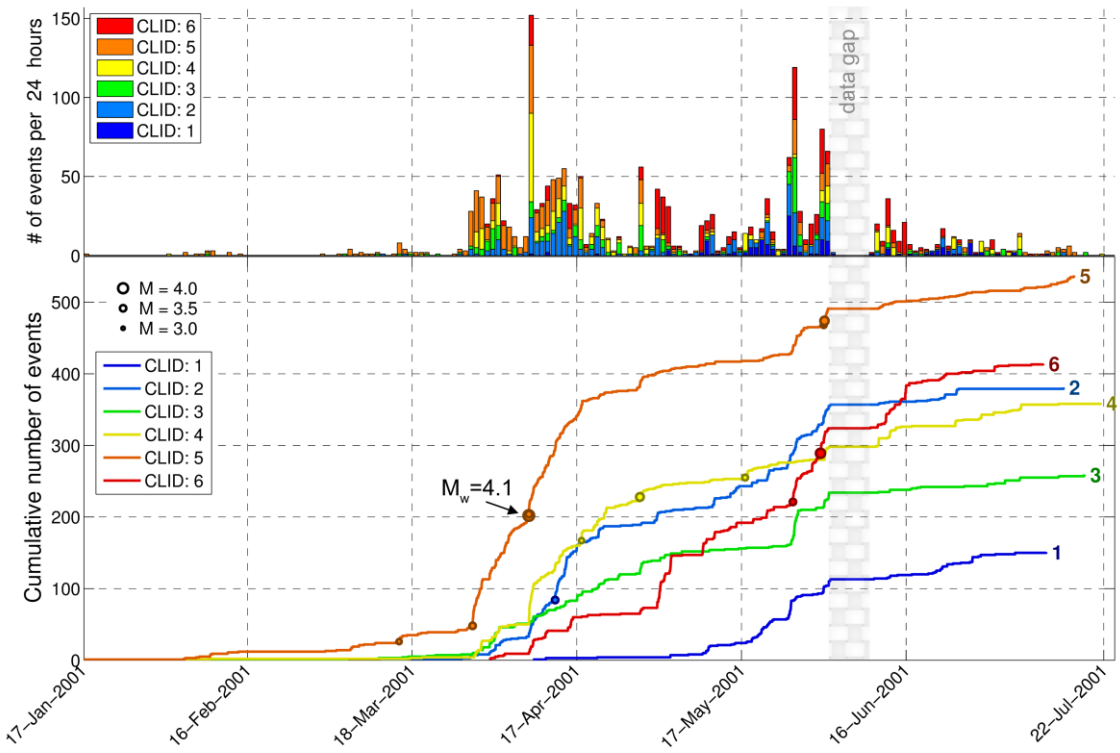

Figure 6.23: (top) stacked histogram of events per day per spatial group (Fig. 6.22) for the seismicity of the 2001 Ayios Ioannis swarm, (bottom) the respective cumulative number of events per group.

ones. The largest multiplets (size>40) were initiated either prior to the M_w=4.1 earthquake or directly triggered by this event, while some others, such as multiplet #57 (sub-group #2) were briefly initiated right after the M_w=4.1 shock but most of their events occurred after the M_w=3.5 event of 26 May 2001.

A better view of the swarm's spatio-temporal evolution is presented in Fig. 6.25, where the y-axis is the distance of the projected epicenters along the N114°E oriented profile-line shown in Fig. 6.22. The early activity is roughly concentrated between the 2 and 3 km marks. By considering this point as the projected center of a fluids injection source, parabolic envelopes are drawn according to the formula of Shapiro *et al.* (1997) for various values of hydraulic diffusivity, D (Eq. 1.16). The value D=0.08m^2/s fits well the expanding triggering front towards ESE, while D=0.1m^2/s is deemed more appropriate for the opposite direction to contain a small cluster in sub-group #4 that is slightly separated from the rest of the swarm (Fig. 6.22, NW). From the point of view provided by this spatiotemporal projection, earthquake migration is observed at a rate of ~30m/day towards both ESE and WNW directions or ~80m/day for the latter if the separated cluster of sub-group #4 is considered as triggered by fluids diffusion.

Small outbursts of increased activity on widespread regions along this projection are presented as thin (short time interval) vertical columns of concentrated points. On a closer look, after detailed examination on how these temporal clusters are distributed on the map, a single source point for radial expansion can be decided. In Fig. 6.26a spatiotemporal distribution is presented relative to a

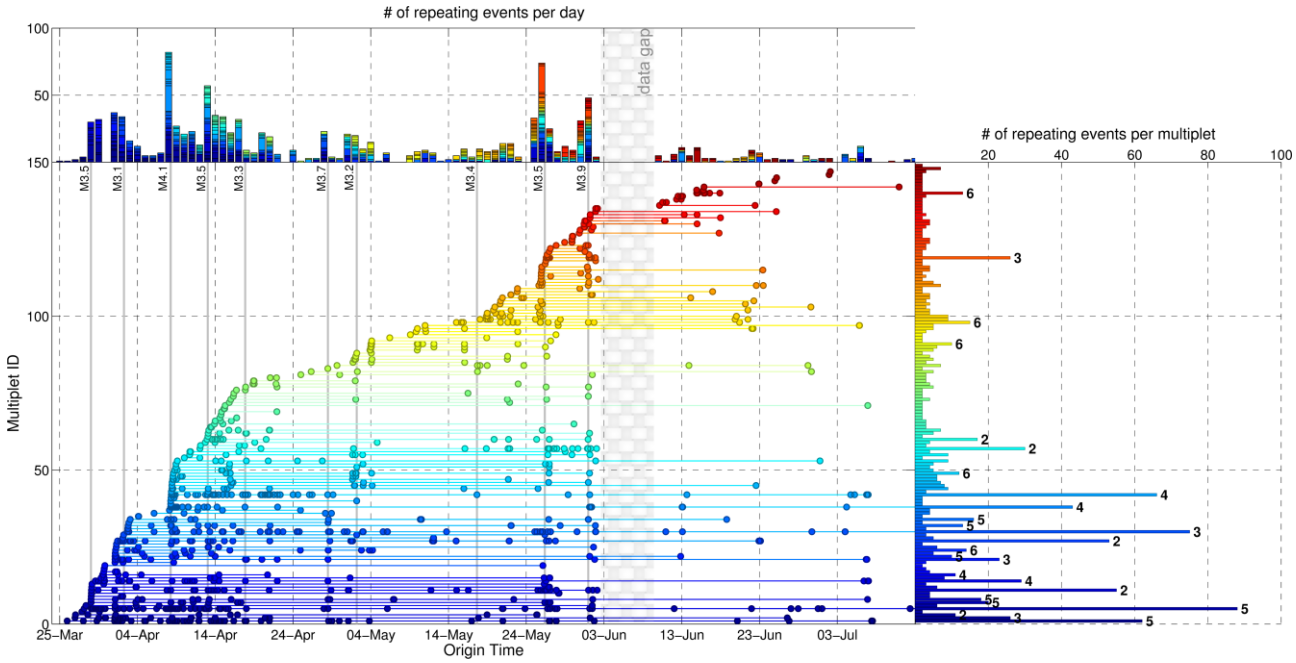

Figure 6.24: (lower-left panel) Multiplet history diagram for the 2001 swarm near Ayios Ioannis calculated using waveforms of station DIMT, filtered between 2 and 15 Hz. Each row represents a multiplet of size≥2 with each repeating earthquake marked with a circle and increasing origin time of the first earthquake in each multiplet from bottom to top. Major events associated with gradual or abrupt increase in new multiplet generation rate are marked with gray vertical lines and the corresponding magnitude at the top. (top panel) Stacked histogram of the total number of repeating earthquakes per day, with colours corresponding to the respective multiplets in the lower-left panel. (right panel) Number of repeating earthquakes or size of the multiplet. Numbers at the end of the largest multiplets' bars mark the respective spatial group numbers as in Fig. 6.22.

fluids source at a point marked by the letter "a" in Fig. 6.22. This diagram ignores direction and is usually more appropriate for simple diffusion procedures. With the fluids pressure pulse starting at about the same time as in Fig. 6.25, on ~50 days, or 8 March 2001, a parabolic envelope with D=0.11m^2/s seems adequate to represent the triggering front. Interestingly, an expansion in depth can also be observed (Fig. 6.26b), at about the same rate of ~30m/day, reaching down to ~9 km by the 80th day, at the distinct cluster of sub-group #4 which, is also the deepest.

In the projection of Fig. 6.25 a pattern that resembles a back-front can be observed, starting shortly after day 100, around 30 April 2001, with a sudden deficit of seismicity near the primary source (2-3 km). In terms of the hydrofracture model (Section 1.3.3; Fig. 1.17) this unidirectional fluids flow pattern could indicate that active fluids triggering (injection) has ceased long before this stage (Parotidis *et al.*, 2004; Dahm *et al.*, 2010) and the rest of seismicity is due to pore-pressure diffusion or stress changes at the edges of the introduced tensile fracture. Alternatively, typical stress-triggering by previous events or, more likely, a combination of stress-transfer with increased pore-pressure could explain the seismicity. The radial expansion diagram of Fig. 6.26a it seems that quite

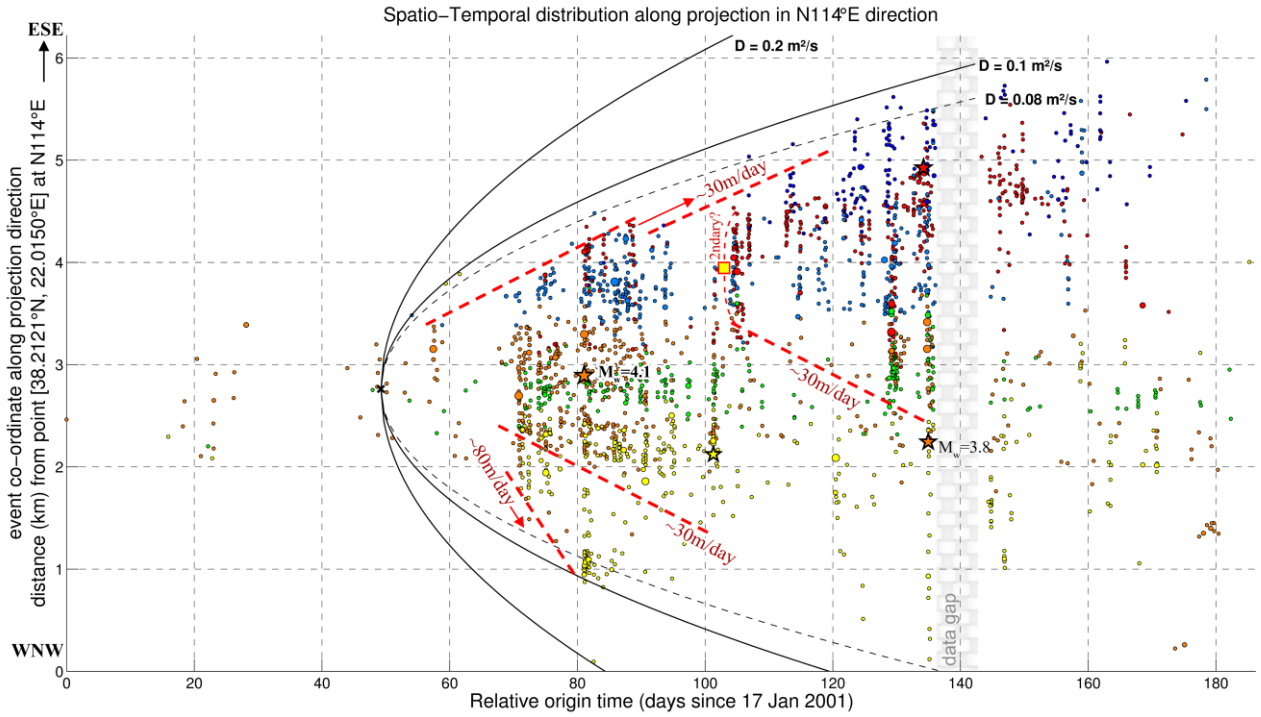

Figure 6.25: Spatiotemporal projection of the 2001 swarm near Ayios Ioannis station in a N114°E direction (Fig. 6.22; WNW→ESE upwards), with the horizontal axis depicting time in days since 17 January 2001. Circle colours correspond to the 6 spatial clusters of Fig. 6.22. Red dashed lines mark possible envelopes of linear migration velocity. Black parabolas are possible non-linear triggering front envelopes of different hydraulic diffusivity values, D, with the source of injection projected roughly on the same point as the M_w=4.1 major event of the swarm. Checkerboard area refers to a data gap between 3 and 9 June 2001. The yellow square at ~102 days, ~3.9km, is the projection of the approximate source of a secondary outbreak (Figs 6.22 and 6.27). Stars mark events with $M_w \geq 3.7$.

a lot of events occur behind the hypothetical back-front. These events could be related to a secondary fluids source whose trace is marked with a square in Fig. 6.25 and by the symbol "b" in Fig. 6.22. A new expanding front at a similar rate of 30m/day is seen after day 100 in both horizontal (Figs 6.25 and 6.26a) and vertical (Fig. 6.26b) spatiotemporal diagrams. Fig. 6.27 shows the radial expansion with respect to the secondary source. Interestingly, from this point of view, the migration rate is, on average, 80m/day, following the parabolic envelope with D=0.22m^2/s until it reaches another major event (M_w=3.8) in Group #5 which in turn triggers a small aftershock sequence. Unfortunately, the latter is interrupted by a data gap between 3 and 9 June 2001.

The 2001 AIO swarm, treated as a single cluster, is well distributed on a roughly flat plane (planarity≈0.85) striking ~240° and dipping at 35° towards NW (Fig. 6B.26a). It is compatible with the focal mechanism of the major M_w=4.1 event of 8 April 2001 as derived by Zahradnik *et al.* (2004), with a fault plane solution φ=220°, δ=40° and λ=-160°. This seems to be in contradiction with the dominant faulting regime in the region of the western Corinth Rift such as the WNW-ESE

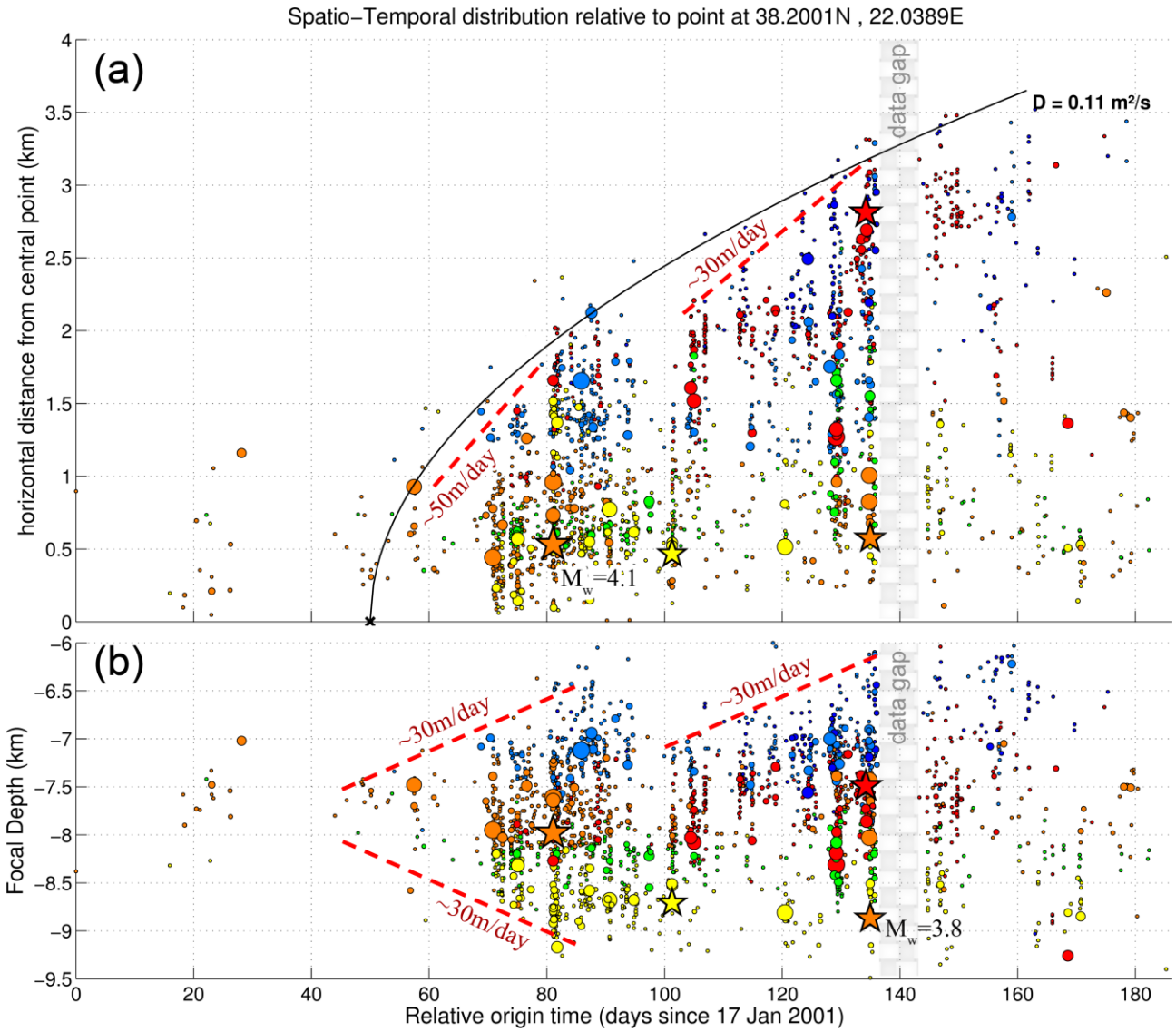

Figure 6.26: Spatiotemporal diagram of the 2001 swarm near Ayios Ioannis station a) horizontal distance from the point at 38.2001°N, 22.0389°E, b) distribution of focal depth. Stars mark events with $M_w \geq 3.7$.

trending, north-dipping Pirgaki and w.Helike faults bounding the epicenters of the swarm. The most likely candidate is the NW-dipping Kerinitis fault, as suggested by Lyon-Caen *et al.* (2004), an old and presumably inactive structure which, however, could provide a weak discontinuity along whose surface slip may occur under the right local stress and pore-pressure conditions. The latter can be strongly influenced by pressurized fluids, whose presence is confirmed by the observed spatiotemporal patterns.

Constraining focal mechanisms with first motion polarities (FMP) in this region is relatively difficult, as the swarm is slightly outside the southernmost end of the CRL network, thus it has a

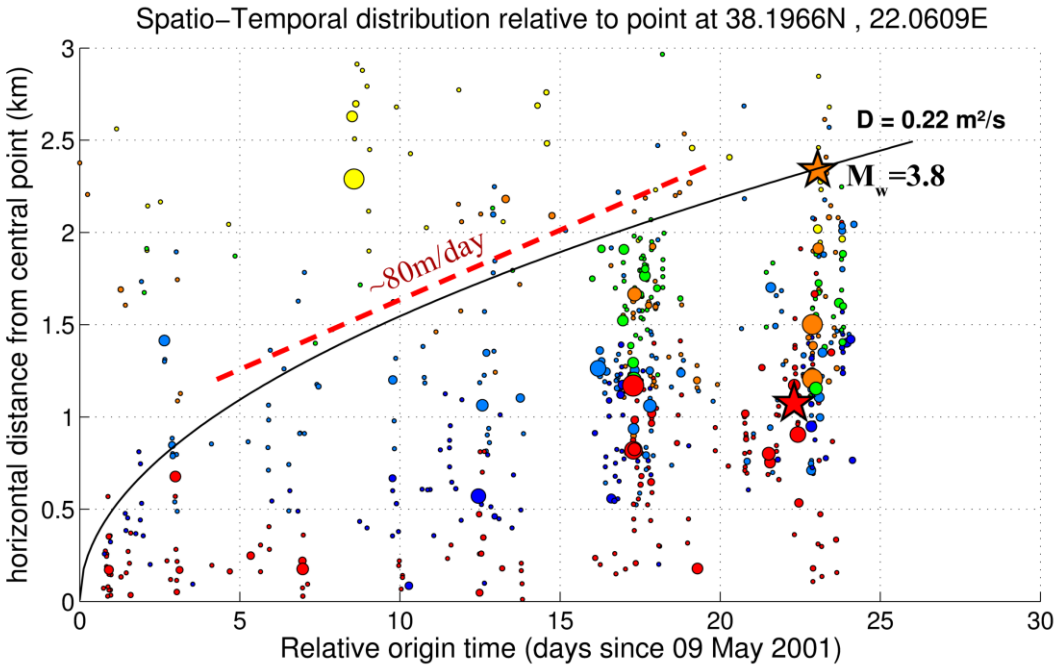

Figure 6.27: Spatiotemporal diagram of a secondary outbreak of the 2001 swarm near Ayios Ioannis station, with the vertical axis representing horizontal distance from the point at 38.1966°N, 22.0609°E (Fig. 6.22; source "b"). Stars mark events with $M_w \geq 3.7$.

significant azimuthal gap. Additional weights by considering S-wave polarization directions and S to P amplitude ratio can balance the high uncertainty, quantified by elevated RMS angular difference values (e.g. Fig. 6B.13a) and by shifting the composite focal mechanism towards a solution that is more compatible with the observed radiation pattern. The results are a mix between oblique-normal dextral-slip faulting, similar to the major M_w=4.1 event, with one of the nodal planes dipping approximately NW and normal / low-angle dip-slip faulting, compatible with the slip on the detachment zone at the northern side of the rift. Fig. 6.28 shows a series of cross-sections drawn at a N310°E direction, transverse to the plane resolved by the geometry of the spatial distribution (a-c) and one roughly perpendicular to the Pirgaki fault (Pi.f.), south of the swarm's epicenters. According to field observations (Ghisetti & Vezzani, 2005) the dip of Pirgaki fault at the surface varies between 50° and 70°. It is immediately apparent that at 60° dip, Pi.f. passes right above the swarm. Even at 70°, provided it does not change at depth, the fault would only intersect with the northernmost / deeper part of the swarm. However, there are no composite focal mechanisms compatible with this scenario and their nodal planes are oblique with respect to the d_1-d_2 cross-section. The perpendicular, thin (±0.3km) cross-sections, on the other hand, show an agreement between NW-dipping nodal planes and the respective profile of the spatial distribution. Kerinitis fault (Ke.f.), hard-linking Pi.f. and Mamousia fault (Mam.f.) at a N242°E strike with a dip of ~70° at the surface, near its junction with Pi.f. (Ghisetti & Vezzani, 2005, fault segment labeled "13d"), "views" the swarm at an angle between 50° and 57°. While not fully compatible, it indicates that the cluster has likely occurred either on this or on another discontinuity with at least the same

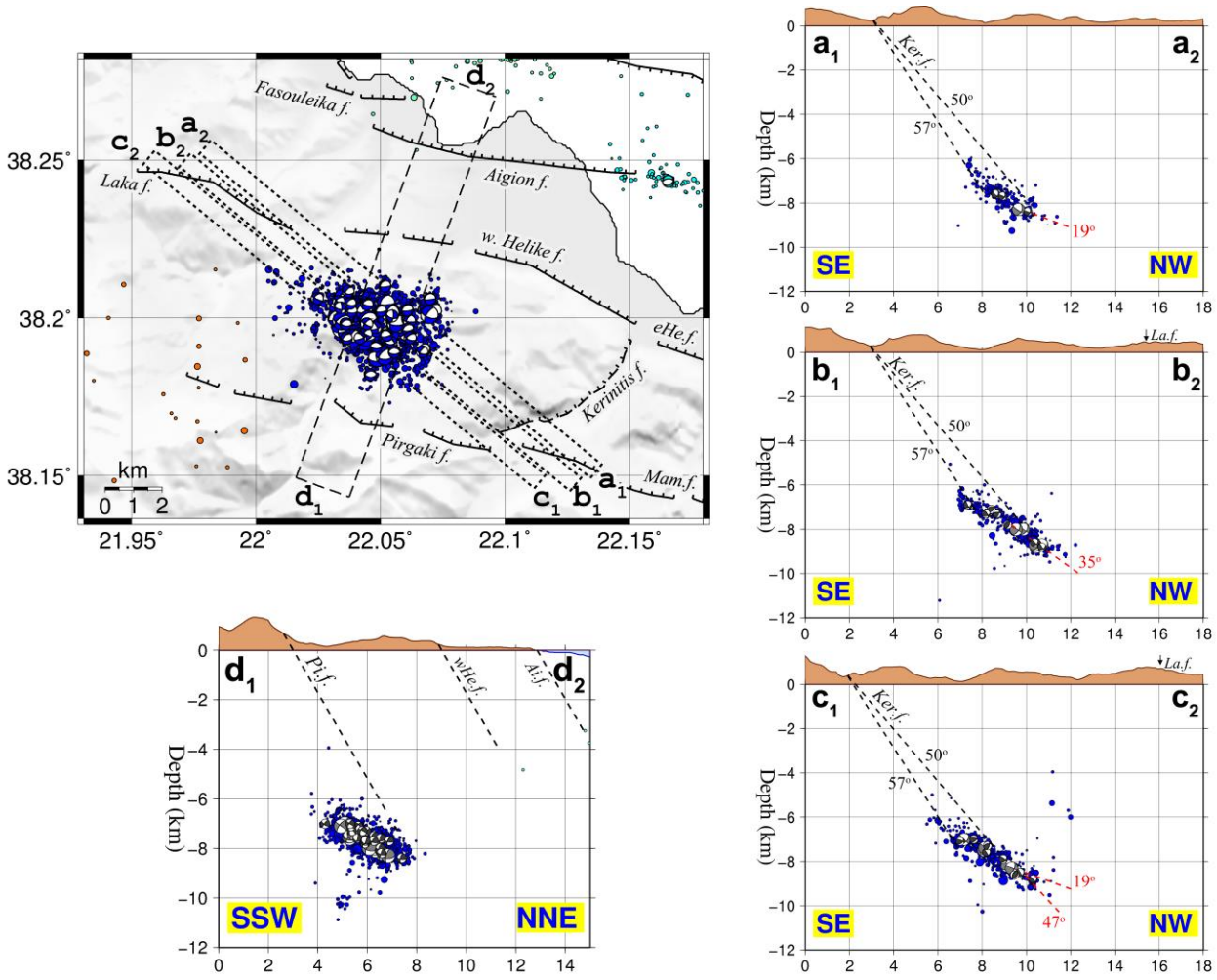

Figure 6.28: (top-left) Seismotectonic map of the 2001 swarm in Ayios Ioannis including composite (small beachballs) and single (large beachballs) focal mechanisms. Cross-sections a-d are drawn in the directions and bounds presented in the map.

strike, a plausible scenario (Lyon-Caen *et al.*, 2004) since Ke.f. is likely crossed by Pi.f. and possibly other minor active E-W striking faults.

6.6.2 Mid-gulf seismic activity (2003-2004)

Another subset of particular interest in the catalogue is the 2003-2004 sequence inside the western Gulf of Corinth. The events belong to the spatial Groups #8, #6 and #5, with their epicenters located north of Selianitika, Fassouleika and Aigion faults (Fig. 6.29). The line drawn at a N120°E direction in Fig. 6.29 is used for the spatiotemporal projection of Fig. 6.30. The catalogue was manually divided in 14 periods (a-n; Fig. 6.30 and 6B.24 in the Appendix) by observing the initiation times of each of the several very distinct sub-clusters which comprise the swarm. The sequence started on 24

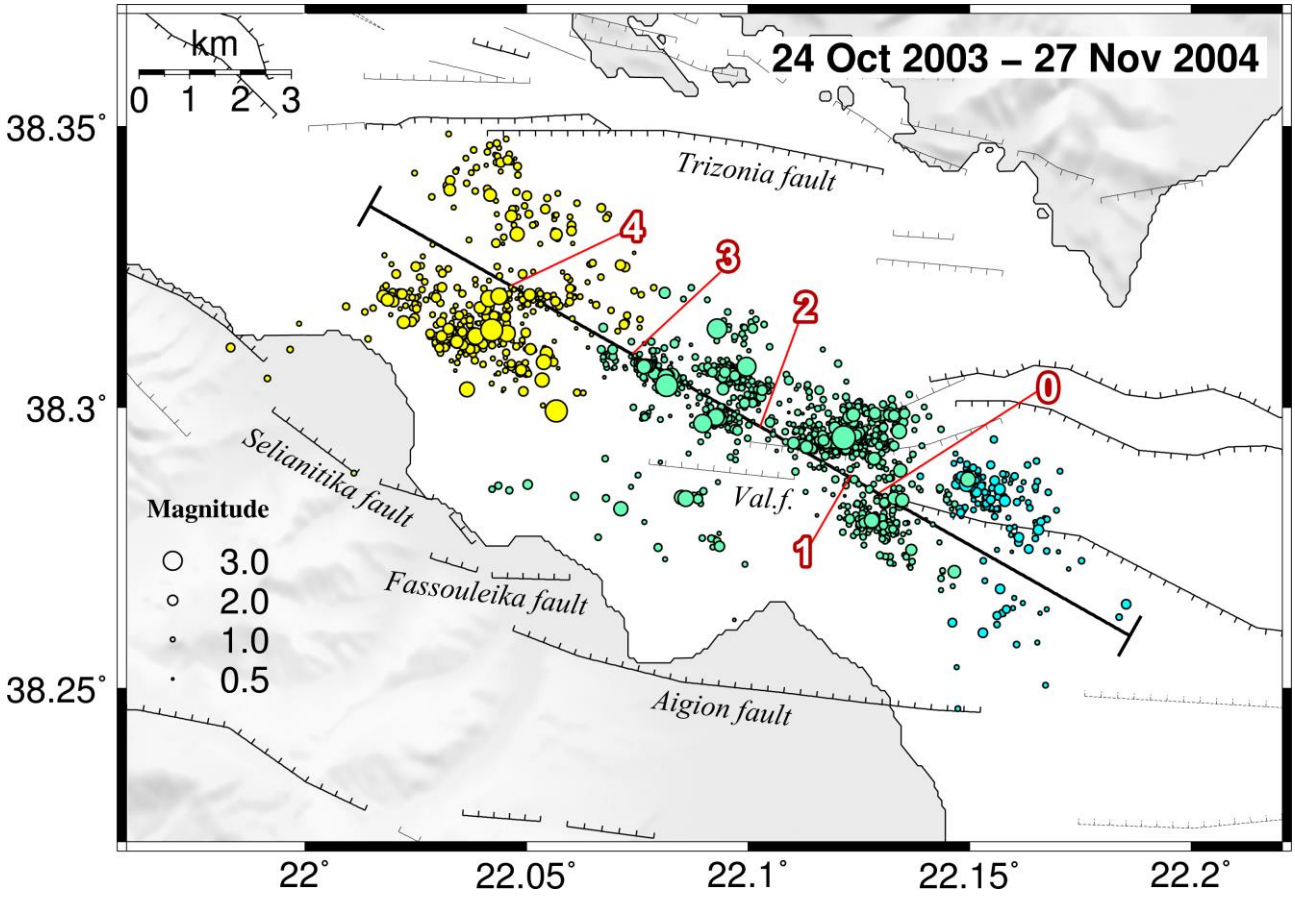

Figure 6.29: Epicenters of relocated seismicity of the 2003-2004 earthquake sequence in the western Corinth Rift. The line drawn at N120°E is used for the spatio-temporal projection of Fig. 6.30. Colours represent the same spatial groups #8, #6 and #5 as in Fig. 6.10. Numbers 1-4 point to the position of potential fluid injection sources (see Fig. 6.30). The point marked with "0" is the center of the radially expanding front of seismicity used in Fig. 6.31.

October 2003 with a series of small events near the 12 km mark (source "1'"), SE of Group #6. Migration patterns are easily observable in Fig. 6.30, initially spreading NW at ~30m/day, then splitting in two fronts, one expanding towards SE at ~50m/day and another NW at ~70m/day. It appears that the latter expands bilaterally relative to a different center than the former, slightly below the 10 km mark (source "2"). The linear dashed envelope that propagates SE at 20m/d encompasses another outburst that includes two events with M_w≈3.5-3.6 in Group #4 during periods h-j. In period g, another source of bilateral diffusion appears at the ~6.5 km mark (source "3"), migration velocities 70-80m/d. The NW branch reaches Group #8 in period j. By the end of period l, a last fluids diffusion source is projected at ~3.8 km (source "4") with slower migration velocities of 30-40 m/day.

Despite the apparent complexity, the whole procedure could be described by spreading from a single starting source roughly located at 38.2833°N, 22.1327°E (point marked with "0" in Fig. 6.29), with a nearly linearly propagating front at 60m/day (Fig. 6.31a). At depth, through periods

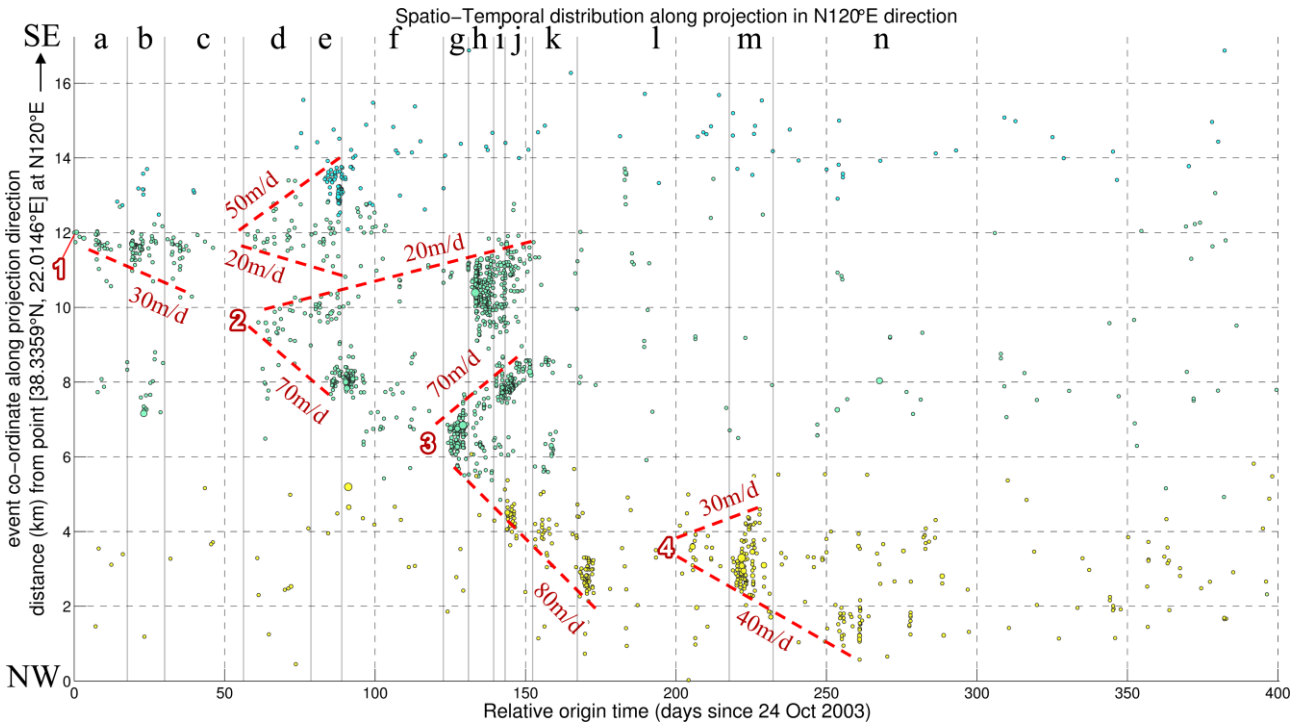

Figure 6.30: Spatiotemporal projection of the 2003-2004 sequence in the western Corinth Rift in a N120°E direction (NW→SE upwards), with the horizontal axis depicting time in days since 24 August 2003. Circle colours correspond to the spatial clusters of Fig. 6.10. The red dashed lines are marking probable migration paths inferred from the patterns of the developing seismicity. Small-case letters on top and solid vertical lines divide the sequence in 14 periods which are presented in the Appendix (Fig. 6B.24). Numbers 1-4 point to the position of potential fluid injection sources also indicated in the map of Fig. 6.29.

a-c (first 40 days) the hypocenters migrate upwards at ~50m/day while the "third wave", during periods g-k (days 120-160), is characterized by a faster migration towards shallower depths at ~100m/day. Interestingly, many of the larger events occurred at the deepest parts of the clusters. Combined with the upwards and horizontal migration that follows, these larger events could have been essential for the opening of paths for fluids to breach into hydraulically conductive channels near the fault's core, increasing pore-pressure and inducing repeating earthquakes.

Fig. 6.32 presents a closer look in the seismotectonics of the activated mid-gulf region during 2003-2004. Most of the focal mechanisms indicate oblique-normal faulting. Four cross-sections are presented to investigate possible relation with mapped faults on the surface. In a_1-a_2, Fassouleika fault (Fas.f.) is a possible candidate structure for the southern part of Group #8, with a dip of ~60°. Selianitika fault (Se.f.), outcropping ~1km N of Fas.f., would have to dip at 65° to reach this part of seismicity. However, there is some incompatibility concerning the strike of the NW-dipping nodal plane and the corresponding strike of Fas.f., as the latter dips NNE rather than NW. The spatial geometry of this cluster also points to a plane dipping 40-70°, depending on the method, directed N11-25°E (NNW). The elongation of the cluster in a WNW-ESE axis is suggestive of the preferred

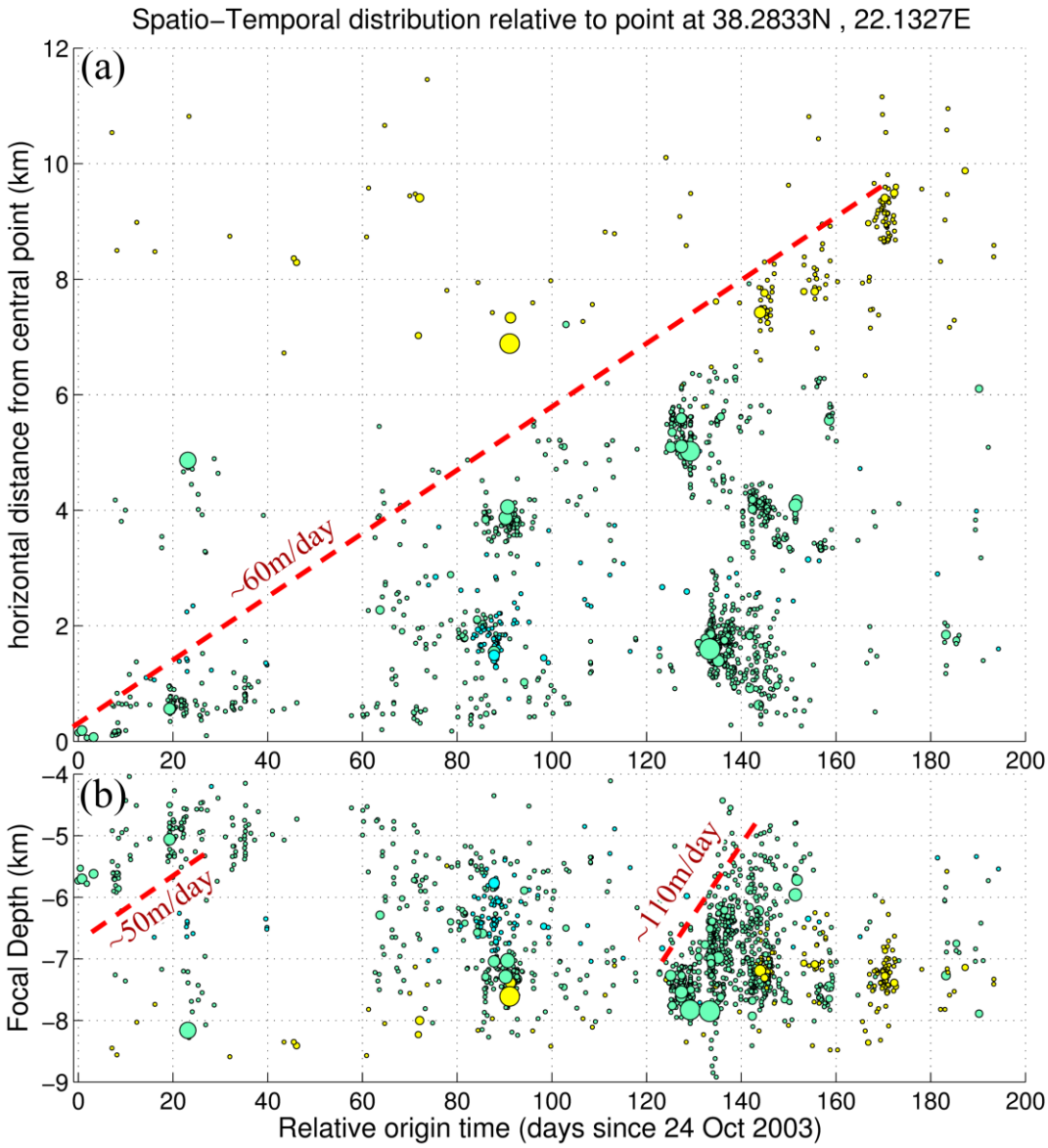

Figure 6.31: Spatiotemporal diagram of the 2003-2004 earthquake sequence within the western Corinth Gulf, a) horizontal distance from the point at 38.2833°N, 22.1327°E (point marked with "0" in the map of Fig. 6.29), b) distribution of focal depth. Circle size is proportional to M_w.

strike. Examples of the oblique-normal composite focal mechanisms from the region involved with cross-section a_1-a_2 (Fig. 6.32) are presented in Fig. 6B.20. These indicate relatively well constrained solutions which do not allow the N-dipping nodal plane's strike to vary much towards a NNE-dipping fault plane. This leaves an ambiguity on whether this activity has occurred at the root of the NNE-dipping Fas.f. or on a small antithetic SW-dipping fault. On the other hand, Se.f. is more compatible with the northern part of Group #8 where the faulting is pure normal in an E-W direction (Fig. 6.19: g_1-g_2, h_1-h_2).

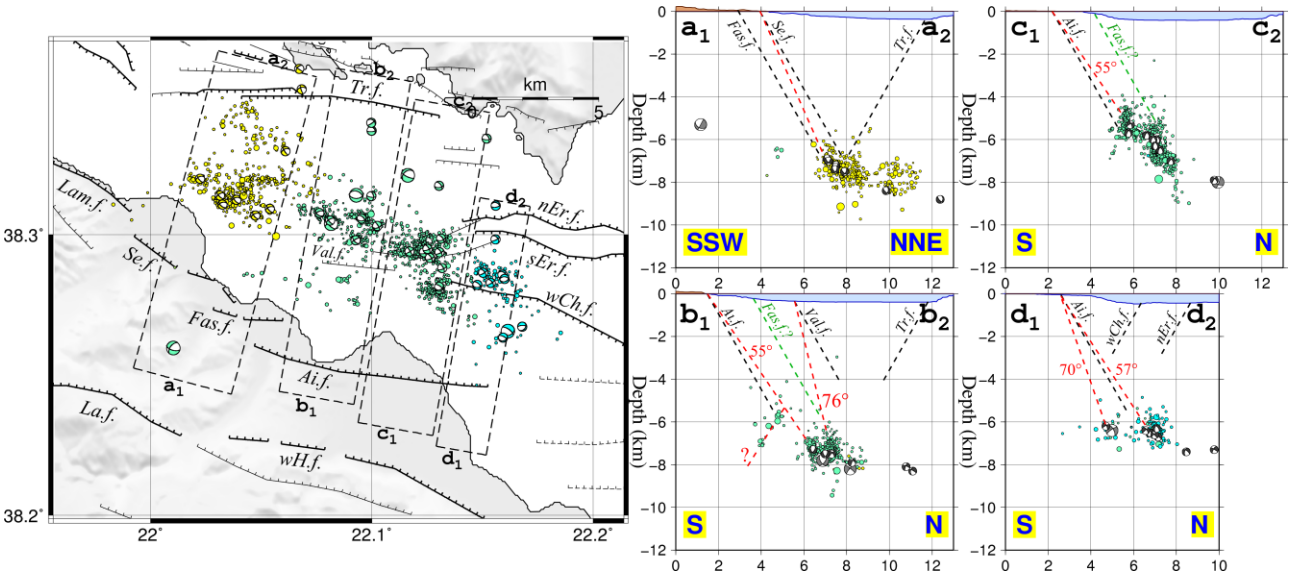

Figure 6.32: (left) Seismotectonic map of the 2003-2004 sequence in the western Corinth Rift including composite (small beachballs) and single (larger beachballs) focal mechanisms. Cross-sections a-d are drawn in the directions (N10°E, except for a_1-a_2 at N15°E) and within the bounds presented in the map. Faults in the cross-sections are drawn at a 60° default dip (black) unless stated otherwise. The red dashed line in a_1-a_2 is drawn at a dip angle of 65°. The green dashed line in cross-sections b_1-b_2 and c_1-c_2 are supposed offshore extensions of Fasouleika fault (Fas.f.). Small beachballs outside the region of the 2003-2004 swarm belong to other multiplets that occurred in 2003-2004.

In b_1-b_2 (Fig. 6.32), some sparse seismicity in the south is either related to Aigion fault or there's a possibility that it belongs to a S-dipping antithetic structure. As with a_1-a_2, most of the focal mechanisms mid-gulf are oblique, contradicting with the expected dip direction of Aigion fault (Ai.f.). However, both Ai.f. and the extension of Fas.f. to the east (green dashed line) are compatible with the southern and northern portions of the activated region, respectively. The offshore Valimitika fault (Val.f.) would have to dip at ~76° to reach the northernmost part of seismicity.

In c_1-c_2 (Fig. 6.32), there are two distinct spatial clusters, a southern one at depths of 4.5-6 km and a northern one at depths of 5-7.5 km. In this part of the swarm, the focal mechanisms are again oblique normal but the nodal planes have different orientations, while, in a few cases, the composite solutions are even pure strike-slip (Fig. 6B.21). It is interesting to note that this is considered to be a region where transition from the highly active western Corinth Rift and the relatively inactive central Corinth gulf occurs (Lambotte *et al.*, 2014) and is near the western extremity of some significant known mapped offshore faults. It is, thus, probable that on a localized scale the stresses are perturbed and deviate from the regional ones, even allowing for transverse structures to be activated. The subvertical southern cluster coincides with Ai.f. at 55°-60° dip while the northern cluster could be compatible with a hypothetical eastern extension of Fas.f., although at a dip angle larger than 60°.

Finally, in d_1-d_2 (Fig. 6.32), Ai.f. dipping at 55°-60° is compatible with a small cluster below the offshore west Channel (wCh.f.) and south Eratini (sEr.f.) faults, and even in agreement with some

of the resolved composite focal mechanisms. A smaller cluster in the south with subvertical N-dipping normal faulting is probably unrelated to Ai.f. or other major mapped structures.

6.6.3 Seismic activity mid-gulf and near Marathias fault (2006-2007)

Intense activity within the western Gulf of Corinth (Fig. 6.33) began by 7 August 2006 in the region of the spatial Group #5 and was soon followed by a complex seismicity pattern of multiple episodes of bilateral migrations and strong outbreaks (Fig. 6.34). The sequence was manually divided in 14 periods by visual observation of the clusters in the spatiotemporal diagram, with the epicenters projected along the major axis of the spatial distribution at N127°E. Maps for each period are presented in the Appendix (Fig. 6B.25). However, to better visualize the observed "flow" of seismicity throughout the consecutive periods, envelope lines have been "free-hand" drawn,

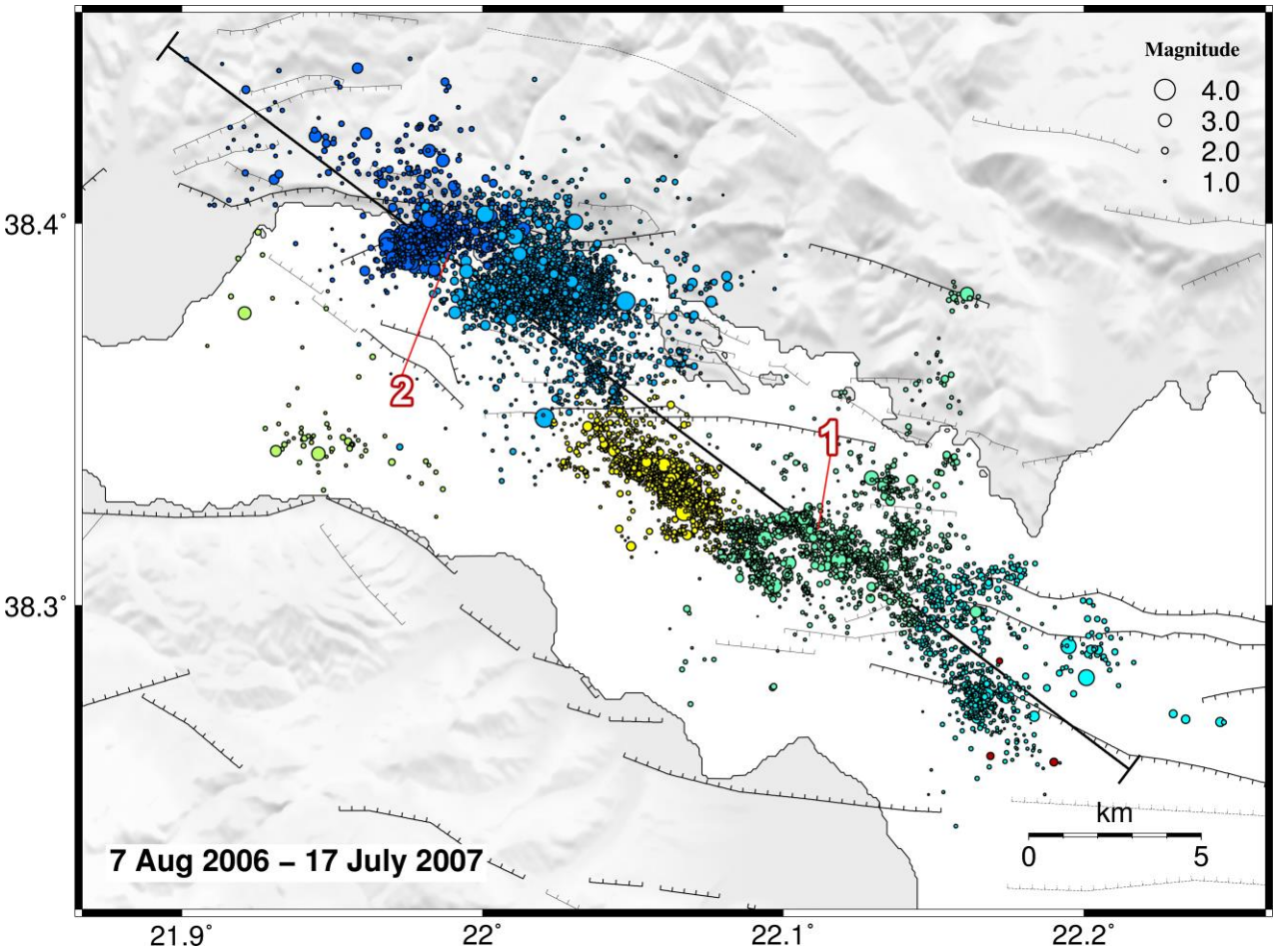

Figure 6.33: Epicenters of relocated seismicity of the 2006-2007 earthquake sequence in the western Corinth Rift. The line drawn at N127°E is used for the spatio-temporal projection of Fig. 6.34. Colours represent the same spatial groups as in Fig. 6.10 for the whole 2000-2007 catalogue.

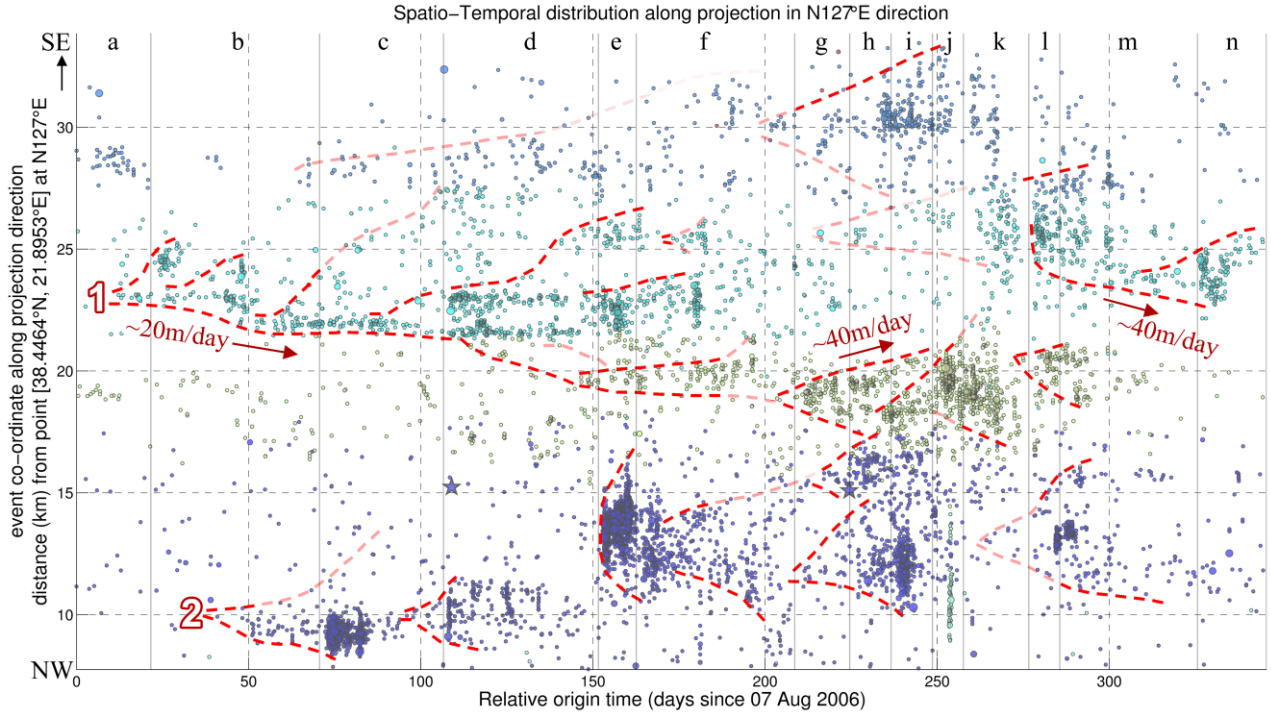

Figure 6.34: Spatiotemporal projection of the 2006-2007 sequence in the western Corinth Rift at N127°E direction (NW→SE upwards), with the horizontal axis depicting time in days since 7 August 2006. Circle colours correspond to the 12 spatial clusters of Fig. 6.10. The free-hand drawn red dashed lines are marking probable migration paths inferred from the patterns of the developing seismicity. Small-case letters on top and solid vertical lines divide the sequence in 14 periods which are presented in the Appendix (Fig. 6B.25). Numbers "1" and "2" point to the position of potential fluid injection sources also indicated in the map of Fig. 6.33.

providing a basis for qualitative description of its evolution. Guided by these lines, a main triggering front can be defined that starts at the 23 km mark in Group #6 (source "1") and propagates at 20m/day towards NW. However, seismicity behind this front is also branching towards the opposite direction at several episodic outbreaks and some others that are not always clearly defined (e.g. in period c, Group #6). Meanwhile, on period b near the NW end of the seismically active region, another source of bilaterally expanding fronts can be observed (source "2"), beginning near the 10 km mark (Group #3). The activity escalates to an intense sequence (period c), triggered by two M_w=3.6 events on 21 and 28 October 2006 near Marathias fault (Mar.f.). This outbreak has a different migration direction, nearly transverse to the projection of Fig. 6.34 but visible in the maps of Figs 5B.25b-d in the Appendix, propagating at 30-40m/day towards NE. It then triggers another outbreak (periods e-f) in the neighboring Group #4, initiated by an M_w=3.6 event on 7 January 2007, migrating at ~160m/day to SE, mainly between 7 and 14 January 2007, while the southern front has reached Group #8 and proceeds NW at 20m/d. Apparently, the two migrating "patches" come together at around mark 17.5km in period h, while another cluster occurs at the SE end. The last outbreak in Group #4 is observed in period i, likely at the western portion of the fault segment that was previously activated during the periods e-f. Seismicity is then

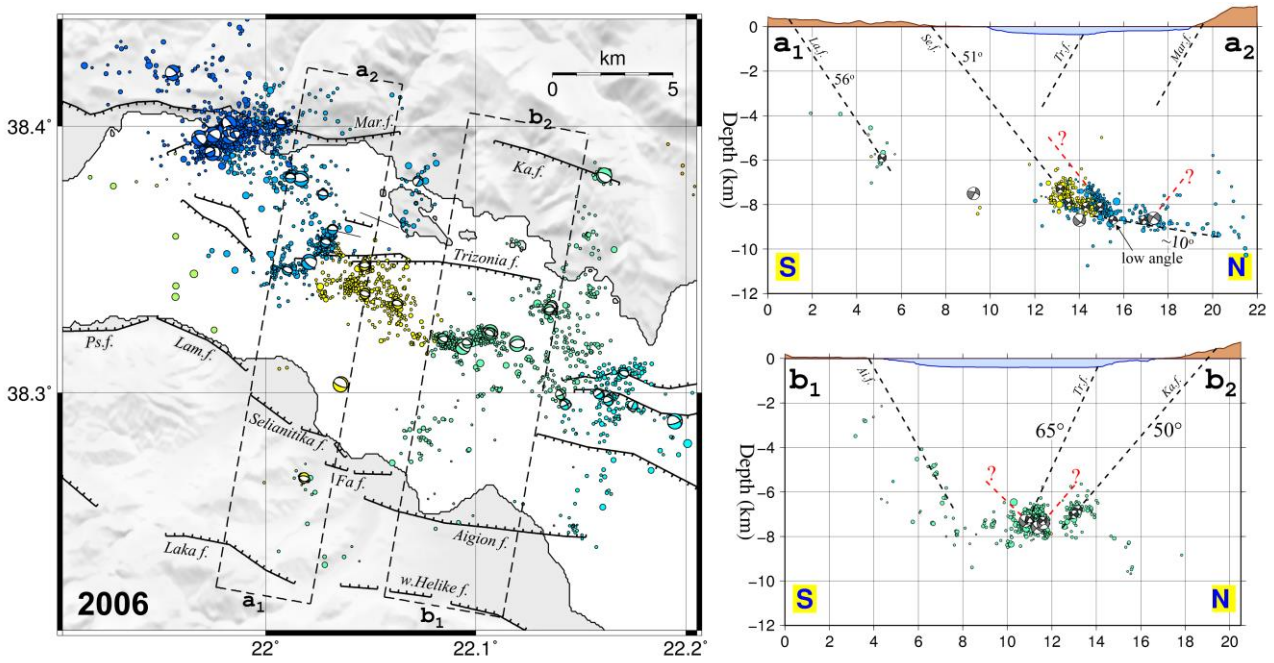

Figure 6.35: (left) Seismotectonic map of the seismicity in the western Corinth Rift during 2006, including composite (small beachballs) and single (larger beachballs) focal mechanisms. Cross-sections a_1-a_2 and b_1-b_2 are drawn in a N10°E direction and within the bounds presented in the map. Faults in the cross-sections are drawn at a 60° default dip unless stated otherwise.

concentrated in the middle of the gulf, at Group #8 (mostly periods g-k) and also at the eastern end in Groups #6 and #5 (periods l, n).

An insight to the seismotectonic characteristics of the western Corinth Rift and particularly the region near Marathias fault has already been given in Section 6.5. However, a clearer view can be provided by selecting a subset of the catalogue in a limited time-interval during the occurrence of spatiotemporally clustered seismicity. In Fig. 6.35 a couple of cross-sections are performed in a N10°E direction for the clusters that were located mid-gulf during 2006. Although the activated structures are not necessarily associated with mapped superficial faults, it is useful to understand their spatial relation to known discontinuities. The clusters in Group #8 appear to correspond to Selianitika fault (Se.f.) at a 51° dip, although the cross-section a_1-a_2 (Fig. 6.35) is not exactly perpendicular to its strike. Activity in Group #4 could possibly correlate with Lambiri fault (Lam.f.). At the eastern side, the activated mid-gulf structures in Group #6 could be related to Trizonia fault (Tr.f.) at a 65° dip, compatible with the observed 64°-72° dip at the surface (Beckers *et al.*, 2015), while a small cluster further north possibly relates to Kallithea fault, supposing a dip angle of 50°, otherwise it could well be a blind small south-dipping fault.

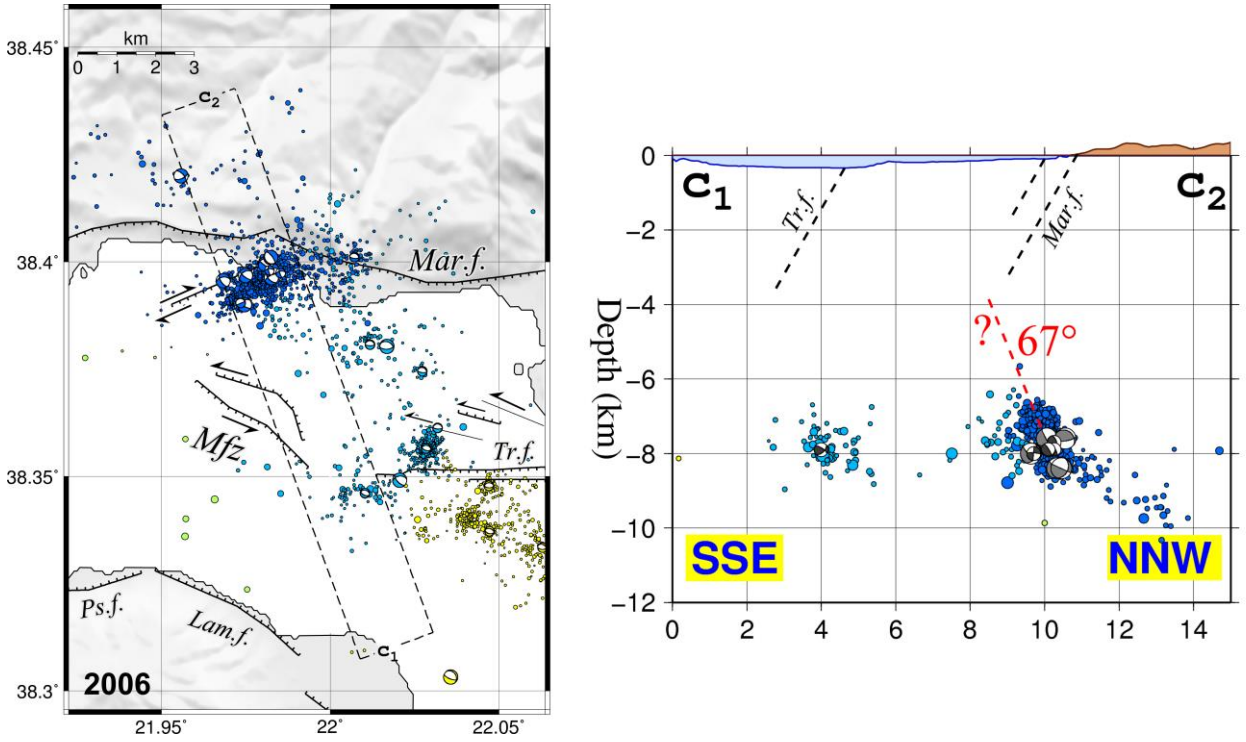

Figure 6.36: (left) Seismotectonic map of the seismicity in the western Corinth Rift during 2006, including composite (small beachballs) and single (larger beachballs) focal mechanisms. Cross-section c_1-c_2 is drawn in a N340°E direction and within the bounds presented in the map. Faults in the cross-sections are drawn at a 60° default dip unless stated otherwise.

Fig. 6.36 presents a cross-section c_1-c_2 at a N340°E direction through the activated patch of Group #3 during 2006 (mainly period c: 17 – 21 November 2006). This is the same structure marked with a yellow rectangle in cross-sections c_1-c_2 and d_1-d_2 of Fig. 6.19. The resolved composite focal mechanisms suggest a NNW-dipping oblique-normal dextral-slip fault. The strike is compatible with the direction of the horizontal elongation of this cluster on the map and the dip direction is confirmed by the examination on the cluster's geometry using the "Three Point" method of Fehler *et al.* (1987) (Fig. 6B.26c,d). At the lowest part of the cluster, some resolved fault plane solutions indicate low-angle NNW-dipping normal faulting. On the surface, Beckers *et al.* (2015) have mapped the undersea Managouli fault zone, south of Marathias fault, with normal faults at oblique directions relative to the E-W strike of the major faults in the western Corinth Rift. Furthermore, they note that these faults have a significant oblique slip component, being dextral on the SE dipping, SW-NE striking fault near the northern shore and sinistral on the offshore NW-SE striking horst. The activated fault patch is not directly associated with the mapped faults; however it has a compatible SW-NE strike and a dextral slip component similar to the fault on the surface.

Concerning the activity during 2007, the most intense cluster is the one that occurred in periods e-f and h-i in Group #4, west of Trizonia island (Fig. 6B.25). Its geometrical characteristics suggest a NW-SE trend (Fig. 6B.27a), compatible with the resolved focal mechanisms that indicate NE-dipping oblique-normal dextral-slip faulting. This is also in agreement with a series of mapped

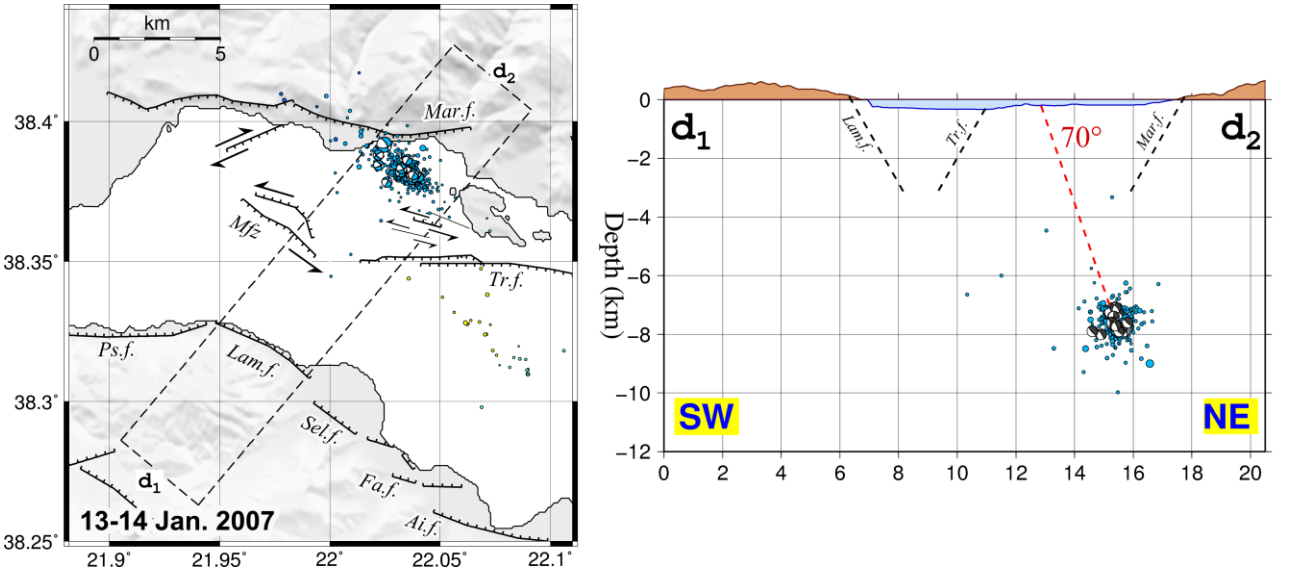

Figure 6.37: (left) Seismotectonic map of the seismicity in the western Corinth Rift during 13-14 January 2007, including composite (small beachballs) and single (larger beachballs) focal mechanisms. Cross-section d_1-d_2 is drawn in a N40°E direction and within the bounds presented in the map. Faults in the cross-sections are drawn at a 60° default dip unless stated otherwise.

faults west of Trizonia island, which are very close to a fault surface, dipping at 70° NE, as inferred by the focal mechanisms (Fig. 6.37, d_1-d_2).

6.6.4 Eratini Group (#9)

The activity in the Eratini group appears to have an almost constant average rate, at about 15-30 events/month, without any significant spatiotemporally clustered outbursts. The western part of the group seems denser than the eastern part, probably due to lower azimuthal gap / higher detectability. Some periods of higher rate include 30 July 2001 – 5 April 2003 with 20 events/month and 26 December 2006 – 10 April 2007 with 23 events/month. The largest events in the group include an M_w=3.7 on 27 January 2002 and an M_w==3.5 on 24 May 2004 (Table 6.10).

The resolved composite focal mechanisms indicate normal, dip-slip faulting at low (western part) to very low-angle (eastern part). Some variations are likely due to the group being at the edge of the network, with significant azimuthal gap. However, the “odd” fault plane solutions are compatible with slip on a low-angle detachment zone with the hanging wall sliding northwards. The overall geometry of the group is also consistent with this hypothesis (Fig. 6B.27b).

6.7 ETAS modeling

The seismic activity of the western Corinth Rift is characterized by continuous background seismicity, mainly offshore, including several outbreaks of spatiotemporally clustered events. The strongest events during 2000-2007 do not surpass M_w=4.2, however, many bursts of intense seismicity appear related to major events. The Epidemic Type Aftershock Sequence (ETAS) model (Ogata, 1988), briefly described in Section 1.3.4, works on the assumption that all earthquakes, independently of their magnitude, are capable of generating their own aftershock sequences. In this section, several subsets of the 2000-2007 catalogue are examined in terms of the ETAS model and their general characteristics are outlined. The SASeis2006 software (Ogata, 2006) is used for the determination of the model parameters μ, K, c, a and p using Maximum Likelihood Estimation (MLE). Forward modeling can then be performed with the estimated parameters for the comparison between model and data. The constants can be calculated for a small subset and then used on a longer time-series to examine how well it performs, or estimated for different phases of a sequence to examine whether one or more parameters have changed.

Deviations of the data from the residual point process (RPP) are generally attributed to one or more of the following reasons:

- One or more of the ETAS model parameters are non-stationary.
- Some of the activated regions require different constants.
- Positive residuals (more observed events than expected) could mean that part of the seismicity cannot be explained by stress-transfer produced by previous events but is rather triggered by other causes (external forcing)
- Negative residuals (deficit of observed events) could indicate seismic quiescence.

The seismicity of Groups #3, #4, #5, #6 and #8 is selected as a subset of the general seismicity along the gulf. The magnitude of completeness M_c=1.2≡M_{th} is used as a threshold or cut-off magnitude while M_r=4.2, the magnitude of the largest event, is considered as a reference magnitude for the ETAS model, a choice that only affects the parameter K. The model parameters are determined by MLE using a total of 10155 events with $M \geq M_{th}$ for a time-span of ~2675 days. Fig. 6.38 shows the result of the ETAS model for the subset. In general, the fit is acceptable, even for the short period of the first 100 days not used in the MLE, with both positive and negative residuals. The best fit is observed up to 26 April 2004, when a long period of "quiescence" (cumulative number of events in data being less than the expected by the model) begins. This period follows the major M_w=4.2 event of 18 November 2003 (marked with star in Fig. 6.38, lower panels), while the most negative residuals are observed during 14 December 2005 – 19 October 2006, when the observed seismicity rate drops to low values. The residual increases abruptly on 19 October 2006, when the sequence of period c (Fig. 6B.25c in the Appendix), described in Section 6.6.3, began, and becomes positive after the other major outbreak on 7 January 2007. The determined aftershock productivity for the whole seismicity is a=0.83 is within the upper bounds that have been known to characterize swarm-like activity in other regions (e.g. Ogata, 1992; Hainzl & Ogata, 2005). During the MLE, the background rate μ has been forced to zero, as the resulting parameters with μ=0

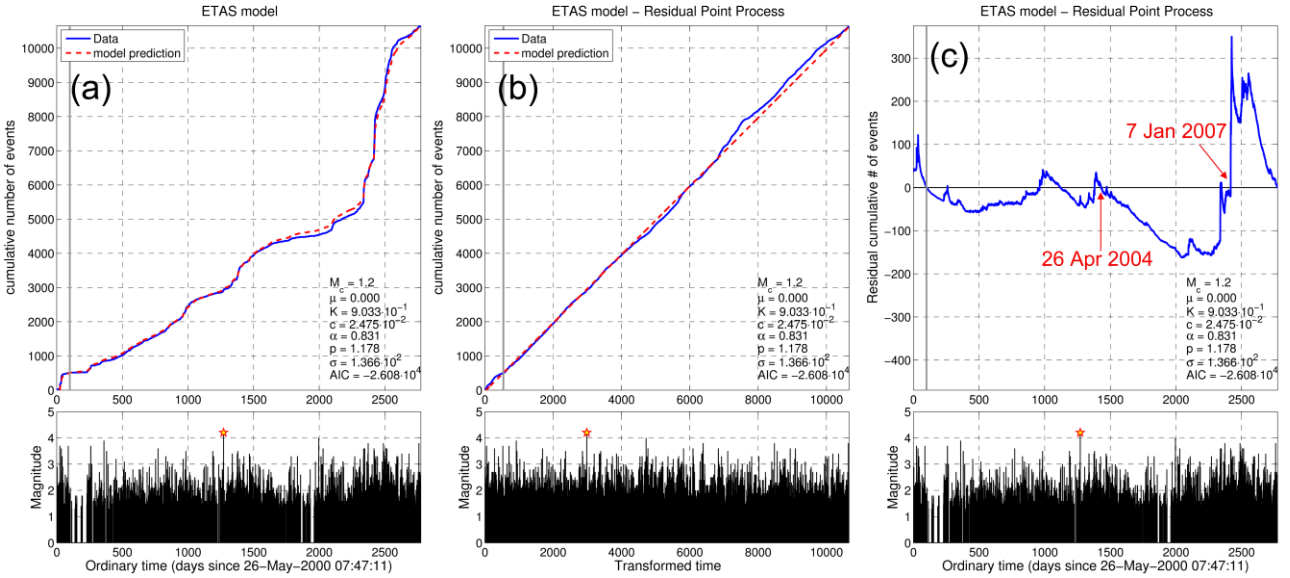

Figure 6.38: ETAS model for the seismicity of 2000-2007 within western Gulf of Corinth (spatial groups #3, #4, #5, #6 and #8), with M_r=4.2, excluding the first 100 days from the modeling (gray vertical line) and forcing μ=0, a) in ordinary time, b) in transformed time and c) residual between data and model in ordinary time.

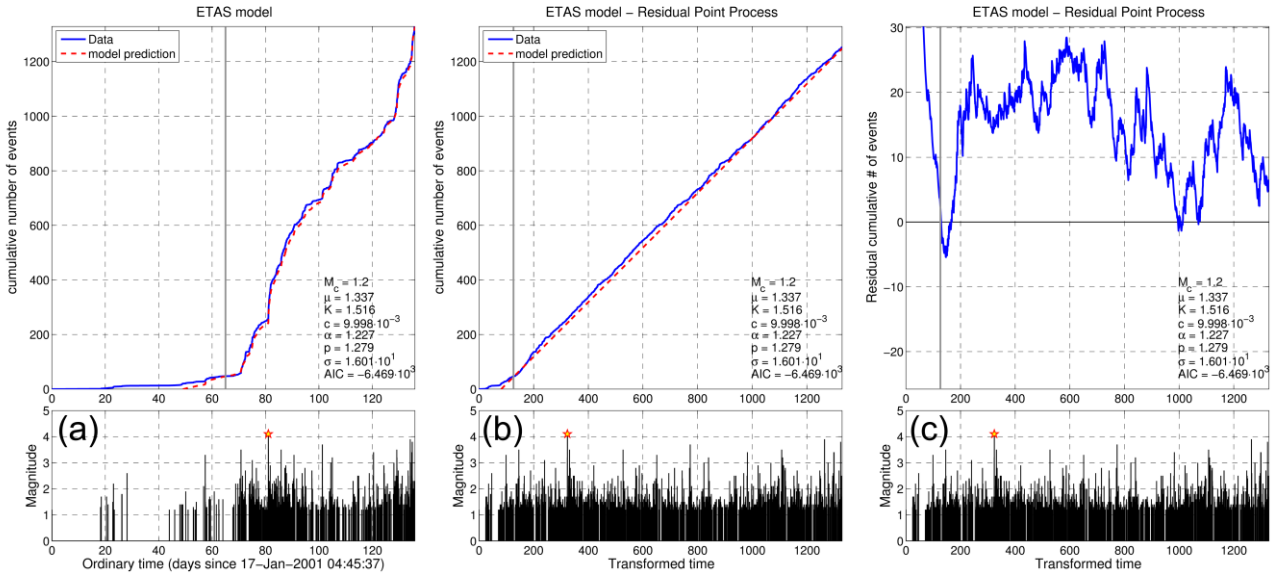

Figure 6.39: ETAS model for the 2001 Ayios Ioannis swarm up to 3 June 2001 (excluding a data gap), a) in ordinary time, b) in transformed time and c) residual between data and model in transformed time. The first 65 days (gray vertical line) are excluded from the modeling. The star (bottom panels) marks the major M_w=4.1≡M_r event of 8 April 2001.

provided a better visual fit to the data (smaller standard deviation, σ), although the Akaike's Information Criterion (AIC) value, which represents the goodness of fit, was slightly smaller for $\mu \neq 0$. In both cases the parameter values are comparable (Table 6.11)

For the 2001 swarm near Ayios Ioannis, the spatiotemporal distribution (Figs 6.25 and 6.26) shows that a few small events occurred within a little more than 50 days since 17 January 2001, before the swarm typically began, following an M_w=3.5 event on 29 March 2001. To determine the parameters for the ETAS model of the swarm, the completeness magnitude M_c=1.2≡M_{th} (Fig. 6.12c) was used as a threshold and M_z≡M_r=4.1 as the reference magnitude, excluding the first 65 days. Although the resulting model follows the observed data closely with a similar shape (Fig. 6.39), it has a residual with a nearly fixed positive sign along most of the set, indicating that stress changes caused by previous earthquakes alone cannot fully describe the observed cumulative number of events. This indicates that aseismic forces likely influence the evolution of the sequence, especially between 29 March and 1 April 2001, when the residual increases to a values of ~20 which remains as an average value up to about 24 April 2001. However, the differences are not very significant, meaning that, on a large part, major events drive their own sub-sequences within the swarm. The residual drops a bit below zero after the beginning of the second phase of the swarm (fluids source "b" on ~9 May 2001, Fig. 6.27), at about 125 days (~22 May 2001), when the seismicity rate has relatively reduced before the next outbreak.

An interesting comparison is presented in Fig. 6.40 where the dataset has been restricted to the period between 8 April 2001 (at the time of the M_w=4.1 major event) and 22 May 2001, before the occurrence of major events during the 2nd phase. An ETAS model is compared against the respective Omori-Utsu model (Modified Omori's Formula or MOF), which attempts to describe the whole sequence as a result of the M_w=4.1 "mainshock". Although in terms of gross characteristics the MOF model adequately describes the average seismicity rate, with alternating signs in the residual, the ETAS model follows the data more closely, albeit with a residual of positive sign, with few, weak alterations. The AIC values are also consistent with the previous observation, as they are of the same order of magnitude for both ETAS and MOF models, but the former has a smaller (more negative) value, which indicates it is preferred over the latter. The standard deviation, σ, is also slightly higher for the MOF model. In addition, the MOF model requires a much higher μ-value for background seismicity while its p-value is significantly smaller, as the whole sequence is supposedly generated by the M_w=4.1 major event, thus it has to be described by a lower decay rate so that the memory is longer. On the other hand, the higher p-value for the ETAS model reflects stronger decay for each subsequence generated by events of various magnitudes. The K, a and p constants for ETAS are of comparable values in both Figs 6.40a and 6.39. By forcing μ≡0, the ETAS model fit in this subsequence becomes even better, with similar AIC but much lower σ (Figs 6.40d-f) and the residual is frequently alternating its sign, indicating strong dependence of the secondary subsequences to the previously generated events without having to assume non-stationarity in the model's parameters. This could indicate that since the major M_w=4.1 the influence of fluids is smaller in the evolution of the swarm and although increased pore-pressure and its diffusion still plays a significant role, as evident from the migration patterns, the sequence is mostly controlled by stress-transfer due to slip caused by the multitude of events.

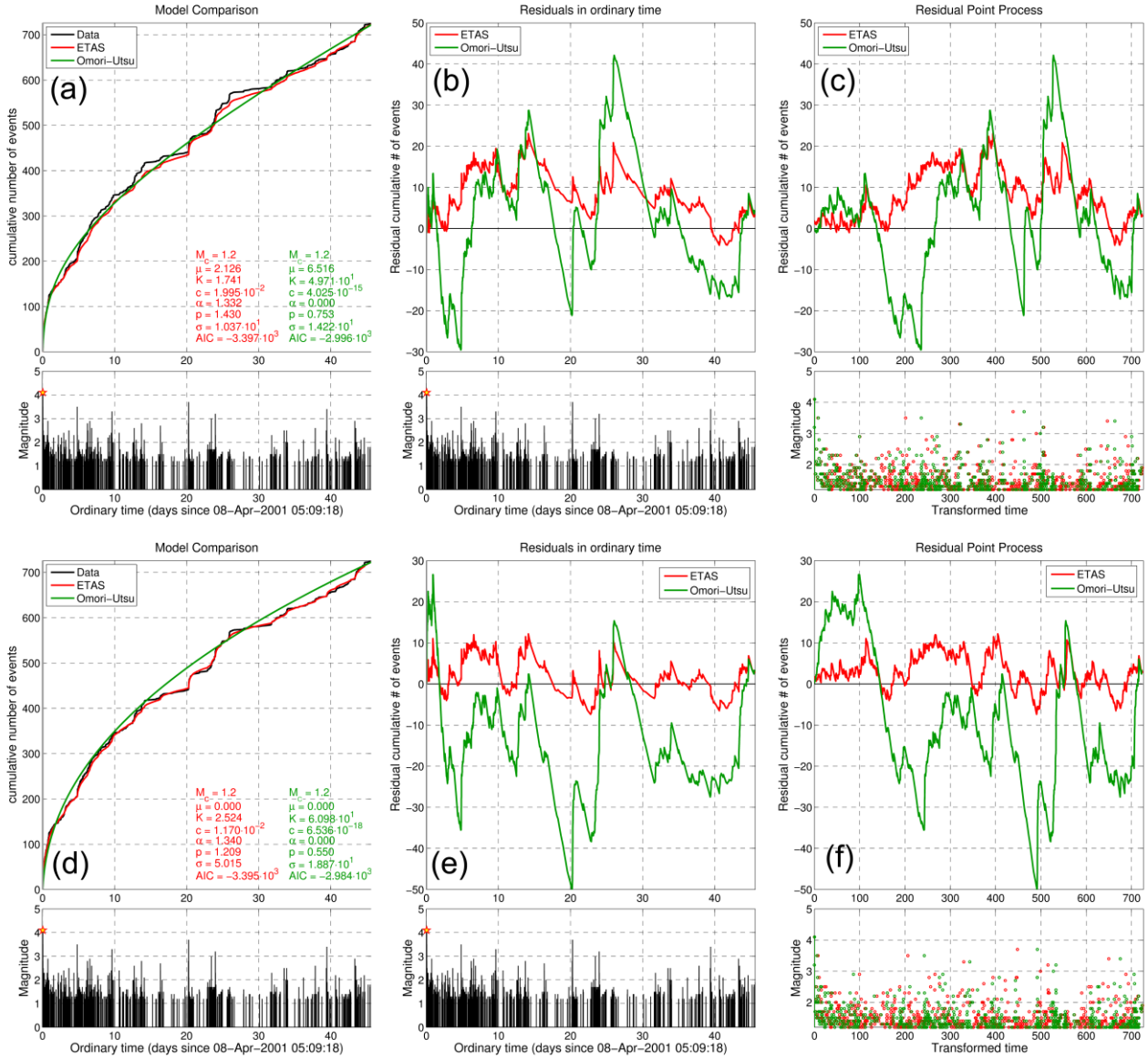

Figure 6.40: ETAS and Omori-Utsu models for part of the 2001 Ayios Ioannis swarm, starting from the M_w=4.1≡M_r event of 8 April up to 22 May 2001 (excluding some other major events that followed), (top row: a, b, c) with μ as a parameter determined by MLE, (bottom row: d, e, f) with fixed μ=0, (a, d) in ordinary time, (b, e) in transformed time and (c, f) residual between data and model in transformed time.

The respective ETAS model for the 2003-2004 sequence is proven harder to fit, with the residual in second part, after the ~130 day mark (Fig. 6.41), deviating significantly. Two sets of parameters were determined for the sequence, the first between 24 October 2003 and 22 March 2004 (150 days) and the latter for the next 235 days, up to 13 November 2004. The best fit is achieved with a fixed μ=0 value. This 2-stage ETAS model (Fig. 6.42) is preferred over the single one (Fig. 6.41) not only for the better visual fit but because of the increased goodness-of-fit, as determined by the summed AIC values of the two models (-1150) compared to the larger AIC value of the single model (-1135). Typically, the changing point for a 2-stage ETAS model is defined as the point that minimizes the sum of the two AIC values calculated for the two individual segments (AIC_1, AIC_2)

for which the parameters for a partial ETAS model are calculated (Ogata, 2001). This is very similar to the method that is used for the AIC phase onset picker (Section 4.2, Eq. 4.3), where the pick defines the separation point so that the applied auto-regressive models maximize their goodness-of-fit to the data segments before and after the pick. The change point analysis is presented in Fig. 6B.28, where the minimum value at 150 days defines the best selection for the separation point, since it is smaller than the respective AIC for the single-stage model.

Both *a* and *p* values are slightly smaller (by ~0.1) in the first period compared to the second one (Fig. 6.42). The main differences appear to be caused by the increased seismicity rate observed between 26 February and 20 March 2004 (periods g-j in Fig. 6.30 and Fig. 6B.24 of the Appendix). While this period includes two major events of magnitude 3.4-3.5, apparently the events of the generated sub-sequence are more than expected by the model. This time-span includes a strong migration pattern towards NW, starting with a small swarm on period g, but also a more mainshock-aftershock-like subsequence further SE, starting on period h. A test with a series of ETAS parameter calculations on a 100-events-long sliding window shows an abrupt increase of the μ parameter (included in the MLE) between 8 and 16 March 2004 (roughly periods h-i), from below 1.0 to around 6.0, which in combination with the observed migration pattern (Hainzl & Ogata, 2005) likely indicates a change in the stressing rate, possibly affected by pressurized fluids.

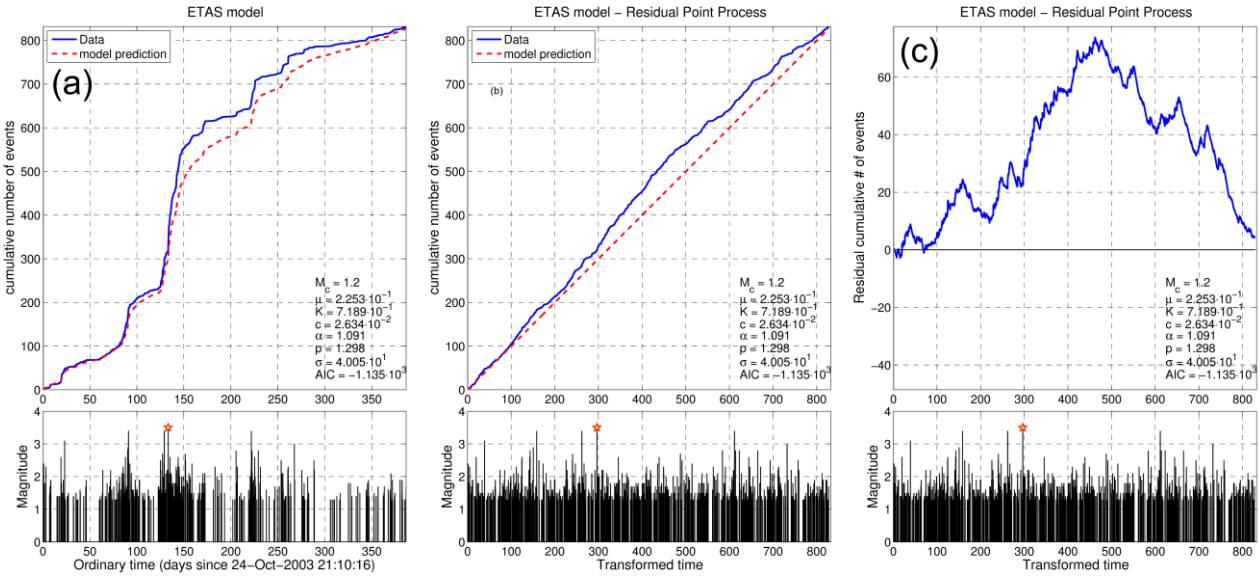

Figure 6.41: ETAS model for the 2003-2004 swarm sequence in the western Corinth Rift, with M_r=3.5, a) in ordinary time, b) in transformed time and c) residual between data and model in transformed time.

Table 6.11: Results of ETAS modeling for the seismicity of 2000-2007 in the western Corinth Rift for seismicity beginning at T_{start}. The parameters μ, K, c, a and p are determined by MLE, except for zero values with (f) which are fixed, with a=0 (f) denoting Omori-Utsu model (MOF) instead of ETAS, σ is the standard deviation between model and data for the subset within the range [T_o, T_{end}] used for the MLE, T_o is the number of days since T_{start} excluded from the MLE and T_{end}, where applicable, is the respective number of days marking the end of the subset range. N is the number of events within the subset range above the M_c magnitude threshold, while the number inside parentheses (when T_o or T_{end} limits are used) is the total number of events.

Dataset	T_{start}	T_o (d)	T_{end} (d)	N	μ	K	c (d)	α	p	σ
2000-2007 (gulf only)	26-May-2000	100	-	10155 (10664)	0 (f)	0.903	2.475E-02	0.831	1.178	136.6
2000-2007 (gulf only)	26-May-2000	100	-	10155 (10664)	0.2147	0.832	3.063E-02	0.805	1.237	155.3
2001 AIO sw.	17-Jan-2001	65	-	1429 (1477)	1.337	1.516	9.998E-03	1.227	1.279	16.0
AIO (major+afters.)	08-Apr-2001	0	-	729	2.126	1.741	1.995E-02	1.332	1.430	10.4
AIO (major+afters.)	08-Apr-2001	0	-	729	6.516	49.71	4.025E-15	0 (f)	0.753	14.2
AIO (major+afters.)	08-Apr-2001	0	-	729	0 (f)	2.524	1.170E-02	1.34	1.209	5.0
AIO (major+afters.)	08-Apr-2001	0	-	729	0 (f)	60.98	6.536E-18	0 (f)	0.550	18.9
2003-2004 seq.	24-Oct-2003	0	-	834	0.2253	0.7189	2.634E-02	1.091	1.298	40.1
2003-2004 seq.(0-150)	24-Oct-2003	0	150	554 (834)	0 (f)	0.9836	7.005E-03	1.14	1.022	9.1
2003-2004 seq. (150-)	24-Oct-2003	150	-	280 (834)	0 (f)	0.7056	1.126E-02	1.206	1.128	5.9
2006-2007 seq.	07-Aug-2006	60	-	6609 (6933)	0 (f)	1.089	2.323E-02	1.079	1.352	65.0
Group #9 (all)	31-May-2000	100	-	488 (507)	0 (f)	1.725	6.094E+00	0.351	1.383	13.1
Group #9 (100-1000)	31-May-2000	100	1000	251 (507)	0.0883	0.1146	2.481E-04	1.11	0.493	9.2
Group #9 (0-1000)	31-May-2000	0	1000	270 (507)	0.1507	0.1429	2.097E-04	0.99	0.731	5.9
Group #9 (1000-)	31-May-2000	1000	-	237 (507)	1.33E-08	6.98E-02	3.998E-04	0.35	0.775	8.2

An adequately good fit is also observed for the ETAS model on the 2006-2007 sequence (Fig. 6.43) with its parameters determined by MLE in the time-span between 6 October 2006 and 17 July 2007. The a-value is near unity ($a \approx 1.08$) while the decay constant is relatively strong ($p \approx 1.35$). The largest deviations between data and model are observed in a period of low rate after the outbreak of 19 October, between 23 October and 24 November 2006. The difference remains stable up to 7

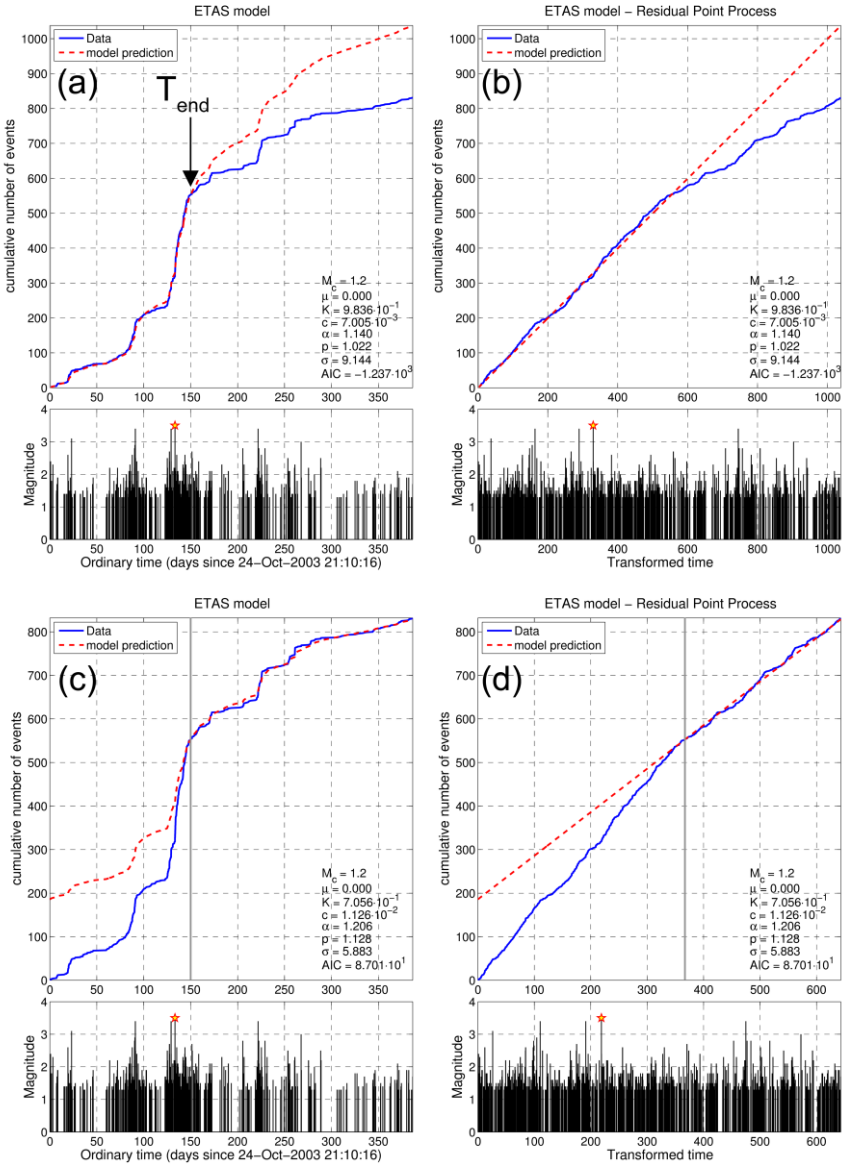

Figure 6.42: ETAS model for the 2003-2004 swarm sequence in the western Corinth Rift with M_r=3.5, forced μ=0 and the rest of the parameters determined by MLE (a, b) for the first 150 days only (up to T_{end}), (c, d) excluding the first 150 days (gray vertical line).

January 2007 when the seismicity rate raises abruptly, surpassing the model significantly until ~12 February.

Lastly, the seismicity of Group #9 was examined by ETAS modeling. As with the 2003-2004 sequence, there appears to be a significant positive residual when the whole subset is used for the parameters determination by MLE (Fig. 6.44a,d). However, an apparently more adequate visual fit is achieved if the model parameters are estimated for the first 1000 days, or up to 25 February 2003 (Fig. 6.44b,e) and for the rest of the subset, separately (Fig. 6.44c,f). Typically, change-point analysis gives various minima, most of which, however, do not correspond to models with a particularly good visual fit for the second part. The best is found for a change-point at ~1030 days

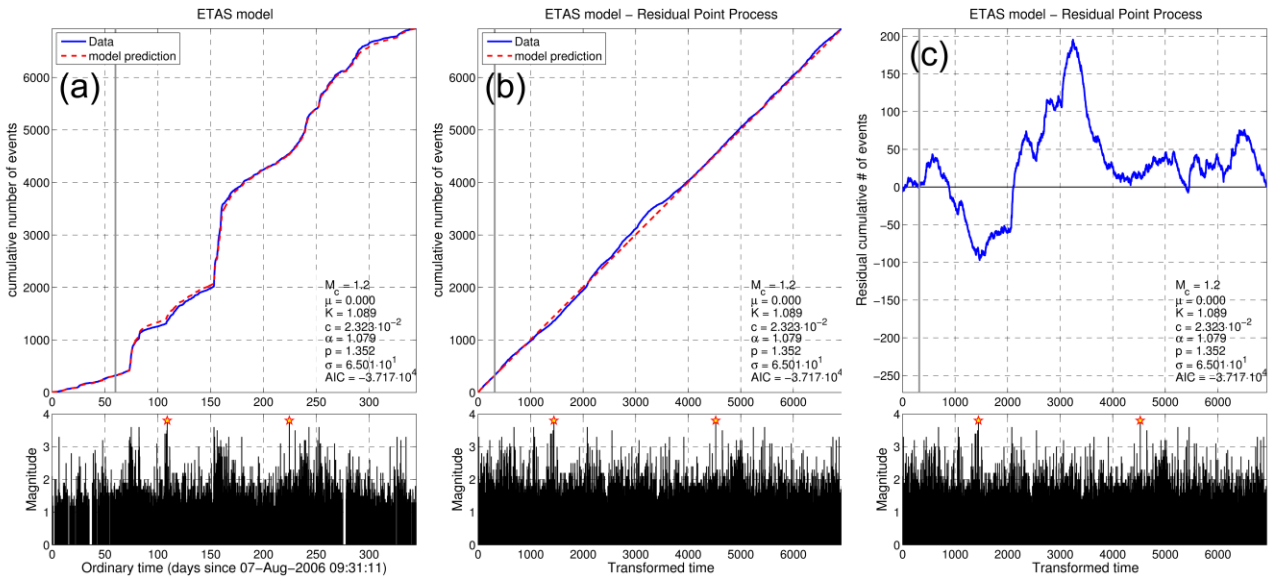

Figure 6.43: ETAS model for the 2006-2007 sequence in the western Corinth Rift, excluding the first 60 days from the modeling (gray vertical line), with M_r=3.8, a) in ordinary time, b) in transformed time and c) residual between data and model in transformed time.

with a μ value free to determine via MLE. However, the respective single model with μ>0 is not fitting well with the data while the same is true for the partial models with $\mu\equiv$0. The two partial models in Fig. 6.44 have a summed AIC_{12} = 2584 > 2526=AIC_o, the AIC value of the single model. However, the latter has been calculated by ignoring the first 100 days. The respective AIC_1 for the first part (by also ignoring the first 100 days) would be 1133, summing up AIC_{12}=2489<2526=AIC_o, with, however, a larger standard deviation, σ (as a measure of the visual fit), than the one of Fig. 6.44b, due to the larger deviation from the RPP after day ~400.

In this respect, Group #9, with an average rate of ~8.5 events/month for $M\geq M_c$=1.4, can be considered as having a rate of 13 events/month for the time-span June 2000 - 25 February 2003 and 6 events/month after the latter date. During the second period, a negative residual is observed between July 2005 and January 2007. The *p*-value is very similar for both periods ($p \approx$ 0.73-0.78) but much smaller than the one obtained for the whole subset ($p \approx$ 1.38), however the aftershock productivity falls from a=0.99 in the first to a=0.35 in the second period (same as for the whole group), reflecting the respective drop in the average seismicity rate. In general, the ETAS modeling for the Eratini Group is really unstable, likely indicating non-stationarity in more than one parameter.

The results of ETAS parameters obtained by MLE on the various subsets are summarized in Table 6.11. The $a\approx$0.83 for the seismicity in the gulf during 2000-2007 is lower than the one obtained for the subsets which are more focused on intense clusters (*a*-values between 1.1 and 1.3). The *p*-value generally ranges between 1.1 and 1.4, except for the partial fits of Group #9 and the Omori-Utsu law fits for the 2001 AIO swarm, where it takes lower values.

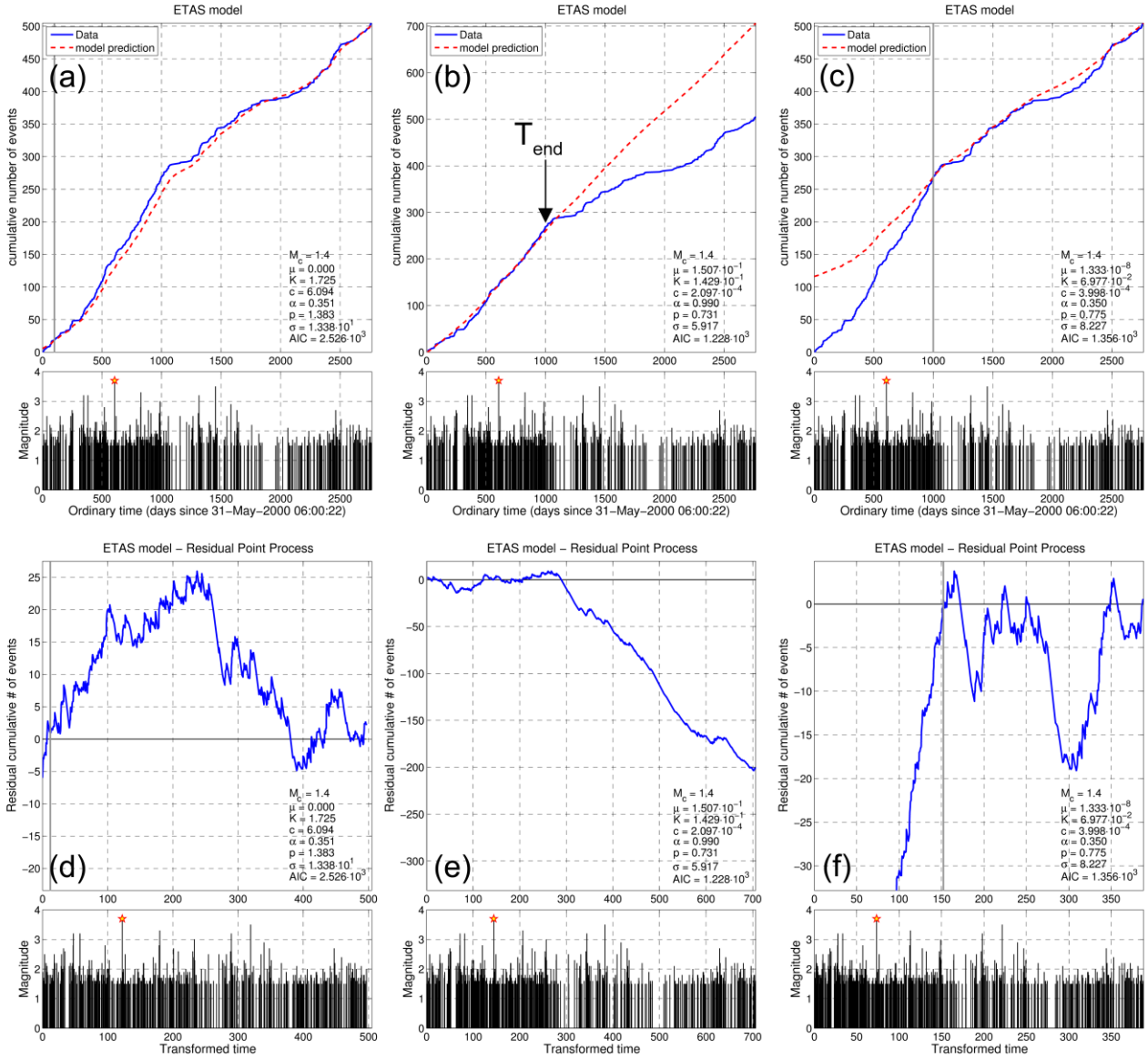

Figure 6.44: ETAS model for Group #9 (Eratini) in the western Corinth Rift, (a, b, c) in ordinary time and (d, e, f) residual between data and model in transformed time, with $M_{th} \equiv M_c = 1.4$, $M_r = 3.7$ parameters determined by MLE (a, d) for the whole period 2000-2007 with forced $\mu = 0$, excluding the first 100 days (vertical gray line), (b, e) only for the first 1000 days (up to T_{end} marked with an arrow), and (c, f) excluding the first 100 days (vertical gray line).

6.8 Discussion

The waveform data acquired by the CRL and collaborating networks in the western Corinth Rift have provided working material for several recent earthquake studies. This includes seismotectonics, relocation, multiplet, spatio-temporal analyses (Pacchiani & Lyon-Caen, 2010; Lambotte *et al.*, 2014; Godano *et al.*, 2014; Kapetanidis *et al.*, 2015; Bourouis & Cornet, 2009) but also earthquake tomography (Gautier *et al.*, 2008; Karakonstantis & Papadimitriou, 2016), measurements of relative velocity changes (Cociani *et al.*, 2010) and others. In the present study the

spatiotemporal and seismotectonic characteristics of the seismicity of the western Corinth Rift through the years 2000-2007 were thoroughly examined.

The seismicity is mainly distributed at focal depths between 5 and 12 km, with the majority of events being concentrated in a thin seismic layer between 7.0 and 8.5 km. Seismic wave propagation velocities at depths between 8 and 12 km are characterized by low $V_p \cdot V_s$, suggesting a highly fractured medium, but also high V_p/V_s ratio, indicating saturation by fluids (Gautier *et al.*, 2008). The lack of microseismicity within the first 4 km has also been observed in previous studies (Rigo *et al.*, 1996; Bernard *et al.*, 1997; Lyon-Caen *et al.*, 2004). This roughly corresponds to the summed thickness of the water body (0.5 - 0.8 km) and the 2-4 km of unconsolidated sediments (Briole *et al.*, 2000) as well as the shallower part of highly fragmented bedrock. These layers are unable to withstand the accumulation of sufficient stress to release as a measurable earthquake and their deformation rather follows that of the underlying crust. On the other hand, the seismicity is limited to a depth of about 10-12 km, where the brittle-ductile transition occurs, supported by results of electrical and magnetic anisotropy which indicate the existence of a high-conductivity layer at these depths, attributed to the presence of fluids in a tectonometamorphic zone (Pham *et al.*, 2000). Avallone *et al.* (2004) calculated extension rate that reached 16 mm/yr near Aigion using GPS data measurements collected between 1990 and 2001. The extension was found to be accommodated mainly in a 10 km narrow band across the gulf near Aigion. The strain rate on the northern side is 120 nstrain/yr, extensional in a N-S direction while in the south it is below the error margin, roughly translated to a strain accumulation of less than 1 mm/yr.

Various models have been suggested to explain the physical mechanism that produces deformation in the seismic layer beneath the western Gulf of Corinth. It's been long considered that the Corinth Rift is an asymmetric half-graben, with the observed deformation being attributed to a major low-angle north-dipping detachment master fault and younger major north-dipping faults. Doutsos & Poulimenos (1992) proposed a model of listric faults, as opposed to planar, for the rift. Geological evidence for a large-scale shallow-dipping fault that acted as a detachment during the early rifting stage was proposed by Sorel (2000), based on field observations of Khelmos fault, or the "northern Peloponnese major fault" (Flotte *et al.*, 2005), outcropping at ~32-35km south of the southern coast of the western Corinth Rift. This detachment later supposedly became inactive, when younger and steeper fault were formed and the activity migrated towards the north. However, the northwards extension of this feature would pass at a depth of ~4km, well-above the observed seismicity within the western Corinth Rift and roughly matching the floor of the unconsolidated sediments. Arguments against the asymmetric half-graben model were made by Moretti *et al.* (2003), who mapped active major south-dipping normal faults in the northern side of the rift. Beckers *et al.* 2015 also suggested that a significant portion of the deformation is accommodated by the south-dipping structures, with the north-dipping ones, however, playing a dominant role.

The seismological evidence in the western part of the rift is really conclusive on the general north-dipping character of the seismogenic layer. Rigo *et al.* (1996) observed the gently north-dipping (15°±10°) mid-gulf seismic layer combined with several "odd", low-angle focal mechanisms during a 6-week experiment in July-August 1991 with a temporary seismological network. They suggested that a significant portion of the deformation could be accommodated on a detachment zone at the bottom of the seismic layer, where the north-dipping faults root at depth. The same data included a

cluster/multiplet with many low-angle focal mechanisms below Efpalio (Rietbrock *et al.*, 1996), further supporting slip on a detachment, at least towards the northern edge of the seismic layer. Hatzfeld *et al.* (2000), on the other hand, suggested that the diffuse mid-gulf microseismicity is associated with the brittle-ductile transition zone rather than a detachment. Arguments against a mid-gulf detachment can be made by the observation of some clusters that "breach" the bottom of the seismogenic layer and are also in good correlation with the extension of south-dipping, antithetic faults such as Trizonia and Kallithea, but also further south with the observation of clusters below the supposed detachment, such as the 2001 AIO swarm (Lyon-Caen *et al.*, 2004) and the 2013 Helike swarm (Kapetanidis *et al.*, 2015). Ghisetti & Vezzani (2005) note that brittle faults may indeed extend at deeper crustal levels into aseismic, ductile shear zones.

Lambotte *et al.* (2014) suggest a sort of compromise between the aforementioned models, with diffuse deformation in a weak seismic layer below the gulf and a growing, yet immature detachment in the north, mostly outlined by the shallow dipping transition zone and Group #9 in the downdip extension of the 1995 major earthquake's rupture plane. In this model, the rift opens in a N-S direction almost symmetrically, with the seismically active zone dipping north due to the formation of a detachment being underway in the northern part. This is compatible with the GPS observations (Briole *et al.*, 2000; Avallone *et al.*, 2004), explaining the mid-gulf high stress accommodation, but also with geophysical data which show sub-horizontal strata in the western Gulf of Corinth (Beckers *et al.* 2015). Lambotte *et al.* (2014) estimated the geometry of multiplets in the western Corinth Rift fitting a plane using grid search, projecting the hypocenters on the plane and estimating an ellipse that contained the projected events on the plane. Some minor differences in the determined absolute focal depths can be attributed to the different location algorithms and distance weighting schemes used, HYPO71 in Lambotte *et al.* (2014) as opposed to HypoInverse in the present study, which in turn may affect dip angles by a few degrees. However, although the methodologies differ, the relative relocations bare significant similarities with the ones of the present study.

The dominant stress regime in the western Corinth Rift is extensional in an average SSW-NNE direction and the large north-dipping faults strike E-W to WNW-ESE. The focal mechanisms of the largest earthquakes, including the M_s=6.2 that struck Aigion in 1995 (Tselentis *et al.*, 1996; Bernard *et al.*,1997), are mostly purely normal dip-slip events on N-dipping faults. However, oblique-normal faulting within the western Corinth Rift has also been observed, especially near its NW edge. Beckers *et al.* (2015) performed high-resolution seismic reflection surveys in that area and detected strike-slip deformation at Nafpaktos basin, mostly on SE dipping faults. A significant oblique-slip component was also found within the Managouli fault zone, the region between Psathopyrgos and Marathias faults. This side of the rift is considered to be an area of triple-junction (Vassilakis *et al.*, 2011). It is a transition zone between normal faulting within the western Gulf of Corinth, right-lateral strike-slip in the SW extending from the Andravida fault, that hosted the 2008 M_w=6.4 earthquake (see Section 5.1; Papadimitriou *et al.*, 2008; Ganas *et al.*, 2009), proceeding NE through the oblique-normal Rion-Patras fault zone (RPfz) and left-lateral strike-slip in the NW, connecting the Nafpaktos basin with Trichonis Lake (see Section 5A.1; Kiratzi *et al.*, 2008; Kassaras *et al.*, 2014a). A series of oblique left-lateral faults has also been mapped west of Trizonia Island (Fig. 6.1).

Throughout years 2000-2007, several episodes of intense seismic activity have occurred, the more significant ones being the 2001 Ayios Ioannis swarm, the 2003-2004 mid-gulf swarm and the 2006-2007 mid-gulf and Marathias seismic crisis. Lyon-Caen *et al.* (2004) have analysed the 2001 Ayios Ioannis swarm. They found that its hypocenters are well distributed on a plane that dips 40° NW. This result is nearly identical to one of the nodal planes of the focal mechanism for the major M_w=4.1 event of 8 April 2001, characterized by oblique-normal, dextral-slip faulting, that was determined by Zahradnik *et al.* (2004) using regional waveform inversion. Pacchiani (2006) and Pacchiani & Lyon-Caen (2010) used first motion polarities (FMP) to resolve focal mechanisms for individual earthquakes. They constrained their solutions using information from the geometry of the multiplet to which they belong, forcing the strike of one of the nodal planes (fault plane) to within ±45° of the plane determined by the "Three-Point" method of Fehler *et al.* (1987) for the relocated hypocenters of the multiplet, where possible. Multiplets were then characterized by both the determined geometry and the focal mechanism solution of a reference earthquake.

In the present study, composite focal mechanisms were calculated using the available data from all or from selected events within each multiplet. The solutions were constrained by incorporating S-wave polarization directions (SWP) and S to P amplitude ratios (SPR) for additional weighting of the individual fault plane solutions that satisfied FMP down to a certain percentage. To resolve fault plane ambiguity the following information was taken into account:

- the extension of mapped faults at depth
- the average location of composite solution's hypocenter
- the orientation of the focal mechanism's nodal planes
- visual observation for extruding features in the spatial distribution of hypocenters around the composite focal mechanism's location.

The "Three-Point" method was only employed in a few cases to determine larger scale geometrical characteristics, such as for spatial groups or sub-clusters. This is due to the relocation procedure being focused on large groups, possibly including weakly linked events, in order to reduce number and percentage of events being ruled out from the procedure. Even if each multiplet is relocated separately, with emphasis on its cross-correlation measurements, there is a good chance that its hypocenters are not distributed on a plane but they are distributed along a line or spread within a small 3d sphere, thus a single plane cannot be determined. However, on a larger scale, chances are that a group of neighboring multiplets have occurred on different patches of the same fault plane, either with similar or varying slip direction, thus the geometrical attributes of a larger plane could represent more than one multiplet.

Several oblique-normal composite focal mechanisms were determined in the spatial Group #2, that is mostly comprised of the Ayios Ioannis swarm (Fig. 6.28), very similar to the solution of Zahradnik *et al.* (2004) for the major event of 8 April 2001. Although their individual solutions satisfy ≥95% of the FMP, most have a significant $\delta\theta_{RMS}$ value (Figs 6B.13a,b). This is due to one of the two nodal planes (in this case, the fault plane) not being adequately constrained by FMP while the other one (auxiliary) varies less, limited by nodal stations such as LAKA and PSAR (Fig. 6B.17). The additional weights provided by SWP and SPR shift the composite solution towards one end of the available range. A pure average with equally weighted individual solutions would result

in a plane with lower dip, or sub-horizontal, or even dipping SE instead of NW, as indeed can be observed in a few solutions. Pacchiani & Lyon-Caen (2010) also found a few variations in faulting types and fault orientations, however they note that the T-axis direction is consistent with the regional extensional stress field. This is also confirmed in Fig. 6.20, where for the majority of T-axes in Group #2 their trend is N-S to NNW-SSE, slightly different from the expected NNE-SSW direction of regional extension. It should be noted, however, that the direction of the T-axis, which is by definition at 45° to the fault plane, does not necessarily correspond to the direction to the regional σ_3 principal stress axis (Section 2.1). This is especially true when the focal mechanism refers to faulting in minor structures that are not representative of the main seismotectonic characteristics of a region.

Concerning the spatio-temporal distribution of the 2001 Ayios Ioannis swarm, the seismicity migration is a strong indicator for triggering by pressurized fluids. In the present study, two different sources of radially expanding triggering fronts were found (Fig. 6.22; marked by "a" and "b", respectively). The first, close to the major event of 8 April 2001, triggered seismicity towards both shallower and deeper portions of the NW dipping structure while the latter started from larger towards smaller depths and activated mostly the eastern/shallower part of the fault. As the fluids cause a pressure pulse which acts as a non-tectonic force, their source does not necessarily coincide with any specific (detectable) seismic cluster. When the fluids are enabling a pre-existing fault to rupture, the seismic activity could be detected even several hundreds of meters away from the source of injection (Skoumal *et al.*, 2015). In this respect, the center of the radially expanding front should be determined by examining the spatiotemporal pattern and extrapolating inwards to a point or a small area and backwards in time to an approximate time of initiation. Selecting the central point is crucial in determining the parameter D or the migration velocity of the propagating front. However, due to the uncertainty in the position / geometry and initiation time of the source there can be multiple combinations that fit the data with different D values. Pacchiani & Lyon-Caen (2004) proposed a single source at a location specified by a certain multiplet and, supposing different initiation times, presented 3 envelope curves using different D values, ranging between 0.08 and 0.20 m^2/s. It is also possible, however, to assign an exact source location and initiation time to the hypocenter and origin time of the first event of a multiplet (Duverger *et al.*, 2015), provided if it bares migration characteristics similar to those expected by the hydraulic diffusion theory (Shapiro *et al.*, 1997; Dahm *et al.*, 2010), on the assumption that the first earthquake created the fracture that connected the fluids reservoir with a hydraulically conductive layer near the fault's core. In the present study, a parabolic line with D=0.11m^2/s was suggested for the primary source (Fig. 6.22, "a"; Fig. 6.26) and a higher hydraulic diffusivity value of D=0.22m^2/s for the secondary source (Fig. 6.22, "b"; Fig. 6.27). The seismicity front propagated at 30-80m/day, depending on the selected source point and direction. The faster rates of ~80m/day were measured taking into account either triggering towards NW and sub-group #4 (Fig. 6.25) or the estimated rate in the secondary source in the middle part of the sub-sequence (Fig. 6.27). Pacchiani & Lyon-Caen (2004) measured migration velocities of 10-20m/day for front and back-front. Such differences may arise from the consideration of a front propagating towards a single direction rather than bilaterally or radially, the different choice of a point in space acting as the fluids source and from the different methodologies adopted for the relocation procedure. The results however are comparable and the main deductions are similar. The easternmost and shallower part appears to be activated later in the swarm,

suggesting an upflow of fluids from a deeper source. ETAS modeling shows a good fit for the 2001 AIO swarm, especially in the period between the major M_w=4.1 event of 8 April 2001 and the major events that occurred after the initiation time of the second source. The more significant deviations from the ETAS model occur at the beginning of the sequence, between 29 March and 1 April 2001, during which it is probable that most of the seismicity was induced by the propagation of fluids rather than belonging to subsequences triggered by previous events. The effect of fluids intrusion to the triggering of a swarm has also been observed in the 2000 Vogtland/NW Bohemia swarm (Hainzl & Ogata, 2005), where non-stationary ETAS modelling revealed a strong external forcing signal right at the beginning and a smaller one 50 days after the initiation of the swarm.

The 2003-2004 swarm has also been examined by several authors. Bourouis & Cornet (2009) presented some of the spatiotemporal characteristics of this sequence using manually picked events. They concluded that the mid-gulf seismicity, despite being concentrated in a relatively thin seismic layer, does not belong to a single, low-dipping plane that could indicate a detachment zone, but rather consists of several structures in various orientations, including even subvertical ones. In Fig. 6.31b it can be observed that the seismicity at the beginning of the swarm (days 0-40) is mostly relatively shallow, between 4 and 6 km. The swarm appears to evolve by triggering clustered seismicity in neighboring fault patches, mainly towards NW but also branching to the opposite direction. While it spreads up to a length of ~10km in a SE-NW direction, seismicity persists near the starting source, within the first 2km (Fig. 6.31a). There appears to be a tendency for upwards migration by 50m/day. Then, during days 60-100, a hint for downwards migration can be observed, followed by upwards migration by ~110m/day between days 120 and ~150.

Bourouis & Cornet (2009) noted that the downgoing migration observed at the beginning of the swarm could be associated with meteoric fluids originating from the mountainous regions, particularly those south of the rift, while the upgoing migration, towards shallower depths, could be related to the circulation of fluids of mantellic origin. The source of the latter could be the subducting slab, whose top is estimated to be at a depth of ~75km below the western Corinth rift (Zelt *et al.*, 2005), with the Moho discontinuity being at ~40 km (Sachpazi *et al.*, 2007). The alternate scenario (Bourouis & Cornet, 2009) is that these fluids travel through a large-scale detachment zone, at depths of 15-20 km, then upwards, via the steep dipping major faults. However, the latter is considered unlikely, as the seismological evidence suggestive of a growing detachment is mostly found at the area of Group #9 and below Efpalio, while the extensional deformation in the western Corinth Rift, according to GPS evidence (Avallone *et al.*, 2004) is almost entirely accommodated offshore, without the necessity of supposing slip on a detachment (Bell *et al.*, 2008).

The sequence cannot be described by a single ETAS model, indicating non-stationarity in its parameters. However, if it is modeled separately for the first 150 days and for the rest, with μ=0, the results for the basic ETAS parameters a and p are comparable, about 1.14-1.20 and 1.02-1.13, respectively. The models deviate after the strongest burst of activity between days 130 and 150. During that time, the NW propagating front is superimposed with a burst near the initial sources, including the stronger event of the swarm. In this short period, more events are generated than can be explained by the single model. However, the good fit for the first 150 days, which contain the majority of events, is suggestive that stress transfer caused by previous events can largely explain the secondary sequences within each cluster. The fluids may “guide” and enable slip in the different

patches by increasing pore-pressure and reducing the coefficient of friction, but then the various events within each spatiotemporal cluster are triggered by local stress permutations. The necessity for two different ETAS models to better describe an earthquake sequence in a region is not abnormal. For example, Ogata & Tsuruoka (2016) observed that the ETAS model of the primary aftershock sequence of the 2015 M_w=7.8 earthquake in Nepal could not predict correctly the evolution of a secondary sequence following an M_w=7.3 major aftershock. More specifically, in the latter sequence the aftershock productivity (ETAS parameter α) was found to be twice that of the former.

Bourouis & Cornet (2009) explain that seismicity on shallow-dipping planes with the maximum principal stress being almost vertical would require a pore-pressure much higher than the subhydrostatic due to the topography-driven downgoing flux. On the contrary, it is likely controlled by the deformation process itself, complemented by transient pulses due to pressurized fluids of deeper origin. It is interesting that very few low-angle normal focal mechanisms are observed within the mid-gulf, low-angle, seismically active layer. In most cases, faulting is associated with steep-dipping planes which sometimes are also resolvable by the geometry of the spatial distribution of the clustered seismicity. While slip on pre-existing major or small/antithetic faults is usually expected to occur, it is also probable that several clusters associated with small multiplets with random geometry, could be attributed to newly-formed small-scale fractures. Duverger *et al.* (2015), have explored the fluids diffusion within multiplets during the 2003-2004 swarm and found that for several of them the smalls-scale migration pattern could be explained by the parabolic envelope of Eq. 1.16 (Shapiro *et al.*, 1997) for a given hydraulic diffusivity constant, with most events of the multiplet being concentrated near their initial source and then a few of them following the edge of the envelope. This is also suggestive of a back-front pattern along the lines of the hydrofracture model (e.g. Fig. 1.17) of Fischer *et al.* (2009) and Dahm *et al.* (2010), in a scale of a few hundreds of meters per multiplet. The latter is evidence for "external" stressing by pressurized fluids, at least in a small-scale, multiplet level, with the active fluids injection stage probably lasting for less than 1 day in each case.

The 2003-2004 swarm took place within the mid-gulf seismic layer near the root of Aigion and Fasouleika faults and probably in smaller structures between them (Fig. 6.32). Duverger *et al.* (2015) suggest that these sub-structures form a relay zone on the hanging wall of Aigion fault. An eastwards, offshore extension of the Fasouleika fault would have to be supposed to explain the northernmost activity in Fig. 6.32 c_1-c_2. Godano *et al.* (2014) also suggests the possibility of involvement of other offshore faults, most likely Valimitika fault (Stefatos *et al.*, 2002). However this would require a very steep dip angle for this fault (~76°; Fig. 6.32,b_1-b_2). Some issues arise from the resolved focal mechanisms concerning the interpretation of this sequence, as the FMP-constrained composite solutions indicate significant obliqueness in the slip. More pure-normal, dip-slip solutions would be incompatible with a great percentage of polarities. Oblique-normal focal mechanisms near the edges of known, mapped faults or in the space between them could indicate the existence of soft relay ramps or zones between approaching or overlapping faults (Morley *et al.* 1990). Oblique slip could occur either near the edge of a major fault, on the same plane, or on oblique / even transverse planes in case the relay zone is very fragmented. Such is a known case of a "hard" linkage between the eastern edge of the west Channel fault and the western edge of the east

Channel fault, where a relay ramp has been observed and is likely bridged by a connecting, transverse fault (Bell *et al.*, 2008). Often, such zones are characterized by high permeability due to their being intensely fragmented in various orientations, increasing probability of openings that create paths through which fluids can flow, bypassing the low permeability barrier set by the major fault segments (Micarelli *et al.*, 2006), and even propagate, eventually, between parallel faults (Fossen & Rotevatn, 2016), increasing the pore-pressure and likely inducing repeating earthquakes. Another effect observed near relay zones is a probable perturbation/rotation of the local stress field (Crider & Pollard, 1998), which may enable slip to occur at different directions or plane orientations, in a pre-existing complex fault network, than expected by the regional stress field. This could well be the case in the volume between the south-dipping west Channel, south Eratini faults and the north-dipping Aigion fault and perhaps several other younger offshore faults N of Ai.f. A similar observation was made by Rigo *et al.* (1996), who determined several oblique focal mechanisms in the aftershock region of the M_L=4.5 event of 3 July 1991, near the root of Pirgaki fault, noting that a transient modification of local stress may enable slip on weak discontinuities. Such could be the case for the fault planes determined for the 2001 AIO swarm but, also, for the more recent 2013 Helike swarm (Section 5A.4; Kapetanidis *et al.*, 2015). They also resolved several oblique focal mechanisms in a cluster west of Trizonia Island, very similar to Fig. 6.37 and even a strike-slip event with positive rake offshore Psaromita, below the traces of the mapped offshore faults.

Godano *et al.* (2014) determined composite fault plane solutions by applying a weighting scheme that involved manual measurements of Sv/P, Sh/P and Sv/Sh ratios with both a 1D (Rigo *et al.*, 1996) and a 3D velocity model (Gautier *et al.*, 2006) for the area of the western Corinth Rift. They also determined several oblique solutions in this area of the rift when using the 1D model. However, they found that by applying the 3D model managed to resolve more stable focal mechanisms with higher weights (score) and more pure-normal fault plane solutions. The seismic rays follow different paths in the 3D model and the stations distribution on the focal sphere is altered significantly, allowing pure-normal solutions. It is, thus, probable that the degree of obliqueness in the composite focal mechanisms of Fig. 6.32 could be reduced and the respective north-dipping planes be more E-W trending to become more compatible with the mapped faults. This is demonstrated in the example of Godano *et al.* (2014) for their multiplet #04432 (Fig. 6.45), roughly located near source "3" of Fig. 6.29 (within the bounds of cross-section b_1-b_2 of Fig. 6.32). Further west, in the 2003-2004 swarm, even using a 3D velocity model, Godano *et al.* (2014) have resolved some oblique events, similar to the respective composite solutions of the present study, as in Fig. 6B.23 (top). At the eastern end, the more oblique solution is that of multiplet #05278 in Godano *et al.* (2014), nowhere near the oblique-normal to strike-slip solutions determined in the present study (e.g. Fig. 6B.21). However, it should be noted that the respective focal mechanism in Fig. 6.45 lacks FMP measurements from station PSAR, which is projected closer to the center with mostly compressive first motions (Fig. 6B.21) and has a decisive role in setting constraints for an oblique-normal solution, most probably even if a 3D model was used. Interestingly, some solutions turn out to be more normal in nearly the same focal area (Fig. 6B.23, bottom). Whether this is an artifact due to the 1D model or an indication of increased complexity of the small structures within the weak seismic layer and strong inhomogeneity in the local stress-field is something that may require further investigation in the future.

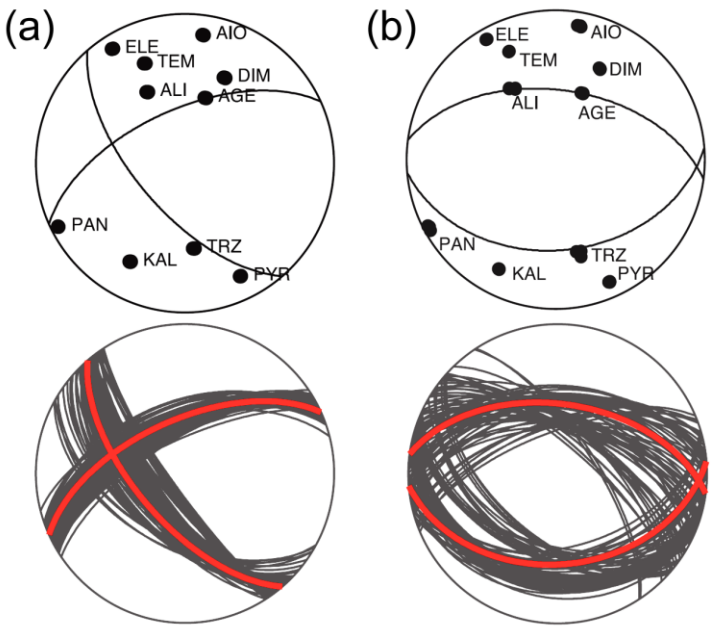

Figure 6.45: Comparison of a composite focal mechanism (multiplet #04432) from Godano *et al.* (2014), a) using the 1D velocity model of Rigo *et al.* (1996), b) using the 3D velocity model of Gautier *et al.* (2006). Upper beachballs show the distribution of stations and the respective first motion polarities (all compressive). Lower beachballs show the optimal fault plane solution (red) with its uncertainty domain within the respective confidence interval (dark nodal planes). Figure modified after Godano *et al.* (2014). The focal mechanism is in the same region and similar to Fig. 6B.23.

The 2006-2007 seismic sequence had not been previously studied in detail. Its spatiotemporal evolution is quite complex, involving migrations both outwards from the middle of the gulf and inwards, from the NW and SE edges towards the center. During a gradual westward earthquake migration at ~20m/day several branches towards the opposite (SE) direction occurred, while the presumed fluids triggering front apparently reached regions SE of its initial source. However, a second front evolved from the NW edge towards the middle, including several very intense earthquake sequences near Marathias fault at the northern shore of the gulf. Bourouis & Cornet (2009) also observed some rough characteristics of this spatiotemporal evolution based on preliminary automatic solutions. They noted that, in contrast with the 2003-2004 swarm, on a large timescale its evolution is complex, with no simple upwards or downwards migration that would allow an association with a simple fluids source, either of meteoric origin or a deep one. They concluded that the pressure pulses caused by propagating fluids were driven by the deformation itself, with short-lived clusters producing stress variations, inducing changes in the pore-pressure and modifying the hydraulic properties of the medium.

While the major events of the 2006-2007 seismicity occurred during the crisis and not at the beginning, consistent with known swarm patterns, most of the stronger earthquakes are associated with short-lived subsequences. This is consistent with the ETAS model that was constructed for the sequence (Fig. 6.43) and is adequately compatible with the observed seismicity. The latter indicates that while fluids might play a crucial role in the propagation of the triggering front, the several sub-sequences are mostly self-explained by stress changes caused by their own earthquakes without the

need to assume a significantly non-stationary parameter, e.g. $\mu(t)$, to account for external forcing (by fluids).

The activated structures near the northern shore are apparently pre-existing faults with oblique normal slip, a NW-dipping, right-lateral one, likely associated with the Managouli fault zone (Mfz) (Fig. 6.36) and a NE-dipping, left-lateral one, consistent with mapped oblique faults west of Trizonia Island or the respective NE-dipping fault of Mfz (Fig. 6.37). The spatiotemporal evolution of the 2006-2007 sequence shows that the former triggered seismicity to the latter neighboring structure, likely with the aid of pore-pressure diffusion due to fluids. The pressure pulse could also facilitate slip on low-angle faults in the same area, as indicated by some composite focal mechanisms as well as previous observations (Rigo *et al.*, 1996; Rietbrock *et al.*, 1996). In the mid-gulf seismically active layer, some of the structures that were involved in the 2006 sequence could be associated with the NNE-dipping Lambiri-Selianitika faults (mainly Groups #4 and #8) and the south-dipping Trizonia fault (Group #6), judging from their location and the respective composite focal mechanisms.

Bourouis & Cornet (2009) remark that spatiotemporal migration patterns are observed throughout years 2000-2007 in multiple scales. Lambotte *et al.* (2014) also mention a tendency for large-scale migration of seismicity, starting mid-gulf and spreading to the north and to the south, the latter at a lower rate, likely obstructed by the major north-dipping onshore faults of the southern shoulder of the rift which may act as barriers to the southwards migration of fluids. To investigate this suggestion, Fig. 6.46 shows a large-scale spatiotemporal projection for roughly the first 1/3 of the study period in a SSW-NNE direction, transverse to the rift's main axis and also the major faults. With hindsight, it appears that an outbreak of seismicity inside the gulf is followed by seismic activity in structures towards the south. It can be speculated that this is also true during the other major mid-gulf sequences of 2003-2004 (Fig. 6B.29) and 2006-2007 (Fig. 6B.30), as well. The only opposite-directed migration incident is the one that occurred in Group #7, likely associated with the Rion-Patras fault zone (RPFZ), in the late 2005 (Fig. 6B.30).

Concerning the latter, it can be argued that the short swarm of 2002 in Group #7 is related to Psathopyrgos fault (Ps.f.). Unfortunately, other than confirming that it occurred at the western side of Ps.f., the resolution, especially at depth, does not permit any more details. It is, however, associated with an interesting anomaly recorded in a strain-meter at Trizonia Island (Bernard *et al.*, 2004). A transient compressional strain was observed on 3 December 2002, lasting for about 1 hour. The strain anomaly was attributed to a silent earthquake of equivalent magnitude M_w=5.3. Superimposed, near the peak of this signal there was an M_w=3.5 event that occurred in Group #4, considered as an "aftershock" of the transient slip and used as reference for its source. Group #4 during 2002 begins with a cluster at the western end of Ps.f., then up to mid-December it spreads NE and then migrates SW again, in the approximate direction of the strike of the RPfz. Within the western Gulf of Corinth, northwards migration is mostly observed along the rift's axis, SE to NW, rather than outwards from the middle towards northern structures. The seismicity rate in Group #9, for example, appears unaffected by the mid-gulf activity.

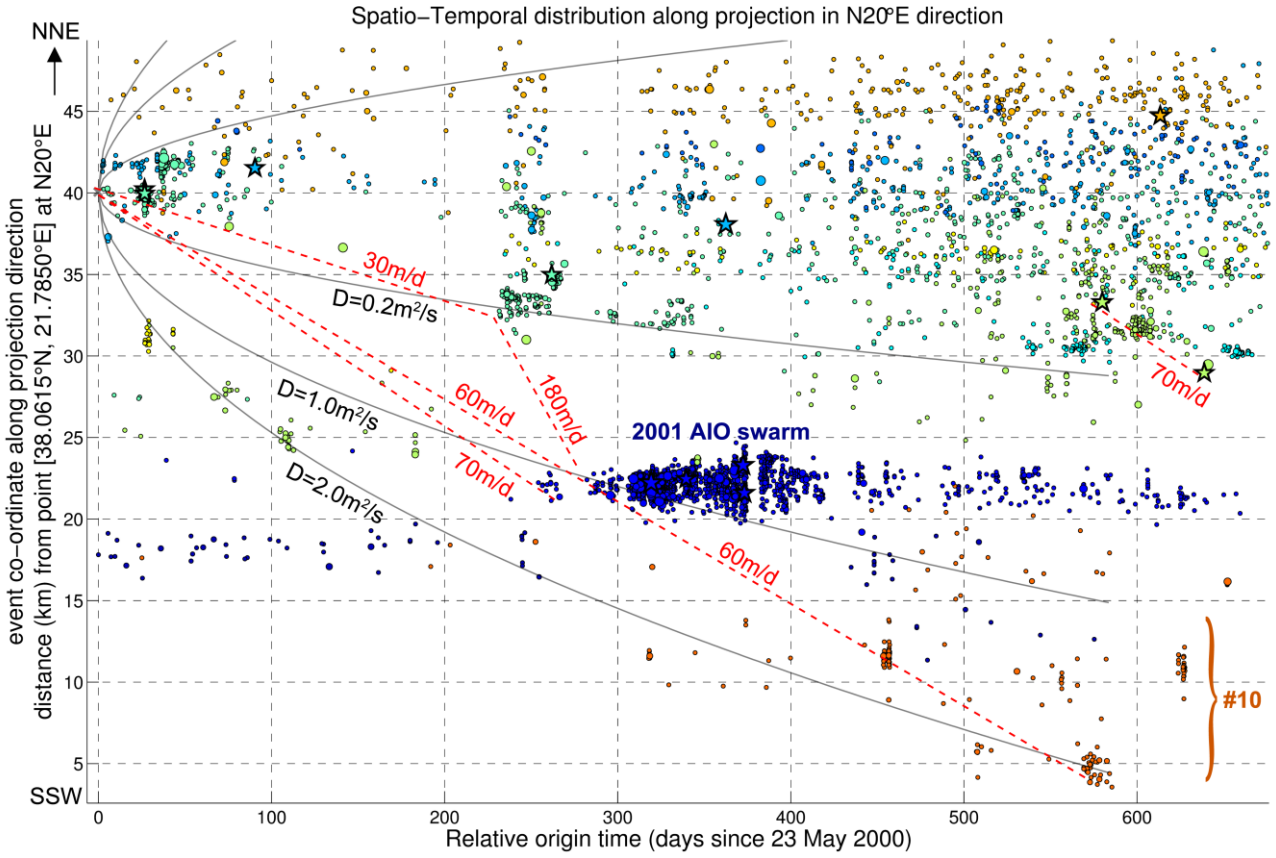

Figure 6.46: Large-scale spatiotemporal projection along a N20°E direction for the seismicity in the western Corinth Rift between 23 May 2000 and 30 March 2002. Parabolic curves correspond to triggering fronts for different values of hydraulic diffusivity, *D*. Red dashed lines indicate migration rates. The events indicated by "#10" refer to the spatial group #10 (Fig. 6.10).

In this view of large-scale seismicity migration, even some clusters in the Patraikos gulf in the west (Group #1) appear to coincide with a "triggering front" originating from the western Corinth Gulf. In all cases, the "migration" of seismicity towards the southern structures appears to propagate at about 60-70m/day, which is a normal rate (slow enough) for fluids diffusion. However, a relatively high hydraulic diffusivity value, $D \approx 1.0$ to $2.0 m^2/s$, would have to be considered in order for the triggering front to match the seismicity in the distant clusters at the south. Such high values are not compatible with triggering fronts observed during local swarm sequences in this region. Whether this sort of apparent temporal dependence of the southern seismicity on preceding mid-gulf outbreaks is truly related to a large-scale migration of fluids or is simply a coincidence and a far-fetched conjecture it would be interesting to examine in other such cases in the future.

Lambotte *et al.* (2014) identified a SSE-NNW zone in the easternmost part of the seismically active region (roughly corresponding to the volume covered by cross-sections j_1-j_2 to l_1-l_2 in Figs 6.18-6.19) as a transition zone between the highly active western zone of the western Corinth Rift and the eastern one. Indeed, the series of parallel cross-sections in Fig. 6.19 show that, starting at about cross-section e_1-e_2, while several structures in various orientations and dips comprise the relatively flat, mid-gulf seismically active layer of variable thickness, mainly at depths between 6 and 8 km,

the activity spreads deeper towards the north in j_1-j_2 to l_1-l_2. This still does not appear to be a single, shallow-dipping structure but is rather composed of several small clusters which are persistently active throughout all the study period, with the exception of 2000, likely not resolved due to the poorer network coverage. This transition zone is very distinct on the yearly maps (Figs 6.2-6.9), along a N-S direction, roughly between Kallithea and north Eratini faults.

The observed high *b*-values along the transition zone and Group #9 (Fig. 6.15) indicate high fragmentation or a region with a multitude of small asperities, possibly combined with high creeping rate and low stress drop. On the contrary, the low *b*-values observed in the region north of Psathopyrgos fault (Ps.f.) could suggest a possible build-up of stress in large asperities, although they do not drop much below 0.8. However, the resolution of seismicity in this part of the study area is very poor and the magnitude of completeness is ~1.7 (Fig. 6.17) or even higher, especially if the EMR method is considered. The strain transient associated with a silent earthquake in the region of Ps.f. (Bernard *et al.*, 2004) as well as an intense swarm that occurred in 2014 (Section 5.4), with a characteristic migration pattern, indicates that Ps.f. could be creeping, rather than being locked. These observations suggest that the *b*-values in that region, despite their adequate goodness of fit, could be slightly underestimated, likely within the upper bounds of δb=±0.10 to ±0.15, closer to b=1.0.

Wyss *et al.* (2008) have also examined the spatial variations of the *b*-value in the western Corinth Rift and observed that the *b*-value mainly decreases with increasing depth (as in Fig. 6.16). This indicates that the stress level tends to increase at larger depths, possibly due to the increasing lithostatic pressure which makes it harder for low-angle faults to rupture as they would require high shear stress while the σ_1 principal stress axis is subvertical. It is also suggestive that stress build-up on large asperities that could generate significant earthquakes is more likely to occur (initiate) at depths between 8 and 10 km. Wyss *et al.* (2008) also noted the abrupt increase of *b*-value at the deepest level (10-12 km) and attributed it to the increased temperature and the brittle-ductile transition, allowing faulting to occur at lower stress levels. These deepest events belong mostly to the seismicity of Group #9 (Fig. 6.11g), also evident from the spatial mapping (Fig. 6.15), but also to the Group #11 in the south, near the epicentral region of the 2001 AIO swarm.

The offshore seismicity ends abruptly east of the transition zone with the exception of the small patch north of Eratini (Group #9). This spatial group, despite its sparseness, is of particular interest as it is considered to be located in the downdip extension of the fault surface that hosted the M_s=6.2 earthquake of 1995 (Bernard *et al.*, 1997). Despite the extensive study of the western Corinth rift in the two decades following this major event (e.g. Bernard *et al.*, 2006; Lambotte *et al.*, 2014), its causative fault remains ambiguous. Coseismic horizontal displacement resolved by GPS shows a 7 cm northward movement at the epicentral area, which rules out the possibility of the slip occurring on the steep south-dipping nodal plane (Bernard *et al.*, 1997). The most prominent theory is that it occurred on a blind low-angle (30°±5°) north-dipping fault, whose extension to the surface would outcrop north of the east Helike fault (eH.f.). However, with the exception of Group #9, there is lack of seismicity in the determined fault surface of the 1995 earthquake, suggesting that this part of the fault is locked (Bernard *et al.*, 2006). Even its aftershocks, including the largest one (M_L=5.2), were registered mainly mid-gulf, highlighting the seismically active layer and the area of Group #9 (Bernard *et al.*, 1997). A model of Taylor *et al.* (2011) suggested a biplanar geometry for eH.f.,

dipping at 35° down to 2.5 km, where it meets the basement, then its dip changes to ~15° down to the hypocenter of the 1995 event and to the activity of Group #9. However, this is incompatible with the resolved 30° dip of the mainshock. An alternative, suggested by Lambotte *et al.* (2014), is a biplanar geometry for eH.f. starting with a dip of 45°-50° at the surface, then bending at 25°-27° down to the 1995 event's hypocenter, rendering the eH.f. a single major structure with a surface 20km-long downdip. ETAS modeling of the Eratini Group has been problematic, with the single model yielding lower AIC than the 2-stage models, although the latter seemed to have a better visual fit to the cumulative number diagram. Very low aftershock productivity values, such as $a \approx 0.35$ as derived for the single model in Group #9, could be related to low viscosity or high heat-flow / fluid activity conditions (Ben-Zion & Lyakhovsky, 2006). For example, in Southern California (Enescu *et al.*, 2009) a weak negative correlation between the spatial distribution of *a*-values and surface heat flow was found. Hainzl *et al.* (2013) note that low *a*-values could result from the underestimation of the respective ETAS parameter when there is a significant degree of aseismic transient forcing that has not been taken into account. These observations suggest that the low *a*-values measured for Group #9 are consistent with the assumption that this region is characterized by relatively low viscosity and high fluid content which increases pore-pressure and enables slip, probably with a significant degree of aseismic creep, on a low-angle detachment.

The detailed examination of the background and clustered seismicity in the western Corinth Rift can help in the assessment of seismic hazard by defining the geometry and seismic potential of the major active faults in the area. This depends on whether they can accumulate enough stress before breaking, their extension at depth, whether they stop at the bottom of the seismogenic layer and on the possibility of *en echelon* faults to rupture in cascade as single large event. In general, the intense but mostly disorganized microseismic activity, combined with the relatively high *b*-values, the inferred strong influence of fluids in the variation of the pore-pressure, triggering swarms and silent earthquakes, and the high degree of fragmentation or porosity derived by tomography, suggest that the mid-gulf portion of the western Corinth Rift is probably not capable of producing destructive events. An important factor that may favor fault segmentation is that the Pindos nappe that crosses the rift's normal faults in a highly oblique direction has a strong structural NNW fabric (Nixon *et al.* 2016). These formations may contain weak discontinuities such as those on which NW-dipping, right-lateral oblique-normal faulting has occurred during the 1991 aftershock sequence, the 2001 AIO swarm and the 2013 Helike swarm.

The low GPS strain rate (Avallone *et al.*, 2004) at the southern shore indicates low accommodation of the extension in the major structures such as Aigion and Helike fault, which translates to longer recurrence time for significant earthquakes (about 500-1000 years for magnitudes 6.5 to 7.0) than the ones on the northern shore. Avallone *et al.* (2004) also suggest that earthquakes on smaller structures, such as the blind offshore fault that hosted the 1995 major event, occur more frequently but they are only capable of producing events of magnitude 5.5 to 6.5. Bernard *et al.* (2006) estimate that a magnitude 6.7-6.9 event could be expected if Ps.f. (with a re-evaluated length of ~12 km by Beckers *et al.*, 2015) and the faults of Kfz and Ai.f. or, equivalently, an offshore north-dipping fault break in cascade, summing a total rupture length of ~25-35km. Otherwise, each fault on their own (9-15 km) could yield a maximum magnitude of 6.0-6.5.

While the background activity in the western Corinth Rift highlights a certain "backbone" of continuous seismicity, including some persistent spatial clusters and multiplets, it is always possible that several other blind and locked structures exist within the western Corinth Rift that have not yet given signs of their location. Continuous monitoring is thus important for the better understanding of the dynamics and the seismic potential of the area. Overlooked, seismically inactive major south-dipping faults, such as Marathias, with a length of 14 km, could rupture with a maximum potential magnitude of ~6.8 (Beckers *et al.*, 2014). Future spatio-temporal anomalies in the measured *b*-values or a long-term quiescence detected through ETAS modelling could possibly indicate an approximate time and place for the occurrence of a major event.

6.9 Conclusions

The continuous seismic activity within the western Corinth Rift generates a large quantity of data that requires a certain degree of automatic treatment. In the present study, over 30,000 events that occurred between May 2000 and December 2007 were located by employing both manual picking and automatic phase detection procedures, then were separated in spatial groups and relocated using both catalogue travel-times and cross-correlation data, yielding a relocated catalogue with 24,000 events. Moment magnitudes were estimated using a spectral fitting technique, employing signal-to-noise criteria, noise level correction and residual reduction. Selected events from multiplets were used for the estimation of composite focal mechanisms using manually determined first motion polarities and automatically estimated S-wave polarization and S to P amplitude ratios. Focal mechanisms for major events were also determined using a similar method.

Spatial analysis of the final catalogue revealed the complex seismotectonic characteristics of the western Corinth Rift. The main seismic cloud is concentrated mid-gulf, following its WNW-ESE orientation, in a thin layer mainly at a depth range of 6.5-8.0 km dipping gently towards the north. The relocation clarified substructures within the otherwise diffuse spatial distribution. The resolved focal mechanisms in combination with the geometry of linear or planar features of the hypocenters enabled their possible association with mapped active faults on the surface or indicated the existence of unknown, buried structures and their kinematics. Several oblique-normal focal mechanisms were resolved in the NW, likely related to mapped offshore faults that also exhibit a certain degree of slip obliquity. An area with several oblique-normal events was defined between the younger north-dipping offshore faults and some major south-dipping ones, possibly related to relay or damage zones between or near the overlapping faults' extremities. Some low-angle focal mechanisms were resolved mainly near Eratini and, also, near and south of Efpalio, providing clues for areas were low-angle faulting may indeed be occurring, likely under special conditions of creep and increased pore-pressure during transient fluid pulse episodes.

Spatio-temporal analysis shed light to the complex dynamics which characterize the observed seismicity patterns in the western Corinth Rift. The attention was mainly focused on a few but significant swarm sequences that occurred during the study period. In all cases, seismicity migration was observed with hydraulic diffusivity values of the order of 0.1m²/s or, equivalently, average triggering front propagation rate at 20-60 m/day, with few exceptions. Some clues on large-scale

interactions between intensification of mid-gulf activity and subsequent major (2001 AIO swarm) or minor activation of southern structures (small clusters) were also hinted.

ETAS modeling that was performed for the seismicity within the western Gulf of Corinth during the whole period, but also in selected subsequences, exhibits an acceptable goodness of fit in most cases. Small positive deviations of the data from the model were attributed to external stressing due to the migration of pressurized fluids, increasing pore-pressure and producing more events than predicted from the model. However, the generally adequate fit of the model indicates that the fluids diffusion is at least partially controlled by the deformation process itself. The resolved aftershock productivity values are in most cases consistent with swarm-like behavior, in agreement with the complex seismicity patterns observed in the rift. Spatial mapping of *b*-values is generally in agreement with the observed high rate of microseismicity, with *b* above unity in most regions. Especially high *b*-values were associated with a transition zone near the eastern part of the seismically active region and particularly with a spatial group at the NE edge of the study area, related with creep on a hypothesized growing detachment.

The data processing and analysis of this massive dataset presented a challenge, but also an opportunity for the development of algorithms that could reduce, eventually, the amount of manual effort for a similar processing workflow on other datasets. The western Gulf of Corinth, despite its large-scale simplicity, proves to be a complex seismotectonic environment in a local scale, continuously generating able amounts of data with persistent, characteristic patterns but also with unforeseen surprises. Future activity could highlight some structures that may help resolve the dispute on the underlying deformation mechanism. Continuous, real-time monitoring, high resolution relocation and investigation of possible anomalies could, therefore, be essential for the construction of a better physical model for the western Corinth Rift and, in a broader perspective, for a time-dependent seismic hazard assessment of the area.

Chapter 7
Summary and results

The present study was mainly focused on exploiting the property of waveform similarity, which is observed for events with similar source parameters, to reduce relative location uncertainties by means of double-difference relocation, perform automatic picking and increase the amount of data in a catalogue. In addition, composite focal mechanisms for groups of similar events provided information on the average faulting type at certain parts of several seismic sequences. This enabled the delineation of features of the activated structures that were previously indiscernible. A proper catalogue is completed by the automatic determination of seismic moment magnitude, incorporating several techniques to enable the proper calculation of seismic moment for small events. For even smaller earthquakes whose waveforms have similarities with larger ones, relative magnitude can also be determined by the scaling between the similar waveforms.

7.1 Waveform similarity and clustering

Two methods for the determination of waveform similarity are considered: the maximum, XC_{max}, of the cross-correlation function in the time-domain and the average spectral coherence, m_{coh}, in a selected band of the frequency domain. The advantages of the former are its faster and more reliable application after filtering in a proper bandwidth. The spectral coherence is only employed as an additional measurement in the "Master-Events" and HADAES methods, rather than being used autonomously, as it has lower tolerance over large shifts, it saturates, yielding large m_{coh} values for events with low XC_{max}, the respective time-lags of best fit are harder to determine via the cross-spectral phase and often problematic due to phase-wrapping. The advantage of the cross-spectral phase for higher precision in the calculation of the time-lag can be approximated in the time-domain by resampling the cross-correlation function around the area of its global maximum to a higher sampling rate.

Grouping of events into multiplets, based on their waveform similarity, is done by performing nearest-neighbour linkage on the cross-correlation matrix and applying a proper threshold. This linkage type is preferred over the furthest-neighbour, as the latter, despite the higher internal consistency within the constructed multiplets, tends to create many smaller groups and quite more orphans. A threshold was considered as the equivalent of the modified Mojena's stopping rule (Mojena, 1977), by finding out the minimum value below which many sub-clusters begin to merge into a single, much larger one. The optimal threshold, $C_{opt.th}$, is defined as the one that maximizes the difference between the size of the largest multiplet and the sum of clustered events. This,

however, is only taken as a minimum allowed threshold, which could be overridden by a larger preset minimum value, e.g. 0.60, to ensure an adequate degree of similarity.

Spatial clustering is performed by applying Ward's linkage on the inter-event distance matrix and selecting a threshold that divides the distribution to the preferred number of clusters. The modified Mojena's stopping rule (Mojena, 1977) can be applied to acquire recommendation for meaningful numbers of samples in terms of the behaviour of the fusion level. The same can be done for a quick division of the temporal distribution into periods, although they usually have to be manually re-divided.

Filtering tests indicated the frequency ranges which provide higher XC_{max} values for events which can be roughly categorized as "local microearthquakes". The widest bandwidth considered is usually 2-23Hz, with the 2Hz high-pass being a usual base for other filters and 23Hz the highest proposed cut-off frequency for a low-pass filter, to allow for enough complexity in the waveforms, usually breaking multiplets into smaller ones and reducing the optimal threshold. Depending on the data, lower low-pass cut-off frequencies can be considered, down to ~10Hz, causing the distribution of XC_{max} values to spread to generally higher values, making it easier for events to be grouped into multiplets but also increasing the optimal threshold. The influence of separation distance and source size (magnitude) to the XC_{max} values was also examined qualitatively. The maximum values of XC_{max} appear to drop with increasing event separation distance, with $XC_{max}>0.6$ at distances below 0.5km and dropping to ~0.2 for inter-event distances above 1.5km. Cross-correlation tests with synthetic sources showed that differences in magnitude of the order of ±0.5 may cause a drop of XC_{max} by 10% to 30% depending on the source's shape. However, tests with real data showed that the tolerance can be greater, allowing for some event-pairs with a difference of even around ~1 order of magnitude to have $XC_{max}>0.9$ at certain stations.

7.2 Focal mechanisms and polarization of particle motion

The focal mechanisms for small local events can be primarily determined by measuring their first motion polarities (FMP) and finding a suitable fault plane solution. A simple automatic procedure has been developed which performs a grid search for all combinations of strike, dip and rake angles, finds individual solutions which satisfy all FMP, which have been manually measured, and estimates an average DC moment tensor which is equivalent to a mean solution for the two nodal planes. The uncertainty of a focal mechanism is calculated as the RMS angular difference between the averaged and the individual solutions. However, the available data may not be enough or of adequate quality to properly constrain a focal mechanism. For this reason, the algorithm can also incorporate automatic measurements of S-wave polarization (SWP) as well as P, SV and SH amplitudes which can be expressed as S/P, SV/P, SH/P and SV/SH ratios (SPR). For each individual solution that satisfies the FMP, a combined weight is calculated that incorporates the deviations of the observed SWP and SPR from the theoretically expected values for the given focal mechanism and the weighted mean moment tensor is determined.

Composite focal mechanisms are also calculated either using solutions determined for individual events in a multiplet or a spatial cluster, using the abovementioned method, or by combining all the

available FMP, SWP and SPR data. In the latter case, an error tolerance for discrepancies between individual solutions and FMP is considered while the percentage of satisfied FMP is also taken into account in the combined weight.

The properties of P-wave polarization have been exploited for the determination of the horizontal orientation of borehole stations or the validation of correct orientation at surface stations. It is also used to determine possible polarity reversals of the vertical component, which may have occurred due to technical issues. These tests have been applied to stations of the CRL network in the western Corinth Rift.

7.3 Seismic moment by spectral fitting

An algorithm was developed for the automatic calculation of the seismic moment magnitude of small earthquakes. The M_o, f_c, γ and κ parameters are determined by performing a non-linear weighted least squares inversion on the seismic moment spectrum. The main issue with the determination of seismic moment is that the SNR of small earthquakes is low, especially at the lower frequencies, masking the plateau and usually causing M_o to become overestimated.

The procedure was tested on the 2013 Helike swarm dataset using various models with more or fewer degrees of freedom, by forcing some parameters to have fixed values. The tests showed remarkable consistency for M_o as determined by the different models, even without restricting its range to $M_{w,avg}\pm0.5$. The M_w as determined from the fit with unrestricted M_o was found to be slightly higher than $M_{w,avg}$, usually by about 0.1, for most magnitudes with the exception of the smaller ones (before the SRF correction). The SRF correction mainly reduces spurious fits for low magnitude events, especially at short-period instruments, but more often than not increases the resulting M_o by slightly raising mid-frequency amplitudes which could happen to be below the level of the fitted function in the preliminary run. The other parameters, such as f_c and κ, require further analysis in order to be physically meaningful, as there is a trade-off between them while f_c also tends to be underestimated in earthquakes of small magnitudes when calculated from single spectra using the abovementioned method.

The model of Boatwright (1978) was considered as a better choice for a default selection because of its steep corner (n=2), a generally acceptable, on average, high-frequency fall-off (γ=2), and $\kappa\geq0$ allowed to vary within a reasonable range. The results were compared to the seismic moment magnitudes of the original catalogue for the 2013 Helike swarm (Kapetanidis *et al.*, 2015), which were determined by applying a similar method (Matrullo *et al.*, 2013) using a Brune-type source (Brune, 1970) and were found to be very similar, especially when using the same type of model. The comparison between M_w and M_L, acquired from the public database of GI-NOA, showed that they follow a nearly linear relation for most magnitudes (Eq. 3.14), generally with $M_L<M_w$ except for the larger magnitudes $3.0<M_L<3.5$ where they are comparable. However, it can also be considered as a quadratic polynomial function for a wider range (Eq. 3.15), with the difference increasing to about M_w-$M_L\approx0.8$ for $M_L<0.5$.

7.4 Automatic picking and location algorithms

The large amounts of available waveform data require at least some minimum level of automatic processing before they are evaluated and manually confirmed or revised. In the present work, two semi-automatic methods were developed for arrival-time picking based on the waveform similarity of repeating earthquakes as well as a classic picking algorithm. They mainly aim for handling intense earthquake sequences, such as aftershocks or swarms, but they can also be used to re-pick or enrich a pre-existing dataset with additional picks.

7.4.1 The AIC-picker

A classic picking algorithm was developed (Section 4.2), based on the Akaike's Information Criterion (AIC), which finds the point that best separates two consecutive waveform segments so that each can be adequately described by a different auto-regressive model. This typically coincides with the point that divides background noise (or coda-waves) before a wave onset and the P- or S-wave train. In the present study, the AIC is calculated at multiple windows of different lengths, centered on a potential wave onset, e.g. a theoretically expected P- or S-wave arrival-time, or determined using a simpler, less accurate automatic method. The pick quality is determined by taking into account the relative level of the AIC minima, their weighted standard deviation, the SNR level as well as the kurtosis and skewness in a window containing mostly noise (before the AIC minimum) and a small segment of (probable) signal (after the AIC minimum).

The AIC-picker, which is an integral part of the HADAES method (Section 4.4), can manage successful picks even at low SNR levels (~1.3). The main weakness of the AIC-picker is that it requires previous knowledge of the approximate arrival time of a P- or S-wave, as it is not efficient for use in sliding windows due to the required processing time.

7.4.2 The Master-Events method

The "Master-Events" method (Kapetanidis & Papadimitriou, 2011) is a semi-automatic picking algorithm that is based on waveform similarity. It works by using a template P or S waveform with known arrival-time, detecting the part of a slave waveform that best matches the template and imposing the pick on the slave-event at the same place relative to the common shape of master and slave waveforms.

The method has the advantage that the correlation detector can detect arrivals which are buried in noise (SNR down to ~0.3, albeit with a very low correlation coefficient) or even superimposed with the coda waves of another event. This is feasible as it is based on the statistical match between the shapes of the template and the slave waveform instead of attempting to distinguish the wave onset from background noise. It is able to discriminate between body-wave types as it uses different templates for P- and S-waves. It can also take advantage of multiple master-events to acquire more observations for a specific pick. The main disadvantage is that it only works with events which are grouped into multiplets and requires sufficient waveform similarity not only at the reference station

but also to the other stations of the network. It is also prone to accumulation of errors as the picks are propagated to the higher order slaves. The latter issue can be mitigated by manual revision of at least the primary slave-events or the addition of more manually picked master-events, mainly for the larger multiplets, by selecting those with the largest number of immediate relatives.

7.4.3 The HADAES method

The Hybrid Automatic Detection and Association of Earthquake Signals (HADAES; Section 4.4) is an alternative algorithm for semi-automatic picking which incorporates key features of the master-events method but exploits it for the association of a temporary set of catalogue and arrival-times meta-data. It then employs a classic picking algorithm, such as the AIC picker, to actually pick the arrival-times. It is also structured in a way that makes possible the processing of large datasets, which may span over long periods of study.

The algorithm was primarily tested with the 2014 Nafpaktos-Psathopyrgos swarm dataset (Section 5.4.1). Over 25000 signals were detected at two reference stations and processed, ~20000 slave-events were initially associated with approximate arrival-times and catalogue meta-data, among which 11271 remained after the removal of duplicates/noise-signals, rejection of solutions with large errors and relocation, using 823 master-events during the period between 15 July and 31 October 2014. The catalogue size was increased by over 12 times, the magnitude of completeness was reduced from 1.4 to 0.5 while the fractal correlation dimension remained similar to the one of the relocated master events, D_2=1.52, but is applicable to a lower minimum scale (was reduced from ~38m to ~12m).

7.5 Applications in case studies

The methodologies described and developed in the present thesis have been applied to several cases of earthquake series that have occurred in various regions of Greece. The main procedures include division into spatial groups, construction of cross-correlation matrices and formation of multiplets, followed by relocation using both catalogue and cross-correlation data. The spatial distribution was examined in thin vertical and horizontal slices to identify the activated structures. This is important in cases where the tectonic regime is complex. For example, in the 2007 Trichonis Lake swarm, the analysis revealed structures which form a conjugate system of normal faults, with the main zone trending NW-SE and dipping NE. In the 2014 Cephalonia sequence different characteristics were associated with the first and the second major earthquakes, the former being related to a complex volume where many different minor structures were activated, while the latter took place in a simpler, nearly linear structure. High resolution relocation also revealed triggered activity in the north, inside Myrtos gulf, likely related to a series of smaller, sub-parallel and sub-vertical, left-lateral structures, trending roughly E-W. The northwards continuation of these antithetic minor faults was activated during the 2015 Lefkada aftershock sequence and was delineated after relocation. In regions were the network coverage was poor, the relocation procedure could not manage adequate improvement in the relative location uncertainties. For example, in the 2008

Andravida sequence, the southern spatial groups were poorly constrained. Even so, the hypocentral dispersion was significantly reduced in some clusters with large numbers of strongly correlated events, mainly associated with activated patches due to stress redistribution near regions of high slip during the main rupture. In the broader area of the Santorini Volcanic Complex the resolution was also very low, especially at depth, leading to widespread vertical distributions in some spatial groups. On the other hand, inside the Caldera of Santorini, which was surrounded by several seismological stations, it was possible to significantly improve the hypocentral distribution. This procedure revealed a SW-NE trending structure, consistent with the Kammeni-Columbo tectonic line.

Detailed spatiotemporal analysis was performed to reveal patterns that could indicate different behaviours in the spreading of seismicity. It can be coupled with the temporal evolution of multiplets, which examines recurrence of (repeating) earthquakes to previously activated structures and the migration of seismicity to previously unbroken areas. A typical characteristic of mainshock-aftershock sequences, such as the cases of the 2008 Andravida, 2014 Cephalonia and 2015 Lefkada earthquakes, is that the seismicity tends to appear almost immediately after the occurrence of the mainshock to the whole aftershock zone. Weak migration of activity to minor neighbouring structures is usually related to stress redistribution or relaxation at later stages. On the other hand, strong migration is consistent with the diffusion of pressurized fluids, mainly observed during swarms. One of the most striking patterns was revealed during the 2011 Oichalia swarm, with unilateral southwards migration of the seismic activity by ~80m/day for the first 80 days, characterized by a parabolic triggering front and a back-front of seismicity deficit. On the contrary, no significant spatiotemporal migration patterns were observed in the 2007 Trichonis lake swarm, besides some weak indications at shallower depths, probably related to stress redistribution. The temporal evolution of the 2013 Helike swarm indicated two different stages of activity. The first exhibited more swarm-like characteristics, including several bursts and migration towards the east. The second phase was more abrupt and activated a different area to the west with little overlap with the seismicity of the first phase, as also confirmed by the reactivation of a few multiplets that were generated during the first one.

In the cases where a local network had been available, composite focal mechanisms were derived from smaller earthquakes for each spatial group or for the largest multiplets. In the 2007 Trichonis swarm, composite solutions indicated significant oblique-slip and even some structures that ruptured with reverse faulting. Inside the Caldera of Santorini several groups were compatible with dextral strike-slip faulting along the Kammeni-Columbo tectonic line. There was also evidence of increased complexity NE of Nea Kammeni, offshore, where the resolved composite focal mechanisms of some groups deviate from their expected trend. This was likely due to localized stress heterogeneities caused by the upwelling magma which facilitates slip on secondary, even antithetic structures with left-lateral strike-slip faulting. In the 2013 Helike swarm, composite solutions revealed mainly N-dipping normal faulting, consistent with the down-dip continuation of Pirgaki fault. However, at least one group was likely related to a steep S-dipping antithetic fault when coupled with the relocated spatial distribution, while certain groups suggested NW-dip and few events were characterized by sub-horizontal faulting with their hanging wall slipping towards NNE, consistent with the regional extension and the developing detachment beneath the gulf.

The outbreak of the 2010 Efpalio sequence stimulated the development of the Master-Events method in an attempt to detect a large number of strongly correlated small earthquakes. Through this algorithm, 388 master-events were used to automatically pick 1945 slave-events that were missing from the routine analysis. An additional 1846 slave-events were automatically determined by the HADAES method. This was possible owed to the availability of data from the CRL seismological network, complemented by local stations of HUSN. High-resolution relocation managed to discriminate three structures out of the initial highly dispersed "cloud": two shallower, north-dipping ones (at depths 7-8km), with one of them mainly associated with the first M_w=5.1 event, and a deeper (~9-10km), south-dipping one that was associated with the second major earthquake. Spatial mapping of the *b*-value during the first phase revealed the existence of a relatively low *b* area (~0.9) around the epicenter of the forthcoming large event of 22 January 2010. This could only be achieved due to the enrichment of the catalogue with additional, smaller events, as the resolution of the initial data was too low to discriminate this pattern. The HADAES method, which was primarily applied to the 2014 Nafpaktos-Psathopyrgos swarm, was also partially employed in the 2015 Lefkada sequence to increase the available data, mainly in the vicinity of the mainshock. Seismic moment magnitudes were calculated by spectral fitting in all case studies where additional events were determined by either Master-Events or HADAES methods.

ETAS modelling complemented most case studies to examine the aftershock productivity rate as to whether the sequences can be explained purely by stress transfer. In most aftershock sequences this is indeed the case, with the Modified Omori's Formula even being preferred over the respective ETAS model for some of them, such as the 2008 Andravida and the 2014 Cephalonia sequence when examined partially before and after its largest aftershock. The ETAS model, is generally better suited in cases where there are multiple bursts of activity, e.g. during swarms. Positive residuals between observed and modelled cumulative number of events, as in the 2011 Oichalia and the 2013 Helike swarms, indicate the contribution of an aseismic factor to the generated seismicity, such as creep or fluids diffusion.

7.6 Seismic activity in the western Corinth Rift during years 2000-2007

A large dataset of tens of thousands of earthquakes recorded by the local CRL network in the western Corinth Rift during the period 2000-2007 was processed by applying methods developed in the framework of the present study. The HADAES method was employed to automatically pick and locate a significant portion of the catalogue, followed by visual inspection and manual re-picking where required. A total of 30000 events were initially located. The catalogue was divided by year, separated into spatial groups per year and each group was further processed individually by applying station corrections, creating cross-correlation matrices and multiplet configurations, followed by double-difference relocation for a total of ~24000 events. Seismic moment magnitudes were determined by spectral fitting using the method of Chapter 3. Composite focal mechanisms were derived for 284 large multiplets containing over 5300 events throughout the study area, using the method of Section 2.4.3, also incorporating S-wave polarization as well as S/P, SV/P, SH/P and SV/SH ratio measurements to provide combined weights.

The detailed spatial analysis delineated a low-angle, north-dipping seismogenic zone beneath the gulf, mainly at depths between 8 and 10km. However, very few low-angle focal mechanisms, only in specific areas, were observed, while the majority indicated normal faulting on steep (~50°-60°) north-dipping planes. In some cases, the relocated clustered seismicity delineated structures which, in combination with the respective composite focal mechanisms, could be associated with the downdip extension of mapped faults on the surface. However, most are likely related to smaller structures, some of which even possibly related to relay zones between the margins of larger faults extremes, as implied by a significant degree of oblique slip. The distribution of the T-axes is consistent with the regional stress regime of N-S extension, with some deviations towards NNW-SSE as estimated from the 2001 Ayios Ioannis swarm and the deeper activity near Eratini, while the B-axis is generally sub-parallel to the strike of the major mapped faults. Seismicity is mainly concentrated in the middle of the gulf, but also spreads onshore near Efpalio and Eratini in the north, while several clusters are also observed on the southern shoulder of the rift. It is shallower offshore between Psaromita and Helike, at a focal depth range of 4-6km, and deeper below Eratini (10-12km). The most notable sequences include a swarm that occurred in 2001 near Ayios Ioannis, ~6km SSW of Aigion, another swarm that took place mid-gulf in 2003-2004 and an intense sequence that occurred in 2006-2007 located near Marathias fault, close to the NW shores of the gulf.

The 2001 swarm, which included an M_w=4.1 event on 8 April 2001, is distributed on a NW dipping plane, oblique to the major E-W trending faults of the rift. It has been mainly attributed to the downdip extension of Kerinitis fault, linking the en echelon Pirgaki and Mamousia faults (Lyon-Caen *et al.*, 2004). Its spatiotemporal distribution exhibits migration patterns radiating outwards from two different centers, one that began ~10 days before the M_w=4.1 event and another that started in early May 2001, with estimated hydraulic diffusivity values D≈0.08 to 0.20 m^2/s and migration velocities of the order of 30-80 m/day, indicating contribution of fluids to the propagation of its activity.

The 2003-2004 swarm likely involved seismicity at the place where the extension of the Aigion, Selianitika and Fasouleika faults meet the weak seismogenic layer and included 2 events with M_w≈3.5-3.6. Its spatiotemporal evolution also presented strong migration patterns, mostly directed towards NW at ~60m/day, but also including several back-propagating branches, likely originating from as many as 4 different injection sources along the activated zone, mostly with slower migration velocities of ~30-40m/day. The observed focal mechanisms are normal with a significant oblique component.

The 2006-2007 sequence involves activity on a ~32km long NW-SE trending zone along the western Corinth Rift, but with the more intense clusters located near Marathias fault. The latter involve interaction between 2 or more structures, one apparently related to a NNW-dipping offshore fault with a small dextral slip component and another, closer to Trizonia Island, with a steep dip towards NE and a significant sinistral slip component. Spatiotemporal analysis revealed very complex migration patterns throughout the sequence, starting at roughly two distinct injection sources, with both triggering fronts radiating bilaterally until their opposite-directed branches converge at average propagation velocities of 20-40m/day, with the exception of some rapidly

spreading, intense clusters near Marathias due to stress transfer by a series of major events (M_w≈3.6) on 21, 28 October 2006 and 7 January 2007.

Spatial mapping highlighted some areas with high *b*-values (~1.5), mainly along the eastern margins of the observed seismicity within the western Corinth Rift, a zone that is considered as a transition zone (e.g. Lambotte *et al.*, 2014) which also includes some of the more shallow activity. Increased b-values are possibly related to highly fragmented volumes where creeping or fluids diffusion is likely to occur. The b-values are also relatively high mid-gulf (~1.2), but also at the region below Eratini, where some low-angle focal mechanisms are detected at depths of 10-12km. The *b*-value generally drops with increasing depth, indicating larger stress due to increasing lithostatic pressure, but below 10km it is again increased, possibly due to the raised temperature and the brittle-ductile transition.

ETAS modelling was attempted for many different subsets of seismic sequences in the western Corinth Rift during years 2000-2007. There haven't been many cases where it could be compared to a MOF model for a mainshock-aftershock pattern, but it was attempted with the major M_w=4.1 event of 8 April 2001 during the Ayios Ioannis swarm, where the ETAS model fitted better than the respective MOF model both in terms of lower standard deviation and lower AIC value. However, it was required in some sequences to calculate a change-point and determine two sets of ETAS parameters to describe two consecutive periods e.g. during the 2003-2004 sequence as well as for the seismicity near Eratini. The generally adequate fits of the ETAS model are suggestive that stress-transfer acts as the main driving force for the evolution of seismicity. However, aseismic factors such as diffused fluids or creep could be responsible for observed positive residuals or sudden changes in some of the ETAS parameters. The characteristic migration patterns with a propagation velocity of the order of 30-60m/day and hydraulic diffusivity D≈0.1m^2/s are the stronger evidence for the contribution of fluids to, at least, controlling the evolution of swarms in the western Corinth Rift, complemented by stress transfer, especially when major events occur.

7.7 Concluding remarks

The main objective of the present study has been the delineation of the geometry of activated structures as well as the detailed investigation of the evolution of several earthquake sequences that have occurred during the years 2000-2015 in Greece. It was also focused on the production of high resolution earthquake catalogues through double-difference relocation and the radical increase of the amount of events in catalogues, mainly by exploiting the property of waveform similarity in repeating earthquakes. This was only made possible after the development of several automatic procedures that were programmed in a MATLAB environment, including, but not limited to: the calculation of waveform similarity, determination of multiplet or spatial clusters, event-detection, classic automatic picking, semi-automatic picking by master-events incorporating the correlation detector algorithm, identification of the geometry of spatial clusters, determination of (composite) focal mechanisms and calculation of seismic moment magnitude, as well as several tools for data management and conversions and a large variety of graphic representation techniques. This enabled the in-depth analysis of several sequences by dividing them into clusters and temporal periods and

studying them through detailed cross-sections and spatiotemporal projections in order to reduce their apparent complexity. The spatial or multiplet clusters' geometry combined with the determined individual or composite focal mechanisms allowed for a complete seismotectonic analysis in several case studies.

The proposed methods of analysis and, more importantly, the detailed presentation of the master-events and HADAES algorithms, are also regarded as a significant part of the contribution of the current study to stimulate further research. The increase of data through the use of single-station-detection and/or correlation detectors could possibly reveal patterns in the dynamics of the evolution of earthquake sequences that are disregarded through routine analysis due to low resolution. For example, there was absolutely no evidence for the existence of a low *b*-value region around the hypocenter of the forthcoming second large event in the 2010 Efpalio sequence before the enrichment of the catalogue with additional slave-events. However, this result was also based on data that became available a posteriori, as master-events both before and after the second major event were used for the detection and picking. On the other hand, the enhancement of the catalogue of the 2014 Nafpaktos-Psathopyrgos swarm using the HADAES method provided more detail on the spatial distribution, enlarging the range for which the fractal law holds true to lower scales, and sharpened the migration pattern in the spatiotemporal projection that was already hinted from the fewer data of routinely analysed seismicity. The decrease of the magnitude of completeness, combined with the improvement in the resolution of the spatial distribution, that is increasing both quantity and quality of the data, could also possibly reveal hidden precursory patterns in cases where they might exist but remain undetectable by conventional methods.

References

1. Abercrombie, R.E., 1995. Earthquake source scaling relationships from -1 to 5 ML using seismograms recorded at 2.5-km depth, *J. Geophys. Res.*, **100** (B12), 24,015 - 24,036.
2. Agius, M.R. & Galea, P., 2011. A Single-Station Automated Earthquake Location System at Wied Dalam Station, Malta, *Seismol. Res. Lett.*, **82**, 545–559, doi: 10.1785/gssrl.82.4.545.
3. Akazawa, T., 2004. A technique for automatic detection of onset time of P and S phases in strong motion records, *Proc. of the 13th World Conf. on Earthquake Engineering*, Vancouver, Canada, Paper No. 786.
4. Ake, J., Mahrer, K., O'Connell, D. & Block, L., 2005. Deep-injection and closely monitored induced seismicity at Paradox Valley, Colorado, *Bull. Seismol. Soc. Am.*, **95**, 664-683, doi: 10.1785/0120040072.
5. Aki, K., 1966. Generation and propagation of G-waves from the Niigata earthquake of June 16, 1964. Part 2. Estimation of earthquake moment, released energy, and stress-strain drop from the G-wave spectrum, *Bull. Earthquake Res. Inst.*, **44**, 73-88.
6. Aki, K., 1984. Asperities, barriers, characteristic earthquakes and strong motion prediction, *J. Geophys. Res.*, **89** (B7), 5867-5872, doi: 10.1029/JB089iB07p05867.
7. Aki, K. & Richards, P.G., 2002. *Quantitative Seismology, 2nd edition*, University Science Books, Sausalito, CA.
8. Akuhara, T. & Mochizuki, K., 2014. Application of cluster analysis based on waveform cross-correlation coefficients to data recorded by ocean-bottom seismometers: results from off the Kii Peninsula, *Earth, Planets Sp.*, **66**, 80, doi: 10.1186/1880-5981-66-80.
9. Albaric, J., Oye, V., Langet, N., Hasting, M., Lecomte, I., Iranpour, K., Messeiller, M. & Reid, P., 2014. Monitoring of induced seismicity during the first geothermal reservoir stimulation at Paralana, Australia, *Geothermics*, **52**, 120-131, doi: 10.1016/j.geothermics.2013.10.013.
10. Allen, R., 1978. Automatic earthquake recognition and timing from single traces, *Bull. seism. Soc. Am.*, **68**, 1521-1532.
11. Allen, R., 1982. Automatic phase pickers: their present use and future prospects, *Bull. seism. Soc. Am.*, **72**, S225–S242.
12. Ambraseys, N., 1960. The seismic sea-wave of July 1956 in the Greek Archipelago, *J. Geophys. Res.*, **65** (4), 1257-1265.
13. Ambraseys, N. & Jackson, J., 1990. Seismicity and associated strain of central Greece between 1890 and 1988, *Geophys. J. Int.*, **101**, 663-708.
14. Amoroso, O., Maercklin, N. & Zollo, A., 2012. S-wave identification by polarization filtering and waveform coherence analyses, *Bull. Seismol. Soc. Am.*, **102**, 854–861.
15. Anderson, J.G., 1986. Implication of attenuation for studies of the earthquake source. *In*: *Earthquake Source Mechanics*, 311–318., doi: 10.1029/GM037p0311.
16. Anderson, J.G. & Hough, S.E., 1984. A model for the shape of the fourier amplitude spectrum of acceleration at high frequencies, *Bull. Seismol. Soc. Am.*, **74**, 1969–1993.
17. Antolik, M., Ichinose, G., Creasey, J. & Clauter, D., 2014. Seismic and Infrasonic Analysis of the Major Bolide Event of 15 February 2013, *Seismol. Res. Lett.*, **85**, 334–343, doi: 10.1785/0220130061.
18. Aoyama, H., Takeo, M. & Ide, S., 2002. Evolution mechanisms of an earthquake swarm under the Hida Mountains, central Japan, in 1998, *J. Geophys. Res.*, **107**, NO. B8, 2174, doi: 10.1029/2001JB000540.
19. Armijo, R., H. Lyon-Caen H. & Papanastassiou, D., 1992. East-west extension and Holocene normal-fault scarps in the Hellenic Arc, *Geology*, **20**(6), 491–494, doi:10.1130/0091-7613.

20. Armijo, R., Meyer, B., King, G.C.P., Rigo, A. & Papanastassiou, D., 1996. Quaternary evolution of the Corinth Rift and its implications for the Late Cenozoic evolution of the Aegean, *Geophys. J. Int.*, **126**, 11–53, doi: 10.1111/j.1365-246X.1996.tb05264.x.
21. Avallone, A., Briole, P., Agatza-Balodimou, A.M., Billiris, H., Charade, O., Mitsakaki, C., Nercessian, A., Papazissi, K., Paradissis, D. & Veis, G., 2004. Analysis of eleven years of deformation measured by GPS in the Corinth Rift Laboratory area, *Comptes Rendus Geosci.*, **336**, 301–311, doi: 10.1016/j.crte.2003.12.007.
22. Bachmann, C.E., Wiemer, S., Goertz-Allmann, B.P. & Woessner, J., 2012. Influence of pore-pressure on the event-size distribution of induced earthquakes, *Geophys. Res. Lett.*, **39**, L09302.
23. Baer, M. & Kradolfer, U., 1987. An automatic phase picker for local and teleseismic events, *Bull. seism. Soc. Am.*, **77**, 1437-1445.
24. Baillard, C., Crawford, W. C., Ballu, V., Hibert, C. & Mangeney, A., 2014. An Automatic Kurtosis-Based P- and S-Phase Picker Designed for Local Seismic Networks, *Bull. seism. Soc. Am.*, **104**, No. 1, 394-409, doi: 10.1785/0120120347.
25. Baisch, S., Ceranna, L. & Harjes, H.P., 2008. Earthquake cluster: What can we learn from waveform similarity? *Bull. Seismol. Soc. Am.*, **98**, 2806–2814.
26. Baisch, S., Vörös, R., Rothert, E., Stang, H., Jung, R. & Schellschmidt, R., 2010. A numerical model for fluid injection induced seismicity at Soultz-sous-Forêts, *Int. J. Rock Mech. Min. Sci.*, **47**, 405-413, doi: 10.1016/j.ijrmms.2009.10.001.
27. Blandford, R.R., 1982. Seismic event discrimination, *Bull. Seismol. Soc. Am.*, **72** , S69–S87.
28. Bardainne, T., Gaillot, P., Dubos-Sallée, N., Blanco, J. & Sénéchal, G., 2006. Characterization of seismic waveforms and classification of seismic events using chirplet atomic decomposition. Example from the Lacq gas field (Western Pyrenees, France), *Geophys. J. Int.*, **166**, 699–718, doi: 10.1111/j.1365-246X.2006.03023.x.
29. Båth, M., 1965. Lateral inhomogeneities of the upper mantle, *Tectonophysics*, **2**, 483-514.
30. Bayrak, Y., Yadav, R.B.S., Kalafat, D., Tsapanos, T.M., Çınar, H., Singh, A.P., Bayrak, E., Yılmaz, Ş., Öcal, F. & Koravos, G., 2013. Seismogenesis and earthquake triggering during the Van (Turkey) 2011 seismic sequence, *Tectonophysics*, **601**, 163–176, doi: 10.1016/j.tecto.2013.05.008.
31. Beckers, A., Hubert-Ferrari, A., Beck, C., Bodeux, S., Tripsanas, E., Sakellariou, D. & De Batist, M., 2015. Active faulting at the western tip of the Gulf of Corinth, Greece, from high-resolution seismic data, *Mar. Geol.*, **360**, 55–69, doi: 10.1016/j.margeo.2014.12.003.
32. Beeler, N.M., Lockner, D.L. & Hickman, S.H., 2001. A simple stick-slip and creep-slip model for repeating earthquakes and its implication for microearthquakes at Parkfield, *Bull. Seismol. Soc. Am.*, **91**, 1797–1804, doi: 10.1785/0120000096.
33. Bell, R.E., McNeill, L.C., Bull, J.M. & Henstock, T.J., 2008. Evolution of the offshore western Gulf of Corinth. *Bull. Geol. Soc. Am.*, **120**, 156–178.
34. Bell, R.E., McNeill, L.C., Bull, J.M., Henstock, T.J., Collier, R.E.L. & Leeder, M.R., 2009. Fault architecture, basin structure and evolution of the Gulf of Corinth rift, central Greece, *Basin Res.*, **21**, 824–855.
35. Bell, R.E., McNeill, L.C., Henstock, T.J. & Bull, J.M., 2011. Comparing extension on multiple time and depth scales in the Corinth Rift, Central Greece, *Geophys. J. Int.*, **186**, 463–470, doi: 10.1111/j.1365-246X.2011.05077.x.
36. Benetatos, C., Kiratzi, A., Kementzetzidou, K., Roumelioti, Z., Karakaisis, G., Scordilis, E., Latoussakis, J. & Drakatos, G., 2004. The Psachna (Evia Island) earthquake swarm of June 2003, *Bull. Geol. Soc. Greece*, **XXXVI**, 1379-1388.
37. Benetatos, C., Kiratzi, A., Roumelioti, Z., Stavrakakis, G., Drakatos, G. & Latoussakis, I., 2005. The 14 August 2003 Lefkada Island (Greece) earthquake: Focal mechanisms of the mainshock and of the aftershock sequence, *J. Seismol.*, **9**, 171–190, doi: 10.1007/s10950-005-7092-1.
38. Benvegna, F., D'Alessando, A., Bosco, G. Lo, Luzio, D., Pinello, L. & Tegolo, D., 2011. A New Dissimilarity Measure for Clustering Seismic Signals. In: Maino, G. & Foresti, G. L. (eds). *Image Analysis and Processing -- ICIAP 2011: 16th International Conference, Ravenna, Italy, September 14-16, 2011, Proceedings, Part II*. Berlin, Heidelberg, Springer Berlin Heidelberg, 434–443, doi: 10.1007/978-3-642-24088-1_45.

39. Ben-Zion, Y. & Lyakhovsky, V., 2006. Analysis of aftershocks in a lithospheric model with seismogenic zone governed by damage rheology, *Geophys. J. Int.*, **165**, 197–210, doi: 10.1111/j.1365-246X.2006.02878.x.
40. Berens, P., 2009. CircStat : A MATLAB Toolbox for Circular Statistics, *J. Stat. Softw.*, **31** (10), 1–21, doi: 10.18637/jss.v031.i10.
41. Bernard, P., Briole, P., Meyer, B., Gomez, J., Tiberi, C., Berge, C., Cattin, R., Hatzfeld, D., Lachet, C., Lebrun, B., Deschamps, a., Courboulex, F., Larroque, C., Rigo, a., Massonnet, D., Papadimitriou, P., Kassaras, J., Diagourtas, D., Makropoulos, K., Veis, G., Papazisi, E., Mitsakaki, C., Karakostas, V. & Papadimitriou, E., 1997. The Ms=6.2, June 15, 1995 Aigion earthquake (Greece): evidence for low-angle normal faulting in the Corinth rift, *J. Seismol.*, **1**, 131–150.
42. Bernard, P., Boudin, F., Sacks, S., Linde, A., Blum, P.-A., Courteille, C., Esnoult, M.-F., Castarède, H., Felekis, S. & Billiris, H., 2004. Continuous strain and tilt monitoring on the Trizonia Island, Rift of Corinth, Greece, *Comptes Rendus Geosci.*, **336**, 313–323, doi: 10.1016/j.crte.2003.11.015.
43. Bernard, P., Lyon-Caen, H., Briole, P., Deschamps, A., Boudin, F., Makropoulos, K., Papadimitriou, P., Lemeille, F., Patau, G., Billiris, H., Paradissis, D., Papazissi, K., Castarède, H., Charade, O., Nercessian, A., Avallone, A., Pacchiani, F., Zahradnik, J., Sacks, S. & Linde, A., 2006. Seismicity, deformation and seismic hazard in the western rift of Corinth: New insights from the Corinth Rift Laboratory (CRL), *Tectonophysics*, **426**, 7–30.
44. Bianco, F., Del Pezzo, E., Saccorotti, G. & Ventura, G., 2004. The role of hydrothermal fluids in triggering the July-August 2000 seismic swarm at Campi Flegrei, Italy: Evidence from seismological and mesostructural data, *J. Volcanol. Geotherm. Res.*, **133**, 229-246, doi: 10.1016/S0377-0273(03)00400-1.
45. Bischoff, M., Cete, A., Fritschen, R. & Meier, T., 2010. Coal Mining Induced Seismicity in the Ruhr Area, Germany, *Pure Appl. Geophys.*, **167**, 63–75, doi: 10.1007/s00024-009-0001-8.
46. Bisrat, S., DeShon, H.R. & Rowe, C., 2012. Microseismic Swarm Activity in the New Madrid Seismic Zone, *Bull. Seismol. Soc. Am.*, **102**, 1167-1178, doi: 10.1785/0120100315.
47. Boatwright, J., 1978. Detailed spectral analysis of two small New York State earthquakes, *Bull. Seismol. Soc. Am.*, **68**, 1117–1131.
48. Bogiatzis, P. & Ishii, M., 2015. Continuous Wavelet Decomposition Algorithms for Automatic Detection of Compressional- and Shear-Wave Arrival Times, *Bull. Seismol. Soc. Am.*, **105**, 1628–1641, doi: 10.1785/0120140267.
49. Bohnhoff, M., Rische, M., Meier, T., Becker, D., Stavrakakis, G. & Harjes, H.P., 2006. Microseismic activity in the Hellenic Volcanic Arc, Greece, with emphasis on the seismotectonic setting of the Santorini-Amorgos zone, *Tectonophysics*, **423**, 17–33.
50. Boore, D.M. & Boatwright, J., 1984. Average body-wave radiation coefficients, *Bull. Seismol. Soc. Am.*, **74**, 1615–1621.
51. Booth, D.C. & Crampin, S., 1985. Shear-wave polarizations on a curved wavefront at an isotropic free surface, *Geophys. J. Int.*, **83**, 31–45, doi: 10.1111/j.1365-246X.1985.tb05154.x.
52. Boschetti, F., Dentith, M. D., List, R. D. A., 1996. A fractal-based algorithm for detecting first arrivals on seismic traces. *Geophysics*, **61** (4), 1095-1102, doi: 10.1190/1.1444030.
53. Bourouis, S. & Bernard, P., 2007. Evidence for coupled seismic and aseismic fault slip during water injection in the geothermal site of Soultz (France), and implications for seismogenic transients, *Geophys. J. Int.*, **169**, 723-732, doi: 10.1111/j.1365-246X.2006.03325.x.
54. Bourouis, S. & Cornet, F.H., 2009. Microseismic activity and fluid fault interactions: some results from the Corinth Rift Laboratory (CRL), Greece, *Geophys. J. Int.*, **178**, 561–580, doi: 10.1111/j.1365-246X.2009.04148.x.
55. Bowers, D. & Hudson, J.A., 1999. Defining the scalar moment of a seismic source with a general moment tensor, *Bull. Seismol. Soc. Am.*, **89**, 1390–1394.
56. Bozzano, F., Lenti, L., Martino, S., Paciello, A. & Scarascia Mugnozza, G., 2011. Evidences of landslide earthquake triggering due to self-excitation process, *Int. J. Earth Sci.*, **100**, 861–879, doi: 10.1007/s00531-010-0514-5.

57. Briole, P., Rigo, A., Lyon-Caen, H., Ruegg, J.C., Papazissi, K., Mitsakaki, C., Balodimou, A., Veis, G., Hatzfeld, D. & Deschamps, A., 2000. Active Deformation of the Corinth Rift, Greece: Results from Repeated GPS Surveys between 1990 and 1995, *J. Geophys. Res.*, **105**(B11), 25605-25625.
58. Brooks, M. & Ferentinos, G., 1984. Tectonics and sedimentation in the Gulf of Corinth and the Zakinthos and Kefallinia channels, Western Greece, *Tectonophysics*, **101**, 25-54.
59. Brune, J., 1970. Tectonic stress and the spectra of seismic shear waves from earthquakes, *J. Geophys. Res.*, **75**, 4997-5009.
60. Buland, R. P., Guy, M., Kragness, D., Patton, J., Erickson, B., Morrison, M., Bryon, C., Ketchum, D. & Benz, H., 2009. Comprehensive seismic monitoring for emergency response and hazards assessment: Recent developments at the USGS National Earthquake Information Center (abstract S11B-1696), *AGU* (Fall Meet.), S11B-1696.
61. Cannata, A., Alparone, S. & Ursino, A., 2013. Repeating volcano-tectonic earthquakes at Mt. Etna volcano (Sicily, Italy) during 1999-2009. *Gondwana Res.*, **24**, 1223–1236.
62. Carmichael, J.D., Pettit, E.C., Hoffman, M., Fountain, A. & Hallet, B., 2012. Seismic multiplet response triggered by melt at Blood Falls, Taylor Glacier, Antarctica, *J. Geophys. Res. Earth Surf.*, **117**, F03004, doi: 10.1029/2011JF002221.
63. Carmona, E., Stich, D., Ibañez, J.M. & Saccorotti, G., 2009. Multiplet focal mechanisms from polarities and relative locations: The Iznajar swarm in southern Spain, *Bull. Seismol. Soc. Am.*, **99**, 3421-3429, doi: 10.1785/0120090036.
64. Cattaneo, M., Augliera, P., Spallarossa, D. & Lanza, V., 1999. A waveform similarity approach to investigate seismicity patterns. *Nat. Hazards*, **19**, 123–138.
65. Cattell, R.B., 1966. The Scree Test For The Number Of Factors, *Multivariate Behav. Res.*, **1**, 245–276.
66. Chouliaras, G., Kassaras, I., Kapetanidis, V., Petrou, P. & Drakatos, G., 2015. Seismotectonic analysis of the 2013 seismic sequence at the western Corinth Rift, *J. Geodyn.*, **90**, 42–57, doi: 10.1016/j.jog.2015.07.001.
67. Chousianitis, K., Ganas, A. & Evangelidis, C.P., 2015. Strain and rotation rate patterns of mainland Greece from continuous GPS data and comparison between seismic and geodetic moment release, *J. Geophys. Res. Solid Earth*, **120**, 3909–3931, doi: 10.1002/2014JB011762.
68. Chun, K.Y., Yuan, Q.Y. & Henderson, G.A., 2010. Precursory rise of P-wave attenuation before the 2004 Parkfield earthquake, *Bull. Seismol. Soc. Am.*, **100**, 509-521, doi: 10.1785/0120090104.
69. Cociani, L., Bean, C.J., Lyon-Caen, H., Pacchiani, F. & Deschamps, A., 2010. Coseismic velocity variations caused by static stress changes associated with the 2001 M_w = 4.3 Agios Ioanis earthquake in the Gulf of Corinth, Greece, *J. Geophys. Res. Solid Earth*, **115**, B07313, doi: 10.1029/2009JB006859.
70. Cornet, F.H., Doan, M.L., Moretti, I. & Borm, G., 2004. Drilling through the active Aigion Fault: the AIG10 well observatory. *Comptes Rendus Geosci.*, **336**, 395–406, doi: 10.1016/j.crte.2004.02.002.
71. Crider, J.G. & Pollard, D.D., 1998. Fault linkage: Three-dimensional mechanical interaction between echelon normal faults, *J. Geophys. Res.*, **103**, 24373-24391, doi: 10.1029/98JB01353.
72. Cua, G. & Heaton, T., 2007. The Virtual Seismologist (VS) Method: a Bayesian Approach to Earthquake Early Warning, *In*: *Earthquake Early Warning Systems*. Berlin, Heidelberg, Springer Berlin Heidelberg, 97–132, doi: 10.1007/978-3-540-72241-0_7.
73. Dahm, T., Hainzl, S. & Fischer, T., 2010. Bidirectional and unidirectional fracture growth during hydrofracturing: Role of driving stress gradients, *J. Geophys. Res. Solid Earth*, **115**, B12322, doi: 10.1029/2009JB006817.
74. Dai, H. & MacBeth, C., 1995. Automatic picking of seismic arrivals in local earthquake data using an artificial neural network, *Geophys. J. Int.*, **120**(3), 758-774, doi: 10.1111/j.1365-246X.1995.tb01851.x.
75. D'Alessandro, A., Papanastassiou, D. & Baskoutas, I., 2011. Hellenic Unified Seismological Network: an evaluation of its performance through SNES method, *Geophys. J. Int.*, **185**, 1417-1430.
76. Davies, R., Foulger, G., Bindley, A. & Styles, P., 2013. Induced seismicity and hydraulic fracturing for the recovery of hydrocarbons, *Mar. Pet. Geol.*, **45**, 171–185.

77. Deichmann, N. & Garcia-Fernandez, M., 1992. Rupture geometry from high-precision relative hypocentre locations of microearthquake clusters, *Geophys. J. Int.*, **110**, 501–517.
78. Delibasis, N., Carydis, P., 1977. Recent earthquake activity in Trichonis region andits tectonic significance, *Ann. Geophys.*, **30**, 19–81.
79. Dewie, J.W., 1971. Seismicity Studies with the Method of Joint Hypocenter Determination, unpubl. doctoral dissertation, Univ. California, Berkeley, 202 p.
80. Dewey, J.W., 1972. Seismicity and tectonics of western Venezuela, *Bull. Seismol. Soc. Am.*, **62**, 1711–1751.
81. Diehl, T., Deichmann, N., Kissling, E. & Husen, S., 2009. Automatic S-Wave Picker for Local Earthquake Tomography, *Bull. seism. Soc. Am.*, **99**, No. 3, 1906-1920, doi: 10.1785/0120080019
82. Dietz, L., 2002. Notes on configuring binder_ew: Earthworm's phase associator, www.ipgp.fr/~tuchais/earthworm/ewdoc/WEB_DOC/ovr/binder_setup.html
83. Di Giacomo, D., Bondár, I., Storchak, D.A., Engdahl, E.R., Bormann, P. & Harris, J., 2015. ISC-GEM: Global Instrumental Earthquake Catalogue (1900–2009), III. Re-computed MS and mb, proxy MW, final magnitude composition and completeness assessment, *Phys. Earth Planet. Inter.*, **239**, 33–47, doi: 10.1016/j.pepi.2014.06.005.
84. Douglas, A., 1967. Joint Epicentre Determination, *Nature*, **215**, 47–48, doi: 10.1038/215047a0.
85. Doutsos, T. & Poulimenos, G., 1992. Geometry and kinematics of active faults and their seismotectonic significance in the western Corinth-Patras rift (Greece), *Journal of Structural Geology*, **14** (6), 689-699, doi:10.1016/0191-8141(92)90126-h.
86. Duverger, C., Godano, M., Bernard, P., Lyon-Caen, H. & Lambotte, S., 2015. The 2003-2004 seismic swarm in the western Corinth rift: Evidence for a multiscale pore pressure diffusion process along a permeable fault system, *Geophys. Res. Lett.*, **42**, 7374–7382, doi: 10.1002/2015GL065298.
87. Eagar, K.C., Pavlis, G.L. & Hamburger, M.W., 2006. Evidence of Possible Induced Seismicity in the Wabash Valley Seismic Zone from Improved Microearthquake Locations, *Bull. Seismol. Soc. Am.*, **96**, 1718–1728, doi: 10.1785/0120050190.
88. Earle, P. & Shearer, P., 1994. Characterization of global seismograms using an automatic picking algorithm, *Bull. seism. Soc. Am.*, **84**, 366-376.
89. Edwards, B., 2008. *On the use of micro-earthquakes to predict strong ground-motion*, PhD thesis, University of Liverpool.
90. Edwards, B., Allmann, B., Fäh, D. & Clinton, J., 2010. Automatic computation of moment magnitudes for small earthquakes and the scaling of local to moment magnitude, *Geophys. J. Int.*, **183**, 407–420, doi: 10.1111/j.1365-246X.2010.04743.x.
91. Einarsson, P. & Brandsdóttir, B., 1979. Seimological Evidence for Lateral Magma Intrusion during the July 1978 Deflation of the Krafla Volcano in NE-Iceland, *Raunvísindastofnun Háskólans - Rep.*, 1–24, doi: 10.2172/890964.
92. Enescu, B. & Ito, K., 2001. Some premonitory phenomena of the 1995 Hyogo-Ken Nanbu (Kobe) earthquake: seismicity, b-value and fractal dimension, *Tectonophysics*, **338**, 297–314, doi: 10.1016/S0040-1951(01)00085-3.
93. Enescu, B., Hainzl, S. & Ben-Zion, Y., 2009. Correlations of Seismicity Patterns in Southern California with Surface Heat Flow Data, *Bull. Seismol. Soc. Am.*, **99**, 3114–3123, doi: 10.1785/0120080038.
94. Fang, L., Wu, J., Wang, W., Du, W., Su, J., Wang, C., Yang, T. & Cai, Y., 2015. Aftershock Observation and Analysis of the 2013 M s 7.0 Lushan Earthquake, *Seismol. Res. Lett.*, **86**, 1135–1142, doi: 10.1785/0220140186.
95. Fedorenko, Y. V., Matveeva, T., Beketova, E. & Husebye, E.S., 2008. Secondary phase validation-Phase classification by polarization, *Phys. Earth Planet. Inter.*, **168**, 231–236, doi: 10.1016/j.pepi.2008.06.006.
96. Fehler, M., House, L., Philips, W. & Potter, R, 1998. A method to allow temporal variation of velocity in travel-time tomography using microearthquakes induced during hydraulic fracturing, *Tectonophysics*, **289**, 189-201.
97. Feng, L., Newman, A. V., Farmer, G.T., Psimoulis, P. & Stiros, S.C., 2010. Energetic rupture, coseismic and post-seismic response of the 2008 MW 6.4 Achaia-Elia Earthquake in northwestern Peloponnese, Greece: an indicator of an immature transform fault zone, *Geophys. J. Int.*, **183**, 103–110, doi: 10.1111/j.1365-246X.2010.04747.x.

98. Ferrucci, F. & Patanè, D., 1993. Seismic activity accompanying the outbreak of the 1991-1993 eruption of Mt. Etna (Italy), *J. Volcanol. Geotherm. Res.*, **57**, 125-135, doi: 10.1016/0377-0273(93)90034-O.

99. Feuillet, N., 2013. The 2011-2012 unrest at Santorini rift: Stress interaction between active faulting and volcanism, *Geophys. Res. Lett.*, **40**(14), 3532-3537.

100. Fischer, T., Hainzl, S. & Dahm, T., 2009. The creation of an asymmetric hydraulic fracture as a result of driving stress gradients, *Geophys. J. Int.*, **179**, 634–639, doi: 10.1111/j.1365-246X.2009.04316.x.

101. Fischer, T., Horálek, J., Hrubcová, P., Vavryčuk, V., Bräuer, K. & Kämpf, H., 2014. Intra-continental earthquake swarms in West-Bohemia and Vogtland: A review, *Tectonophysics*, **611**, 1-27, doi: 10.1016/j.tecto.2013.11.001.

102. Flotté, N., Sorel, D., Müller, C. & Tensi, J., 2005. Along strike changes in the structural evolution over a brittle detachment fault: Example of the Pleistocene Corinth-Patras rift (Greece), *Tectonophysics*, **403**, 77–94, doi:10.1016/j.tecto.2005.03.015.

103. Ford, M., Rohais, S., Williams, E.A., Bourlange, S., Jousselin, D., Backert, N. & Malartre, F., 2013. Tectono-sedimentary evolution of the western Corinth rift (Central Greece), *Basin Res.*, **25**, 3–25, doi: 10.1111/j.1365-2117.2012.00550.x.

104. Fossen, H. & Rotevatn, A., 2016. Fault linkage and relay structures in extensional settings—A review, *Earth-Science Rev.*, **154**, 14–28, doi: 10.1016/j.earscirev.2015.11.014.

105. Fournier, R.O., 1999. Hydrothermal processes related to movement of fluid from plastic into brittle rock in the magmatic-epithermal environment, *Econ. Geol.*, **94**, 1193-1211, doi: 10.2113/gsecongeo.94.8.1193.

106. Frémont, M.-J. & Malone, S.D. , 1987. High precision relative locations of earthquakes at Mount St. Helens, Washington. *J. Geophys. Res. Solid Earth*, **92**, 10223–10236, doi: 10.1029/JB092iB10p10223.

107. Friberg, P., Lisowski, S., Dricker, I. & Hellman, S., 2010. Earthworm in the 21st century, in *European Geosciences Union General Assembly*, 2–7 May 2010, Vienna, Austria, 12654 pp.

108. Friedrich, W.L., 2000. *Fire in the Sea. The Santorini Volcano: Natural History and the Legend of Atlantis*, Cambridge University Press, 2000. ISBN: 0521652901.

109. Galanopoulos, A.G., 1957. The seismic sea wave of July 9, 1956. *Prakt. Akad. Athens*, **32**, 90–101 (in Greek).

110. Gallousi, C. & Koukouvelas, I.K., 2007. Quantifying geomorphic evolution of earthquake-triggered landslides and their relation to active normal faults. An example from the Gulf of Corinth, Greece, *Tectonophysics*, **440**, 85–104, doi: 10.1016/j.tecto.2007.02.009.

111. Gallovič, F., Zahradník, J., Křížová, D., Plicka, V., Sokos, E., Serpetsidaki, A. & Tselentis, G.-A., 2009. From earthquake centroid to spatial-temporal rupture evolution: Mw 6.3 Movri Mountain earthquake, June 8, 2008, Greece, *Geophys. Res. Lett.*, **36**, L21310, doi: 10.1029/2009GL040283.

112. Ganas, A., Serpelloni, E., Drakatos, G., Kolligri, M., Adamis, I., Tsimi, C. & Batsi, E., 2009. The Mw 6.4 SW-Achaia (Western Greece) Earthquake of 8 June 2008: Seismological, Field, GPS Observations, and Stress Modeling, *J. Earthq. Eng.*, **13**, 1101–1124, doi: 10.1080/13632460902933899.

113. Ganas, A., Lekkas, E., Kolligri, M., Moshou, A. & Makropoulos, K., 2012. The 2011 Oichalia (SW Peloponnesus, Greece) seismic swarm: geological and seismological evidence for E-W extension and reactivation of the NNW-SSE normal fault, *Bulletin of the Geological Society of Greece*, vol. **XLVI**, 81-94.

114. Ganas, A., Chousianitis, K., Batsi, E., Kolligri, M., Agalos, A., Chouliaras, G. & Makropoulos, K., 2013. The January 2010 Efpalion earthquakes (Gulf of Corinth, Central Greece): earthquake interactions and blind normal faulting, *J. Seismol.*, **17**, 465–484, doi: 10.1007/s10950-012-9331-6.

115. Gasperini, P. & Vannucci, G., 2003. FPSPACK: a package of FORTRAN subroutines to manage earthquake focal mechanism data, *Comput. Geosci.*, **29**, 893–901, doi: 10.1016/S0098-3004(03)00096-7.

116. Gautier, S., Latorre, D., Virieux, J., Deschamps, A., Skarpelos, C., Sotiriou, A., Serpetsidaki, A. & Tselentis, A., 2006. A new passive tomography of the Aigion area (Gulf of Corinth, Greece) from the 2002 data set, *Pure appl. Geophys.*, **163**, 431-453.

117. Gautier, S., Nolet, G. & Virieux, J., 2008. Finite-frequency tomography in a crustal environment: Application to the western part of the Gulf of Corinth, *Geophys. Prospect.*, **56**, 493–503, doi: 10.1111/j.1365-2478.2007.00683.x.

118. Geller, R.J. & Mueller, C.S., 1980. Four Similar Earthquakes in Central California, *Geophys. Res. Lett.*, **7**, 821–824.

119. Gentili, S. & Michelini, A., 2006. Automatic picking of P and S phases using a neural tree, *J. Seismol.*, **10**, 39–63, doi: 10.1007/s10950-006-2296-6.

120. Gephart, J.W. & Forsyth, D.W., 1984. An Improved Method for Determining the Regional Stress Tensor Using Earthquake Focal Mechanism Data : Application to the San Fernando Earthquake Sequence, *J. Geophys. Res. Solid Earth*, **89**, 9305–9320, doi: 10.1029/JB089iB11p09305.

121. Ghisetti, F. & Vezzani, L., 2005. Inherited structural controls on normal fault architecture in the Gulf of Corinth (Greece), *Tectonics*, **24**, 1–17, doi: 10.1029/2004TC001696.

122. Gibbons, S.J. & Ringdal, F., 2006. The detection of low magnitude seismic events using array-based waveform correlation, *Geophys. J. Int.*, **165**, 149–166.

123. Given, D.D., Cochran, E.S., Heaton, T., Hauksson, E., Allen, R., Hellweg, P., Vidale, J. & Bodin, P., 2014. Technical implementation plan for the ShakeAlert production system—An Earthquake Early Warning system for the West Coast of the United States: U.S. Geological Survey Open-File Report 2014–1097, 25 p., http://dx.doi.org/10.3133/ofr20141097.

124. Godano, M., Larroque, C., Bertrand, E., Courboulex, F., Deschamps, A., Salichon, J., Blaud-Guerry, C., Fourteau, L., Charley, J. & Deshayes, P., 2013. The October-November 2010 earthquake swarm near Sampeyre (Piedmont region, Italy): A complex multicluster sequence, *Tectonophysics*, **608**, 97–111, doi: 10.1016/j.tecto.2013.10.010.

125. Godano, M., Deschamps, A., Lambotte, S., Lyon-Caen, H., Bernard, P. & Pacchiani, F., 2014. Focal mechanisms of earthquake multiplets in the western part of the Corinth Rift (Greece): Influence of the velocity model and constraints on the geometry of the active faults, *Geophys. J. Int.*, **197**, 1660–1680, doi: 10.1093/gji/ggu059.

126. Godano, M., Bernard, P. & Dublanchet, P., 2015. Bayesian inversion of seismic spectral ratio for source scaling: Application to a persistent multiplet in the western Corinth rift, *J. Geophys. Res. Solid Earth*, **120**, 7683–7712, doi: 10.1002/2015JB012217.

127. Gospodinov, D. & Rotondi, R., 2006. Statistical analysis of triggered seismicity in the Kresna region of SW Bulgaria (1904) and the Umbria-Marche region of central Italy (1997), *Pure Appl. Geophys.*, **163**, 1597–1615, doi: 10.1007/s00024-006-0084-4.

128. Gospodinov, D., Karakostas, V. & Papadimitriou, E., 2015. Seismicity rate modeling for prospective stochastic forecasting: the case of 2014 Kefalonia, Greece, seismic excitation, *Nat. Hazards*, **79**, 1039–1058, doi: 10.1007/s11069-015-1890-8.

129. Got, J.-L., Fréchet, J. & Klein, F.W., 1994. Deep fault plane geometry inferred from multiplet relative relocation beneath the south flank of Kilauea, *J. Geophys. Res.*, **99**, 15375–15386.

130. Grassberger, P. & Procaccia, I., 1983. Measuring the strangeness of strange attractors. *Phys. D Nonlinear Phenom.*, **9**, 189–208, doi: 10.1016/0167-2789(83)90298-1.

131. Green, D.N. & Neuberg, J., 2006. Waveform classification of volcanic low-frequency earthquake swarms and its implication at Soufrière Hills Volcano, Montserrat. *J. Volcanol. Geotherm. Res.*, **153**, 51–63.

132. Griffith, A.A., 1921. The Phenomena of Rupture and Flow in Solids, *Philos. Trans. R. Soc. A Math. Phys. Eng. Sci.*, **221**, 163–198.

133. Grünthal, G., Wahlström, R. & Stromeyer, D., 2009. The unified catalogue of earthquakes in central, northern, and northwestern Europe (CENEC)—updated and expanded to the last millennium, *J. Seismol.*, **13**, 517–541, doi: 10.1007/s10950-008-9144-9.

134. Gutenberg, B. & Richter, C.F., 1954. *Seismicity of the Earth and Associated Phenomena, 2nd ed.*, Princeton, N.J.: Princeton University Press.

135. Haakon, F., 2010. *Structural Geology*, Cambridge University Press.
136. Hafez, A.G., Khan, M.T.A. & Kohda, T., 2010. Clear P-wave arrival of weak events and automatic onset determination using wavelet filter banks, *Digit. Signal Process.*, **20**, 715–723, doi: 10.1016/j.dsp.2009.10.002.
137. Häge, M. & Joswig, M., 2009. Mapping local microseismicity using short-term tripartite small array installations - Case study: Coy region (SE Spain), *Tectonophysics*, **471**, 225-231, doi: 10.1016/j.tecto.2009.02.016.
138. Hainzl, S. & Ogata, Y., 2005. Detecting fluid signals in seismicity data through statistical earthquake modeling, *J. Geophys. Res. B Solid Earth*, **110**, 1-10, doi: 10.1029/2004JB003247.
139. Hainzl, S., Fischer, T. & Dahm, T., 2012. Seismicity-based estimation of the driving fluid pressure in the case of swarm activity in Western Bohemia, *Geophys. J. Int.*, **191**, 271-281, doi: 10.1111/j.1365-246X.2012.05610.x.
140. Hainzl, S., Zakharova, O. & Marsan, D., 2013. Impact of Aseismic Transients on the Estimation of Aftershock Productivity Parameters, *Bull. Seismol. Soc. Am.*, **103**, 1723–1732, doi: 10.1785/0120120247.
141. Han, L., Wu, Z., Li, Y. & Jiang, C., 2014. Cross-correlation Coefficients for the Study of Repeating Earthquakes: An Investigation of Two Empirical Assumptions/Conventions in Seismological Interpretation Practice. *Pure Appl. Geophys.*, **171**, 425–437, doi: 10.1007/s00024-012-0515-3.
142. Hanks, T.C. & Kanamori, H., 1979. A moment magnitude scale, *J. Geophys. Res. B Solid Earth*, **84**, 2348–2350, doi: 10.1029/JB084iB05p02348.
143. Hardebeck, J.L. & Shearer, P.M., 2002. A New Method for Determining First-Motion Focal Mechanisms, *Bull. Seismol. Soc. Am.*, **92**, 2264–2276, doi: 10.1785/0120010200.
144. Hardebeck, J.L. & Shearer, P.M., 2003. Using S/P amplitude ratios to constrain the focal mechanisms of small earthquakes, *Bull. Seismol. Soc. Am.*, **93**, 2434–2444, doi: 10.1785/0120020236.
145. Harrington, R.M. & Brodsky, E.E., 2009. Source Duration Scales with Magnitude Differently for Earthquakes on the San Andreas Fault and on Secondary Faults in Parkfield, California, *Bull. Seismol. Soc. Am.*, **99**, 2323–2334, doi: 10.1785/0120080216.
146. Harris, D.B. & Dodge, D.A., 2011. An Autonomous System for Grouping Events in a Developing Aftershock Sequence, *Bull. Seismol. Soc. Am.*, **101** , 763–774, doi: 10.1785/0120100103.
147. Hartigan, J. A., 1975. *Clustering Algorithms (Probability & Mathematical Statistics)*, John Wiley & Sons Inc.
148. Haskell, N.A., 1964. Total energy and energy spectral density of elastic wave radiation from propagating faults, *Bull. Seismol. Soc. Am.* , **54**, 1811–1841.
149. Haslinger, F., Kissling, E., Ansorge, J., Hatzfeld, D., Papadimitriou, E., Karakostas, V., Makropoulos, K., Kahle, H.-G. & Peter, Y., 1999. 3D crustal structure from local earthquake tomography around the Gulf of Arta (Ionian region, NW Greece), *Tectonophysics*, **304**, 201–218, doi: 10.1016/S0040-1951(98)00298-4.
150. Hatzfeld, D., Pedotti, G., Hatzidimitriou, P. & Makropoulos, K., 1990. The strain pattern in the western Hellenic arc deduced from a microearthquake survey, *Geophys. J. Int.*, **101**, 181-202.
151. Hatzfeld, D., Kementzetzidou, D., Karakostas, V., Ziazia, M., Nothard, S., Diagourtas, D., Deschamps, A., Karakaisis, G., Papadimitriou, P., Scordilis, M., Smith, R., Voulgaris, N., Kiratzi, S., Makropoulos, K., Bouin, M.P. & Bernard, P., 1996. The Galaxidi earthquake of 18 November 1992: A possible asperity within the normal fault system of the Gulf of Corinth (Greece), *Bull. Seismol. Soc. Am.*, **86**, 1987–1991.
152. Hatzfeld, D., Karakostas, V., Ziazia, M., Kassaras, I., Papadimitriou, E., Makropoulos, K., Voulgaris, N. & Papaioannou, C., 2000. Microseismicity and faulting geometry in the Gulf of Corinth (Greece). *Geophys. J. Int.*, **141**, 438–456.
153. Hauksson, E. & Shearer, P., 2005. Southern California hypocenter relocation with waveform cross-correlation, part 1: Results using the double-difference method, *Bull. Seismol. Soc. Am.*, **95**, 896–903.
154. Havskov, J. & Alguacil, G., 2014. Seismic Event Detection, *Encyclopedia of Earthquake Engineering SE - 185-1*, Springer Berlin Heidelberg, 1-14, doi:10.1007/978-3-642-36197-5_185-1.

155. Havskov, J. & Alguacil, G. (eds)., 2004. *Instrumentation in Earthquake Seismology*, Dordrecht, Springer Netherlands, Modern Approaches in Geophysics, doi: 10.1007/978-1-4020-2969-1.

156. Hemmann, A., Meier, T., Jentzsch, G. & Ziegert, A., 2003. Similarity of waveforms and relative relocalisation of the earthquake swarm 1997/1998 near Werdau, *J. Geodyn.*, **35**, 191-208, doi: 10.1016/S0264-3707(02)00062-5.

157. Herrmann, R.B., Park, S.-K. & Wang, C.-Y., 1981. The Denver earthquakes of 1967-1968, *Bull. Seismol. Soc. Am.*, **71**, 731–745.

158. Hill, D.P., 1977. A model for earthquake swarms, *J. Geophys. Res.*, **82**, 1347-1352, doi: 10.1029/JB082i008p01347.

159. Horiuchi, S., Horiuchi, Y., Yamamoto, S., Nakamura, H., Wu, C., Rydelek, P.A. & Kachi, M., 2009. Home seismometer for earthquake early warning, *Geophys. Res. Lett.*, **36**, L00B04, doi: 10.1029/2008GL036572.

160. Hotovec, A.J., Prejean, S.G., Vidale, J.E. & Gomberg, J., 2013. Strongly gliding harmonic tremor during the 2009 eruption of Redoubt Volcano, *J. Volcanol. Geotherm. Res.*, **259**, 89–99, doi: 10.1016/j.jvolgeores.2012.01.001.

161. Ibs-von Seht, M., Plenefisch, T. & Klinge, K., 2008. Earthquake swarms in continental rifts - A comparison of selected cases in America, Africa and Europe, *Tectonophysics*, **452**, 66-77, doi: 10.1016/j.tecto.2008.02.008.

162. Ichinose, G.A., Smith, K.D. & Anderson, J.G., 1997. Source parameters of the 15 November 1995 Border Town, Nevada, earthquake sequence, *Bull. Seismol. Soc. Am.*, **87**, 652–667.

163. Ide, S., Beroza, G.C., Prejean, S.G. & Ellsworth, W.L., 2003. Apparent break in earthquake scaling due to path and site effects on deep borehole recordings, *J. Geophys. Res. Solid Earth*, **108**, 2271, doi: 10.1029/2001JB001617.

164. Jackson, J. A., Gagnepain, J., Houseman, G., King, G.C.P., Papadimitriou, P., Soufleris, C. & Virieux, J., 1982. Seismicity, normal faulting and the geomorphological development of the Gulf of Corinth (Greece): the Corinth earthquakes of February and March 1981, *Earth and Planetary Science Letters*, **57**, 377-397.

165. Jenatton, L., Guiguet, R., Thouvenot, F. & Daix, N., 2007. The 16,000-event 2003-2004 earthquake swarm in Ubaye (French Alps), *J. Geophys. Res. Solid Earth*, **112**, B11304, doi: 10.1029/2006JB004878.

166. Jost, M.L. & Herrmann, R.B., 1989. A Student's Guide to and Review of Moment Tensors, *Seismol. Res. Lett.*, **60** , 37–57, doi: 10.1785/gssrl.60.2.37.

167. Jolivet, L., Labrousse, L., Agard, P., Lacombe, O., Bailly, V., Lecomte, E., Mouthereau, F. & Mehl, C., 2010. Rifting and shallow-dipping detachments, clues from the Corinth Rift and the Aegean, *Tectonophysics*, **483**, 287–304.

168. Junek, W.N., Kværna, T., Pirli, M., Schweitzer, J., Harris, D.B., Dodge, D.A. & Woods, M.T., 2014. Inferring Aftershock Sequence Properties and Tectonic Structure Using Empirical Signal Detectors, *Pure Appl. Geophys.*, **172**, 359–373, doi: 10.1007/s00024-014-0938-0.

169. Kabsch, W., 1978. A discussion of the solution for the best rotation to relate two sets of vectors, *Acta Crystallogr. Sect. A*, **34**, 827–828, doi: 10.1107/S0567739478001680.

170. Kagan, Y.Y., 1991. 3-D rotation of double-couple earthquake sources, *Geophys. J. Int.*, **106**, 709–716, doi: 10.1111/j.1365-246X.1991.tb06343.x.

171. Kamberis, E., Pavlopoulos, A., Tsaila-Monopolis, S., Sotiropoulos, S. & Ioakim, C., 2005. Paleogene deep-water sedimentation and paleogeography of foreland basins in the NW Peloponnese (Greece), Geologica Carpathica, **56**(6), 503–515.

172. Kanamori, H. & Anderson, D.L., 1975. Theoretical basis of some empirical relations in seismology, *Bull. Seismol. Soc. Am.*, **65**, 1073–1095.

173. Kanamori, H., 1977. The energy release in great earthquakes, *J. Geophys. Res.*, **82**, 2981–2987, doi: 10.1029/JB082i020p02981.

174. Kanamori, H. & Given, J.W., 1981. Use of long-period surface waves for rapid determination of earthquake-source parameters, *Phys. Earth Planet. Inter.*, **27**, 8–31, doi: 10.1016/0031-9201(81)90083-2.

175. Kanamori, H., Ekström, G., Dziewonski, A., Barker, J.S. & Sipkin, S.A., 1993. Seismic radiation by magma injection: An anomalous seismic event near Tori Shima, Japan, *J. Geophys. Res. Solid Earth*, **98**, 6511–6522, doi: 10.1029/92JB02867.
176. Kanamori, H. & Rivera, L., 2004. Static and dynamic scaling relations for earthquakes and their implications for rupture speed and stress drop, *Bull. Seismol. Soc. Am.*, **94**, 314–319, doi: 10.1785/0120030159.
177. Kanasewich, E. R., 1981. *Time Sequence Analysis in Geophysics*, University of Alberta Press, Edmonton, Alberta, Canada.
178. Kapetanidis, V., 2007. *Μελέτη Σμηνοσεισμών Δυτικού Κορινθιακού κόλπου με χρήση μεθόδων Ετεροσυσχέτισης και Συνοχής: επαναπροσδιορισμός σεισμικών παραμέτρων*, MSc Thesis, 312 pp, National and Kapodistrian University of Athens. (*in Greek*)
179. Kapetanidis, V., Agalos, A., Moshou, A., Kaviris, G., Karakonstantis, A., Papadimitriou, P. & Makropoulos, K., 2008. Preliminary Results from the Study of a Seismic Swarm Occurred in February 2008 in NW Peloponnesus, Greece, *31st General Assembly of the ESC 2008, poster session ACQUIS-3-PROPAG, Oral & Poster Abstracts*, pg. **110**.
180. Kapetanidis, V., Papadimitriou, P. & Makropoulos, K., 2010. A cross-correlation technique for relocation of seismicity in the western Corinth rift, *Bull. Geol. Soc. Greece*, in *Proceedings of the 12th International Congress*, Patras, May 2010, **XLIII**, No **4**, pp. 2015–2025.
181. Kapetanidis, V. & Papadimitriou, P., 2011. Estimation of arrival-times in intense seismic sequences using a Master-Events methodology based on waveform similarity, *Geophys. J. Int.*, **187**, 889–917.
182. Kapetanidis, V., Deschamps, A., Papadimitriou, P., Matrullo, E., Karakonstantis, A., Bozionelos, G., Kaviris, G., Serpetsidaki, A., Lyon-Caen, H., Voulgaris, N., Bernard, P., Sokos, E. & Makropoulos, K., 2015. The 2013 earthquake swarm in Helike, Greece: seismic activity at the root of old normal faults, *Geophys. J. Int.*, **202**, 2044–2073, doi: 10.1093/gji/ggv249.
183. Karakonstantis, A., Papadimitriou, P., 2010. Earthquake relocation in Greece using a unified and homogenized seismological catalogue, *Bull. Geol. Soc. Greece, Proc. of the 12th International Congress, Patras, May 2010*, **XLIII**, No 4, pg. 2043-2052.
184. Karakonstantis, A. & Papadimitriou P., 2016. Local Earthquake Tomography in the broader area of Western Corinth gulf, *Bull. Geol. Soc. Greece, Proc. of the 14th International Congress, Thessaloniki, May, 2016*, vol. **L**, pp. 1143-1152.
185. Karakostas, V.G. & Papadimitriou, E.E., 2010. Fault complexity associated with the 14 August 2003 Mw6.2 Lefkada, Greece, aftershock sequence, *Acta Geophys.*, **58**, 838–854, doi: 10.2478/s11600-010-0009-6.
186. Karakostas, V., Karagianni, E. & Paradisopoulou, P., 2012. Space–time analysis, faulting and triggering of the 2010 earthquake doublet in western Corinth Gulf, *Nat. Hazards*, **63**, 1181–1202, doi: 10.1007/s11069-012-0219-0.
187. Karakostas, V., Papadimitriou, E., Mesimeri, M., Gkarlaouni, C. & Paradisopoulou, P., 2015. The 2014 Kefalonia Doublet (Mw6.1 and Mw6.0), Central Ionian Islands, Greece: Seismotectonic Implications along the Kefalonia Transform Fault Zone, *Acta Geophys.*, **63**, 1–16, doi: 10.2478/s11600-014-0227-4.
188. Karastathis, V.K., Mouzakiotis, E., Ganas, A. & Papadopoulos, G.A., 2015. High-precision relocation of seismic sequences above a dipping Moho: the case of the January–February 2014 seismic sequence on Cephalonia island (Greece). *Solid Earth*, **6**, 173–184, doi: 10.5194/se-6-173-2015.
189. Kassaras, I., Kapetanidis, V., Karakonstantis, A., Kaviris, G., Papadimitriou, P., Voulgaris, N., Makropoulos, K., Popandopoulos, G. & Moshou, A., 2014a. The April-June 2007 Trichonis Lake earthquake swarm (W. Greece). New implications toward the causative fault zone, *Journal of Geodynamics*, **73**, 60-80, http://dx.doi.org/10.1016/j.jog.2013.09.004.
190. Kassaras, I., Kapetanidis, V., Karakonstantis, A., Kouskouna, V., Ganas, A., Chouliaras, G., Drakatos, G., Moshou, A., Mitropoulou, V., Argyrakis, P., Lekkas, E. & Makropoulos, K., 2014b. Constraints on the dynamics and spatio-temporal evolution of the 2011 Oichalia seismic swarm (SW Peloponnesus, Greece), *Tectonophysics*, **614**, 100-127, doi: 10.1016/j.tecto.2013.12.012.
191. Kassaras, I., Kapetanidis, V. & Karakonstantis, A., 2016. On the spatial distribution of seismicity and the 3D tectonic stress field in western Greece, **95**, 50-72, *Phys. Chem. Earth, Parts A/B/C*, doi: 10.1016/j.pce.2016.03.012.

192. Kaviris, G., 2003. Study of Seismic Source Properties of the Eastern Gulf of Corinth, *Ph. D. Thesis*, Geophysics-Geothermics Department, Faculty of Geology, University of Athens, Greece, 2003 (in Greek).
193. Kaviris, G., Papadimitriou, P., Makropoulos, K., 2007. Magnitude scales in Central Greece, *Bull. Geol. Soc. Greece*, **XXXX** (3), 1114–1124.
194. Kaviris, G., Spingos, I., Kapetanidis, V. & Papadimitriou, P., 2016. Preliminary shear-wave splitting results in the broader Aigion area (Greece) during 2013, *Bull. Geol. Soc. Greece*, Proc. of the 14th International Congress, Thessaloniki, May, 2016, **XLVIII**.
195. Ketner, D. & Power, J., 2013. Characterization of seismic events during the 2009 eruption of Redoubt Volcano, Alaska, *J. Volcanol. Geotherm. Res.*, **259**, 45-62.
196. Kikuchi, M. & Kanamori, H., 1991. Inversion of complex body waves – III, *Bull. Seismol. Soc. Am.*, **81** (6), 2335-2350.
197. Kilb, D., Rubin, A.M., 2002. Implications of diverse fault orientations imaged in relocated aftershocks of the Mount Lewis, M_L 5.7, California, earthquake, *J. Geophys. Res.*, **107** (B11), 2294.
198. King, G.C.P., Ouyang, Z.X., Papadimitriou, P., Deschamps, A., Gagnepain, J., Houseman, G., Jackson, J.A., Soufleris, C. & Virieux, J., 1985. The evolution of the Gulf of Corinth (Greece): an aftershock study of the 1981 earthquakes, *Geophys. J. Int.*, **80**, 677–693, doi: 10.1111/j.1365-246X.1985.tb05118.x.
199. King, G., Sturdy, D. & Whitney, J., 1993. The landscape geometry and active tectonics of northwest Greece, *Geol. Soc. Am. Bull.*, **105**, 137–161.
200. Kiratzi, A.A. & Papazachos, B.C., 1984. Magnitude scales for earthquakes in Greece, *Bull. Seismol. Soc. Am.*, **74**, 969–985.
201. Kiratzi, A.A. & Papazachos, C.B., 1995. Active seismic deformation in the southern Aegean Benioff zone, *J. Geodynam.*, **19**, 65–78.
202. Kiratzi, A., Sokos, E., Ganas, A., Tselentis, A., Benetatos, C., Roumelioti, Z., Serpetsidaki, A., Andriopoulos, G., Galanis, O. & Petrou, P., 2008. The April 2007 earthquake swarm near Lake Trichonis and implications for active tectonics in western Greece, *Tectonophysics*, **452**, 51–65, doi: 10.1016/j.tecto.2008.02.009.
203. Kiratzi, A., 2013. The January 2012 earthquake sequence in the Cretan Basin, south of the Hellenic Volcanic Arc: Focal mechanisms, rupture directivity and slip models, *Tectonophysics*, **586**, 160-172.
204. Kissling, E., Ellsworth, W.L., Eberhart-Phillips, D. & Kradolfer, U., 1994. Initial reference models in local earthquake tomography, *J. Geophys. Res.*, **99**, 19635–19646, doi: 10.1029/93JB03138.
205. Kita, S., Okada, T., Hasegawa, A., Nakajima, J. & Matsuzawa, T., 2010. Anomalous deepening of a seismic belt in the upper-plane of the double seismic zone in the Pacific slab beneath the Hokkaido corner: Possible evidence for thermal shielding caused by subducted forearc crust materials, *Earth Planet. Sci. Lett.*, **290**, 415-426, doi: 10.1016/j.epsl.2009.12.038.
206. Klein, F.W., 2002. User's guide to HYPOINVERSE-2000: a Fortran program to solve for earthquake locations and magnitudes, *U.S. Geol. Surv. Prof. Pap.*, **rep. 02-17**, 1–123.
207. Kolaitis, A., 2011. *Tectonic and Volcanological study relating to the seismicity of Santorini*, PhD thesis, National and Kapodistrian University of Athens, Greece (in Greek).
208. Koukouvelas, I. K., Stamatopoulos, L., Katsonopoulou, D. & Pavlides, S., 2001. A palaeoseismological and geoarchaeological investigation of the Eliki fault, Gulf of Corinth, Greece, *Journal of Structural Geology*, **23** (2), 531-543.
209. Koukouvelas, I.K., Kokkalas, S. & Xypolias, P., 2009. Surface deformation during the Mw 6.4 (8 June 2008) Movri Mountain earthquake in the Peloponnese, and its implications for the seismotectonics of western Greece. *Int. Geol. Rev.*, **52**, 249–268, doi: 10.1080/00206810802674329.
210. Kortekaas, S., Papadopoulos, G.A., Ganas, A., Cundy, A.B. & Diakantoni, A., 2011. Geological identification of historical tsunamis in the Gulf of Corinth, Central Greece, *Nat. Hazards Earth Syst. Sci.*, **11**, 2029–2041, doi: 10.5194/nhess-11-2029-2011.
211. Kraft, T., Wassermann, J., Schmedes, E. & Igel, H., 2006. Meteorological triggering of earthquake swarms at Mt. Hochstaufen, SE-Germany, *Tectonophysics*, **424**, 245-258, doi: 10.1016/j.tecto.2006.03.044.

212. Křížová, D., Kiratzi, A. & J. Zahradník, 2010. The 26 June 2009 Santorini Island (Cyclades) earthquake swarm in the Hellenic Volcanic Arc: source characteristics using full moment tensor inversions, *32nd General Assembly of the ESC, Montpellier, France, Extended Abstracts*.

213. Küperkoch, L., Meier, T., Lee, J., Friederich, W. & Working Group, E., 2010. Automated determination of P -phase arrival times at regional and local distances using higher order statistics, *Geophys. J. Int.*, **181** (2), 1159-1170, doi: 10.1111/j.1365-246X.2010.04570.x.

214. Kurzon, I., Vernon, F.L., Rosenberger, A. & Ben-Zion, Y., 2014. Real-Time Automatic Detectors of P and S Waves Using Singular Value Decomposition, *Bull. Seismol. Soc. Am.*, **104**, 1696–1708, doi: 10.1785/0120130295.

215. Kwiatek, G., Plenkers, K., Nakatani, M., Yabe, Y. & Dresen, G., 2010. Frequency-Magnitude Characteristics Down to Magnitude -4.4 for Induced Seismicity Recorded at Mponeng Gold Mine, South Africa, *Bull. Seismol. Soc. Am.*, **100**, 1165–1173, doi: 10.1785/0120090277.

216. Lagios, E., Sakkas, V., Novali, F., Bellotti, F., Ferretti, A., Vlachou, K. & Dietrich, V., 2013. SqueeSAR™ and GPS ground deformation monitoring of Santorini Volcano (1992–2012): Tectonic implications, *Tectonophysics*, **594**, 38–59, doi: 10.1016/j.tecto.2013.03.012.

217. Lambotte, S., Lyon-Caen, H., Bernard, P., Deschamps, A., Patau, G., Nercessian, A., Pacchiani, F., Bourouis, S., Drilleau, M. & Adamova, P., 2014. Reassessment of the rifting process in the Western Corinth Rift from relocated seismicity. *Geophys. J. Int.*, **197**, 1822–1844, doi: 10.1093/gji/ggu096.

218. Langet, N., Maggi, A., Michelini, A. & Brenguier, F., 2014. Continuous Kurtosis-Based Migration for Seismic Event Detection and Location, with Application to Piton de la Fournaise Volcano, La Reunion, *Bull. Seismol. Soc. Am.*, **104**, 229–246, doi: 10.1785/0120130107.

219. Lasocki, S., 2014. Transformation to equivalent dimensions -- a new methodology to study earthquake clustering, *Geophys. J. Int.*, **197**, 1224–1235, doi: 10.1093/gji/ggu062.

220. Latorre, D., Virieux, J., Monfret, T., Monteiller, V., Vanorio, T., Got, J.-L. & Lyon-Caen, H., 2004. A new seismic tomography of Aigion area (Gulf of Corinth, Greece) from the 1991 data set, *Geophys. J. Int.*, **159**, 1013–1031, doi: 10.1111/j.1365-246X.2004.02412.x.

221. Lay, T. & Wallace, T.C., 1995. *Modern Global Seismology*, Academic Press, San Diego.

222. Leclère, H., Fabbri, O., Daniel, G. & Cappa, F., 2012. Reactivation of a strike-slip fault by fluid overpressuring in the southwestern French-Italian Alps, *Geophys. J. Int.*, **189**, 29-37, doi: 10.1111/j.1365-246X.2011.05345.x.

223. Lee, W.H.K. & Lahr, J.C., 1972. HYP071: A computer program for determining hypocenter, magnitude, and first motion pattern of local earthquakes, Open File Report, U. S. Geological Survey, 100 pp.

224. Legrand, D., Barrientos, S., Bataille, K., Cembrano, J. & Pavez, A., 2011. The fluid-driven tectonic swarm of Aysen Fjord, Chile (2007) associated with two earthquakes (Mw=6.1 and Mw=6.2) within the Liquine-Ofqui Fault Zone. *Cont. Shelf Res.*, **31**, 154-161, doi: 10.1016/j.csr.2010.05.008.

225. Le Meur, H., Virieux, J. & Podvin, P., 1997. Seismic tomography of the Gulf of Corinth: a comparison of methods, *Ann. di Geofis.*, **XL**, 1-24.

226. Leonard, M. & Kennett, B.L.N., 1999. Multi-component autoregressive techniques for the analysis of seismograms. *In*: *Physics of the Earth and Planetary Interiors*. 247–263.

227. Levenshtein, V.I., 1966. Binary codes capable of correcting deletions, insertions, and reversals, *Soviet-Physics Doklady*, **10** (8), 707-710.

228. Lin, G., Shearer, P.M. & Hauksson, E., 2007. Applying a three-dimensional velocity model, waveform cross correlation, and cluster analysis to locate southern California seismicity from 1981 to 2005, *J. Geophys. Res.*, **112**, B12309, doi: 10.1029/2007JB004986.

229. Lindenfeld, M., Rümpker, G., Link, K., Koehn, D. & Batte, A., 2012. Fluid-triggered earthquake swarms in the Rwenzori region, East African Rift - Evidence for rift initiation, *Tectonophysics*, **566-567**, 95–104, doi: 10.1016/j.tecto.2012.07.010.

230. Liu, Y., Chen, T., Xie, F., Du, F., Yang, D., Zhang, L. & Xu, L. , 2014. Analysis of fluid induced aftershocks following the 2008 Wenchuan Ms 8.0 earthquake. *Tectonophysics*, **619–620**, 149–158, doi: 10.1016/j.tecto.2013.09.010.

231. Llenos, A.L., McGuire, J.J. & Ogata, Y., 2009. Modeling seismic swarms triggered by aseismic transients, *Earth Planet. Sci. Lett.*, **281**, 59–69, doi: 10.1016/j.epsl.2009.02.011.

232. Lohman, R.B. & McGuire, J.J., 2007. Earthquake swarms driven by aseismic creep in the Salton Trough, California, *J. Geophys. Res. Solid Earth*, **112**, B04405, doi: 10.1029/2006JB004596.

233. Lomax, A., Satriano, C. & Vassallo, M., 2012. Automatic Picker Developments and Optimization: FilterPicker--a Robust, Broadband Picker for Real-Time Seismic Monitoring and Earthquake Early Warning, *Seismol. Res. Lett.*, **83**, 531–540, doi: 10.1785/gssrl.83.3.531.

234. Lowrie, W., 2007. *Fundamentals of geophysics (2nd edition)*. Cambridge University Press.

235. Lyon-Caen, H., Armijo, R., Drakopoulos, J., Baskoutas, J., Delibassis, N., Gaulon, R., Kouskouna, V., Latoussakis, J., Makropoulos, K., Papadimitriou, P., Papanastassiou, D. & Pedotti, G., 1988. The 1986 Kalamata (South Peloponnesus) Earthquake: Detailed study of a normal fault, evidences for east-west extension in the Hellenic Arc, *J. Geophys. Res.*, **93**(B12), 14967–15000.

236. Lyon-Caen, H., Papadimitriou, P., Deschamps, A., Bernard, P., Makropoulos, K., Pacchiani F. & Patau, G., 2004. First results of the CRLN seismic network in the Western Corinth Rift : Evidence for old-fault reactivation. *C. R. Geoscience*, **336**, 343-351.

237. Ma, X.J. & Wu, Z.L., 2013. 'Negative repeating doublets' in an aftershock sequence, *Earth, Planets Sp.*, **65**, 923–927, doi: 10.5047/eps.2013.01.006.

238. Madariaga, R., 1976. Dynamics of an expanding circular fault, *Bull. Seismol. Soc. Am.*, **66**, 639–666.

239. Maeda, N., 1985. A method for reading and checking phase times in autoprocessing system of seismic wave data, Zisin. *J. Seismol. Soc. Jpn.*, **38,** 365–379.

240. Makropoulos, K.C. & Burton, P.W., 1981. A catalogue of seismicity in Greece and adjacent areas, *Geophys. J. R. Astron. Soc.*, **65**, 741-762.

241. Makropoulos, K., Diagourtas, D., Kassaras, J., Kouskouna, V., Papadimitriou P. & Ziazia, M., 1996. The November-December 1994 Lefkas (W. Greece) earthquake sequence: results from in situ seismological survey, *Book of abstracts*, p. 108, XXV General Assembly of ESC, Reykavik, Iceland.

242. Makropoulos, K., Kaviris, G. & Kouskouna, V., 2012. An updated and extended earthquake catalogue for Greece and adjacent areas since 1900. *Nat. Hazards Earth Syst. Sci.*, **12**, 1425–1430, doi: 10.5194/nhess-12-1425-2012.

243. Massa, M., 2010. Selection of empirical green's functions by waveform similarity analysis: An approach to predict ground motion in areas with saturated records, *Bull. Seismol. Soc. Am.*, **100**, 1513-1527, doi: 10.1785/0120090296.

244. Massin, F., Farrell, J. & Smith, R.B., 2013. Repeating earthquakes in the Yellowstone volcanic field: Implications for rupture dynamics, ground deformation, and migration in earthquake swarms, *J. Volcanol. Geotherm. Res.*, **257**, 159-173, doi: 10.1016/j.jvolgeores.2013.03.022.

245. Martinez, W.L., Martinez, A.R. & Solka, J.L., 2010. *Exploratory Data Analysis with MATLAB, 2nd edition*, CRC Press, Boca Raton.

246. Matrullo, E., Satriano, C., Lyon-Caen, H., Bernard, P., Deschamps, A., Papadimitriou, P., Sokos, E. & Plicka, V., 2013. Scaling relationship for source parameters of the seismicity of the Corinth Rift (Greece). In *EGU General Assembly Conference Abstracts*, **15**, p. 7827.

247. McClusky, S., Balassanian, S., Barka, A., Demir, C., Ergintav, S., Georgiev, I., Gurkan, O., Hamburger, M., Hurst, K., Kahle, H., Kastens, K., Kekelidze, G., King, R., Kotzev, V., Lenk, O., Mahmoud, S., Mishin, A., Nadariya, M., Ouzounis, A., Paradissis, D., Peter, Y., Prilepin, M., Reilinger, R., Sanli, I., Seeger, H., Tealeb, A., Toksöz, M. N. & Veis, G., 2000. Global Positioning System constraints on plate kinematics and dynamics in the eastern Mediterranean and Caucasus, *J. Geophys. Res.*, **105**(B3), 5695–5719, doi:10.1029/1999JB900351.

248. Menke, W., 1999. Using waveform similarity to constrain earthquake locations, *Bull. Seismol. Soc. Am.*, **89**, 1143–1146.

249. Mesimeri, M., Karakostas, V., Papadimitriou, E., Schaff, D. & Tsaklidis, G., 2016. Spatio-temporal properties and evolution of the 2013 Aigion earthquake swarm (Corinth Gulf, Greece), *J. Seismol.*, **20**, 595–614, doi: 10.1007/s10950-015-9546-4.

250. Micarelli, L., Moretti, I., Jaubert, M. & Moulouel, H., 2006. Fracture analysis in the south-western Corinth rift (Greece) and implications on fault hydraulic behavior, *Tectonophysics*, **426**, 31–59, doi: 10.1016/j.tecto.2006.02.022.

251. Michael, A.J., 1984. Determination of stress from slip data: Faults and folds, *J. Geophys. Res. Solid Earth*, **89**, 11517–11526, doi: 10.1029/JB089iB13p11517.

252. Michelini, A. & Lomax, A., 2004. The effect of velocity structure errors on double-difference earthquake location, *Geophys. Res. Lett.*, **31**, L09602, doi:10.1029/2004GL019682.

253. Milligan, G. W. & Cooper, M. C., 1985. An examination of procedures for determining the number of clusters in a data set, *Psychometrika*, **50**, 159-179.

254. Mogi, K., 1963. Some discussions on aftershocks, foreshocks, and earthquake swarms: The fracture of a semi-infinite body caused by an inner stress origin and its relation to the earthquake phenomenon, *Bull. Earthquake Res. Inst. Univ. Tokyo*, **41**, 615-658.

255. Mojena, R., 1977. Hierarchical grouping methods and stopping rules: An evaluation, *Computer Journal*, **20**, 359-363.

256. Montalbetti, J.F. & Kanasewich, E.R., 1970. Enhancement of Teleseismic Body Phases with a Polarization Filter, *Geophys. J. Int.*, **21**, 119–129, doi: 10.1111/j.1365-246X.1970.tb01771.x.

257. Moretti, I., Sakellariou, D., Lykousis, V. & Micarelli, L., 2003. The gulf of corinth: an active half graben?, *J. Geodyn.*, **36**, 323-340.

258. Morley, C.K., Nelson, R.A., Patton, T.L. & Munn, S.G., 1990. Transfer zones in the East African rift system and their relevance to hydrocarbon exploration in rifts, *Am. Assoc. Pet. Geol. Bull.*, **74**, 1234–1253, doi: 10.1306/0C9B2475-1710-11D7-8645000102C1865D.

259. Myhill, R., McKenzie, D. & Priestley, K., 2011. The distribution of earthquake multiplets beneath the southwest Pacific, *Earth Planet. Sci. Lett.*, **301**, 87-97, doi: 10.1016/j.epsl.2010.10.023.

260. Nadeau, R.M., Foxall, W. & McEvilly, T. V., 1995. Clustering and Periodic Recurrence of Microearthquakes on the San Andreas Fault at Parkfield, California, *Science*, **267**, 503–507, doi: 10.1126/science.267.5197.503.

261. Nakahara, H., 2004. Correlation distance of waveforms for closely located events - I. Implication of the heterogeneous structure around the source region of the 1995 Hyogo-Ken Nanbu, Japan, earthquake (Mw = 6.9), *Geophys. J. Int.*, **157**, 1255–1268, doi: 10.1111/j.1365-246X.2004.02278.x.

262. Nakamula, S., Takeo, M., Okabe, Y. & Matsuura, M., 2007. Automatic seismic wave arrival detection and picking with stationary analysis: Application of the KM2O-Langevin equations, *Earth, Planets Sp.*, **59**, 567–577, doi: 10.1186/BF03352719.

263. Nishimura, T., Uchida, N., Sato, H., Ohtake, M., Tanaka, S. & Hamaguchi, H., 2000. Temporal changes of the crustal structure associated with the M6.1 earthquake on September 3, 1998, and the volcanic activity of Mount Iwate, Japan, *Geophys. Res. Lett.*, **27**, 269–272.

264. Nixon, C.W., McNeill, L.C., Bull, J.M., Bell, R.E., Gawthorpe, R.L., Henstock, T.J., Christodoulou, D., Ford, M., Taylor, B., Sakellariou, D., Ferentinos, G., Papatheodorou, G., Leeder, M.R., Collier, R.E.L., Goodliffe, A.M., Sachpazi, M. & Kranis, H., 2016. Rapid spatiotemporal variations in rift structure during development of the Corinth Rift, central Greece. *Tectonics*, **35**, 1225–1248, doi: 10.1002/2015TC004026.

265. Ogata, Y., 1983. Estimation of the parameters in the modified omori formula for aftershock frequencies by the maximum likelihood procedure, *J. Phys. Earth*, **31**, 115–124, doi: 10.4294/jpe1952.31.115.

266. Ogata, Y., 1988. Statistical Models for Earthquake Occurrences and Residual Analysis for Point Processes, *J. Am. Stat. Assoc.*, **83**, 9-27, doi: 10.2307/2288914.

267. Ogata, Y., 1989. Statistical model for standard seismicity and detection of anomalies by residual analysis, *Tectonophysics*, **169**, 159–174, doi: 10.1016/0040-1951(89)90191-1.

268. Ogata, Y., 1992. Detection of precursory relative quiescence before great earthquakes through a statistical model, *J. Geophys. Res.*, **97** (B13), 19845-19871, doi: 10.1029/92JB00708.

269. Ogata, Y., 2001. Increased probability of large earthquakes near aftershock regions with relative quiescence. *J. Geophys. Res. Solid Earth*, **106**, 8729–8744, doi: 10.1029/2000JB900400.

270. Ogata, Y., 2004. Space-time model for regional seismicity and detection of crustal stress changes, *J. Geophys. Res.*, **109**, B03308, doi: 10.1029/2003JB002621.

271. Ogata, Y., 2006. Statistical analysis of seismicity—updated version (SASeis2006) Ver. 2. Computer science monographs no. 33., The Institute of Statistical Mathematics, Tokyo. http://www.ism.ac.jp/~ogata/Ssg/ssg_softwares.html

272. Ogata, Y. & Tsuruoka, H., 2016. Statistical monitoring of aftershock sequences: a case study of the 2015 Mw7.8 Gorkha, Nepal, earthquake, *Earth, Planets Sp.*, **68**, 44, doi: 10.1186/s40623-016-0410-8.

273. Okal, E.A., Synolakis, C.E., Uslu, B., Kalligeris, N. & Voukouvalas, E., 2009. The 1956 earthquake and tsunami in Amorgos, Greece, *Geophys. J. Int.*, **178**, 1533–1554.

274. Okubo, P.G. & Wolfe, C.J., 2008. Swarms of similar long-period earthquakes in the mantle beneath Mauna Loa Volcano, *J. Volcanol. Geotherm. Res.*, **178**, 787–794, doi: 10.1016/j.jvolgeores.2008.09.007.

275. Olivieri, M. & Clinton, J., 2012. An almost fair comparison between Earthworm and SeisComp3, *Seismol. Res. Lett.*, **83**, 720–727, doi: 10.1785/0220110111.

276. Omori, F., 1894. On the aftershocks of earthquakes, *J. Coll. Sci. Imp. Univ. Tokyo*, **7**, 111-200.

277. Pacchiani, F., 2006. *Etude sismologique des failles normales actives du Rift de Corinthe*, PhD thesis, 373 pp., Univ. Paris XI, Paris.

278. Pacchiani, F. & Lyon-Caen, H., 2010. Geometry and spatio-temporal evolution of the 2001 Agios Ioanis earthquake swarm (Corinth rift, greece), *Geophys. J. Int.*, **180**, 59-72.

279. Palyvos, N., Pantosti, D., De Martini, P.M., Lemeille, F., Sorel, D. & Pavlopoulos, K., 2005. The Aigion-Neos Erineos coastal normal fault system (western Corinth Gulf Rift, Greece): Geomorphological signature, recent earthquake history, and evolution. *J. Geophys. Res. B Solid Earth*, **110**, B09302, doi: 10.1029/2004JB003165.

280. Pandolfi, D., Bean, C.J. & Saccorotti, G., 2006. Coda wave interferometric detection of seismic velocity changes associated with the 1999 M = 3.6 event at Mt. Vesuvius, *Geophys. Res. Lett.*, **33**, L06306, doi: 10.1029/2005GL025355.

281. Pantosti, D., Martini, P. M. D., Koukouvelas, I., Stamatopoulos, L., Palyvos, N., Pucci, S., Lemeille, F. & Pavlides, S., 2004. Paleoseismological investigations of the Aigion fault (gulf of Corinth, greece), *C. R. Geoscience*, **336**, 335-342.

282. Papadimitriou, P., Kaviris, G. & Makropoulos, K., 2006. The M_w = 6.3 2003 Lefkada Earthquake (Greece) and induced stress transfer changes, *Tectonophysics*, **423**, 73–82.

283. Papadimitriou, P., Agalos, A., Moshou, A., Kapetanidis, V., Kaviris, G., Voulgaris, N. & Makropoulos, K., 2008. Large earthquakes in the broader area of Peloponnesus (Southern Greece) in 2008, *31st General Assembly of the ESC 2008, oral session SIGNIF, Oral & Poster Abstracts*, pg. **322-323**.

284. Papadimitriou, P., Agalos, A., Moshou, A., Kapetanidis, V., Karakonstantis, A., Kaviris, G., Kassaras, I., Voulgaris, N. & Makropoulos, K., 2010a. An important number of recent significant earthquakes in Greece. 32nd General Assembly of the ESC 2010, Oral & Poster Abstracts, pg. **225**.

285. Papadimitriou, P., Kaviris, G., Karakonstantis A. & Makropoulos, K., 2010b. The Cornet seismological network: 10 years of operation, recorded seismicity and significant applications, *Hellenic Journal of Geosciences*, **45**, 193-208.

286. Papadimitriou, P., Voulgaris, N., Kouskouna, V., Kassaras, I., Kaviris, G., Pavlou, K., Karakonstantis, A., Bozionelos, G. & Kapetanidis, V., 2014. The Kefallinia Island earthquake sequence January-February 2014, *Book of Abstracts: Second European Conference on Earthquake Engineering and Seismology (2ECEES)*, 24-29 August, 2014, Istanbul, Turkey.

287. Papadimitriou, P., Kapetanidis, V., Karakonstantis, A., Kaviris, G., Voulgaris, N. & Makropoulos, K., 2015. The Santorini Volcanic Complex: A detailed multi-parameter seismological approach with emphasis on the 2011–2012 unrest period, *J. Geodyn.*, **85**, 32-57.

288. Papadimitriou, P., Karakonstantis, A., Kapetanidis, V., Bozionelos, G., Kaviris, G. & Voulgaris, N., 2016a. The 2015 Lefkada earthquake sequence (W. Greece). *Proceedings of 35th General Assembly of the European Seismological Commission (ESC2016)*.

289. Papadimitriou, P., Karakonstantis, A., Bozionelos, G., Kapetanidis, V., Kaviris, G., Spingos, I., Millas, Ch., Kassaras, I. & Voulgaris, N., 2016b. Preliminary report on the Lefkada 17 November 2015 Mw=6.4 earthquake, report released to EMSC-CSEM.

290. Papadopoulos, G.A. & Pavlides, S.B., 1992. The large 1956 earthquake in the SouthAegean: macroseismic field configuration, faulting, and neotectonics of Amorgos Island, *Earth Planet. Sci. Lett.*, **113** (3), 383–396.

291. Papadopoulos, G.A., Karastathis, V., Ganas, A., Charalambakis, M. & Fokaefs, A., 2009. A storm of strong earthquakes in Greece during 2008, *EOS Trans. Am. Geophys. Union*, **90** (46), 425–426.

292. Papadopoulos, G.A., Karastathis, V., Kontoes, C., Charalampakis, M., Fokaefs, A. & Papoutsis, I., 2010. Crustal deformation associated with east Mediterranean strike-slip earthquakes: The 8 June 2008 Movri (NW Peloponnese), Greece, earthquake (Mw6.4), *Tectonophysics*, **492**, 201–212, doi: 10.1016/j.tecto.2010.06.012.

293. Papadopoulos, G.A., Karastathis, V.K., Koukouvelas, I., Sachpazi, M., Baskoutas, I., Chouliaras, G., Agalos, A., Daskalaki, E., Minadakis, G., Moshou, A., Mouzakiotis, A., Orfanogiannaki, K., Papageorgiou, A., Spanos, D. & Triantafyllou, I., 2014. The Cephalonia, Ionian Sea (Greece), sequence of strong earthquakes of January-February 2014: a first report, *Res. Geophys.*, **4** (1)**,** 19-30, doi: 10.4081/rg.2014.5441.

294. Papazachos, B. & Papazachou, C., 2003. *Earthquakes of Greece*, 3rd edition, Ziti Publications, Thessaloniki, 286 pp.

295. Parcharidis, I., Kokkalas, S., Fountoulis, I. & Foumelis, M., 2009. Detection and monitoring of active faults in urban environments: Time series interferometry on the cities of Patras and Pyrgos (Peloponnese, Greece), *Remote Sens.*, **1**, 676–696, doi: 10.3390/rs1040676.

296. Parotidis, M., Shapiro, S.A. & Rothert, E., 2004. Back front of seismicity induced after termination of borehole fluid injection, *Geophys. Res. Lett.*, **31** (2), L02612, doi: 10.1029/2003GL018987.

297. Parotidis, M., Shapiro, S.A. & Rothert, E., 2005. Determination of criticality and diffusivity heterogeneities based on seismic data analysis - Case study of Vogtland, NW-Bohemia, *Int. J. Rock Mech. Min. Sci.*, **42**, 1088-1093, doi: 10.1016/j.ijrmms.2005.05.010.

298. Peng, Z., Cao, C., Huang, J. & Liu, Q., 2014. Seismic signal recognition using improved BP neural network and combined feature extraction method, *J. Cent. South Univ.*, **21**, 1898–1906, doi: 10.1007/s11771-014-2136-8.

299. Petersen, T., 2007. Swarms of repeating long-period earthquakes at Shishaldin Volcano, Alaska, 2001–2004, *Journal of Volcanology and Geothermal Research*, **166**, 177-192.

300. Pham, V.N., Bernard, P., Boyer, D., Chouliaras, G., Le Mouel, J.L. & Stavrakakis, G.N., 2000. Electrical conductivity and crustal structure beneath the central Hellenides around the Gulf of Corinth (Greece) and their relationship with the seismotectonics, *Geophys. J. Int.*, **142**, 948–969, doi: 10.1046/j.1365-246x.2000.00226.x.

301. Pirli, M., Voulgaris, N., Alexopoulos, J. & Makropoulos, K., 2004. Installation and preliminary results from a small aperture seismic array in Tripoli, Greece, *Bull. Geol. Soc. Greece*, vol. **XXXVI**, 2004, pg. 1499-1508.

302. Pirli, M., Voulgaris, N., Chira, A. & Makropoulos, K., 2007. The March 2004 Kalamata seismic sequence: a case of efficient seismicity monitoring in the area of Peloponnese, southern Greece, by the Tripoli Seismic Array, *J. Seismol.*, **11**, 59–72, doi: 10.1007/s10950-006-9037-8.

303. Pirli, M., Schweitzer, J., Ottemoller, L., Raeesi, M., Mjelde, R., Atakan, K., Guterch, A., Gibbons, S.J., Paulsen, B., Debski, W., Wiejacz, P. & Kvaerna, T., 2010. Preliminary Analysis of the 21 February 2008 Svalbard (Norway) Seismic Sequence, *Seismol. Res. Lett.*, **81**, 63–75, doi: 10.1785/gssrl.81.1.63.

304. Pirli, M., Schweitzer, J. & Paulsen, B., 2013. The Storfjorden, Svalbard, 2008-2012 aftershock sequence: Seismotectonics in a polar environment, *Tectonophysics*, **601**, 192-205.

305. Plenkers, K., Schorlemmer, D. & Kwiatek, G., 2011. On the Probability of Detecting Picoseismicity, *Bull. Seismol. Soc. Am.*, **101**, 2579–2591, doi: 10.1785/0120110017.

306. Plesinger, A., Hellweg, M. & Seidel, D., 1986. Interactive high resolution polarization analysis of broadband seismograms, *J. Geophys.*, **59**, 129–139.

307. Poupinet, G., Ellsworth, W.L. & Frechet, J., 1984. Monitoring velocity variations in the crust using earthquake doublets: An application to the Calaveras Fault, California, *J. Geophys. Res.*, **89**, 5719–5731.

308. Pujol, J., 1995. Application of the JHD technique to the Loma Prieta, California, mainshock-aftershock sequence and implications for earthquake location, *Bull. Seismol. Soc. Am.*, **85**, 129–150.

309. Richter, C.F., 1935. An instrumental earthquake magnitude scale, *Bull. Seismol. Soc. Am.*, **25**, 1–32.

310. Riel, B., Milillo, P., Simons, M., Lundgren, P., Kanamori, H. & Samsonov, S., 2015. The collapse of Bartharbunga caldera, Iceland, *Geophys. J. Int.*, **202**, 446–453, doi: 10.1093/gji/ggv157.

311. Rietbrock, A., Tiberi, C., Scherbaum, F. & Lyon-Caen, H., 1996. Seismic slip on a low angle normal fault in the Gulf of Corinth: Evidence from high-resolution cluster analysis of microearthquakes, *Geophys. Res. Lett.*, **23** (14), 1817-1820.

312. Rigo, A., Lyon-Caen, H., Armijo, R., Deschamps, A., Hatzfeld, D., Makropoulos, K., Papadimitriou, P. & Kassaras, I., 1996. A microseismic study in the western part of the Gulf of Corinth (Greece): implications for large-scale normal faulting mechanisms, *Geophys. J. Int.*, **126**, p. 663-688, 1996.

313. Rodgers, M., Roman, D. C., Geirsson, H., LaFemina, P., Muñoz, A., Guzman, C. & Tenorio, V., 2013. Seismicity accompanying the 1999 eruptive episode at Telica Volcano, Nicaragua, *J. Volcanol. Geotherm. Res.*, **265**, 39–51.

314. Roland, E. & McGuire, J.J., 2009. Earthquake swarms on transform faults, *Geophys. J. Int.*, **178**, 1677-1690, doi: 10.1111/j.1365-246X.2009.04214.x.

315. Roumelioti, Z., Benetatos, C., Kiratzi, A., Stavrakakis, G. & Melis, N., 2004. A study of the 2 December 2002 (M5.5) Vartholomio (western Peloponnese, Greece) earthquake and of its largest aftershocks, *Tectonophysics*, **387**, 65–79, doi: 10.1016/j.tecto.2004.06.008.

316. Roumelioti, Z., Benetatos, C. & Kiratzi, A., 2009. The 14 February 2008 earthquake (M6.7) sequence offshore south Peloponnese (Greece): Source models of the three strongest events, *Tectonophysics*, **471**, 272–284, doi: 10.1016/j.tecto.2009.02.028.

317. Rowe, C.A., Aster, R.C., Borchers, B. & Young, C.J., 2002. An automatic, adaptive algorithm for refining phase picks in large seismic data sets, *Bull. Seismol. Soc. Am.*, **92**, 1660–1674, doi: 10.1785/0120010224.

318. Rowe, C.A., Thurber, C.H. & White, R.A., 2004. Dome growth behavior at Soufriere Hills Volcano, Montserrat, revealed by relocation of volcanic event swarms, 1995-1996. *J. Volcanol. Geotherm. Res.*, **134**, 199–221.

319. Rubinstein, J. L. & Ellsworth, W. L., 2010. Precise estimation of repeating earthquake moment: Example from Parkfield, California, *Bull. seism. Soc. Am.*, **100**(5A), 1952-1961.

320. Ruud, B. O. & Husebye, E. S., 1992. A new three-component detector and automatic single station bulletin production, *Bull. seism. Soc. Am.*, **82**, 221–237.

321. Sabbione, J. I. & Velis, D. R., 2013. A robust method for microseismic event detection based on automatic phase pickers, *Journal of Applied Geophysics*, **99**, 42–50.

322. Sachpazi, M., Galvé, A., Laigle, M., Hirn, A., Sokos, E., Serpetsidaki, A., Marthelot, J.-M., Pi Alperin, J.M., Zelt, B. & Taylor, B., 2007. Moho topography under central Greece and its compensation by Pn time-terms for the accurate location of hypocenters: The example of the Gulf of Corinth 1995 Aigion earthquake, *Tectonophysics*, **440**, 53–65, doi: 10.1016/j.tecto.2007.01.009.

323. Sakellariou, D., Lykousis, V., Moretti, I. & Kaberi, H., 2003. Late quaternary evolution of the cental Gulf of Corinth basin, abstract, CRL workshop, Aigion. June 2.

324. Sakellariou, D., Sigurdsson, H., Alexandri, M., Carey, S., Rousakis, G., Nomikou, P., Georgiou, P. & Ballas, D., 2010. Active tectonics in the Hellenic volcanic arc: the Kolumbo submarine volcanic zone, *Bull. Geol. Soc. Greece*, **XLIII** (2), 1056–1063.

325. Sakkas, V. & Lagios, E., 2015. Fault modelling of the early-2014 ~M6 Earthquakes in Cephalonia Island (W. Greece) based on GPS measurements, *Tectonophysics*, **644**–**645**, 184–196.

326. Saragiotis, C.D., Hadjileontiadis, L.J. & Panas, S.M., 2002. PAI-S/K: A robust automatic seismic P phase arrival identification scheme, *IEEE Trans. Geosci. Remote Sens.*, **40**, 1395–1404, doi: 10.1109/TGRS.2002.800438.

327. Satriano, C., Elia, L., Martino, C., Lancieri, M., Zollo, A. & Iannaccone, G., 2011. PRESTo, the earthquake early warning system for Southern Italy: Concepts, capabilities and future perspectives, *Soil Dyn. Earthq. Eng.*, **31**, 137–153, doi: 10.1016/j.soildyn.2010.06.008.

328. Scarfì, L., Langer, H. & Gresta, S., 2003. High-precision relative locations of two microearthquake clusters in Southeastern Sicily, Italy, *Bull. Seismol. Soc. Am.*, **93**, 1479-1497, doi: 10.1785/0120020146.

329. Schaff, D.P., Beroza, G.C. & Shaw, B.E., 1998. Postseismic response of repeating aftershocks, *Geophys. Res. Lett.*, **25**, 4549-4552.

330. Schaff, D.P., Bokelmann, G.H.R., Ellsworth, W.L., Zanzerkia, E., Waldhauser, F. & Beroza, G.C., 2004. Optimizing correlation techniques for improved earthquake location, *Bull. Seismol. Soc. Am.*, **94**, 705–721.

331. Schaff, D.P. & Waldhauser, F., 2005. Waveform cross-correlation-based differential travel-time measurements at the northern California seismic network, *Bull. Seismol. Soc. Am.*, **95**, 2446–2461.

332. Schaff, D.P., 2008. Semiempirical statistics of correlation-detector performance, *Bull. Seismol. Soc. Am.*, **98**, 1495–1507, doi: 10.1785/0120060263.

333. Schaff, D.P. & Waldhauser, F., 2010. One magnitude unit reduction in detection threshold by cross correlation applied to parkfield (California) and China seismicity, *Bull. Seismol. Soc. Am.*, **100**, 3224–3238.

334. Schaff, D., 2010. Improvements to detection capability by cross-correlating for similar events: A case study of the 1999 Xiuyan, China, sequence and synthetic sensitivity tests, *Geophys. J. Int.*, **180**, 829–846, doi: 10.1111/j.1365-246X.2009.04446.x.

335. Schaff, D.P. & Richards, P.G., 2011. On finding and using repeating seismic events in and near China, *J. Geophys. Res.*, **116**, B03309, doi: 10.1029/2010JB007895.

336. Schaff, D.P. & Richards, P.G., 2014. Improvements in magnitude precision, using the statistics of relative amplitudes measured by cross correlation, *Geophys. J. Int.*, **197**, 335–350, doi: 10.1093/gji/ggt433.

337. Scherbaum, F., 1996. *Of Poles and Zeros: Fundamentals in Digital Seismology*, Volume 15 of Modern Approaches in Geophysics, G. Nolet, Managing Editor, Kluwer Academic Press, Dordrecht, xi + 257 pp., 1996.

338. Schimmel, M. & Paulssen, H., 1997. Noise reduction and detection of weak, coherent signals through phase-weighted stacks, *Geophys. J. Int.*, **130**, 497–505, doi: 10.1111/j.1365-246X.1997.tb05664.x.

339. Schimmel, M., 1999. Phase cross-correlations: Design, comparisons, and applications, *Bull. Seismol. Soc. Am.*, **89**, 1366–1378.

340. Schimmel, M., Stutzmann, E. & Gallart, J., 2011. Using instantaneous phase coherence for signal extraction from ambient noise data at a local to a global scale, *Geophys. J. Int.*, **184**, 494–506, doi: 10.1111/j.1365-246X.2010.04861.x.

341. Schoenball, M., Muller, T. M., Muller, B. I. R. and Heidbach, O., 2010. Fluid-induced microseismicity in pre-stressed rock masses, *Geophys. J. Int.*, **180**, 813–819, doi: 10.1111/j.1365-246X.2009.04443.x

342. Scholz, C.H., 2002. *The Mechanics of Earthquakes and Faulting*, Cambridge Press.

343. Schorlemmer, D., Wiemer, S. & Wyss, M., 2005. Variations in earthquake-size distribution across different stress regimes, *Nature*, **437**, 539–542, doi: 10.1038/nature04094.

344. Seggern, D., 2009. Direct Empirical Estimation of Arrival-Time Picking Error from Waveform Cross-Correlations, *Bull. Seismol. Soc. Am.*, **99** (5), 2749-2758, doi: 10.1785/0120080304.

345. Segou, M., Ellsworth, W.L. & Parsons, T., 2014. Stress Transfer by the 2008 Mw 6.4 Achaia Earthquake to the Western Corinth Gulf and Its Relation with the 2010 Efpalio Sequence, Central Greece. *Bull. Seismol. Soc. Am.*, **104**, 1723–1734, doi: 10.1785/0120130142.

346. Seno, T., 2003. Fractal asperities, invasion of barriers, and interplate earthquakes, *Earth, Planets Sp.*, **55**, 649–665, doi: 10.1186/BF03352472.

347. Serpetsidaki, A., Sokos, E. & Tselentis, G.A., 2010. Study of the 2nd December 2002 Vartholomio earthquake (Western Peloponnese) M5.5 aftershock sequence, Bull. geol. Soc. Gr., XLIII (4), 2174–2182.

348. Serpetsidaki, A., Elias, P., Ilieva, M., Bernard, P., Briole, P., Deschamps, A., Lambotte, S., Lyon-Caen, H., Sokos, E. & Tselentis, G.A., 2014. New constraints from seismology and geodesy on the Mw = 6.4 2008 Movri (Greece) earthquake: Evidence for a growing strike-slip fault system, *Geophys. J. Int.*, **198**, 1373–1386, doi: 10.1093/gji/ggu212.

349. Shapiro, S.A., Huenges, E. & G. Borm, 1997. Estimating the crust permeability from fluid-injection-induced seismic emission at the KTB site. *Geophys. J. Int.*, **131**, 15-18.

350. Shapiro, S. a., Patzig, R., Rothert, E. & Rindschwentner, J., 2003. Triggering of Seismicity by Pore-pressure Perturbations: Permeability-related Signatures of the Phenomenon, *Pure Appl. Geophys.*, **160**, 1051–1066, doi: 10.1007/PL00012560.

351. Shapiro, S.A. & Dinske, C., 2009. Fluid-induced seismicity: Pressure diffusion and hydraulic fracturing, *Geophys. Prospect.*, **57**, 301–310, doi: 10.1111/j.1365-2478.2008.00770.x.

352. Shcherbakov, R. & Turcotte, D.L., 2004. A modified form of Båth's law, *Bull. Seismol. Soc. Am.*, **94**, 1968–1975, doi: 10.1785/012003162.

353. Shearer, P.M., 1998. Evidence from a cluster of small earthquakes for a fault at 18 km depth beneath Oak Ridge, southern California, *Bull. Seismol. Soc. Am.*, **88**, 1327–1336.

354. Shearer, P.M., Hardebeck, J.L., Astiz, L. & Richards-Dinger, K.B., 2003. Analysis of similar event clusters in aftershocks of the 1994 Northridge, California, earthquake, *J. Geophys. Res. Solid Earth*, **108** (B1), 2035, doi: 10.1029/2001JB000685.

355. Shelly, D.R., 2010. Periodic, Chaotic, and Doubled Earthquake Recurrence Intervals on the Deep San Andreas Fault, *Science.*, **328**, 1385–1388, doi: 10.1126/science.1189741.

356. Shuler, A., Nettles, M. & Ekström, G., 2013. Global observation of vertical-CLVD earthquakes at active volcanoes, *J. Geophys. Res. Solid Earth*, **118**, 138–164, doi: 10.1029/2012JB009721.

357. Shuster, M. D., 1993. A Survey of Attitude Representations, *Journal of the Astronautical Sciences*, **41** (4), 439-517.

358. Sigmundsson, F., Hooper, A., Hreinsdóttir, S., Vogfjörd, K.S., Ófeigsson, B.G., Heimisson, E.R., Dumont, S., Parks, M., Spaans, K., Gudmundsson, G.B., Drouin, V., Árnadóttir, T., Jónsdóttir, K., Gudmundsson, M.T., Högnadóttir, T., Fridriksdóttir, H.M., Hensch, M., Einarsson, P., Magnússon, E., Samsonov, S., Brandsdóttir, B., White, R.S., Ágústsdóttir, T., Greenfield, T., Green, R.G., Hjartardóttir, Á.R., Pedersen, R., Bennett, R. a., Geirsson, H., La Femina, P.C., Björnsson, H., Pálsson, F., Sturkell, E., Bean, C.J., Möllhoff, M., Braiden, A.K. & Eibl, E.P.S., 2014. Segmented lateral dyke growth in a rifting event at Bárðarbunga volcanic system, Iceland, *Nature*, **517**, 191-195, doi: 10.1038/nature14111.

359. Skoumal, R.J., Brudzinski, M.R. & Currie, B.S., 2015. Earthquakes Induced by Hydraulic Fracturing in Poland Township, Ohio, *Bull. Seismol. Soc. Am.*, **105**, 189–197, doi: 10.1785/0120140168.

360. Sleeman, R. & van Eck, T., 1999. Robust automatic P-phase picking: an on-line implementation in the analysis of broadband seismogram recordings, *Phys. Earth Planet. Interiors*, **113**, 265–275.

361. Slinkard, M., Schaff, D., Mikhailova, N., Heck, S., Young, C. & Richards, P.G., 2014. Multistation Validation of Waveform Correlation Techniques as Applied to Broad Regional Monitoring, *Bull. Seismol. Soc. Am.*, **104**, 2768–2781, doi: 10.1785/0120140140.

362. Smith, K.D., von Seggern, D., Blewitt, G., Preston, L., Anderson, J.G., Wernicke, B.P. & Davis, J.L., 2004. Evidence for deep magma injection beneath Lake Tahoe, Nevada-California, *Science*, **305**, 1277-1280, doi: 10.1126/science.1101304.

363. Sokos, E., Zahradník, J., Kiratzi, A., Janský, J., Gallovič, F., Novotny, O., Kostelecký, J., Serpetsidaki, A. & Tselentis, G.-A., 2012. The January 2010 Efpalio earthquake sequence in the western Corinth Gulf (Greece), *Tectonophysics*, **530**–**531**, 299–309, doi: 10.1016/j.tecto.2012.01.005.

364. Sorel, D., 2000. A Pleistocene and still-active detachment fault and the origin of the Corinth-Patras rift, Greece, *Geology*, **28**, 83-86, doi: 10.1130/0091-7613(2000)28<83:APASDF>2.0.CO;2.

365. Spudich, P. & Bostwick, T., 1987. Studies of the seismic coda using an earthquake cluster as a deeply buried seismograph array, *J. Geophys. Res. Solid Earth*, **92**, 10526–10546, doi: 10.1029/JB092iB10p10526.

366. Statz-Boyer, P., Thurber, C., Pesicek, J. & Prejean, S., 2009. High precision relocation of earthquakes at Iliamna Volcano, Alaska, *J. Volcanol. Geotherm. Res.*, **184**, 323–332.

367. Stefatos, A., Papatheodorou, G., Ferentinos, G., Leeder, M. & Collier, R., 2002. Seismic reflection imaging of active offshore faults in the Gulf of Corinth: their seismotectonic significance, *Basin Res.*, **14**, 487–502, doi: 10.1046/j.1365-2117.2002.00176.x.

368. Stein, S. & Wysession, M., 2003. *An Introduction to Seismology, Earthquakes and Earth Structure*, Blackwell, Malden, MA.

369. Stiros, S.C., Pirazzoli, P.A., Laborel, J. & Laborel-Deguen, F., 1994. The 1953 earthquake in Cephalonia (Western Hellenic Arc): coastal uplift and halotectonic faulting, *Geophys. J. Int.* , **117**, 834–849, doi: 10.1111/j.1365-246X.1994.tb02474.x .

370. Stiros, S., Moschas, F., Feng, L. & Newman, A., 2013. Long-term versus short-term deformation of the meizoseismal area of the 2008 Achaia–Elia (MW 6.4) earthquake in NW Peloponnese, Greece: Evidence from historical triangulation and morphotectonic data, *Tectonophysics*, **592**, 150–158, doi: 10.1016/j.tecto.2013.02.016.

371. Stucchi, M., Rovida, A., Gomez Capera, A.A., Alexandre, P., Camelbeeck, T., Demircioglu, M.B., Gasperini, P., Kouskouna, V., Musson, R.M.W., Radulian, M., Sesetyan, K., Vilanova, S., Baumont, D., Bungum, H., Fäh, D., Lenhardt, W., Makropoulos, K., Martinez Solares, J.M., Scotti, O.,Zivcic , M., Albini, P., Batllo, J., Papaioannou, C., Tatevossian, R., Locati, M., Meletti, C., Viganò, D. & Giardini, D., 2013. The SHARE European Earthquake Catalog (SHEEC) 1000-1899, *J. Seismol.*, **17** (2), 523-544. http://dx.doi.org/10.1007/s10950-012-9335-2.

372. Suyehiro, S., Asada, T. & Ohtake, M., 1964. Foreshocks and aftershocks accompanying a perceptible earthquake in central Japan: On the peculiar nature of foreshocks, *Pap. Meteorol. Geophys.*, **19**, 427-435.

373. Tape, W. & Tape, C., 2012. Angle between principal axis triples, *Geophys. J. Int.*, **191**, 813–831, doi: 10.1111/j.1365-246X.2012.05658.x.

374. Taylor, K.M., Procopio, M.J., Young, C.J. & Meyer, F.G., 2011. Estimation of arrival times from seismic waves: a manifold-based approach, *Geophys. J. Int.*, **185**, 435–452, doi: 10.1111/j.1365-246X.2011.04947.x.

375. Telesca, L., 2010. Analysis of the cross-correlation between seismicity and water level in the Koyna area of India, *Bull. Seismol. Soc. Am.*, **100**, 2317-2321, doi: 10.1785/0120090392.

376. Thelen, W., West, M. & Senyukov, S., 2010. Seismic characterization of the fall 2007 eruptive sequence at Bezymianny Volcano, Russia, *J. Volcanol. Geotherm. Res.*, **194**, 201–213, doi: 10.1016/j.jvolgeores.2010.05.010.

377. Thelen, W., Malone, S. & West, M., 2011. Multiplets: Their behavior and utility at dacitic and andesitic volcanic centers, *J. Geophys. Res.*, **116**, B08210, doi: 10.1029/2010JB007924.

378. Tselentis, G.-A., Melis, N.S., Sokos, E. & Papatsimpa, K., 1996. The Egion June 15, 1995 ($6.2M_L$) earthquake, western Greece, *Pure Appl. Geophys.*, **147**, 83–98, doi: 10.1007/BF00876437.

379. Tselentis, G.-A., Martakis, N., Paraskevopoulos, P., Lois, A. & Sokos, E., 2012. Strategy for automated analysis of passive microseismic data based on S-transform, Otsu's thresholding, and higher order statistics, *Geophysics*, **77** (6), KS43-KS54, doi: 10.1190/geo2011-0301.1.

380. Turcotte, D.L. & Schubert, G., 2002. *Geodynamics, 2nd edition*, Cambridge University Press.

381. Turino, C., Morasca, P., Ferretti, G., Scafidi, D. & Spallarossa, D., 2010. Reliability of the automatic procedures for locating earthquakes in southwestern Alps and northern Apennines (Italy), *J. Seismol.*, **14**(2), 393-411, doi:10.1007/s10950-009-9171-1

382. Underhill, J.R., 1989. Late Cenozoic deformation of the Hellenide foreland, western Greece, *Geol. Soc. Am. Bull.*, **101**, 613–634.

383. Utsu, T., 1961. A statistical study on the occurrence of aftershocks, *Geophys. Mag.*, **30**, 521-605.

384. Utsu, T., Ogata, Y. & Matsu'ura, S.R., 1995. The Centenary of the Omori Formula for a Decay Law of Aftershock Activity, *J. Phys. Earth*, **43**, 1–33.

385. Valkaniotis, S., 2009. Correlation between Neotectonic structures and Seismicity in the broader area of Gulf of Corinth (Central Greece). *Ph.D. Thesis*, Aristotle University of Thessaloniki, Thessaloniki.

386. Valkaniotis, S., Ganas, A., Papathanassiou, G. & Papanikolaou, M., 2014. Field observations of geological effects triggered by the January–February 2014 Cephalonia (Ionian Sea, Greece) earthquakes, *Tectonophysics*, **630**, 150–157, doi: 10.1016/j.tecto.2014.05.012.

387. Vassilakis, E., Royden, L. & Papanikolaou, D., 2011. Kinematic links between subduction along the Hellenic trench and extension in the Gulf of Corinth, Greece: A multidisciplinary analysis, *Earth Planet. Sci. Lett.*, **303**, 108–120, doi: 10.1016/j.epsl.2010.12.054.

388. Vavryčuk, V., Bouchaala, F. & Fischer, T., 2013. High-resolution fault image from accurate locations and focal mechanisms of the 2008 swarm earthquakes in West Bohemia, Czech Republic, *Tectonophysics*, **590**, 189-195, doi: 10.1016/j.tecto.2013.01.025.

389. Vidale, J.E. & Shearer, P.M., 2006. A survey of 71 earthquake bursts across southern California: Exploring the role of pore fluid pressure fluctuations and aseismic slip as drivers, *J. Geophys. Res.*, **111**, B05312, doi:10.1029/2005JB004034.

390. Waldhauser, F. & Ellsworth, W.L., 2000. A Double-difference Earthquake location algorithm: Method and application to the Northern Hayward Fault, California, *Bull. Seismol. Soc. Am.*, **90**, 1353–1368.

391. Waldhauser, F., 2001. HypoDD: a computer program to compute double-difference earthquake locations, *U.S. Geol. Surv. open-file report*, 01-113, Menlo Park, California.

392. Waldhauser, F., Ellsworth, W.L., Schaff, D.P. & Cole, A., 2004. Streaks, multiplets, and holes: High-resolution spatio-temporal behavior of Parkfield seismicity, *Geophys. Res. Lett.*, **31**, L18608, doi: 10.1029/2004GL020649.

393. Waldhauser, F. & Schaff, D.P., 2008. Large-scale relocation of two decades of Northern California seismicity using cross-correlation and double-difference methods, *J. Geophys. Res.*, **113**, B08311, doi: 10.1029/2007JB005479.

394. Wang, J. & Teng, T., 1995. Artificial Neural Network-Based Seismic Detector, *Bull. Seismol. Soc. Am.*, **85**, 308–319.

395. Wang, J., Chen, J. H., Liu, Q. Y., Li, S. C. & Guo, B., 2006. Automatic onset phase picking for portable seismic array observation, *Acta Seismologica Sinica*, **19**(1), 44-53.

396. Ward, J.H., 1963. Hierarchical Grouping to Optimize an Objective Function. *J. Am. Stat. Assoc.*, **58**, 236–244, doi: 10.1080/01621459.1963.10500845.

397. Wells, D.L. & Coppersmith, K.J., 1994. New Empirical Relationships among Magnitude, Rupture Length, Rupture Width, Rupture Area, and Surface Displacement, *Bull. Seismol. Soc. Am.*, **84**, 974–1002.

398. White, R.S., Drew, J., Martens, H.R., Key, J., Soosalu, H. & Jakobsdottir, S.S., 2011. Dynamics of dyke intrusion in the mid-crust of Iceland, *Earth Planet. Sci. Lett.*, **304**, 300–312, doi: 10.1016/j.epsl.2011.02.038.

399. Wiemer, S. & Wyss, M., 1997. Mapping the frequency-magnitude distribution in asperities: An improved technique to calculate recurrence times? *J. Geophys. Res. Solid Earth*, **102**, 15115–15128, doi: 10.1029/97JB00726.

400. Wiemer, S. & Wyss, M., 2000. Minimum magnitude of completeness in earthquake catalogs: Examples from Alaska, the Western United States, and Japan, *Bull. Seismol. Soc. Am.*, **90**, 859–869.

401. Wiemer, S., 2001. A Software Package to Analyze Seismicity: ZMAP, *Seismol. Res. Lett.*, **72**, 373–382, doi: 10.1785/gssrl.72.3.373.

402. Woessner, J. & Wiemer, S., 2005. Assessing the quality of earthquake catalogues: Estimating the magnitude of completeness and its uncertainty, *Bull. Seismol. Soc. Am.*, **95**, 684–698, doi: 10.1785/0120040007.

403. Wolfe, C.J., Brooks, B.A., Foster, J.H. & Okubo, P.G., 2007. Microearthquake streaks and seismicity triggered by slow earthquakes on the mobile south flank of Kilauea Volcano, Hawai'i, *Geophys. Res. Lett.*, **34**, L23306, doi: 10.1029/2007GL031625.

404. Wyss, M., 1973. Towards a Physical Understanding of the Earthquake Frequency Distribution, *Geophys. J. Int.*, **31**, 341–359, doi: 10.1111/j.1365-246X.1973.tb06506.x.

405. Wyss, M., Shimazaki, K. & Ito, A. (eds)., 1999. *Seismicity Patterns, Their Statistical Significance and Physical Meaning*, Basel, Birkhäuser Basel, doi: 10.1007/978-3-0348-8677-2.

406. Wyss, M., Pacchiani, F., Deschamps, A. & Patau, G., 2008. Mean magnitude variations of earthquakes as a function of depth: Different crustal stress distribution depending on tectonic setting, *Geophys. Res. Lett.*, **35**, L01307, doi: 10.1029/2007GL031057.

407. Xu, P., 2004. Determination of regional stress tensors from fault-slip data, *Geophys. J. Int.*, **157**, 1316–1330, doi: 10.1111/j.1365-246X.2004.02271.x.

408. Yang, H., Zhu, L. & Chu, R., 2009. Fault-plane determination of the 18 April 2008 mount Carmel, Illinois, earthquake by detecting and relocating aftershocks, *Bull. seism. Soc. Am.*, **99**, 3413–3420, doi: 10.1785/0120090038.

409. Yoon, C.E., OReilly, O., Bergen, K.J. & Beroza, G.C., 2015. Earthquake detection through computationally efficient similarity search, *Sci. Adv.*, **1** (11), e1501057, doi: 10.1126/sciadv.1501057.

410. Yukutake, Y., Tanada, T., Honda, R., Harada, M., Ito, H. & Yoshida, A., 2010. Fine fracture structures in the geothermal region of Hakone volcano, revealed by well-resolved earthquake hypocenters and focal mechanisms, *Tectonophysics*, **489**, 104-118, doi: 10.1016/j.tecto.2010.04.012.

411. Zahradnik, J., Jansky, J., Sokos, E., Serpetsidaki, a, Lyon-Caen, H. & Papadimitriou, P., 2004. Modeling the ML 4.7 mainshock of the February-July 2001 earthquake sequence in Aegion, Greece, *J. Seismol.*, **8**, 247–257, doi: 10.1023/B:JOSE.0000021376.21087.2d.

412. Zahradnik, J., Serpetsidaki, A., Sokos, E. & Tselentis, G.-A., 2005. Iterative Deconvolution of Regional Waveforms and a Double-Event Interpretation of the 2003 Lefkada Earthquake, Greece, *Bull. Seismol. Soc. Am.*, **95**, 159–172, doi: 10.1785/0120040035.

413. Zahradnik, J., Gallovic, F., Sokos, E., Serpetsidaki, A. & Tselentis, A., 2008. Quick Fault-Plane Identification by a Geometrical Method: Application to the Mw 6.2 Leonidio Earthquake, 6 January 2008, Greece, *Seismol. Res. Lett.*, **79**, 653–662, doi: 10.1785/gssrl.79.5.653.

414. Zamani, A. & Hashemi, N., 2004. Computer-based self-organized tectonic zoning: a tentative pattern recognition for Iran, *Comput. Geosci.*, **30**, 705–718, doi: 10.1016/j.cageo.2004.04.002.

415. Zelt, B.C., Taylor, B., Sachpazi, M. & Hirn, A., 2005. Crustal velocity and Moho structure beneath the Gulf of Corinth, Greece, *Geophys. J. Int.*, **162**, 257–268, doi: 10.1111/j.1365-246X.2005.02640.x.

416. Zhang, H., Thurber C. & Rowe, C., 2003. Automatic P-wave arrival detection and picking with multiscale wavelet analysis for single-component recordings, *Bull. Seism. Soc. Am.*, **93**(5), 1904-1912.

417. Zhang, M. & Wen, L., 2014. Seismological Evidence for a Low-Yield Nuclear Test on 12 May 2010 in North Korea, *Seismol. Res. Lett.*, **86**, 138–145, doi: 10.1785/02201401170.

418. Zhao, Y. & Takano, K., 1999. An artificial neural network approach for broadband seismic phase picking, *Bull. Seismol. Soc. Am.*, **89** , 670–680.

419. Zhizhin, M.N., Rouland, D., Bonnin, J., Gvishiani, A.D. & Burtsev, A., 2006. Rapid Estimation of Earthquake Source Parameters from Pattern Analysis of Waveforms Recorded at a Single Three-Component Broadband Station, Port Vila, Vanuatu, *Bull. Seismol. Soc. Am.*, **96**, 2329–2347, doi: 10.1785/0120050172.

420. Zoback, M. Lou., 1992. First- and second-order patterns of stress in the lithosphere: The World Stress Map Project, *J. Geophys. Res.*, **97**, 11703–11728, doi: 10.1029/92JB00132.

421. Zobin, V.M. & Ivanova, E.I., 1994. Earthquake swarms in the Kamchatka-Commander region, *Geophys. J. Int.*, **117**, 33-47, doi: 10.1111/j.1365-246X.1994.tb03302.x.

422. Zobin, V. M., 2003. *Introduction to Volcanic Seismology*, Amsterdam: Elsevier.

NATIONAL AND KAPODISTRIAN UNIVERSITY OF ATHENS

SCHOOL OF SCIENCE
FACULTY OF GEOLOGY AND GEOENVIRONMENT
DEPARTMENT OF GEOPHYSICS AND GEOTHERMICS

Spatiotemporal patterns of microseismicity for the identification of active fault structures using seismic waveform cross-correlation and double-difference relocation.

PHD DISSERTATION

KAPETANIDIS VASILIS

VOLUME II
APPENDIX

ATHENS

MARCH 2017

ΕΘΝΙΚΟ ΚΑΙ ΚΑΠΟΔΙΣΤΡΙΑΚΟ ΠΑΝΕΠΙΣΤΗΜΙΟ ΑΘΗΝΩΝ

ΣΧΟΛΗ ΘΕΤΙΚΩΝ ΕΠΙΣΤΗΜΩΝ
ΤΜΗΜΑ ΓΕΩΛΟΓΙΑΣ ΚΑΙ ΓΕΩΠΕΡΙΒΑΛΛΟΝΤΟΣ
ΤΟΜΕΑΣ ΓΕΩΦΥΣΙΚΗΣ - ΓΕΩΘΕΡΜΙΑΣ

Μελέτη χωροχρονικών προτύπων μικροσεισμικότητας για την σκιαγράφηση χαρακτηριστικών ενεργών ρηγμάτων τη χρήσει της μεθόδου διπλών διαφορών και ετεροσυσχέτισης σεισμικών κυματομορφών.

ΔΙΔΑΚΤΟΡΙΚΗ ΔΙΑΤΡΙΒΗ

ΚΑΠΕΤΑΝΙΔΗΣ ΒΑΣΙΛΕΙΟΣ

ΤΟΜΟΣ Β΄
ΠΑΡΑΡΤΗΜΑ

ΑΘΗΝΑ

ΜΑΡΤΙΟΣ 2017

ADVISORY COMMITTEE	P. PAPADIMITRIOU	Professor, NKUA (supervisor)
	N. VOULGARIS	Professor, NKUA
	K. MAKROPOULOS	Professor Emeritus, NKUA

EXAMINATION COMMITTEE	P. PAPADIMITRIOU	Professor, NKUA
	N. VOULGARIS	Professor, NKUA
	K. MAKROPOULOS	Professor Emeritus, NKUA
	G. TSELENTIS	Professor, NKUA
	A. KIRATZI	Professor, AUTH
	I. KASSARAS	Assistant Professor, NKUA
	G. KAVIRIS	Assistant Professor, NKUA

ΣΥΜΒΟΥΛΕΥΤΙΚΗ ΕΠΙΤΡΟΠΗ	Π. ΠΑΠΑΔΗΜΗΤΡΙΟΥ	Καθηγητής ΕΚΠΑ (Επιβλέπων)
	Ν. ΒΟΥΛΓΑΡΗΣ	Καθηγητής ΕΚΠΑ
	Κ. ΜΑΚΡΟΠΟΥΛΟΣ	Ομότιμος Καθηγητής ΕΚΠΑ

ΕΞΕΤΑΣΤΙΚΗ ΕΠΙΤΡΟΠΗ	Π. ΠΑΠΑΔΗΜΗΤΡΙΟΥ	Καθηγητής ΕΚΠΑ
	Ν. ΒΟΥΛΓΑΡΗΣ	Καθηγητής ΕΚΠΑ
	Κ. ΜΑΚΡΟΠΟΥΛΟΣ	Ομότιμος Καθηγητής ΕΚΠΑ
	Γ. ΤΣΕΛΕΝΤΗΣ	Καθηγητής ΕΚΠΑ
	Α. ΚΥΡΑΤΖΗ	Καθηγήτρια ΑΠΘ
	Ι. ΚΑΣΣΑΡΑΣ	Επίκουρος Καθηγητής ΕΚΠΑ
	Γ. ΚΑΒΥΡΗΣ	Επίκουρος Καθηγητής ΕΚΠΑ

Table of Contents

Appendix 1A

Supplementary figures for Chapter 1

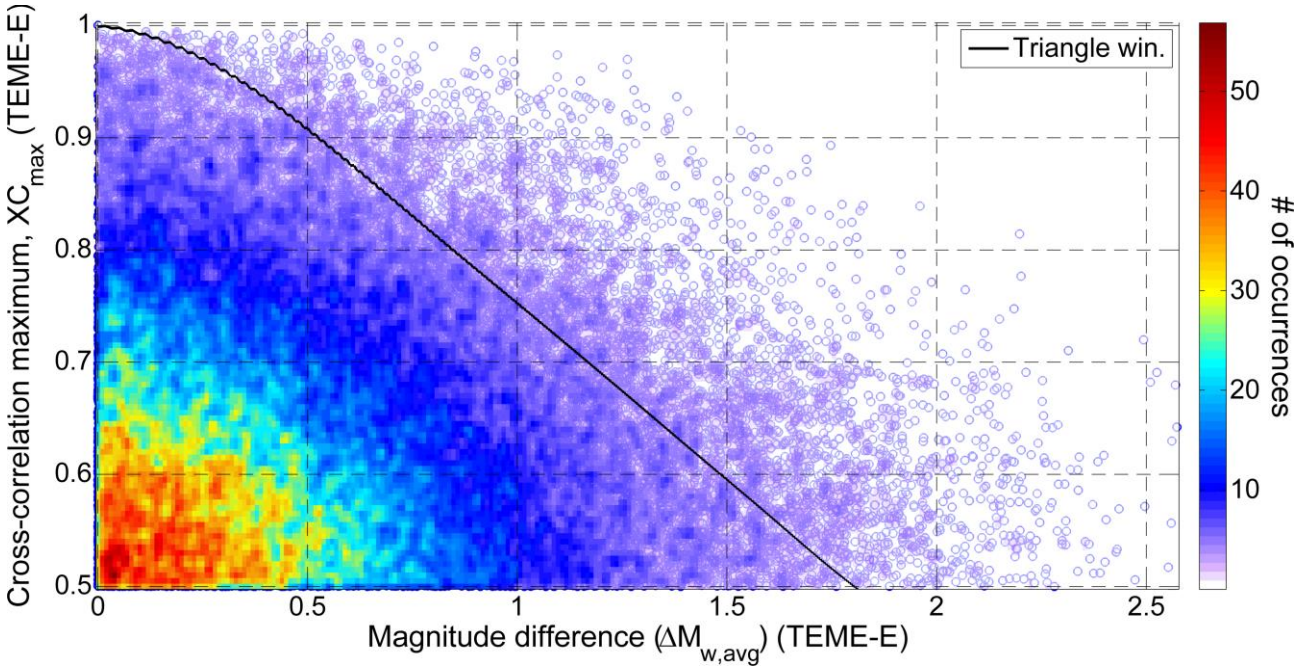

Figure 1A.1: Test for XC_{max} with respect to magnitude difference as determined from average spectral amplitude (See Section 3.3 for the calculation of $M_{w,avg}$) for earthquakes of the 2013 Helike swarm dataset recorded at the E-W component of station TEME, located within the epicentral area.

Figure 1A.2: Synthetic test for the distinction of 5 partially overlapping spatial clusters using Ward's linkage (a) initial distribution and true grouping, (b) differential of the modified Mojena's stopping rule (Martinez et al., 2010) with its global minimum suggesting 6 clusters, (c) the 6 reconstructed clusters.

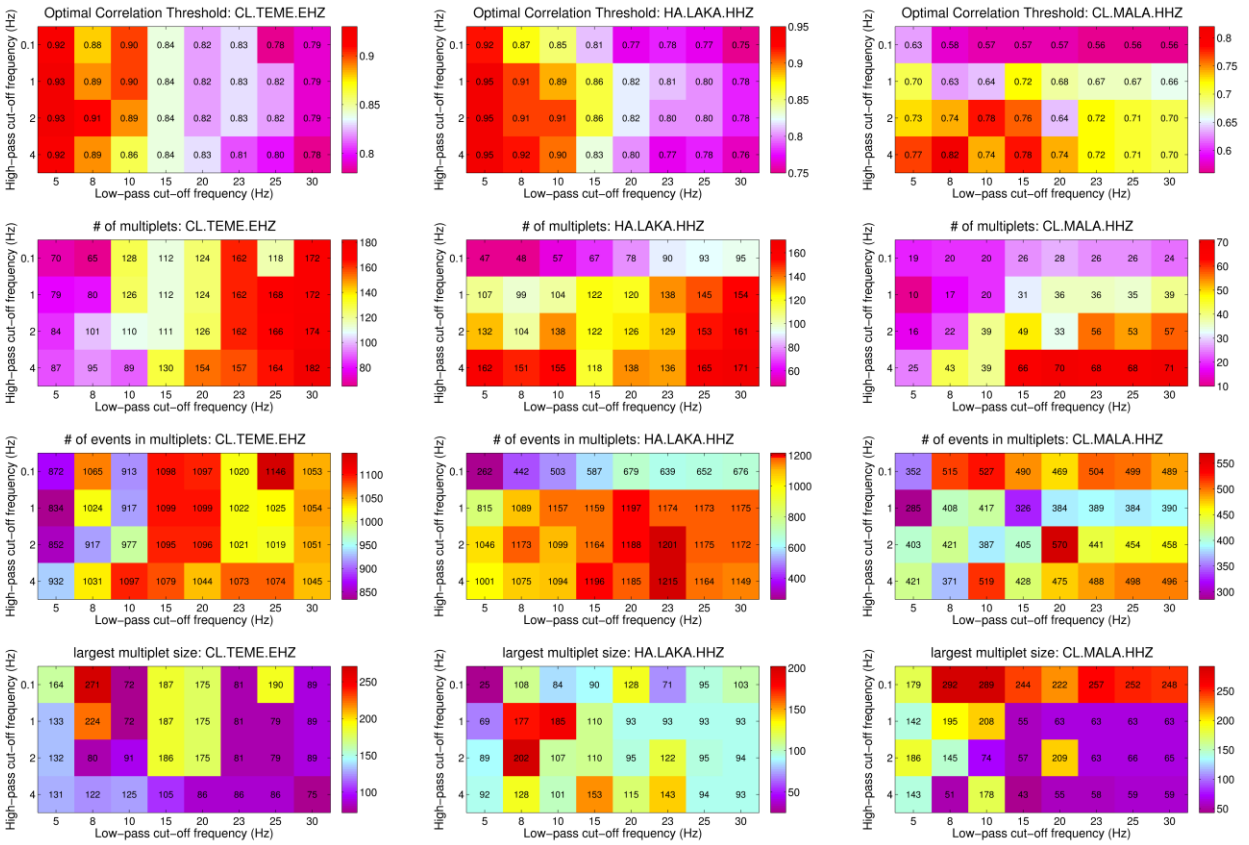

Figure 1A.3: Same test as in Fig. 1.1, but for the seismic swarm of 2013 in Helike (Kapetanidis *et al.*, 2015), where station TEME (short-period) is within the epicentral area while and LAKA and MALA, at average epicentral distances ~10 and ~26 km, respectively, are equipped with broad-band sensors.

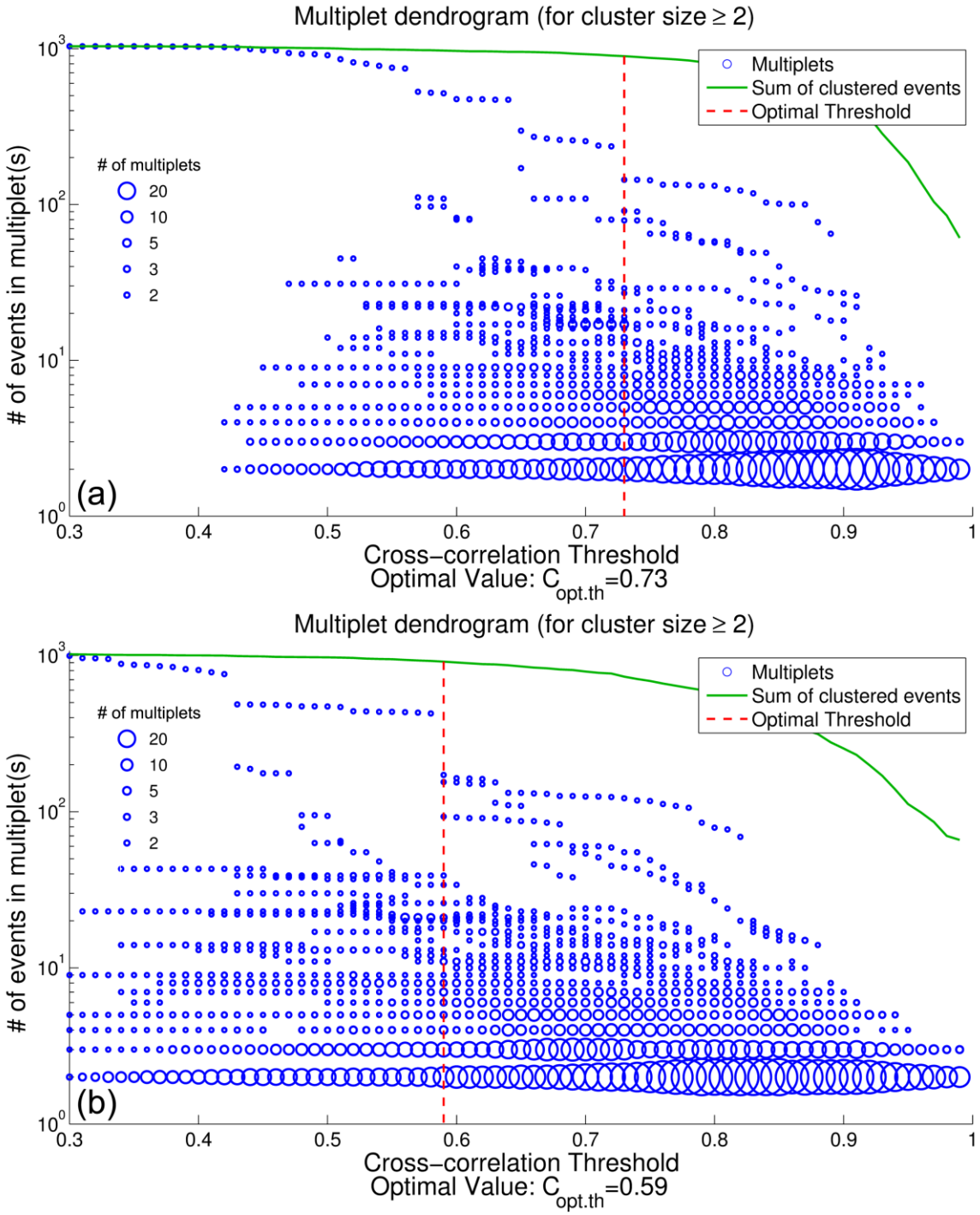

Figure 1A.4: Multiplet dendrograms for events of the seismicity of the western Corinth rift in 2004, Group #4 (Section 6.3.5) using data from the vertical component of station AIOA at average epicentral distance 13km, filtered at 2 – 23 Hz, (a) with a window length of 3 sec, (b) with a window length of 30 sec.

Appendix 2A

Supplementary figures for Chapter 2

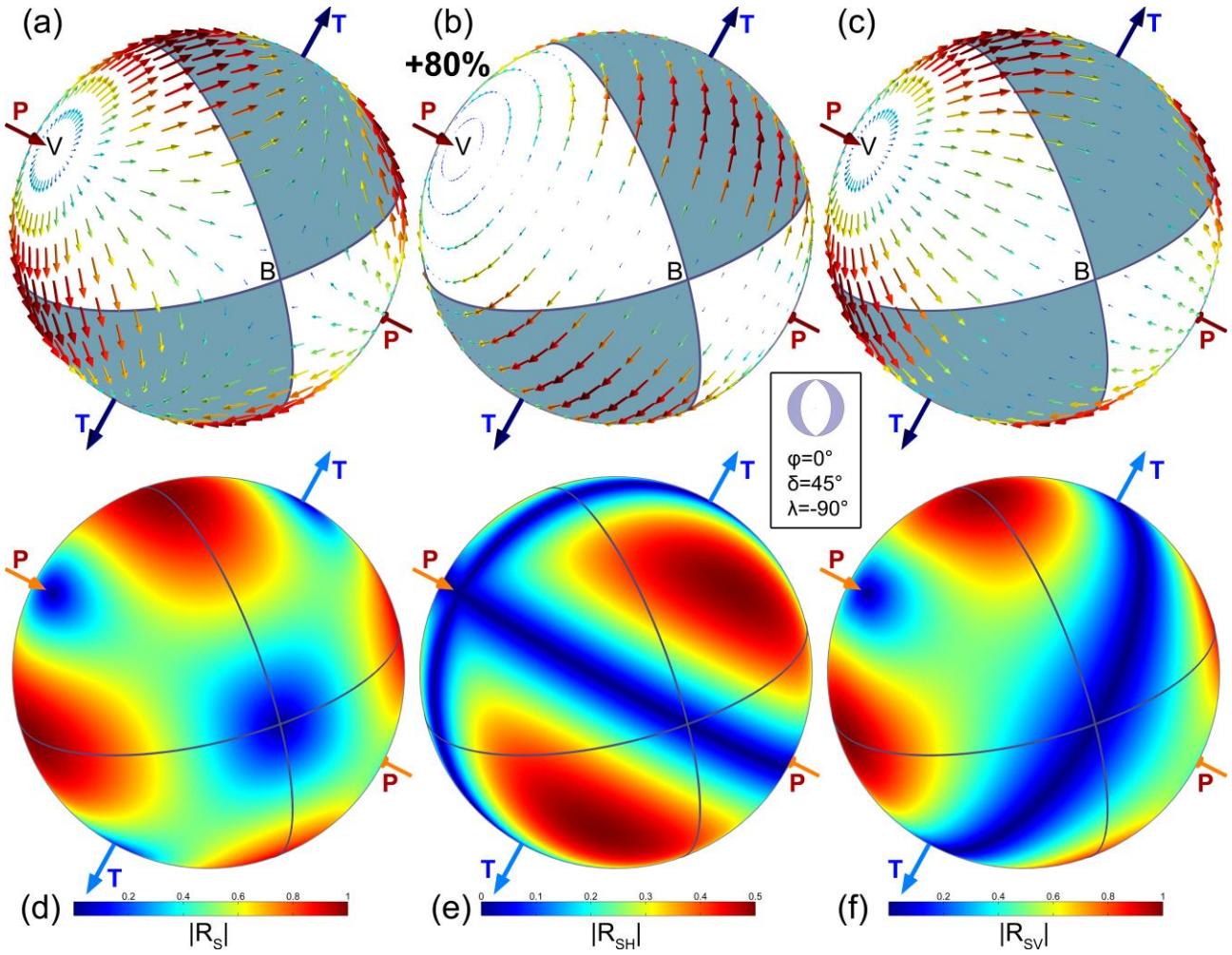

Figure 2A.1: 3D representation of the S-wave radiation pattern (same as Fig. 2.10) for a pure normal, dip-slip, double-couple focal mechanism: φ=0°, δ=45°, λ=-90° (see embedded icon with the respective lower hemisphere stereographic projection), a) S, b) SH and c) SV first motion vectors, d-f) distribution of the $|R_S|$, $|R_{SH}|$ and $|R_{SV}|$ amplitude values of the respective wave-types. B marks the trace of the **B**-axis while V marks the trace of the vertical axis, which in this case coincides with the **P**-axis.

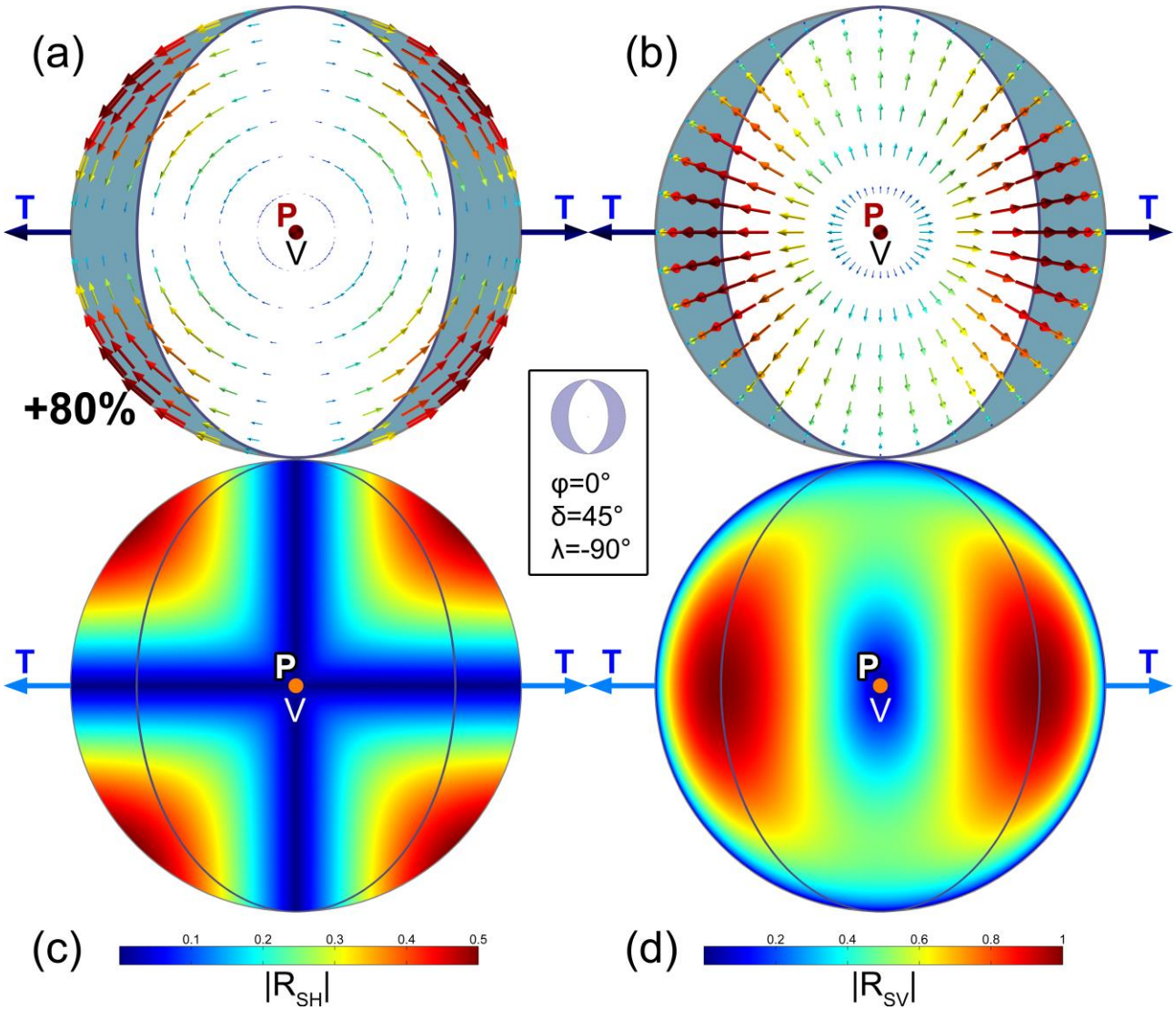

Figure 2A.2: Vertical view for the normal focal mechanism of Fig. 2A.1, with φ=0°, δ=45°, λ=-90° (see embedded icon with the respective lower hemisphere stereographic projection), a) SH, b) SV first motion vectors, c-d) distribution of the $|R_{SH}|$ and $|R_{SV}|$ amplitude values of the respective wave-types. V marks the trace of the vertical axis, which in this case coincides with the **P**-axis.

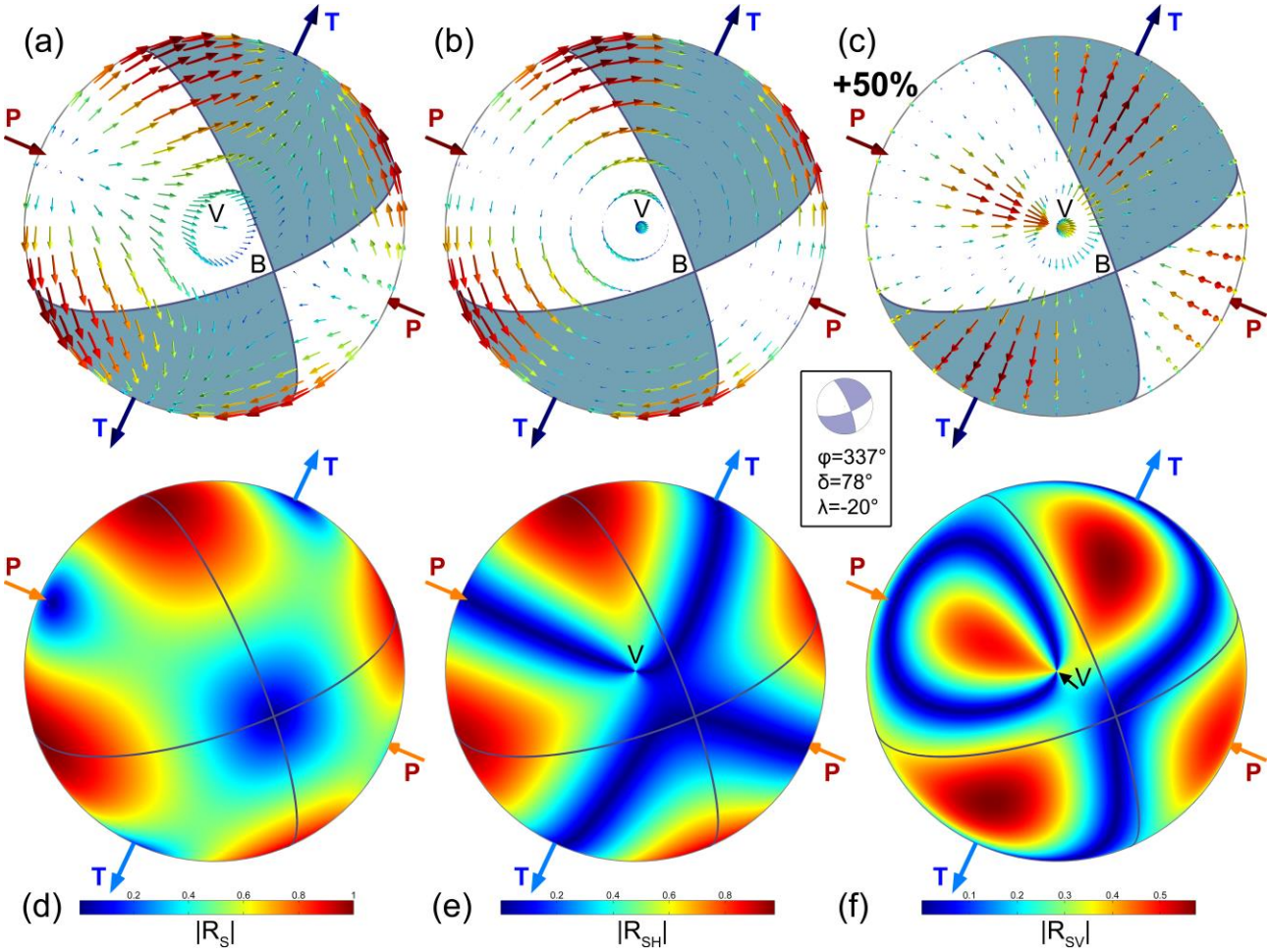

Figure 2A.3: 3D representation of the S-wave radiation pattern (same as Fig. 2A.1) but for an oblique-normal double-couple focal mechanism: φ=337°, δ=78°, λ=-20° (see embedded icon with the respective lower hemisphere stereographic projection), a) S, b) SH and c) SV first motion vectors, d-f) distribution of the $|R_S|$, $|R_{SH}|$ and $|R_{SV}|$ amplitude values of the respective wave-types. B marks the trace of the **B**-axis while V marks the trace of the vertical axis.

Appendix 3A

Instrument transfer functions

The seismometers are instruments which convert oscillations of real ground motion into proportional oscillations of electric potential. They exploit the principle of inertia of suspended masses which tend to remain stationary with respect to the reference frame of the instrument that moves along with the ground. The physical properties of the mechanism, which is in principle a system of damped harmonic oscillators, define a range of frequencies over which the seismometer is sensitive. The frequency response of any such system that is constructed of mechanical and electrical components can be described with a transfer function, $T(\omega)$, of the general form (Stein & Wysession, 2003; Havskov & Alguacil, 2004):

$$T(\omega) = \frac{a_o + a_1(i\omega) + a_2(i\omega)^2 + \ldots}{b_o + b_1(i\omega) + b_2(i\omega)^2 + \ldots} = A_o \frac{\prod_{i=1}^{Nz}(i\omega - z_i)}{\prod_{j=1}^{Np}(i\omega - p_j)} \tag{3A.1}$$

where the A_o is the normalization constant and the complex numbers z_i and p_j are the zeros and poles, respectively. The construction is such that the sensor has a flat velocity response over a certain frequency band, so that ground oscillations at these frequencies produce voltage oscillations defined by a constant proportion. This parameter is called *sensitivity*, *S*, and is typically measured in V/(m/s) for seismometers.

The analogue signal produced by the seismometer then passes through another instrument/module called digitizer or data-logger, which converts it to a digital signal and records it to a memory medium or transmits it to an acquisition server. In the past, the analog seismographs registered the ground motion on paper, with the waveform being enlarged, with respect to the real ground motion, by a dimensionless value called *magnification*. The respective parameter of digital data-loggers is called *gain*, *G*, and is measured in count/V or, more usually in μV/count (G^*).

The final digital signal, *W*, can be described in terms of the convolution of the real ground motion, *R*, with a series of filters:

$$W = R * (T \cdot S) * D \tag{3A.2}$$

where *T* the sensor's transfer function (Eq. 3A.1), *S* the sensitivity and *D* the Digitizer's transfer function. The latter refers to the procedures and transformations of the analogue signal to digital at a certain sampling rate. The more significant influence of *D* on the waveform's shape is caused by a

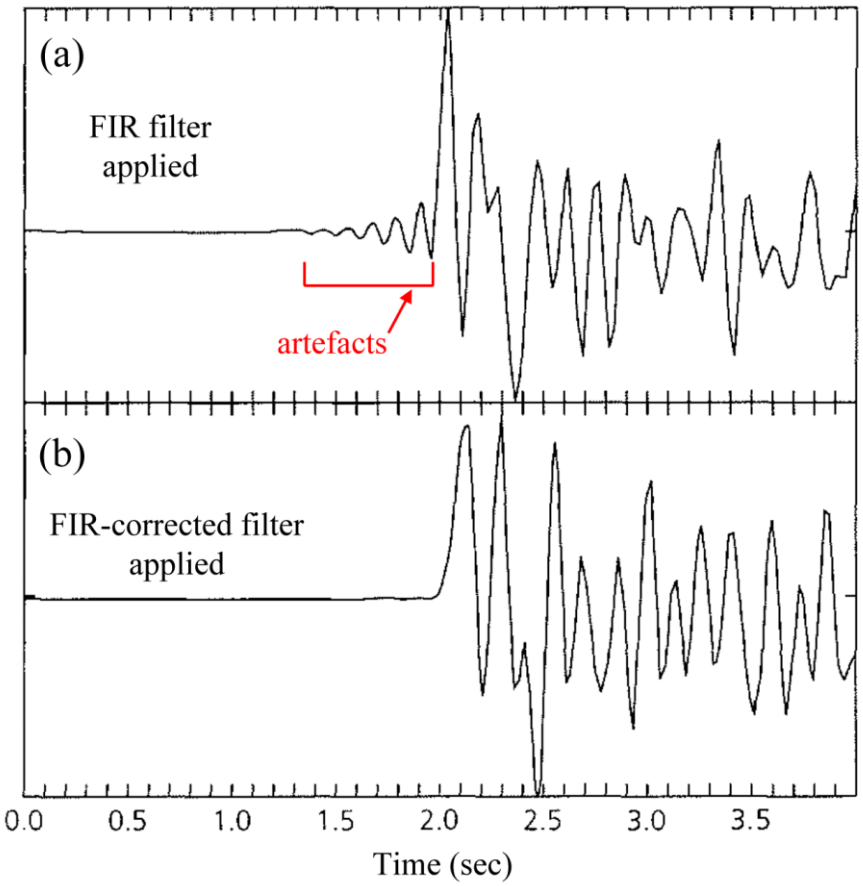

Figure 3A.1: a) High-frequency artefacts preceding an impulsive wave onset due to the applied non-causal FIR filter for digital anti-aliasing, b) the same waveform corrected for the distortion caused by the FIR filter. (Figure modified after Stein & Wysession, 2003, original by Scherbaum, 1996)

non-causal FIR filter that is used for digital anti-aliasing but may introduce spurious artefacts preceding impulsive onsets (Fig. 3A.1). These can be removed by a proper FIR filter correction. However, for most applications, D can be simply replaced by the digitizer's gain, G. This leaves $T(\omega)$, along with factors S and G, which can be incorporated in a combined constant:

$$C = A_o \cdot S \cdot G \tag{3A.3}$$

where C can be expressed in count/(m/s) units. In case the argument of the transfer function (Eq. 3A.1) requires to be the simple frequency, f, instead of the angular frequency, ω, the poles and zeroes can be converted to Hz by simply being multiplied by 2π, while the normalization constant has the following relation between rad/s and Hz units (Scherbaum, 1996):

$$A_o(rad/s) = A_o(Hz) \cdot 2\pi^{Np-Nz} \tag{3A.4}$$

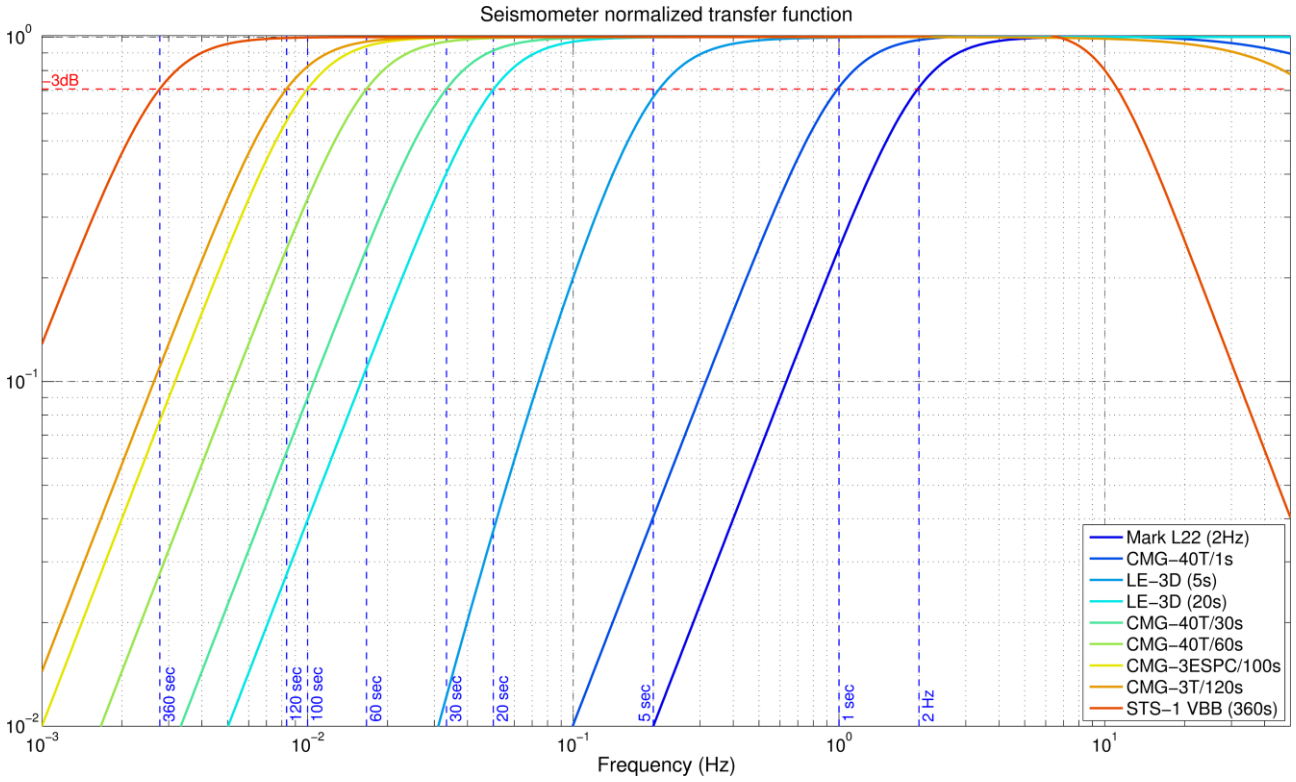

Figure 3A.2: Normalized transfer functions for several different types of seismometers. The corner frequencies and the -3dB level are also marked.

Seismometers are generally divided in short-period (SP), broad-band (BB) and very-broad-band (VBB) or long-period (LP), depending on the frequency range where they exhibit approximately flat response to the real ground motion. The seismometer's transfer function usually resembles a band-pass Butterworth filter, with its sensitivity at low frequencies marked by a corner frequency where the amplitude of the normalized transfer function has dropped by 3dB, approximately at 0.707. A set of normalized (using only the A_o factor) transfer functions is presented in Fig. 3A.2 for various instruments, most of which are used in the Hellenic Unified Seismological Network (HUSN) as well as the Corinth Rift Laboratory network (CRLnet). Note how the -3dB level intersects each instrument's normalized transfer function near their respective corner frequency.

An example of an earthquake spectrum recorded at a broad-band CMG-40T/30sec seismometer is presented in Fig. 3A.3a. The spectra are such that the maximum amplitude of the raw signal is unity. The normalized transfer function, depicted in purple, is almost flat in the entire band, as the signal window is not much larger than 30 sec, which is the corner frequency of the seismometer. Thus, a deconvolution would not affect the spectral shape but only transform its units, which is not included in this figure, resulting in an overlap between raw and deconvoluted spectra. On the other hand, an integration, which is effectively a multiplication by $i{\cdot}2\pi f$, which results in a relative increase of the amplitude at the lower frequencies and decrease at the higher ones. Also note the theoretically expected plateau at the lower frequencies where the M_o can be measured when the

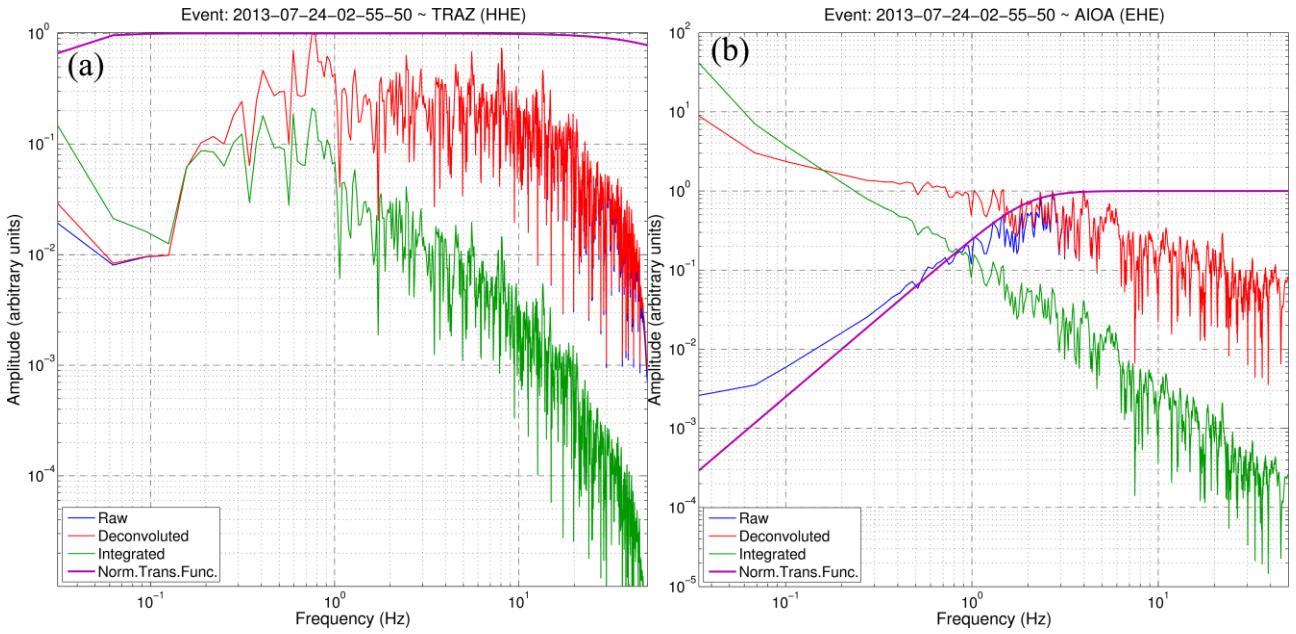

Figure 3A.3: Spectral amplitudes for raw signals (blue), signals after the deconvolution (red) of the normalized transfer function (purple) and after integration (green) for a) a broad-band CMG-40T/30sec seismometer and b) a short-period Mark L22 (2Hz) seismometer.

Table 3A.1: Poles and zeros for a CMG-40T/30sec broadband seismometer. Its typical sensitivity is 800V/m/s.

(Hz)		**(rad/sec)**	
Ao	2304000	**Ao**	571507692
ZEROS (Nz=2)		**ZEROS (Nz=2)**	
real	**imag.**	**real**	**imag.**
0	0	0	0
0	0	0	0
POLES (Np=5)		**POLES (Np=5)**	
real	**imag.**	**real**	**imag.**
-80	0	-5.026548E+02	0.000000E+00
-160	0	-1.005310E+03	0.000000E+00
-180	0	-1.130973E+03	0.000000E+00
-0.02356	0.02356	-1.480318E-01	1.480318E-01
-0.02356	-0.02356	-1.480318E-01	-1.480318E-01

spectrum has been converted to the proper seismic moment units. The poles and zeros of the transfer function are presented in Table 3A.1, in both Hz and rad/sec units. In this case, the sensitivity is S=800V/m/s. Coupled with e.g. a Reftek-72A data-logger, with a gain of G^*=1.907μV/count=1/G the combined constant (in rad/sec) would be:

$$C = A_o(rad/s)\cdot S\cdot G = 571507692\cdot\frac{800V/m/s}{1.907\cdot 10^{-6}V/count} = 2.397515\cdot 10^{17}\,\text{count}/(\text{m/s}) \qquad (3A.5)$$

so that a deconvolution of the transfer function with the combined constant from the raw signal (which is in counts) would result in a spectral amplitude measured in velocity units, m/s.

On the other hand, a short-period instrument (Fig. 3A.3b), such as the Mark-L22, has a corner frequency at f_c=2Hz. While this enables the quick view of a seismogram for local microearthquakes in the time-domain, as its transfer function also works as a high-pass filter that greatly reduces long period noise, it is not sensitive to the low frequency content of large/regional earthquakes. In this case, the flat region of the instrument's response is for about f>3Hz, where the blue and red spectra in Fig. 3A.3b overlap. The deconvolution of the normalized instrument response, which is a division in the spectral domain, which in turn is a subtraction in the spectral log-domain, significantly raises the level of noise at the lower frequencies, which can greatly affect the inversion procedure for the determination of M_o (Section 3.2), as integration may result in a ramp rather than a plateau at the lower frequencies. For this particular instrument, the transfer function is such that it has a unitary normalization constant, A_o (Table 3A.2). Furthermore, because N_p=N_z=2, the A_o value is the same whether expressed in Hz or rad/sec units (see Eq. 3A.4).

Table 3A.2: Poles and zeros for a Mark-L22 (2Hz) short-period seismometer. Its typical sensitivity is 88V/m/s.

(Hz)		**(rad/sec)**	
Ao	1.0000E+00	**Ao**	1.000E+00
ZEROS (Nz=2)		**ZEROS (Nz=2)**	
real	**imag.**	**real**	**imag.**
0	0	0	0
0	0	0	0
POLES (Np=2)		**POLES (Np=2)**	
real	**imag.**	**real**	**imag.**
-1.399927	1.428256	-8.796000E+00	8.974000E+00
-1.399927	-1.428256	-8.796000E+00	-8.974000E+00

Appendix 3B

Supplementary figures for Chapter 3

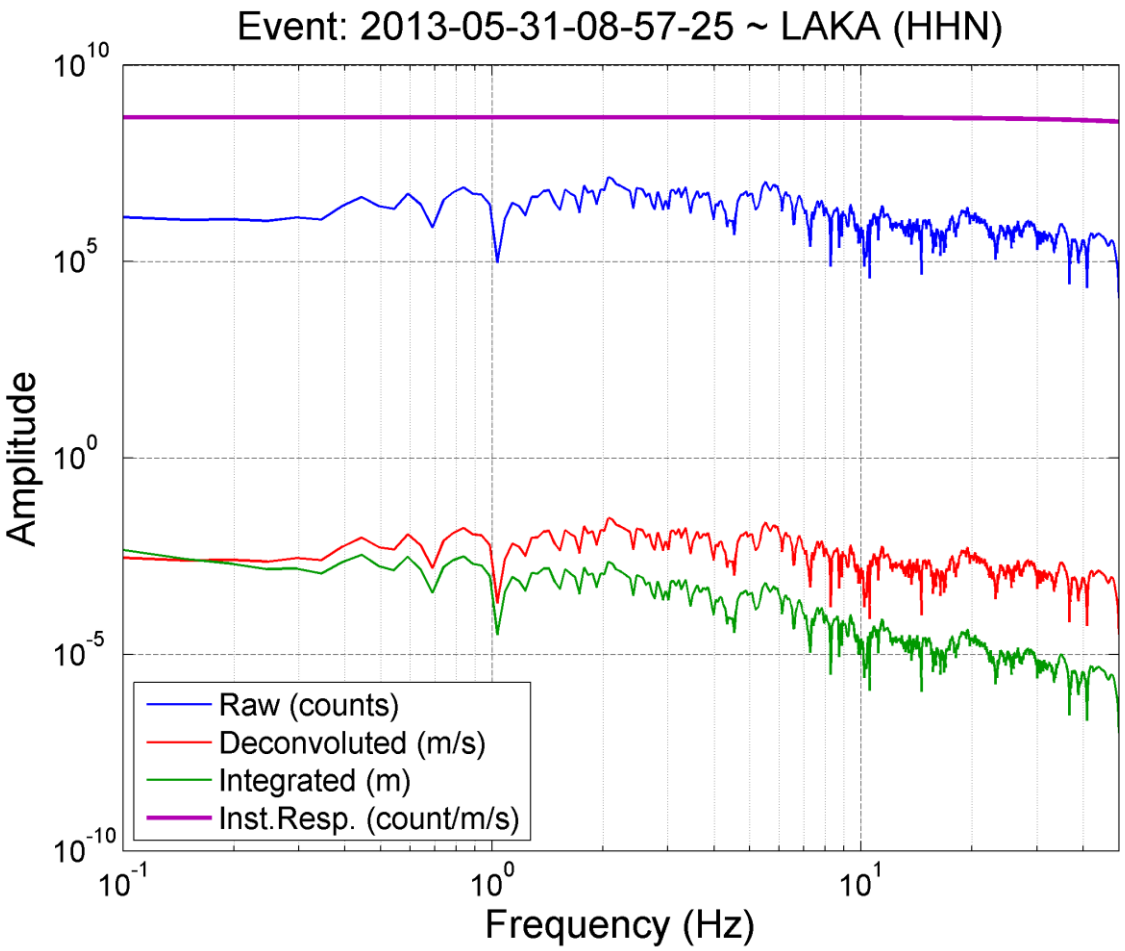

Figure 3B.1: Spectra of raw signal (blue), after deconvolution (red) of the instrument response (purple) and after integration (green).

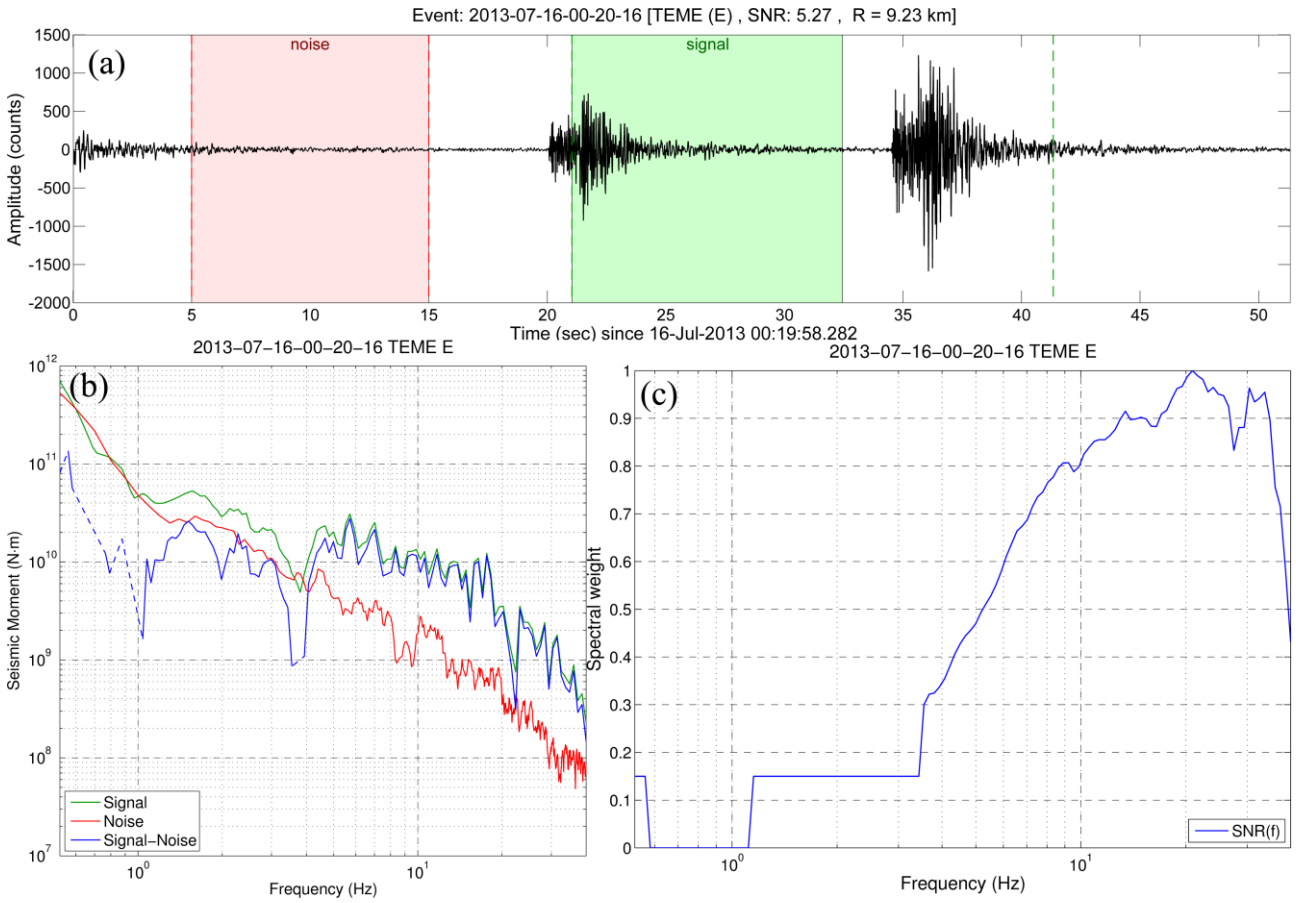

Figure 3B.2: Processing of a small event (M_w=0.8) with *SNR*≈5 at station TEME, equipped a short-period (Mark-L22) seismometer, a) signal and noise windows, b) signal and noise spectra and c) spectral weight, *w*(f), before the SRF correction. No extra weights have been added to the lower frequencies as the SNR is low (<50).

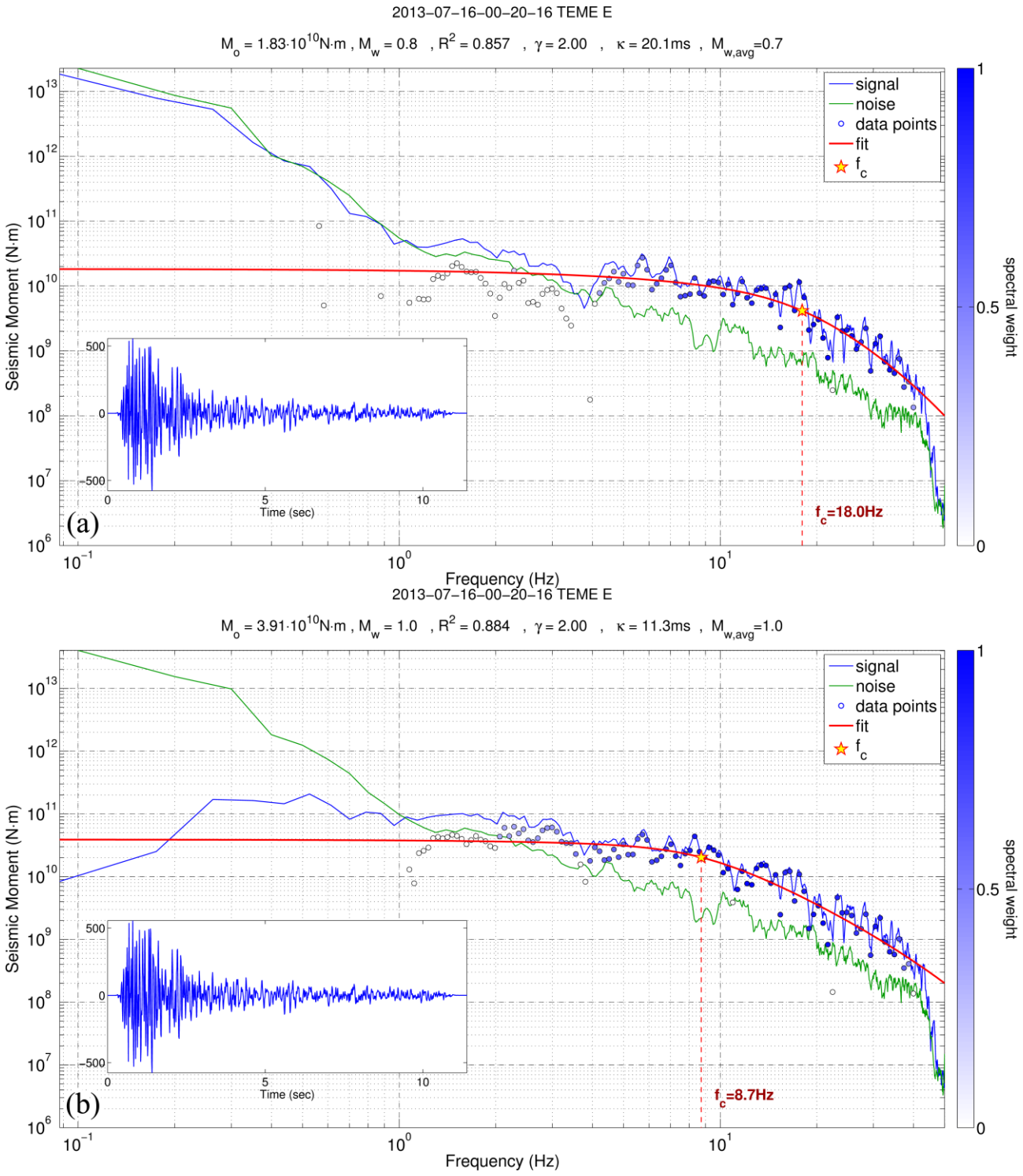

Figure 3B.3: Fit on the seismic moment spectrum of the signal of Fig. 3B.2a using the model of Boatwright (1978) a) before and b) after the SRF correction.

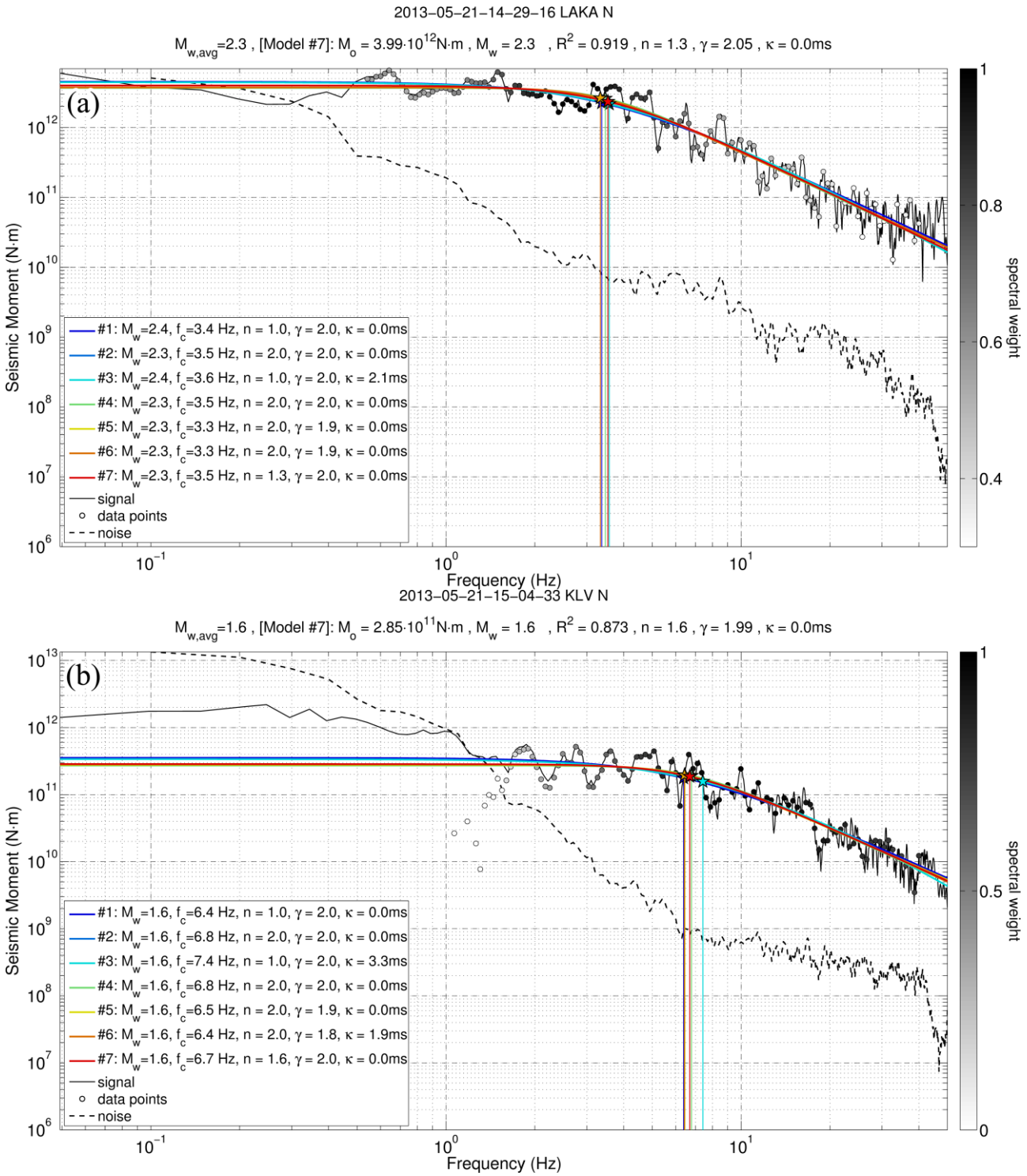

Figure 3B.4: Spectral fit of multiple models (Table 3.1). Both signal spectra have been corrected for the SRF. The fit parameters are displayed in the legend. The parameters of the model with the largest correlation coefficient, R^2 are shown on top.

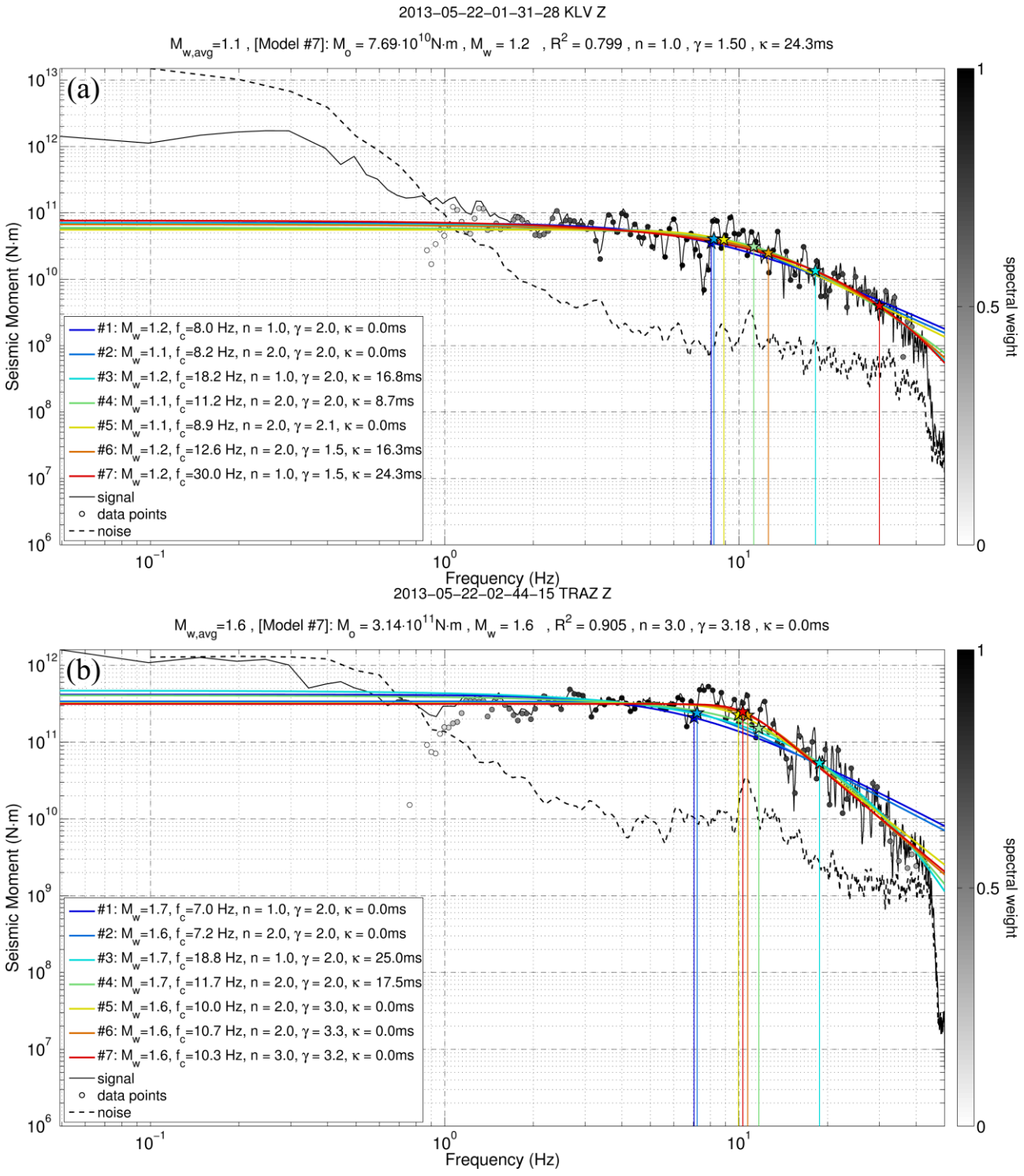

Figure 3B.5: Same as Fig. 3B.4, but for two examples which exhibit a large range of f_c values.

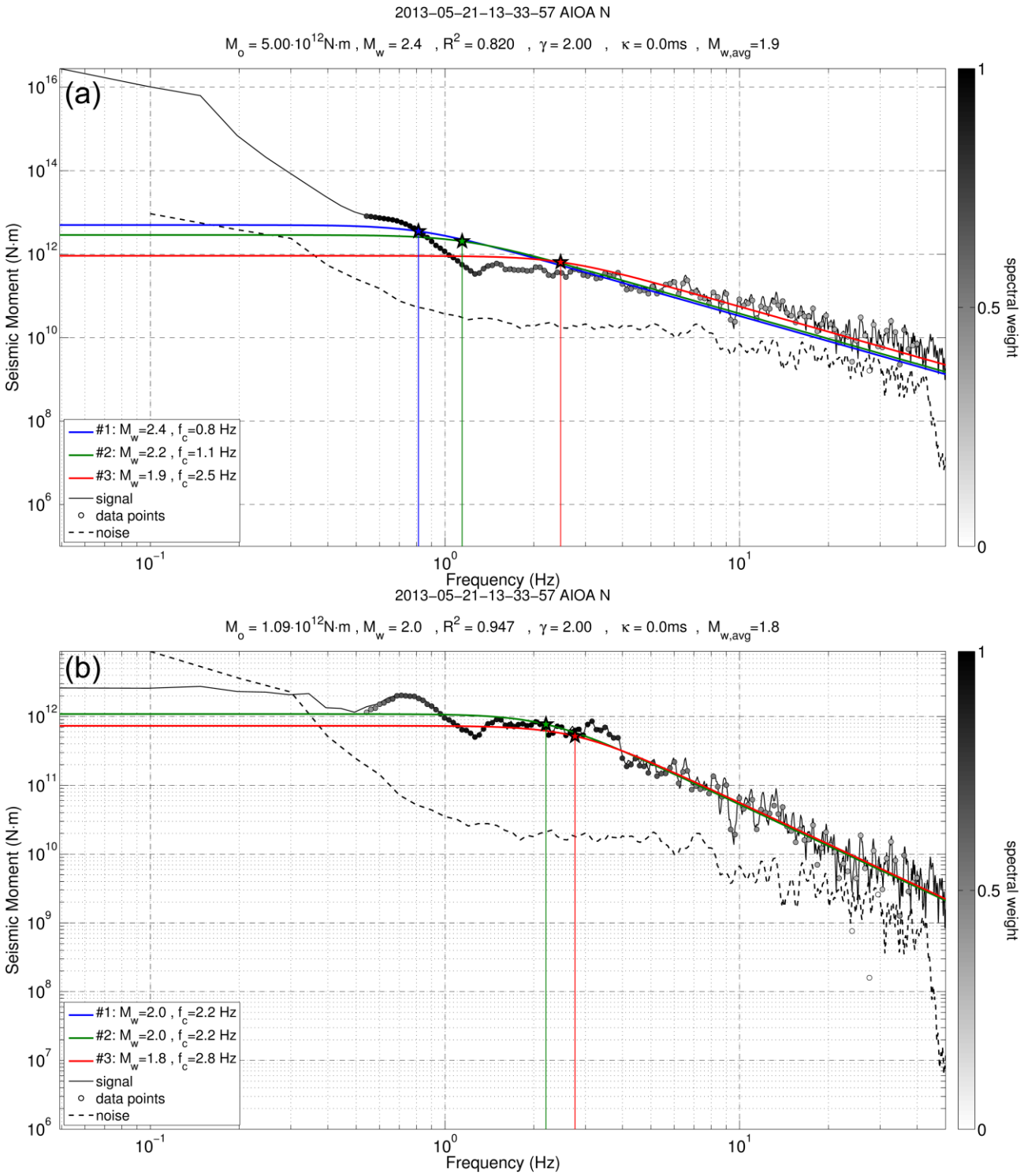

Figure 3B.6: Spectral fit of model #4 with three different ranges for M_o, #1: free to vary within the range of Table 3.2, #2: restricted within a range of equivalent moment magnitude $M_{w,avg}$±0.5, and #3: fixed at $M_{w,avg}$, a) before and b) after correction for the SRF. In case (b) both #1 and #2 have identical solutions.

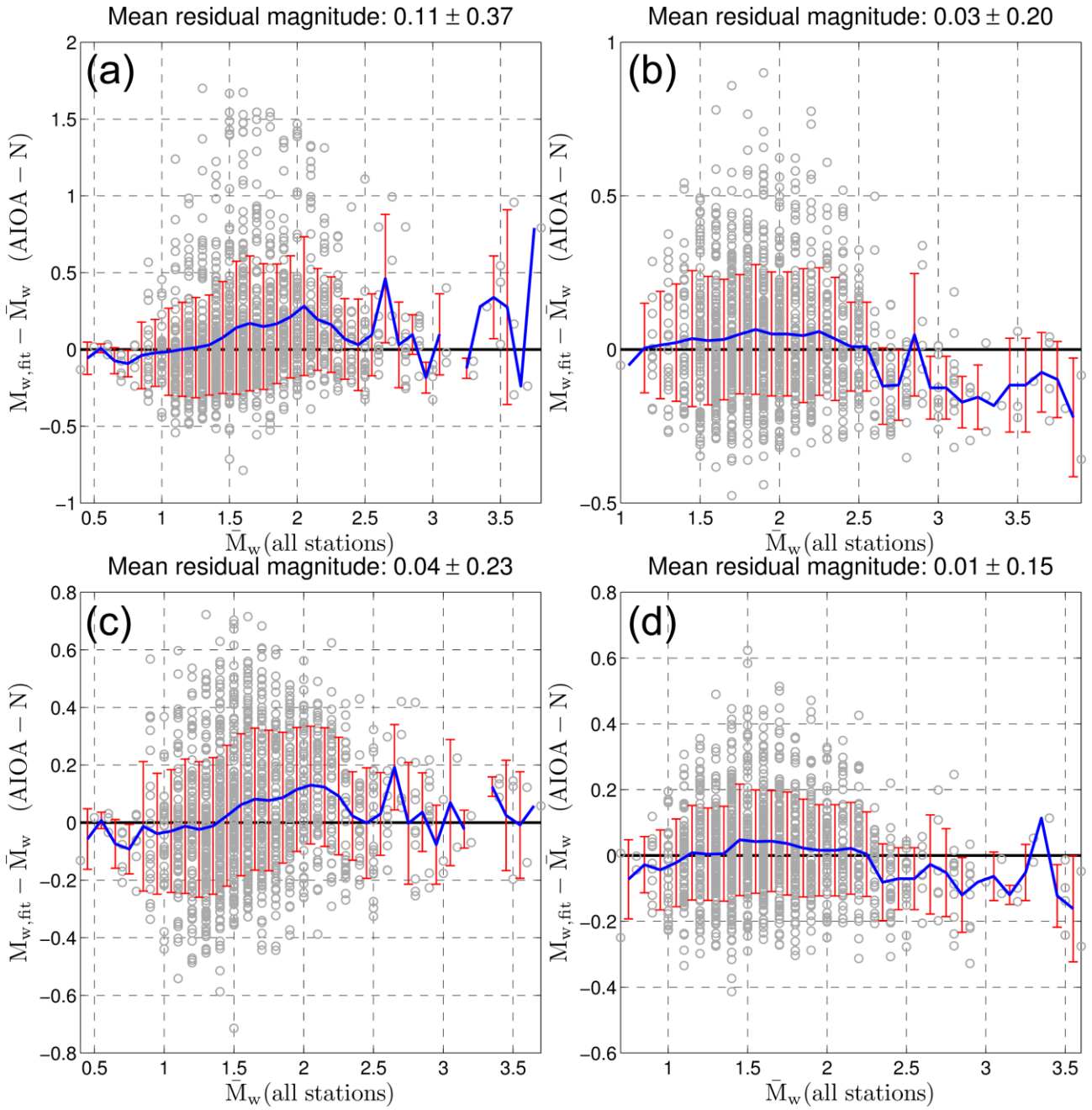

Figure 3B.7: Differences between M_w derived by spectral fit on the N-S component of station AIOA and the respective trimmed weighted mean M_w from all stations for the dataset of the 2013 Helike swarm using model #4, a-b) with M_o free to vary according to Table 3.2, c-d) with M_o restricted within $M_{w,avg}$±0.5, before (a,c) and after the correction for the average M_w offset and the SRF (b,d).

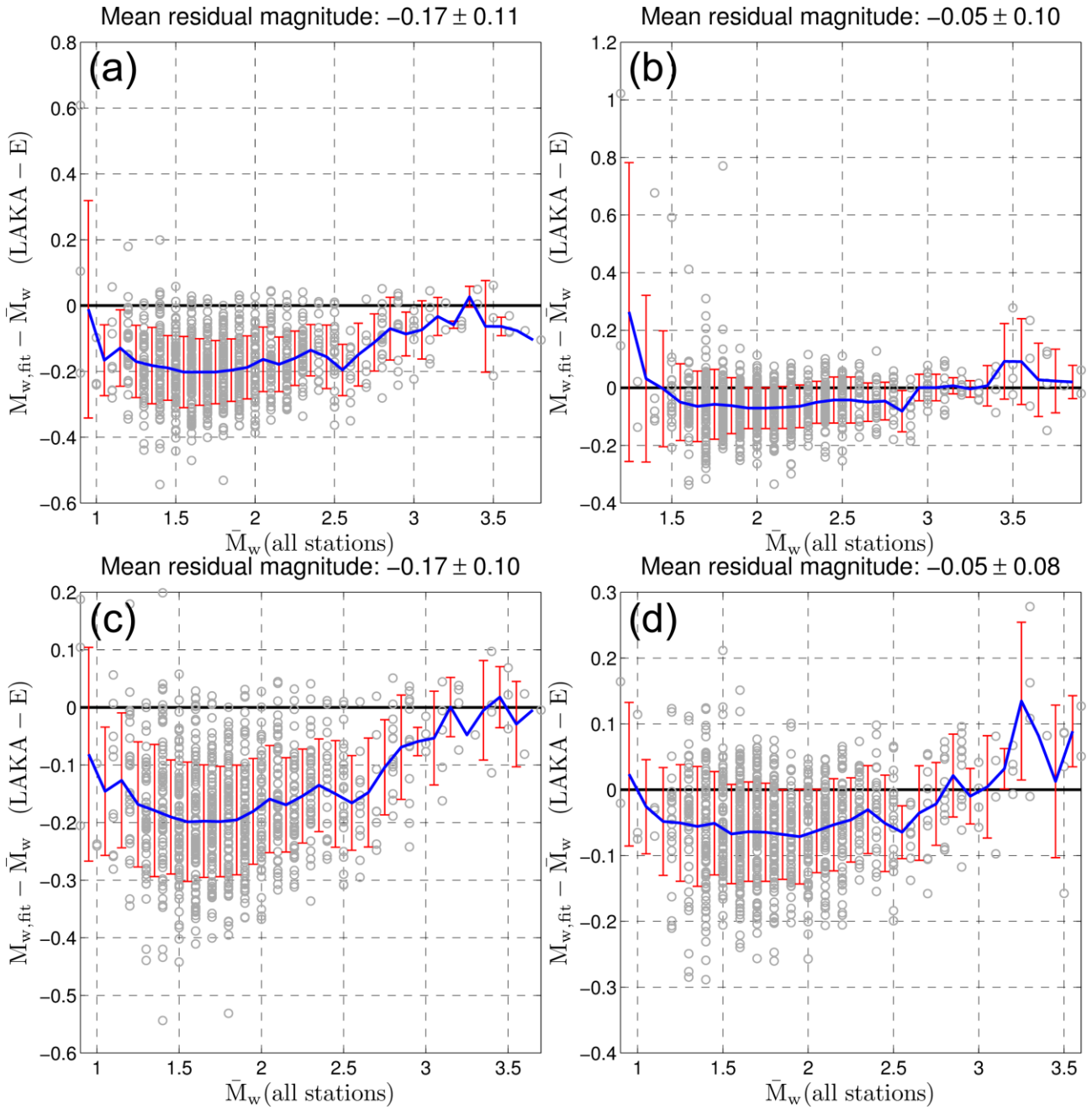

Figure 3B.8: Differences between M_w derived by spectral fit on the E-W component of station LAKA and the respective trimmed, weighted mean M_w from all stations for the dataset of the 2013 Helike swarm using model #4, a-b) with M_o free to vary according to Table 3.2, c-d) with M_o restricted within $M_{w,avg}$±0.5, before (a,c) and after the correction for the average M_w offset and the SRF (b,d).

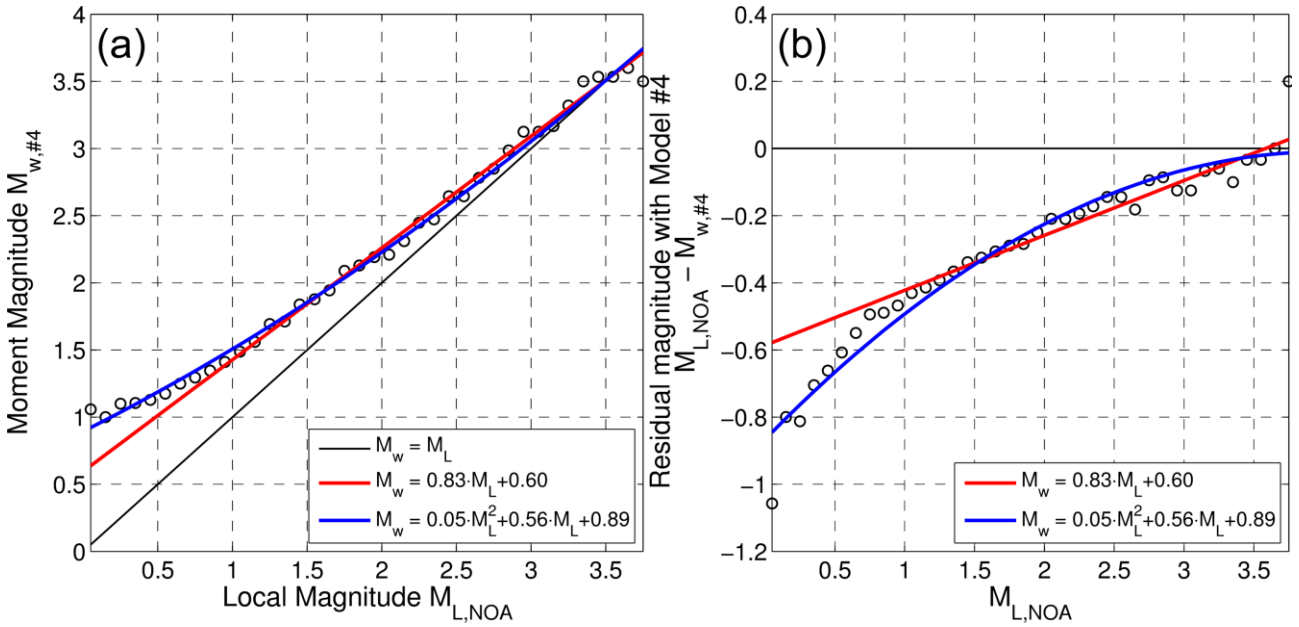

Figure 3B.9: a) Linear (red) and quadratic polynomial (blue) relations between the moment magnitude $M_{w,\#4}$ derived from Model #4 and the respective local magnitude $M_{L,NOA}$ from the database of GI-NOA, for the 2013 Helike swarm, b) same as (a) but in the form of difference $M_{L,NOA}$-$M_{w,\#4}$ (as in Fig. 3.16d).

Appendix 4A

Filtering out gaps in waveform data

In procedures which involve processing and analysis of digital waveform data, the existence of gaps can be a major issue. Gaps can be systematic or sporadic, in various lengths and occurring at different offsets on different components of the same seismological station (Fig. 4A.1a,b). They may be caused by connection or re-transmission problems in real-time telemetry, power failures or digitizer malfunctions. During the application of the HADAES method in Section 5.4, this issue had to be eliminated before performing either signal detection or master-event association with slave-events. The main problem is that during the data processing, gaps are primarily replaced by zeroes in the original waveforms. However, the data amplitudes usually have a non-zero mean and the zero-padded data gaps appear as step functions which are as large as the mean amplitude offset. When Butterworth filtering is applied, both gaps and their neighboring data are transformed into pulses of significant amplitude due to the Gibbs phenomenon (Fig. 4A.1c). This can lead to three types of problems:

1. False positive during the signal detection procedure, as the artificial pulses may affect the STA window and be registered as a trigger.
2. When these pulses are cross-correlated they may result in significant values of $XC_{\max}$, M_{coh} and $D_{\max}$. Consequently, a large number of these false signals may be grouped in a multiplet.
3. In rare cases, these false multiplets may be erroneously associated with a master-event (especially if there are also gaps in the master-event waveforms), leading to a false assignment of P- and S-wave arrival-times.

All these issues can be eliminated by smoothing out the gaps before further processing the waveform data. The following method has been applied in the framework of the present study:

Gap detection

Gap patterns in a segment of waveform data can be identified as a continuous sequence of exact amplitude values. In a more generic case, if the data have been detrended by the removal of their mean, the value which corresponds to the gaps may be non-zero. A histogram is performed to measure the frequency of each unique amplitude value in the raw waveform. The most frequent value is considered as a possible "gap-value". The waveform segment is then examined for sequential samples with the aforementioned gap-value. Blocks of at least three sequential samples with this value are registered as "gap blocks". All other segments are labeled as "data blocks". Optionally, small segments of one or two samples can be replaced by the mean value of their neighboring samples (which differ from the "gap-value") in case they are, indeed, small gaps.

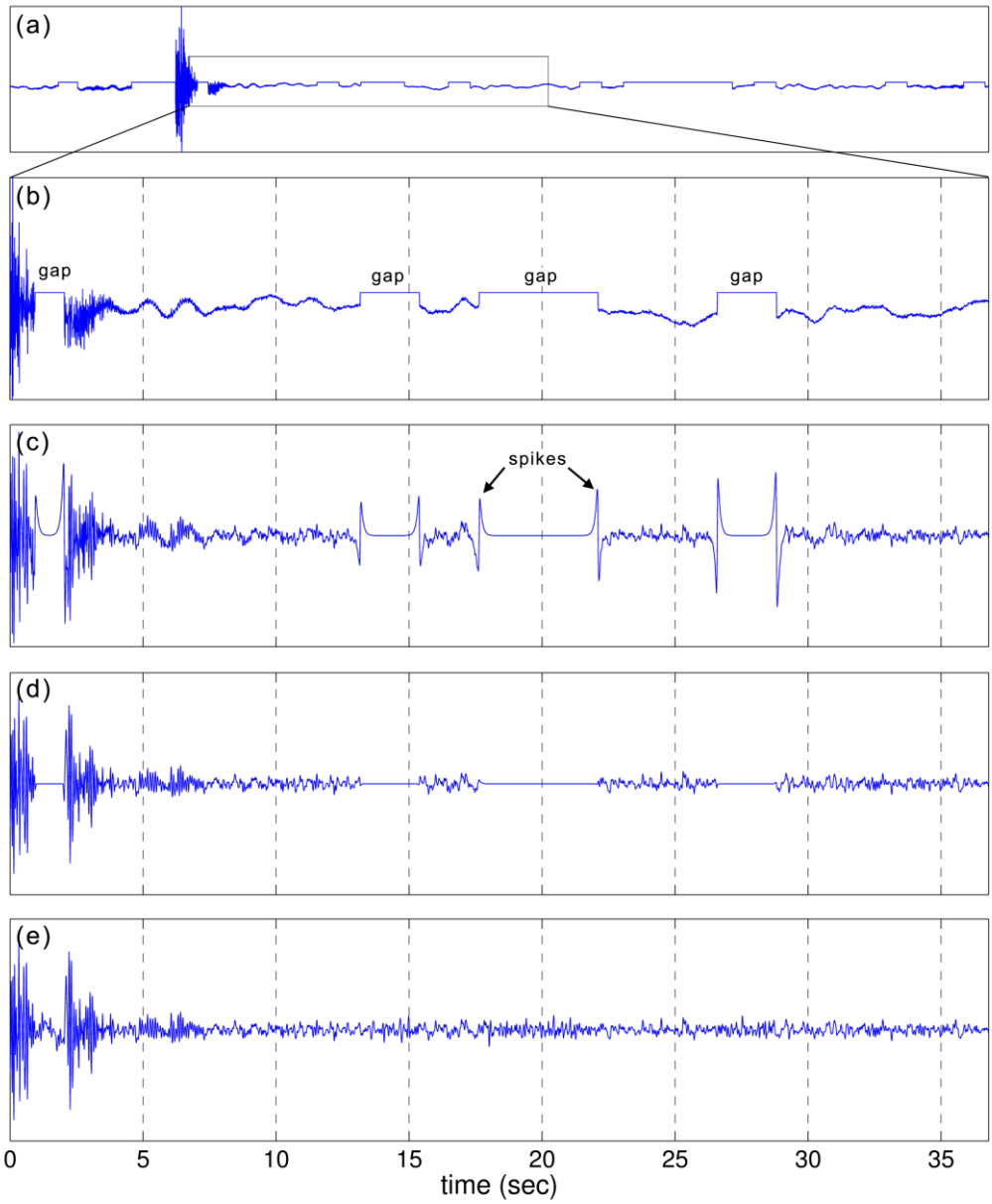

Figure 4A.1: (a) gap-riddled, unfiltered seismic waveform recording, (b) zoom on the rectangle of panel (a), the gaps are replaced by a constant amplitude value, e.g. zero, (c) simple filtering between 2-15 Hz with emphasis on the spike artifacts at the edges of the gaps, (d) smoothed gaps, filled with reverse tapering to enable cross-correlation procedures, (e) smoothed gaps, filled with Gaussian noise to enable the STA/LTA signal detection procedure.

Gap reduction

A first attempt to minimize the influence of gaps in data is performed by replacing the gap blocks with values which would introduce a smaller step function in the data. The median of data blocks could be considered, but it may be unsuitable when the raw data includes significant low frequency spectral content. A better solution is the interpolation (or extrapolation, if the gap is at the boundaries of the data segment) of the nearest-neighbor value. While this minimizes the step at the edges of each gap block with its immediate neighboring data, it may also introduce a step in the

middle of the gap block, if the data values at its two ends differ significantly. Afterwards, a copy of the whole data segment is smoothed e.g. with a moving average of ~50 samples, and the gap blocks of the original waveform are replaced by the smoothed values before filtering.

Reverse tapering or additive noise

The final step of the gap-filtering procedure depends on the type of processing that is about to follow. At this point, the application of a Butterworth filter already exhibits a significant improvement over the original waveform, with minimal effect at the edges of the gaps on the data blocks. However, the influence of the gaps themselves can be further reduced by:

Reverse-tapering on the gap blocks (Fig. 4A.1d). This creates a smooth transition from unity at the edges to zero in the rest of the gap block, which is useful to eliminate the effect of the gaps in the cross-correlation procedures and also nullify some spike artefacts which may have been introduced within the gap at the mid-block step due to the nearest neighbor interpolation.

Superimposing zero-mean Gaussian noise on the gap blocks, with a standard deviation measured by the amplitude distribution of the neighboring data blocks (Fig. 4A.1e). This can be useful in the signal detection procedure, to minimize the effect of a sudden energy increase being detected at the end of a large gap block which might have reduced the LTA significantly. The noise must be added after reverse-tapering has been applied for the elimination of mid-block spikes.

Appendix 5A

Published case studies

5A.1 The 2007 Trichonis Lake swarm

Trichonis Lake is located in Central Greece, at about 30 km N of Patraikos gulf and NW of the western Corinth Rift (Fig. 5A.1). It is the largest natural lake in Greece, with its mid-western part bounded between an E-W trending system of antithetic normal faults and its eastern part, bending SE, formed by another system of NW-SE trending oblique-normal faults. The latter is related to an immature NW-SE sinistral strike-slip structure linked to a possibly triple junction point between

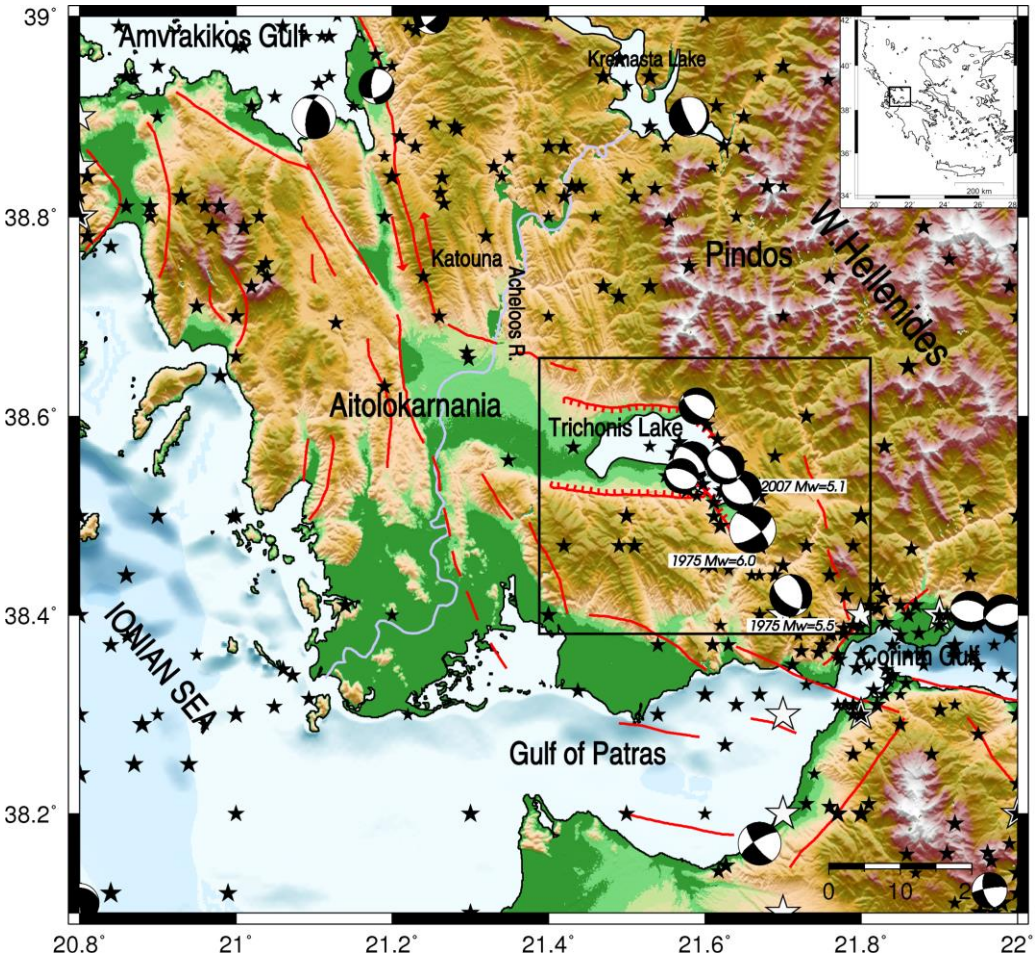

Figure 5A.1: Seismotectonics of the broader area in the vicinity of Trichonis Lake. Figure after Kassaras *et al.* (2014a).

continental Greece, Peloponnese and Ionian Island-Akarnania blocks (Beckers *et al.*, 2015), connecting with the NE extension of the right-lateral strike-slip Andravida fault towards the Rion-Patras fault zone and the E-W normal faulting of the Corinth Rift. Left-lateral, NNW-SSE strike-slip faulting (Amphilochia fault zone) also links the western end of Trichonis basin with Amvrakikos gulf in the NW. This essentially renders Trichonis a typical pull-apart basin (Vassilakis *et al.*, 2011). The strongest earthquake that has been recorded in the region during the instrumental era is the 31 December 1975, with M_w=6.0, at about 3 km SE of Trichonis Lake (Delibasis and Carydis, 1977), a sinistral strike-slip event with a small normal component that relates with the NW-SE zone between Trichonis basin and Nafpaktos (Kiratzi *et al.*, 2008).

On 10 April 2007, three moderate size shallow earthquakes of M_w=4.9-5.1 occurred within a time interval of 7 hours in the area of Trichonis Lake, initiating a swarm that lasted until June 2007. Most of the seismic activity appeared to be concentrated in the NW-SE trending easternmost portion of the basin. One day after the initiation of the sequence, a temporary seismological network composed of 12 portable, 3-component stations was deployed in the epicentral area around the lake for a period of 3 months by the Seismological Laboratory of the University of Athens and the Greek EPPO (Earthquake Planning and Protection Organization), with the purpose of better constraining the location, geometry and kinematics of the activated structures. The relocation procedure, clustering, spatiotemporal analysis and composite focal mechanisms determined for the swarm are mainly presented in the present section. A complete account on the results has been published in the work of Kassaras *et al.* (2014a).

5A.1.1 Location - Relocation

More than 1600 earthquakes were located with HYPOINVERSE (Klein, 2002) using an optimized 1D local velocity model that has been determined using a selected subset of the best located events (Kassaras *et al.*, 2014a) while magnitudes, M_d, were calculated based on the signal duration and an empirical relation (Kaviris *et al.*, 2007). A subset of 1640 earthquakes were selected for the determination of multiplets and relocation. The catalogue P- and S-wave travel-times, their observation weights and their respective cross-correlation measurements are the direct input for the double-difference relocation algorithm, HypoDD (Waldhauser & Ellsworth, 2000) which is used to minimize relative errors mostly due to unmodeled velocity structure and arrival-time reading errors. For the 2007 Trichonis Lake swarm, the combined cross-correlation matrix was constructed using measurements from four different reference stations (avar, kers, lith, thrm) for 1564 events that occurred between 11 April 2007 and 3 July 2007. The usage of multiple stations was required in order to cover some data gaps, as well as to provide more reliable similarity values for the events of the westernmost cluster, whose epicenters are closer to the kers station. After calculating all cluster configurations for the complete range of threshold values, the optimal one was found at C_{th}=0.73. This resulted in 127 multiplets, containing a total of 1093 correlated events. Most of these clusters consist of less than 5 events, while 6 of them contain more than 20 events. The largest multiplet is composed of 367 events (Fig 5C.1, CLID:6).

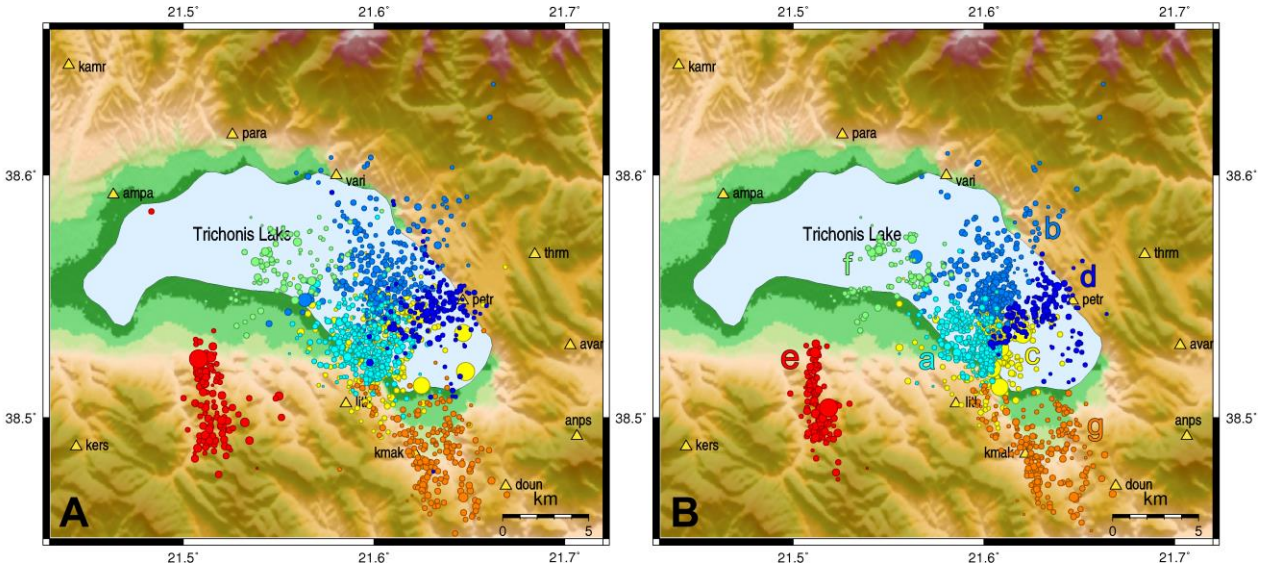

Figure 5A.2: Epicenters of aftershocks A) before and B) after relocation with HypoDD. Colours and lower-case letters (Panel B only) represent the 7 major spatial clusters that could be discriminated. Events which were not successfully relocated are not presented in panel (A). Figure after Kassaras *et al.* (2014a).

The relocation process was divided in two sets of 7 iterations each, minimizing the double-difference residuals for pairs of events at each station using the conjugate gradient method (LSQR) employed in the HypoDD inversion scheme. In the first one the procedure mainly uses the catalogue data, while the *a priori* weights of cross-correlation data are reduced to a minimum non-zero value required to maintain the links between correlated events. This achieves a rough relocation of the main bodies of the spatial clusters. In the second stage the *a priori* weights of the cross-correlation data are maximized at the expense of the corresponding values for the catalogue data. A re-weighting scheme that removes links between pairs of events according to their inter-event distance and the RMS error of their travel-time differences is also used. The latter set of iterations manages to relocate the strongly correlated events locally, closer to their multiplet's centroid, providing higher detail in the spatial distribution. A total of 1490 events (representing about 90% of the initial solutions) were successfully relocated, including 66 events prior to 11 April 2007 relocated independently with regional catalogue data only, using the SVD iterative method of HypoDD.

5A.1.2 Spatio-temporal analysis

Spatial clustering was performed on the 3D spatial distribution of hypocenters using Ward's linkage and imposing a specific threshold that would result in 7 spatial clusters, after consulting Mojena's plot. The acquired HypoDD solutions (Figs 5A.2B and 5A.3B) suggest a significantly denser foci distribution compared to their initial locations (Figs 5A.2A and 5A.3A). The hypocentral cross-section at N50° direction (Fig. 5A.3B) reveals the tight clustering achieved with the double-difference procedure. Following the pattern of the relocated events, shallow seismicity (<2 km) is either excluded or moved deeper. Deeper foci do not exceed 15 km in depth. Certain trends in the

spatial distribution identify three zones. A main NE-dipping (spatial clusters a, c, f, and g), an antithetic SW-dipping zone (spatial clusters b and d), crosscutting the main NE-dipping zone at ~7 km depth, and a third westernmost zone (cluster e) spatially separated from the others, restricted between 8 and 11 km depth.

The spatial distribution of the multiplets reveals that the largest one (CLID:6 in Fig. 5C.1) includes many of the events that were separated in different spatial clusters (labeled a and b in Figs 5A.2 and 5A.3). Excluding multiplet #5 of the western and mostly apart spatial cluster "e", the other large multiplets (#1, #2 and #3) are close together. However, as shown in Fig. 5C.1, their waveform recordings on the vertical component (at station lith) are significantly different from those of multiplet #6. The latter can be attributed to differences in hypocentral locations and focal mechanisms. Multiplet #2 mostly includes events of the SW-dipping cluster "d". It is also worth noting that the largest multiplet of the southernmost spatial cluster "g" was composed of only 10 events (hence not shown in Fig. 5C.1). Several smaller multiplets comprise this cluster, which indicates a higher level of dissimilarity between event waveforms compared to the others. This may be due to the fact that this spatial cluster is less concentrated around its centroid than the others and is composed of several smaller clusters which are separated both horizontally (as seen in Fig. 5A.2) and vertically (Fig. 5A.3). In addition, this cluster has a wider depth range than the others, spreading between 3 and 10 km.

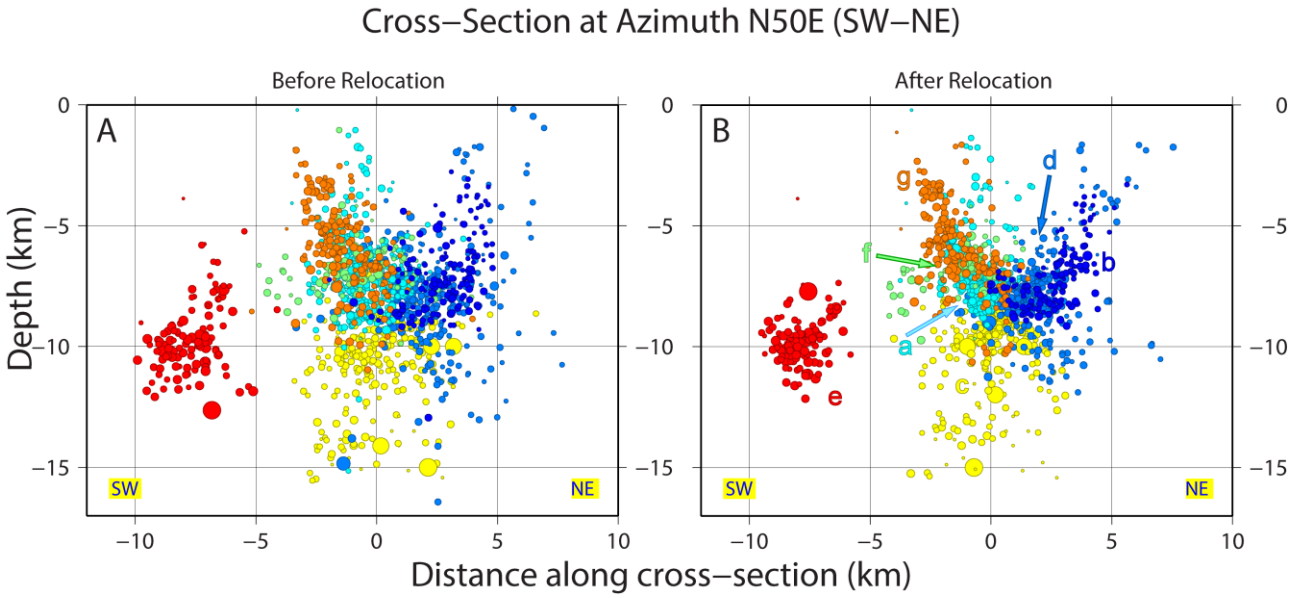

Figure 5A.3: Cross-section of aftershocks at N50°E (SW-NE), centered at 38.5250°N, 21.6096°E, A) before and B) after relocation with HypoDD. Colours and lower-case letters represent the 7 spatial clusters that were distinguished and correspond to the same colour/letter labels as shown in Fig. 5A.2B. Events which were not successfully relocated are not presented in panel (A). Figure after Kassaras *et al.* (2014a).

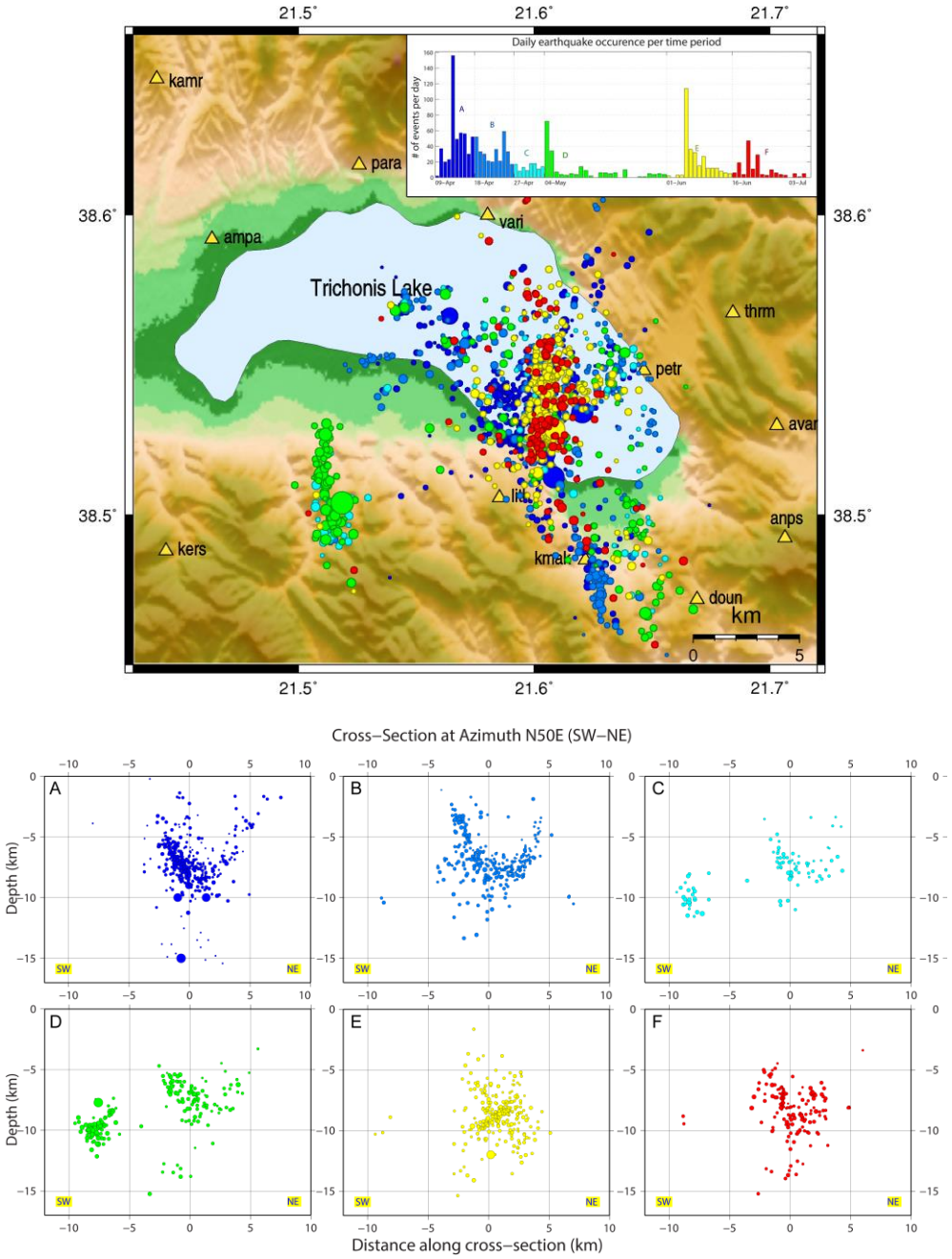

Figure 5A.4: (top) Map of temporal evolution of the relocated events with different colours representing the 6 consecutive time periods in which the aftershock sequence has been divided. The embedded histogram shows the daily number of earthquakes per time-period (A-F), (bottom) Cross-section of the aftershocks at N50°E (SW-NE), centered at 38.5250°N, 21.6096°E. Panels A-F represent the 6 periods: A) 10-18 April 2007, B) 18-27 April 2007, C) 28 April – 4 May 2007, D) 4-30 May 2007, E) 1-16 June 2007 and F) 17 June – 3 July 2007. Figure after Kassaras *et al.* (2014a).

The temporal distribution of the swarm (Fig. 5A.3) reveals that there have been several stages in the evolution of the sequence with three major outbursts of activity occurring after large events (periods A-C, D and E-F in Fig. 5A.4). The first phase (A) covers the period between 10 and 18 April 2007, following the occurrence of the three moderate events a larger one (M_w=4.2) on 15 April. The activated part spreads through most of the activated zone that is located under the lake, including

multiplet #6 or spatial cluster “a”. During the next period B (18-27 April) the seismicity beneath the lake has migrated to the eastern part that includes multiplet #2 or cluster ”d” but also at the NW part of the lake including spatial cluster “f”. Period C (28 April – 4 May) has only a few events, mostly on the NE part of cluster “g”, but also displays some precursory micro-earthquakes in the westernmost cluster “e” whose outbreak took place during period D (4-30 May), following an M_d=3.1 event on 4 May, almost one month after the beginning of the swarm. Period E (1-16 June) is the second most seismically active in the entire sequence due to the occurrence of the largest earthquake on 5 June 2007 (M_w=4.8). It spreads across the central part of the large multiplet #6 and includes some of the deepest events beneath the lake with the activation of both the NE-dipping and the antithetic SW-dipping faults (Fig. 5A.3). During the last period F (17 June – 3 July) the seismicity on both faults has migrated to shallower depths.

5A.1.3 Composite focal mechanisms

A total of 173 focal mechanisms were determined for events with $M_d \geq 2.0$ after manual measurement of the first motion polarities (FMP) in the stations of the local network (Kassaras *et al.*, 2014a). The relocated foci and the determined local velocity model were considered for the values of station azimuths and seismic ray take-off angles. Take off angles were computed based on the custom 1D velocity model and the relocated hypocenters provided by HypoDD. In this application, the fault plane solutions were manually determined by manual adjustment of planes that satisfied all FMP or taking into account the uncertainty of some measurements that could indicate a proximity to a nodal plane. To reduce the effect of focal mechanisms uncertainties, the selected earthquakes were first grouped according to their corresponding spatial cluster. A temporary mean focal mechanism that satisfied most of events’ first-motion polarities was considered by visual inspection and was used to aid the procedure of individual solution determination in case of events with few available data. In some cases more than one mean focal mechanism was required for the same spatial group, as for cluster “g” which had to be separated in two sub-clusters, g_1 and g_2.

The composite focal mechanisms presented in Fig. 5A.5 have been calculated for each cluster by summing the normalized moment tensors of each event’s fault plane solution, multiplied by an appropriate weight, and then calculating the nodal planes and axes from the resulting moment tensor. Weight multipliers can either be all unity (in that case every solution will be equally considered) or a function of the event’s magnitude or the number of polarities used to constrain each individual solution. This is similar to the method described in Section 2.4.1, but without considering S-wave polarization or S to P amplitude ratio. After calculating the mean focal mechanisms using each of the aforementioned weighting schemes, the one which was more consistent with the observed polarities of the first motions was selected.

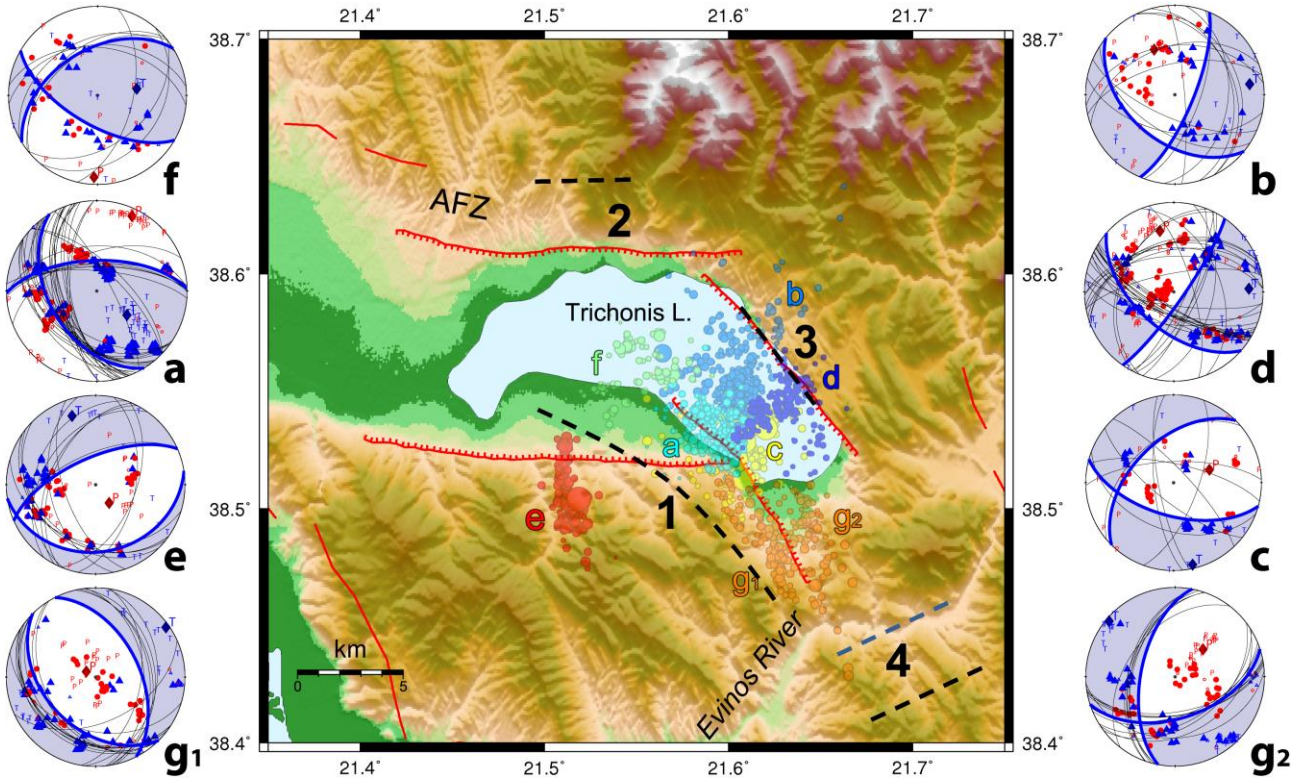

Figure 5A.5: Traces of the activated structures (black dashed lines; 1-4, see text) when extrapolated to the surface, and composite focal mechanisms. Nodal plane projections drawn with thick lines on the focal spheres denote the averaged solution for each spatial cluster (labeled a-f and g1, g2 next to their corresponding relocated epicenters). Filled circles on the focal spheres indicate all observations of dilatational first motion while triangles denote observations of compressional first motion. Individual solutions' P- or T-axis traces are marked with the letters P and T, respectively, while the averaged solution's axes are represented by a filled diamond symbols. Figure after Kassaras *et al.* (2014a).

The types of the obtained focal mechanisms are predominantly normal and strike-slip, however some earthquakes exhibit reverse faulting. For the special case of the two sub-groups "g_1" and "g_2" different types of normal mechanisms could be discriminated, one striking NW-SE and another striking roughly NE-SW. The variability of faulting mechanisms in such a small volume is supported by the lack of large multiplets, as mentioned earlier, which could indicate a high degree of variability in the parameters of the activated secondary fault 4 in a strongly fractured zone.

5A.1.4 Discussion

The 2007 seismic swarm in Lake Trichonis has offered an opportunity to investigate the geometry of the active faults in this tectonically complex region, which combines two normal faulting systems, striking E-W and NW-SE, respectively, with a likely high degree of obliqueness due to the NW-SE lateral strike-slip faulting at the SE of the lake. The major feature of the hypocentral spatial distribution can be described by two conjugate, NW-SE trending structures, likely related to the respective basin that is responsible for the bend of the eastern portion of the lake towards SE. These are also possibly listric or kinked, as their dip apparently reduces from ~85° at shallow depths (3-

5km) to about 60° at middle depths and 35° at larger depths (7-10km). SW-NE extension or NW-SE sinistral strike-slip faulting would be expected in this region. However, its interaction with the E-W trending basin, mid-west of the lake, possibly creates a more complicated fault network and likely a local stress field which differs from the regional one and can also be significantly perturbed after the occurrence of major events.

Stress-tensor inversion (Kassaras *et al.*, 2014a) shows that the prevailing extensional stress axis in the activated region beneath the lake is oriented in a WSW-ENE direction near the eastern bank, almost perpendicular to the major axis of the Hellenides, and gradually turns WNW-ESE in the middle to NW-SE near the SW coast, while both P- and T-axes of the individual focal mechanisms have relatively shallow plunge angles, indicating significant oblique-slip. However, the composite focal mechanisms of groups "b" and "d" that correspond to the SW-dipping feature have a respective nodal plane that would indicate right-lateral, rather than sinistral oblique faulting, opposite to what would be expected taking into account the NW-SE sinistral slip faulting supported by the 1975 event (Kiratzi *et al.*, 2008).

Focal mechanisms determined by regional body-wave modeling for the 5 largest events of the swarm Kassaras *et al.* (2014a) indicate normal to oblique-normal faulting, compatible with either a south-dipping fault with a small right-lateral component or a ENE- to NE-dipping fault with a sinistral-slip component. Reverse focal mechanisms are mostly associated with seismicity near the SW bank of the lake, but a few were also observed in around the middle of the lake (Fig. 5A.5). In the separated group "e", despite the variability, the T-axis indicates N-S extension at a relatively shallow angle, compatible with E-W striking normal faulting observed at the north, possibly related to structure #2, related to the Agrinio fault zone. Its temporal evolution shows a tendency for northwards migration, towards structure #2 and shallower depths, indicating dip-slip that is further supported by its N-S spatial elongation. In group "g" the P-axis is at a generally steep angle of ~60° while the T-axis is sub-horizontal in a NW-SE direction. Its eastern portion (g_2) can be roughly associated with structure #4 (parallel to Evinos fault) while the western half (g1) is mostly compatible with structure #1. The latter is probably the extension or a sub-parallel structure to the one that hosted the 1975 M_w=6.0 event (Kiratzi *et al.*, 2008) as well as the three largest events of 10 April 2007 with M_w=4.9-5.1 (Kassaras *et al.*, 2014a). This fault, however, is not the one that bounds the south-eastern bank of the lake but offset by about 3 km SW. The two structures, #1 and #4, likely interact with each other at depth, increasing the complexity of the small-scale fault network and causing local perturbations in the stress field.

During the 2007 seismic swarm, the activity beneath Trichonis Lake has been generally continuous, especially at depths between 8 and 10 km, but some horizontal migrations at shallower depths were also observed, rather related to stress redistributions. The secondary outbreak of Period D was followed by a relative quiescence, lasting for about one month before the major M_w=4.8 event of 5 June 2007. Although migration effects are not strong, as with other seismic swarms in the literature, fluids may likely play a key role either in its initiation or in its evolution. The interaction between major faults that bound the lake at different orientations provides a complex network of pre-existing fractures. While this could create diffuse deformation, the observed focal mechanisms, when grouped by spatial cluster, have a certain degree of homogeneity. Major events cause perturbations in the stress field which in turn trigger slip in neighboring structures. Coulomb stress transfer

calculations (Kassaras *et al.*, 2014a) showed that the activated area of the 2007 swarm lies in a positive stress lobe of the 1975 earthquake while stress redistribution caused by the 3 major events of 2007 can explain the triggering of deeper activity in the later stage of the swarm (Period E).

The variety of focal mechanisms observed during the 2007 swarm in Lake Trichonis makes sense when the region is examined at a larger scale. In contrast with the Corinth Rift, which is trending E-W and is dominantly normal with little contribution to lateral slip, Trichonis basin is much smaller and bound between larger NNW-SSE strike-slip fault zones. Kassaras *et al.* (2016) showed that in terms of the 3D stress field, Lake Trichonis lies in a transition zone between the normal faulting of the Corinth Rift and the left-lateral strike-slip zones between the latter, Amvrakikos Gulf as well as the right-lateral Cephalonia-Lefkada Transform Fault zone further west. Similar to the extensional vector of the strain field as derived by differential GPS measurements (Chousianitis *et al.*, 2015), the σ_3 minimum principal stress-axis at shallow depths has a generally low plunge angle and is directed N-S in the Corinth Rift, then rotates to NE-SW near Trichonis while further west it becomes oriented NW-SE. However, the study of the 2007 swarm revealed that, on a local scale, NW-SE extension is also present at the south-eastern part of the lake while the localized complexity of the stress field apparently produced some reverse slip events on parts of pre-existing structures as well.

The activity of group "e" may also be important, since it is likely associated with the major south-dipping Agrinion fault zone. Continuous monitoring of seismic activity by the Hellenic Unified Seismological Network has shown that this particular region has been activated by short-lived clusters or swarms in several cases, such as in September 2008 and July 2016. Other regions around the lake have exhibited clustered activity by the end of February 2011 and June 2013 at the SE side and November 2015 west of the lake. However, the strongest events have had magnitudes between 3.5 and 3.8 and the increased activity lasted for a few days, at most. If the E-W Agrinion fault zone is locked on most of its part, accumulating stress, it could have the potential to generate a major event, filling another possible gap in the catalogues of the instrumental era.

5A.2 The 2011 Oichalia swarm

The region of Messenia, SW Peloponnese, is mostly characterized by N-S trending normal fault zones (Armijo *et al.*, 1992), owed to the dominant E-W extensional deformation that has been observed by GPS (e.g. McClusky *et al.*, 2000). It has been the site of the major M_s=6.0 earthquake that struck the city of Kalamata on 13 September 1986, also characterized by N-S normal faulting (Lyon-Caen *et al.*, 1988). In the period between August and December 2011, a seismic swarm took place in the vicinity of Oichalia, north Messenia (Ganas *et al.*, 2012; Kassaras *et al.*, 2014b; Fig. 5A.6), with the largest earthquakes having magnitudes between 4.6 and 4.8. The swarm was recorded and detected by the regional stations of the Hellenic Unified Seismological Network (HUSN). As it seemed not to be a short-lived occurrence of clustered seismicity, the area was later reinforced with 7 temporary seismological stations by a joint effort of the National and Kapodistrian University of Athens and the Geodynamics Institute of the National Observatory of Athens. The temporary network remained operational between 14 October 2011 and January 2012. In the current

section, the spatiotemporal evolution and seismotectonic interpretation of the 2011 Oichalia seismic swarm are briefly described. An extensive study has been presented by Kassaras *et al.* (2014b).

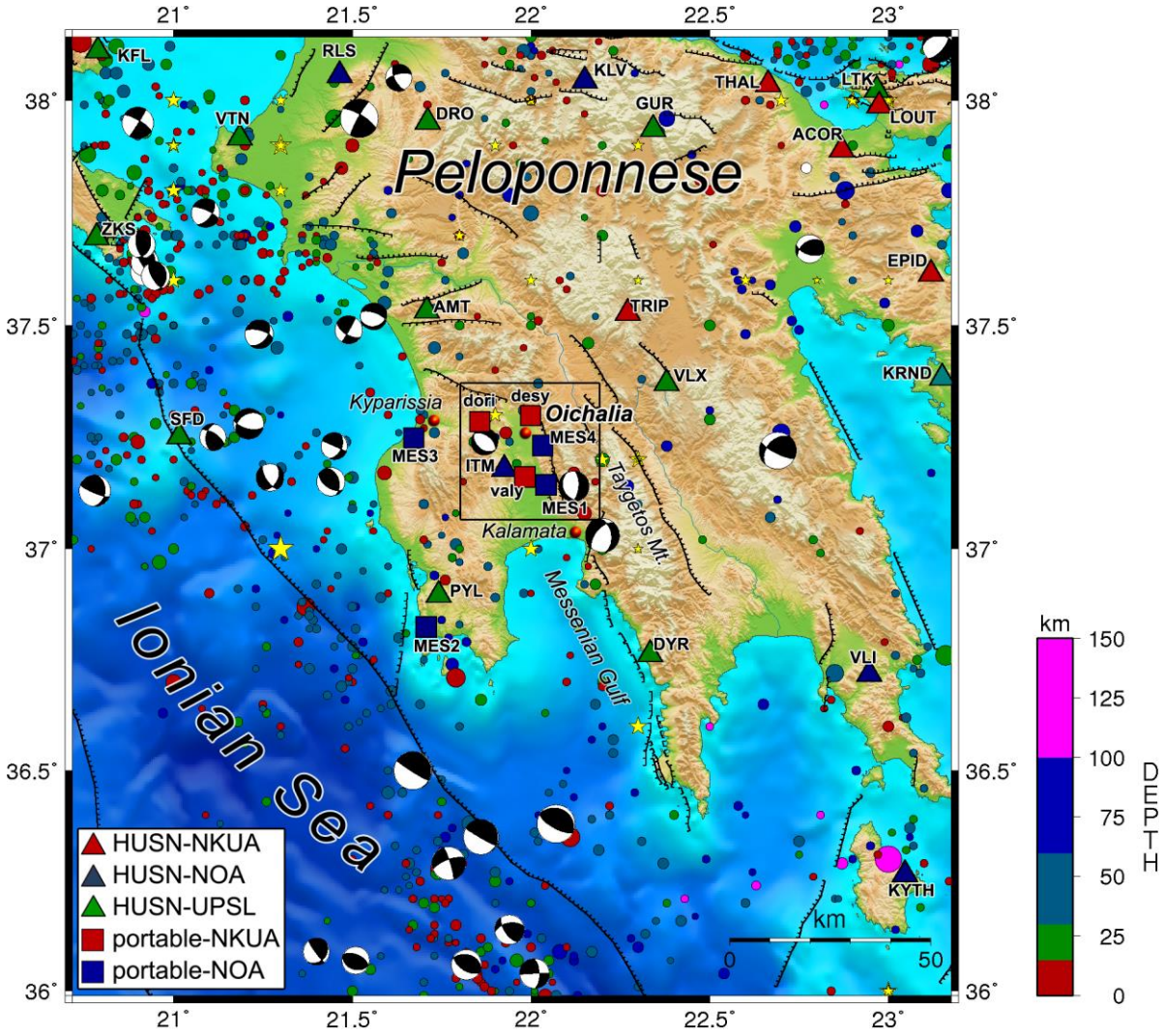

Figure 5A.6: Seismotectonic map of Peloponnesus. Stars represent epicenters of historical earthquakes that occurred before 1900 (Papazachos and Papazachou, 2003). Solid circles are earthquakes of the instrumental era, with origin time after the year 1900 ($M_s \geq 4.0$, Makropoulos *et al.*, 2012). Focal mechanisms are CMT solutions (1976-2012) for events with $M_w \geq 5.0$. Permanent (HUSN) and temporary seismological stations are represented by solid squares and triangles. Fault lines are from Lyon-Caen *et al.* (1988) and Armijo *et al.* (1992). Figure modified after Kassaras *et al.* (2014b).

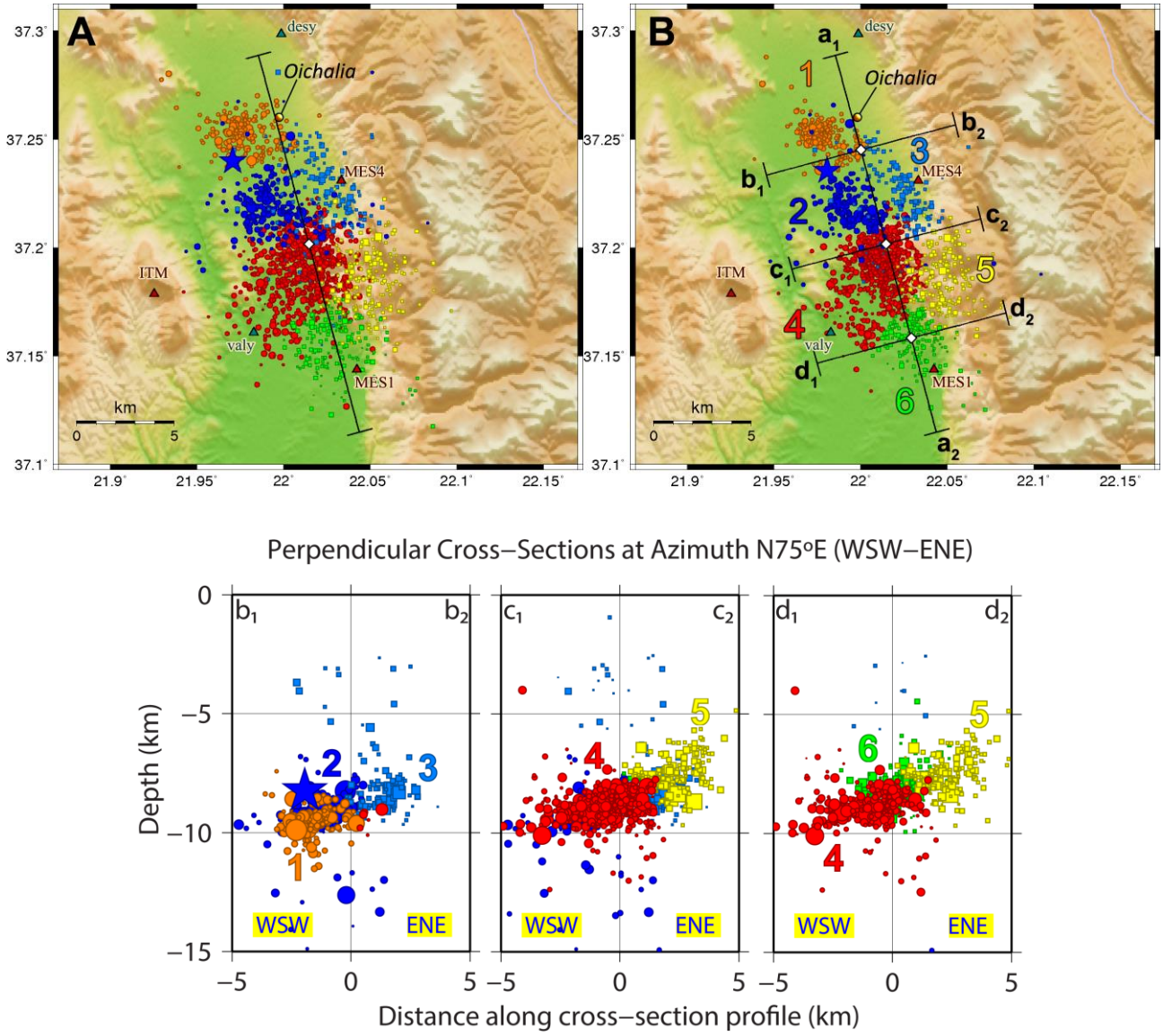

Figure 5A.7: (Top) Epicenters of the seismic swarm sequence A) before and B) after relocation with HypoDD. Local stations are represented by triangles. (Bottom) Cross-sections along the profile lines b_1-b_2, c_1-c_2 and d_1-d_2, drawn at N75°E azimuth, perpendicular to the main axis of the swarm's distribution. The star denotes the major event of 14 August 2011. Colours and numbers (Panel B only) correspond to 6 major spatial Groups that could be distinguished. Figure modified after Kassaras *et al.* (2014b).

5A.2.1 Relocation - Clustering

A total of 1615 events were manually analyzed and located using a custom 1D velocity model that was determined by minimizing the average RMS errors and location uncertainties for a subset of selected events (Kassaras *et al.*, 2014b). The differences between the custom model and a regional model for the broader area of Peloponnese (Hatzfeld *et al.*, 1990), especially in the distribution of focal depths, are striking (Fig. 5C.10a,b).

Station ITM, at an average epicentral distance of ~7km, was selected as a reference station for the primary cross-correlation procedure, being the closest station of the HUSN to the swarm that was

operational during the whole period of study. Nearest-neighbor linkage was applied and multiplets were formed using the optimal correlation threshold $C_{th} \equiv C_{opt.th}$=0.75 which resulted in 998 events contained in 223 multiplets (with two or more events). A sum of 406 events belongs to the 19 largest multiplets of size ≥10, with more than half of them included in multiplets of size ≥20. The uncertainties of the hypocentral distribution were further reduced by applying the relocation algorithm HypoDD (Waldhauser & Ellsworth, 2000), incorporating both catalogue and cross-correlation differential travel-times. The data between the two periods (before and after the installation of the temporary local network) intertwine through catalogue links of the observed travel-times from the HUSN network and cross-correlation measurements from station ITM.

The parameterization of the configuration files for HypoDD was determined by trial-and-error, aimed to achieve smoothly stepped relocation with minimal event rejection and small origin shift. The HypoDD procedure was divided in 4 sets with 10 steps in total. The sets begin with low a priori weight on the cross-correlation data (CC) and high weight on catalogue data (CT). Then, on the later stages, the CC weights gradually increase with decreasing CT weights. At the same time, stronger re-weighting thresholds are being applied on distance between linked event-pairs and residuals on both types of data. This achieves a crude relocation of the whole distribution in the first sets and refined relative relocation concentrated on multiplets at the later sets. Starting with 1516 sufficiently linked events, 1480 were successfully relocated, representing 91.6% of the full catalogue. The mean origin shift was ~22m, which is important, as it shows that there is only minimal systematic shift of the hypocenters and that the events' locations were mostly concentrated closer to the main body of the original distribution or to their cluster's centroid. This result is displayed in Figs 5A.7B and 5C.10d in comparison to the respective initial locations (Figs 5A.7A and 5C.10c).

The 3D distribution of the relocated events was divided into 6 spatial groups (labeled as shown in Figs 5A.7B and 5C.10d) using Ward's linkage and an appropriate threshold for the fusion levels. Concentrations within individual clusters during the relocation procedure are mainly due to strongly correlated events that form multiplets. A least-squares best-fit plane has been calculated from the 3D distribution of the relocated hypocenters, striking N177°E with a dip angle ~W18°. The cross-sections of Fig. 5C.10c,d, which are almost parallel to the strike of the aforementioned plane, also indicate that the seismicity tends to be deeper in the North than in the South, although this does not imply that the fault is dipping NNW. The total length of the spatial distribution is ~18 km in the NNW-SSE direction.

Furthermore, the major M_w=4.8 event of 14 August 2011 which started the sequence, is located at a gap in the spatial distribution between Groups #1 and #2 in the northern tip and has been classified to the latter one. The gap around the major event is consistent with the rupture of an asperity that caused redistribution of stress in its neighboring region, triggering Groups #1 and #2. Other identifiable gaps are separating the Groups #2 and #4 from the slightly shallower #3 and #5 respectively, but these can't be directly associated with a major shock. Some smaller sub-clusters belonging to #4 also seem to be more detached from the main body of the group. However, following the current clustering hierarchy, a threshold constructing at least 10 spatial clusters would be required for their partition, which was not deemed necessary for the description of the seismic swarm activity.

Fig. 5A.7 (bottom) shows cross-sections of the relocated hypocenters at azimuth N75°E, almost perpendicular to the main direction of the swarm's distribution, at three partially overlapping segments. The low dip angle of the fault is more prominent in its deeper portion, as seen at the northernmost segment (b_1-b_2). In the middle cross-section (c_1-c_2) the shallower Group #5 tends to connect to the rest of the distribution at a higher angle, almost 45°. It is evident from the comparison between the parallel (Fig. 5C.10) and perpendicular cross-sections (Fig. 5A.7) that the distribution is becoming shallower primarily towards ENE rather than SSE, which is consistent with a low-angle fault striking SSE-NNW and dipping WSW.

5A.2.2 Spatio-temporal Distribution

The temporal distribution of the seismic swarm can also be divided in 6 groups that correspond to periods of main/secondary outbreaks in the seismicity (Figs 5A.8, 5A.9 and 5C.11). Period A (14-22 August 2011) with 170 events, begins with the major M_w=4.8 earthquake of 14 August and spatially concentrated activity at the northern part of the distribution, involving almost exclusively the spatial Groups #1 and #2. Period B (22 August – 13 September 2011) with 137 events, is a secondary sequence that follows the M_w=4.1 and M_w=4.0 events of 22 and 23 August, when a more southerly segment of the rupture zone was activated, mostly involving Group #2 but also reaching Groups #3 and #4. The next outbreak (period C: 13 September – 9 October 2011) was triggered by an M_w=4.6 event on 14 September and contains several events with $M_L \geq 3.0$. Seismicity within the spatial Group #5 was also recorded during this period, while the activity keeps spreading towards the South. The next three major events of the sequence (M_w = 4.3, 4.3 and 4.7, respectively, on 10 October 2011) generated the major outbreak that occurred during Period D (9 October – 7 November 2011) with a total of 457 events, ranging mainly at the southern portion of Groups #4 and 5 but also reaching Group #6. During the last two periods (E and F) a couple of spatio-temporal sub-clusters occurred in the northern part (occupying Group #1), induced by an M_w = 4.1 event on 12 November, while the activity in the rest of the rupture zone continues to spread towards the southern end, at the shallower portion of the activated zone.

As far as the 6 largest multiplets are concerned, in the northern and the middle part of the activated zone, two of them (#4 and #5 in Fig. 5C.9) were simultaneously generated at the beginning of the sequence, strongly clustered both in time and space. Later, starting on September 14th and for more than a month, there was sporadic activation of three large multiplets on the southern part, namely #2, #3 and #6 (Fig. 5C.9). The last large multiplet is located in the North (#1 in Fig. 5C.9). It emerged on December 1st after a few pre-shocks, probably triggered by another, smaller spatio-temporal cluster that was activated on November 12th. It is qualitatively different from multiplet #4, which occurred at the beginning of the sequence, as no pair of events with a cross-correlation maximum value over C_{th}=0.75 could link the two of them. The relocated foci of these large multiplets are concentrated in volumes of about 1-2 km diameter, following the general direction and dip of the rest of the swarm's distribution. However, multiplets #1 and #4 appear to be slightly dislocated from the others, mainly because of the gap between these two and multiplet #5.

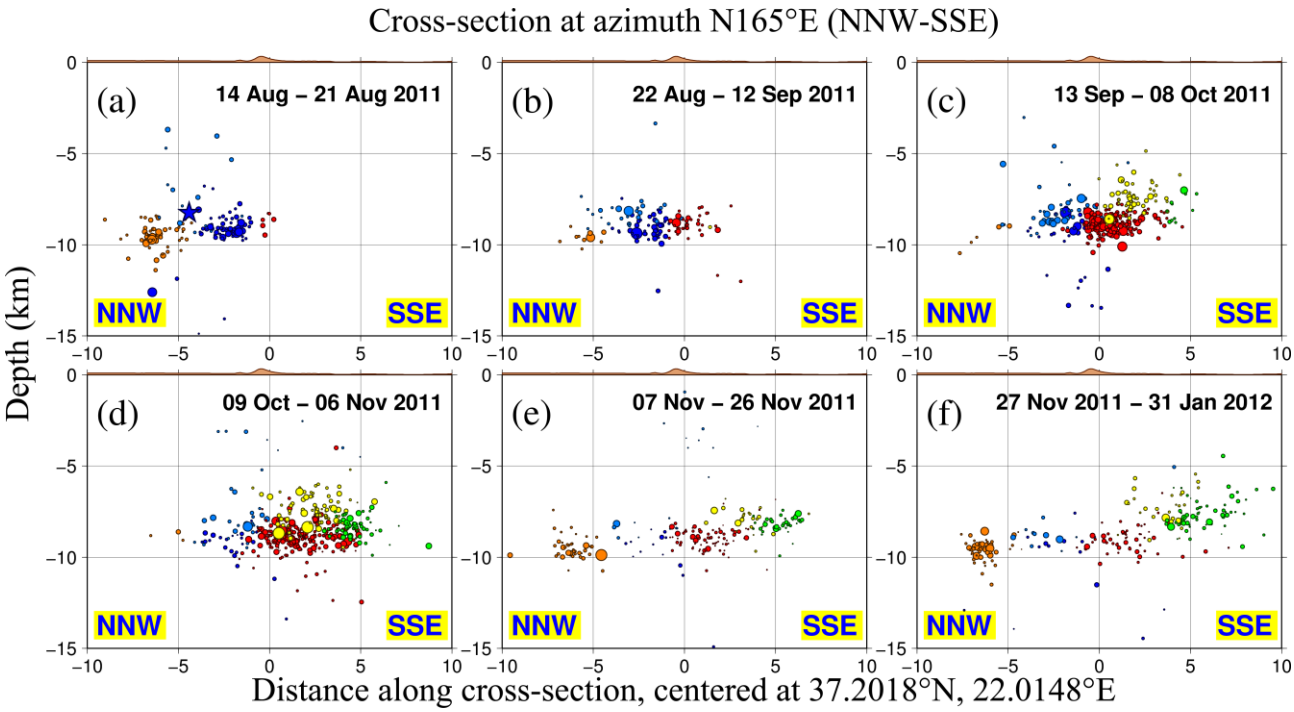

Figure 5A.8: Cross-sections along the a_1-a_2 profile line of Fig. 5A.7B, at a N165°E direction, for 6 successive periods (a-f). Colours represent the 6 spatial Groups.

It is noteworthy that a gradual migration of seismic activity can be observed from the Northern to the Southern part of the rupture zone. Although this is evident from the cross-sections of Fig. 5A.8 it is more clearly demonstrated in the diagram of Fig. 5A.9, which shows the projection of epicenters on a line that passes through the middle of the spatial sequence at N165°E azimuth with respect to the relative origin time (X-axis). The sequence begins with the M_w=4.8 event of 14 August, triggering seismicity in both Groups #1 and #2, then gradually spreads towards SSE, as it starts triggering events from Group #4 and a few in the smaller Group #3. The second outbreak (period C) causes a jump of seismicity in the area of Groups #5 and #6, while activity in Group #2 diminishes. A back-propagation occurs in periods E-F with two small spatiotemporal clusters in Group #1. Fig. 5A.10 shows the evolution of the cumulative number of events per spatial Group, with nearly 600 events while the other groups have a total of 150-200 events. In terms of the total number of events, Group #4 is the largest one. It begins with a small, almost constant seismicity rate and is mainly kick-started by the M_w=4.6 event of 14 September. It also receives a small boost after the M_w=4.7 event that occurred on 10 October in the less populated Group #5. Seismicity in Group #2 decays smoothly, without being significantly affected by major events. Group #6 at the southern end has a generally steady seismicity rate. Group #1, on the other hand, at the northern end, exhibits a more step-like behavior, including the outburst on 12 November, due to an M_w=4.1 event and a smaller one near 2 December.

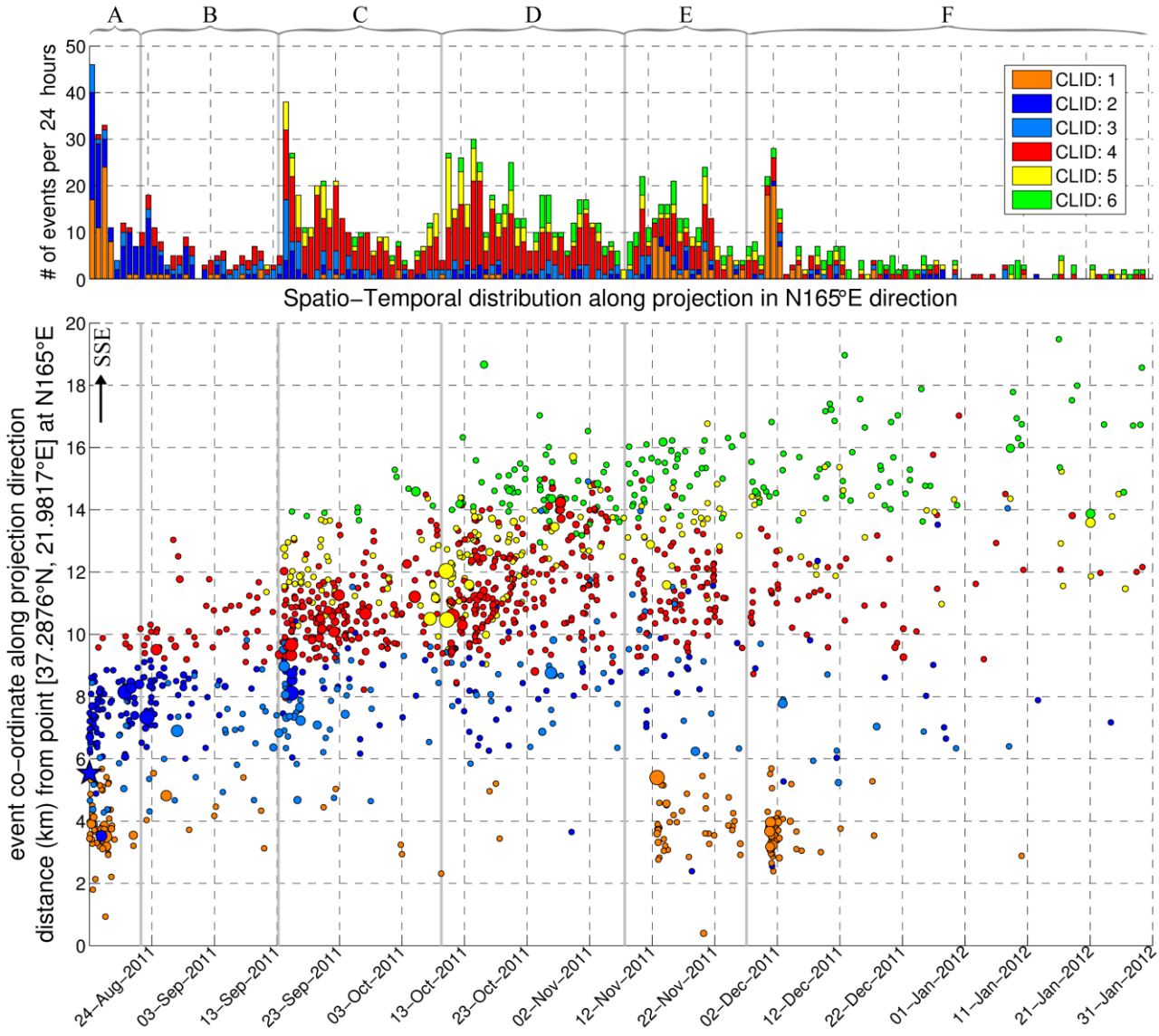

Figure 5A.9: (Top) Stacked histogram of the daily number of earthquakes per spatial Group, represented by different colours, during the 2011 Oichalia swarm. (Bottom) Spatio-temporal projection along the 20km-long, a_1-a_2 profile line (Fig. 5A.7B) at a N165°E direction. The blue star represents the M_w=4.8 event of 14 August 2011. Vertical thick gray lines divide the 6 successive temporal periods, labeled A-F at the top.

The quantitative properties of spatiotemporal migration are presented in the projection of Fig. 5A.11, which is similar to Fig. 5A.9 but without colours for groups. The temporal derivative of the thick parabolic curve drawn through the middle of the distribution represents the migration rate. A linear approximation for the average rate of migration of the seismic activity towards the south during the first 80 days is about 80m/day. At the same time, it appears to ascend to relatively shallower depths in the southern part. Since the first outbreak of 14 August 2011, starting from ~18 August and up to about ~28 October, the seismicity occurs on a migrating active patch, about 6-8km long (~8 km, roughly represented by the 95% confidence bounds drawn with dashed lines) in

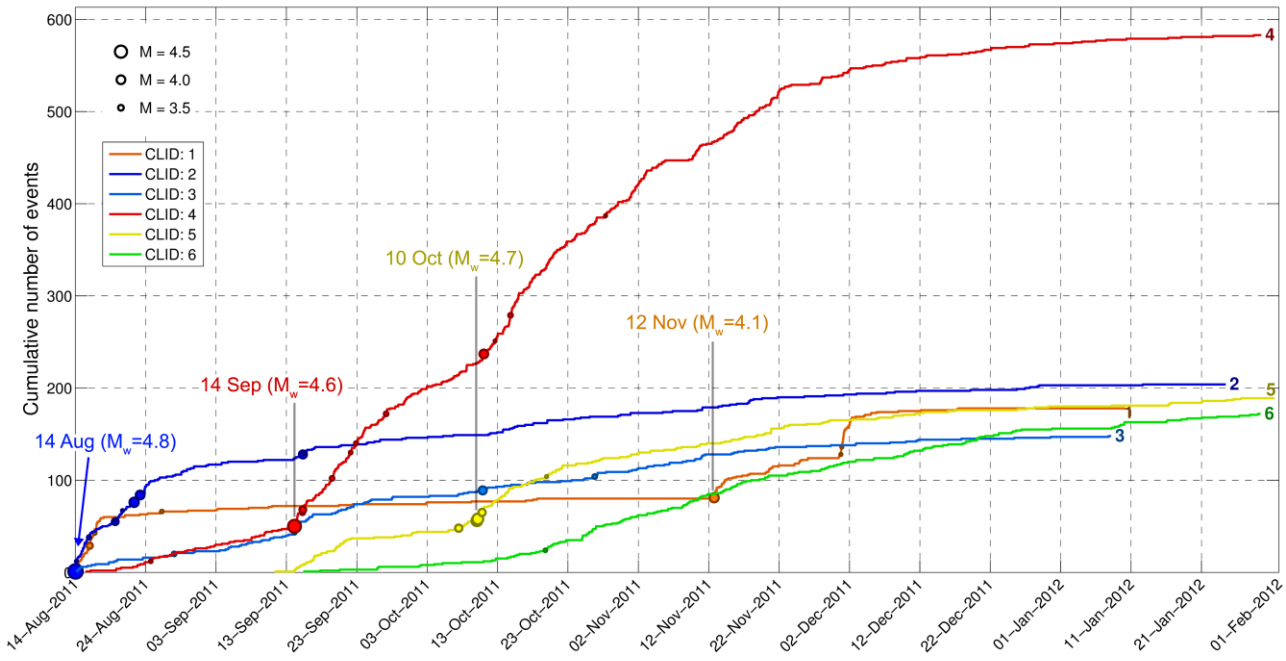

Figure 5A.10: Cumulative number of events per spatial Group, during the 2011 Oichalia swarm. Circles depict the stronger events of the sequence.

the N165°E direction. The occurrence of two small sub-clusters around days ~90 and ~110 (at about 12 November and 1 December) with Y<-4 km, located in the northern part, likely contributed to the more dispersed distribution of events within the whole length of the rupture zone. The migration speed apparently slows down after day 80, as the seismicity reaches its full expansion, being gradually diminished afterwards.

The thick envelope curve in Fig. 5A.11 corresponds to the distance of the triggering front $r = r(t)$ (Eq. 1.16) from the source of fluid infiltration, relative to the time $(t - t_o)$ since the occurrence of the injection, as defined by Shapiro *et al.* (1997), starting at t_o = 6 days before the origin time of the major event (14 August 2011), with hydraulic diffusivity D = 1.10 m^2/s. This is by no means the only plausible solution, as various combinations of D, temporal and spatial offsets can define a satisfactory envelope line. Additionally, the exact time, location and geometry of the fluid injection source are unknown. However, this set of parameters provides an envelope curve for the triggering front with approximately the same slope as the seismicity migration curve. We have also imposed the t_o value so that the source of fluids (y_o) coincides with the projection of the hypocenter of the major event. The same curve mirrored downwards can also be thought of as an envelope of the events occurring NNW of the major earthquake, at the beginning of the sequence, along the same direction.

The triggering front model for the migration of seismicity provides evidence that the spatio-temporal distribution of the seismic swarm can be explained by an injection of fluids (Schoenball *et al.*, 2010). Their source is assumed to be close to the hypocenter of the major event of 14 August, starting about a week before its occurrence. It is interesting at this point to note that the NOA database has registered about 120 events between July and August 2011, with epicenters

concentrated at the area where the 14 August event occurred. This means that the fluid injection could have possibly started more than a month before $t = 0$.

5A.2.3 ETAS model

The 2011 Oichalia sequence exhibits patterns which are characteristic of earthquake swarms, such as the occurrence of several major events of comparable magnitude, with no single event being characterized as a mainshock, the large dimensions of the activated area relative to the released seismic moment and significant seismicity migration. The latter is a clear sign for pressurized fluids

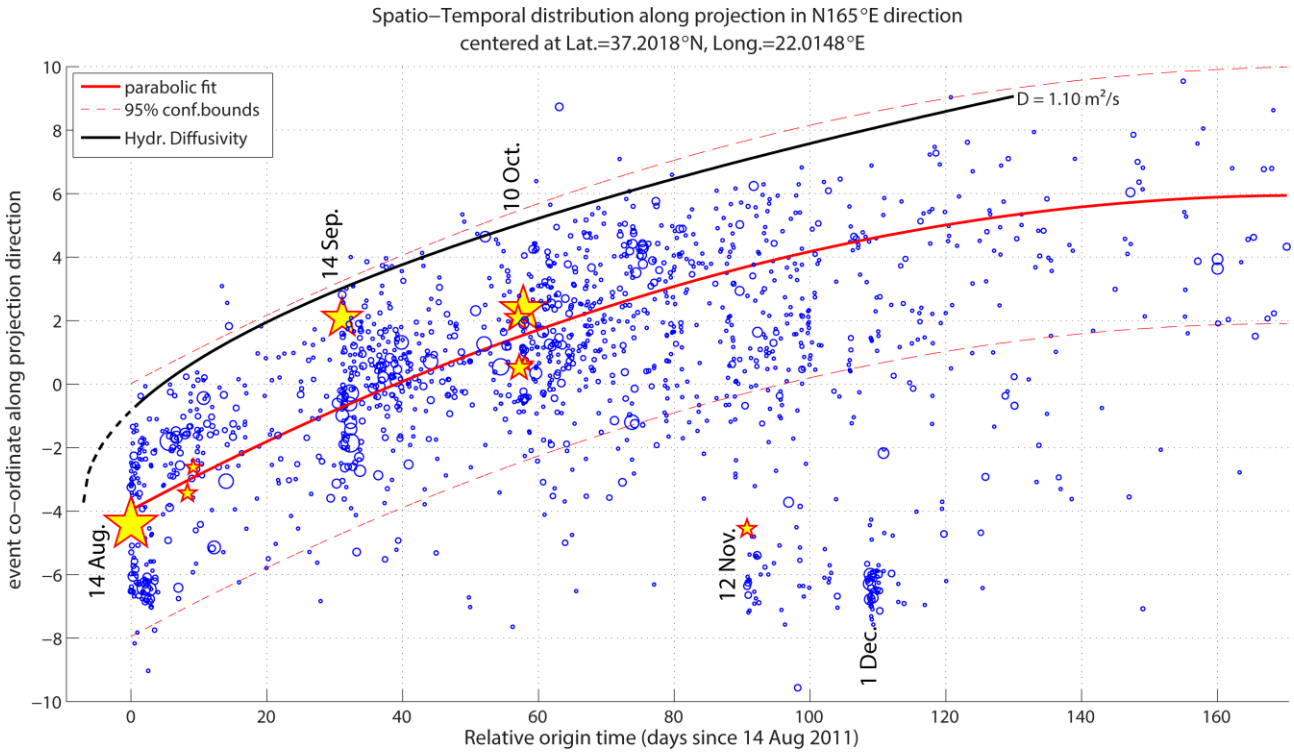

Figure 5A.11: Spatio-temporal diagram of the swarm activity. The vertical axis represents the projection of epicenters along the a_1-a_2 line shown in Fig. 5A.7B, centered at Y=0 or 37.2018°N, 22.0148°E (white diamond in the middle of the respective line in Fig. 5A.7A), drawn at N165°E azimuth, with Y=-10 km being at the NNW end (37.2887°N, 21.9855°E) and Y=10 km being at the SSE end (37.1149°N, 22.0440°E). The horizontal axis denotes the relative origin time measured in days since 14 August 2011. The solid curve is a parabolic-fit estimate of the mean migration rate of seismicity along the N165°E direction with a mean slope of ~80m/day for the first 80 days. Dashed lines mark the 95% confidence bounds with a width of about 8 km. Stars denote events with $M_w \geq 4.0$. The envelope curve corresponds to the position of the triggering with the source of fluid infiltration at the same position as the 14/8 event's hypocenter, starting at t_o = 6 days before the origin time of the major event and defined for hydraulic diffusivity D=1.10m^2/s. Figure after Kassaras *et al.* (2014b).

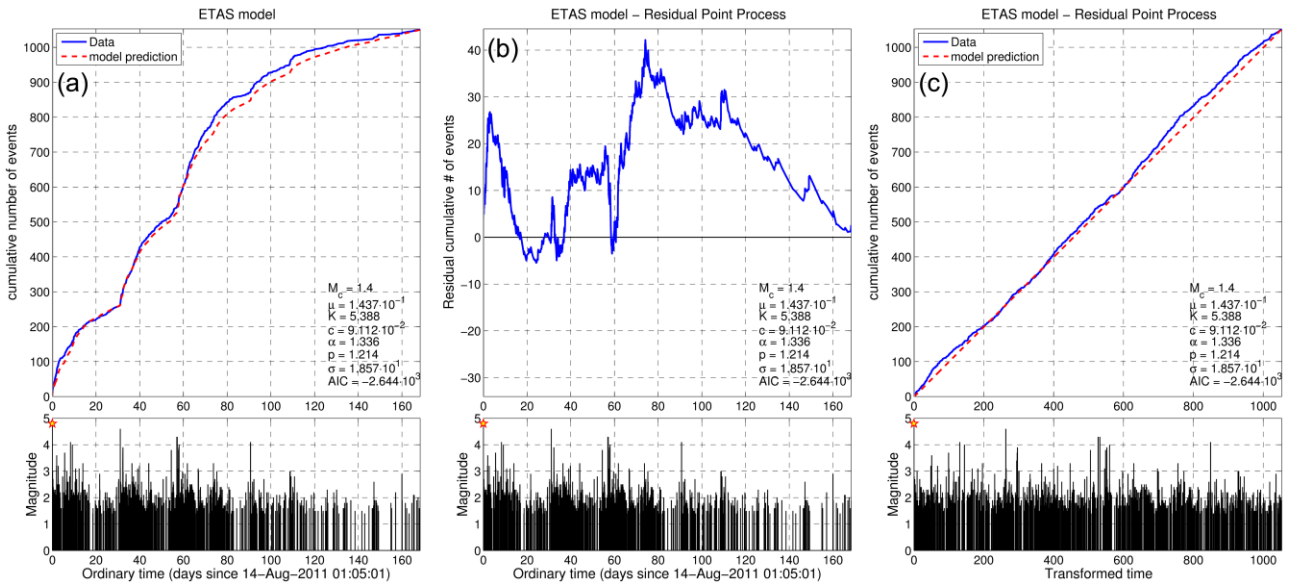

Figure 5A.12: ETAS model for the seismicity of the 2011 Oichalia swarm, using a threshold value at $M_{th} \equiv M_c = 1.4$ and $M_r \equiv M_{main} = 4.8$, a) data and model curves in ordinary time, b) in transformed time, c) residual between data and model in transformed time. The two $M_w = 5.1$ events are marked with a star in the histograms (lower panels).

being at least partially responsible for the propagation of the seismicity front. However, seismicity is also triggered by stress-transfer and perturbations of the local stress field caused by the earthquakes themselves during the swarm.

For this reason, ETAS modeling was performed for the 2011 Oichalia sequence (Fig. 5A.12). Kassaras *et al.* (2014b) have shown a variation of the magnitude of completeness, M_c, starting from a high value of ~1.8 and dropping down to 1.2, mainly due to the installation of the temporary stations in mid-October, roughly 60 days after the beginning of the study period (14 August 2011). After experimenting with various thresholds above 1.2, a value of $M_{th}=1.4$ was selected, which resulted in smaller residuals between the data and the model. The a and p values, at ~1.34 and ~1.22, respectively, do not change much (±0.1) if the threshold is varied between 1.2 and 2.0. Positive residuals are related to the first two outbursts of periods A and C, and the longer period D-F. The latter begins roughly after the installation of the temporary local stations. However, even if treated separately (e.g. using change point analysis, various thresholds etc.) the positive residuals persist, indicating non-stationarity. Estimation of the ETAS model parameters on a sliding window shows temporary increase of the μ parameter during the 3 main outbreaks and gradual decrease to lower values during periods E-F. This suggests a possible aseismic component to the triggering of seismicity, which is compatible with the contribution of fluids to the propagation of the seismic front, as indicated by the migration pattern. A small deficit of the data with respect to the ETAS model is also observed shortly before the major event of 14 September, which is a possible sign of short-term quiescence.

5A.2.4 Discussion - Conclusions

The geometry of the temporary seismological network allowed for the determination of 146 focal mechanisms, with 128 of them been constrained using P-wave first motion polarities and 18 using regional moment tensor inversion solutions (Kassaras *et al.*, 2014b). The fault plane solutions mostly indicate dip-slip N-S trending normal faulting. However, quite a few have a significant strike-slip component while a few cases of reverse faulting were also observed, mainly at the southwestern part of the epicentral area. The overall geometry of the activated zone is a ~18 km long dip-slip normal structure, trending NNW-SSE and dipping ~32° WSW, slightly tilted so that it also becomes shallower towards the south. The orientations of the sub-horizontal T-axes are consistent with the results of stress-tensor inversion performed at a regional scale (Kassaras *et al.*, 2016) which showed that the region of Messenia is characterized by WSW-ENE extension, with the σ_3 minimum principal stress axis gradually rotating northwards to a N-S direction in the region of the Corinth Rift, consistent with GPS observations (Chousianitis *et al.*, 2015).

The shallow dip (20°WSW) of the spatial geometry of the swarm defines a single major structure which can be extrapolated to the surface at about 12 km east of the swarm, within an area along the western ramps of Taygetos Mt. (Fig. 5A.6). However, taking into account the focal mechanisms average dip of 42°WSW, Kassaras *et al.* (2014b) suggest that more than one structures are involved, interacting with each other, forming a complex fault network which is compatible with the NW-SE striking and west dipping normal fault observed at the eastern flanks of the Upper Messenia basin. It may be a similar case to the one observed in the western Corinth Rift, where diffuse seismicity is observed in a weak seismogenic layer that appears to be dipping to the north, however the majority of focal mechanisms are steep-dipping, indicating steep faults which root to the seismogenic layer (see Chapter 6).

Kassaras *et al.* (2014b) also studied the spatial distribution of the *b*-value and its temporal variations and found relatively low *b*-values during the first phase of the swarm (up to 14 September 2001), highly variable *b*-values during the second phase (up to 12 November 2011) and a smoother distribution of *b*-values in the rest of the sequence, tending towards unity thus signifying the end of the swarm activity. Lower *b*-values were generally associated with the northern part of the spatial distribution, where the swarm began. This indicates a higher concentration of stress (Wiemer and Wyss, 1997), likely associated with an asperity that may rupture in the future. Differential increase of b-values in the northern part during the third phase indicates that stresses became relatively more relaxed. Kassaras *et al.* (2014b) also measured coulomb stress transfer by the major events and found it to be of the order of 0.5 bars or less. The authors suggested that, although not impossible, these values are too low to support triggering by stress-transfer alone and proposed that there is likely a significant degree of aseismic component to the triggering of the major outbursts of the second and third phase. This could be caused either by creep or transient increase of pore-pressure due to the intrusion of fluids, which is supported by the strong migration patterns.

The spatio-temporal hypocenters migration is bound by the parabolic envelope of the triggering front (Eq. 1.16) with hydraulic diffusivity $D \approx 1.10$ m^2/s, supposing that the fluid injection event that started 6 days before the major shock of August 14th, in the vicinity of its hypocenter. However, the occurrence of several events at the northernmost part of the swarm during June-July 2011, points

towards external triggering, most probably due to diffusion of pressurized fluids that could have started more than a month before the major event. The average rate of the seismicity migration towards the south during the first 80 days was found at about 80m/day. At the same time, the diffusion appears to ascend to shallower depths towards the southern part. However, this vertical migration is not exclusively upwards but appears to be more complex, turning downwards from period C onwards.

Kassaras *et al.* (2014b) attributed the observed migration patterns to crustal fluids of meteoric origin circulating in depth, justified by the existence of many mineral thermal springs in the area. However, as also discussed in the case of the western Corinth Rift (Chapter 6), the seismicity migration from larger to shallower focal depths could also indicate triggering by fluids of deeper origin, such as mantelic fluids rising upwards from the subducting lithospheric slab (Bourouis & Cornet, 2009). The complex vertical migration leads to the conclusion that while the seismicity during the 2011 Oichalia swarm is controlled by fluids, mainly as far as its horizontal propagation is concerned, earthquake triggering mostly depends on stress field changes caused by the earthquakes themselves. The latter is supported by the fact that the ETAS model follows the real data closely. Systematic positive residuals, however, indicate a significant degree of aseismic component, most likely due to the diffusion of pressurized fluids.

5A.3 The 2011-2012 seismic crisis in the Santorini Volcanic Complex

Santorini Island is an active stratovolcano, located in the Volcanic Arc of the southern Aegean Sea (Fig. 5A.13). Its peculiar shape is owed to the destructive "Minoan eruption" of about 1630 BCE, the submersion of its caldera and the following growth of the Palea Kammeni and Nea Kammeni islands in a rich history of explosive and effusive activity (Friedrich, 2000). The regional stress-field is extensional in an approximate NW-SE direction, creating the SW-NE trending Santorini-Amorgos normal fault zone (Kiratzi and Papazachos, 1995), part of which, the Amorgos fault, hosted the immense M_w=7.8 Amorgos earthquake of 9 July 1956 (Fig. 5A.14; Okal *et al.*, 2009), the largest ever recorded in Greece during the instrumental era and responsible for a catastrophic tsunami (Galanopoulos, 1957; Ambraseys, 1960; Papadopoulos & Pavlides, 1992).

Anydros basin, SW of Amorgos, contains a series of volcanic cones whose spatial distribution is controlled by dextral strike-slip faults running parallel to the long axis of the basin (Sakellariou *et al.*, 2010). The latter faulting type is observed in two volcano-tectonic features striking SW-NE, one cutting through the interior of Santorini Island (Kammeni line) and another reaching NE of Santorini (Columbo line), along which most of the current seismicity is recorded, which also act as paths for the propagation of magma. The whole group of Santorini, Nea and Palea Kammeni, Aspronisi islands and the undersea features of Columbo comprise what is called the Santorini Volcanic Complex (SVC).

Despite the increasing detectability due to the installation of local seismological stations since 1990, the background seismicity rate in the SVC has been generally low, with the exception of several earthquake swarms occurring mostly in the vicinity of Columbo volcano (e.g. Kolaitis, 2011), while

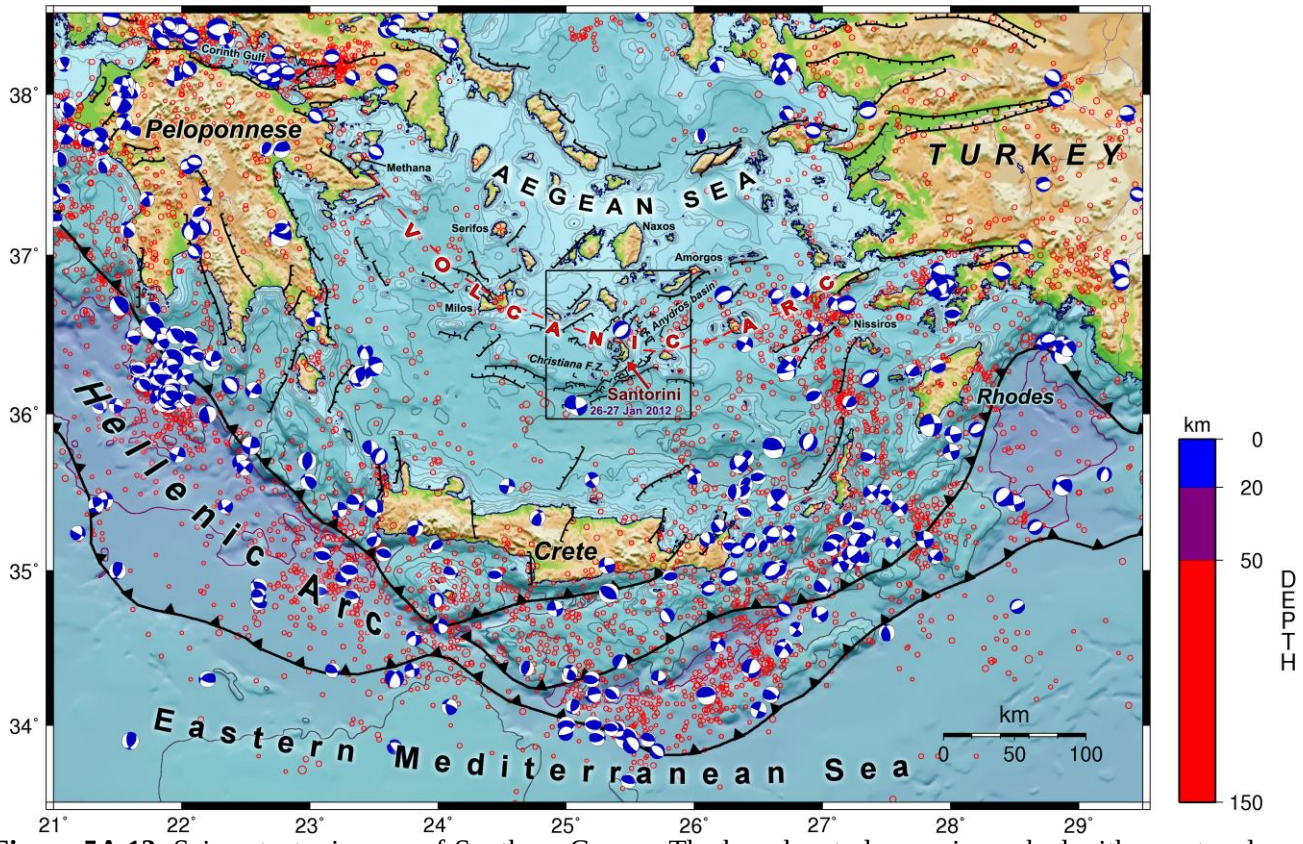

Figure 5A.13: Seismotectonic map of Southern Greece. The broader study area is marked with a rectangle. Figure after Papadimitriou *et al.* (2015).

the recorded seismicity within the caldera has been very low. However, during 2011-2012 this pattern changed as intense seismic activity was detected inside the Santorini Caldera (Papadimitriou *et al.*, 2015). The sequence within the caldera was swarm-like, while increased activity was also present in the vicinity of Columbo volcano. In January 2012, two M_w=5.1-5.2 strike-slip events occurred in the region south of Christiana Islands, ~40km SW of Santorini Island (Kiratzi, 2013).

In this section, the spatiotemporal and seismotectonic analysis of the 2011-2012 seismic crisis in the SVC is briefly described with emphasis in the period between September 2011 and March 2013. The full account is presented in detail by Papadimitriou *et al.* (2015), including polarization, spectral analysis and seismic travel-time tomography. The waveform data were acquired mainly from regional stations of the Hellenic Unified Seismological Network (HUSN), which have been available since 2007, but were improved after the installation of more local stations since 2011.

5A.3.1 Clustering and relocation

Initial locations for the seismicity of 2011-2013 in the SVC were obtained using a regional velocity model (Fig. 5A.15A). It was then divided into spatial groups by calculating a matrix of the Euclidean distances between all pairs of hypocenters and then applying the Ward's linkage with a

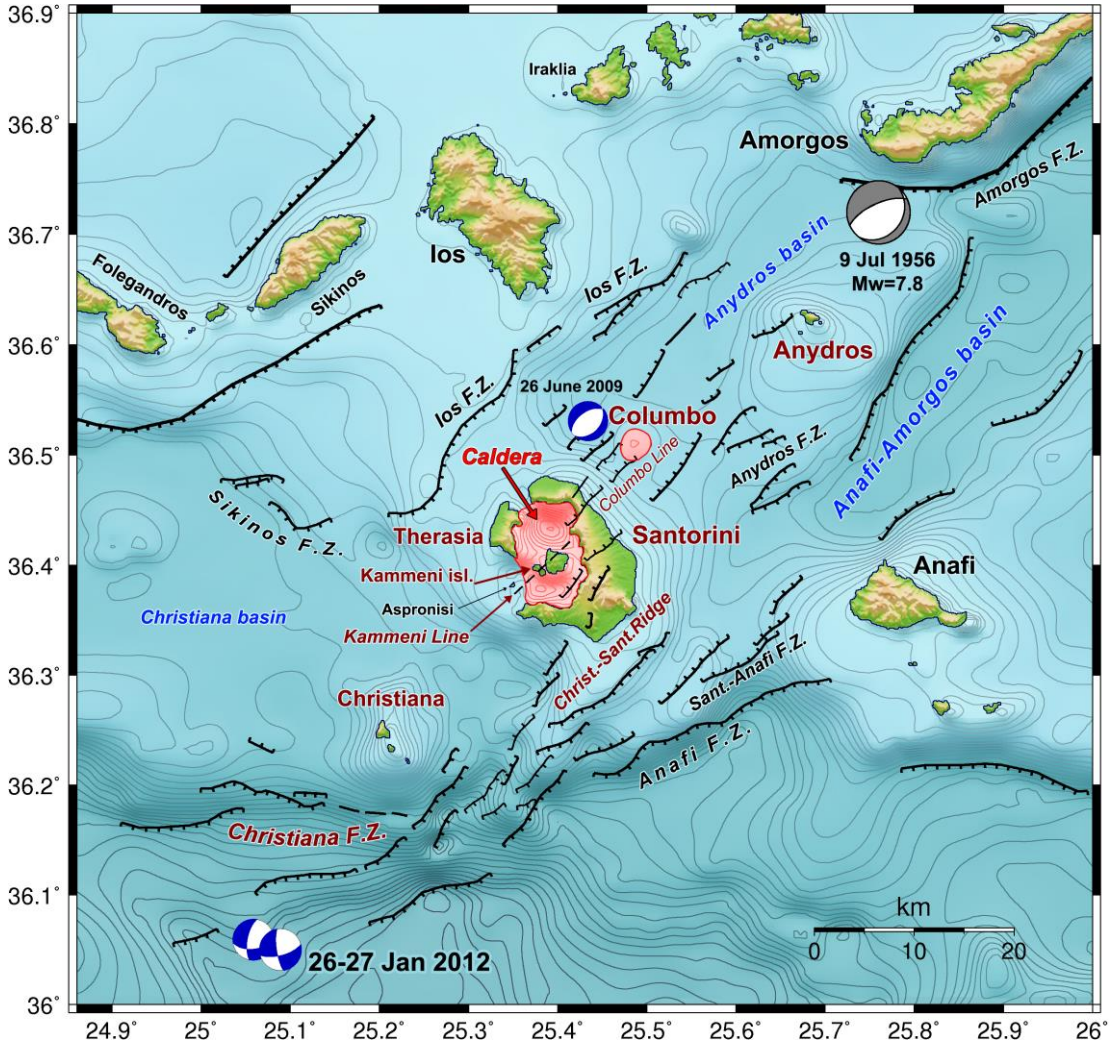

Figure 5A.14: Map of the broader area of study, including the Santorini Volcanic Complex and several local fault zones. Figure after Papadimitriou *et al.* (2015).

threshold value that produced a custom number of spatial clusters. A total of 5 groups were considered: A) the Caldera region, B) an important cluster about 40 km SW of Santorini Island, C) seismicity around the submarine volcano Columbo, along with a small cluster south of it and east of Santorini Island, D) seismicity around Anydros Island, NE of Columbo and E) sparse seismicity south of Santorini Island. In addition, some deep events were recorded, almost exclusively during 2012 with one exception on 24 December 2011. They are mostly located South of Santorini, at focal depths of about 80 km - 100 km, which suggests they are of tectonic origin and likely belong to the Wadati - Benioff zone. These events could not be included in any other group and were not processed any further. The largest groups are A and B including over 500 events each, groups C and D contain about 150 events and group E is sparse with only 67 events. A region-specific 1D velocity model was estimated for each group to further improve the initial hypocentral solutions (Papadimitriou *et al.*, 2015). The most significant change in the distribution of focal depths, due to the custom velocity models, has occurred to the SW Cluster (group B), where many mis-located events close to the surface shifted to lower depths towards the main body of the cluster.

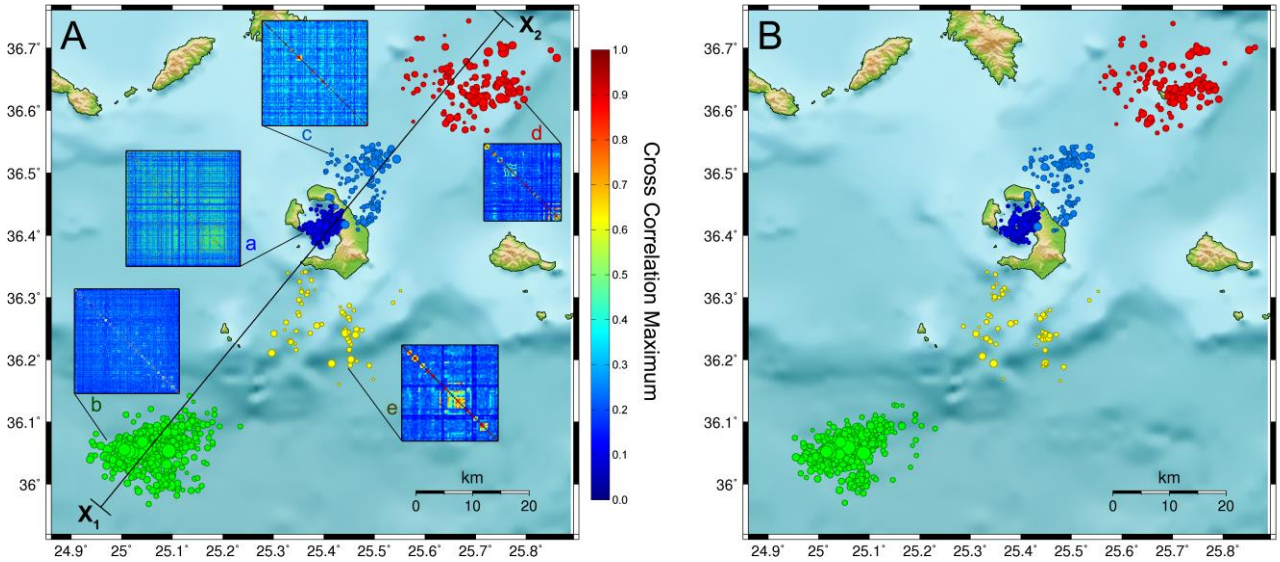

Figure 5A.15: Seismicity in the broader area of Santorini Island during the period between September 2011 and March 2013, (A) solutions derived from a regional model and (B) solutions derived using a region-specific model per spatial group. Colours and lower-case letters (a-e) represent the 5 independent groups: a) Caldera group, b) SW group, c) Columbo group, d) Anydros group, e) Southern group. Figure after Papadimitriou *et al.* (2015).

The double-difference relocation algorithm, HypoDD (Waldhauser & Ellsworth, 2000), was employed to reduce uncertainties due to the unmodeled inhomogeneities velocity structure as well

as arrival-time reading errors in strongly correlated events. The latter were very likely to be significant in some local low resolution stations for signals with low SNR. For Group A in particular, station corrections were also applied prior to relocation to improve the initial locations. Residual corrections for the other groups were less effective and thus they were dismissed. Cross-correlation matrices were constructed for each spatial group, taking into account the vertical recordings of the full signal (P-wave, S-wave and coda) in several stations with relatively high SNR. The waveforms were band-pass filtered in a range between 1 Hz - 20 Hz, to remove high frequency and long-period noise, which can affect the correlation measurements. For every pair of events, each reference station provided a cross-correlation maximum, the highest of which was registered in the corresponding cell of the matrix. This procedure provides a general description for the similarity between all combinations of pairs of events' waveforms that is related to similarity in their source parameters. The matrices for each group are embedded in the map of Fig. 5A.15A.

Afterwards, the events of each group were classified into multiplets according to the degree of their similarity. The hierarchical clustering was calculated with the nearest neighbor linkage using the values of the combined cross-correlation matrix. The optimal threshold, $C_{th} \equiv C_{opt.th}$, was calculated for each group. The largest C_{th} value was calculated for the seismicity inside the Santorini Caldera (C_{th} = 0.77) which resulted in a total of 326 out of 536 events contained in 62 multiplets of 2 or more events each. Group B (SW of Santorini) consists of a large number of events (582) but the closest station is located about 40 km away, which would usually mean lower SNR compared to events of Group A. However, it consists of relatively stronger events, so there should be more

energy to compensate for the longer hypocentral distances. Its estimated optimal threshold was as low as C_{th} = 0.39, with 382 events contained in 60 multiplets, the largest of which was composed of 45 events. Multiplet statistics for all groups are displayed in Table 5A.1. Although the number of multiplets formed in the two major groups is similar, the ones in Caldera have much stronger correlation since they are surrounded by stations in local distances, hence the larger C_{th} value. This has also enabled the detection of smaller events, which are more likely to be similar to each other, providing a large multiplet with 47 events. These statistics have strong influence to the quality of the relocation for each group, since it is mostly guided by cross-correlation data. The other part depends on the catalogue data, which provide links between neighboring events, independently of their waveform similarity.

Table 5A.1: Statistics concerning the multiplet analysis and relocation procedure.

Group	# evt.	C_{th}	# evt. in multiplets	# multiplets	Largest multiplet size	# of evt. relocated	% of evt. relocated
A) Caldera	536	0.77	326	62	47	502	94%
B) SW Group	582	0.39	382	60	45	541	93%
C) Columbo	145	0.53	45	17	6	126	87%
D) Anydros	163	0.35	55	10	18	141	87%
E) S. Group	67	0.46	39	9	13	55	82%

A more specific cross-correlation procedure was then performed for every pair of events in each multiplet, in order to calculate the input data required for HypoDD. The parameterization of the HypoDD procedure includes the linking scheme for catalogue data, the number of sets with different a priori weights for the two types of input data, the re-weighting scheme, the dumping and the number of iterations. It was determined by trial-and-error, aiming for gradual relocation to be achieved with minimal systematic shift of the absolute locations and a stable result in the final iterations. Each hypocenter was relocated relatively to its neighbors with whom it shares links of travel-time observations by catalogue or cross-correlation data as well. The latter usually provide stronger links, which consequently tend to concentrate the hypocenters of multiplets close together. The usual weighting method is to begin with low a priori weights on the cross-correlation data (CC) and high weights on catalogue data (CT), then gradually increase CC and lower CT weights, while stronger thresholds on distance between linked event-pairs and residuals are being applied on both types of data. Variations on the strength of the re-weighting procedure, as well as the damping parameter used for the least-squares inversion, depend mainly on the quantity and quality of available data.

The relocation procedure has achieved reduction in the hypocentral dispersion and, consequently, provided a clearer image of the spatial distribution. This is shown in the seismicity map of the broader area (Fig. 5A.15) and can be also represented numerically as a decrease of dispersion in relative locations within sub-clusters (Table 4 in Papadimitriou *et al.*, 2015). More specifically, the relocation in group A has achieved a reduction of ~30% in horizontal dispersion within sub-clusters and ~7% for the group as a whole. In addition, its vertical dispersion has been reduced by about 12%, which is in general better than in the other groups with the exception of the relative vertical locations in group C which were improved by 15%. A 10% reduction was achieved for the epicenters of group B, while some shallow events have been relocated deeper. Changes in the

horizontal dispersion of other groups are generally smaller and more significant in the EW direction than in NS. The depth distribution of group E did not benefit from the relocation procedure, as the vertical dispersion was apparently increased. Focal depths within the Santorini Caldera mainly vary between 3 km and 8 km. In the surrounding areas, several events are located deeper than 10 km, possibly due to the insufficient station coverage and to the fact that the minimum epicentral distance is greater than the focal depth.

5A.3.2 Spatio-temporal analysis

Papadimitriou *et al.* (2015) present a detailed analysis on the spatiotemporal distribution of seismicity in the broader SVD area since 2000, with additional arrival-time data for years 2000-2006 being incorporated from a homogenized catalogue (Karakonstantis & Papadimitriou, 2010) as well as data from local temporary networks which operated in the study area in 2001 and 2003 (Kolaitis, 2011). In the years between 2000 and 2010, most of the seismic activity was mainly concentrated in the region of the submarine volcano, Columbo, NE of the Santorini Island (area of group C), but also in the area South of Santorini (region of group E, also known as the Christiana-Santorini ridge). The most notable outbreaks were observed in 2003, when an M_w=4.3 event occurred in the vicinity of Columbo on 25 September, followed by an aftershock sequence that was recorded by a local network (Kolaitis, 2011), a spatiotemporal cluster in the area of group E occurred between 24 and 28 August 2007, followed by an increase of activity in the Group C region, and a significant seismic crisis took place by the end of June 2009 in Columbo (Fig. 5C.12), starting with a few foreshocks and culminating with an M_w=4.9 event on 26 June, which was followed by a very short but dense aftershock sequence that lasted up to 1 July 2009 (Křížová *et al.*, 2010).

Inside the Caldera, there has been lack of seismicity during the last decade, with only few sporadic events. That situation changed in February 2011, when the Caldera region was activated with events concentrated under Nea Kammeni, roughly along a NE-SW direction. Another seismically quiet region during 2000 - 2011 has been the Group B area, 40 km SW of Santorini. However, on 26 January 2012, an M_w=5.1 earthquake, followed by an M_w=5.2 event the next day, initiated aftershock activity. These major events have been largest earthquakes in the broader area since 1956 (Makropoulos *et al.*, 2012). This signaled a halt in the seismicity inside the main island of Santorini, peaking shortly before the activation of Group B, around 23 - 25 January 2012, then gradually diminishing during 2012. The major event of 26 January 2012 was also followed by small increase of activity in Group D.

The temporal evolution of the detected multiplets in the 5 spatial groups, for the period October 2011 - August 2012, is displayed in Fig. 5A.16 (bottom-left panel). As expected, the caldera Group A dominates the first part (Period I), with the first couple of multiplets also being the largest ones (size > 20, right panel). It is noteworthy that the increased activity inside the Caldera prior to the 26 January 2012 event of the SW Cluster (Group B) is reflected in the generation of new multiplets for Group A, but also in the reactivation of previously generated multiplets. This led to a peak in

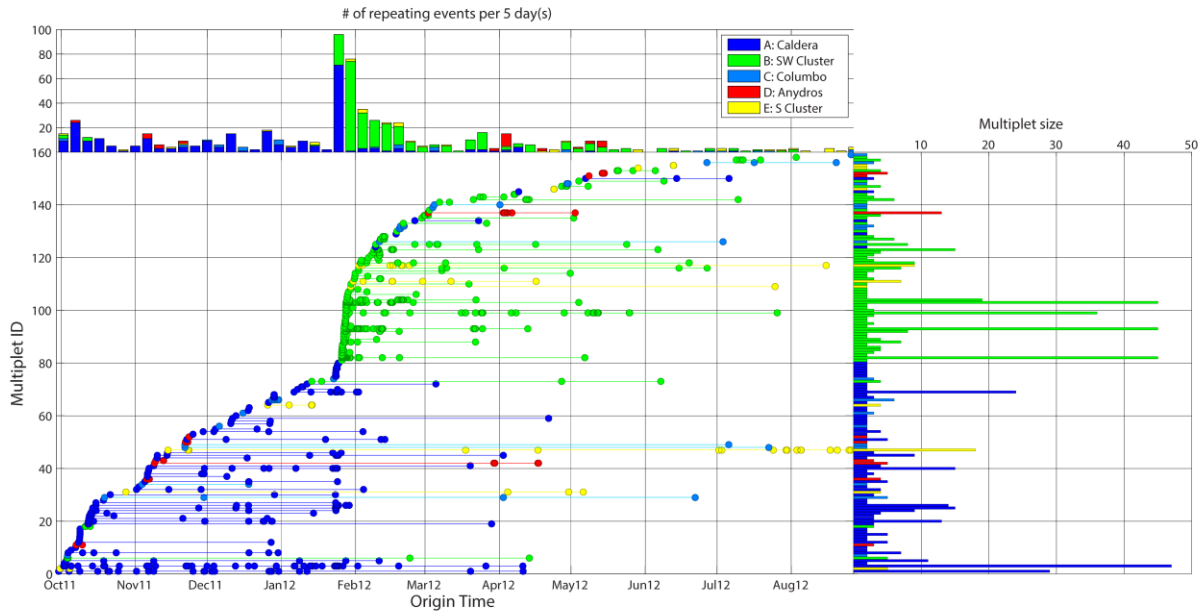

Figure 5A.16: (Bottom left) Multiplet history dendrogram of the broader area of Santorini for the period between October 2011 and August 2012. The circles represent repeating earthquakes linked by horizontal lines to indicate that they belong to the same multiplet. The vertical axis shows the Multiplet ID, sorted by the origin time of the first event of each multiplet. Multiplets with lower ID were initiated earlier than others with higher ID. Horizontal axis represents the origin time. (Right) Multiplet size, indicating the number of events contained in each multiplet. The vertical axis is shared with the history dendrogram. (Top) stacked histogram of the total number of repeating events occurring per 5 days. The horizontal axis is shared with the history dendrogram. The legend shows the correspondence of colour coding with the spatial groups A-E, similar to other figures. Figure after Papadimitriou *et al.* (2015).

multiplet activity inside Group A during the period 23 - 25 January 2012, with over 60 repeating earthquakes in 5 days (Fig. 5A.16, top panel), along with the activation of Group B. It is important to note that, while the generated multiplets of Group B seem numerous and more abruptly generated, each group has a different correlation threshold, with Group B having one of the smallest (C_{th}=0.39). This means that events inside them are more weakly correlated than in Group A, at least as far as their detected signals are concerned, because of their larger epicentral distance from the stations. Groups D and E contain a few well-defined multiplets, the largest having size over 10 (mainly during early April 2012) and 15 events (mainly after June 2012), respectively (right panel of Fig. 5A.16). The otherwise highly active area of Group C (Columbo) in the past decade does not contain any significant multiplets during the more recent period (October 2011 - August 2012), or any important spatio-temporal clusters. The period between April 2012 and March 2013 was characterized of low multiplet activity and is not presented in Fig. 5A.16.

The spatiotemporal analysis revealed that, while no unilateral migration of seismicity has been observed in either small or large scale, the various regions in the broader area of the Santorini

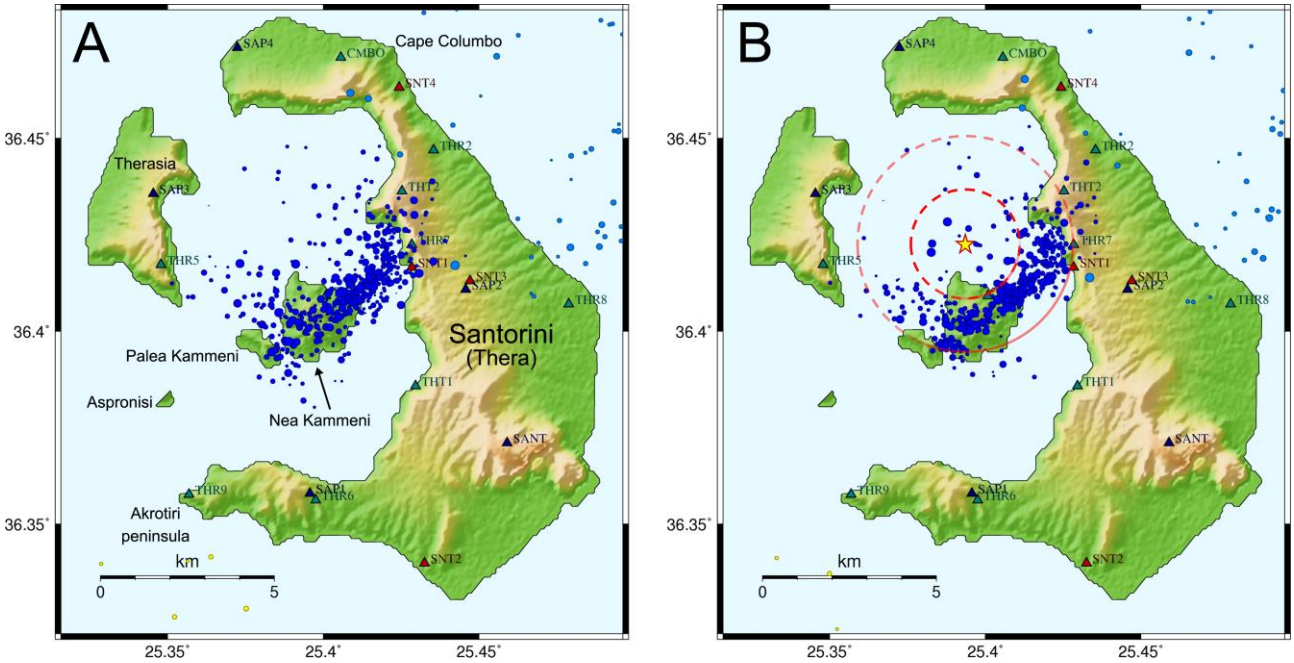

Figure 5A.17: Seismicity inside the caldera of Santorini Island (group A) during the period of September 2011 - March 2013, (A) before and (B) after relocation with HypoDD. The red star in panel (B) is the center of the concentric circles (shown in red) inside which the major part of the seismicity of the caldera group is included. Figure after Papadimitriou *et al.* (2015).

Volcano Complex have exhibited different behaviors during the past decade. The regions of Anydros (Group D) and Columbo (Group C) presented more or less continuous, moderate seismicity with several outbreaks in the past years. The area south of Santorini (Group E) was activated during certain periods, with a peak in 2007. Intense seismicity in Group B appeared for the first time in January 2012, due to the M_w=5.1 and 5.2 events and their aftershock sequence, with at least 17 events having $M_w \geq 3.7$ being detected up to 15 February 2012. The Santorini Caldera (Group A) was characterized by very low, sporadic activity until 2011, when a yearlong seismic unrest was initiated. More details concerning the Caldera region are discussed in the following section.

The intense seismic activity within the Santorini Caldera, which was initiated in February 2011, lasted for more than one year. Its main characteristics are the relatively small magnitudes (the largest events do not exceed M_L=3.5) and the shallow depth distribution, with the deeper events reaching up to 10 km. More than 1000 events have been detected inside the Caldera since the beginning of 2011, with their epicenters mainly located between the Palea and Nea Kammeni Islands and the central-west scarp of Santorini Island (Fig. 5A.17A for the latter part of 2011). The relocated events for the study period in Group A are shown in Fig. 5A.17B. The relocation results in this area are more efficient than for any of the other groups, which is due to the local seismological stations of HUSN that have been installed, mostly on the main island of Santorini but also on Nea Kammeni and Therasia.

The spatial distribution of the seismicity on Nea Kammeni tends to be aligned along a NE-SW direction. This is mainly due to the three main clusters located on or very close to Nea Kammeni,

one on its central part and the other two close to its NE and SW coast. These constitute the main part of the recorded seismicity in the Caldera. In addition, a small cluster is located west of Nea Kammeni, while only sparse events are observed north of it. Finally, an important spatial cluster is located NE of Nea Kammeni, close to the west coast of Santorini Island, on the mainland of which some sparse events have also been located. Taking into account the spatial distribution of the seismicity, an alternative interpretation can be considered. More specifically, it appears to be located along a circular ring with its center north of Nea Kammeni. The southern part of the ring is characterized by high activity, whereas the northern by low.

The seismicity inside the Caldera spans across a 5 km long zone oriented in a NE-SW direction. The whole zone is more or less activated at any period, although in some cases it appears that seismicity under Nea Kammeni is more dense than towards the central-west scarp of the Caldera or the opposite side. There is no evidence of unilateral spatiotemporal migration. In early 2012, the whole zone was activated, including a small cluster over Nea Kammeni and another between Nea and Palea Kammeni, right before the onset of the 26 January 2012, M_w=5.1 event in Group B.

The largest multiplets of Group A (with size ≥ 10 events) are displayed in the map of Fig. 5A.18, along with waveforms for a pair of events from each one. As this visualization indicates, the most complicated volume appears to be under the NE coast of Nea Kammeni, where 4 of the largest multiplets (#3, #4, #5 and #8) are located very close (few hundreds of meters) to each other. This patch of events is separated by about 1 km from two other multiplets (#1 and #6) located NE, close to the coast of the Caldera, that appear to have quite different characteristics from the rest, as observed during the multiplet analysis. A very well relocated multiplet (#2) is situated in the middle of Nea Kammeni, while at the SW portion of the activated zone there is another large multiplet (#7), with most of its events having occurred during January 2012. Several other earthquakes with waveforms displayed in Fig. 5A.18 have origin times either in January 2012 or, more specifically, a few days before the M_w=5.1 event in Group B, period during which a high concentration of repeating events was also observed inside the Caldera (Fig. 5A.16). It is worth noting that despite the fact that the spatial distribution of the multiplets of Group A is restricted within a relatively small volume, significant variability in the recorded waveforms can be observed, implying complexity of the activated structure.

5A.3.3 Focal mechanisms

To investigate in detail the kinematics of microseismicity within the Caldera of Santorini Island (group A), the relocated hypocenters were further divided in 9 spatial sub-clusters, whose epicentral areas are roughly outlined by ellipses in Fig. 5A.19. First motion polarities were measured and fault plane solutions were manually determined for 131 events spread throughout the sub-clusters (Papadimitriou *et al.*, 2015). Composite focal mechanisms were also calculated for each sub-cluster using a similar technique as in Section 5A.1.3 for the 2007 Trichonis lake swarm. This method is based on the assumption that closely spaced events have a high probability to belong to the same activated fault plane and to be characterized by similar focal mechanisms. It is an extension of the

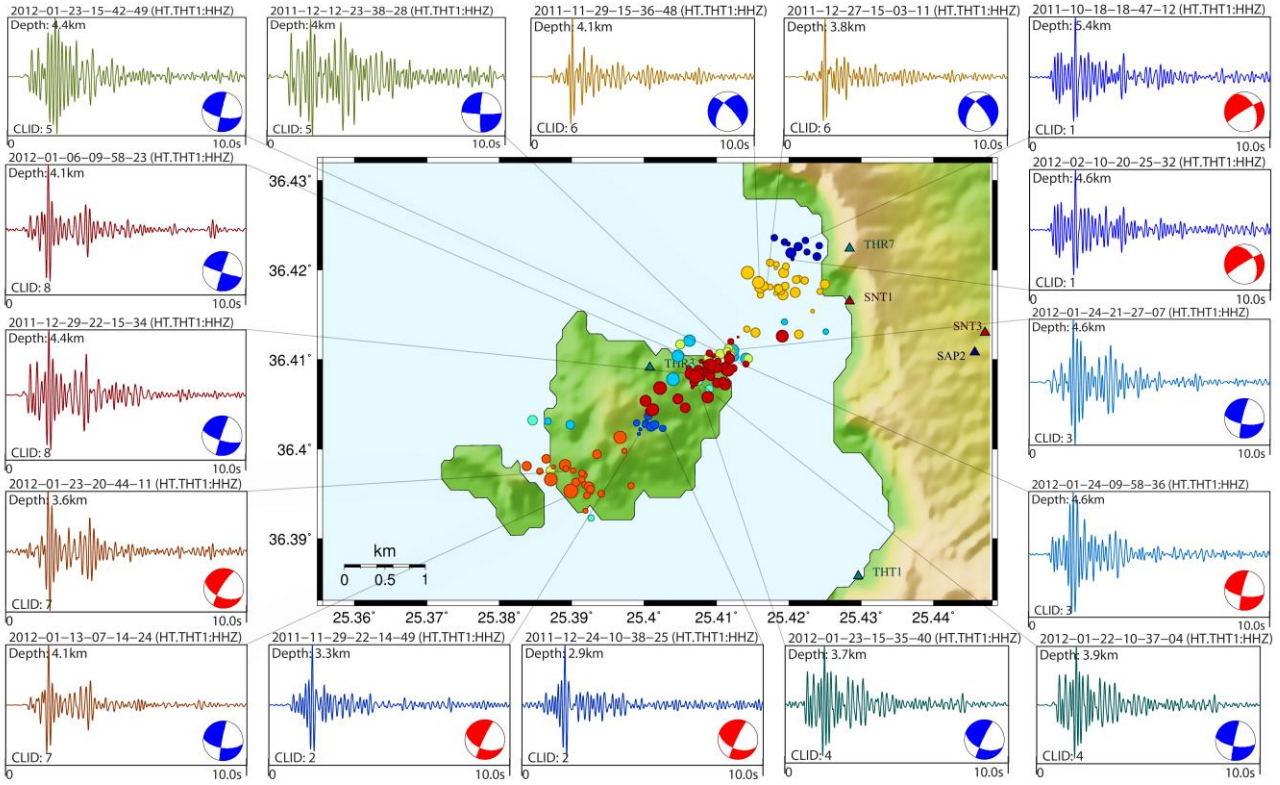

Figure 5A.18: Map of the 8 largest multiplets of the Caldera group (A), with size ≥ 10. The waveforms in the periphery of the figure are recordings from the vertical component of station THT1 (see bottom-right corner of the map) for two events from each multiplet. The corresponding focal mechanisms of individual events, where available, are displayed with blue colour in the compressive quadrants, while those with red colour are the approximate solutions acquired from the average focal mechanism of the corresponding cluster (for events with smaller magnitudes). The waveforms are band-pass filtered in the range 3-8Hz for visualization purposes. Figure after Papadimitriou *et al.* (2015).

definition of a multiplet to spatially clustered events, without directly considering waveform similarity. However, the distribution of relocated events is a result of both catalogue and cross-correlation data. Consequently, spatial clusters can be considered as multiplets in a broader sense. Such groups of events may share a similar focal mechanism, which enables the calculation of composite focal mechanisms per cluster. The major part of the fault plane solutions for individual events (Fig. 5A.19) indicates strike-slip type faulting. In general, one plane strikes in an almost NE-SW direction with an approximately vertical dip, while the other strikes NNW-SSE. The NE-SW striking plane can be considered as the activated fault plane, since it is almost parallel to the Santorini-Amorgos Fault Zone. Deviations from the described type of faulting can be observed towards the SW and NE edges, which suggests increased complexity. This is also outlined by the composite solutions have a strong strike-slip component with one of the two sub-vertical planes striking NE-SW, being almost parallel to the mean direction of the events spatial distribution. The aforementioned observation suggests that this is probably the fault plane, characterized by dextral

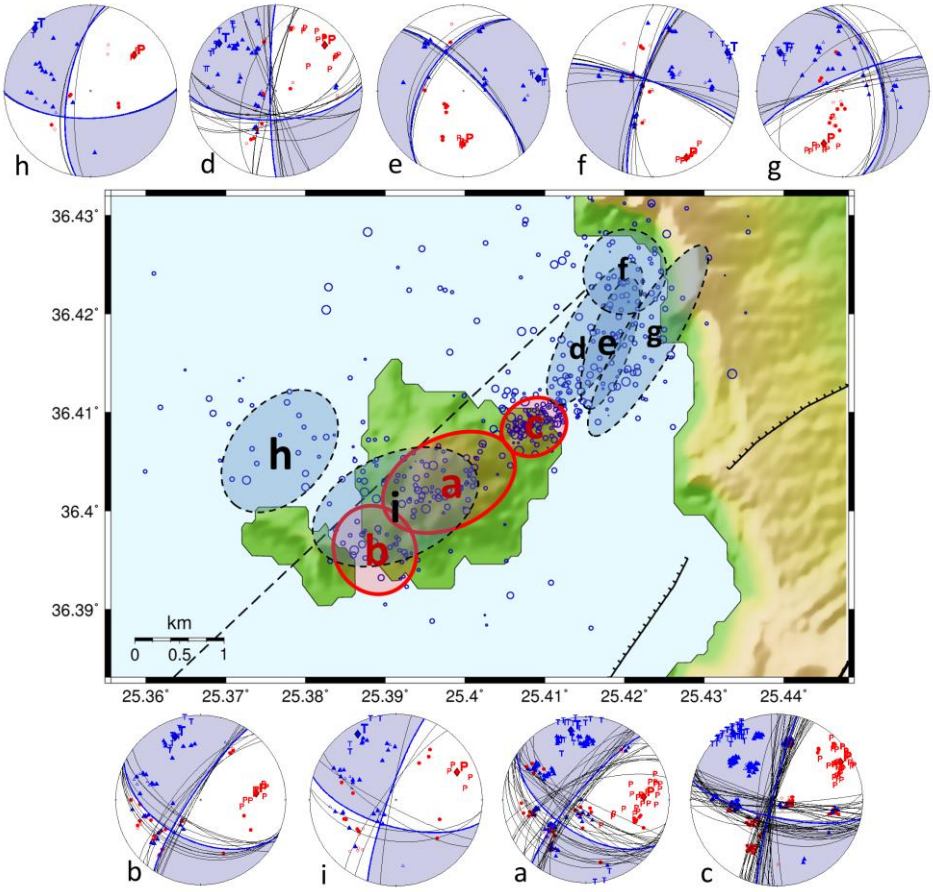

Figure 5A.19: Composite focal mechanisms calculated for the strongest events in 9 spatial clusters within the caldera group. The labeled ellipses inside the map depict the approximate regions covered by each cluster's epicenters. Blue and red symbols inside the focal spheres represent compressional and dilatational P-wave onset motions recorded at the various stations. Blue T and red P letters in each focal sphere correspond to the T and P axes of individual solutions. The corresponding axes for the composite solution are denoted by a larger, bold letter and a diamond symbol. The nodal planes for individual solutions are drawn with thin, black lines while the ones of the average solution with thick blue line. Blue and white regions typically correspond to the compressive and extensive quadrants of the composite mechanism. Blue open circles in the map depict the relocated epicenters of the caldera group. Figure modified after Papadimitriou *et al.* (2015).

slip. Nevertheless, towards the ends of the distribution the situation deviates, with stronger normal component at the SW edge and different orientation of the two planes at the NE end. The mean direction of the T-axis, as deduced from the determined focal mechanisms, is NE-SW, similar to the Santorini-Amorgos Fault Zone. However, towards the NE of the activated area in the Santorini Caldera the T axis is differentiated.

5A.3.4 Conclusions

The 2011-2012 seismic crisis in the Caldera of Santorini (Papadimitriou *et al.*, 2015) has been unique in terms of the usual patterns that have been observed during the past decades. High-

resolution relocation revealed intense microearthquake activity, with focal depths ranging between 4 km and 8 km, concentrated in several small spatial clusters. The spatiotemporal distribution has not indicated any significant migration patterns. Since March 2012, the activity inside the Caldera has returned to its low background rates, while in the broader study area seismicity occurs at low rates in vicinity of the 4 other groups (B-E).

The determination of composite focal mechanisms using first motion P-wave polarities mainly indicated NNE-SSW strike-slip faulting and a NW-SE oriented extension, almost parallel to the orientation of the larger-scale Anydros basin. This is also in agreement with the spatial alignment of hypocenters within the Caldera. Dispersion from the linear distribution of the epicenters is also observed towards the edges of the activated region. A circular ring area can be considered, centered north of Nea Kammeni, with the seismicity being located mainly in its southern part, while its northern part was characterized by very low seismicity. The center of the ring is compatible with the magmatic chamber that was identified by tomographic inversion, at depths between 4 km and 7 km depth, north of Nea Kammeni Island (Papadimitriou *et al.*, 2015) and with the location of the best-fit Mogi source of the observed deformation during the seismic crisis period, as measured by a combination of GPS - SqueeSAR modeling (Lagios *et al.*, 2013).

Variability of fault plane solutions was observed at the edges of the seismically activated zone inside the Caldera, related to local stress changes. These variations in the focal mechanisms are generally consistent with the theoretically predicted behavior of the stress field inside the caldera due to magmatic inflation combined with an extensional stress regime in a NW-SE direction (Feuillet, 2013). Therefore, monitoring possible future systematic changes of fault plane solutions in this area can be proven of significant importance to detect stress changes induced by magma movement (Zobin, 2003). Furthermore, the focal mechanisms determined for the sub-groups c, d, h and i (Fig. 5A.19) are similar to the ones of the major events of the cluster located approximately 40 km SW of the Santorini Island, implying a similar stress regime in a region where no information was available until recently.

5A.4 The 2013 Helike swarm

One of the most recent intense seismic swarms in the western Corinth Rift occurred in the vicinity of the city of Helike, at the southern coast of the gulf (Fig. 5A.20), between May and August 2013. The epicentral region is between the W. Helike and Aigion fault scarps, one of the areas which do not present continuous background seismicity. The last known activity had been in 1991, with an aftershock sequence following an M_w=4.5 mainshock on 3 July 1991, part of which was located and described by Rigo *et al.* (1996) with data from a temporary seismological experiment that took place between July and August 1991. In 2013, the Helike swarm was recorded by the local Corinth Rift Laboratory (CRL) network, a temporary station at Helike (HELI), installed on 23 May 2013

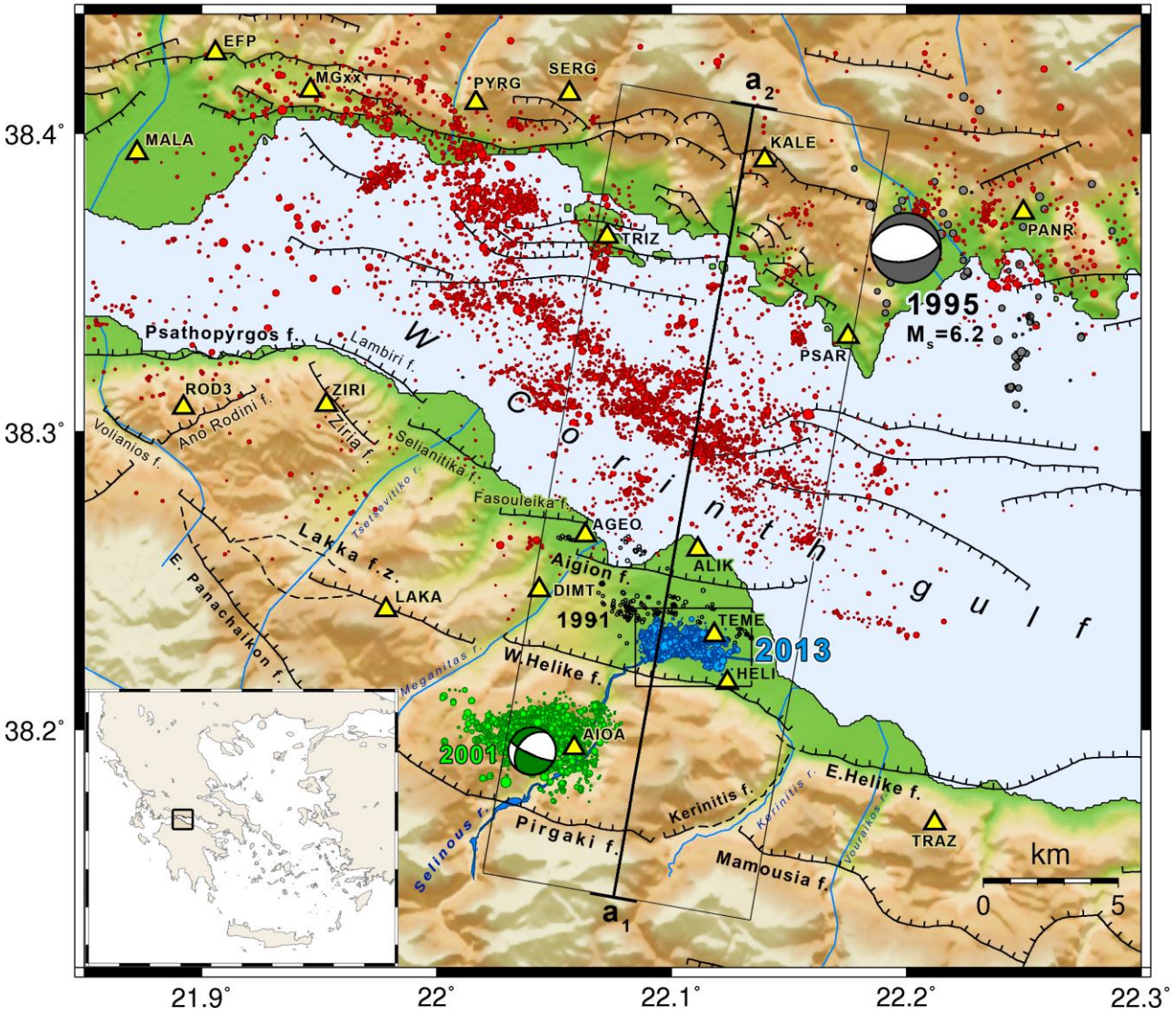

Figure 5A.20: Seismotectonic map of the Western Corinth Gulf (see mini-map of Greece at the lower-left corner for its location). Red circles represent relocated background seismicity of the period 2001 - 2007 (Lambotte *et al.* 2014), black open circles represent selected seismicity of the period July-August 1991 (Rigo *et al.* 1996), green circles represent the relocated epicenters of the 2001 swarm near Agios Ioannis (Lyon-Caen *et al.* 2004; Kapetanidis *et al.* 2010) and blue circles represent the relocated epicenters of the 2013 swarm (this study). Local stations are displayed with yellow triangles. The fault lines are based on Moretti *et al.* (2003); Palyvos *et al.* (2005); Bell *et al.* (2008). Figure after Kapetanidis *et al.* (2015).

within the epicentral area as well as from local and regional stations of the Hellenic Unified Seismological Network (HUSN), up to an average epicentral distance of 30 km. The data were manually analysed by the Seismological Laboratory of the University of Athens. A detailed study has been conducted in cooperation with the Institut du Globe de Paris (IPGP), France, and is described by Kapetanidis *et al.* (2015), hence only a brief description of the procedures and results is presented in this section, including an additional calculation of ETAS models.

5A.4.1 Location/Relocation – Multiplet classification

More than 1500 events of the swarm during the period between 21 May and 31 August 2013 were detected, manually picked and located, initially, using a local velocity model (RM) for the area of Western Corinth Rift (Rigo *et al.*, 1996). A custom velocity model (CM) was then determined using an average travel-time residuals and location uncertainties minimization technique (Kapetanidis *et al.*, 2015) to acquire better estimates of the initial hypocentral locations and to take advantage of the available local network. Both RM and CM models have the same V_p/V_s ratio (1.80), similar layer ceiling depths and yield hypocenters within a comparable depth range (8-10 km). However, the new model has reduced RMS errors by about 17% while the horizontal and vertical location errors were reduced by 6-7%. The hypocentral distribution was further improved by calculating the mean P- and S-wave travel-time residuals and applying station corrections to reduce errors due to lateral velocity variations, geology or topography characteristics at each station.

The typical procedure described in the introduction of Chapter 5 was followed for multiplet classification. Two reference stations were used, TEME, situated within the epicentral region, and LAKA, in an average distance of ~10 km from the center of the swarm. For each pair events, the respective waveforms (of the same station/component) were band-pass filtered prior to the cross-correlation procedure to remove long-period and high-frequency noise in the frequency band between 2.5 Hz and 23 Hz that is usually adequate in most cases of local micro-earthquakes (Section 1.2.2). A combined cross-correlation matrix was constructed by averaging the XC_{max} for up to 6 measurements per event-pair, using their RMS value. The optimal correlation threshold for

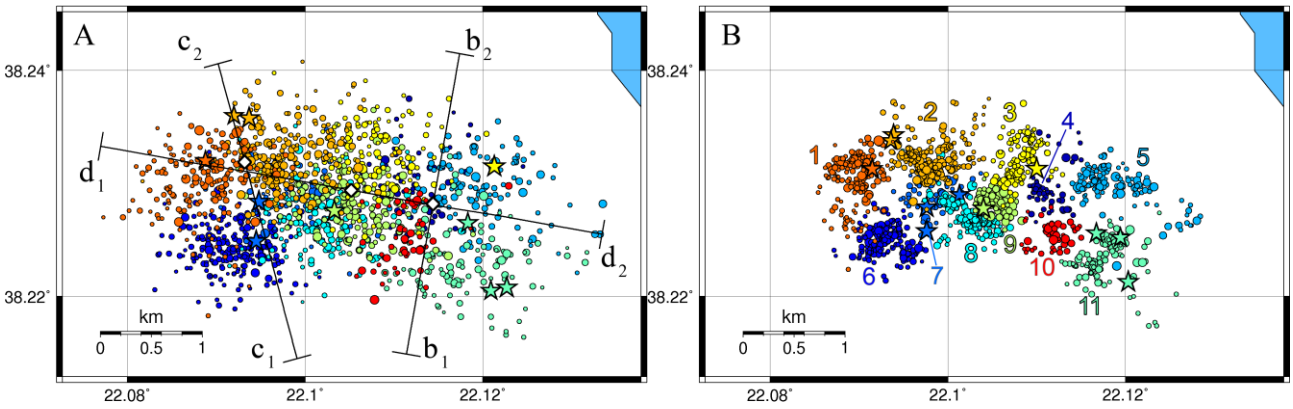

Figure 5A.21: Epicenters of the 2013 seismic swarm in Helike, A) before and B) after the relocation procedure with HypoDD. Colours and numerical labels (panel B) represent the 11 spatial clusters. Profile lines (panel A) correspond to the cross-sections of Fig. 5A.22. Figure after Kapetanidis *et al.* (2015).

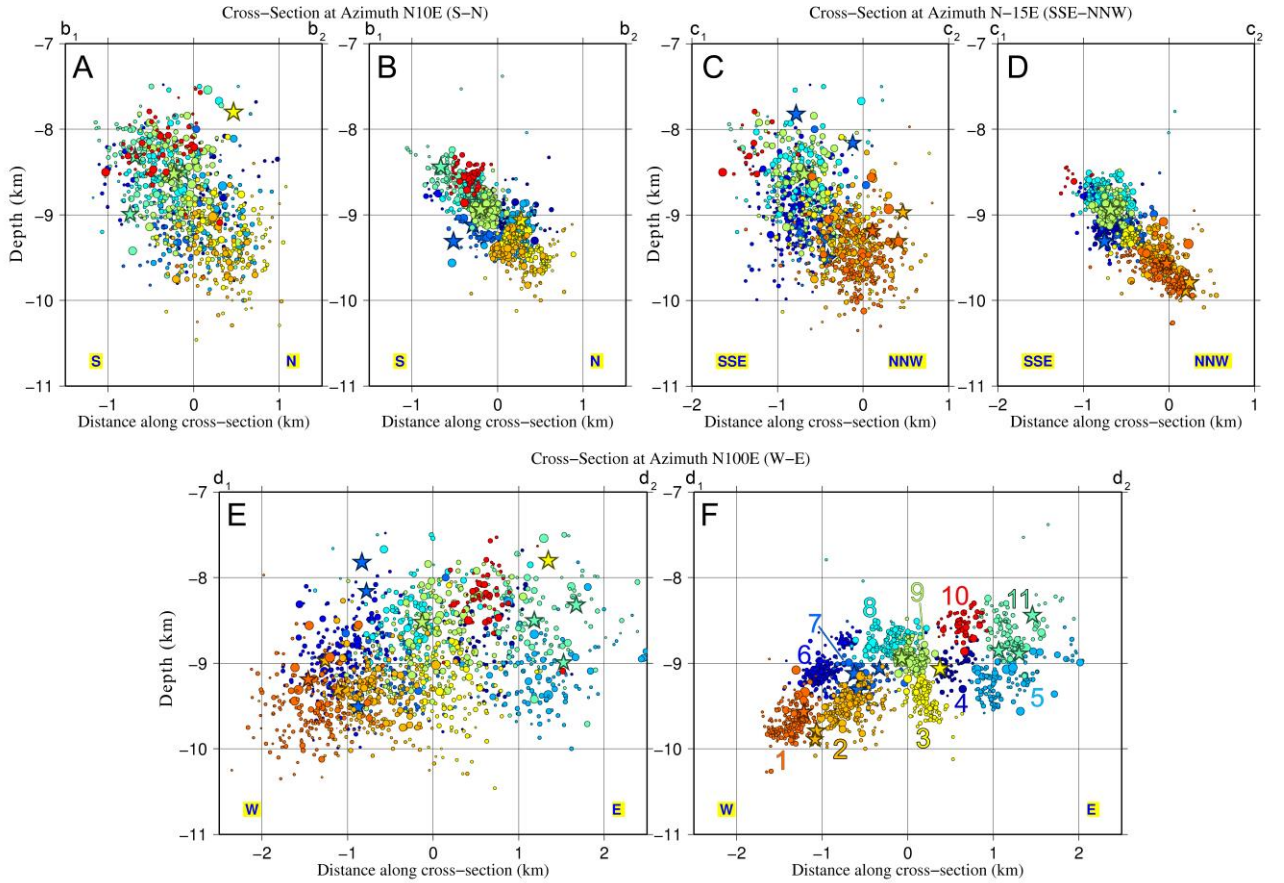

Figure 5A.22: Hypocenters of the 2013 seismic swarm in Helike, before (A, C, E) and after (B, D, F) the relocation procedure with HypoDD. The N10°E and N15°W cross-sections (A, B and C, D, respectively) correspond to the b_1-b_2 and c_1-c_2 profile lines of Fig. 5A.21A, while the N100°E cross-sections E and F correspond to the d_1-d_2 profile lines of the same figure. Colours and numerical labels (panel D) represent the 11 spatial clusters. The thickness of the perpendicular cross-sections A, B and C, D is ±1.5 and ±1.3 km, respectively. The profile lines b_1-b_2, c_1-c_2 and d_1-d_2 are centered at [38.2282N, 22.1144E], [38.2319N, 22.0932E] and [38.2294N, 22.1052E], respectively (white diamonds in Fig. 5A.21A). Figure after Kapetanidis *et al.* (2015).

nearest neighbor linkage was found at $C_{th} \equiv C_{opt.th} = 0.80$, resulting in 113 multiplets which contained a total of 1189 events (~80% of the catalogue). Cross-correlation measurements for all combinations of pairs of events within each multiplet, at all stations, for P- and S-waves separately, yielded mean absolute time-lags of about 0.05 sec and 0.09 sec, for P- and S-waves, respectively, justifying the choice of the average arrival-time reading error of 0.15 sec for the estimation of the initial location errors, with median uncertainty values *ERH* = 0.25 km and *ERZ* = 0.40 km.

Double-difference relocation followed, using the HypoDD algorithm (Waldhauser, 2001), parameterized in two sets, the first with strong a priori weights on catalogue data and the latter on cross-correlation data, resulting in a stable solution with minimal origin shift. A second pass was also considered, using the relocated foci of the first one as initial positions and repeating the

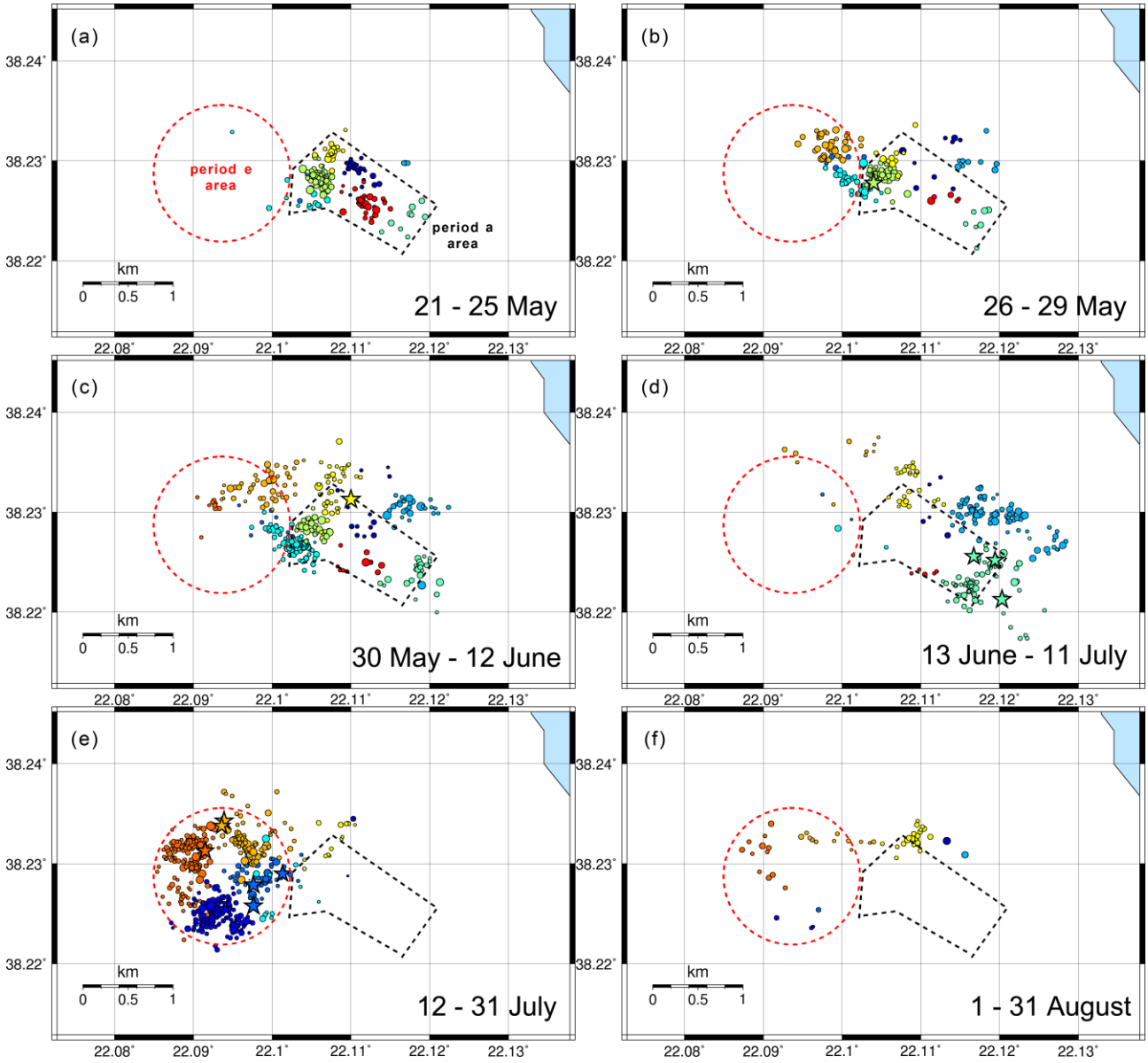

Figure 5A.23: Epicentral maps of the relocated catalogue for 6 consecutive periods of year 2013: A) 21 - 25 May, B) 26 - 29 May, C) 30 May - 12 June, D) 13 June - 11 July, E) 12 July - 31 July and F) 1 - 31 August. The colours correspond to different spatial clusters. The dashed black polygon and dashed red circle correspond roughly to the epicentral area activated during periods A and E, respectively, and are used for spatial reference. Figure from Kapetanidis *et al.* (2015).

procedure on each of the individual multiplets separately, using the Singular Value Decomposition (SVD) method for the smaller ones and the weighted least-squares (LSQR) method for the larger ones. The dispersion of the spatial distribution was significantly reduced, especially in the vertical axis, and multiplets were compacted in dense spatial clusters. A total of 1489 events (99%) were successfully relocated (Figs 5A.21 and 5A.22), including those which were only linked through catalogue data (they did not belong to multiplets). Both horizontal and vertical scattering were decreased, with the epicenters becoming concentrated in a 3 km × 2 km patch, oriented approximately E-W. A 3D visualization of the relocated spatial distribution suggests that the events have occurred at a depth range between 8 and 10 km, on a curved surface with an uncertainty of

about ±250m (the width of the distribution can be observed in the perpendicular cross-sections of Fig. 5A.22B and 5A.22D), striking approximately N270°-280°E at its north-dipping middle and eastern part and N260°E at its NNW-dipping western side. Its estimated horizontal extent is ~3.7 km in a N100°E direction. The surface is not evenly covered with hypocenters but the activity is focused in strong spatial clusters, separated by gaps, some of which may correspond to asperities which have hosted the stronger events of the sequence.

5A.4.2 Spatio-temporal / multiplet analysis

The characteristics of the spatiotemporal distribution, which can shed light on the dynamics, reveal patterns in its behavior and provide clues for the interpretation of the phenomenon, are being thoroughly examined in this section. A spatial segmentation of the distribution in groups was performed, using Ward's linkage, to provide visual aid for better understanding of the hypocentral shifts achieved by the relocation procedure, but also to enable the spatially targeted analysis. A threshold value was imposed, dividing the distribution in exactly 11 clusters (Fig. 5A.22B), after consulting Mojena's plot and confirming the choice visually. Although the clustering is 3-dimensional, the horizontal projections of the clusters are also well-separated. The clusters appear to be divided in two rows (both horizontally and vertically), with the exception of the middle region of the swarm which is shared by clusters #3, 8 and 9.

The Helike seismic swarm was initiated on 21 May 2013 by a series of small earthquakes, escalating up to an M_w = 3.1 event on 23 May 05:31 UTC, spreading through the polygon area marked in Fig. 5A.23A. A second outbreak (Fig. 5A.23B) began in 27 May 2013, culminating to an M_w = 3.6 earthquake on 28 May 01:13 UTC. The latter event occurred at the westernmost point of the main cluster of activity of period A and triggered a patch of the fault surface further to the west (Fig. 5A.24, 1st star). This was followed by another burst of seismicity (period C) including a major M_w = 3.7 event on 31 May 08:57 UTC (2nd star in Fig. 5A.24, cluster #3), which occurred in a spatial gap of the previous activity, approximately in the middle of the swarm's epicentral distribution. By the end of period C, since 10 June, the seismicity started to migrate gradually towards the eastern portion, while at the western and middle part the activity diminished. The eastwards migration continued during period D with small bursts every few days, including one with three earthquakes of magnitude between 3.0 and 3.5, followed by two more clusters, the latter of which involved an M_w = 3.6 event on 27 June 17:24 (the fourth event of the sequence with $M_w \geq$ 3.5) that generated smaller events at the easternmost edge of the distribution.

A sudden change in the spatiotemporal pattern occurred in mid-July (Fig. 5A.23E, with a dashed circle marking the epicentral area in all panels for spatial reference), when the western portion of the swarm was activated, with several $M_w \geq 3.0$ events, including an M_w = 3.7 earthquake on 15 July, 20:07:55 UTC, one of the major events of the sequence. It is worth noting that the latter occurred in a gap between spatial clusters #1, 2 and 6 which were initiated one day earlier with some smaller events. The last period (F) is characterized by a small spatiotemporal cluster at the middle-northern part of the swarm and a gradual decline of activity towards the end of August.

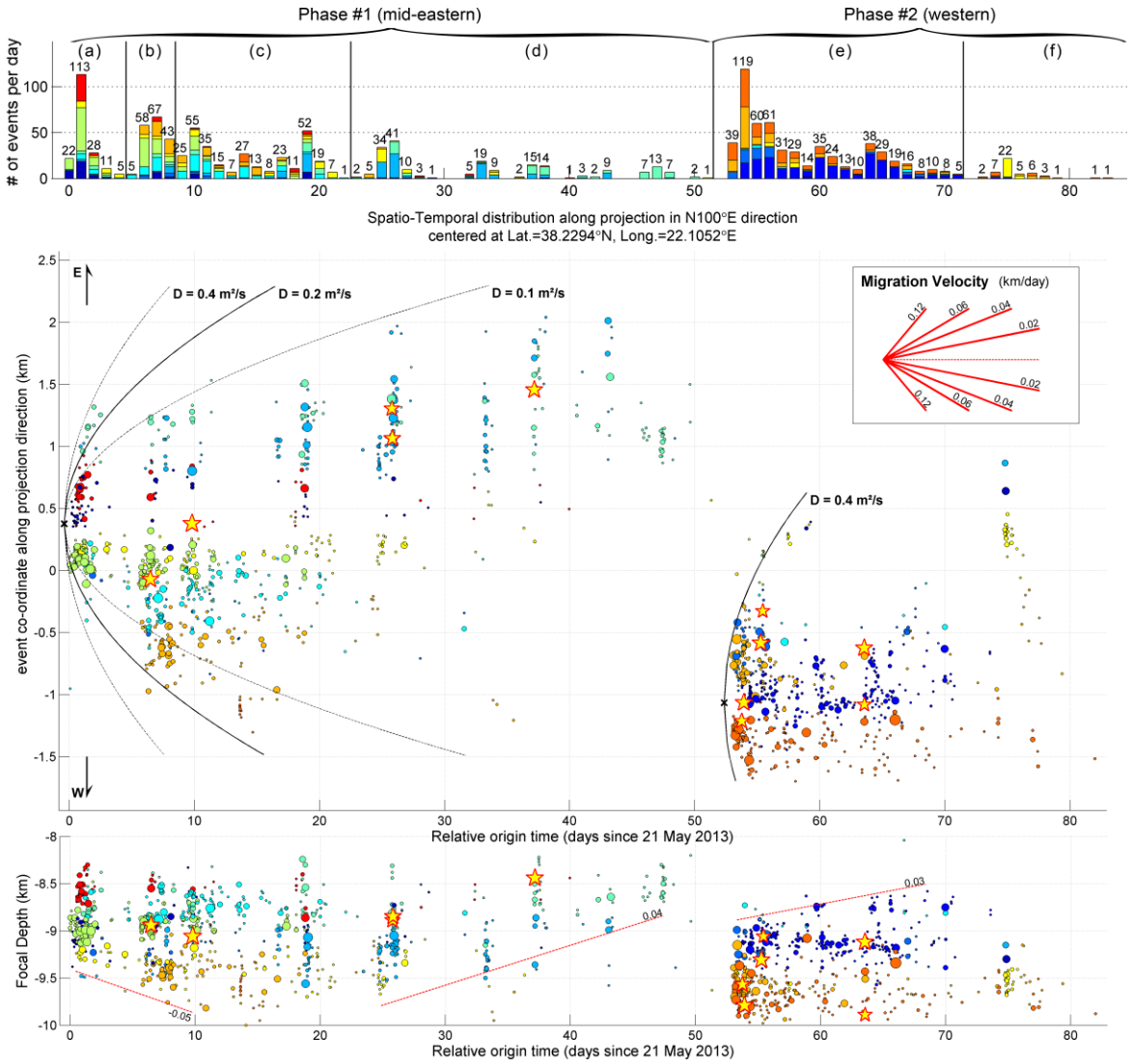

Figure 5A.24: (upper panel) stacked histogram of earthquakes per day with different colours corresponding to the 11 spatial clusters. (Middle panel) spatio-temporal diagram for the evolution of the 2013 earthquake swarm in Helike. The vertical axis represents the projection along a line in a N100°E direction, centered at [38.2294°N, 22.1052°E] (similar to the profile d_1-d_2 of Fig. 5A.21A). Colours correspond to different spatial clusters (similar to Figs 5A.21B and 5A.22F). The circle size is proportional to the event magnitude. Major events (M_w > 3.2), are displayed with stars. The parabolic theoretical curves of probable triggering fronts for hydraulic diffusivity values D = 0.4m²/s, D = 0.2m²/s and D = 0.1m²/s are also displayed for 2 distinct fluid intrusion events (see the discussion section for details). The "Migration Velocity" aiding lines at the box in the upper-right corner refer to horizontal migration. (Bottom panel) the same as in the middle panel but for focal depth against origin time. The dashed lines show approximate vertical migration rates in km/day (±0.01 km/day). Figure from Kapetanidis *et al.* (2015).

Several differences exist between the first (periods A-D) and the second (periods E-F) phase of the sequence. The "middle region" (in the range of Y between 0 and 0.5 km in Fig. 5A.24) is mostly active during the first 30 days. The eastern region (Y > 0.5 km), active during the first phase, exhibits a gradual migration of seismicity from the middle of the swarm towards the east, with a ~400-500 m long patch of activity propagating at a rate of ~30-40 m/day, mostly during June. In the

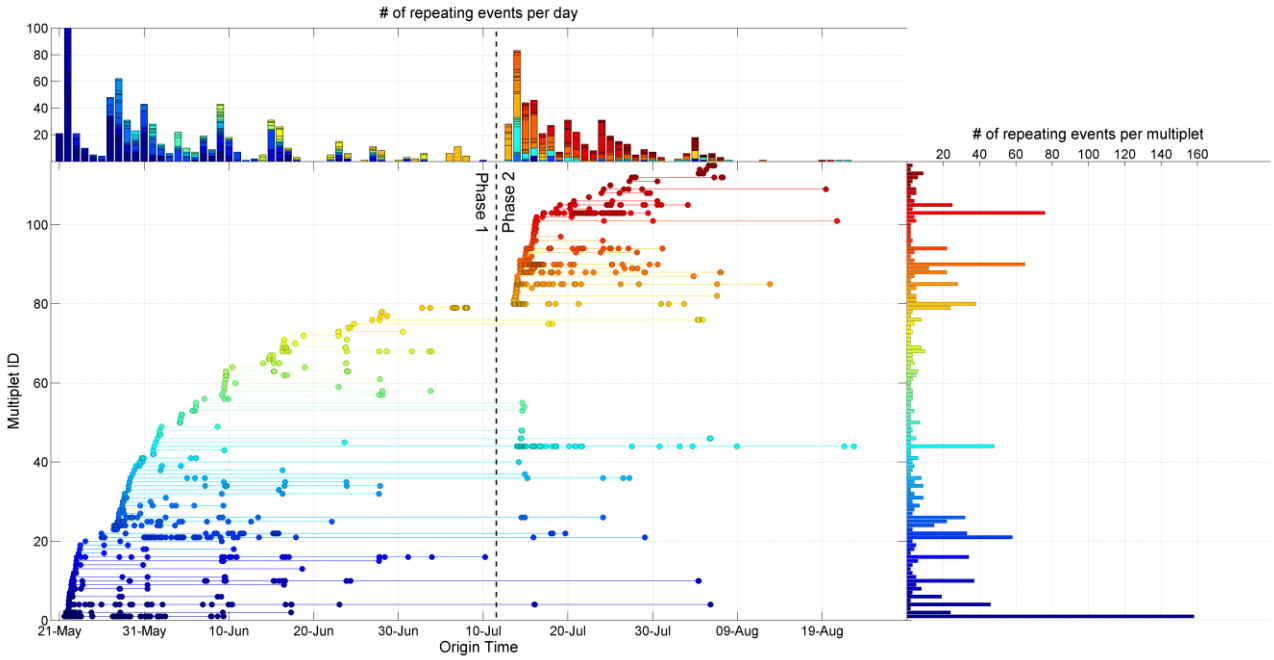

Figure 5A.25: Multiplet history for the seismic swarm of Helike, 2013. The circles represent repeating earthquakes linked by horizontal lines to indicate that they belong to the same multiplet. The vertical axis shows the Multiplet ID, sorted by the origin time of the first event of each multiplet. Multiplets with lower ID were initiated earlier than others with higher ID. The horizontal axis represents origin time. (Right) Multiplet size, indicating the number of events contained in each multiplet. The vertical axis is shared with the history dendrogram. (Top) Histogram of the total number of repeating events occurring per day. The horizontal axis is shared with the history dendrogram. Figure after Kapetanidis *et al.* (2015).

second phase, the activity is almost exclusively occupying the westernmost portion of the swarm, for a range of *Y* between -1.5 and -0.5 km (Fig. 5A.24), with the exception of a small spatiotemporal cluster in the middle of the swarm during period F. The focal depths during phase #1 are constrained between 8.5 and 9.5 km, gradually reaching ~10 km by the end of the second week (Fig. 5A.24, bottom panel). In phase #2, the activity is more constrained between 9 and 10 km, mostly involving spatial clusters #6 and 1 with persistent activity in a constant volume. Cluster #2 was also triggered at the beginning of period E and cluster #3 by period F, both concentrated at about 9.5 km.

The differences between the two phases were also evident in both the cross-correlation matrix and the consequent hierarchical clustering. A history of the occurrence of repeating events, with increasing IDs reflecting the origin time of the first event in each multiplet, can be observed in Fig. 5A.25. Sudden bursts of seismic activity are usually accompanied by the generation of new multiplets in regions previously unbroken. With the initiation of phase #2, about 20 new multiplets were formed during the first 4 days, some of which containing over 10 events. There are also a few groups of repeating earthquakes, mostly doublets with the first event of the pair having already occurred in phase #1 (among IDs 4-25 and 35-55). The same is true for one of the larger ones (ID #44), with all events but one in phase #2. This shows that there is some overlap between the activated regions in the two phases. The largest multiplet, by far, is the first that was generated (ID #1), containing 158 events, and occurring between 21 May and 9 June, 2013. This corresponds to

the spatial cluster #9, which lies in the middle of the swarm. The largest 18 multiplets contain over 20 events and have been generated in regions of strongly spatially (and often temporally) clustered activity.

The spatiotemporal distribution of the 2013 swarm revealed that the earthquake activity during the first phase was developed bilaterally in several sudden bursts, with a partial, weak gradual migration towards the east. The parabolic curves drawn in Fig. 5A.24 correspond to the theoretical triggering front (Eq. 1.16) caused by fluids infiltration and pore-pressure migration (Section 1.3.3; Shapiro *et al.* 1997). The theoretical envelope curves have been drawn bilaterally for different values of D with a pair of (y_o, t_o) parameters, starting location and initiation time of the fluids injection, estimated by visual inspection of the spatio-temporal diagram for each of the two phases. The y_o corresponds approximately to the projection of the major events of 31 May and 14 July, for the first and second phase, respectively, while t_o has been chosen ~1 day before the initiation of the corresponding sub-sequence. The eastwards migration of the first phase nearly follows this pattern for D = 0.1 m^2/s, while the western branch is better enveloped by the D = 0.2 m^2/s line. Although the second phase is within the bounds of the triggering front of the first one, it should most likely be considered independently. A fast, bilateral migration during the latter phase, lasting for about 7 days, is implied by the D = 0.4 m^2/s curve in Fig. 5A.24, combined with persistent activity near its initial source.

An alternate view is provided in Fig. 5A.26, which shows the radial distance from the starting point of each phase. The D = 0.4 m^2/s curve fits well on the beginning of the first phase, while D = 0.1 m^2/s fits better its later part, after day 15, at least in terms of migration rate. In the second phase, the D = 0.4 m^2/s curve does not manage to envelope the events of cluster #2 ($y \geq 0.5$ km) as they occurred almost simultaneously to those at Cluster #1. It does, however, match well the major events of July 14 and 15 which are displayed by stars in Fig. 5A.26. A similar pattern can be observed for the first phase if the D = 0.1 m^2/s line is shifted to the right by ~5 days. What is common in both phases is that, as in other cases of swarms in the literature (Aoyama *et al.* 2002; Vidale & Shearer 2006; Roland & McGuire 2009; Legrand *et al.* 2011), the stronger events appear later in the sequence, rather than the beginning. In many instances they are preceded by a number of foreshocks, while they behave as part of the sequence without triggering large series of aftershocks.

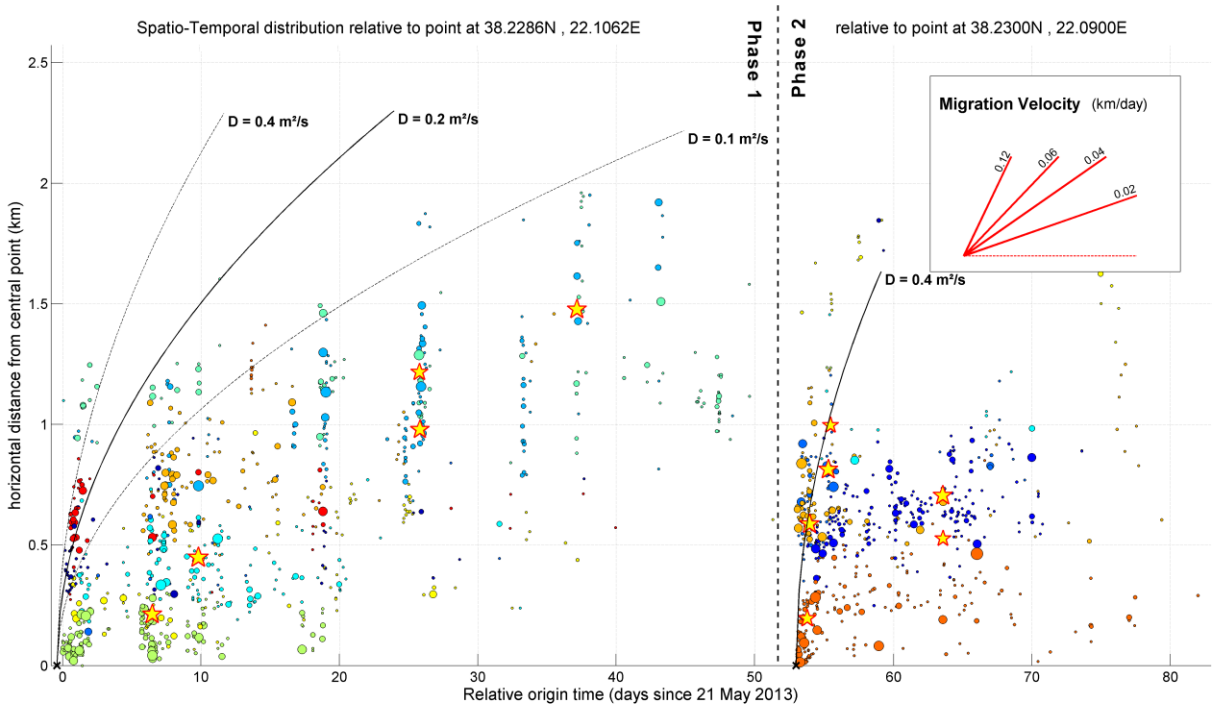

Figure 5A.26: Spatiotemporal distribution of epicenters relative to possible fluid intrusion sources located at [38.2286°N, 22.1062°E] (left, phase 1, eastern part) and [38.2300°N, 22.0900°E] (right, phase 2, western part). Colours correspond to different spatial clusters. Parabolic theoretical curves of probable triggering fronts for hydraulic diffusivity values $D = 0.4\text{m}^2/\text{s}$, $D = 0.2\text{m}^2/\text{s}$ and $D = 0.1\text{m}^2/\text{s}$ are also displayed.

There are significant similarities between the histogram of repeating events per day (Fig. 5A.25, top panel) and the total number of events per day (Fig. 5A.24, top). This was expected, as their majority (80%) has been found to belong to multiplets, although not necessarily large ones. However, the most striking similarity is between the diagram of the cumulative seismic moment (Fig. 5C.13b) and the multiplet history dendrogram (Fig. 5A.25, main panel). This shows that periods of outbursts in the seismic activity were followed by generation of new multiplets, which is interpreted as a spread of the activity in new areas rather than repeated slip in places that were ruptured earlier, even though repeating events tend to occur on a fault patch soon after the generation of a new multiplet. The major event of 31 May 2013 did not seem to cause an adequate number of aftershocks reflecting its magnitude (no sudden increase in Fig. 5C.13a). It was, however, soon followed by events that belong to multiplets which were briefly re-activated during the second phase of the sequence, such as the event of 1 June, 04:36 UTC, which belongs to multiplet #44 with more than 45 repeating earthquakes in phase #2 (Fig. 5A.25). These events belong to spatial cluster #2 and are located within the bounds of the circle marking the epicentral region of period E, at its northern part (Fig. 5A.23E). This implies influence of the seismicity during the first phase in the preparation of the region that was activated in the second one.

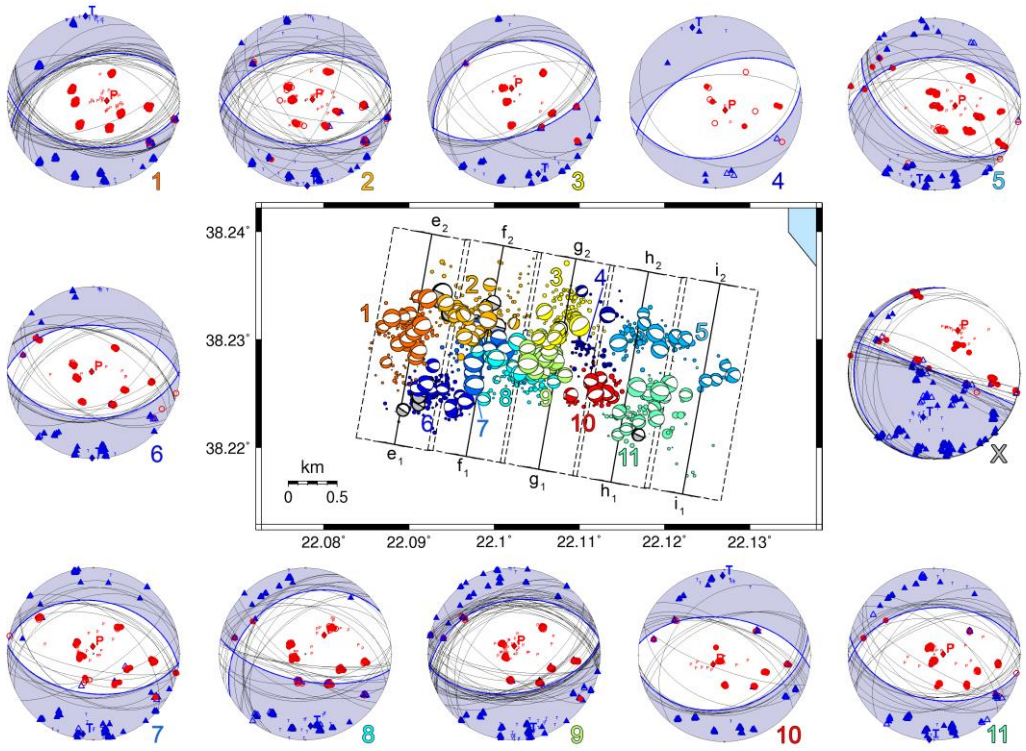

Figure 5A.27: 179 focal mechanisms belonging to the 11 spatial clusters (same colour coding and labels as in Figs 5A.21B and 5A.22F), with an additional special case (gray) for a group of sub-horizontal solutions. Composite focal mechanisms for each cluster are displayed in the periphery of the figure. Nodal plane projections drawn with thick blue lines denote the averaged solution for each group. Filled red circles indicate all observations of dilatational first motion, while blue triangles denote observations of compressional first motion. Individual solutions' P- or T-axis traces are marked with small letters P and T, respectively, while the corresponding axes for the average solution are represented by filled diamond symbols and a larger letter. The composite solution labeled with "X" (right hand side) corresponds to the gray individual solutions shown in the map. Labeled parallel lines on the map in N10°E direction are the cross-section profiles for Fig. 5A.28. The dashed rectangles represent the width for each cross-section (± 0.4 km, with 0.05 km overlap). Figure after Kapetanidis *et al.* (2015).

The behavior of Phase #1 is characterized by energy release in several intermittent bursts. Furthermore, it begins smoothly rather than abruptly, and proceeds with a few significant events accompanied by a large number of smaller events which do not contribute significantly to the released seismic moment. The second phase, beginning roughly around 12 July, is more typical of a mainshock-aftershock sequence, starting with a large number of events, including some with $M_w \geq$ 3.5, accompanied by strong energy release, then slowly decaying with relatively smaller shocks. The released energy can be described in terms of cumulative moment magnitude (CMM) (Fig. 5C.14). The CMM for the whole sequence reaches 4.55, while the corresponding values are 4.39 and 4.30 for the first and second phase, respectively. Although the total energy is comparable for both phases, the latter released it more abruptly than the former (dashed red line compared to the blue line in Fig. 5C.14). This is mainly explained by the fact that most of the major events of phase #2 occurred in a very short interval of 1-2 days (14 - 15 July, stars in Fig. 5A.26), while the corresponding events of phase #1 were wide-spread in a time-span of ~30 days, which is more typical of swarm-like behavior. This observation indicates that the first phase, possibly triggered by

fluids intrusion, has contributed to the preparation of the more abrupt second phase, which resembles a typical mainshock-aftershock behavior in terms of temporal energy release, without, however, starting with a major event that could be characterized as a mainshock of significantly higher magnitude than the rest of the events in its sequence.

5A.4.3 Focal Mechanisms

The highly detailed spatial distribution provides some clues on the geometry of the activated fault surface. In order, however, to gain a more complete understanding of the seismotectonic characteristics of the 2013 seismic crisis in Helike, Focal Mechanisms (FMs) estimated for over 170 events by first-motion polarities (FMP), complemented by S-Wave Polarizations (SWP) and S to P amplitude Ratios (SPR) to better constrain the solutions. The used method is similar to the one described in Section 2.4.1 for each event, with a grid-search for the determination of individual fault plane solutions which satisfy the FMP and a mean solution averaged over the individual ones weighted by a factor that takes into account the discrepancies between theoretical and observed SWP and SPR. In addition, Kapetanidis *et al.* (2015) determined focal mechanisms for the stronger events via regional waveform modeling, which were found to be compatible with the solutions derived from FMP.

Table 5A.2: Results of composite focal mechanisms per spatial cluster identified by CLID. Column "# evt." refers to the total number of events in each spatial cluster, while column "# f.m." is the number of focal mechanisms that corresponds to the cluster. (Kapetanidis *et al.*, 2015)

CLID	# evt.	# f.m.	Depth[a] (km)	Strike	Dip	Rake	T-axis		P-axis	
							Azim.	Plunge	Azim.	Plunge
1	190	24	9.7	253	47	-108	355	1	88	77
2	209	20	9.5	262	45	-100	179	1	82	83
3	127	10	9.4	250	33	-100	162	12	349	78
4	62	2	9.0	247	55	-97	343	10	131	78
5	126	12	9.2	266	45	-118	195	4	95	70
6	220	12	9.1	273	44	-88	181	1	297	88
7	76	12	9.2	279	38	-88	187	7	355	83
8	139	15	8.8	101	64	-70	176	17	45	65
9	164	31	9.0	259	38	-92	171	7	1	83
10	53	10	8.5	278	54	-77	359	8	232	77
11	110	14	8.6	265	45	-102	183	1	90	81
"X"	-	17	(9 - 10)	188	8	166	194	46	29	43
All	1476[b]	179	(8 - 10)	258	39	-103	177	7	46	79
All -X[c]	1459[b]	162	(8 - 10)	261	41	-98	177	4	49	83

[a] for the spatial clusters the depth column refers to median depth.
[b] some outliers were removed before the spatial clustering procedure was applied.
[c] excluding group "X".

A composite solution per spatial cluster was calculated for the events with FMs determined by either FMP or waveform modeling (Fig. 5A.27 and Table 5A.2), by averaging their normalized moment tensors, weighted by the number of FMP available for each individual solution. This is a procedure similar to the one applied in the case of the 2007 Trichonis Lake swarm (Section 5A.1.3; Kassaras *et al.* 2014a), and in the Santorini Volcanic Complex (Section 5A.3.3; Papadimitriou *et al.* 2015). The analysis revealed that most clusters exhibit a consistent composite solution that is more or less similar to the mean mechanism, averaged over all 179 individual observations. This corresponds to a normal fault, striking ~258° and dipping 39° to the north, which is favored against its auxiliary, south-dipping plane, as it is in agreement with the plane indicated by the relocated spatial distribution (Fig. 5A.22).

However, some events have been found with significantly different P-waveform onsets. While the FMP in most observations are dilatational in the middle and compressive at the top and bottom of

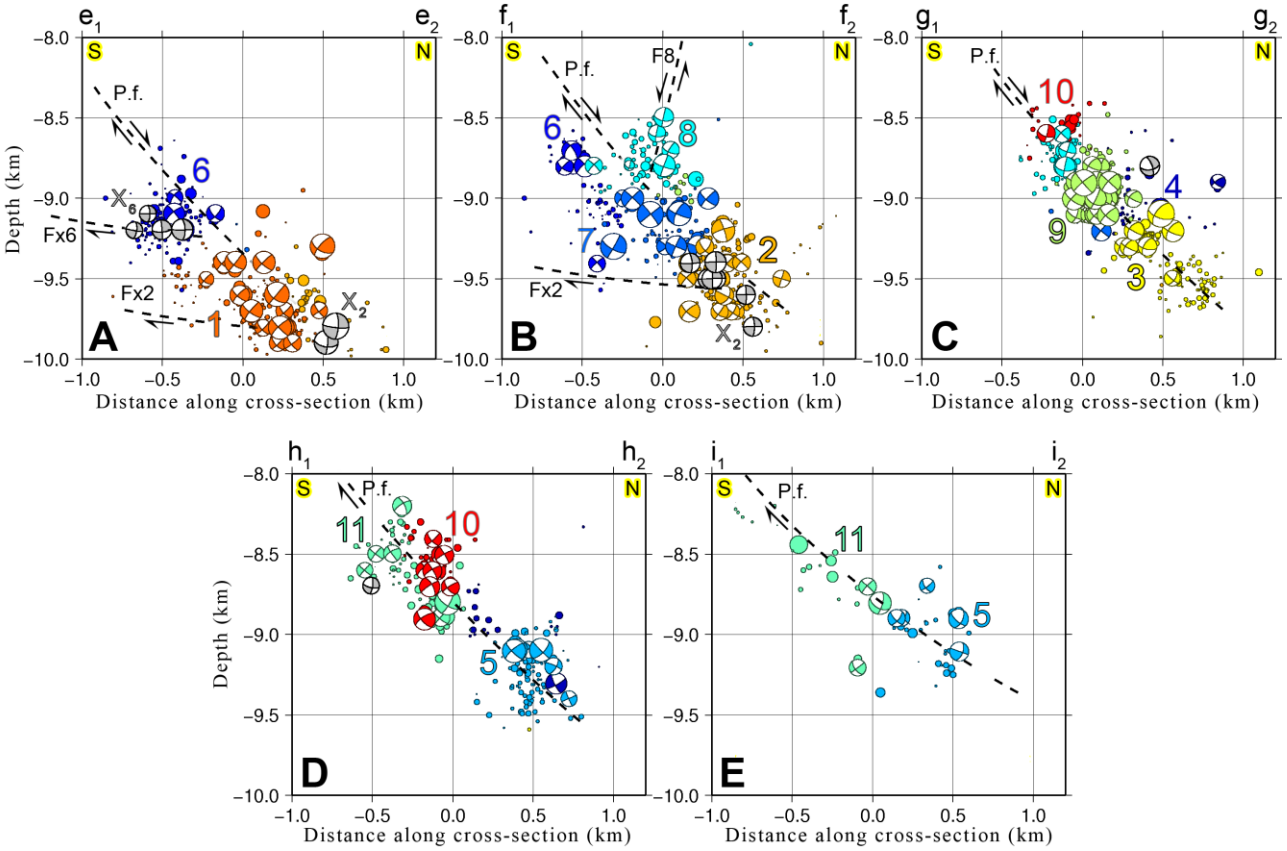

Figure 5A.28: Vertical cross-sections of hypocenters and focal mechanisms for the profile lines displayed in Fig. 5A.27: A) e_1-e_2, B) f_1-f_2, C) g_1-g_2, D) h_1-h_2 and E) i_1-i_2. The profiles are parallel (N10°E), equidistant (0.75 km apart), with the same length (±1.25 km from the center of each cross-section) and width (±0.4 km, displayed with dashed rectangles in Fig. 5A.27). Their individual centers are distributed on a line oriented at N100°E, centered at [38.2269°N, 22.1072°E], which coincides with the center of the middle cross-section g_1-g_2. The colours and numerical labels correspond to the spatial clusters defined in Figs 5A.21B and 5A.22F. X_2 and X_6 mark the sub-horizontal focal mechanisms of group "X" (Fig. 5A.27) belonging to clusters #2 and #6, respectively. Dashed lines represent possible faults involved in the swarm, P.f.: Pirgaki fault, F8: possible antithetic fault corresponding to cluster #8, Fx2 and Fx6: possible sub-horizontal faults corresponding to sub-clusters X_2 and X_6, respectively. Figure after Kapetanidis *et al.* (2015).

the stereo-net, group "X", displayed on the right hand side of Fig. 5A.27, has compressive polarities in the SSW half of the circle and dilatations are limited to the NNE half. These solutions were mostly found in spatial clusters #2 and #6, at average depths of ~9.5 and ~9.2 km, respectively, located almost exclusively at the western part of the swarm, with occurrence times mostly on 28-29 May or after 14 July. However, they were grouped separately for the calculation of a composite mechanism (Fig. 5A.27 and Table 5A.2, group "X"). Its rake is marginally positive (considering the angle wrapping at 180°), primarily due to the influence of the stations TEME, ALIK (compressive

first motion) and LAKA (dilatational motion) which constrain the sub-vertical auxiliary nodal plane. The sub-horizontal rupture plane dips slightly WNW, however the slip direction of the footwall is towards SSW. This is in agreement with the motion of the low-angle detachment which lies underneath the northern coast of the Western Corinth Rift at similar depth, where evidence of similar focal mechanisms has been found previously (Rietbrok *et al.* 1996). The coexistence of purely normal faulting events in the same volume with events that have occurred on a sub-horizontal rupture plane with horizontal slip and a small reverse component increases the complexity in the western part of the swarm. It is noteworthy that the major event of 14 July also belongs to this group and similar FMs have been derived through waveform modeling.

FMs belonging to the spatial clusters with CLIDs 2, 5, 6, 7, 9 and 11 are mostly suggestive of a north-dipping normal fault. FMs for CLID 8 have a NW-dipping nodal plane and a steeper SSW-dipping counterpart. In this case, the latter could well be a small antithetic rupture plane (Fig. 5A.28B, fault line labeled "F8" in cross-section f_1-f_2). The same could be true for CLID 10, or at least for some of its individual events. Both clusters #8 and #10 are located in relatively shallower average depths of ~8.8 and 8.5 km, respectively. CLID #1, located at the westernmost and deepest (~9.7 km) part of the swarm, dips roughly N-NNW, in agreement with the change in the curved surface that can be fitted to the spatial distribution. Clusters #4 and #3, the latter of which includes the oblique-normal, major event of 31 May, although they are located in the middle of the swarm, also suggest a NW-dipping or a steeper SE-dipping rupture plane. In general, the dip angles of the majority of the composite solutions vary near 45°, while the corresponding rake is around -90°, indicating mostly normal faulting with a small lateral component in some groups. Both pure- and oblique-normal solutions are obtained throughout the whole sequence, both spatially and temporally.

For most groups, the P-axes are generally sub-vertical, oriented in various directions but with their plunge angle around or above 80°. The T-axes, on the other hand, are mostly horizontal, with plunge angles below 10°, in a general NNE-SSW direction. That is with the exception of clusters #8 and #3, where the T-axis is less horizontal and, more importantly, group "X", which is the obvious exception, as it represents rupture on a sub-horizontal plane. Even in the latter case, both P- and T-axes for the composite solution of group "X" are directed roughly NNE-SSW, with azimuths 29° and 194°, respectively. These observations are compatible with both the known tectonic regime of the Western Corinth Rift and the regional extension field.

5A.4.4 Magnitude distribution – ETAS modeling

In the work of Kapetanidis *et al.* (2015), seismic moments were calculated using a spectral fitting technique (Matrullo *et al.*, 2013), much similar to the one described in Section 3.2 (see comparative results in Fig. 3.16), using a Brune-type (Brune, 1970) source model (Model #3 in Section 3.3). Examination of the energy release rates showed, at first impression, a qualitative difference between the two different phases of the evolution of the 2013 Helike swarm. In the first phase, the energy was released gradually, in a series of small bursts, while the second phase bared characteristics more akin to a mainshock-aftershock sequence, with most energy being released in the beginning of the phase, with several events with $M_w \geq 3.0$, including an M_w=3.7 on 15 July 2013 and gradually lower energy release rate later. The Gutenberg-Richter frequency-magnitude distribution diagram showed a *b*-value of ~1.1, calculated by linear regression between the completeness magnitude M_c = 1.7 and 3.5.

In this section, the application of ETAS modelling is described to investigate whether a common set of parameters for earthquake productivity, seismicity rate decay etc. can describe the sequence, either as a whole or at least partially. Fig. 5A.29 shows the ETAS model for the whole 2013 Helike swarm. There have been instabilities to the determination of the (constant) parameters, mainly depending on the starting and ending times. The best fit was achieved by ignoring the first 2 days of the sequence, where a short-lived outburst occurred with the strongest events having $M_w \approx 3.0$ halfway through. Although the model follows the data closely, there is an almost constantly positive residual, mainly attributed to the seismicity between the first M_w=3.6 of 28 May and the largest event, M_w=3.7, of 31 May, 2001. Had the residual level been reduced by ~15 events, a short period of quiescence would be detected ~15-20 days before the beginning of Phase #2. The latter increased the residual back to about 10-15 events. The sequence practically ends at about 80 days. The positive residual could indicate a contribution of fluids, especially to some of the outbursts, which cannot be modeled as a stationary process. However, the relative stability of the residual shows a strong dependence of the seismicity that followed from stress changes induced by previous (mainly the stronger ones) events of the sequence. The *a*-value of the model (a=0.841) is low enough to suggest a swarm-type sequence.

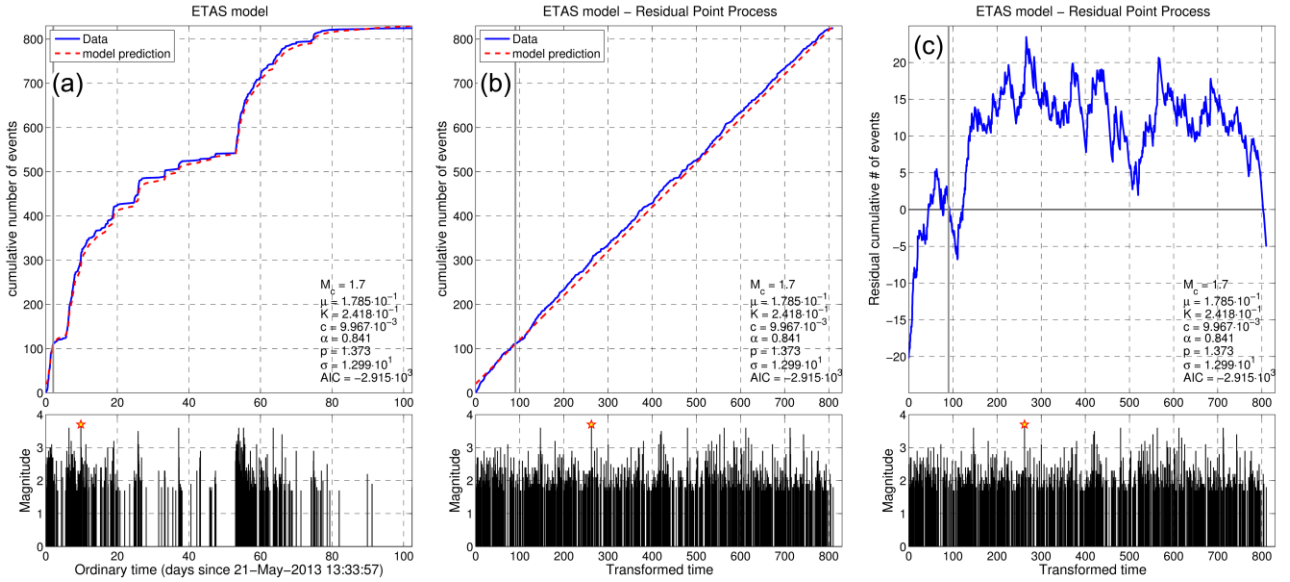

Figure 5A.29: ETAS model for the 2013 Helike swarm (21 May – 31 August), using a threshold $M_{th} \equiv M_c = 1.7$ and $M_r = 3.7$, with the model parameters estimated by MLE ignoring the first $T_o = 2$ days, a) data and ETAS model curves in ordinary time, b) the residual point process, c) residuals between data and model in transformed time.

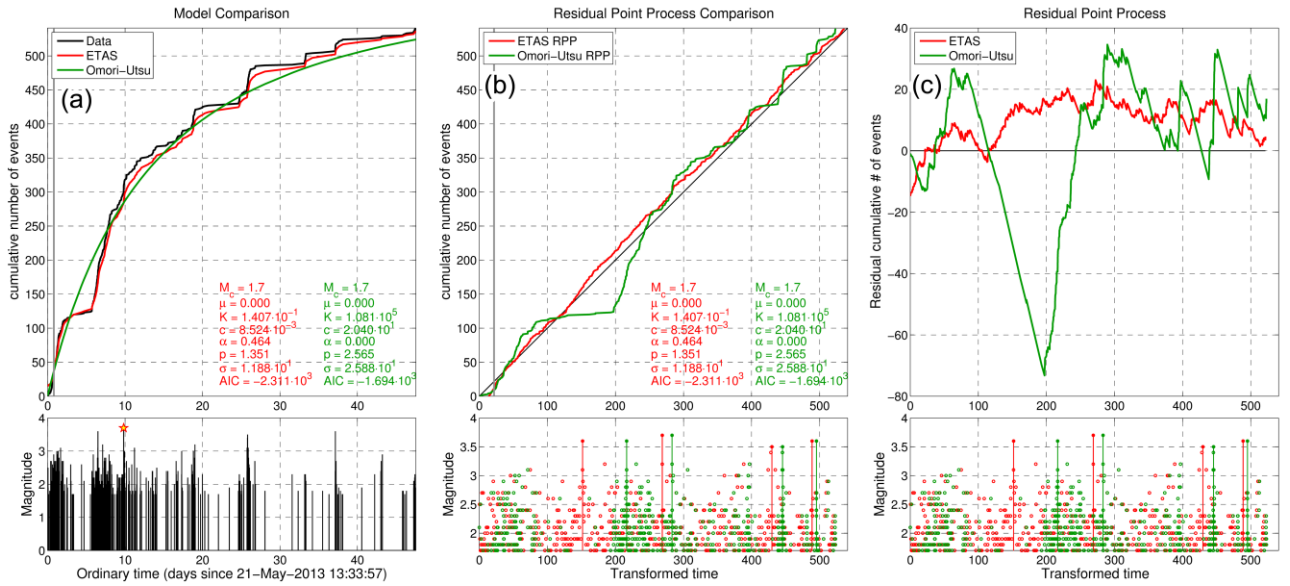

Figure 5A.30: ETAS and MOF models for the first phase of the 2013 Helike swarm (21 May – 12 July, $T_{end} = 52$ days), using a threshold $M_{th} \equiv M_c = 1.7$ and $M_r = 3.7$, with the model parameters estimated by MLE ignoring the first $T_o = 0.8$ days, a) data and ETAS model curves in ordinary time, b) the residual point process, c) residuals between data and model in transformed time.

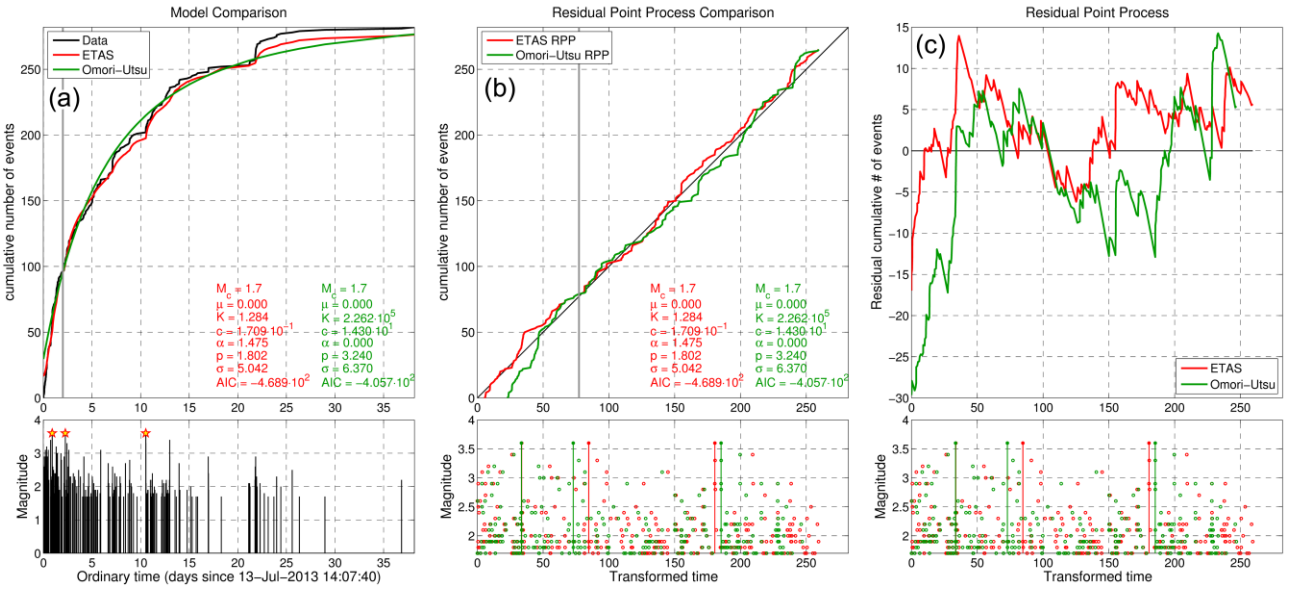

Figure 5A.31: ETAS and MOF models for the second phase of the 2013 Helike swarm (12 July – 31 August), using a threshold $M_{th} \equiv M_c = 1.7$ and $M_r = 3.6$, with the model parameters estimated by MLE ignoring the first $T_o = 2$ days, a) data and ETAS model curves in ordinary time, b) the residual point process, c) residuals between data and model in transformed time.

A closer look on Phase #1 with independent ETAS and Modified Omori's Formula (MOF) modeling is presented in Fig. 5A.30. This part of the sequence clearly cannot be modeled by MOF, as it does not begin with a single strong event and contains many secondary "aftershock" sequences. This is clearly suggested by the much lower (more negative) *AIC* value of the ETAS model compared against the respective value of the MOF model. Again, the ETAS residual is mostly positive, with a short-time negative (quiescence) before the first $M_w = 3.6$ event. The *a*-value ($a = 0.464$) is even lower than for the whole sequence, strongly supporting the swarm-type energy release pattern, while the aftershock decay p-value is relatively high ($p = 1.351$) but within normal margins and similar to the one for the whole sequence ($p = 1.373$).

Regarding Phase #2, the ETAS and MOF models (Fig. 5A.31) appear to have more comparable *AIC* values, although the ETAS model is still preferred over MOF, both in terms of *AIC* and visual fit, quantified by the standard deviation σ which is lower for the ETAS model. However, in this case the a-value is high enough ($a = 1.475$) to suggest a more mainshock-aftershock type pattern. The decay parameter p is also higher, consistent with the energy being released during a much shorter time-span in the second phase than the first one. Interestingly, if the last part of Phase #2 is omitted, which concerns the last outburst at the mid-northern part of the spatial distribution (cluster 3) the *AIC* value of the MOF model (which was preferred for Phase #2 by Chouliaras *et al.*, 2015) comes closer to the one of the ETAS model, but is still more positive, while the a-value of the ETAS model becomes lower (Fig. 5C.15). However the latter fit requires a fixed $p = 3$ due to instabilities, and also a lower threshold value $M_{th} = 1.5$, which is within the accepted range for M_c during the second phase. The ETAS model in this application appears to detect a short quiescence before the $M_w = 3.5$ event of 24 July 2001 and towards the end of the window, before the outburst at the mid-northern part.

5A.4.5 Discussion

The seismic crisis of 2013 in Helike, one of the most intense sequences that have occurred in the vicinity of Aigion city during the last decade, has offered the opportunity to investigate the fault geometry and mechanics at depth in a poorly known region of the Western Corinth Rift which has been relatively inactive since 1991. The high-resolution relocation and a multitude of focal mechanism solutions determined in the framework of the study of Kapetanidis *et al.* (2015) have enabled the detailed description of both spatial and temporal characteristics of this swarm. The coarse geometry of the spatial distribution in combination with the normal FMs is in agreement with the known tectonic regime, suggesting a north-dipping normal fault. Its geometry is a slightly curved surface which dips about 50° N-NW, a result which is also confirmed by the focal mechanisms, consistent with the eastern, downdip continuation of the presently inactive Pirgaki fault. The thickness of the swarm's spatial distribution (~500 m), which may be considered large relative to the relocation uncertainties, combined with the observation of sub-horizontal planes for some of the events in the western part at depths between 9.0 and 9.5 km and, possibly, some antithetic south-dipping faults at 8.0 - 8.5 km, are indicative of fault branching and, likely, fault edge.

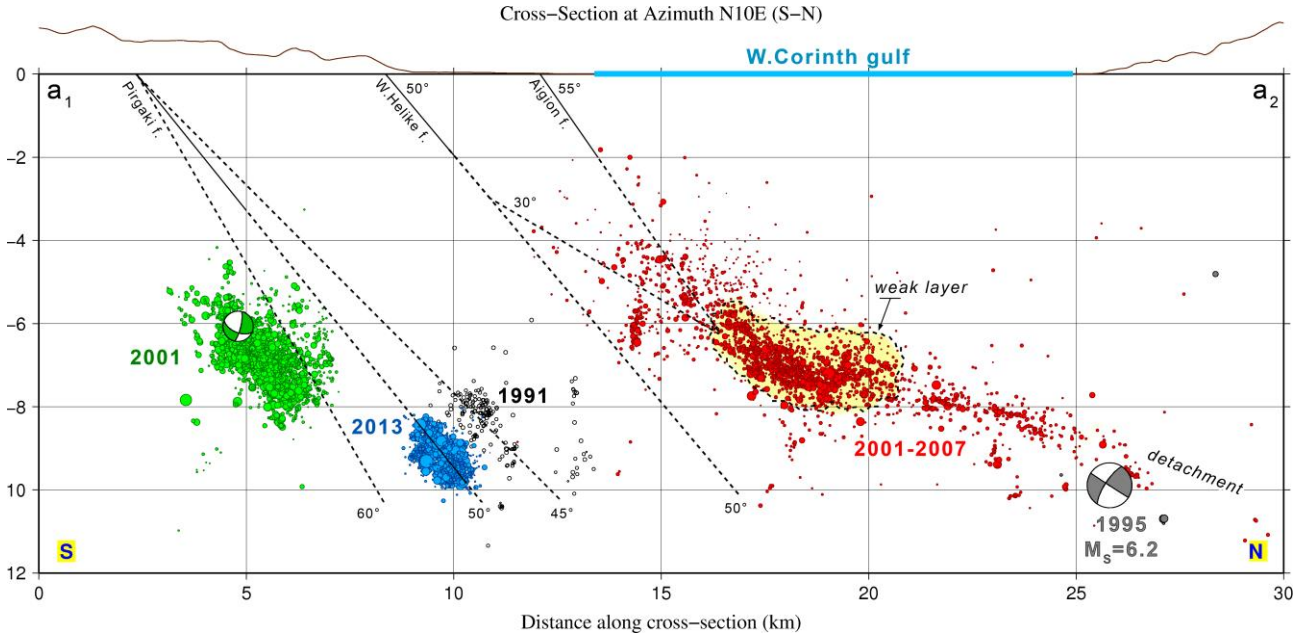

Figure 5A.32: 30 km long, ±5 km wide, N10°E cross-section across the Western Corinth Gulf, along the profile line a_1-a_2 displayed in Fig. 5A.20, approximately perpendicular to the dominant strike of the normal fault system and parallel to the direction of the extension of the gulf. Red circles represent relocated background seismicity for the period September 2001 - 2007, black open circles correspond to relocated seismicity of the period July-August 1991, green circles are the relocated epicenters of the 2001 swarm near Agios Ioannis (Lambotte *et al.* 2014) and blue circles represent the relocation results of the 2013 swarm (this study). The topography of the southern and northern coasts of the Western Corinth Gulf is also displayed on top. Solid, labeled diagonal lines represent known faults and their hypothetical extensions at depth along with other aiding lines (dashed). Angle values refer to the apparent dip of the corresponding linear segments. Figure after Kapetanidis *et al.* (2015).

A possible interpretation is that the main fault that hosted the swarm is the Pirgaki fault, which outcrops about 8 km to the south (Fig. 5A.20). Its strike direction ranges N095°-100° while the dip angle varies between 40° and 70° to the north (Micarelli *et al.* 2006). This is consistent with the mid-eastern portion of the spatial distribution which is aligned in an E-W direction dipping roughly 40° towards the north. The high-resolution analysis which was undertaken in the study of Kapetanidis *et al.* (2015) has also provided details on secondary faults which were implicated at the western part of the swarm that was activated at a later temporal phase. There are a couple of spatial clusters (CLIDs: 1 and 6) which deviate from the N100°E oriented plane and make the spatial distribution appear curved at its western portion, dipping ~45° NNW. The activated fault segment is located about 2 km deeper than the seismically active weak layer of diffuse deformation (Lambotte *et al.* 2014) which is situated at 6-8 km beneath the gulf (Fig. 5A.32). The extension of the fault plane, as indicated by the mean focal mechanism (strike = 261°, dip = 41°) at 9 km focal depth, meets the surface near the western end of Pirgaki fault and Kerinitis fault, which links it with the *en échelon* Mamousia fault. The intense swarm of 2001 near station AIOA (Agios Ioannis village) has been attributed to Kerinitis fault, which is roughly parallel to the orientation of the Hellenic napes and is characterized as a structure that is cross-cutting the currently active N100°E trending faults (Lyon-Caen *et al.* 2004; Lambotte *et al.* 2014).

It is safe to assume that there are at least two parallel sub-horizontal discontinuities at the westernmost segment, which are depicted by the dashed lines Fx2 and Fx6 in Fig. 5A.28A, as they are grouped in clusters 2 and 6, respectively. The small-scale sub-horizontal fault Fx2, which also hosted the major event of 14 July, likely extends to the next segment, shown in Fig. 5A.28B (profile f_1-f_2). The FMs of group "X" have an average dip of 8° towards W-WNW, likely occurring on sub-horizontal weakenings in the crust, while providing a SSW-NNE slip direction consistent with the regional extension. The FM of the major event of the 2001 swarm is similar (one sub-vertical WNW-ESE plane), but with larger dip angle on the NW-dipping plane. Regarding a subset of oblique-normal FM solutions which were observed during the 2013 crisis, these could be attributed either to a small antithetic south-dipping fault or to a NW-dipping one. This suggests that while the swarm most likely took place on the easternmost, deepest part of Pirgaki fault, the focal zone is probably affected by an interaction either with Kerinitis fault or by other tectonic features.

In addition to the 2001 sequence, important seismic activity had occurred earlier, in 1991, in the vicinity of the 2013 swarm. That was an aftershock sequence which followed an M_L = 4.5 event on 3 July 1991, described as the Aigion cluster "Cl1" by Rigo *et al.* (1996). A relocated subset of its spatial distribution (Lambotte *et al.* 2014) is displayed in Fig. 5A.32. Its hypocenters are concentrated at a depth of around 8 km, shifted slightly towards the north (Fig. 5A.20). Rigo *et al.* (1996) observed that they are diffused through the whole block bounded by Pirgaki and Helike faults. The divergence from the hypocentral region of the 2013 swarm could also be due to the difference in network geometry or data quality. Another possible explanation could be that the 1991 sequence has occurred on a different (possibly blind) normal fault, parallel to the Pirgaki one. A third possibility would be that the 1991 sequence has occurred on a fault segment with its superficial trace a bit more southerly of Pirgaki fault, with a smaller dip angle. This fault segment intersects with the main Pirgaki fault at about 1 km depth (segment 13b described by Ghisetti & Vezzani 2005), retaining its lower dip angle, which means it should reach the depth of ~8 km more

northerly than Pirgaki fault. The location uncertainties are such that the spatial distribution of the 1991 sequence does not permit the definition of a fault plane dipping north. According to a different scenario, it would have occurred on a small antithetic, south-dipping fault. It is noteworthy that the mean FM solution for the 1991 sequence (Rigo *et al.* 1996) is quite similar to the one estimated for the 2013 swarm.

Clustering and spatio-temporal analysis revealed evidence for triggering by diffusion of pressurized fluids, especially during the first phase of the sequence, which lasted for ~50 days and was characterized by a series of outbursts with a weak migration to the east. The western portion of the swarm was then activated abruptly, releasing roughly the same amount of energy in a much shorter time. The sudden nature of the activity during the second phase is also reflected by larger migration rate, which is described by a hydraulic diffusivity parameter $D = 0.4$ m^2/s compared to the $D = 0.1$ m^2/s value that better describes the eastern migration of seismicity during the first phase. The fast, radial migration during the first day of the swarm's activity (Fig. 5A.26), with a roughly constant rate of 1 km/day, suggests a significant contribution of creep propagation and faulting interaction for this early stage. A possible mechanism could involve a combination between creeping and pore-pressure diffusion (e.g. Bourouis & Bernard, 2007), as indicated by the low migration rates of 20-100m/day and relatively low hydraulic diffusivity values of 0.1 to 0.2m²/s. As Kapetanidis *et al.* (2015) note, the faster stress relaxation during the second phase could be due to the transfer of coseismic stresses and possibly of the high pore-pressure from the first phase to the western fault system: the latter would thus have been loaded closer to its failure strength, making it more reactive when failure started diffusing within it. This combination of triggering mechanisms (fluid diffusion and tectonic stress transfer) has been previously observed in seismic swarms, such as the 2000 swarm in Vogtland/NW Bohemia (Hainzl & Ogata 2005). The limited extension of the swarm upwards and northwards may be due to the interaction of the Pirgaki fault with others that are intersecting it, like the NW-dipping Kerinitis fault, which may act as barriers for stress migration through creep and/or pore-pressure diffusion.

The narrow depth range of the hypocenters can be mainly attributed to their strong clustering and relatively small magnitudes. Similarly narrow ranges, however, are also observed in cases of induced seismicity by man-made hydraulic stimulations (Ake *et al.* 2005; Baisch *et al.* 2010; Bachmann *et al.* 2012; Albaric *et al.* 2014), which makes the fluid intrusion hypothesis even more likely. The 2013 swarm possibly took place at the deepest edge of the Pirgaki fault where brittle fracture is feasible. At larger depths, the deformation of the crust becomes gradually ductile and, even if the Pirgaki fault extends deeper, it is not expected to be seismogenic. Kapetanidis *et al.* (2015) estimated a cumulative seismic moment magnitude for the swarm of the order of $M = 4.5$, which would cause a Coulomb stress change by less than 0.01 MPa (increase or decrease, depending on the position of the sub-faults), representing a clock advance of less than one year for the major west Helike fault, supposing a recurrence time of 300 years and a 3 MPa stress drop (Briole *et al.* 2000).

Complementary to the study of Kapetanidis *et al.* (2015), the determination of parameters for the ETAS in this section confirms the swarm-type behavior for the whole sequence, with implications for a contribution of aseismic processes to account for abnormally higher seismicity rate than expected from the model due to simple stress transfer. It also revealed a quantitative distinction

between the first and the second phase, with the latter resembling the pattern of an aftershock-type decay in the seismicity rate (although still lacking a single major event that could be labeled as a "mainshock") while the former being more consistent with a swarm-type pattern.

Appendix 5B

Main application of the HADAES method

The HADAES method has been applied to the case study of the 2014 Nafpaktos-Psathopyrgos swarm, described in Section 5.4. In this Appendix, the step-by-step procedures and technical aspect of the application are described in detail. Routine analysis by the Seismological Laboratory of the University of Athens has provided a set of over 800 manually located earthquakes which can be used, potentially, as master-events (ME). It is crucial that arrival-times of both P- and S-waves are

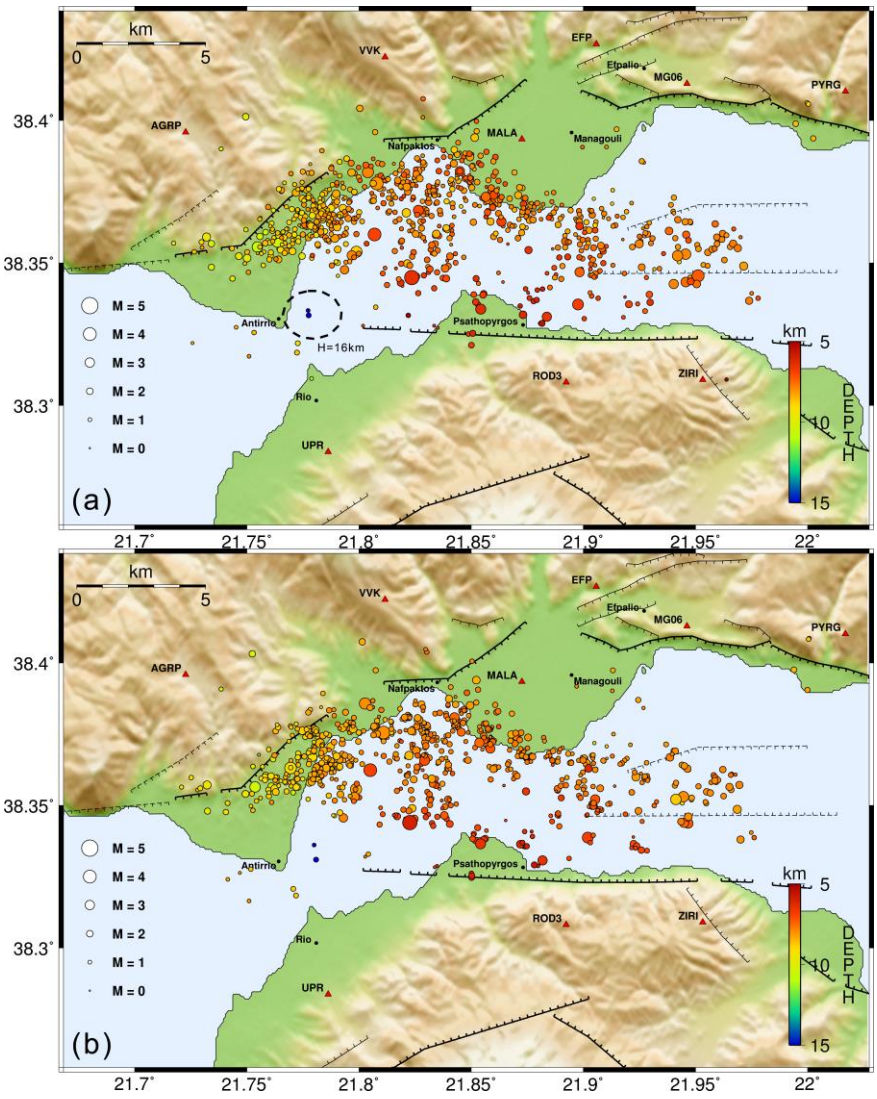

Figure 5B.1: Hypocenters of manually located master-events (a) before and (b) after relocation with HypoDD.

available at all Stations of Interest (SoI), if possible, as their travel-times are used as guides for the theoretical arrivals of the corresponding waves of the detected slave-events. Any missing arrivals from the routine analysis can be added either manually or automatically by applying the AIC-picker algorithm, as described in Section 4.2. Initially, these ME were located using HYPOINVERSE (Klein, 2002) and the velocity model of Rigo *et al.* (1996) for the region of the western Corinth Rift. The ME were post-processed using a standardized method for the identification of multiplets and double-difference relocation with both catalogue and cross-correlation data (see Section 5.4). This is important, as their absolute locations are used for reference in the initial (dummy) locations of slave events which will be detected by the algorithm.

The results of the relocation procedure are presented in Fig. 5B.1. The seismicity is mainly distributed on a curved surface which can be roughly divided in two halves. The eastern one is a sub-horizontal plane, striking N350°E and dipping ~20° towards the north. The western half appears to have a slightly steeper dip angle and is a bit rotated counterclockwise with respect to the eastern half. A deeper cluster was also identified in the western region, at a focal depth of $H \approx 16$ km. One of the closest stations to the epicentral area with available continuous waveform data for the most part of the study period is station EFP of the HUSN, which was chosen as the primary reference station for this application. Station AGRP, at the western edge of the CRL network, was used in addition, to cover some data gaps of EFP during August and especially in October 2014. A total of 550 out of 765 events with available waveforms at the primary reference station, EFP, inside the Area of Interest (AoI) were grouped to 94 multiplets with a correlation threshold C_{th}=0.64. One event was selected from each multiplet, following the procedures of Section 4.4, and along with the remaining orphan ME they comprise a database of 309 external ME, or "M_{ext}". The rest of the manually analysed events in the AoI were only used as internal master-events (M_{int}) at their DS multiplets, or externally via cross-day links (Section 4.4.5).

The continuous recordings on the vertical component were filtered between 1.5 and 15 Hz, inspected for data gaps which were smoothed and filled with Gaussian noise to prevent false triggers (see Appendix 4A). Afterwards, the waveforms were loaded in 30-minute buffers and processed with the STA/LTA method and additional selection criteria, as described in Section 4.1, to detect probable earthquake signals and reject low SNR or multiple triggers. Day-Specific (DS) cross-correlation matrices were constructed for the selected signals. This step was followed by nearest neighbor linkage, determination of the optimal threshold and construction of DS multiplets.

Triggers which coincided with the arrival-time of P- or S-waves of ME (which occurred on the same day) to the reference station were directly associated to them. Any of these ME which belong to one of the DS multiplets provides a starting point for the association of approximate source parameters and arrival-times to the rest of the events in their corresponding multiplet. Multiplets which did not contain a DS master-event were cross-correlated against the database of M_{ext}, excluding those which have occurred on the same day. For (first-order) slave events which could be directly related to ME, their P- and S-wave arrival-times on the reference station were determined by the waveform similarity approach (Section 4.3; Kapetanidis & Papadimitriou 2011), controlled by a third cross-correlation using the full master waveform (P & S) as template. The XC_{max} values were used as weights for the calculation of approximate P- and S-wave travel-times in all SoI, as well as the rough estimates of hypocentral parameters. The "dummy" origin time was estimated by

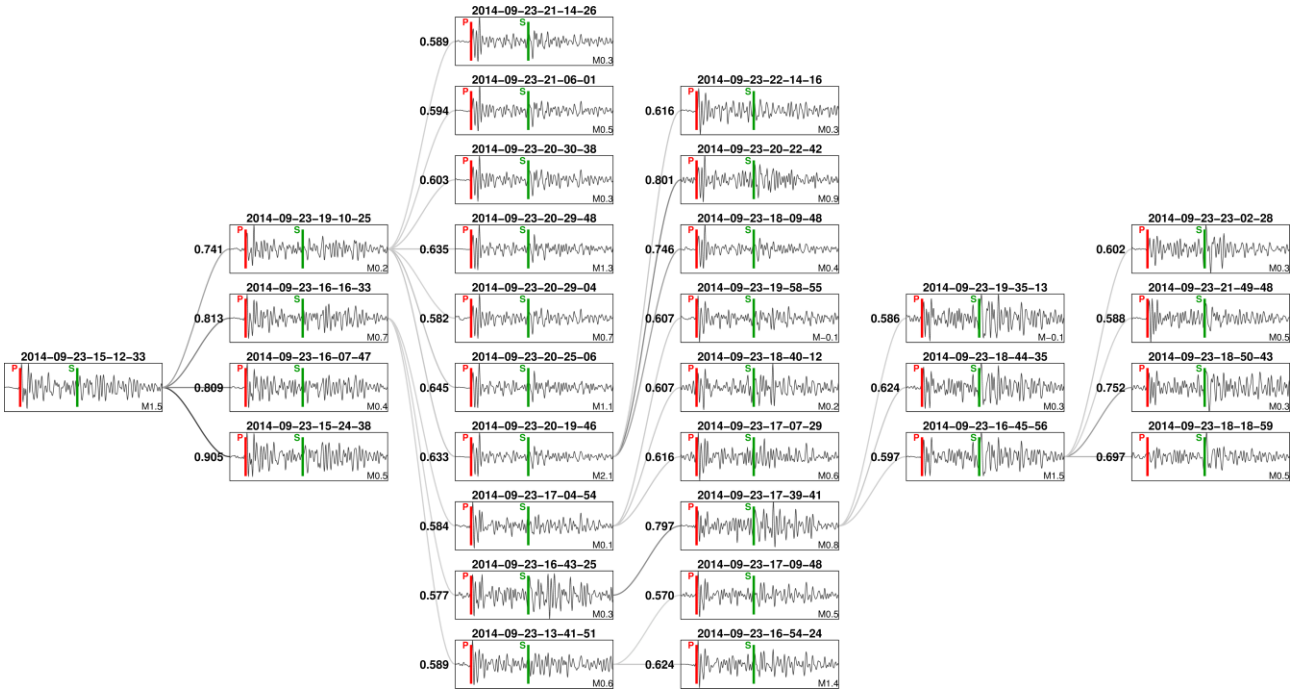

Figure 5B.2: An example of hierarchical relations within a day-specific multiplet and inheritance of P- and S-wave arrival-time associations with the correlation detector technique. Codes on top of waveforms denote the approximate origin time, numbers on the right of the waveform panels refer to the cross-correlation maximum between each secondary slave and its parent. The relative magnitude of each event is denoted on the lower-right corner of the corresponding panel. For each child only a single parent is presented for better clarity.

subtracting the travel-times of P- or S-waves from the corresponding arrival-time at the reference station. The first-order slaves were then used as ME (Slaves-as-Masters, or SaM) and the procedure was repeated to propagate the arrival-times and seismic source parameters to the rest of unassociated slaves within the multiplet. An example of this internal hierarchy is presented in Fig. 5B.2. Orphans were cross-correlated against the M_{ext} for possible associations.

Each DS multiplet was assigned a reference waveform, either by phase-weighted stacking or highest SNR, as described in Section 4.4.5. From the second day of the study period onwards, the reference waveforms were cross-correlated against those of the previous days (up to a maximum of 5 days). Similarity information between DS multiplets of different days was registered for later use. In case of strong similarity between the reference waveform of an unassociated multiplet of day B with one from a previous day, A, an association was attempted with the internal ME used for the multiplet of day A (if available). The original ME may even be "internal" (M_{int}) to a multiplet that belongs to another day, C, if the association of the multiplet of day A was achieved by reference to a multiplet of day C which contained a particular M_{int} that is not part of the M_{ext} database. If this does not yield a high XC_{max} value, a cross-correlation may be performed between the events of the multiplet in day B with the associated slaves of the multiplet in day B. As a last resort, the reference waveform of the multiplet of day A, which had provided the initial high-correlation match between the multiplets of different days, may be used as an ME itself, as it is also assigned with dummy

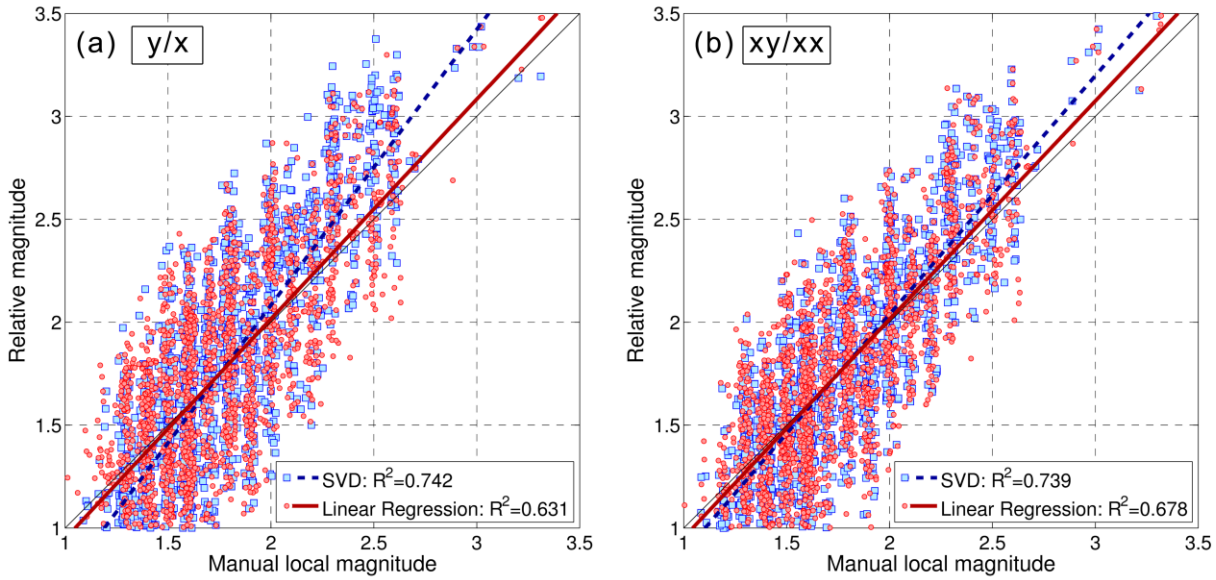

Figure 5B.3: (a) Automatically calculated relative magnitude against manually determined local magnitude for combinations of similar master-events with correlation threshold C_{th}=0.5, with the magnitude calculated using all samples in the best-fit window of the waveform pairs, filtered in the range 2-23Hz, (b) same as (a) but with the relative magnitude calculations being made on the (xy)/(xx) scatterplot (see Fig. 4.19c). The wide spread of the scatterplots corresponds to a standard deviation of ~0.36, which indicates the degree of imprecision of catalogue magnitudes.

source parameters and P and S travel-times. Similarity measurements between reference waveforms of associated multiplets are also useful for the later linkage between multiplets of different days into larger families. Also, reference waveform cross-day links between unassociated DS multiplets are used for the secondary loops of the algorithm (Section 4.4.5).

When primary and secondary loops are finished, a draft catalogue of "dummy" source parameters for associated slaves will be readily available. This can provide a first, draft image of the detected events and their associated origin times and hypocenters. However, it may contain groups of earthquakes with equal coordinates, when they are associated with exactly the same master-event, or linear artefacts when a set of slaves is related to a couple of master-events with varying weights. It also may contain artificial / anthropogenic noise "events" which were accidentally associated due to chaining effects and errors in the propagation of meta-data information. While it would be more efficient for the whole procedure if such signals were filtered out during the first stage of event-detection, any remaining noise-events will likely fail to be located and relocated at later stages. However, for better results, such signals should be discarded from the catalogue after manual examination (Ketner & Power 2013).

The correlation detector procedures also include measurements of relative magnitudes by the ratio of the similar parts of master and slave P, S or whole waveforms. The amplitude ratio can be calculated either by least-squares linear regression (LSQR) or Singular Value Decomposition (SVD), as described in Section 4.4.4. The ME already have manually determined duration, local or moment magnitudes. In order to calibrate the procedure, the filtered waveforms of similar ME at the

reference station (R_{st}) were cross-correlated to one another and relative magnitude was measured for those with XC_{max} > 0.5 with both LSQR and SVD methods. Their comparison with the corresponding manually determined magnitude is presented in Fig. 5B.3a. The results of the LSQR appear to scale properly (the slope, 1.07 ± 0.02, is close to unity), while the slope with the SVD method is higher, 1.34 ± 0.02, indicating larger bias. Both linear fits cross the $y=x$ line at $x=y=1.76$ (which is equal to the mean magnitude of the events), leading to, statistically, underdetermined lower magnitudes ($M<1.76$) and overestimated higher ones ($M>1.76$), mostly with the SVD method. If, on the other hand, the *xy*/*xx* data scatterplot is used for the relative magnitude calculation (see Section 4.4.4), the slopes of the linear fit are reduced to 1.06 ± 0.02 and 1.16 ± 0.02 for the LSQR and SVD methods, respectively (Fig. 5B.3b), while the corresponding correlation coefficient, R_2, appears to increase for the LSQR from 0.63 to 0.68. The standard deviation around the linear fit line is also slightly reduced with the *xy*/*xx* data but it is still rather high, at the level of ~0.3 for most magnitude ranges, which can be reckoned as an average uncertainty in the estimation of relative magnitude at the first level (for the immediate relatives of ME). The case of selected data with amplitudes above a certain threshold e.g. $>3\sigma$ (not presented here) yields a better correlation between relative and local magnitudes, with R_2 = 0.79, slopes closer to unity and lower standard deviation (~0.24) for both SVD and LSQR methods. However, it is safer that this technique is

Table 5B.1: Performance tables presenting the relation between assigned weights for manually and automatically defined arrival-times of P- and S-waves at the Stations of Interest (SoI), as well as missed or newly added picks with the automatic AIC-picker. Weight classes increase from best (0) to worst (3), representing the quality of a pick.

P-waves

		Automatic					
	Weight class	**0**	**1**	**2**	**3**	**Missed (2^{nd} pass)**	**Missed (1^{st} pass)**
Manual	**0**	445	2	2	0	4	4
	1	1607	194	12	6	28	34
	2	48	3	8	0	1	1
	3	9	0	1	2	1	1
	New picks	1032	57	76	57	-	-

S-waves

		Automatic				
	Weight class	**1**	**2**	**3**	**Missed (2^{nd} pass)**	**Missed (1^{st} pass)**
Manual	**1**	172	113	83	11	95
	2	901	518	275	82	530
	3	9	5	2	1	2
	New picks	605	209	244	-	-

applied only for whole waveforms (including both P- and S-waves) to ensure that an adequate number of samples are available for the correlation. Similar results are acquired with filters in different frequency ranges, such as 2-10Hz.

At this point, while the spatial information still has some uncertainties, the temporal distribution given by the draft catalogue, merged with the ME, is generally representative. The frequency-magnitude distribution is also expected to be more complete, although the calculated relative magnitudes may include some events with large deviations and there is a possibility for errors when applied between signals of environmental noise that may be accidentally present in the data. This is due to the fact that with the procedures that have been run so far the detection sensitivity is high, as a result of the SSD technique.

The automatic AIC-picker was then applied for all associated slaves, searching for P- and S-wave onsets around their predicted arrival-times at all SoI, including the R_{st}. Although this algorithm is not expected to work well at distant stations when an event's magnitude (and, consequently, its SNR) is low, it provides useful input data at the closer stations which can be exploited in the last step of the HADAES method for the generation of the final catalogue. The picker was tested on a dataset of manually picked master-events in order to evaluate its ability to successfully pick arrivals and reject cases of low SNR or otherwise large uncertainties (see Section 4.2 for details). The performance of the algorithm and its weighting scheme is presented in Table 5B.1. The P-wave arrival-times tend to be picked by the AIC-picker with generally high weights while only a 1.5 per cent of the original manual P-wave picks were missed by the automatic procedure. A broader distribution of weights is observed for the S-waves, whose picking has some inherent difficulties, as described in Section 4.2. The column "Missed (1st pass)" denotes arrivals with available manual picks that failed to be automatically picked on the first attempt. This means that, while an automatic arrival-time may have been determined, the resulting uncertainty was larger than allowed for a valid pick. On a second attempt, the dummy arrival-time of the 1st pass was used as the central point of the W_{max} window in the targeted AIC-picker, which can possibly lead to a successful pick. The algorithm failed to pick an S-wave on the 4.5 per cent of cases with manually picked arrivals. The "new picks" row refers to additional arrivals that were not available in the routine locations, either because they were ignored by an analyst or because data from some stations were not available.

The residuals between manual and automatic picks at the reference station, EFP, are presented in Fig. 5B.4. For the P-waves, most of the picks were made with the maximum weight (zero denoting the smallest uncertainty) and the difference is, on average, around ±0.1 sec. Some bias on a small number of picks towards +0.4sec is attributed to the Gibbs phenomenon due to filtering on strong and impulsive P-wave onsets (see Fig. 4.7). For the S-waves, on the other hand, the variance is higher, which is due to the generally larger uncertainty in the picking of P-waves both by the analyst and the algorithm. This is also reflected in the significant number of picks with lower weights (2 and 3). A different approach on the performance of the AIC-picker is presented for slave-events in Fig. 5B.5, which shows the differences between dummy arrival-times, acquired either by direct measurements of the correlation detector at the reference station, EFP, or by association of travel-times of other SoI available for the master-events (e.g. station UPR). The

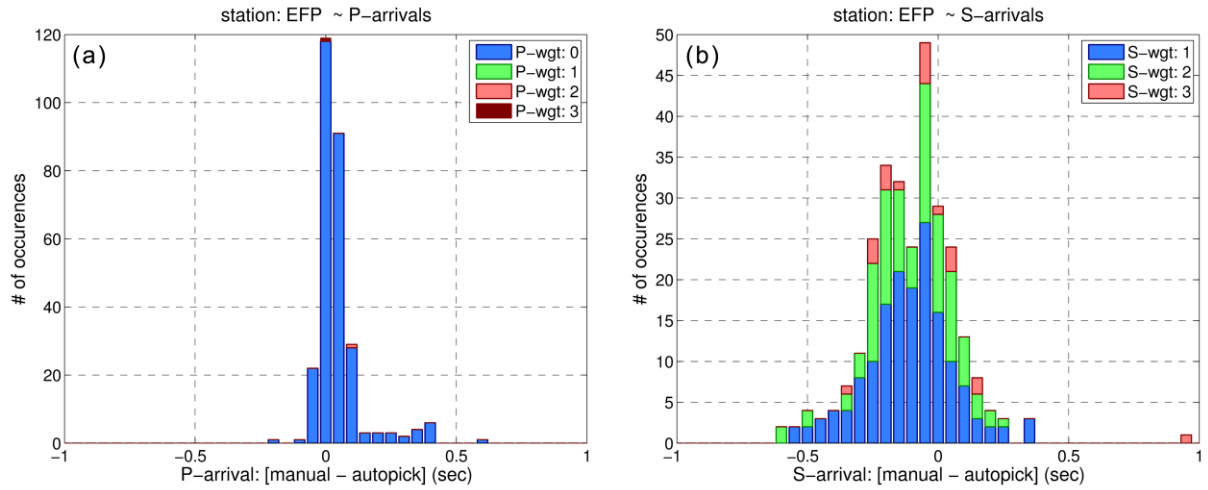

Figure 5B.4: Residuals between manual and automatically picked arrival-times of master-events with the AIC-picker: (a) for P- and (b) S-waves on the reference station, EFP. Colours refer to the pick weight; with 0 to 3 corresponding to a decrease from best to worst pick quality.

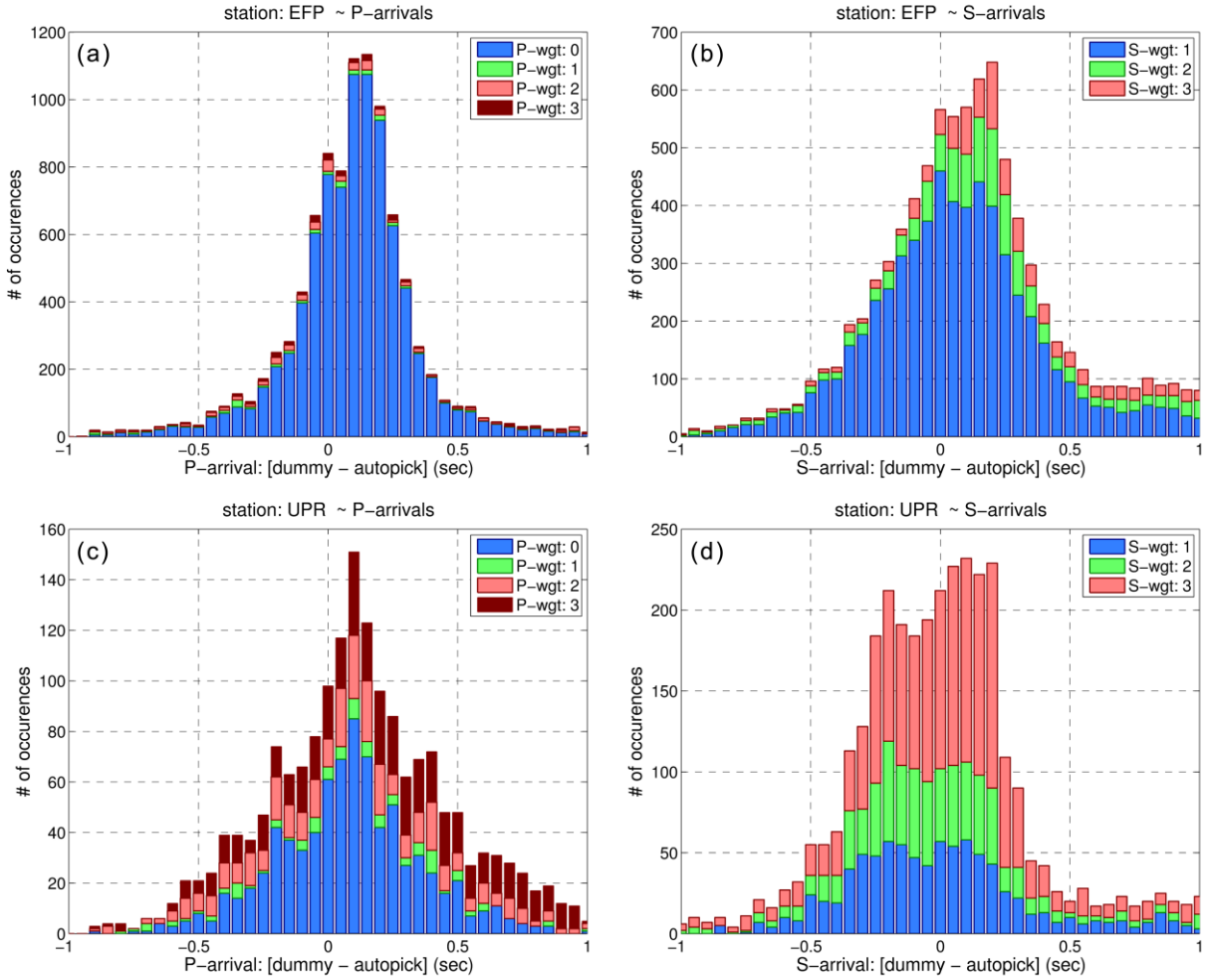

Figure 5B.5: Residuals between dummy and automatically picked arrival-times of slave events with the AIC-picker: (a) for P- and (b) S-waves on the reference station, EFP, and (c) for P- and (d) S-waves on station UPR.

variance is, of course, larger than the one for the manually picked arrival-times, as the uncertainty of the dummy-arrivals is larger and also prone to an increase of bias due to error propagation (Kapetanidis & Papadimitriou, 2011). Part of this bias may be included in the larger deviations, especially in the S-waves (residuals larger than 0.5 sec). There is, however, a clear peak in all the histograms close to zero residual. Station UPR was selected for comparison, as its records have a generally lower SNR due to increased level of background noise. This results in a lower count of successful picks but also in an increased percentage of picks with lower weights, especially in the S-waves.

Groups of associated multiplets are merged into large families using linkage information stored in each one. These families also include ME used in the primary associations. While the families are, in general, spatially constrained, they may actually contain several sub-clusters due to chaining effects. The internal structure can be revealed by creating a cross-correlation matrix and performing nearest neighbor linkage on the optimal threshold. At this point, a secondary R_{st} may be considered to cross-check the similarity and filter out artificial signals that were recorded in the primary R_{st}. In that case, a combined cross-correlation matrix can be constructed by averaging the XC_{max} values of the corresponding event-pairs in the individual XC matrices, using a vector-length approach (Kapetanidis *et al.* 2010). This procedure, however, will also possibly remove events with low SNR (and XC_{max}) at the second station.

Running a single-event location algorithm, such as HYPOINVERSE (Klein, 2002), with the automatically picked arrival-times acquired via the AIC-picker may be meaningful for slave-events of higher magnitudes. However, considering the fact that the HADAES method aims to significantly lower the detection threshold, many signals may actually only be readable on the reference station or a few of the closest ones. This may lead to dispersion of the hypocenters, large errors and even significant bias; a systematic shift of the hypocenters with respect to the ME. The last step of the proposed method includes cross-correlation measurements between the manually (for ME) or automatically (slave-events) picked P- or S-waves at all SoI on the multiplets revealed within each family. This will provide cross-correlation input for a double-difference relocation which aims to relocate the slave-events relative to their corresponding ME. To reduce the bias, the "dummy" hypocenters are used as initial locations and travel-time residuals are calculated using the roughly estimated origin time, the theoretical travel-times of the dummy solutions and the real arrival-times acquired by the AIC-picker. While in other studies the dispersion is usually reduced after relocation, as a result of the reduction of double-difference residuals, in the case of the HADAES method the hypocenters begin from a collapsed state (e.g. same hypocenter for a whole group or family of events) to a stable relative location. This is analogous to using the option for "single source", where all events start with their initial hypocentral location at the cluster's centroid, instead of "network sources", where the catalogue locations are used instead, in HypoDD (Waldhauser 2001). For this reason, it is important that the initial locations of the ME be constrained, preferably by carrying out preliminary relocation before the beginning of the event-detection and association procedures. The relocation is performed on a per-family basis with the weighted least squares inversion method and appropriate configuration parameters according to the number of events in each family.

Appendix 5C

Supplementary figures for Chapter 5

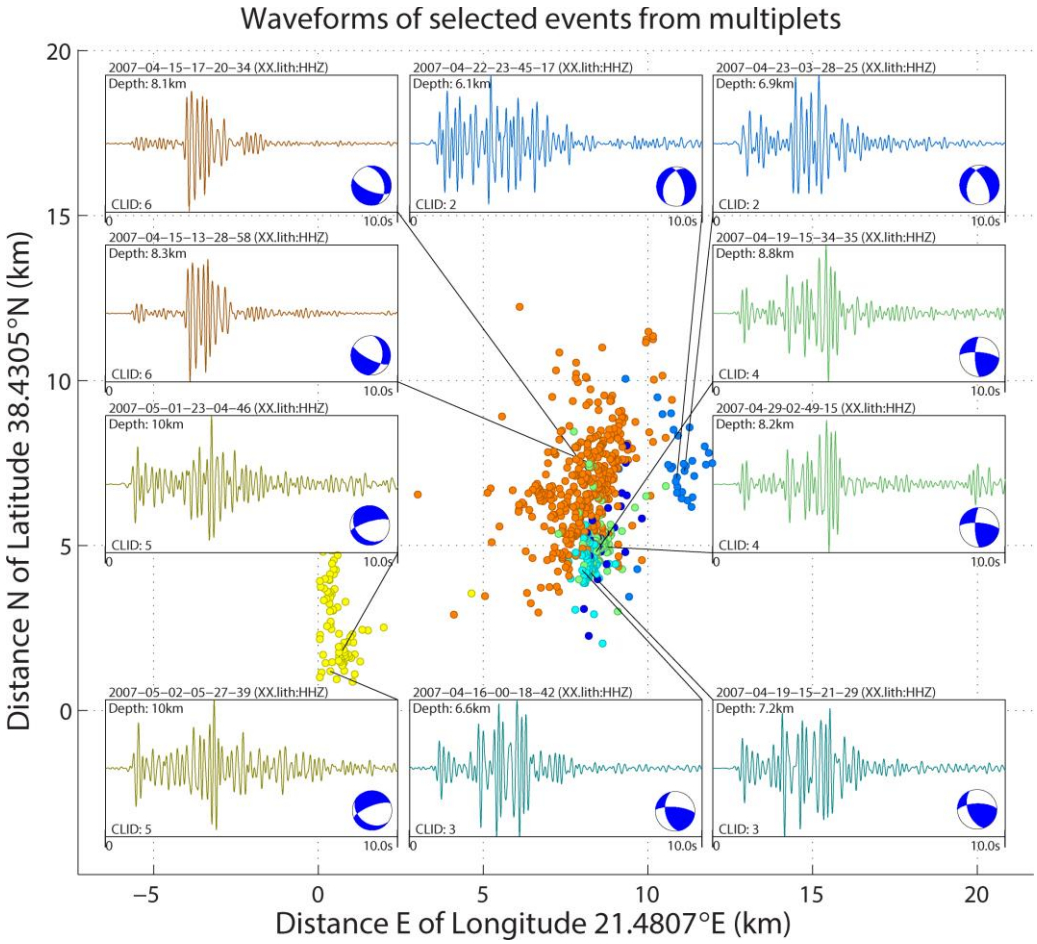

Figure 5C.1: Waveform recordings of the vertical component of station lith for 5 doublets selected from the largest multiplets. The CLID number (Cluster Id) mark different multiplets. The focal mechanisms that were determined for these events are also shown at the lower-right of each waveform panel. Figure after Kassaras *et al.* (2014a).

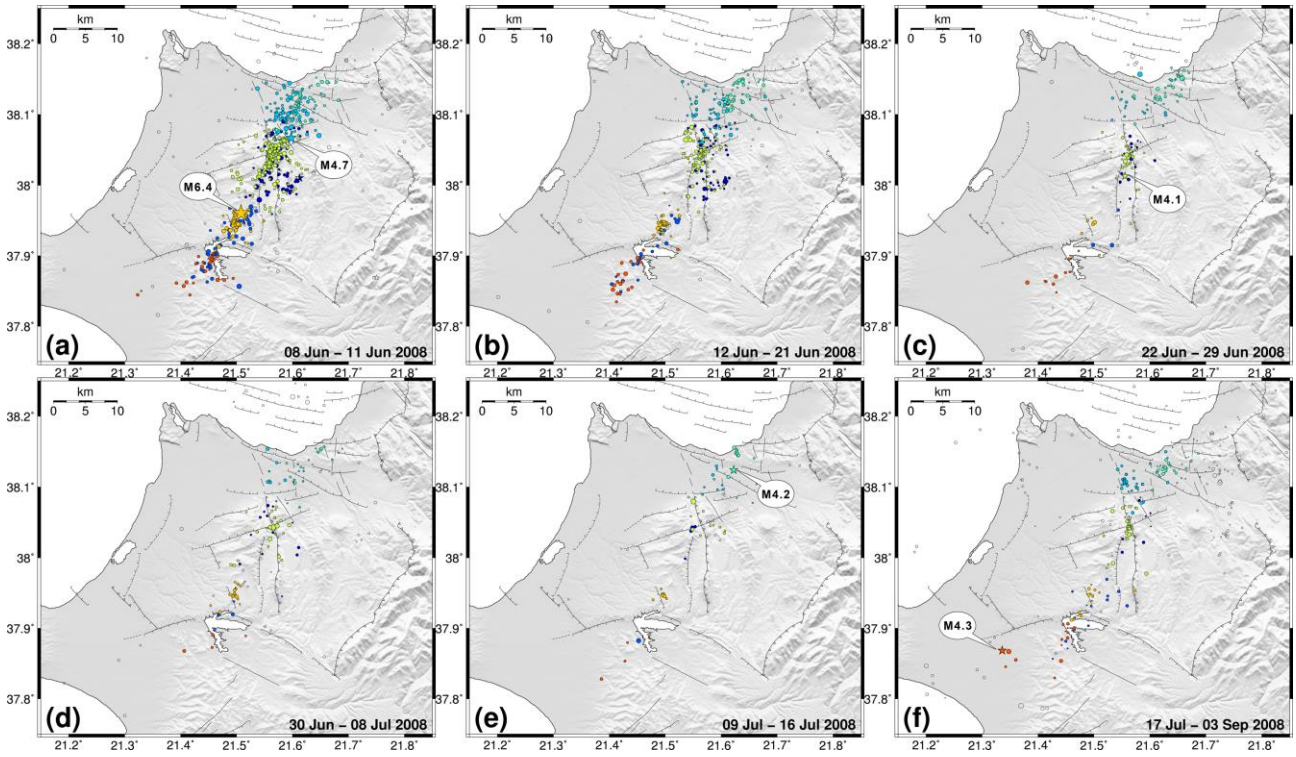

Figure 5C.2: Maps of consecutive periods during the 2008 Andravida aftershock sequence.

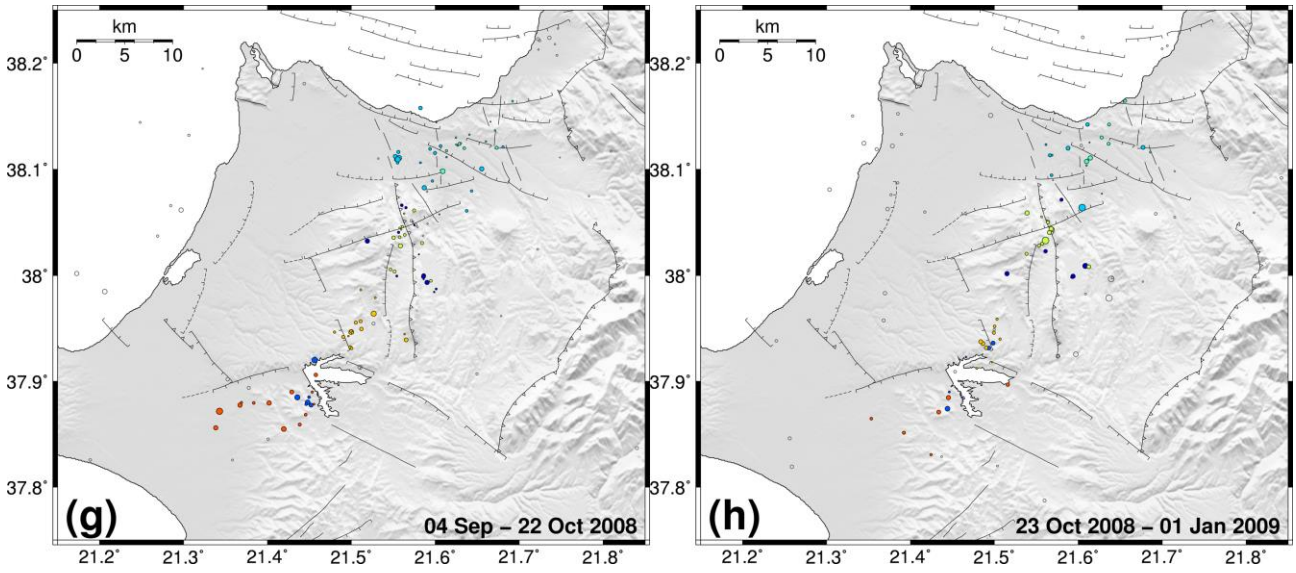

Figure 5C.2: (continued).

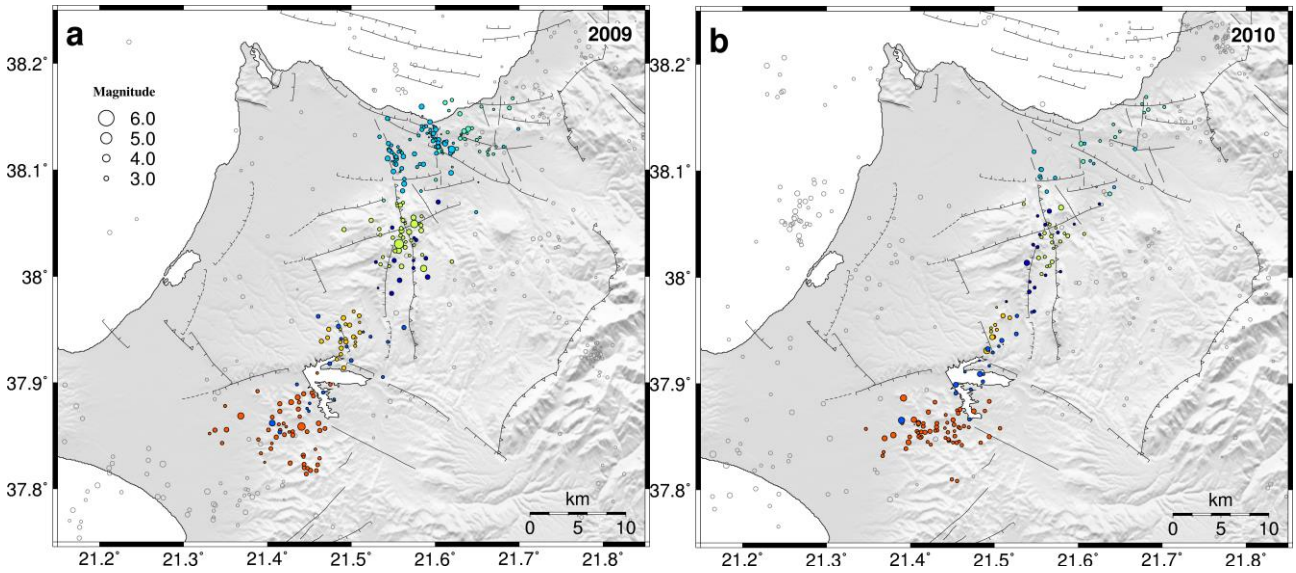

Figure 5C.3: Seismicity in the area of the aftershock sequence of the 8 June 2008 M_w=6.4 earthquake a) during 2009, b) during 2010.

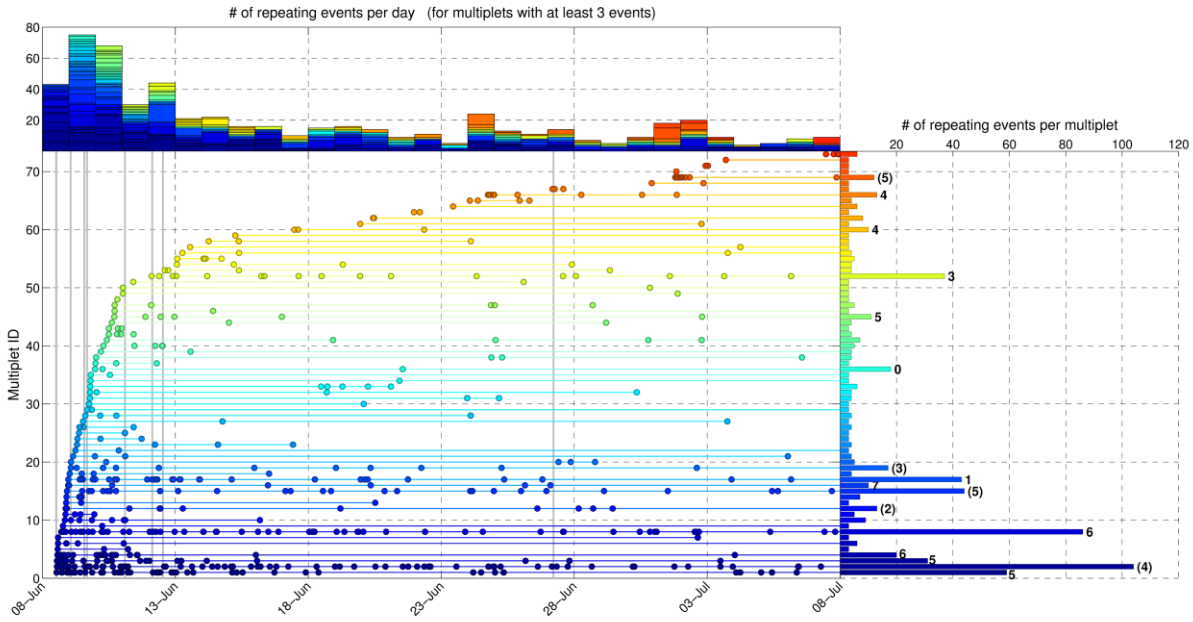

Figure 5C.4: (bottom-left) Multiplet evolution history during the first month of the 2008 Andravida aftershock sequence, for multiplets with at least 3 events. Each row represents a single multiplet, with IDs sorted in increasing order according to the origin time of the first event in each multiplet. Circles represent repeating earthquakes. Vertical gray lines correspond to the origin times of major events. (top) histogram of the daily number of repeating earthquakes, with colours corresponding to multiplet ID, (right) total number of repeating earthquakes per multiplet. Numerical labels next to certain large multiplets (size≥10) correspond to the spatial group to which they belong.

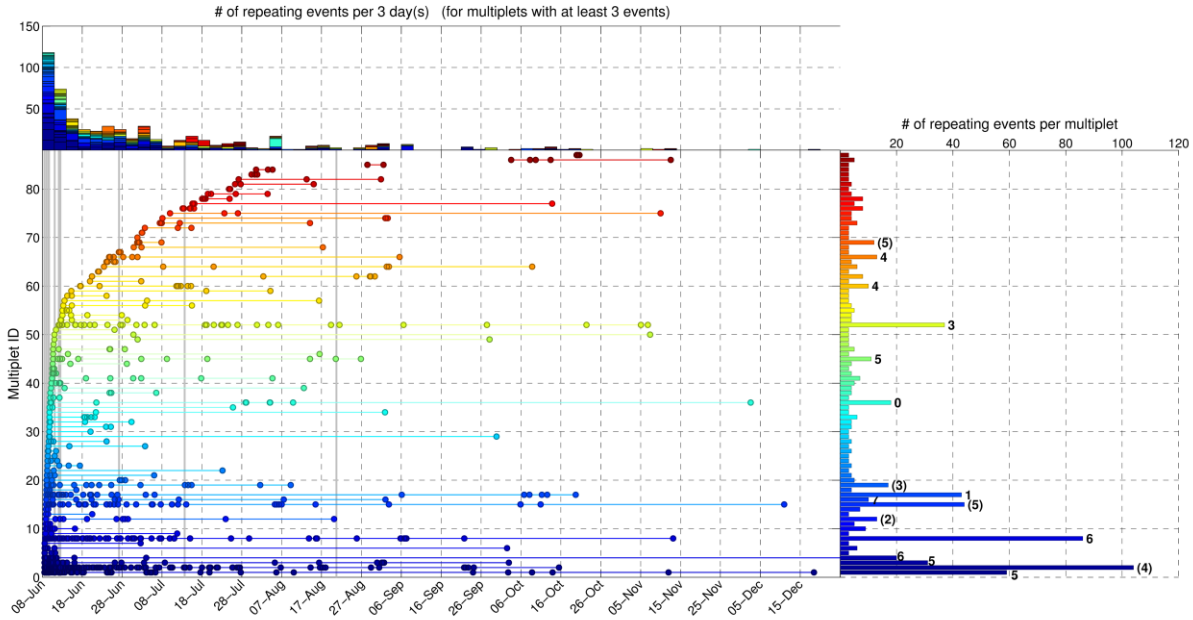

Figure 5C.5: Same as Fig. 5C.4, but covering the whole year 2008 and with the top histogram counting the number of repeating earthquakes per 3 days.

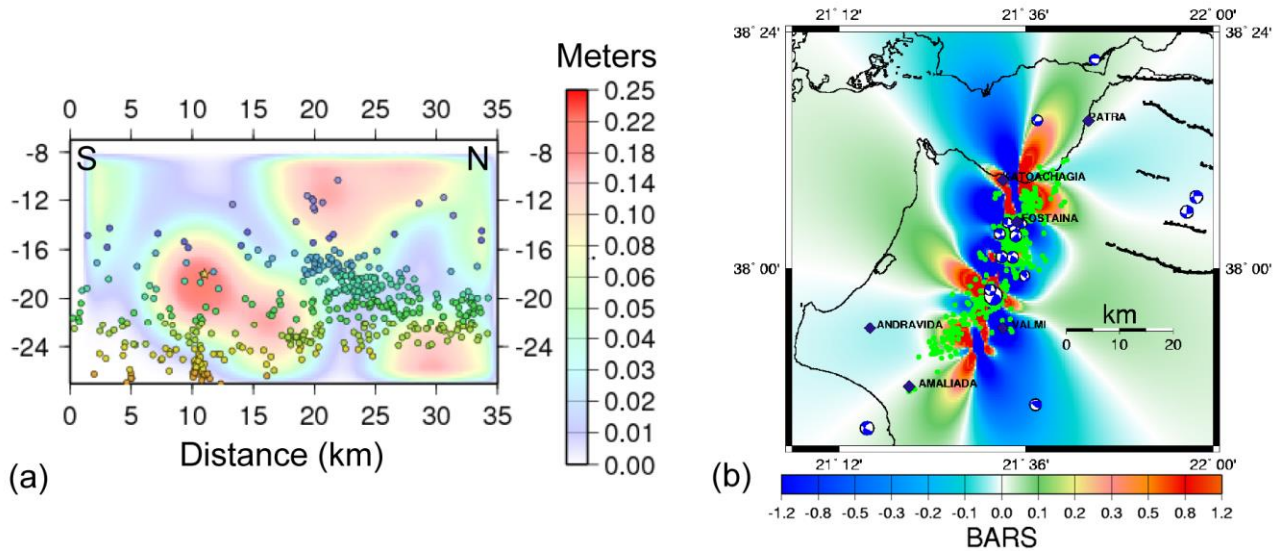

Figure 5C.6: a) Slip model for the 2008 Andravida earthquake with superimposed preliminarily relocated aftershock hypocenters, b) coulomb stress transfer using the slip model of panel (a). (Figures modified after Papadimitriou *et al.*, 2010)

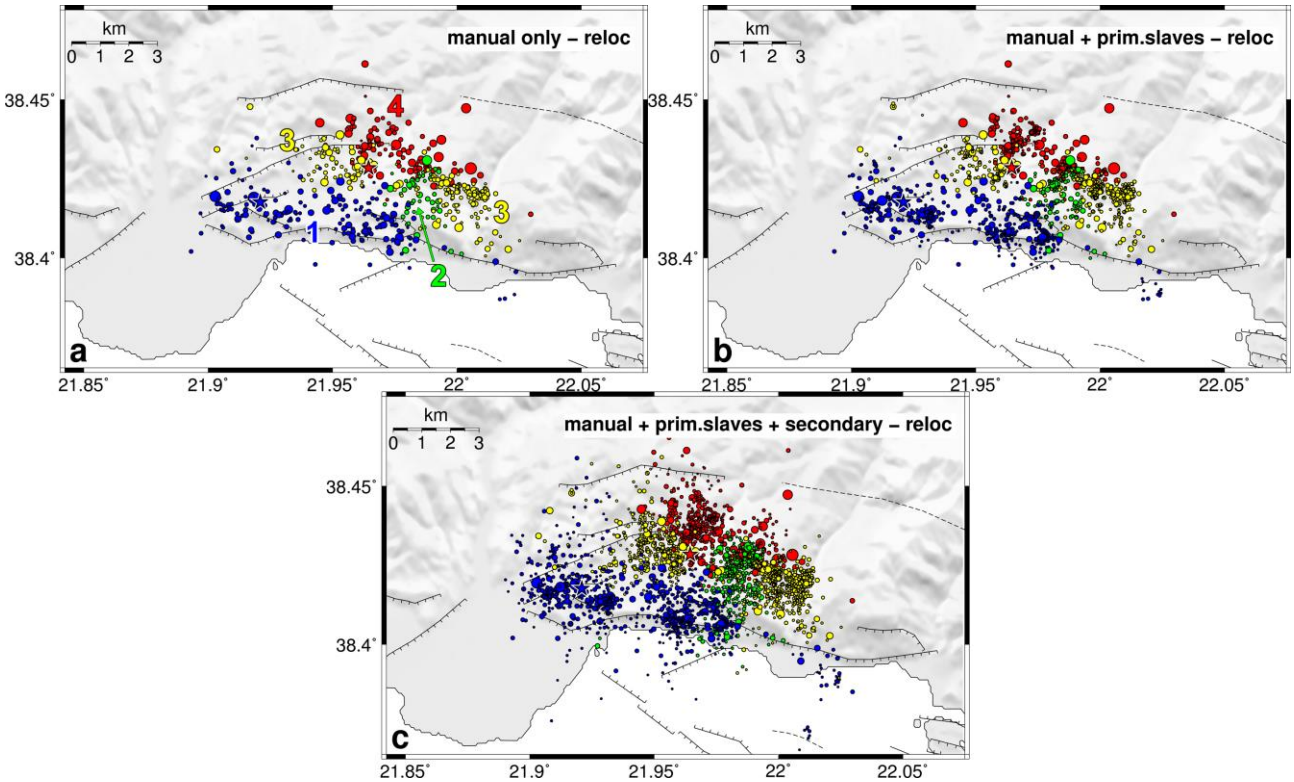

Figure 5C.7: Comparison of the relocated catalogues of the 2010 Efpalio sequence a) routine solutions, b) subset A, c) subset B.

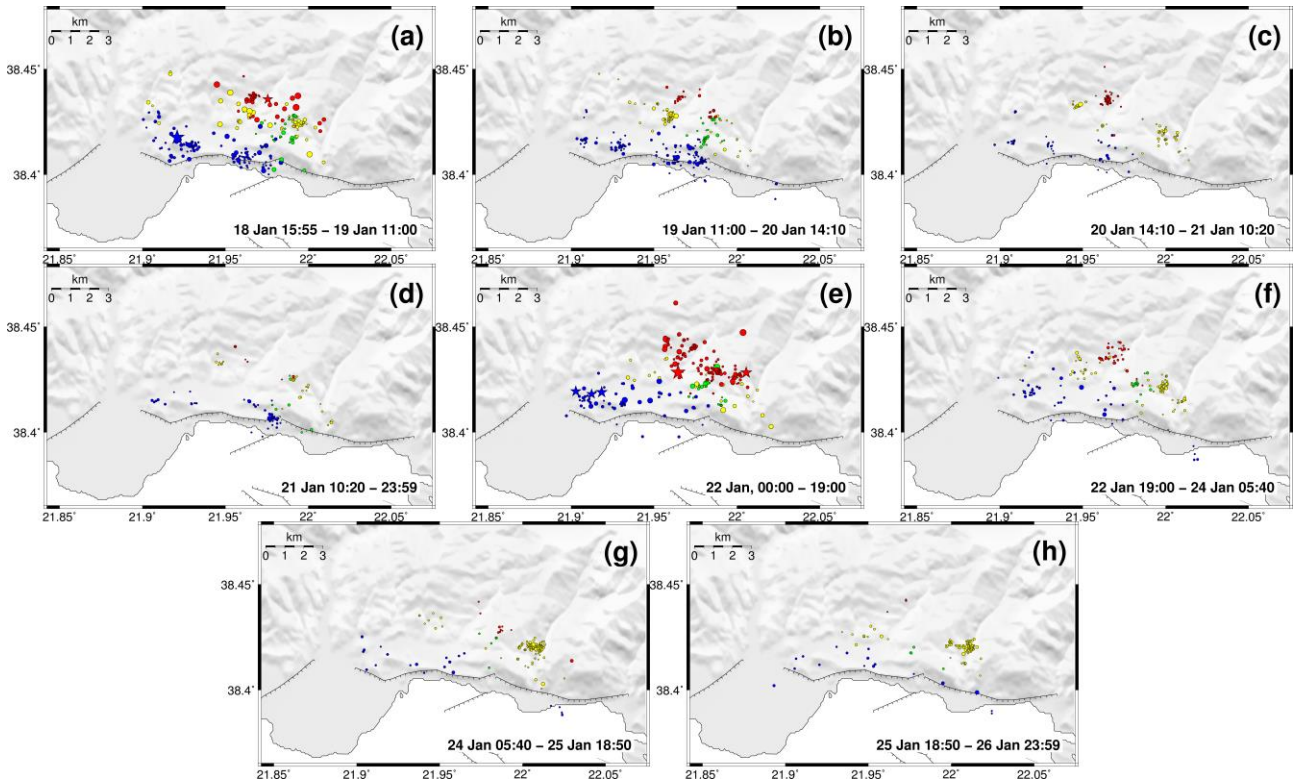

Figure 5C.8: Maps of the relocated epicenters of the 2010 Efpalio sequence (Subset A) for the 8 successive periods (a-h) to which it has been divided. Colours correspond to the 4 spatial groups.

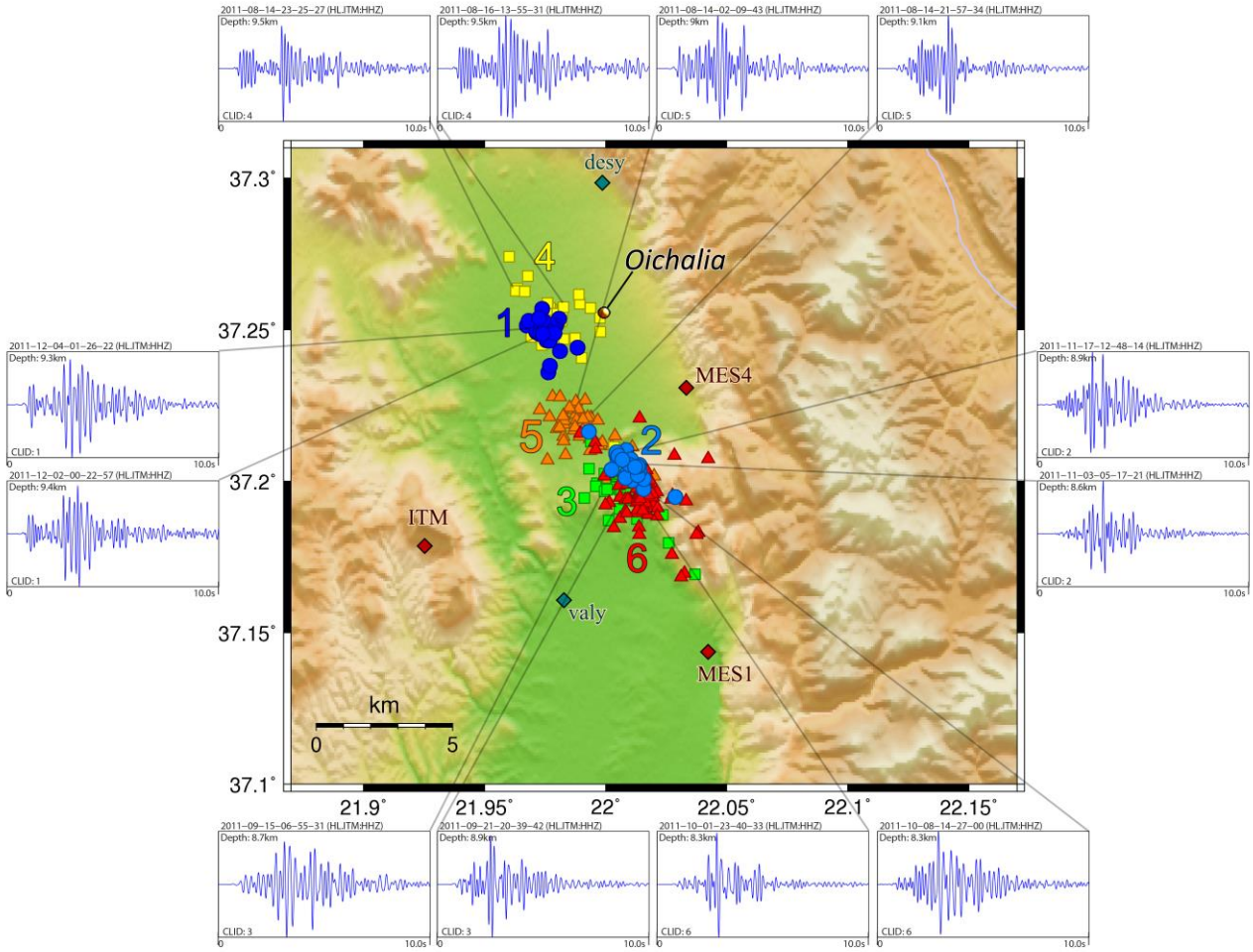

Figure 5C.9: Relocated epicenters of the 2011 Oichalia swarm for the 6 largest multiplets with size ≥ 20. Different colours and shapes represent different multiplets, labeled with numbers from 1 to 6. Waveforms in the periphery of the figure depict the vertical component of the permanent station ITM for pairs of events that belong to the same multiplet. The waveform panels also include information about the origin time and depth of the corresponding event. Local stations are marked as diamonds. Figure after Kassaras *et al.* (2014b).

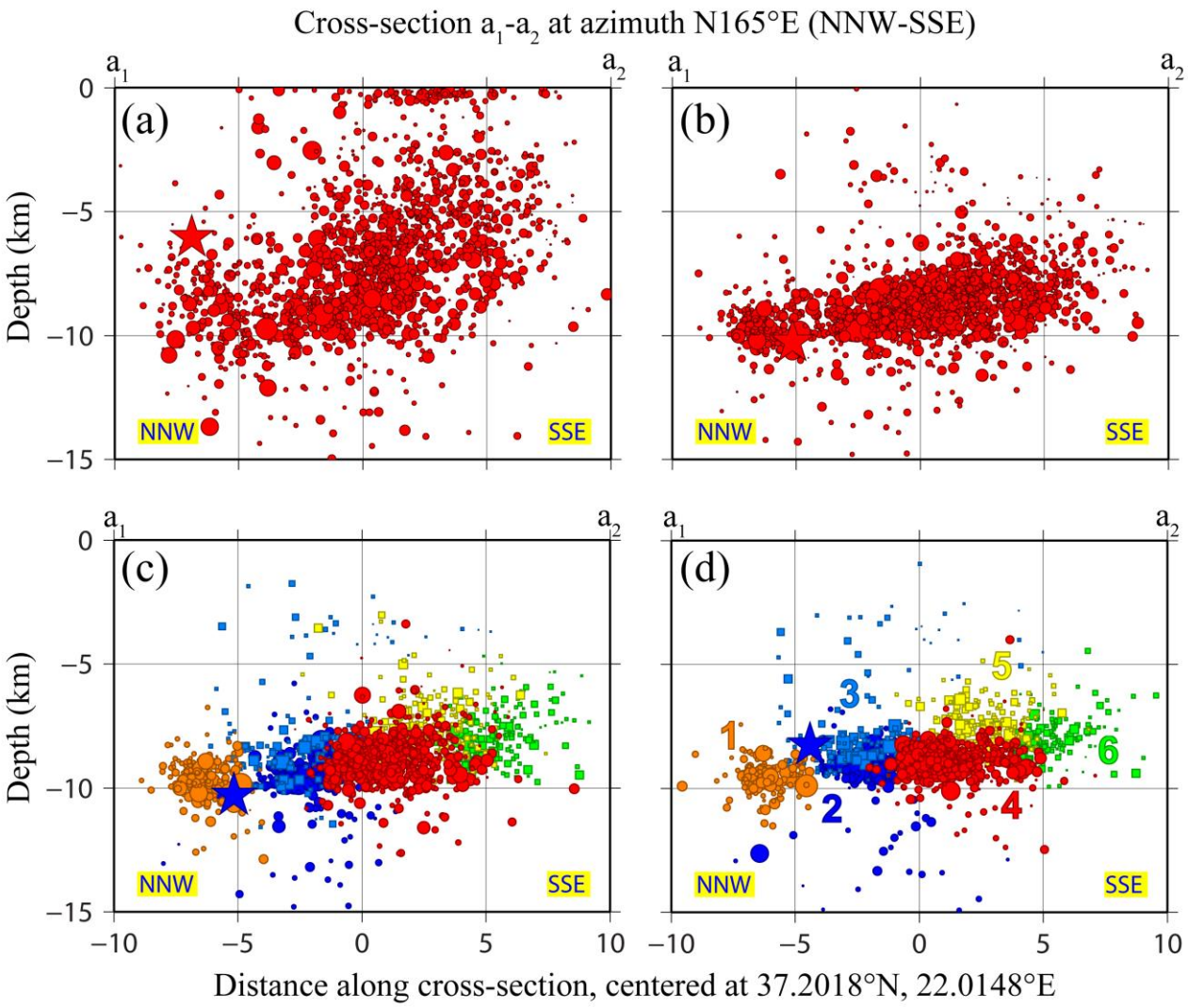

Figure 5C.10: (Top) Cross-section of the 1615 located earthquakes of the 2011 Oichalia swarm along the a_1-a_2 profile line (see Fig. 5A.7) at N165°E direction (NNW-SSE), centered at 37.2018°N, 22.0148°E, a) with the regional velocity model (Hatzfeld *et al.*, 1990) and b) with the new local model calculated in this paper. (Bottom) Same as (b) but with colours representing the 6 spatial clusters, c) before and d) after relocation with HypoDD. The star denotes the major M_w=4.8 event of 14 August 2011. Figure modified after Kassaras *et al.* (2014b).

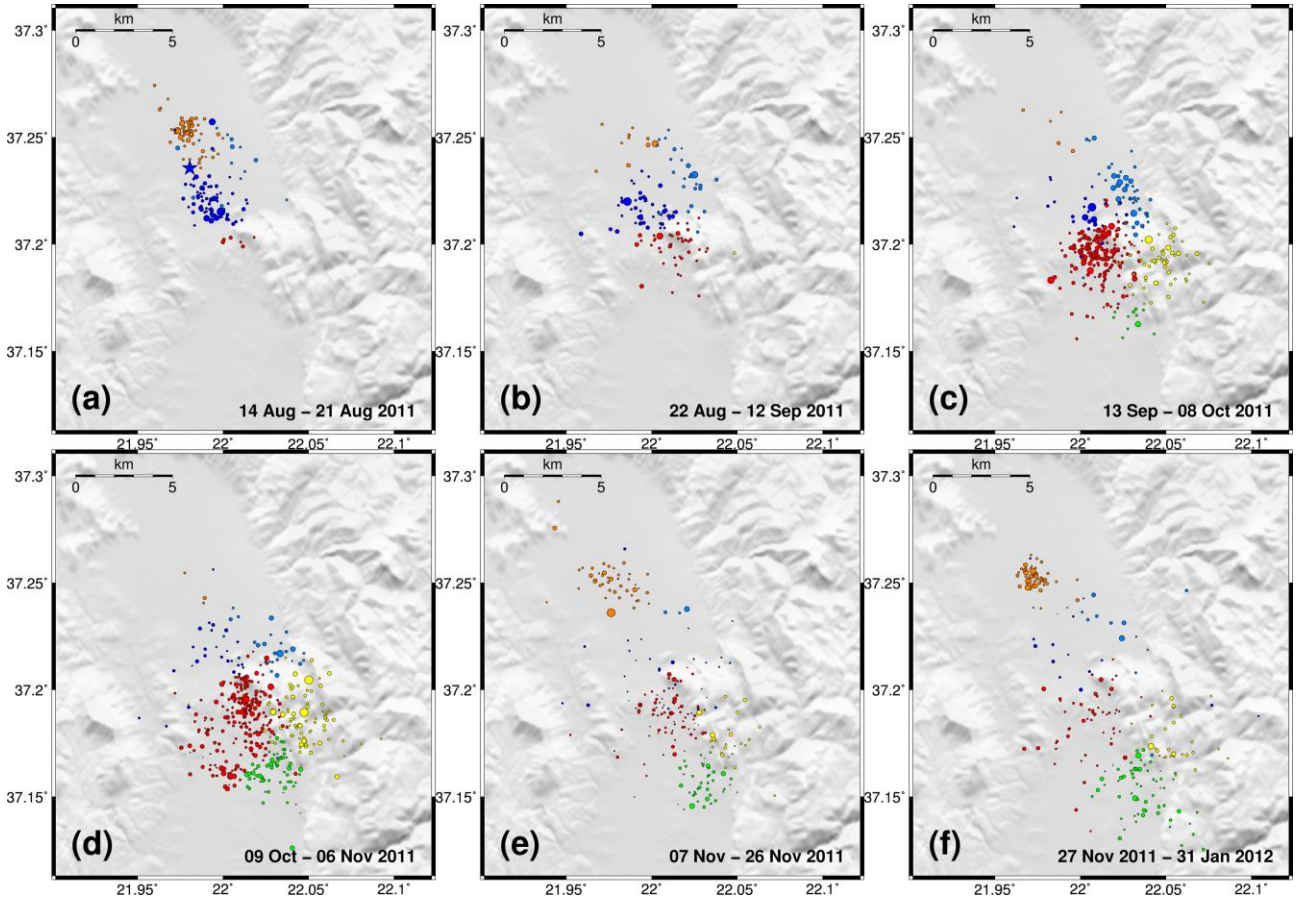

Figure 5C.11: Maps of the relocated epicenters of the 2011 Oichalia swarm for the 6 successive periods (a-f) to which it has been divided. Colours correspond to the 6 spatial groups.

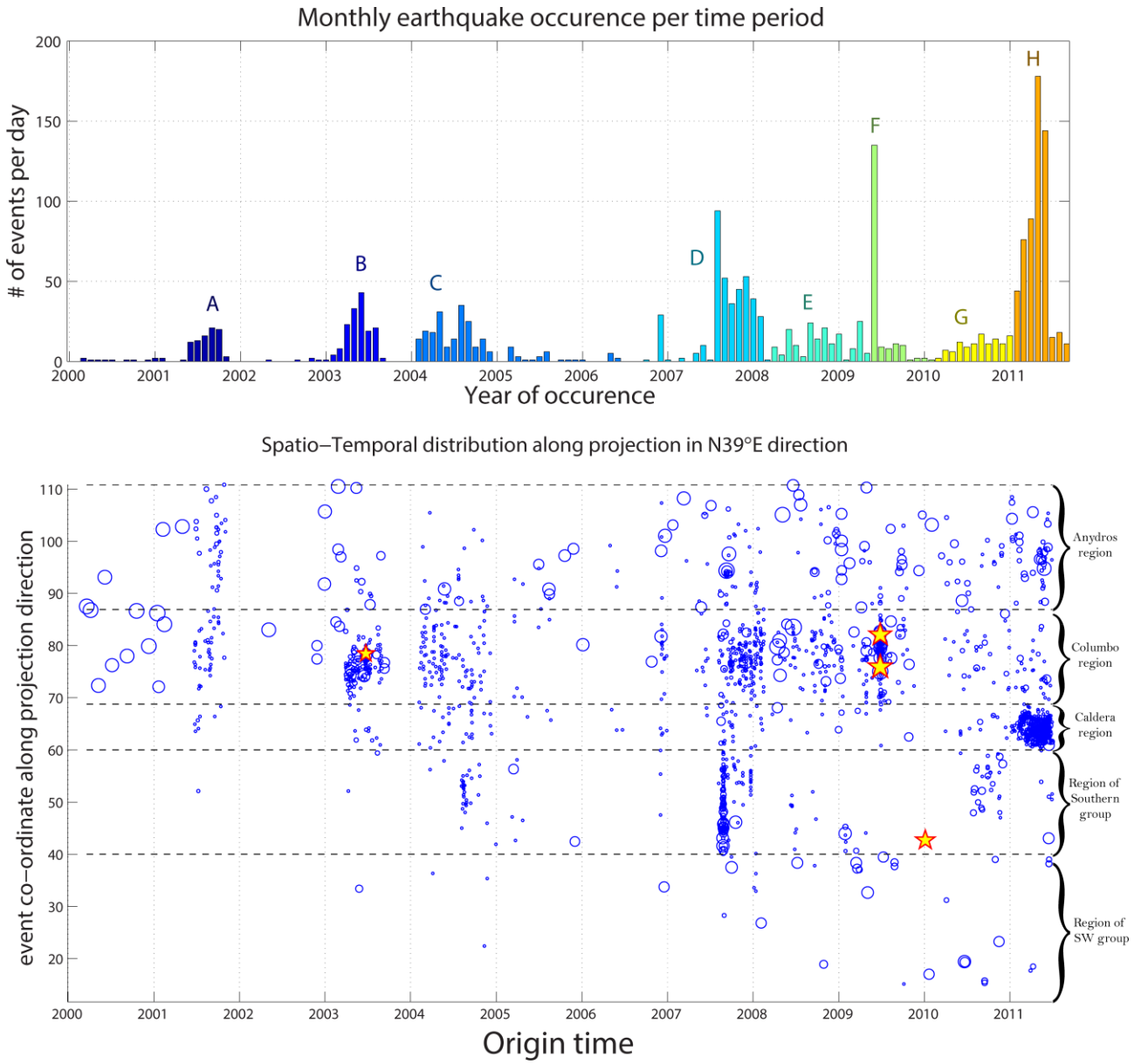

Figure 5C.12: (Top panel) histogram of monthly occurrence of earthquakes for the seismicity between March 2000 and August 2011. (Lower panel) Spatio-temporal diagram projected along the profile line X_1–X_2 (Fig. 5A.15A), for the time-period between March 2000 and August 2011. The circle size is proportional to the seismic magnitude. Large events ($M_w \geq 4$) are marked with stars. Both top and bottom panels share a common temporal horizontal axis. Figure after Papadimitriou et al. (2015).

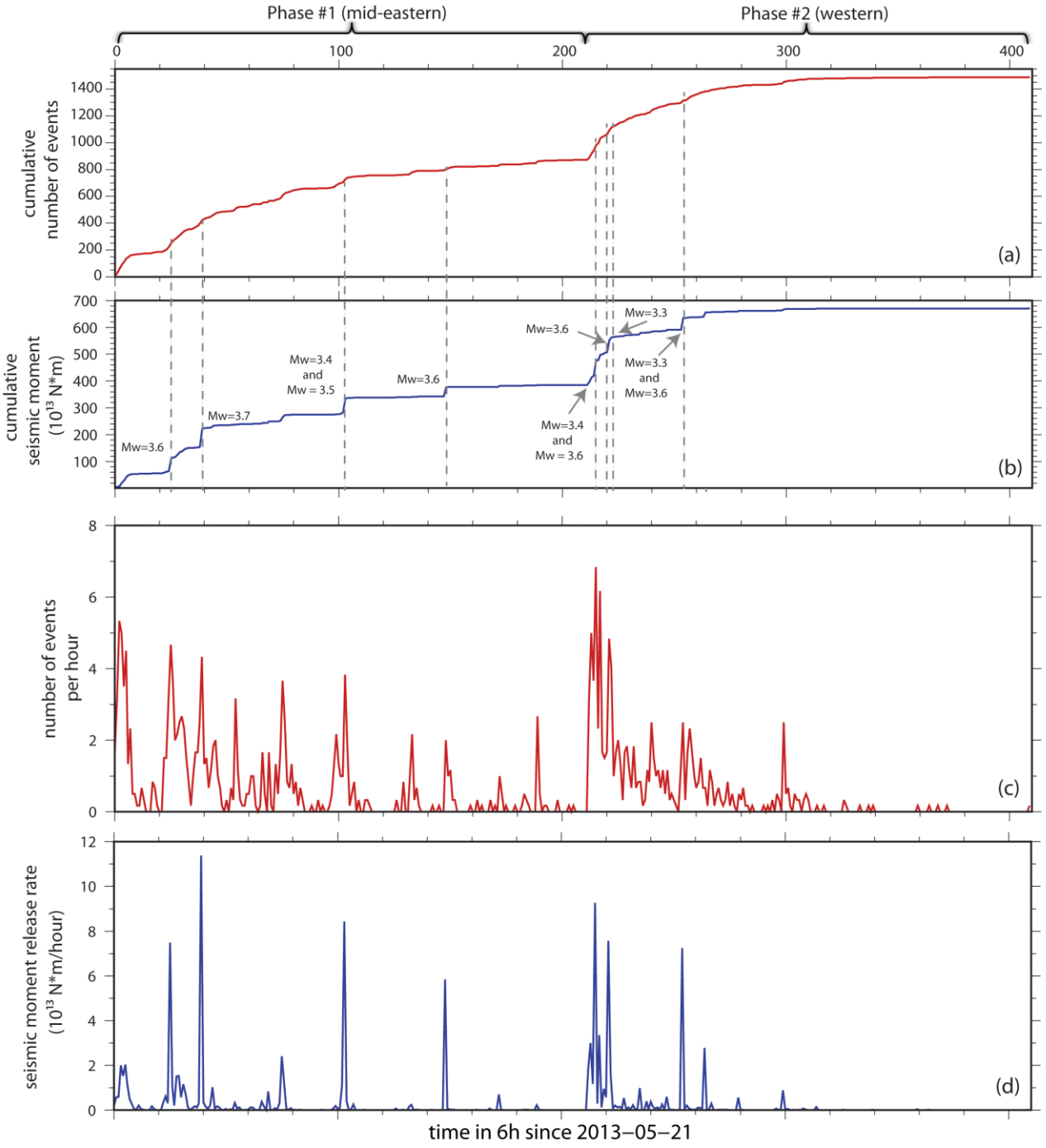

Figure 5C.13: (a) cumulative number of events, (b) cumulative seismic moment (dashed vertical lines mark the origin time of 11 major events with M_w > 3.2), (c) temporal derivative of the cumulative number of events and (d) seismic moment hourly release rate. Figure after Kapetanidis *et al.* (2015).

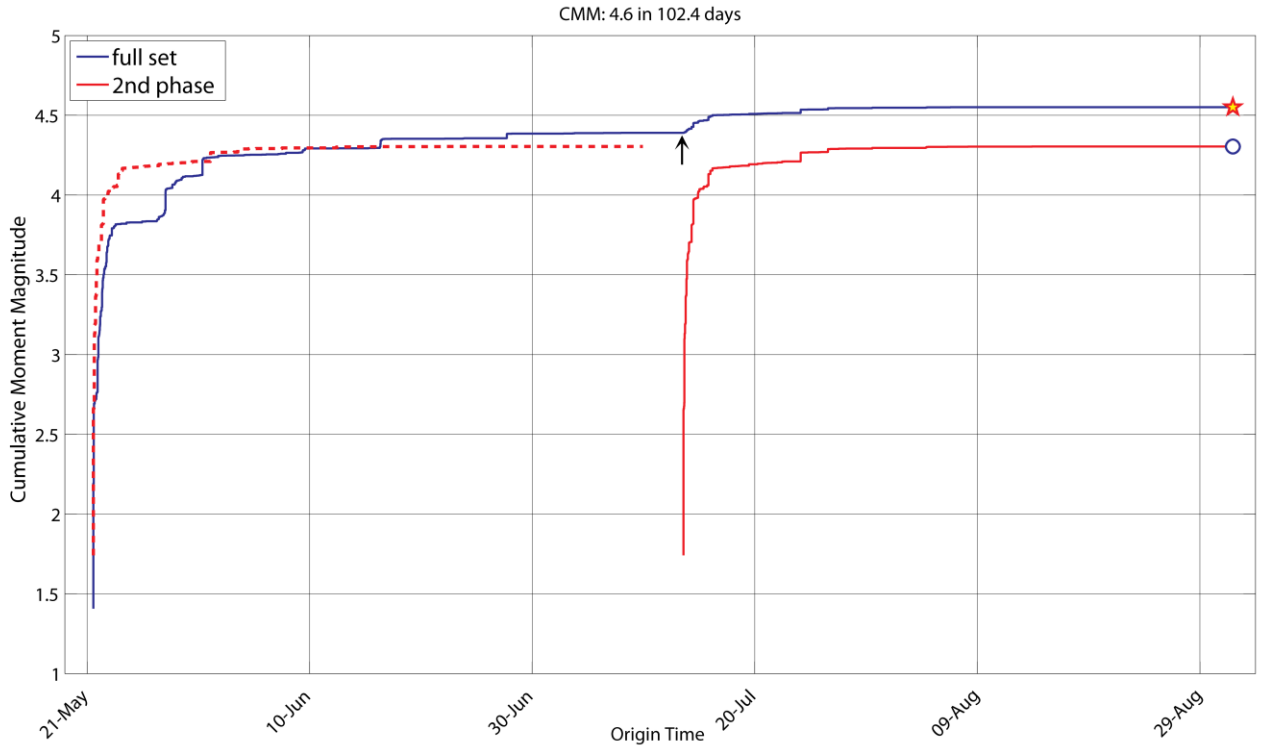

Figure 5C.14: Cumulative Moment Magnitude (CMM) for the whole sequence (blue line) and the second phase only (red solid line). The red dashed line is similar to the solid one but beginning simultaneously with the blue solid line for direct comparison. The CMM maxima are: 4.55 for the whole sequence (star), 4.39 at the end of the first phase (arrow) and 4.30 at the end of the second phase (circle). The maximum CMM is practically met at the end of July (~70 d). Figure after Kapetanidis *et al.* (2015).

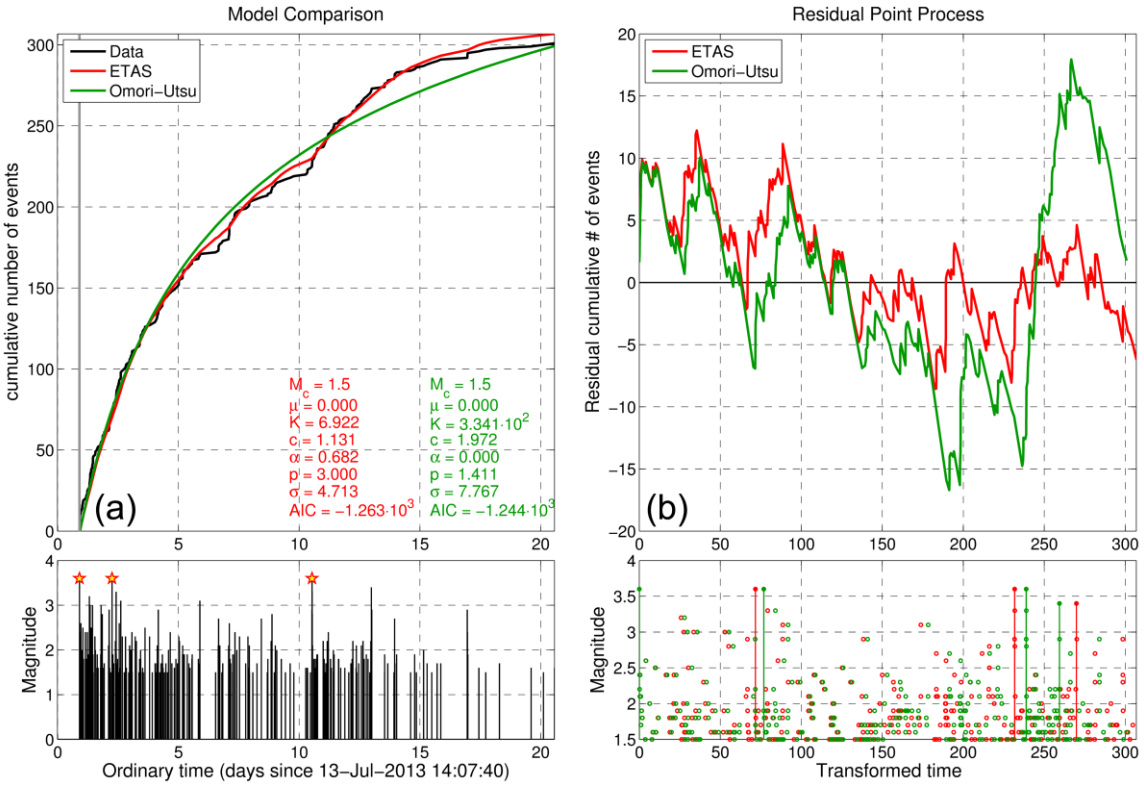

Figure 5C.15: Alternative ETAS and MOF models for the second phase of the 2013 Helike swarm (12 July – 3 August, omitting the last outburst of cluster 3), using a threshold M_{th}=1.5 and M_r=3.6, with the model parameters estimated by MLE, starting at the time of the first major M_w=3.6 of this phase (gray bold line, 14 July), a) data and ETAS model curves in ordinary time, b) residuals between data and model in transformed time.

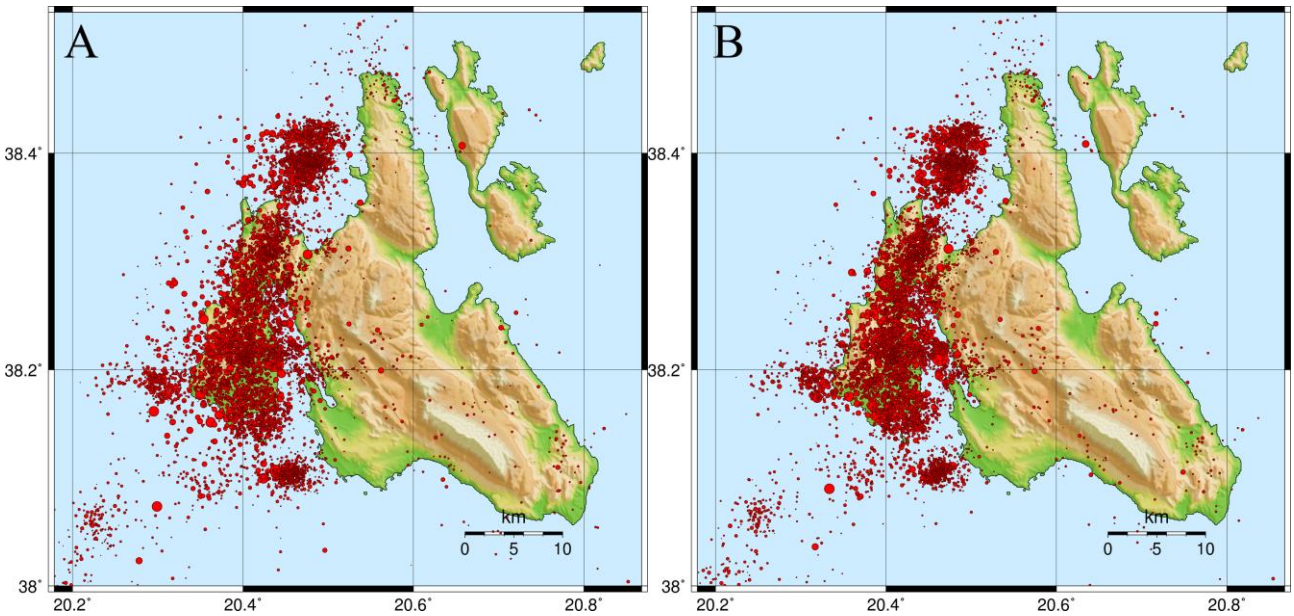

Figure 5C.16: Preliminary epicenters of the 2014 earthquake sequence in Cephalonia A) using the regional velocity model of Haslinger *et al.* (1999) and B) using the custom velocity model of Papadimitriou *et al.* (2014).

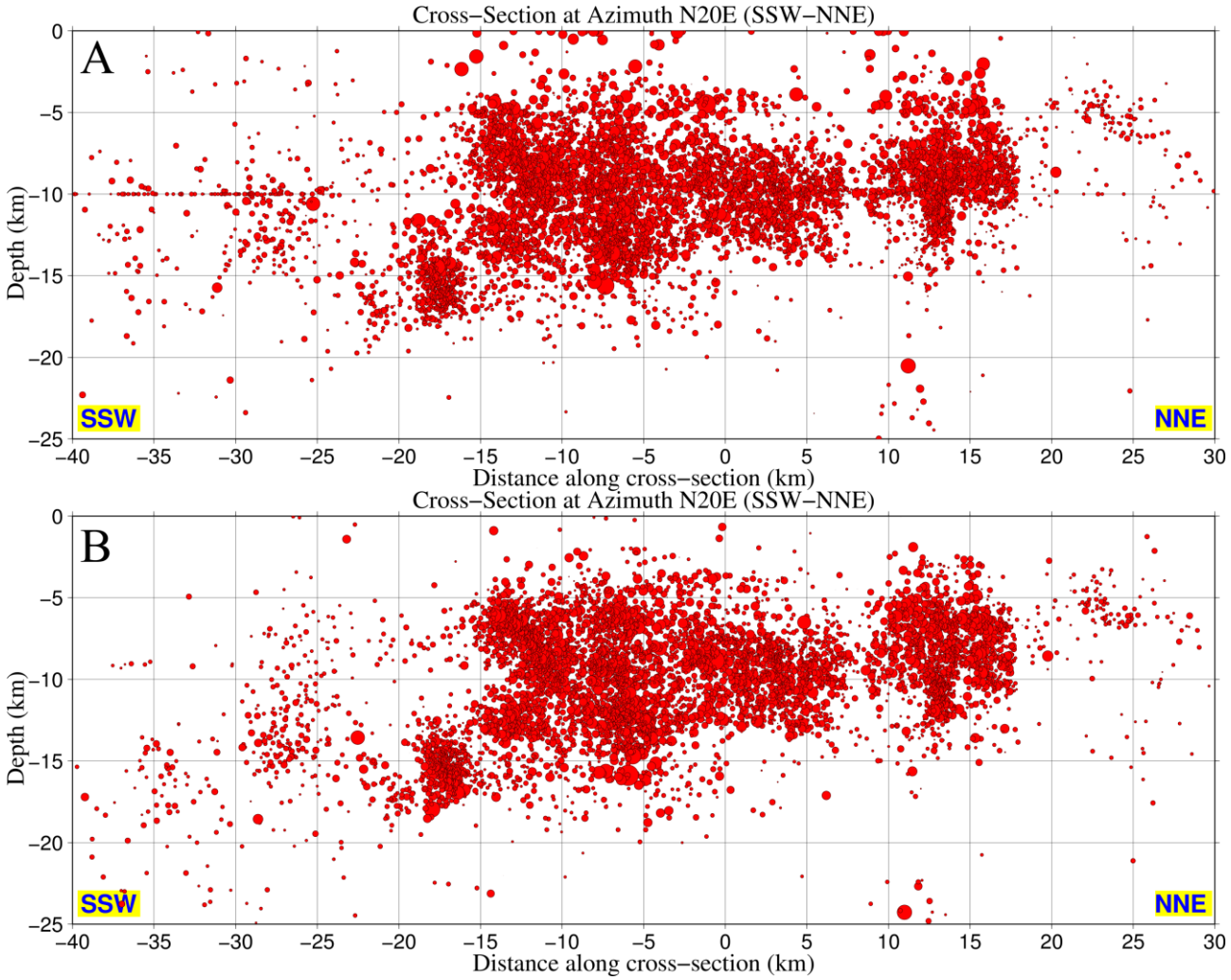

Figure 5C.17: Cross-sections of the 2014 earthquake sequence in Cephalonia, drawn in N20°E direction using solutions obtained with A) the regional velocity model of Haslinger *et al.* (1999) and B) the local velocity model of Papadimitriou *et al.* (2014). The cross-sections are centered (x=0) at 38.2790°N, 20.4263°E.

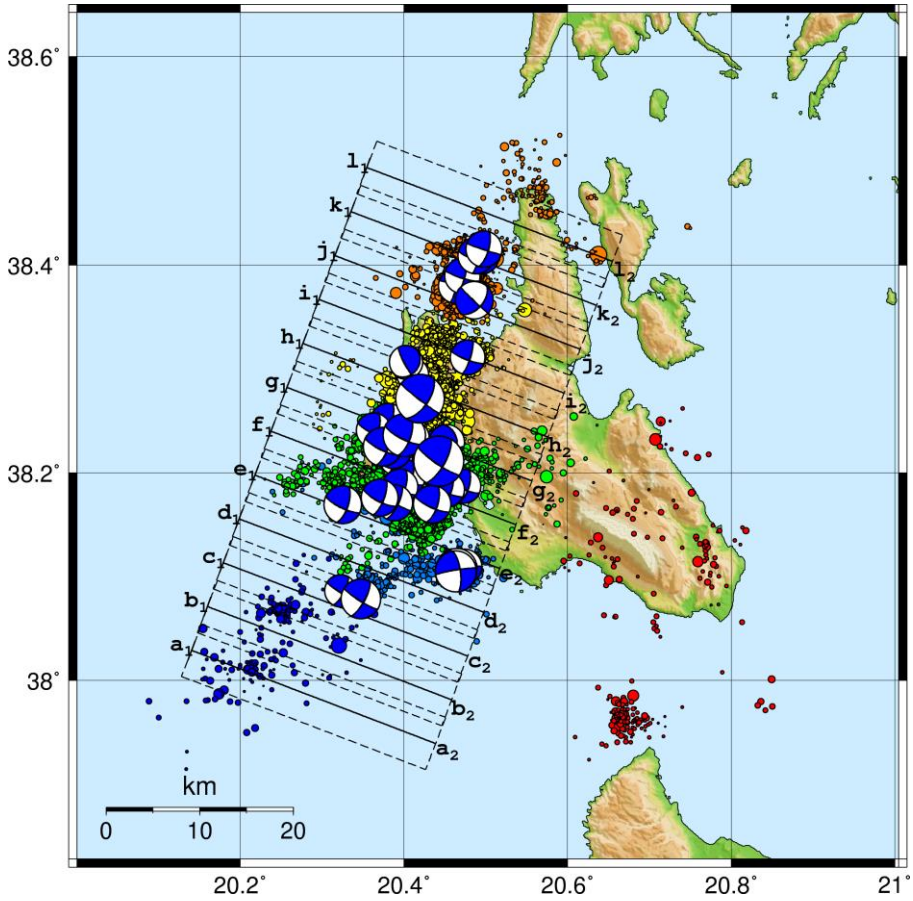

Figure 5C.18: Map of the relocated epicenters of the 2014 aftershock sequence in Cephalonia along with focal mechanisms determined for the largest events (Papadimitriou *et al.*, 2014). Profile lines a-l are used for the cross-sections of Fig. 5C.19.

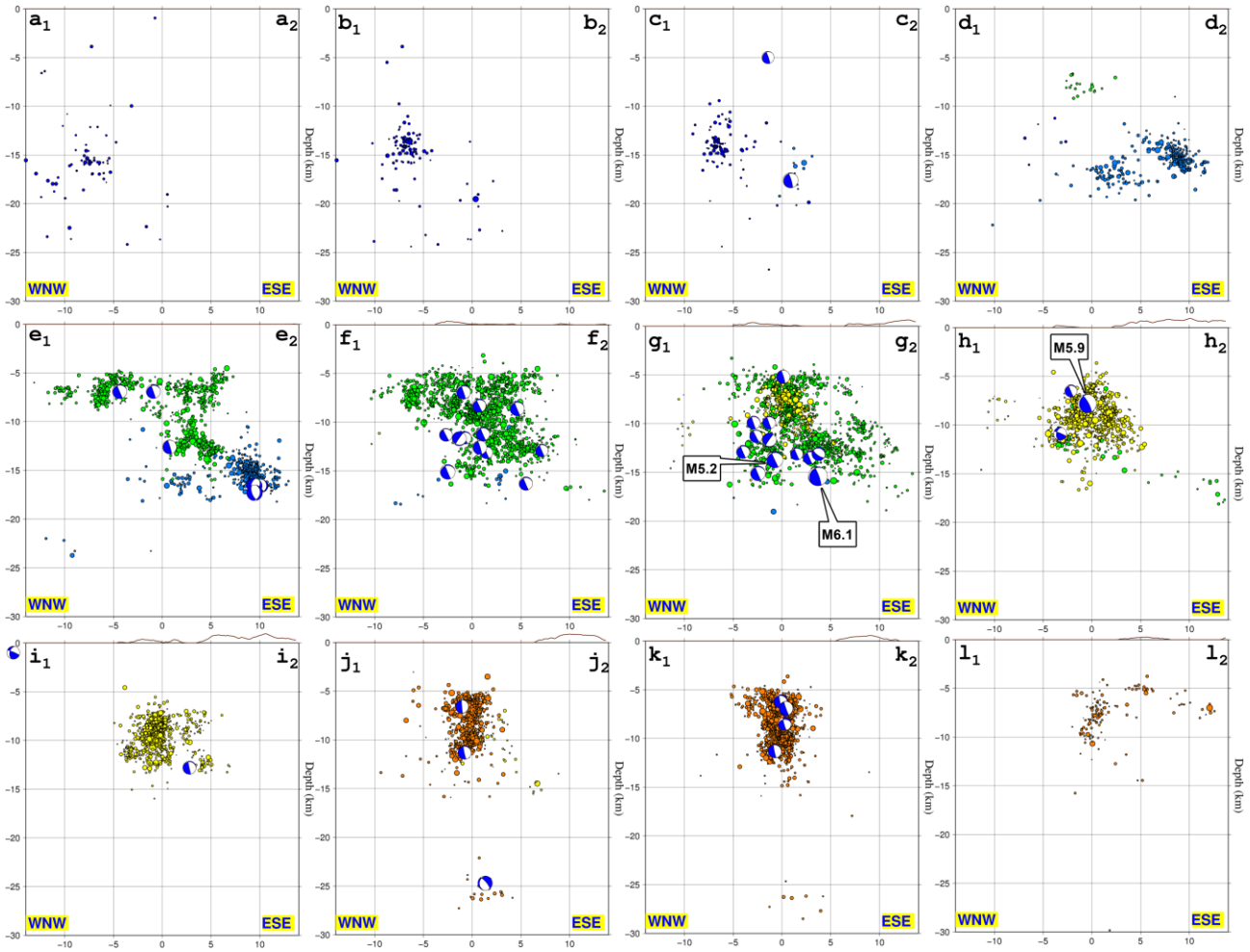

Figure 5C.19: Vertical, thin (±3km), partially overlapping, parallel, sequential cross-sections along the N110°E directed profile lines of Fig. 5C.18, perpendicular and centered to the main axis of the 2014 Cephalonia aftershock sequence. The far-hemisphere projections of the largest events' focal mechanisms are also depicted.

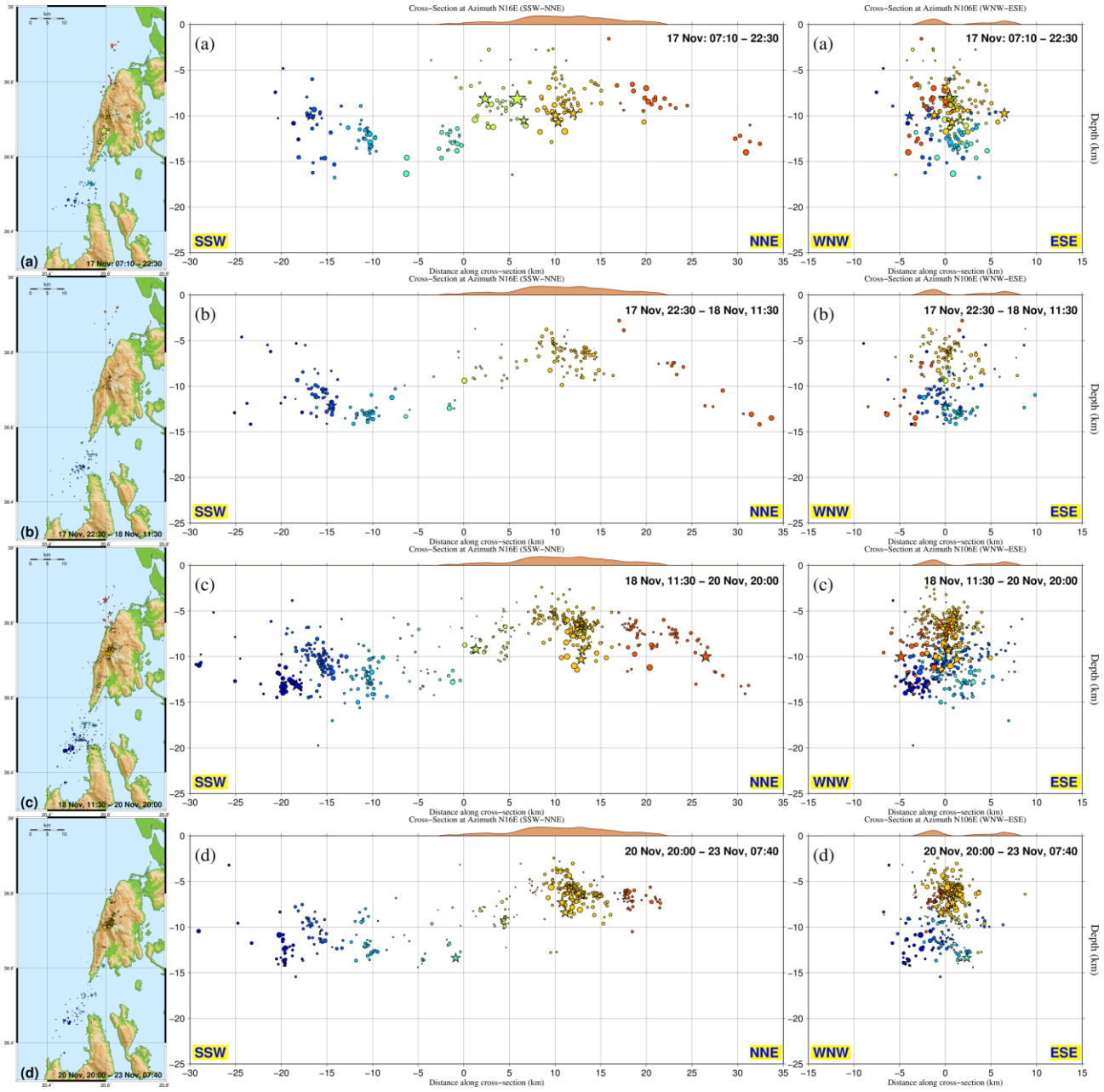

Figure 5C.20: (left side) Maps, (middle) cross-sections along the main axis of the spatial distribution (N16°E), (right side) transverse cross-sections (N106°E direction) for the temporal evolution of the aftershock activity divided in 8 periods (Figs 5.60 and 5.61). Colours represent the 7 spatial clusters (Fig. 5.58).

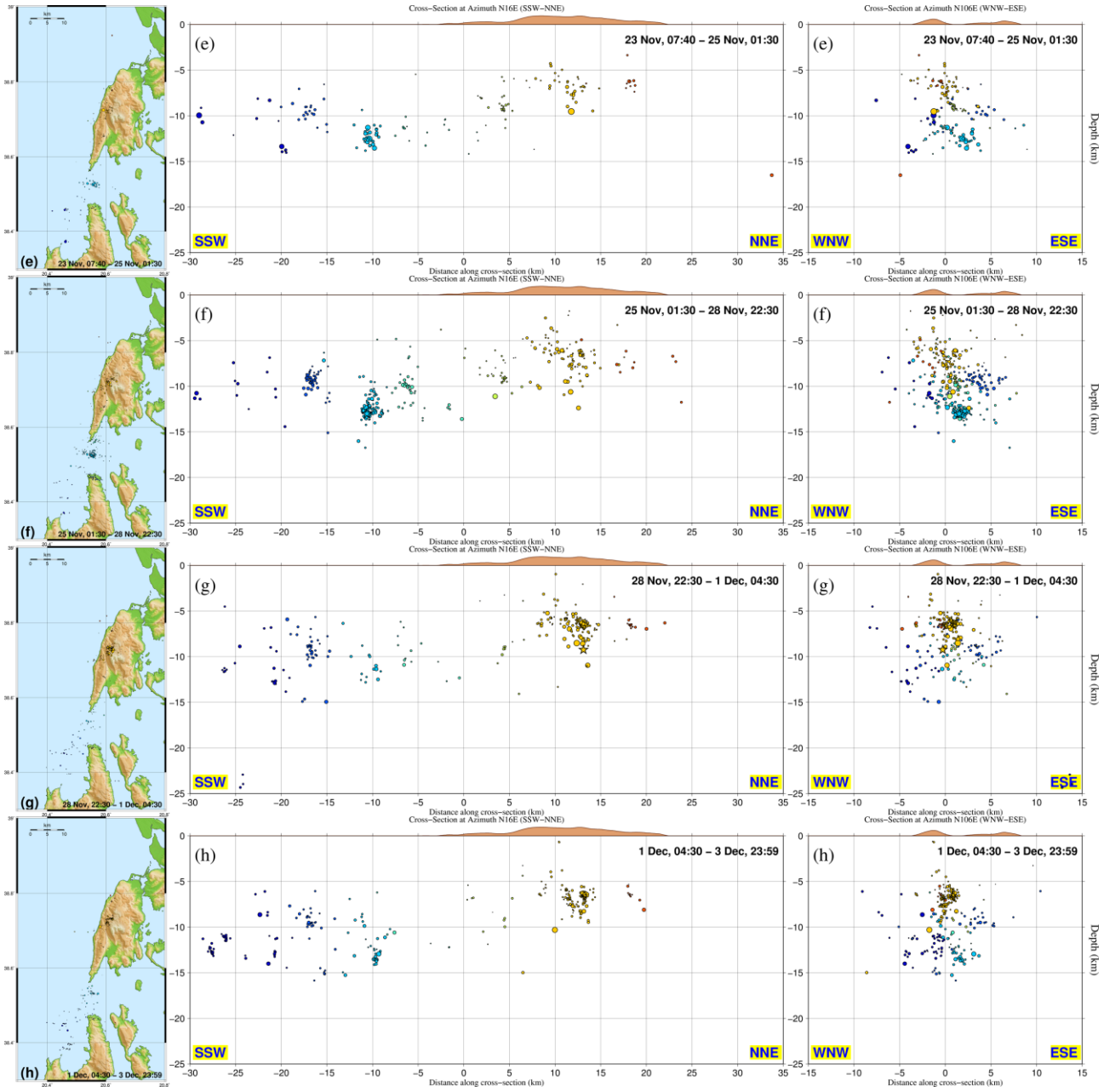

Figure 5C.20: (continued).

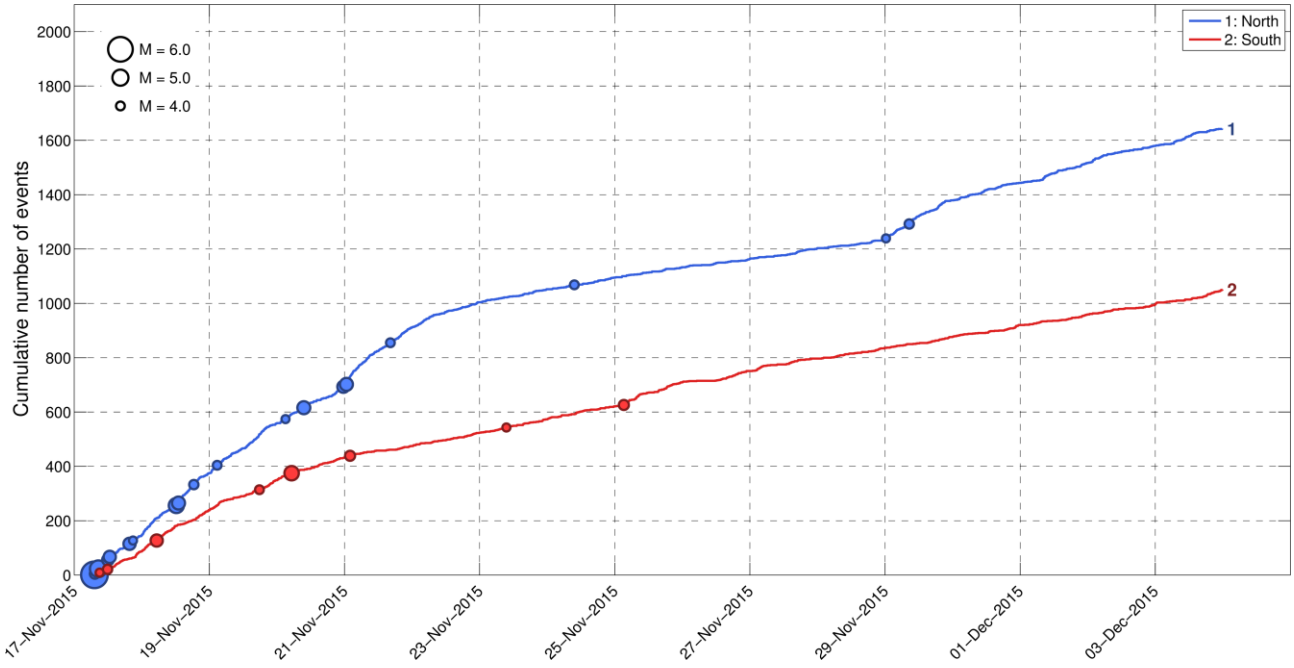

Figure 5C.21: Cumulative number of events during the 2015 Lefkada aftershock sequence for the northern (blue) and southern (red) group. Circles denote major events ($M_w \geq 4.0$)

Appendix 6A

Seismicity of the western Corinth Rift during 2008-2015

Some of the more significant earthquake occurrences and sequences in the western Corinth Rift during the years 2008-2015 include:

- A swarm ~15 km NW of Kalavryta, on 4 February 2008, including two M_w=4.5-4.6 events (Fig. 6A.1; Kapetanidis et al., 2008).
- An M_L=3.8 event on 24 July 2008, south of Psathopyrgos, followed by an aftershock sequence.
- An M_L=4.2 event on 7 June 2009, followed by an aftershock sequence, likely at the root of the Kamarai fault zone.
- Two M_w=5.1-5.2 earthquakes in Efpalio (Section 5.2) in January 2010, the strongest events in the western Corinth Rift since the 1995 Aigion earthquake and its aftershock sequence.
- A swarm near Rio that started on 23 July 2011, including an M_w=4.0 event on 24 July 2011 and an M_w=4.5 on 28 July 2011. It was also followed by an M_w=4.7 event near Nafpaktos.
- A swarm near Sergoula in 4-7 February 2011, including an M_L=3.4 event on 5 February 2011.
- An M_w=4.1 event on 11 February 2011 followed by a short aftershock sequence near Nafpaktos.
- The 2013 Helike swarm between 21 May and November 2013. (Section 5A.4)
- An intense swarm in the Rion straits in 2014 (Section 5.4).
- An M_w=5.0 event, the strongest since the 2010 Efpalio events, followed by an aftershock sequence, mid-gulf on 7 November 2014 (Fig. 6A.4).

Preliminary data of relocated seismicity from the period 2011-2014 (Fig. 6A.3), analysed in the framework of the REAKT project, using stations from both CRL and HUSN networks, show evidence for:

- A thin north-dipping zone in the westernmost part, in the slice of a_1-a_2 (Fig. 6.18) which seems to pass below Psathopyrgos fault.
- A complex structure west of Trizonia island, in the area of the 2007 crisis (Fig. 6.18, e_1-e_2), with the hypocenters extending to shallower depths than the weak layer.
- An overlooked region with seismicity in the easternmost part of the study area, offshore SE of Eratini, were some sparse earthquakes were also recorded in 2000-2007.
- Several small clusters along the N-S transition zone (Fig. 6.18, k-l).
- Many earthquakes near the western part of Psathopyrgos fault in Nafpaktos basin, where only a few could be resolved during 2000-2007.
- Persistent but sparse seismicity in the area of Group #9.
- Several clusters in Patraikos gulf at a depth of ~15km.
- A few intermediate depth events (~50km) in the region of the deep Group #12 and to the south near the region of the 2001 AIO swarm.

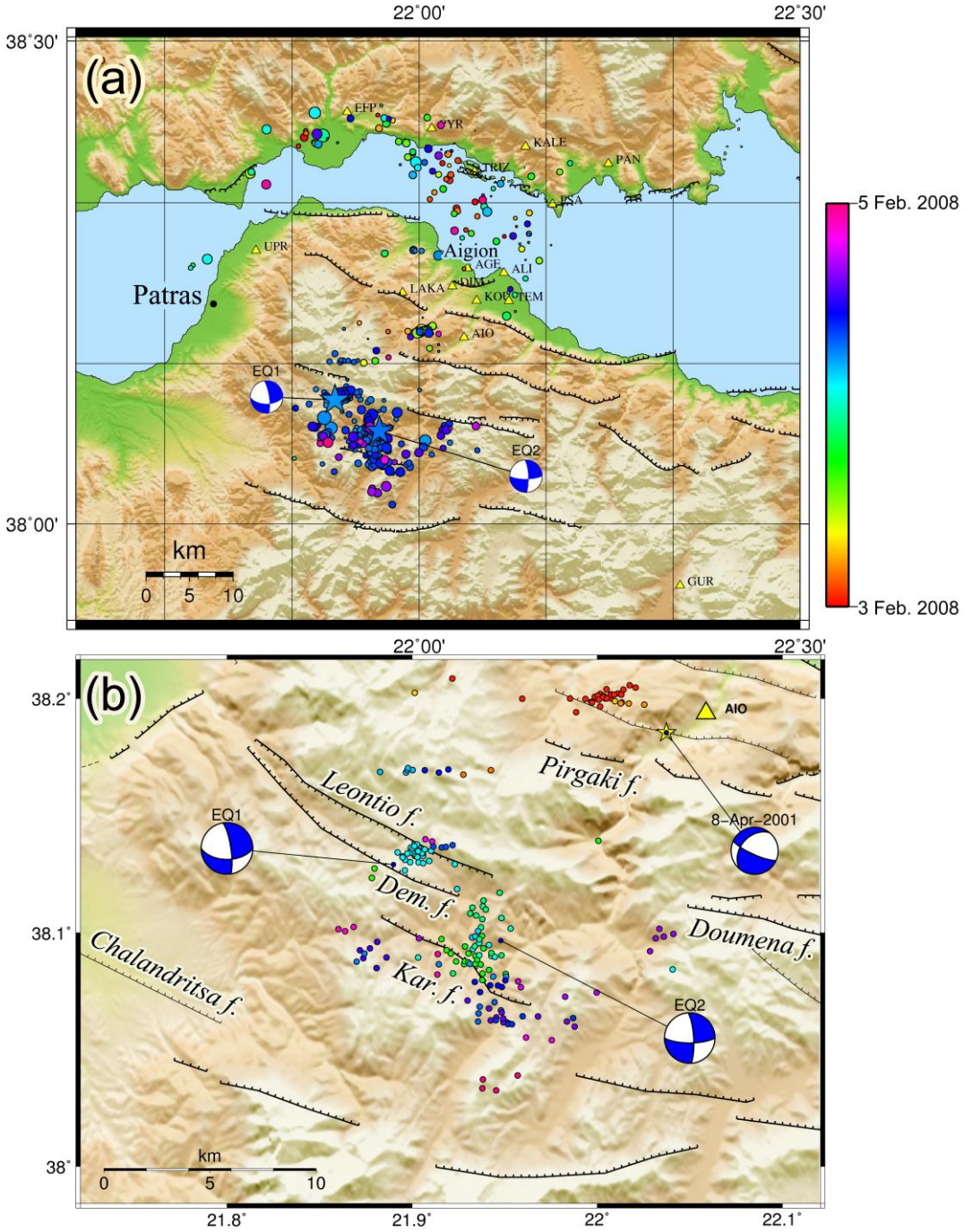

Figure 6A.1: The 3-5 February 2008 swarm near Leontio-Demesticha faults (modified after Kapetanidis *et al.*, 2008). The sequence is probably associated with a relay zone between the eastern end of Leontio and Demesticha (Dem.f.) faults and the north-dipping Karousi fault (Kar.f.), hence it refers to probably N-S dextral strike-slip faulting. The rotation of the T-axis to SW-NE is also consistent with the transition between N-S extension in the Corinth Rift and E-W extension in southern Peloponnese (Kassaras *et al.*, 2016). Colours represent a) origin time, b) different multiplets.

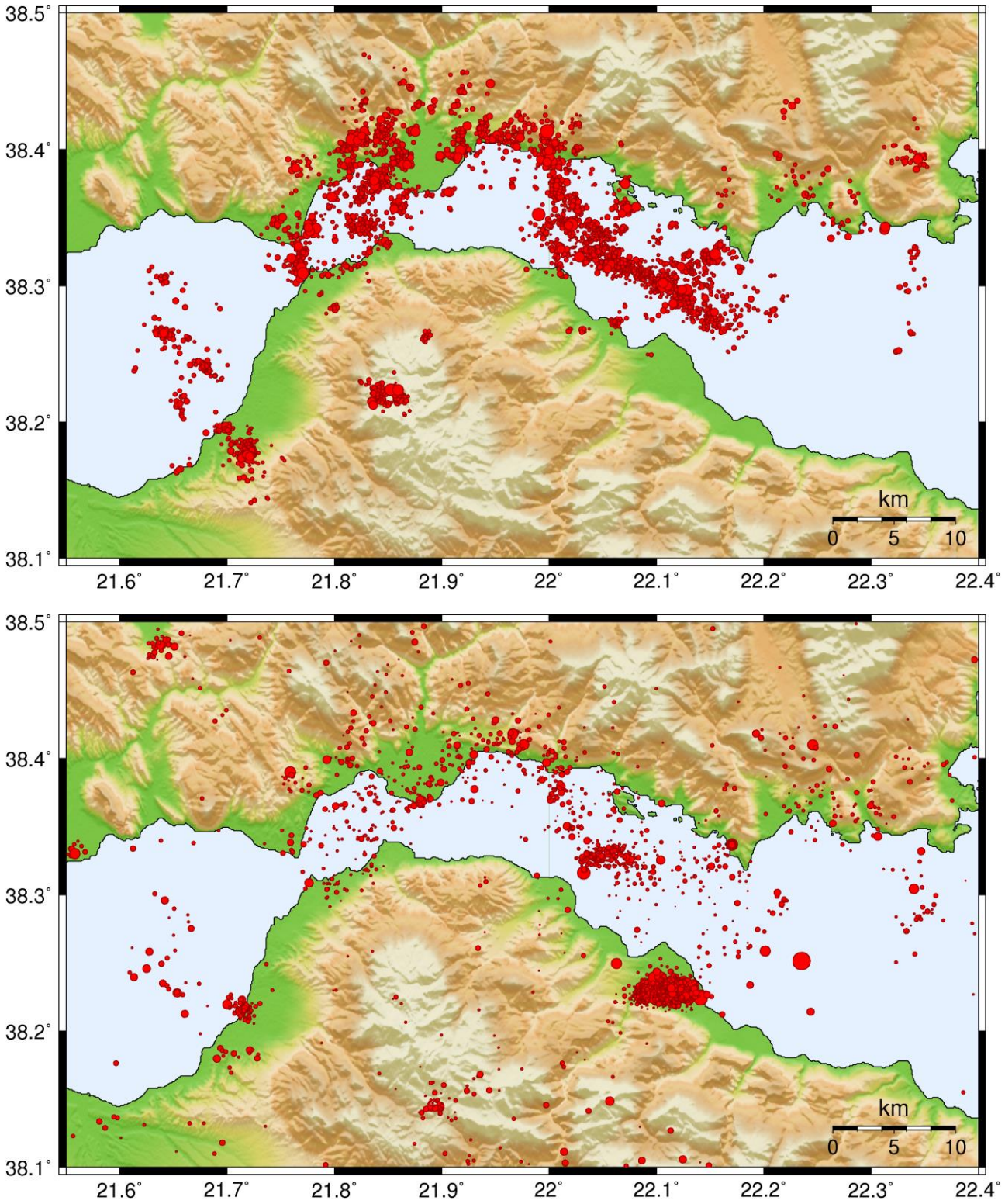

Figure 6A.2: Preliminary relocations (top) September 2011 – March 2013, (bottom), March 2013 – August 2013. (REAKT Project)

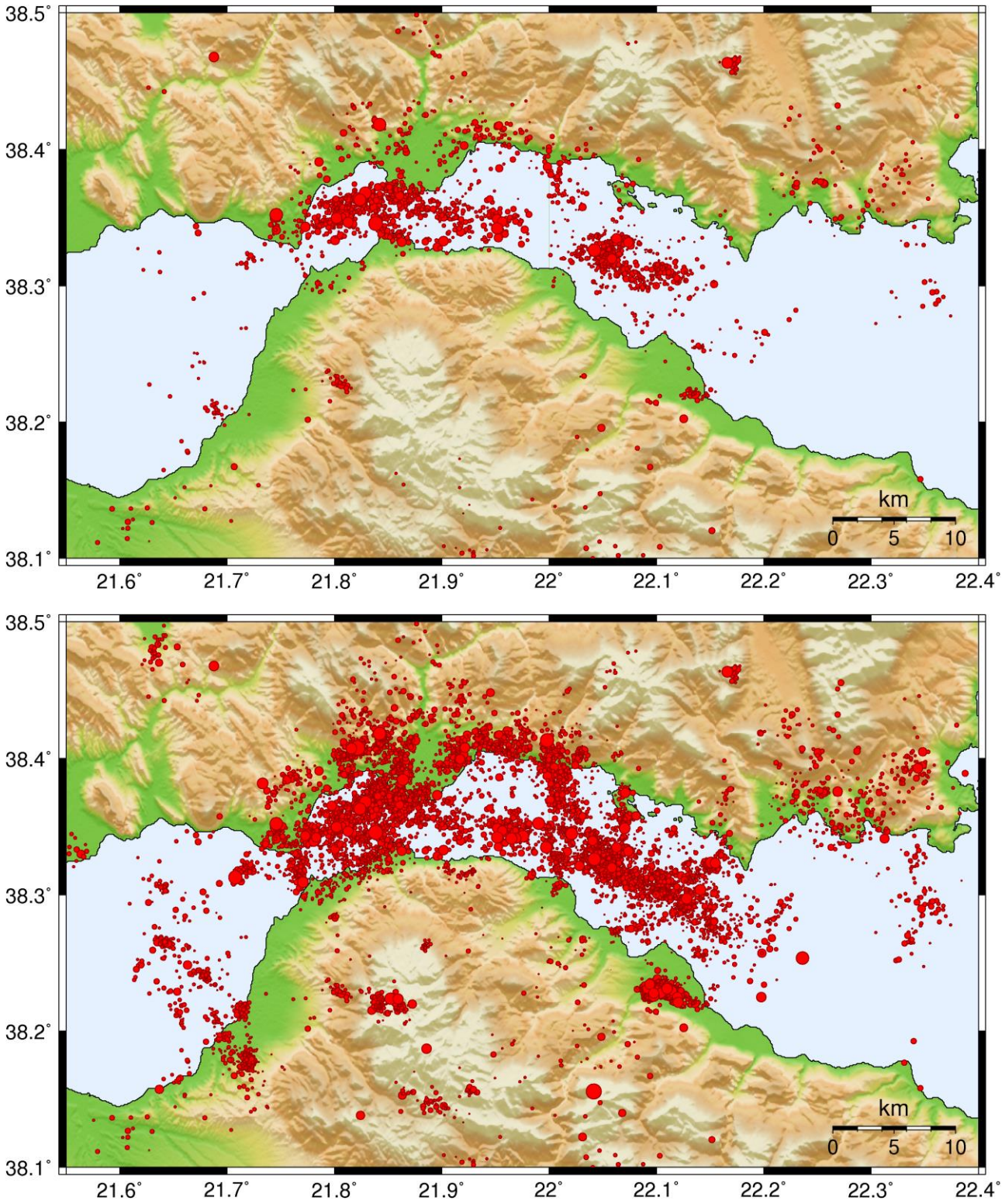

Figure 6A.3: Preliminary relocations (top) April – October 2014, (bottom) September 2011 – October 2014. (REAKT Project)

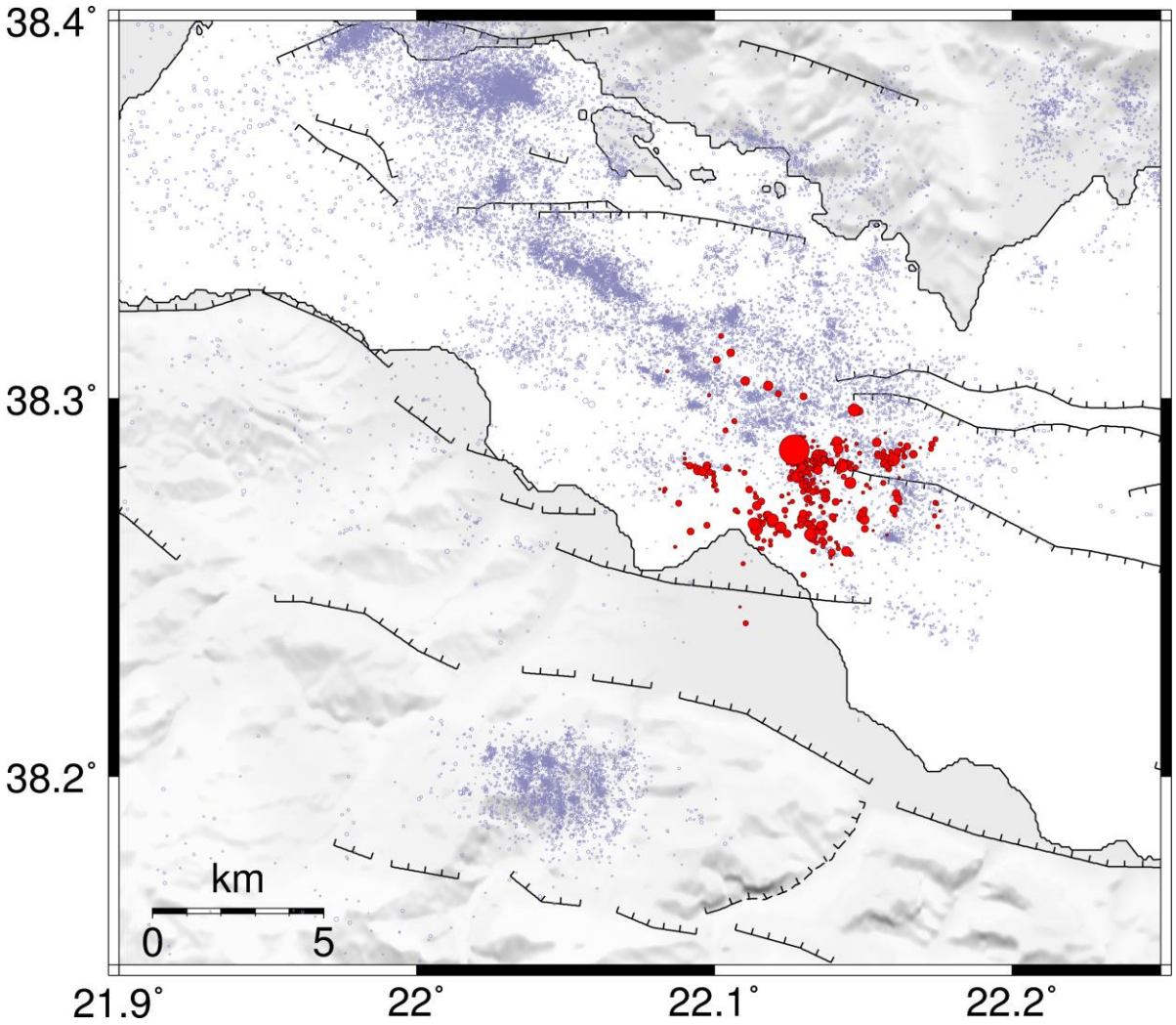

Figure 6A.4: Preliminary solutions for the aftershock sequence of the 7 November 2014 M_w=5.0 event (red), superimposed on the relocated catalogue of 2000-2007 (thin, light blue).

Appendix 6B

Supplementary material for Chapter 6

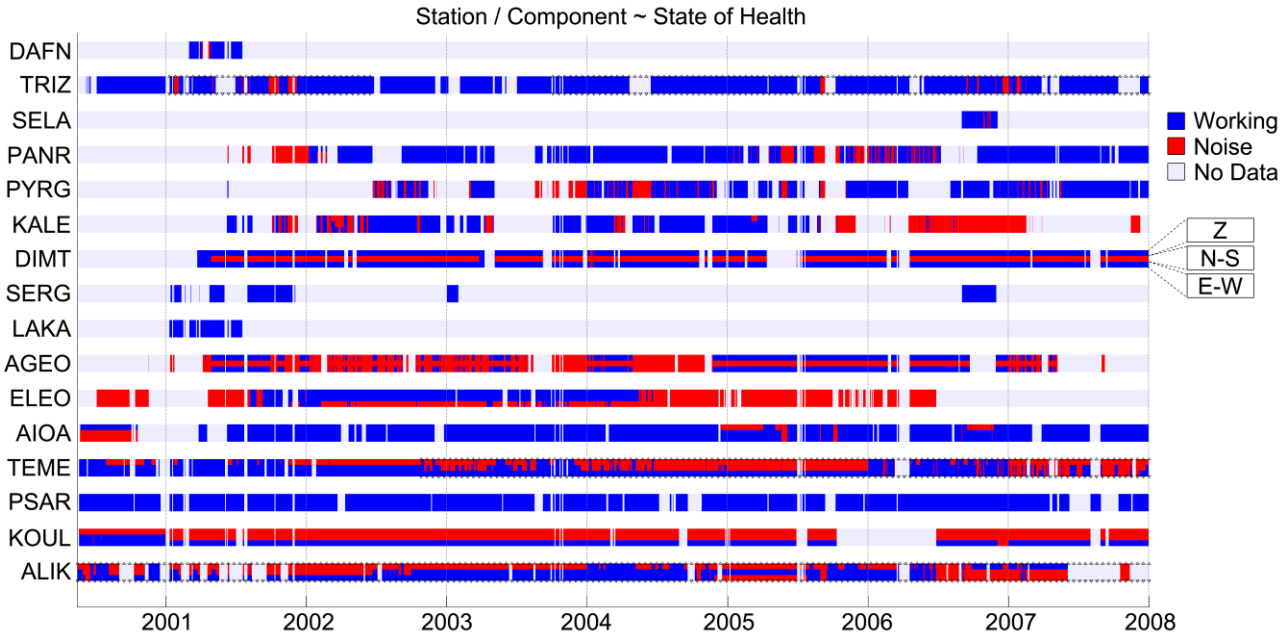

Figure 6B.1: State of Health per station and component for the seismological stations of CRL network in the period between 2000 and 2007. Observations were made on random samples and the rules on component rejection were then decided on the permanent character of problematic behavior of certain components over a long period.

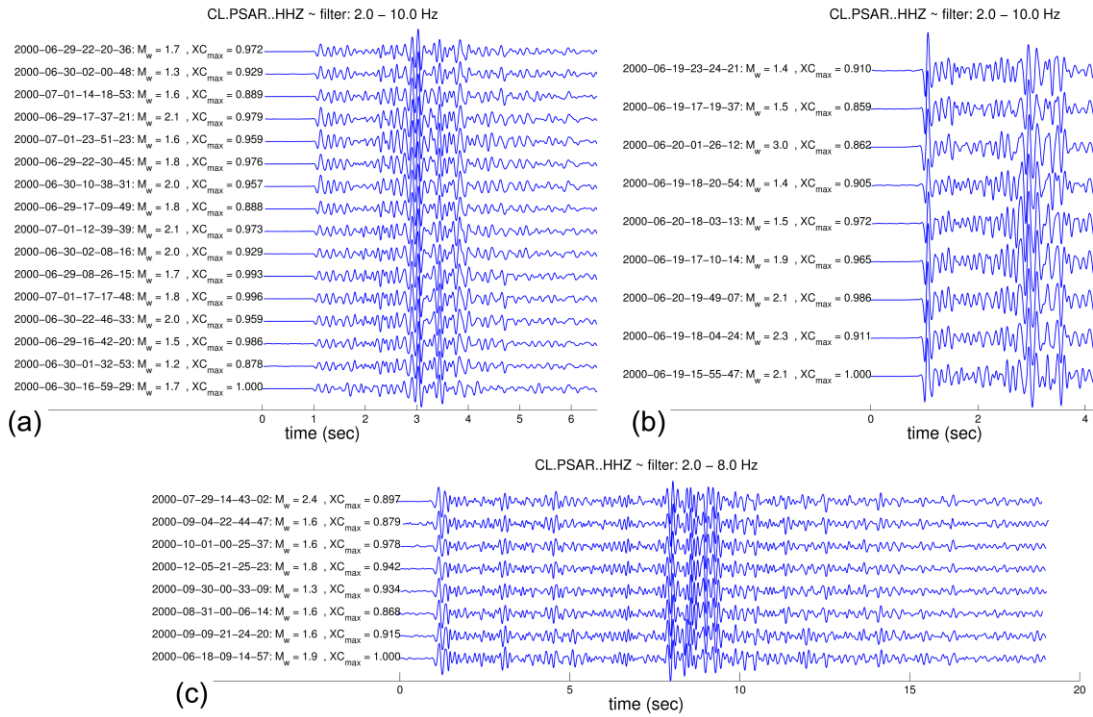

Figure 6B.2: Waveforms of the vertical component of station PSAR from selected multiplets, a) southern cluster of 2000-Group #1 (east of Trizonia island), b) northern cluster of 2000-Group #1, c) 2000-Group #2 (Patraikos gulf). Each waveform has been cross-correlated with the one below and shifted by the respective t_m.

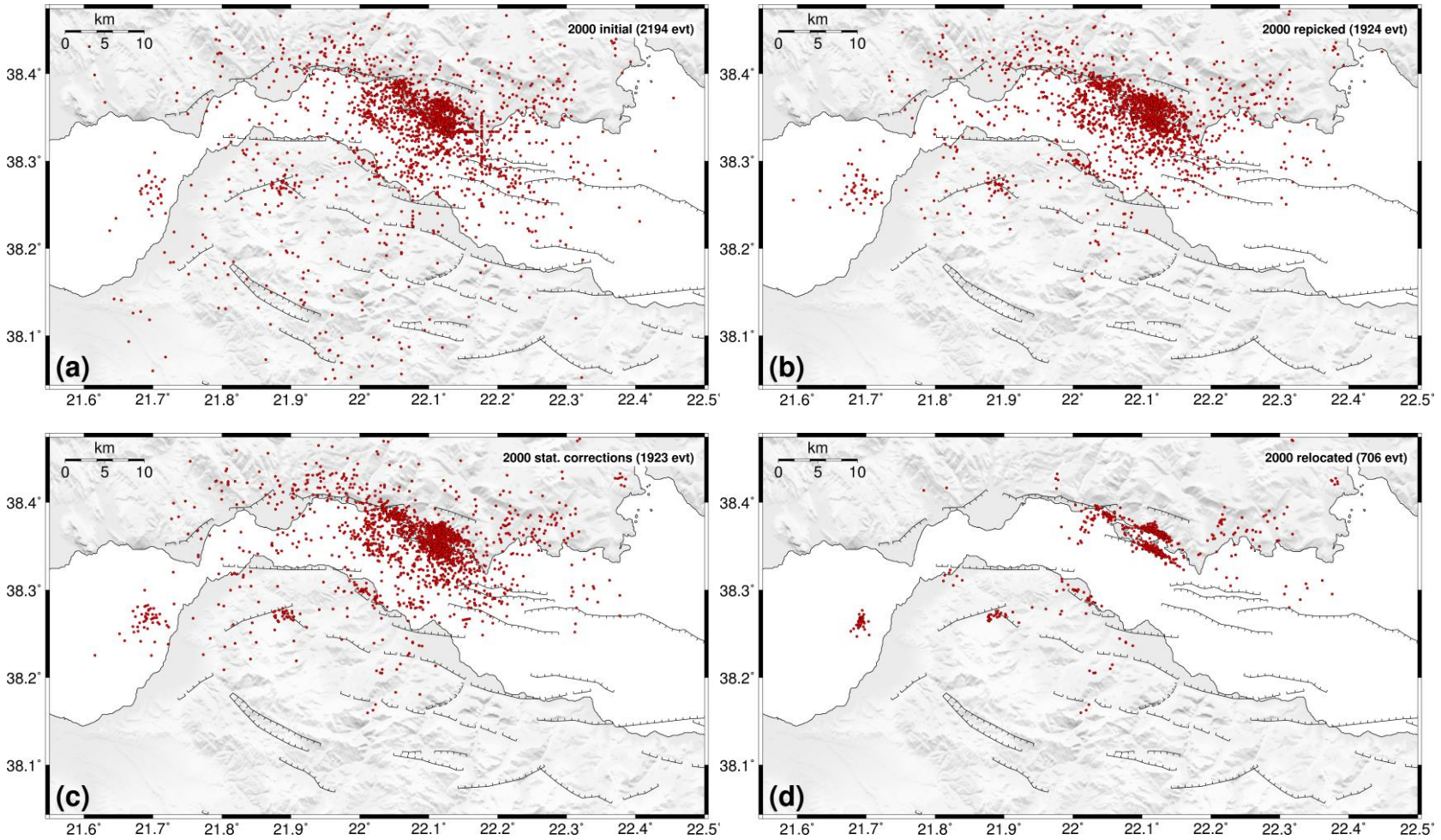

Figure 6B.3: Seismicity of 2000 in the western Corinth Rift, a) initial locations, b) re-picked solutions, c) solutions after station corrections per spatial group, d) relocated epicenters.

Table 6B.1: Statistics of initial locations and after the application of station corrections per spatial group for the seismicity of 2000 in the western Corinth rift.

2000	**Group #1**		**Group #2**		**Group #3**		**Group #4**	
	initial	**stat.corr.**	**initial**	**stat.corr.**	**initial**	**stat.corr.**	**initial**	**stat.corr.**
# Events	797		48		63		72	
Epic. Region	*near Trizonia isl.*		*Patraikos gulf*		*Sela - Rio*		*Selianitika*	
Mean RMS (s)	0.088	0.047	0.107	0.064	0.098	0.070	0.073	0.060
Median RMS (s)	0.090	0.040	0.110	0.060	0.090	0.060	0.080	0.060
Median ERX (km)	1.830	1.650	2.000	1.730	0.910	0.890	0.985	0.885
Median ERY (km)	3.550	3.230	6.370	5.825	1.180	1.100	1.545	1.460
Median ERZ (km)	2.550	2.400	17.280	15.600	18.400	17.480	2.730	2.450
Mean ERX (km)	1.880	1.689	2.391	1.968	1.044	1.002	1.399	1.288
Mean ERY (km)	3.097	2.793	4.549	4.217	1.220	1.229	2.009	1.901
Mean ERZ (km)	2.731	2.645	14.292	11.383	18.694	17.718	4.052	3.868
Mean Depth (km)	8.739	8.606	10.161	8.711	8.000	8.031	8.609	8.541
Median Depth (km)	8.710	8.560	9.385	8.580	8.000	8.000	8.995	8.920

	Group #5		**Group #6**	
	initial	**stat.corr.**	**initial**	**stat.corr.**
# Events	428		120	
Epic. Region	*Trizonia*		*Eratini*	
Mean RMS (s)	0.084	0.058	0.075	0.064
Median RMS (s)	0.090	0.060	0.070	0.060
Median ERX (km)	1.065	1.030	1.280	1.260
Median ERY (km)	1.125	1.100	1.325	1.290
Median ERZ (km)	1.995	1.810	1.685	1.730
Mean ERX (km)	1.253	1.310	1.815	1.791
Mean ERY (km)	1.400	1.508	1.874	1.819
Mean ERZ (km)	8.116	7.028	3.746	3.736
Mean Depth (km)	7.475	7.882	10.803	10.810
Median Depth (km)	8.000	8.000	10.440	10.300

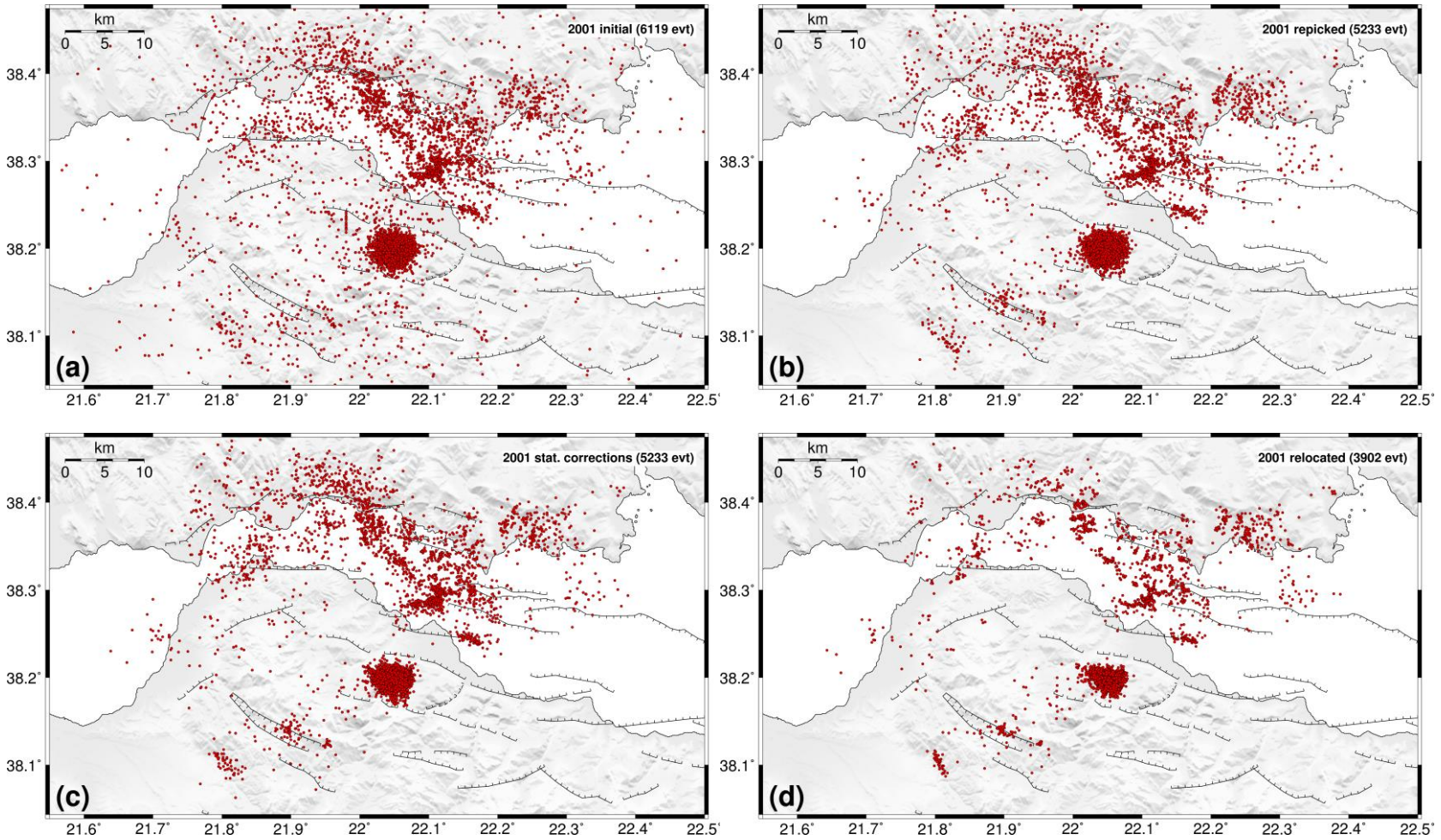

Figure 6B.4: Seismicity of 2001 in the western Corinth Rift, a) initial locations, b) re-picked solutions, c) solutions after station corrections per spatial group, d) relocated epicenters.

Table 6B.2: Statistics of initial locations and after the application of station corrections per spatial group for the seismicity of 2001 in the western Corinth rift.

2001	**Group #1**		**Group #2**		**Group #3**		**Group #4**	
	initial	**stat.corr.**	**initial**	**stat.corr.**	**initial**	**stat.corr.**	**initial**	**stat.corr.**
# Events	240		977		303		743	
Epic. Region	*Eratini*		*mid-gulf*		*Psathopyrgos*		*Sergoula*	
Mean RMS (s)	0.088	0.061	0.067	0.058	0.113	0.083	0.089	0.061
Median RMS (s)	0.090	0.060	0.060	0.050	0.110	0.080	0.090	0.060
Median ERX (km)	0.990	0.900	0.460	0.450	0.910	0.830	0.750	0.700
Median ERY (km)	1.090	1.020	0.690	0.670	1.020	0.960	0.990	0.920
Median ERZ (km)	1.165	1.080	1.390	1.340	18.530	17.720	1.500	1.400
Mean ERX (km)	1.093	1.045	0.567	0.548	1.074	0.984	0.959	0.873
Mean ERY (km)	1.241	1.227	0.794	0.774	1.448	1.386	1.157	1.089
Mean ERZ (km)	2.643	2.630	1.579	1.514	14.608	14.276	3.039	2.977
Mean Depth (km)	9.945	9.929	7.192	7.084	8.994	8.233	9.111	8.913
Median Depth (km)	10.000	10.000	7.130	7.060	8.000	8.000	8.900	8.780

	Group #5		**Group #6**	
	initial	**stat.corr.**	**initial**	**stat.corr.**
# Events	2863		219	
Epic. Region	*Agios Ioannis (AIOA) swarm*		*near Chalandritsa*	
Mean RMS (s)	0.071	0.049	0.099	0.073
Median RMS (s)	0.070	0.040	0.100	0.070
Median ERX (km)	0.900	0.860	1.290	1.230
Median ERY (km)	0.640	0.620	1.230	1.140
Median ERZ (km)	1.030	0.950	3.630	4.470
Mean ERX (km)	1.078	1.057	1.456	1.387
Mean ERY (km)	0.774	0.749	1.707	1.616
Mean ERZ (km)	1.217	1.130	8.452	8.742
Mean Depth (km)	7.594	7.676	11.266	10.543
Median Depth (km)	7.740	7.690	9.580	9.260

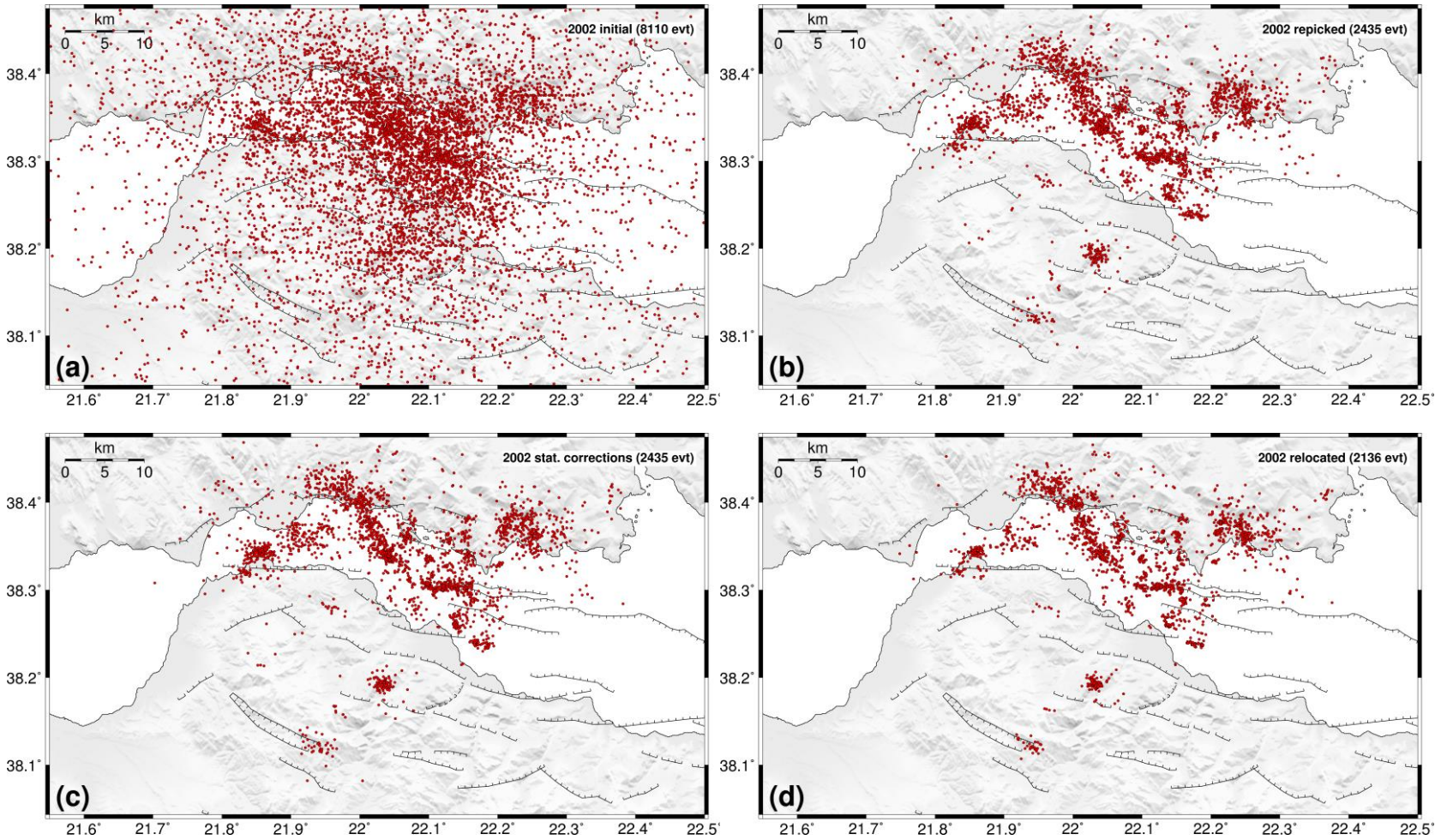

Figure 6B.5: Seismicity of 2002 in the western Corinth Rift, a) initial locations, b) re-picked solutions, c) solutions after station corrections per spatial group, d) relocated epicenters.

Table 6B.3: Statistics of initial locations and after the application of station corrections per spatial group for the seismicity of 2002 in the western Corinth rift.

2002	**Group #1**		**Group #2**		**Group #3**		**Group #4**	
	initial	**stat.corr.**	**initial**	**stat.corr.**	**initial**	**stat.corr.**	**initial**	**stat.corr.**
# Events	480		503		498		416	
Epic. Region	*mid. gulf (S)*		*mid. gulf (N)*		*Sergoula*		*Psathopyrgos*	
Mean RMS (s)	0.102	0.085	0.105	0.072	0.106	0.078	0.120	0.095
Median RMS (s)	0.100	0.080	0.100	0.070	0.110	0.080	0.120	0.090
Median ERX (km)	0.320	0.310	0.350	0.330	0.540	0.510	0.750	0.700
Median ERY (km)	0.540	0.520	0.580	0.540	0.730	0.700	0.890	0.830
Median ERZ (km)	0.940	0.900	0.940	0.880	1.110	1.040	18.935	18.040
Mean ERX (km)	0.337	0.321	0.382	0.360	0.589	0.553	0.803	0.745
Mean ERY (km)	0.557	0.533	0.603	0.567	0.761	0.723	1.000	0.951
Mean ERZ (km)	0.960	0.945	0.983	0.916	2.559	2.267	14.346	14.004
Mean Depth (km)	6.882	6.747	7.988	7.944	8.774	8.645	8.825	8.312
Median Depth (km)	7.040	7.030	8.070	7.910	8.650	8.620	8.000	8.000

	Group #5		**Group #6**	
	initial	**stat.corr.**	**initial**	**stat.corr.**
# Events	141		397	
Epic. Region	*near AIOA*		*Eratini*	
Mean RMS (s)	0.109	0.076	0.100	0.076
Median RMS (s)	0.110	0.080	0.100	0.080
Median ERX (km)	0.680	0.660	0.550	0.520
Median ERY (km)	0.750	0.690	0.700	0.680
Median ERZ (km)	0.740	0.630	0.830	0.790
Mean ERX (km)	0.719	0.689	0.592	0.562
Mean ERY (km)	0.776	0.730	0.724	0.700
Mean ERZ (km)	2.573	2.401	1.229	1.161
Mean Depth (km)	8.839	8.761	10.039	9.999
Median Depth (km)	8.330	8.120	10.010	9.930

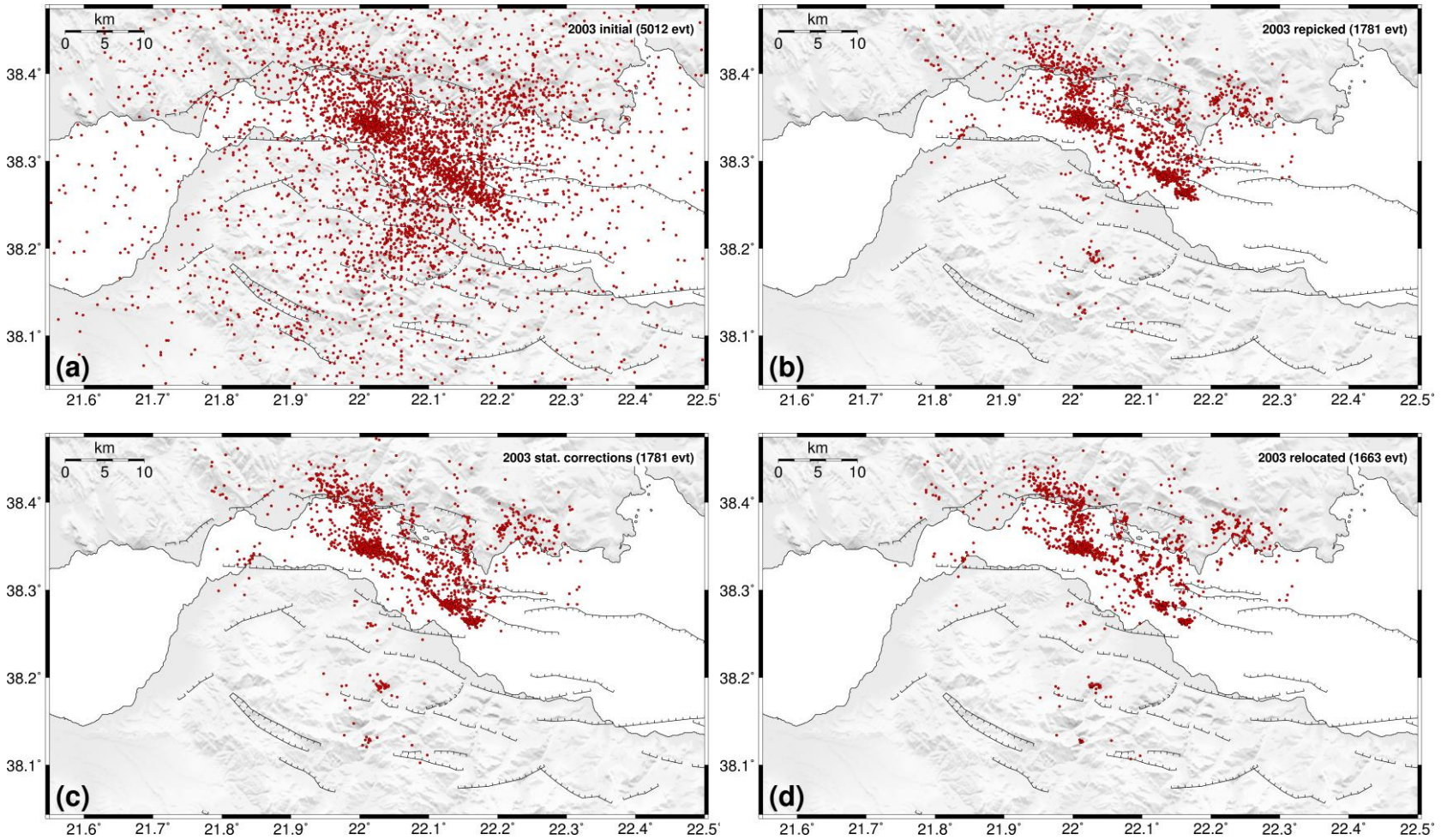

Figure 6B.6: Seismicity of 2003 in the western Corinth Rift, a) initial locations, b) re-picked solutions, c) solutions after station corrections per spatial group, d) relocated epicenters.

Table 6B.4: Statistics of initial locations and after the application of station corrections per spatial group for the seismicity of 2003 in the western Corinth rift.

2003	**Group #1**		**Group #2**		**Group #3**		**Group #4**		**Group #5**	
	initial	**stat.corr.**	**initial**	**stat.corr.**	**initial**	**stat.corr.**	**initial**	**stat.corr.**	**initial**	**stat.corr.**
# Events	151		161		90		264		380	
Epic. Region	*Sergoula*		*Sergoula-Nafpaktos*		*Psaromita*		*mid. gulf*		*mid. gulf, W patch*	
Mean RMS (s)	0.110	0.077	0.111	0.084	0.092	0.075	0.094	0.077	0.111	0.081
Median RMS (s)	0.110	0.070	0.110	0.080	0.090	0.070	0.100	0.080	0.110	0.080
Median ERX (km)	0.590	0.560	0.690	0.650	0.455	0.430	0.380	0.360	0.410	0.390
Median ERY (km)	0.780	0.730	0.760	0.720	0.550	0.550	0.600	0.580	0.760	0.690
Median ERZ (km)	1.060	0.990	1.420	1.540	0.890	0.865	0.940	0.915	1.220	1.135
Mean ERX (km)	0.635	0.566	0.736	0.680	0.508	0.483	0.442	0.422	0.476	0.436
Mean ERY (km)	0.873	0.793	0.830	0.773	0.661	0.633	0.651	0.631	0.772	0.713
Mean ERZ (km)	2.617	2.517	6.473	5.661	0.957	0.909	1.126	1.101	2.604	2.376
Mean Depth (km)	9.152	9.023	8.702	8.596	8.807	8.736	7.883	7.778	8.466	8.265
Median Depth (km)	9.020	8.950	8.410	8.410	8.705	8.710	8.010	8.000	8.285	8.190

Table 6B.4: (continued)

2003	Group #6		Group #7		Group #8		Group #9	
	initial	stat.corr.	initial	stat.corr.	initial	stat.corr.	initial	stat.corr.
# Events	38		49		491		157	
Epic. Region	*Psathopyrgos*		*near AIOA*		*mid. gulf, E patch*		*Eratini*	
Mean RMS (s)	0.118	0.091	0.108	0.074	0.112	0.083	0.096	0.076
Median RMS (s)	0.120	0.090	0.100	0.060	0.110	0.080	0.090	0.080
Median ERX (km)	0.875	0.900	0.700	0.630	0.310	0.290	0.520	0.500
Median ERY (km)	0.850	0.800	0.800	0.790	0.550	0.510	0.690	0.660
Median ERZ (km)	16.835	3.405	0.750	0.680	0.950	0.910	0.780	0.730
Mean ERX (km)	1.078	0.992	0.866	0.815	0.359	0.334	0.585	0.563
Mean ERY (km)	1.212	0.975	1.070	1.026	0.584	0.545	0.727	0.704
Mean ERZ (km)	11.619	8.942	0.904	0.859	0.985	0.966	0.961	0.944
Mean Depth (km)	8.977	8.482	8.570	8.613	6.269	6.149	10.239	10.208
Median Depth (km)	8.270	8.000	7.820	7.860	6.400	6.170	10.070	9.930

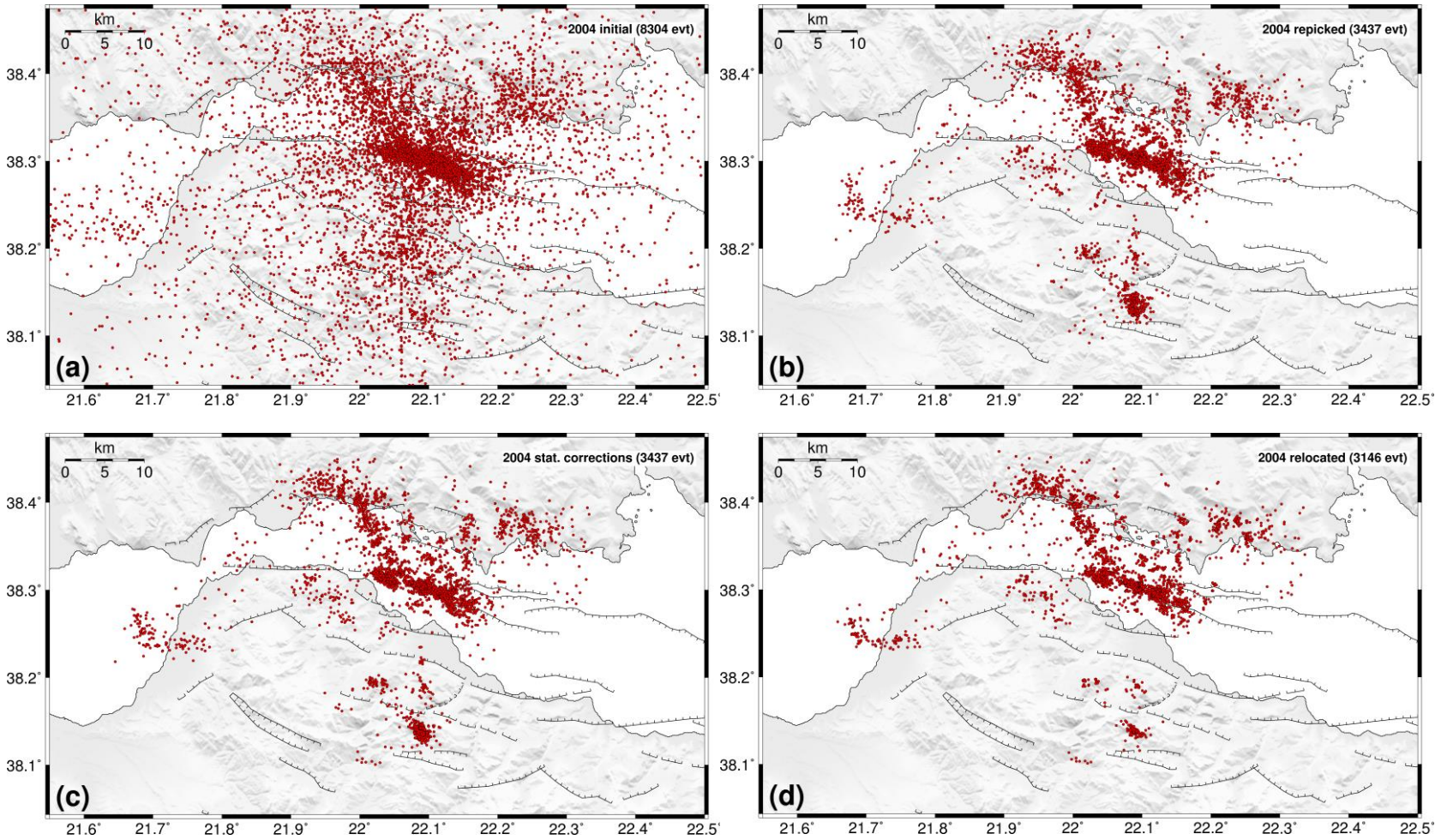

Figure 6B.7: Seismicity of 2004 in the western Corinth Rift, a) initial locations, b) re-picked solutions, c) solutions after station corrections per spatial group, d) relocated epicenters.

Table 6B.5: Statistics of initial locations and after the application of station corrections per spatial group for the seismicity of 2004 in the western Corinth rift.

2004	**Group #1**		**Group #2**		**Group #3**		**Group #4**	
	initial	**stat.corr.**	**initial**	**stat.corr.**	**initial**	**stat.corr.**	**initial**	**stat.corr.**
# Events	203		410		123		1040	
Epic. Region	*Sergoula*		*mid. gulf*		*Psathopyrgos*		*swarm offshore Aigion*	
Mean RMS (s)	0.093	0.071	0.100	0.069	0.117	0.097	0.102	0.071
Median RMS (s)	0.090	0.070	0.100	0.070	0.110	0.100	0.100	0.070
Median ERX (km)	0.730	0.710	0.500	0.460	0.510	0.450	0.310	0.290
Median ERY (km)	0.780	0.740	0.690	0.650	0.910	0.840	0.520	0.490
Median ERZ (km)	1.050	0.970	0.980	0.925	2.110	2.350	0.960	0.900
Mean ERX (km)	0.788	0.774	0.542	0.515	0.561	0.526	0.339	0.311
Mean ERY (km)	0.792	0.759	0.721	0.683	1.001	0.924	0.574	0.540
Mean ERZ (km)	4.400	4.120	1.636	1.509	7.311	7.687	1.044	0.999
Mean Depth (km)	8.810	8.886	8.555	8.488	8.360	7.902	7.640	7.439
Median Depth (km)	8.910	8.940	8.525	8.505	8.000	8.000	7.530	7.490
	Group #5		**Group #6**		**Group #7**		**Group #8**	
	initial	**stat.corr.**	**initial**	**stat.corr.**	**initial**	**stat.corr.**	**initial**	**stat.corr.**
# Events	915		239		119		388	
Epic. Region	*mid. gulf, W. patch*		*Eratini*		*Patraikos gulf*		*near AIOA*	
Mean RMS (s)	0.107	0.084	0.094	0.073	0.120	0.085	0.090	0.065
Median RMS (s)	0.110	0.080	0.090	0.070	0.120	0.080	0.090	0.060
Median ERX (km)	0.310	0.300	0.640	0.620	1.210	1.150	0.790	0.750
Median ERY (km)	0.490	0.460	0.620	0.600	2.110	1.880	1.000	0.995
Median ERZ (km)	0.940	0.900	0.820	0.780	16.510	12.900	0.945	0.830
Mean ERX (km)	0.352	0.333	0.678	0.660	1.307	1.207	0.819	0.793
Mean ERY (km)	0.527	0.499	0.672	0.653	3.196	2.890	1.009	0.994
Mean ERZ (km)	0.973	0.936	0.870	0.910	13.700	9.948	1.091	0.961
Mean Depth (km)	6.957	6.861	10.280	10.206	10.832	8.946	9.653	9.852
Median Depth (km)	6.950	6.860	10.220	10.090	9.800	8.680	10.155	10.965

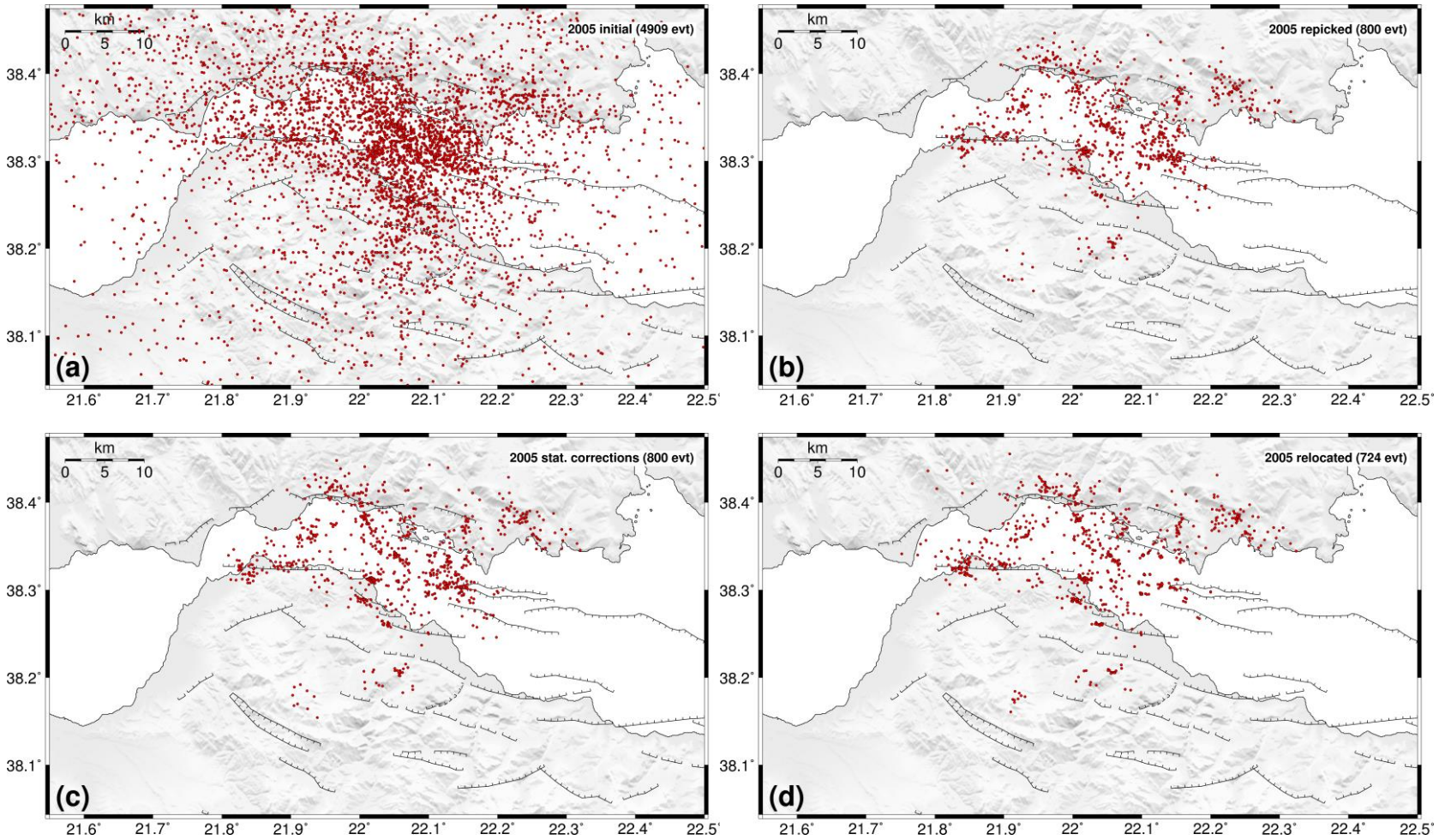

Figure 6B.8: Seismicity of 2005 in the western Corinth Rift, a) initial locations, b) re-picked solutions, c) solutions after station corrections per spatial group, d) relocated epicenters.

Table 6B.6: Statistics of initial locations and after the application of station corrections per spatial group for the seismicity of 2005 in the western Corinth rift.

2005	**Group #1**		**Group #2**		**Group #3**		**Group #4**		**Group #5**	
	initial	**stat.corr.**	**initial**	**stat.corr.**	**initial**	**stat.corr.**	**initial**	**stat.corr.**	**initial**	**stat.corr.**
# Events	78		91		78		84		10	
Epic. Region	*mid. gulf*		*mid-S gulf*		*mid-NW gulf*		*Napfaktos, W. gulf*		*near SELA*	
Mean RMS (s)	0.105	0.068	0.115	0.085	0.103	0.072	0.109	0.081	0.089	0.072
Median RMS (s)	0.100	0.065	0.110	0.080	0.100	0.070	0.100	0.080	0.080	0.065
Median ERX (km)	0.360	0.330	0.380	0.360	0.520	0.480	0.610	0.590	1.180	1.060
Median ERY (km)	0.625	0.580	0.810	0.750	0.730	0.690	0.870	0.825	0.985	0.860
Median ERZ (km)	1.015	0.955	1.300	1.180	0.995	0.930	1.365	1.250	1.910	1.390
Mean ERX (km)	0.371	0.336	0.414	0.376	0.542	0.498	0.666	0.629	1.175	1.116
Mean ERY (km)	0.633	0.583	0.833	0.780	0.741	0.698	0.888	0.842	1.046	0.962
Mean ERZ (km)	1.034	0.980	1.879	1.945	1.041	0.967	2.413	2.393	6.355	4.427
Mean Depth (km)	7.885	7.759	7.326	7.155	8.578	8.535	8.950	8.797	10.543	10.291
Median Depth (km)	8.010	7.955	7.160	7.060	8.690	8.665	8.900	8.750	10.155	9.820

Table 6B.6: (Continued)

2005	Group #6		Group #7		Group #8		Group #9		Group #10	
	initial	stat.corr.	initial	stat.corr.	initial	stat.corr.	initial	stat.corr.	initial	stat.corr.
# Events	61		164		77		80		77	
Epic. Region	*S. of Aigion*		*mid-E gulf*		*Trizonia-Psaromita*		*Psathopyrgos*		*Eratini*	
Mean RMS (s)	0.098	0.080	0.098	0.081	0.108	0.075	0.119	0.092	0.093	0.071
Median RMS (s)	0.100	0.080	0.100	0.080	0.110	0.070	0.120	0.090	0.090	0.070
Median ERX (km)	0.360	0.340	0.355	0.340	0.450	0.410	0.755	0.735	0.710	0.670
Median ERY (km)	0.570	0.550	0.540	0.520	0.510	0.480	1.000	0.930	0.650	0.630
Median ERZ (km)	0.870	0.790	0.990	0.960	0.950	0.900	18.850	18.015	0.820	0.750
Mean ERX (km)	0.414	0.389	0.380	0.367	0.486	0.449	0.886	0.817	0.716	0.704
Mean ERY (km)	0.596	0.584	0.565	0.547	0.526	0.508	1.063	0.986	0.684	0.654
Mean ERZ (km)	0.830	0.763	1.030	0.988	1.214	1.035	14.725	14.315	0.842	0.793
Mean Depth (km)	5.568	5.503	7.244	7.206	8.294	8.339	9.026	8.634	10.056	10.022
Median Depth (km)	5.030	4.870	7.210	7.140	8.720	8.650	8.000	8.000	10.040	9.990

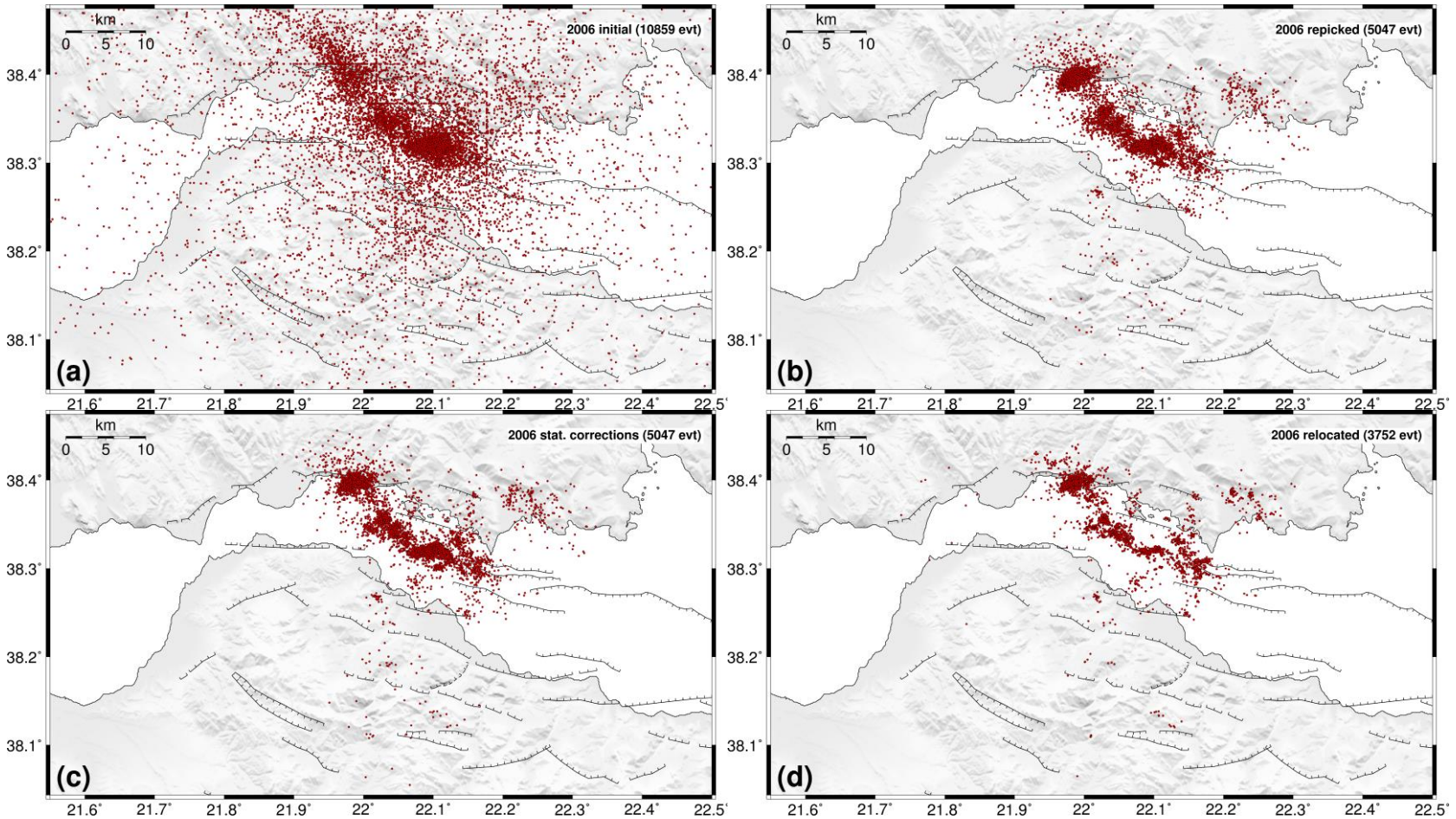

Figure 6B.9: Seismicity of 2006 in the western Corinth Rift, a) initial locations, b) re-picked solutions, c) solutions after station corrections per spatial group, d) relocated epicenters.

Table 6B.7: Statistics of initial locations and after the application of station corrections per spatial group for the seismicity of 2006 in the western Corinth rift.

2006	Group #1		Group #2		Group #3		Group #4	
	initial	stat.corr.	initial	stat.corr.	initial	stat.corr.	initial	stat.corr.
# Events	81		1679		325		280	
Epic. Region	*offshore Aigion*		*mid. gulf*		*mid-E gulf*		*mid.gulf*	
Mean RMS (s)	0.097	0.088	0.096	0.068	0.098	0.079	0.090	0.077
Median RMS (s)	0.100	0.080	0.100	0.070	0.100	0.080	0.090	0.070
Median ERX (km)	0.390	0.400	0.320	0.300	0.420	0.410	0.400	0.390
Median ERY (km)	0.630	0.600	0.450	0.430	0.600	0.560	0.470	0.450
Median ERZ (km)	0.900	0.880	0.990	0.930	0.930	0.920	0.960	0.940
Mean ERX (km)	0.456	0.443	0.372	0.350	0.542	0.518	0.498	0.490
Mean ERY (km)	0.778	0.752	0.473	0.450	0.711	0.680	0.547	0.535
Mean ERZ (km)	0.893	0.904	1.036	0.977	1.074	1.041	0.982	1.030
Mean Depth (km)	6.069	5.945	7.328	7.263	6.395	6.436	7.418	7.392
Median Depth (km)	6.220	5.930	7.300	7.270	6.510	6.550	7.325	7.255

Table 6B.7: (continued)

2006	Group #5		Group #6		Group #7		Group #8	
	initial	stat.corr.	initial	stat.corr.	initial	stat.corr.	initial	stat.corr.
# Events	53		1330		1113		186	
Epic. Region	*near AIOA*		*near Sergoula*		*mid-W gulf*		*Eratini*	
Mean RMS (s)	0.096	0.076	0.101	0.075	0.100	0.070	0.093	0.069
Median RMS (s)	0.090	0.070	0.100	0.070	0.100	0.070	0.090	0.070
Median ERX (km)	0.870	0.820	0.580	0.550	0.410	0.380	0.755	0.740
Median ERY (km)	0.890	0.880	0.730	0.710	0.640	0.610	0.700	0.665
Median ERZ (km)	0.970	0.840	0.830	0.800	1.080	1.010	0.840	0.795
Mean ERX (km)	0.906	0.853	0.622	0.590	0.492	0.458	0.871	0.849
Mean ERY (km)	1.059	1.040	0.712	0.688	0.667	0.629	0.770	0.738
Mean ERZ (km)	1.185	1.103	1.185	1.159	1.194	1.131	0.867	0.826
Mean Depth (km)	9.706	10.080	7.926	7.935	7.947	7.921	10.007	10.134
Median Depth (km)	8.860	9.140	7.900	7.880	7.950	7.960	10.130	10.180

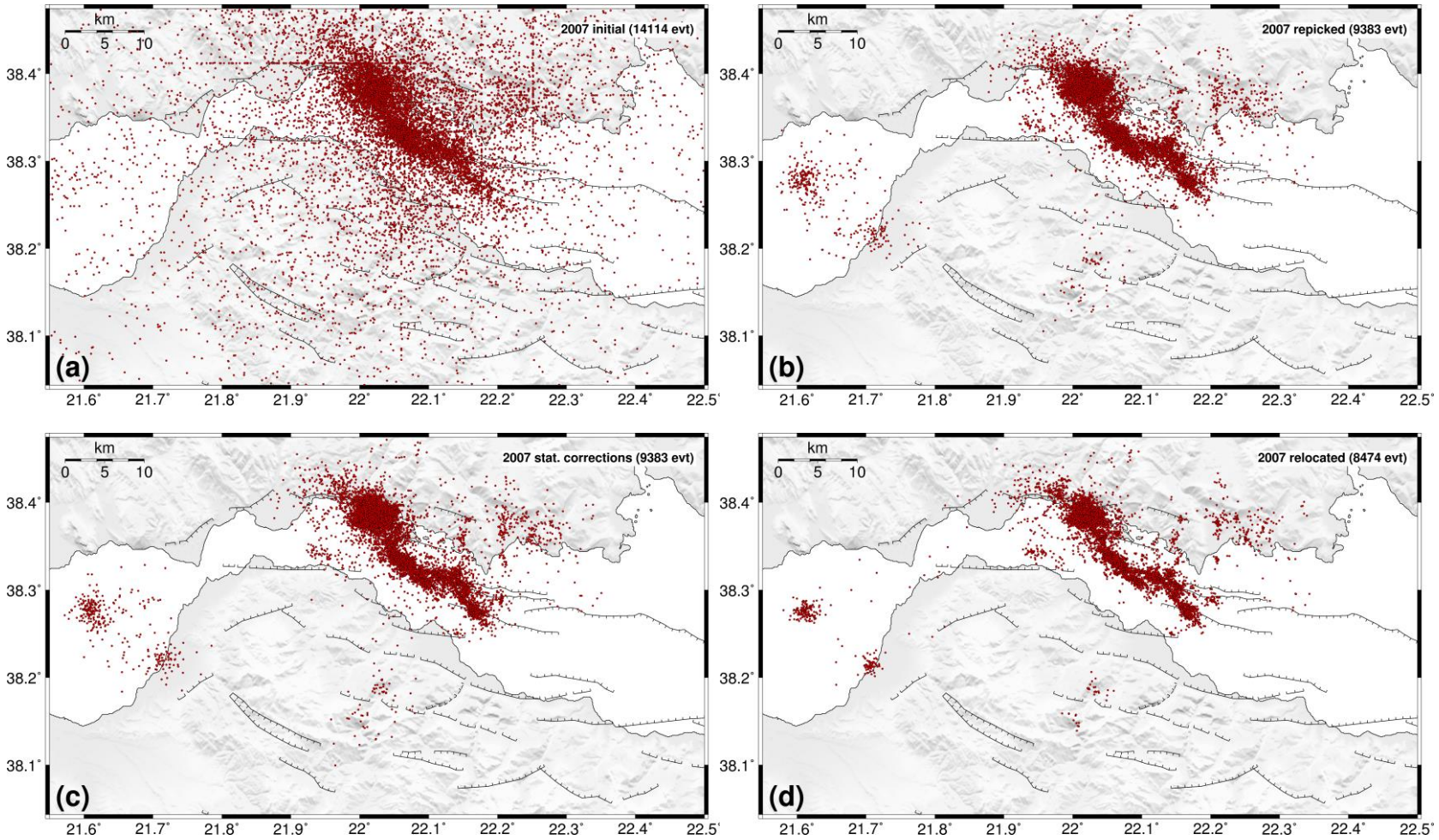

Figure 6B.10: Seismicity of 2007 in the western Corinth Rift, a) initial locations, b) re-picked solutions, c) solutions after station corrections per spatial group, d) relocated epicenters.

Table 6B.8: Statistics of initial locations and after the application of station corrections per spatial group for the seismicity of 2007 in the western Corinth rift.

2007	**Group #1**		**Group #2**		**Group #3**		**Group #4**	
	initial	**stat.corr.**	**initial**	**stat.corr.**	**initial**	**stat.corr.**	**initial**	**stat.corr.**
# Events	525		1678		67		1712	
Epic. Region	*mid-E gulf*		*mid. gulf*		*near AIOA*		*mid. gulf*	
Mean RMS (s)	0.106	0.081	0.097	0.078	0.090	0.071	0.091	0.063
Median RMS (s)	0.110	0.080	0.100	0.080	0.090	0.070	0.090	0.060
Median ERX (km)	0.520	0.500	0.380	0.360	0.800	0.800	0.370	0.350
Median ERY (km)	0.670	0.630	0.500	0.470	1.160	1.100	0.520	0.490
Median ERZ (km)	1.170	1.170	1.080	1.040	0.810	0.720	1.110	1.050
Mean ERX (km)	0.608	0.598	0.530	0.513	0.855	0.823	0.531	0.486
Mean ERY (km)	0.753	0.729	0.682	0.654	1.257	1.233	0.680	0.628
Mean ERZ (km)	1.840	1.591	1.277	1.257	1.320	1.249	1.208	1.217
Mean Depth (km)	5.875	5.970	7.277	7.153	8.773	8.891	7.871	7.623
Median Depth (km)	6.200	6.250	7.200	7.180	9.160	9.360	7.540	7.430

	Group #5		**Group #6**		**Group #7**	
	initial	**stat.corr.**	**initial**	**stat.corr.**	**initial**	**stat.corr.**
# Events	278		4809		314	
Epic. Region	*Eratini*		*offshore Sergoula*		*Patraikos gulf*	
Mean RMS (s)	0.086	0.078	0.106	0.080	0.143	0.108
Median RMS (s)	0.090	0.070	0.110	0.080	0.140	0.100
Median ERX (km)	0.800	0.790	0.500	0.470	1.610	1.430
Median ERY (km)	0.690	0.675	0.620	0.590	6.390	6.165
Median ERZ (km)	0.895	0.850	0.890	0.840	17.160	15.645
Mean ERX (km)	0.973	0.994	0.557	0.533	1.760	1.591
Mean ERY (km)	0.796	0.816	0.670	0.647	5.152	4.718
Mean ERZ (km)	1.328	1.431	1.216	1.112	14.749	12.902
Mean Depth (km)	10.926	10.907	7.660	7.662	9.111	8.045
Median Depth (km)	10.405	10.310	7.670	7.690	8.035	7.930

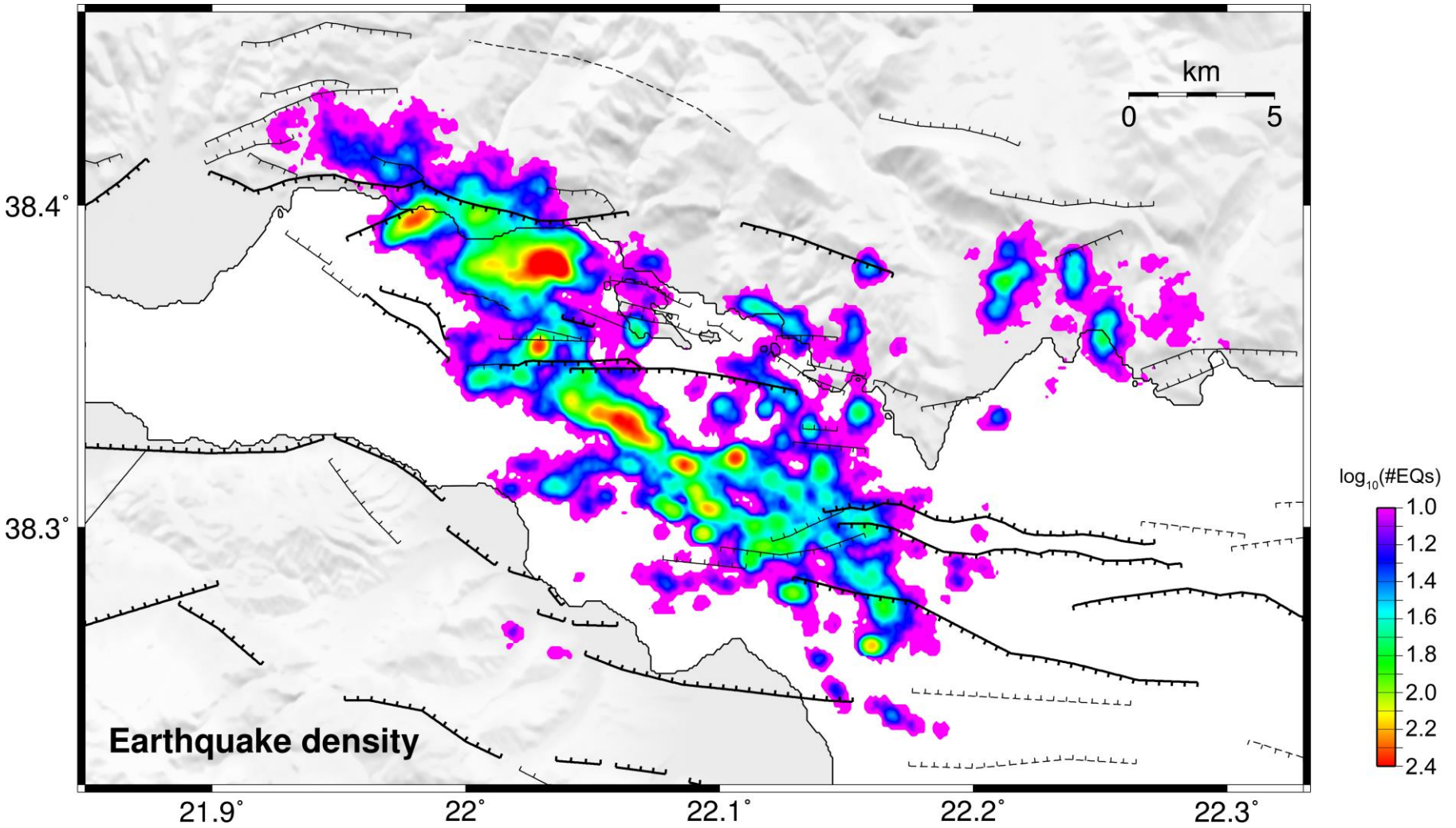

Figure 6B.11: Log_{10} density of earthquakes in a 0.3 km radius for the seismicity of 2000-2007 in the western Corinth Rift.

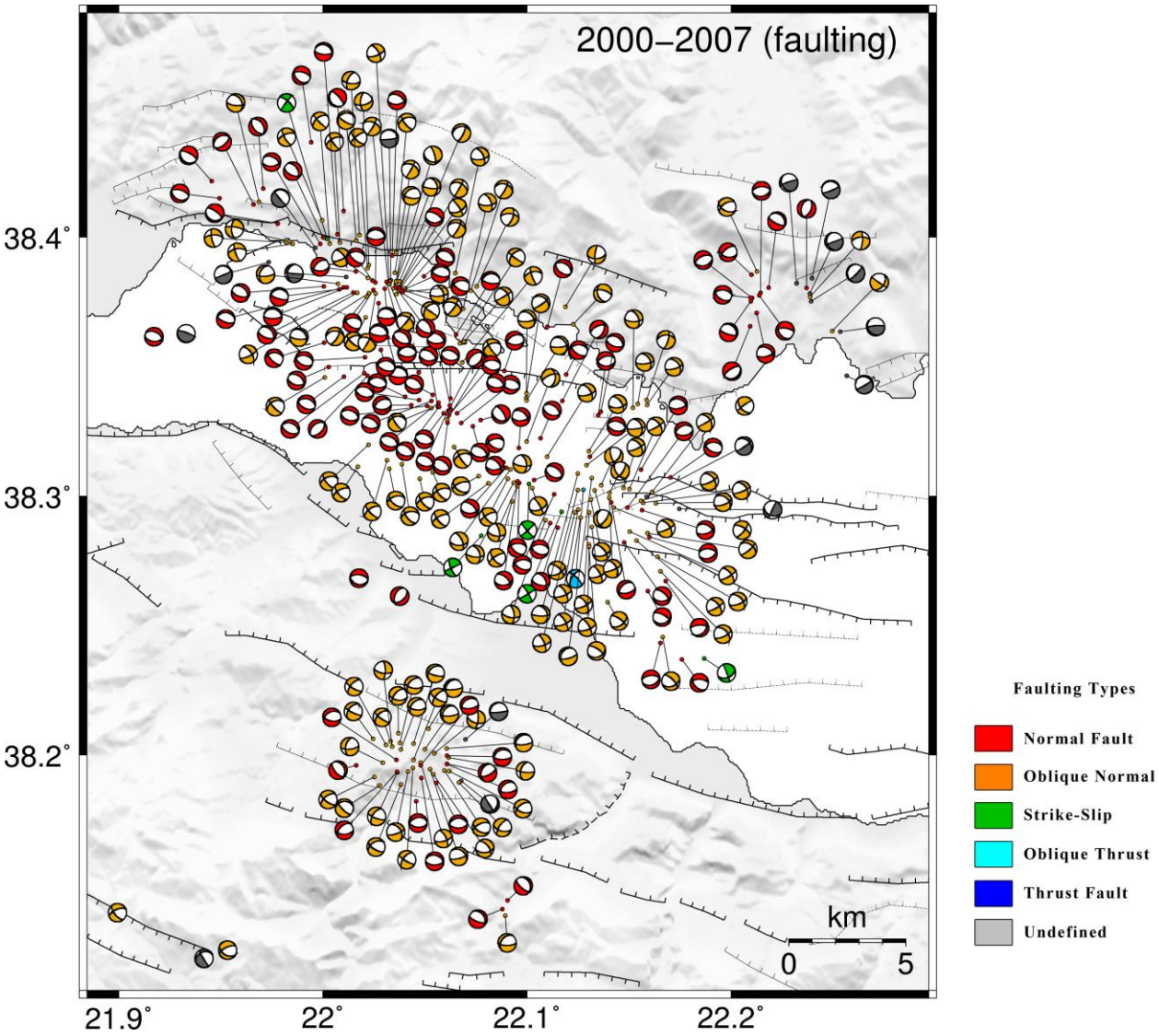

Figure 6B.12: Composite focal mechanisms for multiplets in the western Corinth Rift during 2000-2007 with colours representing faulting type according to the criteria of Zoback (1992) (Table 2.1).

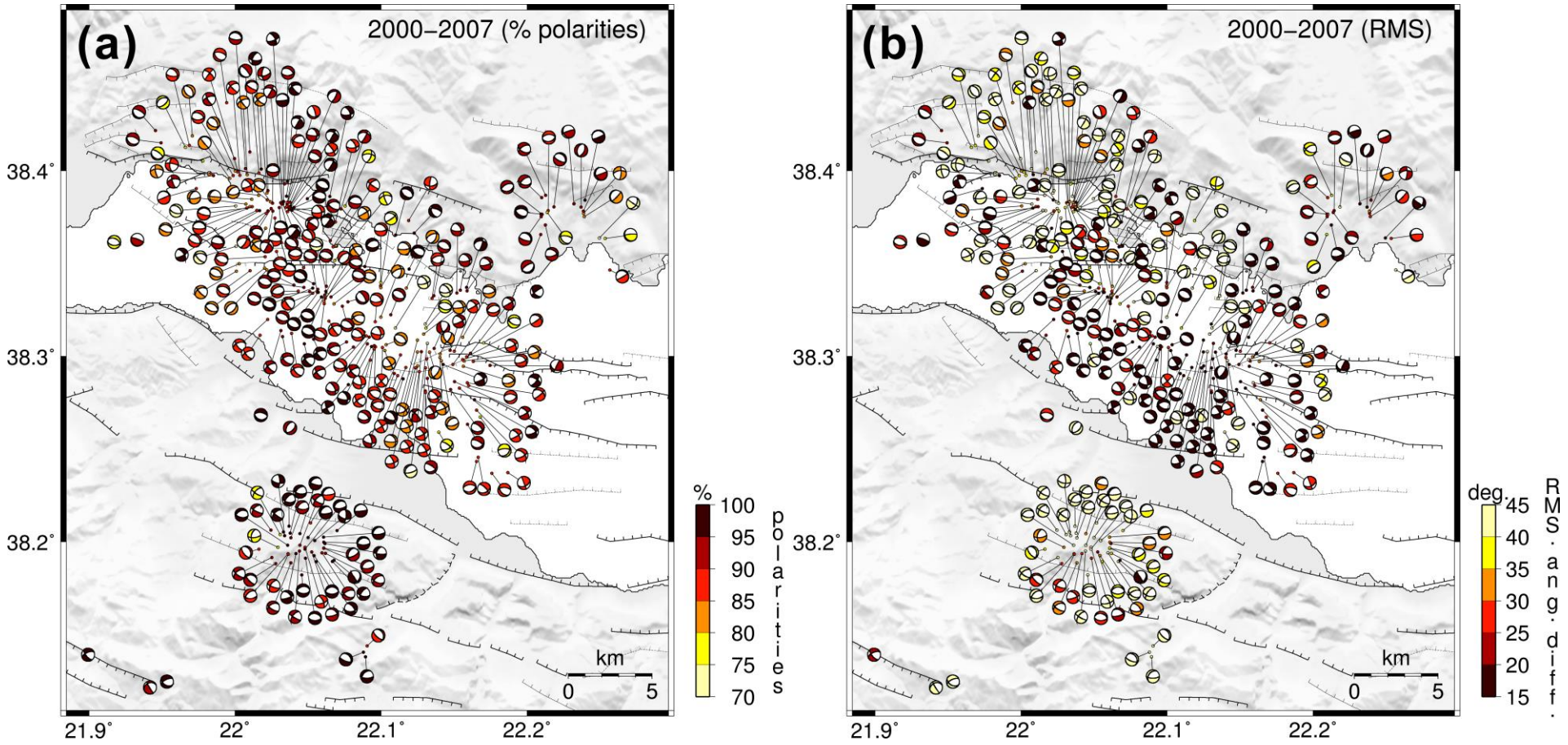

Figure 6B.13: Composite focal mechanisms for multiplets in the western Corinth Rift during 2000-2007 with colours representing a) minimum percentage of first motion polarities satisfied by individual solutions, b) RMS angular difference of individual solutions.

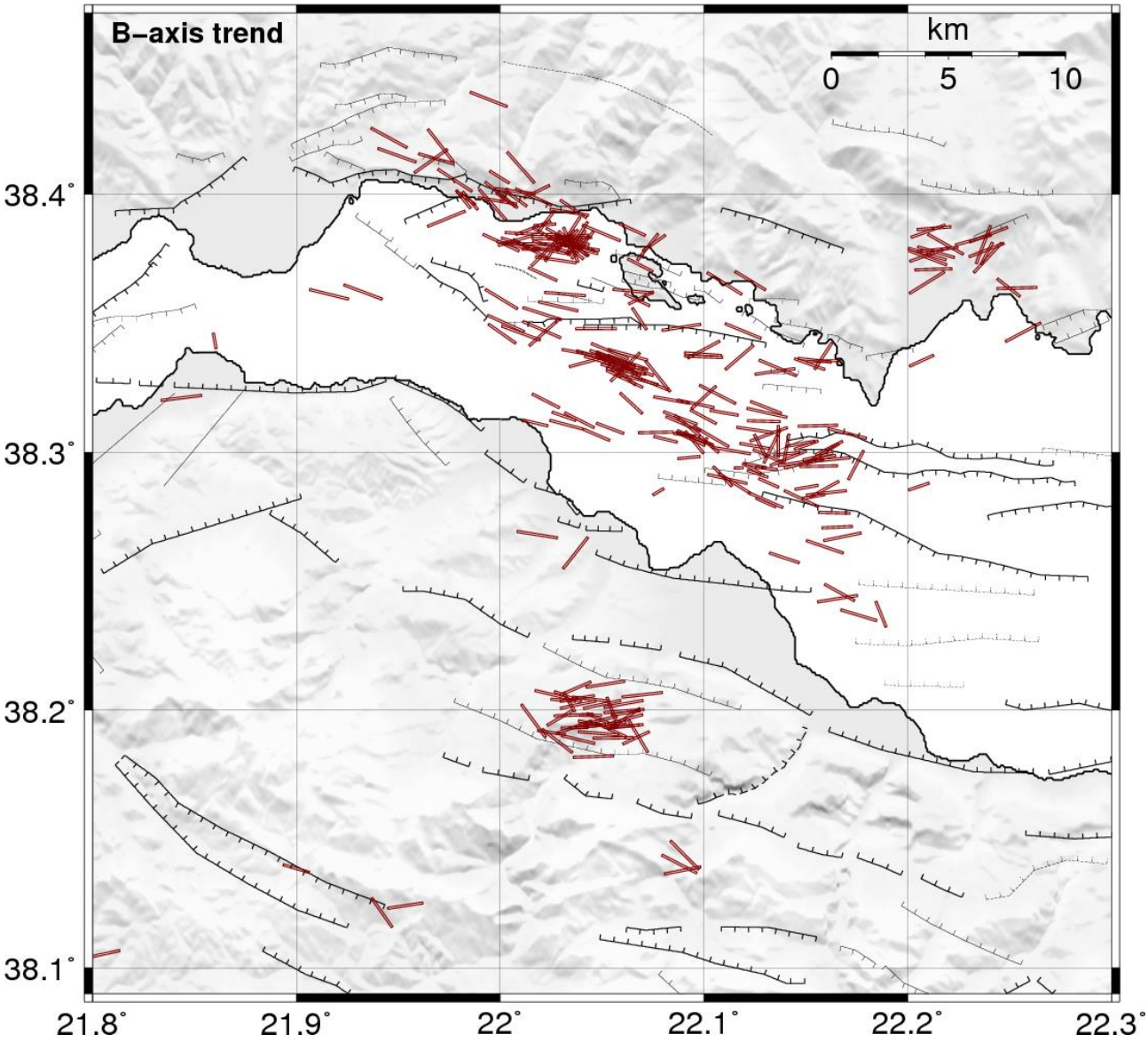

Figure 6B.14: Directions of the composite focal mechanisms' B-axes for multiplets in the western Corinth Rift in 2000-2007. Line length is proportional to $\cos B_{pl}$, where B_{pl} is the B-axis plunge angle.

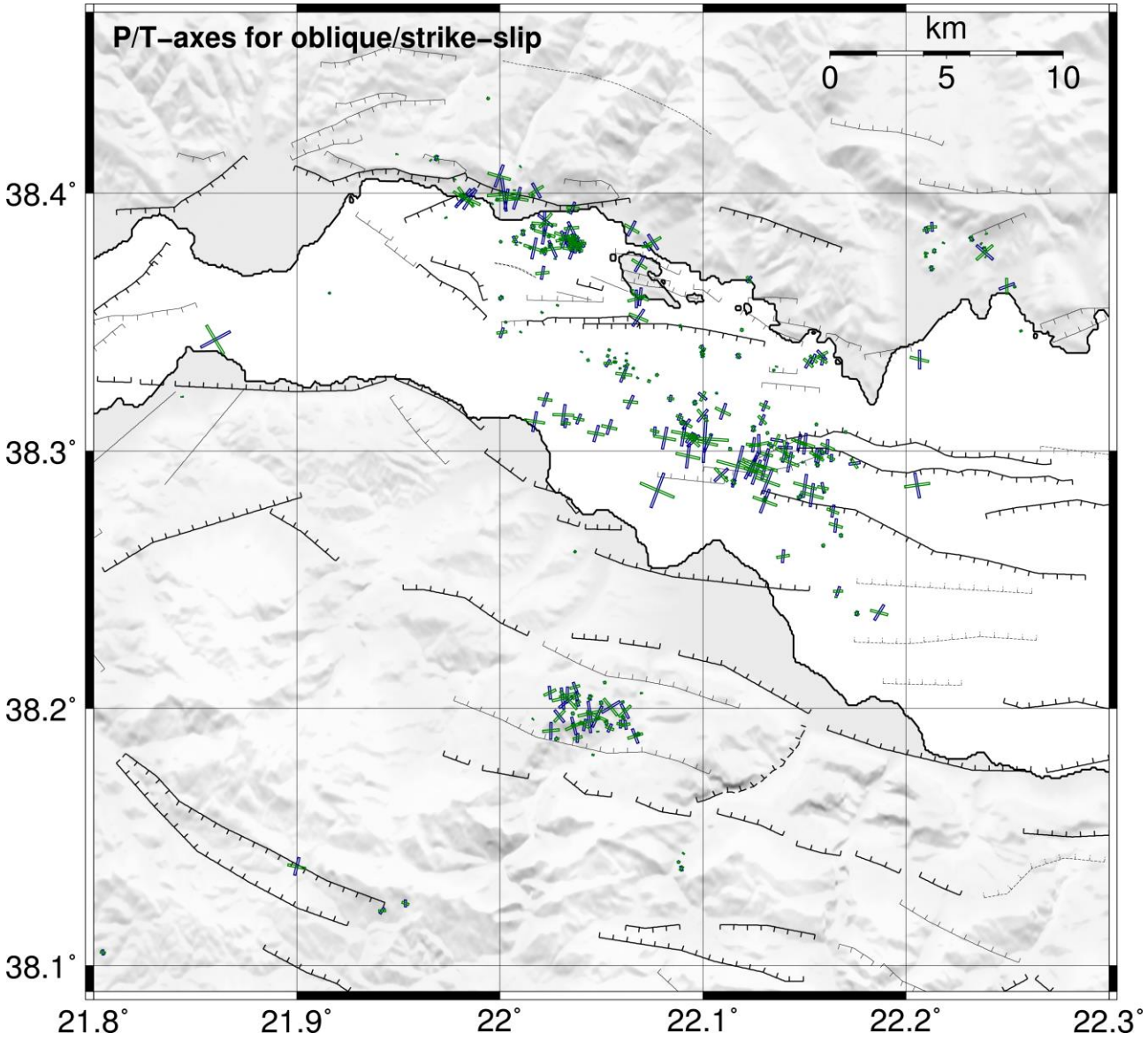

Figure 6B.15: Directions of the composite focal mechanisms' P- (green) and T-axes (blue) for multiplets in the western Corinth Rift in 2000-2007. The length of each pair of lines is proportional to (1-cosB_{pl}), where B_{pl} is the B-axis plunge angle, to emphasize on cases with a significant oblique-slip component.

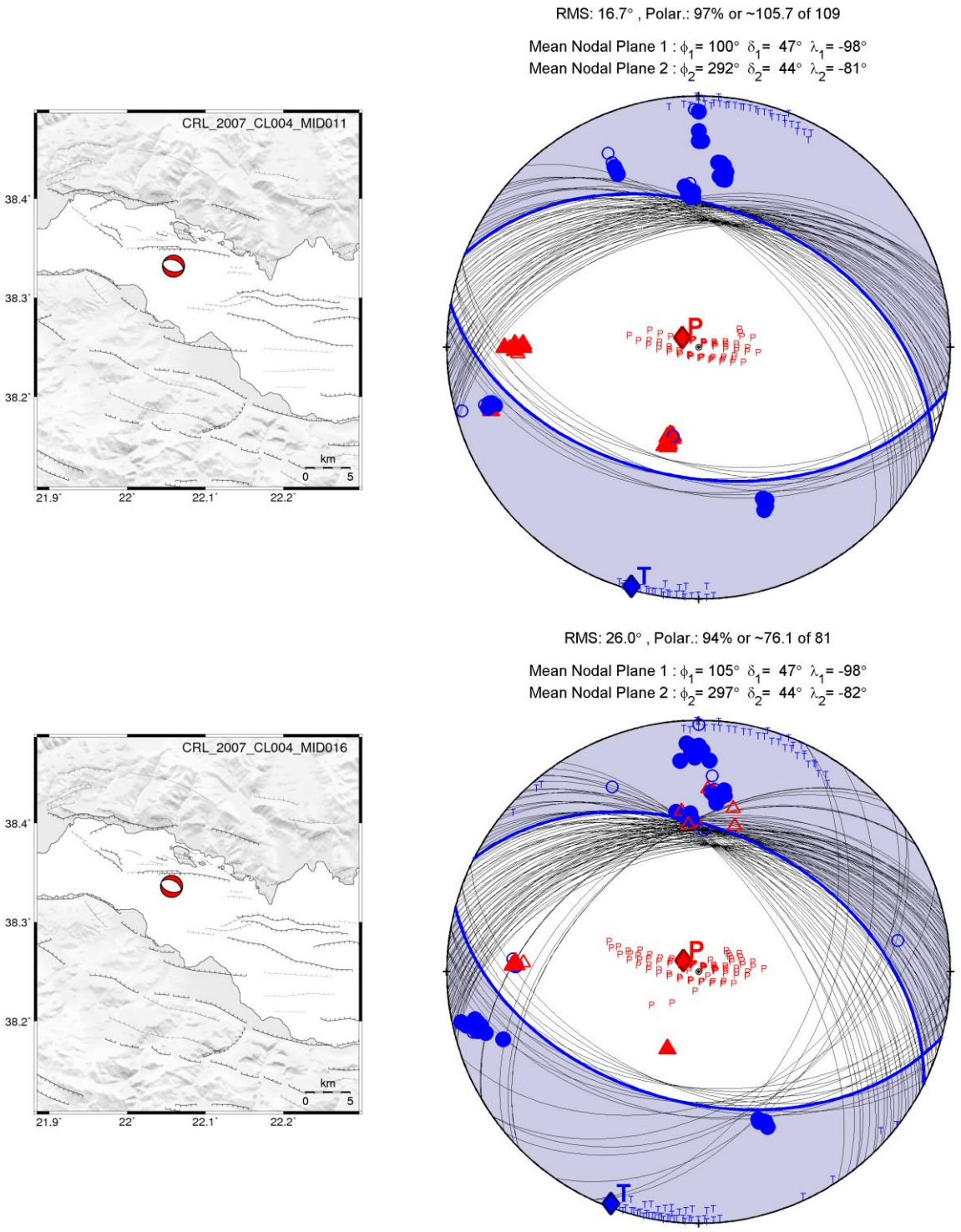

Figure 6B.16: Examples of composite focal mechanisms. Blue circles indicate compressional and red triangles dilatational first motion polarity, open symbols mark uncertain measurements. Thin black arcs are individual (trial) solutions, blue bold arcs are the weighted average solution.

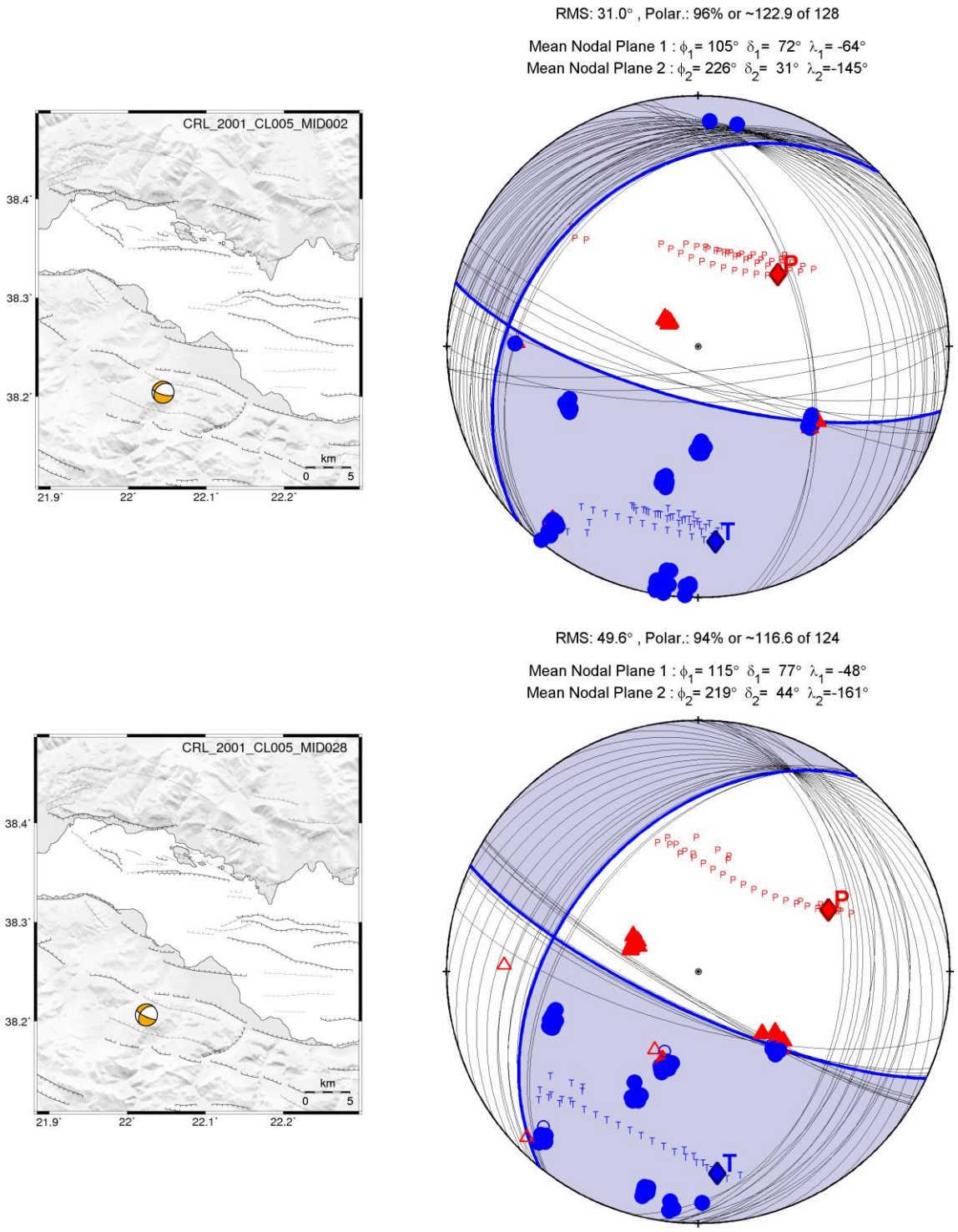

Figure 6B.17: Examples of composite focal mechanisms. Blue circles indicate compressional and red triangles dilatational first motion polarity, open symbols mark uncertain measurements. Thin black arcs are individual (trial) solutions, blue bold arcs are the weighted average solution.

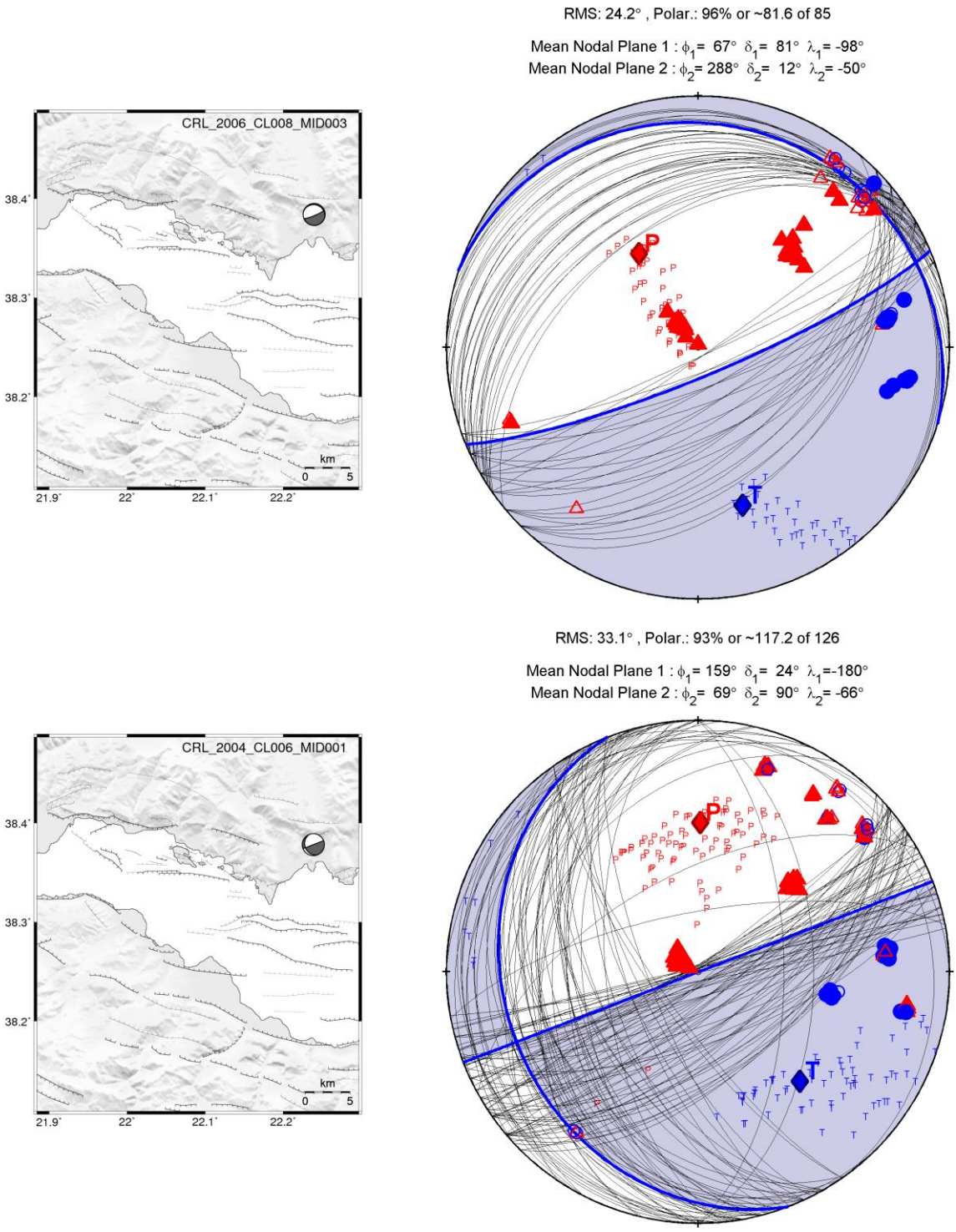

Figure 6B.18: Examples of composite focal mechanisms. Blue circles indicate compressional and red triangles dilatational first motion polarity, open symbols mark uncertain measurements. Thin black arcs are individual (trial) solutions, blue bold arcs are the weighted average solution.

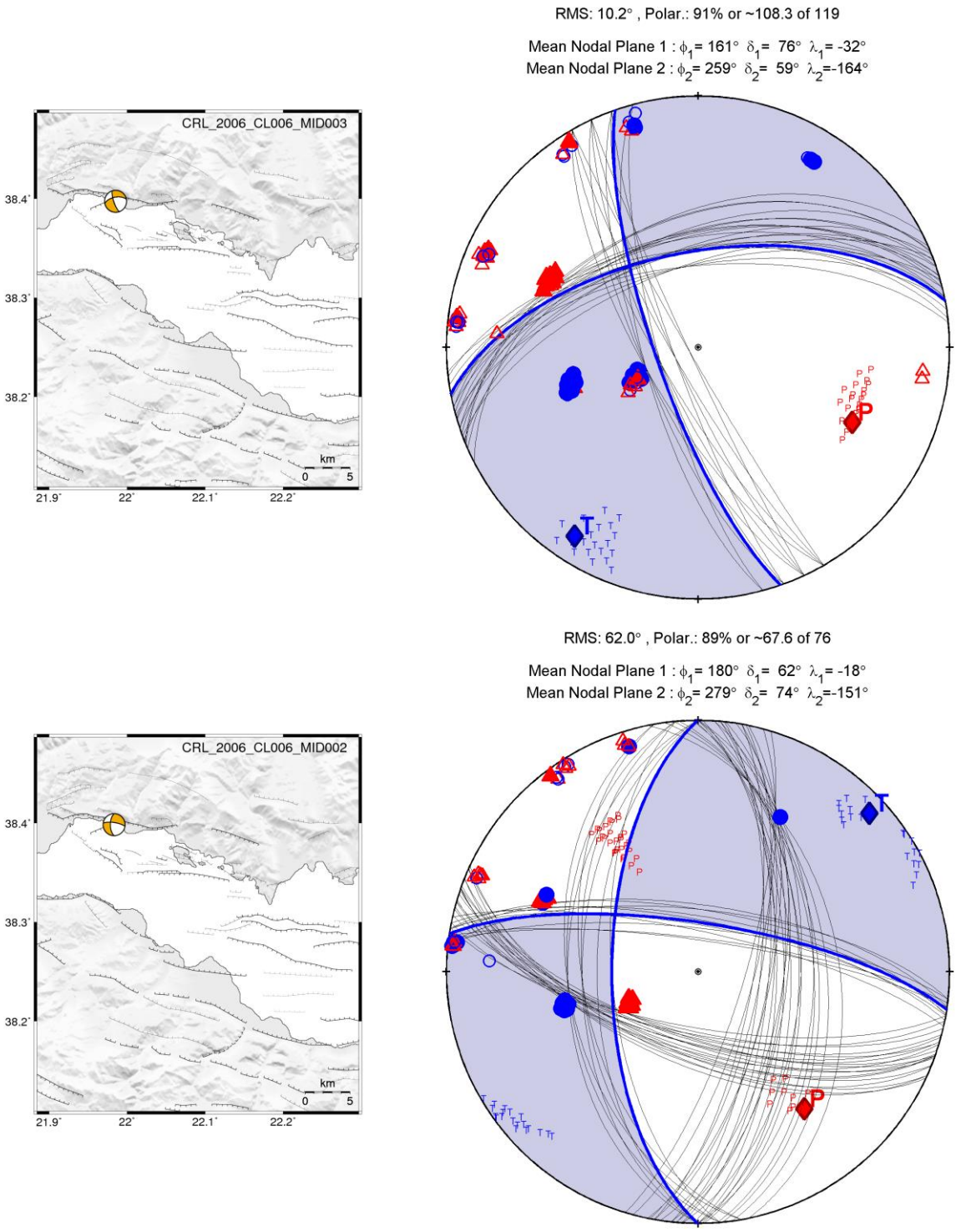

Figure 6B.19: Examples of composite focal mechanisms. Blue circles indicate compressional and red triangles dilatational first motion polarity, open symbols mark uncertain measurements. Thin black arcs are individual (trial) solutions, blue bold arcs are the weighted average solution.

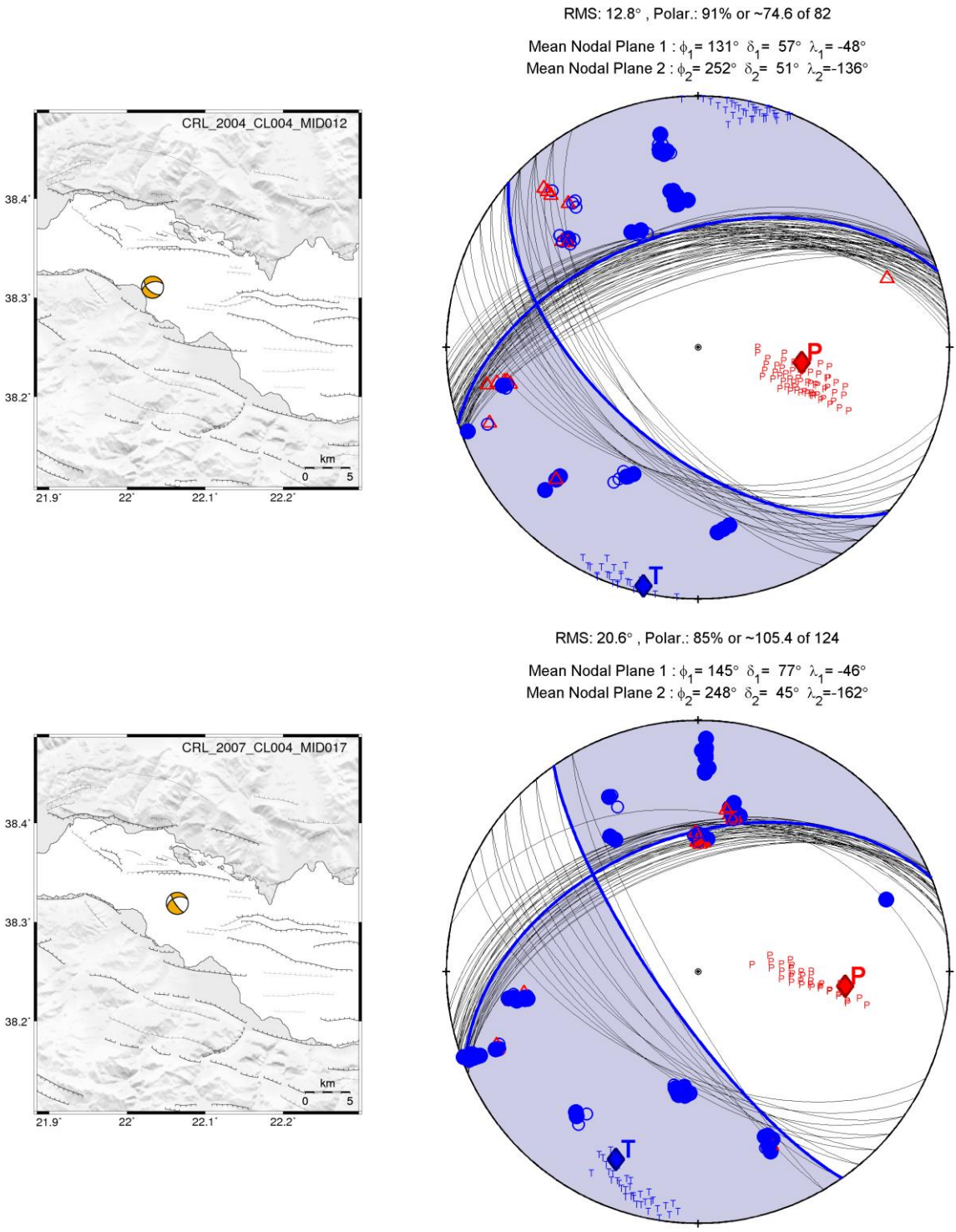

Figure 6B.20: Examples of composite focal mechanisms. Blue circles indicate compressional and red triangles dilatational first motion polarity, open symbols mark uncertain measurements. Thin black arcs are individual (trial) solutions, blue bold arcs are the weighted average solution.

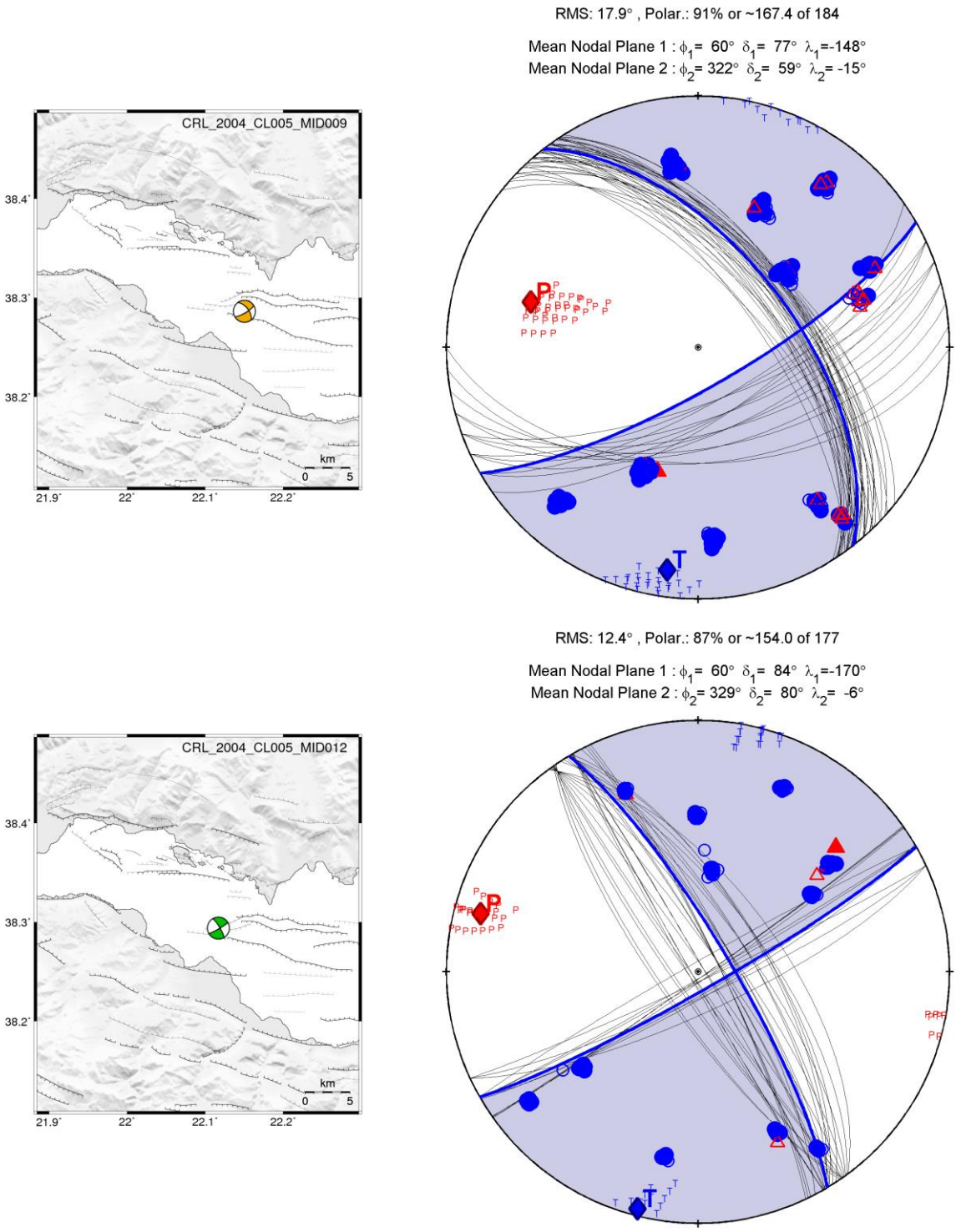

Figure 6B.21: Examples of composite focal mechanisms. Blue circles indicate compressional and red triangles dilatational first motion polarity, open symbols mark uncertain measurements. Thin black arcs are individual (trial) solutions, blue bold arcs are the weighted average solution.

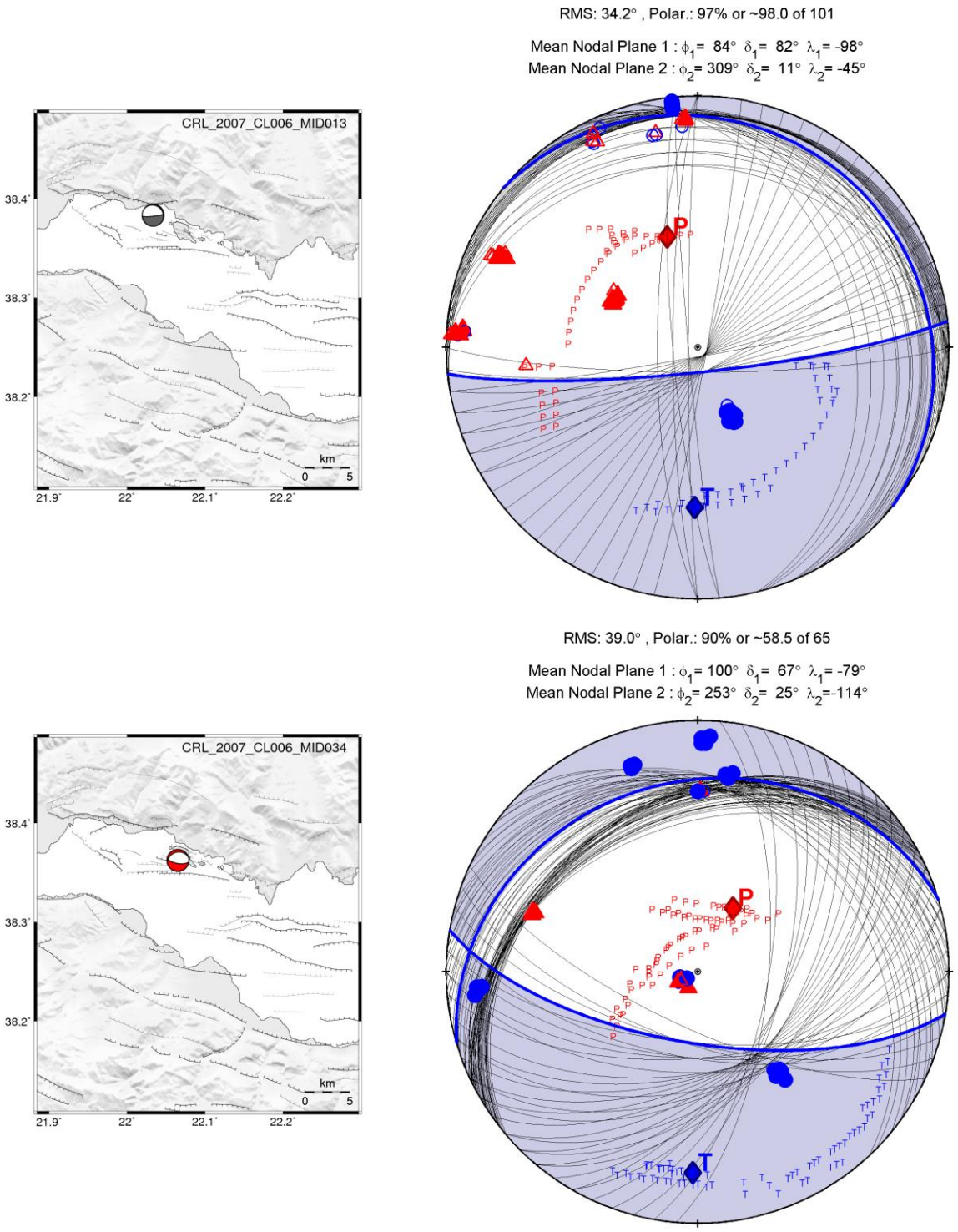

Figure 6B.22: Examples of composite focal mechanisms. Blue circles indicate compressional and red triangles dilatational first motion polarity, open symbols mark uncertain measurements. Thin black arcs are individual (trial) solutions, blue bold arcs are the weighted average solution.

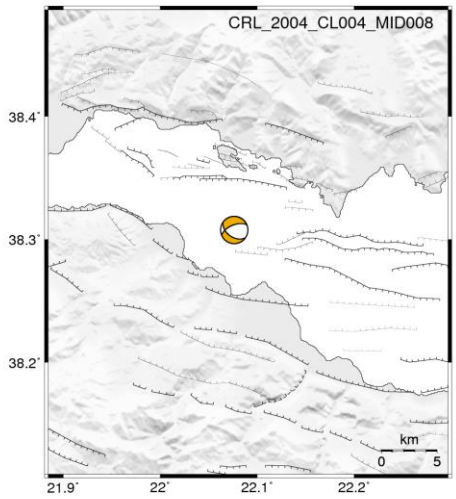

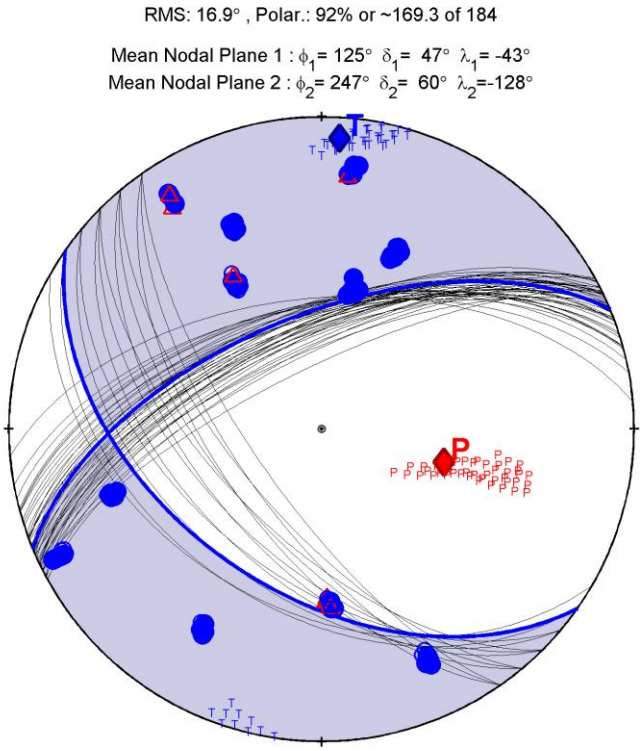

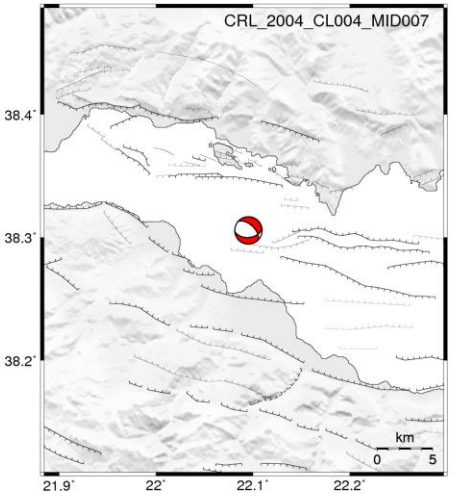

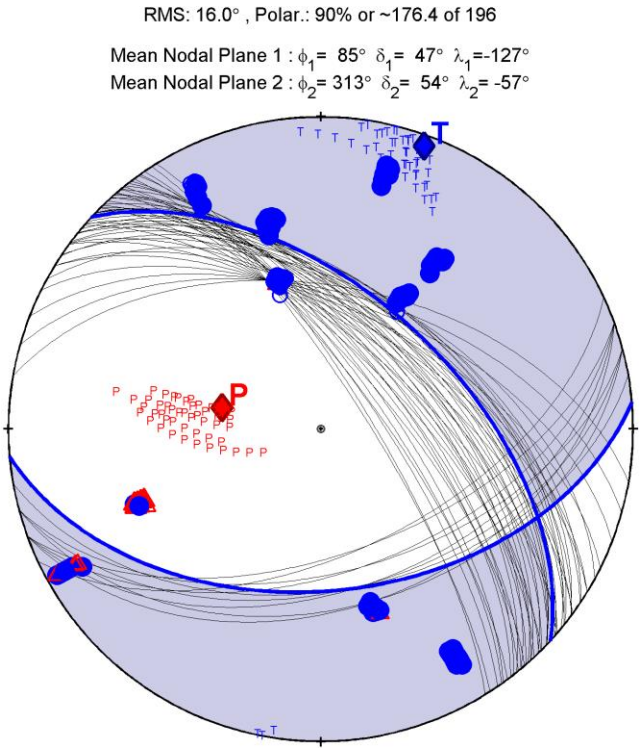

Figure 6B.23: Examples of composite focal mechanisms. Blue circles indicate compressional and red triangles dilatational first motion polarity, open symbols mark uncertain measurements. Thin black arcs are individual (trial) solutions, blue bold arcs are the weighted average solution. The upper panel is an example similar/comparable to that of Fig. 6.45.

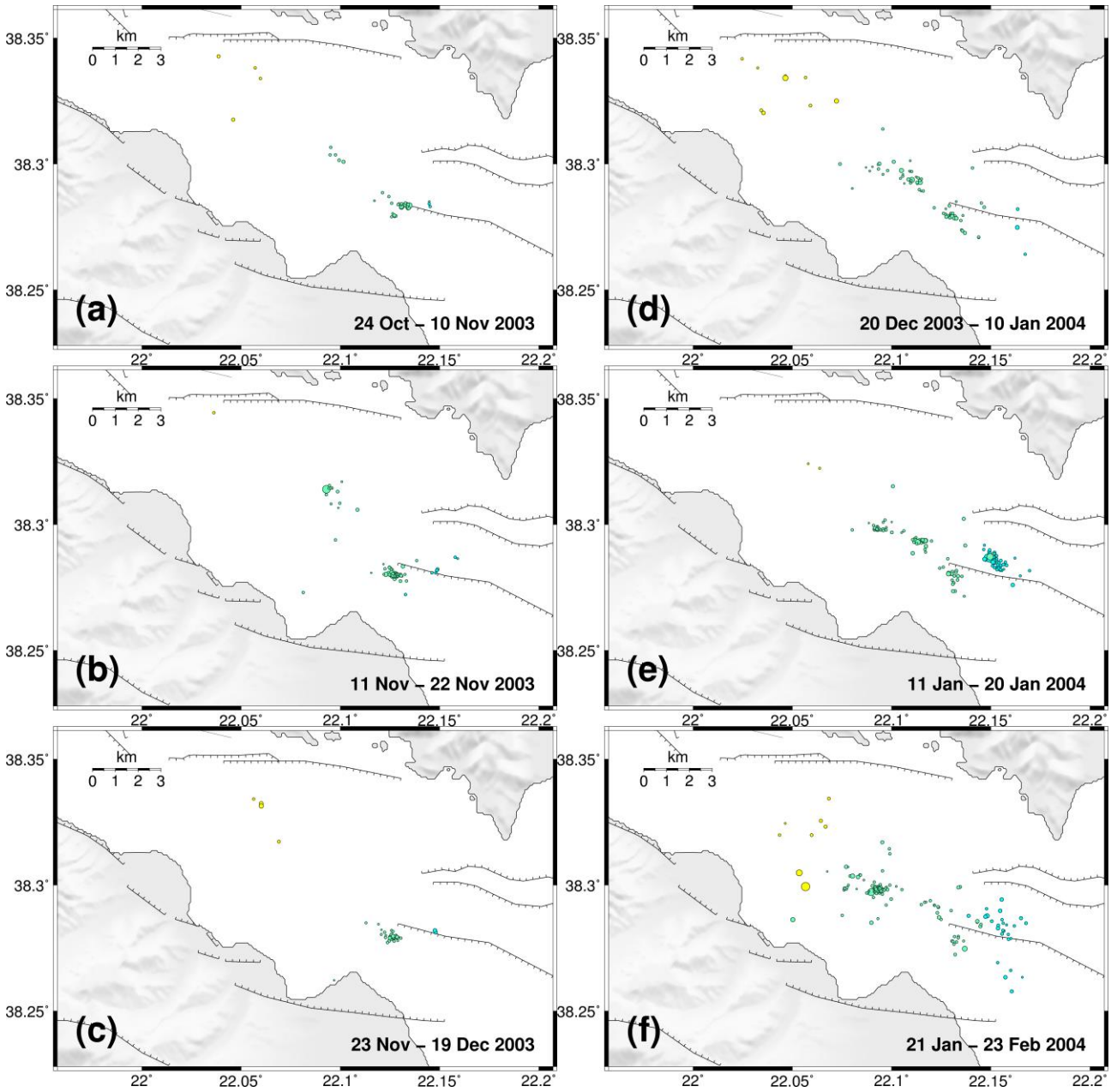

Figure 6B.24: Maps of relocated seismicity for 14 consecutive periods during the 2003-2004 swarm sequence in the western Corinth Rift.

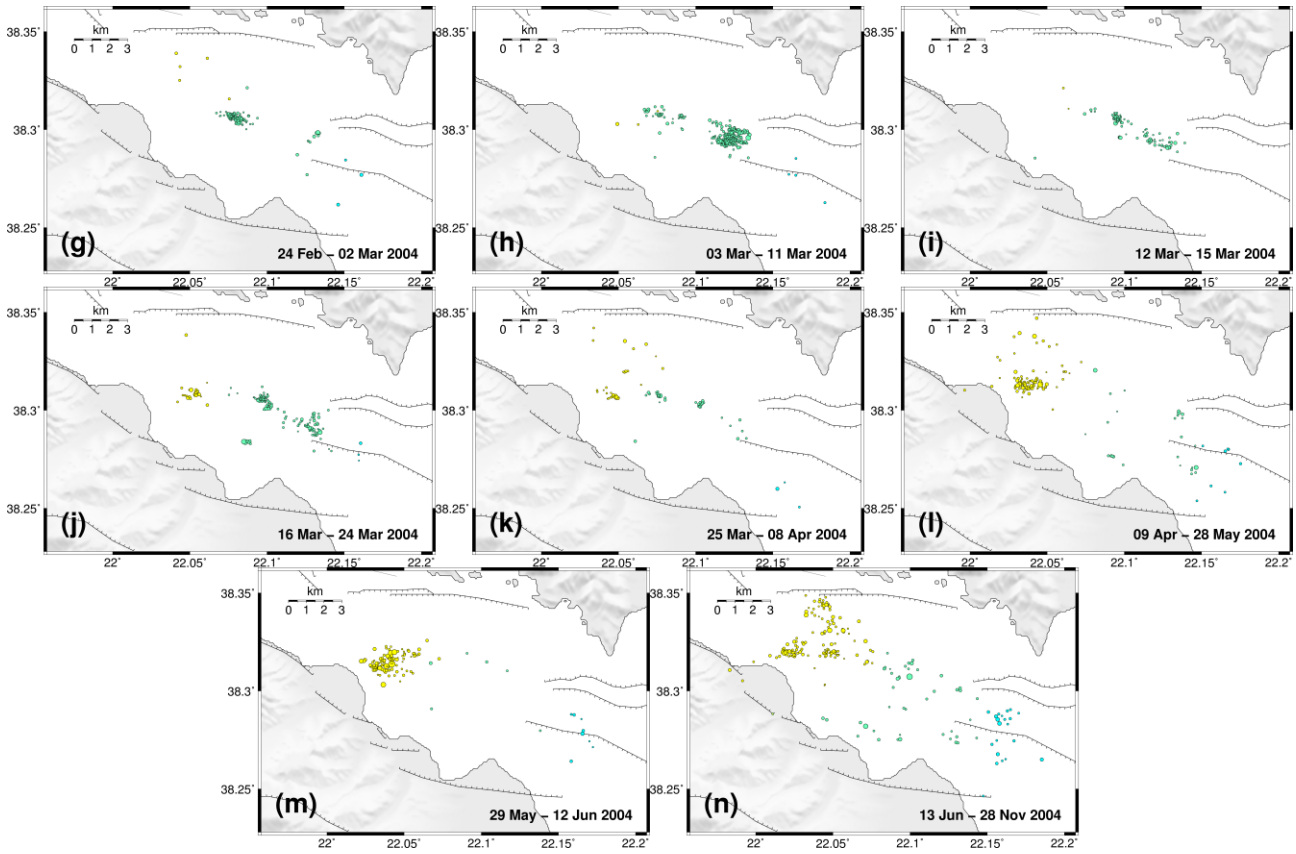

Figure 6B.24: (continued).

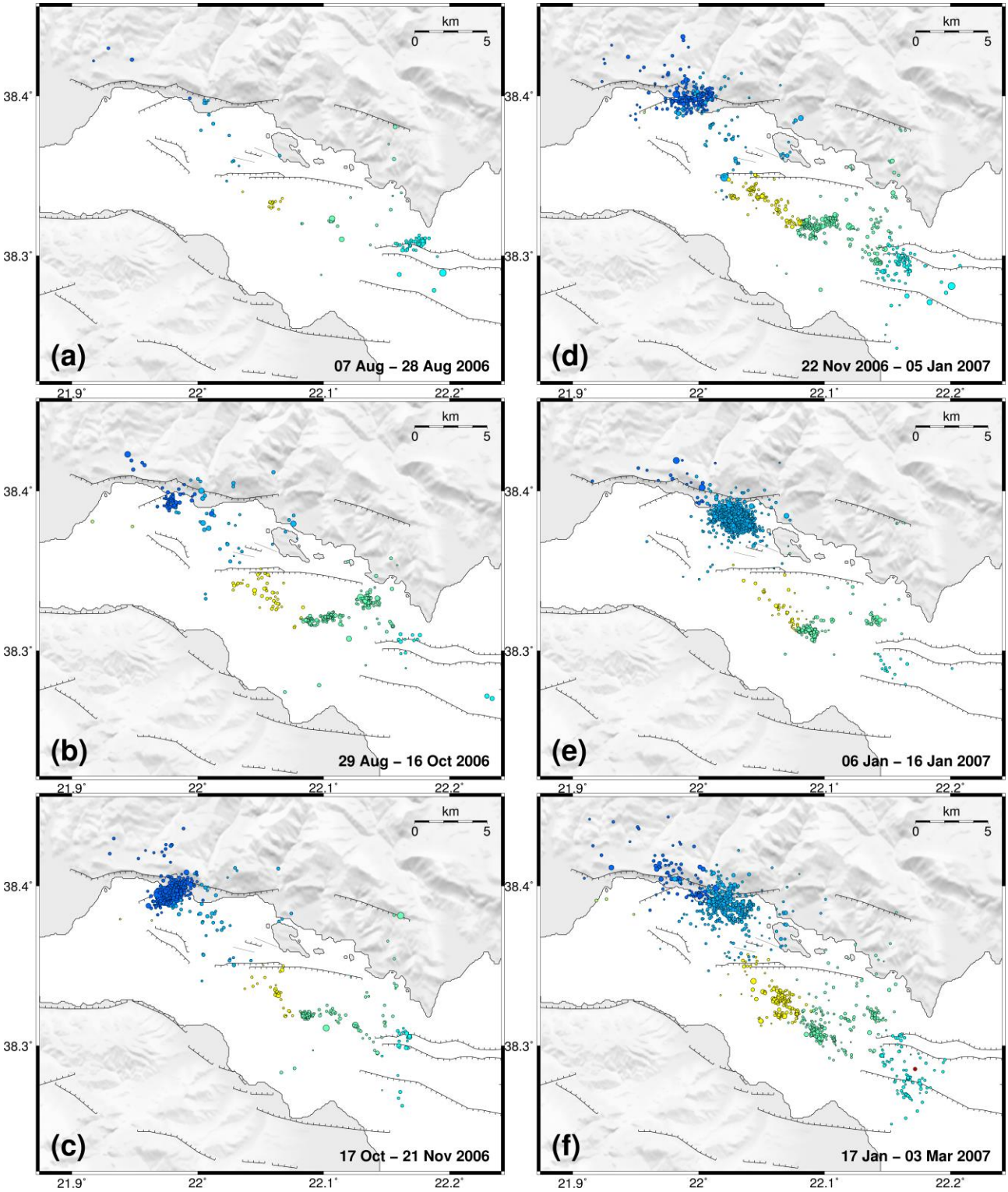

Figure 6B.25: Maps of relocated seismicity for 14 consecutive periods during the 2006-2007 sequence in the western Corinth Rift.

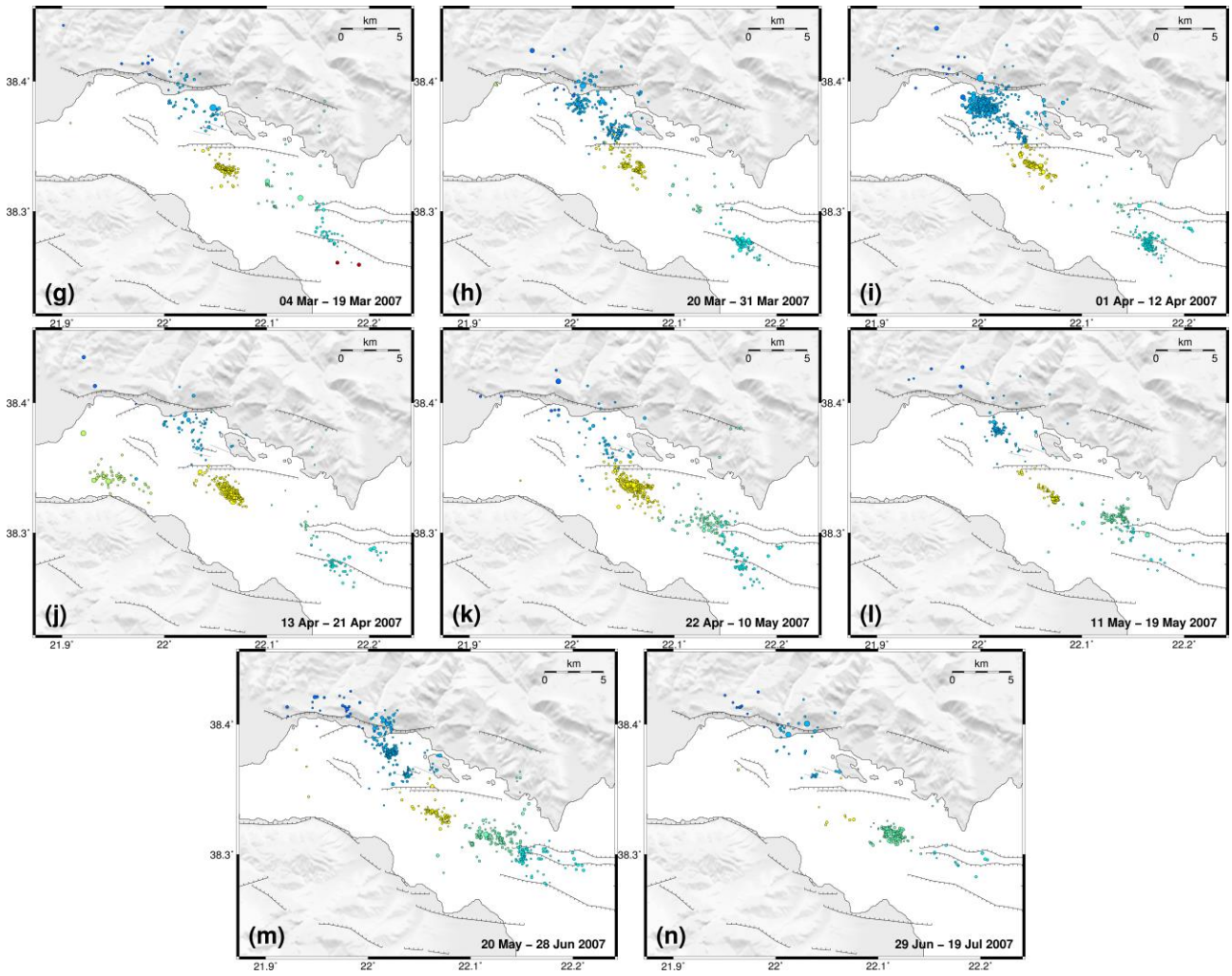

Figure 6B.25: (continued).

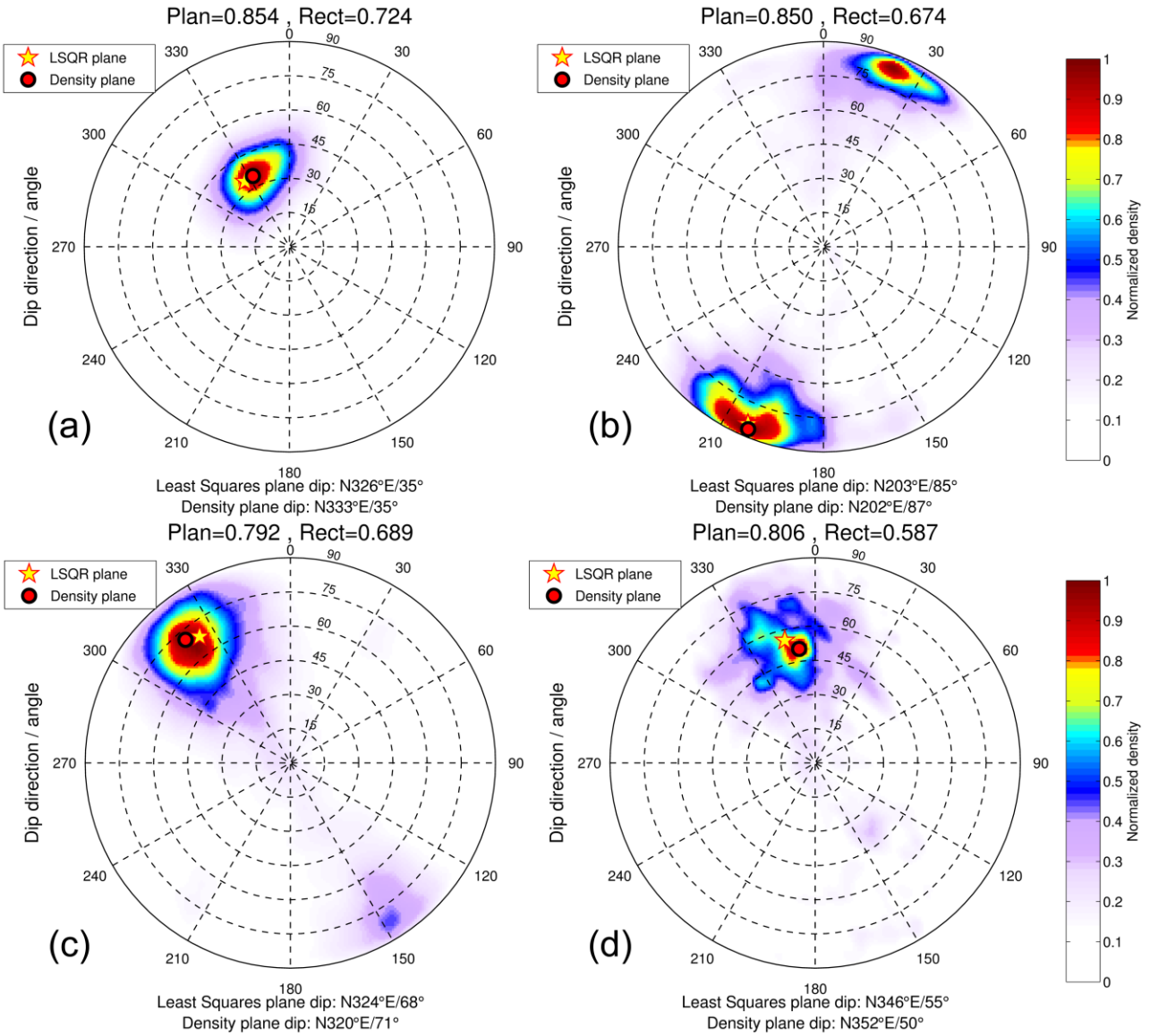

Figure 6B.26: Plane geometry for spatially clustered events in the western Corinth Rift, a) for the 2001 swarm in Ayios Ioannis, b) for the mid-gulf cluster in the period between 25 February and 3 March 2004 (period "g" of the 2003-2004 swarm, near source "3" of Fig. 6.29), c) for the cluster near Marathias fault between 19 and 23 October 2006 and d) for the cluster in the same region between 23 and 24 November 2006. The colours represent dip direction and dip angle derived using the "Three Point" method of Fehler *et al.* (1987). The direction and dip angle at the point of maximum density is marked with a circle. The respective direction and dip of the least squares plane is depicted with a star. Planarity and Rectilinearity values are also presented at the top of the polar diagram.

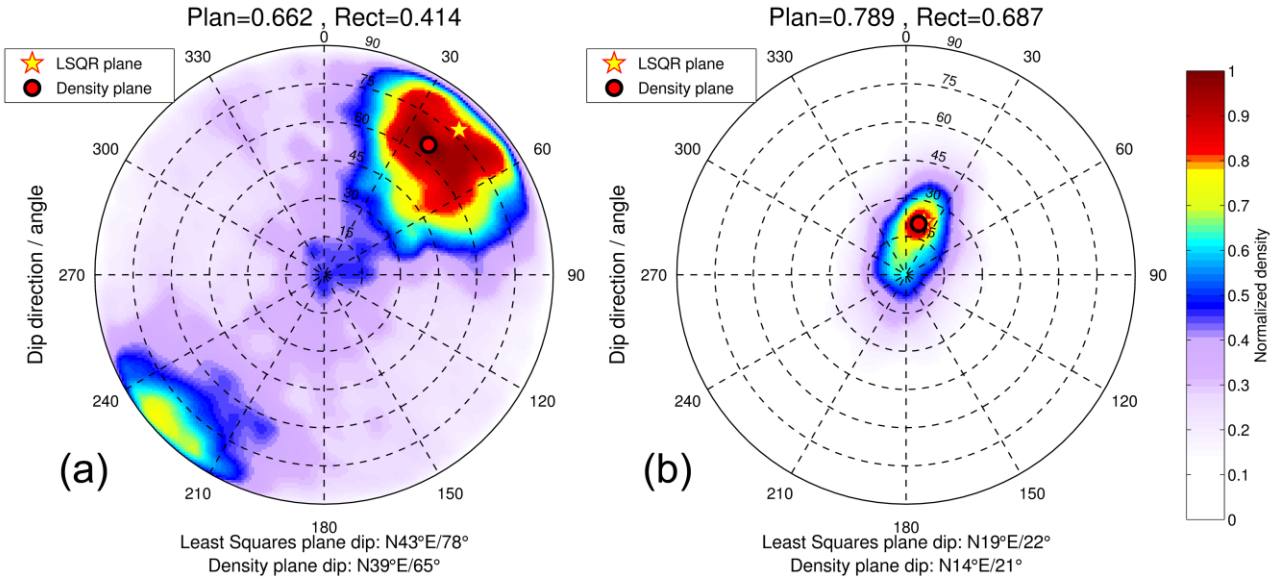

Figure 6B.27: Same as in Fig. 6B.26 a) for the cluster west of Trizonia Island between 13 and 14 January 2007 and b) for Group #9 (Eratini).

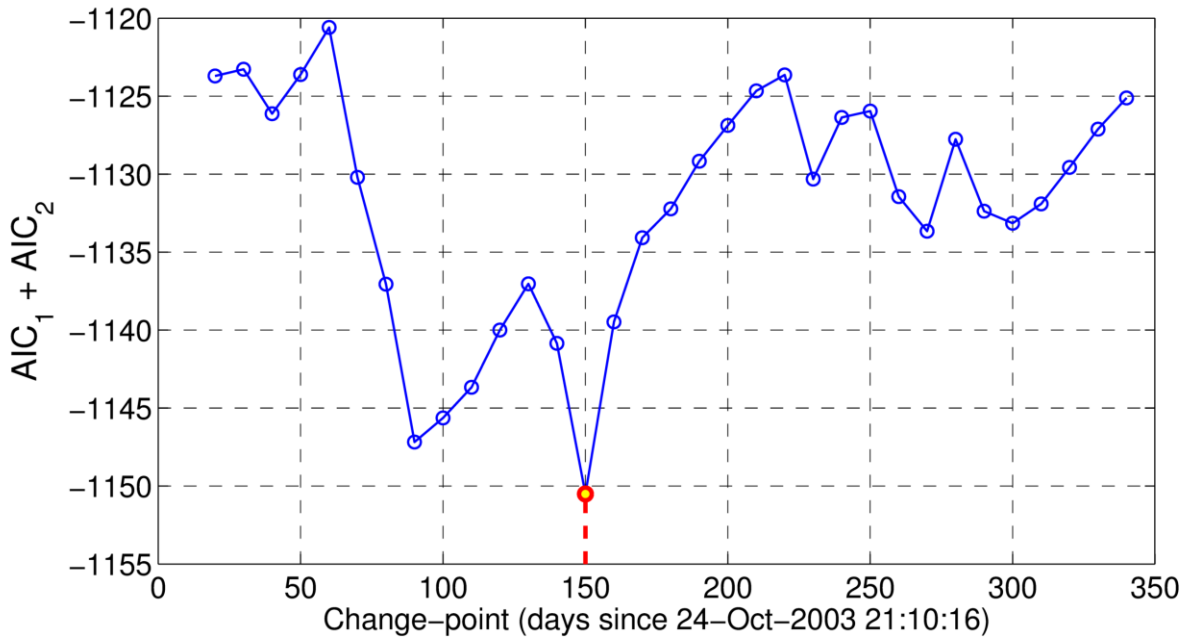

Figure 6B.28: Change point analysis for the 2-stage ETAS model of the 2003-2004 sequence (Fig. 6.42).

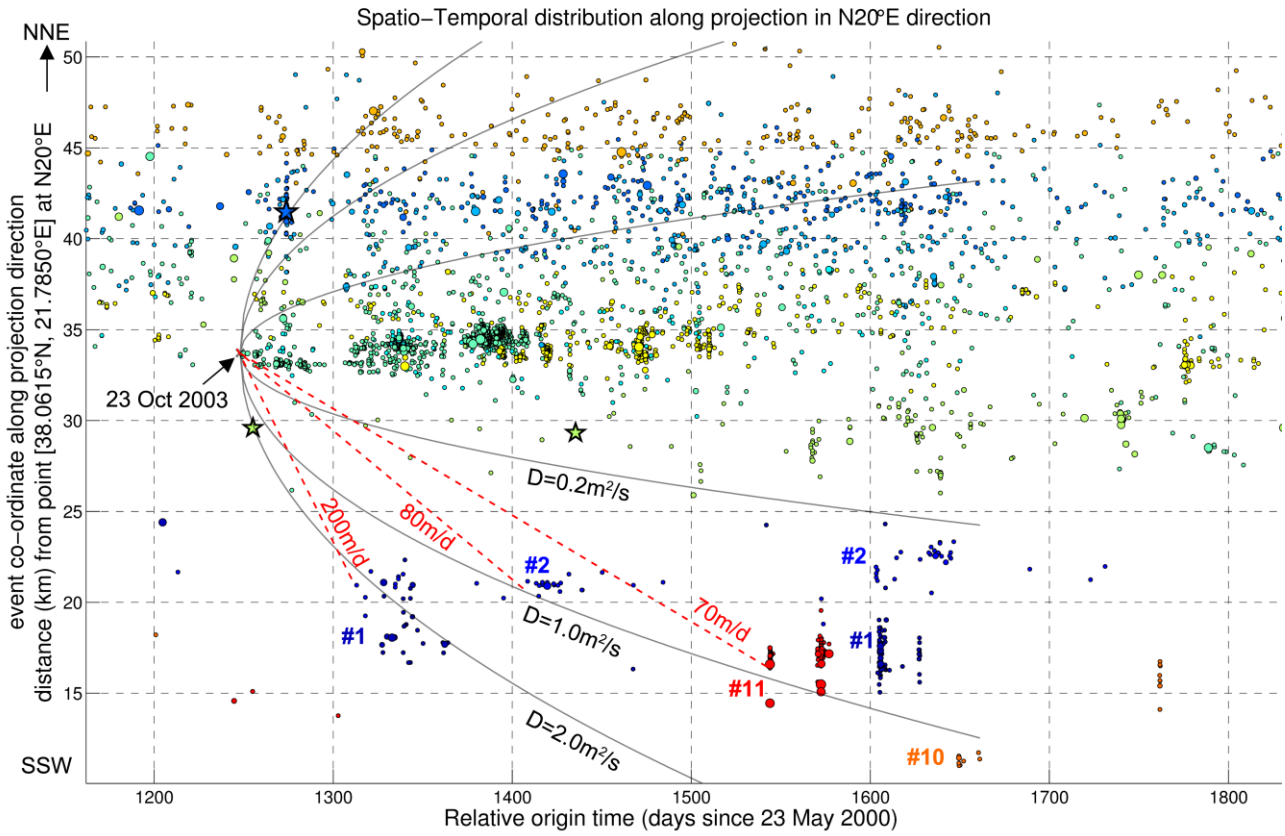

Figure 6B.29: Large-scale spatiotemporal projection along a N20°E direction for the seismicity in the western Corinth Rift between 1 Aug 2003 and 27 May 2005. Parabolic curves correspond to triggering fronts for different values of hydraulic diffusivity, *D*. Red dashed lines indicate migration rates. Clusters marked with # correspond to the respective spatial group (Fig. 6.10).

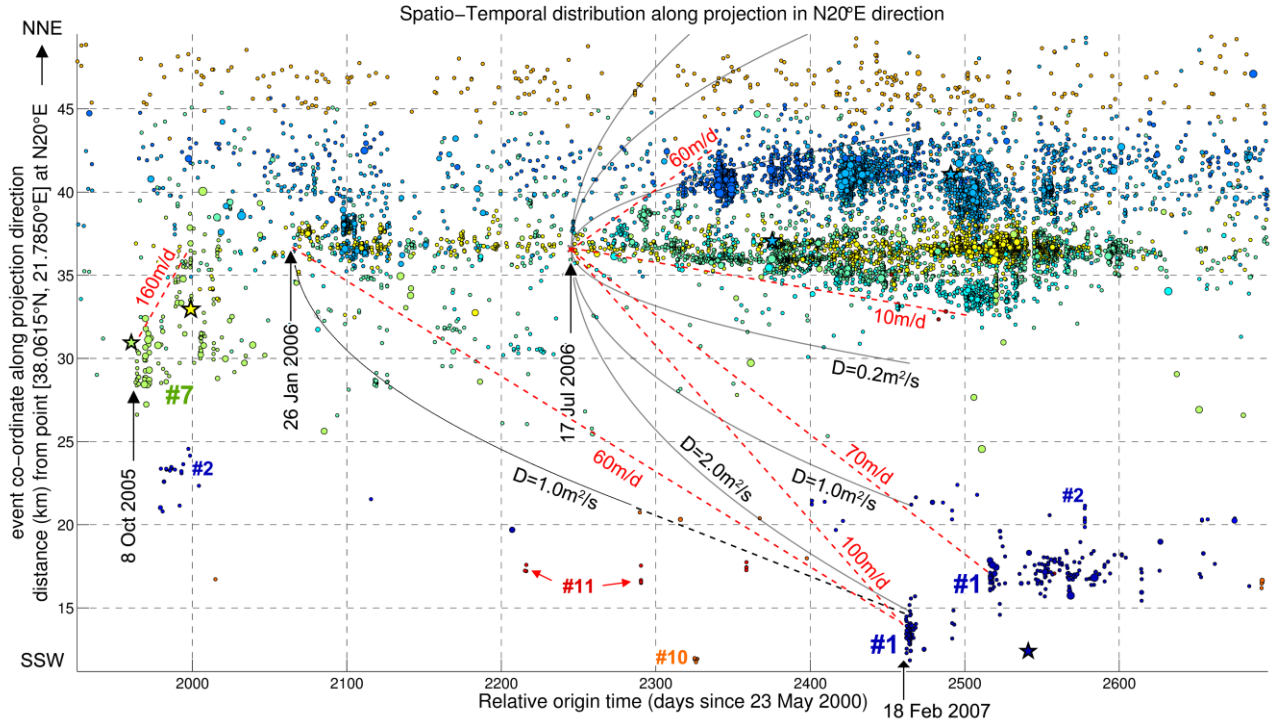

Figure 6B.30: Large-scale spatiotemporal projection along a N20°E direction for the seismicity in the western Corinth Rift between 31 Aug 2005 and 11 Oct 2007. Parabolic curves correspond to triggering fronts for different values of hydraulic diffusivity, *D*. Red dashed lines indicate migration rates. Clusters marked with # correspond to the respective spatial group (Fig. 6.10).

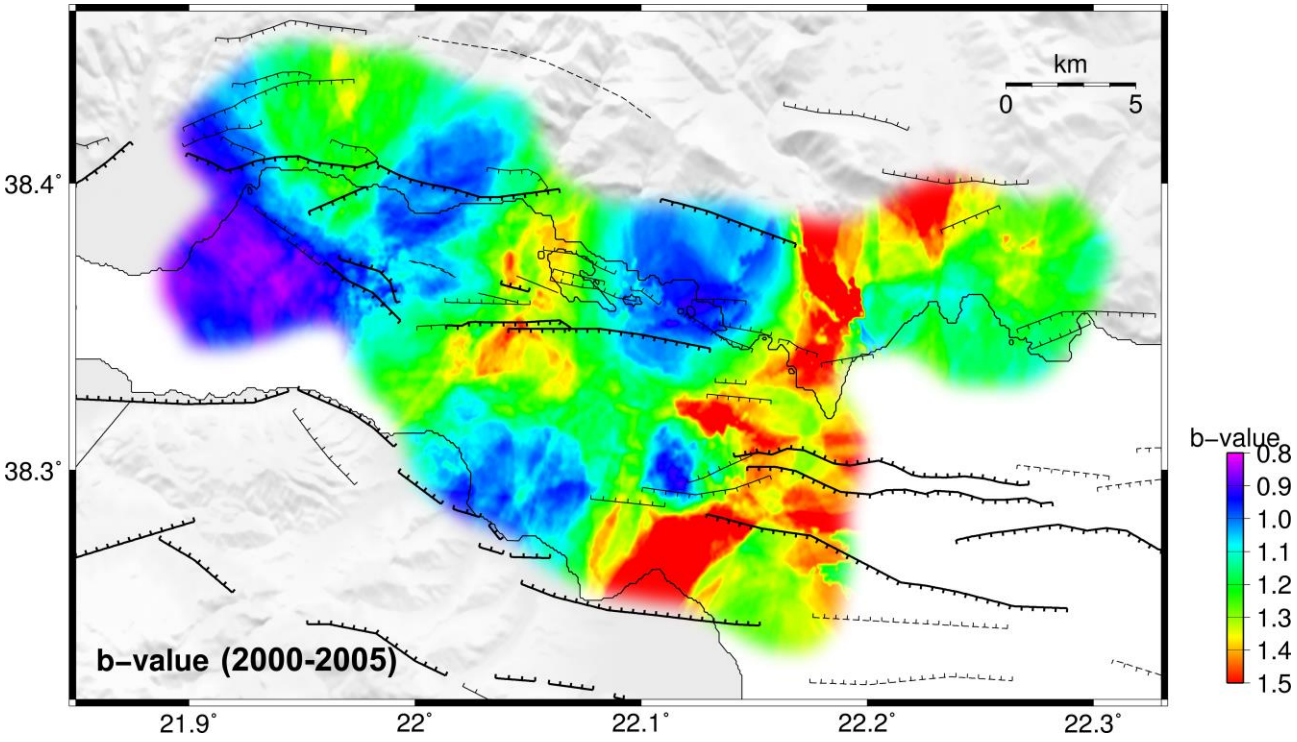

Figure 6B.31: Spatial distribution of the *b*-value in the western Corinth Rift for the seismicity of 2000-2005. The values were calculated on a grid with ~0.1km spacing in volumes defined by vertical cylinders of variable radius, each containing 400 events. The results were masked in regions with available seismicity within a radius of ~3km. The M_c values were calculated using the maximum curvature method.

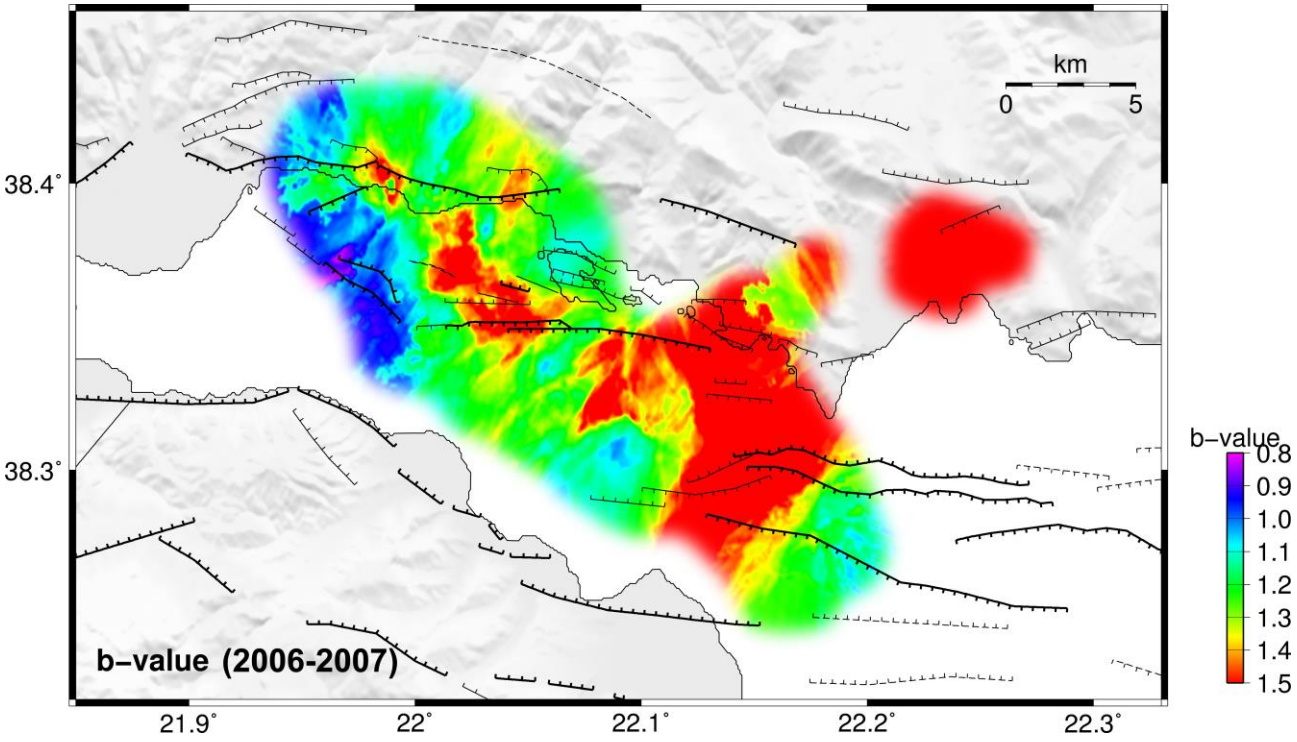

Figure 6B.32: Spatial distribution of the *b*-value in the western Corinth Rift for the seismicity of 2006-2007. The values were calculated on a grid with ~0.1km spacing in volumes defined by vertical cylinders of variable radius, each containing 400 events. The results were masked in regions with available seismicity within a radius of ~3km. The M_c values were calculated using the maximum curvature method.

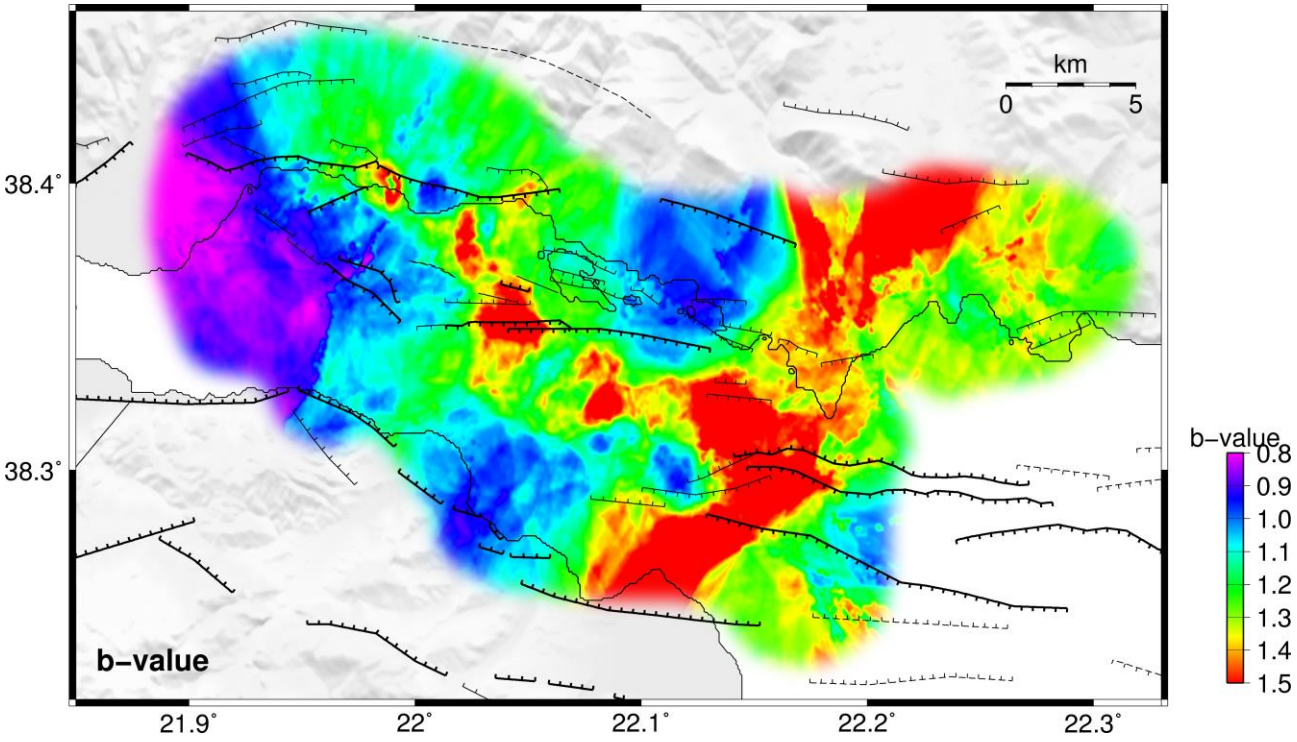

Figure 6B.33: Spatial distribution of the *b*-value in the western Corinth Rift for the seismicity of 2000-2007. The values were calculated on a grid with ~0.1km spacing in volumes defined by vertical cylinders of variable radius, each containing 400 events. The results were masked in regions with available seismicity within a radius of ~3km. The M_c values were calculated using the maximum curvature method. The result is directly comparable with that of Fig. 6.15 where the b-value was calculated in cylinders with a constant radius of 3km.

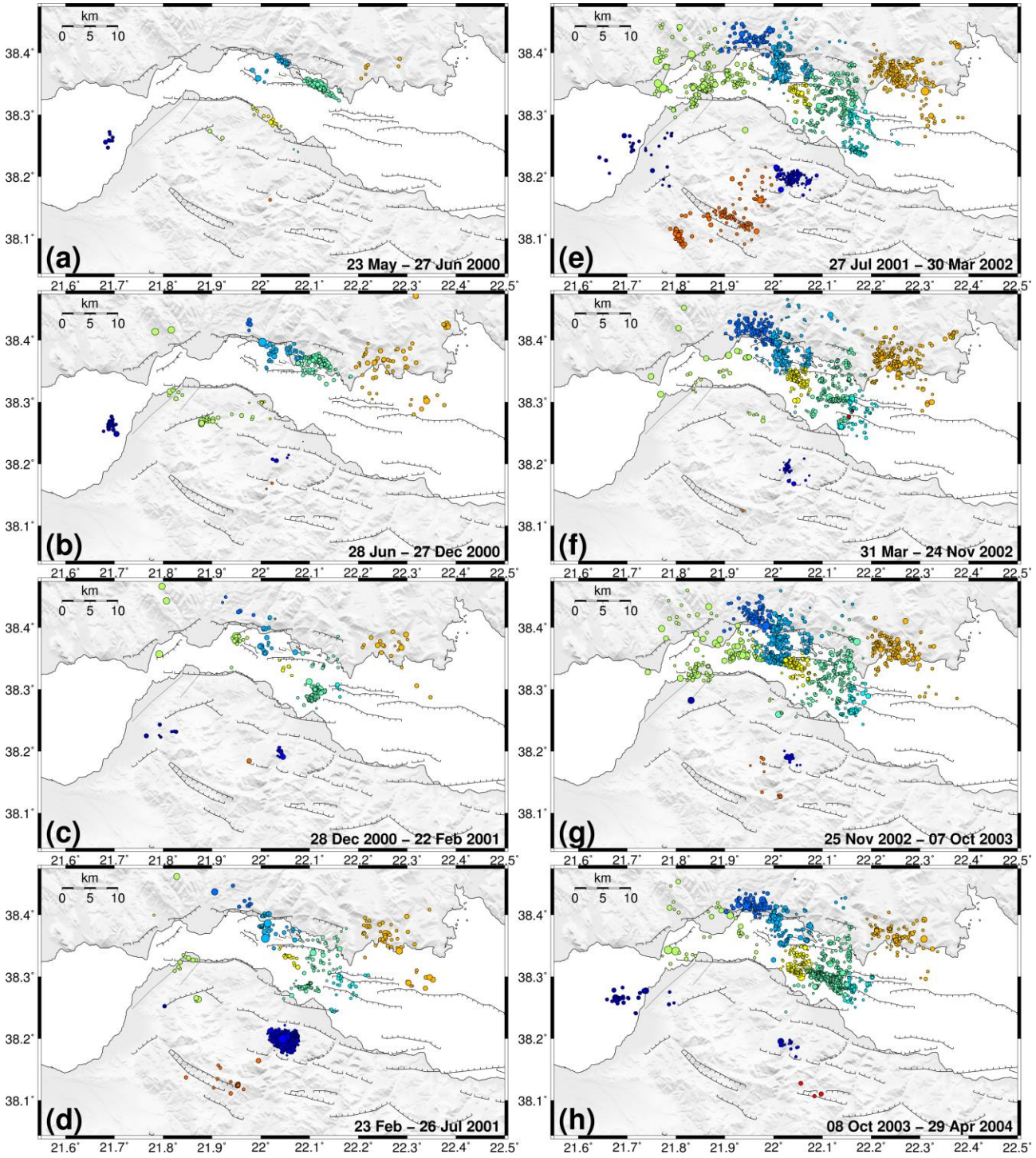

Figure 6B.34: Maps of relocated seismicity for 19 consecutive periods during 2000-2007 in the western Corinth Rift (see Fig. 6.21).

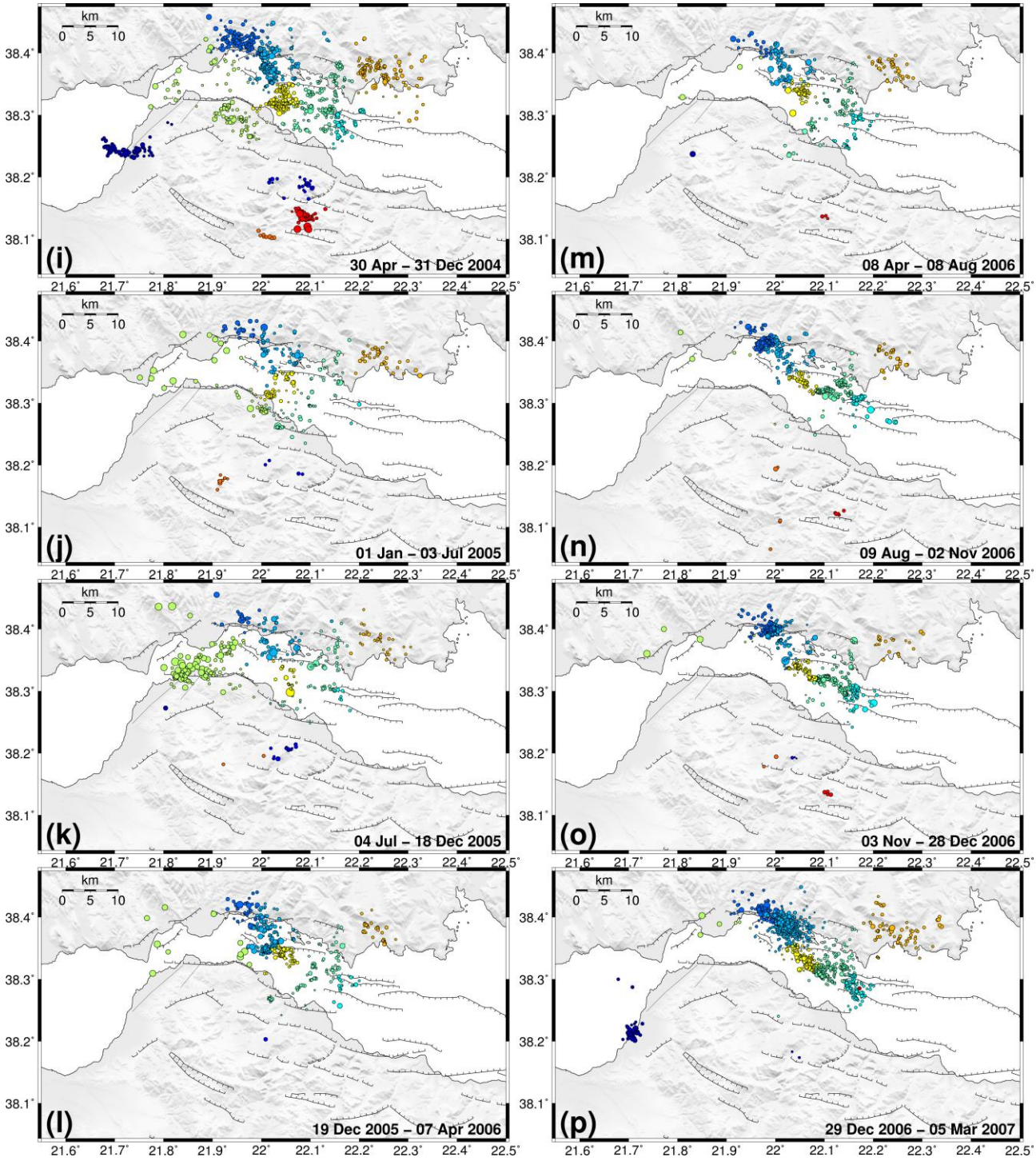

Figure 6B.34: (continued)

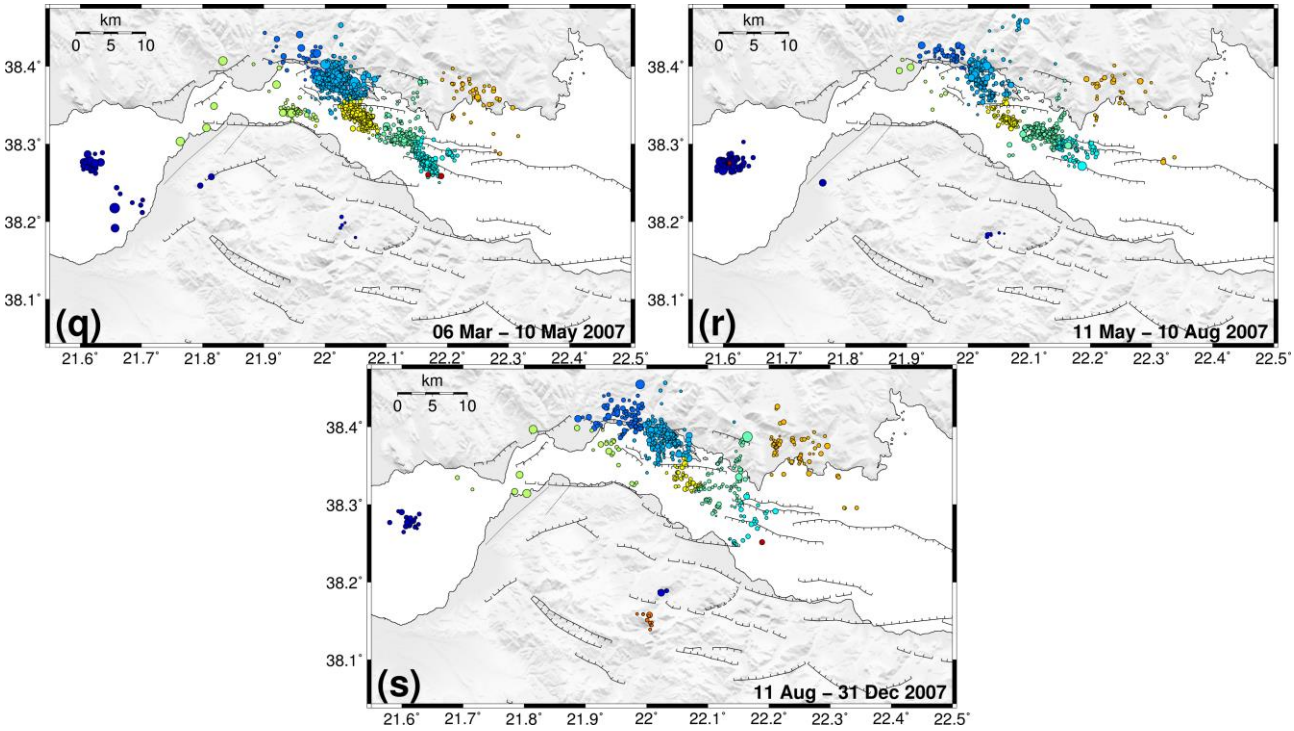

Figure 6B.34: (continued)